

Lawrence Berkeley National Laboratory

Lawrence Berkeley National Laboratory

Title

Proceedings of the TOUGH Symposium 2009

Permalink

<https://escholarship.org/uc/item/1zf1b81h>

Author

Moridis, George J.

Publication Date

2009-10-15

Peer reviewed



Proceedings of the TOUGH Symposium 2009

September 14—16, 2009

Lawrence Berkeley National Laboratory
Berkeley, California

Editors

George Moridis, Christine Doughty, Stefan Finsterle, and
Eric Sonnenthal

*Lawrence Berkeley National Laboratory
Earth Sciences Division
1 Cyclotron Road, Mail Stop 90-1116
Berkeley, CA 94720*

This work was supported by the U.S. Department of Energy under Contract No. DE-AC02-05CH11231.



Foreword

Welcome to the TOUGH Symposium 2009. Within this volume are the Symposium Program for eighty-nine papers to be presented in both oral and poster formats. The full papers are available as pdfs linked from the Symposium Program posted on the TOUGH Symposium 2009 website

<http://esd.lbl.gov/newsandevents/events/toughsymposium09/program.html>

Additional updated information including any changes to the Program will also be available at the website.

The papers cover a wide range of application areas and reflect the continuing trend toward increased sophistication of the TOUGH codes. A CD containing the proceedings papers will be published immediately following the Symposium and sent to all participants. As in the prior Symposium, selected papers will be invited for submission to a number of journals for inclusion in Special Issues focused on applications and developments of the TOUGH codes. These journals include, *Transport in Porous Media*, *Geothermics*, *Energy Conversion and Management*, *Journal of Nuclear Science and Technology*, and the *Vadose Zone Journal*.

The Organizing Committee wishes to thank in advance the session chairs, presenters, key note speakers, and participants for their ongoing interest in the TOUGH codes. The support from various agencies and offices in the U.S. and around the world for the development and application of the TOUGH codes is greatly appreciated. We also are grateful to Tecplot, Inc., Thunderhead Engineering, and RockWare, Inc. for financial support of the Poster Session, Symposium Banquet, and lunchtime presentations.

George Moridis
Christine Doughty
Eric Sonnenthal
Carol Valladao

Berkeley, September 14, 2009

CONTENTS (BY CATEGORY)

CARBON DIAGENESIS AND GAS HYDRATES	3
CO₂ STORAGE	36
ENVIRONMENTAL ENGINEERING	187
GENERAL	277
GEOHERMAL	348
NUCLEAR WASTE	399
NUMERICAL METHODS	550

CARBONATE DIAGENESIS & GAS HYDRATES

LARGE-SCALE SIMULATION OF OCEANIC GAS HYDRATE DISSOCIATION IN RESPONSE TO CLIMATE CHANGE

Matthew T. Reagan, George J. Moridis, and Keni Zhang

Lawrence Berkeley National Laboratory
1 Cyclotron Rd.
Berkeley, CA 94720 USA
e-mail: MTRegan@lbl.gov

ABSTRACT

Vast quantities of methane are trapped in oceanic hydrate deposits, and there is concern that a rise in the ocean temperature will induce dissociation of these hydrate accumulations, potentially releasing large amounts of carbon into the atmosphere. Because methane is a powerful greenhouse gas, such a release could have dramatic climatic consequences. The recent discovery of active methane gas venting along the landward limit of the gas hydrate stability zone (GHSZ) on the shallow continental slope west of Svalbard suggests that this process may already have begun, but the source of the methane has not been determined. This study performs a 2D simulation of hydrate dissociation in conditions representative of the Svalbard margin to assess whether such hydrates could be responsible for in the observed gas release. The results show that shallow, low-saturation hydrate deposits, if subjected to recent measured or predicted temperature changes at the seafloor, can release quantities of methane at the magnitudes recorded, and that the releases will be localized near the landward limit of the top of the GHSZ as observed. Both gradual and rapid warming is simulated, and localized gas release is observed for both cases. These suggest that hydrate dissociation and methane release as a result of climate change may be a real phenomenon, and that it already may be occurring.

INTRODUCTION

Gas hydrates are solid crystalline compounds in which gas molecules are lodged within a clathrate crystal lattice (Sloan, 1998). Natural gas hydrate deposits occur in geologic settings where the necessary low temperatures and high pressures exist for their formation and stability. Vast quantities of methane are trapped in oceanic hydrate deposits (Klauda and Sandler, 2005). Because methane is a powerful greenhouse gas (about 26 times more effective than CO₂), there is considerable concern that a rise in the ocean temperature will induce dissociation of these hydrate accumulations, potentially releasing large amounts of carbon into the atmosphere.

Initial investigations estimated the total amount of methane hydrate currently residing in the deep ocean and along continental margins, beginning with an early “consensus value” of 10,000 gigatons (Gt, 20×10¹⁵ m³ STP) of methane carbon (Gornitz and Fung, 1994; Kvenvolden, 1999; Borowski, 2004). However, more recent studies have produced widely different results—one yielding an upper estimate of 27,300 Gt of methane in hydrate along continental margins (74,400 Gt globally) (Klauda and Sandler, 2005) and the other a lower estimate of 3,000 Gt of methane in hydrate and 2,000 Gt of underlying gaseous methane (Buffett and Archer, 2004).

In oceanic deposits, the depth at which hydrates remain stable depends on the pressure (as imposed by the water depth) and the temperature. An increase in water temperature at the seafloor changes the extent of the gas hydrate stability zone (GHSZ), and such a shift could induce hydrate dissociation and lead to methane release. Deep ocean surveys have found pockmarks and other structures that indicate large fluid releases at the seafloor in the past (Hovland et al., 2005), and computational studies show the potential for hydrate instability under warming conditions (Reagan and Moridis, 2008).

Such a release could have dramatic climatic consequences because it could amplify atmospheric and oceanic warming and possibly accelerate dissociation of the remaining hydrates. This positive-feedback mechanism has been proposed as a significant contributor to rapid and significant climate changes in the late Quaternary period (Kennett et al., 2000). The Clathrate Gun Hypothesis (Kennett et al., 2002) proposes that past increases in water temperatures near the seafloor may have induced such a large-scale dissociation, with the methane spike and isotopic anomalies reflected in polar ice cores and in benthic foraminifera. While this hypothesis is controversial, and the relationship between hydrates and climate has not yet been established, the role of methane in climate cycles is currently an active area of research, and hydrates are considered to be a potential source (Mascarelli, 2009).

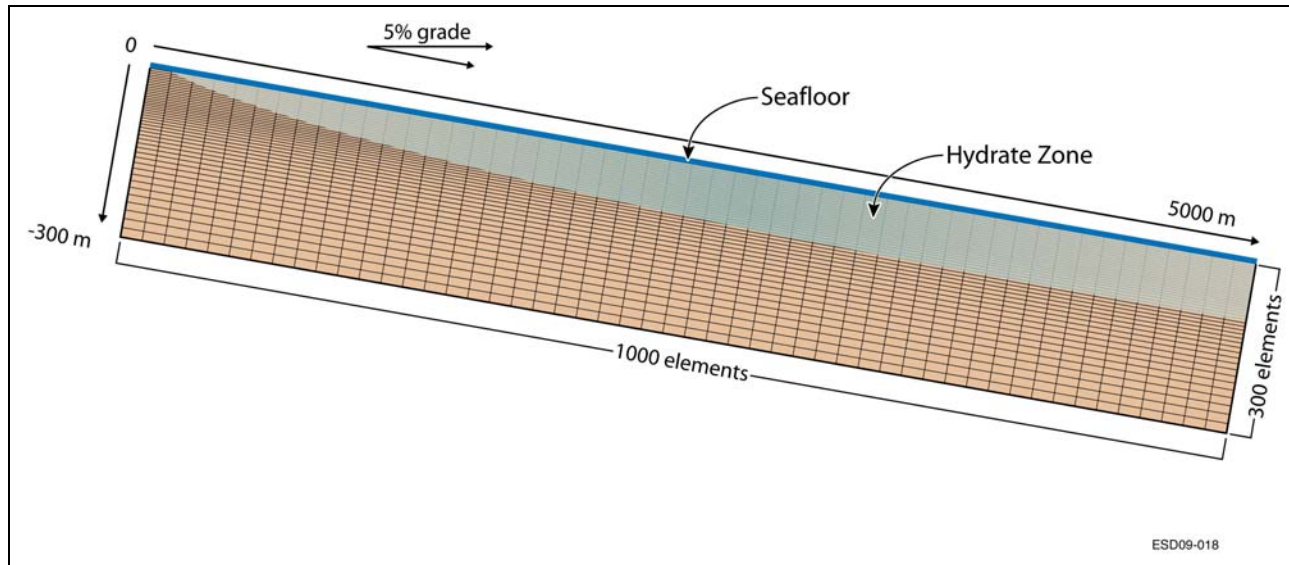


Figure 1. Illustration of the domain discretization, GHSZ extent, and boundaries for the 2D sloping system (not to scale). Gridlines are a schematic representation only.

The recent discovery of active gas venting along the shallow continental slope west of Svalbard creates new cause for concern (Westbrook et al., 2009). The observed plumes release a sizeable quantity of methane—enough that some methane reaches the ocean surface. While methane seeps are known to exist in other locations, this system is notable in that the locations of the plumes coincide with the landward limit of the GHSZ, suggesting that recent changes in ocean temperature at the seafloor have interacted with shallow hydrates in the subsurface. Two hydrate-related phenomena are proposed: (1) that dissociating shallow hydrates are responsible for the methane itself; and (2) that methane arriving from deeper sources forms hydrate in the shallow GHSZ, and this hydrate (due to the change in effective permeability) may act to block or channel methane that migrates upward from deeper sources. To test this hypothesis, this study performs a large-scale, 2D simulation of shallow hydrates in conditions representative of the western Svalbard margin to assess the potential for hydrate dissociation, methane release, and methane plume formation in arctic continental shelf environments subjected to ocean warming.

MODELS AND METHODS

We evaluate the stability and dissociation of shallow oceanic hydrates subjected to short-term temperature variations and the flow of methane in the subsurface using the massively parallel version of the TOUGH+HYDRATE code (pT+H) (Moridis et al., 2008). T+H models the nonisothermal hydration reaction, phase behavior and flow of fluids and heat in complex geologic media (Moridis and Kowalsky, 2007; Moridis and Sloan, 2007) and has been used in

earlier 1D studies of hydrate dissociation in response to ocean temperature change (Reagan and Moridis, 2008). This study is the first simulation of fully coupled hydrate dissociation, heat transport, and multiphase flow applied to a climate-driven system of this magnitude.

Domain Discretization and Initial Configuration

The model is a 2D sloping system 5,000 m in length and extending to 300 m below the seafloor. The western Svalbard continental shelf has a 3%–5% slope, as indicated by local averages from GEBCO bathymetry data for the western Svalbard region (GEBCO, 1997) and as reported by Westbrook (2009) in the region of methane plume formation. We select a 5% grade (20 m per 1 m depth) to constrain the horizontal extent of the system. The top of the slope is located at a depth of 300 m, above the top of the GHSZ at local temperatures, with the bottom of the slope at 550 m for a 5% grade. Figure 1 shows a schematic of the mesh (not to scale), including the system boundaries and the extent of the GHSZ. To represent the system at a suitable level of detail, we use 300,000 gridblocks (1000×300), with a horizontal discretization of $dx = 5$ m, a 2D slice thickness of $dy = 1$ m, and a variable vertical discretization, beginning with $dz=0.25$ m from the seafloor to $z=-50$ m, $dz = 0.5$ m between $z = -50$ m and $z = -75$ m, and a logarithmic progression ($dz=0.5-15.8$ m) from $z=-75$ to $z = -300$ m.

The initial condition involves a hydrostatic pressure distribution based on depth and 3.5 wt% salinity, initial temperature based on a geothermal gradient of $8.7^{\circ}\text{C}/100$ m (Haacke et al., 2008), and a uniform initial hydrate saturation of 3% in the sediment column within the GHSZ. The extent of the GHSZ is

computed directly from the depth and initial temperature using T+H (Moridis, 2003; Moridis et al., 2008) and the initial state of the system was brought to thermal equilibrium and hydrostatic conditions. A preexisting region of free gas, often inferred to exist underneath shallow stratigraphic hydrate deposits, is not included in this simulation, as the actual quantity of gas under systems of this type has not been directly measured and our goal is to assess the quantity of gas that may be released due to hydrate dissociation alone.

System Properties

The intrinsic permeability for this base case, $k = 1$ mD, is within the reported range of hydrate-bearing oceanic sediments (Ginsberg and Soloviev, 1998) and represents a baseline stratigraphic or “Class 4” hydrate deposit (Moridis and Sloan, 2007), in contrast to the less common, more permeable, and often more saturated structures near sites of active methane seepage and/or venting. The porosity $\phi = 0.55$ reflects measurements taken at deeper locations further offshore (Haake et al., 2008). The physical properties parameters used in the simulations are summarized in Table 1.

The top of the sediments is bounded by an open boundary representing heat and mass transfer between the sediments and the bulk ocean. The pressure at the upper boundary (set according to hydrostatic conditions at the initial salinity) is held constant, representing constant ocean levels. The domain bottom is a closed boundary at $z = -300$ m, beyond the expected range of temperature propagation on short time scales, and is held at a constant temperature selected to match the known initial geothermal gradient and supply the expected geological heat flux from lower strata.

Climate Change Scenarios

Recent climate simulations coupling ocean circulation, atmospheric circulation, and atmospheric chemistry (Meehl et al., 2007) indicate that, under current climate conditions and a 1%/yr increase in atmospheric CO₂, the temperature at the seafloor would rise by 1°C over the next 100 yr, and possibly by another 3°C in the following century. Historical temperature data from the Svalbard region (Westbrook et al., 2009) suggest that a 1°C change in bottom-water temperature has already occurred over the last 30 years. Previous work on the response of shallow hydrates to ocean temperature change (Reagan and Moridis, 2008) indicates that temperature changes as small as 1–3°C can have significant effects on shallow hydrates.

Table 1. Physical properties and simulation parameters for the 2D hydrate-bearing system

Parameter	Value
Initial pore water salt mass fraction, X_0	0.035
Permeability, k	10^{-15} (= 1 mD)
Porosity, ϕ (Haake et al., 2008)	0.55
Dry thermal conductivity, k_{sd}	1.0 W/m/K
Wet thermal conductivity, k_{sw}	3.3 W/m/K
Composite thermal conductivity k_ϕ model (Moridis et al., 2005)	$k_\phi = (\sqrt{S_H} + \sqrt{S_A}) * (k_{sw} - k_{sd}) + k_{sd}$
Capillary pressure model (van Genuchten, 1980)	$P_{cap} = -P_0 \left[(S^*)^{-1/\lambda} - 1 \right]^2$ $S^* = \frac{(S_A - S_{irA})}{(S_{mA} - S_{irA})}$
P_0	2000 Pa
Relative permeability model (Stone, 1970)	$k_{rA} = (S_A^*)^n$ $k_{rG} = (S_G^*)^n$ $S_A^* = (S_A - S_{irA}) / (1 - S_{irA})$ $S_G^* = (S_G - S_{irG}) / (1 - S_{irA})$
λ	0.45
n	4
S_{irG}	0.02
S_{irA}	0.20

Therefore, we vary the temperature at the upper boundary to represent these changes in the bulk ocean temperature above the seafloor. As a base case, we assume an initial seafloor temperature of $T_0 = 0^\circ\text{C}$ (Westbrook et al., 2009). We increase the overlying ocean temperature by 1°C/100 yr, a conservative representation of possible temperature changes over the last century, and also a conservative projection of potential warming in the near future. We simulate the evolution of the system for a total of 300 yr to capture a range of conditions and create a significant variation in the extent of the GHSZ. In addition, to assess the effect of more rapid change, we also extrapolate the reported 1°C/30 yr trend (Westbrook et al., 2009) to 3°C/100 yr for comparison. In both cases, the total simulation time is restricted, as extrapolation of recent temperature trends over many centuries is speculative at best, and we are most interesting in capturing century-scale phenomena that

may already be occurring, and that may already be observable.

RESULTS AND DISCUSSION

While simulating the evolution of the representative hydrate deposit, we record localized methane fluxes through the upper boundary, hydrate dissociation rates, and phase saturations throughout the 2D system. To simulate such a large system, 80–100 processors were required to produce significant results in a manageable amount of time, as the solution of the problem requires the coupled solution of 1.2×10^6 equations at each timestep.

Base Case: Gradual Change

The base case represents a 3°C temperature change at the seafloor (at all depths from 300 to 550 m) over a 300 yr period. The temperature was varied linearly at a rate of $1^\circ\text{C} / 100 \text{ yr}$, with an initial temperature of $T_0 = 0^\circ\text{C}$ at $t = 0$. The upslope limit of the GHSZ at initial conditions is located at $x = 290 \text{ m}$, or a water depth of approximately 314 m.

Figure 2 describes the evolution of hydrate saturation, S_H , with time. Minimal change is observed at $t = 50 \text{ yr}$, but by $t = 100 \text{ yr}$ significant recession is apparent (corresponding to the new upper extent of the GHSZ at time t). At the end of the 300 yr simulation period, the upper (leftmost) extent of methane gas hydrate has receded over 1,700 m downslope.

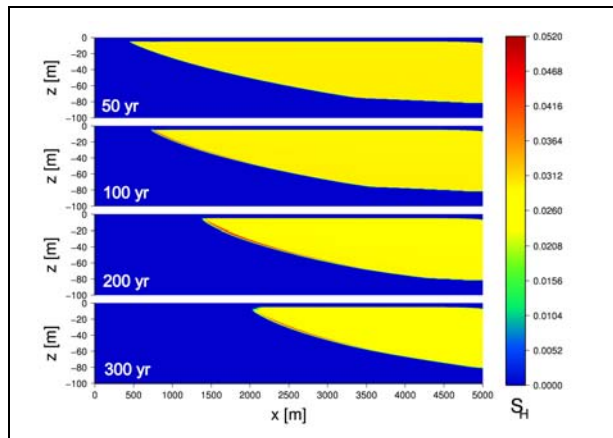


Figure 2. Hydrate saturation, S_H , for the 2D system at $t = 50, 100, 200,$ and 300 yr for the base case. The top of the 5% slope is at $x = 0$.

Figure 3 shows the evolution of gas saturation, S_G , with time. At $t = 50 \text{ yr}$ (18,200 days), only a thin layer of gas is seen along the bottom of the region of hydrate-bearing sediments. By $t = 100 \text{ yr}$ (36,400 days), a significant region of gas has formed in place of the receding hydrate, with the highest

concentration along the bottom of the remaining hydrate and the landward (leftmost) limit of the GHSZ at $x = 750 \text{ m}$ downslope. This gas, now at saturations in excess of the irreducible gas saturation (2%), is moving upward toward the seafloor ($z = 0$). By $t \sim 200 \text{ yr}$ (75,129 days), a “plume” of high gas saturation is observed, as gas moves along the bottom of the remaining hydrate deposit and reaches the seafloor at $x \sim 1400 \text{ m}$ downslope. At $t = 300 \text{ yr}$ (109,201 days), the plume of highest gas saturation is located 2,000 m downslope, and the entire region of the seafloor from $x = 500 \text{ m}$ to $x = 2000 \text{ m}$ is receiving mobile methane gas from below.

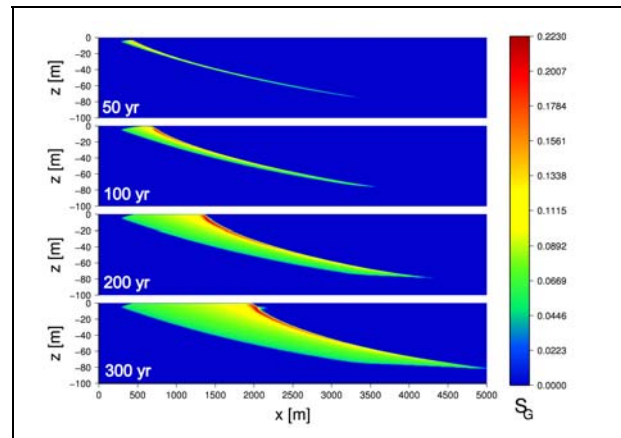


Figure 3. Gas saturation, S_G , for the 2D system at $t = 50, 100, 200,$ and 300 yr for the base case. The top of the 5% slope is at $x = 0$.

Note the increase in hydrate saturation ($S_H > S_{H,0}$) in a thin zone along the bottom of the hydrate-bearing sediments for $t > 100 \text{ yr}$ seen in Figure 2. As gaseous methane (Figure 3) travels along the bottom of the remaining hydrate mass (guided by the reduced effective permeability of the overlying hydrate-bearing sediments), secondary hydrate re-forms as some gas enters the (now less extensive) GHSZ. The localized increase in S_H further reduces the effective permeability at the base of the hydrate zone, and the result is a channeling of gas into a plume of high saturation.

Simulation outputs indicate that the first appearance of gaseous methane at the seafloor occurs around $t = 97 \text{ yr}$. In Figure 4, the evolution of gas flux, Q_{CH_4} , presented here as $\text{mol CH}_4 \text{ per m}^2$ at downslope position x for a 1 m-wide 2D slice of the overall system, is plotted as a function of time, t . The peak of the Q_{CH_4} profile corresponds almost exactly to the location of contact between the gas-phase “plume” observed in Figure 3 and the seafloor. The peak Q_{CH_4} , as does the plume, moves downslope over time. Localized methane gas flux peaks at 45 mol/yr-m^2 (at $t \sim 250 \text{ yr}$), but significant fluxes of gaseous methane

occur over a wide area, locally decreasing with time as the subsurface plume moves downslope.

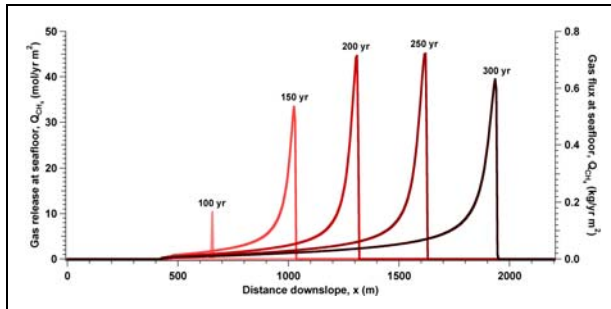


Figure 4. Flux of gaseous methane, Q_{CH_4} , at the seafloor at $t = 100, 150, 200, 250,$ and 300 yr. Q_{CH_4} is presented here as mol CH_4 per m^2 at downslope position x for a 1 m-wide 2D slice of the real system, for the base case.

The evolution of the total methane release at the seafloor, in both aqueous and gaseous form, for the entire $5000 \text{ m} \times 1 \text{ m}$ seafloor boundary is shown in Figure 5. Methane release into the ocean begins just before $t = 100$ yr, increases continuously over the simulated timeframe, and is still increasing at the end of the simulation at $t = 300$ yr, having reached 8900 mol/yr .

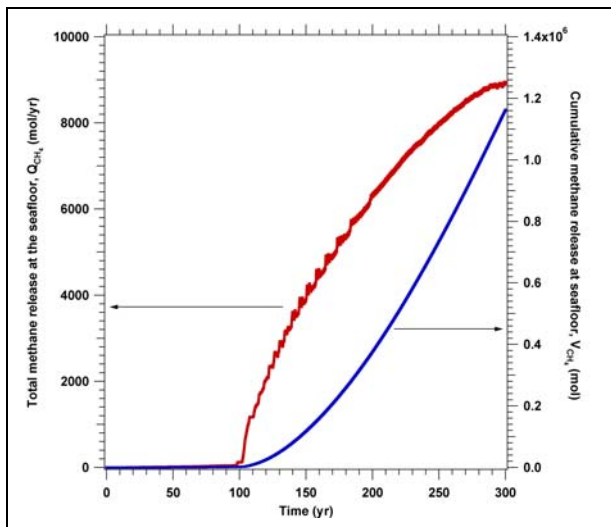


Figure 5. Total methane release (aqueous and gaseous phases), $Q_{CH_4,T}$, and cumulative methane release, V_{CH_4} , for the entire simulated seafloor boundary, a 1 m wide, 5000 m long section, for the base case

Figure 5 also describes the time evolution of the cumulative methane release, V_{CH_4} , for the entire $5000 \text{ m} \times 1 \text{ m}$ seafloor boundary. By $t = 300$ yr, over $1.16 \times 10^6 \text{ mol}$ of CH_4 has been released in the overlying ocean.

Case II: Rapid Change

While the base case assumed conservative projections, some observations suggest that warming may in fact be occurring at a considerably faster pace. A change in the temperature of the West Spitsbergen current of 1°C over the past 30 yr has been reported (Westbrook, 2009) with an average rate of 0.03°C/yr . We model this rapid change with a linear 3°C temperature increase at the seafloor (at all depths from 300 to 550 m) over a 100 yr period with an initial temperature of $T_0 = 0^\circ\text{C}$ at $t = 0$. After 100 years of simulation, the ocean temperature is held constant for additional 100 yr to assess the consequences of the rapid warming. No additional warming is simulated for the reasons stated previously. The simulation is otherwise performed in an identical manner to the base case.

Figure 6 describes the evolution of hydrate saturation, S_H , with time for the case of rapid change. Over the 200 yr simulation period, the upper (leftmost) extent of methane gas hydrate recedes by approximately 1500 m downslope. More so than the base case, here we clearly see the effects of the lowering of the top of the GHSZ, as an upper dissociation front is apparent at $t = 50$ yr, 100 yr, and 130 yr. Note that in all contour plots, the 2D system has a 5% slope, with the top of the slope located at $x = 0$, and as such the angle to the observed dissociation front reflects this slope.

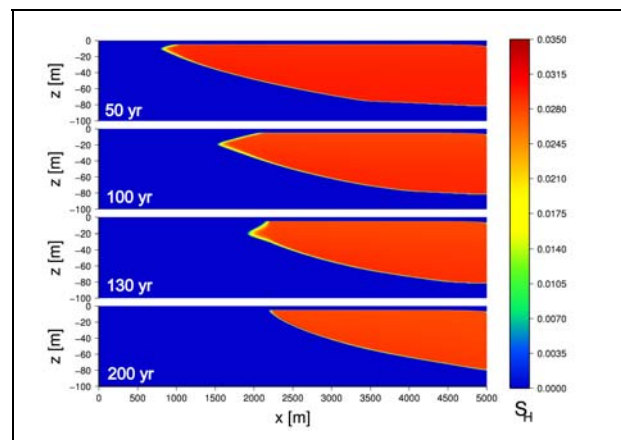


Figure 6. Hydrate saturation, S_H , for the 2D system at $t = 50, 100, 130,$ and 200 yr for Case II. The top of the 5% slope is at $x = 0$.

Simulations of 1D hydrate-bearing sediment columns under shallow Arctic conditions (Reagan and Moridis, 2008) have demonstrated that the rate of dissociation is regulated by heat transfer limitations, as hydrate dissociation is strongly endothermic, and thus we see the formation of a sharp dissociation front in both the previous 1D study and in this 2D simulation. Secondary hydrate formation is less apparent in this case, with only a slight increase in S_H

to 0.035 along the bottom of the hydrate-bearing zone at $t = 200$ yr (72,746 days).

Figure 7 shows the evolution of gas saturation, S_G , with time. At $t = 50$ yr (18,200 days), a large region of free gas already fills the sediments as the top and bottom of the GHSZ has receded substantially and mobile gas is moving upward toward the seafloor. As in the base case, the gas forms a localized plume of high S_G , which in this case remains well-defined as the gas travels through the region between the upper dissociation boundary and the seafloor. This plume contacts the seafloor at $x \sim 750$ – 1500 m, and as in the base case, moves downslope over time, but in this case gas saturations decrease noticeably by $t = 130$ yr. By $t = 200$ yr, the entire region of the seafloor from $x = 500$ m to $x = 2200$ m is receiving mobile methane gas from below, but S_G within the plume has declined substantially, and the plume is no longer well-defined.

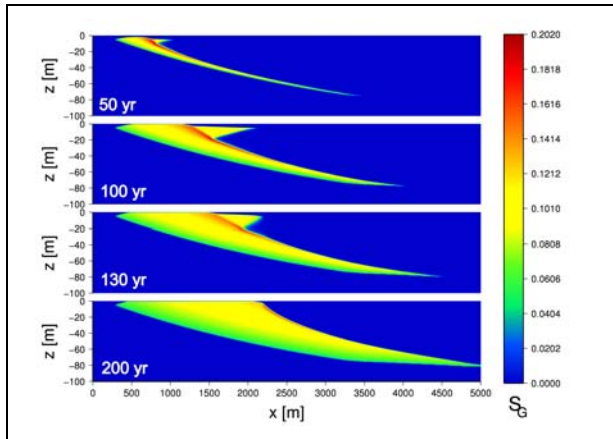


Figure 7. Gas saturation, S_G , for the 2D system at $t = 50$, 100, 130, and 200 yr for Case II. The top of the 5% slope is at $x = 0$.

Simulation outputs indicate that the first appearance of gaseous methane at the seafloor occurs around $t \sim 80$ yr, and that the onset of gas release is rapid. In Figure 8, the evolution of gas flux, Q_{CH_4} ($\text{mol}/\text{yr}\cdot\text{m}^2$), is presented as a function of time, t , and downslope position, x . As in the base case, the peak of the gaseous flux corresponds closely to the location of the gas-phase plume observed in the 2D plots of S_G . However, in Case II, methane gas flux peaks immediately at $15 \text{ mol}/\text{yr}\cdot\text{m}^2$ and then slowly decreases with time.

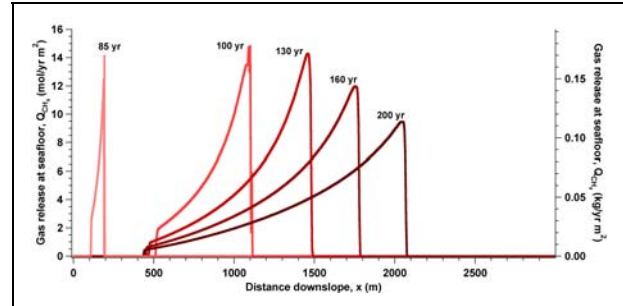


Figure 8. Flux of gaseous methane, Q_{CH_4} , at the seafloor at $t = 85$, 100, 130, 160, and 200 yr for Case II. Q_{CH_4} is presented here as mol CH_4 per m^2 at downslope position x for a 1 m wide 2D slice of the real system.

However, in contrast to the base case, the distribution of venting is broader, reflecting the greater extent of high-saturation gas present within the sediment at a given time t compared to the base case. As seen in Figures 3 and 7, the region of free gas extends 750 m further downslope at $t = 200$ yr when compared to the base case, reflecting more rapid dissociation of the hydrate and also indicating that the transport of gas to the seafloor is not necessarily increased simply due to the rapidity of dissociation.

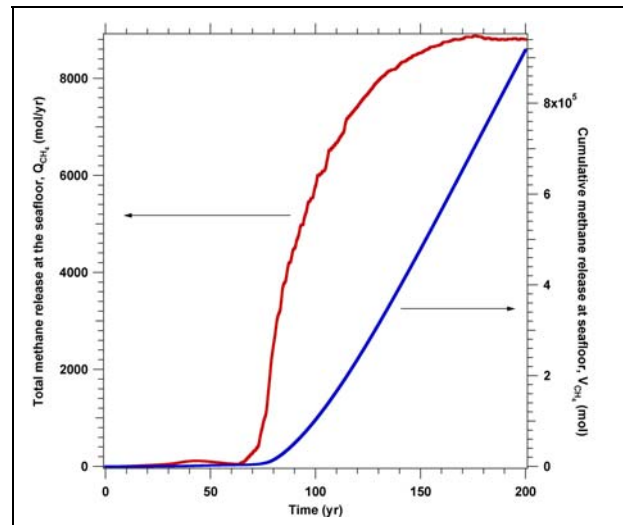


Figure 9. Total methane release (aqueous and gaseous phases), $Q_{CH_4,T}$, and cumulative methane release, V_{CH_4} , for Case II over the entire simulated seafloor boundary, a 1 m wide, 5000 m long section.

The evolution of the total methane flux, in both aqueous and gaseous form, for the entire $5000 \text{ m} \times 1 \text{ m}$ seafloor boundary is shown in Figure 9. Methane release into the ocean begins at approximately $t = 30$ yr in the aqueous phase, but increases rapidly after $t = 65$ yr until a peak at $t = 175$ yr at

8800 mol/yr for the 1 m wide 2D slice of the overall system. Despite a much more rapid disappearance of hydrate compared to the base case, the peak flux is nearly identical. Figure 9 also shows the evolution of cumulative release over time, with this case releasing a total of 9.2×10^5 mol of CH_4 by $t = 200$ yr. In comparison, at $t = 200$ yr the base case has released only 3.8×10^5 mol of CH_4 . While instantaneous fluxes may be similar for different warming scenarios, more rapid warming clearly results in faster rates of gas release at the seafloor, as would be expected.

CONCLUSIONS

Comparison to 1D results

Previous simulations of 1D hydrate-bearing sediment columns (Reagan and Moridis, 2008) indicated that hydrate dissociation due to both gradual and rapid change does not produce violent eruptions of methane gas, rather, dissociation and the resultant gas release tend to occur in an orderly fashion, regulated by heat transfer limitations and gas migration through sediments containing multiple phases. Extending the model system to a 2D sloping domain introduces horizontal migration of fluids and dissociation of hydrate along multiple fronts. However, the rate of dissociation and the rate of gas release into the environment are still constrained by heat and fluid flow limitations, and as such these deposits release gas at the seafloor in an orderly fashion. In both the base case and Case II in particular, we see the formation of a sharp upper dissociation boundary and instantaneous total methane fluxes that asymptotically approach a constant value, similar to the example of a 1D Arctic hydrate system at $T = 0.4^\circ\text{C}$ and 320 m depth (Reagan and Moridis, 2008). Substantial but not catastrophic releases appear to be the likely consequence of climate-driven hydrate dissociation.

Comparison to Observations

A team led by Westbrook (Westbrook et al., 2009) recently observed over 250 plumes of methane gas erupting from the seabed off the West Spitsbergen (Svalbard) continental margin at the present landward limit of the GHSZ. These gas plumes, which extend along 30 km of the slope, have been hypothesized to be partly the result of hydrate dissociation as a consequence of recent ocean warming in the area, and partly due to diversion and channeling of upwelling methane by hydrate-bearing sediments. Using hydrate saturations taken (about 4.5% average) from further downslope, the observers estimated a potential release of 900 kg/yr CH_4 per 1 m of margin length.

The simulations presented in this paper closely represent the type and extent of hydrate-bearing system thought to exist along the Svalbard margin,

and allow us to make several conclusions about the nature of this system:

(1) Our simulations, using a slightly lower average $S_{H,0}$, suggest that at least 141 kg/yr CH_4 per 1 m width of slope can be released solely due to dissociating hydrate. Integrated over the 30 km plume region, this would be 0.004 Tg/yr of CH_4 from this one hydrate system alone, small in comparison to the global atmospheric flux of methane but significant to the ocean biochemistry of the region.

(2) A second conclusion from this study is that hydrate alone can provide a significant quantity of methane gas in climate change-driven release scenarios, in addition to any geological methane source that may be providing free gas or dissolved aqueous methane to the region below the GHSZ.

(3) A third conclusion is that the hydrate-bearing sediments can divert and channel the flow of aqueous and gaseous methane, despite the very low hydrate saturations expected for disperse, unconfined stratigraphic deposits. In both the base and rapid-warming cases, we observe channeling of mobile gas along the bottom of the GHSZ due to the reduced effective permeability of hydrate-bearing sediments, the trapping of methane through the formation of secondary hydrate when methane enters the GHSZ, and the formation of localized subsurface plumes of higher methane saturation that directly correlate to localized gaseous fluxes at the seafloor. These processes provide a clear model for the formation of gas plumes at the landward limit of the GHSZ, as observed.

ACKNOWLEDGMENT

This research was funded by the Assistant Secretary for Fossil Energy, Office of Natural Gas and Petroleum Technology, through the National Energy Technology Laboratory. The authors would like to thank Katie L. Boyle for the development of the 2D data visualization tools.

REFERENCES

- Borowski, W.S., A review of methane and gas hydrates in the dynamic, stratified system of the Blake Ridge region, offshore southeastern North America. *Chem. Geology*, 205, 311-346, 2004.
- Buffett, B., and D. Archer, Global inventory of methane clathrate: Sensitivity to changes in environmental conditions, *Earth Planetary Sci. Lett.*, 227, 185-199, 2004.
- GEBCO, Published by the British Oceanographic Data Centre on behalf of Intergovernmental Oceanographic Commission and International Hydrographic Organization, 1997.

- Ginsburg, G.D. and V.A. Soloviev, Submarine Gas Hydrates. St. Petersburg, 1998.
- Gornitz V., and I. Fung, Potential distribution of methane hydrate in the world's oceans, *Global Biogeochem. Cycles*, 8, 335-347, 1994.
- Haake, R.R., Westbrook, G.K., and M.S. Riley, Controls on the formation and stability of gas hydrate-related bottom-simulating reflectors (BSRs): A case study from the west Svalbard continental slope, *J. Geophys. Res.*, 113, B05104, doi: 10.1029/2007JB005200, 2008.
- Hovland, M., Svensen, H., Forsberg, C.F., Johansen, H., Fichler, C., Fossa, J.H., Jonsson, R., and H. Rueslatten, Complex pockmarks with carbonate-ridges off mid-Norway: Products of sediment degassing, *Marine Geology*, 218, 191-206, 2005.
- Kennett, J.P., Cannariato, K.G., Hendy, L.L., and R.J. Behl, Carbon isotopic evidence for methane hydrate instability during quaternary interstadials. *Science*, 288, 128-133, 2000.
- Kennett, J.P., Cannariato, K.G., Hendy, L.L., and R.J. Behl, *Methane hydrates in quaternary climate change: The Clathrate Gun Hypothesis*, AGU Publishing, Washington, DC, 2002.
- Klauda, J.B., and S.I. Sandler, Global distribution of methane hydrate in ocean sediment. *Energy and Fuels*, 19, 459-470, 2005.
- Kvenvolden, K.A., Potential effects of gas hydrate on human welfare, *Proc. Nat. Acad. Sci.*, 96, 3420-3426, 1999.
- Mascarelli, A.L., A Sleeping Giant? *Nature Reports Climate Change*, 3(4), doi: 10.1038/climate.2009.24, 2009.
- Meehl, G., et al., Global climate projections, *Climate Change 2007: The Physical Basis*, 789-844, Cambridge Univ. Press, Cambridge, UK, 2007.
- Moridis, G.J., Numerical Studies of Gas Production from Methane Hydrates, *SPE Journal*, 32(8), 2003.
- Moridis, G.J., Seol, Y., and T. Kneafsey, Studies of reaction kinetics of methane hydrate dissociation in porous media (Paper 1004), *Proceedings of the 5th International Conference on Gas Hydrates*, Trondheim, Norway, 12-16 June 2005.
- Moridis, G.J., and M.B. Kowalsky, Response of Oceanic Hydrate-Bearing Sediments to Thermal Stresses, *SPE Journal*, 12(2), 253-268, doi:10.2118/111572-PA, 2007.
- Moridis, G.J., and E.D. Sloan, Gas production potential of disperse low-saturation hydrate accumulations in oceanic sediments, *Energy Conv. Manag.*, 48, 1834-1849, doi:10.1016/j.enconman.2007.01.023, 2007.
- Moridis, G.J., Kowalsky, M.B., and K. Pruess, *TOUGH+HYDRATE v1.0 User's Manual: A Code for the Simulation of System Behavior in Hydrate-Bearing Geologic Media*, Report LBNL-0149E, Lawrence Berkeley National Laboratory, Berkeley, CA.
- Reagan, M. T., and G. J. Moridis, Dynamic response of oceanic hydrate deposits to ocean temperature change, *J. Geophys. Res.*, 113, C12023, doi:10.1029/2008JC004938, 2008.
- Sloan, E.D. and C. Koh, *Clathrate Hydrates of Natural Gases*, CRC Press, New York, NY, 2008.
- Stone, H.L., Probability model for estimating three-phase relative permeability, *Trans. SPE AIME*, 249, 214-218, 1970.
- Westbrook, G.K., Thatcher, K.E, Rohling, E.J., Piotrowski, A.M., Palike, H., Osborne, A.H., Nisbet, E.G., Minshull, T.A., Lanoiselle, M., James, R.H., Huhnerbach, V., Green, D., Fisher, R.E., Crocker, A.J., Chabert, A., Bolton, C., Beszczynska-Moller, A., Berndt, C., and A. Aquilina, Escape of methane gas from the seabed along the West Spitsbergen continental margin *Geophys. Res. Lett.*, in press, doi: 10.1029/2009GL039191, 2009.
- Van Genuchten, M.T., A closed-form equation for predicting the hydraulic conductivity of unsaturated soils, *Soil Sci. Soc.*, 44, 892-898, 1980.

EXPERIMENTAL DESIGN APPLIED TO SIMULATION OF GAS PRODUCTIVITY PERFORMANCE AT
RESERVOIR AND LABORATORY SCALES UTILIZING FACTORIAL ANOVA METHODOLOGY

Evgeniy M. Myshakin^{1,2}, Isaac K. Gamwo¹, and Robert P. Warzinski¹

¹United States Department of Energy, National Energy Technology Laboratory
P.O. Box 10940, Pittsburgh, PA 15236
E-mail: Evgeniy.Myshakin@netl.doe.gov

²NETL Support Contractor, Parsons, P.O. Box 618, South Park, PA 15129

ABSTRACT

Using the TOUGH+HYDRATE simulation code, we developed an experimental design involving analysis of variance (ANOVA) at two scales, for the simulation of gas production from methane hydrates. Heterogeneous and homogeneous hydrate-bearing reservoirs were studied, as well as a laboratory-scale reactor filled with methane hydrate in wetted sand. We chose vertical intrinsic permeability, intrinsic permeability multiplier, pore compressibility, thermal conductivity, and irreducible water saturation as three-level controllable factors in these studies. For every scenario, the design constitutes a total of 243 individual production simulations, according to the combinations of the factor settings (3^5). A factorial ANOVA approach was used to study the designed simulations with respect to the responses of average

production rate and recovery ratio. Estimated main effects and second-order interactions among the factors were determined and ranked with respect to their impact on the responses. An analysis of estimated marginal means for significant interactions was also conducted, to compare the effects of these factors. The results obtained are discussed in light of model specifics, and predictions are made to optimize the performance of the systems studied. Using the ANOVA approach, as opposed to a sensitivity analysis, defines both the first-order effects of the variables being studied, similar to a sensitivity analysis, *and* the significance of second-order interactions among the studied variables. Such information could be useful in developing improved correlations for models to describe the behavior of hydrate decomposition in both small- or large-scale scenarios.

EVALUATION OF THE GAS PRODUCTION POTENTIAL OF CHALLENGING HYDRATE DEPOSITS

George J. Moridis, Matthew T. Reagan, Katie L. Boyle, and Keni Zhang

Lawrence Berkeley National Laboratory
1 Cyclotron Rd.
Berkeley, CA 94720, USA
e-mail: GJMoridis@lbl.gov

ABSTRACT

We use the TOUGH+HYDRATE code to assess the production potential of challenging hydrate deposits, i.e., deposits that are characterized by any combination of the following factors: absence of confining boundaries, high thermodynamic stability, low temperatures, low formation permeability. Using high-resolution grids, we show that a new horizontal well design using thermal stimulation coupled with mild depressurization yields production rates that appear modest and insufficient for commercially viable production levels. The use of parallel horizontal wells (with the lower one providing thermal stimulation through heat addition, direct injection or circulation of warm water, and the upper one producing under a mild depressurization regime) offers tantalizing possibilities, and has the potential of allowing commercial production from a very large number of hydrate deposits that are not currently considered as production candidates if the problem of the corresponding large water production can be solved.

INTRODUCTION

Gas hydrates are solid crystalline compounds in which gas molecules are lodged within a clathrate crystal lattice (Sloan and Koh, 2008). Vast amounts of CH_4 stored in hydrates in geologic media in the permafrost and in the oceans. The current study is part of a larger effort to determine the technical feasibility of gas production from a wide range of hydrate deposits in geologic media.

Recent studies have determined the conditions, methods and characteristics that enhance production from such deposits. The most important features (Moridis et al., 2008) include (a) high temperatures and pressures (the deepest, warmest deposits are the most desirable), (b) thermodynamic proximity to the H-V-Lw equilibrium conditions (Figure 1), (b) the use of depressurization, because pure thermal stimulation appears to be very slow and ineffective (Moridis and Reagan, 2007a;b), (c) the presence of impermeable boundaries and, in the case of Class 2 systems, thin water zones, and (d) high intrinsic permeabilities of the hydrate-bearing sediments. If these conditions are met, hydrate deposits can yield

methane at high rates (well in excess of 10 MMSCFD) for long periods using conventional production technology (Moridis and Reagan, 2007a;b).

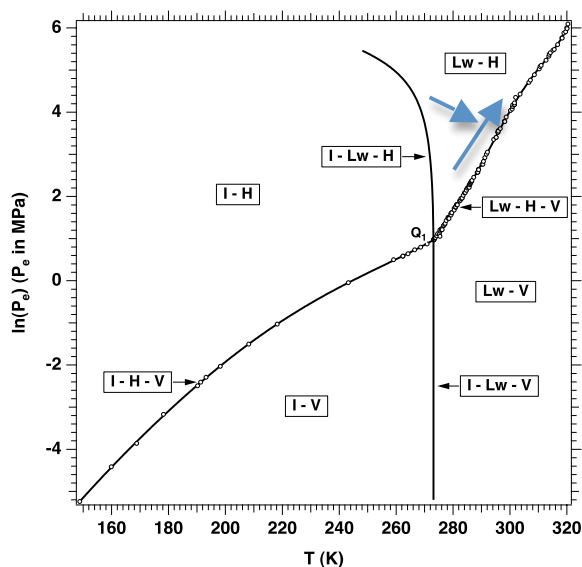


Figure 1. Pressure-temperature equilibrium relationship in the phase diagram of the water- CH_4 -hydrate system (Moridis, 2003). The two arrows show the direction of increasing thermodynamic desirability of a deposit as a production target.

Challenging Hydrates

In this study we address the issue of gas production from “challenging” hydrates (CG), i.e. those that do not meet the desirability criteria discussed earlier. Such CG include: (a) absence of impermeable boundaries (CG-B), (b) low initial temperatures, and, consequently, pressures (CG-T), (c) increased stability, as indicated from their thermodynamic distance from the hydrate equilibrium conditions (CG-S), (d) extremely low effective permeability k_{eff} , caused either by very high hydrate saturations S_H (CG-H), and/or by occurrence in fine-textured sediments, low- k media such as silts and clays (CG-k). An additional type of CG includes hydrate chimneys (CG-C), i.e., marine hydrates that occur at high S_H in near-vertical cylindrical structures that are associated with past CH_4 plumes, often extend to the

ocean floor, and usually have limited diameters (usually < 30 m) and no confining boundaries.

Dissociation is orders of magnitude more effective than thermal stimulation as a dissociation method for gas production (Moridis and Reagan, 2007b). However, a common feature of all cases of CG is that depressurization cannot be effectively applied because of (1) the absence of low- k boundaries and high water production (CG-B, CG-C), (2) the very low k_{eff} , (CG-H, CG-k, CG-C), (3) the impracticality of effecting the very large pressure drops needed to cause dissociation of very stable hydrates (CG-S), or (4) low sensible heat to sustainably fuel depressurization-induced dissociation (CG-T). The high cost and progressively diminishing effectiveness of chemical inhibitors precludes their intensive use for gas production from CG, and pure thermal stimulation has been shown to be ineffective (Moridis and Reagan, 2007b). Conjunctive use of thermal stimulation with depressurization appears to be a plausible method for gas production from CGs.

Objectives

In this study we investigate by means of numerical simulation the production potential of some types of CGs. We focus on CG-B, but we also investigate production from CG-T and CG-k through sensitivity analysis. Additionally, we investigate the effectiveness of two different well designs. We evaluate production according to two criteria: the *absolute* criterion of gas production, and the *relative* criterion of the gas-to-water ratio.

GEOLOGIC AND NUMERICAL MODEL

The geologic system in this study is based the Tigershark area, located in the Alaminos Canyon Block 818 of the Gulf of Mexico. Log data from a specially designed exploration well in about 2750 m (9000 ft) of water at the site indicated the presence of an 18.25-m (60-ft) thick sandy hydrate-bearing layer (HBL) corresponding to a drilling depth. The HBL has a porosity ϕ of about 0.30 and Darcy-range intrinsic permeability k . Initial estimates of gas hydrate saturation S_H derived from analyses of the resistivity and p-wave velocity data indicate a range from 0.6 to over 0.8. Preliminary calculations indicated that the base of the gas hydrate stability zone at this location occurs at or slightly below the base of the HBL. Because of uncertainty about its boundaries, Moridis and Reagan (2007a;b) investigated production from the Tigershark deposit both as a Class 2 deposit (HBL overlying a mobile water zone) and a Class 3 system (HBL bounded by impermeable strata, with no underlying zone of mobile fluids). They showed that the presence of near-impermeable boundaries can yield very high

rates (as high as 17 MMSCFD in Class 2, up to 15 MMSCFD in Class 3). However, sensitivity analysis (Reagan et al., 2008; Boswell et al. 2009) indicated that lack of impermeable boundaries can dramatically reduce gas production (Figure 2), while yielding very large amounts of water. Here we investigate the production potential of the Tigershark formation under the hypothesis of a worst-case scenario, i.e., absence of impermeable boundaries, and contact of the hydrate layer with practically infinite aquifers.

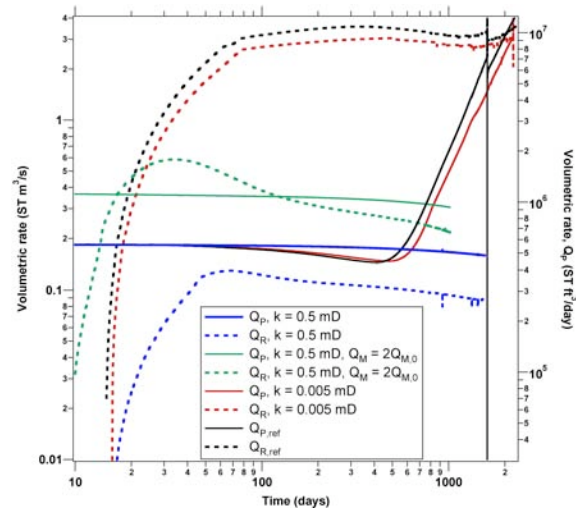


Figure 2. Effect of boundary permeability on gas production from a Tigershark Class 3 deposit (Reagan et al., 2008).

This study involves horizontal wells because of their significant advantages over vertical wells in production from Class 2 and Class 3 deposits (Moridis and Reagan, 2008). We investigated two different horizontal well designs. The single-well of the first design (Figure 3) provides heat to the hydrate-bearing sediment (HBS) by means of hot water that circulates inside the wellbore without coming in contact with the hydrate. The resulting higher T is expected to promote hydrate dissociation and gas production through the configuration of Figure 3 that operates at a pressure P_w that is slightly lower than the initial pressure P_0 . By avoiding direct injection of the warm water into the HBS we do not create adverse relative permeability conditions for the flow evolving gas, and the mild depressurization limits the water production. The second design is akin to that used in heavy oil production, and involves two parallel horizontal wells. Heat (through circulation of warm water, electrical or microwave heating, or direct water injection into the HBL) is added to the HBL through the lower well, while the upper well (positioned on the same vertical plane) is the gas collection well operates at a mild depressurization regime. In both well designs, the source of the warm water is assumed to be a deeper warmer reservoir.

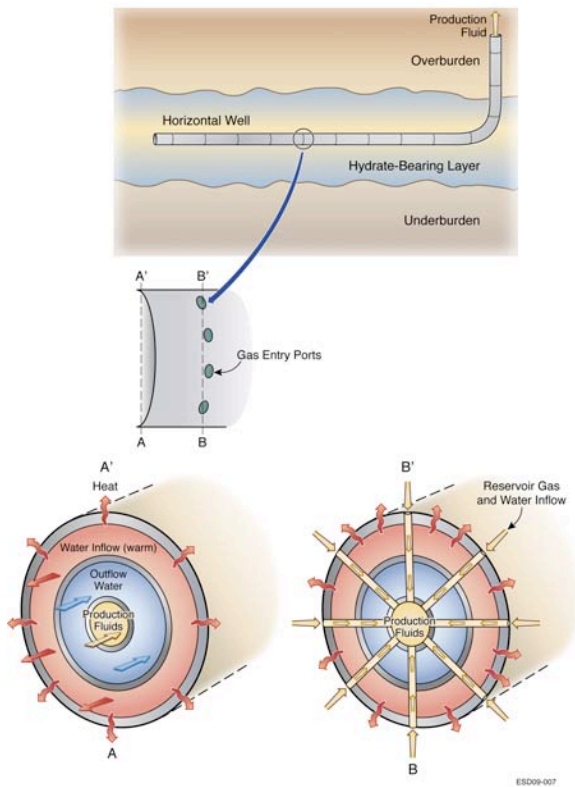


Figure 3. The new well design for concurrent heat addition and gas production.

We conducted the simulations using the TOUGH+HYDRATE code (Moridis et al., 2008). This code can model the non-isothermal hydration reaction, phase behavior, and flow of fluids and heat under conditions typical of natural CH₄-hydrate deposits in complex geologic media. It includes both an equilibrium and a kinetic model of hydrate formation and dissociation. The model accounts for heat and up to four mass components (i.e., water, CH₄, hydrate, and water-soluble inhibitors such as salts or alcohols) that are partitioned among four possible phases: gas, aqueous liquid, ice, and hydrate. A total of 15 states (phase combinations) can be described by the code, which can handle any combination of hydrate dissociation mechanisms.

We used 2-D grids because of symmetry. The unstructured hybrid grids used in the simulations are shown in Figures 4 and 5, and comprised 47,000 and 27,000 elements, respectively (resulting in 288,000 and 108,000 coupled equations). The system properties and initial conditions are as described by Moridis and Reagan (2007a;b) and shown in Table 1. Both grids had open top and bottom boundaries, i.e., the HBL was connected with the permeable overburden and underburden, allowing fluid and heat flow through the boundaries. The $x = 40$ m boundary was closed, indicating a well spacing of 80 m.

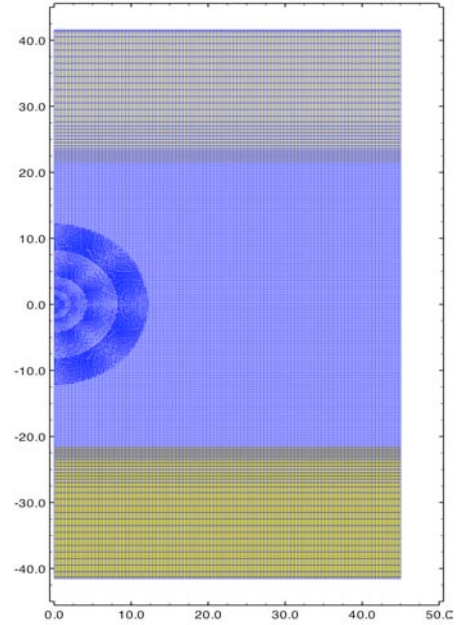


Figure 4. Grid used in the study of the performance of the new well design of Figure 3.

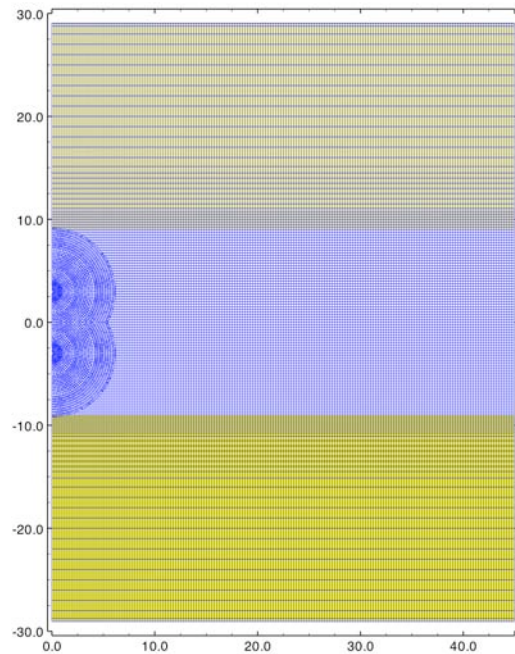


Figure 5. Grid used in the study of the performance of the two parallel horizontal well system.

THE SINGLE WELL DESIGN

In the evaluation of the single-well design, the reference case involved the sandy HBS ($k = 7.5 \times 10^{-13}$ m²) described in the Moridis and Reagan (2007a;b) study, and the temperature of the circulating hot water was $T_w = 90$ °C. Sensitivity analysis was investigated through the following additional cases: (a) $T_w = 120$ °C, (b) a silty medium with $k = 7.5 \times 10^{-14}$

m², (c) a clayey medium with $k = 7.5 \times 10^{-15}$ m², and (d) lower (by 10 °C) initial T , i.e., a more stable hydrate at the prevailing P .

Table 1. Physical properties and simulation parameters for the 2-D hydrate-bearing system.

Parameter	Value
Hydrate zone thickness	18.25 m
Initial pressure P_B (at base of HBL)	3.3×10^7 Pa
Initial temperature T_B (at base of HBL)	294.15 K (21 °C)
Gas composition	100% CH ₄
Initial saturations in the HBL	$S_H = 0.7, S_A = 0.3$
Water salinity (mass fraction)	0.03
Initial saturations in the HBL	$S_H = 0.7, S_A = 0.3$
Intrinsic permeability $k_r = k_z$ (HBS and boundaries)	7.5×10^{-13} m ² (= 0.75 D)
Grain density r_R (all formations)	2750 kg/m ³
Dry thermal conductivity	0.5 W/m/K
k_{QRD} (all formations)	
Wet thermal conductivity	3.1 W/m/K
k_{QRW} (all formations)	
Composite thermal conductivity model (Moridis et al., 2005)	$k_{QC} = k_{QRD} + (S_A^{1/2} + S_H^{1/2})(k_{QRW} - k_{QRD}) + f S_I k_{QI}$
Capillary pressure model (vanGenuchten, 1980)	$P_{cap} = -P_0 \left[(S^*)^{-1/\lambda} - 1 \right]^{-\lambda}$ $S^* = \frac{(S_A - S_{irA})}{(S_{mA} - S_{irA})}$
S_{irA}	1
l	0.45
P_0	10^5 Pa
Relative permeability Model (Moridis et al., 2008)	$k_{rA} = (S_A^*)^n$ $k_{rG} = (S_G^*)^n$ $S_A^* = (S_A - S_{irA}) / (1 - S_{irA})$ $S_G^* = (S_G - S_{irG}) / (1 - S_{irA})$
n (from Moridis and Reagan, 2007a;b)	3.572
S_{irG}	0.02

The Reference Case and the $T_w = 120$ °C Case

Figure 6 to 9 show respectively the evolutions of the following variables over time: P , T , S_H and S_G . The very low pressure drop ΔP (Figure 6) is evident in that it creates an anomaly fully confined in a limited zone around the well. This is caused by the low effective permeability k_{eff} of the HBL in the area surrounding the dissociated zone (Figure 8). As expected, the temperature disturbance does not propagate far from the well because of the limited efficiency of conduction as the main heat transfer

mechanism, and the rate of its propagation declines significantly over time as the volume around the well increases as a function of r^2 . A direct consequence of the limited advance of the temperature front is the limited extent of the dissociated region (Figure 8).

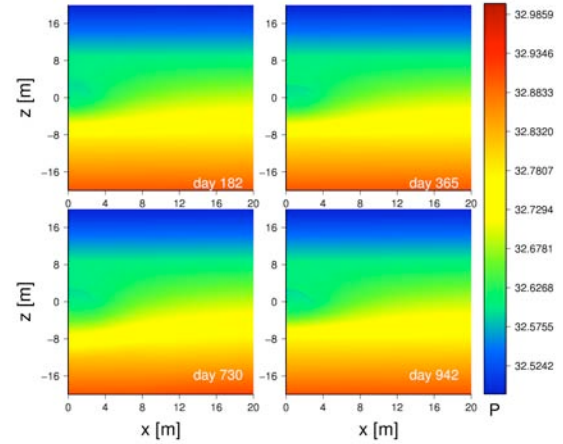


Figure 6. Evolution of pressure P over time during production from the single well of Figure 3.

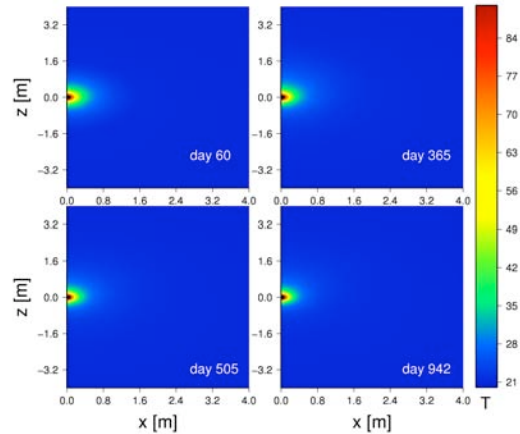


Figure 7. Evolution of temperature T during production from the single well of Figure 3.

Of particular interest is the high- S_H region immediately ahead of the dissociation front (Figure 8). This occurs because the edge of this front is the locus of local maximum of P in the system, with fluids moving both away and toward the well. Gas moving deeper into the hydrate body (away from the well) encounters conditions that are conducive to secondary hydrate formation that result in S_H higher than the initial one. The S_G distribution in Figure 10 indicates that practically all the dissociated gas that has not been produced is trapped within the hydrate-free cylindrical zone defined by the dissociation front. Because of buoyancy, gas accumulates at the top of the cylindrical dissociated zone, while the water released from dissociation drains and accumulates at the bottom of the cylindrical hydrate-free zone.

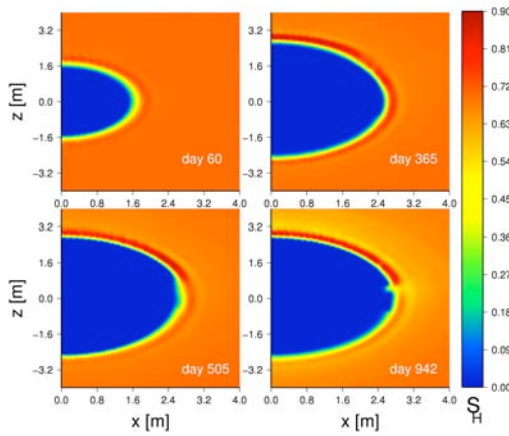


Figure 8. Evolution of hydrate saturation S_H during production from the single well of Figure 3.

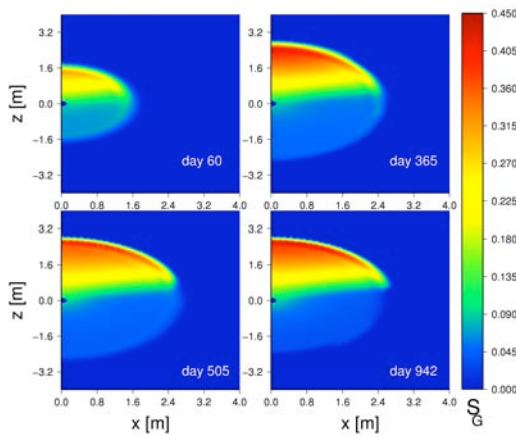


Figure 9. Evolution of gas saturation S_G during production from the single well of Figure 3.

Figure 10 shows the volumetric rates (per linear m of the horizontal well) of CH_4 (a) release Q_R , (b) production in the gas phase Q_{PG} , and (c) total gas production Q_{PT} , i.e., both in the gas and aqueous phase for the $T_w = 90^\circ\text{C}$ and 120°C cases. Note that Q_{PT} exceeds Q_R , and that the majority of the produced gas comes from CH_4 dissolved in the water rather than from the free gas phase, and that. The production rates appear to be quite low, even if we assume that all the dissolved CH_4 (a very significant fraction of Q_{PT}) is recovered. Additionally, the higher T_w appears to have a limited effect on gas production, increasing Q_{PT} only slightly over the 90°C case. The corresponding water production rates Q_w and gas-to-water ratios $R_{GW} = V_P/M_w$ in Figure 12 show the larger T_w has slight (if any) practical effect, that water production is manageable and that the R_{GW} is not prohibitively low. However, for a 1000 m well, long-term $Q_{PT} < 7,000 \text{ ST m}^3$ (245 MSCFD), and about 40 times lower than the rule-of-thumb for commercially viable production rates from offshore gas wells.

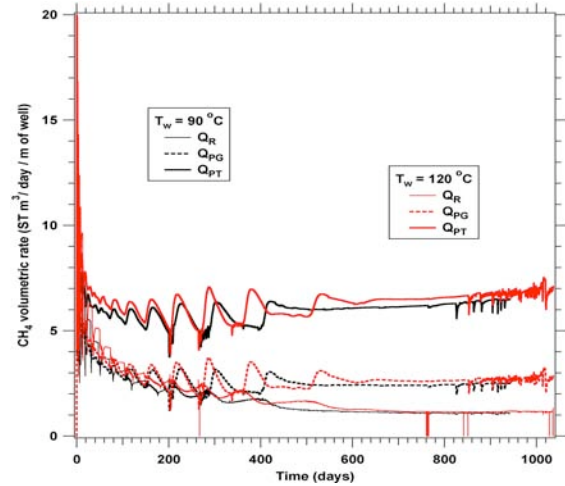


Figure 10. Evolution Q_R , Q_{PG} and Q_{PT} during production from the single well of Figure 3.

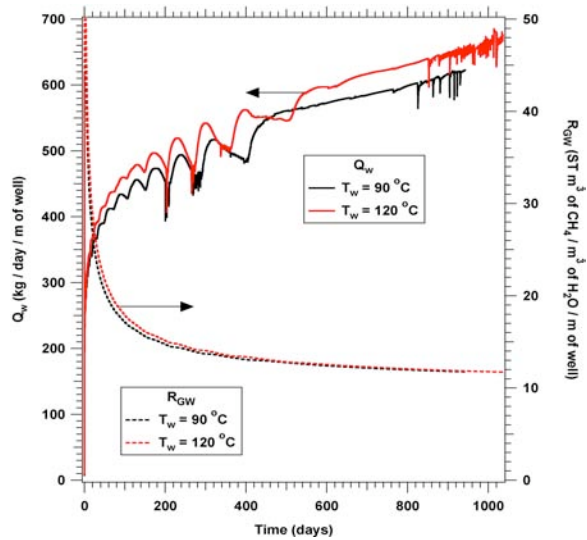


Figure 11. Evolution Q_w and R_{GW} during production from the single well of Figure 3

Effect of Finer Texture-Media (Lower k)

Figure 12 shows Q_R , Q_{PG} , and Q_{PT} in (a) the reference case of a sandy HBL, (b) the case of a silt, (c) a clay with a low well pressure drop $\Delta P_w = 1 \text{ atm}$ (Case Clay-LP), and (d) a clay case of a higher $\Delta P_w = 5 \text{ atm}$ (case Clay-HP). The decreasing permeability k and increasing capillary pressure P_{cap} of a progressively finer texture (moving from a sand to a clay) leads to an increasing Q_R , but a decreasing Q_{PT} . Thus, Q_{PT} from the sandy system (already quite low) is the highest of all cases. Additionally, the contribution of production in the gas phase Q_{PG} increases with a decreasing permeability. As expected, the higher ΔP_w leads to higher Q_R , Q_{PG} , Q_{PT} , Q_w , and R_{GW} , but Q_{PT} is still lower than that for the sandy HBS.

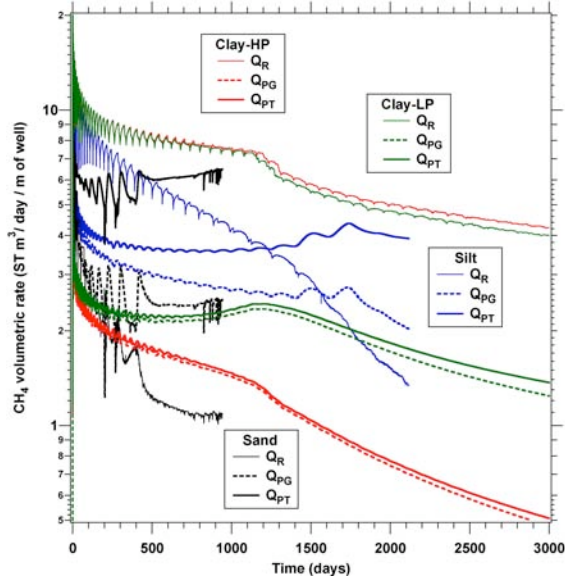


Figure 12. Effect of HBS texture on Q_R , Q_{PG} and Q_{PT} during production from the single well.

The corresponding Q_w and R_{GW} in Figure 13 show that water production increases with the fineness (decreasing k and increasing P_{cap}) of the HBS texture, but R_{GW} exhibits the opposite pattern. The high R_{GW} in silt and clay systems (relative criterion) cannot compensate for the low production (absolute criterion).

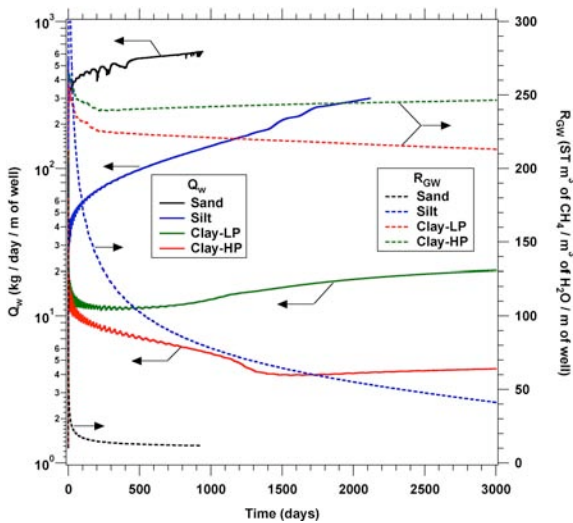


Figure 13. Effect of HBS texture on Q_w and R_{GW} during production from the single well.

Effect of Temperature

Figure 14 shows Q_R , Q_{PG} , and Q_{PT} in a silty HBL with (a) the reference initial $T_0 = 21\text{ }^\circ\text{C}$, and (b) in a colder system with $T_0 = 11\text{ }^\circ\text{C}$ at the same pressure, and indicates that lower T_0 results in significantly lower gas production. Additionally, Figure 15 indicates that the lower Q_{PT} of the colder case is further

burdened by a lower R_{GW} despite a decreasing Q_w . This was expected because the k_{eff} and the corresponding Q_w remain low during the longer time it takes for the colder (and thermodynamically more stable) HBL to reach the dissociation temperature at the prevailing pressure.

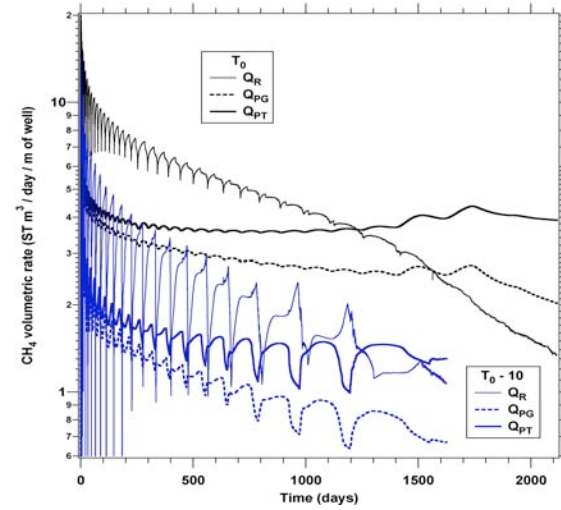


Figure 14. Effect of temperature on Q_R , Q_{PG} and Q_{PT} during production from the single well.

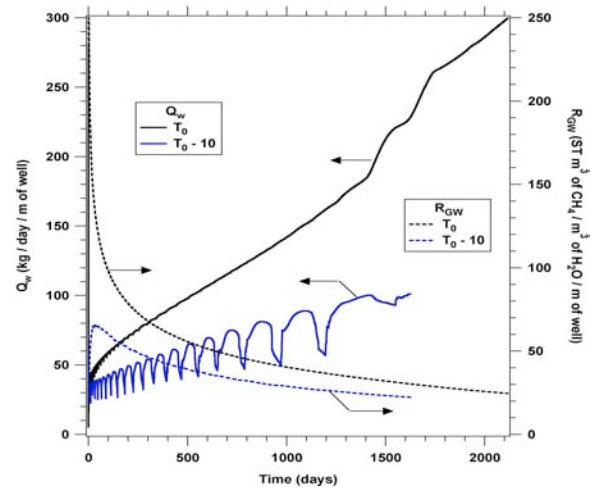


Figure 15. Effect of temperature on Q_w and R_{GW} during production from the single well.

THE TWO-WELL DESIGN

We study the following cases, all involving sandy systems: (a) Case A, with hot water ($T_w = 90\text{ }^\circ\text{C}$) circulating in the lower well (LW) without entering the HBL, and the upper well (UL) operating at a $\Delta P_w = 1\text{ atm}$, (b) Case B1, with heat added to the HBL at a rate of 1000 W/m , and a $\Delta P_w = 1\text{ atm}$ at the UW, (c) Case B2, differing from B1 in that $\Delta P_w = 0.2 P_0$, (d) Case C1, with warm water ($T_{iw} = 60\text{ }^\circ\text{C}$) injected into the HBL through the LW at a rate of $Q_{iw} = 5 \times 10^{-3}\text{ kg/s/m}$ of the well, and $\Delta P_w = 1\text{ atm}$ at the UW, (e)

Case C2, differing from C1 in that $\Delta P_w = 0.1 P_0$, and (f) Case C3, differing from C1 in that $\Delta P_w = 0.2 P_0$.

Cases A, B1 and B2

Figure 16 shows that in Cases A and B1, no CH_4 is ever produced in the gas phase ($Q_{PG} = 0$), i.e., all the produced gas originated from CH_4 dissolved in the aqueous phase. The low Q_{PT} ceases completely after only about 52 days. Q_R continues past that time because of the continuous heat addition, but this does not lead to continuous gas production because the released gas remains trapped in a dissociated, hydrate-free cylindrical zone that is surrounded by hydrate at very high saturations that exceed the initial S_H (Figure 17). This is caused by gas from dissociation moving into the HBL and creating secondary hydrates that reach levels resulting in a reduction of k_{eff} to practically zero. Note that secondary hydrates are also formed around the producing UW. In Figure 17, the gas and water accumulation at the top and the bottom, respectively, of the isolated cylindrical zone are evident.

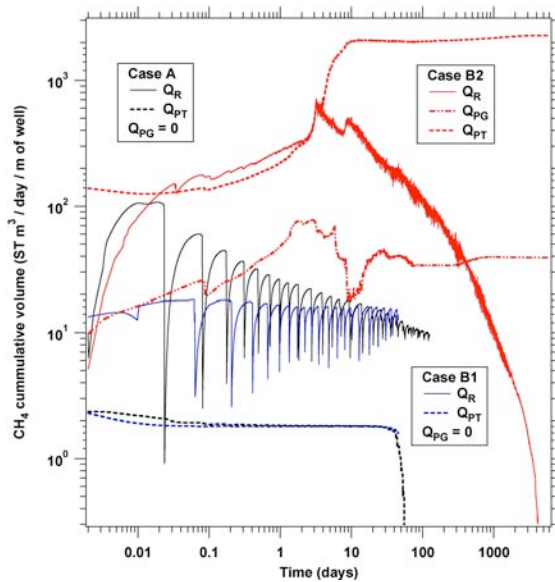


Figure 16. Evolution of Q_R , Q_{PG} and Q_{PT} during production from the two-well system (Cases A, B1, and B2).

Figure 18 confirms the creation of the isolated zone by showing Q_w declining to zero at the same time that Q_{PT} tends to zero. This was expected because no free gas is ever produced, and flow of the aqueous phase is necessary to obtain the dissolved CH_4 (the only gas source in these cases).

Case B2 appears very different. Figure 16 indicates order of magnitude higher Q_R and Q_{PT} in addition to a large Q_{PG} , all of which are attributable to the stronger depressurization (as the thermal regime remains the same). Thus, the thermal

stimulation in the LW serves only to develop an initial Q_R reaches a maximum after about 3 days, and then declines continuously until it is reduced to zero after about 4,000 days when the hydrate is exhausted. Q_{PG} is practically constant after about 60 days, while Q_{PT} exhibits a jump at 3 days (corresponding roughly to the depressurization front reaching the upper boundary of the HBL), and remains practically constant after 10 days.

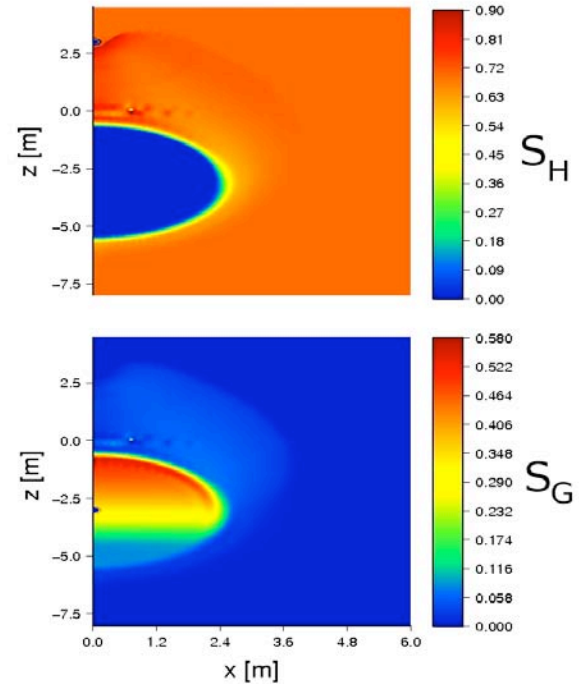


Figure 17. Distribution of S_H and S_G during production from the two-well system at $t = 60$ days (Case A).

This is confirmed by Figure 18, which shows a step increase in Q_w at $t = 3$ days, and a constant Q_w after about 10 days that corresponds to a significant reduction in R_{GW} . Thus, Q_{PT} for a 1000 m well system reaches a long-term near-constant level of 2.2×10^6 ST m^3/day (76 MMSCFD), this is hampered by a large water production.

The reason for this promising Q_{PT} performance is the effectiveness of depressurization as a dissociation method, as demonstrated by the S_H distribution over time in Figure 19. The corresponding P and T distributions in Figures 20 and 21, respectively, show the establishment of a steady state pressure regime (because of the permeable boundaries) and the negligible effect of the warm water injection, which appears to be completely overwhelmed by the effects of depressurization (evident by the changes in the T

distribution over time in the vicinity of, and within, the hydrate body).

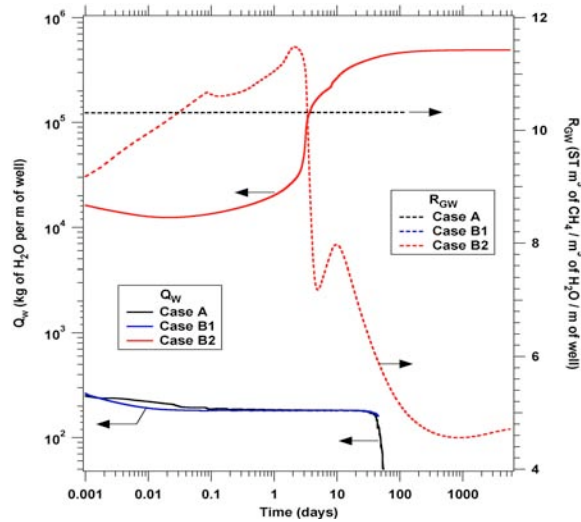


Figure 18. Evolution of Q_R , Q_{PG} and Q_{PT} during production from the two-well system (Cases A, B1, and B2).

Cases C1, C2 and C3

The Q_R , Q_{PG} , and Q_{PT} in Figure 22 indicate that, in Case C1, warm water injection appears to have a worse overall effect than the heat addition methods in Cases A and B1. As in these cases, no CH_4 is ever produced in the gas phase ($Q_{PG} = 0$), but the low Q_{PT} ceases completely after 21.6 days because of significant secondary hydrate creation around the UW and around the hydrate-free cylindrical zone of complete dissociation (Figure 23), which brings k_{eff} down to zero levels at these locations. The Q_R curve is entirely analogous to that of Case A in Figure 16, as are the S_H and S_G distributions in Figure 20.

The Q_R , Q_{PG} , and Q_{PT} of Case C3 in Figure 22 are indistinguishable from those in Case B2, indicating (a) large production potential for this approach, and (b) that the heat addition method plays a minimal role in the pattern of the system response (and possibly only to create an initial high- k_{eff} zone to allow further dissociation by means of depressurization). Figure 24 shows the similarity of the Q_W and R_{GW} between Cases A, B1 and C1, in addition to the practical coincidence of the system behavior in Cases B2 and C3.

Case C2 appears quite different. While its Q_R , Q_{PG} , and Q_{PT} curves in Figure 19 initially appear to track those for Case C2 (albeit at a lower level because of the lower ΔP_w), Q_R and Q_{PG} are reduced to zero levels after 34 and 18 days, respectively, because ΔP_w is insufficient to prevent the formation of an isolated hydrate-free zone surrounded by high S_H . Water production continues past this point because the flow to the UW is not blocked (Figure

24), but Q_{PT} is reduced because dissolved gas is the only source of CH_4 .

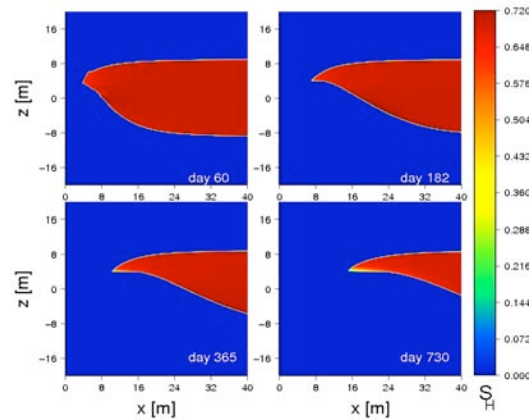


Figure 19. Evolution of hydrate saturation S_H distribution during production in Case C3.

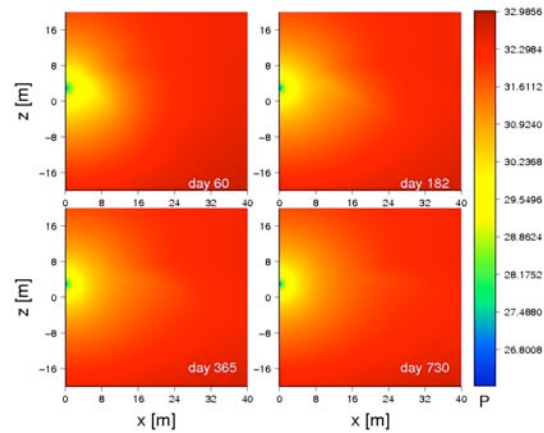


Figure 20. Evolution of pressure P distribution during production in Case C3.

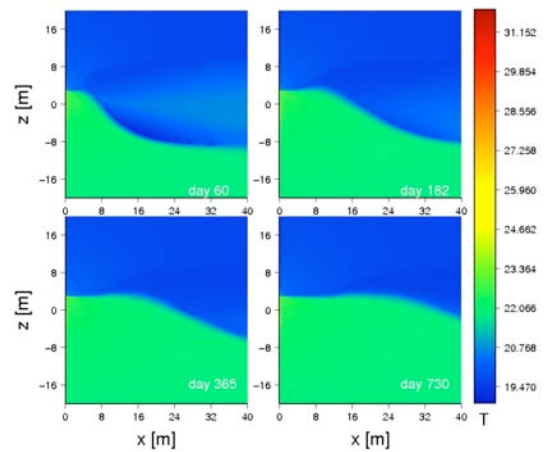


Figure 21. Evolution of reservoir temperature T distribution during production in Case C3.

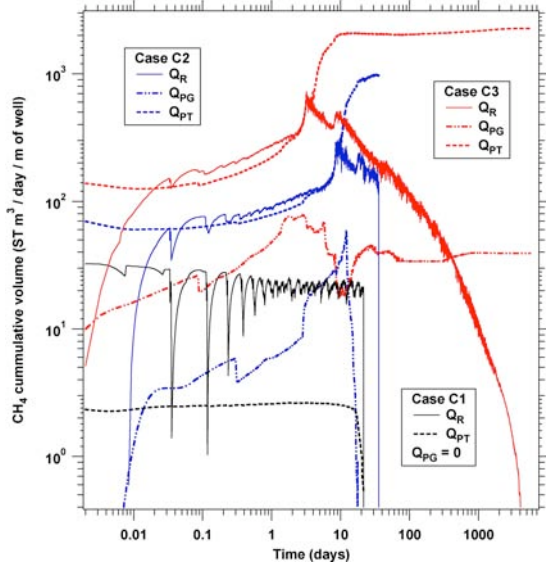


Figure 22. Evolution of Q_R , Q_{PG} and Q_{PT} during production from the two-well system (Cases C1, C2, and C3).

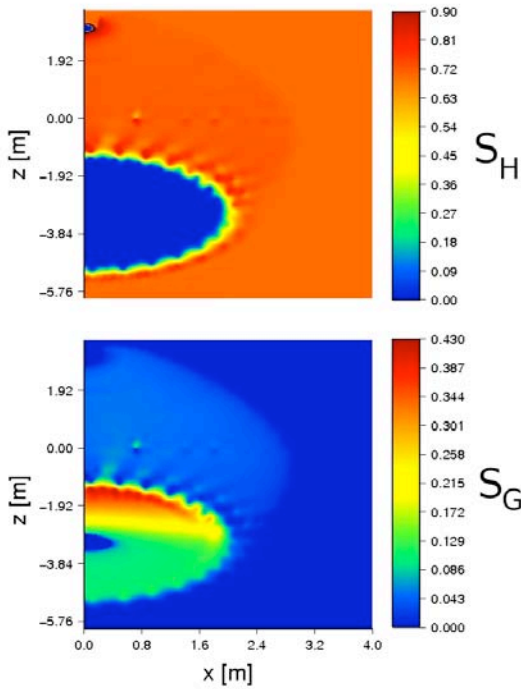


Figure 23. Distribution of S_H and S_G during production from the two-well system at $t = 21.6$ days (Case C1).

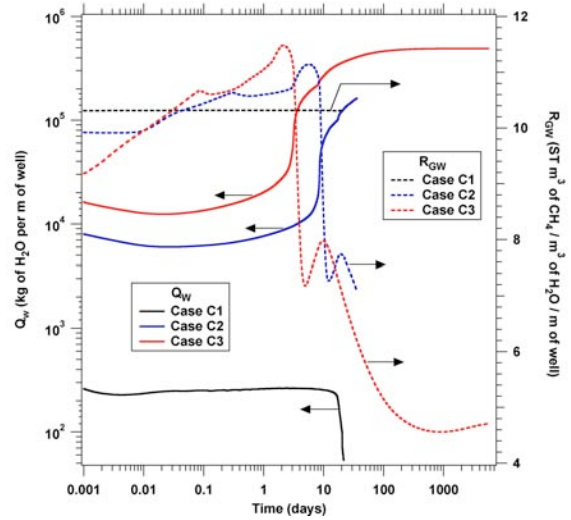


Figure 24. Evolution of Q_R , Q_{PG} and Q_{PT} during production from the two-well system (Cases C1, C2 and C3).

CONCLUSIONS

We reach the following conclusions from this study:

- The use of the new, single-well design involving concurrent HBL heating and production from different segments along the same wellbore does not appear a promising solution to the problem of production from challenging hydrates because it results in very low gas production rates and unfavorable gas-to-water ratios.
- Using the new, single-well design, production increases with the coarseness of the HBS (i.e., with an increasing k and P_{cap} , thus favoring sandy over silty and clayey HBS) and with the initial temperature of the deposit. Using a lower well (bottomhole) pressure P_w increases gas production, but it also increases the undesirable water production.
- If the P_w of the UW is maintained at levels very close to P_0 , the two parallel horizontal well system appears to be very ineffective, resulting in very short production times before flow to the UW is blocked by secondary hydrate that brings the k_{eff} to zero levels.
- If $P_w = 0.8 P_0$ in the UW, then depressurization is by far the dominant process and effective dissociation occurs, resulting in high gas production rates (up to 76 MMSCFD). However, the gas production is accompanied by a large water production.

ACKNOWLEDGMENT

This work was supported by the Assistant Secretary for Fossil Energy, Office of Natural Gas and Petroleum Technology, through the National Energy Technology Laboratory, under the U.S. Department of Energy, Contract No. DE-AC02-05CH11231. The

authors are indebted to John Apps and Dan Hawkes for their careful review.

REFERENCES

- Boswell, R., D. Shelander, M. Lee, T. Latham, T. Collett, G. Guerin, G. Moridis, M. Reagan and D. Goldberg, Occurrence of gas hydrate in Oligocene Frio sand: Alaminos Canyon Block 818: Northern Gulf of Mexico, *J. Mar. Pet. Geo.*, 26, 8, 1499-1512, 2009.
- Moridis, G.J., Numerical Studies of Gas Production from Methane Hydrates, *SPE Journal*, 32(8), 2003.
- Moridis, G.J., Seol, Y., and T. Kneafsey, Studies of reaction kinetics of methane hydrate dissociation in porous media (Paper 1004), *Proceedings of the 5th International Conference on Gas Hydrates*, Trondheim, Norway, 12-16 June 2005.
- Moridis, G.J., and M.T. Reagan, Strategies for Gas Production From Oceanic Class 3 Hydrate Accumulations, OTC-18865, *Proceedings of the 2007 Offshore Technology Conference*, Houston, Texas, 30 April – 3 May, 2007a
- Moridis, G.J., and M.T. Reagan, Gas Production From Oceanic Class 2 Hydrate Accumulations, OTC 18866, *Proceedings of the 2007 Offshore Technology Conference*, Houston, Texas, U.S.A., 30 April–3 May 2007.
- Moridis, G.J., Kowalsky, M.B., and K. Pruess, *TOUGH+HYDRATE v1.0 User's Manual: A Code for the Simulation of System Behavior in Hydrate-Bearing Geologic Media*, Report LBNL-0149E, Lawrence Berkeley National Laboratory, Berkeley, CA.
- Reagan, M.T., Moridis, G.J., and Zhang, K., Sensitivity Analysis of Gas Production from Class 2 and Class 3 Hydrate Deposits, OTC 19554, *Proceedings of the 2008 Offshore Technology Conference*, Houston, Texas, USA, 5-8 May 2008.
- Sloan, E.D. and C. Koh, *Clathrate Hydrates of Natural Gases*, CRC Press, New York, NY, 2008.
- Van Genuchten, M.T., A closed-form equation for predicting the hydraulic conductivity of unsaturated soils, *Soil Sci. Soc.*, 44, 892-898, 1980.

REACTIVE TRANSPORT MODELS OF STRUCTURALLY CONTROLLED HYDROTHERMAL DOLOMITE IN CARBONATE RESERVOIRS

Ipsita Gupta, University of South Carolina
Gareth D. Jones, Chevron Energy and Technology Company
Eric Sonnenthal, Lawrence Berkeley National Laboratory

ABSTRACT

Hydrothermal dolomitization is the dominant control on reservoir quality in several hydrocarbon accumulations—for example, the Ordovician Trenton-Black River trend in the USA and Ladyfern and Clarke Lake fields in the Devonian of Canada. Furthermore, there is increasing recognition of hydrothermal modification in several giant Middle East reservoirs, including Ghawar in Saudi Arabia and the North Field in Qatar. Structurally controlled hydrothermal dolomitization describes the replacement of limestone with dolomite and/or the precipitation of dolomite cement and associated Mississippi Valley-type minerals (anhydrite, sulfides, quartz and fluorite) as a consequence of subsurface brines that ascend upwards through extensional fault and fracture systems. The resulting fluid rock interaction in the burial environment has the potential to both improve and/or degrade reservoir quality, depending on the properties of the host rock and spatial position relative to structure.

In this study we used the numerical Reactive Transport Model TOUGHREACT, which couples fluid flow with chemical reactions to simulate hydrothermal dolomitization in a carbonate reservoir. Specifically, we investigated the sensitivity of hydrothermal dolomite to: fault permeability/flow rates of ascending fluids, reservoir heterogeneity (alternating high- and low-permeability strata), temperature of host rock and ascending fluids (including their temperature difference), fault spacing/multiple fault scenarios, fault vertical separation and strata juxtaposition, episodic versus continuous brine injection, and subsurface brine composition (in particular Na-Cl vs. Ca-Cl brines).

Results suggest that diagenetic changes due to hydrothermal dolomitization are a complex function of the hydrodynamics and fluid chemistry. Variations in fault and matrix permeability strongly control the spatial patterns of diagenesis. Convective flow generated as a consequence of temperature and brine-induced fluid-density variations further complicates the transport of reactants and the resultant diagenesis. Brine chemistry of both the host rock and the fault fluids affect the extent and distribution of dolomitization. In general, Na-Cl brines produce more dolomite than Ca-Cl brines, because of higher Mg/Ca ratios, but this result is salinity and temperature dependent. Interestingly, the down-thrown fault block is preferentially dolomitized in our simulations. Relay zones between faults can act as groundwater flow divides such that, depending on permeability variations, flow rates and timing of fault activation can remain undolomitized. For the systems simulated, hydrothermal dolomitization enhances matrix porosity and permeability; however, fault zones begin to seal due to the precipitation of anhydrite cement. Reactive Transport Models cannot currently simulate the development of breccias, which is often an important hydrothermal dolomite pore type.

Finally, we present preliminary results, including 3D simulations with multiple faults, to evaluate this predictive diagenesis technology as applied to improving our understanding of the distribution of hydrothermal dolomite in the Cretaceous Upper Toca Formation in Chevron's Kambala field, Angola.

Special thanks to Nic Spycher (Lawrence Berkeley National Laboratory) and Jason Francis (Chevron)

APPARENT STRATIGRAPHIC CONCORDANCE OF REFLUX DOLOMITE:
NEW PREDICTIVE CONCEPTS FROM HIGH-FREQUENCY CYCLE SCALE
SYNSEDIMENTARY REACTIVE TRANSPORT MODELS

Beatriz Garcia-Fresca¹, Gareth D. Jones², Tianfu Xu³

¹ Jackson School of Geosciences, The University of Texas at Austin

² Chevron Energy Technology Company

³ Lawrence Berkeley National Laboratory, Earth Sciences Division, Berkeley, California

ABSTRACT

Our Reactive Transport Model investigates the dolomitization potential of reflux brines at the high-frequency cycle scale. One-dimensional simulations were constrained by outcrops of the partially dolomitized Cretaceous Upper Glen Rose Formation in central Texas. Rock properties (porosity and permeability) were specified based on reconstructed depositional values that varied by facies, and the initial mineralogy was predominantly calcite. A brine was placed at the top boundary of the model and flowed downward, driven by density gradients (“reflux”) and progressively replaced calcite with dolomite. Precipitation of gypsum cement was a byproduct of the dolomitization process. Simulations predict that the top 1.5 m of a Glen Rose high-frequency cycle can be dolomitized in approximately 550 yrs with brine concentration four times that of seawater (~ 140 ppt), and confirm that reflux dolomitization can operate at time scales interpreted from the rock record. Sensitivity analyses demonstrated that the specified kinetic-rate constant of dolomite precipitation is a critical parameter; other variables tested (brine salinity, duration of brine source, and permeability) controlled the amount but not the occurrence of dolomite. Stratigraphic controls were investigated using a quasi-dynamic grid to simulate episodic brine reflux as three consecutive high-frequency cycles

were deposited. Our results reveal the potential for the complex evolution, migration, and convergence of multiple dolomite fronts. Discrete dolomite fronts separated by limestone intervals could advance simultaneously as the result of a single brine reflux event. The incomplete consumption of magnesium along a flow path and the variable rate of dolomitization due to the dolomite “seed-effect” are primarily responsible for this phenomenon. Both complete and partially dolomitized cycles were simulated in the range of sensible parameter space. These results suggest that the observed relationships between dolomite patterns and sequence stratigraphic surfaces may be casual, which challenges the current paradigm and has significant implications for interpreting diagenetic patterns. Future simulations will include 2D and 3D simulations of reflux dolomitization and other styles of carbonate diagenesis, with the goal of improving predictions of carbonate reservoir quality.

RELATED PUBLICATION

Garcia-Fresca, B and Jones G.D. (in review) Apparent stratigraphic concordance of reflux dolomite: New predictive concepts from high-frequency cycle scale synsedimentary reactive transport models. *Geology*. Submitted May 2009.

MODELING DYNAMIC INTERACTIONS BETWEEN GEOTHERMAL AND REFLUX CIRCULATION USING TOUGHREACT: THE IMPORTANCE OF TEMPERATURE IN CONTROLLING DOLOMITIZATION AND ANHYDRITE CEMENTATION

Anwar Al-Helal¹, Fiona F. Whitaker¹, Yitian Xiao²
¹Department of Earth Sciences, University of Bristol,
Bristol BS8 1RJ, England,
An.Alhelal@bristol.ac.uk
²ExxonMobil Upstream Research Company,
PO Box 2189, Houston TX 77027, USA

ABSTRACT

This study uses TOUGHREACT to investigate interactions between heat, solute and fluid flow driven by geothermal convection and brine reflux, and the resultant diagenesis in a generic carbonate platform. Reflux of brines (85‰) rapidly restricts geothermal convection to the margin, eliminating lateral temperature contrasts. Brines penetrate to >2 km depth within 1 M.y., but fluid flux is most rapid at shallow depth due to the initial permeability-depth relationship, specified anisotropy, and positive feedbacks among dolomitisation, porosity and permeability. Below the brine pool, dolomitization is complete to 150-200 m depth within 1 M.y., and beneath this extends a zone of partial dolomitization. In contrast, there is only minor dolomitization of the platform margin by geothermal convection.

Although reflux dolomitization significantly enhances reservoir quality at shallow depth, associated anhydrite precipitation occludes porosity beneath the main dolomite body. The predicted anhydrite volume is almost double that suggested by simulations that fail to incorporate heat transport, while the zone of partial dolomitisation beneath the main dolomite body is also greater. Increasing geothermal heat flux provides little support for geothermal circulation, but does accelerate rates of reflux diagenesis. Reduction of platform top temperature from 40 to 25°C results in slower reactions and downward displacement of the anhydrite diagenetic zone, which may become completely decoupled from the brine source.

When brine-generating conditions cease, subsurface brine flow will continue and has been suggested as a drive for continued dolomitisation (a variant of reflux circulation termed “latent reflux”). TOUGHREACT simulations demonstrate that latent reflux does not form a significant amount of dolomite due to prior Mg²⁺ consumption at shallow depth, although as geothermal circulation becomes re-established, platform margin dolomitization rates increase.

INTRODUCTION

Density-driven fluid flow occurs in carbonate platforms in response to geothermal heating and brine

reflux, and both of these systems have been invoked to explain early dolomitization. The drive for geothermal (Kohout) convection is the density gradient set up by spatial variations in temperature between ocean water and pore fluids warmed by the geothermal heat flux (GTHF, Figure 1). In the case of reflux, flow occurs in response to density gradients set up by spatial variations in salinity generated by evaporation of seawaters in restricted parts of the platform.

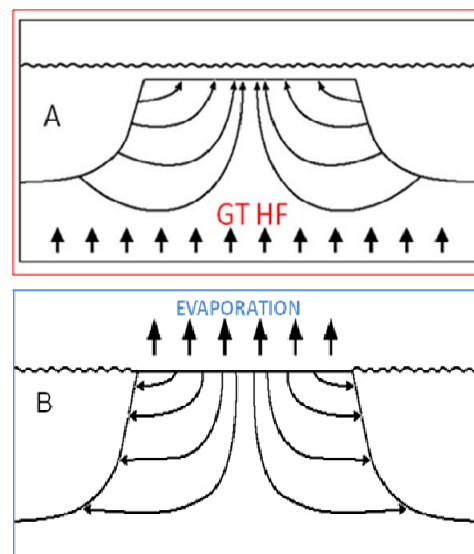


Figure 1. Conceptual model of geothermal (Kohout) convection (A) and brine reflux (B).

Previous reactive transport (RTM) simulations of carbonate diagenesis have focused on individual fluid flow mechanisms. Geothermal convection of normal seawater can form a wedge-shaped dolomite body which is thickest at the platform margin over a period of 10–30 M.y. (Whitaker and Xiao, 2009). When brines are present on the platform top, isothermal simulations of Jones and Xiao (2005) indicate that in <1 M.y. reflux of brines can drive relatively rapid reactions, with formation of a tabular dolomite body that thins away from the fluid source. All studies have shown formation of gypsum/anhydrite cements where sufficiently high temperatures occur downstream of the zone of dolomitisation, which provides a source of Ca²⁺.

However, in natural systems fluid flow is commonly a product of a number of different drives acting simultaneously. The balance between drives will change over time with variations for example, in relative sea-level and climate. To date, simulations of dolomitisation have assumed constant boundary conditions and thus fail to account for dynamic interactions between flow systems. Here, we use TOUGHREACT to investigate dynamic interactions between geothermal and reflux systems, their impact on dolomitisation and anhydrite cementation, and the importance of temperature as a controlling factor in a generic carbonate platform.

METHODS

Flow was simulated in a 2D linear (Cartesian) coordinates flow domain representative of half of an isolated carbonate platform, assuming flow is symmetrical. The shelf measures 25 km from the interior to the margin, with a steep margin sloping down into a 2 km deep basin. The grid system comprises 2964 active blocks of non-uniformly specified node spacing ($x=50-500$ m $z= 5-50$ m). (Figure 2).

Right and left boundaries are specified as no-flow boundaries, while the lower boundary is closed to flow and solute transport but open to heat transport, with a specified heat flux of 60 mW/m^2 , representative of a passive margin setting. The upper boundary is a fluid-pressure boundary, allowing the recharge or

discharge of fluids at the platform top and slope. The temperature at the platform top is 40°C . In the basin temperatures decline exponentially with depth after Sanford et al. (1998).

Initial porosity declines exponentially with depth, based on core data for the Cenozoic and Mesozoic Florida carbonates (Schmoker and Halley, 1982). Permeability is derived from porosity based on grain-size-dependent relations of Lucia (1995). Permeability anisotropy is specified as 1000 based on flow-based scale-up simulations (Jones 2000). Diagenetic changes in permeability are calculated from changes in porosity using the Carman-Kozeny relation, ignoring changes in grain size, tortuosity, and specific surface area.

The initial temperature and pressure reflects advective heat transport by geothermal convection. The fluids surrounding the platform are seawater evolved to equilibrium with respect to calcite. The brine pool temperature is set as 40°C and the salinity is 85‰ ($2.5 \times$ seawater), with Mg/Ca molar ratio of 5.6 and pH of 7.7, based on Ibis Pond, Lake MacLeod evaporite basin (Logan, 1987). Simulations incorporate three solid phases (calcite, dolomite and anhydrite), with initial mineralogy specified to be 99% calcite and 1% “seed” dolomite. Effective reactive surface area (RSA) is set as $10^3 \text{ cm}^2/\text{g}^1$, representative of packstone/wackestone (Lucia, 1995) and/or medium crystalline mud-dominated dolostone (Lucia, 2004).

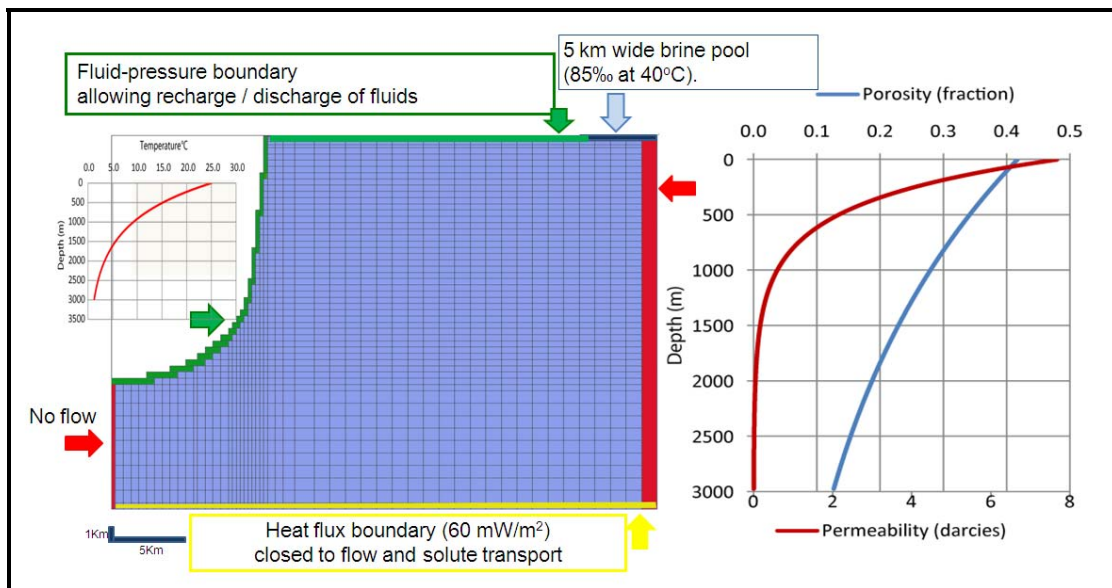


Figure 2: Numerical mesh, boundary and initial conditions for platform-scale reflux RTM. Porosity-depth curve based on data for Florida (Schmoker and Halley, 1982) and permeability derived using Class 2 (pack-wackestone) relationship from Lucia (1995).

Simulations assume that dolomitisation results from calcite dissolution and dolomite precipitation rather than a single reaction. Because dolomite precipitation is much slower than calcite dissolution and anhydrite precipitation, the latter are modeled as thermodynamic minerals. Dolomite precipitation is modeled as a kinetic process, using the rate equation of Arvidson and Mackenzie (1999; Equation 1).

$$r_{dol} = A_s A e^{\frac{-Ea}{RT}} \left(\frac{Q}{K_{eq}} - 1 \right)^{2.26} \quad (1)$$

where r_{dol} is the reaction rate of dolomite precipitation; A_s is the specific reactive surface area of dolomite; Q is the activity quotient; K_{eq} is the equilibrium constant for ordered dolomite, Q/K_{eq} ; define the saturation index; A is the pre-exponential factor (11.22 mol/cm^2); Ea is the activation energy ($1.335 \times 10^5 \text{ J/mol}$); R is the universal gas constant; T is the temperature (K) and 2.26 is the reaction order.

RESULTS

With development of a brine pool in the platform interior, the flow of cold ocean waters into the platform is rapidly reversed by refluxing brines. Chloride concentrations reflect the development of a large brine plume extending towards the margin, largely eliminating lateral temperature contrasts (Figure 3). However, magnesium concentrations decline rapidly at relatively shallower depth, due to consumption by dolomitisation beneath the brine pool.

Reflux leads to development of a tabular dolomite body, up to 200 m thick after 1 My (Figure 4B). This is underlain by a partially dolomitised zone where anhydrite cements form up to 20% of the total rock fraction. Anhydritisation occurs at temperatures $>40^\circ\text{C}$ where Ca^{2+} released by dolomitisation reacts with SO_4^{2-} in the brines. Thus, while dolomitisation enhances reservoir quality at shallow depth, beneath this, there is a net reduction in porosity and permeability. This has the effect of lateral focusing of flow and extending the dolomite body towards the platform margin.

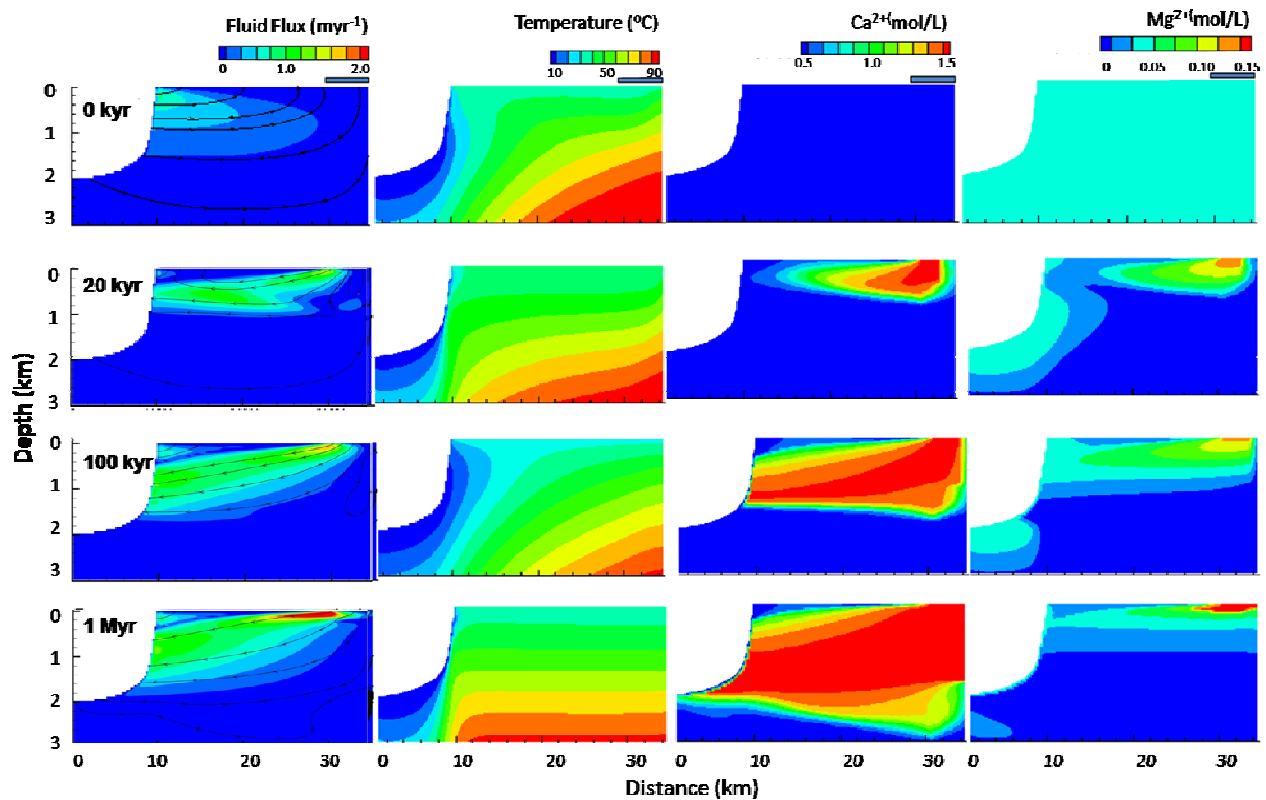


Figure 3. Evolution of fluid flux (illustrative streamlines), temperature, Ca^{2+} and Mg^{2+} concentrations for baseline simulations from initial geothermal convection, over 1 Myr of reflux from platform interior brine pool (blue bar).

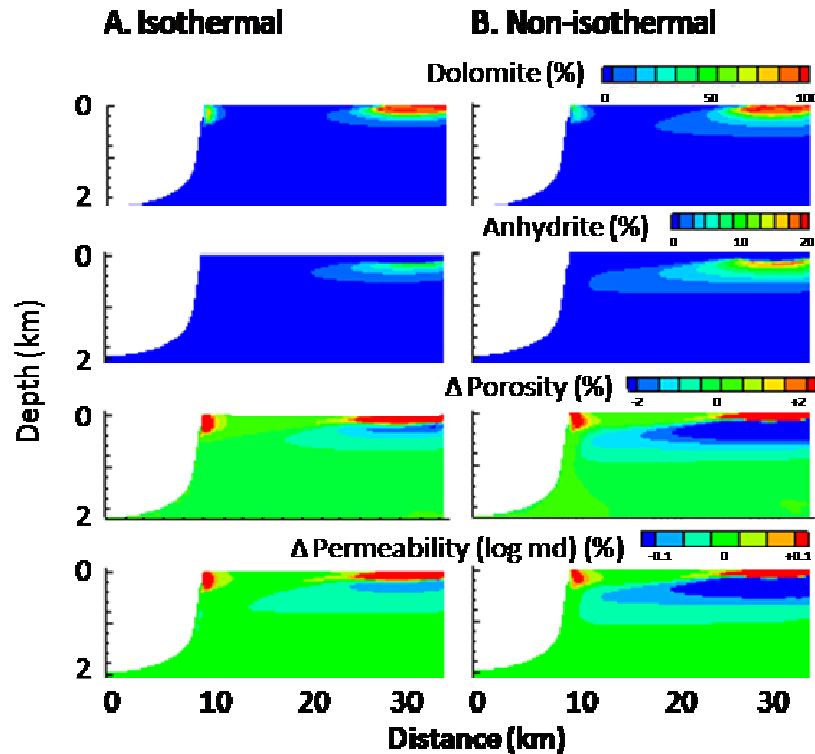


Figure 4: Comparison of dolomite and anhydrite abundance and change (Δ) in porosity and permeability after 1 Myr of reflux for isothermal simulation (A) and non-isothermal (baseline) simulation (B) for top 2 km of platform.

The difference between simulating brine reflux within a spatially variable temperature field and an equivalent isothermal simulation (at 40°C) is shown in Figure 4. Previous RTM studies of reflux dolomitisation by Jones and Xiao (2005) focused at shallow depth and assumed isothermal conditions. Where spatial and temporal constraints allow brines to reflux through thicker carbonate sequences, this assumption leads to considerable underestimation of the resulting diagenetic alteration. Additional dolomite and, more notably, anhydrite precipitation occurs due to gradient reactions as descending reflux brines are heated in the nonisothermal simulations. This has significant implications for porosity and permeability, and demonstrates why meaningful prediction of how reflux impacts reservoir quality demands consideration of spatial variations in temperature.

Given focusing of diagenetic reactions at shallow depth, the temperature of the platform top waters is of key importance (Figure 5). Reduction of the upper boundary temperature from 40°C to 25°C cools the entire platform. This dramatically reduces rates of dolomitisation and anhydritisation, and results in

significant downward displacement of the zone of porosity occlusion, which can become completely decoupled from the reflux dolomite body. This suggests that latitude is a key control on the diagenetic efficacy of reflux brines, with increased solar insolation creating favorable temperatures, independent of any control on degree of evaporative concentration.

Maintaining a platform top temperature of 40°C, we have also investigated the sensitivity of dolomitisation and anhydritisation to varying the heat flux, by $\pm 20 \text{ mW/m}^2$ (results not shown). While the crustal heat flux alters the temperature at the base of the platform and the thermal gradient, the effect on the shallow dolomite body is minor. With a higher heat flux, anhydrite is slightly more abundant (maximum 18% at 40 mW/m^2 compared to 22% at 80 mW/m^2).

Brine generation is sensitive to changing sea-level and temporal variations in the salinity of platform top waters would affect reflux. Jones et al. (2002) used a hydrological model to demonstrate that refluxed

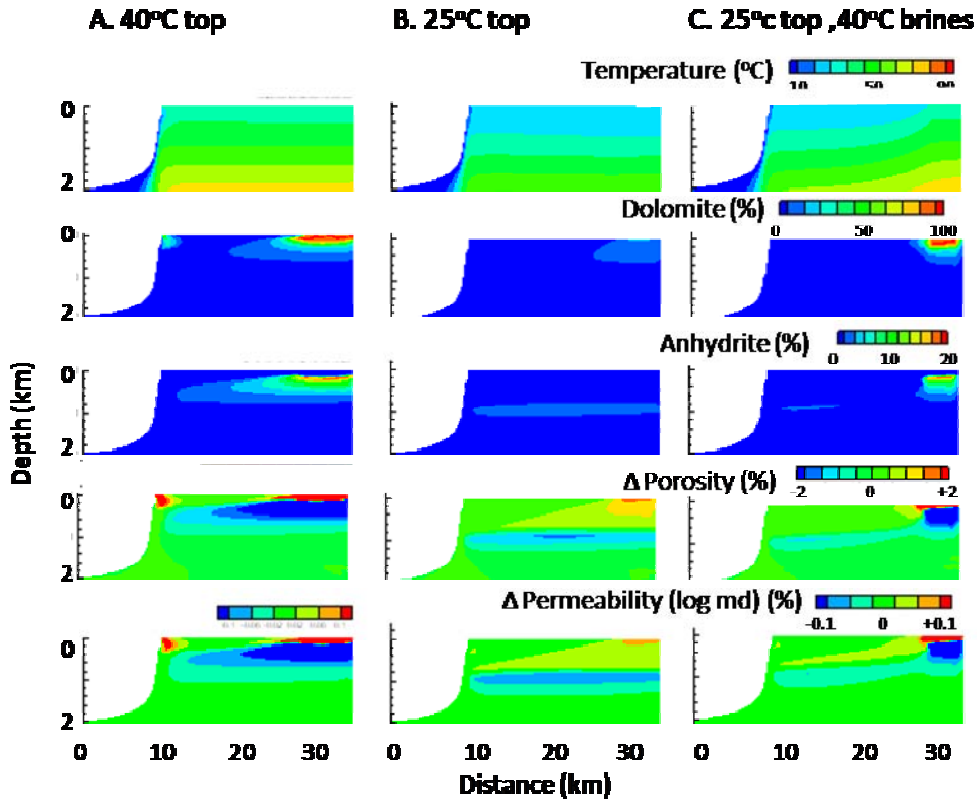


Figure 5: Sensitivity of dolomite and anhydrite abundance and change in porosity and permeability after 1 Myr to upper boundary temperature. Platform top at 40°C (A), 25°C (B and C), with brine pool at 40°C (C). Plot for top 2 km of platform

brines would continue to move through the platform after brine generation had ceased (a variant termed “latent reflux”) and could deliver a significant quantity of Mg^{2+} for dolomitisation. After 1 M.y. of reflux, brine generation was turned off and normal seawater specified for the entire platform top boundary (time 0, Figure 6). Over the next 1 M.y. brines continue to sink into the platform and discharge to the ocean basin (latent reflux). Above the brine plume, geothermal convection gradually extends, drawing seawater into the platform predominantly via the platform margin. This results in dolomitisation of the margin, but in the interior, flow rates are relatively low and fluids are Mg^{2+} -depleted due to prior reaction, limiting further dolomitisation. Although the direct diagenetic impact of latent reflux is rather limited (note 10x change in scale for change in dolomite in Figure 6), the persistence of brines within the platform has long-term implications for geothermal circulation.

CONCLUSIONS

Reactive transport models offer considerable potential for improving our understanding of diagenetic reactions and their impact on reservoir quality in such hybrid flow systems. However, the veracity and

utility of predictions depend on specification of meaningful boundary and initial conditions. In particular, temperature regime appears to play a critical role in prediction of dolomitisation and anhydritisation.

Reflux rapidly restricts geothermal circulation of the platform margin, and drives much more rapid dolomitisation close to the brine source. Variations in platform temperature are important in controlling the distribution and extent of reflux dolomitisation and anhydritisation, with significant implications for the evolution of porosity and permeability. Isothermal simulations systematically under-predict the extent of reflux diagenesis. Because reflux diagenesis is focused at shallow depth, it is more critical to correctly specify platform top temperatures than crustal heat flux.

Results are dependent upon specification of thermal conductivity within TOUGHREACT. This is currently tied to initial depth-dependent porosity, but improved predictions require incorporation of feedbacks among porosity, mineralogy and effective thermal conductivity.

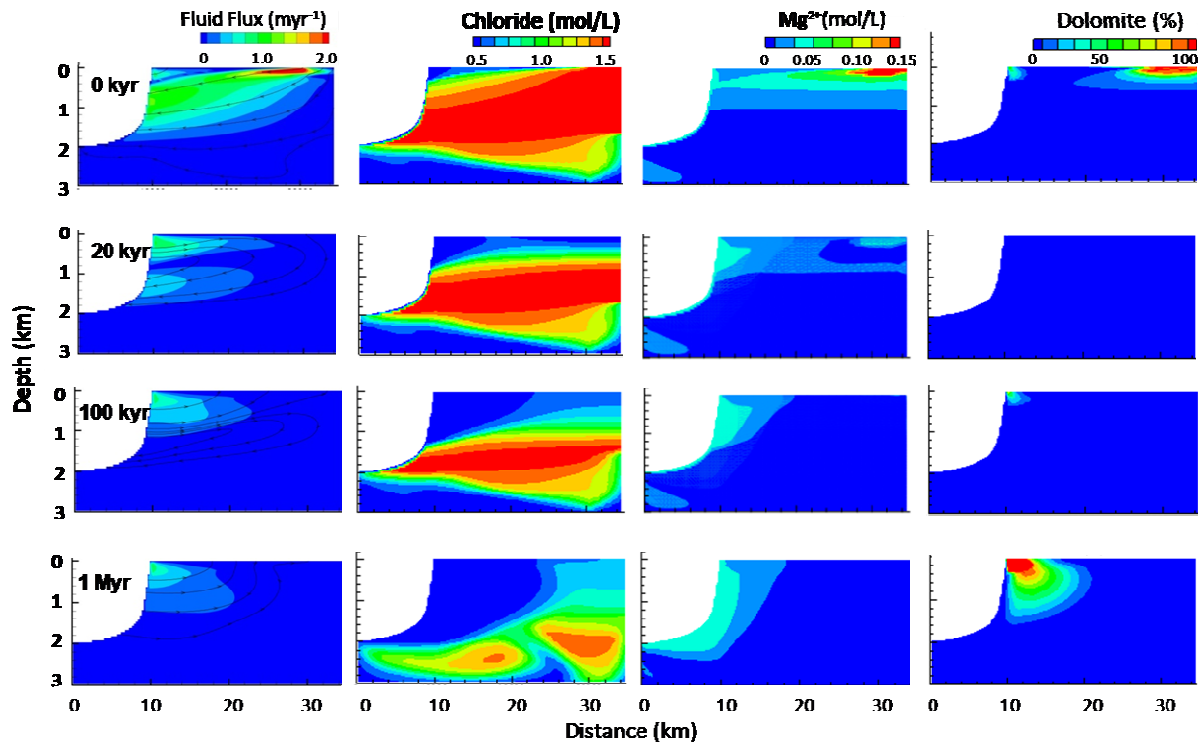


Figure 6. Fluid flux (illustrative streamlines), Cl^- and Mg^{+2} concentrations and change in dolomite abundance during latent reflux following 1 My of reflux (baseline simulation gives initial dolomite abundance).

ACKNOWLEDGMENTS

Funding for this study was provided by the public authority for applied education and training 'Kuwait'. AA thanks the Kuwait Foundation for the advancement of Sciences (KFAS) for funding to attend the 2009 TOUGH symposium. FFW thanks ExxonMobil URC for supporting stimulating academic exchange visits between URC and Bristol. The views expressed in this paper by Yitian Xiao are his own and not necessarily those of ExxonMobil.

REFERENCES

- Arvidson, R. S., and Mackenzie, F. T., The dolomite problem: Control of precipitation kinetics by temperature and saturation state: *American Journal of Science*, 299, 257– 288. 1999
- Schmoker, J. W., and Halley, R. B., Carbonate porosity versus depth - A predictable relation for South Florida, *AAPG Bulletin*, 66, 2561-2570, 1982
- Jones, G. D., and Xiao, X., Dolomitization, anhydrite cementation, and porosity evolution in a reflux system: Insights from reactive transport models, *AAPG Bulletin*, 89, 577 – 601, 2005
- Jones, G. D., Whitaker, F. F., Smart, P. L., and Sanford, W. E., Fate of reflux brines in carbonate platforms, *Geology*, 30, 371-374, 2002
- Jones, G. D., and Rostron, B. J., Analysis of fluid flow constraints in regional-scale reflux dolomitization: constant versus variable-flux hydrogeological models: *Bulletin of Canadian Petroleum Geology*, 48, 230-245, 2000
- Logan, B.W., The MacLeod evaporite basin, Western Australia: *AAPG Memoir*, 44, 140 p., 1987
- Lucia, F. J., Origin and petrophysics of dolostone pore space, *Geological Society of London Special Publication*, 235, 141-155, 2004
- Lucia, F. J., Rock-fabric petrophysical classification of carbonate pore-space for reservoir characterization: *AAPG Bulletin* 79, 1275-1300, 1995
- Whitaker, F.F. and Xiao, Y., geothermal convection, a viable mechanism for early burial dolomitisation of platform carbonates: *AAPG Bulletin (in press)* 2009

GEOHERMAL CONVECTION: A VIABLE MECHANISM FOR EARLY BURIAL DOLOMITISATION OF PLATFORM CARBONATES?

Fiona F. Whitaker¹, Yitian Xiao²

¹Department of Earth Sciences, University of Bristol,
Bristol BS8 1RJ, England,
Fiona.Whitaker@bristol.ac.uk

²ExxonMobil Upstream Research Company,
PO Box 2189, Houston TX 77027, USA

ABSTRACT

Geothermal convection of seawater cools the margins of carbonate platforms, warming the interior. Previous reactive transport model (RTM) studies suggested this process can drive dolomitisation in the platform interior at depth at >50°C. However, extrapolation from short (0.1 Myr) simulations suggested complete dolomitisation requires at least 30–60 Myr. Our more extended (30 M.y) TOUGHREACT (Xu et al., 2006) simulations indicate significant nonlinearities in the system, with complete dolomitisation within 15 Myr. Reactions rapidly become flux controlled, forming a shallower wedge-shaped dolomite body that thins from the margin to the interior temperatures of 20–30°C.

Geothermal dolomitisation is relatively insensitive to changes in boundary conditions such as relative sea-level and platform geometry, but is slower in radial than linear platforms. Sediment permeability and reactive surface area (RSA), often inversely related, are key controls. Low fluid flux limits dolomitisation to the platform margin of low-permeability muddy platforms, despite high RSA. Dolomitisation of more permeable grainy platforms is limited by RSA and occurs only in the platform core, due to widespread platform cooling. Layering of sediment types produces a complex vertical diagenetic stratigraphy, favoring more reactive beds at shallow depth where permeability is not limiting, but switching to more permeable beds at depth. Bank-marginal fracturing limits dolomitisation of the interior, irrespective of whether the fractures are open or sealed.

INTRODUCTION

Dolomites are important hydrocarbon reservoirs, and the process of dolomitisation is a critical control on reservoir quality and consequent producibility. Dolomitisation also plays an important role in the secular changes in seawater chemistry through the Phanerozoic (Holland, 2005).

Most dolomites are considered secondary, formed by replacement of original limestone (Equation 1):



Despite the abundance of dolomite in the rock record and dolomite super-saturation of modern seawater, dolomites are rare in modern carbonate sediments. Laboratory experiments at elevated temperatures show dolomitisation rate depends on $Mg^{2+}:Ca^{2+}$ in solution, reactant mineralogy, RSA, temperature, and the presence of kinetic inhibitors, such as sulfate (see review by Machel, 2004).

Critically, dolomitisation also relies upon an efficient fluid flow mechanism, to transport reactants and products (Whitaker et al., 2004). Unlike many proposed dolomitisation models, geothermal convection is essentially independent of boundary conditions such as relative sea-level (Sanford et al., 1998), and thus will operate in all platforms with sufficient permeability. The forced convection cells draw on an infinite reservoir of Mg^{2+} and affect large volumes of platform carbonates for extended time periods. Such convection operates in modern carbonate platforms ranging from small-scale atolls (e.g., Aharon et al., 1987) to the extensive Floridian platform (Kohout, 1965).

Early RTM simulations of geothermal convection over 100 ky suggested that dolomitisation was focused in a sweet spot in the deeper (>1.5 km) platform interior (Wilson et al., 2001). This implied dolomitisation is not simply transport-limited, which would give a distribution mirroring that of fluid flux, but rather occurs as a gradient reaction along a 60–70°C isotherm where there is an optimum balance between transport and reaction rate. However, extrapolation from these short-term simulations suggests that, even in the most favorable locations, less than 2% dolomite will form in 1 million years, and complete dolomitisation will require more than 60 Myr.

Here we report RTM simulations of geothermal convection over a time scale of millions of years and address three important questions

1. Can geothermal convection form significant volumes of dolomite within geologically reasonable timescales?
2. If so, do geothermal dolomite bodies have characteristic geometries and/or geochemical signatures such as temperature of formation?

3. To what extent is geothermal dolomitisation controlled by the characteristics of the sediments and/or the platform geometry?

METHODS

We use TOUGHREACT to simulate geothermal convection in a 2-D flow domain 3×35 km representing half an isolated carbonate platform, assuming symmetrical flow. The platform is a rimmed shelf flooded with seawater to 5 m depth and measuring 25 km from interior to margin, sloping steeply into a 2 km deep basin. The flow domain is discretized into 4305 active blocks 350–500 m wide and 5–50 m high, and in the baseline simulation employed linear (Cartesian) coordinates. Additional simulations using narrower and shallower platforms and a radial grid to investigate sensitivity to platform geometry.

Right and left boundaries are no-flow boundaries, while the lower boundary is closed to flow and solute transport but open to heat transport, with a specified heat flux of 60 mW/m^2 , representative of passive margins. The upper boundary, from the basin and slope to the platform top, is a fluid-pressure boundary, allowing the recharge or discharge of fluids, where temperature and pressure are defined from depth below sea-level. Initial temperature distribution reflects advective heat transport by geothermal convection prior to initiation of any reactions. Although effective thermal conductivity will vary with mineralogy and porosity, TOUGHREACT does not at present include these feedbacks. A thermal conductivity of $2.2 \text{ W/m}^\circ\text{C}$ was specified, with a specific heat capacity of $1000 \text{ J/kg}^\circ\text{C}$.

Initial porosity is an exponential function of depth based on data for Florida (Schmoker and Halley, 1982; Figure 1). Permeability is derived from porosity based on Lucia's (1995) analysis of core-scale measurements (Figure 1). The base case uses the Class 2 relationship for packstone-wackestones. Sensitivity to porosity-permeability relationship is explored using by increasing permeability by one order of magnitude (grainy platform) and by using Lucia's Class 3 poro-perm relationship (muddy platform). Permeability anisotropy in platform carbonates reflects depositional layering and early diagenesis, and is specified as 1,000, based on flow-based scale-up of core data. The effect of dolomitisation on the porosity-permeability relationship is highly variable. Mimetic dolomites can exhibit remarkable preservation of sedimentary textures, but recrystallisation can completely destroy depositional fabrics (Lucia, 2004). We used a simplified Carmen-Kozeny Equation to modify permeability, ignoring the effects of changes in grain size, tortuosity, and specific surface area.

The initial mineralogy is 99% calcite, with 1% "seed" dolomite representing minor syndepositional dolomitisation and providing nucleation sites. In

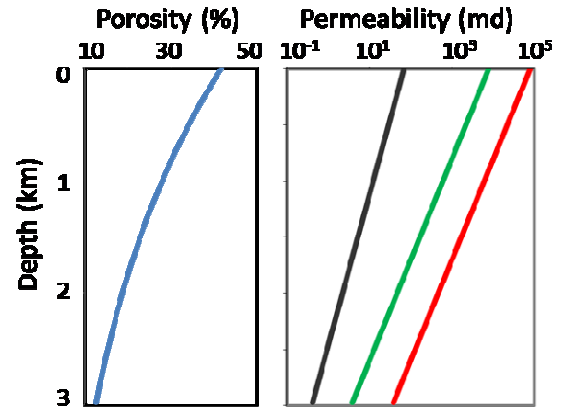


Figure 1. Relationship between permeability and depth below the platform top based on the Schmoker and Halley (1982) porosity depth curve for Florida and the porosity-permeability relationships of Lucia (1995)

addition, anhydrite is incorporated as a secondary mineral. Initial fluid composition is seawater modified to equilibrium with respect to calcite but remaining supersaturated with respect to dolomite, to represent diagenesis in very shallow pore waters.

Dolomitisation is assumed to occur via calcite dissolution followed by dolomite precipitation (Machel, 2004). Dolomite precipitation is modeled as a kinetic process, since it is orders of magnitude slower than calcite dissolution and anhydrite precipitation, which are modeled as thermodynamic processes. We use the kinetic expression for dolomite precipitation of Arvidson and Mackenzie (1999; Equation 2):

$$r_{dol} = A_s A e^{-E_a/RT} (1 - (Q/K_{eq}))^{2.26} \quad [2]$$

where r_{dol} is the reaction rate of dolomite precipitation, A_s is the specific reactive surface area, and together Q , the activity quotient, and K_{eq} , the equilibrium constant for ordered dolomite, define the saturation index. The rate constant as defined from laboratory experiments where A the pre-exponential factor is 11.22 mol/cm^2 ; E_a the activation energy is $1.335 \times 10^5 \text{ J/mol}$; R is the universal gas constant; T is temperature (K) and 2.26 is the reaction order.

We assume an RSA of $1,000 \text{ cm}^3/\text{g}$, which equates to an average diameter of idealized grains of $50 \mu\text{m}$ diameter, or larger morphologically more complex grains. Geometric considerations suggest that RSA is inversely proportional to the average grain diameter, and thus permeability and RSA are likely to co-vary. For the lower-permeability muddy sediments, we

assume an RSA of $10,000 \text{ cm}^3/\text{g}$, while for the grainier sediments, we set the RSA to $100 \text{ cm}^3/\text{g}$.

RESULTS

Cold ocean water enters along the platform slope and flows laterally and upwards to discharge from platform top, with highest flux in the upper platform adjacent to the margin (Figure 2). The depth dependence arises from the specified reduction in initial permeability with depth, and the lateral penetration arises from the high anisotropy. Over time, diagenesis increases porosity and permeability, enhancing fluid flow and also advective cooling. Cooling extends across most of the platform, with a tongue of $<20^\circ\text{C}$ water extending progressively from the margin over time, but ascending waters result in limited advective warming of the platform interior.

Dolomite forms within two distinct zones that develop at different rates and over time merge to create a single dolomite body. A broad inclined dolomite ellipse forms parallel to the isotherms and shallowing with distance from the margin, where the balance between temperature and fluid flow is favorable. Dolomite initially forms very slowly, but after $>10 \text{ Ma}$, reaction rates accelerate and the ellipse extends towards the platform margin. A second dolomite zone develops at shallow depth ($<500 \text{ m}$) within 10 km of the platform margin up to 15 Ma , but later extends further towards the interior. Reactions

are most rapid at the shallowest part of the platform due to the very high flux of sea-water close to 25°C .

The transition from complete to undolomitised rock occurs vertically over $2\text{--}300 \text{ m}$ and horizontally over $1\text{--}2 \text{ km}$ rather than forming a sharp reaction front.

These simulations reveal important nonlinearities in the rate of dolomitisation, with an increase in reaction rate as dolomite abundance increases, giving complete dolomitisation locally within 5 Ma and over significant areas of the platform in $10\text{--}15 \text{ Ma}$. This is consistent with high-temperature experiments, which show that once the dolomitization reaction starts, it proceeds very quickly.

The calcite distribution mirrors that of dolomite, but the mol:mol replacement of calcite by the denser dolomite enhances porosity by up to 13% , although precipitation of some dolomite cement (“over-dolomitisation”) reduces porosity by up to 3% near the platform margin. In the platform interior, there is a smaller inclined zone of minor anhydrite cementation at $1\text{--}2 \text{ km}$ depth down-flow of the 50°C isotherm, where porosity is reduced by up to 7.5% , due to precipitation of calcium sulfate (most likely at this pressure and temperature as anhydrite). Anhydrite precipitation rate is initially rapid, but the reaction becomes self-limiting with progressive reduction of fluid flow, caused by the reduction of porosity and permeability.

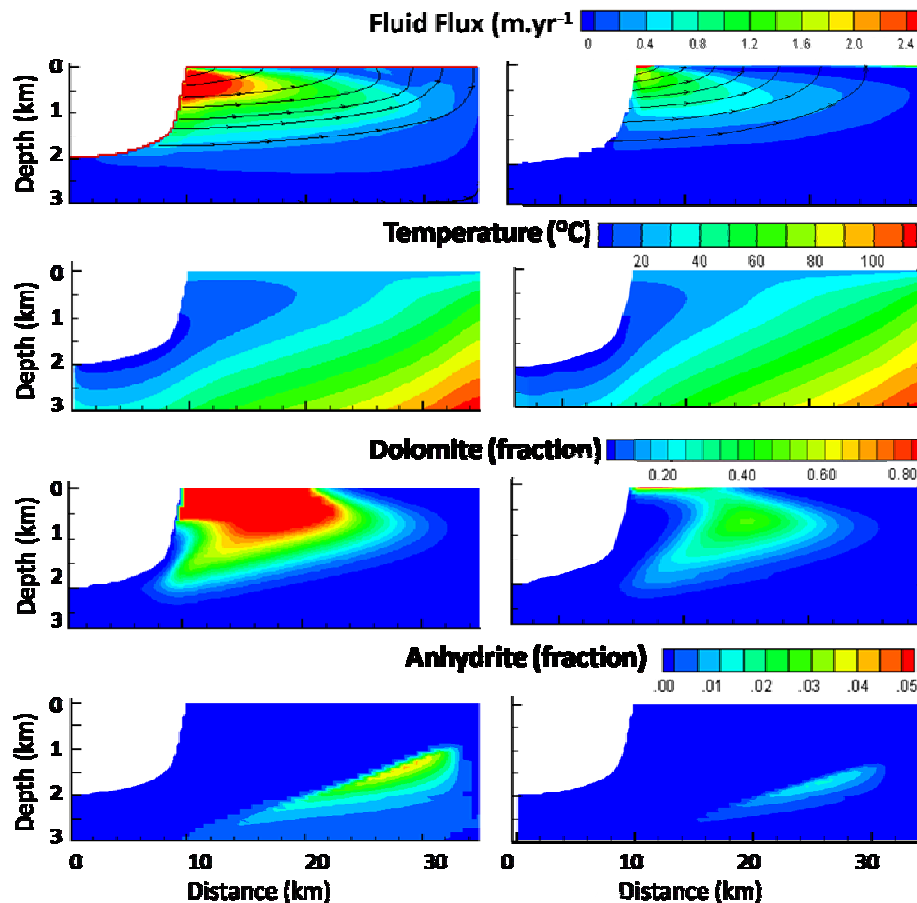


Figure 2. Geothermal convection in linear (left) and radial (right) platform geometries, showing distribution of fluid flux (including representative streamlines), temperature, dolomite and anhydrite (as a fraction of the total rock volume) after 15 Ma .

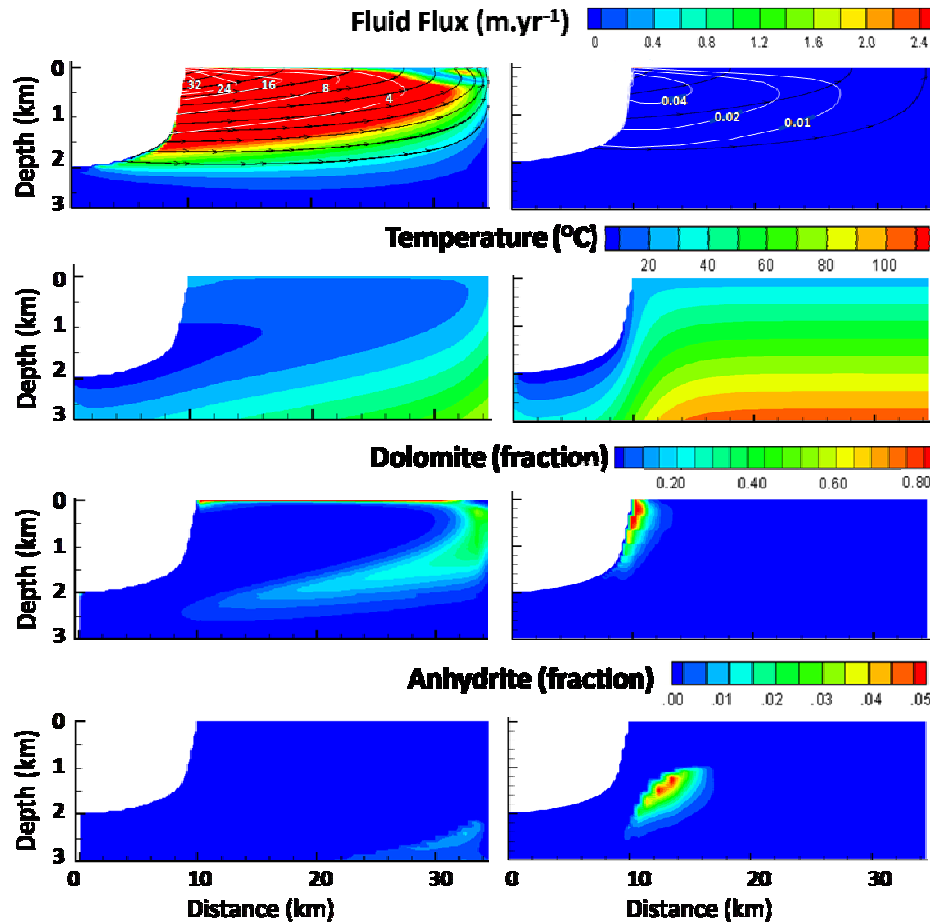


Figure 3. Geothermal convection in grainy (left) and muddy (right) linear platforms showing distribution of fluid flux (including representative streamlines), dolomite and anhydrite (as a fraction of the total rock volume) after 15 Ma.

The baseline simulation uses planar (Cartesian) coordinates, appropriate for platforms with a length/width ratio of more than 4–5. Flow in more circular platforms can be approximated using radial coordinates (Figure 2). Flow enters the circular platform from the entire circumference of the margin and convergences towards the platform interior. The lower flow rates mean less advective cooling. The distribution and extent of dolomite and anhydrite after 15 Ma in the radial simulations resemble that of the linear coordinate simulations after only 1.5 Ma.

Previous RTM simulations (e.g., Wilson et al., 2001) have demonstrated that dolomitisation is highly sensitive to variations in both permeability and RSA. Results of simulations co-varying permeability and RSA are shown in Figure 3. In the grainier platform, the fluid flux is an order of magnitude greater than in the baseline simulation, resulting in widespread and significant platform cooling. Despite the higher fluid flux, a combination of the significantly lower temperatures and lower RSA result in only partial dolomitisation of the platform interior. At these low temperatures, no anhydrite cements are precipitated.

In the muddier platform, fluid flux is reduced by some two orders of magnitude relative to the baseline simulation, and temperatures are almost entirely conductive. Fluid flux limits dolomitisation to a narrow zone within a few kilometers of the margin, where temperatures are mostly $<30^{\circ}\text{C}$. Anhydrite forms more rapidly than in the cooler baseline simulation, in a zone located just downstream of the platform margin dolomitisation.

Real platforms are characteristically heterogeneous at a range of scales, often with pronounced vertical layering reflecting changes in depositional regime over time. We simulated a very simple vertically stacked sequence within the upper 2 km of the platform, alternating 150 m thick units of pack-wackestone (Class 2) sediments with intermediate RSA ($1,000\text{ cm}^2\cdot\text{g}^{-1}$) and 50 m thick layers of either low permeability but more reactive (muddy) sediments or high permeability less reactive (grainy) sediments (Figure 4).

Grainy layers effectively pirate the flow, with very high fluxes ($>50\text{ m}\cdot\text{yr}^{-1}$) adjacent to the margin, although fluxes within the Class 2 sediments are an order of magnitude lower than in the baseline

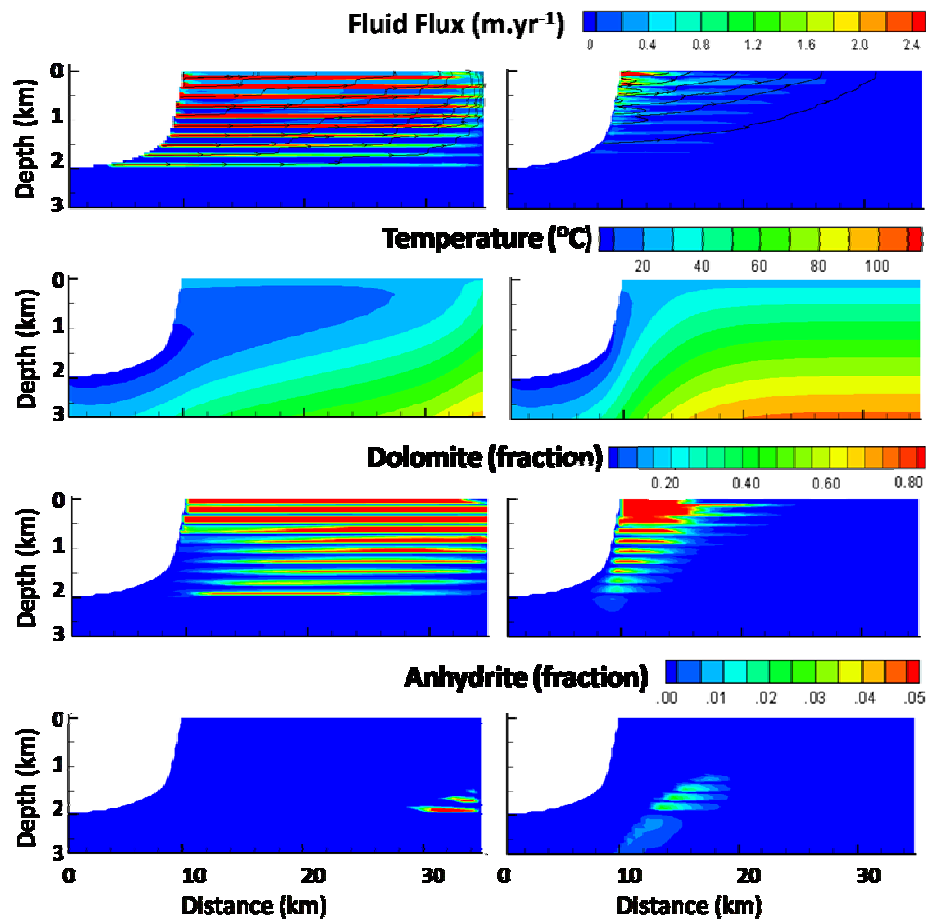


Figure 4. Geothermal convection in a pack-wackestone platform with grainy layers (left) and muddy layers (right), showing distribution of fluid flux (including representative streamlines), temperature, dolomite and anhydrite (as a fraction of the total rock volume) after 15 Ma.

simulation. Flow in the higher permeability layers significantly cools the platform, and conduction prevents any vertical temperature stratification. The resulting pattern of dolomitisation shows marked layering, with complete dolomitisation of almost all Class 2 sediments in the upper 600 m of the platform. While fluid flux rarely exceeds 0.4 m.y^{-1} , in these sediments, they are preferentially dolomitised due to their higher RSA. At depths of 600–1600 m, dolomitisation continues to favor the more reactive Class 2 sediments, but within each Class 2 layer, dolomite abundance increases with depth as Mg^{2+} is sourced from the underlying grainier layer. Below 1600 m, the Class 2 sediment permeability has reduced sufficiently such that dolomitisation occurs preferentially within the grainier layers despite their lower reactive surface area. Anhydrite formation is restricted to a couple of these grainier layers at depth in the very interior of the platform.

With the introduction of muddy layers, fluid flux is significantly reduced compared to the baseline simulation, with most flow occurring within the Class 2 sediments adjacent to the platform margin. Advective cooling of the platform is significantly reduced. By 15 Ma, dolomitisation is complete within 4 km of the margin in this high flow zone, and at

shallow depth tongues of dolomite extending towards the interior are developed preferentially within the more reactive, less permeable beds. The decreasing permeability with depth of both sediment types is mirrored by the fluid flux, and below 600 m, fluid flux is insufficient to dolomitize the muddy layers and occurs only within the more permeable Class 2 sediments. A minor amount of anhydrite forms at depths >1 km downstream of the platform margin dolomites within the Class 2 sediments.

CONCLUSIONS

Geothermal convection of normal sea-water can form a large dolomite body within millions to a few tens of millions of years, and is accompanied by precipitation of anhydrite cements downstream of the dolomite body, but only very minor dolomite cements. The rate of geothermal dolomitisation and the size of the dolomite body formed have previously been significantly underestimated, owing to nonlinearities in the rate of dolomitisation. The dolomite body is characteristically thicker at the platform margin and at shallow depth, thinning towards the platform interior, and forms at temperatures that are rather cooler than previously suggested, mostly in the range 20–40°C. The rate of

dolomitisation is significantly reduced in circular rather than in elongate platforms, although the general pattern remains similar.

Dolomitisation is critically sensitive to sediment permeability and reactive surface area, which are often inversely related. Despite much higher rates of fluid flow in grainier platforms, a combination of lower temperatures and RSA restricted fluid flux results in only partial dolomitisation within the center of the platform. In muddier platforms, dolomitisation is also reduced, but in this case reactions are flux limited, with dolomitisation restricted to the platform margin. The introduction of horizontal layers of grainy or muddy sediments produces a complex vertical diagenetic stratigraphy, favoring more reactive beds at shallow depth where permeability is not limiting, but switching to more permeable beds at depth.

While at present TOUGHREACT does not consider feedbacks between evolving porosity and thermal conductivity, this is unlikely to significantly alter our conclusions. There are a number of important challenges to improving our RTM simulations of dolomitisation. These arise from uncertainties in physical and chemical parameters (especially permeability and reactive surface area), uncertainties in dolomitisation kinetics at low temperatures, appropriate representation of such inherently heterogeneous systems, and the nonstationarity of boundary conditions over such long times.

ACKNOWLEDGMENTS

Funding for this study was provided by the public authority for applied education and training 'Kuwait'. FFW thanks ExxonMobil URC for supporting stimulating academic exchange visits between URC and Bristol. The views expressed in this paper by Yitian Xiao are his own and not necessarily those of ExxonMobil. A more extended version of this paper is presented by Whitaker and Xiao (2009).

REFERENCES

- Aharon, P., Socki, R.A, and Chan, L., Dolomitisation of atolls by sea water convection flow: tests of a hypothesis at Niue, South Pacific: *Journal of Geology*, 95, 187-203. 1987.
- Arvidson, R. S., and Mackenzie, F. T., The dolomite problem: Control of precipitation kinetics by temperature and saturation state: *American Journal of Science*, 299, 257–288. 1999
- Schmoker, J. W. and Halley, R. B., Carbonate porosity versus depth - A predictable relation for South Florida, *AAPG Bulletin*, 66, 2561-2570, 1982.
- Holland, H.H., Sea level, sediment and the composition of seawater: *American Journal of Science*, 305, 220-239. 2005.
- Kohout, F.A, A hypothesis concerning cyclic flow of salt water related to geothermal heating in the Floridan aquifer: *Transactions of the New York Academy of Science* (2) 28, 249-271. 1965
- Lucia, F. J., Rock-fabric petrophysical classification of carbonate pore-space for reservoir characterization: *AAPG Bulletin* 79, 1275-1300, 1995.
- Lucia, F. J., Origin and petrophysics of dolostone pore space, *Geological Society of London Special Publication*, 235, 141-155, 2004.
- Machel, H.G., Concepts and models of dolomitization; a critical reappraisal: *Geological Society of London Special Publication* 235, 7-63 2004.
- Sanford, W. E., Whitaker, F. F., Smart, P. L. and Jones, G. D., Numerical Analysis of seawater circulation in carbonate platforms: I geothermal circulation: *American Journal of Science* 298, 801-828. 1998.
- Whitaker, F.F. and Xiao, Y., Geothermal convection, a viable mechanism for early burial dolomitisation of platform carbonates: *Bulletin of the American Association of Petroleum Geologists* (in press). 2009.
- Whitaker, F.F., Smart, P.L. and Jones, G.D., Dolomitisation: from conceptual to numerical models. *Geological Society London Special Publication* 235, 99-139. 2004.
- Wilson, A. M., Sanford, W. E., Whitaker, F. F. and Smart, P. L. Spatial patterns of diagenesis during geothermal circulation in carbonate platforms: *American Journal of Science* 301, 727-752. 2001.
- Xu, T., E. Sonnenthal, N. Spycher and K. Pruess, TOUGHREACT: A simulation program for non-isothermal multiphase reactive geochemical transport in variably saturated geologic media. *Computers and Geosciences*, 32, 145-165, 2006.

CO₂ STORAGE

SINGLE-WELL EXPERIMENTAL DESIGN FOR STUDYING CO₂ RESIDUAL TRAPPING, OTWAY BASIN, AUSTRALIA

Yingqi Zhang¹, Stefan Finsterle¹, Lincoln Paterson^{2,3}, Martin Leahy^{2,3},
Jonathan Ennis-King^{2,3}, Barry Freifeld¹, Tess Dance^{2,3}

1. Lawrence Berkeley National Laboratory, Berkeley, CA, USA
2. CSIRO Petroleum, Clayton, Victoria, Australia
3. Cooperative Research Centre for Greenhouse Gas Technologies, Australia
e-mail: yqzhang@lbl.gov

ABSTRACT

The geologic sequestration of greenhouse gases to mitigate climate change is receiving increasing attention as a means to allow some continued use of fossil fuels while reducing emissions. Numerous demonstration programs are currently under way to understand the mechanisms by which CO₂ can be safely stored and to develop analytical tools to manage reservoirs. The objective of our research is to design a single-well injection-withdrawal test to investigate nonstructural (residual) trapping mechanisms. The proposed design consists of a sequence of tests—including hydraulic, thermal, and tracer tests—to provide complimentary data to constrain the estimate of residual gas saturation (S_{gr}), and to reduce the bias caused by formation heterogeneity. Numerical simulations were conducted using the EOS7C module of TOUGH2, incorporated into the iTOUGH2 simulation-optimization code. The proposed approach is applied to CO2CRC's Otway Project Site, Victoria, Australia. iTOUGH2 provides means not only for joint analysis of different types of data to be collected at Otway, but also for characterization and estimation of attributes of the heterogeneous property field that are likely to affect test performance and data interpretation. The results of the study suggest that uncertainty in the estimate of S_{gr} can be reduced by using multiple data types and repeated tests.

INTRODUCTION

The geologic sequestration of anthropogenic greenhouse gases to mitigate climate change is receiving increasing attention as a means to reduce the impact of atmospheric CO₂ releases from the use of fossil fuels. However, to be able to safely store CO₂ in the reservoirs, we need to understand the trapping mechanisms that keep CO₂ underground. While four trapping mechanisms—structural trapping, residual phase trapping, solubility trapping and mineralization trapping (IPCC, 2005)—have been identified, the focus of this study is on residual phase trapping.

To achieve the pressure and temperature conditions required for supercritical CO₂ storage, the depth of the target formation must be at least ~800 m below

ground surface. The high cost associated with drilling wells at such depth leads to an effort to minimize the number of wells.

The objective of this study is to propose a test sequence that uses a single well for quantifying the amount of injected CO₂ trapped as residual gas in brine aquifers. We will demonstrate the approach by applying it to the Otway injection project in Australia. However, the proposed method is general, i.e., it can be applied to other CO₂ injection projects.

DESIGN APPROACHES

The proposed test consists of a carefully designed sequence of hydraulic, tracer and thermal tests. This test combination is needed to sufficiently constrain the estimate of S_{gr} given uncertainty and variability in formation properties. The basic idea for the design is to (1) perform a series hydraulic, thermal, and tracer tests under fully water-saturated conditions (referred to as *reference tests*; Stage 1); (2) create a system at residual CO₂ saturation (Stage 2); (3) repeat the sequence of hydraulic, thermal and tracer tests in the formation containing residual CO₂ (referred to as *characterization tests*; Stage 3); and (4) analyze the differences between the reference and characterization tests to estimate S_{gr} .

Hydraulic test

The hydraulic tests provide a distinct pressure signal to infer the amount of gas trapped in the formation. When water is injected into (a) a fully water-saturated formation; (b) a formation at residual gas saturation with a low S_{gr} ; or (c) a formation at residual gas saturation with a high S_{gr} , the liquid relative permeability is highest in (a) and lowest in (c), which means the injected water in Case (a) can move away from the vicinity of the well with less resistance than in Cases (b) and (c). Therefore, the pressure increase observed in Case (c) is the highest. While the observed pressure effects can be quite pronounced, uncertainty in the relative permeability will lead to uncertainty in the estimate for S_{gr} . Therefore, we seek additional observations that can further constrain the S_{gr} estimate.

Tracer test

Tracer is injected into the formation and pushed further away from the injection well by continuous injection of water, before being pulled back into the borehole, where a breakthrough curve (BTC) is measured. The BTC in Stages 1 and 3 are distinctly different, because in Stage 3, part of the tracer partitions into the trapped gas and thus becomes immobile. The differences between the two BTCs can be used to infer how much gas is trapped in the system. We propose to use noble gases as tracers, because they (1) partition between the aqueous and CO₂-rich phase, (2) are chemically inert and nonhazardous, and (3) can be measured with great precision. We propose to use Kr and Xe and compare the BTCs obtained from the residual gas field (Stage 3) with the BTCs from the reference test (Stage 1).

Thermal test

Supercritical CO₂ has a significantly smaller thermal diffusivity than water. We can take advantage of the contrast between the thermal diffusivity of a brine-saturated formation and one that contains CO₂, and perform a well-based thermal transport test in which the temperature response is used to estimate gas saturation. The basic mechanics of such a test are shown in Freifeld et al. (2008). Figure 1 shows the temperature increase as a function of gas saturation for a system initially at 65°C after 2 days of heating at 40 W/m. Because the effective thermal conductivity is treated in TOUGH2 as a linear function of gas saturation, the maximum temperature increases linearly as gas content increases; however, a laboratory-derived relationship between gas saturation and thermal conductivity can be used to more accurately interpret field observations. Since temperature can be measured very accurately, even small changes in gas saturation, and thus thermal diffusivity, can be identified. However, this method has the limitation that the scale of the formation "interrogated" is a cylinder of 1 to 2 m around the wellbore.

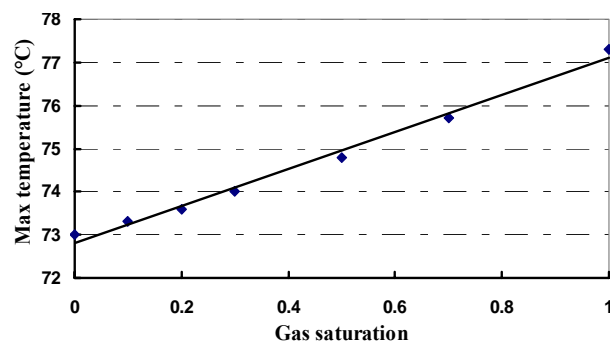


Figure 1. Maximum temperature after 2 days of heating at 40 W/m for systems with different gas saturations

APPLICATION TO OTWAY I INJECTION PROJECT

Recognizing the importance of saline aquifers for CO₂ storage, the CO₂CRC Otway Project proposed a test to better understand residual trapping in sedimentary formations that lack clear stratigraphic traps. A predetermined volume of CO₂-rich gas (80% CO₂ and 20% CH₄ by volume; or 90% CO₂ and 10% CH₄ by mass) will be piped to a new well (CRC-2) and injected at a supercritical state into the Paaratte Formation. The proposed injection formation is at a depth of 1481–1507 m at the base of the Paaratte's 400 m thick sequence of sands and shales. There are two lithofacies in our targeted zone: sand (59%) and shale (41%). The mean permeability used to represent the sand is 1 darcy in the horizontal direction and 0.01 darcy in the vertical direction; mean porosity is 0.28. All the shale layers are considered to have one milli-darcy permeability.

Test Sequence

The proposed test sequence can be summarized as follows (Figure 2):

1. Stage 1: Reference Tests Under Fully Water-Saturated Conditions

- 1.1. *Reference Thermal Test*: Heating of borehole for 2 days, followed by 3 days of cooling; temperature is measured using fiber-optic distributed temperature sensors
- 1.2. *Reference Hydraulic and Tracer Test*:
 - 1.2.1. Injection: Water injection for 1 day; combined with injection of 2-hour tracer pulse (water injection 4 hours; water+tracer injection 2 hours; water injection 18 hours); pressure measurements
 - 1.2.2. Production: Pull back for 7 days; pressure and tracer concentration measurements (reference BTC)

2. Stage 2: CO₂ Injection and Creation of Trapped Gas Field

- 2.1. *CO₂ Injection*: Injection of CO₂ for 2 day, followed by a 1-day shut-in period
- 2.2. *Thermal test*: Heating of borehole for 2 days, followed by 3 days of cooling
- 2.3. *Water Injection*: Injection of CO₂-saturated water for 3 days, followed by a 1-day shut-in period

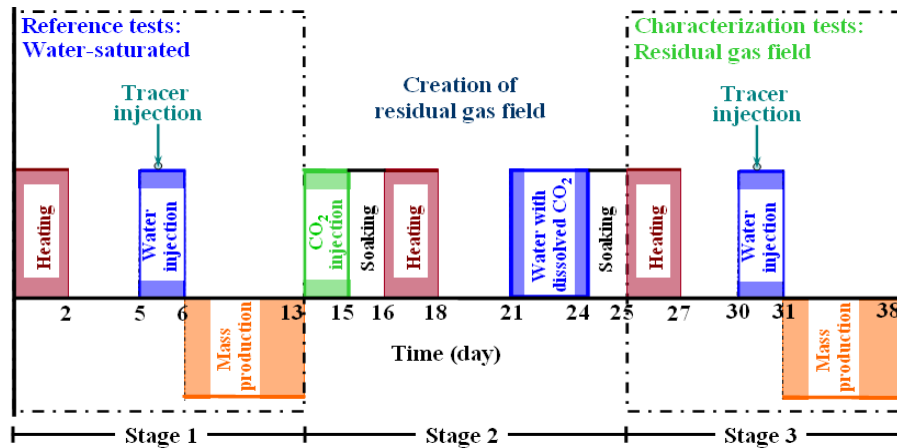


Figure 2. Proposed test sequence

3. Stage 3: Characterization Tests for a System at Residual Gas Saturation

- 3.1. *Characterization Thermal Test:* Heating of borehole for 2 days, followed by 3 days of cooling; temperature is measured using fiber-optic distributed temperature sensors
- 3.2. *Characterization Hydraulic and Tracer Test:*
 - 3.2.1. Injection: Water injection for 1 day; combined with injection of 2-hour tracer pulse; pressure measurements
 - 3.2.2. Production: Pull back for 7 days; pressure and tracer concentration measurements (characterization BTC)

Model Description

Numerical simulations were conducted using the EOS7C module (Oldenburg, 2004) of TOUGH2, a numerical simulator for nonisothermal multiphase, multicomponent flows in porous media. EOS7C was developed to model multicomponent gas mixtures of methane and a noncondensable gas (in our case: CO₂), with one tracer present.

The EOS7C module was incorporated into the iTOUGH2 (Finsterle, 2007) simulation-optimization code in preparation for formal sensitivity and parameter identification analyses. Moreover, iTOUGH2 is expected to be used for parameter estimation by automatic model calibration (inverse modeling), the method of choice for the joint analysis of the hydrologic, thermal, and tracer data to be collected at Otway. iTOUGH2 also provides the means to characterize and estimate attributes of the heterogeneous property field that are likely to affect test performance and data interpretation.

The injection zone was modeled as a 2D radial system, extending 1000 m in the lateral direction and 26 m in depth. A heterogeneous permeability field was created using an indicator-based algorithm from the geostatistical software library GSLIB, which is incorporated into iTOUGH2. The permeability field is conditioned on well log and core data. The corresponding capillary-strength parameter of the van Genuchten constitutive relationships is calculated using Leverett scaling. Figure 3 shows the permeability field used in the simulation up to 100 m from the well. The well is perforated between -7 and -12 m. Vertical discretization of the model is 0.5 m for the upper 14 m and 1 m for the lower 12 m.

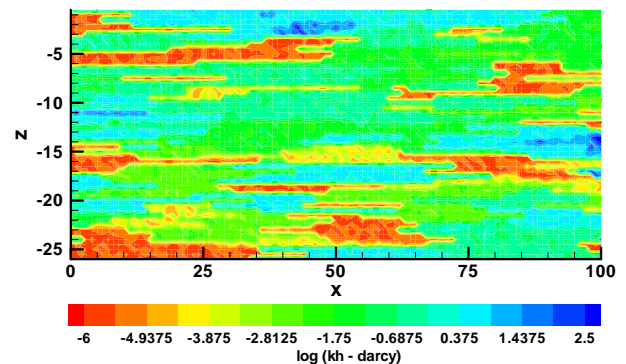


Figure 3: Simulated property field: logarithm of horizontal permeability

Results

Simulations were performed for residual gas saturations of $S_{gr}=0.1$, $S_{gr}=0.2$, and $S_{gr}=0.35$. Time-series data of pressure, temperature, and tracer concentration are used for a sensitivity analysis of entrapped gas volume and residual gas saturation.

Gas saturation

Figure 4 shows the liquid saturation for a system with $S_{gr}=0.2$ at 15 days (immediately after gas injection) and 25 days (immediately after water injection). At Day 15, the system reaches the highest gas saturation. Some of the injected gas moved above the injection area due to the buoyancy of CO_2 . At Day 25, CO_2 moves a little further away, and gas saturation stays mostly at 20%.

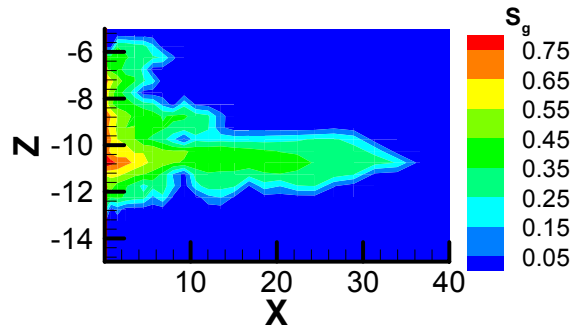


Figure 4(a): Liquid saturation at 15 days

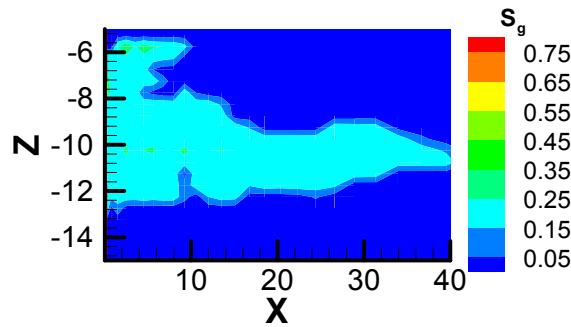


Figure 4(b): Liquid saturation at 25 days

Pressure responses

Pressure responses at the wellbore during the test period for the three systems are shown in Figure 5. The four pressure increases seen within the time series for each of the systems are due to (1) water injection into the fully water-saturated system; (2) gas injection into a fully water-saturated system (drainage); (3) water injection into a gas field (imbibition); (4) water injection into a residual gas field (imbibition).

Temperature responses

Temperature responses at the wellbore over the test period are shown in Figure 6. The three temperature increases correspond to the three heating periods. The last heating of a residual gas-saturation field shows some sensitivity to the amount of entrapped gas. While the differences in temperature for the residual gas field appear small, the high accuracy of temperature measurements are expected to result in relatively well constrained estimates for S_{gr} . For this

plot, one should compare the first and third temperature increases to infer S_{gr} . The second temperature increase is difficult to interpret, because the temperature change during this period depends on borehole conditions, the details of the heterogeneous property field, and the residual pressure disturbance, all of which cause convective fluid flow and associated heat flows.

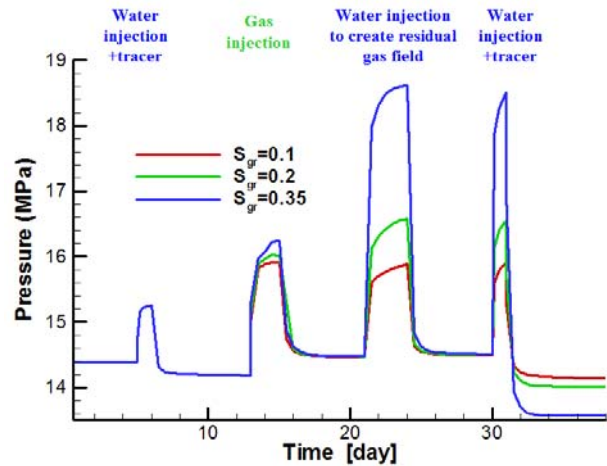


Figure 5. Pressure responses at the wellbore as a function of time for different residual gas saturations

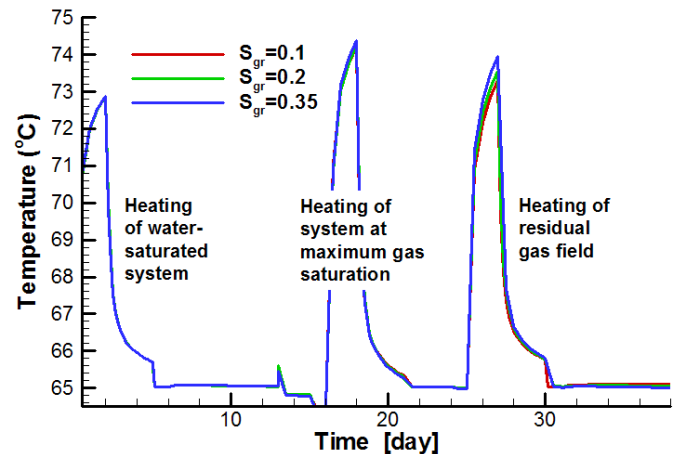


Figure 6. Temperature responses at the wellbore as a function of time for different residual gas saturations

Tracer breakthrough curves

Tracer breakthrough curves are plotted in Figure 7. Two noble gases are used as tracers in our simulations: Krypton (^{84}Kr) and Xenon (^{132}Xe). The Henry coefficients are 3.860×10^9 Pa for Kr and 2.634×10^9 Pa for Xe at $65^\circ C$. A highly volatile tracer is not suitable for our test purpose, because a large amount of highly volatile tracer will partition into the trapped gas phase. As a consequence, the amount of

recoverable tracer in the liquid phase would be drastically reduced. A reasonable, expected reduction is seen in Figure 7 between the reference curves and the final tracer tests. Due to the reduced peak concentrations of the second recovery, the sensitivity of the curves to residual gas saturation is reduced correspondingly, making it difficult to infer S_{gr} when real data are used.

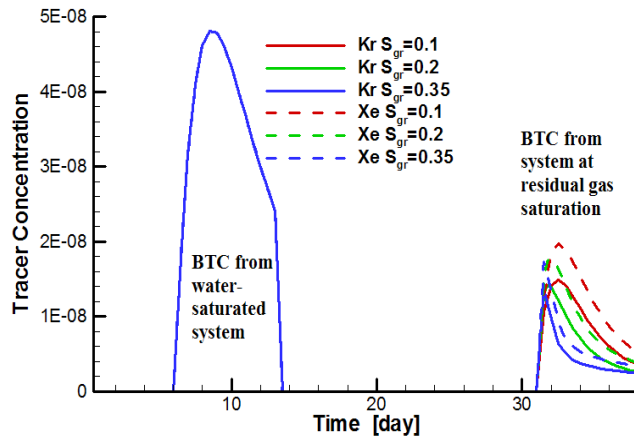


Figure 7. Tracer breakthrough curves for different residual gas saturations

CONCLUSION

Single-well-derived data sets to assess reservoir properties can cost-effectively reduce uncertainties in the appraisal phase for finding commercial scale storage sites. Having multiple data sources and constraining the measurements, it is possible to design a single-well CO₂ sequestration experiment to determine the key factors influencing residual trapping of CO₂ in saline storage reservoirs. The proposed test design (1) provides complementary data that are sensitive to residual CO₂ trapping, and (2) reduces ambiguity by using reference tests in the interpretation of hydraulic, thermal, and tracer data to arrive at S_{gr} estimates. Given the inherent uncertainty caused by subsurface heterogeneity and measurement errors, the joint inversion of all three data sets is proposed as a practical approach to best constrain S_{gr} .

ACKNOWLEDGMENT

Funding to support this study has been provided by Australia's CO2CRC and through the Assistant Secretary of the Office of Fossil Energy, U.S. Department of Energy, National Energy Technology Laboratory under contract DE-AC02-05CH11231.

REFERENCES

- Finsterle, S., *iTOUGH2 User's Guide*, Report LBNL-40040, Lawrence Berkeley National Laboratory, Berkeley, Calif., 2007.
- Freifeld, B. M., S. Finsterle, T.C. Onstott, P. Toole and L.M. Pratt, Ground surface temperature reconstructions: using in situ estimates for thermal conductivity acquired with a fiber-optic distributed thermal perturbation sensor, *Geophys. Res. Lett.*, 35, L14309, doi:10.1029/2008GL034762, 2008.
- IPCC (Intergovernmental Panel on Climate Change) Special Report on CO₂ Capture and Storage, 208-210, 2005.
- Oldenburg, C. M., G. J. Moridis, N. Spycher, and K. Pruess, *EOS7C Version 1.0: TOUGH2 Module for Carbon Dioxide or Nitrogen in Natural Gas (Methane) Reservoirs*, Report LBNL-56589, Lawrence Berkeley National Laboratory, Berkeley, Calif., 2004.

TOUGH+CO₂: A MULTIPHASE FLUID-FLOW SIMULATOR FOR CO₂ GEOLOGIC SEQUESTRATION IN SALINE AQUIFERS

Keni Zhang, George Moridis, and Karsten Pruess

Earth Sciences Division, Lawrence Berkeley National Laboratory
e-mail: kzhang@lbl.gov

ABSTRACT

TOUGH+CO₂ is a new simulator for modeling of CO₂ geologic sequestration in saline aquifers. It is a member of TOUGH+, the successor to the TOUGH2 family of codes for multicomponent, multiphase fluid and heat flow simulation. The code accounts for heat and up to three mass components, which are partitioned into three possible phases. By solving coupled equations of mass and heat balance, TOUGH+CO₂ can model nonisothermal or isothermal CO₂ injection, phase behavior, and flow of fluids and heat under typical conditions of temperature, pressure, and salinity in CO₂ geologic storage projects. The new simulator inherits all the capabilities of TOUGH2 in handling fractured media and using unstructured meshes for complex simulation domains. The FORTRAN 95 OOP architecture and other new language features have been extensively used to enhance memory use and computing efficiency. In addition, a domain decomposition approach has been implemented for parallel simulation. All these features lead to increased computational efficiency, and allow applicability of the code to multi-core/multi-processor parallel computing platforms with excellent scalability.

INTRODUCTION

CO₂ geologic sequestration in saline aquifers involves complex multiphase flow processes, such as advection and diffusion, convective mixing, phase appearance/disappearance, dissolution and precipitation of minerals, and other chemical reactions. Mathematical models are effective tools for understanding the behavior of CO₂ in geological formations. Numerical modeling can in fact play an important role in evaluating the feasibility and reliability of CO₂ disposal. However, modeling of such a complex process as CO₂ geologic sequestration can be a large computational challenge.

One of the most popular numerical simulators for modeling sequestration of supercritical CO₂ into deep saline aquifers is the general-purpose reservoir simulator TOUGH2, in combination with the ECO2N fluid property module (Pruess et al., 1999; Pruess, 2005). TOUGH2/ECO2N models nonisothermal, multiphase flows of mixtures of water, salt (NaCl), and CO₂. Because of the complexity of these types of subsurface flow processes, most simulations are

limited to simplified systems, mostly in two dimensions. However, for field-scale or refined-mesh applications, a simulator with more sophisticated modeling functionalities and efficiency is needed to represent geologic heterogeneities and the complicated multiphase, multicomponent flow processes.

In this study, an efficient simulator, TOUGH+CO₂, for modeling CO₂ geologic sequestration in saline aquifers, was developed. The simulator is a member of TOUGH+ (Moridis et al. 2007), the successor to the TOUGH2 family of codes. TOUGH+CO₂ is developed based on (and retaining) all the process-modeling capabilities of TOUGH2/ECO2N. The code can be used to model nonisothermal multiphase flow in systems with H₂O-NaCl-CO₂ mixtures. It represents fluids as consisting of two mobile phases—a water-rich aqueous phase and a CO₂-rich gas phase—and one immobile solid halite phase. The code partitions water and CO₂ between gas and aqueous phase under different temperature, pressure, and salinity conditions using the correlations developed by Spycher and Pruess (2005). Dissolution and precipitation of salt is treated by means of local equilibrium solubility. Associated changes in medium porosity and permeability, and the wettability phenomena, may also be modeled. As special cases, the simulator may be used for investigation of sea water intrusion (no CO₂) and saturated/unsaturated groundwater (no CO₂ and NaCl).

In this new development, the FORTRAN 95 OOP architecture and new language features—such as pointers, lists and trees, data encapsulation, defined operators and assignments, operator extension and overloading, use of generic procedures, and maximum use of the powerful intrinsic vector and matrix processing operations—have been extensively used. In addition, a domain decomposition approach has been implemented for parallel simulation. TOUGH+CO₂ adopts a similar parallelization scheme as developed for the TOUGH2-MP code by Zhang et al (2001, 2007), which has been successfully applied to many large-scale simulations. The domain decomposition approach and parallel computation enhance model simulation capabilities in terms of problem size and complexity to a level that cannot be reached by single-CPU codes. By using the TOUGH+CO₂ simulator, multimillion gridblock

problems can be run on a typical Linux cluster with several tens to hundreds of processors, to achieve ten to hundred times improvement in computational time or problem size.

In this paper, the concepts, physics, and governing equations of the new simulator are summarized. Design, implementation, and parallelization of the code are discussed. The simulator is used to simulate a site scale CO₂ sequestration in deep saline aquifers.

THEORIES AND GOVERNING EQUATIONS

Modeled Components, Phases and Flow processes

Under typical geologic conditions for CO₂ sequestration, fluids may be present in three different phases: an aqueous phase that is mostly water, but may contain dissolved NaCl and CO₂; a liquid CO₂ phase that may contain some water; and a gaseous CO₂ phase that also may contain some water. Liquid and gaseous CO₂ may coexist along the saturated vapor-pressure curve of CO₂, which ends at the critical points (31.04°C, 73.82 bar; Vargftik, 1975). If the geologic system is a saline aquifer, a third component, NaCl (salt), must also be considered. Salt can be dissolved in the aqueous phase or precipitate as solid phase. In TOUGH+CO₂, the thermophysical properties are accurately calculated for gaseous as well as for liquid CO₂, but no distinction between them is made in the treatment of flow. This simplifies the phase combinations in the water-NaCl-CO₂ system, but limits applications to processes that do not involve phase change between liquid and gaseous subcritical CO₂. Table 1 shows the phases of a system that can be simulated:

*Table 1. Fluid phase conditions modeled by the simulator***

Phase condition	Major constituent	Minor constituents
Single aqueous phase	Liquid water	Dissolved CO ₂ and NaCl.
Single gaseous phase*	Liquid CO ₂ or Gaseous CO ₂	H ₂ O
Two phases	Liquid water and CO ₂ (can be in liquid or gaseous phase)	Dissolved CO ₂ in water; dissolved water in CO ₂ -rich phase.

*All sub- and supercritical CO₂ is considered as a single nonwetting phase and referred to as “gaseous” phase.

** In all cases, solid salt (NaCl) may be present or absent.

The simulator was designed for simulation of the following processes and phenomena in saline aquifers: (1) the partitioning of the mass components among the possible phases; (2) the flow of gases and liquids in the geologic system; (3) precipitation and

dissolution of halite, with associated changes in porosity and permeability; and (4) the corresponding heat flow and transport. One of the primary assumptions of the model is that Darcy’s law is assumed valid in the simulated domain. All phases may appear or disappear in any location during the course of a simulation. Thermodynamic conditions covered include a temperature range from ambient to 100°C, pressures up to 60 MPa, and salinity from zero to full halite saturation.

The Mass- and Energy-Balance Equation

Following *Pruess et al.* [1999], mass- and heat-balance equations in every subdomain (gridblock) into which the simulation domain is been subdivided by the integral finite difference method can be written in the form:

$$\frac{d}{dt} \int_{V_n} \mathbf{M}^\kappa dV_n = \int_{\Gamma_n} \mathbf{F}^\kappa \cdot \mathbf{n} d\Gamma_n + \int_{V_n} q^\kappa dV_n \quad (1)$$

$\kappa=1, \dots, 4$ (representing water, NaCl, CO₂, and heat)
 $n=1, \dots, MN$ (total number of gridblocks).

The integration is over an arbitrary subdomain V_n of the flow system under study, which is bounded by the closed surface Γ_n . The quantity \mathbf{M} appearing in the accumulation term (left hand side) represents mass or energy per volume, \mathbf{F} denotes mass or heat flux (see below), q denotes sinks and sources, and \mathbf{n} is a normal vector on surface element $d\Gamma_n$, pointing inward into V_n .

The integral finite difference (IFD) method (Edwards, 1972) is used for space discretization, while time is discretized fully implicitly as a first-order backward finite difference. One of the most important advantages of IFD is that the discretized gridblocks can have irregular shape. This feature provides flexibility for discretization of complex simulation domains, such as discrete fractures. Time and space discretization of Equation (1) results in a set of coupled nonlinear equations. These nonlinear equations are solved by Newton/Raphson iteration.

Thermophysical Properties and Constitutive Relations

A set of primary variables will be obtained at each Newton step. The simulated brine-CO₂ system is characterized and its state can be fully defined by the set of primary variables. However, to complete the mathematical description of the multiphase flow and heat transfer in porous or fractured media for CO₂ geologic sequestration, Equation (1) needs to be supplemented with a number of constitutive equations. These constitutive correlations express the interrelationships and constraints of physical processes, variables, and parameters, and allow the evaluation of secondary variables or parameters as

functions of the set of primary variables. The constitutive relations include:

$$\text{Constraint of fluid saturations: } \sum_{\beta} S_{\beta} = 1$$

$$\text{Constraint of mass fractions: } \sum_{\kappa} X_{\beta}^{\kappa} = 1$$

In the above equations, $\kappa = 1, \dots, 3$ representing water, NaCl, and CO_2 components, and $\beta = 1, 2, 3$ representing aqueous, gas, and solid phases.

The relation between capillary pressure and phase saturation: $P_{c\beta} = P_{c\beta}(S_{\beta})$. In the code, seven different functions have been implemented, including: linear, Pickens et al. (1979), Narasimhan et al. (1978), Milly (1982), Udell and Fitch (1985), Van Genuchten (1980), and Brooks and Corey (1966).

The relation between relative permeability and phase saturation: $k_{r\beta} = k_{r\beta}(S_{\beta})$. The following relative permeability functions have been included: linear, Pickens et al. (1979), Corey (1954), Grant (1977), Udell (1982), van Genuchten (1980), Verma et al. (1985), Stone (1970), and Aziz and Settari (1979).

Other parameters—such as fluid density, viscosity, specific enthalpy of liquid and gas, thermal conductivity, and mass partitioning between components—are all determined by the primary variables. Many of these correlations for estimating properties and interrelationships are determined by experimental studies from the literature.

Mass partitioning and phase change are also very important to the description of the multiphase and multicomponent flow system. The partitioning of water and CO_2 among co-existing aqueous and gas phases is calculated from a slightly modified version of the corrections developed by Spycher and Pruess (2005) with Altunin's correlation (1975) for calculation of CO_2 molar volumes. The predicted equilibrium compositions for the two phases are functions of temperature, pressure, and salinity. The phase equilibrium between aqueous and gas corresponds to the dissolved CO_2 mass fraction in the aqueous phase. When CO_2 mass fraction is less than its equilibrium-partitioning mass fraction in liquid, the system will be in a single-phase liquid condition; when mass fraction of water does not exceeds its equilibrium-partitioning mass fraction in gas, the system will be in single-phase gas condition. Intermediate values of mass fractions correspond to two phase conditions.

Influence of Salt on flow system

Precipitation and dissolution of solid salt in a porous medium changes the void space available for fluids. Such change in porosity will cause change in permeability as well. In TOUGH+ CO_2 , several choices for the functional dependence of relative change in permeability on the relative change in porosity are offered. In general, the relation can be written as

$$\frac{k}{k_0} = f\left(\frac{\phi - \phi_c}{\phi_0 - \phi_c}\right) \quad (2)$$

The subscript “0” denotes the original property and ϕ_c is “critical porosity.” It is obvious that permeability effects depend not just on the magnitude of porosity change, but on geometric properties of the pore channels, and on where and how solid salt deposition in those channels occurs. The critical porosity is the porosity at which the throats of flow channel become clogged, so that permeability is reduced to zero. For a simplified model, the ϕ_c effect may be neglected, and a power law dependence of permeability k on porosity ϕ may be selected as the relational function.

Solid salt deposition may not only involve permeability change, but may also influence capillary pressure. Precipitation of salt will alter the pore size distribution, generally reducing pore sizes, and thereby giving rise to stronger capillary pressures. Scaling factors of intrinsic permeability and capillary pressure are computed with OPM or EPM models developed by Moridis et al. (2008). In addition, the functions for the tubes-in-series model developed by Verma and Pruess (1988) have also been adopted as an alternative choice.

PROGRAM DESIGN AND IMPLEMENTATION

Primary Variables

The thermodynamic state and mass partition of different components among phase conditions are determined from the equation of state. Using the same approach as TOUGH2/ECO2N (Pruess, 2005), the multiphase flow system for CO_2 sequestration is defined by four primary variables. According to Gibbs' phase rule, the number of thermodynamic degrees of freedom for a system involving three mass components and heat component in two (mobile) phases is four, which indicates that the four primary variables can completely define the flow system state of CO_2 geologic sequestration. All other (secondary) variables can be computed from the four primary variables.

An important consideration in the program design is the choice of the primary variables (PV). When a phase appears or disappears, the set of appropriate thermodynamic variables may change. In this study, a primary variable switching scheme is used. Different primary variables are chosen under different phase conditions (Table 2). Experience has proven variable-switching to be a very robust method for treating such multiphase flow systems as CO₂ storage in saline aquifers. The four primary variables include pressure, salt mass fraction/solid salt saturation, CO₂ mass fraction, and temperature for single phase; and pressure, salt mass fraction/solid salt saturation, gas-phase saturation, and temperature for two phases. When no solid salt is present, the second primary variable is salt mass fraction dissolved in the two-component water-NaCl system. When solid salt is present, solid saturation is selected as the second primary variable, because the salt mass fraction is no longer an independent variable: it is determined by the equilibrium solubility of NaCl, which is a function of temperature. In Table 2, we note some primary variables plus 10.0 are used in model calculations, because the second and third primary variables all have a value ranging from 0 to 1.0. By adding a number 10.0, the presence or absence of solid salt, and single- or two-phase fluid conditions, can be recognized simply from the numerical value of the second and third primary variable. For the isothermal cases, heat transport is ignored and temperatures are maintained at their initial values.

Table 2. Phases, system states, and primary variables*

Phase	State ID	PV1	PV2	PV3	PV4
1-Phase: Gaseous, with salt	GsS	P	S _s +10	X _{CO2}	T
1-Phase: Gaseous, no salt	Gas	P	X _{NaCl}	X _{CO2}	T
1-Phase: Aqueous, with salt	AqS	P	S _s +10	X _{CO2}	T
1-Phase: Aqueous, no salt	Aqu	P	X _{NaCl}	X _{CO2}	T
2-Phase: Gas+Aqu with salt	AGS	P	S _s +10	S _g +10	T
2-Phase: Gas+Aqu no salt	AqG	P	X _{NaCl}	S _g +10	T

* The primary variables: P is pressure, S_s is solid salt saturation, X_{NaCl} is NaCl mass fraction in the two-component system water-NaCl, X_{CO2} is CO₂ mass fraction in gaseous or aqueous phase, and S_g is gas saturation; T is temperature.

Program implementation

The code is implemented with the standard FORTRAN 95/2003, except for the libraries for domain decomposition and parallel linear solver, which are written in C by third parties. Object-oriented programming architecture and some new language features are used to enhance code performance, such as pointers, lists and trees, data encapsulation, defined operators and assignments, operator extension and overloading, use of generic procedures, and maximum use of the powerful intrinsic vector and matrix processing operations. In addition, many utility functions are carefully designed for higher efficiency, such as the use of an efficient binary index searching scheme. Dynamic memory allocation for all larger arrays, together with the domain decomposition approach, allows large-scale problems to be solved on distributed memory computers. The code has been designed for maximum portability, scalability, and efficiency.

Parallelization

The massively parallel simulation scheme implemented into the TOUGH+CO₂ simulator uses the same approach as discussed in Zhang et al. (2001). The code partitions the simulation domain, defined by an unstructured grid, using a partitioning algorithm from the METIS software package (Karypis and Kumar, 1998). In a parallel simulation, each processor will treat one portion of the simulation domain for updating thermophysical properties, assembling mass and energy-balance equations, solving linear equation systems, and performing other local computations. Local linear-equation systems are solved in parallel by multiple processors with the Aztec linear solver package (Tuminaro et al., 1999). This parallel simulator has been built with an efficient communication scheme. Detailed discussion of the prototype of the data-exchange scheme can be found in Elmroth et al. (2001), and improvements in the communication scheme are further discussed in Zhang and Wu (2006).

APPLICATION EXAMPLE: CO₂ INJECTION INTO A 3D LAYERED SALINE AQUIFER

Continuous long-term injection of CO₂ into a saline aquifer will cause a buildup of groundwater pressures in extensive regions. The injection activities may induce significant hydrological and geochemical impacts on groundwater resources. One of the most common applications of TOUGH+CO₂ is for simulating such a CO₂ injection process and its influence on the groundwater flow system. We use a three-dimensional (3D) example to demonstrate application of the code and its performance.

The first industrial scale CO₂ storage project to become operational is at the Sleipner Vest field in the Norwegian sector of the North Sea, where approximately 10⁶ tons of CO₂ per year have been injected, since 1996, through a horizontal well into sands of the Utsira formation. A two-dimensional model has been designed based on this project for intercomparison of modeling codes (Pruess, 2005). The model was patterned after conditions at Sleipner and was designed to investigate CO₂ migration in heterogeneous sand-shale interlayers. In this paper, a three-dimensional version of the model is developed.

Even for the 3D model, significant simplifications have to be made. One of the most important simplifications is the assumption of isothermal conditions with a constant temperature of 37°C, which is the approximate ambient temperature of the formation. CO₂ injection rates, system geometry, and system permeabilities correspond approximately to those at Sleipner, although no attempt was made to accurately represent details of the permeability structure within the host formation. Injection of the supercritical CO₂, which is less dense than the saline formation waters into which it is injected, causes it to rise through the formation. Its rate of ascent, however, is limited by the presence of four relatively low-permeability shale layers (Figure 1). The top and bottom of the formation are assumed to be impermeable. The only reactive chemistry considered in this problem is the dissolution of CO₂ in the aqueous phase.

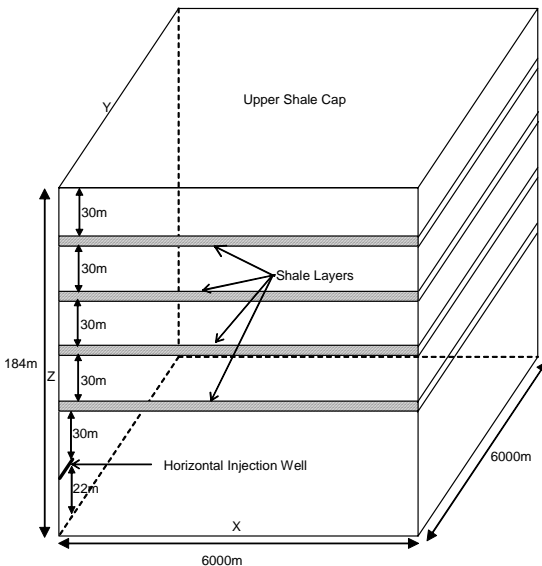


Figure 1. Schematic representation of the 3D geometry for CO₂ injection in the Utsira Formation.

The sequestration system is idealized as a 3D symmetric domain. The model needs only to cover one quarter of the domain because of symmetry.

Figure 1 shows the 3D model range. The horizontal injection well, which has a screen length of 100 meters (50 m for the model) with a 1m×1m cross-sectional area, is along the Y direction. The well is 30 m below the lowest shale unit, while the bottom of the aquifer is another 22 m below the well. The thickness of the formation at the site is 184 m. The injection point is 940 m below the sea floor, while the ocean depth at the site is 80 m. The formation is assumed to include four lower permeability shale units of 3 m thickness distributed within the high-permeability sand at 30 m distance. Top and bottom of the simulation domain are impermeable boundaries. The two sides with X=0 and Y=0 are also impermeable boundaries, due to model symmetry. No heat and mass flux is allowed across the impermeable boundaries. The other two sides with X=6,000 m and Y=6,000 m are chosen as fixed hydrostatic pressure boundaries, which allows flow into and out of the domain. The two constant pressure boundaries are ~6,000 m away from the injection well, which is far enough that the CO₂ cannot reach the two boundaries after 2 years of injection.

The model mesh is designed with refined grid around the well and near shale layers where significant gradients may occur. Gridding in the X-direction starts with 1 m increments at the well, and becomes coarser at increasing distance with a total 29 gridblocks to reach 6000 m. In the Y-direction, the 50 m length horizontal well is discretized into 25 gridblocks at 2 m each. The Y-direction is discretized into a total of 50 gridblocks. Gridding in the Z-direction also uses a 1 m increment blocks at the well and coarser grid below and above, with a total 34 of gridblocks. With this discretization scheme, the model consists of 49,300 elements and 143,764 connections. The most important parameters for the model include intrinsic permeability $3 \times 10^{-12} \text{ m}^2$ for sand and 10^{-14} m^2 for shale, corresponding porosity of 0.35 and 0.1025. Other parameters can be found in Pruess et al. (2002).

The initial conditions of the model are generated based on the measurements and estimations: (1) isothermal conditions with $T=37^\circ\text{C}$ for the entire model domain, (2) hydrostatic pressure conditions with a pressure of 110 bars at the injection level, (3) a salinity of 3.2% mass fraction of NaCl, (4) CO₂ in the aqueous phase in equilibrium with a PCO₂ of 0.5 bars, a typical value for sedimentary formation waters at the temperature of 37°C, which is about 0.04541% CO₂ mass fraction. The initial conditions are obtained by specifying the thermodynamic properties of $P = 110 \text{ bars}$, $T = 37^\circ\text{C}$, salinity $X_s = 0.032$, CO₂ mass fraction $X_{\text{CO}_2} = 4.541 \times 10^{-4}$ for all gridblocks with fixed pressure at the horizontal level of the injection well, and running the simulation to steady state for gravity equilibrium.

The injection of 10^6 tons of CO_2 per year to the system represents an injection rate of about 31.7 kg/s, corresponding to 0.317 kg/s for each 2 m long injection gridblock. The total injection applied to the model is $\frac{1}{4}$ of the total injection rate. The model is run with the given initial conditions, boundary conditions, and injection rate for 2 years of continuous injection. Figures 2–7 show some simulation results.

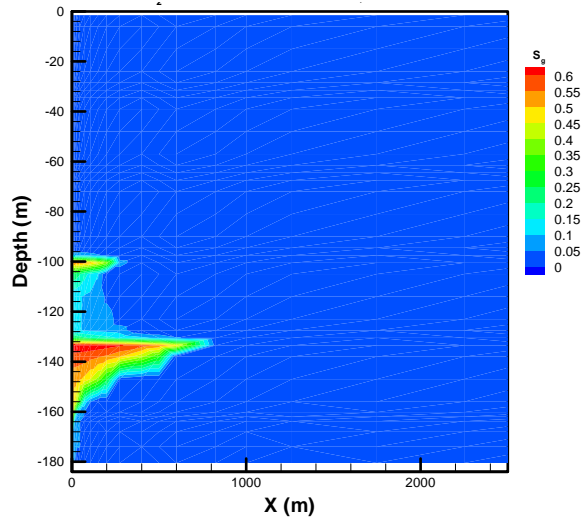


Figure 2. Distribution of gas saturation at $Y=1.0\text{m}$ after 2 years of CO_2 injection

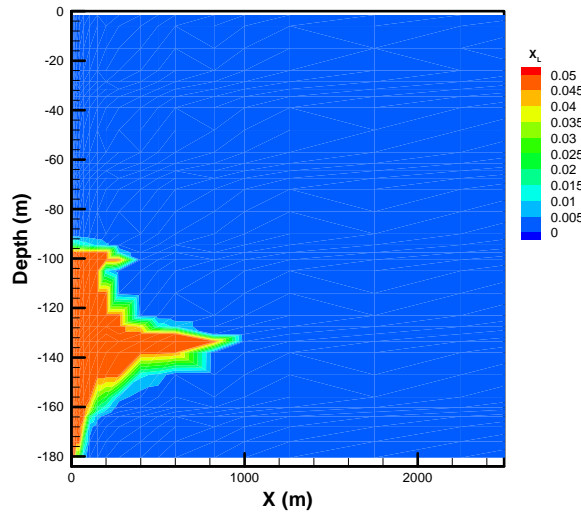


Figure 3. Distribution of dissolved CO_2 mass fraction at $Y=1.0\text{m}$ after 2 years of CO_2 injection

Figure 2 shows the distribution of gas saturation at the $Y=1.0\text{ m}$ (the vertical cross section which is perpendicular to the horizontal injection well) after two years of simulation time. The peak gas saturations of approximately 60% occur beneath the shale layers at elevations of -123 m and -99 m. When CO_2 is injected into the target sand aquifer, it partially displaces the resident brine and partially

dissolves in it. Under the site subsurface temperature and pressure conditions, CO_2 is buoyant (less dense) compared to brine, and the injected CO_2 moves upward towards the bottom of the shale layers. Eventually, the carbon dioxide is partially distributed among sand layers beneath the shale, and partially migrates through the low-permeable shale layer into the next sand layer. At the time of 2 years, the injected CO_2 goes through only one shale layer. When CO_2 accumulates beneath the shale layers, it slowly dissolves in brine. Dissolution of CO_2 leads to an increase in the density of aqueous phase by a small amount. Although small, the density increase may be sufficient to generate convection flow in the formation. The distribution of dissolved CO_2 mass fraction (Figure 3) may confirm this process. The range of dissolved CO_2 mass fraction for 4.5% or higher covers most of the two-phase zone. The plume is significantly larger than the gas-phase distribution. By comparing the 3D model results with previous 2D results (Pruess et al., 2002), we can find that the 3D model predicts much smaller plumes of CO_2 in gas saturation and mass fraction distribution. This suggests that a 3D model may be necessary for field-scale investigation.

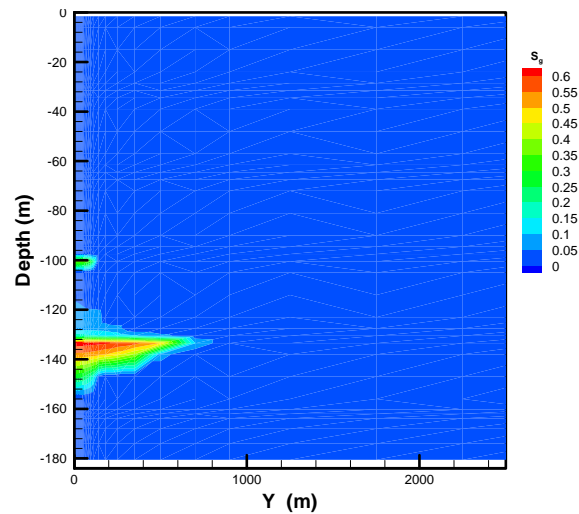


Figure 4. Distribution of gas saturation at $X=200.0\text{m}$ after 2 years of CO_2 injection

Figure 4 shows a contour map of gas saturations at $X=200\text{ m}$. The cross section of $X=200\text{ m}$ is parallel to the horizontal injection well, at a distance of 200 m from the well. The figure shows the front of gas CO_2 distribution at the location, which has a similar pattern as the distribution at $Y=1.0\text{ m}$, except a smaller range. The figure also shows that CO_2 migration along the horizontal well direction is very significant.

Figure 5 shows pressure changes with time at 4 gridblocks. AU111 (0.5 m, 1.0 m, -162 m) and AUP11(0.5 m, 49 m, -162 m) are gridblocks at the center and end of the horizontal injection well,

respectively. Both APQ1C (200 m, 52 m, -138 m) and ASQ1C (200 m, 52 m, -156 m) are located near the end of the injection well ($x=200$ m, $y=52$ m), but APQ1C is 18 m above ASQ1C. CO₂ injection causes pressures to rise initially, most strongly and rapidly in the well center gridblock. The two well gridblocks have very similar patterns of pressure evolution curves, except the one located at the well end shows less pressure buildup. Pressure changes at APQ1C and ASQ1C are less strong and with some time delay. Once the system establishes a quasi-steady flow condition at the injection well, pressures of the well gridblocks start to decline slowly.

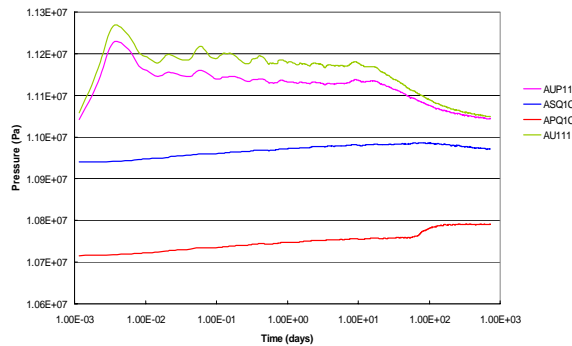


Figure 5. Pressure evolution with time at 4 locations

The correctness of these simulation results has been confirmed by comparing with the corresponding 3D model results obtained by TOUGH2/ECO2N code.

The simulations were run on a Linux cluster equipped with 10 nodes using infiniband switch connection, and each node consists of 2 INTEL Xeon 3.6 GHz CPUs. Series and parallel simulations with different numbers of CPUs were run for the first 0.2 years of CO₂ injection, to examine the code performance. The total execution time reduces from 30,504 seconds by series simulation, to 7112 seconds by parallel simulation with 8 CPUs and 3,178 seconds with 16 CPUs. The code demonstrates very good performance with near-linear or even super-linear speedup.

CONCLUSIONS

An efficient numerical simulation program, named TOUGH+CO₂, has been developed for modeling of CO₂ geologic sequestration in saline aquifers. The program is a member of TOUGH+, the successor to the TOUGH2 family of codes for multicomponent, multiphase fluid- and heat-flow simulation. TOUGH+CO₂ was developed based on TOUGH2/ECO2N. In addition to inheriting all functionalities from the TOUGH+ platform, the code retains all the process-modeling capabilities from TOUGH2/ECO2N. The new code is a three-dimensional, fully implicit model that solves large, sparse linear systems arising from discretization of the partial differential equations for mass and energy

balance in porous and fractured media. The code uses the FORTRAN 95 OOP architecture, adopts new language features, and redesigns the program data structure to enhance memory use and computing efficiency. In addition, a domain decomposition approach has been implemented for parallel simulation. All these features lead to increased computational efficiency and allow application of the code to multi-core/processor parallel computing platforms with excellent scalability.

The program was applied to simulate a CO₂ sequestration project with a 3D model. The model was patterned after conditions at the Sleipner site and was designed to investigate CO₂ migration in heterogeneous sand-shale interlayers. The exercise demonstrates good performance of the new code. Reasonable simulation results have been reached.

ACKNOWLEDGMENT

The authors would like to thank Lehua Pan for his review of this paper. This work was supported by funding from TOUGH royalty funds at the Earth Sciences Division, LBNL.

REFERENCES

- Altunin, V.V., *Thermophysical Properties of Carbon Dioxide*, Publishing House of Standards, 551 pp., Moscow (in Russian), 1975.
- Aziz, K. and A. Settari, *Petroleum Reservoir Simulation*, Elsevier, London and New York, 1979
- Brooks, R. H., and A.T. Corey, Properties of media affecting fluid flow. *J. Irrig. Drain. Div., Am. Soc. Civil Engineering*. 92 (IR2):61-88, 1966.
- Corey, A.T., The Interrelation Between Gas and Oil Relative Permeabilities, *Producers Monthly*, 38-41, November, 1954.
- Edwards, A.L., *TRUMP: A Computer Program for Transient and Steady State Temperature Distributions in Multidimensional Systems*, National Technical Information Service, National Bureau of Standards, Springfield, VA, 1972.
- Elmroth, E., C. Ding, and Y.S. Wu, High performance computations for large-scale simulations of subsurface multiphase fluid and heat flow, *The Journal of Supercomputing*, 18(3), pp. 233-256, 2001.
- Grant, M.A., *Permeability Reduction Factors at Wairakei*, paper 77-HT-52, presented at AIChE-ASME Heat Transfer Conference, Salt Lake City, Utah. 1977.

- Karypis, G. And V. Kumar, *METIS: A Software Package for Partitioning Unstructured Graphs, Partitioning Meshes, and Computing Fill-Reducing Orderings of Sparse Matrices, V4.0*, Technical Report, Department of Computer Science, University of Minnesota, 1998.
- Milly, P.C.D., Moisture and Heat Transport in Hysteretic, Inhomogeneous Porous Media: A Matrix-Head Based Formulation and a Numerical Model, *Water Resour. Res.*, Vol. 18, No. 3, pp. 489 – 498, 1982
- Moridis, G., M. Kowalsky, S. Finsterle, and K. Pruess, *TOUGH+: The New Generation of Object-Oriented Family of Codes for the Solution of Problems of Flow and Transport in the Subsurface*, Proceedings of TOUGH Symposium 2006, Lawrence Berkeley National Laboratory, Berkeley, California, May 15-17, 2006.
- Moridis, G.J., M. Kowalsky, and K. Pruess, *TOUGH+HYDRATE v1.0 User's Manual*. Report LBNL-0149E, Lawrence Berkeley National Laboratory, Berkeley, CA, 2008.
- Pickens, J.F., R.W. Gillham, and D. R. Cameron, Finite Element Analysis of the Transport of Water and Solutes in Tile-Drained Soils, *J. of Hydrology*, 40, 243-264, 1979.
- Pruess, K., and T. N. Narasimhan, On Fluid Reserves and the Production of Superheated Steam from Fractured, Vapor-Dominated Geothermal Reservoirs, *J. Geophys. Res.*, Vol. 87, No. B11, pp. 9329 – 9339, 1982.
- Pruess, K. and T. N. Narasimhan, A Practical Method for Modeling Fluid and Heat Flow in Fractured Porous Media, *Soc. Pet. Eng. J.*, Vol. 25, No. 1, pp. 14 – 26, 1985
- Pruess, K., C. Oldenburg. and G. Moridis, *TOUGH2 User's Guide, V2.*, Lawrence Berkeley National Laboratory Report LBNL-43134, Berkeley, CA, 1999.
- Pruess, K. and J. García, Multiphase Flow Dynamics During CO₂ Injection into Saline Aquifers, *Environmental Geology*, Vol. 42, pp. 282 – 295, 2002.
- Pruess, K., J. García, T. Kovscek, C. Oldenburg, J. Rutqvist, C. Steefel and T. Xu. *Intercomparison of Numerical Simulation Codes for Geologic Disposal of CO₂*, Lawrence Berkeley National Laboratory Report LBNL-51813, Berkeley, CA 94720, December 2002.
- Pruess, K., *ECO2N: A TOUGH2 Fluid property module for mixtures of water, NaCl, and CO₂*, Lawrence Berkeley National Laboratory Report LBNL-57952, Berkeley, CA, 2005.
- Spycher, N. and K. Pruess, CO₂-H₂O Mixtures in the Geological Sequestration of CO₂. II. Partitioning in Chloride Brines at 12–100 °C and up to 600 bar, *Geochim. Cosmochim. Acta*, 69, No. 13, pp. 3309–3320, doi:10.1016/j.gca.2005.01.015, 2005
- Tuminaro, R.S., M. Heroux, S. A. Hutchinson, and J. N. Shadid, *Official Aztec user's guide, Ver 2.1*, Massively Parallel Computing Research Laboratory, Sandia National Laboratories, Albuquerque, NM, 1999.
- Udell, K.S. and J. S. Fitch, *Heat and Mass Transfer in Capillary Porous Media Considering Evaporation, Condensation, and Non-Condensable Gas Effects*, paper presented at 23rd ASME/AIChE National Heat Transfer Conference, Denver, CO, 1985
- van Genuchten, M.Th., A Closed-Form Equation for Predicting the Hydraulic Conductivity of Unsaturated Soils, *Soil Sci. Soc. Am. J.*, 44, pp. 892 – 898, 1980.
- Vargftik, N. B., Tables on the Thermophysical Properties of Liquids and Gases. 2nd ed, New York : John Wiley & Sons, 1975.
- Verma, A. K., K. Pruess, C. F. Tsang, and P. A. Witherspoon, *A Study of Two-Phase Concurrent Flow of Steam and Water in an Unconsolidated Porous Medium*, Proc. 23rd National Heat Transfer Conference, Am. Society of Mechanical Engineers, Denver, CO, 135–143, 1985.
- Verma, A. and K. Pruess, Thermohydrologic Conditions and Silica Redistribution Near High-Level Nuclear Wastes Emplaced in Saturated Geological Formations, *Journal of Geophysical Res.*, Vol. 93 (B2), pp. 1159-1173, 1988.
- Zhang, K., Y. S. Wu, C. Ding, K. Pruess, and E. Elmroth, *Parallel computing techniques for large-scale reservoir simulation of multi-component and multiphase fluid flow*, Paper SPE 66343, Proceedings of the 2001 SPE Reservoir Simulation Symposium, Houston, Texas, 2001.
- Zhang, K. and Y. S. Wu, *Enhancing Scalability and Efficiency of the TOUGH-MP for Linux Clusters*, proceedings of TOUGH Symposium 2006, Berkeley, CA, 2006.
- Zhang K., C. Doughty, Y. S. Wu, and K. Pruess., *Efficient Parallel Simulation of CO₂ Geologic Sequestration in Saline Aquifers*, Paper SPE 106026, Proceedings of the 2007 SPE Reservoir Simulation Symposium, Houston, Texas, 2007.

INVESTIGATION OF GRIDDING EFFECTS FOR NUMERICAL SIMULATION OF CO₂ GEOLOGIC SEQUESTRATIONS

Hajime Yamamoto¹ and Christine Doughty²

¹ Taisei Corporation, 344-1 Nase-cho Totsuka-ku, Yokohama, 245-0051, Japan

² Lawrence Berkeley National Laboratory, #1 Cyclotron Rd, MS 90-1116, Berkeley, California, 94708, USA
e-mail: hajime.yamamoto@sakura.taisei.co.jp; cadoughty@lbl.gov

ABSTRACT

Uncertainties caused by gridding effects (in terms of grid shape and resolution) are investigated for the numerical simulation of CO₂ geologic sequestration in the WESTCARB Phase III pilot test. This pilot test involves a large-volume CO₂ injection into a saline formation in California's Central Valley, and preliminary simulations using a coarse rectangular grid have already been performed to predict CO₂ plume migration and trapping mechanisms. For this study, we generated a high-resolution model with Voronoi discretization. In the model, the lithologies (sand/shale distribution) in the original geological model of the injection formation were fully represented. To solve the high-resolution model efficiently, a parallelized version of TOUGH2, TOUGH-MP/ECO2N, was used. Our results indicate that (1) high-order Voronoi discretization significantly reduces grid-orientation effects; (2) Coarse grids considerably underestimate gravity override, and thus the maximum lateral extent of CO₂ plumes is also underestimated to a few tens of percent for our cases; (3) A fine-grid resolution in the vicinity of the injection well may be needed to simulate near-well phenomena. Salt precipitation associated with formation dryout could be highly over- or underestimated by the use of coarse grids when the capillary-driven backflow to the well is significant.

INTRODUCTION

In two-phase flow simulation, it is well known that geometry and grid resolution can significantly change the shape of two-phase fronts. For example, when CO₂ is injected into a single well and the shape of the CO₂ saturation front should be essentially radial, the use of a five-point finite difference scheme results in a "diamond" shape for the front. In a vertical cross section, coarse grids underestimate gravity override (less dense CO₂ flows over denser groundwater), and thus the maximum radial extent of the plume is also underestimated. Limitation of computational power often requires reducing the number of model gridblocks, by simplifying or upscaling a heterogeneous lithology model originally interpreted and developed by geologists.

In this paper, the following gridding effects are investigated for numerical simulations of CO₂ geologic sequestration.

- (1) Shape of two-phase fronts
 - Grid-orientation phenomenon
 - Gravity override
- (2) Salt precipitation
- (3) Subgrid-scale heterogeneity

The early part of the paper will illustrate gridding effects (1) and (2), using simple 1D/2D radial models. Then all three effects are investigated as part of a numerical simulation of a CO₂ injection pilot test that is planned for a saline formation in California.

GRIDDING EFFECTS IN A SIMPLE MODEL

Shape of Two-phase Front

Grid-orientation phenomenon

When CO₂ is injected into a single well and the shape of the CO₂ saturation front should be essentially radial, the use of a five-point finite difference scheme results in a "diamond" shape for the front, as shown in Figure 1. This phenomenon is well known as "grid-orientation effect" (Aziz and Settari, 1979), which commonly occurs whenever there is gas injection. The effect is not a result of truncation errors alone and remains prominent as the grid is refined. The grid-orientation error increases as the saturation front becomes sharper, which occurs with an increasing mobility ratio and decreases with an increasing dispersion term (i.e., capillary pressure, mechanical dispersion). This effect can be removed by employing a nine-point difference scheme (Doughty and Pruess, 2004) or a two-point upstream weighting scheme, but these approaches significantly increase the computational load.

Here, we examine high-order Voronoi discretization as a way to remove grid-orientation effects, as schematically shown in Figure 1c.

We consider a horizontal storage formation (1 m thick) at 2 km depth (T=81°C, P=220 bars, X_s=0.05) for the simulation. The formation is homogeneous and isotropic. Throughout this paper, we assume isothermal conditions, and diffusions in aqueous and

gaseous phases are neglected for the simulations. The effect of diffusion will be negligible for this short time frame. Permeability k and porosity ϕ of the formation are 200 md and 28% respectively. The relative permeability is given by the van Genuchten model, with $m=0.457$ and $S_{lr}=0.2$. CO_2 is injected at a constant rate of 0.1 kg/s. The Voronoi grid is shown in Figure 2, along with a rectangular grid for comparison. These are one-layer models, so no gravity effects are involved. The CO_2 saturation fronts at 4 years are shown for both grids in Figure 2. In Figure 2, it is seen that the shape of the saturation contour for the rectangular grid is distorted. This is caused by grid-orientation effects, which favor fluid flow along the grid axis directions. Figure 2b shows that a circular front is obtained for the Voronoi grid, indicating that the Voronoi grid can remove the grid-orientation effect.

Gravity Override

Gravity override occurs when less dense CO_2 flows over denser groundwater. In CO_2 geologic sequestration, gravity override is important for

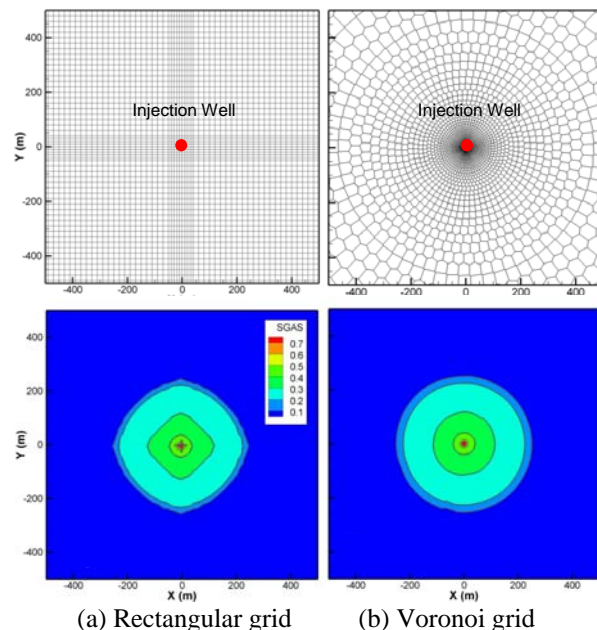
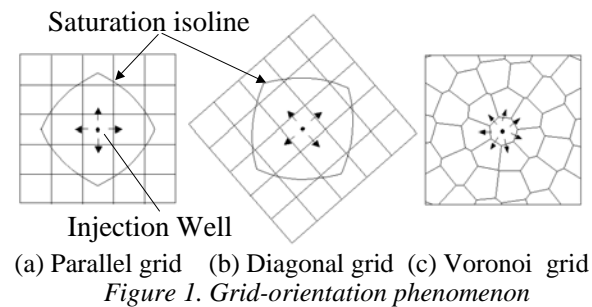


Figure 2. Example of CO_2 saturation contours (below) calculated for rectangular and Voronoi grid models (above) of a horizontal formation

evaluating the maximum lateral extent of CO_2 plumes, and also the storage efficiency or capacity of CO_2 storage in a formation. When there is a difference in density between the injected fluid and the fluid initially present, the slope of the interface between the fluids depends on the ratio of viscous forces to gravitational forces. The degree of gravity override increases as the difference in density between the two fluids increases, as the permeability of the medium increases, and as the mobility ratio increases. At a given injection site, one operational parameter that affects override is the CO_2 injection rate (Davis, 1998).

It is also well known that coarse gridding in a vertical cross section underestimates gravity override, and thus the maximum radial extent of the plume is also underestimated (Aziz and Settari, 1979).

Examples of gravity override of CO_2 over groundwater are shown in Figure 3. This simulation considers a horizontal storage formation of 100 m thickness. The other formation parameters are the same as above. Two-dimensional radial models with different vertical grid-resolution ($dz=1$ m and 10 m) are used, as shown in Figure 3a. CO_2 is injected with a constant rate of 0.01 Mt/year and 1 Mt/year. The CO_2 saturation contours after 20 years' injection at the vertical cross section for the two cases of different injection rates are shown in Figures 3b and 3c, respectively. The radial extent of the CO_2 plume obtained from the coarse grid is obviously shorter than that from the fine grid. In the case of 0.01 Mt/year, where the gravitational force is comparatively dominant, the radial extent of the CO_2 plume obtained from the coarse grid is underestimated by about 30% compared to that from the fine grid.

Formation Dry-out and Salt Precipitation

Injection of CO_2 into a saline aquifer may cause formation dryout and precipitation of solid salt near the injection well, which may reduce porosity, permeability, and injectivity (Pruess and Müller, 2009). This section presents how resolution of lateral grid spacing affects the formation dryout and salt precipitation encountered in this study.

Without capillarity

A basic problem similar to Test Problem 3 of a code intercomparison study (Pruess et al., 2004), and used in the recent salt precipitation study by Pruess and Müller (2009), is adapted for the current study. A CO_2 injection well fully penetrates a homogeneous, isotropic, infinite-acting aquifer of 100 m thicknesses, at conditions of 120 bar pressure, 50°C temperature, and a salinity of 25% by weight NaCl. CO_2 is injected uniformly at a constant rate of 5kg/s. Formation parameters are as follows: $k=33$ md,

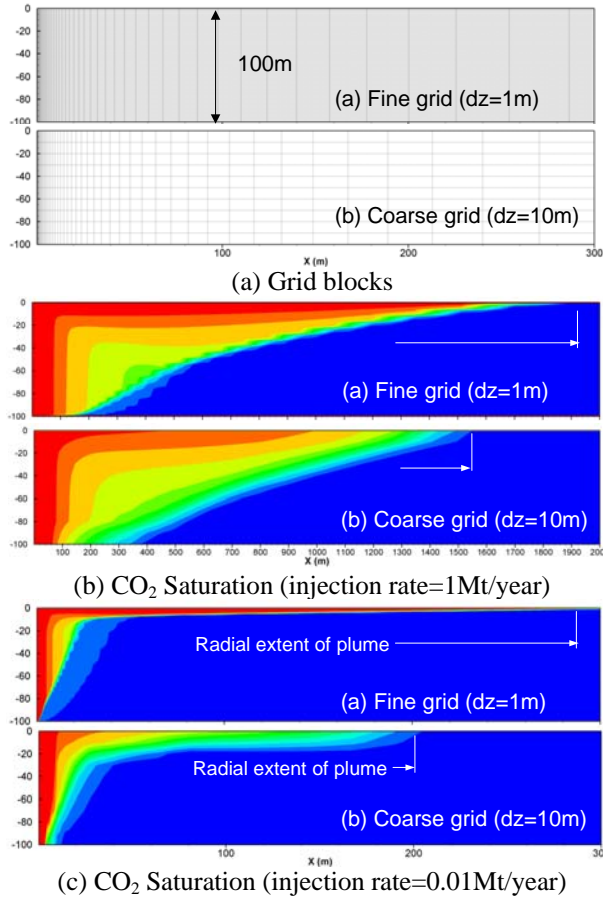


Figure 3. Examples of CO₂ saturation profile in vertical cross section from fine and coarse grids.

$\phi=20\%$, $S_{lr}=0.263$, $m=0.187$, $S_{gr}=0.05$. A one-dimensional radial grid is used for the simulation, neglecting gravity effects. Starting from the well radius of 0.1 m, different grid spacings (dr) are examined ($dr=0.02$ m, 0.2 m, 1 m, 5 m, 10 m, 20 m, and 50 m) within a radial distance of 10 m. Permeability reduction with decreasing porosity is not considered.

Figure 4 shows formation dryout and salt precipitation after 1-year injection obtained from the simulation with 0.02 m grid spacing. It is seen that salt precipitation occurs only within the dryout zone with a constant solid saturation. Pruess (2009) developed an analytical model for the salt precipitation as follows.

$$M_s = \pi r_d^2 \phi (1 - \bar{S}_{g,d}) \rho_{aq} X_s \quad (1)$$

$$S_s = \left(1 - \bar{S}_{g,d}\right) \frac{\rho_{aq} X_s}{\rho_s} \quad (2)$$

where M_s is mass of solid salt precipitated, r_d radial distance from the injection point to the dryout front at time t , S_s solid salt saturation, ϕ porosity, ρ_{aq} : aqueous phase density, X_s the mass fraction of salt, $\bar{S}_{g,d}$ average gas saturation in the region behind the dryout front. The parameters r_d and $\bar{S}_{g,d}$ can be calculated based on the fractional flow theory (see Pruess, 2009 for details).

In Figure 5a, an excellent match is found between the analytical solution of salt precipitation (M_s) given by Equation (1) and numerical results for the fine grid of $dr=0.02$ m, whereas the coarse grids underestimate salt precipitation. The delay of the start of precipitation is attributed to the larger amount of water initially presents in coarser grids, because much CO₂ can flow into the gridblock before sufficient evaporation of water causes salinity to reach the solubility limit of salt. In the figure, the position of the dryout front (r_d) as calculated by Pruess (2009) is also plotted on the graph. It is confirmed that the numerical simulations with coarse grids underestimate the total solid salt until the dryout front reaches the first grid interface (=grid block size). As expected, such error can occur not only at the first gridblock, but also at every gridblock sequentially along the CO₂ plume movement. In Figure 5b, it is seen that coarser grids generally underestimate the salt precipitation more, except for the times, indicated by the arrows, at which the dryout front reaches each gridblock interface, and analytical and numerical results correspond to each other.

With capillarity

Capillary pressures will provide a driving force for backflow of aqueous phase toward the injection well, which provides a supply of dissolved salt to be precipitated, especially near the dryout front where capillary pressure gradients are largest (Pruess and Müller, 2009).

Figure 6 shows salt precipitation profiles obtained from the simulation with capillarity. Here, we used the same model and parameters as in the previous “without capillarity” case, except that capillary pressure is introduced using the van Genuchten model with $m=0.457$ and $P_0=19.6$ kPa. In addition, the injection rate is reduced to 1/10 (0.5kg/s) and absolute permeability is increased to 66 md, so as to emphasize the capillary-driven backflow of aqueous phase to the well.

In Figure 6a, without capillarity, solid salt saturation throughout the dryout region becomes constant independent of space and time, as analytically described in Equation (2) from Pruess (2009). On the other hand, with capillarity (see, $dr=0.02$ m in the figure), the backflow has the considerable effect of

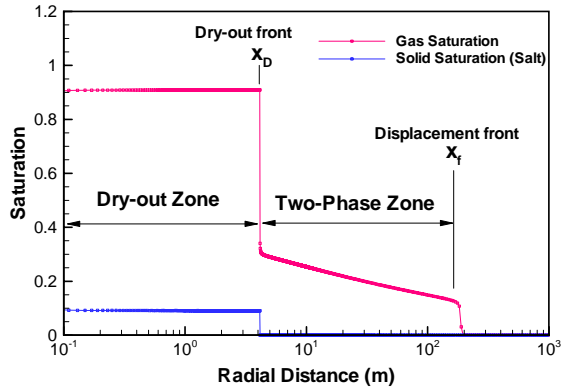
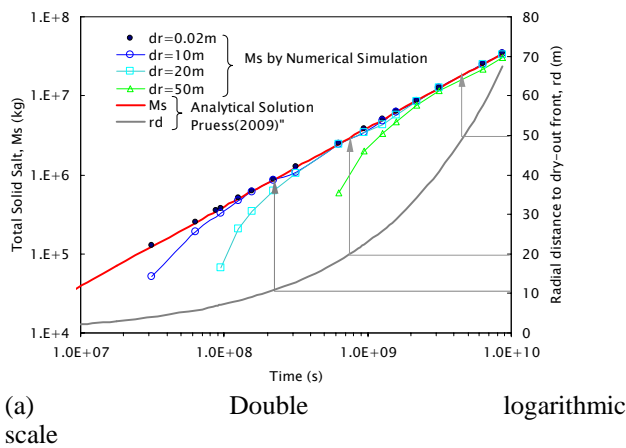
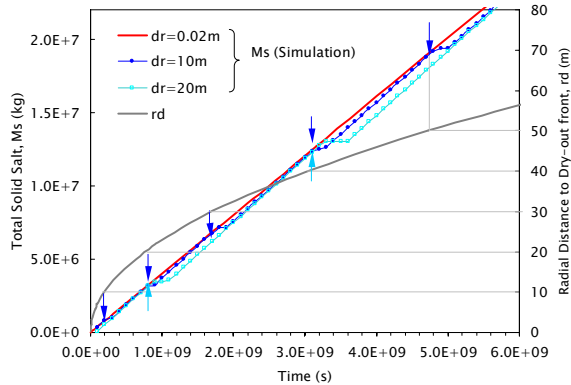


Figure 4. Formation dryout and salt precipitation for a simulation using 0.02 m grid spacing



(a) Double logarithmic scale



(b) Linear scale

Figure 5. Time evolutions of solid salt precipitation at the first gridblock. Analytical and numerical solutions for fine and coarse grids

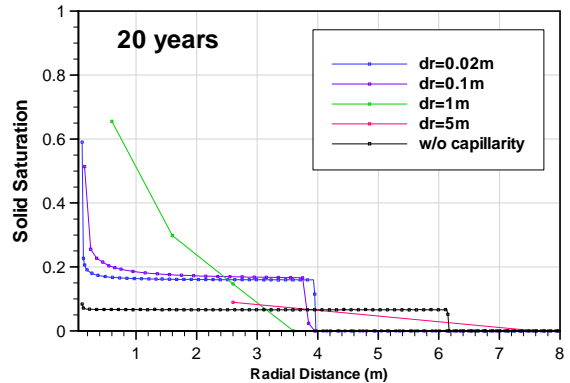
thrusting back the dryout front, increasing solid salt saturation above the w/o capillarity case.

The capillary-driven backflow of the aqueous phase toward the well becomes prominent for slow injection rate, high liquid permeability (absolute permeability \times liquid relative permeability), or steep capillary pressure gradients. For example, the larger m value of van Genuchten's relative permeability curve will yield larger salt precipitation in the dryout

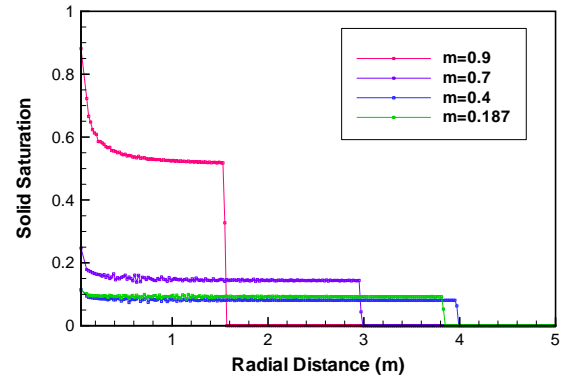
zone, as shown in Figure 6b, at 10 years, since the injection start for an example case of $k=200$ md and injection rate = 5kg/s. It is seen that the use of $m = 0.9$ yields a very high solid saturation in a narrow precipitation zone, that can result in near-zero permeability, deteriorating the well injectivity, if the permeability reduction option is adapted in the model. The rapid rise of solid saturation around the well, especially at the early stages of injection, is attributed to the fast backflow to the well.

In terms of the effect of grid size, in Figure 6a, the backflow continuously supplies solute to a gridblock just behind the dryout front, until the water in the next-downstream gridblock reaches the solubility limit of salt. This results in greater salt precipitation in the coarser grids than in the fine-grid case. At the same time, as discussed above, coarser grids may also underestimate the solid saturation due to the delay in the start of salt precipitation, as demonstrated by the $dr = 5$ m case in the figure.

These results suggest that the simulation of salt precipitation at field scales can be computationally challenging, because it may require a very high-resolution grid, when capillary-driven backflow is



(a) Effect of grid size



(b) Effect of van Genuchten's m value

Figure 6. The effect of grid size and a parameter for salt precipitation with capillary-driven backflow of saline water.

significant, depending on the injection rate, liquid permeability, and capillary pressure distribution.

GRID SENSITIVITY STUDY FOR THE SIMULATION OF CO₂ INJECTION PILOT TEST AT KIMBERLINA SITE

WESTCARB (West Coast Regional Carbon Sequestration Partnership) led by the California Energy Commission is planning a commercial-scale, large-volume CO₂ sequestration test (LVST) in the San Joaquin Valley, California. The oxy-combustion “Zero-Emissions Power Plant” (ZEPP-1) plans to provide 250,000 metric tons of CO₂ per year for four years’ injection of the LVST. A numerical model using a coarse rectangular grid has already been developed for preliminary simulations performed to predict CO₂ plume migration and trapping mechanisms (Doughty, 2009).

In this study, a high-resolution model is developed to investigate uncertainties due to gridding effects (geometry and resolution) present in the previous simulation. In addition, phenomena near the injection well are also explored.

Model Setup

The target formation for the injection is the Vedder Formation, a high-permeability sand about 150 m thick, located at a depth of 2 km. The Vedder Formation consists of alternating sand and shale layers, and is covered by a low-permeability shale formation. The geologic model has been developed by Lawrence Livermore National Laboratory, using 180 layers to represent the sand and shale distribution in the Vedder Formation (Wagoner, 2009).

In the previous simulation by Doughty (2009), a TOUGH2 model of the Vedder Formation was developed for the 11 km by 11 km area centered on the injection well. The thickness and dip of the formation are respectively 157.5 m and 7°. The sand/shale ratio is assumed to be 50%. For the initial reservoir conditions, we assumed a hydrostatic pressure distribution with average 220 bars at the injection well; an initial temperature of 81°C; and an initial salinity of 50,000 mg/L. Material properties used for the base-case model in Doughty (2009) are shown in Table 1. A no-flow boundary condition was applied for the top/bottom boundary and lateral y-direction boundary, while a constant-pressure boundary was applied for the lateral x-direction boundary. Permeability reduction with decreasing porosity associated with salt precipitation was not considered.

In this study, the conceptual model and parameters are the same as Doughty (2009), except (1) the hysteretic formulations of relative permeability and

capillary pressure are not involved, which is very important for the fate of CO₂ in the postinjection period; (2) the van Genuchten parameter m for liquid relative permeability was reduced from 0.917 to 0.457, to avoid heavy NaCl precipitation occurring near the wellbore, especially when the high-resolution grid is used. As discussed above, a larger m value increases relative permeability of the liquid phase, and generates rapid backflow of the liquid phase to the well.

The isothermal two-phase flow simulation ran for the 4-year injection period at a rate of 250,000 tons of CO₂ per year, resulting in one million tons of CO₂ injected. In the models, the injection rate is uniformly assigned to wellbore elements located in the sand layers. To solve the high-resolution model efficiently, a parallelized version of TOUGH2, TOUGH-MP ECO2N (Zhang et al., 2008) was used.

Table 1. Material properties for the simulation (based on Doughty, 2009)

Property		Sand	Shale
Porosity	n	28%	15%
Horizontal permeability	$k_{x,y}$	200md	0.1md
Vertical permeability	k_z	20md	0.01md
Relative permeability parameters			
Residual liquid saturation	S_{lr}	0.2	0.3
van Genuchten parameter	m	0.457*	0.457*
Capillary pressure parameters			
Capillary pressure strength	P_0	1.88X10 ⁴ Pa	8.41X10 ⁵ Pa
van Genuchten parameter	m	0.412	0.412

* 0.917 is adopted in Doughty(2009)

Grid Models

Four grid models with different grid shapes and resolutions are compared to investigate the gridding effects as shown in Table 2. The R30-30 model is the rectangular grid employed in Doughty (2009) with varying lateral grid spacing: maximum 55 m within CO₂ plume footprint and 5 m at injection well, as shown in Figure 7a. Each TOUGH2 model layer combines six geologic model layers, resulting in 30 layers each 5.25 m thick. A plan view of the Voronoi discretization used in this study is shown in Figure 7b. To explore near-well phenomena, gridblocks are refined in the vicinity of the well, representing the 0.1 m-diameter well accurately.

In the three Voronoi grid models (V30-30, V30-180, and V180-180) the first and second numbers represent the number of geological and TOUGH2 model layers, respectively (Table 2). The vertical cross sections of the three models are shown in Figure 8. The V180-180 model fully represents the 180 layers, each 0.875 m thick, of the original geologic model in the corresponding 180 layers of the TOUGH2 model. The V30-30 model represents the same 30 geologic layers used in the R30-30

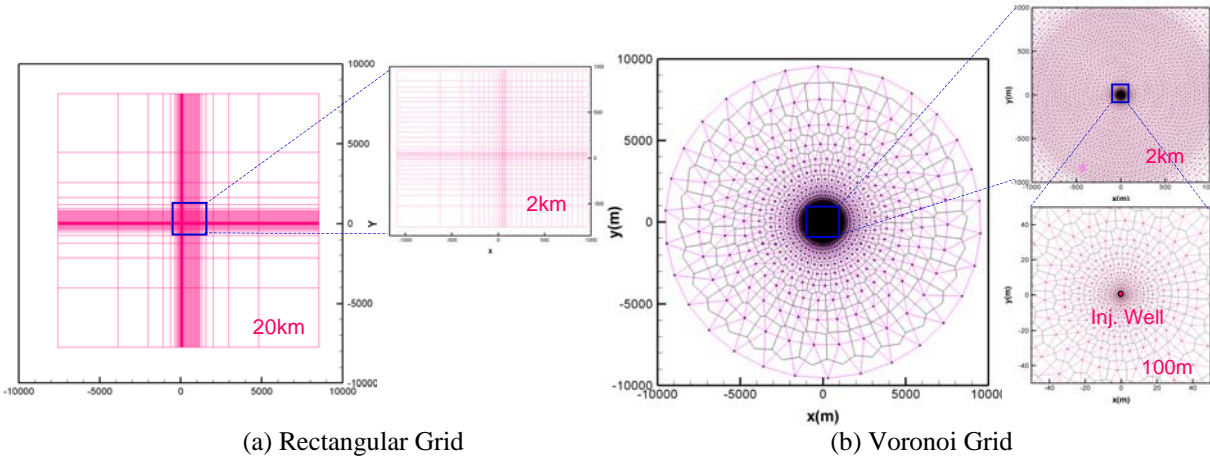


Figure 7. Plan views of grids (pink: connections, black: element polygons, closed circles: node points).

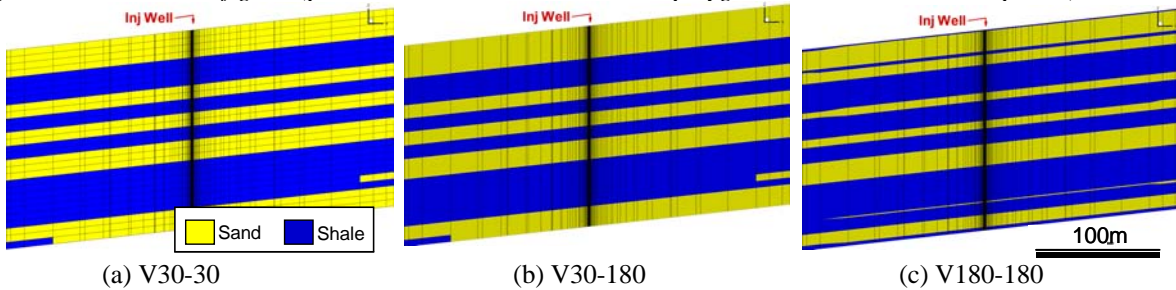


Figure 8. Vertical cross sections ($y=0$) near the injection well for three TOUGH2 grid models investigated in this study. For visibility, only about 300 m wide areas centered on the injection well are depicted.

model. In addition, to investigate the vertical grid-resolution effect in the V30-30 model, the V30-180 model was constructed assigning the simplified geologic model of 30 layers to the 180-layer TOUGH2 grid (Figure 8b).

Table 2. Studied grid models

Model	Grid type	Geologic Layers	TOUGH2 Layers	Number of elements	Number of Connections
R30-30*	Rectangular	30	30	63,360	185,208
V30-30	Voronoi	30	30	73,170	289,221
V30-180	Voronoi	30	180	439,020	1,747,521
V180-180	Voronoi	180	180	439,020	1,747,521

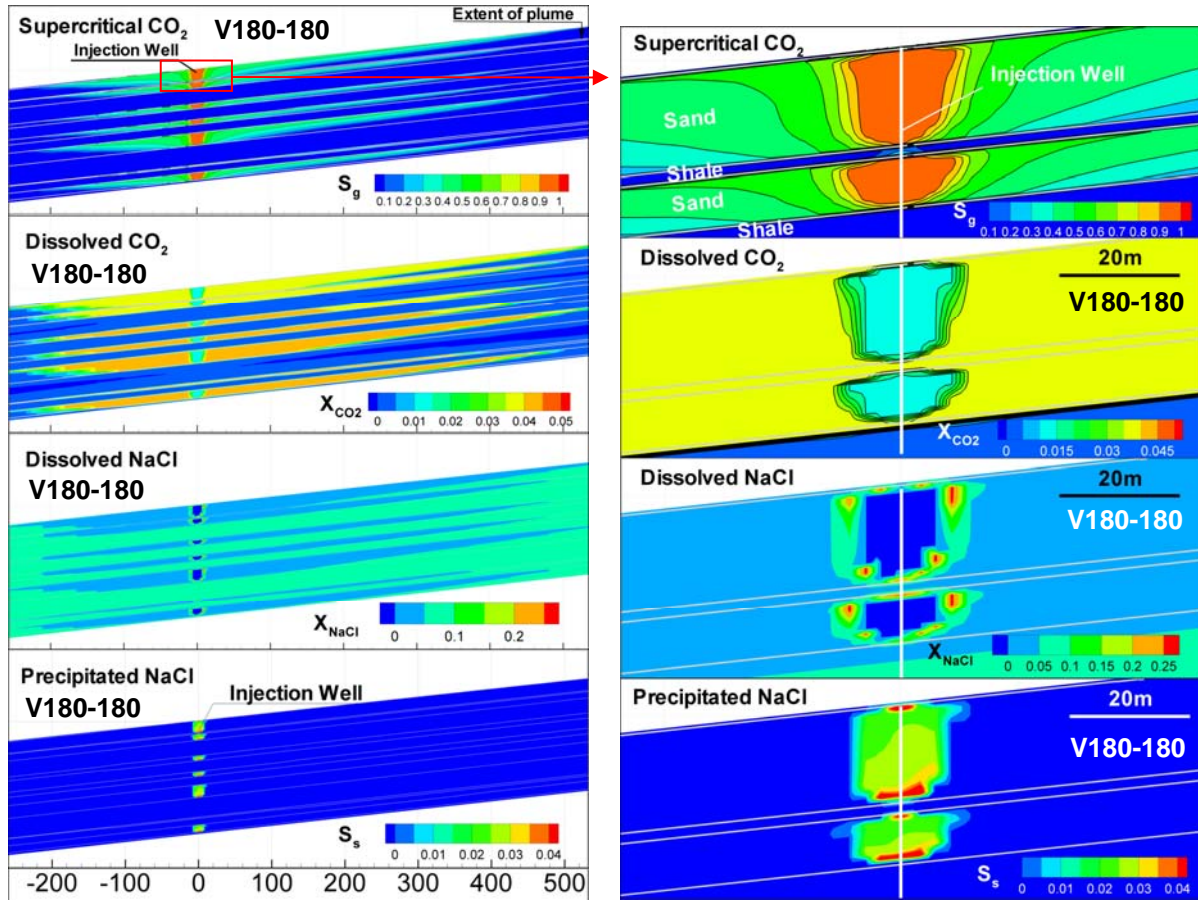
* Doughty(2009)

Simulation Results

Figure 9 shows the simulation results obtained from the V180-180 model after 4 years of injection on the cross section at $y=0$, for supercritical CO_2 saturation, mass fractions of dissolved CO_2 and NaCl, and solid salt saturation. The white lines on the cross section in Figures 9 and 10 align with the sand-shale interfaces. A key feature is the strong buoyancy flow to the top of each layer and in the up-dip direction. Near the well bore (Figure 9b), we note that solid saturation increases mostly along the sand/shale interfaces at the top and bottom of the sand formation. This is because of enhanced vertical capillary-driven flow at the sand/shale interface, essentially perpendicular to the major flow direction. Figure 10 compares CO_2 saturation profiles from the three models with 30-layer discretization of the geologic model. Comparing Figures 8b and 8c shows that several additional thin sand and shale layers can be resolved with the V180-180 grid compared to the V30-180

grid. Doing so causes differences in the details of the simulated distributions of CO_2 and salt, but the overall CO_2 plume evolution, including the up-dip extent of the supercritical CO_2 plumes, is very similar for the two grids (compare Figures 9a and 10 bottom).

The CO_2 saturation near the injection well is sharply higher in the Voronoi grids (V30-30 and V30-180), because of the fine lateral resolution of grids near the wellbore, whereas it is absent in the R30-30 model, in which grid spacing is rather coarse (5 m) near the well. The lateral extents of the CO_2 plumes obtained from the two 30-layer models (R30-30 and V30-30) are almost identical, while much larger extent is obtained from the 180-layer model (V30-180). The maximum difference in the extent is found in the up-dip direction, whereas no significant difference is found in the down-dip direction. This is the aforementioned effect of vertical grid resolution on gravity override. Figure 10 also compares the precipitation patterns of solid salt near wellbore. R30-180 represents the asymmetrical distribution of the salt precipitation, probably due to the CO_2 plume movement to the up-dip direction by gravity effects, while it is symmetrical in R30-30 and V30-30. Figure 11 shows a plan view of the CO_2 plume front, drawn along the contour line of CO_2 saturation =10%. Comparing R30-30 with V30-30, the planar size of the CO_2 plumes are almost identical, except for the “diamond”-like shape in R30-30, due to grid-orientation effects, which emphasize the movement of the plume in the x- and y-directions.



(a) Overview

(b) Near wellbore

Figure 9. East-west cross-section of the V180-180 model in the plane $y=0$ at 4 years

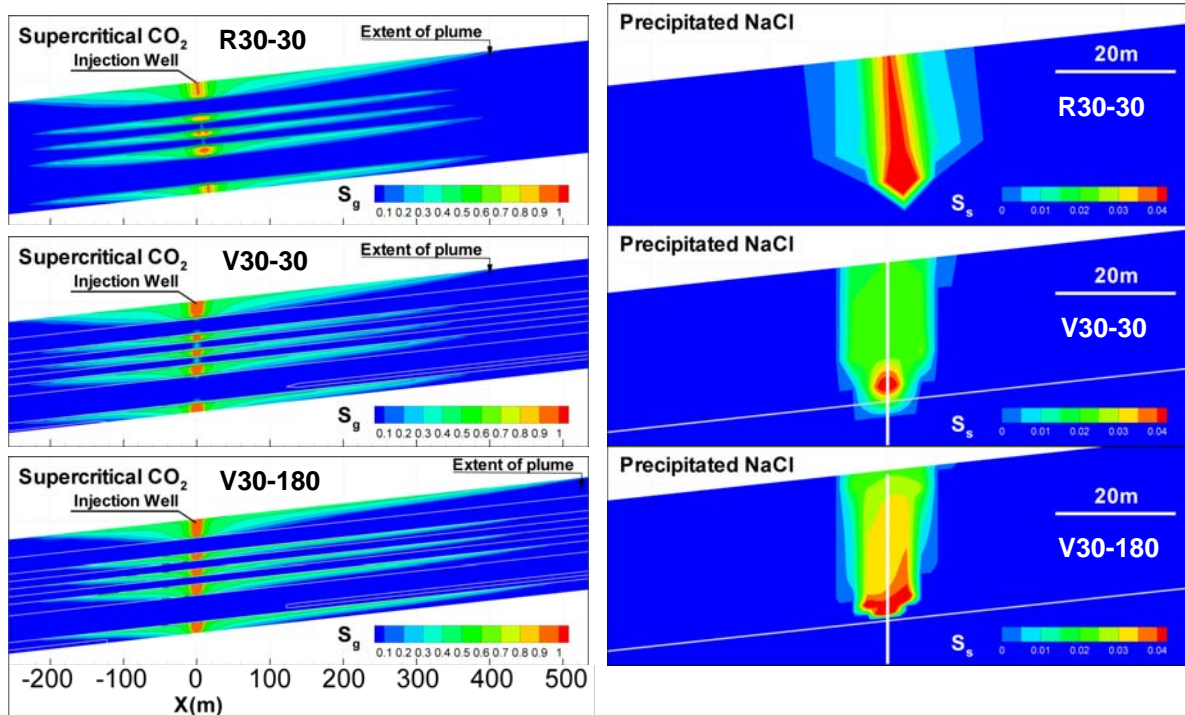


Figure 10. CO_2 saturation on the EW cross-section (left) and solid salt saturation near wellbore (right) at 4 years, for R30-30 (upper), V30-30 (middle), and V30-180 (bottom). The white lines on the cross-sections align with the sand-shale interfaces

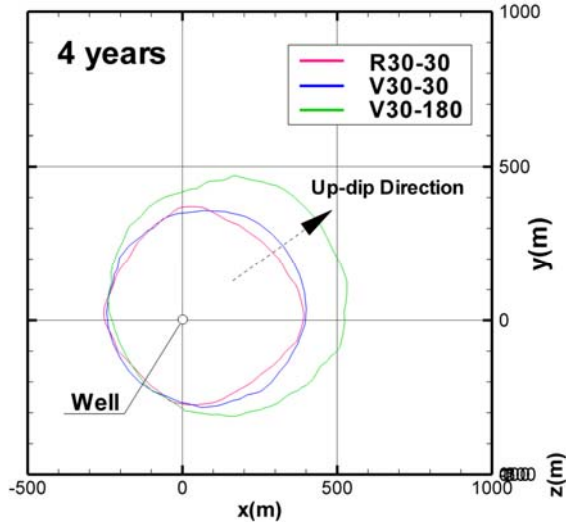


Figure 11. Plan view of CO₂ plume front ($S_g=10\%$) in the uppermost layer of the model

of the plume in the x- and y-directions. However, both the two 30-layer models underestimate the extent of CO₂ plume by about 30% in the up-dip direction, compared to the 180-layer model.

CONCLUSIONS

In this study, uncertainties due to gridding effects in terms of shapes and resolutions were investigated for the numerical simulation of CO₂ geologic sequestration in the WESTCARB Phase III pilot test.

Our results indicate that:

- (1) High-order Voronoi discretization can significantly reduce grid-orientation effects, and is necessary to clearly illustrate the shape and movement direction of CO₂ plumes.
- (2) Coarse grids considerably underestimate gravity override, and thus the maximum lateral extent of CO₂ plumes is also underestimated. The effect is prominent in flow to the up-dip direction, where the gravity force has an important role. In the simulation of the pilot test, the plume extent obtained from a coarse model was a few tens of percent shorter than that from a fine model.
- (3) To simulate near-well phenomena exactly, much finer grid resolution in the vicinity of the injection well may be needed. The use of coarse grids may result in considerable over- or underestimation of salt precipitation, especially in flow conditions where the capillary-driven backflow to the well is significant.
- (4) In terms of the sand/shale lithology, the uncertainties due to the model resolution seem insignificant for the current geological model and simulation settings. Nevertheless, in general, the representation of heterogeneous lithology is a very important uncertainty factor that should be investigated in the future, along with geology and facies modeling.

ACKNOWLEDGMENTS

The authors appreciate Jeff Wagoner of Lawrence Livermore National Laboratory for providing the geological model of the Kimberlina site. We thank Larry Myer and Curt Oldenburg of Lawrence Berkeley National Laboratory, and Satoshi Imamura and Tomoyuki Aoki of Taisei Corporation for encouragement and support. Thanks are also due to Keni Zhang for the extensive support on the use of TOUGH2-MP code. This work is partly supported by Taisei Corporation, and in part by the U.S. Department of Energy under contract No. DE-AC02-05CH11231.

REFERENCES

- Aziz, K. and A. Settari, *Petroleum Reservoir Simulation*, Applied Science Publishers, London, 1979.
- Davis, E.L., *Steam injection for soil and aquifer remediation*, EPA/540/S-97/505, 1998.
- Doughty, C., Investigation of CO₂ plume behavior for a large-scale pilot test of geologic carbon storage in a saline formation, *Transport in Porous Media*, doi:10.1007/s11242-009-9396-z, 2009.
- Doughty, C. and K. Pruess, Modeling supercritical carbon dioxide injection in heterogeneous porous media, *Vadose Zone Journal*, 3, 837-847, 2004.
- Pruess, K., C. Oldenburg, and G. Moridis, *TOUGH2 User's Guide, Version 2.0*, Rep. LBNL-43134, Lawrence Berkeley National Laboratory, Berkeley, CA, 1999.
- Pruess, K. and N. Müller, Formation dry-out from CO₂ injection into saline aquifers: 1. Effects of solids precipitation and their mitigation, *Water Resour. Res.*, 45, W03402, doi:10.1029/2008WR007101, 2009.
- Pruess, K., Formation dry-out from CO₂ injection into saline aquifers: 2. Analytical model for salt precipitation, *Water Resour. Res.*, 45, W03403, doi:10.1029/2008WR007102, 2009.
- Wagoner, J., *3D geologic modeling of the southern San Joaquin basin for the Westcarb Kimberlina demonstration project – a status report*. Rep. LLNL-TR-410813. Lawrence Livermore National Laboratory, Livermore, CA, 2009.
- Zhang, K., Y.S. Wu, and K. Pruess, *User's Guide for TOUGH2-MP - A Massively Parallel Version of the TOUGH2 Code*, Rep. LBNL-315E, Lawrence Berkeley National Laboratory, Berkeley, CA, 2008.

A GEOCHEMICAL STUDY OF CO₂ INJECTION INTO DEPLETED GAS FIELDS IN THE NETHERLANDS

T.J. Tambach, T. Benedictus, F. van Bergen, V.P. Vandeweyer, and L.G.H. van der Meer

Business Unit Geo-energy and Geo-information, TNO Geological Survey of the Netherlands
Princetonlaan 6, P.O. Box 80015
3508 TA Utrecht, The Netherlands
e-mail: tim.tambach@tno.nl

ABSTRACT

Natural analogues of CO₂-dominated gas reservoirs indicate that subsurface CO₂ containment over geological time scales is stable. However, CO₂ injection into depleted gas fields leads to CO₂ dissolution in the formation water and lowering of the pH. Consequently, geochemical dissolution and precipitation reactions of minerals could lead to injectivity problems (e.g., clogging) in the reservoir or degradation of the sealing cap rock and well materials. It is therefore important to quantify the geochemical response of the reservoir to CO₂ injection.

Several models are available to model the geochemical impact of CO₂ injection into depleted gas fields. In this study, reactive transport modeling (via TOUGHREACT) is used to study CO₂ injection into a simplified reservoir structure, representative of a depleted gas field in the Netherlands, for a relatively short period of 10 years. The results show that physical and chemical properties in the reservoir change during time. Dry-out of the near-well zone and salt precipitation are observed during the CO₂ injection phase, which is caused by water uptake by dry CO₂. The salt precipitation reduces the porosity in the near-well zone with a maximum of 0.5%. After shut-in of the well, the gas saturation (S_g) does not change. Mineral reactions depend on the availability of water and therefore do not take place in the zone that is completely dried out ($S_g = 1$). In the near-well zone, up to a distance of 74.3 m, S_g declines from 1 to the initial S_g of 0.85. In this zone, a retardation of mineral reactions occurs, due to the limited water availability. Beyond the near-well zone, the final S_g is 0.845. Several mineral reactions were predicted to take place in the reservoir. Pyrite is oxidized and glauconite, muscovite, and calcite dissolve. Illite, quartz (or chalcedony), and anhydrite precipitate. Mineral trapping of CO₂ occurs in dolomite and siderite. On the relatively small simulated time scale of 10 years, the reactions take place slowly. A limited increase in porosity (<0.01%) and permeability (<0.02%) is predicted after 7.2 years shut-in time. Longer simulation time is necessary to predict the long-term stability of CO₂ in depleted gas fields, but this requires sufficient CPU time.

INTRODUCTION

Carbon dioxide (CO₂) is one of the most prominent greenhouse gases in the Earth's atmosphere. To limit global warming and climate change, CO₂ emission (from industrial sources) needs to be reduced. Carbon Capture and Storage (CCS) through CO₂ injection into geological formations is a promising way for isolating the gas from the atmosphere for a long time span (Benson and Cook, 2005). Potential onshore and offshore injection sites include depleted oil and gas reservoirs, deep saline aquifers, and unminable coal seams. Several projects worldwide have successfully demonstrated CO₂ storage, for example K12-B in the offshore part of the Netherlands (Van der Meer et al., 2005; Audigane et al., 2008).

Once present in reservoirs, four types of CO₂ trapping can be considered, their dominance depending on the time (Benson and Cook, 2005). Structural trapping and residual trapping refer to storage in open and isolated pores, respectively. Solubility trapping indicates the dissolution of CO₂ in the formation water, which depends on the salinity (Duan and Sun, 2003). In contrast to these three trapping types, mineral trapping becomes more dominant at a later stage and is related to a complex geochemical response of the system. As CO₂ dissolution into the formation water lowers the pH, it induces solubility of primary minerals and precipitation of secondary minerals. The geochemical reactivity of each mineral varies, depending on the kinetics and accessibility of the minerals in the reservoir. Fixation of CO₂ in several carbonate minerals (e.g., calcite, dolomite, dawsonite, siderite, and magnesite) leads to CO₂ immobility and increases storage security. However, local variations in mineral dissolution and precipitation affect the permeability and may lead to injectivity problems, especially near the wellbore, or migration out of the reservoir into the overburden. The time scales and extent to which all trapping mechanisms occur (Benson and Cook, 2005) remain speculative and require further study.

Due to the practical limitations involved in observing the *in situ* behavior of CO₂ in reservoirs experimentally, its fate has been extensively modeled (i.e., Van der Meer, 1996; Van der Meer, 2000; Xu et

al., 2004, Xu et al. 2005, Gaus et al. 2005, Audigane et al. 2008). Numerical modeling provides a fast and cost-effective way for evaluating the consequences of CO₂ storage in the reservoir. Several physical and chemical processes are accounted for in simulators nowadays, such as multiphase fluid flow, mineral reactivity, and solute transport. It was shown that mineral alteration, porosity changes, and the amount of CO₂ trapped in minerals depend on the mineralogical composition of the reservoir (Xu et al., 2004). Also, a few simulation studies predict dry-out and salt precipitation in the near-well zone (André et al., 2007; Giorgis et al., 2007; Pruess and Müller, 2009; Müller et al., 2009), which may have implications for porosity, permeability, and injectivity. The progression of dry-out and precipitation depends on many factors, such as CO₂ injection rate and reservoir properties (Pruess and Müller, 2009).

In this study reactive transport modeling of CO₂ injection into a depleted gas field is carried out using TOUGHREACT and the ECO2N module (Xu et al., 2006). The reservoir geometry was kept simple, and the geophysical and geochemical properties of the reservoir are based on the subsurface of the Netherlands.

BACKGROUND

CO₂ storage in the Netherlands

The Netherlands play a key role in the implementation of CCS in northwestern Europe, because CO₂ sources and storage reservoirs are situated at relatively short mutual distances, and infrastructure is already installed for (cross-border) gas transport over large distances. Early application of CCS, within the next 5 years, is promoted in the Netherlands—first, because of a strong commitment to reach the emission reductions, and second, because the oil and gas production in the country is maturing, and it is expected that many fields will be abandoned in the coming two decades. CCS should be applied within the same period or shortly after, to benefit from the use of (adapted) existing infrastructure such as platforms, wells, and pipelines. Various types of oil and gas fields in the subsurface of the Netherlands are currently evaluated as potential location for CO₂ storage. There is a need for finding a consistent methodology to support policy makers and field operators to evaluate the short-term operational effects and long-term containment of CO₂ storage in the reservoir.

Geological details

The main CO₂ storage capacity is expected in Permian Rotliegendes reservoirs, Triassic Buntsandstein reservoirs, and Cretaceous Rijnland reservoirs. The Rotliegendes reservoirs are good

candidates because of the overlying thick Permian Zechstein salt, which has provided an effective seal for gas generated from the Carboniferous. Cretaceous reservoirs that contain Jurassic oil are less likely candidate reservoirs, because of their expected small storage capacity.

The area near the Port of Rotterdam is an attractive location for early CCS application, because of its abundant industrial point sources with highly concentrated CO₂. However, sealing Zechstein salt is lacking here, and Carboniferous gas migrated towards the Mesozoic reservoirs. These are mainly sealed by intercalated shale layers, locally by thinner salt or evaporite layers. In this study, the De Lier Member of the Cretaceous Vlieland Sandstone Formation was selected, which is a typical sandstone-dominated interval that forms the reservoir of several gas fields in the proximity of the Port of Rotterdam. It is an alternation of thin-bedded, very fine- to fine-grained argillaceous sandstones, generally glauconitic and lignitic, and sandy claystones, commonly glauconitic, with shell fragments and frequent bioturbation. Siderite concretions are common. Sediments consist of decimeter-scale fining-upward beds. It is covered by the Lower Holland Marl Member that generally consists of grey and red-brown marl or calcareous, glauconitic, fissile claystone, frequently with intercalated bituminous claystone beds (Van Adrichem Boogaert and Kouwe, 1993-1997). The claystone beds provide the seal for the trapped gas in the underlying sandstone.

METHODS

Reservoir

A simplified model of a small reservoir was created representing a depleted Cretaceous gas field in the Netherlands at a depth of 1670 m. The grid model of the reservoir has x and y dimensions of 400 m by 1,000 m, a thickness of 20 m, and hence a total volume of 8.0×10^6 m³. The model has no-flow boundaries, representing impermeable layers and bounding faults surrounding the reservoir. The number of grid cells in the x,y,z direction is 11, 17, and 5, respectively, adding to a total number of 935. The size of the grid cells in the z direction is uniform (i.e., 4.0 m), whereas the cell dimensions in the x and y directions increase further away from the wellbore. The minimum and maximum grid cell sizes are 3.6 m and 100.0 m, respectively. A projection on the xy -plane (top view) is shown in Figure 1.

The assumed temperature in the reservoir is 72°C, with an initial CO₂ partial pressure of 2.0 bar. Although depleted gas fields usually contain remaining CH₄, it was not taken into account here, because the ECO2N module only describes the interactions between brine and CO₂. Chemically, CH₄ was assumed to behave as an inert phase. The

porosity in the reservoir was defined as 20%, with a water saturation of 15%. The permeability is 100 mD in all three directions, and no faults are present in the reservoir. The relatively low and irreducible water content implies no water flow (relative permeability of 0) and full gas flow (relative permeability of 1.0).

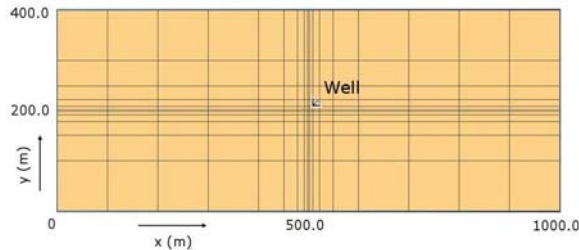


Figure 1. XY-projection (top view) of the reservoir model grid

CO₂ injection

Injection of CO₂ was carried out through a single vertical well, penetrating the entire depth interval in the middle of the *xy*-plane of the reservoir. The injection rate is 8.7 kg/s, which corresponds to a total injected mass of 275 kton per year. Continuous injection was carried out for 2.8 years, followed by a simulation of permanent shut-in of the well for 7.2

years. It should be noted that in practice a sequential scheme of CO₂ injection and shut-in could be carried

out (the effects of such discontinuous injection are not evaluated here). Temperature effects such as Joule-Thomson cooling (Oldenburg, 2006) were not taken into account.

Mineralogy and formation water

The average matrix density of the sandstone reservoir (ρ_{res}) is assumed to be 2,600 kg/m³. The mineralogy predominantly consists of quartz and significant amounts of clay minerals (kaolinite, muscovite, and illite), as well as small amounts of carbonates (calcite, dolomite, and dawsonite), and other minerals (K-feldspar, glauconite, and pyrite). The initial mineralogical volume fractions present in the simulations are given in Table 1.

Formation water composition data from the De Lier sandstone was present for several wells showing a relatively large variation in ionic species and concentrations. Throughout the reservoir, a sensitive equilibrium exists between the reservoir rock composition, formation water, and the gas phase. Constructing this balance in a geochemical model is relatively complex and requires a workflow, for example described by Xu et al. (2005) and Audigane et al. (2008). Here it was chosen to estimate the element concentrations in the formation water from the initial mineralogical and gas compositions in the reservoir.

Table 1. Initial volume fraction ($V_{frac,ini}$) (-) and parameters describing the kinetics of the mineral reactions at 25 °C (Palandri and Kharaka, 2004): dissolution rate constant (k in mol/m²s), activation energy (E in kJ/mol), reaction order parameter (n), and mineral surface area ($A_{minsurf}$) (cm²/g).

	$V_{frac,ini}$	Acid Mechanism			Neutral Mechanism		Base Mechanism			$A_{minsurf}$
		Log k	E	n	Log k	E	Log k	E	n	
Alunite	-	<i>Instantaneous</i>								
Anhydrite	-	-	-	-	-3.19	14.3	-	-	-	9.8
Calcite	3.73E-03	<i>Instantaneous</i>								
Chalcedony	-	-	-	-	-13.40	90.9	-	-	-	9.8
Dawsonite [#]	6.85E-05	-	-	-	-7.00	62.8	-	-	-	9.8
Diaspore [*]	-	-	-	-	-13.33	47.5	-23.60	47.5	-1.503	9.8
Dolomite-ord [#]	1.30E-04	-3.76	56.7	0.500	-8.60	95.3	-5.37	45.7	0.500	9.8
Glauconite [*]	1.30E-02	-4.80	85.0	0.700	-9.10	85.0	-	-	-	9.8
Illite [*]	6.20E-02	<i>Set to kaolinite</i>								
Kaolinite [*]	3.51E-02	-11.31	65.9	0.777	-13.18	22.2	-17.05	17.9	-0.472	151.63
K-Feldspar [*]	6.01E-03	-10.06	51.7	0.500	-12.41	38.0	-21.20	94.1	-0.823	9.8
Magnesite [#]	-	-6.38	14.4	1.000	-9.34	23.5	-5.22	62.8	1.000	9.8
Muscovite [*]	8.56E-03	-11.85	22.0	0.370	-13.55	22.0	-14.55	22.0	-0.220	151.63
Pyrite [*]	9.68E-04	-7.52	56.9	-0.500	-4.55	56.9	-	-	-	9.8
Quartz	0.6702	-	-	-	-13.40	90.9	-	-	-	9.8
Siderite	-	<i>Instantaneous</i>								
	0.800									

^{*} Reaction order with respect to H⁺; [#] Reaction order with respect to P(CO₂)

Table 2. Computed composition of the formation water in the reservoir, in equilibrium with the mineral and gas composition

Species	Concentration* (mol/kg H ₂ O)
Na ⁺	1.69
Ca ²⁺	3.56E-02
Fe ²⁺	2.47E-04
H ⁺	1.63E-03
K ⁺	1.24E-02
Mg ²⁺	6.14E-12
Cl ⁻	1.66
HCO ₃ ⁻	2.08E-03
SO ₄ ²⁻	6.69E-02
AlO ₂ ⁻	1.79E-07
SiO ₂	3.76E-04

* The total concentration of primary species and aqueous complexes are given.

The equilibrium state of pure water equilibrated with surplus amounts of measured minerals and gas was computed using PHREEQC (Parkhurst and Appelo, 1999) and the LLNL database, followed by equilibration in TOUGHREACT using the thermXu4 database. Minor differences are expected, owing to the use of different databases. Precipitation of new minerals (e.g., dawsonite and dolomite-ord) was allowed during equilibration, but was limited to very small volume fractions by lowering the reactants (predominantly slow-reacting clay minerals). The final composition of the formation water used for a reservoir grid is given in Table 2, with a corresponding pH of 5.3. Precipitation of secondary minerals alunite, chalcedony, siderite, diaspore, and magnesite was predicted with preliminary PHREEQC simulations using the mineralogy, equilibrated formation water, and a CO₂ partial pressure of 170 bar. Precipitation of the abovementioned minerals was therefore also enabled for computations with TOUGHREACT. Kinetics of precipitation and dissolution of most minerals were taken into account using the kinetic law of Lasaga (1984), as described in more detail elsewhere (Audigane et al., 2008). Most parameters are taken from the literature (Palandri and Kharaka, 2004; Audigane et al., 2008), or assumed to be instantaneous. The total set of parameters used here is listed in Table 1. The reactive surface area of clay minerals was set to 151.63 cm²/g, whereas a value of 9.8 cm²/g was assigned to the other minerals (Xu et al., 2005, Audigane et al. 2008). The grain radius for each mineral is assumed to be 1.0 mm.

RESULTS AND DISCUSSION

The pressure in the reservoir as a function of the time is given in Figure 2. During the CO₂ injection phase (i.e., 0–2.8 years), the pressure steadily increases up to approximately 170 bar. During the first few weeks, the pressure increases faster close to the well than further away from the well, for example 150 m, as illustrated in Figure 2. Immediately after shut-in of the well, the bottomhole pressure will equalize with the surrounding reservoir pressure. During the following 7.2 years, the pressure slowly declines with 0.4 bar due to CO₂ solubility and mineral trapping.

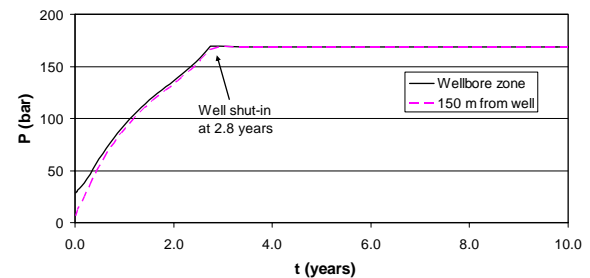


Figure 2. Pressure (P) in the reservoir as a function of time (t) near the well and 150 m away from the well

Dry-out of the wellbore zone

Initially the gas saturation (S_g) in the pores is 0.85. Injection of pure CO₂ leads to water evaporation from the reservoir into the CO₂ gas stream, also known as a dry-out effect. In Figure 3, the gas saturation is plotted as a function of the distance from the wellbore at several moments during the CO₂ injection phase (0–2.8 years). After shut-in of the well, only marginal changes are encountered. As becomes clear, the radius of the zone that is completely dried out ($S_g=1.0$) increases over time, with a final value of 35.4 m. This also holds for a transition zone, for which S_g varies from 0.85 to 1.0. Further away from the well, S_g is computed to be relatively stable, with a value of 0.845.

During dry-out of the near-well zone, the mass fraction of salt (NaCl) in the formation water increases, leading to precipitation. This is illustrated in Figure 4, showing the mass fraction of salt as a function of time. Relatively close to the wellbore (i.e., 15.4 m), the mass fraction of salt increases rapidly within a period of three months, followed by approximately 1 month of a stable mass fraction. This indicates that the formation water is saturated with NaCl and precipitation occurs, enhanced by the absence of water flow and solute transport. When all water has evaporated into the dry CO₂, then all salt

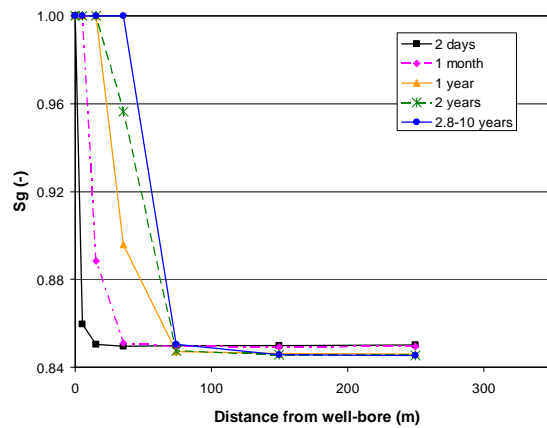


Figure 3. Gas saturation (S_g) in the reservoir as a function of the distance from the wellbore in the xz -plane ($x=200$ m; $z=-1680$ m)

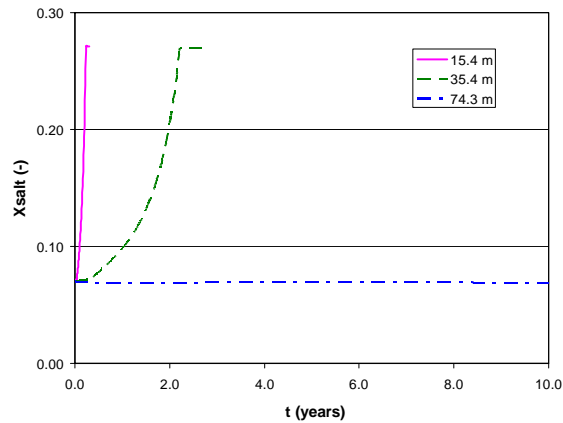


Figure 4. Mass fraction of salt (or NaCl) (X_{salt}) in the formation water as function of time (t) at three distances away from the wellbore in the xz -plane ($x=200$ m; $z=-1680$ m)

has precipitated, taking up 0.5% of the pore volume. Similar trends are also encountered closer to the wellbore (not shown) and further away from the wellbore (i.e., 35.4 m). A constant S_g is observed at a minimum distance of 74.3 m away from the wellbore (see Figure 3). Beyond this distance, the mass fraction of salt remains almost constant and close to the initial value of 0.07. Dry-out of the near-well zone was also predicted for saline aquifers (Pruess and Muller, 2009) with a corresponding salt precipitation fraction of 9.1% of the pore volume. This value is much higher in comparison with the one computed in the current study. In the work of Pruess and Muller (2009), more water is present, as all pores are initially filled with water ($S_g=0$), and the brine has a higher salt mass fraction. Consequently, more salt can precipitate.

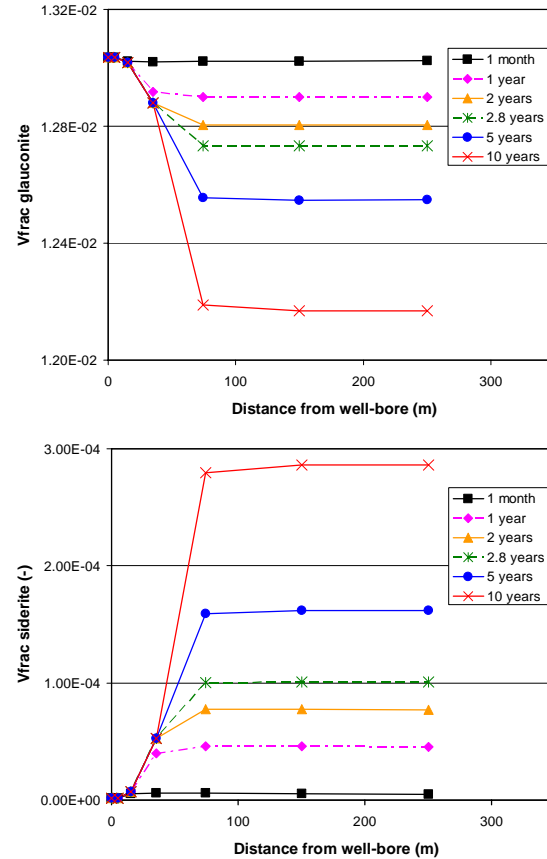


Figure 5. Volume fraction (V_{frac}) glauconite (top) and siderite (bottom) as a function of the distance from the wellbore in the xz -plane ($x=200$ m; $z=-1680$ m)

Mineral reactions

Geochemical reactions of minerals occur in the reservoir during the CO_2 injection and shut-in phases. This is illustrated for glauconite dissolution and siderite precipitation in Figure 5. Initially, the volume fractions of glauconite and siderite in the reservoir are constant throughout the reservoir. Dissolution or precipitation of these minerals depends on the mineralogy and composition of the formation water, as well as the kinetic parameters (see Table 1). Dry-out of the near-well zone also influences mineral reactions. Obviously, no reactions will take place in the zone that is completely dried out ($S_g=1$), because water is required for these reactions to occur. In the transition zone, more water is present with increasing distance from the wellbore (see Figure 3). This means that larger amounts of minerals can dissolve before saturation is reached. Beyond the distance where a constant S_g is observed (i.e., at 74.3 m from the wellbore), the largest changes in the amounts of glauconite and siderite are observed (see Figure 5). Similar behavior is encountered for the other dissolving and precipitating minerals, as described above.

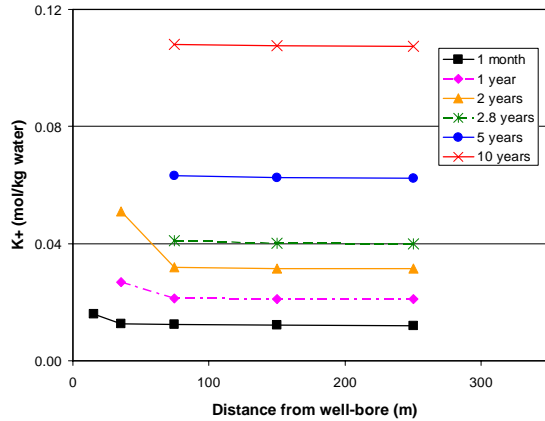


Figure 6. K^+ concentration as a function of the distance from the wellbore in the xz -plane ($x=200$ m; $z=-1680$ m)

During the simulation, a relatively small change in Al^{3+} concentration was computed, whereas a substantial increase of the K^+ concentration was found. This is illustrated in Figure 6. The increasing concentrations close to the well are caused by dry-out of the near-well zone, which was also discussed above for salt and shown in Figure 4. Since solute transport through water flow does not occur, all other ions also precipitate upon dry-out.

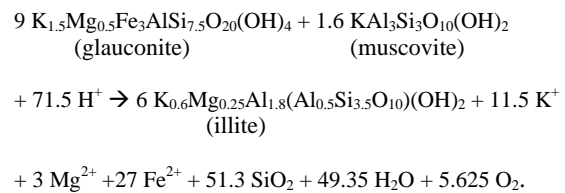
In Table 3, the final volume fractions of the minerals outside the dry-out zone (>74.3 m) are shown, as well as the relative change in volume fraction. As can be derived from Table 3, the simulations predict that trapping of CO_2 in carbonate minerals primarily occurs in dolomite and siderite during the first 10 years. It should be noted that instantaneous dissolution and precipitation was assumed for siderite (see Table 1). The amount of calcite is reduced, no trapping is observed in magnesite, and the initial traces of dawsonite disappear. Fixation of CO_2 in dawsonite has been predicted in several numerical studies (Xu et al., 2004; Xu et al., 2005), although on much larger time scales (i.e., 100,000 years). Apparently, precipitation of the other carbonate minerals is favored during the first 10 years for this reservoir.

Newly formed minerals are anhydrite and chalcedony (microcrystalline quartz), whereas diasporite and alunite are not formed. Significant amounts of muscovite and pyrite dissolve, while considerable amounts of illite precipitate. Transformations of K-feldspar and kaolinite are limited to less than 0.1%. The pH in the reservoir slowly decreases from 5.3 to a value of approximately 4.9. A limited increase in porosity ($<0.01\%$) and permeability ($<0.02\%$) is predicted beyond the near-well zone after 7.2 years of

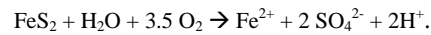
Table 3. Final volume fraction ($V_{frac,final}$) (-) and the relative change in volume fraction (ΔV_{frac}), with respect to $V_{frac,ini}$, outside the dry-out zone (>74.3 m)

	$V_{frac,final}$ (-)	ΔV_{frac} (%)
Alunite	0.0	-
Anhydrite	2.32E-05	>100
Calcite	3.67E-03	-1.4
Chalcedony	1.62E-04	>100
Dawsonite	0.0	-100
Diasporite	0.0	-
Dolomite-ord	1.85E-04	43.1
Glaucosite	1.22E-02	-6.7
Illite	6.23E-02	0.5
Kaolinite	3.51E-02	<0.1
K-Feldspar	6.02E-03	<0.1
Magnesite	0.0	-
Muscovite	8.50E-03	-0.8
Pyrite	9.55E-04	-1.4
Quartz	6.70E-01	<0.1
Siderite	2.86E-04	>100

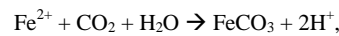
shut-in time. Using the observations discussed above, the most important geochemical mineral reactions can be summarized as follows. Glaucosite and muscovite dissolve, while illite precipitates:



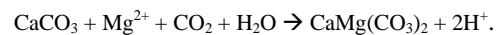
In the reaction given above, no Al^{3+} is formed, and the released O_2 is used to oxidize pyrite (FeS_2):



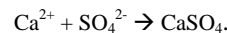
Mineral trapping of CO_2 occurs through siderite ($FeCO_3$) precipitation:



and transformation of calcite ($CaCO_3$) into dolomite ($CaMg(CO_3)_2$):



Anhydrite ($CaSO_4$) is formed with the released Ca^{2+} and SO_4^{2-} ions:



Note that the pH is lowered due to release of H^+ during pyrite oxidation and during the dissolution of

CO₂ with H₂O, embedded in the mineral trapping reactions of CO₂.

The composition of the mineralogy used here, as well as the trends that are found, compare with the glauconitic sandstone used in a batch reaction study that describes CO₂ injection in aquifers (Xu et al., 2004). In this study, dissolution of glauconite and precipitation of illite were also predicted, as well as CO₂ trapping in dolomite and siderite. The simulations in the abovementioned study were carried out up to 100,000 years—practically impossible for reactive transport modeling in 935 grid cells (as in the current study), due to CPU time constraints.

Implications for well integrity

Dry-out of the near-well zone reduced the water saturation to 0 in a radius of 1.8 m around the well after only 2 days of CO₂ injection. This could have significant implications for well integrity. Since both degradation of well cement and corrosion of steel casing and tubulars are governed by reactions requiring the presence of aqueous CO₂ (e.g., Kutcho et al., 2007; López et al., 2003), dehydration is expected to diminish the chemical reactivity of well materials with CO₂ and likely limits significant chemical degradation of the injection well. However, extraction of water from the cement itself is reported to affect its chemistry and microstructure (Hartmann et al., 1999). Further research is required to investigate this phenomenon in more detail.

Model sensitivity to the kinetic parameters

The results presented here depend on the kinetic parameters listed in Table 1. With respect to these parameters, a few assumptions need to be mentioned here that could influence the final results. The listed parameters describe mineral dissolution (Palandri and Kharaka, 2004). It is usually assumed that the dissolution and precipitation parameters are the same, since precipitation rates are usually more complicated to measure than dissolution rates. Often the measured data were acquired through experiments with unconsolidated and single mineral samples at atmospheric conditions. Reaction rates of coated minerals or minerals in a consolidated rock assemblage of several minerals are expected to be different. It is difficult to characterize the reactive surface areas of minerals (Audigane et al., 2008).

CONCLUSIONS AND FUTURE WORK

This work describes geochemical modeling of CO₂ injection into a relatively simple reservoir model representing a depleted gas field in the subsurface of the Netherlands. The simulations show that a radially increasing zone around the wellbore is relatively quickly dried out while CO₂ is injected. After shut-in of the well, no significant changes are observed for the gas saturation throughout the reservoir. The dry-out influences the dissolution and precipitation of mineral reactions, which need water to take place. In the zone beyond 74.3 m from the wellbore, the gas saturation is almost stable. The most dominant reactions in the reservoir are predicted to be oxidation of pyrite and dissolution of glauconite, muscovite, and calcite. Illite, quartz (or chalcedony), and anhydrite precipitate. Mineral trapping of CO₂ occurs in dolomite and siderite.

Overall it is concluded that CO₂ injection into the modeled depleted gas field leads to:

- A maximum porosity reduction of 0.5% in the near-well zone, due to dry-out and salt precipitation. Temperature effects and the impact on permeability were not computed.
- Dry-out of the near-well zone affects the chemical integrity of the wells, which should be studied in future work.
- A limited porosity increase (<0.01%) and permeability increase (<0.02%) due to mineral reactions beyond the near-well zone after 7.2 years shut-in time.

The model presented here does not contain any heterogeneity, but it is admitted that this may play an important role in, for example, preferential flow. Such heterogeneity, more complex representations of reservoirs, and the impact on well integrity will be taken into account in future work. Longer simulation times will also be considered, as they are required for estimating the long-term stability of CO₂ in depleted gas fields.

ACKNOWLEDGMENT

We thank Elja Huibregtse and Kalijn Peters for their contributions to this work and Pascal Audigane for helpful discussions.

REFERENCES

- André, L., P. Audigane, M. Azaroual, and A. Menjot, Numerical modeling of fluid-rock chemical interactions at the supercritical CO₂-liquid interface during CO₂ injection into a carbonate reservoir, the Dogger aquifer (Paris Basin, France), *Energy Convers. Manag.* 48(6), 1782-1797, 2007.
- Audigane, P., J. Lions, I. Gaus, C. Robelin, P. Durst, C.M. Oldenburg, T. Xu, L.G.H. van der Meer, and K. Geel. Geochemical modeling of CO₂ injection into a methane gas reservoir at the K12-B field, North Sea. In: Carbon dioxide sequestration in geological media-State of the science, Eds. M. Grobe, J.C. Pashin, and R.L. Dodge, AAPG Studies 59, 1-20, 2008.
- Benson, S. and P. Cook, Underground geological storage, Chapter 5. In: IPCC Special report on carbon dioxide capture and storage, Cambridge University Press, Eds. Metz, B., Davidson, O., De Coninck, H., Loos, M., Meyer, L., 2005.
- Duan, Z. and R. Sun, An improved model for calculating CO₂ solubility in pure water and aqueous NaCl solutions from 273 to 533 K and from 0 to 2000 bar. *Chem. Geol.* 193, 257-271, 2003.
- Gaus, I., M. Azaroual, and I. Czernichowski-Lauriol, Reactive transport modeling of the impact of CO₂ injection on the clayey cap rock at Sleipner (North Sea). *Chem. Geol.* 217, 319-337, 2005.
- Giorgis T., M. Carpita, A. Battistelli, 2D modeling of salt precipitation during the injection of dry CO₂ in a depleted gas reservoir, *Energy Convers. Manag.* 48(6), 1816-1826, 2007.
- Hartmann, T., P. Paviet-Hartmann, J.B. Rubin and K.E. Sickafus, Supercritical CO₂ carbonation of cemented radioactive waste-forms – Influence of leachability and structure. *Cement Concrete Res.* 29, 1359, 1999.
- Kutchko, B.G., B.R. Strazisar, D.A. Dzombak, G.V. Lowry and N. Thaulow, Degradation of Well Cement by CO₂ under Geological Sequestration Conditions. *Environ. Sci. Technol.* 41, 4787-4792, 2007.
- Lasaga, A.C., Chemical kinetics of water-rock interaction. *J. Geophys. Res.* 89, 4009-4025, 1984.
- López, D.A., T. Pérez and S.N. Simison, The influence of microstructure and chemical composition of carbon and low alloy steel in CO₂ corrosion. A state-of-the-art appraisal. *Mater. Design* 24, 561-575, 2003.
- Müller, N., R. Qi, E. Mackie, K. Pruess, and M.J. Blunt, CO₂ injection impairment due to halite precipitation, *Energy Procedia* 1, 3507-3514, 2009.
- Oldenburg, C.M., Joule-Thomson cooling due to CO₂ injection into natural gas reservoirs. TOUGH Symposium Lawrence Berkeley National Laboratory, California, U.S.A. Paper LBNL-60158, 2006.
- Palandri, J. and Y.K. Kharaka. A compilation of rate parameters of water-mineral interaction kinetics for application to geochemical modeling. US Geological Survey Open File Report 2004-1068, USGS, 2004.
- Parkhurst, D.L. and C.A.J. Appelo, User's guide to PHREEQC (version 2)—a computer program for speciation, batchreaction, one-dimensional transport, and inverse geochemical calculations: U.S. Geological Survey Water-Resources Investigations, Report 99-4259, 1999.
- Pruess, K. and N. Müller, Formation dry-out from CO₂ injection into saline aquifers: 1. Effects of solids precipitation and their mitigation, *Wat. Resour. Res.* 45, W03402, 2009.
- Strazisar, B.R., C. Zhu, and S.W. Hedges, Preliminary modeling of the long-term fate of CO₂ following injection into deep geological formations. *Env. Geosci.*, 13(1), 1-15, 2006.
- Van Adrichem Boogaert, H.A. and W.F.P. Kouwe, Stratigraphic nomenclature of the Netherlands, revision and update by RGD and NOGEP. Mededelingen Rijks Geologische Dienst, 50. Haarlem, Sections A-J separately paginated, 1993-1997.
- Van der Meer, L.G.H., Computer Modeling of Underground CO₂ Storage, *Energy Convers. Manag.* 37 (6-8), 1155-1160, 1996.
- Van der Meer, L.G.H., R.J. Arts, and L. Paterson, Prediction of Migration of CO₂ Injection in a Saline Aquifer: Reservoir History Matching of 4D Seismic Image with a Compositional Gas/Water Model, *Greenhouse Gas Control Technologies: Proceedings of the 5th International Conference on Greenhouse Gas Control Technologies*, Cains, Australia, 2000.
- Van der Meer, L.G.H., E. Kreft, E., C. Geel, and J. Hartman, K12-B a Test Site for CO₂ Storage and Enhanced Gas Recovery, SPE 94128, 2005.
- Xu, T, J.A. Apps, and K. Pruess, Numerical simulation of CO₂ disposal by mineral trapping in deep aquifers, *Appl. Geoch.*, 19, 917-936, 2004.
- Xu, T, J.A. Apps, and K. Pruess, Mineral sequestration of carbon dioxide in a sandstone-shale system, *Chem. Geochem.*, 217, 295-318, 2005.
- Xu, T., E. Sonnenthal, N. Spycher, and K. Pruess, TOUGHREACT—a simulation program for non-isothermal multiphase reactive geochemical transport in variably saturated geologic media: applications for geothermal injectivity and CO₂ geologic sequestration. *Comp. Geosci.* 32(2), 145-165, 2006.

THE WABAMUM AREA CO₂ SEQUESTRATION PROJECT: TOUGHREACT MODELING OF CO₂ INJECTION INTO A SALINE AQUIFER CONTAINING H₂S

Maurice Shevalier, Michael Nightingale, Bernhard Mayer and Ian Hutcheon

University of Calgary
Applied Geochemistry Group, Dept. of Geoscience
Calgary, AB, T2N 1N4, Canada
e-mail: maurice@earth.geo.ucalgary.ca

ABSTRACT

This paper presents a numerical modeling study of the initial stages of CO₂ injection into a saline aquifer in the Nisku formation at Wabamum Lake, Central Alberta. The aim of the simulation was to evaluate potential differences between injection into brine with an ambient amount of dissolved H₂S and the same brine without dissolved H₂S. The simulation covers a CO₂ injection period of 50 years.

A 1D radial symmetrical model was used for the model and was assumed to be a uniform carbonate formation. This study found that a significant amount of the injected CO₂ was sequestered in the brine through solubility trapping and ranged from ~33% after 1 year to ~56% after 50 years.

BACKGROUND

CO₂ injection into saline aquifers is considered a promising option for sequestering large amounts of CO₂ captured from point source emitters such as coal-burning power plants. Many deep saline aquifers, however, contain H₂S, wherever even minor amounts of anhydrite or other sulfate sources are present in the formation. If the unit in question has been buried to reach a temperature of 120°C, H₂S will almost certainly form via the process of thermochemical sulfate reduction (TSR) (Krouse et al. 1988; Hutcheon, 1999; Simpson, 1999). On a volume basis, the amount of anhydrite required to produce 50% H₂S in gas at 5% porosity is less than 1% of the rock. Typical anhydrite amounts (e.g., in Devonian strata of the Western Canadian Sedimentary Basin) are much higher.

Figure 1 shows the distribution of H₂S in the Devonian system in Alberta (Hutcheon, 1999). Note that concentrations (mole fraction) increase to the west, which corresponds to increasing depth of burial and increasing temperature. Concentration may exceed 0.8 mole fraction H₂S in the disturbed belt of the Rocky Mountains.

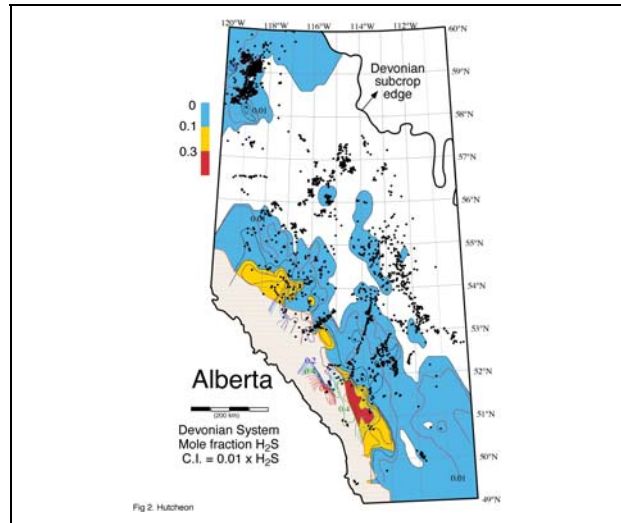


Figure 1. Concentration of H₂S in gas samples in the Devonian system in Alberta (Hutcheon, 1999).

LOCATION

The Wabamun Area CO₂ Sequestration Project (WASP) investigates the feasibility of injecting one gigaton of CO₂ (20 Mt-CO₂ year⁻¹ for 50 years) into a saline aquifer in the Western Canadian Sedimentary Basin. The Devonian Nisku formation in the WASP study area in central Alberta (see Figure 2) was identified as a suitable aquifer for CO₂ injection due to its nonassociation with current oil and gas production, adequate depth, adequate containment, and good reservoir quality.

NUMERICAL METHOD

All of the simulations were performed using TOUGHREACT v. 1.2 (Xu et al., 2006). The code was developed by using the existing multiphase fluid and heat flow code, TOUGH2 v. 2 (Pruess, 1991) and adding in the geochemical reactive transport code. The integral finite difference method for space discretization (Narasimham and Witherspoon, 1976) is the basis for the numerical method for simulation of fluid flow. Coupling between the geochemical

reactions and the fluid transport requires a sequential iterative approach (Yeh and Tripathi, 1991). The fluid property module ECO2N was used in the modeling.

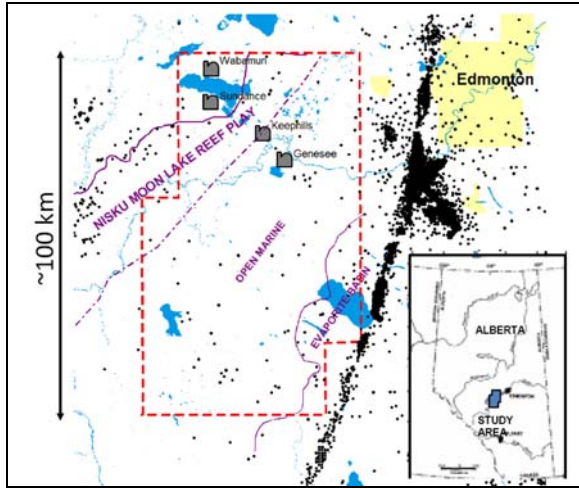


Figure 2. The WASP study area (dashed line) in central Alberta (Canada) and location of four large power plants. Black circles show wells that penetrate the targeted stratigraphic interval, the Nisku Formation. Important depositional boundaries in the Upper Devonian section are also indicated.

SETUP OF THE MODEL

Geometry

A single layer uniform carbonate formation with a thickness of 70 m is considered in the present model. The formation is assumed to be uniform throughout and extend infinitely in the horizontal direction. A 1D radial symmetrical was used with non-uniform spacing.

The simplifications in the model geometry resulted in a number of shortcomings, and hence we were not able to consider non-uniform sweeps, buoyancy forces, convective mixing, etc. Some justification for these simplifications are that the slow reaction rates and the long time scales for geological changes will, in the long run, make the CO₂ distribution more or less uniform over time (Xu et al., 2007).

Initial and boundary conditions

The hydrogeological parameters used in the simulations are shown in Table 1. The carbonate formation was assumed to be homogeneous. Injection of carbon dioxide was simulated at 31.69 kg/s (1 MT/year) for 50 years. The initial pressure was 16 MPa at the top of the formation.

Table 1. Hydrogeological parameters for the Nisku carbonate formation

Parameter	Carbonate
Permeability (m ²)	0.3x10 ⁻¹³
Porosity	0.10
Temperature (°C)	60
Pore Compressibility (Pa ⁻¹)	4.5x10 ⁻¹⁰
Tortuosity	0.3
Compressibility (Pa ⁻¹)	1x10 ⁻⁸
Diffusivity (m ² /s)	1x10 ⁻⁹
Relative Permeability	
Liquid (Van Genuchten, 1980):	
$k_{rl} = \sqrt{S^* \{1 - (1 - [S^*]^{1/m})^m\}^2}$ $S^* = (S_l - S_{lr}) / (1 - S_{lr})$	
S _{lr} : irreducible water saturation	S _{lr} = 0.3
m: exponent	m=0.457
Gas (Corey, 1954)	
$k_{rg} = (1 - \widehat{S})^2 (1 - \widehat{S}^2)$ $\widehat{S} = (S_l - S_{lr}) / (S_l - S_{lr} - S_{gr})$	
S _{gr} : irreducible gas saturation	S _{gr} = 0.05
Capillary pressure	
Van Genuchten (1980)	
$P_{cap} = -P_0([S^*]^{-1/m} - 1)^{1-m}$ $S^* = (S_l - S_{lr}) / (1 - S_{lr})$	
S _{gr} : irreducible gas saturation	S _{gr} = 0.0
m: exponent	m = 0.457
P ₀ : strength coefficient (kPa)	P ₀ = 19.61

Initial geochemical conditions

The initial mineral composition of a representative sample of the Nisku formation used in the modeling is shown in Table 2 (Nightingale et al., 2009). Given that H₂S was present in the aquifer, pyrite was included as a secondary mineral in one set of the models. Also, K-feldspar was substituted for orthoclase.

Table 2. Initial mineral volume fractions and potential secondary mineral phases of the Nisku formation

Mineral	Chemical Formula	Volume percent	
		of Solid	of Solid
<i>Primary</i>			
Dolomite	CaMg(CO ₃) ₂	81.22	80.49
Calcite	CaCO ₃	15.45	16.04
Illite	K _{0.6} Al _{1.8} Mg _{0.25} (Al _{0.5} Si _{3.5} O ₁₀)(OH) ₂	1.89	1.89
K-feldspar	KAlSi ₃ O ₈	0.86	0.95
Low-Albite	NaAlSi ₃ O ₈	0.58	0.62
<i>Secondary</i>			
Kaolinite	Al ₂ Si ₂ O ₅ (OH) ₄		
Na-smectite	Na _{0.29} Mg _{0.26} Al _{1.77} Si _{3.97} O ₁₀ (OH) ₈		
Ca-smectite	Ca _{0.145} Mg _{0.26} Al _{1.77} Si _{3.97} O ₁₀ (OH) ₈		
Dawsonite	NaAlCO ₃ (OH) ₂		
Aragonite	SrCO ₃		
Siderite	FeCO ₃		
Ankerite	CaMg _{0.3} Fe _{0.7} (CO ₃) ₂		
Magnesite	MgCO ₃		
Pyrite	FeS ₂		

Table 3 shows the measured water composition from brine obtained from a well located in the Nisku formation (Shevalier and Mayer, 2009). The water composition was re-equilibrated with gases such as CO₂, H₂S and CH₄, since degassing occurred when the brine was pumped from depth to surface. This was done using SOLMINEQ88 (Kharaka et al., 1988). Two species shown in Table 3 were not

measured, AlO₂⁻ and O_{2(aq)}. A small amount of each was added, since the first would probably be present due to the presence of silicate minerals and traces of O_{2(aq)} were necessary for redox reactions to occur.

Table 3. Initial chemical species concentrations used in the ToughReact simulations

Species	Concentration (mol/kg)
pH	6.10
Ca ²⁺	0.41
Mg ²⁺	9.33 x 10 ⁻²
Na ⁺	2.56
K ⁺	0.10
Sr ²⁺	1.08 x 10 ⁻²
Fe ²⁺	9.35 x 10 ⁻⁶
SiO _{2(aq)}	4.56 x 10 ⁻⁴
HCO ₃ ⁻	2.01 x 10 ⁻²
SO ₄ ²⁻	5.21 x 10 ⁻³
Cl ⁻	3.44
AlO ₂ ⁻	1.36 x 10 ⁻⁷
O _{2(aq)}	4.88 x 10 ⁻⁷⁰
H ₂ S _(aq)	3.97 x 10 ⁻²

Table 4 provides the parameters for the kinetics of dissolution and precipitation for the minerals used in the models (Palandri and Kharaka, 2004). Calcite was used as an equilibrium mineral in the simulations. Specific details about the kinetics used in the simulations can be found in Xu et al. (2007).

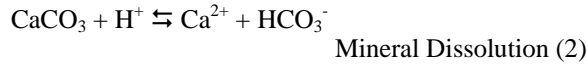
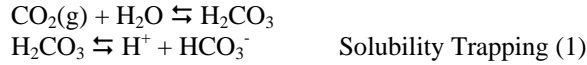
Table 4. Parameters for calculating kinetic rate constants of minerals used in the simulations (Palandri and Kharaka, 2004)

Mineral	A (cm ² /g)	Parameters for kinetic rate law							
		Neutral Mechanism		Acid Mechanism			Base Mechanism		
		k ²⁵ (mol/m ² /s)	E (kJ/mol)	k ²⁵	E	n(H ⁺)	k ²⁵	E	n(H ⁺)
Dolomite	9.1	2.9512 10 ⁻⁸	52.2	6.4565 10 ⁻⁰⁴	36.1	0.500			
Illite	108.7	1.6596 10 ⁻¹³	35.0	1.0471 10 ⁻¹¹	23.6	0.340	3.02 10 ⁻¹⁷	58.9	-0.400
K-feldspar	9.1	3.8905 10 ⁻¹³	38.0	8.7096 10 ⁻¹¹	51.7	0.500	6.3096 10 ⁻²²	94.1	-0.823
Low-Albite	9.1	2.7542 10 ⁻¹³	69.8	6.9183 10 ⁻¹¹	65.0	0.457	2.5119 10 ⁻¹⁶	71.0	-0.572
Kaolinite	108.7	6.9183 10 ⁻¹⁴	22.2	4.8978 10 ⁻¹²	65.9	0.777	8.9125 10 ⁻¹⁸	17.9	-0.472
Na-smectite	108.7	1.6596 10 ⁻¹³	35.0	1.0471 10 ⁻¹¹	23.6	0.340	3.0200 10 ⁻¹⁷	58.9	-0.400
Ca-smectite	108.7	1.6596 10 ⁻¹³	35.0	1.0471 10 ⁻¹¹	23.6	0.340	3.0200 10 ⁻¹⁷	58.9	-0.400
Dawsonite	9.1	1.2598 10 ⁻⁰⁹	62.76	6.4565 10 ⁻⁰⁴	36.1	0.500			
Aragonite	9.1	4.5709 10 ⁻¹⁰	23.5	4.1687 10 ⁻⁰⁷	14.4	1.000			
Siderite	9.1	1.2598 10 ⁻⁰⁹	62.76	6.4565 10 ⁻⁰⁴	36.1	0.500			
Ankerite	9.1	1.2598 10 ⁻⁰⁹	62.76	6.4565 10 ⁻⁰⁴	36.1	0.500			
Magnesite	9.1	4.5709 10 ⁻¹⁰	23.5	4.1687 10 ⁻⁰⁷	14.4	1.000			
Pyrite	12.87	2.8184 10 ⁻⁰⁵	56.9 n(O _{2(aq)})=0.5	3.2022 10 ⁻⁰⁸	56.9 n(H ⁺) = -0.5, n(Fe ³⁺)=0.5				

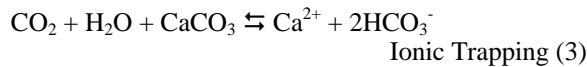
- Notes: (1) all rate constants are for dissolution
(2) A is specific area, k²⁵ is kinetic rate constant at 25 °C, E is activation energy, n is power term (Eq. (3), Xu et al., 2007)
(3) power terms n for both acid and base mechanism are with respect to H⁺
(4) for pyrite, the neutral mechanism has n with respect to O_{2(aq)}, the acid mechanism has two species involved: one n with respect to H⁺ and another n with respect to Fe³⁺ (Eq. (3), Xu et al., 2007)

GEOCHEMICAL REACTIONS

The dissolution of CO₂ in water forms carbonic acid via Reaction 1, also known as solubility trapping, resulting in a decrease in the pH. If there are any reactant minerals present, such as calcite, then mineral dissolution occurs (Reaction 2), resulting in a free cation and a bicarbonate ion, causing both the pH and the cation concentration to increase.



Thus, the net reaction between injected CO₂ and calcite is as follows, also known as ionic trapping:



SIMULATION RESULTS

The simulations conducted for this study considered the fate of injected CO₂ in the reservoir through geochemical interactions with the brine, with minerals present in the formation and residual trapping, i.e., how much CO₂ remained as a gas in the reservoir. The information is presented in graphical form as a function of radial distance from the injector well and at discrete time intervals, 1, 10, 25, and 50 years. Two sets of simulations were performed, one with and one without dissolved H₂S present in the brine, to evaluate the effect of ambient dissolved H₂S on the geochemistry of the reservoir when large amounts of CO₂ (1 MT/year for 50 years) are injected.

Brine Chemistry

The pH distribution along the radial distance is shown in Figure 3. The initial observation is that for all the simulations, both with and without H₂S present, the pH appears to increase from values below 4.0 to 5.11. The region of pH < 4.0 is the region where there is no water present, i.e., the value of the gas saturation is ~1.0. This complete dehydration was probably due to the high rate of CO₂ injection, 1 MT/yr (31.69 kg/sec). The dehydration region ranges from 18.7 m after 1 year to 136.1 m after 50 years. Beyond this region, the pH is initially at a value of 5.11 and remained constant, then increased over a very short distance from 5.11 to 6.44 and remained constant over the rest of the radial distance. This represents the region where CO₂ had diffused into the reservoir fluids and solubility trapping (Reaction 1) is occurring, causing the pH to remain slightly acidic. This pattern was observed for both H₂S and non-H₂S aquifers (Figure 3).

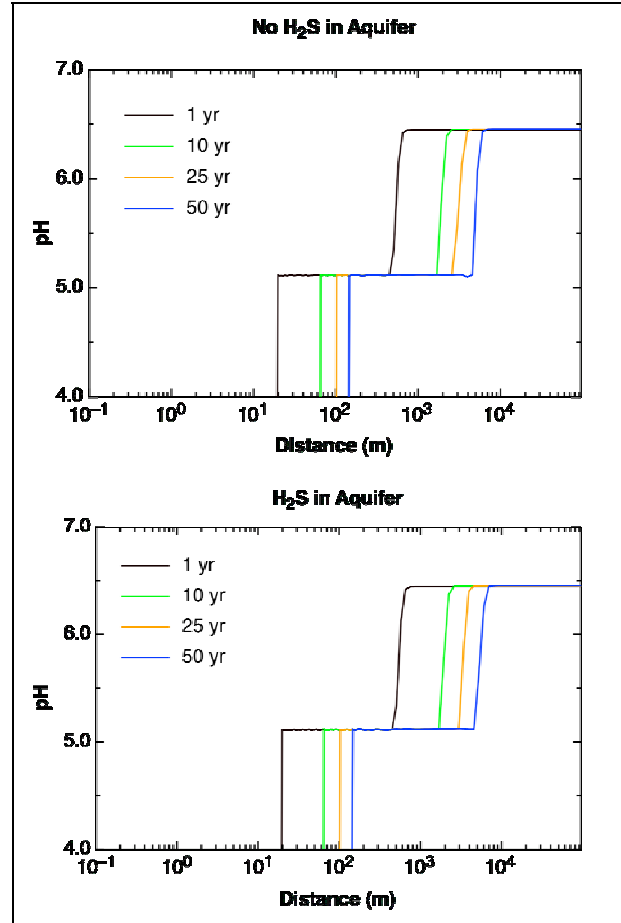


Figure 3. pH of brine as a function of radial distance and time after initiation of CO₂ injection for both non-H₂S (top) and H₂S (bottom) containing aquifers

Figure 4 shows the concentration of bicarbonate (in moles/kg) as a function of distance. The initial concentration of bicarbonate in the water is ~0.02 moles/kg across the entire modeling area. After 1 year, for both models, the concentration of bicarbonate in the water was ~1.25 moles/kg at a distance of ~20 m from the injector. At a distance of ~500 m, the concentration decreased to the ambient value of ~0.02 moles/kg. A similar increase and decrease in bicarbonate concentration was evident for all times but at increasing distances from the injector. The increase in bicarbonate concentrations along with the decrease in pH and no significant changes in Ca²⁺ and Mg²⁺ concentrations (not shown), indicated that solubility trapping was occurring in this region. Table 5 summarizes the amount of CO₂ sequestered in the brine by solubility trapping over the 50-year injection phase. The gradual increase in sequestration of CO₂ over time was due to the larger fluid volumes available as the CO₂ travels radially outward into the reservoir. Further, as time progressed, the amount of CO₂ sequestered by solubility trapping increased from 34% to 56%.

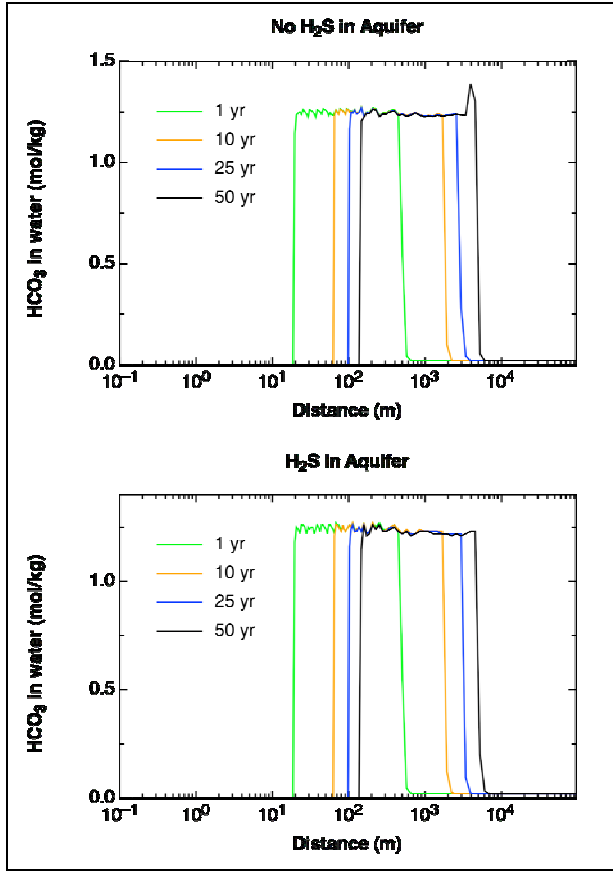


Figure 4. HCO_3^- concentrations in brine as a function of radial distance and time after initiation of CO_2 injection for both non- H_2S (top) and H_2S (bottom) containing aquifers

Table 5. Amount of CO_2 stored as HCO_3^- in the brine as a function of time

Time (years)	Amount of CO_2 stored in brine as HCO_3^- (MT)	Percentage of injected CO_2 stored as HCO_3^-
1.0	0.28	34%
5.0	1.66	33%
10.0	3.96	39%
12.5	5.50	44%
25.0	10.8	43%
37.5	17.8	48%
50.0	27.8	56%

Mineral Reactions

Figures 5 and 6 show the change in the volume fraction of the two main minerals present in the reservoir, calcite and dolomite. There was a small decrease in dolomite present to ~100 m. Thereafter, the amount of dolomite present remained constant as the radial distance increased, followed by a small increase. The radial distance of this volume change increased with time, from ~500 m after 1 year of injection to ~5000 m after 50 years. Calcite displayed an opposite trend, i.e., the volume fraction of calcite

increased at similar radial distances, then remained stable, and then decreased slightly at similar distances to the dolomite change. Mineral precipitation represents another method of CO_2 sequestration, but in this case the net C sequestration via mineral trapping was negligible compared to the amount of CO_2 sequestered as HCO_3^- .

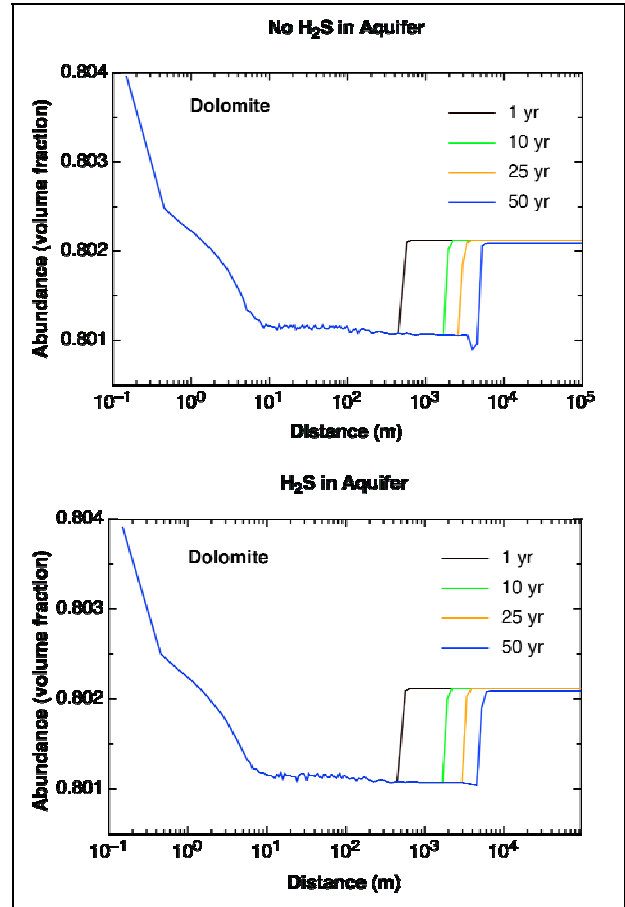


Figure 5. Dolomite abundance as a function of radial distance and time after initiation of CO_2 injection for both non- H_2S (top) and H_2S (bottom) containing aquifers

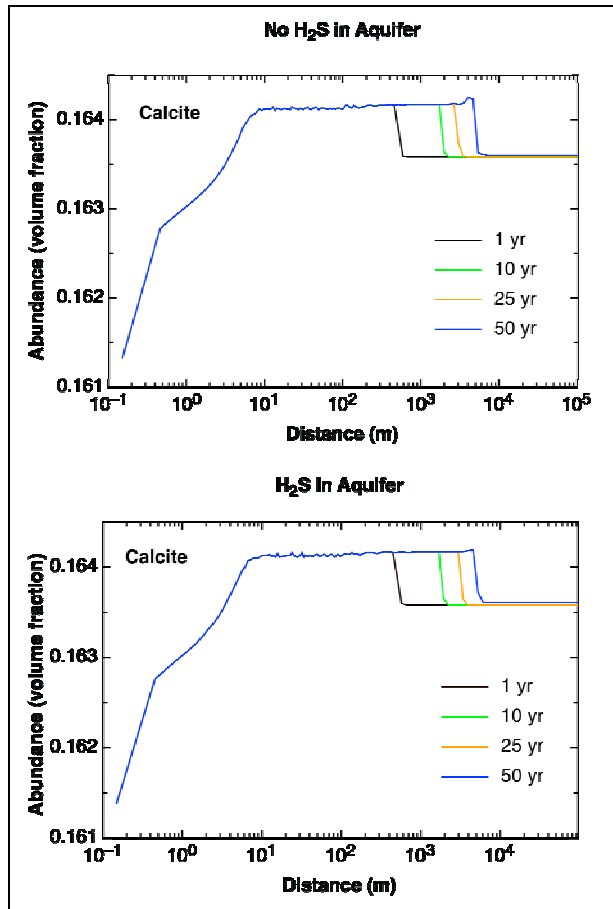


Figure 6. Calcite abundance in brine as a function of radial distance and time after initiation of CO₂ injection for both non-H₂S (top) and H₂S (bottom) containing aquifers.

CONCLUSIONS

1. CO₂ injection created a dehydrated region around the injection wellhead, with the radius increasing from 18.7 m after 1 year to 136.1 m after 50 years.
2. A significant amount of injected CO₂ was sequestered in the brine as HCO₃ due to solubility trapping. Based on the simplified model, from ~33% after one year to ~56% after 50 years, of the injected CO₂ was sequestered via solubility trapping.
3. Small amounts of dolomite and calcite were dissolved/precipitated in the reservoir.
4. There were no significant observable differences in the chemical or mineralogical reactions between the H₂S and non-H₂S containing aquifers.

ACKNOWLEDGMENT

This work was supported by a grant from the Wabamun Area CO₂ Sequestration Project (WASP), University of Calgary.

REFERENCES

- Corey, A.T., The interrelation between gas and oil relative permeabilities. *Prod. Mon.* 38–41, 1954.
- Hutcheon, I., Controls on the distribution of non-hydrocarbon gases in the Alberta Basin, *Bull. Can. Pet. Geol.*, 47(4), 573-593, 1999.
- Kharaka, Y. K., Gunter, W., Aggarwal, P. K., Perkins, E. H. and De Braal, J. D., *SOLMINEQ88: a computer programme for geochemical modelling of water-rock reactions*. USGS Water Resources Investigation Report, 88-4227, 1988.
- Krouse, H.R., Viau, C.A., Eliuk, L.S., Ueda, A. and Halas, S., Chemical and isotopic evidence of thermochemical sulphate reduction by light hydrocarbon gases in deep carbonate reservoirs, *Nature*, 333, 415-419, 1988.
- Narasimhan, T.N., Witherspoon, P.A., An integrated finite difference method for analyzing fluid flow in porous media, *Water Resour. Res.*, 12, 57–64, 1976.
- Nightingale, M., Shevalier, M., Mayer, B., *Wabamun Area Sequestration Project: Mineralogy Report*, Wabamun Area CO₂ Sequestration Project (WASP) Internal Report, U. of Calgary, 2009
- Palandri, J., Kharaka, Y.K., *A compilation of rate parameters of water–mineral interaction kinetics for application to geochemical modeling*. US Geol. Surv. Open File Report 2004-1068.64, 2004.
- Pruess, K., *TOUGH2: A General Numerical Simulator for Multiphase Fluid and Heat Flow*, Lawrence Berkeley Laboratory Report LBL-29400, Berkeley, California, 1991.
- Shevalier, M., Mayer, B., *Wabamun Area Sequestration Project: Baseline Geochemistry and Preliminary Geochemical Modelling*, Wabamun Area CO₂ Sequestration Project (WASP) Internal Report, University of Calgary, 2009
- Simpson, G., *Sulfate reduction and fluid chemistry of the Devonian Leduc and Nisku formations in south-central Alberta*. Ph.D. Thesis, University of Calgary (unpublished) 1999.
- van Genuchten, M.Th., A closed-form equation for predicting the hydraulic conductivity of unsaturated soils. *Soil Sci. Soc. Am. J.*, 44, 892–898, 1980.

- Xu, T., E. Sonnenthal, N. Spycher and K. Pruess, TOUGHREACT: A simulation program for non-isothermal multiphase reactive geochemical transport in variably saturated geologic media. *Computers and Geosciences*, 32, 145-165, 2006.
- Xu, T., Apps, J., Pruess, K., Yamamoto, H., Numerical modeling of injection and mineral trapping of CO₂ with H₂S and SO₂ in a sandstone formation, *Chem. Geol.*, 242, 319-346, 2007.
- Yeh, G.T., Tripathi, V.S., A model for simulating transport of reactive multispecies components: model development and demonstration, *Water Resour. Res.*, 27, 3075-3094, 1991.

GEOLOGIC SEQUESTRATION OF CARBON DIOXIDE: MODELS, CODES, AND FEDERAL REGULATIONS

Gregory Schnaar
Daniel B. Stephens & Associates

ABSTRACT

Computational modeling will likely be an integral part of management and regulation of geologic sequestration projects. For example, proposed US-EPA Underground Injection Control (UIC) regulations for geologic sequestration sites require owner/operators of geologic sequestration projects to include computational modeling results as a key component of a permit application. Modeling may be required for delineation of the project area of impact (e.g., area of review), and demonstration of non-dangerment of drinking water resources. In addition, the proposed regulations would require periodic calibration of computational models to site monitoring data. Peer-reviewed studies of geologic sequestration modeling have used a range of numerical, semi-analytical, and analytical codes that are capable of simulating multiphase flow, heat transport, reactive transport, and geomechanical processes. Of over 40 peer-reviewed studies of geologic sequestration modeling that have been compiled and critically reviewed, nearly half used a model based on the TOUGH code. These existing studies have demonstrated the use of modeling in design of geologic sequestration projects, interpretation of site characterization data, assessment of potential leakage through faults, fractures, and abandoned well bores, design of site monitoring strategies, estimation of plume stabilization time, and assessment of

geochemical impacts, as well as model calibration to site monitoring data. Particularly informative components of existing studies include parameter sensitivity analyses, evaluation of numerical artifacts, code comparison, and demonstration of model calibration to site monitoring data. Sensitivity analyses have demonstrated that model results are sensitive to several parameters prone to a significant degree of uncertainty, such as relative permeability-saturation functional relationships and mineral precipitation/dissolution kinetics. For the most part, good agreement has been found in code intercomparison. Most discrepancies between codes have been traced to differences in the fluid property physicochemical parameters used. Evaluations of numerical artifacts have demonstrated that overly coarse grids do not capture specific migration pathways and may artificially impact predicted CO₂ movement and trapping processes. Preliminary comparisons of site monitoring data from early geologic sequestration projects to model predictions demonstrate the necessity of ongoing model calibration when feasible.

RELATED PUBLICATION

Schnaar G., and D.C. Digiulio, Computational Modeling of the Geologic Sequestration of Carbon Dioxide. *Vadose Zone Journal*, 8(2) 389-403, 2009.

NUMERICAL SIMULATION STUDIES OF THE LONG-TERM EVOLUTION OF A CO₂ PLUME UNDER A SLOPING CAPROCK

Karsten Pruess*, Jan Nordbotten** and Keni Zhang*

* Earth Sciences Division, Lawrence Berkeley National Laboratory

** Department of Mathematics, University of Bergen/Norway

e-mail: K_Pruess@lbl.gov

ABSTRACT

We have used the TOUGH2-MP/ECO2N code to perform numerical simulation studies of the long-term behavior of CO₂ stored in an aquifer with a sloping caprock. This problem is of great practical interest, and is very challenging due to the importance of multiscale processes. We find that the mechanism of plume advance is different from what is seen in a forced immiscible displacement, such as gas injection into a water-saturated medium. Instead of pushing the water forward, the plume advances because the vertical pressure gradients within the plume are smaller than hydrostatic, causing the water column to collapse ahead of the plume tip. The CO₂ plume becomes thinner as it advances, yet the speed of advancement remains constant over the entire simulation period of up to 400 years, with migration distances of more than 80 km. Our simulation includes dissolution of CO₂ into the aqueous phase and associated density increase, and molecular diffusion. However, no convection develops in the aqueous phase, because it is suppressed by the relatively coarse (sub-)horizontal gridding required in a regional-scale model. A first, crude sub-grid-scale model was implemented to represent convective enhancement of CO₂ dissolution. This process is found to greatly reduce the thickness of the CO₂ plume, but surprisingly does not affect the speed of plume advancement.

INTRODUCTION

Geologic storage as a greenhouse gas mitigation strategy will be workable only if long-term secure containment of CO₂ can be assured. At typical subsurface temperature and pressure conditions in terrestrial crust, separate-phase supercritical CO₂, henceforth for simplicity referred to as "gas," is less dense than aqueous phase. It will thus experience an upward buoyancy force and will tend to migrate towards shallower depth whenever suitable permeable pathways are available.

As the CO₂ plume spreads out under a cap rock, it will become partially immobilized by capillary forces ("trapped gas"; Kumar et al., 2005), while also partially dissolving in the aqueous phase. CO₂

dissolution functions as a gateway towards potential eventual fixation of CO₂ as carbonates of low solubility, and it induces a small increase in aqueous phase density, thus alleviating concerns about upward buoyancy flow. The progression from free gas to trapped gas, aqueous phase dissolution, and precipitation of solid carbonates increases CO₂ storage security, and the quantitative aspects of CO₂ inventories and characteristic times involved are of great practical interest (IPCC, 2005).

In this paper, we consider the long-term evolution of a large CO₂ plume that is emplaced beneath a sloping cap rock. Our focus is on understanding the role and significance of different multiphase, multicomponent flow and transport processes, including the rate of advance of the CO₂ plume, mechanisms of gas and water flow, and CO₂ transport and inventory in gas and aqueous phases. We neglect chemical interactions between CO₂ and rock minerals.

DEFINITION OF REFERENCE CASE

The problem is patterned after the Carrizo-Wilcox aquifer in Texas (Nicot, 2008; Hesse et al., 2008). We assume that a substantial number of CO₂ storage projects will be operating in the Wilcox, and we model a 2-D vertical section along the dip of the aquifer. The aquifer is modeled as a rectangular domain of 200 m thickness and 110 km length, tilted with an angle of $\alpha = 1.5^\circ$ against the horizontal (Fig. 1). We consider the upper right hand corner of the domain to be at the land surface; the lower left hand corner is then at a depth of $110,000 \sin(\alpha) + 200 \cos(\alpha)$, which for $\alpha = 1.5^\circ$ corresponds to 3,079.4 m. Formation properties include a uniform and isotropic permeability of 500 mD, a porosity of 15 %, and a compressibility of $4.5 \times 10^{-10} \text{ Pa}^{-1}$ (similar to compressibility of water at ambient conditions). The domain is initialized as a fully (fresh-)water-saturated medium in hydrostatic equilibrium, held in a geothermal gradient of 30 °C/km relative to a land surface temperature of 10 °C. Boundary conditions are "no-flow" everywhere, except that the upper right hand corner of the domain is held at land surface conditions of $(T_0, P_0) = (10^\circ\text{C}, 1.013 \times 10^5 \text{ Pa})$.

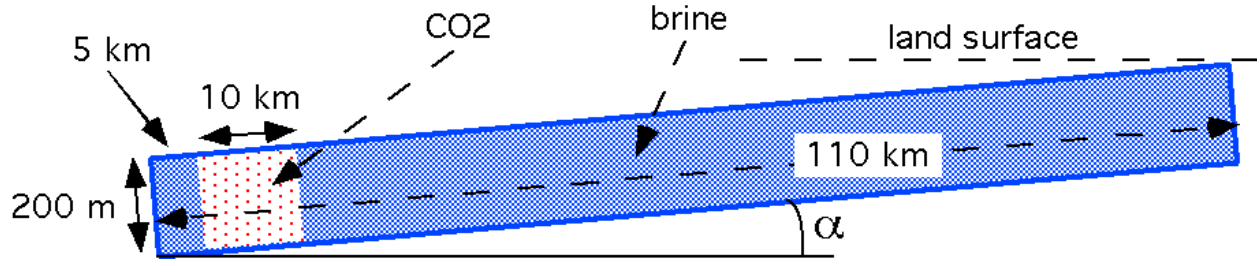


Figure 1. 2-D rectangular domain modeled with geometric dimensions shown (not to scale; note the extreme aspect ratio). The domain is dipping upward by an angle α . The initial CO₂ plume is shown by light shading.

The initialization is accomplished in two steps. First, we use a free-standing utility program to read in a TOUGH2 MESH file and write out an INCON file with temperature and pressure data assigned as $T(Z) = T_0 + \text{grad}(T)*Z$, $P(Z) = P_0 + \text{grad}(P)*Z$. Here, Z is the true depth relative to a reference point with conditions (T_0, P_0) , and an approximate value of $\text{grad}(P) \approx 10^4$ Pa/m is used. Subsequently we initialize a TOUGH2 simulation with these INCON data, maintaining temperatures at their initial values, and allowing pressures to come to an accurate gravitational equilibrium relative to a pressure of 1.013×10^5 Pa at the land surface.

The CO₂ plume is then emplaced instantaneously by using another utility program to assign a uniform gas saturation of $S_g = 80\%$, corresponding to aqueous phase at irreducible saturation of $S_{lr} = 20\%$, to the subdomain labeled “CO₂” in Fig. 1; for the CO₂ emplacement, pressures, and temperatures are maintained at their initial values. Plume evolution takes place under the combined action of gravity and pressure forces, with CO₂ buoyancy due to lower density being the primary driving force. For the simulations reported here, we neglect capillary pressures. Effects of aqueous diffusion, and enhancement of CO₂ dissolution through convective mixing, are explored in sensitivity studies—see below. Relative permeabilities for liquid (k_{rl}) and gas (k_{rg}) were assumed as follows,

$$k_{rl} = \sqrt{S^*} \left\{ 1 - \left(1 - [S^*]^{1/m} \right)^m \right\}^2 \quad (1a)$$

$$k_{rg} = (1 - \hat{S})^2 (1 - \hat{S}^2) \quad (1b)$$

where $S^* = (S_1 - S_{lr}) / (1 - S_{lr})$, $\hat{S} = (S_1 - S_{lr}) / (1 - S_{lr} - S_{gr})$, with S_1 the liquid (aqueous phase) saturation, and S_{lr} , S_{gr} the irreducible liquid and gas saturations, respectively. Equation (1a) for liquid was developed

by van Genuchten (1980); Equation (1b) for gas is from Corey (1954). Parameters used are $S_{lr} = S_{gr} = 20\%$, $m = 0.457$. The relative permeabilities given by Eq. (1) are nonhysteretic; problem variations with hysteretic relative permeabilities will be explored in the future (Doughty, 2007).

Obtaining accurate results for this problem, and interpreting simulated behavior, is made difficult by the extreme aspect ratio of the flow system. This is illustrated by a contour map of densities that CO₂ would have throughout the flow domain for the applied hydrostatic-geothermal conditions (Figure 2). Temperatures and pressures, hence CO₂ densities, are a function of depth only, so the isolines of constant density shown in Figure 2 are in fact horizontal. Additional difficulties arise from the multiscale nature of the flow processes, from effects of space and time discretization, and from orders-of-magnitude variations in mass fluxes in space and time.

CO₂ was introduced into the 10 km by 200 m large domain highlighted in Figure 1 under conditions corresponding to the initial hydrostatic pressure equilibrium in a geothermal gradient. Due to its lower density as compared to aqueous phase, CO₂ experiences a buoyancy force that drives it upward, towards shallower depth. Figure 2 shows that pressure and temperature effects on CO₂ density nearly compensate for one another at deeper levels, with density showing small variations for $Y < 75,000$ m, corresponding to true depths in excess of $\sin(\alpha) \times (110,000 - 75,000) = 916$ m; the buoyancy force experienced by CO₂ is then also nearly constant in the deeper regions. As has been mentioned, we hold temperatures constant at initial geothermal gradient values throughout the simulation.

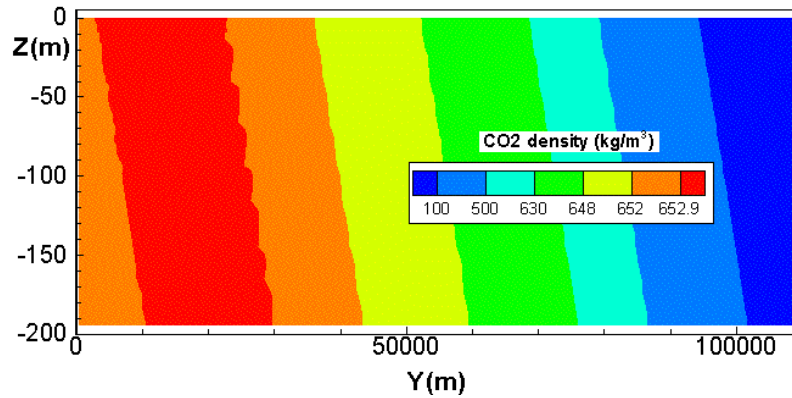


Figure 2. Variation of the density of free-phase CO_2 throughout the model domain. Note that CO_2 density depends on temperature and pressure, both of which are a function of true depth only, so that density isolines are actually horizontal.

The evolution of the CO_2 plume was modeled with a parallelized version TOUGH2-MP of our general-purpose reservoir simulator TOUGH2 (Pruess, 2004; Zhang et al., 2008), augmented with a fluid property module ECO2N that provides accurate correlations for thermophysical properties of fluids, including the partitioning of H_2O and CO_2 between brine and gas phases (Pruess and Spycher, 2007). The basic space discretization was 10 m in the subvertical and 1000 m in the subhorizontal direction, but we did some experimentation with grid refinement to achieve a compromise between spatial resolution and efficient execution. Most of the simulations presented here were done with a grid that involved refinement to $\Delta Z = 1$ m near the top, to better resolve the CO_2 plume, as well as refinement to $\Delta Y = 10$ m in the Y-direction near $Y = 50$ km. The latter refinement was done to be able to monitor updip plume advancement with a spatial resolution down to 10 m, and thereby obtain a more accurate depiction and understanding of flow mechanisms at the advancing phase front. The MESH has 7300 gridblocks. The simulations were performed on a Dell T5400 dual quad core computer with a total of eight cores. For parallelized execution, we would normally partition the simulation domain into eight subdomains and assign each processor core the computations corresponding to one subdomain. However, in most cases, we partitioned the computations into 16 parallel processes (two per processor), because this was found to reduce execution time compared to running eight processes. Individual runs typically took about 1 to 1.5 hours.

RESULTS

Figure 3 shows gas saturations at three different times, from early to late, and indicates strong gravity override as the plume migrates updip near the top of the permeable interval. The plume thins out as it migrates under the sloping cap rock, and mass flows of CO_2 generally decrease with distance from the original CO_2 emplacement. One might expect that the

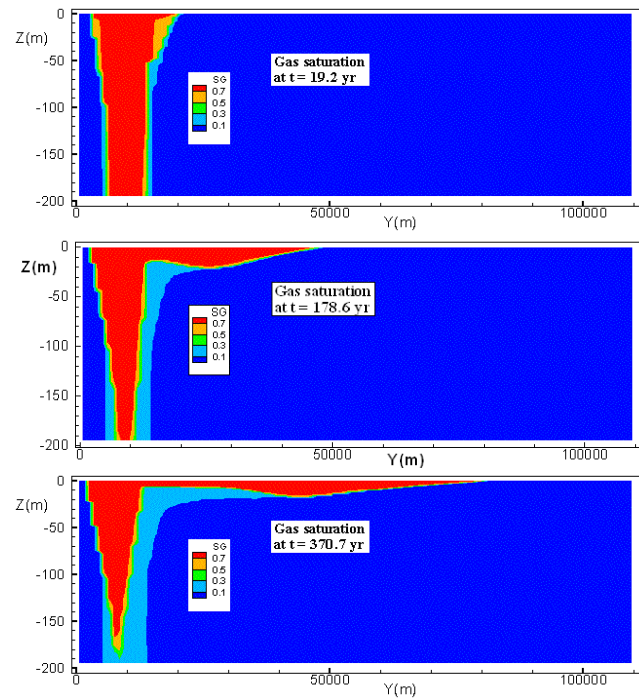


Figure 3. Simulated gas saturations at different times

advancement of the plume may slow over time, but this is not the case. Figure 4 shows that the plume advances with constant speed. The (small) scatter of points about the straight line is due to space and time discretization effects. The plume reaches a distance of 80.5 km after $t = 11.7 \times 10^9$ s (370.7 yr; Fig. 4), for an average speed of plume advancement of $V_p = (80.5 - 15) \times 10^3 / 11.7 \times 10^9 = 5.60 \times 10^{-6}$ m/s (176.7 m/yr). The speed of plume advancement is given by the pore velocity of CO_2 at the front. Its near-constancy can be understood by noting that (1) the plume advances with a constant frontal saturation, corresponding to constant relative permeability and fluid mobility, (2) the pressure field remains close to

hydrostatic, and (3) CO₂ density, hence buoyancy force in a given pressure gradient, is nearly independent of position (depth). The nearly constant gas-phase density together with the nearly constant pore velocity further implies that the updip CO₂ mass flux is nearly independent of position and time.

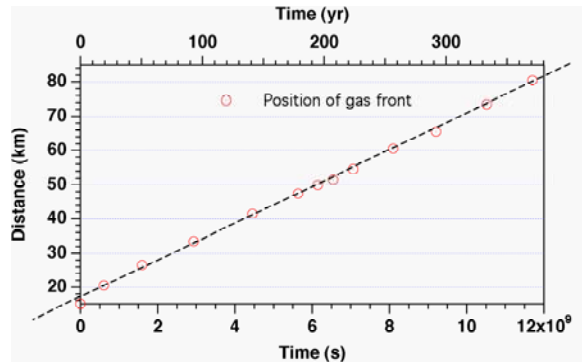


Figure 4. Advancement of the gas front over time. Distance is measured with respect to the l.h.s. of the domain, so that at time $t = 0$, the plume extends to $Y = 15$ km.

The aqueous phase plays a four-fold role in affecting the evolution of the CO₂ plume: (1) it serves as a medium for pressure transmission, (2) it occupies pore space that must be vacated to enable advancement of the CO₂ plume, (3) it can dissolve CO₂, thus serving as a sink, and (4) it serves as a transport medium for dissolved CO₂ by diffusive and advective processes. Inspection of simulated results reveals that water near the plume tip experiences a less-than-hydrostatic vertical pressure gradient. This causes water to flow downward and to vacate pore space at the top of the permeable interval into which the CO₂ plume may advance. One could say that the groundwater column “collapses” upon the approach of the CO₂ plume with its smaller (sub-) vertical pressure gradient. This mechanism of gas invasion into the aqueous zone is quite different from what would be encountered near a CO₂ injection well, where a gas plume would advance by displacing water outward under a pressure gradient maintained by the injection operation.

The initial CO₂ inventory in the flow domain is 158.7 kt (for a section of 1 m thickness), of which only about 3.1 kt (2.0%) is dissolved in the aqueous phase. Equilibrium dissolved CO₂ mass fraction is approximately 5.2% throughout most of the flow domain. With a total initial aqueous phase inventory of 3.03×10^9 kg, dissolution equilibrium would correspond to a total amount of dissolved CO₂ of 157.6×10^6 kg = 157.6 kt, which is almost exactly equal to the total initial CO₂ inventory. This indicates that the aqueous phase represents a very large sink, which potentially can dissolve almost the entire CO₂ inventory. The critical issue is, how readily is this

sink available, how fast is dissolution happening? Over time, the dissolved CO₂ inventory increases, reaching 14.2 kt, or 9.0% of the total, after 13.18×10^9 s (417.7 yr; see Figure 5). Figure 5 also shows free phase and dissolved CO₂ inventories for a simulation in which molecular diffusion of CO₂ in the aqueous phase was included. It is seen that aqueous diffusion has very small effects and leads to a slight increase in dissolved CO₂, which can be understood by noting that such diffusion will transport CO₂ away from the interface between aqueous and gas phases, providing a mechanism for solubilizing additional CO₂. The diffusivity of CO₂ for the pressure and temperature conditions of interest here is approximately $D = 2 \times 10^{-9}$ m²/s (Tewes and Boury, 2005; Farajzadeh, 2009); our simulation includes porous medium tortuosity effects and uses an effective diffusivity of $D_{\text{eff}} = 1 \times 10^{-9}$ m²/s. Diffusion is a slow process, and after 300 years ($= 9.5 \times 10^9$ s) would penetrate a distance of only $L = \sqrt{D_{\text{eff}} t} = \sqrt{9.5} = 3.1$ m into the aqueous phase.

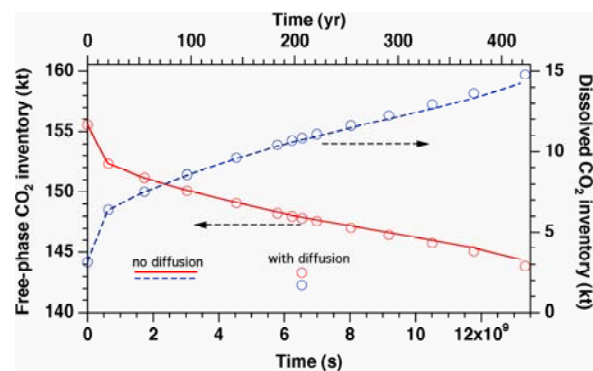


Figure 5. Time dependence of free-phase and dissolved CO₂ inventory.

DISSOLUTION, DIFFUSION, CO CONVECTION (DDC)

There is another effect that arises from CO₂ dissolution and subsequent diffusion, one that has been neglected in the simulations presented above, and that can potentially make much larger contributions to solubilizing CO₂. Dissolution of CO₂ into aqueous phase induces an increase in aqueous phase density that, depending on salinity, is typically in the range of 1% (for pure water) to 0.1% (for highly saline brine). Although small, this density increase gives rise to a gravitationally unstable configuration of denser fluid above less-dense fluid. This can induce convection in the aqueous phase, which can transport CO₂ downward, away from the dissolution boundary, at much larger rates than molecular diffusion. However, even though our simulations properly account for increase in aqueous-phase density from CO₂ dissolution, they do not generate any buoyancy-driven aqueous-phase convection over the time period simulated. This is

because the development of such convection is suppressed by the relatively coarse gridding in our field-scale model.

We have performed high-resolution simulations of the dissolution-diffusion-convection (DDC) process, using a 1 m wide by 5 m tall rectangular domain (Pruess and Zhang, 2008). Vertical grid resolution was 1 mm near the top of the domain, gradually coarsening to 1 cm at larger distance from the boundary; horizontal resolution was 1 cm. The computational mesh has 52,300 gridblocks with 104,500 connections. Typical run times on a Dell T5400 dual quad core computer are approximately seven hours. By comparing CO₂ mass transfer rates with an analytical solution for diffusion only, we deduce an incubation time of 4.0×10^6 s for onset of convective activity, and a stabilized long-term convectively enhanced CO₂ dissolution rate due to DDC of 1.0×10^{-7} kg/s/m² (Figure 6). Accordingly, the enhanced dissolution process will start practically instantaneously relative to characteristic time scales of plume migration.

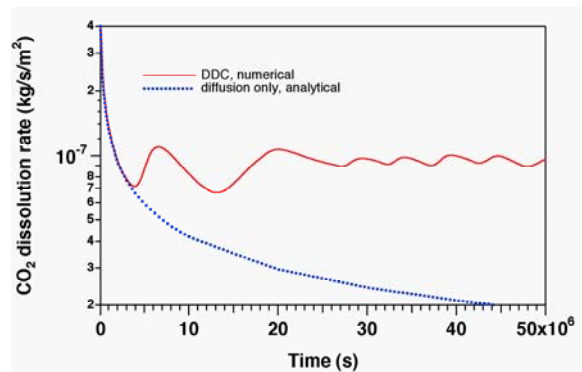


Figure 6. CO₂ dissolution rate due to convective enhancement, obtained from high-resolution simulations.

What ramifications can be expected from accelerated CO₂ dissolution for the long-term behavior of the plume? The simulations presented above showed that gas saturations and updip CO₂ fluxes in the mobile (upper) part of the plume are approximately constant, independent of space and time. This holds true even though plume thickness is a complicated function of time and distance, and it is the reason why the plume advances with constant speed. On the basis of these findings we expect that accelerated dissolution will reduce the thickness of the plume, but will have little impact on gas saturations and CO₂ fluxes in the upper, mobile portion of the plume. Accordingly, we hypothesize that the speed of plume advancement will be unaffected by accelerated dissolution from DDC.

This hypothesis was tested by implementing a first, admittedly crude model of sub-grid-scale DDC into TOUGH2-MP. Our approach represents enhanced CO₂ dissolution by means of a sink term applied to the region with free-phase CO₂. The DDC process is expected to remove free-phase CO₂ primarily from the lower portions of the CO₂ plume, near the boundary between two-phase fluid above and a single aqueous phase below. This boundary is time-dependent, and gas-phase saturations immediately above the boundary are small over much of the plume, near the irreducible limit of $S_{gr} = 20\%$, raising significant issues for incorporating a dynamic, self-consistent DDC sink into a numerical model. We avoid these issues by adopting a highly simplified model that applies the DDC sink to the top row of gridblocks throughout the entire region with two-phase conditions. This will overestimate effects of dissolution on the mobile part of the plume, and therefore should overestimate the reduction in the speed of plume advancement from DDC, if indeed any such reduction occurs. Other approximations invoked in our model for sub-grid-scale enhanced dissolution include neglecting the (small) incubation time for onset of convection; assuming convective CO₂ flux to be constant, independent of time; applying a threshold criterion of $S_g > 20\%$ before turning on DDC in a gridblock; and lagging DDC flux by one time step.

Simulations of plume migration subject to DDC were performed for two different values of the dissolution flux, $F_{DDC} = 1 \times 10^{-7}$ kg/s/m² as determined in our fine-grid simulation (Figure 6), and a value half this large, $F_{DDC} = 0.5 \times 10^{-7}$ kg/s/m², to explore the sensitivity to reduced vertical permeability. Figure 7 compares results for the CO₂ plumes after about 335 years with the previous simulation that ignored DDC. As had been expected, the main effect of enhanced dissolution is to reduce the thickness of the upper, highly mobile portions of the plume, while impacts on the advancement of the plume appear to be minor. A plot of plume advancement versus time indeed shows that plume advancement is essentially unaffected by CO₂ solubilization due to DDC (Figure 8). Finding no reduction in the speed of plume advancement, even when making an approximation that would overestimate such effects, is strong evidence that plume advancement indeed is little affected by convectively enhanced dissolution.

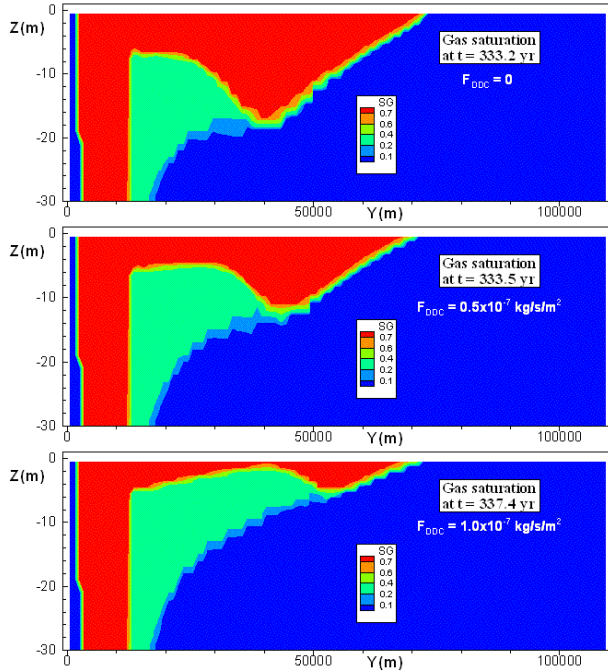


Figure 7. Gas saturations after approximately 335 years, for different strengths of convectively enhanced CO₂ dissolution rates.

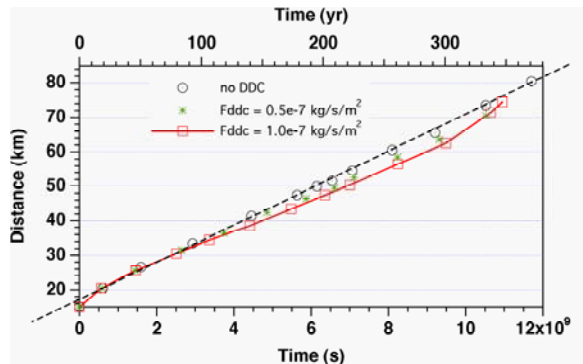


Figure 8. Plume advancement versus time for different convectively enhanced CO₂ dissolution rates.

Mass balances for free-phase and dissolved CO₂ show substantial increase in CO₂ solubilization from DDC (Figure 9). In plotting Figure 9, we included the free-phase CO₂ removed by our sub-grid-scale representation of DDC as dissolved CO₂. For the case with $F_{DDC} = 1 \times 10^{-7} \text{ kg/s/m}^2$, at the end of the simulation (340 years) approximately 1/3 of the initial CO₂ inventory has been dissolved into the aqueous phase, while 2/3 remain as a free supercritical phase.

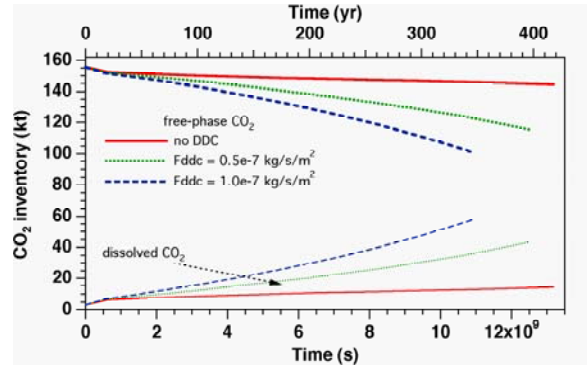


Figure 9. Free-phase and dissolved CO₂ inventory for different CO₂ dissolution rates.

CONCLUDING REMARKS

The migration of a CO₂ plume under a sloping cap rock involves processes on a wide range of space and time scales, and poses difficult challenges for numerical modeling. We have used the TOUGH2-MP/ECO2N simulator on a plume migration problem with parameters applicable to the Carrizo-Wilcox aquifer in Texas. Plume behavior was simulated for time scales of a few hundred years, and covering a migration distance of order 100 km. In addition, we performed high-resolution simulations of the convective instability that develops when CO₂ dissolves and diffuses into aqueous phase, increasing fluid density, and inducing convectively enhanced CO₂ dissolution. Our main findings are as follows.

- Gas saturations in the advancing CO₂ plume are nearly uniform, and updip migration occurs at constant speed, independent of plume thickness.
- The mechanism of plume advancement is quite different from displacement behavior in the vicinity of an injection well. Near a CO₂ injection well, the plume advances by pressure-driven displacement of aqueous phase away from the injection point. In contrast, at the tip of a CO₂ plume advancing under a sloping cap rock, water flow is mostly downward rather than outward. One can say that the plume advances updip due to a collapse of the water column ahead of the plume tip, induced by the approaching smaller vertical pressure gradient in the CO₂ plume.
- In a coarsely-gridded field-scale model, the process of dissolution and diffusion of CO₂ into the aqueous phase does not give rise to convective mixing, because the large scale of spatial averaging suppresses the convective instability.

- High-resolution simulations have shown that the process of CO₂ dissolution-diffusion-convection (DDC) gives rise to CO₂ dissolution at an enhanced rate that stabilizes over time.
- A first rough model for subgrid-scale DDC was implemented into TOUGH2-MP, and was used to explore the impact of DDC on long-term behavior of the plume. The results showed that enhanced dissolution made the advancing CO₂ plume thinner, and reduced the up dip CO₂ flow rate. Surprisingly, it did not affect the speed of plume advancement.

The models developed here did not include hysteresis in relative permeability and capillary pressure. Hysteretic effects are known to be important for long-term trapping of CO₂ (Doughty, 2007), and will be explored in the future.

ACKNOWLEDGMENT

Thanks are due to Curt Oldenburg and Christine Doughty for a careful review of the manuscript and the suggestion of improvements. This work was supported by the Office of Basic Energy Sciences and by the Zero Emission Research and Technology project (ZERT) under Contract No. DE-AC02-05CH11231 with the U.S. Department of Energy.

REFERENCES

- Corey, A.T. The Interrelation Between Gas and Oil Relative Permeabilities, *Producers Monthly*, pp. 38 - 41, November 1954.
- Doughty, C. Modeling Geologic Storage of Carbon Dioxide: Comparison of Non-hysteretic and Hysteretic Characteristic Curves, *Energy Conv. Managmt.*, Vol. 48, pp. 1768–1781, 2007.
- Farajzadeh, R. *Enhanced Transport Phenomena in CO₂ Sequestration and CO₂ EOR*, PhD thesis, Technical University Delft, The Netherlands, 2009.
- Hesse, M.A., F.M. Orr, Jr., and H.A. Tchelepi. Gravity Currents with Residual Trapping, *J. Fluid Mech.*, Vol. 611, pp. 35–60, 2008.
- IPCC (Intergovernmental Panel on Climate Change), *Special Report on Carbon Dioxide Capture and Storage*, 2005.
- Kumar, A., R. Ozah, M. Noh, G.A. Pope, S. Bryant, K. Sepehrnoori and L.W. Lake. Reservoir Simulation of CO₂ Storage in Deep Saline Aquifers, *SPE Journal*, Vol. 10, issue 3, pp. 336–348, 2005.
- Nicot, J.-P. Evaluation of Large-Scale CO₂ Storage on Fresh-Water Sections of Aquifers: An Example from the Texas Gulf Coast Basin, *Int. J. Greenhouse Gas Control*, Vol. 2, Issue 4, pp. 583–593, 2008.
- Pruess, K. The TOUGH Codes—A Family of Simulation Tools for Multiphase Flow and Transport Processes in Permeable Media, *Vadose Zone J.*, Vol. 3, pp. 738 - 746, 2004.
- Pruess K. and N. Spycher. ECO2N – A Fluid Property Module for the TOUGH2 Code for Studies of CO₂ Storage in Saline Aquifers, *Energy Conversion and Management*, Vol. 48, No. 6, pp. 1761–1767, doi:10.1016/j.enconman.2007.01.016, 2007.
- Pruess, K. and K. Zhang. Numerical Modeling Studies of the Dissolution-Diffusion-Convection Process During CO₂ Storage in Saline Aquifers, Lawrence Berkeley National Laboratory Report LBNL-1243E, November 2008.
- Tewes, F. and F. Boury. Formation and Rheological Properties of the Supercritical CO₂-Water Pure Interface, *J. Phys. Chem. B*, Vol. 109, No. 9, pp. 3990–3997, 2005.
- van Genuchten, M.Th. A Closed-Form Equation for Predicting the Hydraulic Conductivity of Unsaturated Soils, *Soil Sci. Soc. Am. J.*, Vol. 44, pp. 892 - 898, 1980.
- Zhang, K., Y.S. Wu and K. Pruess. User's Guide for TOUGH2-MP - A Massively Parallel Version of the TOUGH2 Code, Lawrence Berkeley National Laboratory Report LBNL-315E, May 2008.

NUMERICAL MODELING OF FLUID-ROCK CHEMICAL INTERACTIONS DURING CO₂ SATURATED WATER INJECTION INTO A SANDSTONE RESERVOIR, USING THE MARTHE-REACT CODE

Picot-Colbeaux G., Pettenati M., Thiéry D., Kervévan C., André L., Azaroual M.

BRGM
3 av. C. Guillemin
BP 36009, 45 060 Orléans, FRANCE
e-mail: g.picot@brgm.fr

ABSTRACT

This study describes the numerical modeling of fluid-rock chemical interactions during CO₂-saturated water injection into a sandstone reservoir, using the MARTHE-REACT code (Thiéry et al., 2009, presented in the same TOUGH symposium). The reservoir is modeled in a 2D radial geometry with a thickness of 100 m, divided into three horizontal layers. The layers are characterized by contrasting hydrodynamic properties (porosity between 4 to 7%, permeability between $2 \times 10^{-16} \text{m}^2$ and $2.3 \times 10^{-15} \text{m}^2$), but all layers initially contain the same material (mineralogical assemblage and water composition). CO₂-saturated water is injected vertically over the entire thickness of the reservoir.

The simulation results confirm the high reactivity of CO₂-saturated water with respect to carbonate and sulphate minerals, which are totally dissolved in the water-saturated zone of the near-well field. Reactions occur to a larger extent in the upper layer, where the permeability is higher. Dissolution of calcite, dolomite, and anhydrite induces some pH buffering and a significant increase in porosity, reaching 41% in the first few meters of the water-saturated zone after ten years. Just behind the dissolution front, one can observe precipitation of dolomite, kaolinite, and quartz. Albite dissolution presents the first step in destabilization of the alumino-silicates. This can be explained by the slow kinetics of alumino-silicate mineral dissolution compared to the faster kinetics of carbonates. Consequently, the porosity evolution of the reservoir is essentially constrained by the magnitude of carbonate- and sulphate-mineral dissolution-precipitation reactions.

This study is a first step in the assessment of CO₂-saturated water leakage from the reservoir to the surface in a sedimentary basin, where physical-functionality approaches implemented in the MARTHE simulator are essential for modeling complex hydrodynamic systems (supporting the link between hydrogeology and hydrology, including, for instance, mass exchanges with the atmosphere and river subsystems).

INTRODUCTION

We describe physical and chemical phenomena occurring during the injection of acidic solutions (CO₂-rich solutions) with the establishment of reactive and mobile fronts.

Previous studies of geochemical processes occurring during CO₂ injection in an aquifer forecast the existence of five contrasting reactive zones extending radially from the injector (Figure 1): a full drying-out of the medium (Zone 5); a highly saline aqueous solution (Zone 4); a multiphase system with pH controlled by CO₂ (Zone 3); a saturated and acidified (CO₂-rich solution) aqueous solution (Zone 2); and an aqueous solution at equilibrium with reservoir minerals at reservoir pH (Zone 1) (Gaus et al., 2008; André et al., 2007; Azaroual et al., 2007).

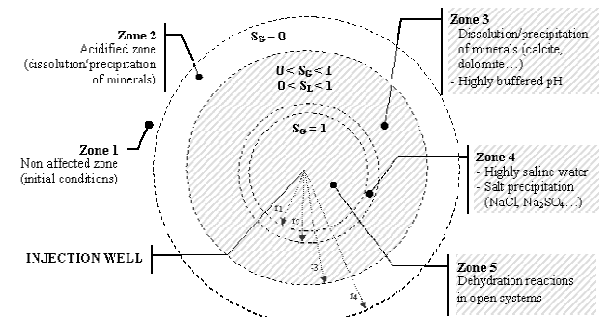


Figure 1. Conceptual diagram of the geochemical processes believed to occur during CO₂ injection in an aquifer. r_1 , r_2 , r_3 , r_4 are the different radii; S_G is gas saturation and S_L is liquid saturation (from Gaus et al., 2008; André et al., 2007 and Azaroual et al., 2007).

These reactions may change the porosity and connectivity of the porous/fractured medium, and therefore have an impact on the performance of the injection. This study is focused on Zone 1 and Zone 2, which have single-phase flow. In our study, we assume the point zero is located at the interface between supercritical CO₂ and water (Zone 3–Zone 2). We analyze the main physical chemical processes involved with injection of CO₂ and saturated water into the deep Keuper aquifer in the Paris Basin

(France), using a reactive transport modeling approach.

NUMERICAL TOOLS

The simulations presented in this study were performed using the MARTHE-REACT code (Thiéry et al., 2009, presented in the same TOUGH symposium), which was formed by coupling the MARTHE code (flow and transport in porous media) with the chemical part of the TOUGHREACT code.

TOUGHREACT reactive code

TOUGHREACT is a nonisothermal multicomponent reactive fluid flow and geochemical transport simulator (Xu et al., 2004) that can be applied under various thermohydrological and geochemical conditions of pressure (1 bar to several hundred bars), temperature (0–300°C), water saturation (dry to saturated), and ionic strength (up to 6 mol/kg H_2O for NaCl-dominant solutions). Note that only the chemical part of TOUGHREACT is taken into account for the coupling with MARTHE.

MARTHE transport code

The MARTHE code (Modelling Aquifers with Rectangular cells, Transport and Hydrodynamics) is designed by BRGM for the hydrodynamic and hydro-dispersive modeling of groundwater flow in porous media (Thiéry, 1990). Hydrodynamic calculations are carried out by a finite volume algorithm based on a matrix resolution of conjugate gradients with Choleski preconditioning. Several methods can be used for transport calculation (total variation diminishing, finite volumes, MOC, or random walk).

MARTHE-REACT coupling approach

MARTHE has already been coupled to specific chemical simulators (SCS) (Thiéry, 1995). The approach used to couple it with the TOUGHREACT chemical simulator is essentially the same as before. Flow calculations and mass and energy transport are performed by the MARTHE code with no modifications. The chemical simulations are performed by the chemical part of the TOUGHREACT code. The coupling sequence is the following at each time step: (1) coupled flow calculation in aquifers and river networks integrating evaporation, infiltration, runoff, overflow, etc.; (2) transport in aquifer and river networks of every primary dissolved chemical species; (3) chemical reactions in each aquifer cell and river reach using the concentrations at the end of the time step. There is no iteration; hence, it is a SNIA (Sequential Non Iterative Algorithm) scheme. The important point is that with this sequential scheme, after transport, the chemical-reaction calculations are independent in each cell.

INJECTION OF CO_2 -SATURATED WATER INTO THE KEUPER AQUIFER

Keuper aquifer properties

The study site is located in the Paris Sedimentary Basin, which includes deposits from the Mesozoic to the Cenozoic on a pre-Permian basement. The Keuper formation within the Paris Basin was recently studied for its CO_2 storage feasibility (Bonijoly et al., 2003; Delmas, 2007). Several aquifers in the east and south-central parts of the Paris Basin could be affected by CO_2 storage; we focus our study on the Donnemarie sandstone formation, a multilayered reservoir located at a depth of around 2,000 m with a thickness of 100 m. The reservoir, which is entirely sealed by anhydritic clays, is still exploited for hydrocarbons deposits and natural gas storage. Three layers (an upper, middle, and lower part) can be distinguished, with thicknesses of 35 m, 20 m, and 45 m, respectively. The upper part of the reservoir is the most permeable layer, whereas the porosity of the three parts is similarly low (*Table 1*). Water salinity is in the range 30–180 g $kg^{-1} H_2O$. Temperature and pressure conditions in the reservoir (1,500 to 3,000 m depth) vary respectively from 70 to 120°C and 200 to 300 bars (Bonijoly et al., 2003).

Table 1. Physical properties of the Keuper aquifer (Donnemarie).

	Reservoir part		
	Upper	Middle	Lower
Porosity (-)	0.06	0.04	0.07
Permeability (m^2)	$2.3 \cdot 10^{-15}$	$0.3 \cdot 10^{-15}$	$0.2 \cdot 10^{-15}$

Geometry

The Keuper aquifer (Donnemarie) is modeled as a sandstone reservoir represented by a cylindrical geometry with three layers, here representing the upper, middle, and lower parts of the reservoir (Figure 2).

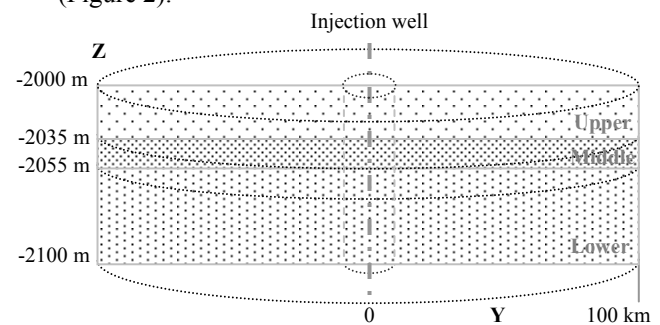


Figure 2. Two-dimensional radial geometry of the Keuper reservoir model with three layers representing upper, middle and lower parts of Donnemarie sandstones

The grid is composed of 300 cells: along the Y axis, 1 cell with a radius of 0.2 m contains the vertical injection well, whereas 99 cells represent a radius following a logarithmic progression up to 100 km; the Z axes is divided by 3 cells corresponding to the upper (35 m), middle (20 m), and lower (45 m) parts of the Donnamarie sandstone. Each layer is assumed to be homogeneous, isotropic, and without slope.

Basin mineralogy

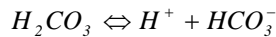
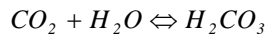
Donnamarie sandstone mineralogy has been chosen and identified through numerous data sets. In the first step, an aqueous speciation calculation of Keuper saltwater (Azaroual et al., 1997) is performed with the geochemical code PHREEQC (Parkhurst and Appelo, 1999). In this way, minerals at thermodynamic equilibrium are hypothesized. For the missing mineralogy, data are taken from the literature. Thus, Renoux (2005) suggests the presence of quartz, feldspar, anhydrite, dolomite, and illite. To attribute relative quantities for each mineral, proportions (in volume fraction) are determined with help of the Elghali et al. (2009) study: 52.85% of quartz, 25% of dolomite, 9% of calcite, 8% of albite, 3% of anhydrite, 1% of illite, 0.9% of Fe(OH)₃ and 0.25% of kaolinite.

Formation water

The composition of the Keuper aquifer formation water is calculated at equilibrium with the mineralogy cited above. For the following simulation, the reservoir is assumed to be saturated by saline brine ($\approx 150 \text{ g/kg}_{\text{H}_2\text{O}}$), with the chemical composition given in Table 2 at a temperature of 100°C and 200 bars pressure.

CO₂-saturated injected water

CO₂-saturated injected water is created from the equilibrium between initial dilute formation water with a pure CO₂ phase at 100°C and a pressure of 200 bars (equivalent to a CO₂ fugacity of 123.1 bars). As mentioned in André et al. (2007), this reaction produces bicarbonate ions, which gives an acid solution (pH of 3.15).



The resulting CO₂-saturated solution, with a concentration about $1.3 \text{ mol CO}_2 \text{ kg}^{-1}_{\text{H}_2\text{O}}$ and a pH of 3.15, is injected into the reservoir (Table 2). A tracer is also injected in the reservoir to show the velocity of a nonreactive compound in the different layers (its concentration is $5 \times 10^{-5} \text{ mol} \cdot \text{kg}^{-1}_{\text{H}_2\text{O}}$).

Table 2. Chemical composition of water from the Keuper aquifer (formation water) and of CO₂-saturated water injected into the Keuper aquifer ($\text{mol} \cdot \text{kg}^{-1}_{\text{H}_2\text{O}}$)

	Formation Water	CO ₂ -saturated Water
Temperature	100°C	100°C
pH	6.46	3.15
C	3.343e-3	1.3069
Ca	3.068e-2	3.071e-5
Mg	8.064e-3	8.061e-6
Na	2.468	2.468e-3
K	1.376e-3	1.376e-6
Fe	1.844e-13	1.010e-13
H4SiO4	8.93e-4	8.932e-7
SO4	6.183e-2	8.181e-5
Al	3.028e-7	3.028e-10
Cl	2.42	2.42e-3
Tracer	5.063e-8	5.00e-5

Geochemical approach

Kinetic rates are taken into account to examine the different mineral behaviors. Mineral (n) dissolution (+) –precipitation (-) rate (r_n) in mol/s is expressed by Lasaga et al. (1994):

$$r_n = \pm k_n A_n |1 - \Omega_n^\theta|^\eta$$

with k_n the rate constant ($\text{mol}/\text{m}^2/\text{s}$), A_n the specific reactive surface area (m^2), Ω_n the mineral saturation ratio (-) and θ and η power terms defined from experiments. Calcite and iron hydroxides are assumed to dissolve-precipitate at equilibrium, because their reaction rates are quite rapid. Other minerals are kinetically controlled by acid, neutral, alkaline (1), and carbonation (2), mechanisms depending on temperature (Lasaga et al., 1994; Palandri and Kharaka, 2004):

$$k = k_{25}^{nu} \exp \left[\frac{-E_a^{nu}}{R} \left(\frac{1}{T} - \frac{1}{298.15} \right) \right] + k_{25}^H \exp \left[\frac{-E_a^H}{R} \left(\frac{1}{T} - \frac{1}{298.15} \right) \right] a_H^{n_H}$$

$$+ \begin{cases} k_{25}^{OH} \exp \left[\frac{-E_a^{OH}}{R} \left(\frac{1}{T} - \frac{1}{298.15} \right) \right] a_H^{n_{OH}} & 1) \\ k_{25}^{OH} \exp \left[\frac{-E_a^{OH}}{R} \left(\frac{1}{T} - \frac{1}{298.15} \right) \right] a_{\text{CO}_2, \text{aq}}^{n_{OH}} & 2) \end{cases}$$

with k_{25} the rate constant at 25°C, E_a the activation energy, R the gas constant, T the absolute temperature, a the activity of species, and n a power term, where the subscripts nu and H indicate neutral and acid mechanisms respectively.

The acid catalysis is considered only for mineral dissolution. Table 3 provides all parameters defining the kinetic rate constrained for the simulation. For several minerals, the volume fraction is null, because minerals are not initially present in the reservoir, but allowed to precipitate.

Table 3. Kinetic rate parameters of each mineral for neutral and acid mechanism and associated volume fraction
*Dissolve and precipitate at equilibrium.

Minerals	volume fraction (Vmin/Vs)	Acid Mechanism			Neutral Mechanism		Carbonation Mechanism		
		Log k	Ea	n	Log k	Ea	Log K	Ea	m
Dolomite	0.25	-3.19	36.1	0.5	-7.53	52.2	-5.11	34.8	0.5
Siderite	0.0								
Dawsonite	0.0	-	-	-	-7	62.8	-	-	-
Magnesite	0.0	-6.38	14.4	1	-9.34	23.5	-5.22	62.8	1
Calcite*	0.09								
Fe(OH) ₃ *	0.009			-					
							Alkaline mechanism		
							Log k	Ea	n
Albite	0.08	-10.16	65	0.457	-12.56	69.8	-15.6	71	-0.572
Kaolinite	0.0025	-11.31	65.9	0.777	-13.18	22.2	-17.05	17.9	-0.472
Illite-Mg	0.01	-10.98	23.6	0.34	-12.78	35.0	-16.52	58.9	-0.4
Quartz	0.5285				-13.4	90.9			
Halite	0.0	-	-	-	-0.21	7.4	-	-	-
Anhydrite	0.03	-	-	-	-3.19	14.3			

Simulation scenario

The scenario is a hypothetical injection of a CO₂-saturated water conducted to test the reactive geochemical model in Zone 2 (acidified zone) and observe the dissolution-precipitation phenomena on Keuper mineralogy. Injection rate of CO₂-saturated water is chosen to have an increase in pressure lower than 20% of the initial pressure (200 bars) in each layer. Deduced injection rates correspond to 8.4×10^{-4} m³/s, 6×10^{-5} m³/s, and 9.45×10^{-5} m³/s into upper, middle, and lower layers respectively. An amount of 300,000 m³ of CO₂-saturated water flows over 10 years, which corresponds to 18,720 tons of dissolved CO₂ considering 1.3 mol CO₂ kg⁻¹H₂O. A hydrostatic pressure is considered initially and is fixed in the outermost column of the grid during the simulation. No exchanges of fluids are considered under and above the system.

Simulation results

Hydrodynamics

The tracer included within the CO₂-saturated water is represented on a profile (Figure 3) from 0 to 350 m after 10 years of injection. Its behavior confirms different flow velocities for the three layers, with the fastest transport in the upper layer (the most permeable). After 10 years, originally injected CO₂-saturated water reaches a radius of 150 m in the upper layer, 70 m in the middle layer, and 45 m in the lower layer. We can expect preferential geochemical reactivity in these zones.

Geochemical reactivity

As original injected CO₂-saturated water reaches a radius of 150 m in the upper layer, we could expect a pH of 3.15 in this area. But the pH of 3.15 exists only in the first few meters around the injection well (Figure 4). Further into the upper layer (radius 3–150 m), the pH is 4.8, which indicates that geochemical reactivity is buffering the pH. Estimated changes in porosity and permeability are located in the same area as well (Figure 5).

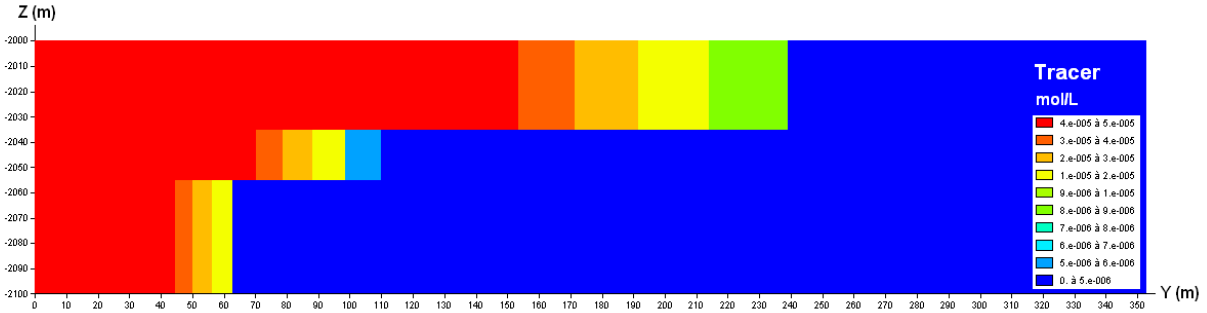


Figure 3. Profile of tracer after 10 years of CO₂-saturated water injection. Initial concentration of tracer is equal to 5 10⁻⁸ mol.kg⁻¹_{H2O} and injected tracer concentration is equal to 5 10⁻⁵ mol.kg⁻¹_{H2O}.

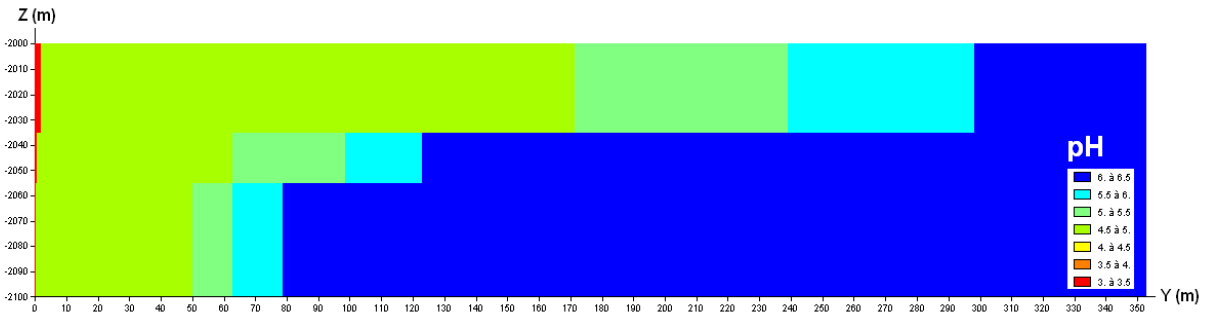


Figure 4. Profile of pH after 10 years of CO₂-saturated water injection. The pH of injected CO₂-saturated water and formation water are equal to 3.15 and 6.46 respectively.

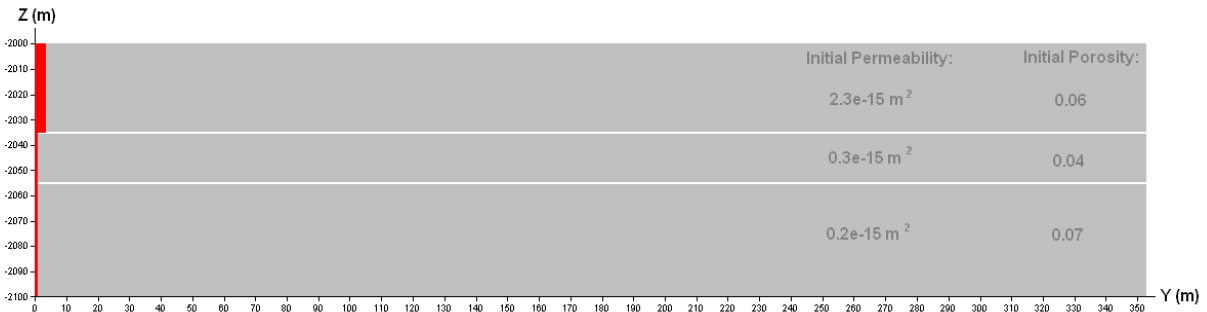
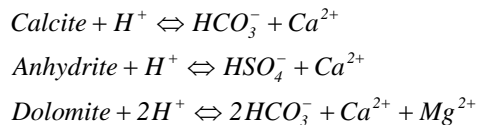


Figure 5. Profile of potential impact on porosity and permeability (red zone) after 10 years of CO₂-saturated water injection. Maximal porosity is estimated around 0.41 and maximal permeability is deduced equal to 7×10⁻¹³ m².

For a better understanding, we focus on the geochemical reactivity of the upper layer (Figure 6). As observed previously, the pH of 3.15 extends a few meters (0 to 2.5 m), forming an acidic front: Zone 2a (A). The total dissolution of dolomite, calcite (B), and anhydrite (C) is observed in the same area.



Dissolution of albite (D) is observed in lower quantities as a result of smaller kinetic rates.



The potential impact of mineral dissolution on porosity is estimated (A), but not taken into account in the flow calculation. A maximal increase in porosity (41% from 6% initially) is estimated, which corresponds to the total dissolution of carbonate and sulphate minerals.

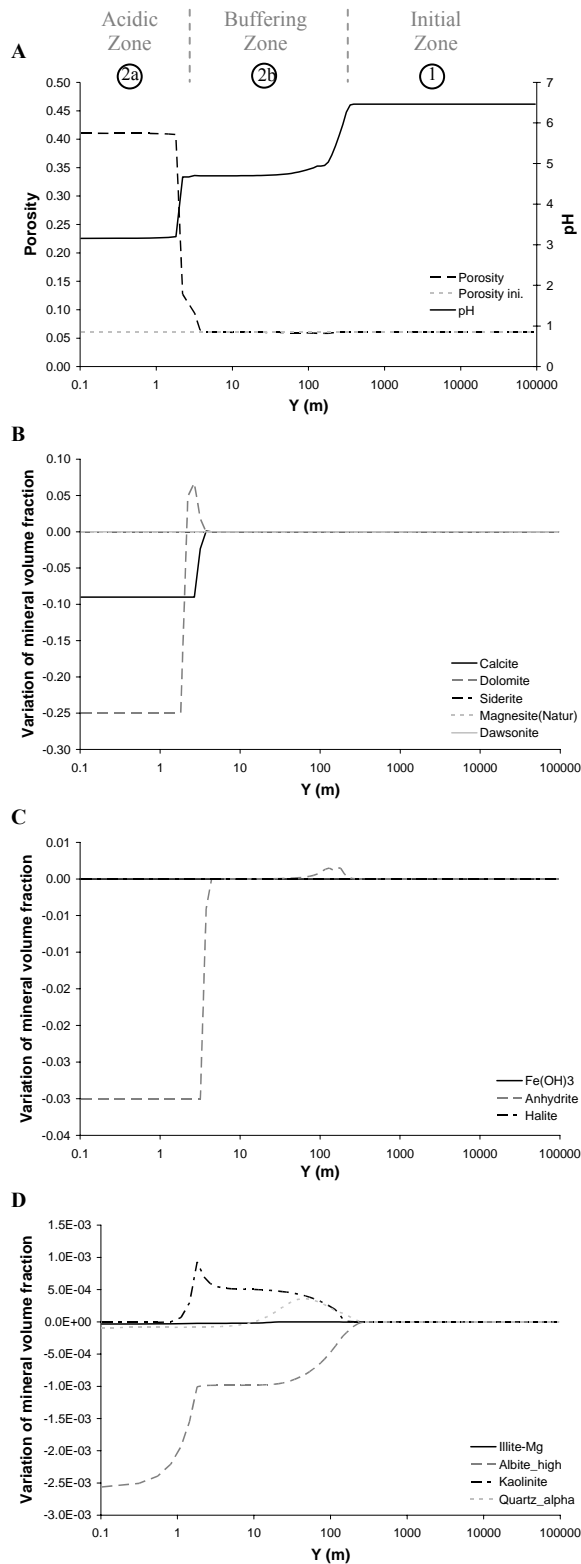
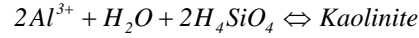
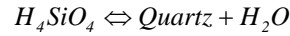


Figure 6. Variation of porosity, pH, and mineral volume fractions (V_{min}/V_s) in the upper layer of Donnamarie aquifer from the injection cell to the outermost after 10 years of CO_2 -saturated water injection. Curves are plotted on semilog scales.

These dissolutions release Ca^{2+} , Mg^{2+} , HCO_3^- , HSO_4^- , Al^{3+} , and H_4SiO_4 in solution, allowing precipitation of kaolinite and dolomite just after the acidic zone (2.5 to 3 m).



Further (3 to 150 m), we can observe a second area where the pH is buffered by carbonate and sulphate, and where kaolinite and quartz precipitate (zone 2b = buffering zone).



Precipitations of kaolinite and quartz have a minor impact on porosity changes compared to dissolution of carbonates. But at this time scale (10 years), porosity changes are limited by the amount of carbonate, because of the slow reactivity of silicates. Further, in the buffered zone (from 150 m to 100 km), pH increases to reach the pH of formation water, and any dissolution-precipitations are observed because of the equilibrium between minerals and formation water (zone 1 = initial zone).

The simulation results confirm the high reactivity of CO_2 -saturated water with respect to the carbonate minerals (André et al., 2007), which are totally dissolved in the water-saturated zone of the near-well field. Reactions occur on a larger extent in the superior layer, where the permeability is higher. Dissolution of calcite, dolomite, and anhydrite induces some pH buffering and a significant increase in porosity, reaching 41% in the first meters of the water-saturated zone after ten years, when the dissolution is total. Albite dissolution presents the first step in destabilization of the aluminosilicates in lower quantities. This can be explained by the slow kinetics of dissolution for aluminosilicate minerals compared to that for carbonates. This is in accordance with observations by Audigane et al. (2007), who simulate CO_2 injection into sandstone. Just behind the acidic zone, one can observe precipitation of dolomite, kaolinite, and quartz. The porosity evolution of the reservoir is essentially constrained by the magnitude of carbonate and sulphate mineral dissolution, and the impact on injectivity still depends on the location of mineral dissolution-precipitation (connected pores or not).

CONCLUSION

A 2D-radial numerical model of CO_2 -saturated water injection into the sandstone Keuper aquifer in the Paris Basin has been presented using the MARTHE-REACT code. The simulation was performed over 10 years of continuous injection considered as a high reactivity level compared to supercritical CO_2 injection as studied by André et al (2007). Three reactive zones were identified:

- 1) An **acidic zone** where dolomite, calcite, and anhydrite are totally dissolved, and where albite starts to dissolve from the acidic conditions (pH = 3.15), with a maximal porosity increase of 41%,
- 2) A **buffered zone** where carbonate and sulphate minerals buffer the acidic injection (pH = 4.8) and where transported ions allow precipitation of kaolinite, quartz, and dolomite with minor impact on porosity,
- 3) An **initial zone** where minerals are in equilibrium with formation water (pH = 6.46) without changes in porosity.

The results obtained confirm similar findings from other studies on the reactivity of carbonate and sandstone aquifers, and provides further confidence in the coupling tool.

This study is a first step before the assessment of CO₂-saturated water leakage from a reservoir to the surface in a sedimentary basin, where functionalities of the MARTHE simulator are essential for modeling complex hydrodynamic systems (providing a link between hydrogeology and hydrology, including, for example, atmosphere and river subsystems).

ACKNOWLEDGMENT

This study is carried out in the framework of the PROCHE PUIITS project co-funded by the French National Research Agency (ANR, in French).

REFERENCES

- André, L., P. Audigane, M. Azaroual, A. Menjoz, Numerical modeling of fluid-rock chemical interactions at the supercritical CO₂-liquid interface during CO₂ injection into a carbonate reservoir, the Dogger aquifer (Paris Basin, France), *Energy Conversion & Management*, 48, 1782-1797, 2007.
- Audigane, P., I. Gaus, I. Czernichowski-Lauriol, K. Pruess and T. Xu, Two-dimensional reactive transport modelling of CO₂ injection in a saline aquifer at the Sleipner site, North Sea, *American Journal of Science*, 307, 974-1008, 2007.
- Azaroual, M., K. Pruess, C. Fouillac, Feasibility of using supercritical CO₂ as heat transmission fluid in the EGS integrating the carbon storage constraints, *Engine Workshop 2*, 1-4 April 2007, Volterra, Italy, p. 47, 2007.
- Azaroual, M., C. Fouillac, J.M. Matray, Solubility of silica polymorphs in electrolyte solutions, II. Activity of aqueous silica and solid silica polymorphs in deep solutions from the sedimentary Paris Basin, *Chemical Geology*, 140, 167-179, 1997.
- Bonijoly, D., J. Barbier, J.M. Matray, C. Robelin, C. Kervevan, D. Thiéry, A. Menjoz, C. Cotiche, B. Herbrich, Feasibility of CO₂ storage in geothermal reservoirs. Example of the Paris Basin, France, Report BRGM/RP-52349-FR, 2003.
- Delmas, J., Etude pétrophysique des aquifères gréseux triasiques dans le secteur d'étude de PICOREF (Sud Champagne, Bassin de Paris), Porosité et perméabilité mesurées sur carottes, Rapport d'avancement Projet PICOREF: Volet 3, 2007, restricted.
- El-ghali, M.A.K., S. Morad, H. Mansurbeg, M.A. Caja, M. Sirat, N. Ogle, Diagenetic alterations related to marine transgression and regression in fluvial and shallow marine sandstones of the Triassic Buntsandstein and Keuper sequence, the Paris Basin, France, *Marine and Petroleum Geology*, 26, 289-309, 2009.
- Gaus, I., P. Audigane, L. André, J. Lions, N. Jacquemet, P. Durst, I. Czernichowski-Lauriol, M. Azaroual, Geochemical and solute transport modelling for CO₂ storage, what to expect from it?, *International journal of greenhouse gas control*, 2, 605 – 625, 2008.
- Lasaga, A. C., J. M. Soler, J. Ganor, T. E. Burch, K. L. Nagy, Chemical weathering rate laws and global geochemical cycles, *Geochim. Cosmochim. Acta*, 58, 2361-2386, 1994.
- Palandri, J.L., and Y.K. Kharaka, A compilation of rate parameters of water-mineral interaction kinetics for application to geochemical modeling, U.S. Geological Survey Open file report (of 2004-1068), 2004.
- Parkhurst, D.L., and C.A.J. Appelo, User's Guide to PHREEQC (Version 2)--A Computer Program for Speciation, Batch-Reaction, One-Dimensional Transport, and Inverse Geochemical Calculations, *Water Resources investigations report*, 99-4259, 1999.
- Renoux, P. Aquifères : Etude diagraphique du puits Limoreau 101. Projet GEOCARBONE-PICOREF-ANR CO₂ Edition 2005, 150-151, 2005.
- Thiéry, D., N. Jacquemet, G. Picot-Colbeaux, C. Kervevan, L. André and M. Azaroual, Validation of MARTHE-REACT coupled surface and groundwater reactive transport code for modeling hydro systems, TOUGH Symposium 2009, 14-16 September, submitted.

- Thiéry, D, Modélisation des écoulements avec interactions chimiques avec le logiciel MARTHE Release 5.5, Report BRGM/R38463-HYT/DR-95, 1995.
- Thiéry, D. Software MARTHE, Modelling of aquifers with a rectangular grid in transient state for hydrodynamic calculations of heads and flows, Release 4.3, Report BRGM/R32548, 1990.
- Xu, T., E. Sonnenthal, N. Spycher and K. Pruess, TOUGHREACT User's Guide: A simulation program for non-isothermal multiphase reactive geochemical transport in variably saturated geologic media, Report LBNL-55460, Lawrence Berkeley National Laboratory, 2004.

NUMERICAL STUDIES OF DENSITY-DRIVEN FLOW IN CO₂ STORAGE IN SALINE AQUIFERS

George S. H. Pau, John B. Bell, Karsten Pruess, Ann S. Almgren, Michael J. Lijewski, and Keni Zhang

Lawrence Berkeley National Laboratory
1 Cyclotron Road MS50A-1148
Berkeley, CA 94720, USA
e-mail: gpau@lbl.gov

ABSTRACT

Simulations are routinely used to study the process of carbon dioxide (CO₂) sequestration in saline aquifers. In this paper, we look at some numerical aspects of the accurate modeling and simulation of the dissolution-diffusion-convection process. We perform convergence studies with respect to solver tolerances, grid resolutions, fluctuation strength, and domain size. We show that stringent tolerances and grid resolutions are needed to accurately predict onset time. Domain size must be sufficiently large to contain at least 2 extended fingers to accurately predict the long-term stabilized mass flux of CO₂; otherwise, finite domain effects will adversely change the flow behavior of the system we are modeling.

INTRODUCTION

Carbon dioxide (CO₂) sequestration involves injecting CO₂ into a saline aquifer. While the primary mechanism of securing the CO₂ relies on a leak-proof formation, secondary geochemical mechanisms may play a significant role, especially in a geological time frame. At long time, an immiscible CO₂ gas layer will form on top of the brine in the rock formation. Under ambient temperature and pressure conditions in a typical aquifer, CO₂ will dissolve into the brine and increase the density of the brine at the interface of the layers by 0.1–1%, depending on the salinity of the brine (Pruess and Zhang, 2008). Due to gravitational instability and the heterogeneity in the rock properties of the aquifer, CO₂-rich brine fingers will form, leading to convective flow that transports these CO₂-rich brines downward, while driving brine with low CO₂ concentration upwards. This then accelerates the rate at which CO₂ is dissolved and provides a more secure mechanism by which CO₂ can be stored.

This dissolution-diffusion-convection process has been analyzed in a number of studies. In Ennis-King

and Paterson (2003) and Riaz et al. (2006), linear stability analyses yield useful relations for the onset time for convection, dominant wavelength for growth of convective fingers, and the growth rates of these fingers. Numerical simulations were also performed to further elucidate the process and to validate the linear stability analyses. For example, Riaz et al. (2006) performed numerical simulation of a single-phase two-component model with the Boussinesq assumption and demonstrated that the simulation results are consistent with their analysis. Pruess and Zhang (2008) examined long-term behavior of the CO₂ flux, in addition to the onset of convection. Their simulation uses a full compressible model with very accurate equations of state.

In this work, we examine some of the numerical aspects of studying the dissolution-diffusion-convective process of CO₂ through simulation. We use a second-order accurate adaptive method that is described in the next section. Specifically, we examine how simulation parameters, such as solver tolerances, grid resolution, strength of perturbations, and domain size, affect our solution. The results are compared to those obtained through TOUGH2-MP, a parallelized version of the general-purpose simulator TOUGH2/ECO2N (Zhang et al., 2008; Pruess, 2004; Pruess and Spycher, 2007).

NUMERICAL SCHEME

We assume that a layer of CO₂-saturated brine is formed at the interface of the brine and CO₂ gas, and the dissolution rate is sufficiently high that the layer remains saturated for the length of the simulation. This assumption allows us to use a variable-density single-phase incompressible model to treat the dissolution-diffusion-convection process. The variable-density formulation we use is similar to the formulation of Douglas et al. (2002), and different from that of Riaz et al. (2006), since it does not make

the Boussinesq assumption. Here, we provide an overview of the methodology; details of the approach are given in Pau et al. (2009).

The basic integration scheme is based on the total-velocity splitting approach. Due to the dependence of fluid density on the mass fraction of dissolved CO₂, the velocity divergence constraint is given by

$$\nabla \cdot u = \sum_{i=1}^2 \frac{1}{\rho_i} \nabla \cdot \phi \rho D \nabla X_i,$$

where the summation is over components $i = 1$ (CO₂) and $i = 2$ (H₂O). Here, u is the Darcy velocity, ρ_i and X_i are the density and the mass fraction of CO₂(aq), ρ_2 and X_2 are the density and the mass fraction of H₂O, respectively, ρ is the density of the mixture, ϕ is the porosity and D is the diffusion coefficient. Expressing u in terms of pressure p , this divergence constraint leads to a second-order elliptic pressure equation, given by,

$$-\nabla \cdot \frac{\kappa}{\mu} (\nabla p - \rho \mathbf{g}) = \sum_{i=1}^2 \frac{1}{\rho_i} \nabla \cdot \phi \rho D \nabla X_i,$$

that we can solve to obtain u ; κ is the permeability of the porous media, μ is the viscosity of the mixture and \mathbf{g} is the gravity. This velocity is then used to recast component conservation equations as nonlinear hyperbolic equations.

The discretization procedure we have adopted is similar to the IMPES approach. The pressure equation is solved implicitly using a finite difference method and the mass conservation equations are solved semi-explicitly using an explicit second-order Godunov method for advection and an implicit Crank-Nicholson discretization of diffusion. Unlike the basic IMPES algorithm, however, our method is second-order accurate in both space and time.

The overall time-stepping procedure is integrated into an adaptive mesh refinement (AMR) framework (Almgren et al., 1994) to efficiently accommodate the difference in scale between the diffusive boundary layer and the large-scale convective fingers. Our approach to adaptive refinement uses a nested hierarchy of logically rectangular grids with simultaneous refinement of the grids in both space and time. The grid changes with time based on a set of user-defined refinement criteria. Shown in Figure 1 is a snapshot of the grid; finer grids are placed in region where small features with large concentration gradients are present. The resulting algorithm is parallelized and shows good scaling behavior up to 1024 CPUs.

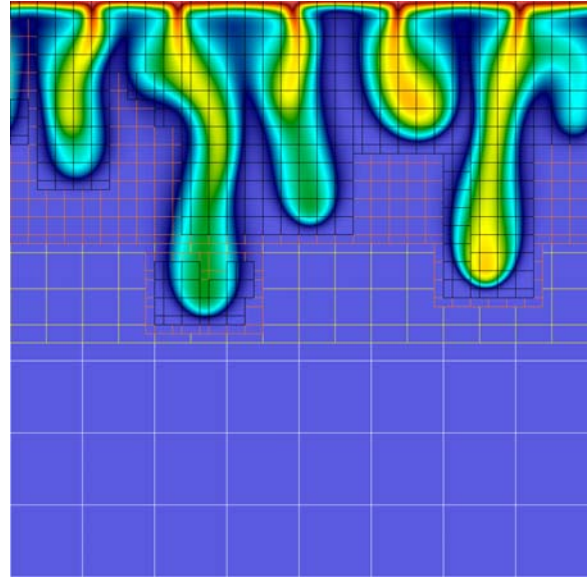


Figure 1. AMR grid with four levels of refinement. Refinement criterion is based on concentration gradient of all components.

PROBLEM SETUP

The fluid properties, as specified in Table 1, are derived from the ECO2N fluid module of TOUGH2 and correspond to pure water (no salinity) at temperature and pressure conditions of $T = 45^\circ\text{C}$, $P = 100$ bar, as would be encountered in a typical sedimentary basin near 1,000 m depth. A two-dimensional domain was used as shown in Figure 2. In most cases, a domain size of $1 \text{ m} \times 4 \text{ m}$ is used.

Table 1. Fluid and formation properties

Property	Magnitude
Viscosity, μ	0.5947 mPas
Water density, ρ_w	994.56 kg/m ³
Saturated CO ₂ mass fraction, X_1	0.049306
Density increase due to CO ₂ dissolution, $\Delta\rho$	10.45 kg/m ³
Diffusivity, D	$2 \times 10^{-9} \text{ m}^2/\text{s}$
Mean permeability, κ	10 D
Mean porosity, ϕ	0.3

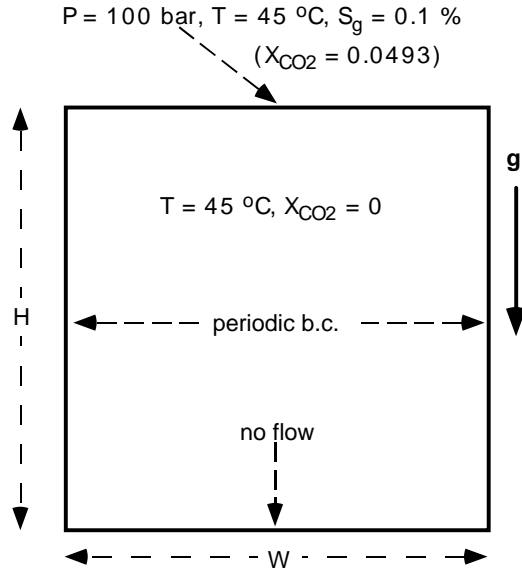


Figure 2. Schematic of specifications used for numerical simulations. Different heights H and widths W were employed for the simulation domain. Periodic boundary conditions mean that the same conditions were maintained on the left and right boundaries.

The flow system is initialized in gravity equilibrium (hydrostatic pressure gradient). The top boundary is impermeable and only diffusion of dissolved CO_2 into the simulation domain is permitted at the top boundary. Isothermal conditions are assumed throughout. The medium is assumed homogeneous, but small random variations, described by maximum per cent deviation from the mean, in permeability or porosity are imposed to seed the convective activity.

RESULTS

Figure 3 shows the concentration of CO_2 after the initialization of convective flow. Small fingers that form at the top boundary of the domain grow and merge into one or more extended fingers, the main conduits by which aqueous CO_2 is transported efficiently downward. These extended fingers grow wider as they traverse downward, due to diffusion. In addition, the dynamics within each of these extended fingers can be quite complex. Specifically, we observe that blobs of aqueous CO_2 with higher concentration may pinch off from an extended finger, and move downward at a greater speed. These blobs

eventually diffuse to a point where they are indistinguishable from the extended finger. The dynamics of convective flow is thus complex and exhibits highly nonlinear behavior.

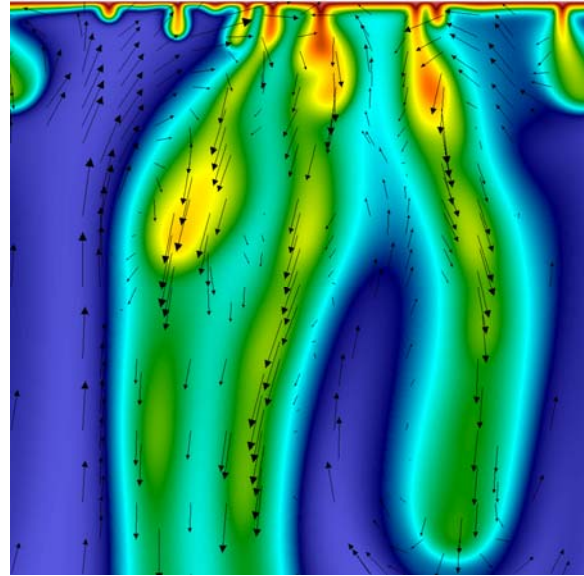


Figure 3. A snapshot of the concentration of CO_2 after onset of convection. The arrows show the velocity field.

In subsequent analyses, we will focus on two quantities of interest. First is the onset time of convection, t_{onset} , which determines the time at which convection becomes an important transport mechanism. We define t_{onset} as the time at which the average mass flux at the top boundary, F_0 , has a relative deviation of 1% from a pure diffusive mass flux.

Second is the stabilized mass flux, $\langle F_0 \rangle$, at the top boundary. The existence and the quantification of $\langle F_0 \rangle$ provide a simple model for larger-scale simulations of CO_2 injection. To determine $\langle F_0 \rangle$, we first compute the moving average $F_m(t)$ defined as

$$F_m(t) = \frac{1}{\Delta t} \int_{t-\Delta t/2}^{t+\Delta t/2} F_0(s) ds,$$

where Δt is chosen such that F_m does not fluctuate more than 5% over a time interval ΔT . The stabilized mass flux is then given by

$$\langle F_0 \rangle = \frac{1}{\Delta T} \int_{T-\Delta T}^T F_m(t) dt,$$

where $T+\Delta t/2$ is time at end of simulation. We ensure that the fingers have not reached the bottom of the simulation domain at time $T+\Delta t/2$.

Both the definitions we adopted above are admittedly arbitrary, but they provide consistent measures for performing our convergence studies. We note that F_0 is numerically equal to the CO_2 dissolution rate. Thus, F_0 denotes the rate at which CO_2 is removed from the highly mobile and buoyant gas phase, and put into a less mobile and negatively buoyant aqueous phase. This rate has important ramifications for storage security.

Effects of solver tolerances on the onset time

We begin this section with an analysis of the influence of numerical errors on the onset time. For homogeneous permeability and porosity, the two-dimensional problem at hand can be essentially reduced to a one-dimensional diffusion problem. Convective transport is only induced when a non-uniform flow field is generated by the heterogeneity in the permeability or the porosity function. However, linear solvers with finite tolerances may introduce small non-uniform errors that can also eventually lead to instability and convective flow. It is then important that we ensure that any convective transport observed in our simulation is induced by heterogeneities in formation's properties, and not due to finite tolerances of the linear solver we use. In particular, the tolerances must be sufficiently small that it has limited influence on the dynamics of the flow, and thus the onset time.

Since the Darcy velocity is computed from the pressure, we shall look at tolerances of the linear solver used to solve the pressure equation in our numerical scheme. Our multigrid linear solver uses two tolerances to control the accuracy of the linear solve: the relative error tolerance, ε_{rel} and the absolute error tolerance, ε_{abs} . Figure 4 shows that for 1% fluctuation in κ and $\varepsilon_{\text{rel}} = 10^{-12}$, the onset time converges to a value of 2.3×10^5 s when $\varepsilon_{\text{abs}} < 10^{-14}$. We note that the numerically-induced onset time is larger by a factor greater than 2. In addition, as we decrease ε_{abs} , the numerically induced onset time increases, but the true onset time remains unchanged. Decreasing ε_{rel} to 10^{-14} also does not change the results. Thus, we can conclude that with $\varepsilon_{\text{rel}} = 10^{-12}$ and $\varepsilon_{\text{abs}} = 10^{-14}$, the convective behavior that we observed is induced only by the heterogeneity in the permeability, and not by effects of finite tolerances in the linear solver.

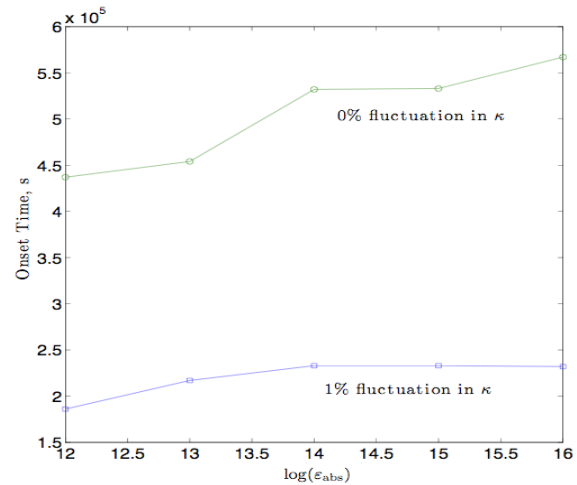


Figure 4. Effects of numerical errors on the determination of onset time. The onset time has converged when the absolute tolerance is 10^{-14} .

Effects of grid resolution on the onset time

Riaz et al. (2006) derived a critical wavelength λ_c from the linear stability analysis for examining the onset of convective flow. To fully capture the dynamics during the onset of convection, the dimensions of the simulation domain must be much larger than λ_c . For the parameters given in Table 1, $\lambda_c = 0.1$ m. Thus, our simulation domain, which has a width that is 10 times larger, is adequate.

However, the grid resolution must still be sufficiently high to resolve λ_c so that we can capture the initiation of convective flow accurately. We perform a grid convergence study to determine the appropriate grid size. Initial experiments show that we need to adjust the fluctuations value with grid size so that the underlying statistics are consistent for an uncorrelated random distribution. It reflects the notion that for a truly random medium, as gridblocks become larger, the variance of the fluctuations will be lower because of averaging. For example, an initial 1% fluctuation for a given resolution has to be reduced by half when the grid size in each direction is doubled.

We examine four different grid sizes: $\Delta x = 1/256$, $1/512$, $1/1024$, and $1/2048$. The corresponding fluctuations are given by 0.25%, 0.5%, 1% and 2%. Figure 5 shows that the onset time converges to a single value. From Table 2, we can conclude that the onset time converges to 2.23×10^5 s. An effective resolution of $\Delta x = 1/1024$, which is a factor of 100 smaller than λ_c , is thus sufficient.

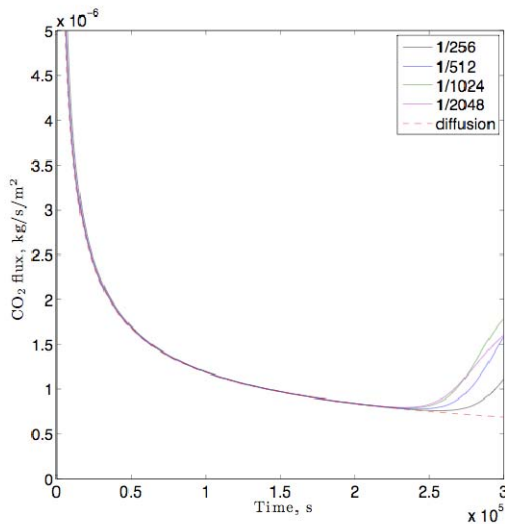


Figure 5. Effects of numerical errors on onset time. The onset time has converged when the absolute tolerance is 10^{-14} .

Table 2. Onset time, t_{onset} , at different resolutions.

h, m	$t_{onset} \times 10^{-5}$ s
1/256	2.44
1/512	2.33
1/1024	2.26
1/2048	2.23

Effects of fluctuation strength on the onset time

As the fingering phenomenon is driven by the heterogeneity in the permeability and porosity, we would like to study what influence fluctuations in permeability and porosity have on the onset time. Figure 6 shows that for similar level of relative per cent fluctuation, fluctuation in ϕ leads to faster onset time than fluctuation in κ . The variations with respect to per cent fluctuation are, however, similar; the onset time decreases with increasing fluctuation strength.

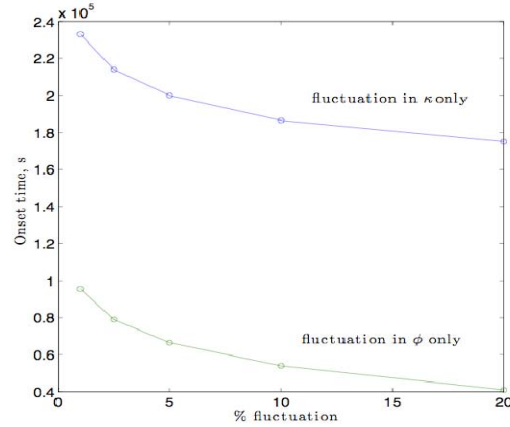


Figure 6. Variation of onset time with % fluctuation in permeability κ and porosity ϕ

Effects of domain size on the stabilized mass flux

At long time, the flow is characterized by fingers that extend along the length of the domain. Initial experiments show that boundary effects will adversely affect the solutions if the simulation domain cannot accommodate at least two extended fingers. To provide a good averaging to F_0 , there should be a modest number of these extended fingers. In Table 3, we show the computed stabilized mass fluxes, the maximum relative deviations from the $\langle F_0 \rangle$ in the sample set used to compute $\langle F_0 \rangle$, and the number of fingers for domains with different widths.

Table 3. Stabilized mass fluxes for different domain size. The deviation shown is the maximum absolute relative deviation of F_0 from $\langle F_0 \rangle$.

width, m	$\langle F_0 \rangle \times 10^6$ kg/m ² /s	deviation	number of fingers
1	1.46	0.27	2
2	1.48	0.12	4
8	1.52	0.07	8
16	1.50	0.06	17

The fluctuation decreases with increasing width; the relative deviation of F_0 from $\langle F_0 \rangle$ for $W = 16$ m is about a factor of 5 smaller than the relative deviation for $W = 1$ m. The mean also appears to converge to 1.5×10^{-6} kg/m²/s, although the variation is less drastic compared to the variation in the relative deviation. This shows that having a width that can accommo-

date two fingers may be sufficient, but larger width will lead to better averaging.

COMPARISON TO TOUGH2-MP

The same problem of convective instability discussed above was simulated with a parallelized version TOUGH2-MP (Zhang et al., 2008) of the general-purpose reservoir simulator TOUGH2. Initial calculations used the ECO2N fluid property module (Pruess and Spycher, 2007). However, since the conditions in the present problem are limited to a single aqueous phase, a more efficient simulation can be obtained by using EOS7, in which the fluid is represented as a two-component mixture of H₂O and brine. We use the brine component to represent density changes in the aqueous phase from CO₂ dissolution. Numerical work is approximately proportional to NEQ², where NEQ is the number of equations per gridblock. Accordingly, a given problem can be solved with EOS7 (NEQ = 2) in less than half the time required with ECO2N (NEQ = 3). Our test calculations have confirmed excellent agreement between simulations using EOS7 and ECO2N.

We experimented with different domain sizes and grid resolutions, to achieve results with “small” space discretization errors. Most calculations were performed for a domain of width $W = 1$ m, height $H = 5$ m, and a vertical grid resolution of 1 mm near the top boundary, which gradually was coarsened going downward. Horizontal grid resolution was 10 mm, and the total number of gridblocks was 52,300. Simulations presented here were performed on a Dell T5400 dual quad core computer with a total of 8 cores, and in most cases 16 processes were run (two per processor), because this was found to reduce total execution time compared to running eight processes. Depending on grid resolution and simulation time, individual runs typically took from 1/2 to 4 hours.

Results

The convective activity shows similar features as seen in the adaptive grid simulations discussed previously, including fingering convection, merging and pinch-off of fingers, and continuous generation of new fingers as older ones grow. As an example, Figure 7 shows convective patterns for three different random number seeds after a time of 101.6 days. The resolution of features is somewhat inferior in comparison to the adaptive gridding (Figure 3).

Specifics of the convective activity are very sensitive to small problem variations, but we observe that integral measures of the process, such as onset time of

convection and long-term behavior of the CO₂ mass flux carried by the convection, are quite robust to modest changes in problem parameters. Indeed, for the three cases with different random permeability fields shown in Figure 7, onset times of convection are identical, and long-term stabilized fluxes show random fluctuations of $\pm 15\%$ about the same mean of approximately 1.3×10^{-6} kg/s/m².

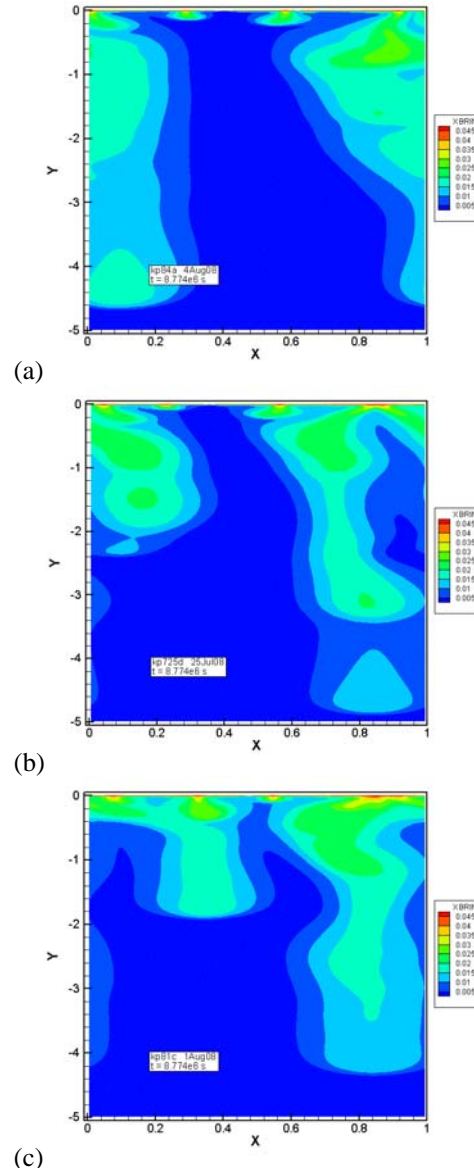


Figure 7. Simulated distribution of dissolved CO₂ after 101.6 days for three different random number seeds to generate permeability heterogeneity (a-0.7; b-0.8; c-0.9). Note the different horizontal and vertical scales.

We explored the sensitivity of the onset time for convection to the random perturbations applied to the medium. Figure 8 shows that the onset time for convection decreases with increasing strength of the applied perturbation of the medium. Porosity perturbations are seen to be more effective in triggering convective instability than permeability perturbations. These results are consistent with the results in the previous section, as shown in Figure 6.

A comparison calculation with a perfectly homogeneous medium yields a substantially larger onset time, as in this case convective instability arises only from numerical roundoff. The onset times obtained from TOUGH2-MP simulations are around $6\text{-}9 \times 10^4$ s, about a factor 3 smaller than obtained with the adaptive algorithm. The reason for this significant discrepancy is unknown. At a nominal onset time of 7.5×10^3 s, the thickness of the diffusive boundary layer is $= 12.2$ mm, which is well resolved with our 1 mm grid resolution.

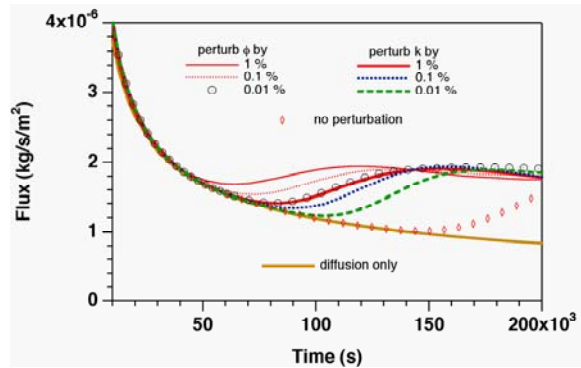


Figure 8. Simulated CO_2 fluxes at the top boundary at early times, for different random perturbations of the porosity or permeability field.

The convective CO_2 flux at the top is equal to the CO_2 dissolution rate per unit area. Due to the partially chaotic nature of the convection process, this rate fluctuates, but the fluctuations are modest in size, and fluxes stabilize at 1.3×10^{-6} kg/s/m^2 ($\pm 15\%$), regardless of how the instability was triggered (Figure 9). This is approximately 13% smaller than the value obtained from adaptive gridding simulations.

We also performed simulations with different boundary conditions at the sides and bottom of the domain, such as no-flow conditions on the sides, and constant pressure conditions on the bottom. Onset times for convection and long-term stabilized fluxes were found to be insensitive to boundary conditions. A more extensive account of TOUGH2 analyses of the dissolution-diffusion-convection process is available in a laboratory report (Pruess and Zhang, 2008).

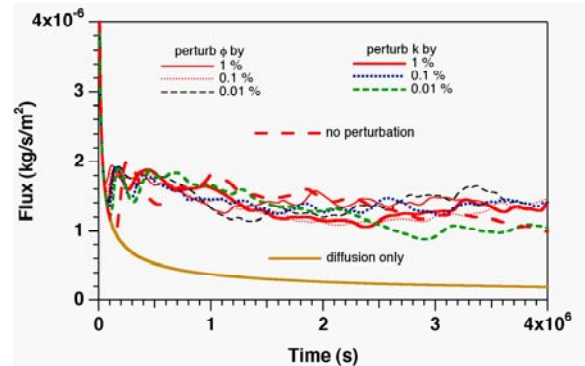


Figure 9. Longer-term behavior of simulated CO_2 fluxes at the top boundary.

CONCLUSION

High-resolution simulations of the diffusion-convection process in CO_2 sequestration were performed using a block structured adaptive mesh refinement method. Some numerical aspects of the simulations were examined, specifically variations in the onset time and stabilized mass flux with respect to solver tolerances, grid resolution, fluctuation strength, and domain size. Our main findings are as follows.

The diffusion-convection process involves complex fluid dynamics on multiple scales, including creation, growth, movement, merging, and pinch-off of convective fingers. While details of the convection process are chaotic in nature, integral measures, such as onset time for convection, and long-term CO_2 mass flux associated with the convective activity, are robust and insensitive to modest problem variations. By employing an adaptive gridding method combined with semi-implicit time stepping, we were able to control discretization errors and demonstrate convergence of onset times for convection. High-resolution simulations with TOUGH2-MP, using fixed gridding with resolution down to 1 mm at the CO_2 dissolution boundary, showed similar features as

the simulations with adaptive gridding. Long-term stabilized CO₂ fluxes obtained from adaptive gridding simulations and TOUGH2-MP agree to within 13%. Onset time for convection with TOUGH2-MP was only about 1/3 of what was obtained with the adaptive gridding approach. The reason for these differences is unknown at present, but may have to do with different approximations made for the flow physics.

ACKNOWLEDGMENT

Support for this work was provided by the LDRD program at Lawrence Berkeley National Laboratory (LBNL) and by the Office of Basic Energy Sciences under Contract No. DE-AC02-05CH11231 with the U.S. Department of Energy. This research used resources of the National Energy Research Scientific Computing Center and the Lawrence Livermore computational cluster resource provided by the LBNL's IT Division, both of which are supported by the Office of Science of the U.S. Department of Energy under Contract No. DE-AC02-05CH11231.

REFERENCES

- Almgren, A. S., J. B. Bell, L. H. Howell, and P. Colella, An Adaptive Projection Method for the Incompressible Navier-Stokes Equations. In *Proceedings of the IMACS 14th World Conference*, Atlanta, GA, July 11-15, 1994.
- Douglas, J. Jr., D. Frias, N. Henderson, and F. Pereira, Simulation of Single-Phase Multi-Component Flow Problems in Gas Reservoirs by Eulerian-Lagrangian Techniques, *Transport in Porous Media*, 50:307–342, 2002.
- Ennis-King, J., and L. Paterson, Role of Convective Mixing in the Long-Term Storage of Carbon Dioxide in Deep Saline Formations, paper SPE-84344, presented at *Society of Petroleum Engineers Annual Fall Technical Conference and Exhibition*, Denver, CO, October 2003.
- Pau, G. S. H., A. S., Almgren, J. B. Bell, and M. J. Lijewski, A Parallel Second-Order Adaptive Mesh Algorithm for Incompressible Flow in Porous Media, *Phil. Trans. R. Soc. A*, 2009. To be published.
- Pruess, K. The TOUGH Codes—A Family of Simulation Tools for Multiphase Flow and Transport Processes in Permeable Media, *Vadose Zone J.*, Vol. 3, pp. 738 - 746, 2004.
- Pruess K. and N. Spycher. ECO2N – A Fluid Property Module for the TOUGH2 Code for Studies of CO₂ Storage in Saline Aquifers, *Energy Conversion and Management*, 48(6), 1761-1767, 2007.
- Pruess, K., and K. Zhang, Numerical Modeling Studies of the Dissolution-Diffusion-Convective Process during CO₂ Storage in Saline Aquifers, Paper LBNL-1243E, Lawrence Berkeley National Laboratory, Berkeley, Calif., 2008.
- Riaz, A., H. A. Tchelepi, and F. M. Orr, Onset of Convection in a Gravitationally Unstable Diffusive Boundary Layer in Porous Media, *Journal of Fluid Mechanics*, 548:87–111, 2006.
- Zhang, K., Y. S. Wu and K. Pruess. *User's Guide for TOUGH2-MP - A Massively Parallel Version of the TOUGH2 Code*, LBNL-315E, Lawrence Berkeley National Laboratory, Berkeley, Calif., 2008.

CO₂ FLOW AND MIXING IN THE SHALLOW SUBSURFACE AND IN DEPLETED GAS RESERVOIRS

C.M. Oldenburg, J.L. Lewicki, L. Pan, and B.M. Freifeld
Earth Sciences Division 90-1116
Lawrence Berkeley National Laboratory
Berkeley, CA USA
e-mail: cmoldenburg@lbl.gov

ABSTRACT

We are using TOUGH2/EOS7CA and EOS7C to model CO₂ injection and migration in (1) near-surface leakage studies and (2) in depleted gas reservoir studies. EOS7CA is applicable to shallow leakage and seepage, while EOS7C finds application in studies related to gas reservoirs. Use of EOS7CA to address the question of the origin of patchy emissions at the ZERT shallow-release experiment in Montana suggests that packer locations within the horizontal well influence emission patterns. Preliminary results of EOS7C simulations relevant to the CO₂CRC Otway project in Victoria, Australia, show that the presence of residual gas, regardless of composition, decreases injectivity due to the lower effective permeability of brine that must be displaced. The mixing between residual CH₄ and injected CO₂ and corresponding density increase is a secondary effect.

INTRODUCTION

Modeling of CO₂ injection and migration is a powerful tool for providing insight into the behavior and performance of geologic carbon sequestration sites. In this study, we present results of modeling using TOUGH2/EOS7CA and EOS7C aimed at two specific questions that arise in two diverse field studies. The first field study is the Zero Emissions Research and Technology (ZERT) shallow-release experiment in Montana. The second field study is the CO₂CRC Otway Project in Victoria, Australia (Sharma et al., 2007). While these two field projects share little in common in terms of depth of injection, scale of release, and overall field-test objectives, we show in this paper that the two closely related TOUGH2 equation-of-state modules, EOS7CA and EOS7C, can be applied to these field studies to address key questions.

METHODS

TOUGH2/EOS7CA and EOS7C (Pruess et al., 1999; Oldenburg et al., 2004) model five components (water, brine, CO₂, a tracer, and air (EOS7CA) and

CH₄ (EOS7C), respectively). Both modules use the GasEOS (Reagan and Oldenburg, 2006) approach to accurately model the density and viscosity of gas mixtures. EOS7CA uses Henry's law for solubility of gas species in the aqueous phase, an approach only accurate at low pressure, while EOS7C uses an approach that is well-suited for high pressure situations (Oldenburg et al., 2004). We used WinGridder (Pan, 2008) for generating the three-dimensional grid used in the ZERT simulation study.

EFFECT OF PACKER LOCATION

Patchy CO₂ emissions at the ZERT shallow-release experiment (e.g., Lewicki et al., 2007) appear to correlate with the locations of packers in the shallow horizontal injection well, as illustrated in Figure 1, which shows flux data in the top of the figure with packer locations below. The process hypothesized to create this patchy emission pattern is that CO₂ injected into each zone of the well flows within the pipe upward by buoyancy forces along the slightly sloping water-filled sections of each zone, until it encounters a packer, at which point it accumulates and moves through the perforations of the pipe into the cobble-soil system, effectively forming a local point source of gaseous CO₂, which is seen at the surface as a patchy emission pattern. We undertook modeling with EOS7CA to test this hypothesis.

We used WinGridder (Pan, 2008) to develop a 3D grid as shown in Figure 2. The grid was designed to capture the details of the release of CO₂ from the horizontal well. The discretization represents one-half of the horizontal well and its elevation variations in detail. The 3D grid consists of 11 replications of a two-dimensional slice. Though replicated in the direction perpendicular to the pipe (Z-direction), there is no pipe material in the model anywhere except in the plane at Z = 8.975 m (the mirror plane) and cobble or soil is specified in the other planes as appropriate even where the discretization mimics the pipe geometry. Each of the 11 XY planes contains 4779 gridblocks, for a total of 52,569 gridblocks and 147,486 connections.

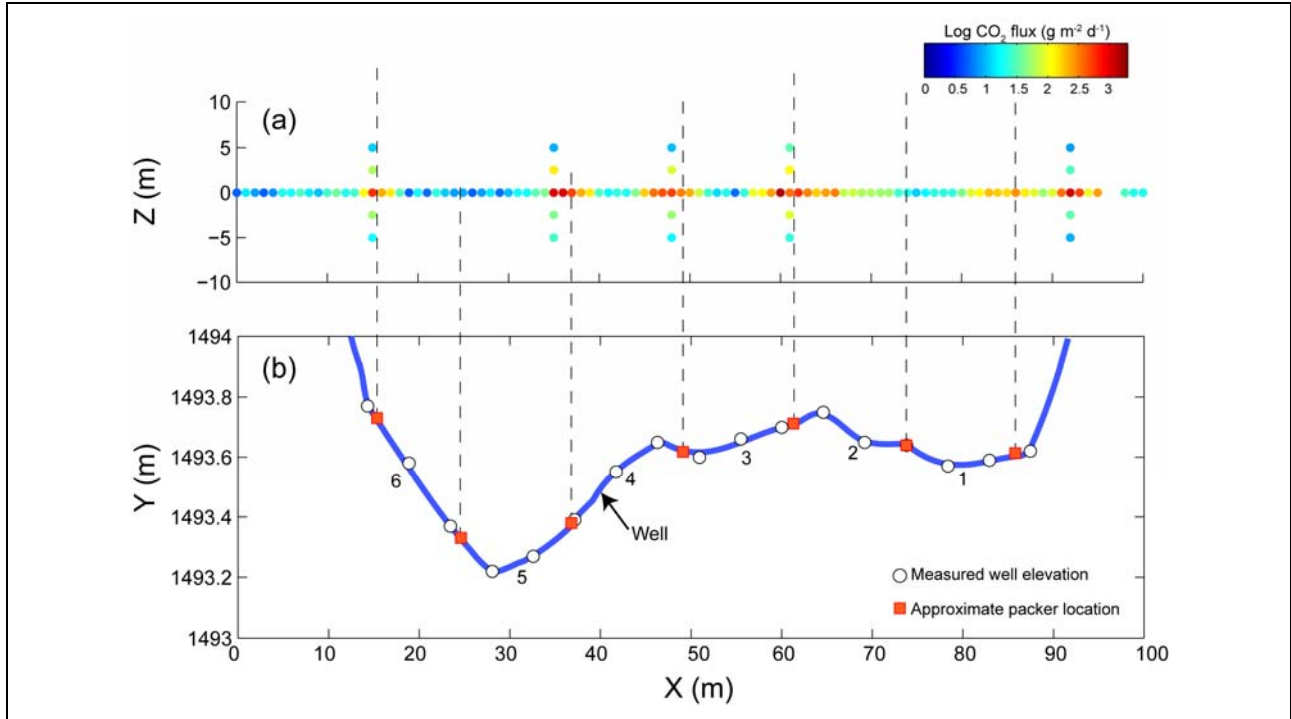


Figure 1. (a) Log soil CO₂ fluxes measured along surface trace of well on Day 9 of the first CO₂ release carried out in 2007 (see Lewicki et al., 2007). (b) Elevation of nominally horizontal well (note vertical exaggeration) and packer locations. Focused areas of high CO₂ flux (patches) are generally correlated with packer locations.

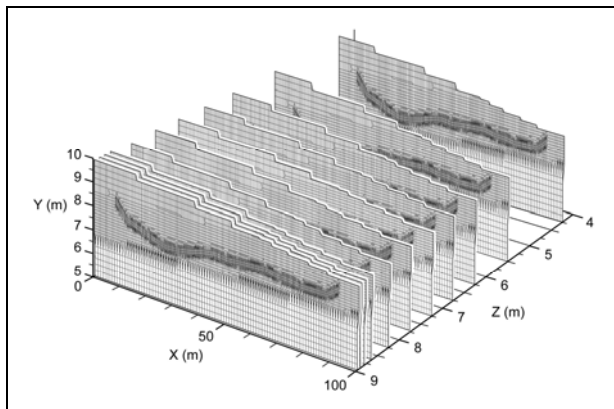


Figure 2. Three-dimensional grid showing the plane at $Z = 8.975$ m (mirror plane) that contains the pipe and the ten planes to the right-hand side (northwest). Horizontal Z -direction connections between planes are not shown.

Boundary conditions are no-flow at the bottom and atmospheric conditions at the top represented by elevation-dependent pressure that is constant with time. The mass fraction in the aqueous phase at the top boundary is set equal to 5.76×10^{-4} which corresponds to a gas-phase concentration of 380 ppmv and is also the initial condition throughout the system. The sides ($X = 0.0$ and $X = 96.5$ m) are closed

(no-flow boundary condition), while conditions at the rear XY plane ($Z = 4.5$ m) are constant with time and equal to the initial condition. The front XY plane ($Z = 8.975$ m) is a no-flow boundary and serves as the mirror plane of the symmetric model system. All simulations assume fresh water (salinity equal to zero) and are isothermal at 15°C.

The properties we use for the two layers (soil and cobble) and the pipe are given in Table 1. Rainfall infiltration was set to zero as the CO₂ releases from the horizontal well were carried out in summer months, during which there is little precipitation. The pipe was approximated as a high-porosity and high-permeability porous medium with low capillarity. This assumption clearly does not allow a rigorous modeling of intrawell flow processes, but will capture the key effect of faster flow and transport of CO₂ within the well and stronger capillary suction of the formation than of the pipe in unsaturated conditions.

The total injection rate of CO₂ into the pipe is 100 kg/d distributed evenly into each packed-off section and divided by two to honor the mirror symmetry of the system. Note that not all zones are the same length, and therefore this injection specification differs slightly from that in the field experiment, which injected the same amount of CO₂ per unit length.

Table 1. Properties of Materials in the Near-Surface Model

	Soil	Cobble	Pipe
Temperature (T)	15 °C	15 °C	15 °C
Porosity (ϕ)	0.35	0.35	0.99
Permeability (k)	$5 \times 10^{-11} \text{ m}^2$	$3.2 \times 10^{-12} \text{ m}^2$	$1 \times 10^{-10} \text{ m}^2$
Capillary Pressure (P_c)	van Genuchten ^{1,2} $\lambda = 0.291, S_{lr} = 0.15, \alpha = 2.04 \times 10^{-4} \text{ Pa}^{-1}, P_{max} = 5 \times 10^5 \text{ Pa}, S_{ls} = 1.$	van Genuchten ^{1,2} $\lambda = 0.627, S_{lr} = 0.10, \alpha = 1.48 \times 10^{-3} \text{ Pa}^{-1}, P_{max} = 5 \times 10^5 \text{ Pa}, S_{ls} = 1.$	No capillary pressure
Relative permeability (k_r)	Liquid: van Genuchten (1980); Gas: Corey (1954) $S_{lr} = 0.17, S_{gr} = 0.05$	Liquid: van Genuchten (1980); Gas: Corey (1954) $S_{lr} = 0.12, S_{gr} = 0.05$	Linear with saturation ¹ $S_{lr} = 0.1, S_{gr} = 0.05$
Molec. diffusivity coefficients (d_{ij}^k)	Liquid: $10^{-10} \text{ m}^2 \text{ s}^{-1}$ Gas: $10^{-5} \text{ m}^2 \text{ s}^{-1}$ $\theta = 1.0, P_0 = 10^5 \text{ Pa}$	Liquid: $10^{-10} \text{ m}^2 \text{ s}^{-1}$ Gas: $10^{-5} \text{ m}^2 \text{ s}^{-1}$ $\theta = 1.0, P_0 = 10^5 \text{ Pa}$	Liquid: $10^{-10} \text{ m}^2 \text{ s}^{-1}$ Gas: $10^{-5} \text{ m}^2 \text{ s}^{-1}$ $\theta = 1.0, P_0 = 10^5 \text{ Pa}$
Tortuosity (τ_D)	1.0	1.0	1.0
Saturation-dependent tortuosity (τ_p)	Equal to relative permeability	Equal to relative permeability	Equal to relative permeability

¹Pruess et al. (1999)

² λ is m in van Genuchten, 1980.

The base-case three-dimensional result is shown in Figure 3. As shown, the model qualitatively produces patchy emissions, although no effort was made to match the emission patterns in number or location exactly between model and field observation. Instead, we carried out numerous simulations using a two-dimensional slice of the three-dimensional model and changed the number of packers to investigate the dependence of patchy emission patterns on number of packers.

As shown in Figure 4, the number of upward-flowing CO₂ plumes increases with the number of packers, and the locations of the most advanced tip of the plumes correlates with packer location. The main conclusion from this study is that patchy emission patterns originate from packers located in up-sloping regions of the pipe. Further, the point-source nature of the resulting CO₂ injection is preserved at the ground surface. As time goes on, these individual plumes merge in the model, whereas in the field the patches are long-lived. While these modeling results seem to confirm the hypothesis being tested, it must be kept in mind that other features of the subsurface not modeled here could be influencing the patchy emission pattern observed in the field experiment.

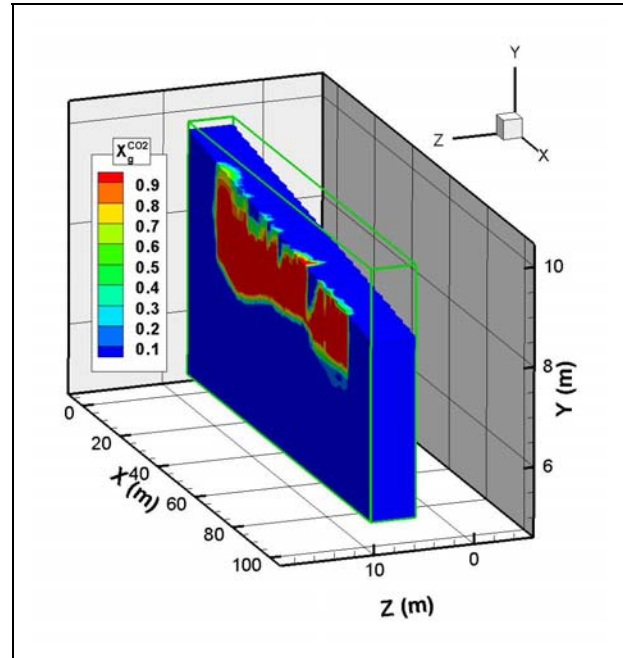


Figure 3. Three-dimensional result of the Base Case showing mass fraction of CO₂ in the gas phase ($X_g^{CO_2}$) in a patchy emission pattern at $t = 3$ days.

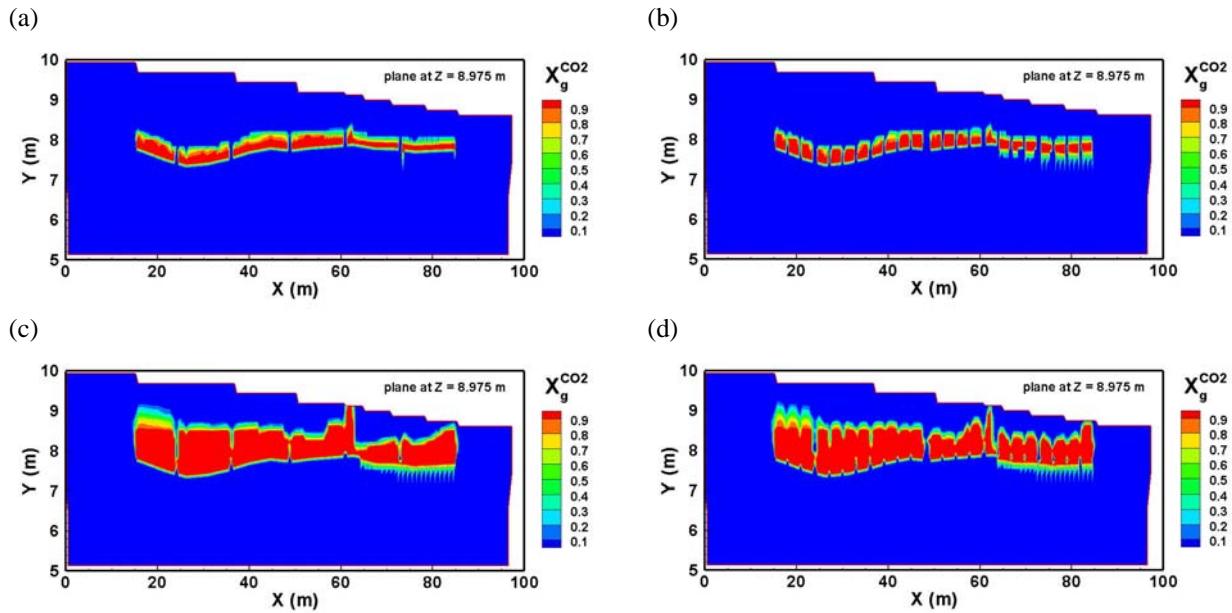


Figure 4. Mass fraction of CO₂ in the gas phase at $t = 0.06$ and 0.5 days for the case of injection into six zones (left-hand side (a, c)) and 23 zones (right-hand side (b, d)).

EFFECT OF RESIDUAL GAS ON INJECTION

The CO2CRC Otway Project is injecting CO₂ into the water leg of the natural-gas-depleted Waarre-C formation. Wellbore logging has indicated that the Waare-C is at or close to saturated with residual gas. In this preliminary study, we used EOS7C to investigate the effect of the presence of residual gas on injection in a simplified geometry. Residual gas may affect an injection process in many different ways, e.g., inhibiting the displacement of brine through relative permeability effects, enhancing injection of gas as residual gas becomes mobile at the leading edge of the injected gas plume, or changing the composition of the gas as injected gas mixes with residual gas of different composition. The purpose of

This preliminary study was to investigate the processes of interaction between injected supercritical CO₂ and residual gas to understand potential implications for the Waarre-C injection. A simplified one-dimensional radial geometry is used to focus on the mobility and gas composition effects.

Three different situations are shown in Figure 5 to illustrate the question being addressed. The base case is the injection of CO₂ with no residual gas (Figure 5a), while the two other cases explore the effect of mixing of injected supercritical CO₂ with (Figure 5b) residual CO₂, and with residual CH₄ (Figure 5c). The question being addressed is, what is the effect of residual gas on the injection of supercritical CO₂?

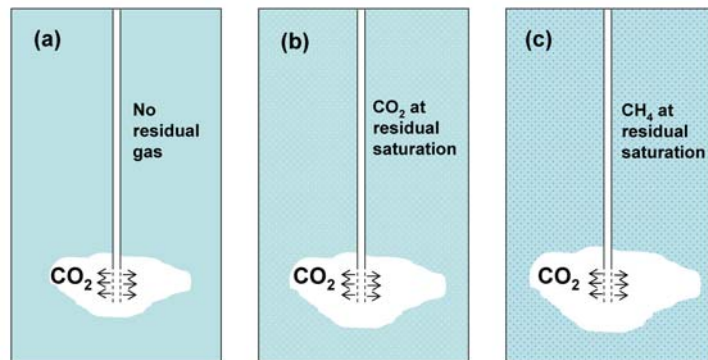


Figure 5. Three alternative cases for injection of CO₂. (a) zero residual gas. (b) 20% residual gas consisting of CO₂ represented (white stipple). (c) 20% residual gas consisting of CH₄ (blue stipple).

Simulations were carried out using EOS7C to accurately model CO_2 and CH_4 gas-mixture properties. The injection rate is 100 t CO_2/day into a layer with permeability of 500 mD ($5 \times 10^{-13} \text{ m}^2$), porosity equal to 0.16, isothermal conditions of 90°C , zero salinity, and layer thickness 30 m. The residual gas saturation is set to 0.01 for the base case and 0.21 for the CO_2 and CH_4 residual gas cases. Hysteretic relative permeability is not used for this case of constant injection.

Pressure (P), liquid saturation (S_l), mass fraction of CO_2 in the gas ($X_g^{\text{CO}_2}$), gas density, and mass fraction of CH_4 in the gas ($X_g^{\text{CH}_4}$) for the three cases considered are shown in Figures 6–8. Kinks in the curves arise from the relatively coarse resolution of the mesh for $R > 100$ m. The first-order observation from Figures 6–8 is that the pressure increase at the well is larger for the cases with residual gas (Figures 7 and 8) than for the case of zero residual gas (Figure 6). This occurs because of the decreased mobility of brine in the cases where residual gas is present. By this mechanism, rather than enhancing injectivity as might be expected, residual gas inhibits injectivity by limiting the mobility of the brine that must be displaced in order for injection to occur.

The second observation is that the plume radius as defined by the region in which gas is mobile is larger in Figures 7 and 8. Apparently, the reduced volume of pore space occupied by mobile brine when there is residual gas present makes the injected plume extend farther. The injected gas is then augmented by the initial residual gas and incorporated into the plume.

A third-order effect is shown by the gas density curves of Figures 7 and 8, which show the large effect that CH_4 has in decreasing the density of supercritical CO_2 . Note the small amount of CH_4 present in the result of Figure 7 does not affect the main conclusions. In short, as supercritical CO_2 mixes with residual CH_4 , the total volume of gas increases. This effect is expected to be less important at Otway, because the injected gas is already 20% CH_4 and does not attain the high density at supercritical conditions that pure CO_2 attains. In summary, this preliminary set of simulations suggests that rather than enhancing injectivity by providing existing gas saturation for improved gas mobility, the presence of residual gas reduces injectivity by reducing the mobility of brine.

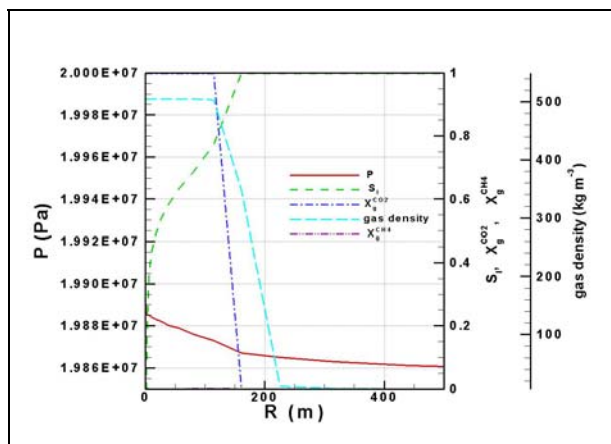


Figure 6. Results after two years of injection of CO_2 for the case of zero residual gas.

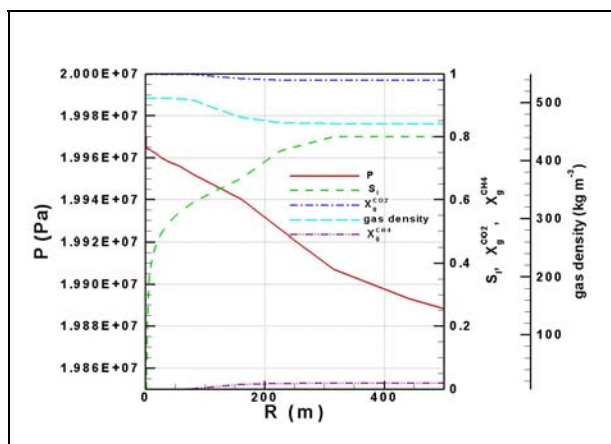


Figure 7. Results after two years of injection of CO_2 for the case 20% residual gas consisting of pure CO_2 .

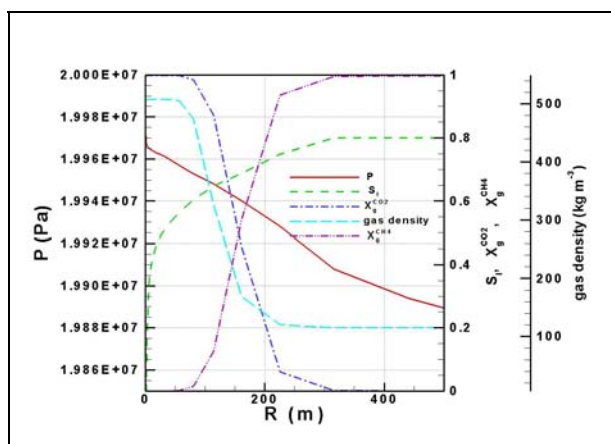


Figure 8. Results after two years of injection of CO_2 for the case 20% residual gas consisting of pure CH_4 .

CONCLUSIONS

We have used the closely related TOUGH2/EOS7CA and EOS7C models to address questions relevant to two different field tests related to geologic carbon sequestration. In the first study, simulations of multiple packer scenarios suggest that packers control the location of the leading upward-flowing CO₂ gas plumes at the ZERT shallow-release experiment. The model results show merging of plumes with time, while in the field experiment the patchy emission is long-lived. This discrepancy suggests other features (e.g., macropores, or cracks in the soil) are present at the ZERT site that are not included in the model. In the second study, applications of EOS7C to the question of the effects of residual gas saturation for injections into depleted gas reservoirs suggest that residual gas reduces injectivity by reducing the mobility of the brine that has to be displaced. With this understanding, the composition of the residual gas and its possible impact on reducing CO₂ density is likely a second-order effect.

ACKNOWLEDGMENT

We thank Chris Doughty (LBNL) for comments on an earlier draft. This work was carried out with funding from the ZERT and GEO-SEQ projects funded by the Assistant Secretary for Fossil Energy, Office of Sequestration, Hydrogen, and Clean Coal Fuels, through the National Energy Technology Laboratory, U.S. Department of Energy under Contract No. DE-AC02-05CH11231.

REFERENCES

- Corey, A.T., The interrelation between gas and oil relative permeabilities, *Producers Monthly*, 38-41, November 1954.
- Lewicki, J.L., G.E. Hilley, and C.M. Oldenburg, An improved strategy to detect CO₂ leakage for verification of geologic carbon sequestration, *Geophys. Res. Letts.*, 32, L19403, *LBNL-57414*, 2005.
- Oldenburg, C.M., G.J. Moridis, N. Spycher, and K. Pruess, EOS7C Version 1.0: TOUGH2 Module for Carbon Dioxide or Nitrogen in Natural Gas (Methane) Reservoirs, Lawrence Berkeley National Laboratory Report *LBNL-56589*, March 2004.
- Oldenburg, C.M., J.L. Lewicki, L. Dobeck, and L. Spangler, Modeling Gas Transport in the Shallow Subsurface During the ZERT CO₂ Release Test, *Transport in Porous Media*, LBNL-1529E, available online, DOI 10.1007/s11242-009-9361-x, 2009 in press.
- Pan, L., User information for WinGridder Version 3.0, (May 30, 2008). Lawrence Berkeley National Laboratory. Report *LBNL-273E*, 2008.
<http://repositories.cdlib.org/lbnl/LBNL-273E>
- Pruess, K., C. Oldenburg, and G. Moridis, *TOUGH2 User's Guide, Version 2.0*, Report *LBNL-43134*, Lawrence Berkeley National Laboratory, Berkeley, Calif., 1999.
- Reagan, M.T. and C.M. Oldenburg, WebGasEOS v1.0 User Guide, Lawrence Berkeley National Laboratory Report *LBNL-3188*, June 2006.
- Sharma, S., Cook, P., Berly, T. and Anderson, C., Australia's first geosequestration demonstration project - the CO₂CRC Otway Basin Pilot Project. *The APPEA Journal*, 47(1), 257-68, 2007.
- van Genuchten, M.Th, A closed-form equation for predicting the hydraulic conductivity of unsaturated soils, *Soil Sci. Soc.*, 44, 892-898, 1980.

STORAGE OF CO₂ IN DEEP SALINE AQUIFERS VIA INJECTION IN HORIZONTAL WELLS

Roland T. Okwen, Mark Stewart, and Jeffrey A. Cunningham

University of South Florida
4202 E. Fowler Avenue
Tampa, Florida, 33620, USA
e-mail: rokwen@mail.usf.edu

ABSTRACT

Effects of well orientation and length on the storage of CO₂ in deep saline aquifers were evaluated and quantified by conducting numerical simulations with TOUGH2. Simulations of CO₂ injection into confined, homogeneous, isotropic, saline aquifers were conducted for both vertical and horizontal wells. The metrics used in quantifying the performances of different strategies included changes in pressure near the well, mass of CO₂ dissolved into brine, fraction of injected CO₂ dissolved into brine, and storage efficiency, all evaluated over a simulated injection period of 50 years. These metrics were quantified as functions of well length and CO₂ injection rate. When equal injection rates and well lengths were compared, there was not a significant difference between the performances of horizontal wells and vertical wells. However, the length of a horizontal well may exceed the length of a vertical well, because the length of the horizontal well is not constrained to the vertical thickness of the geologic formation. As the length of the horizontal well was allowed to increase, the geologic formation could receive a significantly higher injection rate of CO₂ without exceeding a maximum allowable pressure. This results in a higher CO₂ storage efficiency in the formation, because storage efficiency increases with injection rate. These results suggest that horizontal wells could be utilized to improve CO₂ storage capacity in confined aquifers, especially under pressure-limited conditions.

INTRODUCTION

Subsurface injection of CO₂ from large point sources has been recommended as a potential strategy for isolating significant quantities of CO₂ from the atmosphere (Pruess et al., 2001; Bruant et al., 2002; Ennis-King and Paterson, 2002; IEA, 2004; IPCC, 2005). Potential deep geologic formation types for CO₂ sequestration include abandoned oil and gas fields, unminable coalbed seams, and saline aquifers (Bruant et al., 2002; Pruess and Spycher, 2005; IPCC, 2005; Kovscek and Cakici, 2005; Kristian et al., 2005). The latter formation type (saline aquifers) is reported to have the largest storage capacity, owing to its worldwide availability and lack of competitive uses (Law and Bachu, 1996; Holloway, 2001; Pruess

and Garcia, 2002; Bachu and Adams, 2003; Obi and Blunt, 2006).

Previous work on numerical simulation of CO₂ injection into confined saline aquifers via fully perforated vertical wells showed the CO₂-rich ("gas") phase to migrate radially from the injection well. The gas phase was also reported to overlie resident brine and rise until it reaches the upper confining layer of formation, resulting from differences in density and viscosity between CO₂ and brine (van der Meer, 1993; Law and Bachu, 1996; Nordbotten et al., 2005). The tendency of CO₂ to simultaneously migrate laterally at a faster rate than brine while rising to the upper section of a formation has a negative effect on the quantity of CO₂ stored per unit volume of aquifer (storage efficiency). As a result, the injection strategy adopted in a CO₂ storage project must take into consideration differences in the physical properties of CO₂ and resident formation fluid(s) in order to enhance storage.

The injection strategies considered in this study were based on well orientation and well length. The orientation of an injection well can be horizontal, vertical, or slanted. The completed length of vertical wells is limited to the aquifer's thickness, while those of horizontal wells can be as long as current technology permits. Horizontal wells can now be drilled to lengths up to 9–11 km (Donnelly, 2008). Research in the oil and gas industry has shown that a vertical well drains a cylindrical volume of formation, while a horizontal well drains an ellipsoid volume of formation (Joshi, 1991). As a result, the latter generally produces larger volumes of natural gas and/or crude oil than the former. Preliminary numerical simulations of CO₂ injection via vertical and horizontal wells suggest the latter to be more efficient than the former, based on injectivity and storage potential (Ozah et al., 2005; Jikich et al., 2003). However, the conditions under which these predictions are valid are unknown.

This study evaluates and quantifies the effects of well orientation and length on CO₂ storage potential of saline aquifers under isotropic conditions. It also addresses conditions under which horizontal injection wells may be technologically more viable than their

vertical counterparts for CO₂ storage. Findings were achieved by conducting a series of numerical simulations of CO₂ injection via vertical and horizontal wells to quantify the effects of well orientation and length on CO₂ storage. The metrics used to quantify performances of the different injection strategies include the maximum pressure near the injection well (P_w), total mass of CO₂ dissolved ($M_{CO_2, aq}$), fraction of injected CO₂ dissolved into brine (f_c), and storage efficiency (ϵ_s). Comparison of the results based on the metrics predict that CO₂ injection via horizontal wells of length greater than the vertical thickness of an aquifer is a more efficient injection strategy than utilizing fully perforated vertical wells.

APPROACH

A series of numerical simulations of CO₂ injection into a homogeneous, isotropic confined saline aquifer, using the TOUGH2 numerical software, was conducted by varying well orientation and well length (L_w) while keeping other parameters constant, in order to quantify the effects of the latter on CO₂ storage. Additional TOUGH2 numerical simulations were also conducted to study the effects of CO₂ injection rate (Q) on the storage performance. The input parameters applied in all the simulations are presented in Table 1.

Table 1. Hydrogeologic and numerical parameters applied in all simulations

Parameter	Value
Dimension ($L:W:H$), m	$10^5 : 10^5 : 100$
Gridblocks ($X:Y:Z$)	$65 : 65 : 10$
Aquifer depth, m	1200–1300
Initial pressure (P_{init}), bar	120–131
Temperature, °C	45
Average porosity (ϕ)	0.12
Average permeability (k), m ²	1.0×10^{-13}
Rock compressibility (c), Pa ⁻¹	4.5×10^{-10}
Residual brine saturation (S_{br})	0.3
Residual gas saturation (S_{gr})	0.05

In all simulations, the relationships developed by van Genuchten (1980) were used to describe the fluid relative permeabilities and brine capillary pressure (P_{cap}) as functions of the liquid phase saturation. An S_{br} value of 0.0 was used in the relationship between P_{cap} and brine saturation in order for the former to be finite at all saturations (Pruess, 1997).

The completed portions of vertical wells extended across the vertical thickness of the aquifer, while those of horizontal wells were varied between 100 m and 3000 m. The simulations were conducted using a

3D grid of dimension 100 km by 100 km by 100 m, with the injection wells positioned at the center (vertical well) or at the bottom of the central portion of the formation along the x-axis (horizontal wells). Horizontal wells were positioned at the bottom of the aquifer to maximize the contact between CO₂ and the aquifer, since the former will rise due to buoyancy. The mesh grid was refined close to the injection well and at the upper portion of the formation, in order to closely study fluid flow dynamics in these regions. Grid refinement was concentrated around the central portion of the mesh, extending 10 to 20 km from its center. This was predetermined by conducting trial simulations to ensure that the CO₂ plume extent in all simulations was within the above-mentioned range. Constant pressures were imposed at the boundaries of the formation by setting very large volume factors ($> 1 \times 10^{30}$ m³) to gridblocks at the boundaries. As a result, any flow into the gridblocks at the boundaries will have negligible impact on their pressures. CO₂ was continuously injected for 50 years in all simulations. Results obtained from the numerical simulations were compared and analyzed based on the metrics listed previously.

Values of near-wellbore pressures (P_w) and total mass of dissolved CO₂ ($M_{CO_2, aq}$) were obtained directly from the simulation results. The fraction of injected CO₂ dissolved into brine (f_c) was calculated by dividing $M_{CO_2, aq}$ by the total mass of CO₂ injected, which is a product of the mass injection rate (Q) and time of continuous injection (t). The CO₂ storage efficiencies (ϵ_s) of the simulations were estimated from their gas saturation (S_g) distributions within the confined aquifer. ϵ_s is calculated as the ratio between volume of CO₂ injected (V_{inj}) and the utilized porous volume of aquifer (V_{max}). V_{inj} is calculated as the product of Q and injection time (t) divided by the average density of CO₂ ($\rho_{c, av}$). We estimated V_{max} based on a plan view of the CO₂ plume shape. Depending on the well orientation and injection time, the plume extent in the X and Y directions may be similar or different. When the plume extent in the X and Y directions are equal, the plume occupies a cylindrical volume of the aquifer. Otherwise, the plume occupies an ellipsoidal volume of the aquifer when the plume extents in the X and Y directions are different. The former is generally encountered in vertical wells and the latter in horizontal wells (Joshi, 1991). The mathematical expressions for calculating cylindrical ($V_{max, c}$) and ellipsoidal ($V_{max, e}$) plume volumes are as follows:

$$V_{max, c} = \phi \pi (r_{max})^2 B \quad (1)$$

$$V_{max, e} = \phi \pi a b B \quad (2)$$

where ϕ is the average porosity of the formation, r_{max} is the radius (maximum radial extent) of the cylindrical gas plume, a and b are the equatorial radii of the ellipsoid-shaped gas plume along the X - and Y -axes, respectively.

RESULTS AND DISCUSSION

Analysis of the metrics

Results show saturations of CO₂-rich (“gas”) phase (S_g) to be maximum near injection wells and vanish far from the wells. The diameter of the gas plume in all simulations was less than 20 km, indicating that the plume did not migrate beyond the region of high-resolution grid. Detailed analysis of these results is discussed subsequently.

Results from the simulations conducted herein predict pressures to be highest at the injection well and lowest at the boundaries of the aquifers. Results from the simulations also predict increases in pressure as CO₂ mass injection rate (Q) is increased. This phenomenon was most pronounced near the injection wells.

For a fixed well length, the total mass of CO₂ dissolved in brine ($M_{CO_2,aq}$) increased with CO₂ mass injection rate (Q). This is because of a corresponding increase in formation pressure as more CO₂ is injected per unit length of well. Results reported in previous studies on CO₂ solubility in water also indicate that the amount of dissolved CO₂ in solution increases with pressure (Kohl and Nielsen, 1997; Spycher et al., 2003; Spycher and Pruess, 2005). However, the fraction of the injected CO₂ that dissolves (f_c) slightly decreased as Q is increased.

The CO₂ storage efficiencies (ϵ_s) estimated from the S_g profiles of the simulations indicate that ϵ_s also increases with Q for fixed well length. Similar observations have been reported in the technical literature in which increases in ϵ_s with Q were also achieved (van der Meer, 1995). As Q decreases, gravity becomes relatively more dominant. This causes the gas plume (CO₂) to occupy a thin but broad region at the top of the formation, leading to a decrease in ϵ_s .

Sensitivity analyses

The effects of injection-well orientation were determined by comparing the performances of CO₂ injection simulations using a vertical well and a horizontal well of equal length at a constant mass injection rate (Q). Results in Table 2 indicate that no significant difference in the performances of both simulations was achieved. Therefore, it can be concluded that CO₂ injection via a vertical well or a horizontal well of equal length have similar performances. Results in

Table 2 also support the arguments made in the previous subsection that $M_{CO_2,aq}$ and ϵ_s increase with CO₂ mass injection rate (Q) for a fixed well length.

When the length of the horizontal well (L_w) was systematically increased from 100 m to 3,000 m while keeping Q constant, P_w decreased. It can be deduced that P_w decreases with increasing well length due to reduction in the mass of CO₂ injected per unit well length. The average density of the gas phase also decreased as a result. These results indicate that additional quantities of CO₂ can be injected into the aquifer without exceeding a limiting pressure as L_w is increased.

Table 2. Comparison of performances from simulations using vertical wells and horizontal wells with equal length (100 m) for 50 years injection

Metrics	Well orientation			
Q (kg/s)		50	100	200
P_w (bar)	vertical	163	195	248
	horizontal	164	196	247
$M_{CO_2,aq}$ (Mtons)	vertical	6.1	11.5	22.1
	horizontal	6.1	11.5	21.4
f_c	vertical	0.077	0.073	0.070
	horizontal	0.077	0.073	0.068
ϵ_s (%)	vertical	10.5	12.0	13.7
	horizontal	10.5	12.0	13.5

However, in order to avoid risk of possible CO₂ leakage, P_w must not surpass the fracturing pressure of the aquifer. Therefore, evaluating the performances of the simulations under pressure-limiting conditions is warranted. The performances of simulations using vertical injection wells and horizontal injection wells were evaluated and compared by estimating a maximum CO₂ injection rate (Q_{max}) at specified maximum pressure increases (ΔP) for different well lengths. Correlation between ΔP and Q_{max} was achieved by fitting P_w data points as functions of Q , with a straight line passing through the origin. The correlations were made at 50 years of CO₂ injection, which roughly corresponds to the average lifespan of heavy-duty industrial facilities that emit large quantities of CO₂. The resulting linear equations depicting the relationship between P_w and Q are as follows:

$$\Delta P = 0.59 Q \quad L_w = 100 \text{ m (vertical)} \quad (3)$$

$$\Delta P = 0.59 Q \quad L_w = 100 \text{ m} \quad (4)$$

$$\Delta P = 0.50 Q \quad L_w = 1000 \text{ m} \quad (5)$$

$$\Delta P = 0.48 Q \quad L_w = 2000 \text{ m} \quad (6)$$

$$\Delta P = 0.46 Q \quad L_w = 3000 \text{ m} \quad (7)$$

where $\Delta P = P_w - P_{init}$ and P_{init} is the initial pressure.

In these equations, ΔP and Q are in bar and kg/s, respectively. These correlations were determined by using TOUGH2 simulation results to determine maximum values of P_w at different values of Q . Results showed excellent agreement between pressures estimated using the above equations and those predicted by TOUGH2, with relative errors of less than 2%.

At a given maximum allowable pressure (ΔP_{max}), the required CO₂ mass injection rate (Q_{max}) using vertical or horizontal injection wells can be estimated using Equations (3)–(7) based on the well orientation or length. Table 3 presents results of Q_{max} , $M_{CO_2, aq}$, f_c , and ε_s at different well lengths for a value of ΔP_{max} equal to 100 bar. It can be deduced from Table 3 that at any specified ΔP_{max} , the maximum allowable CO₂ mass injection rate (Q_{max}) increases with well length and consequently the storage efficiencies (ε_s) also increase. $M_{CO_2, aq}$ also increased as Q was increased, because horizontal wells are reported to sweep a greater cross-sectional area of a formation than vertical wells (Joshi, 1991). This also indicates that horizontal wells have better vertical sweep than vertical wells, thereby enhancing mixing between CO₂ and brine as the former rises to the top of the aquifer (Ozah et al., 2005). Despite the increases in ε_s and $M_{CO_2, aq}$ with increasing Q , the fraction of CO₂ dissolved in brine (f_c) slightly decreased as Q is increased (Table 3). This may be because as Q increases, there is a decrease in the ratio of CO₂-brine interfacial area relative to CO₂ plume volume.

Table 3. Maximum allowable CO₂ injection rate, total mass of dissolved CO₂, fraction of dissolved CO₂, and storage efficiency at different well length (for $\Delta P = 100$ bar and after 50 years injection).

L_w (m)	Q_{max} (kg/s)	$M_{CO_2, aq}$ (Mtons)	X_C	ε_s (%)
100	170	18.4	0.0686	13.0
1000	201	21.0	0.0662	14.7
2000	211	22.0	0.0660	15.1
3000	217	22.6	0.0660	15.5

Figure 1 shows the estimated additional mass of CO₂ that can be stored using horizontal injection wells of different lengths as opposed to a vertical injection at different values of ΔP_{max} . The results in Figure 1 indicate that the additional mass of CO₂ that can be stored via horizontal injectors increases with well length and the maximum allowable pressure increase

(ΔP_{max}) within an aquifer. For example, at ΔP_{max} equal to 300 bar, an additional 228 million tons (Mtons) of CO₂ can be stored in a confined aquifer using a horizontal injector of length 30 times its thickness. This can accommodate CO₂ emissions from a 1,000 MWe (electric) coal-fired plant for over 20 years (Pruess et al., 2003). It can be concluded that significantly large quantities of CO₂ could be stored using long horizontal wells at little or no change in pressure, as reported in previous works by Jikich et al. (2003) and Ozah et al. (2005).

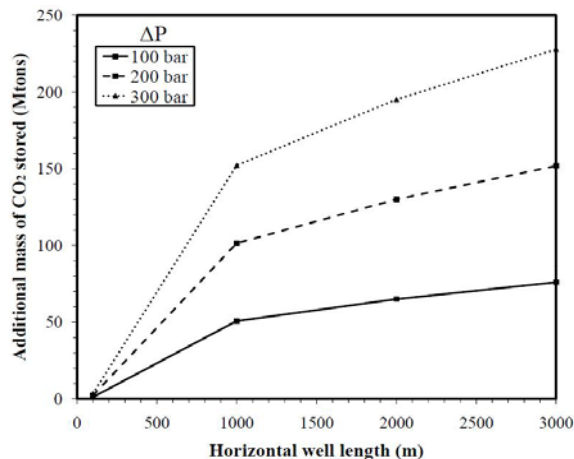


Figure 1. Additional mass of CO₂ that can be stored using horizontal injectors for 50 years

Results from simulations conducted herein indicate that a decline in pressure as a result of well length increment at constant injection rates subsequently leads to corresponding reductions in the average density and solubility of CO₂. However, the pressure decay also leads to reductions in the amount of solids (NaCl in this study) precipitated and an increase in injectivity.

Sensitivity studies on the effect of injection rate on the flow dynamics and storage of CO₂ indicate that pressure, average density, mass of CO₂ dissolved, and storage efficiency generally increase as the CO₂ mass injection rate is increased. It can be deduced from the results presented in Table 3 that the mass of CO₂ dissolved in formation brine increases with CO₂ injection rate. Results from the simulations conducted herein suggest that substantial quantities of additional CO₂ could be sequestered using horizontal wells of lengths at least ten times the aquifer's thickness.

This study addresses only the technical feasibilities of using vertical and horizontal wells for CO₂ sequestration. Economic and technical aspects related to drilling and completion of horizontal and vertical wells are beyond the scope of this study.

CONCLUSIONS

This study was conducted to evaluate and quantify the effects of well orientation and well length on the storage of CO₂ under isotropic conditions. Our findings show horizontal injection wells to be viable under certain conditions. Under isotropic conditions, CO₂ storage efficiencies in simulations using horizontal injectors are greater than those of their vertical counterparts. Horizontal wells of lengths at least ten times the aquifer's thickness could be used to significantly improve the storage capacity of an aquifer under pressure-limited conditions. These findings suggest that horizontal injection wells could be utilized to significantly improve CO₂ storage capacities in confined aquifers, under pressure-limited conditions.

The following additional conclusions were arrived at based on analyses of the results obtained from the simulations conducted in this study:

- (1) The pressure at the injection well decreases with well length, but increases with CO₂ injection rate.
- (2) Pressures at vertical injection wells are higher than those of long horizontal wells, because completion lengths of the former are limited to the aquifer's thickness.
- (3) The average CO₂ density increases with injection rate, but decreases with increasing well length. CO₂ densities in simulations using horizontal injectors are generally lower than those using vertical injectors, because pressures encountered in the former are lower than those in the latter.
- (4) The CO₂ plume in simulations using long horizontal and vertical injection wells are generally ellipsoidal and cylindrical in shape, respectively.

To enhance CO₂ storage, the injection strategy should account for the differences in physical properties of CO₂ and the resident fluid at conditions suitable for deep geologic storage. The effects of permeability anisotropy or/and aquifer heterogeneity coupled with changes in well length on CO₂ flow dynamics and storage will be addressed in future work.

ACKNOWLEDGMENT

This material is based on work supported by the Florida Energy Systems Consortium (FESC). Financial support has been awarded to Roland Okwen by the Alfred P. Sloan Foundation and by a Diverse Student Success (DSS) Fellowship at the University of South Florida (USF). Any opinions, findings, conclusions, or recommendations are those of the

authors and do not necessarily reflect the views of FESC, USF, or the Alfred P. Sloan Foundation.

REFERENCES

- Bachu, S. and Adams, J. J.: 2003, Sequestration of CO₂ in geological media in response to climate change: capacity of deep saline aquifers to sequester CO₂ in solution, *Energy Conversion and Management* 44, 3151–3175.
- Bruant, R., Guswa, A., Celia, M. and Peters, C.: 2002, Safe storage of carbon dioxide in deep saline aquifers, *Environmental Science and Technology* 36(11), 241A–245A.
- Donnelly, J.: 2008, Regional update: Europe, Exxon Neftegas, *Journal of Petroleum Technology (JPT)* 60(5), 10–12.
- Ennis-King, J. and Paterson, L.: 2002, *Engineering aspects of geological sequestration of carbon dioxide*, Vol. SPE-77809, Asia Pacific Oil and Gas Conference and Exhibition, Melbourne, Australia, SPE and CSIRO Petroleum.
- Holloway, S.: 2001, Storage of fossil fuel-derived carbon dioxide beneath the surface of the earth, *Annual Review of Energy and the Environment* 26, 145–166.
- IEA: 2004, Prospects for CO₂ capture and storage, Technical report, International Environmental Agency, Paris, France.
- IPCC, 2005: IPCC Special Report on Carbon Dioxide Capture and Storage. Prepared by Working Group III of the Intergovernmental Panel on Climate Change [Metz, B., O. Davidson, H. C. de Coninck, M. Loos, and L. A. Meyer (eds.)]. Cambridge University Press, Cambridge, United Kingdom and New York, NY, USA, 442 pp.
- Jikich, S., Sams, W., Bromhal, G., Pope, G., Gupta, N. and Smith, D.: 2003, *Carbon dioxide injectivity in brine reservoirs using horizontal wells*. Second Annual Conference on Carbon Sequestration, May 5–8, Alexandria, Virginia. <http://204.154.137.14/publications/proceedings/03/carbon-seq/PDFs/107.pdf>
- Joshi, S. D.: 1991, *Horizontal well technology*, PennWell Books, Tulsa, Colorado, USA.
- Kohl, A. and Nielsen, R.: 1997, *Gas purification*, Technical report, Gulf Publication Company, Houston, Texas.
- Kovscek, A. and Cakici, M.: 2005, Geologic storage of carbon dioxide and enhanced oil recovery: II. Co-optimization of storage and recovery, *Energy Conversion and Management* 46, 1941–1956.

- Kristian, J., Kavscek, A. and Orr, F.: 2005, Increasing CO₂ storage in oil recovery, *Energy Conversion and Management* 46, 293–311.
- Law, D. and Bachu, S.: 1996, Hydrogeological and numerical analysis of CO₂ disposal in deep aquifers in the Alberta sedimentary basin, *Energy Conversion and Management* 37(6–8), 1167–1174.
- Nordbotten, J. M., Celia, M. A. and Bachu, S.: 2005, Injection and storage of CO₂ in deep saline aquifers: Analytical solution for CO₂ plume evolution during injection, *Transport in Porous Media* 58, 339–360.
- Obi, O. and Blunt, M.: 2006, streamline-based simulation of carbon dioxide storage in a North Sea aquifer, *Water Resources Research* 42 (W03414, doi:10.1029/2004WR003347), 1–13.
- Ozah, R., Lakshminarasimhan, G., Sepehrnoori, K. and Bryant, S.: 2005, *Numerical simulation of the storage of pure CO₂ and CO₂-H₂S gas mixture in deep saline aquifers*, SPE Annual Technical Conference and Exhibition, SPE 97255, Society of Petroleum Engineers, Society of Petroleum Engineers, Dallas, Texas, USA, pp. 1–12.
- Pruess, K.: 1997, On vaporizing water flow in hot sub-vertical rock fractures, *Transport in Porous media* 28, 335–372.
- Pruess, K. and Garcia, J.: 2002, Multiphase flow dynamics during CO₂ disposal into saline aquifers, *Environmental Geology* 42, 282–295.
- Pruess, K., Oldenburg, C. and Moridis, G.: 2001, Process modeling of CO₂ injection into natural gas reservoirs for carbon sequestration and enhanced gas recovery, *Energy and Fuels* 15, 293–298.
- Pruess, K. and Spycher, N.: 2005, *ECO2N - A new TOUGH2 fluid property module for studies of CO₂ storage in saline aquifers*, Lawrence Berkeley National Laboratory, Berkeley, California. TOUGH2 symposium, May 15–17.
- Pruess, K., Xu, T., Apps, J. and Garcia, J. E.: 2003, Numerical modeling of aquifer disposal of CO₂, *Society of Petroleum Engineering Journal* 8(1), 49–60.
- Spycher, N. and Pruess, K.: 2005, CO₂-H₂O mixtures in the geological sequestration of CO₂. II. Partitioning in chloride brines at 12 to 100°C and up to 600 bar., *Geochim. Cosmochim. Acta* 69, 3309–3320.
- Spycher, N., Pruess, K. and Ennis-King, J.: 2003, CO₂-H₂O Mixtures in the Geological Sequestration of CO₂. I. Assessment and calculation of mutual solubilities from 12 to 100°C and up to 600 bar., *Geochim. Cosmochim. Acta* 67, 3015–3031.
- van der Meer, L. G. H.: 1993, The Conditions Limiting CO₂ Storage in Aquifers, *Energy Conversion and Management* 34.
- van der Meer, L. G. H.: 1995, The CO₂ storage efficiency of aquifers, *Energy Conversion and Management* 36(6–9), 513–518.
- van Genuchten, M. T.: 1980, A closed-form equation for predicting the hydraulic conductivity of unsaturated soils, *Soil Sci. Soc. Am. J.* 44, 892–898.

EFFECT OF SOIL LAYERING ON THE CROSSWIND–TOPOGRAPHY INTERACTION

Egemen Ogretim and Donald D. Gray

National Energy Technology Laboratory
Morgantown, West Virginia, USA

West Virginia University
Civil & Environmental Engineering, PO BOX 6103
Morgantown, West Virginia, USA
e-mail: egemen.ogretim@mail.wvu.edu

Grant S. Bromhal

National Energy Technology Laboratory
Morgantown, West Virginia, USA

ABSTRACT

Several factors are important in determining the near-surface behavior of a CO₂ leak from a sequestration site. The atmospheric pressure at the ground's surface is particularly important because it helps define the pressure gradients in the vadose zone that drive advective flow. Known effects of the atmosphere on the vadose zone are due to the turbulent boundary layer at the ground surface, barometric pumping, and the interaction between wind and the topography. This study will focus on the third effect, the crosswind-topography interaction, through simulations performed with TOUGH2 and its EOS7CA module. Previous studies have shown that the acceleration of a crosswind over a hill-like topography imposes a spatially-varying pressure boundary condition across the ground's surface, which generates underground gas currents. A potential leak of CO₂ that has made its way into the vadose zone is likely to get entrained in these underground gas currents and express itself at the surface accordingly. As a result, one can expect seepage anomalies due to this interaction. In the present study, we looked at the effect of soil layering in terms of directing the underground gas currents and the resultant effect on the CO₂ expression at the surface. A stacked series of layers with isotropic hydrologic properties was used. The results show that the presence of an unfractured, low-permeability layer under the high permeability soil layers near the surface inhibits the effect of wind-topography interaction on seepage. However, as fractures are introduced to the low permeability layer, the mentioned effect become quite visible through CO₂ seepage enhancement. This result suggests that the performance of the monitoring networks can be improved by placing detection devices near the peak regions of wavy topographies with fracture networks.

INTRODUCTION

Geologic sequestration of CO₂ is an essential component of the efforts to prevent the increase of anthropogenic greenhouse gasses in the atmosphere. For the success of this method, one needs to be able to predict the long term fate of the injected CO₂ whether in the reservoir or out of it in case of a potential leakage. The interaction between the monitoring-mitigation and verification efforts is thus dependent on the relevant computer simulations.

Currently, there is a great amount of simulations to see how the CO₂ plume is going to behave in the reservoir into which it is injected. Since the reservoirs are deep in the earth, these simulations mostly look at the interactions in the saturated media. However, in the case of a possible leak from these reservoirs, the CO₂ plume is likely to get into the vadose zone and possibly to the near surface. Therefore, the migration of the CO₂ plume must be investigated in the vadose zone and in the near surface where it is going to be exposed to atmospheric effects not present in the saturated zone or deep underground.

So far, researchers have listed three atmospheric effects in near-surface vadose zone. These result from the dynamic nature of the atmosphere that energizes the slow processes of the underground.

Barometric pumping is the induced flow of gas due to changes in atmospheric pressure. As atmospheric pressure rises, air flows into the ground; conversely, the soil gas returns to the atmosphere in response to a decrease in atmospheric pressure. Although components of all frequencies are present, the diurnal temperature cycle and the passage of large scale weather systems every several days are predominant. As this alternation of induced gas flow occurs, migration of a gas contained in the vadose zone is thus affected. In case of CO₂ leakage into the vadose

zone from below, barometric pumping can suppress or enhance the seepage into the atmosphere.

An atmospheric turbulent boundary layer forms due to the effect of the no-slip condition at the ground surface on the wind. This turbulent boundary layer enhances the mixing processes both above and below the ground surface.

Finally the crosswind–topography interaction, which is the topic of the present paper, refers to the induced effects when the wind blows over a hill–like surface, thus creating an extra suction effect near the peak region. This suction effect strongly depends on the wind speed as well as the permeability of the porous medium. Soils with high permeability or rock structures with fracture networks are highly prone to this effect. The wind can be strong enough to completely suppress the seepage from the skirts of the hill and direct it to the peak region. In case of very low permeability layers with fracture networks, the presence of the wind can reveal a leakage that would otherwise not be observable at the surface.

So, the seepage of a CO₂ leak into the atmosphere is thus affected due to the atmospheric dynamics. Aside from the underground effects, the atmospheric dynamics are of concern, owing to their impact on the distribution of a potential leak in the habitat of living organisms, including humans.

In the context of geologic sequestration of CO₂, the first study involving the crosswind-topography

interaction, to our knowledge, was presented at the GHGT-9 conference (Ogretim et al, 2008). Later, the authors were informed of a study on moist air seepage anomalies at Yucca Mountain (Weeks, 1987). In that study, unable to explain the observed anomalies via other mechanisms, the researchers, after considering the crosswind-topography interaction mechanism, were able to account for most of the otherwise unaccountable moist air seepage. This unrelated work provides an experimental verification to the concept of the present study.

Our previous studies on this effect were rather simplistic studies to establish a proof of concept. They involved 2D domains and a single soil type that had homogeneous and isotropic properties. In the present study, we included fractures and faults, and imposed a topsoil on the base rock. The fractures, except for those that faded away within the rock, extended to the surface or the topsoil, depending on the case. When determining the properties of these soil types (Table 1), we used as reference the values that were used for the ZERT site modeling by Oldenburg et al. (2003).

The atmospheric wind speed is set at a constant speed of 5 m/s, which represents a realistic yearly average wind speed. The hill geometry and the resulting pressure distribution at the surface (Figure 1) are obtained by using the Rankine Ovals in the potential flow theory (Munson et al., 2006). The hydrostatic pressure in this figure refers to the barometric pressure without the presence of wind. The static

Table 1. Soil properties.

Property	ROCK	TOPSOIL	FRACTURE	ATMOSPHERE
Porosity	0.15	0.35	0.225	0.99
Permeability	1 mD	100 D	100 D	100 D
Relative Permeability				
function	Van Genuchten	Van Genuchten	Van Genuchten	Van Genuchten
λ	0.4	0.6	0.46	0.99
S_{lr}	0.12	0.12	0.05	0.05
S_{ls}	1.0	1.0	1.0	1.0
S_{gr}	0.05	0.05	0.05	0.05
Capillary Pressure				
function	Van Genuchten	Van Genuchten	Van Genuchten	Van Genuchten
λ	0.4	0.6	0.46	0.99
S_{lr}	0.12	0.12	0.05	0.05
$1/P_0$ (Pa ⁻¹)	5×10^{-4}	1×10^{-3}	1×10^{-3}	1.48×10^{-3}
P_{max}	5×10^5	5×10^5	5×10^5	5×10^5
S_{ls}	1.0	1.0	1.0	1.0

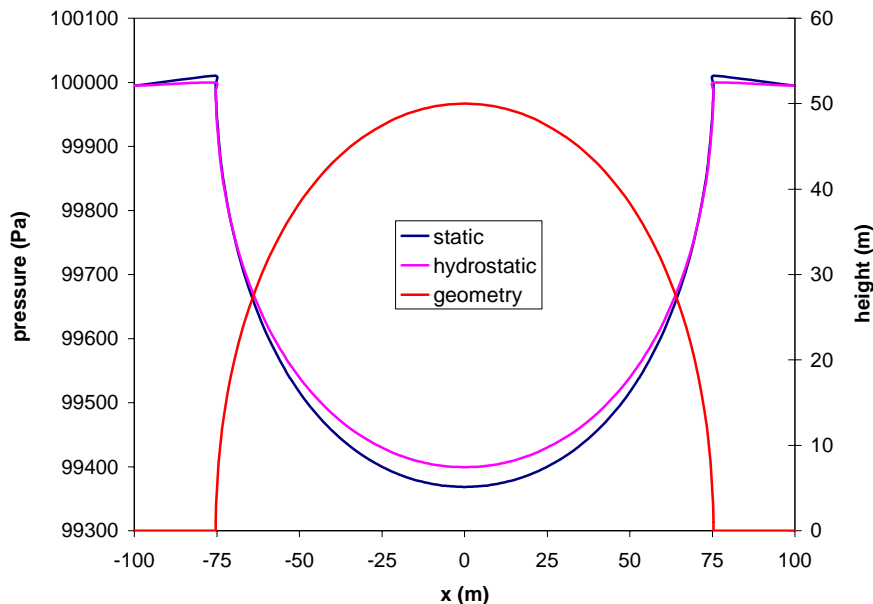


Figure 1. Depiction of domain geometry and the static pressure distribution at the surface

pressure in the same figure refers to the pressure in case of a wind with the specified magnitude. Note the increase in static pressure at the skirts of the hill due to the stagnation of the wind. Also note the slight difference between the two pressure values around the peak region. This difference results from the acceleration of the wind over the hill geometry. Its magnitude depends on the speed of the wind. Although the average wind speed in this study is relatively slow, in an actual storm, this value may temporarily increase tremendously, which will have an exponential effect on the extra suction due to the wind, and hence the enhancement of the seepage values around the peak region.

The water table was set at 10 m for all cases; the entire volume above this level formed the vadose zone. The liquid saturation distribution in the domain before CO₂ leakage is shown in Figure 2. The low capillary-retention properties of the fracture zones are seen as the penetration of low saturation zones into the high saturation zones above the water table. The cells in the rock zone exhibit a higher capillary-retention compared to the topsoil, which is seen at the interface between the two.

In presenting the results, we will show the state of the CO₂ flux at the surface after 1 year of simulated leakage into the domain. Also, the state of the CO₂ plume is provided for one case where it is needed for further insight into the processes.

METHOD

For the simulations of this study, the TOUGH2 (Pruess et al., 1999) simulator was used with its EOS7CA module which can account for air, water,

brine, CO₂, and a tracer. We prepared the 2D domain for the leakage simulation by first obtaining a stable water table at the desired depth, then by imposing the wind boundary condition on the surface and obtaining a stable gas pressure field within the domain. This second step is achieved by modifying the pressure value at each cell along the hill surface (for which we used an in-house pre-processor called 7CAINCON) and simulating the domain for 1 year with the modified boundary condition. This second step gave steady-state results before injection.

The leakage of the CO₂ into the domain was modeled by assigning source properties to a cell at the depths of a fracture. In our case, the leakage amount was 16.7 kg/day at 8 m below the water table. The leakage was also simulated for 1 year with the wind conditions at the top boundary. The source of the leakage was chosen to be at two locations, both in the fractures; but in a single simulation, a single leakage location was used. The first one of these locations was under the onset of the hill, where a fracture is formed due to high stress. The second one was more towards the center of the hill, but at the same depth. At this lateral location, the upper end of the fracture is more exposed to the low-pressure region near the peak. Thus, we are going to be able to study the consequences of leakage from different paths.

To mimic the presence of the atmosphere at the top of the domain, we used a generic soil type, which we called “atmosphere” (Table 1), that had low capillary-retention properties and high porosity and permeability. These atmosphere cells were assigned as fixed property cells, and the flow of CO₂ into them was regarded as seepage into the real atmosphere.

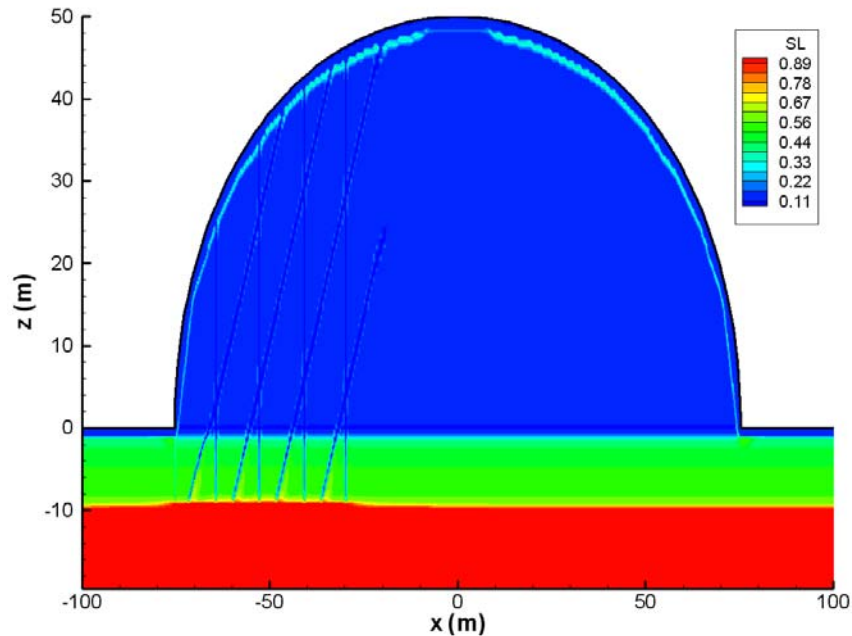


Figure 2. Liquid saturation distribution in the domain before the leakage

To model the fractures, we used weighted averages that accounted for the rock properties and the highly permeable fracture with low capillary-retention properties. This was done to avoid the overwhelming grid requirements that would have been required for a realistic representation of the fractures.

To conduct a parametric study of the effects of a topsoil layer, we used three cases. The first case is the base case, which has no topsoil in it, and the rock layer is directly connected to the atmosphere layer. The second case has a thin topsoil whose thickness varies between 1-2 m. For the third case, we used a 10 m thick topsoil between the rock layer and the atmosphere. To distinctly show the effects of the wind and the soil layering, we present these three cases with wind and without wind boundary conditions, which make a total of 12 simulations, including the leakage source location.

RESULTS

As mentioned before, the results will be presented with respect to their point of leakage and the wind boundary conditions.

Leakage under hill skirt without wind conditions

In the base case, i.e., with no topsoil between the rock and the atmosphere, the CO_2 makes its way quickly to the surface through the fractures, and exhibits itself as a strong point-leakage with very limited spatial spreading at the locations where the fractures meet the atmosphere (Figure 3). The presence of the topsoil in the thin- and thick-soil

cases not only dampens out the spiky behavior of the seepage but also allows the buoyancy to work on the CO_2 , which is heavier than air. As a result, the plume, having exited the fracture, flows downhill in the topsoil, and unifies to a single seepage feature at the base of the hill.

Leakage under hill skirt with wind conditions

The introduction of wind conditions to the previous case does not bring a significant difference at the scales shown in Figure 4. This is because the pressure differences are not strong enough to cause a significant communication between the leakage locations and the suction regions near the peak. However, when zoomed in for the thick topsoil case, one can see a point source of seepage around the peak area ($0.03 \text{ micromol/m}^2/\text{s}$) that is detectable by flux measurement devices.

Leakage towards the center without wind conditions

In the base case, the migrating CO_2 exits directly into the atmosphere, and a strong point source of seepage is observed about 30 m from the center (Figure 5). Proportional to the thickness of the topsoil in the other two cases, the plume flows downhill within the topsoil due to negative buoyancy and seeps to the atmosphere as a distributed source. However, for the thick-soil case, the soil thickness is high enough to allow an almost-complete underground flow for the CO_2 plume, such that a strong source of seepage is observed at the skirt of the hill.

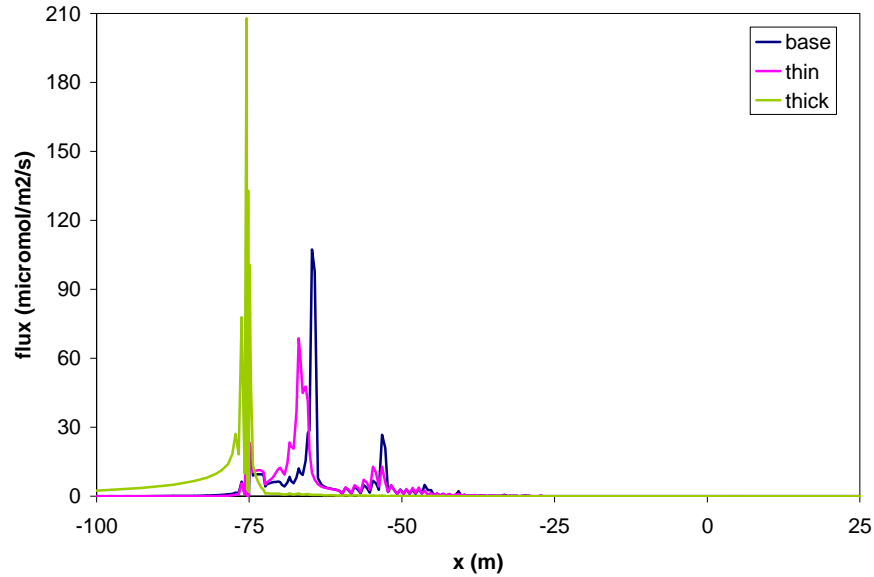


Figure 3. Seepage distribution for the leakage under the hill skirt without wind boundary condition

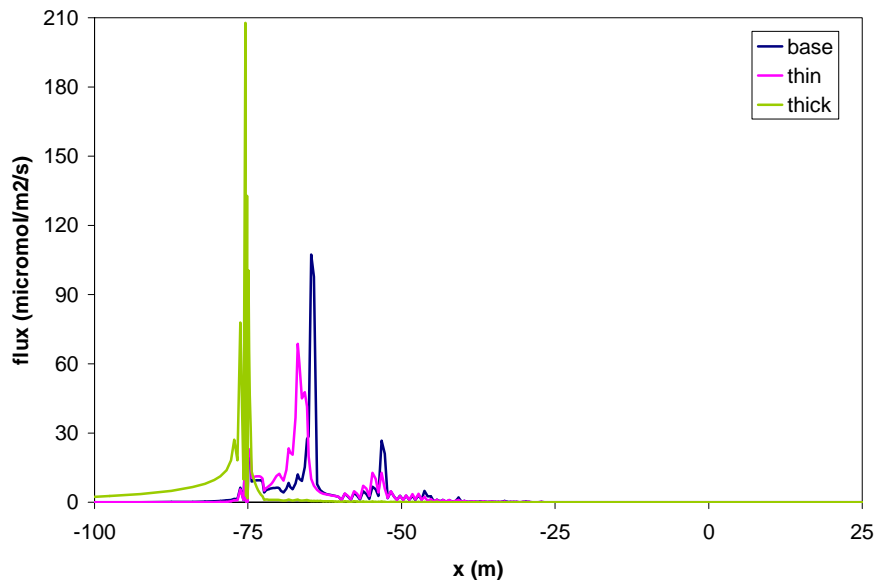


Figure 4. Seepage distribution for the leakage under the hill skirt with wind boundary condition

Leakage towards the center with wind conditions

This case is the most striking one of all, since it reveals the effect of the wind at the visible scale, except for the base case where the wind has no room to show its effect. The suction effect due to the wind directs some of the CO_2 exiting the fractures towards the peak region. In terms of the surface seepage values (Figure 6), this effect is visible in the thick-soil case and is detectable for the thin case. The state of the plume is shown in Figure 7 where a significant vent has formed under the peak region for the thick case.

CONCLUSIONS

The presence of a soil layer or a highly fractured rock layer on top of a rock structure with minor fractures has varying effects on the seepage of CO_2 into the atmosphere. A leak that follows a path around the skirts of a hill flows downhill in the soil layer due to the negative buoyancy. Thus, there is an accumulation of seepage at the onset of the hill proportional to the thickness of the soil layer. If the leak follows a path towards the center of the hill, then it is more likely to interact with the suction created by the wind

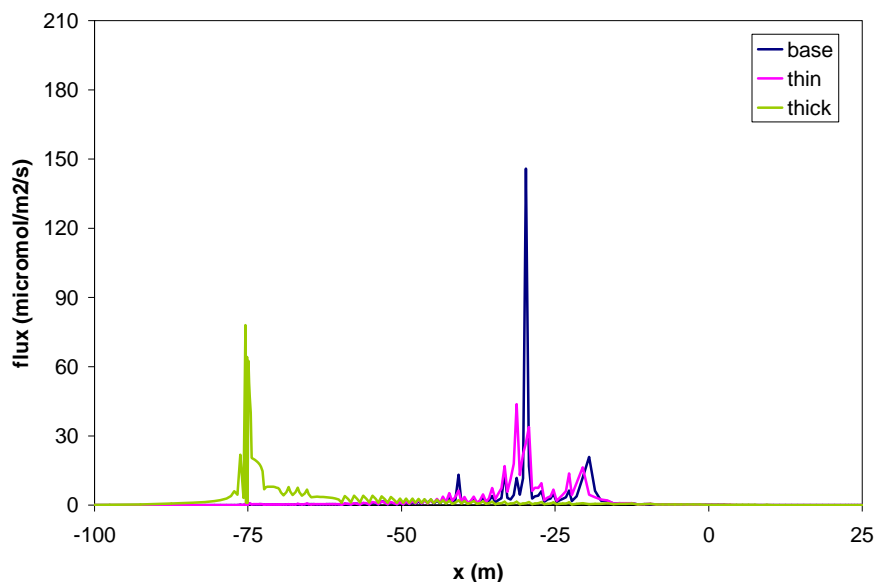


Figure 5. Seepage distribution for the leakage towards the center without wind boundary condition

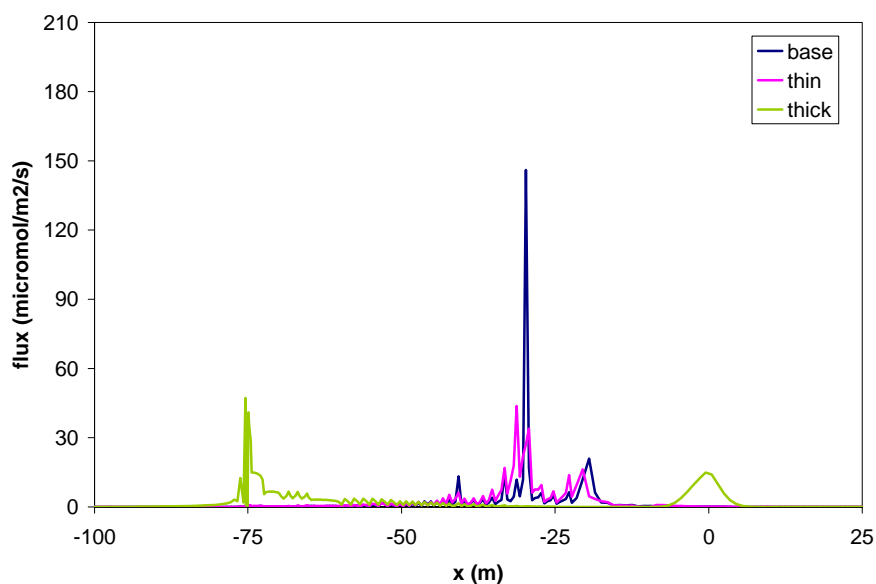


Figure 6. Seepage distribution for the leakage towards the center with wind boundary condition

flow over the hill surface. As a result, some of the plume that exits into the soil layer is directed to the peak region, where it forms a distinct, easily detectable signature at the surface. The amount of redirected gas depends on the wind speed and the soil layer thickness. For future studies, better simulation of the fractures and accounting for the variation in the wind as weekly averages could give better and further insight into the effects of wind-topography interaction on CO₂ seepage.

ACKNOWLEDGMENT

This work was performed in support of the National Energy Technology Laboratory's on-going research in carbon sequestration under the RDS contract DE-AC26-04NT41817.

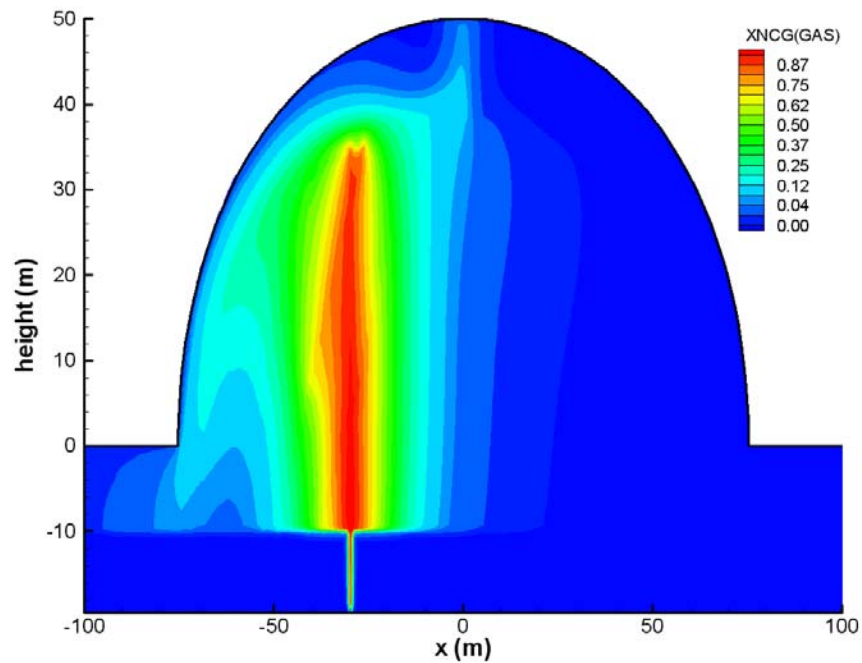


Figure 7. CO_2 mass fraction in the gas phase for the thick topsoil case with leakage towards the center and wind boundary condition

REFERENCES

- Munson, B.R., Young, D.F., and Okiishi, T.H., *Fundamentals of Fluid Mechanics*, John Wiley & Sons, Inc., USA, 2006.
- Oldenburg, C.M. and Unger, A.J.A., On Leakage and Seepage from Geologic Carbon Sequestration Sites: Unsaturated Zone Attenuation, *Vadose Zone Journal*, Vol. 2, 287-296, 2003.
- Pruess, K., C. Oldenburg, and G. Moridis, *TOUGH2 User's Guide, Version 2.0*, Report LBNL-43134, Lawrence Berkeley National Laboratory, Berkeley, Calif., 1999.
- Weeks, E.P., Effects of topography on gas flow in unsaturated fractured rock--concepts and observations, *Am. Geophys. Union Geophysical Monograph*, Vol. 42, 165-170, 1987.

BARRIER EFFECT IN A CO₂ CAPTURE AND STORAGE FEASIBILITY STUDY

¹G. Montegrossi, ²B. Cantucci, ³G. Biccocchi, ^{1,3}O. Vaselli, ²F. Quattrocchi

¹CNR – IGG, Via G. La Pira 4, 50121 Florence, Italy

²INGV, Via Vigna Murata 605, 00141 Roma, Italy

³University of Florence, Dept. Earth Sciences, Via G. La Pira 4, 50121 Florence, Italy
e-mail: montegrossi@igg.cnr.it

ABSTRACT

CO₂ Capture & Storage (CCS) in saline aquifers is one of the most promising technologies for reducing anthropogenic emission of CO₂. Feasibility studies for CO₂ geosequestration in Italy have increased in the last few years. Before planning a CCS plant, appropriate precision and accuracy in the prediction of the reservoir evolution during injection is required, in terms of both geochemical calculation and fluid flow properties. In this work, a geochemical model will be presented for an offshore well in the Tyrrhenian Sea, where the injection of 1.5 million ton/year of CO₂ is planned. The dimension of the trapping structure requires the study of an area ~100 km² and 4 km deep. Consequently, three different simulations were performed by means of the TOUGHREACT code, specifically using the Equation of State (EOS) module ECO2N.

The first simulation is of a stratigraphic column with a size of 110×110×4,000 m and 10-m resolution in the injection/cap-rock area (total of 8,470 elements) conducted to assess the geochemical evolution of the cap rock and to ensure the sealing of the system. The second simulation, at large-scale, was conducted in order to assess the CO₂ path from the injection towards the spill point (total of about 154,000 elements).

During these simulations, the effect of the full coupling of chemistry with fluid flow and the related effect in the expected CO₂ diffusion velocity were recognized. Owing to the effect of the chemical reaction and coupling terms (porosity/permeability variation with mineral dissolution/precipitation), the diffusion velocity results were 20% slower than in a pure fluid flow simulation. To give a better picture of this “barrier” effect, where the diffusion of the CO₂-rich acidic water into the carbonate reservoir initiate a complex precipitation/dissolution sequence, a small-volume simulation with a 1-m grid was conducted.

This barrier effect may potentially (i) have a significant impact on CO₂ sequestration, due to the reduction in available storage volume reached by the CO₂ plume in 20 years and/or the enhanced injection pressure; and (ii) demonstrate the relevance of a full

geochemical simulation in an accurate prediction of the reservoir properties.

DATA ACQUISITION

The petrophysical data used in the simulations of CO₂ injection described in the present work were obtained in a previous study (Montegrossi et al., 2008). A brief report of the procedure is reported here. Each formation recognized from the well-log (Table 1), was collected in-shore.

The mineralogical composition was calculated by combining calcimetric determination with a Dietrich-Fruhling apparatus for calcite and a XRD Rietveld analysis to quantify the main minerals. A correction for dolomite was applied to the calcimetry determination. A Rietveld quantification procedure was performed by using Maud v2.2. After the separation of the clay fraction (<2 μm), clay minerals were determined by XRD with the analysis of oriented-, glycol- and 450 and 600°C treated samples. The key concept of the models is that, once the mineralogy of each geological formation is defined, a relationship among thermal capacity, conductivity, porosity and permeability can be established (Montegrossi et al. 2008). The thermal properties are computed by simply using a weighted sum of the thermal properties of each mineral, using 1% porosity as an initial value from literature data (Singh et al., 2007; Clauser and Huegens, 1995). With the well located offshore, we can indeed reasonably assume that rock pores are filled with water, and they obviously have thermal properties sensibly different from those of minerals: the higher the porosity, the lower the thermal capacity and conductivity. One limitation of this model is the assumption that no turbulent heat transport is present. This is valid for permeability values up to 10⁻¹² m/s. Thus, the thermal properties are expressed as a function of porosity.

The correlation models between porosity and permeability are well known as functions of the main mineralogical composition of each stratum. On the basis of the mineralogical analysis reported in Table 2, we decided to use a clay coating for the upper formations (Zone 1–5, Table 1) and a calcite coating for the other strata (Zone 6-11, Table 1).

Table 1. Average pressure (P) and temperature (T) for each formation are reported. K_i : permeability, ϕ_i : initial porosity, ϕ_c : critical porosity

Formation	Zone	P bar	T °C	Density kg/m ³	Cond. T. W/m °C	Capac. T. J/kg 25°C	K_i m ²	ϕ_i	ϕ_c
Gray Clay	1	24	25	2400	02.08.00	1280	2.95e-17	0.14	-
Carbonatic Flysch	2	46	32	2600	2.21	940	7.65e-18	0.03	-
Sandstone	3	115	55	2500	2.55	1370	7.65e-18	0.03	-
Clay Shale	4	181	76	2600	1.70	1170	7.65e-18	0.03	-
Schist	5	189	79	2600	1.70	870	2.04e-17	0.05	-
Limestone and Jasperoids	6	193	80	2600	2.13	900	2.04e-17	0.05	0.046
Cherty Limestones	7	204	84	2600	2.13	920	2.04e-17	0.10	0.055
Marly Limestones	8	213	87	2600	2.04	940	1.02e-16	0.10	0.044
Limestones	9	232	93	2600	2.04	940	2.48e-14	0.10	0.055
Dolomite Limestones	10	280	108	2600	1.96	940	2.48e-14	0.10	0.055
Anhydrites	11	308	118	2800	4.08	1870	1.84e-16	0.06	0.043

Table 2. Mineralogical composition (volume fraction) of considered formations in the model

Zone	Calcite	Quartz	Dis. Dolom.	K-felds.	Smectite	Illite	Chlorite	Kaolinite	Muscov..	Montmor.	Anhydrid..	Dawsonite	Calcedony	Phlogopite
1	0.2559	0.0698	0.0155	0.062	0.185	0.0035	0.0606	0.025	0.0785	1e-05	-	1e-05	1e-05	1e-05
2	0.9520	0.0307	1e-05	-	-	0.0130	0.0012	1e-05	-	0.0028	-	1e-05	1e-05	1e-05
3	0.7041	0.1558	0.0176	-	-	0.0513	0.0202	1e-05	-	0.0404	-	1e-05	1e-05	1e-05
4	0.8380	0.0536	1e-05	-	-	0.0350	0.0324	1e-05	-	0.0410	-	1e-05	1e-05	1e-05
5	0.6105	0.3595	1e-05	-	-	0.0118	0.0021	1e-05	-	0.0152	-	1e-05	1e-05	1e-05
6	0.9540	0.0336	1e-05	-	-	0.0123	-	1e-05	-	1e-05	-	1e-05	1e-05	1e-05
7	0.6630	0.3140	1e-05	-	-	0.0020	0.0015	1e-05	-	0.0196	-	1e-05	1e-05	1e-05
8	0.9610	0.0367	1e-05	-	-	-	-	1e-05	-	0.0020	-	1e-05	1e-05	1e-05
9	0.9941	0.0059	1e-05	-	-	-	-	1e-05	-	1e-05	-	1e-05	1e-05	1e-05
10	0.7478	0.0060	0.2398	-	-	-	-	1e-05	-	0.0064	-	1e-05	1e-05	1e-05
11	0.0080	-	0.0020	-	-	-	-	-	-	-	0.989	1e-05	1e-05	-

A coating model assumes the presence of a small channel whose tortuosity and connectivity depend on the filling material (i.e., calcite or clay in our assumption) with a correction for the presence of quartz as vein filler material. A summary of the correlation models is reported in Table 1, using the equations of Verma and Pruess (1988) and Steefel and Lasaga (1994) for Zones 6–11 (with $n = 5$) and Zone 1–5, respectively.

Once a correlation model between porosity and permeability is established, porosity is the only

independent variable in our system. For the calculation of porosity, we used the software package SHEMAT (Kuhn and Chiang, 2003) that also allows us to compute heat flow from fluid advection. As a boundary condition, the surficial heat flow reported in Calore et al. (1988) was considered. Using a trial-and-error procedure, the best fit between our temperature profile and the well-log temperature profile was computed, thus obtaining a porosity profile. From the model, detailed temperature, porosity and permeability profiles and the thermal

properties for each rock formation were calculated (Table 1).

To construct a geochemical model, the database of Wolery (1992) was adopted. The database is corrected to take into account the pressure: the pressure of the centroid of the reservoir unit (namely Cherty Limestone Formation), which is 204 bar, was used. The pressure correction of the database was performed by means of SUPCRT92 (Johnson et al., 1992).

The pristine formation water was computed by means of PHREEQC 2.15 (Parkhurst and Appelo, 1999) using the NaCl-equivalent salinity measured in the well log, as suggested by Cantucci et al. (2009), with the pressure corrected database. The same database was also used for the TOUGHREACT (Xu and Pruess, 2001; Xu et al., 2006) model with the specific EOS for CO₂ (ECO2N EOS, Spycher and Pruess, 2005).

The geochemical model strategy proceeds through a fully kinetic approach. With the kinetic database from

Palandri and Kharaka (2004 and references therein), the acquisition of the mineral specific surface was performed with a geometric approach based on a morphology investigation carried out by means of a Scanning Electron Microscope equipped with an Energy Dispersive System (SEM-EDS). This system measures for each mineral the isodistribution of the grain size, which is then transformed into a specific reaction area (Table 3) and converted according to the geometric grain shape used in TOUGHREACT. For secondary minerals, an area corresponding to a 10⁻⁶ m radius grain size was adopted.

The relative permeability and capillary pressure equation used were from Corey (1954), with an irreducible liquid saturation assumed at 0.1. Diffusivity coefficients of water and CO₂ were computed according to Palmer (1994), Frank et al. (1996), Wang et al. (1996), Hashimoto and Suzuki (2002), and Tamini et al. (1994) from viscosity of the fluids at the reservoir temperature. The resulting diffusion coefficients are 4.04×10⁻⁹ m²/s for water and 1.59×10⁻³ m²/s for CO₂.

Table 3. Minerals reactive surface (Area) computed as geometric area from SEM-EDS morphological analysis. Bold: Reactive surface of secondary minerals with initial radius of 1×10⁻⁶ m.

Zona	1	2	3	4	5	6	7	8	9	10	11
	Area cm ² /g	Area Cm ² /g	Area cm ² /g	Area cm ² /g	Area cm ² /g	Area cm ² /g	Area cm ² /g	Area cm ² /g	Area cm ² /g	Area cm ² /g	Area cm ² /g
Calcite	5844.4	2859.2	71.480	2144.4	4108.2	3160.0	10236	4435.6	4435.6	6653.4	634.55
Dolomite	68.208	3769.23	769.2	3769.23	769.23	769.2	3769.23	769.23	769.2	9767.5	605.50
Quartz	5976.7	10544	349.61	1271.5	6845.7	751.75	680.41	336.86	336.86	618.55	-
K-feld.	6211.1	-	-	-	-	-	-	-	-	-	-
Smectite	6599.3	-	-	-	-	-	-	-	-	-	-
Illite	5759.4	6363.6	1636.4	3636.4	1621.9	7785.2	6556.7	-	-	-	-
Chlorite	5596.6	6183.7	1374.2	3553.6	1576.1	-	6371.3	-	-	-	-
Montmor.	5325.7	8706.5	1954.5	4975.1	2219.0	5325.7	8970.6	-	-	11608	-
Anhydride	-	-	-	-	-	-	-	-	-	-	933.37
Muscov.	5596.6	-	-	-	-	-	-	-	-	-	-
Kaolinite	6045.1	4085.74	085.7	4085.74	085.74	085.7	4085.74	085.74	085.7	4085.7	4085.7
Dawsonite	4351.54	351.54	351.5	4351.54	351.54	351.5	4351.54	351.54	351.5	4351.5	4351.5
Calcedony	4039.54	039.54	039.5	4039.54	039.54	039.5	4039.54	039.54	039.5	4039.5	4039.5
Phlogopite	3782.53	782.53	782.5	3782.53	782.53	782.5	3782.53	782.53	782.5	3782.5	-

MODELING STRATEGY

The data show that the reservoir, located in the Cherty Limestone Formation, has a low permeability and a medium porosity. The limiting factor of CO₂ injection in such a system is either the velocity of the displaced water or the injection overpressure needed to provide the expected injection rate; the request is an injection rate of 1.5 Mton/year for 20 years. A preliminary modeling study on the whole structure without chemistry, considering only CO₂ solubility, led to the conclusion that the injection overpressure should be 40 bars to obtain the desired injection rate. The same overpressure leads to a lower injection rate while using a fully coupled model, with a kinetic model for mineral reactions and a variable porosity-permeability model using the correlation curves reported in Table 1.

To study which processes could induce such variation, a horizontal model extending from one side of the CO₂ plume to a point of water displacement (a “spill-point”) was created, and then a column model was developed, with the results of both models used to plan an injection strategy for the entire three-dimensional structured model.

HORIZONTAL PATHWAYS

The horizontal model is composed of 99×11×11 elements, each one being a cube with 1 m long side. Reservoir conditions were considered, i.e., 200 bars of pressure and a left-side CO₂ plume with 40 bars of overpressure, located in the central element of the left-hand side of the model. On the bottom of the right side, there is a “spill point”, simulated as an extraction well for water on deliverability at 201 bars. The results are summarized in Figure 1, where the contour lines show permeability in 10⁻²⁰ m² after 2 years of simulation. On the left-hand side, near the CO₂ plume, there is a small increase in permeability (original permeability was 2,040×10⁻²⁰ m²), and on top of the model an area of slightly increased permeability is observed. This is due to the buoyancy of the CO_{2(aq)}-rich water with respect to normal water.

Then the water goes through the spill point on the right-hand bottom side of the figure; the CO_{2(aq)} rich water shows a pH of 6,6, slightly aggressive with respect to the calcite in the Cherty Limestone Formation. Thus, along the migration pattern, we observe a slight increase in permeability. The upper pattern will be filled by CO_{2(g)}. The red-colored area, mainly on the bottom of Figure 1, where permeability decreases to 2,038×10⁻²⁰ m², denotes the deposition of secondary calcite. To study this effect, we conducted a simulation of the stratigraphic column.

THE COLUMN MODEL

The column model is made of 10 m long 11×11 elements on X- and Y-axis, and 70 elements on Z-axis, whose dimensions are 10 m in Zones 5 to 8 (Table 1). The injection is performed at the center of the reservoir zone, i.e., at a depth of 1900 m and a pressure of 190 bars (hydrostatic pressure), plus 40 bars of injection overpressure. The spill point is at a depth of 2,400 m on deliverability at hydrostatic pressure. After five years of simulations, an increased permeability area around the injection point and a lowered permeability area below the injection point are highlighted. From the permeability contour, we could define a convective cell generated by the buoyancy of the CO_{2(aq)}-rich water and the more dense water generated by calcite dissolution. The nearly saturated water at acidic pH migrates downward, and when it encounters the reservoir basic water, CO_{2(aq)} is neutralized. The pH increase gives rise to a deposition of secondary calcite and, to a minor extent (0.01%), dolomite. Carbonates are in fact the only minerals in the simulation able to form deposits outside the CO₂ plume, with other secondary minerals depositing only within the plume. Nevertheless, the carbonate dissolution effect on porosity and permeability is by far the most important process, also due to their generally faster kinetics. Summarizing, around the injection point, the permeability increases up to 2,075×10⁻²⁰ m² and a barrier is formed downward due to water stratification (Figure 2). This effect is apparently small, but it is important to stress that it is caused mainly by the dissolved calcite, which will precipitate when the acidic saline water is diluted in the reservoir water.

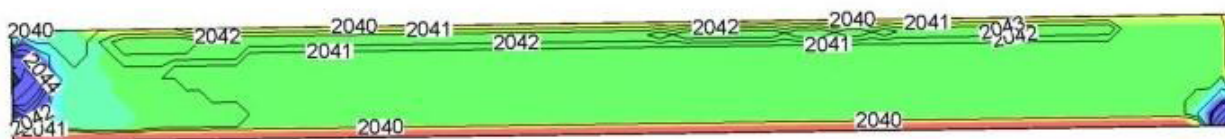


Figure 1. Simulation of the horizontal model after 2 years of simulation time. Numbers represent permeability in 10⁻²⁰ m², colors represent porosity change from -0.002 (blue), 0.0 (green), to +0.002 (red).

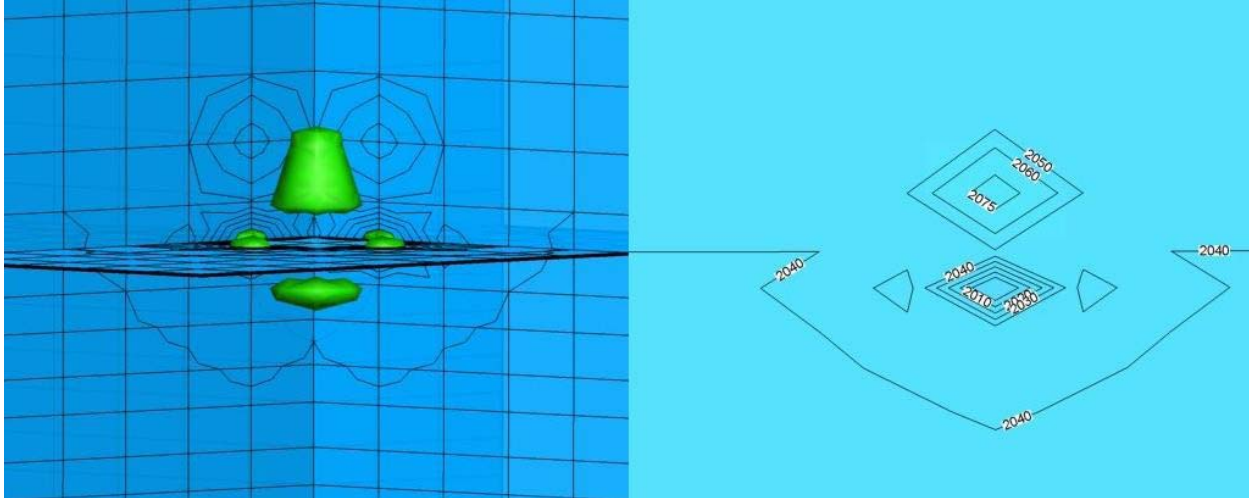


Figure 2. Column after 5 years of simulation. Numbers represent permeability in 10^{-20} m^2 . On the left-hand side the 3D image shows the $2,040 \times 10^{-20} \text{ m}^2$ contour, while on the right-hand side the corresponding 2D vertical section is drawn; elements are $10 \times 10 \times 10 \text{ m}$.

STRUCTURED MODEL

The grid of the trapping structure is made by $54 \times 51 \times 55$ (151,470) elements, with dimensions of $250 \times 250 \text{ m}$ along the X- and Y-axis, and variable Z with a thickness of 10 m in the reservoir units (Zones 5–8) (dark green, Figure 3). The irregular hexahedric elements follow the contact surfaces between the different geological formations, the structure obtained directly by seismic data. This kind of structure, though very common in nature for shape and dimension, requires long computation times with a relatively low resolution. On the basis of the previous simulation, the position of the injection point was located on the middle of the reservoir along the Z-axis, and shifted on the right boundary of the cap rock (Figure 3, pink dot). This is due to the fact that the $\text{CO}_{2(\text{aq})}$ -rich water and $\text{CO}_{2(\text{g})}$ originated around the injection point will arise up to the top of the structure along the cap-rock boundary. The Ca^{2+} - HCO_3^- enriched solution will move down along the side of the structure, thus protecting the cap rock and allowing CO_2 to fill out of the right side of the structure, a volume that may not otherwise be available for CO_2 storage. As the injection was performed, the injection pressure was adjusted to obtain $1.5 \text{ Mton CO}_2/\text{year}$. The result was an

injection pressure of 190 bars of hydrostatic pressure and 50 bars of injection overpressure. A simulation of both the CO_2 flux and mineral precipitation leads to the results shown in Figure 4. After 5 years of simulation, there is a contribution to SMCO₂ (total CO_2 sequestered in mineral phases) related almost exclusively to calcite, that reaches its maximum just beyond the spill point, all around the structure with an average value of about 0.02 Kg/m^3 . Just at the outlet of the structure, the elements show a slightly increased permeability ($2,360 \times 10^{-20} \text{ m}^2$ with respect to the reference value of $2,040 \times 10^{-20} \text{ m}^2$), while the main depositing elements are the nearest elements outside the structure (250 m away) and show a permeability of $260 \times 10^{-20} \text{ m}^2$. The escaping pathways of the displaced water, aligned along the Y-axis in Figure 4, show a permeability value of $1,240 \times 10^{-20} \text{ m}^2$, thus the main permeability barrier is very localized. Along the Z-axis, the flux is limited by the marly limestone formation where, owing to the interaction with basic reservoir water, the formation of a depositing area just along the contact of the two strata beds is favored, showing the same permeability barrier effect observed on the spill point level.

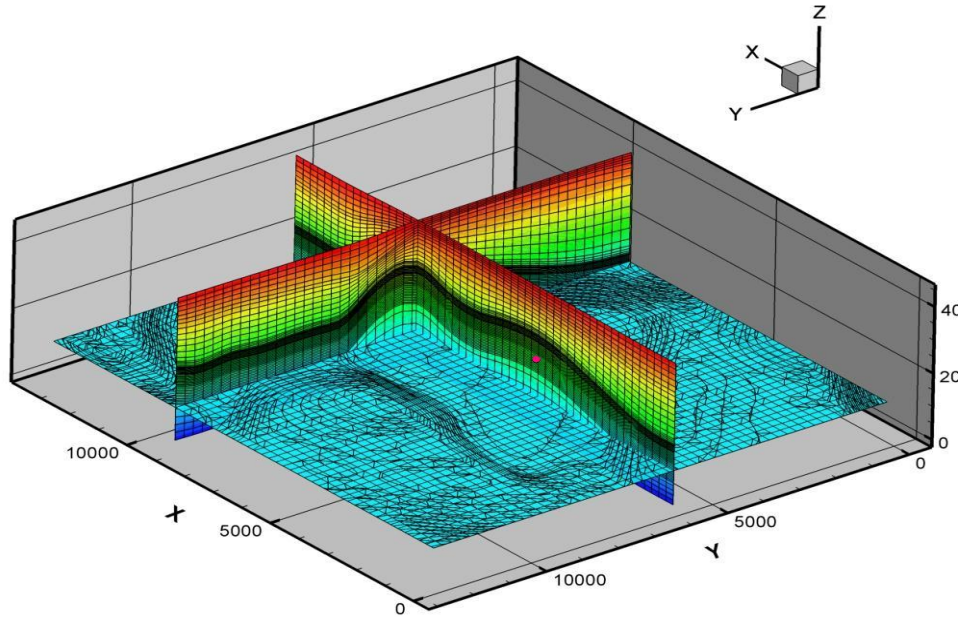


Figure 3. Structure meshing—54x51x55 elements, with dimensions of 250x250 m along X- and Y-axis, and variable Z with 10 m thick elements in the reservoir (dark green). Pink dot is the injection point.

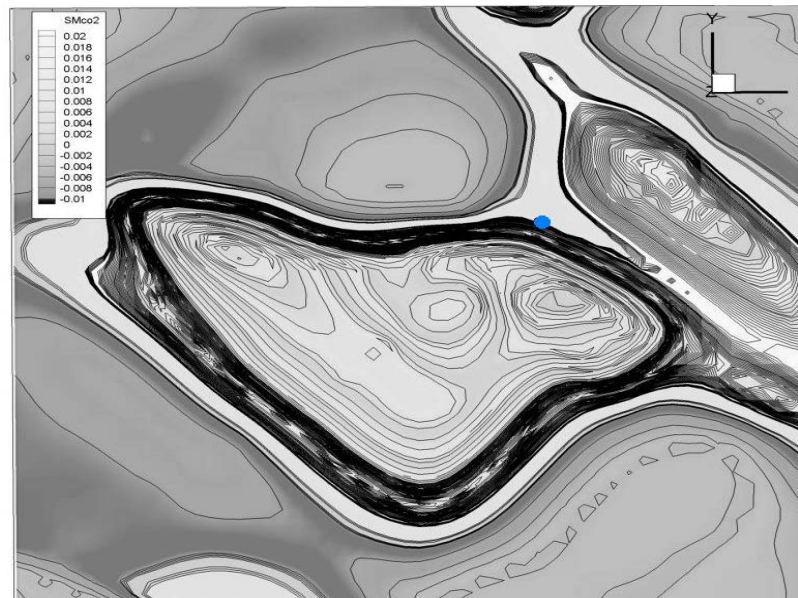


Figure 4. Plan view showing SMCO₂, total sequestered CO₂ in mineral phases in kg m⁻³. The blue dot shows the position of the spill point, and all around the structure the precipitating area at the spill point level.

CONCLUSION

Permeability plays an important role in CO₂ injection, especially in a low-permeability reservoir. In this work, we show that an important effect occurs, mainly due to the formation of secondary calcite deposits on the spill point. The depositing site is where the water displaced from the trapping structure encounters the “fresh” water of the reservoir. This process is relatively fast, and the secondary calcite

barrier is fully formed just after 5 years of injection in a large (5×3×0.5 km) trapping structure; the barrier reduces the outflow velocity of the CO₂-displaced water, thus reflecting a lower CO₂ injectivity. A low-permeability reservoir may present many difficulties, but the low permeability itself guarantees against CO₂ leakage. Therefore, a major effort should be made to study this kind of system.

REFERENCES

- Calore C., R. Celati, P. Squarci, L. Taffi, *Temperature map of Italy at 1000, 2000 and 3000 m*, Intl. Inst. for Geothermal Research-CNR, Pisa, 1988.
- Cantucci, B., G. Montegrossi, O. Vaselli, F. Tassi, F. Quattrocchi, and E.H. Perkins, *Geochemical modeling of CO₂ storage in deep reservoirs: The Weyburn Project (Canada) case study*, Chemical Geology, 265, Issues 1-2, 181-197, 2009.
- Clauser C. & Huenges E., *Thermal Conductivity of Rocks and Minerals, Chapter 3 of A Handbook of Physical Constants*. AGU Ref. Shelf 3, 1995.
- Corey, A.T. *The Interrelation Between Gas and Oil Relative Permeabilities*, Producers Monthly, 38-41, November 1954.
- Frank M.J.W., Kuipers J.A.M., Van Swaaij W.P.M., *Diffusion Coefficients and viscosities of CO₂+H₂O, CO₂+CH₃OH, NH₃+H₂O, and NH₃+CH₃OH Liquid Mixtures*, J. Chem. Eng. Data, 41, 297-302, 1996.
- Hashimoto S. and Suzuki M., *Vertical distribution of carbon dioxide diffusion coefficients and production rates in forest soils*, Soil. Sci.Soc.Am.J., 66, 1151-1158, 2002.
- Kuhn M., and W.-H. Chiang, *Processing Schemat, Ver. 4.0.0, SHEMAT Ver. 8.0*, J. Bartels, C. Clauser, M. Kuhn, D. Mottaghy, V. Rath, R. Wagner & A. Wolf, Springer-Verlag, Berlin, Heidelberg, 2003.
- Johnson, J.W., E.H. Oelkers, H.C. Helgeson, *SUPCRT 92: A software package for calculating the standard molal thermodynamic properties of minerals, gases, aqueous species, and reactions from 1 to 5000 bars and 0 to 1000 °C*. Comput. Geosci. 18, 899-947, 1992..
- Lutterotti, L., S. Matthies, H-R. Wenk, *MAUD (Material Analysis Using Diffraction): a user friendly Java program for Rietveld Texture Analysis and more*, Proceeding of the Twelfth International Conference on Textures of Materials (ICOTOM-12), 1, 159, 1999.
- Montegrossi, G., B. Cantucci, O. Vaselli, and F. Quattrocchi, *Reconstruction of porosity profile in an off-shore well*, Bollettino di Geofisica Teorica ed Applicata, 49 (2), 408-410, 2008.
- Palandri, J., Y.K. Kharaka, *A compilation of rate parameters of water-mineral interaction kinetics for application to geochemical modelling*, US Geol Surv. Open File Report 2004-1068, 2004, p. 64.
- Palmer, B.J, Calculation of thermal-diffusion coefficients from plane-wave fluctuations in the heat energy density, Physical Review E, 49 (3), 2049-2057, 1994.
- Parkhurst, D.L., C.A.J. Appelo, *User's guide to PHREEQC (version 2)-A computer program for speciation, batch-reaction, one-dimensional transport, and inverse geochemical calculations*, U.S. Geological Survey Water-Resources Investigations Report 99-4259, pp. 312, 1999.
- Singh T.N., Sinha S., Singh V.K., *Prediction of thermal conductivity of rock through physico-mechanical properties*. Building and Environment, 42, 146-155, 2007
- Spycher, N., K. Pruess, *CO₂-H₂O mixtures in the geological sequestration of CO₂ center dot. II. Partitioning in chloride brines at 12-100 °C and up to 600 bar*, Geochim. Cosmochim. Acta 69 (13), 3309-3320, 2005.
- Steefel, C.I, A.C. Lasaga, *A coupled model for transport of multiple chemical species and kinetic precipitation/dissolution reactions with applications to reactive flow in single phase hydrothermal system*, Am. J. Sci.; 294:529-92, 1994.
- Tamini, A., Rinker, B., Sandall, O.C., *Diffusion Coefficients for Hydrogen Sulfide, Carbon Dioxide, and Nitrous Oxide in water over the Temperature Range 293-368 K*, J.Chem.Eng.Data, 39, 330-332, 1994
- Verma, A. and K. Pruess, *Thermohydrologic Conditions and Silica Redistribution Near High-Level Nuclear Wastes Emplaced in Saturated Geological Formations*, J. of Geophys. Res., Vol. 93, No. B2, pp. 1159-1173, 1988.
- Wang L.S., Lang Z.X., Guo T.M., *Measurement and correlation of the diffusion coefficients of carbon dioxide in liquid hydrocarbon under elevated pressures*, Fluid Phase Equilibria, 117, 364-372, 1996
- Wolery, T.J., *EQ3/6: Software package for geochemical modeling of aqueous systems: package overview and installation guide (version 7.2)*, Lawrence Livermore National Laboratory Report UCRL-MA-10662 PT I, Livermore, California, 1992.
- Xu, T., K. Pruess, *Modeling multiphase non-isothermal fluid flow and reactive geochemical transport in variably saturated fractured rocks: I Methodology*, Am. J. Sci. 301, 16-33, 2001.
- Xu, T., E.L. Sonnenthal, N. Spycher, K. Pruess, *TOURGHREACT: a simulation program for non-isothermal multiphase reactive geochemical transport in variably saturated geologic media*, Comput. Geosci. 32, 145-165, 2006.

INJECTION OF CO₂ IN AN EXPLOITED GAS RESERVOIR: MODELING OF ROCK AND CEMENT ALTERATION USING THE TOUGHREACT-TMGAS SIMULATOR

Claudio Geloni, Thomas Giorgis and Alfredo Battistelli

RISAMB Dept., Environmental Engineering Unit, Saipem SpA (Eni Group), 61032 Fano (PU), Italy
e-mail: claudio.geloni@saipem.eni.it, thomas.giorgis@saipem.eni.it, alfredo.battistelli@saipem.eni.it

ABSTRACT

The injection of CO₂ in exploited natural gas reservoirs as a means to reduce GHG emissions is highly attractive, since it takes place in well-known geological structures of proven integrity with respect to gas leakage. The injection of a reactive gas such as CO₂ puts emphasis on the possible alteration of reservoir and caprock formations and especially of the wells' cement sheaths induced by the modification of chemical equilibria. Within an R&D project funded by Eni, we set up a numerical model to investigate the rock–cement alterations driven by the injection of CO₂ into a depleted sweet natural gas pool. CO₂ is captured from natural gas produced from sour gas pools of the same field.

The simulations are performed with the TOUGHREACT simulator coupled to the TMGAS EOS module developed for the TOUGH2 family of reservoir simulators (Pruess et al., 1999). On the basis of field data, the system is considered to be under isothermal (50°C) and isobaric (130 bar) conditions. The effects of the evolving reservoir gas composition are taken into account before, during, and after CO₂ injection. Fully water-saturated conditions were assumed for the cement sheath and caprock domains. The gas phase does not flow by advection from the reservoir into the interacting domains, so that molecular diffusion in the aqueous phase is the unique process controlling the mass transport occurring in the cement sheath and caprock domains under study.

INTRODUCTION

In the framework of activities related to wellbore integrity and risk assessment for a storage site, an important potential escape mechanism is the CO₂ leakage from poorly plugged wells (or old, abandoned wells) at the cement interfaces with casing and formation, or through the well materials (inside of corroded casings and within the cement plug itself). The potential for long-term degradation of cement and metal casing in the presence of CO₂ is a topic of extensive investigation at this time, especially with wellbore simulation models that couple geomechanics, geochemistry, and fluid transport. Some studies emphasize that the primary paths for possible CO₂ movement are along the cement interfaces with casing and/or formation, rather than the CO₂-resistant

cement that provides an effective barrier (IPCC, 2005).

In our numerical model, we make no assumptions based on the complex annular tolerance that can occur between cement and casing and caprock interfaces. Rather, we focus on the diffusion processes that occur between cement and caprock fluids (i.e., aging processes) near to and at a distance from an evolving reservoir. Despite the lack of specific scanning electron microscope (SEM) analysis, our model is able to give a good representation of the mineralogical alteration of cement interfaces in contact with a reservoir acid aqueous solution, typical of the chemical processes reported in literature. The simulations are aimed to reproduce the evolution of an idealized reservoir corresponding to the ongoing gas production operations and to the possible future CO₂ re-injection operations in the field under study. Attention is focused on the possible effects at near-wellbore scale to better understand the degradation dynamics that can occur in cement completion.

THE TOUGHREACT-TMGAS SIMULATOR

An updated version of the TOUGHREACT numerical simulator (Xu et al., 2004) was employed in our simulations. The reactive transport module of this version of the code is coupled to the new TMGAS EOS module (Battistelli and Marcolini, 2009), able to model the two-phase flow of an aqueous (Aq) and nonaqueous (NA) phase in deep geological structures. TMGAS can simulate the behavior of NaCl-dominated brines in equilibrium with a NA mixture containing hydrocarbons and inorganic gases such as CO₂, H₂S, and CH₄. The NA phase can be in either gas, supercritical, or liquid (condensed) conditions, with the limitation that such conditions cannot coexist within the same grid element. Starting from the fluid–phase equilibria computed in the thermodynamic module of the flow section, an effective Henry constant—depending on temperature, pressure, and composition of the gaseous and aqueous phase—is obtained and passed to the geochemical module for the aqueous speciation step. In fact, the Henry constant substitutes the thermodynamic constant (depending only on temperature) contained in the geochemical database used by the TOUGHREACT code in the reactive transport section.

CONCEPTUAL MODEL AND GEOMETRICAL DETAILS

The exploitation history of the gas reservoir was schematically divided into four subsequent stages, representing the chronological evolution of the entire natural gas pool:

- *Phase 0*—a preliminary phase in which the reservoir-caprock interactions develop a concentration gradient within the caprock domain (This phase represents a possible maturation of the impermeable layer above the storage formation, before the start of mining exploitation.);
- *Phase 1*—from 0 to 40 years: wellbore cement interaction with the caprock and reservoir fluids, during gas exploitation, before CO₂ re-injection in the gas pool;
- *Phase 2*—from 40 to 60 years: CO₂/CH₄ displacement up to a CO₂/CH₄ ratio in the gas phase of 95:5 by mass fraction;
- *Phase 3*—from 60 to 140 years: reservoir-cement-caprock evolution after the end of CO₂ re-injection.

These four phases are simulated considering a three-domain region close to a generic well existing prior to CO₂ injection (Figure 1).

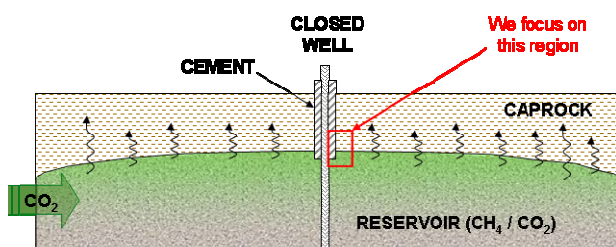


Figure 1. Conceptual model of the system at the reservoir scale after CO₂ injection, with the region focused by the simulations

The system is modeled as a cylinder, with its symmetry axis centered on the vertical axis of the well, as shown in Figure 2-left). The nodal network, represented by a 2D radial grid (Figure 2-right), consists of 57 layers corresponding to an overall thickness of 5 m and 42 columns to a radial extent of 5 m. The well casing, considered as an inactive, closed boundary (inner surface), is located at a radius of 12.5 cm and surrounded by a 4 cm thick cylindrical cement sheath. The reservoir is represented by a single layer at the bottom of the cement and caprock domains acting as a (re)active boundary with time-variable geochemical conditions. The upper and lateral surfaces of the system represent closed boundaries. To study the near wellbore effects, we use a fine mesh at the domain interfaces (internodal distance = 5×10^{-3} m) with a logarithmic progression of grid increments in the radial direction.

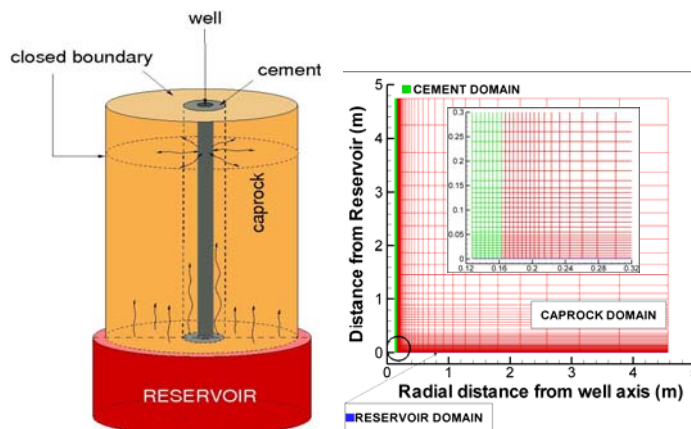


Figure 2. Representation of the rock domains at the near-wellbore scale (left); numerical model discretization grid (right).

INITIAL CONDITIONS

The initial porosity (ϕ) of reservoir and caprock formations was fixed at the average values measured on field cores (Table 1). The value for cement porosity was set according to the volume of the capillary porosity of a hydrated cement, estimated by means of empirical models available in the literature, such as Powers-Brownyard's model of phase distribution in hydrated cement paste (Powers and Brownyard, 1948, and modified versions, e.g., see Young and Hansen, 1987; Jensen and Hansen, 2001; Taylor, 1997) for a degree of hydration of 0.99 and a water/cement ratio of 0.44. This value is the water requirement for an American Petroleum Institute (API) Class G cement.

Table 1. Initial values of the thermodynamic and petrophysical properties assigned to the rock domains: reservoir (RES), cement (CEM) and caprock (CAP).

P	128.5 bar		
T	50 °C		
	S _w	Porosity (ϕ)	Tortuosity (τ)
RES	0.22	0.18	0.10
CEM	1.00	0.10	0.05
CAP	1.00	0.05	0.05

The reservoir is in a two-phase condition, close to the irreducible aqueous-phase saturation, while the cement and caprock domains were assumed to be in fully water-saturated conditions. Disregarding the capillary pressure and any possible leakage through fractures, the gas phase does not flow by advection from the reservoir into the overlying media, so molecular diffusion is the unique mechanism of transport. Porosity changes related to geochemical processes affect the diffusion of solutes in the

aqueous phase according to an effective diffusion coefficient depending on tortuosity (τ). Unfortunately, the tortuosity coefficients are not constrained by experimental data, and no definitive information is available in the literature on its variability in geological media; consequently, average reference values are used in the simulations (Table 1). This model does not account for an ionic multispecies approach to the diffusion process (Samson and Marchand, 2007) that can prove significant only in the very short term (< 10 days). The diffusion coefficient in free water has been set at $8 \times 10^{-10} \text{ m}^2/\text{s}$ @ 50°C (Oelkers, 1996).

Petrophysical, mineralogical, and geochemical data are derived from rock samples collected at the field and from SEM laboratory analysis. The reservoir formation is sandstone (Table 2) mainly consisting of (by volume) carbonates (35%), quartz (35%), clay minerals (muscovite, kaolinite and chlorite, up to 20%) and feldspars (K-feldspar and albite, 10%). The caprock is a carbonate-rich shale composed of (by volume) 27% calcite plus dolomite, 48% silicate clay minerals and (the remaining) 25% non-clay minerals (K-feldspar and quartz). The detailed mineralogical composition is reported in Table 2. The cement is a hydrated Geocem™, an API Class G High Sulphate Resistant grade commercial oilwell cement, whose composition (Table 2) has been determined in the laboratory. Laboratory data indicate that at 50°C , amorphous phases are predominant in this cement. We made the assumption that all amorphous materials (about 82% by volume) are represented by the calcium silicate hydrate (CSH:1.7, $\text{Ca}_{1.7}\text{SiO}_{6.317}\text{H}_{5.234}$). Other mineral phases are portlandite (12%) and minor quantities of ettringite, brownmillerite, and calcite. Chemical analyses are available for reservoir pore waters only.

Table 2. Initial mineralogical compositions of the rock domains (% by volume)

Minerals	RES	CEM	CAP
calcite	30	1.38	26
dolomite-dis	5	-	0.78
quartz	35	-	3.8
albite	3	-	-
K-feldspar	7	-	19.37
chlorite	5	-	0.99
kaolinite	3.5	-	traces
muscovite	11.5	-	35.07
smectite-Na	-	-	10.6
smectite-Ca	-	-	2.76
CSH:1.7	-	81.83	-
portlandite	-	11.87	-
ettringite	-	2.6	-
brownmillerite	-	2.31	-
monosulphate	-	traces	-

These data have been used to constrain the concentration of the main ions in solution, in order to compute the composition of an “evolved” water at least partially equilibrated with the primary local mineralogy of both reservoir and caprock domains (Table 3). The chemical composition of the cement pore water has been totally reconstructed by means of simplified numerical 0D models, allowing a low-salinity NaCl solution to react with the primary minerals of the cement. A pH of 11.63 at 50°C is obtained, comparable with the values reported in the literature for cement pore waters at thermodynamic equilibrium with portlandite (Glasser, 1997). The chloride content was set at $6 \times 10^{-3} \text{ mol/kgw}$, in order to obtain a OH/Cl ratio equal to 5 (Page et al., 1986). The Na and K concentrations were initially set to 0.01 mol/kgw , in agreement with literature data (Hong and Glasser, 2002).

Table 3. Initial aqueous solutions of reservoir, cement, and caprock domains (mol/kgw)

	RES	CEM	CAP
pH	7.432	11.630	6.069
Ca^{2+}	1.586×10^{-3}	6.960×10^{-3}	8.590×10^{-2}
Mg^{2+}	2.583×10^{-3}	5.619×10^{-11}	4.492×10^{-2}
Na^+	4.723×10^{-1}	1.015×10^{-2}	3.426×10^{-1}
K^+	2.150×10^{-3}	1.002×10^{-3}	5.312×10^{-2}
Fe^{2+}	3.371×10^{-9}	4.440×10^{-10}	6.766×10^{-4}
$\text{SiO}_{2(\text{aq})}$	2.889×10^{-4}	1.270×10^{-5}	2.501×10^{-4}
Al_3^+	2.411×10^{-7}	1.100×10^{-4}	1.540×10^{-8}
Cl^-	4.770×10^{-1}	6.000×10^{-3}	5.747×10^{-1}
HCO_3^-	6.750×10^{-3}	8.540×10^{-6}	5.802×10^{-3}
SO_4^{2-}	9.693×10^{-6}	3.980×10^{-4}	1.831×10^{-8}
CH_4	8.298×10^{-2}	-	9.193×10^{-6}

THERMODYNAMICS DATA AND KINETICS PARAMETERS

The database ThermXu4.dat of the TOUGHREACT simulator was modified to include additional thermodynamic data on the cement mineral phases. Missing data were taken from the data bases:

- (i) *data0.ymp.R2.dat*, of EQ3/6 code (Wolery, 1992);
- (ii) *thermo.com.v8.r6+.dat*, of The Geochemist’s Workbench software package (Bethke, 1992);
- (iii) *Thermodem.dat*, released in 2008 by BRGM (BRGM, 2008).

Solids were allowed to dissolve and precipitate according to a kinetic reaction mechanism (Lasaga et al., 1994). The kinetic data for the non-cement phases are mainly taken from Palandri and Kharaka (2004). Data for ettringite, monosulphate, CSH (Baur et al., 2004) and portlandite (Halim et al., 2005) are available at ambient temperature (25°C). Brownmillerite kinetic constants, not available in the literature, were set at the same order of magnitude of ettringite. Mineral reactive surfaces for non-cement phases

were set according to literature data (Xu et al., 2004). To have a consistent group of values, we decided to set the reactive specific surface of cement phases equal to those of the non-cement minerals. A reactive specific surface similar to that of clay minerals was instead assigned to the CSH gel.

RESULTS

Following the time schedule reported in the conceptual model description (above), the evolution of the three rock domains during the different phases is discussed.

Caprock maturation (Phase 0)

The interaction between the reservoir and the caprock, simulated for a period of 300 years, creates a gradient in the solute concentration inside the caprock, as shown in Figure 3 for the main ions. The CH_4 and Ca concentrations show typical diffusion profiles, while Na undergoes retardation effects due to the reactive processes (mainly Na-smectite precipitation), also constraining the Mg behavior in the zone at the contact with the reservoir. The $\text{CH}_{4(\text{aq})}$ diffusion front reaches a distance from the reservoir of about 1 m; pH also increases at the caprock-reservoir interface. The moderate reactivity of the caprock in this aging period leaves porosity unchanged around the initial value (0.05). The final results of this step are used as a starting point for the next simulations.

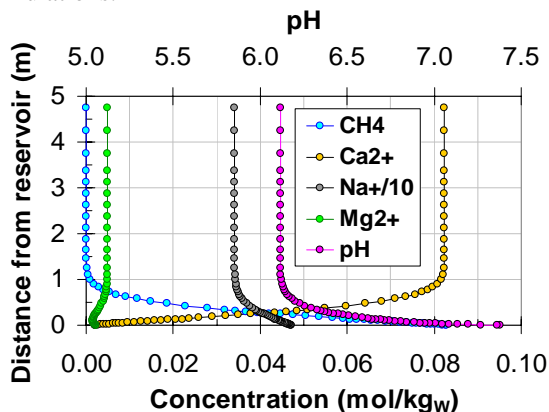


Figure 3. Caprock aging process prior to CO_2 injection

Reservoir evolution

Following the gas-pool exploitation history and planned CO_2 injection scenario, the reservoir geochemical system evolves along different phases varying its initial aqueous-phase composition and mineral assemblage given in Tables 2 and 3. The evolution of the reservoir boundary is made up of:

- *Phase 1*: water-rock interaction for 40 years, before CO_2 re-injection takes place, in the presence of the cement sheath. In this period, no relevant reactivity effects are observed in the reservoir formation, as shown in Figures 4–6.

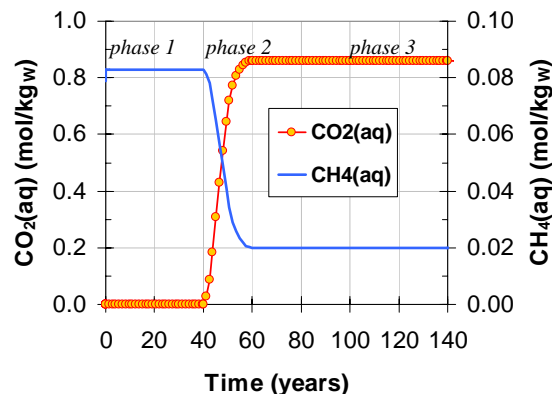


Figure 4. Reservoir evolution: concentration of CH_4 and CO_2 in the reservoir brine

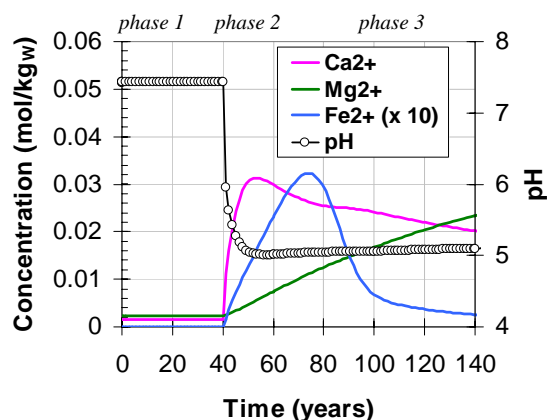


Figure 5. Reservoir evolution: pH and concentration of Ca^{2+} , Mg^{2+} and Fe^{2+} in the aqueous phase

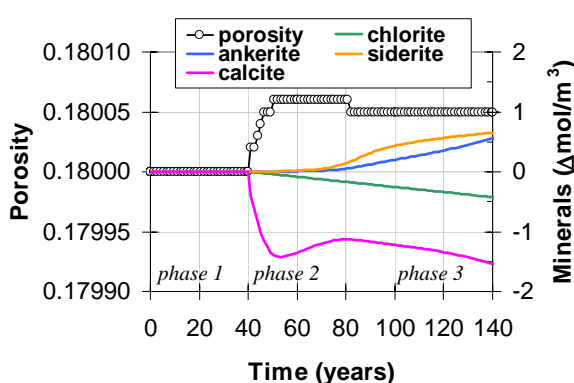


Figure 6. Reservoir evolution: porosity and mineral abundance in mol/m^3 of porous medium

- *Phase 2*: gradual CH_4 displacement by the injected CO_2 along a period of 20 years (Figure 4). The pH of the reservoir brine decreases to a value of 5.0, with a small increase in porosity due to weak calcite dissolution (about 1 mol/m^3 , Figure 6).

- *Phase 3*: an increased mineral reactivity takes place during these additional 80 years of simulation (Figure 6): chlorite starts dissolving, and the released Fe and Mg promote the precipitation of ankerite and siderite.

An excess of iron and magnesium remains in the aqueous phase owing to this conversion. Dissolution of calcite and precipitation of the secondary carbonate also constrain the Ca concentration. Minor porosity changes are obtained within the limited simulated time, compared to the slow kinetics of the mineral phases.

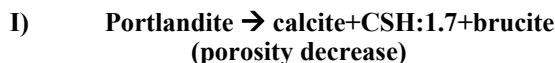
Below, the results from the end of the simulated period are presented by means of 1D profiles along sections of the cylindrical model shown in Figure 2. The selected sections are: (1) a vertical section inside the cement domain at a radial distance $R = 0.1425$ m, to highlight cement-reservoir reactivity, and (2) a radial section at a height of $Z = 1.65$ m, to highlight cement-caprock mutual interactions.

1D Reservoir–Cement interaction

The reservoir-cement interface interaction is closely related to the reservoir reactivity, in other words, to the contact of the well cement completion by the CO_2 plume. During Phase 1, the reservoir brine, which is only weakly alkaline ($\text{pH}=7.4$) compared to the hyper-alkaline cement pore water, promotes the portlandite ($\text{Ca}(\text{OH})_2$) dissolution and the calcite (CaCO_3) precipitation favored by the migration of HCO_3^- ions of the connate reservoir pore water. Inside the cement, in a very alkaline context, the magnesium of the reservoir precipitates as brucite ($\text{Mg}(\text{OH})_2$). This reactivity induces an increase in global porosity.

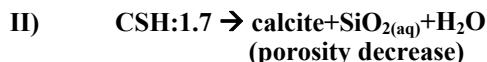
After the CO_2 arrival, the geochemical evolution of the cement is characterized by the propagation of two distinct reactive fronts which control the distribution of porosity inside the cement matrix and divide the cement annular radius in three zones (Kutchko, 2007). We present a possible scenario at the simulation time of 140 years. The first zone (I in Figure 7) is the most advanced altered zone inside the cement matrix. It is characterized by the occurrence of portlandite dissolution, precipitation of secondary calcite,

brucite, and CSH:1.7, with an overall reduction in porosity of 2% with respect to the initial cement matrix porosity (10%). This reactivity, leading to cement carbonation, can be formalized as in reaction I):



This process is active in a narrow zone where portlandite maintains the pH at alkaline values (around 11), holding over until some portlandite is present in the cement. This is a very effective process, because of the fast kinetics of the reaction in the presence of H^+ ions migrating from the reservoir. Dawsonite precipitation, predicted by the model in this zone (Figure 7), is likely due to the aluminum made available by the aluminosilicates (smectite and muscovite) reactivity occurring at the cement-caprock interface (see next paragraph).

The next zone (II in Figure 7) begins as soon as portlandite is totally dissolved and is therefore characterized by mild acidic pH values. In this portion of the cement matrix, the diffusion of carbon and magnesium coming from the reservoir makes possible a further calcite precipitation using calcium of CSH:1.7, which dissolves. The net balance in terms of volume fraction of the CSH:1.7/calcite conversion is a porosity reduction to a value around 9%. The reactivity can be described as in reaction II):



The H^+ ions coming from the reservoir cause brucite destabilization and its subsequent dissolution.

The inner zone (III in Figure 7) is characterized by dissolution of the secondary calcite, only partially compensated by ankerite ($\text{CaMg}_{0.3}\text{Fe}_{0.7}(\text{CO}_3)_2$) precipitation (Fe, Mg and HCO_3^- supplied by the reservoir). The reactivity can be described by the following reaction:

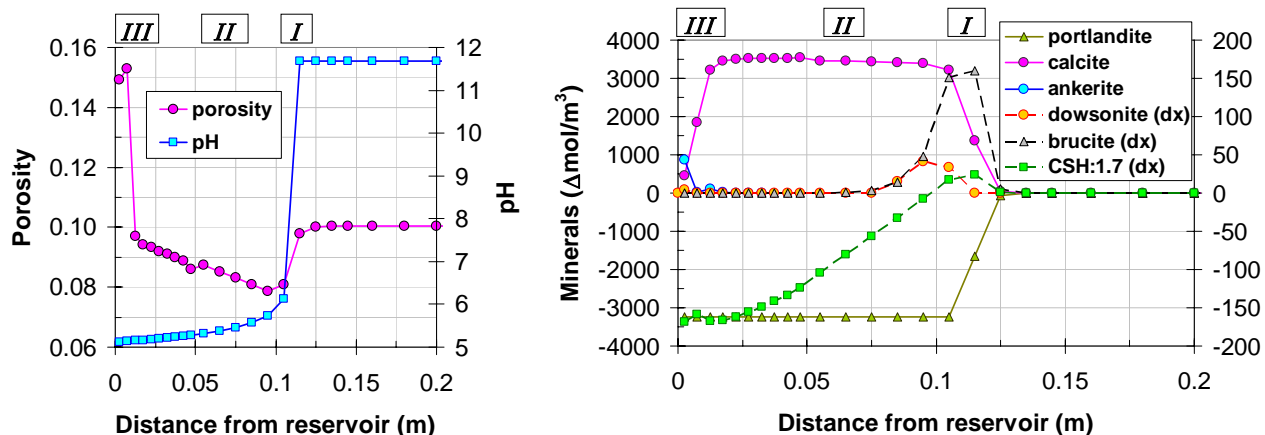


Figure 7. Spatial distribution in the first 0.2 m of cement sheath at the end of simulated period: (left) pH and porosity profiles; (right) abundance change (in mol/m^3 of medium) of the most reactive mineral

III) $\text{calcite} + \text{Mg} + \text{Fe} + \text{HCO}_3^- \rightarrow \text{ankerite}$ (porosity increase)

The reduced buffer capacity of the cement matrix due to portlandite disappearance brings the pH values close to those of the reservoir. In this condition, CSH.1.7 also dissolves. This is the most damaged zone, experiencing a pronounced increase in porosity (up to 15%) associated with a significant increase of $\text{SiO}_{2(\text{aq})}$ (not shown here), but without amorphous silica precipitation as experimentally demonstrated by the laboratory tests.

1D Cement–Caprock interaction

To describe the interaction between cement and caprock, we present the results along a radial section of the system at a distance from the reservoir interface (1.65 m), such as to not be affected by the reservoir itself. The very different mineralogy and chemistry between the two considered domains leads to a heavy modification of both media, in a narrow region across the cement–caprock interface.

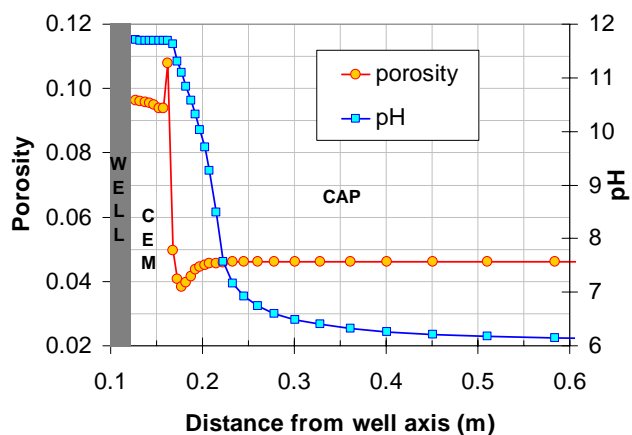


Figure 8. Spatial distribution of pH and porosity at the cement sheath–caprock interface.

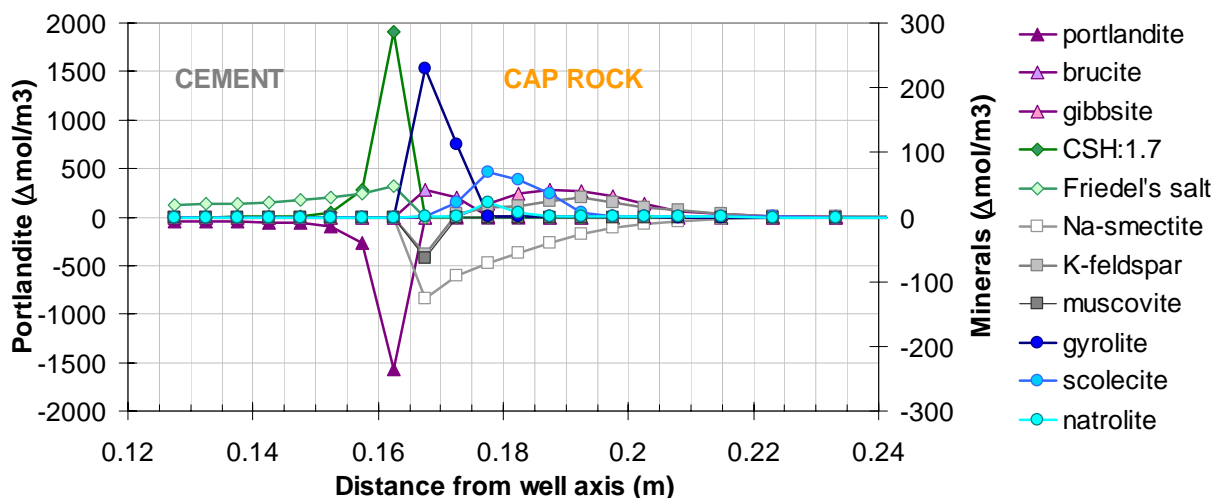


Figure 9. Spatial distribution of the mineral abundance changes (in mol/m^3 of medium) of the most reactive mineral phases at the cement–caprock interface at the end of the simulation period. K-feldspar pattern is hidden by that of muscovite.

The wide pH difference between the cement and caprock causes a diffusive flux of OH^- ions from the cement alkaline fluids into the caprock (Figure 8). A portlandite destabilization, which dissolves (Figure 9), is associated with this process. The calcium released by this reaction promotes the CSH precipitation favored by the incoming Al and Si from the caprock (see below). Although the molar volume of CSH is much higher than that of portlandite ($\text{CSH}=107.097 \text{ cm}^3/\text{mol}$, $\text{Ca}(\text{OH})_2=33.056 \text{ cm}^3/\text{mol}$) the net balance of this interconversion in terms of volume results in an increase in the cement porosity (about 1.5% at the end of simulated period, Figure 8). The chloride diffusion of the caprock brine into cement moreover induce the precipitation of Friedel's salt (a calcium aluminum chlorohydroxide, $\text{Ca}_2\text{Al}(\text{OH})_6\text{Cl}\cdot 2\text{H}_2\text{O}$). The very high molar volume of this salt ($276.24 \text{ cm}^3/\text{mol}$) causes a porosity reduction in the inner portion of the cement (Figure 8). This process can be a source of potential damage to and mechanical property degradation of the cement matrix (Taylor, 1997).

The major mineralogical alterations occurring within the caprock concern a partial conversion of the aluminosilicate mineral fraction (Na-smectites, muscovite and K-feldspar) into zeolites, with a concomitant release in solution of an excess of aluminum, silicon, and magnesium. As mentioned above: (i) Al and Si, migrating into the cement, promote the precipitation of CSH and Friedel's salt, (ii) Mg is sequestered by the precipitation of brucite ($\text{Mg}(\text{OH})_2$) and sepiolite ($\text{Mg}_4\text{Si}_6\text{O}_{15}(\text{OH})_2\cdot 6\text{H}_2\text{O}$, in minor amounts and not shown in Figure 9). Other reactions include a precipitation of gibbsite, an aluminum hydroxide in nature often associated with natrolite, further from the cement interface. In the caprock region very close to the cement interface, the interactions with the hyperalkaline fluids favor consistent zeolite precipitation and a remarkable

reduction in porosity (Figure 8). The kinetics of zeolite reactivity strongly affects the role played by each of the three types of zeolites inserted in the model. A sensitivity study on the kinetic rate constants (Geloni, 2009) showed that gyrolite and scolecite are the two most important minerals in porosity reduction. Given the parameters used in the present study, the model predicts a sealing effect of the caprock at a simulation time of 500 years (Figure 10).

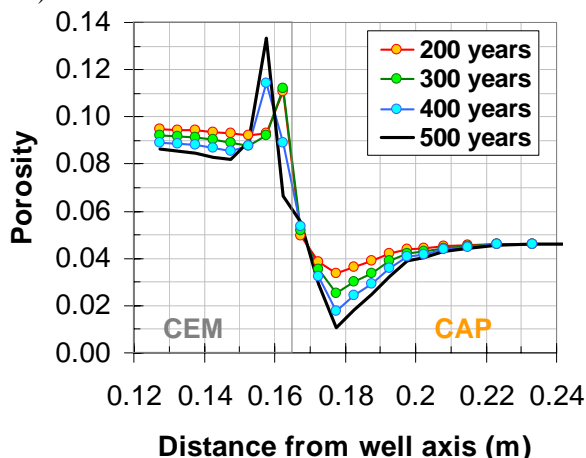


Figure 10. Time evolution of porosity spatial distribution at the cement–caprock interface

CONCLUSIONS

Although the numerical model proposed is quite idealized, and a few problems persist in the thermodynamic description of cement phases (e.g., lack of kinetic and thermodynamic data for iron phases and CSH gel), the simulations are able to predict the main mineralogical alterations occurring at the cement–reservoir and cement–caprock interfaces as documented in the literature (such as muscovite dissolution and zeolites and brucite precipitation, Gaucher and Blanc, 2006, and reference cited therein).

Some of the results obtained with our simulations can be schematically summarized as follows:

- 1) The macro process of cement carbonation reproduced by the numerical model is characterized by portlandite dissolution and the precipitation of secondary calcite, with a concomitant minor dissolution of the calcium silicate hydrate (CSH). A slight reduction in porosity is associated with this process.
- 2) The onset of the second major mineralogical transformation is related to the total removal of primary portlandite, characterized by a decrease in pH and a progressive dissolution of the secondary neo-formed calcite and ankerite formation at the contact with the reservoir. Increased porosity is associated with this process.

- 3) The diffusive migration of chemical complexes from the mild acidic reservoir brine induces alterations only in the first few centimeters of the wellbore cement and caprock (10 cm at the end of the simulated period, as shown in Figure 11). Under these conditions, cement sheath and caprock alteration due to reservoir interactions does not seem to cause any concern about their containment capacity over time.
- 4) The diffusion of hydroxyl ions from the cement into the caprock increases the pH in the portion of the caprock at the contact with the cement, far from the reservoir interface where the acidification effects of CO₂ are not yet felt (Figure 11). The interaction of the caprock minerals with the hyper-alkaline fluids induces: (i) a destabilization of portlandite, which converts into CSH:1.7 inside the cement (slight increase in porosity); (ii) zeolite precipitation in the caprock close to the cement surface (a sealing effect is observed for times higher than 500 years); (iii) Friedel's salt formation inside the cement, related to an only partial conversion between the aluminum-silicate phases into zeolites (availability of Al and Si at this interface).

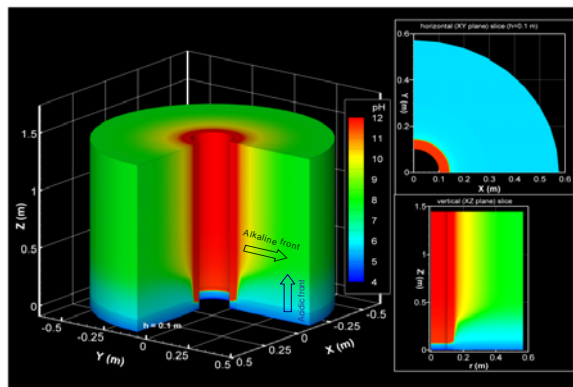


Figure 11. 3D view of pH distribution in the modeled domain, showing the acid front coming from the reservoir and the alkaline front migrating from the cement sheath into the caprock, at the end of the simulated period.

Under conditions of pure diffusion, it is now well known and proven that the cement alterations due to CO₂ brine acidification are very localized at the rock-domain interfaces. For the carbonation process, under diffusion control, a front thickness (e) estimation could be given by a very simplified equation (Barlet-Gouédard et al., 2009) $e = 0.22 (time)^{1/2}$ with e (mm) and time (h). After 100, the estimated front thickness would equal 20 cm, which is the same order of magnitude for the carbonation layer we found with our simulations. This model is further confirmation that the cement sheath could be more damaged by aging effects resulting from the caprock, rather than by CO₂ migration from a gas-depleted reservoir.

ACKNOWLEDGMENTS

The study was performed within the R&D program “GHG-GreenHouse Gases” financed by Eni SpA. Thanks are due to Eni E&P and R&M Divisions for making available the reservoir and laboratory data. Simona Biagi of IGG-CNR is gratefully thanked for the valuable help in the analysis and compilation of thermodynamic data of the cement mineral phases. Finally, thanks are due to Tianfu Xu of LBNL, who coded the first coupling of a prototypal version of TMGAS to TOUGHREACT.

REFERENCES

- Battistelli, A. and M. Marcolini, TMGAS: a new TOUGH2 EOS module for the numerical simulation of gas mixtures injection in geological structures, *Intl. J. Greenhouse Gas Control*, 3, 481-493, 2009.
- Barlet-Gouédard, V., Rimmelé, G., Porcherie O., Quisel, N., and Desroches, J, A solution against well cement degradation under CO₂ geological storage environment. *Intl. J. Greenhouse Gas Control*, 3, 206-216, 2009.
- Baur, I., P. Keller, D. Mavrocordatos, B. Wehrli, and C.A. Johnson, Dissolution-precipitation behaviour of ettringite, monosulfate, and calcium silicate hydrate. *Cem. Concr. Res.*, 34, 341-348, 2004.
- Bethke, C.M., The Geochemist's Workbench™, release 4.0. A user's guide to Rxn, Act2, Tact, React, and Gtplot. Hydrogeology Program, University of Illinois, 2002.
- BRGM, <http://thermoddem.brgm.fr>, 2008
- Geloni C., T. Giorgis, S. Biagi, E. Previde Massara, and A. Battistelli, Modelling of Well Bore Cement Alteration as a Consequence of CO₂ Injection in Exploited Gas Reservoirs. 5th Meeting of the Wellbore Integrity Network, IEA-GHG, Calgary May 12-13, 2009.
- Glasser, F.P., Fundamental aspects of cement solidification and stabilisation. *J. Hazard. Mater.*, 52, 151-170, 1997.
- Gaucher, E.C., and P. Blanc, Cement/clay interactions – A review: experiments, natural analogues, and modeling. *App. Geochem.*, 26, 776 – 788, 2006.
- Halim, C.E., S.A. Short, J.A. Scott, R. Amal, and G. Low, Modelling the leaching of Pb, Cd, As, and Cr from cementitious waste using PHREEQC. *J. Hazard. Mat.*, A125, 45-61, 2005.
- Hong, S.Y., and F.P. Glasser, Alkali sorption by C-S-H and C-A-S-H gels Part II. Role of alumina. *Cem. Concr. Res.*, 32, 1101-1111, 2002.
- IPPC – Intergovernmental Panel on Climate Change, IPCC Special Report on Carbon Dioxide Capture and Storage, Underground geological storage (Chapter 5), pp. 197-276, 2005.
- Jensen, O.M., and P.F. Hansen, Water-entrained cement-based materials I. Principles and theoretical background. *Cem. Concr. Res.*, 31, 647-654, 2001.
- Kutchko, B., B. Strazisar, D. Dzombak, G. Lowry, and N. Thaulow, Degradation of well cement by CO₂ under geologic sequestration conditions. *Environ. Sci. Technol.*, 41, 4787 – 4792, 2007.
- Lasaga, A.C., J.M. Soler, J. Ganor, T.E. Burch, and K.L. Nagy, Chemical weathering rate laws and global geochemical cycles. *Geochim. Cosmochim. Acta*, 58, 2361-2386, 1994.
- Oelkers E.H., Physical and chemical properties of rocks and fluids for chemical mass transport calculations. In: Lichtner, P.C., Steefel, C.I., Oelkers, E.H. (Eds.) *Reactive Transport in Porous Media: Review in Mineralogy*, vol.34. Washington, DC. The Mineralogical Society of America, pp. 131-191, 1996.
- Page, C.L., N.R. Short, and W.R. Holden, The influence of different cements on chloride-induced corrosion of reinforcing steel. *Cem. Concr. Res.*, 16, 79-86, 1996.
- Palandri, J.L., and Y.K. Kharaka, A compilation of rate parameters of water-mineral interaction kinetics for application to geochemical modeling. U.S. Geological Survey Open File Report 2004-1068. 64 pp., 2004.
- Powers, T.C., and T.L. Brownyard, Studies of the Physical Properties of Hardened Portland Cement Paste. Bull. 22, 992 pp., Portland Cement Association, Chicago, IL; reprinted from 1947. *J. Am. Concr. Inst. (Proc.)* 43, 101, 249, 469, 549, 669, 845, 993, 1948.
- Pruess K., C. Oldenburg, and G. Moridis, *TOUGH2 User's Guide, Version 2.0*, Report LBNL-43134, Lawrence Berkeley National Laboratory, Berkeley, CA, 1999.
- Samson E., and J. Marchand, Modeling the effect of temperature on ionic transport in cementitious materials. *Cem. Concr. Res.*, 37, 455-468, 2007.
- Taylor, H.F.W., Cement chemistry. 2nd edition. Thomas Telford ed., London, 1997.
- Xu T., E. Sonnenthal, N. Spycher, and K. Pruess, *TOUGHREACT User's Guide: A Simulation Program for Non-isothermal Multiphase Reactive Geochemical Transport in Variably Saturated Geologic Media*. Report LBNL-55460, Lawrence Berkeley National Laboratory, Berkeley, CA, 2004.
- Wolery, T.J., EQ3/6, a software package for geochemical modelling of aqueous systems: Package overview and installation guide. Lawrence Livermore National Laboratory, Livermore, CA., 1992.
- Young, J.F., and W. Hansen, Volume Relationships for C-S-H Formation Based on Hydration Stoichiometries. Materials Research Society Symposium Proceedings, 85, 313-322, 1987.

IMPACT OF LARGE-SCALE CO₂ GEOLOGIC STORAGE IN DEEP SALINE AQUIFERS: AN EXAMPLE FROM THE SONGLIAO BASIN, CHINA

Yanhui Dong, Guomin Li, Ming Li and Runjian Wu

Institute of Geology and Geophysics, Chinese Academy of Sciences
P.O.Box 9825
Beijing, 100029, China
e-mail: lemondyh@mail.iggcas.ac.cn

ABSTRACT

To reduce greenhouse gas content, CO₂ may be stored in deep saline aquifers. The pressure buildup caused by large-scale injections may impact a volume of the basin significantly larger than the CO₂ plume itself. A numerical simulation of CO₂ geologic storage that predicts CO₂ migration as well as its impact was performed. A hypothetical large-scale injection of CO₂ at the Daqingzi oilfield in the Songliao Basin, China, was selected as a case study. The model domain, with an area of ~ 45 km×60 km, included a multilayered groundwater system, with a sequence of aquifers and aquitards (sealing layers). In the simulation, CO₂ was injected into a storage aquifer at about 1,400 m depth under the Songliao Basin. The results suggest that large-scale pressure buildup can occur even in shallow aquifers, and that the seal permeability is the most important factor controlling the simulated pressure buildup. Furthermore, injection well optimization should be considered for industrial-scale CO₂ storage projects in deep saline aquifers.

INTRODUCTION

Geologic carbon sequestration in deep saline aquifers has drawn increasing consideration as a promising method for reducing greenhouse gas content in the atmosphere. Saline aquifers, which offer the largest storage potential of all of the geological CO₂ storage options, are widely distributed throughout the globe in all sedimentary basins. For CO₂ storage to have a significant impact on atmospheric levels of greenhouse gases, the amounts of CO₂ injected and sequestered underground need to be extremely large (Holloway, 2005). In industrial-scale CO₂ geologic storage projects, it is expected that the amount of CO₂ fluid injected into an aquifer could be several million tons per year for each storage site. Large-scale injection of CO₂ will impact subsurface volumes much larger than the CO₂ plume. Thus, even if the injected CO₂ itself is safely trapped in suitable geological structures, pressure changes and brine displacement may affect shallow groundwater resources, for example by increasing the rate of discharge into a lake or stream, or by mixing of brine into drinking-water aquifers (Bergman and Winter, 1995). Continuous long-term injections for more than

several decades will build up groundwater pressures over large regions.

Nicot (2007) first investigated the impact of a hypothetical large-scale injection on regional groundwater at the Texas Gulf Coast Basin, using conventional groundwater flow models, and suggests that large-volume CO₂ injection can cause groundwater pressure perturbation at up-dip aquifers. Birkholzer (2009) conducted a systematic sensitivity study of pressure response in a radially symmetrical stratified system. Their results suggest that seal permeability has a significant impact on pressure buildup, and that pressure perturbation of shallow units may occur only when the permeability of sealing layers is comparably high (higher than a microdarcy). Yamamoto (2009) performed a large-scale numerical simulation of CO₂ geologic storage at Tokyo Bay, Japan, to predict CO₂ migration and its impact on regional groundwater flow. Their results suggest that even if containment of CO₂ plume is ensured, pressure buildup on the order of tens of meters can occur in shallow, confined layers over extensive regions, including urban inlands.

In this study, we conducted a numerical simulation of CO₂ geologic storage that evaluates CO₂ trapping capacity and its impact. The simulation is designed for a preliminary investigation of hypothetical industrial-scale CO₂ injection at the Songliao Basin. The hydrogeological model covers the Daqingzi oilfield in the central Songliao Basin, an area approximately 45 km×60 km. The thickness of the model layers is determined using data from hundreds of deep boreholes. To ensure that pressure propagation in both lateral and vertical directions, and saline water migration, have no negative impact on near-surface aquifers, the model fully represents the entire hydrogeological system in the area, including surface topography, freshwater aquifers for drinking water, sealing layers, and CO₂ storage aquifers.

The primary goal of this study is to understand the behavior of CO₂ and its influence when it is stored in a geologic storage site, where the permeabilities of sealing layers are comparatively high. Numerical simulations are performed to determine: the extent to which the CO₂ moves within the geological

formations, and the range of possible pressure buildup in the near-surface and storage aquifers. The results are important for assessing whether the sequestration will impair the geological integrity of the underground formations, and whether CO₂ storage under such an industrial and populated area is secure and environmentally acceptable. The multiphase flow simulator TOUGH2 (Pruess, 1999) with ECO2N (Pruess, 2003) fluid properties module of sub/supercritical CO₂ was used to simulate the spatial CO₂ plume evolution and transient pressure buildup.

MODEL SETUP

Songliao Basin and Daqingzi Oilfield

The Songliao Basin, the most important oil-productive basin in China, is located in northeastern China (Figure 1 and Figure 2), with an area of about 260,000 km². The Songliao Basin is one of the largest Jurassic-Cenozoic continental basins in China related to the rifting process. It consists of a central depression and surrounding basin margins. There are minimal faults, fractures, or folds in the Basin. The stratigraphic sequences of the Basin are dominated by Cretaceous fluvial and lacustrine strata with volcanic and volcanoclastic rocks, which can be classified into five hydrostratigraphic units from bottom to top (Figure 3): the Upper Jurassic to Lower Cretaceous formation, the Late Cretaceous Quantou Formation, the Qingshankou Formation, the Yaojia Formation, and the Nenjiang Formation. The average thickness of the saline aquifer in the Basin is about 320 m (Figure 4). It also has extensive intra-informational lacustrine seals. The presence of shale formations within the Basin would provide a succession of barriers to vertical migration of CO₂ and contain any leak of CO₂ if it occurs from the main cap rock.

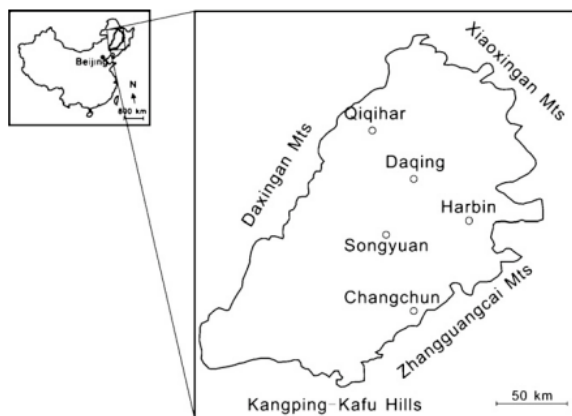


Figure 1. Location of the Songliao Basin in northeastern China

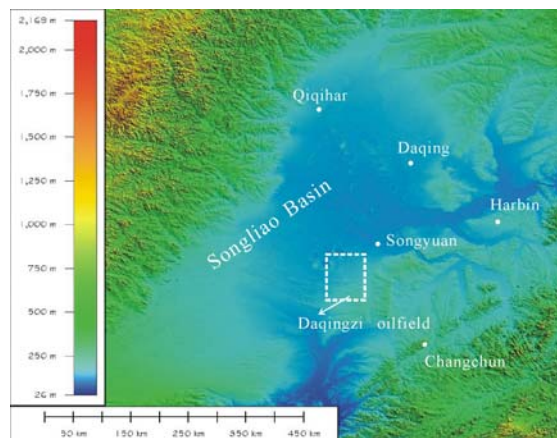


Figure 2. Topographic map of Songliao Basin

Zhang (2009) and Huang (2004) discussed the possibility of CO₂ geologic storage in the Qingshankou Formation at depths greater than 1,000 m, supposing sealing capabilities of the overlying Yaojia and Nenjiang Formations. At the Daqingzi Oilfield (Figure 2), located in the central Songliao Basin, the Qingshankou formation (Figure 3) is about 320 m thick. If CO₂ were injected into the Qingshankou Formation at the bottom of the Daqingzi Oilfield, it could result in deep saline groundwater in the Qingshankou Formation being pushed up-dip into shallow aquifers, the buildup of groundwater pressures, and a change in the water salinity of freshwater wells.

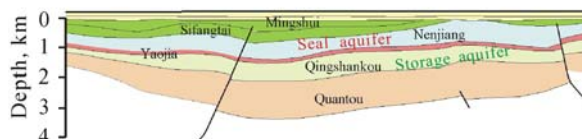


Figure 3. Geologic cross section

It should be emphasized that there is no plan for CO₂ geologic storage at the Daqingzi Oilfield at present. We selected this area for a case study, because the geologic data is relatively abundant.

Conceptual Model

We constructed a three-dimensional geological structure model for the 45 km×60 km area in Daqingzi Oilfield, as shown in Figure 5. The surface topography is represented by 90 m grid SRTM DEM (digital elevation model) data published by NASA. The geological structure was developed by interpolating formation boundaries identified by borehole loggings. Locations of the boreholes used for the interpolation are shown in Figure 4, a map of geological stratigraphy is shown in Figure 6, and the hydrogeological model is shown in Figure 7.

The Qingshankou Formation (siltstone), located at depths of about 1,400 m to 1,720 m belowground, was selected as the CO₂ storage aquifer. The selected storage formation is bounded at the top by two sealing layers, the Yaojia (mudstone) and Nenjiang (mudstone) Formation, with a thickness of about 500 m to 550 m. The bottom of the Quantou Formation (mudstone) is an additional sealing layer.

A temperature of 15°C was assumed at the surface. Temperature varies linearly with depth, and the average temperature gradient in this area is about 3.76°C per 100 m depth (see Figure 8). The pressure also increases linearly with depth, and the average pressure gradient is about 1.16 MPa per 100 m (see Figure 9). Salinity was assumed to be very low, and no density-driven flow occurs. Geomechanical effects such as land-surface uplift were not explicitly considered.

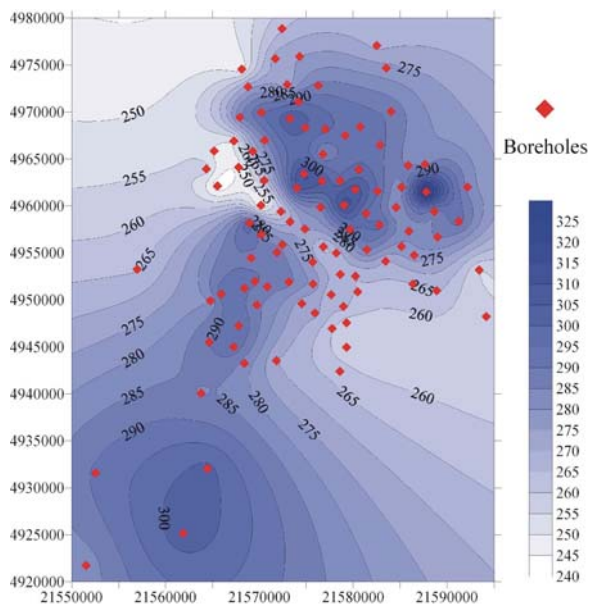


Figure 4. Thickness of the Qingshankou Formation in Daqingzi oilfield

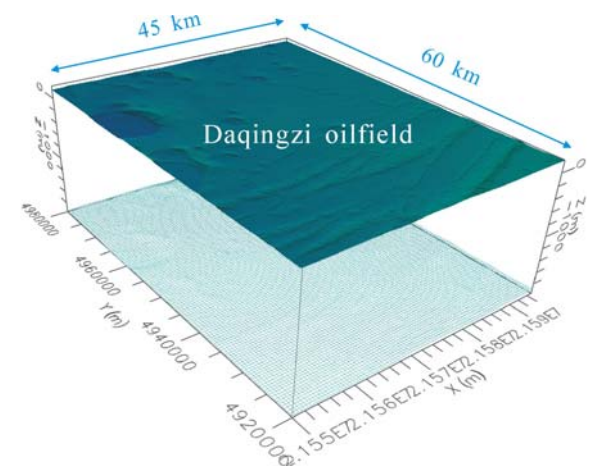


Figure 5. Modeled region

Carbon dioxide was assumed to be injected through one or five boreholes in the center of the oilfield, with an annual rate of 1 or 0.2 MtCO₂/year/well, respectively, over 30 years, resulting in a total annual rate of 30 MtCO₂/year. The simulation runs covered a time period of 100 years, including a post-injection period of 70 years.

PERIOD	STRATIGRAPHY	THICKNESS (m)	LITHOLOGY	HYDROGEOLOGY
CRETACEOUS	Mingshui Fm	80-100	Siltstone	Aquifer
		475-500	Mudstone	Aquitard
	Sifangtai Fm	60-100	Siltstone	Aquitard Aquifer
		222-280	Mudstone	Aquitard
	Nenjiang Fm	22-112	Siltstone	Aquifer
		440	Mudstone	Aquitard
	Yaojia Fm			
	Qingshankou Fm	300	Mudstone	Aquitard Aquifer
		170	Siltstone	Aquifer
		70	Siltstone	Aquitard Aquifer
140		Siltstone	Aquifer	
Quantou Fm				

Figure 6. Map of geological stratigraphy

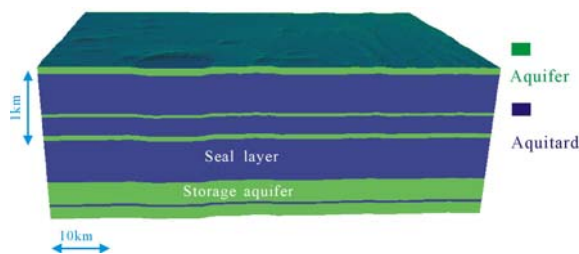


Figure 7. Hydrogeological model

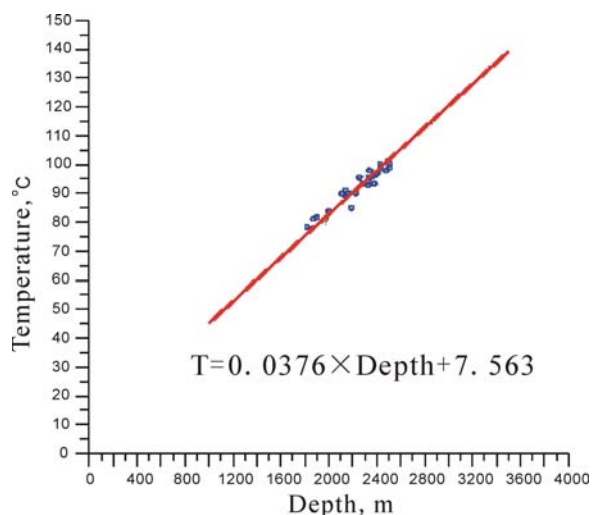


Figure 8. Temperature vs. depth in Daqingzi area

The surface and side boundaries were hydraulically open, while the bottom was closed. The large lateral extent of the 45 km × 60 km model was chosen to ensure that the boundary conditions have minimal effect on the simulation results. At the lateral boundary, the initial hydrostatic pressure was specified, and the boundary was open for fluids to escape from the model domain. The surface boundary was also open, so that the pressure was fixed at the atmospheric pressure. The bottom of the model was closed (no-flow), representing the very low permeability of the Quantou mudstone.

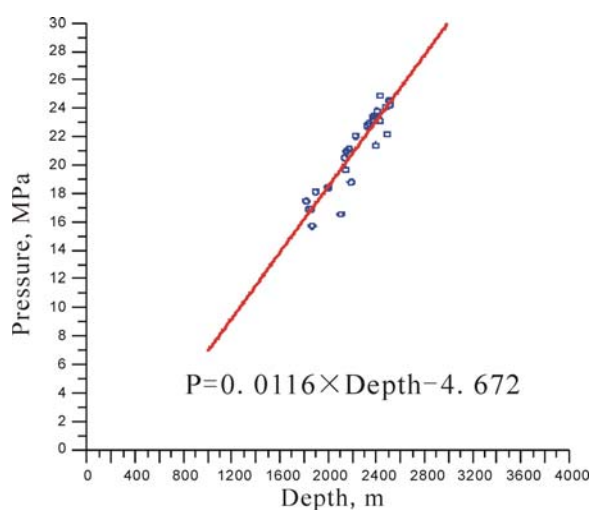


Figure 9. Pressure vs. depth in Daqingzi area

Model Parameters and Sensitivity Cases

The hydrogeologic parameters chosen for this case study are given in Table 1, based on well logs and laboratory test data. For simplification, in most

Table 1. Hydrogeologic properties for the aquifer-aquitard system used in the simulations (base case)

Properties	Aquifers	Aquitards
Permeability, m ²	2.65×10^{-13}	1×10^{-19}
Porosity	0.11	0.03
Pore compressibility, Pa ⁻¹	1×10^{-9}	5×10^{-10}

simulation cases, all aquifers and aquitards were assigned the same set of properties without variation in depth. Vertical/horizontal ratio of permeability was assumed to be 1/10 in all the layers. The van Genuchten model was used to calculate the capillary pressure and relative permeability of the two-phase flow of CO₂ and water. The model parameters were basically adopted from Pruess (2003). In the base case, CO₂ was injected through one borehole with an annual rate of 1 MtCO₂/year.

Sensitivity cases are summarized in Table 2. The first sensitivity case (Case 2) reduces the permeability for aquitards, whereas the second sensitivity case (Case 3) increases the permeability for aquitards. In addition, the sensitivities to number of boreholes and injection rate are also explored in Case 4.

Table 2. Sensitivity cases.

Case	Properties	Changes
2	Permeability for aquitards	1×10^{-22}
3	Permeability for aquitards	1×10^{-17}
4	Number of boreholes	5
	Injection rate	0.2 Mt/year

RESULTS AND DISCUSSION

Spatial distribution of CO₂ plume

The CO₂ plumes at the end of the injection period for the base case and Case 4 are shown in Figure 10a and 10b, respectively. The evolution of CO₂ gas saturation for a plume on a cross section for the base case is shown in Figure 11. The plume is concentrated at the top of the storage formation, a result of buoyancy forces. The plume basically continues to be contained under the sealing layer, indicating that CO₂ may be safely trapped over longer time periods.

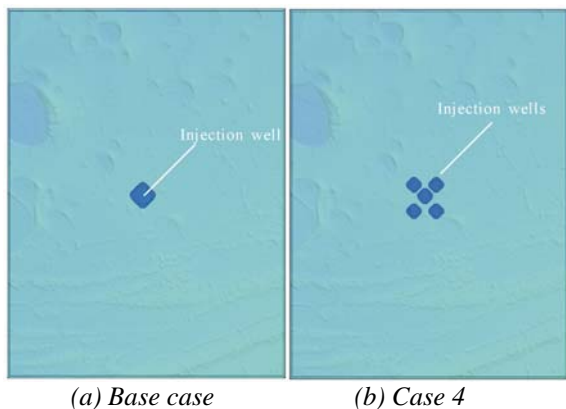


Figure 10. Simulated CO₂ plumes (30 years since injection)

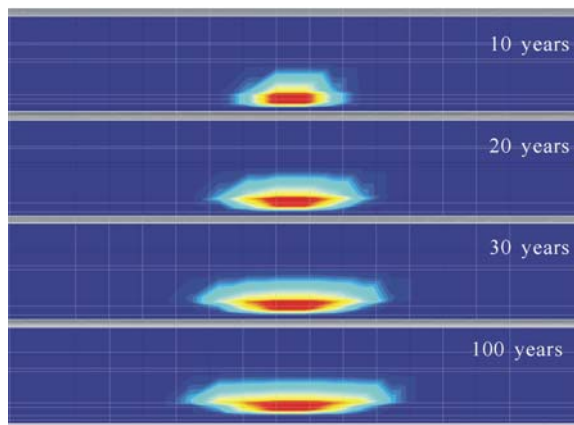


Figure 11. CO₂ plume on a cross section during and after injection (base case)

Pressure buildup

In this section, we evaluate the large-scale pressure perturbations in the subsurface in response to CO₂ injection. Pressure buildup at the injection points was about 10 bars. Figure 12 shows spatial distribution of calculated pressure buildup on a cross section, showing that the pressure buildup can occur over a wide area of the region. Figure 13 shows vertical-pressure profiles at the injection point at the time of 30 years. This result suggests that significant pressure buildup can occur in shallow aquifers. For the sensitivity cases, the comparison of pressure buildup at 200 m depth at the injection point is shown in Figure 14. As expected, the larger the seal permeability, the higher the pressure buildup—within the simulation, the seal permeability is the most important factor for pressure buildup. It is obvious from Figure 12 and Figure 14 that the permeability of the sealing layers has a strong effect on both the vertical and the lateral pressure propagation. Figure 15 shows that for a total annual rate of 30 MtCO₂/year injection, using five wells can reduce

pressure buildup compared to using one well. Given these results, well optimization should be taken into account when planning industrial-scale CO₂ storage projects in deep saline aquifers.

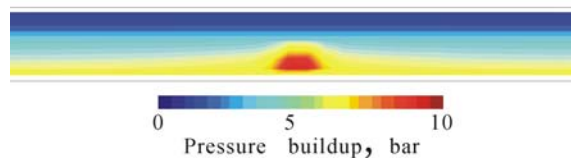


Figure 12. Distribution of pressure buildup

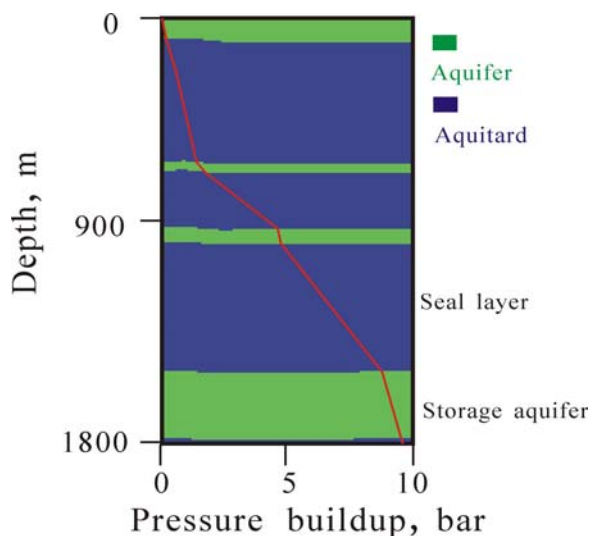


Figure 13. Pressure buildup changes in depth at 30 years of injection

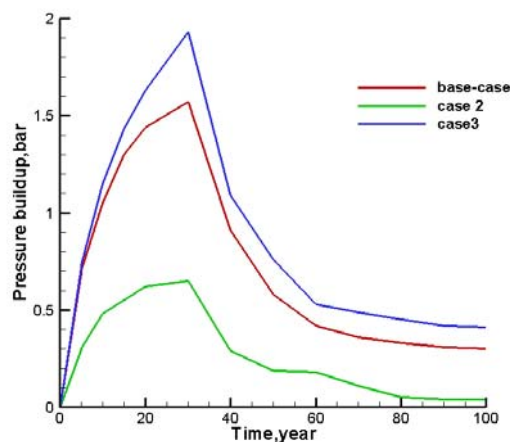


Figure 14. Comparison of pressure buildup in base case, Case 2, and Case 3

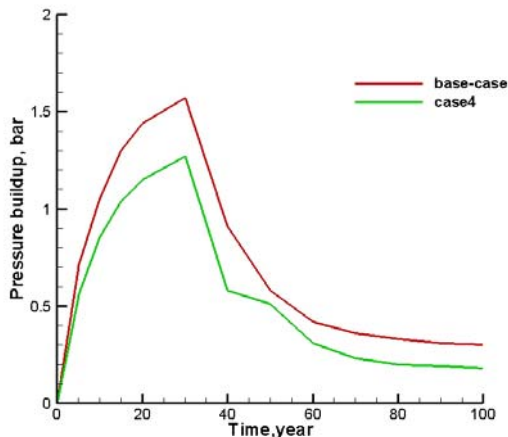


Figure 15. Comparison of pressure buildup in base case and Case 4

CONCLUSION

Through numerical modeling of an idealized representation of the subsurface formations at the Daqingzi Oilfield in the Songliao Basin, China we have simulated CO₂ migration and evaluated the impact of large-scale CO₂ geologic storage in deep saline aquifers. According to our simulations, large-scale pressure changes appear to be of more concern to groundwater resources than changes in water quality, due to (for example) the lateral migration of saline waters. Also, seal permeability appears to have a significant impact on pressure buildup. As a result, the pressure buildup in the storage formation can be strongly reduced compared to that obtained for a perfect seal with zero or close-to-zero permeability. Pressure perturbation of shallow units may occur only when the permeability of sealing layers is comparably high. Also, CO₂ injection well optimization should be considered to reduce pressure buildup. The results show that it is very important to evaluate the large-scale hydrologic perturbations generated by CO₂ storage, and to that end, sensitivity studies should be conducted during site assessment. In the future, the hydrogeological model will be improved, and more detailed geologic structure will be represented in the model.

REFERENCES

- Bergman, P.D., Winter, E.M., Disposal of carbon dioxide in aquifers in the US, *Energy Conv. Manage*, 36, 523–526, 1995.
- Birkholzer, J.T., Zhou, Q., Tsang, C.F., Large-scale impact of CO₂ storage in deep saline aquifers: a sensitivity study on pressure response in stratified systems, *Int. J. Greenhouse Gas Control*, 3 (2), 181–194, 2009.
- Holloway, S., Underground sequestration of carbon dioxide—a viable greenhouse gas mitigation option, *International Symposium on CO₂ Fixation and Efficient Utilization of Energy*, 30(11-12), 2318–2333, 2005.
- Huang H., Jie Yang, Yufeng Yang, and Xiujuan Du, Geochemistry of natural gases in deep strata of the Songliao Basin, NE China, *Int. J. Coal Geol.*, 58, 231-244, 2004.
- Nicot, J.P., Evaluation of large-scale CO₂ storage on fresh-water sections of aquifers: an example from the Texas Gulf Coast Basin, *Int. J. Greenhouse Gas Control*, 2, 582–593, 2007.
- Pruess, K., C. Oldenburg, and G. Moridis, *TOUGH2 User's Guide, Version 2.0*, Report LBNL-43134, Lawrence Berkeley National Laboratory, Berkeley, Calif., 1999.
- Pruess, K., *ECO2N: a TOUGH2 fluid property module for mixtures of water, NaCl, and CO₂*, Report LBNL-57952, Lawrence Berkeley National Laboratory, Berkeley, Calif., 2003.
- Yamamoto H, Keni Zhang, Kenzi Karasaki, Atsunao Maruic and Hitoshi Ueharad, Noriaki Nishikawad, Numerical investigation concerning the impact of CO₂ geologic storage on regional groundwater flow, *Int. J. Greenhouse Gas Control*, 3, 586–599, 2009.
- Zhang W., Yilian Li, Tianfu Xu, Huilin Cheng, Yan Zheng, and Peng Xiong, Long-term variations of CO₂ trapped in different mechanisms in deep saline formations: A case study of the Songliao Basin, China, *Int. J. Greenhouse Gas Control*, 3, 161–180, 2009.

INTEGRATED MODELING OF BASIN- AND PLUME-SCALE PROCESSES RELATED TO GEOLOGIC CARBON SEQUESTRATION IN THE ILLINOIS BASIN

Jens Birkholzer and Quanlin Zou
Lawrence Berkeley National Laboratory
Earth Sciences Division
Berkeley California
JTBirkholzer@lbl.gov

ABSTRACT

If employed at the scale necessary to help mitigate climate change, geologic carbon sequestration (GCS) may be conducted in the near future at multiple storage sites in a sedimentary basin. Assessment of GCS-induced flow and transport processes at the basin scale will then become important, in addition to the transport processes of stored and potentially leaking CO₂ at the plume scale. In this research, an integrated high-performance model for basin- and plume-scale transport processes was applied to a hypothetical scenario of CO₂ injection and storage in the extensive Mt. Simon Formation in the Illinois Basin, USA. A three-dimensional unstructured mesh was generated with grid resolution adequate for detailed modeling of multiscale transport processes. Local mesh refinement was achieved around 20 hypothetical injection sites, spaced approximately 30 km apart within the center of the basin. The two-phase CO₂-brine flow at the plume scale and the single-phase density-dependent brine flow at the basin scale were simulated using a parallel version of the TOUGH2/ECO2N simulator. Our simulation results suggest that the small-scale layering within

the Mt. Simon Formation helps retard upward migration of CO₂ and thereby reduces adverse impacts of CO₂ buoyancy on the integrity of the regional seal. No plume interference is expected between individual storage operations. However, injection-induced pressure perturbations propagate quickly away from injection sites, interfere with other storage operations after less than a year, and eventually reach the basin margins. A pressure increase of a few bar is predicted as far as 200 km from the basin center, affecting northern Illinois, where valuable groundwater resources exist in overlying freshwater aquifers. If local conduits existed there, e.g., permeable faults and/or open boreholes, such a pressure increase could cause upward migration of native brine.

RELATED PUBLICATION

Birkholzer, J.T. and Zhou, Q. (2009) Basin-Scale Hydrogeologic Impacts of CO₂ Storage: Capacity and Regulatory Implications, International Journal of Greenhouse Gas Control, published online on 8/8/2009, DOI: 10.1016/j.ijggc.2009.07.002.

INJECTION OF ACID GAS MIXTURES IN SOUR OIL RESERVOIRS: ANALYSIS OF NEAR-WELLBORE PROCESSES USING TMGAS

Alfredo Battistelli⁽¹⁾, Paola Ceragioli⁽²⁾, Marica Marcolini⁽¹⁾

(1) RISAMB Dept., Environmental Engineering Unit, Saipem SpA (Eni Group), 61032 Fano (PU), Italy

(2) TERA Dept., E&P Division, Eni SpA, 20097 San Donato Milanese (MI), Italy

e-mail: alfredo.battistelli@saipem.eni.it, paola.ceragioli@eni.it, marica.marcolini@saipem.eni.it

ABSTRACT

The reinjection of sour or acid gas mixtures is often required for the exploitation of hydrocarbon reservoirs containing remarkable amounts of acid gases (H₂S and CO₂) to reduce the environmental impact of field exploitation and provide pressure support for enhanced oil recovery (EOR) purposes. Sour and acid gas injection in geological structures can be modeled with TMGAS, a new EOS module for the TOUGH2 reservoir simulator. TMGAS can simulate the two-phase behavior of NaCl-dominated brines in equilibrium with a non-aqueous (NA) phase, made up of inorganic gases such as CO₂ and H₂S and hydrocarbons (pure as well as pseudocomponents), up to the high pressures (~100 MPa) and temperatures (~200°C) found in deep sedimentary basins.

This work is focused on the near-wellbore processes driven by the injection of acid gas mixtures in a hypothetical high-pressure sour oil reservoir at a well sector scale and at conditions for which the injected gas is fully miscible with the undersaturated oil. Relevant coupled processes are simulated—including the displacement of oil originally in place, the evaporation of connate brine, the salt concentration and consequent halite precipitation, as well as nonisothermal effects generated by the injection of the acid gas mixture at temperatures lower than initial reservoir temperatures.

INTRODUCTION

The exploitation of hydrocarbon reservoirs containing remarkable amounts of acid gases (H₂S and CO₂) is increasing all over the world, requiring appropriate reservoir engineering management approaches. Among them, the reinjection of sour or acid gas mixtures is often considered to reduce the environmental impact of field exploitation and provide pressure support for EOR purposes. For instance, the injection of sour and acid gas mixtures is a common practice in Canada (IEA, 2003; Bachu and Gunter, 2004) and is now applied in other regions where many sour oil and gas reservoirs are located, such as the North Caspian basin and the Middle East. One conventional scheme used to reinject gas mixtures containing acid gases is composed of: the separation of acid gases from the sour hydrocarbon mixture; the multistage compression of the gas mixture; the piping

of compressed gas; and the injection through suitable wells. With respect to reservoir behavior, the numerical modeling of injected mixtures requires reservoir simulators able to model phase equilibria, evaluate fluid-phase properties, and solve mass- and heat-balance equations in multiphase compositional environments. Gas injection promotes the displacement of oil originally in place with the potential for EOR. Under fully miscible conditions, gas injection may provide the complete displacement of reservoir oil. On the other hand, the recirculation of gas, particularly when the acid gas content is higher in the injected gas than in oil, may increase the costs for sourer hydrocarbon treatment and handling at surface. The injection of sour and acid gases, which are undersaturated with respect to water at reservoir conditions, drives a suite of near-wellbore processes that need to be evaluated to assess the possible changes in injectivity over time. The connate brine present at irreducible saturation behind the gas displacement front is progressively evaporated, due to the solubility of water in the injected gas. At the dryout front, NaCl concentration increases until salts precipitate, potentially affecting formation porosity and permeability. The increase in gas fugacities drives the solution of CO₂ and H₂S in the reservoir brines, promoting changes in chemical equilibria in the aqueous phase and fluid-rock interactions able to modify the porosity and permeability distribution in the formations interested by gas injection.

We briefly review the main characteristics of the TMGAS EOS module (Battistelli and Marcolini, 2009) developed for the TOUGH2 V.2.0 reservoir simulator (Pruess et al., 1999). Then we discuss the processes occurring around a vertical injection well when the injected acid gas mixture is fully miscible with the undersaturated reservoir oil, using a simple 1D radial model for which the results can be described in terms of a similarity variable. Finally, a 2D radial model is used to show how the transients occurring in the injection well may affect the displacement of oil and the abovementioned near-wellbore processes. The near-wellbore processes described are similar to those occurring when injecting supercritical CO₂ in a natural gas reservoir (Giorgis et al., 2007) where the aqueous phase is present at saturation levels close to the irreducible saturation.

THE TMGAS EOS MODULE

TMGAS (Battistelli and Marcolini, 2009) is a new EOS module developed for the TOUGH2 V.2.0 reservoir simulator starting from TMVOC (Pruess and Battistelli, 2002). It can model the injection within deep geological structures of mixtures of greenhouse or acid gases. TMGAS can simulate the two-phase behavior of NaCl-dominated brines in equilibrium with non-aqueous (NA) phases made up of inorganic gases, such as N₂, CO₂ and H₂S and hydrocarbons (pure as well as pseudo-components).

The NA phase can be either in gas, supercritical, or condensed conditions, with the limitation that such conditions cannot coexist within the same grid element. The PR EOS (Peng and Robinson, 1976) with the Soreide and Whitson (1992) modifications is used for phase equilibria calculations. Specifically, CO₂-brine and H₂S-brine binary interactions coefficients for the aqueous phase were calibrated by reproducing the solubility calculations performed with the accurate EOSs developed by Duan and Sun (2003) and Duan et al. (2007), respectively. NA phase density is computed using the PR EOS, accounting for the conventional volume shift correction (Penelux et al., 1982), whereas departure enthalpy and dynamic viscosity are computed using the LK EOS (Lee and Kesler, 1975) and the Friction Theory Model (Quiñones-Cisneros et al., 2001), respectively. Brine properties are evaluated using enhanced versions of the correlations implemented in the EWASG EOS module (Battistelli et al., 1997) for water and sodium chloride mixtures.

ACID GAS INJECTION SIMULATIONS

TOUGH2-TMGAS is used to simulate the processes driven at a well-sector scale by the injection of an acid gas mixture in a hypothetical high-pressure sour oil reservoir, at conditions for which the injected gas is fully miscible with the undersaturated oil.

Petrophysical properties

Reservoir formation is assumed to be a homogeneous porous medium with a vertical to horizontal permeability ratio of 10. Main reservoir petrophysical properties are shown in Table 1.

Table 1. Reservoir petrophysical properties

Horizontal permeability	$3 \times 10^{-15} \text{ m}^2$
Vertical permeability	$3 \times 10^{-16} \text{ m}^2$
Porosity	0.10
Rock grain density	$2700 \text{ kg} \cdot \text{m}^{-3}$
Rock heat conductivity	$2.50 \text{ W} \cdot \text{m}^{-1} \cdot \text{°C}^{-1}$
Rock specific heat	$950 \text{ J} \cdot \text{kg}^{-1} \cdot \text{°C}^{-1}$
Pore compressibility	$4.5 \times 10^{-10} \text{ Pa}^{-1}$

The aqueous phase (AQ) relative permeability is described using a van Genuchten formulation with an irreducible water saturation of 0.20, whereas a Corey's formulation is used for the NA phase relative permeability. A connate water saturation of 0.10 is assigned; consequently, the relative permeability is 1 and 0 for the NA and the AQ phases, respectively. The capillary pressure is described using a van Genuchten formulation, even though it has no practical effect, with NA the only mobile phase. The permeability reduction due to halite precipitation is described using the series tube model of Verma and Pruess (1988) with a residual porosity of 0.60 and a fraction length of wider pore of 0.80.

Initial conditions and fluids composition

Initial reservoir pressure and temperature of 50 MPa abs and 100°C are assigned to the reservoir formation. A 2 molal NaCl concentration is assumed for the connate brine. The composition of the under-saturated sour oil in equilibrium with the connate brine is listed in Table 2. Oil composition is described using six pure components, including CO₂ and H₂S, and two pseudocomponents whose mass fraction amounts to about 0.60. Relevant pseudocomponent properties are listed in Table 3.

Table 2. Composition of reservoir oil at equilibrium with the 2 molal NaCl connate brine at 50 MPa and 100°C

Component	Molar fract.	Mass fract.
H ₂ S	0.1500	0.0934
CO ₂	0.0500	0.0402
CH ₄	0.4500	0.1319
C ₂ H ₆	0.0500	0.0275
C ₃ H ₈	0.0500	0.0403
C ₅ H ₁₂	0.0500	0.0659
C ₆₋₈	0.1000	0.1700
C ₉ ⁺	0.0939	0.4288
H ₂ O	0.0061	0.0020

Table 3. Properties of pseudocomponents

Comp.	T _C (K)	P _C (bar)	V _C (l/mol)	ω	MW
C ₆₋₈	525	32	0.36	0.29	93
C ₉ ⁺	760	16	0.91	0.73	250

We consider that the acid gases are captured from the gas phase separated at the surface from the produced two-phase oil-gas mixture. For simplicity, without performing any flash calculations, we assume that the composition of the acid gas mixture to be injected is that listed in Table 4. The density, dynamic viscosity, and water content at equilibrium with the connate brine of both reservoir oil and injected gas are listed in Table 5 at initial reservoir conditions and at a lower temperature of 60°C, to highlight the effect of temperature on fluid properties. In fact, downhole injection temperature is likely to be lower than reservoir temperature as a function of wellhead injection temperature, heat transfer between the tubing and surrounding rock formations, and Joule-Thomson effects. Table 5 shows that injected gas has a higher density and a lower viscosity than reservoir oil. As a consequence, its mobility is higher, and the displacement of oil with the acid gas will be characterized by an unfavourable mobility ratio. It should also be noted that the acid gas mixture can have a water content 10 times higher than the reservoir oil.

Table 4. Composition of dry acid gas injection mixture

Component	Mole fract.	Mass fract.
H ₂ S	0.6750	0.66659
CO ₂	0.2250	0.28692
CH ₄	0.1000	0.04649

Table 5. Main properties of reservoir oil and injected acid gas mixture

	Reservoir conditions (100°C, 50 MPa)		Injection conditions (60°C, 50 MPa)
	Wet reservoir oil	Dry Injection Mixture	Dry Injection Mixture
Density (kg/m ³)	566.33	703.69	786.51
Viscosity (Pa·s)	.1527×10 ⁻³	.0975×10 ⁻³	.1279×10 ⁻³
Mobility (s/m ²)	3.71×10 ⁺⁶	7.22×10 ⁺⁶	6.15×10 ⁺⁶
Mobility Ratio	-	1.95	1.66
Water content	2.0×10 ⁻³	4.3×10 ⁻²	2.0×10 ⁻²

1D radial simulation (similarity solution)

The suite of processes driven around the well during the injection of the acid gas mixture is first analyzed by modeling the constant rate injection in a large 1D radial system whose behaviour is infinite-acting and can be described in terms of a similarity solution (O'Sullivan, 1981). The reservoir formation has a thickness of 100 m and is discretized using a 1D radial grid, starting with an initial radius of 0.05 m and extending to a total radius of 100 km with 500 grid elements. By an appropriate choice of the first grid increment, the grid constructed using the MESHMAKER facilities available in TOUGH2 has node coordinates following a logarithmic progression. The injection takes place on the inner element on the axis of the radial grid, whereas the outer boundary element is held at constant conditions equal to the initial reservoir conditions. Rock petrophysical properties, oil and injection gas compositions are those listed in Tables 1, 2, and 3, respectively. The acid gas mixture is injected at a constant rate of 10 kg/s with an enthalpy corresponding to 60°C at initial reservoir pressure. The pressure and temperature distribution after 30 days and 6 months of gas injection are shown in Figure 1 as a function of the similarity variable. The distribution at 6 months is identical to that at 30 days, proving that the numerical solution preserves the similarity nature of the problem. Figure 1 shows that the reservoir is not yet affected by the injection for similarity values exceeding ~6 m²/s; the oil-gas displacing front is located at a similarity value of 2×10⁻⁴ m²/s. The change in the pressure gradient shown in Figure 1 is linked to the different mobilities of oil and acid gas mixtures.

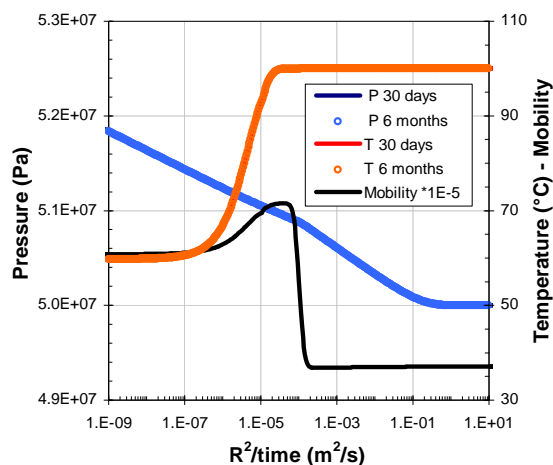


Figure 1. *P* and *T* profiles as a function of the similarity variable after 30 days and 6 months of constant acid gas injection

The positions of the displacement and dryout fronts are better shown in Figure 2, where the profiles of AQ saturation, H₂S, and C₉⁺ mass fractions in the NA phase are displayed. The change of pressure gradient

clearly corresponds to the gradual change from the oil to the acid gas composition, with the increase in H_2S concentration and the complete displacement of the C_9^+ pseudo-component. The mobility profile in Figure 1 also shows the effect of temperature: the maximum mobility is reached in a narrow zone where the injected gas has been warmed up to the initial reservoir temperature, while it is slightly lower where the injected gas is still at the lower injection temperature. Between the dryout and displacement fronts, the solution of CO_2 and H_2S due to the increase in their fugacity determines a slight swelling

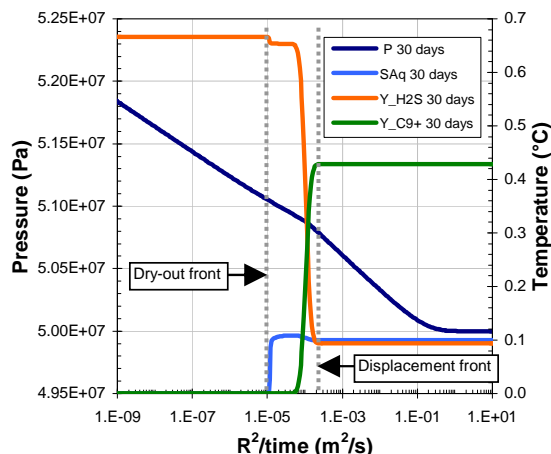


Figure 2. P , AQ saturation, H_2S and C_9^+ mass fraction in the NA phases as function of the similarity variable.

of the connate water phase (Figure 3). Close to the dryout front, the evaporation of water into the dry injected gas drives the rapid concentration of salt, which finally precipitates. Halite saturation is constant, as the brine is immobile and the $NaCl$ initially dissolved in it precipitates locally. Diffusive fluxes, albeit present, give a negligible contribution to the salt mass balance. Note that the acid gas mixture can hold a considerable amount of water; as a consequence, the dryout front travels slightly faster than the thermal front, and the two-phase zone between the dryout and the displacement fronts is practically at, or close to, the initial reservoir temperature. In a previous paper, Battistelli and Marcolini (2009) showed for a similar application that the injected sour gas mixture (60% CH_4 , 30% H_2S and 10% CO_2) held a lower amount of water, and the dryout front was always located within the zone already cooled at the injection temperature.

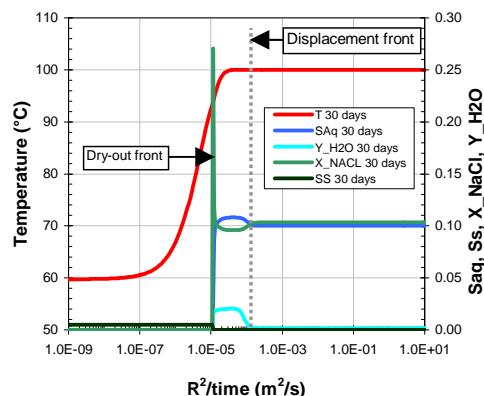


Figure 3. T , AQ and Ss saturation, $NaCl$ brine mass fraction, and water content in the NA phase as a function of the similarity variable

Finally, it is interesting to highlight the effects on the AQ phase composition: the mass fraction of injected gases in the AQ phase is shown in Figure 4. Their solubility is affected mainly by the change of NA phase composition, as the temperature and salinity effects are localized in a narrow zone in proximity of the dryout front. The increased solubility of the acid gases, CO_2 and H_2S , between the dryout and the displacement fronts suggests that this is the more reactive area, where the strong changes in aqueous phase composition can drive rock-water reactions.

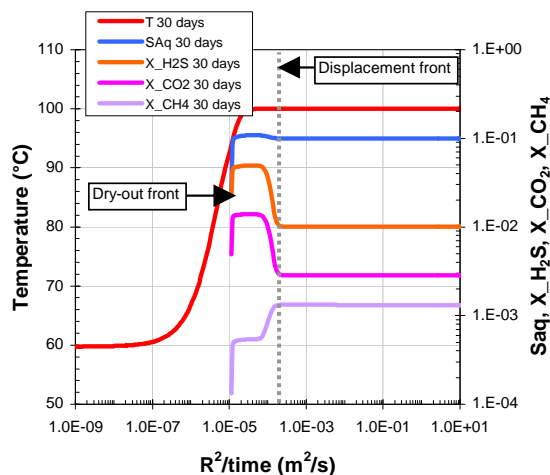


Figure 4. T , AQ saturation, and mass fraction of H_2S , CO_2 and CH_4 in the AQ phase as a function of the similarity variable

From the 1D radial simulation, it can be observed that the major effects on the injection pressure come from the mobility change linked to the displacement of reservoir oil by the more mobile acid gas. The nonisothermal injection reduces the acid-gas mobility by about 10%, a change high enough to be taken into account for a reliable prediction of injection requirements. On the other hand, the halite precipitation is so low ($Ss=5 \times 10^{-3}$) that no major effects on forma-

tion permeability are likely to occur. With the permeability reduction function chosen, rock permeability is reduced to 98% of its initial value. This conclusion can be extended to all cases in which dry gas injection takes place in an oil reservoir with an immobile AQ phase having low initial saturation: the amount of salt per unit formation volume is low, and no local accumulation processes are possible, because the AQ phase is immobile.

2D radial simulations

Two-dimensional simulations are performed by discretizing the 100 m thick reservoir formation into 10 layers of equal thickness, with the injection wellbore explicitly modeled with a column of elements on the axis of the cylindrical grid. The wellbore has a 0.1 m radius. The *reservoir grid* has 100 additional elements with node radial coordinates increasing, following a logarithmic progression from 0.1 m up to 1400 m; a further grid increment from 1,400 to 1,420 m is added on the lateral grid boundary. Wellbore flow from the surface down to a depth of 3,000 m, assumed to be the depth of reservoir-caprock contact, is explicitly modeled using a 2D radial grid divided into 29 layers of 100 m thickness and two layers of 50 m thickness at the top and the bottom of the grid. The acid gas is injected into a tubing string modeled with a column of elements of 0.05 m radius located on the grid axis and connected with the top element of the reservoir grid representing the wellbore. The *tubing grid* has 20 additional radial grid increments reaching an outer radius of 50 m to model the conductive heat transfer from the tubing towards the surrounding rock formation. While the acid gas is injected at a constant rate of 10 kg/s and at constant enthalpy, the reservoir oil is extracted from the top element of the outer column of the *reservoir grid* at a constant rate of 20 kg/s. The dimensions of the cylindrical well sector are chosen to approximately emulate a 5-spot well pattern with injectors and producers located on the opposite corners of a 1,000 m side square.

2D simulation: Darcy's law for tubing flow

The first simulation is performed modeling the friction losses within the tubing string using Darcy's law. Tubing elements have unit porosity and a vertical permeability of $1 \times 10^{-6} \text{ m}^2$, which is evaluated to give friction losses equivalent to those computed with the conventional equation for turbulent flow in a cylindrical conduit having an internal radius of 0.05 m and a surface roughness of $1 \times 10^{-4} \text{ m}$. Due to the oil extraction at the lateral radial boundary at a mass rate, which is twice that of injected acid gas, the reservoir pressure is soon controlled by the oil production as shown in Figure 5.

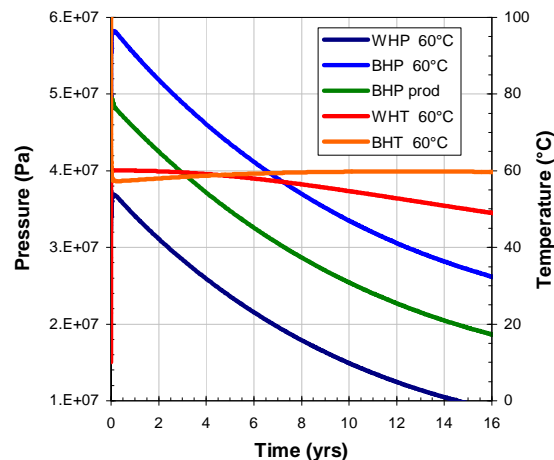


Figure 5. WH and BH pressure and temperature at the injection well, and BHP at the production element as a function of time.

Bottomhole pressure (BHP) at the injection well and production element shows a nearly constant pressure gradient throughout the reservoir. Figure 5 clearly shows that this exploitation strategy cannot sustain the reservoir pressure at levels sufficient to guarantee the assigned extraction rate for times greater than about 10 years, when the pressure at the production element falls below 25 MPa. WHT and BHT at the injection well change slowly after the rapid initial transient. WHT declines after 4 years because of WHP decline, because the injection is performed at constant enthalpy. Tubing flow is dominated by pressure and temperature transients only at early times, as shown in Figure 6 where WH and BH parameters are plotted as a function of the logarithm of time. After < 9 hours, BH temperature is nearly constant, and the WHP is almost entirely affected by the pressure losses in the reservoir. The evolution of flowing pressure profile within the tubing is shown at different injection times in Figure 7.

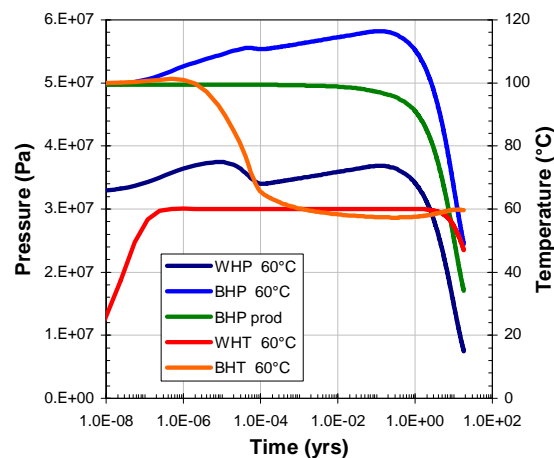


Figure 6. WH and BH pressure and temperature at injection well, and BHP at the production element on logarithmic time scale

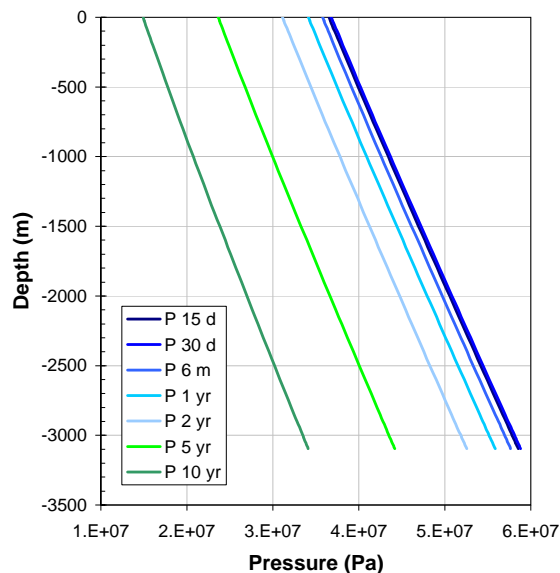


Figure 7. Tubing flowing pressure profile at different injection times

The maximum pressure is obtained after about 1 month of injection, whereas, as time proceeds, the flowing pressure profile is mainly controlled by the reduction of average reservoir pressure due to the modeled exploitation scenario. In spite of pressure and temperature effects, the pressure gradient is almost constant over the tubing length. The flowing temperature profiles in Figure 8 show that temperature variations in the 3,000 m tubing are quite low, between 52°C and 60°C. Cooling prevails in the upper half, where the injected acid gas is hotter than the surrounding rock formation; warming occurs in the lower half, where the injected gas loses heat towards the surrounding rocks.

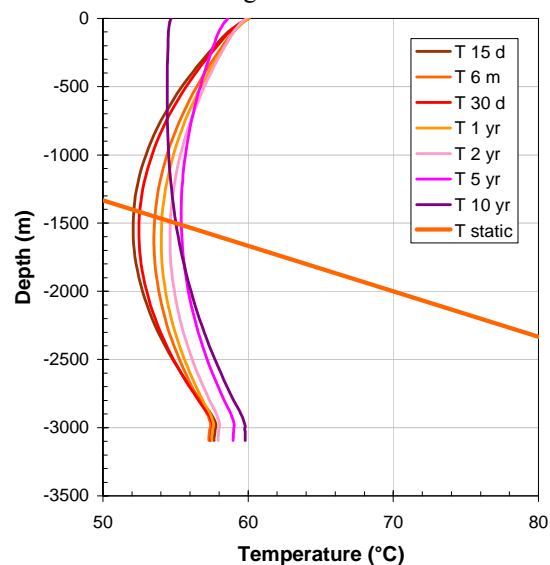


Figure 8. Tubing flowing temperature profile at different injection times

As for the processes occurring within the reservoir formation, the description made for the infinite acting 1D radial reservoir basically applies to the injection in the 2D radial well sector. Even though there is a consistent difference in fluid densities, and the injected acid gas mixture is denser than reservoir oil, density driven flow does not develop due to: (i) the high radial pressure gradient driven by the fairly high injection rate (0.1 kg/(s m)) and the extraction at the outer boundary; and (ii) the high contrast between horizontal and vertical permeability. As a result, the injection rate is distributed almost uniformly over the 10 layers in which the reservoir formation is discretized. The vertical profiles of acid gas flux at the wellbore-reservoir interface are shown at different injection times in Figure 9. In spite of the evolution shown, with an increase in the upper section and a decrease in the lower one, the difference between upper and lower injection fluxes remains on the order of $\pm 1\%$ only. As a consequence, the velocity of displacement, thermal, and dryout fronts is almost the same in every layer. Since the aqueous phase is immobile, evaporation processes and halite precipitation are uniformly distributed in all layers.

It can be concluded that for the simulated conditions in which the horizontal pressure gradients dominate over the density driven flow, the solution obtained with a 1D radial model is a good approximation for the more complex 2D radial system. A different scenario can be envisaged if the acid-gas injection is performed close to the oil-water contact where the AQ phase is mobile, as already described by Giorgis et al. (2007) for CO₂ injection in an exploited gas reservoir.

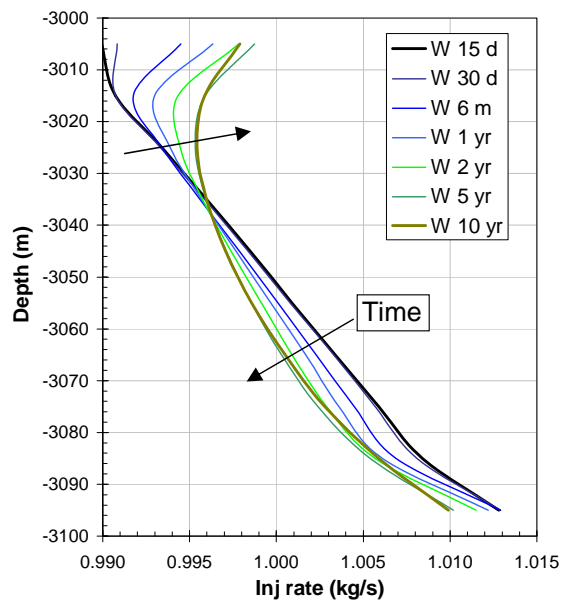


Figure 9. Distribution of injection fluxes (W) into the 10 reservoir grid layers at different injection times

2D simulation: friction losses for tubing flow

For high-density injected acid-gas mixtures, the hydrostatic head usually gives the greatest contribution to the overall pressure head (Carroll and Maddocks, 1999). At a high injection rate, and thus at high fluid speed within the tubing, the contribution of frictional pressure losses may become significant, and their evaluation needs to be improved compared to the simple application of Darcy's law available within TOUGH2 V.2.0. Disregarding the acceleration pressure drop, the change in pressure along the vertical tubing is described according to:

$$dP = \rho g dz \pm \frac{2f}{D\rho} \left(\frac{W}{A}\right)^2 dz \quad (1)$$

where g is the acceleration of gravity, f the Fanning's friction factor, D the conduit internal diameter, A the conduit cross sectional area, and W the mass flow rate. The sign of friction loss term depends on the direction of flow with respect to the vertical axis z . The previous simulation was performed using a vertical permeability for tubing grid elements computed to give pressure losses with Darcy's law equal to those computed with eq. (1). By equating Darcy's and frictional losses for single-phase flow:

$$\frac{W\mu}{k\rho A} = \frac{2f}{D\rho} \left(\frac{W}{A}\right)^2 \quad (2)$$

the equivalent absolute permeability can be evaluated:

$$k = \frac{\mu AD}{2fW} \quad (3)$$

where the Fanning's friction factor can be evaluated on the Moody's diagram as a function of Reynolds' number or with a suitable correlation, such as that given by Churchill (1977), which conveniently covers both laminar and turbulent flow regimes at any conduit relative roughness values. The previous simulation is replicated with a modified version of MULTI subroutine in which pressure losses are computed using Equation (1). At the injection rates experienced under field conditions, the Reynolds number is often so high that the Fanning's friction factor is a function of the relative conduit roughness only. When:

$$Re > 3500 \frac{\varepsilon}{D} \quad (4)$$

the Fanning's friction factor is given by:

$$f = \frac{0.25}{(1.14 - 2\log(\varepsilon/D))^2} \quad (5)$$

Under the constraint given by Equation (4), the mass flow W through the generic tubing connection is computed inside MULTI using Equation (6) below,

where the sign depends on the direction of flow along the generic connection:

$$W = \pm A \sqrt{\left[\frac{dP}{dz} + \rho g \right] \frac{D\rho}{2f}} \quad (6)$$

Equation (6) takes care of the changes in fluid density due to pressure and temperature transients within the tubing, whereas the previous approach requires the preliminary calculation of the equivalent Darcy's absolute permeability at average density, viscosity, and fluid mass rate. WHP and WHT as a function of time obtained with the original and the modified code versions are shown in Figure 10. Except for a lower WHP evaluated by the modified code version at very early times, the solutions are in good agreement, suggesting that in this particular case, with limited temperature transients within the tubing, the approaches are equivalent. The lower WHP calculated at early times with the modified code results from the fact that at the very beginning of injection, the fluid velocity is low, and the approximation made to compute the Fanning's friction factor fails.

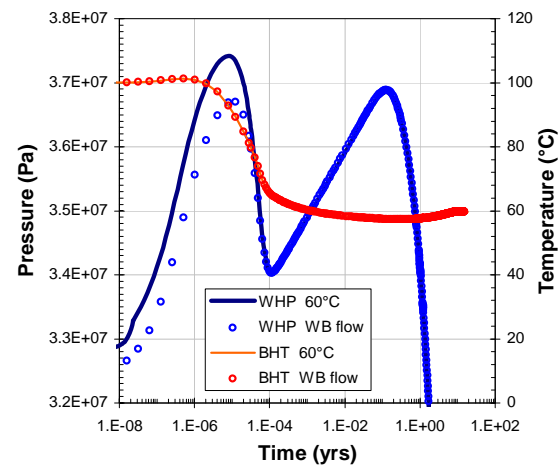


Figure 10. WH pressure and temperature at the injection well: friction losses vs Darcy's law for tubing flow.

It must be pointed out that the approaches followed for wellbore-flow simulation can be applied to single-phase flow when flowing conditions evolve smoothly and acceleration pressure losses can be neglected. Rapid changes in flow rate, when high compressible fluids are present, cannot be handled in a reliable way, and a true wellbore flow approach needs to be applied, as done by Pan et al. (2009) for the ECO2N EOS module of the TOUGH2 simulator.

CONCLUSIONS

TMGAS, a new EOS module developed for the TOUGH2 V.2.0 reservoir simulator, has been used to model injection at a well-sector scale of an acid-gas mixture into a high-pressure undersaturated sour oil

reservoir. At the reservoir conditions modeled, the acid gas is fully miscible with the sour oil, which can then be completely displaced. One-dimensional radial simulation of constant rate injection shows the development of three distinct fronts traveling at different speed from the injection well into the reservoir: the oil-gas displacement, the dryout, and the thermal fronts. The dryout front corresponds to the complete evaporation of connate brine by the injected dry acid gas. NaCl concentration and precipitation of halite occurs close to the dryout front, with only minor effects on formation permeability. As already shown in previous work (Giorgis et al., 2007) dealing with the GHG injection in gas reservoirs, the immobile AQ phase originally in place prevents any localized vaporization and halite precipitation. The simulation also suggests that a reliable evaluation of injection pressure requires nonisothermal effects to be taken into account.

Two-dimensional radial simulations of acid-gas injection and oil production at a well-sector scale are performed to simulate the flow within the injection tubing and the reservoir flow in a coupled fashion—to evaluate, in a realistic way, the evolution of wellhead pressure as a function of time. Because of the high horizontal pressure gradient between the injection well and the lateral boundary where oil extraction takes place, density-driven flow is negligible in the reservoir, and the suite of processes described with the 1D simulation apply to the 2D simulation as well. At the relatively high injection pressure simulated (10 kg/s), temperature transients within the tubing are limited, and injection BHT is nearly constant around values close to the injection WHT. Because both temperature and pressure affect the fluid density and then the hydrostatic head term, a reliable modeling of transient tubing flow is mandatory for WHP evaluation. An attempt to improve tubing flow calculation within the TOUGH2 simulator has been made by calculating the friction losses with the conventional equation for turbulent flow in cylindrical conduits, in a modified version of subroutine MULTI. Results obtained are in good agreement with the calculations performed using Darcy's law, provided that the correct equivalent tubing vertical permeability is used.

TMGAS successfully accomplished the challenging simulation of acid-gas-mixture injection into a sour high-pressure oil reservoir, accounting for nonisothermal, compositional, brine evaporation, and halite precipitation processes.

ACKNOWLEDGMENTS

The TMGAS EOS module was developed within R&D programs sponsored and coordinated by Eni E&P Division, who also sponsored the R&D project within which the present work was performed.

REFERENCES

- Bachu, S., and W.D. Gunter, Overview of acid-gas injection operations in Western Canada. In: Rubin, E., Keith, D., Gilbo, C., (Eds), Proceedings of the 7th Intl. Conf. on Greenhouse Gas Technologies, Sept. 5-9, 2004, Vancouver, BC, 2004.
- Battistelli A. and M. Marcolini, TMGAS: a new TOUGH2 EOS module for the numerical simulation of gas mixtures injection in geological structures, *Intl. J. Greenhouse Gas Control*, 3, 481-493, 2009.
- Battistelli A., C. Calore and K. Pruess, The simulator TOUGH2/EWASG for modelling geothermal reservoirs with brines and a non-condensable gas. *Geothermics*, 26, 4,437-464, 1997.
- Carroll J.J and J.R. Maddocks, Design considerations for acid gas injection. Laurance Reid Gas Conditioning Conf., Oklahoma, Feb. 1999, pp. 26.
- Churchill S.W., Friction factor equation spans all fluid flow regimes. *Chem. Eng.*, Vol. 84, pp. 91-92, 1977.
- Corey A. T., The interrelation between gas and oil relative permeabilities. *Producers Monthly*, 38-41, November, 1954.
- Duan, Z.H., and R. Sun, An improved model calculating CO₂ solubility in pure water and aqueous NaCl solutions from 273 to 533 K and from 0 to 2000 bar. *Chem. Geol.*, 193, (3-4), 257-271, 2003.
- Duan, Z.H., R. Sun, R. Liu, and C. Zhu, An accurate thermodynamic model for the calculation of H₂S solubility in pure water and brines. *Energ. Fuel*, 21(4), 2056-2065, 2007.
- Giorgis, T., M. Carpita, and A. Battistelli, 2D modeling of salt precipitation during the injection of dry CO₂ in a depleted gas reservoir. *Energ. Convers. Manag.* 48, 6, 1816-1826, 2007.
- International Energy Agency, 2003. Acid gas injection: A study of existing operations. Phase 1: Final Report. Greenhouse gas R&D Programme, Report n. PH4/18.
- Lee B.I. and M.G. Kesler, A generalized thermodynamic correlation based on three-parameter corresponding states, *AICHE J.*, 21, 3, 510-527, 1975.
- O'Sullivan, M.J., 1981. A similarity method for geothermal well test analysis. *Water Resour. Res.*, 17, 2, 390-398.
- Pan L., C.M. Oldenburg, Y.-S. Wu, and K. Pruess, Wellbore flow model for carbon dioxide and brine. *Energy Procedia*, 1, 1, 71-78, 2009.

- Peneloux, A., E. Rausy, and R. Freze, A consistent correction for Redlich-Kwong-Soave volumes, *Fluid Phase Equilib.*, 8, 7-23, 1982.
- Peng D.Y. and D.B. Robinson, A New Two-Constant Equation of State. *Ind. Eng. Chem. Fund.* 15, 59-64, 1976.
- Pruess K., C. Oldenburg, and G. Moridis, *TOUGH2 User's Guide, Version 2.0*, Report LBNL-43134, Lawrence Berkeley National Laboratory, Berkeley, CA, 1999.
- Pruess K. and A. Battistelli, *TMVOC, a numerical simulator for three-phase non-isothermal flows of multicomponent hydrocarbon mixtures in saturated-unsaturated heterogeneous media*. Report LBNL-49375, Lawrence Berkeley National Laboratory, Berkeley, CA, 2002.
- Quiñones-Cisneros, S.E., C.K. Zéberg-Mikkelsen, and E.H. Stenby, The friction theory for viscosity modeling: extension to crude oil systems, *Chem. Eng. Sci.*, 56, 7007-7015, 2001.
- Soreide, I., and C.H. Whitson, Peng-Robinson predictions for hydrocarbons, CO₂, N₂, and H₂S with pure water and NaCl brine. *Fluid Phase Equilib.*, 77, 217-240, 1992.
- van Genuchten, M.Th., A closed-form equation for predicting the hydraulic conductivity of unsaturated soils. *Soil Sci. Soc.*, 44, 892-898, 1980.
- Verma, A. and K. Pruess. Thermohydrologic conditions and silica redistribution near high-level nuclear wastes emplaced in saturated geological formations. *J. Geophysical Res.*, 93, B2, 1159-1173, 1988.

MODELING OF CO₂ LEAKAGE THROUGH AN ABANDONED WELL FROM A DEEP SALINE AQUIFER TO FRESH GROUNDWATER

Pascal Audigane, Christophe Chiaberge, Julie Lions, and Pauline Humez

BRGM, French Geological Survey
3 Avenue Claude Guillemin, BP 36009
45000, Orléans, Cedex 2, France
e-mail: p.audigane@brgm.fr

ABSTRACT

This paper presents a numerical modeling of CO₂ geological storage in a deep saline aquifer directly connected to an overlying, shallow, potable water aquifer by a leaky abandoned well. The objective of such modeling is to assess the complete path of migration for supercritical CO₂, from the injection storage zone to the shallow aquifer. Because of density differences, the CO₂ migrates upwards through the leaky well, approximated as a 1D vertical porous medium.

Estimates are obtained of the CO₂ migration rate and CO₂ amounts arriving as a free gas state, dissolving first in the storage waters and then in the water of the overlying aquifer. Also assessed are the impacts on water quality in terms of chemical composition and mineral phase representative of the porous rock, by estimating fluid-rock interactions in both aquifers. To perform such estimates, we used the reactive transport code TOUGHREACT. Specific local grid-mesh refinement techniques for this code have been developed to reduce numerical dispersion near injection and leaky wells.

Finally, one case study is presented using the Paris Basin context. The Dogger formation is considered as the geological target for storage. This geological formation has been extensively used for geothermal purposes and is now under consideration as a target for the French national program of greenhouse gas emission reduction and CO₂ geological storage. The Albien Aquifer, situated above the Dogger Aquifer, may therefore be considered as one of the potable water aquifers potentially impacted by leaky CO₂ in case of integrity failure. Simulations presented in this study aim at helping in defining guidelines and selecting criteria with respect to environmental risks.

INTRODUCTION

In the context of carbon dioxide geological storage, potential leakage of CO₂ back into the atmosphere, while considered unavoidable in the long term, is acceptable if it is small enough—that is, less than 1% of the stored volume (Hepple and Benson, 2003). Investigations of CO₂ leakage through abandoned wells have been extensively performed by means of analytical or semi-analytical solutions, and applied to

(for example) the province of Alberta, Canada, where the density of wells is particularly high (Nordbotten et al., 2005). Such well leakage models serve as inputs for certification framework and risk analysis (Oldenburg et al., 2009).

Numerical modeling offers an alternative method for risk assessment, including a better description of the geological features and also a coupling between hydrological, thermal, and geochemical processes. But numerical modeling performance is limited by mesh resolution and time of calculations. Benchmark studies provide a way to evaluate codes performance and precisions. So far, two main studies have been conducted in the context of carbon capture and storage (CCS), providing the pertinent status of actual code performance (Pruess et al., 2004; Class et al., 2009). Our contribution to the benchmark study proposed by Class et al. (2009) and using TOUGH2 is described in this paper. Local grid refinement (LGR) was essential for successfully fitting the proposed analytical solution. Three-dimensional visualization-tool implementation became crucial for easily handling output files from a TOUGH2 run.

We extend our domain application from this benchmark experience to a case study of potential leakage through an abandoned well, considering the Dogger Aquifer (Paris Bassin, France) as the storage target. The assumed leaky well is connected to an overlying freshwater aquifer (Albien Formation). The geochemical impact on water quality is assessed using the geometrical configuration developed for the benchmark study, and using TOUGHREACT for reactive transport modeling of the simulated leakage, utilizing a pertinent data set for implementing the hydrogeological and hydrogeochemical properties of the 3D model.

WORKFLOW

The need for 3D model geometry and a fluid-flow run execution of heterogeneous media is of great importance when simulating carbon dioxide injection into saline aquifers at the basin scale. Developments of a GUI (Graphical User Interface) for handling TOUGH2 and TOUGHREACT simulation runs have been already investigated by several authors (Sato et al., 2003; Burnell et al., 2003; Alcott et al., 2006;

Pan, 2008). The main advantage of these GUIs are the very user friendly interface supplied for 3D model elaboration, the gridding options (Voronoi mesh generation), and the postprocessing visualization. On the other hand, one main drawback of these GUIs is the lack of flexibility, because of the integrated aspect of the tool, meaning that in case of slight modifications, the GUI user is strongly dependent on the GUI developers. Therefore, an ensemble of modules coded in Fortran (and therefore easily modifiable to a specific requirement) that are able to create, execute, and postprocess TOUGH2 and TOUGHREACT models has been developed for CCS purposes (Chiaberge, 2009; Audigane et al., 2009). The main objective is to provide modules able to use input and output files from a TOUGH2/TOUGHREACT run.

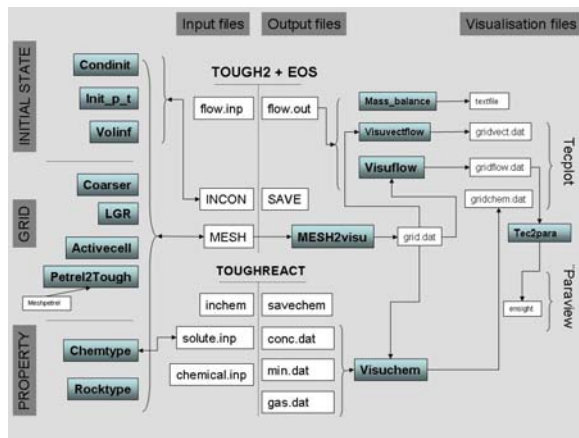


Figure 1. Workflow chart description for handling TOUGH2 and TOUGHREACT models

The chart description of the modules represented in Figure 1 summarizes the 15 modules developed for elaborating the workflow. The gridding elaboration is limited to a Cartesian mesh, but LGR, coarsening, and inactive cell options can be managed. Outputs are provided in Tecplot (<http://www.tecplot.com/>) or Paraview (<http://www.paraview.org/>) format. Heterogeneous property assignment is managed for both hydrodynamics and geochemical processes. So far, the workflow has been tested with the ECO2N, EOS7C, and EOS3 modules. A direct application with the ECO2N module is presented in the next section. Every module is described in the User's Manual in Chiaberge (2009) or in Audigane et al. (2009).

BENCHMARK (STUTTART UNIVERSITY)

University of Stuttgart recently submitted a problem-oriented benchmark assessing code performance for CCS modeling (Class et al., 2009). Three exercises on modeling multiphase hydrodynamics have been proposed. We participated in Problem 1.1, dedicated

to “CO₂ plume evolution and leakage through an abandoned well.”

Problem 1.1 Description

Problem 1.1 aimed at determining the CO₂ flux rate of a leaky abandoned well simulated as a porous 1D vertical medium, situated 100 m from the injection point (Figure 2). The lateral extension of the model is 1,000×1,000 m.

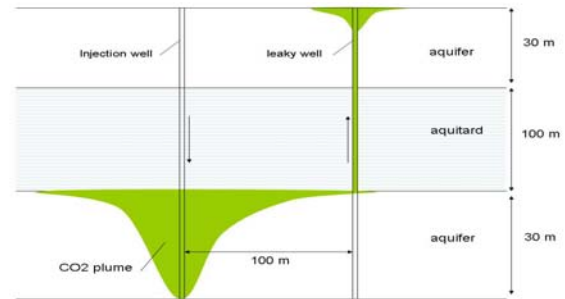


Figure 2. Benchmark Problem 1.1 description (Class et al., 2009)

Aquifer and aquitard hydrodynamic parameters are simplified in order to compare simulation results with the semi-analytical solution (Nordbotten et al., 2005). The aquitard is assumed to be completely impermeable, and permeability and porosity is homogeneous for both aquifers. The storage zone is considered deep enough (~3,000 m) to keep the density and viscosity of water and CO₂ constant and independent of pressure and temperature. Capillary pressure is neglected, and relative permeability models are assumed linear.

Mesh

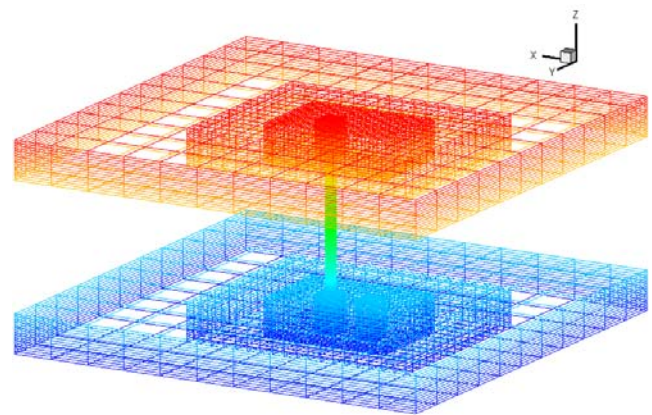


Figure 3. 3D Mesh built with the workflow for Problem 1.1 of the Stuttgart Benchmark

To build up the model, we first create a 3D grid with the **MESHMAKER** tool provided by TOUGH2. This 3D grid includes the storage aquifer and the overlying aquifer, as well as the impermeable

aquitard. Then, using the **LGR** module (Figure 1), we refined locally around the leaky well for the entire domain, and around the injection well inside the storage aquifer exclusively. Finally, using the **Activecell** module, we removed all the gridblocks defining the aquitard domain except those located at 1 m around the leaky well. **Mesh2Visu** allows the visualization of the final 3D grid mesh (Figure 3). Using the **Init_p_t** module, we initialized the pressure for the entire system (temperature is assumed constant for this exercise). Constant hydrostatic pressure was imposed on each side of the grid with the module **Volinf**.

Comparison with analytical solution

Flow rate inside the leaky well is estimated according to the percentage of leaky CO₂ rate versus the injected rate. A comparison between the TOUGH2 simulation results and a semi-analytical solution shows good agreement (Figure 4).

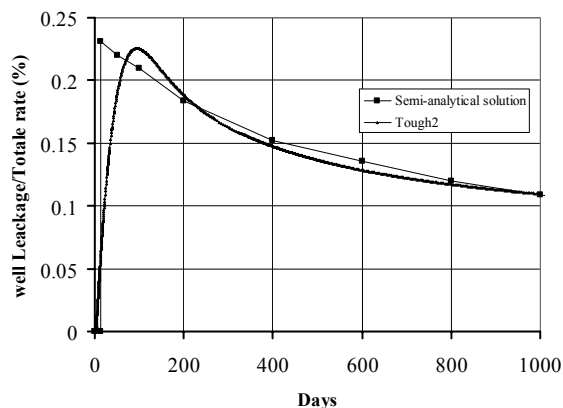


Figure 4. Comparison between TOUGH2 run and semi-analytical solution for the leaky rate in Problem 1.1 of the Stuttgart Benchmark

Results differ mainly because of the grid resolution and associated numerical dispersion, which becomes crucial near the wells. The main difference is observed in the maximum rate, which is predicted earlier with the semi-analytical model. More explanations and results from other codes can be found in Class et al. (2009).

APPLICATION TO PARIS BASIN

Our main concern in this study is the dissolution of minerals in the aquifer induced by the lowering of the pH, a lowering directly connected to the ingress of CO₂ in the system. Indeed, after being injected, supercritical CO₂ will dissolve in the brine to produce H⁺ ions and therefore decrease the pH in the system. At the same time, this release of H⁺ is buffered by the dissolution of minerals, mainly carbonates. This brine enriched with CO₂, in combination with supercritical CO₂ is intended in our scenario to leak through the

1D porous-medium column to reach the overlying freshwater aquifer. The mineralogical composition of this impacted aquifer is therefore crucial for correctly estimating which elements may possibly be released during the arrival of CO₂ and dissolved CO₂ in fresh water.

Geological context

The intracratonic Paris Basin (France) was a quasi-continuous subsidence and sedimentary site during Mesozoic time. It is made up of a maximum of 3 km in indurated sediments from the Triassic to the Tertiary, resting on a basement (Guillocheau et al., 2000). This complex, multilayered aquifer system provides two suitable aquifers (Triassic and Dogger) for large-scale CO₂ storage in a deep saline aquifer. In this study, we consider CO₂ injection into the Dogger Aquifer and observe the impact of leakage on the Albian fresh groundwater. The study area is located in southeast of the Paris Basin (Figure 5).

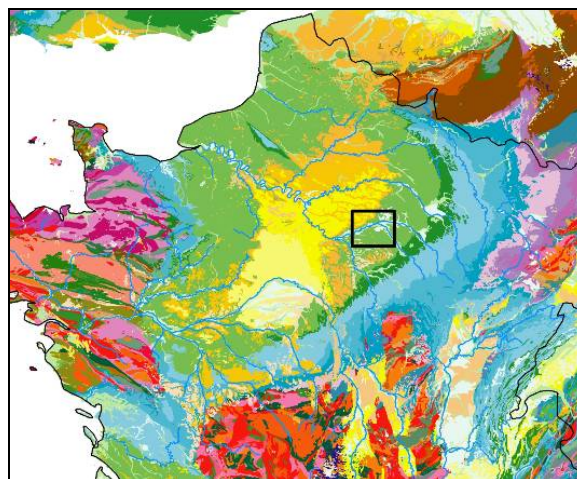


Figure 5. Site localization and geological units of the northern part of France.

Hydrogeology

The aquifer investigated for CO₂ storage is in the Middle Jurassic (Dogger) aquifer in the center of the Paris Basin, at a depth of 1,500–2,000 m. This aquifer, exploited for geothermal and petroleum resources, is mainly composed of carbonates. Sedimentary studies of this aquifer (Rojas et al., 1989) show that the most permeable facies, the oolitic limestone, retains or even increases its initial porosity by fracturing and dissolution. The groundwater in the Dogger, recharged by meteoric water, flows from the east and southeast to the center of the Basin. Wei et al. (1990) estimated, by modeling, the Darcy average horizontal velocity in the Dogger, to be on the order of 0.33 m.y⁻¹, in the southern area of Paris.

The Albian confined aquifer, a sandy, multilayered aquifer, covers an area of about 75 000 km² in the Paris Basin (Raoult et al. 1997). An upward vertical flow from the Neocomian aquifer (up to 24%), located under the Albian aquifer, has been measured in the Paris area. Nevertheless, in the present area of interest, vertical flow is not significant and not considered in the model. The Cenomanian Chalk Aquifer, located above the Albian aquifer, does not contribute to its recharge.

Hydrogeochemistry

The aquifer is mainly composed of quartz, glauconite, kaolinite, muscovite, carbonates (siderite, calcite, dolomite), phosphates, barite, and pyrite (Mégnyen 1980). The Albian waters present several chemical compositions according to their recharge origins, with some constant characteristics. Albian waters are anoxic with high concentrations of Fe, pH around 7 and low mineralized (0.3 to 0.6 g/L). The present study is based on average chemical composition measured in the study area.

The Neocomian aquifer, above the Albian confined aquifer, is characterized by high concentrations of Na and Mg, as well as F and Sr. The influence of Neocomian waters on the Albian waters is observed for the NW Paris area, but not in the study area, confirming the absence of vertical flow (Raoult et al. 1997).

Numerical modeling

Flow modeling

In the model, we consider only the oolitic limestone to be the productive layer of the Dogger aquifer. The Albian multilayer aquifer is represented as a homogeneous layer formation (Vernoux et. 1997), because the aquitards are not continuous. Injection of CO₂ is simulated into the Dogger Aquifer, represented as a horizontal formation with a thickness of 30 m and an area of 5 by 5 km, at a representative depth of 1525 m. The Albian Aquifer is also represented as a horizontal formation 80 m thick, with an extension of 3 by 3 km at 625 m deep. The abandoned well is simulated as a 1D porous media connecting the two aquifers, located 100 m away from the injection well, with a horizontal area of 5 by 5 m and a length of 820 m. Mesh refinement has been applied with inactivation of the cap-rock gridblocks to build up a 3D model of the scenario with 5326 mesh elements (Figure 6). Hydrogeological parameters chosen for each formation are summarized in Table 1.

Table 1. Hydrogeological parameters

Dogger		Albian	Leak
Pressure (bar)	57	150	gradient
porosity	0.12	0.2	0.15
K (m ²)	6.67E-13	1E-9	1E-8

Pressure and temperature gradients, applied to initiate calculations though simulation runs, are performed in an isothermal mode in the following (Figure 7). Temperature at the top of the Dogger fm. corresponds to the isotherm measured in the considered area (Brosse et al., 2007), while for the Albian formation it was determined from measured temperatures.

Log temperature was based on geothermal gradients of 3°C/100 m for Albian aquifer and 4°C/100 m for Dogger aquifer. A hydrostatic pressure was initialized using a pressure value at the top of the Albian formation of 57 bar.

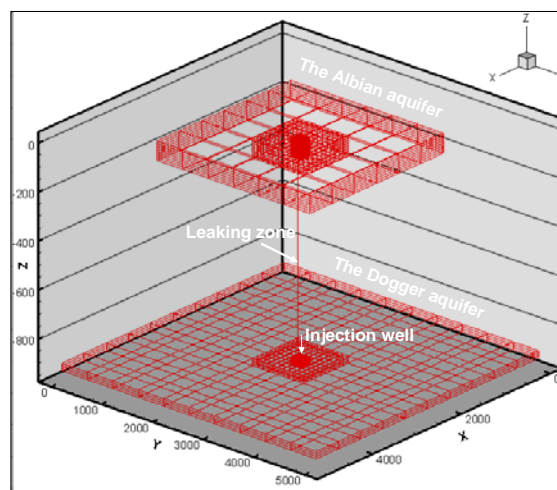


Figure 6. 3D mesh representation for modeling leakage from the Dogger Aquifer to the Albian formation, through an abandoned well simulated as a 1D porous media

Multiphase hydrodynamic parameters are more difficult to constrain. We use a conventional van Genuchten model with the Sleipner field parameters (Utsira sandstone) to describe relative permeability and capillary pressure curves (Table 2).

Table 2. Multiphase hydrodynamics parameters

Relative permeability (Van Genuchten)	
$\lambda = 1 - 1/n$	0.63
Residual liquid phase saturation (Slr)	0.05
Liquid phase saturation (SlS)	1.0
Irreducible gas saturation (Sgr)	0.2
Capillary pressure (Van Genuchten)	
$\lambda = 1 - 1/n$	0.63
Residual liquid phase saturation (Slr)	0.05
Po (Pa)	1400
Initial liquid phase saturation (SlS)	1.0

Geochemical Batch modeling

The first step involves elaborating a geochemical system representative of each aquifer according to measured data, for describing the mineralogical and aqueous-phase compositions of each media. All chemical elements likely to have a quantitative influence on dissolution or precipitation reactions have to be taken into account. To constrain the geochemical model, we need iterative procedures between modeling assessment and calibration with measured data compiled in the literature.

The initial geochemical conditions for the three domains were determined using the following different assumptions:

- Since the Dogger fm. is mainly composed of calcite (until 99%), other minerals are neglected as a first stage in the study. Water analysis from Rojas et al. (1989) is used for constraining the composition of the brine (Table 3).
- The equivalent mineralogy of the Albian formation (Table 3) was determined using Phreeqc. These calculations were made using analysis of water from several wells located in the study area, to simulate a water composition similar to the mean of the observed chemical compositions (Table 3).
- The leaky abandoned well defined as a 1D porous column is composed of a similar chemical composition to the Albian for the aqueous phase without any solid-phase minerals (Table 3).

Table 2. Chemical composition of the solid and liquid phase for the three domains

	Dogger	Albian	Leak
range Temp. (°C)	65 – 66.2	30-32.4	32.4-65
pH	6.7	7.36	7
pCO ₂ (bar)	0.183	0.0141	0.0141
Salinity (g.kgw ⁻¹)	5	1	1
Minerals (Vol %)			
Calcite	100	19.2	-
Glauconite	-	14.43	-
Quartz	-	49	-
Siderite	-	2.18	-
Kaolinite	-	15.23	-
Pyrite	-	0.5	-
Elements (mol/kgw)			
[Ca]	2.26e ⁻³	1.54e ⁻³	1.54e ⁻³
[Na]	7.74e ⁻²	8.65e ⁻⁵	8.65e ⁻⁵
[Fe]	1.60e ⁻⁵	3.01e ⁻⁵	3.01e ⁻⁵
[CO _{2aq}]	7.48e ⁻³	3.11e ⁻³	3.11e ⁻³
[Cl]	6.96e ⁻²	8.58e ⁻⁵	8.58e ⁻⁵
[Mg]	-	1.01e ⁻⁴	1.01e ⁻⁴
[K]	-	5.93e ⁻⁵	5.93e ⁻⁵
[SiO _{2aq}]	-	9.40e ⁻⁵	9.40e ⁻⁵
[Al]	-	8.74e ⁻⁹	8.74e ⁻⁹
[SO ₄ ²⁻]	-	3.02e ⁻⁴	3.02e ⁻⁴

In the simulation, calcite siderite dissolution and precipitation are considered at equilibrium, while for the others minerals, kinetic parameters are taken into account according to the rates and kinetic laws proposed by Palandri and Kharaka (2004).

Reactive transport modeling

Injection is conducted with a rate of 9 kg/s (0.3 Mt/y) over the entire thickness of the Dogger fm. divided into three cells (3 kg/s by cell). We keep the system open by imposing constant pressure at the lateral boundary of both aquifers. No regional flow is assumed in the first stage of the study. Since the lateral extension is limited to 2.5 km away from the injection point, the impact of a close boundary condition may play a role in the flow system (see discussion in Nordbotten et al., 2005). Therefore, we limit the scenario to a 5-year injection period.

According to this scenario, supercritical CO₂ reaches the Albian formation after 90 days (Figure 7) at a flow rate of 0.2 kg/s, which rises to 1.38 kg/s after 5 yrs at the end of the simulation. CO₂ intrusion is accompanied by water with a flow rate decreasing from 0.028 kg/s after 90 days to 0.004 kg/s after 5 years. After 5 years of injection, the lateral extension of the gas bubble in the Dogger fm. reaches ~1,300 m around the injection point, in which a few tens of meters are completely flushed by dried supercritical CO₂.

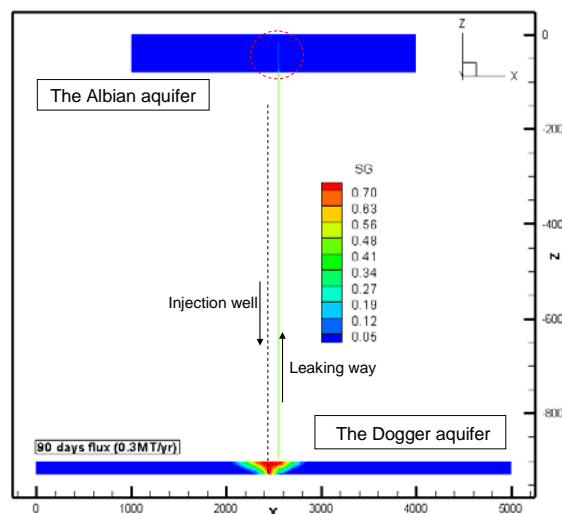


Figure 7. Gas phase saturation after 90 days

The gravity effect and the impact of vertical permeability are clearly visible in both aquifers. In the Dogger fm., the CO₂ injection rate is high enough so that the gas phase lighter than the brine reaches the top of the formation, forming a reverse bell shape envelope of gas where CO₂ dissolves (Figure 8). On the opposite, when the gas phase slowly migrates through the leaky zone and enters the Albian aquifer,

only the 1D vertical column is invaded by the gas. Because the permeability is much higher in the Albian formation, the enriched CO₂ liquid phase, heavier than the brine, drops down to the bottom of the Albian aquifer faster than the upward migration of the gas (Figure 8).

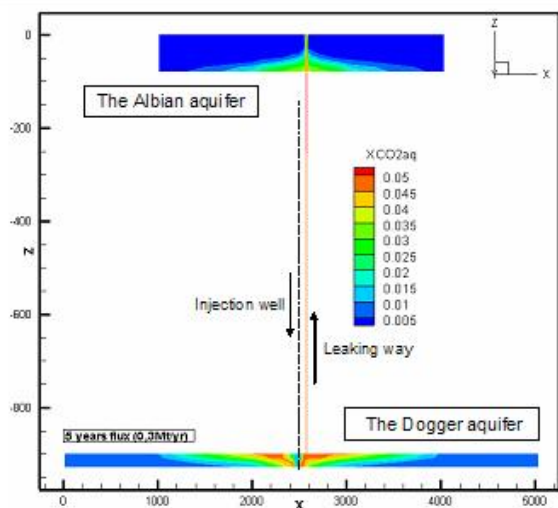


Figure 8. Dissolved CO₂ (in mol/kgw) after 5 years

During its upward migration, CO₂ density is modified as pressure and temperature of the system is correlated to depth. From these calculations, CO₂ is injected under supercritical conditions into the Dogger before switching progressively to a gas state at the Albian depth (Figure 9).

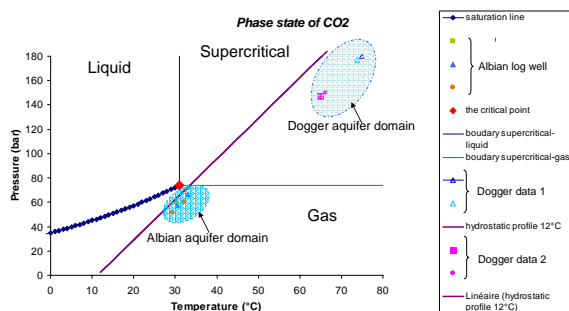


Figure 9. CO₂ phase states for Dogger fm. and Albian formation based on data from Brosse et al. (2007); André et al. (2007); Vernoux et al. (1997).

The decrease in pH precisely follows the dissolved CO₂ pathway; after 5 years of injection, the extension of pH in the lowering zone reaches about 1 km around the leaky well in the Albian formation (Figure 10).

Looking at the geochemical modifications in the aqueous and solid phases of the system, at the exit

point of the leaky well in the Albian formation, provides information on the correlation between gas saturation arrival and pH buffering (from 7.3 to 4.9), along with dissolution of CO₂ in the aqueous phase (from 3 mmol/kgw to 1.36 mol/kgw) (Figure 10).

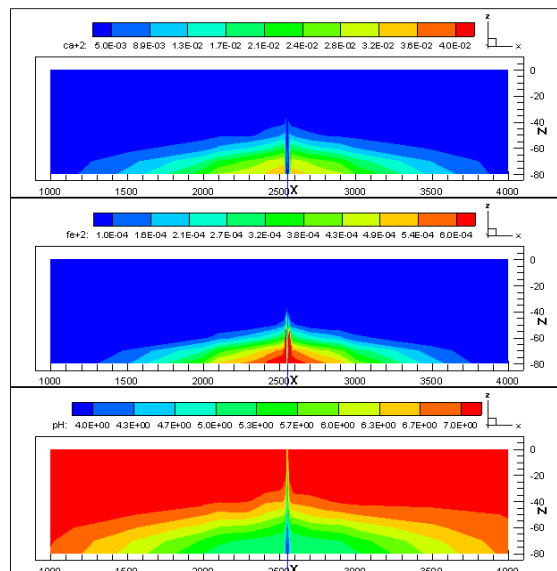


Figure 10. Aqueous concentrations (Ca, Fe in mol/kgw) and pH in Albian formation after 5 years

The solution becomes undersaturated with regard to most of the minerals contained in the Albian aquifer (and initially in equilibrium with the chemical elements), owing to the dissolution of solid phases, affecting porosity, permeability, and chemical composition modifications in the water formation.

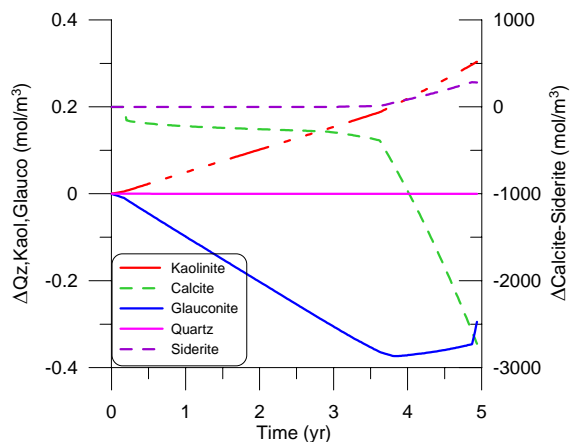


Figure 11. Evolution of mineral phases during CO₂ arrival in the Albian formation (cell at the top of the leaking well) during CO₂ leakage.

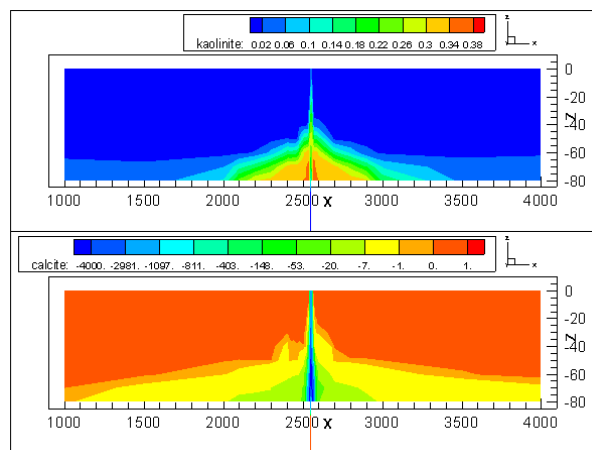


Figure 12. Calcite and kaolinite variation after 5 yr in Albian formation (in mol/m³ of porous media)

As can be observed in Figure 11, calcite and glauconite start to dissolve at the CO₂ intrusion point, with a high and rapid impact on the concentrations of calcium and iron. Figure 12 shows that calcite dissolution is mainly localized above the intrusion point, with small impact around it. Indeed, in the first cell, localized just above the leaky well, calcium concentration increases from 1.72 to 41.7 mmol/kgw and iron concentration increases from 16.10 to 831 μmol/kgw, which is significant. In fact, iron is not a health concern at concentrations normally observed in drinking water, but the taste and appearance of water are affected below the health-based value (WHO). In France, health guidelines for iron are set to 3.6 μmol/L. In the Albian aquifer, groundwaters are naturally above this value, and they are already submitted to water treatment. Siderite precipitates over time around the intrusion point, with little impact on iron concentration variation.

Whereas carbonate chemistry and formation of an acid plume due to leakage of CO₂ is well understood, glauconite (phyllosilicate group) dissolution mechanisms are not, and they could play a prominent part in the Albian chemical impact. Dissolution rates for the glauconite were evaluated in Palandri and Kharaka (2004); this entailed a mineral dissolution assumed fast enough to be rapidly in equilibrium with a fast release of iron and siliceous rock, touching off the precipitation of kaolinite and quartz around the intrusion point (Figure 12).

A change in redox conditions causes pyrite dissolution, which releases iron and sulphate elements. Arsenic is often associated with pyrite, and this dissolution of pyrite could impact water quality by releasing the associated arsenic. The impact of CO₂ intrusion on water quality will be characterized to quantify the potential environmental impact of CO₂ leakage on fresh groundwater.

The porosity calculated from solid volume changes, due to mineral dissolution, increases from 0.2 to almost 0.29 and permeability increases from 1.10⁻⁹ to 3.1x10⁻⁹ m² provoking a considerable increase of the flow rate and the amount of CO₂ in the system.

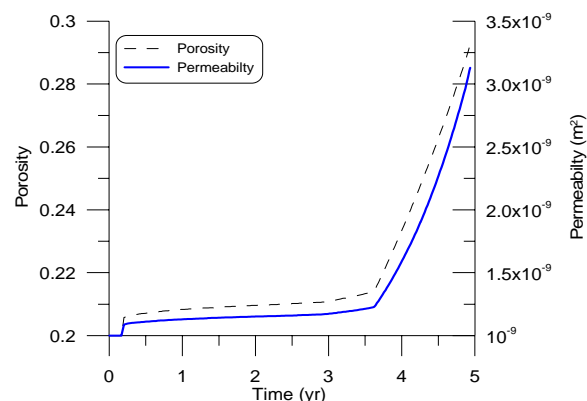


Figure 13. Evolution of porosity and permeability in Albian formation. (cell at the top of the leaking well) during CO₂ leakage.

CONCLUSION

We conducted a modeling study of the geochemical impact on fresh groundwaters of a CO₂ intrusion during geological storage. This work provides a 3D model including (i) the storage saline aquifer, (ii) the impacted overlying aquifer containing freshwaters and (iii) a leaky abandoned well, represented as a 1D porous column. Mesh refinement techniques and specific 3D pre- and postprocessing tools have been developed specifically for this numerical modeling study with TOUGHREACT.

We applied our model to the carbonate saline Dogger Aquifer as a storage reservoir in the Paris Basin, and the Albian formation as a fresh groundwater aquifer. The main geochemical process simulated was acidification of groundwater due to CO₂ dissolution, inducing Albian minerals dissolution and element release. Specific attention was paid to iron, originally present in high concentrations in the geochemical aqueous system. Estimates of increasing element concentrations were presented, simultaneously with a direct control of the injection procedure.

Iron mobilization remains very high in our system, an issue that needs further investigation. Reduction in oxidation levels can also control the mobilization of potential trace elements such as arsenic, known to be associated with pyrite in various quantities, according to the geological settings. In our model, we did not take into account trace elements, or adsorption and desorption processes via surface complexation, which can play a very important role in potential toxic mobilization caused by CO₂ intrusion (Kharaka et al. 2006; Birkholzer et al., 2008). This will be added in the future part of this work.

REFERENCES

- André, L., Audigane P; Azaroual M, Menjot A.. Numerical modeling of fluid-rock chemical interactions at the supercritical CO₂-liquid interface during CO₂ injection into a carbonate reservoir, the Dogger aquifer (Paris Basin, France) *Energy Conversion and Management*, 48(6), 1782-1797, 2007
- Audigane, P., Chiaberge Ch., Mathurin F., Lions J., Picot G., A workflow for handling heterogeneous 3D model with TOUGH2 code's family: application to numerical modeling of CO₂ geological storage, submitted to *Comp. & Geosc.*, 2009.
- Alcott, A., Swenson D., Hardeman B. Using PETRASIM to create execute and post-process TOUGH2 models, in *Proceedings of TOUGH Symposium*, Berkeley, California, USA, May 15-17, 2006
- Birkholzer, J., Apps, J. Zheng, L. Zhang, Y. Xu, T. Tsang., C. Water Quality Effects Caused by CO₂ Intrusion into Shallow Groundwater Lawrence Berkeley National Laboratory Technical Report No. LBL 60000, 450 p, 2008
- Burnell, J.G., S.P., White, K. Osato, and T. Sato, GeoCad, a pre and post-processor for TOUGH2, in *Proceedings of TOUGH Symposium*, Berkeley, California, May 11-14, 2003
- Brosse É., Hasanov V., Bonijoly D., Garcia D., et al., The PICOREF project : Selection of geological sites for pilot CO₂ injection and storage in the Paris Basin, 1st French-German Symposium on Geological Storage of CO₂, Potsdam, June 21st and 22nd, pp 36-37, 2007
- Chiaberge, Ch., Audigane, P., Manuel d'utilisation des outils de pre et post processing pour la modélisation de stockage géologique de CO₂ avec les logiciels TOUGH. Brgm Report RP57457, 50 pp 2009
- Class, H., A., Ebigo, R., Helmig, H. K., Dahle, J. M. Nordbotten, et al., A benchmark study on problems related to CO₂ storage in geologic formations, *Computational and Geosciences*, DOI 10.1007/s10596-009-9146-x, 2009
- Guillocheau F., Robin C., Allemand P., et al., Meso-Cenozoic geodynamic evolution of Paris Basin: 3D stratigraphic constraints. *Geodyn. Acta* vol. 13: pp. 189-246, 2000
- Hepple, R. P., and S. M. Benson, Implication of surface seepage on the effectiveness of geological storage of carbon dioxide as a climate change mitigation strategy. In *Proceedings of the Sixth International Greenhouse Gas Technologies Conference*, Kyoto, Japan, October 1-5, 2002; Gale, J., Kaya, Y., Eds.; Pergamon; Vol. I, pp 261-266, 2003
- Kharaka, Y.K., Cole, D.R., Hovorka, S.D., Gunter, W.D., et al. Gas-water-rock interactions in Frio Formation following CO₂ injection: Implications for the storage of greenhouse gases in sedimentary basins. *Geology* 34, 577-580, 2006
- Mégnyen, C., Mégnyen L., Synthèse géologique du Bassin de Paris. Stratigraphie et paléogéographie. Mémoire BRGM n°101-102-103, Orléans, France. 1980
- Nordbotten, JM; Celia, MA, Bachu, S., Dahle, H.K., Semianalytical solution for CO₂ leakage through an abandoned well, *Environmental Science & Technology*, Vol. 39, pp 602-611, 2005
- Oldenburg, C.M., S.L. Bryant, and J-Ph. Nicot, Certification framework based on effective trapping for geologic carbon sequestration, *International Journal of Greenhouse Gas Control*, Vol. 3, pp 444-457, 2009
- Palandri, J., Kharaka, Y.K., A compilation of rate parameters of water-mineral interaction kinetics for application to geochemical modeling. US Geological Survey Open File Report 2004-1068, 64 p, 2004
- Pan, L., User information for WINGRIDDER Version 3.0, Lawrence Berkeley National Laboratory Report LBNL-273E, University of California, p 76, 2008
- Pruess, K; Garcia, J; Kovscek, T, et al., Code inter-comparison builds confidence in numerical simulation models for geologic disposal Of CO₂, Conference Information: 6th International Conference on Greenhouse Gas Control Technologies, 1-4 Oct. 2002, Kyoto Japan, *Energy*, Vol: 29, Issue: 9-10, pp: 1431-1444, 2004
- Raoult, Y., Boulègue, J., Lauverjat, J. Olive, P., Geochemistry of the Albian aquifer in the Paris Basin area contributes to understanding complex hydrogeological behaviour. *Comptes Rendus de l'Académie des Sciences - Series IIA - Earth and Planetary Science*, vol 325, n°6, pp. 419-425, 1997
- Rojas J., Giot D., Le Nindre Y.-M, Criaud A., Fouillac C. et Lambert M., Caractérisation et modélisation du réservoir géothermique du Dogger Bassin Parisien, France. Rapport Final. BRGM IRG SGN 89, 1989
- Sato, T., K., Ohsato, and T. Shiga, G-StAR-BASE (G*BASE)- A data base system for underground information and post-processing for TOUGH2, in *Proceedings of TOUGH Symposium*, Berkeley, Californian, May 12-14 2003
- Vernoux J.F., Maget P., Afzali H., et al., Synthèse hydrogéologique du Crétacé inférieur du Bassin de Paris, rapport BRGM DSGR/IDF R39702, 93p., 1997
- Wei, H.F., Ledoux, E. and Marsily, G.de, Regional modelling of groundwater flow and salt and environmental tracer transport in deep aquifers in the Paris Basin. *J. Hydrol.*, vol 120, pp. 341-358, 1990

DEVELOPMENT OF A COUPLED REACTIVE FLUID FLOW MODEL FOR MINERAL CO₂ CAPTURE IN HELLISHEIDI, ICELAND

Edda S.P. Aradottir^{1,2}, Eric Sonnenthal³, Grimur Bjornsson⁴, Einar Gunnlaugsson² and Hannes Jonsson¹

¹ University of Iceland, Saemundargotu 2, IS-101, Reykjavik, Iceland

² Reykjavik Energy, Baejarhalsi 1, IS-110, Reykjavik, Iceland

³ Lawrence Berkeley National Laboratory, 1 Cyclotron Rd, Berkeley CA 94720, USA

⁴ Reykjavik Geothermal, Kollunarklettsvegi 1, IS-104, Reykjavik, Iceland

e-mail: edda.sif.aradottir@or.is

ABSTRACT

CarbFix, a joint research project of the University of Iceland, Reykjavik Energy, Columbia University, and CNRS in Toulouse, is aimed at studying the behavior of CO₂ injected into basalts.

Geochemical modeling plays an important role in the project, and TOUGHREACT and iTOUGH2 have been used for the development of a coupled reactive fluid flow model of the mineral CO₂ capture. The model is being developed in stages. The first stage consisted of defining physical and chemical properties of the system and developing an internally consistent thermodynamic database. In the current, ongoing second stage, field data is used to calibrate hydrological parameters. Reactive chemistry is then coupled to the model, which consequently can be used to simulate different scenarios for the CO₂ injection. The third and final stage of the reactive fluid flow development consists of validating the model by comparing its numerical results to laboratory and field data.

INTRODUCTION

CO₂ mineral storage in basalts may provide a long lasting, thermodynamically stable and environmentally benign solution to reduce greenhouse gases in the atmosphere. CarbFix, a joint research project of the University of Iceland, Reykjavik Energy, Columbia University, and CNRS in Toulouse, is aimed at studying the behavior of CO₂ injected into basalts.

The Hellisheidi geothermal power project, situated in the Hengill area, SW Iceland, comprises ideal conditions for studying permanent mineral CO₂ storage in basaltic rocks. Reykjavik Energy operates the power plant, which currently generates 213 MW_e and will be expanded to 303 MW_e and 133 MW_{th} in 2010–2011. The power plant currently releases 0.8 kg/s CO₂ of geothermal origin into the atmosphere. The CO₂ emissions will be captured at the power plant and dissolved in water. The CO₂-loaded water will then be re-injected at intermediate depths (400–800 m) into relatively fresh basaltic lavas. As the CO₂-rich and low pH fluid is injected into the basaltic host rock, dissolution reactions will take place,

releasing cations from the basalt into the liquid phase. Once the cations are in aqueous form, they can immobilize the injected CO₂ by reacting with dissolved carbon species to form carbonates.

Figure 1 shows a topological map of the planned CO₂ injection site¹. The site is located ~ 3 km SW of the Hellisheidi power plant. A one-year experimental CO₂ injection will start at Hellisheidi this fall. During the experiment, 0.05–0.07 kg/s CO₂ will be injected into basaltic rocks. If the experiment is successful, full-scale injection could start in 2013–2014.

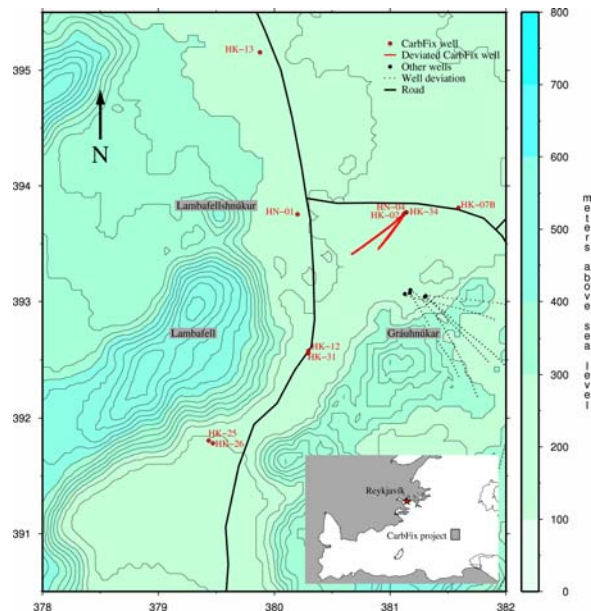


Figure 1. Topological map of the CarbFix target injection zone, located 3 km SW of the Hellisheidi geothermal power plant. CarbFix wells are denoted by red bullets and well deviation by red lines.

Geochemical and hydrological modeling plays an important role in the project, providing tools to predict and optimize long-term management of the

¹ Wells at Grauhnukar will not affect this study. They serve as re-injection wells for brine from the power plant and are cased down to 800 m depth.

injection site, as well as to quantify the amount of CO₂ that can be mineralized.

In this paper, we present development of a reactive fluid flow model that simulates hydrology and mineral alteration associated with injecting dissolved CO₂ into basalts. TOUGHREACT (Xu et al., 2005) and iTOUGH2 (Finsterle, 1999) are used in the model development.

CONCEPTUAL MODEL

Figure 2 shows a simplified cross-sectional view of the reservoir volume that is in consideration in the CarbFix project.

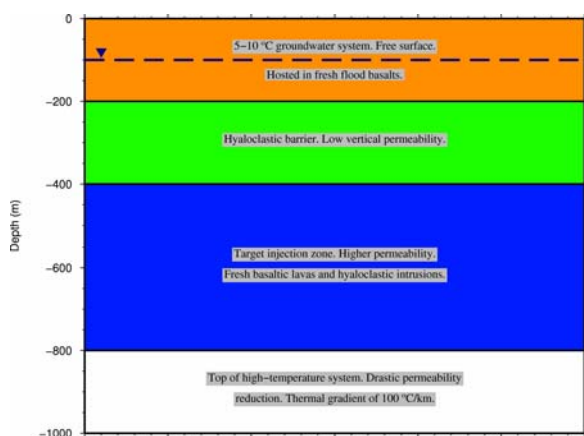


Figure 2. Simplified cross-sectional view of the CarbFix reservoir volume

Fresh flood basalts govern the bedrock from surface down to 200 m depth. These basalts host a cold (5–10°C) groundwater system, with the water table located at about 100 m depth. This groundwater system supplies potable water to nearby communities.

Below the cold groundwater system lies a 200 m thick hyaloclastic layer that ranges down to 400 m depth. This layer has significantly lower vertical permeability than the fresh flood basalts above and the CarbFix target injection zone below, and acts as a barrier, separating these two systems.

The target injection zone extends from about 400 to 800 m depth. It is composed of fresh basaltic lavas interbedded with minor hyaloclastic layers/intrusions. Highest permeability is encountered between 400 and 500 m depth, while good permeability is also found near the base at 800 m depth.

Permeability drops drastically below 800 m depth. This reduction in permeability and changes in secondary mineralogy indicate that the top of the Hengill

high-temperature geothermal system has been reached.

HYDROLOGICAL CHARACTERIZATION

The CarbFix project has ten wells at its disposal. HN-01, HN-02, HN-04, HK-34, HK-26 and HK-31 are drilled through the target injection zone. Wells HK-12, HK-25, HK-7, and HK-13, however, only penetrate the shallow groundwater system. Table 1 gives more detailed information on the CarbFix wells.

Table 1. Depth of CarbFix wells and feed zones between 400 and 800 m. Wells will be used for injection (I), production (P), monitoring the shallow groundwater system (SM) or monitoring the target injection zone (DM).

Well	Depth	Feed zone	Usage
HN-01*	1306	600-725	P, DM
HN-02	1997	520	I, DM
HN-04**	980	420	DM
HK-07B	78.7	X	SM
HK-12	138	X	SM
HK-13	137	X	SM
HK-25	300	X	SM
HK-26	855	400	DM
HK-31	790	400	DM
HK-34**	801	530	DM

* Well HN-01 has several small feed zones below 650 m depth. These are neglected in the model and feed zones only assumed to be at 600-650 m depth.

** Well is deviated.

Water from well HN-01 will be used for dissolving CO₂, and the CO₂ rich water will then be re-injected into well HN-02. The main permeable section in HN-02 is located around 520 m depth, so most of the injected fluid should enter the reservoir there. Wells HN-04, HK-34, HK-31, and HK-26 will serve as monitoring wells in the intermediate target injection zone. Wells HK-31 and HK-26 are located about 1750 and 3,000 m downstream from Well HN-02, while the main permeable zones in HN-04 and HK-34 are at about 70 and 300 m vertical distance from HN-02. Regional groundwater flow is believed to be from NE to SW. Thus, deeper monitoring wells are all downstream from the injection well.

The intermediate target injection zone is believed to be confined from the cold shallow groundwater system by a low-permeable hyaloclastic layer (Figure 2). This is supported by ~2 days lag in water level fluctuations between wells only penetrating the shallow system and wells that are drilled through the intermediate system. Water level changes in wells

HN-04 and HK-13, caused by a 6.3 size earthquake in S-Iceland in June 2008, also confirmed this separation. Water level in HK-13 rose less than 5 cm, whereas water level in HN-04 rose 2 m. The small water-level rise in Well HK-13 is normal for a well connected to a free surface reservoir, but the 2 m rise in HN-04 suggests the well is connected to a confined reservoir.

Two tracer tests have been carried out at the injection site as part of comprehensive research conducted to understand and characterize the nature of the regional ground water flow and estimate the reservoir volume available for CO₂ injection. The tests involve a forced-gradient short-scale tracer test using 0.5 kg sodium fluorescein and a large-scale natural gradient test using 13.8 g sulfur hexafluoride (SF₆) and 50 kg sodium fluorescein. The short-scale tracer test was launched November 13, 2007 and ran until May 26th 2008. Tracer was injected into Well HN-02 as a slug and a gradient forced between HN-02 and HN-04 by continuously pumping 6 kg/s into the previous well (water from HN-01) and producing 10 kg/s from the latter. The short-scale test was followed by a large-scale tracer test, which was launched on June 10, 2008, and is ongoing.

A comprehensive chemistry background monitoring has been ongoing in the CarbFix target injection zone since July 2008. Temperature, pH, alkalinity, conductivity, major and trace elements, dissolved organic carbon, nutrients, ¹⁸O, ¹³C, dD and ³⁴S isotopes have been measured in all CarbFix wells. Loggers that continuously measure temperature and pressure are also located in all deep wells, as well as in three shallow wells.

BASALT ALTERATION

Studies from Iceland and Greenland have shown the mineralogy associated with basalt alteration to be highly affected by CO₂ concentration. At low CO₂ conditions, which are (e.g.) typical for low-temperature (<100°C) geothermal fields in Iceland, alteration products are dominated by clay minerals and zeolites, calcite and chalcedony and/or quartz (e.g. Walker, 1960; Kristmannsdóttir and Tómasson, 1978; Gíslason et al., 1996; Neuhoff et al., 1999). In comparison, secondary minerals commonly associated with basalt weathering are amorphous Al(OH)₃ and Fe(OH)₃, allophane and/or imogolite, opal or chalcedony, kaolinite, Mg-Ca-Fe rich smectites and amorphous Fe-Ti-Al phases (Crovisier et al., 1987; Arnalds, 1990; Wada et al., 1992; Arnalds et al., 1995).

Low-temperature alteration and weathering of basalt is considered to result from interaction of the primary rocks with low CO₂ waters of meteoric origin (e.g., Rogers et al., 2006). Under these conditions,

amorphous silica, celadonite, smectites, and chlorite initially form, but with increasing time, calcite and zeolites form as well (e.g. Neuhoff et al., 1999; Neuhoff et al., 2006).

Neuhoff et al. (2006) reported results of basalt alteration under elevated CO₂ conditions at Nuussuaq, W Greenland. There, regional mineralogy (clays and carbonates) has been replaced with quartz and carbonates, the latter being dominantly Fe-Mg carbonates and Mg-Ca carbonates, and at later stages, also calcite.

GEOCHEMICAL DATA

TOUGHREACT requires vast amount of thermodynamic and kinetic data for aqueous species, minerals, and gases. Effort was put into updating mineral reactions in the database, providing an internally consistent database suitable for mineral reactions of interest for this study.

Thermodynamic data

The EQ3/6 V7.2b database (Woolery, 1992) is the primary source for equilibrium constants used in this study. However, thermodynamic properties of several minerals relevant to this study have been revised or added to the database. All revisions were generated by SUPCRT92 (Johnson et al., 1992) to ensure consistency with unmodified equilibrium constants. Thermodynamic properties of zeolites (analcime, Camordenite, Ca-stilbite, Ca-chabazite, heulandite, laumontite, mesolite, scolecite and thomsonite) were generated based on the work of Neuhoff (2000). Thermodynamic properties of kaolinite, magnesite, calcite, dolomite, siderite, Fe-celadonite and Mg-Fe smectite were revised after Holland and Powell (1998), whereas data from Stefansson and Gíslason (2001) was used to calculate thermodynamic properties of allophane and imogolite. The thermodynamic properties of phyllosilicates (chlorite, Mg-Fe smectite and Ca-Mg-Fe smectite) and carbonate solid solutions (Fe-Mg carbonate) were calculated using data from Stefansson (2008), whereas Majzlan et al. (2000) was used to calculate the thermodynamic properties of iron hydroxide.

Kinetic data

In the present study, dissolution and precipitation are described using the following general rate expression, which is based on transition state theory (Lasaga et al., 1994; Steefel and Lasaga, 1994).

$$r = kA \left[1 - \left(\frac{Q}{K} \right)^{\sigma} \right]^{\eta} \quad (1)$$

where r is rate of dissolution or precipitation, k is the temperature dependent rate constant, A is the specific

reactive surface area, K is the equilibrium constant for the dissolution/precipitation reaction taking place, and Q is the reaction quotient; θ and η must be determined by experiment, but are often set to unity.

Since dissolution and precipitation of minerals are often catalyzed by H^+ (acid mechanism) or OH^- (base mechanism), the rate constant in Equation (1) is the sum of three mechanisms:

$$k = k_{nu}^{25} \exp\left[\frac{-E_{nu}}{R}\left(\frac{1}{T} - \frac{1}{298.15}\right)\right] + k_H^{25} \exp\left[\frac{-E_H}{R}\left(\frac{1}{T} - \frac{1}{298.15}\right)\right] a_H^{\eta_H} \quad (2) + k_{OH}^{25} \exp\left[\frac{-E_{OH}}{R}\left(\frac{1}{T} - \frac{1}{298.15}\right)\right] a_{OH}^{\eta_{OH}}$$

where nu, H and OH denote neutral, acid, and base mechanisms, respectively. E is activation energy, k_{25} the rate constant at 25°C, R the gas constant, T absolute temperature and a activity of a species. Here, θ and η have been set to unity.

Gislason and Oelkers (2003) measured basaltic-glass dissolution kinetics far from equilibrium at temperatures ranging from 6 to 300°C and pH between 1 and 11. The resulting rate law describing basalt glass dissolution is:

$$r_{geo} = A_{geo} k_{geo} \exp\left[\frac{E_A}{RT}\right] \left(\frac{a_{H^+}^3}{a_{Al^{3+}}}\right)^{\frac{1}{3}} \left(1 - \frac{Q}{K}\right) \quad (3)$$

where $A_{geo}=250 \text{ cm}^2/\text{g}$, $k_{geo} = 10^{-5.6}$ and $E_A=25.5 \text{ kJ/mol}$. Unfortunately, the current release of TOUGHREACT does not support this type of rate law so it had to be approximated, using the option of varying reaction rate with pH (Xu et al., 2005).

Parameters used for the kinetic rate expression are given in Table 2. Rate constants for dissolution and precipitation reactions for minerals other than basaltic glass were taken from Palandri and Kharaka (2004). Mineral reactive surface areas are taken from Xu et al. (2007). All zeolites are assumed to have the same rate law parameters as heulandite. Allophane, imogolite, iron hydroxide, aluminum hydroxide, calcite and chalcedony are assumed to react at equilibrium.

CARBFIX FIELD MODEL DEVELOPMENT

Model setup

Figure 3 shows the geographical location of the CarbFix field model. The model lies in the direction of the regional groundwater flow which, as previously stated, is believed to be from NE to SW.

The CarbFix field model is 3000×1500×600 m in size, covering all wells in the target injection zone except HK-13 and HK-07B. The mesh is horizontal, except around Well HN-2, where it is radial to get a reasonable distribution of injected fluids and chemicals (Figure 4). Elements close to the injection well are small (<1 m radius), but their size gradually increases as they move away from the well. Total elements is 52,488; connections are 156,772.

The model consists of nine layers, from 300 to 900 m depth, as is shown in Figure 5. Generally, layers containing feed zones are narrow (25 or 50 m), but those that do not contain feed zones are thicker (50, 100, or 150 m). Top and bottom layers (A and I) are inactive, and the horizontal hydraulic gradient that drives natural flow through the bedrock is 5 m/1000 m. Thus, pressure at the models NE boundary is 1.5 bar higher than at the SW boundary. Elements at NE and SW boundaries have thousand-fold volumes.

Table 2. Parameters for calculating kinetic rate constants of secondary minerals

Mineral*	A (cm ² /g)	Parameters for kinetic rate law								
		Neutral mechanism		Acid mechanism			Base mechanism			
		k ²⁵ (mol/m ² /s)	E (kJ/mol)	k ²⁵	E	n (H ⁺)	k ²⁵	E	n (OH ⁻)	
Kaolinite	108.7	6.981E-14	22.2	4.898E-12	65.9	0.777	8.913E-18	17.9	-0.472	
Magnesite	9.1	4.571E-10	23.5	4.169E-07	14.4	1				
Dolomite	9.1	2.95E-08	52.2	6.46E-04	36.1	0.5				
Siderite	9.1	1.260E-09	62.8	6.457E-04	36.1	0.5				
Mg-Fe carbonate	9.1	1.260E-09	62.8	6.457E-04	36.1	0.5				
Chlorite	9.1	1.260E-09	62.8	6.457E-04	36.1	0.5				
Celadonite	151.6	1.660E-13	35.0	1.047E-11	23.6	0.34	3.020E-17	58.9	-0.4	
Fe celadonite	151.6	1.660E-13	35.0	1.047E-11	23.6	0.34	3.020E-17	58.9	-0.4	
Mg-Fe smectite	151.6	1.660E-13	35.0	1.047E-11	23.6	0.34	3.020E-17	58.9	-0.4	
Ca-Mg-Fe smectite	151.6	1.660E-13	35.0	1.047E-11	23.6	0.34	3.020E-17	58.9	-0.4	
Zeolites**	145	1.585E-12	58.0							

*Allophane, imogolite, Fe hydroxide, Al hydroxide, calcite and chalcedony react under equilibrium

**Assumed to be equal to heulandite parameters for all zeolites

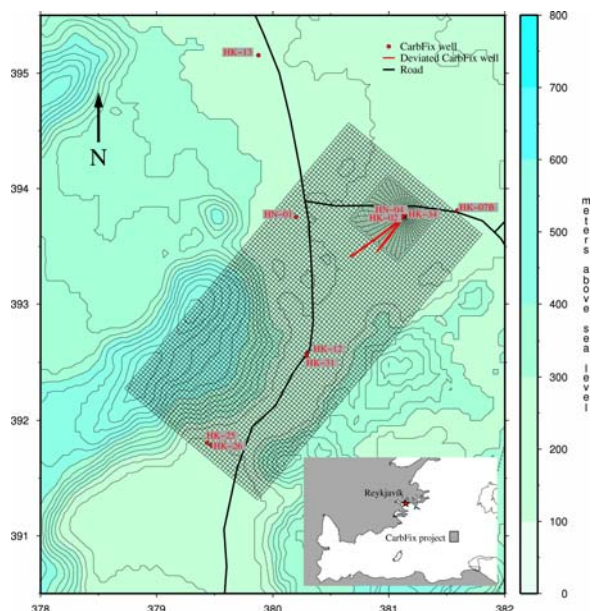


Figure 3. Geographical location of the CarbFix field model

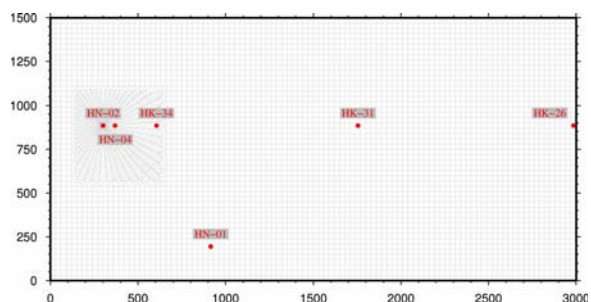
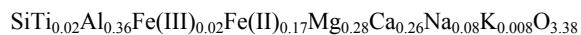


Figure 4. Top view of the CarbFix field model mesh. Distance is in meters.

Basaltic glass from Stapafell, SW-Iceland, is the only primary phase used in the CarbFix model. The chemical composition of the Stapafell glass normalized to one Si atom is:



Reactive surface area of basaltic glass is assumed to be $56 \text{ cm}^2/\text{g}$. This value is based on TOUGHREACT simulations on a basaltic glass dissolution experiment (Sigfusson, 2009).

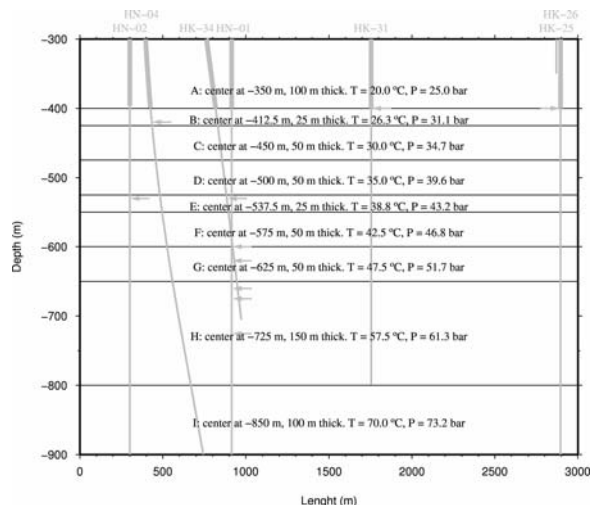


Figure 5. Cross sectional view through the field model, showing distribution of layers, along with wells and their feed zones. (T,P) are steady state values at the right vertical boundary ($x=3000$). Pressure at the left vertical boundary ($x=0$) is 1.5 bar higher due to horizontal hydraulic gradient.

The following secondary phases, which are known to form in basalt alteration and weathering, are allowed to precipitate.

allophane	$\text{Al}_2\text{O}_3(\text{SiO}_2)_{1.22}(\text{H}_2\text{O})_{2.5}$
imogolite	$\text{Al}_{25}\text{O}_3(\text{OH})_4$
kaolinite	$\text{Al}_{25}\text{O}_5(\text{OH})_4$
Fe hydroxide	$\text{Fe}(\text{OH})_3$
Al hydroxide	$\text{Al}(\text{OH})_3$
magnesite	MgCO_3
calcite	CaCO_3
dolomite	$\text{CaMg}(\text{CO}_3)_2$
siderite	FeCO_3
Fe-Mg carbonate	$\text{FeMg}(\text{CO}_3)_2$
chlorite	$\text{Fe}_{3.15}\text{Mg}_{1.85}\text{Al}_2\text{Si}_3\text{O}_{10}(\text{OH})_8$
celadonite	$\text{KMgAlSi}_4\text{O}_{10}(\text{OH})_2$
Fe-celadonite	$\text{KFeAlSi}_4\text{O}_{10}(\text{OH})_2$
Mg-Fe smectite	$\text{Na}_{0.04}\text{K}_{0.10}\text{Ca}_{0.21}\text{Mg}_{1.44}\text{Fe}_{1.78}\text{AlSi}_3\text{O}_{10}(\text{OH})_2$
Ca-Mg-Fe smectite	$\text{Ca}_{0.50}\text{Mg}_{1.05}\text{Fe}_{1.30}\text{AlSi}_3\text{O}_{10}(\text{OH})_2$
chalceony	SiO_2
analcime	$\text{NaAlSi}_2\text{O}_6$
Ca-mordenite	$\text{Ca}_{0.5}\text{AlSi}_5\text{O}_{12}$
Ca-stilbite	$\text{CaAl}_2\text{Si}_7\text{O}_{18}$
Ca-Chabazite	$\text{CaAl}_2\text{Si}_4\text{O}_{12}$
heulandite	$\text{CaAl}_2\text{Si}_7\text{O}_{18}$
laumontite	$\text{CaAl}_2\text{Si}_4\text{O}_{12}$
mesolite	$\text{Ca}_{0.667}\text{Na}_{0.666}\text{Al}_2\text{Si}_3\text{O}_{10}$
scolecitet	$\text{CaAl}_2\text{Si}_3\text{O}_{10}$
thomsonite	$\text{CaNaAl}_5\text{Si}_5\text{O}_{20}$

Initial water composition is given in Table 3. Boundary water solutions have the same composition except for CO_2 loaded water, which has CO_2 concentration corresponding to 25 bar CO_2 partial pressure.

Table 3. Initial water composition in mmol/L

pH/°C	8.82/25
CO ₂	1.9
SiO ₂	2.11
Na	1.57
K	0.03
Ca	0.18
Mg	0.33
SO ₄	0.08
Cl	0.25
F	0.02

Simulations

Hydrological properties of the model were calibrated using iTOUGH2 and TOUGHREACT to simulate the tracer tests that have been ongoing in Hellisheidi since 2007. Water level, temperature changes, and tracer recovery have been monitored in injection and monitoring wells during the tests, providing numerous datasets that were used in the calibration. Permeability was calibrated using inverse and forward EOS1 iTOUGH2 runs, but calibration of the system's porosity was done with forward TOUGHREACT EOS1 runs. This had to be done because the two-water EOS1 option did not work on a system of this size. Reactive transport was added to the model after calibrating hydrological properties of the system. TOUGHREACT is used for reactive transport simulations, which are ongoing. The system was allowed to reach steady state (chemical and hydrological) prior to all simulations.

RESULTS

Hydrological parameters

The system's porosity and three different permeabilities were calibrated (k_{xy} , k_z and skin zone permeability next to each well). Our current "best" hydrological model has horizontal permeability of approximately 500 mD (k_{xy}) and vertical permeability (k_z) of 300 mD, while $k_{\text{skin zone}}$ is an order of magnitude higher. The corresponding calibration resulted in only 4% porosity, a value much lower than usually seen in Icelandic basalts. Simulations are, however, ongoing so these values might still change. Figures 6 and 7 show comparison between calculated and measured values for some of the data sets that were used for model calibration.

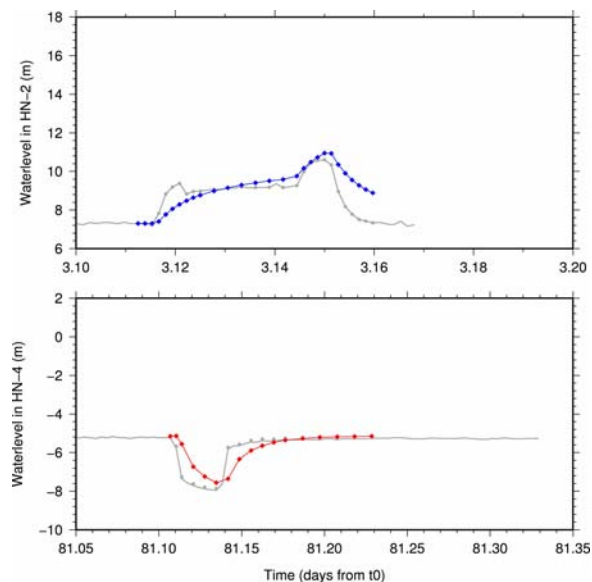


Figure 6. Calculated and measured water level fluctuations in HN-04 due to injection stop in HN-02 are shown on the lower figure and water level fluctuations in HN-02 due to production stop in HN-04 on the top figure. Measured water level values are shown in gray, whereas calculated values for wells HN-02 and HN-0 are shown in red and blue, respectively.

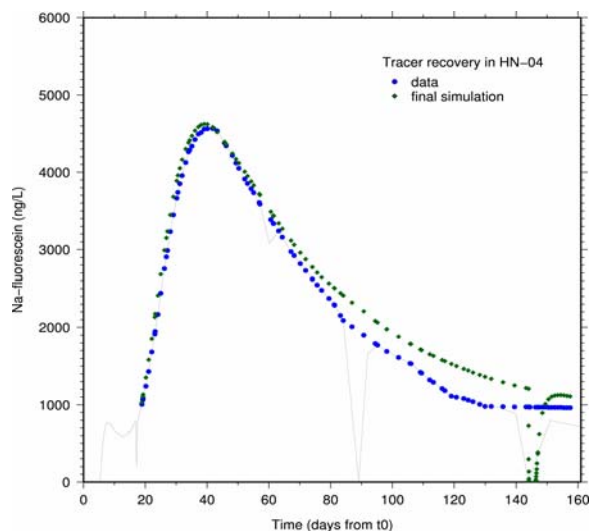


Figure 7. Calculated and measured tracer recovery.

Back-of-the-envelope calculations using the estimated permeability and porosity values above, along with the system's horizontal gradient of 5 m/1,000 m, indicate groundwater velocity in the target injection zone to be ~ 25 m/year, which is much lower than previously anticipated. However, the large-scale tracer test, launched on June 10, 2008, supports this, as no tracer has yet been detected in any downstream wells.

This slow groundwater velocity calls for revision of injection plans, because it might be necessary to increase groundwater flow in the reservoir by producing downstream wells at low rates after CO₂ injection has started. The main objective of this potential production would be to pull highly concentrated CO₂-loaded water away from the immediate surroundings of the injection well to prevent clogging. Managing plans for the potential production would, however, have to be carefully designed to minimize the amount of CO₂ that would be pumped out of downstream production wells.

Mineral alteration

Calibrated hydrological parameters are currently being used to develop reactive fluid flow models that simulate different scenarios for the CO₂ injection. Since these reactive fluid flow simulations have not been running for long, it is still too early to tell which secondary phases will form in greatest quantities. However, TOUGHREACT has already been used to simulate laboratory-scale plug flow reactor experiments that will be carried out to study distribution of secondary phases as dissolved CO₂ reacts with basaltic glass, as well as to determine the efficiency of the carbonization process. TOUGHREACT simulations have been used to optimize conditions for the experiment. Water with dissolved CO₂ was pumped through a pipe filled with Stapafell basaltic glass. Simulations were carried out at 25, 50 and 75°C, pCO₂ = 2-30 bars, and flow rate between 0.1–10 mL/min. Basaltic glass was allowed to dissolve according to approximation to the rate expression of Gislason and Oelkers (2003). Secondary minerals allowed to form were the same as previously presented in this paper.

Numerical simulations show that the plug flow experiments must be carried out at 50 or 75°C for carbonates to form, and that low flow rates are needed for carbonate precipitation. Calcite and dolomite are the most abundant carbonates to form. Among other secondary phases that form, chalcedony, imogolite, and chlorite are most abundant. This is in agreement with batch experiments ongoing at the Institute of Earth Sciences at the University of Iceland. Results from the plug-flow reactor simulations will not be covered in more detail here; they will be presented in another paper that is currently in preparation (Aradottir, 2009).

SUMMARY AND CONCLUSIONS

CarbFix, a joint research project of the University of Iceland, Reykjavik Energy, Columbia University and CNRS in Toulouse, is aimed at studying the behavior of CO₂ injected into basalts. Geochemical modeling plays an important role in the project, and TOUGHREACT and iTOUGH2 have been used for developing a coupled reactive fluid flow model of the

mineral CO₂ capture. The CarbFix field model is 3000×1500×600 m in size, covering all wells in the target injection zone except HK-13 and HK-07B. Total number of elements is 52,488 and connections are 156,772.

Hydrological properties of the model are being calibrated using iTOUGH2 and TOUGHREACT to simulate the tracer tests that have been ongoing in Hellisheidi since 2007. The calibration resulted in horizontal permeability of approximately 500 mD, and 4% porosity. Reactive transport was added to the model after calibrating hydrological properties of the system. TOUGHREACT is being used for ongoing reactive transport simulations. Optimally, these simulations should determine which injection scenario will maximize mineralization of the injected CO₂, as well as show the depth and temperature range best suited for the mineralization.

ACKNOWLEDGEMENT

We thank Andri Arnaldsson and Gunnar Gunnarsson for helpful discussions and support. This work was partly supported by the University fund of Eimskipafelag Islands and by GEORG, Geothermal Research Group.

REFERENCES

- Aradottir, E.S.P., Numerical modeling of CO₂ mineralization in basaltic glass, in preparation, 2009.
- Arnalds, O., Characterization and erosion of andisols in Iceland, Ph.D. Thesis, Texas A&M University, Texas, 1990.
- Arnalds, O., Hallmark, C.T., Wilding, L.D., Andisols from four different regions of Iceland. *Soil Sci. Soc. Amer. J.* 59, 161-169, 1995.
- Crovisier, J.L., Honnerez, J., Fritz, R., Petit, J.C. Dissolution of subglacial volcanic glasses from Iceland. Laboratory study and modeling, *Applied Geochem. Suppl.*, 1, 55-81, 1992.
- Finsterle, S. iTOUGH2 User's Guide. Report LBNL-40040, Lawrence Berkeley National Laboratory, Berkeley, Calif., 1999.
- Gislason, S.R., Arnorsson, S., Arnmannsson, H. Chemical weathering of basalts Southwest Iceland: Effect of runoff, age rocks and vegetative/glacial cover, *Amer. J. Sci.* 296, 837-907, 1996.
- Gislason, S.R., Oelkers, E.H. Mechanisms, rates and consequences of basaltic glass dissolution: II. An experimental study of the dissolution rates of basaltic glass as a function of temperature, *Geochim. Cosmochim. Acta* 67, 3817-3832, 2003.

- Holland, T.J.B., Powell, R., An internally consistent thermodynamic data set for phases of petrological interest, *J. Metam. Geol.* 16, 309-343, 1998.
- Johnson, J.W., Oelkers, E.H., Helgeson, H.C., SUPCRT92: a software package for calculating the standard molal thermodynamic properties of minerals, gases, aqueous species and reactions from 1 to 5000 bars and 0 to 1000 degrees C. *Comput. Geosci.*, 18, 899-947, 1992.
- Kristmannsdottir, H., Tomasson, I., Zeolite zones in geothermal areas in Iceland, *Natural Zeolites*, eds. L.B. Sand and F.A. Mumpton, Pergamon Press, 277-284, 1978.
- Lasaga, A.C., Soler, J.M., Ganor, J., Burch, T.E., Nagy, L.L., Chemical weathering rate laws and global geochemical cycles, *Geochim. Cosmochim. Acta* 58, 2361-2386, 1994.
- Majzlan, J., Navrotsky, A., Schwertmann, U., Thermodynamics of iron oxides: Part III. Enthalpies of formation and stability of ferrihydrite ($\text{Fe}(\text{OH})_3$), schwertmannite ($\text{FeO}(\text{OH})_{3/4}(\text{SO}_4)_{1/8}$) and $\epsilon\text{-Fe}_2\text{O}_3$. *Geochim. Cosmochim. Acta* 68, 1049-1059, 2004.
- Neuhoff, P.S., Thermodynamic properties of parageneses of rock-forming zeolites., Ph.D. Thesis, Stanford University, Stanford, Calif., 2000.
- Neuhoff, P.S., Fridriksson, Th., Arnorsson, S., Bird, D.K., Porosity changes and mineral paragenesis during low-grade metamorphism at Teigarhorn, eastern Iceland, *Amer. J. Sci.* 299, 467-501, 1999.
- Neuhoff, P.S., Fridriksson, Th., Arnorsson, S., Bird, D.K., Pedersen, A.K., Regional very low-grade metamorphism of basaltic lavas, Disko-Nuussuaq region, West Greenland, *Lithos*, 92, 33-54, 2006.
- Palandri, J.L., Kharaka, Y.K., A compilation of rate parameters of water-mineral interaction kinetics for application to geochemical modeling. USGS Report 2004-1068, 2004.
- Rogers, K.L., Neuhoff, P.S., Pedersen, A.K., Bird, D.K., CO_2 metasomatism in a basalt-hosted petroleum reservoir, Nuussuaq, West Greenland. *Lithos*, 92, 55-85, 2006.
- Sigfusson, B., Reactive transport of arsenic through basaltic porous media, Unpublished Ph.D. thesis, University of Aberdeen, Aberdeen, 2009.
- Sonnenthal, E., Ito, A., Spycher, N., Yui, M., Apps, J., Sugita, Y., Conrad, M., Kawakami, S., Approaches to modeling coupled thermal hydrological and chemical processes in the Drift Scale Heater Test at Yucca Mountain, *Int. J. Rock Mech. Min. Sci.* 42, 687-719, 2005.
- Steefel, C.I., Lasaga, A.C., A coupled model for transport of multiple chemical species and kinetic precipitation/dissolution reactions with applications to reactive flow in single phase hydrothermal systems, *Am. J. Sci.* 294, 529-592, 1994.
- Stefansson, A., Numerical simulation of CO_2 -water basalt interaction, Report RH-2-2008, Institute of Earth Sciences, University of Iceland, Reykjavik, 2008.
- Stefansson, A., Gislason, S.R., Chemical weathering of basalts, Southwest Iceland: effect of rock crystallinity and secondary minerals on chemical fluxes to the ocean, *Am. J. Sci.* 301, 513-556, 2001.
- Wada, K., Arnalds, O., Kakuto, Y., Wilding, L.P., Hallmark, C.T., Clay minerals of four soils formed in eolian and tephra materials in Iceland, *Geoderma* 52, 351-365, 1992.
- Walker, G.P.L., Zeolite zones and dike distribution in relation to the structure of the basalts of eastern Iceland, *J. Geol.* 68 515-528, 1960.
- Wolery, T.J., EQ3/6: software package for geochemical modeling of aqueous systems: package overview and installation guide (version 7.0). Lawrence Livermore National Laboratory Report UCRL-MA-210662 PT I. Livermore, Calif., 1992.
- Xu, T., Sonnenthal, E.L., Spycher, N., Pruess, K. TOUGHREACT User's Guide: a simulation program for non-isothermal multiphase reactive geochemical transport in variably saturated geologic media. Report LBNL-55460, Lawrence Berkeley National Laboratory, Berkeley, Calif., 2005.
- Xu, T., Apps, J.A., Pruess, K., Yamamoto, H., Numerical modeling of injection and mineral trapping of CO_2 with H_2S and SO_2 in a sandstone formation, *Chem. Geology* 242, 319-346, 2007.

MODELING OF SALT PRECIPITATION DURING SUPERCRITICAL CO₂ INJECTION IN A SALINE RESERVOIR: POSSIBLE IMPACT ON THE INJECTIVITY OF THE TARGETED RESERVOIR

Laurent ANDRE and Mohamed AZAROUAL

BRGM - Water Division,
3 Avenue Claude Guillemin, BP 36009,
F-45060 ORLEANS Cedex 2, France
e-mail: l.andre@brgm.fr; m.azaroual@brgm.fr

ABSTRACT

Geological sequestration of CO₂ offers a promising solution for reducing net emissions of greenhouse gases into the atmosphere. In the framework of this concept, CO₂ can be injected into saline aquifers in the supercritical state ($P > 7.4$ MPa and $T > 31.1^\circ\text{C}$) in order to achieve a higher density and therefore occupy less volume underground. Previous experimental and numerical simulations have demonstrated that massive CO₂ injection in saline reservoirs causes a major disequilibrium in the physical and geochemical characteristics of the host aquifer. The near-well injection zone seems to constitute an underground hydrogeological system particularly impacted by supercritical CO₂ injection—and the most sensitive area, where reversible chemical phenomena (e.g., mineral dissolution/ precipitation) can have a major impact on porosity and permeability. This study, based on numerical multiphase simulations, investigates the chemical effects of CO₂ injection into a deep saline reservoir containing various types of brines. It demonstrates the impact of salt precipitates on rock porosity, according to the nature of the salt.

INTRODUCTION

Massive carbon dioxide injection in a fully water-saturated reservoir causes many physical, geochemical, thermal and geomechanical reactions, the most important ones occurring in the near-well injection zone (André et al., 2007). Among these perturbations, the desiccation of the porous medium appears to be a major phenomenon, with various potential repercussions such as salt precipitation, modification of the local geomechanical constraints (due to the salt precipitation and the new distribution of internal forces), and the impact of injected fluids on the interfacial tensions. This study investigates the consequences of porous media desiccation on well injectivity, through the geochemical reactivity and petrophysical properties of the different subsystems.

Desiccation of porous media submitted to gas injections is a well-known process at laboratory or field scales (Rosenbauer et al., 2005; Kaszuba et al., 2003; Kleinitz et al., 2003; Mahadevan, 2005;

Mahadevan et al., 2007). First, the massive and continuous injection of CO₂ in a porous medium involves water displacement and evaporation: mobile water is removed by the injected supercritical CO₂. At the end of this phase, immobile residual water, entrapped in pores or distributed on a grain surface as a thin film, is in contact with the flowing dry CO₂ (i.e., with very low relative humidity). Consequently, a continuous and extensive evaporation process leads both to the appearance of a drying front moving into the medium, and the precipitation of salts and possibly secondary minerals (André et al., 2007). According to the nature of the initial brine, a large variety of salts having contrasting molar volumes can precipitate: while some salts have only a minimal impact on porosity and permeability, some other salts can dramatically affect the behavior of the flow field around the injection well.

This study focuses on the geochemical behavior of different types of brines modeled with TOUGHREACT based on the THERMODDEM database (Piantone et al., 2006), a new thermodynamic database containing more than 160 elements and 500 mineral phases.

The precipitated salt volumes are estimated according to CO₂ injection temperature, and they are then related to porosity decreases. Moreover, a sensitivity analysis is also proposed to estimate the relationship between the precipitated amounts of salts and the petrophysical rock properties. The volumes of immobile water, stabilized in pores and able to evaporate, is related to capillary pressure, wettability of the porous medium, and the relative permeability characteristics of the porous medium. With an increase in irreducible water threshold and according to the ionic strength of the brine, high salt volumes are expected, involving possible porosity clogging. Finally, this study highlights not only the parameters (chemical, petrophysical, and thermal) influencing both salt precipitation and deposit volumes, but also defines relevant conditions for sustaining well injectivity for long-term CO₂ injection periods.

NUMERICAL APPROACH

Coupled code

The TOUGHREACT simulator (Xu and Pruess, 2001) was used for all the simulations of this study. This code, adapted from TOUGH2 V2 (Pruess et al. 1999), couples thermal, hydraulic and chemical (THC) processes and is applicable to one-, two-, or three-dimensional geologic systems with physical and chemical heterogeneity. TOUGHREACT is coupled with ECO2N (Pruess 2005), a fluid property module developed specifically to deal with geologic sequestration of CO₂ in saline aquifers. It can be used to model isothermal or nonisothermal multiphase flow in water/brine/CO₂ systems.

TOUGHREACT simulates the chemical reactivity of systems based on a thermodynamic database, THERMODDEM (Piantone et al., 2006) developed at BRGM and available from Internet at <<http://thermoddem.brgm.fr/>>. It is valid for the 0–300°C range, 1 bar below 100°C, and water saturation pressure above 100°C.

Equilibrium between the gas phase and the aqueous phase is assumed for CO₂ dissolution. An extension of Henry's law, including the salting out effect, is used to estimate the dissolution of CO₂ in aqueous phase at high pressure. For these calculations, the dissolution and precipitation reactions of minerals proceed under chemical equilibrium.

Mineral dissolution and precipitation reactions involve temporal changes in reservoir porosity and permeability. Variations in the mineral volume fraction due to chemical reactions allow the resulting porosity to be computed. Modification of permeability is calculated from porosity changes using a cubic law. The current TOUGHREACT version uses an extended Debye-Hückel model (Helgeson et al., 1981) to determine activity coefficients of dissolved species:

$$\text{Log } \gamma_i = -\frac{A_\gamma z_i^2 I^2}{1 + a B_\gamma I^{1/2}} + \text{Log} (1 + 0.018053 m^*) - \left[\omega_i b_{\text{NaCl}} + b_{\text{Na}^+, \text{Cl}^-} - 0.19 (|z_i| - 1) \right] I$$

where i refers to each ion, γ is the activity coefficient of the ion, z is the ion electric charge, m^* is the total molality of all species in solution, I is taken as the true ionic strength of the solution, ω is the Born coefficient, $b_{\text{Na}^+, \text{Cl}^-}$, b_{NaCl} , are Debye-Hückel parameters, and \hat{a} is calculated from ion radii. A_γ and B_γ are temperature- and pressure-dependent parameters.

The Debye-Hückel approach for calculating activity coefficients is unsuitable for solutions with high ionic strengths, as is the case when desiccation occurs. A Pitzer approach would be more appropriate when the ionic strength is higher than 0.5–0.7. André et al. (2007) did calculations with TOUGHREACT and an in-house code, SCALE2000 (Azaroual et al., 2004), a geochemical simulator designed for highly saline solutions. There are discrepancies between the two codes, and the conclusions highlight the advantage of using the Pitzer formalism for such complex systems. Nevertheless, TOUGHREACT enables a first qualitative approach to the main geochemical processes and general evolutionary trends of the system.

Geometrical model

A 1D column model 10 m long is proposed as a conceptual framework for determining the evolution of geochemical reactivity induced by the injection of CO₂, in both time and space. The system under consideration is represented by 10 gridblocks composing the model mesh. The thickness of each grid cell is constant (1 m). A hydrostatic status is initially assumed for the pressure within the reservoir and maintained constant at the lateral boundary. The initial pressure of the targeted reservoir is 18 MPa.

The physical properties of the reservoir correspond to a generic reservoir with a porosity of 0.20 and an isotropic reservoir permeability of 10⁻¹² m² (1 D) ($K_v/K_H = 1.0$). The rock constituting the matrix is supposed inert with respect to CO₂, i.e., without chemical reactivity.

Variations in relative permeability and capillary pressure according to water saturations are given on Figures 1 and 2. Relative permeability for aqueous phase and capillary pressure models are described using the van Genuchten formulation, whereas a fourth-degree polynomial function is used to represent the relative permeability of gaseous phase.

For the liquid phase:

$$k_{rl} = \sqrt{S^*} \left\{ 1 - \left(1 - [S^*]^{1/m} \right)^m \right\}^2 \quad \text{with} \quad S^* = \frac{S_l - S_{lr}}{1 - S_{lr}}$$

k_{rl} is the relative permeability of the liquid phase, S_l the liquid-phase saturation, S_{lr} the residual liquid-phase saturation, and m a non-dimensional characteristic parameter of the law.

For the gas phase:

$$k_{rg} = 1.3978 - 3.7694 S_1 + 12.7090 S_1^2 - 20.6420 S_1^3 + 10.3090 S_1^4$$

where k_{rg} is the gas-phase relative permeability.

Capillary pressure P_{cap} is calculated by the following expression:

$$P_{cap} = -P_0 \left([S^*]^{1/m} - 1 \right)^{1-m} \quad \text{with} \quad S^* = \frac{S_l - S_{lr}}{1 - S_{lr}}$$

where P_0 is the pressure coefficient in Pa, and m a nondimensional exponent.

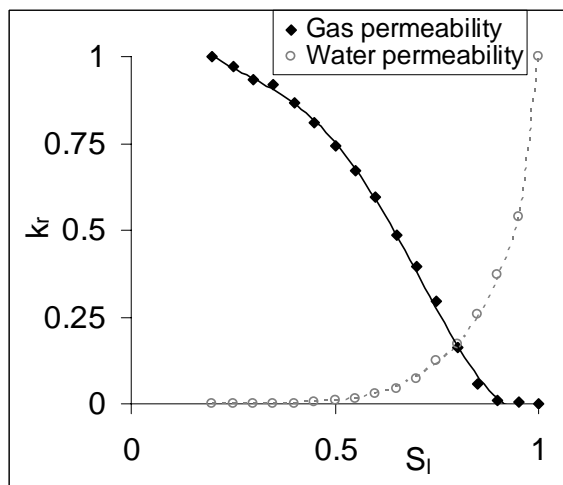


Figure 1. Variations in relative permeability according to water saturation (S_l). Points represent experimental data whereas lines symbolize models (IFP data).

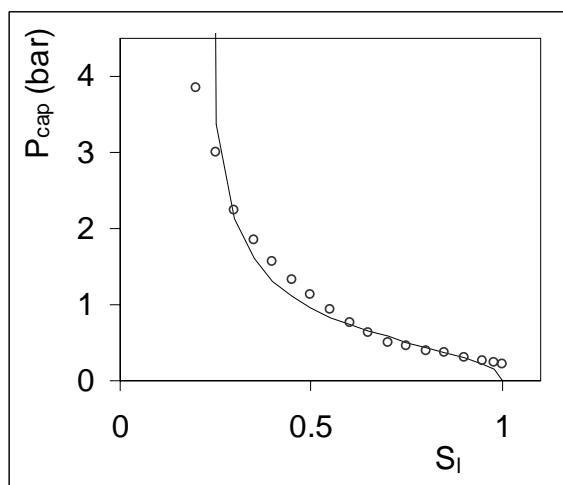


Figure 2. Variations in capillary pressure according to water saturation (S_l). Points represent experimental data whereas line symbolizes model (IFP data).

The parameters used in the simulations for relative permeability and capillary pressure models are summarized in Table 1.

Table 1. Physical properties of the aquifer. Each of the characteristic curves for water permeability and capillary pressure are fitted with the van Genuchten model.

Relative permeability parameters for brine (Van Genuchten model - 1980)	
$m = 1 - 1/n$	0.600
Residual liquid saturation	0.200
Liquid saturation	1.000
Residual gas saturation	0.050
Capillary pressure parameters (Van Genuchten model - 1980)	
$m = 1 - 1/n$	0.600
Residual liquid saturation	0.199
P_0 (Pa)	54000
P_{max} (Pa)	10^7

During the brine evaporation process driven by dry CO_2 injection, the capillary pressure is limited to a maximum value of 10 MPa. This value is quite large, but it is not unreasonable compared to values proposed by many authors who predict values up to 100 MPa during the desiccation process of a porous medium (Rossi and Nimmo, 1994; Pettenatti et al., 2008 and references cited therein).

All the simulations presented hereafter are performed in isothermal mode, neglecting the thermal effects associated with water vaporization, compression, decompression of CO_2 , and the heat of dissolution of gas in brine.

NUMERICAL RESULTS

Salinity impact

The column is initially fully saturated with a solution containing different concentrations of Na^+ and Cl^- at 100°C . Concentrations are less than $6.68 \text{ mol kg}_w^{-1}$, the maximal solubility of halite at this temperature: the solution is initially undersaturated with respect to halite. The injection of supercritical CO_2 is performed at a constant flow rate of 1 kg s^{-1} during one day.

Injection of dry supercritical CO_2 involves the desiccation of the porous medium. Figure 3a indicates that the CO_2 injection modifies the gas saturation in the system. After 4 hours, all the cells of the column contain gas. But halite precipitation occurs only in the first cell (= first meter), where the gas saturation is higher. With the increase in injection time, salt precipitation occurs in the first eight cells (Figure 3b).

The amount of halite precipitated depends on the initial composition of the brine. With the increase in the salinity of the initial solution, different halite amounts deposit, particularly in the injection cell

(Figure 4). Scaling affects the porosity of the medium with a decrease of about 15% for a highly saline solution (decrease from 0.2 to 0.17).

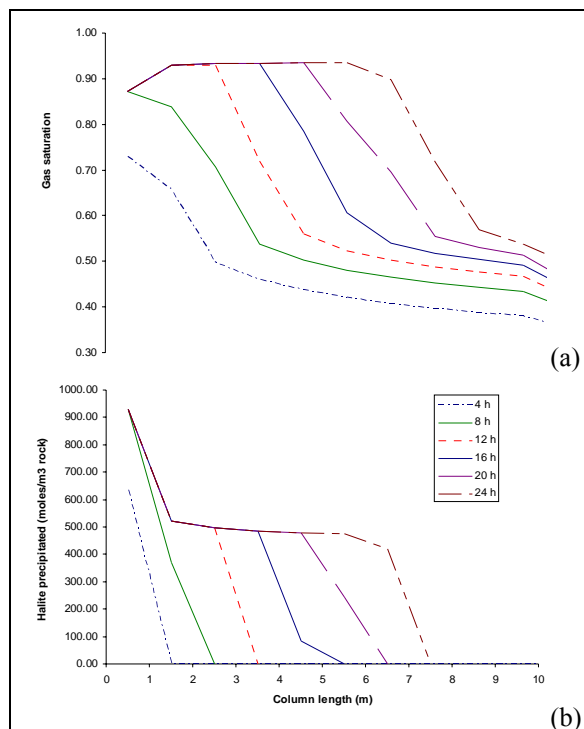


Figure 3: Variations with time in (a) gas saturation and (b) amount of halite precipitated in the column. The composition of initial brine is 5 mol kg_w^{-1} of NaCl.

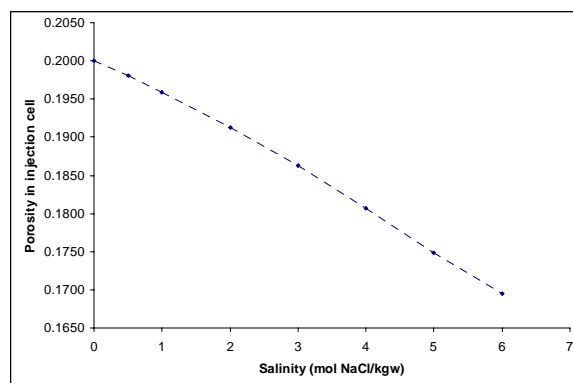


Figure 4. Variations in porosity in the injection cell according to different NaCl salinity of the initial solution

Type of brine

NaCl brine is now replaced by KCl brine. Initially, the solution is undersaturated with respect to sylvite, i.e., the K^+ and Cl^- concentrations are less than $7.12 \text{ mol kg}_w^{-1}$, the maximal solubility of sylvite at 100°C .

The injection of supercritical CO_2 is performed at a constant flow rate of 1 kg s^{-1} during one day.

As demonstrated by Figure 5, the injection of dry CO_2 involves the precipitation of sylvite in the porous medium. We note that, for a given salinity of both NaCl and KCl between 0 and 5 mol kg_w^{-1} , the same total amounts of sylvite and halite precipitate, but the porosity response is different for the two salts. The porosity decrease is more important for KCl solution than for NaCl solution. This difference results from the molar volume of salts: $37.53 \text{ cm}^3 \text{ mol}^{-1}$ for sylvite and $27.02 \text{ cm}^3 \text{ mol}^{-1}$ for halite. Consequently, as presented in Figure 5, the porosity of injection cell is more affected by sylvite precipitation (showing decrease of about 20% for KCl against 15% for NaCl).

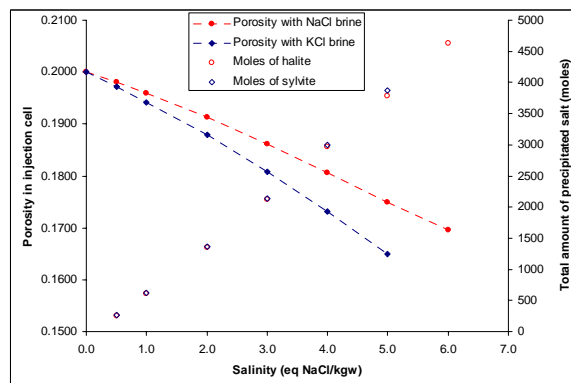


Figure 5. Total amount of salts precipitated (halite and sylvite) in the entire column and variations in porosity within the injection cell according to different salinity of NaCl and KCl brines.

These porosity variations (and consequent permeability variations) can appear as negligible. But as calculations are made at a constant flow rate, these perturbations of rock properties (porosity and permeability) have an impact on pressure.

A test case was performed with the evaporation of deionized water: this process does not generate salt deposits in the column, and the increase in pressure due to CO_2 injection is lower than for KCl brine (Figure 6). With NaCl brine, the precipitation of halite involves an increase in pressure (with respect to distilled water), but this increase is less important than for KCl brine (Figure 6).

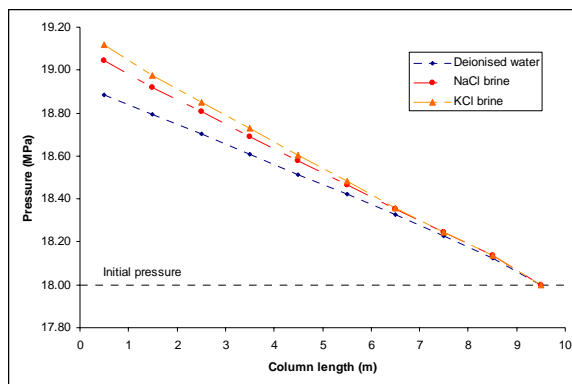


Figure 6. Profile of pressure in the column according to the salinity of the initial solution: deionised water (without salt), undersaturated NaCl brine (5 mol kg_w^{-1}), undersaturated KCl brine (5 mol kg_w^{-1}).

Temperature impact

The column is now saturated with a solution containing Na^+ and SO_4^{2-} , with an initial concentration of $1.0 \text{ mol kg}_w^{-1}$ of Na_2SO_4 . The saline solution is undersaturated with respect to thenardite ($\text{Na}_2\text{SO}_4(s)$) in the temperature range between 40 and 100°C . We assume the injection of supercritical CO_2 at a constant flow rate of 1 kg s^{-1} during one day.

As shown by Figure 7, the increase in temperature enhances the desiccation phenomenon. At 40°C , only the first two cells are impacted by the drying, whereas at 100°C , the first eight meters are affected. This process is explained by the thermodynamic properties of CO_2 , which is more hydrophilic at 100°C than at 40°C .

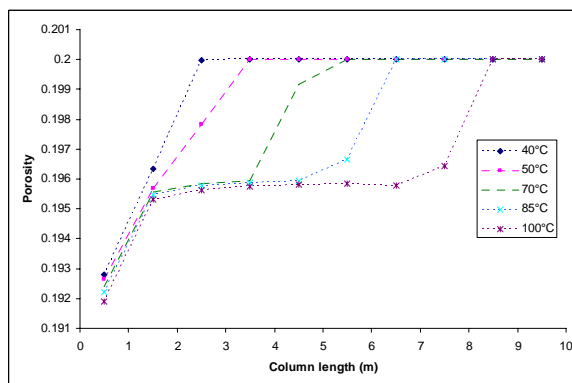


Figure 7: Variations in porosity in the entire column according to the temperature after a CO_2 injection period of one day.

Moreover, except in the first cell where the salt scaling is more important, we observe that the salt deposits are constant in the entire column. This constant scaling is related to the residual liquid

saturation. To illustrate this, we conducted a simulation with a more substantial residual liquid saturation ($S_{lr} = 0.4$ instead of 0.2). Figure 8 indicates that an increase in this parameter results in the precipitation of higher amounts of salts and, consequently, a more significant decrease in porosity.

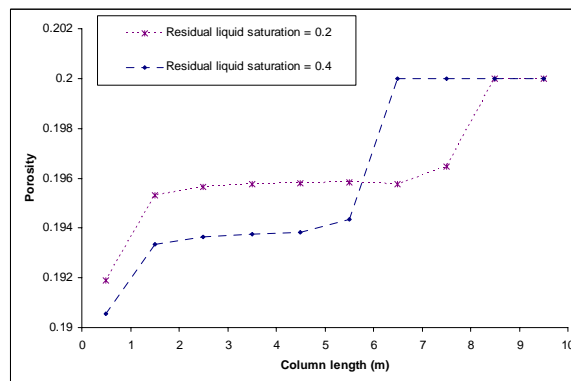


Figure 8: Variations in porosity after a CO_2 injection period of one day at 100°C in the entire column according to two values of residual liquid saturation.

Figure 6 demonstrated that the molar volume of salts constitutes a key factor in determining the evolution of porosity. We confirm this hypothesis by comparing the impact of thenardite precipitation with respect to halite deposits (Figure 9). A solution with the same concentration of NaCl ($= 1.0 \text{ mol kg}_w^{-1}$) initially saturates the porous medium. The total amounts of halite and thenardite precipitated in the entire column due to CO_2 injection are quite similar. But the molar volume of thenardite ($= 53.30 \text{ cm}^3 \text{ mol}^{-1}$) is twice as great as that of halite. Consequently, the porosity decrease is more significant when thenardite deposits (Figure 9).

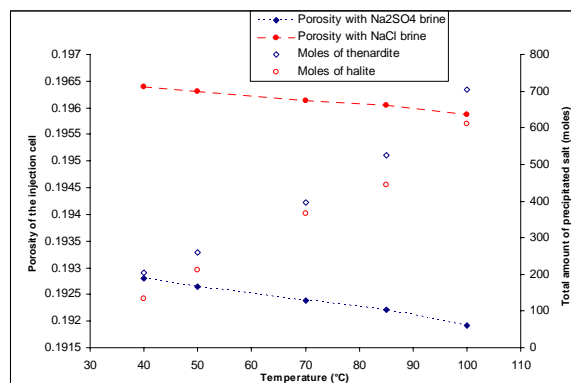


Figure 9: Total amount of salts precipitated (halite and thenardite) in the entire column and variations in porosity within the injection cell according to different temperatures

Complex brines

After observing the behavior of three mono-salt brines, more complex solutions are studied. The objective is to determine if the complexity of a brine composition can have an impact on salt precipitation due to CO_2 injection.

$\text{NaCl} + \text{Na}_2\text{SO}_4$

A solution containing $1.0 \text{ mol kg}_w^{-1}$ NaCl and $0.5 \text{ mol kg}_w^{-1}$ Na_2SO_4 is initially present in the porous rock. Temperature is 100°C . At this temperature, the solution is undersaturated with respect to halite and thenardite.

As previously shown, injection of dry CO_2 desiccates the porous medium causing salt precipitation. In this case, two salts are able to precipitate during the evaporation process: halite and thenardite. Figure 10 confirms the precipitation of these two salts, with halite precipitation higher than thenardite precipitation. Figure 10 also demonstrates a hierarchy in the precipitation order of the salts within the column: thenardite precipitates first, before halite. This succession in salt precipitation is governed exclusively by equilibrium constraints.

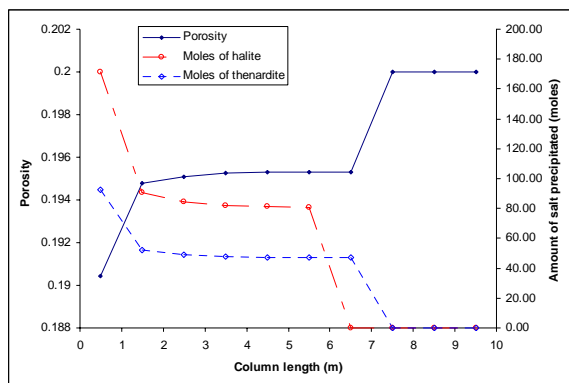


Figure 10. Total amount of salts precipitated (halite and thenardite) and variations in porosity within the entire column after a CO_2 injection period of one day. Initial solution contains $(\text{Na} + \text{Cl} + \text{SO}_4)$.

$\text{KCl} + \text{Na}_2\text{SO}_4$

A solution containing 1 mol kg_w^{-1} KCl and $0.5 \text{ mol kg}_w^{-1}$ Na_2SO_4 is initially present in the porous rock, at a temperature of 100°C . At this temperature, the solution is undersaturated with respect to halite ($\text{SI} = -1.88$), sylvite ($\text{SI} = -1.61$), and thenardite ($\text{SI} = -0.99$).

Injection of dry CO_2 desiccates the porous medium causing salt precipitation. The salts able to precipitate during the evaporation process are halite, sylvite, and thenardite. But as shown by Figure 11, only two salts precipitate: sylvite and thenardite. Halite stays undersaturated during the entire process.

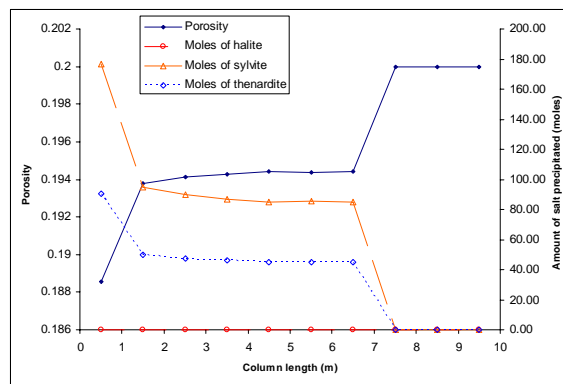


Figure 11. Total amount of salts precipitated (halite, sylvite and thenardite) and variations in porosity within the entire column after a CO_2 injection period of one day. Initial solution contains $(\text{Na} + \text{K} + \text{Cl} + \text{SO}_4)$.

The amount of sylvite precipitated is the same as the amount of halite determined in the mix ($\text{NaCl} + \text{Na}_2\text{SO}_4$). But because of differences in the molar volume of halite and sylvite, the decrease in porosity with sylvite is much more significant.

Nevertheless, it is interesting to note the competition between sylvite and halite to precipitate. The limiting factor is dissolved Na . As sodium precipitates to form thenardite, it is not available to form halite. But if sodium is added to the initial solution (1 mol kg_w^{-1} $\text{NaCl} + 1 \text{ mol kg}_w^{-1}$ $\text{KCl} + 0.5 \text{ mol kg}_w^{-1}$ Na_2SO_4), then the evaporation of the solution produces the three salts—halite, sylvite, and thenardite (Figure 12). The resulting porosity is also lower in this case than in the two previous cases.

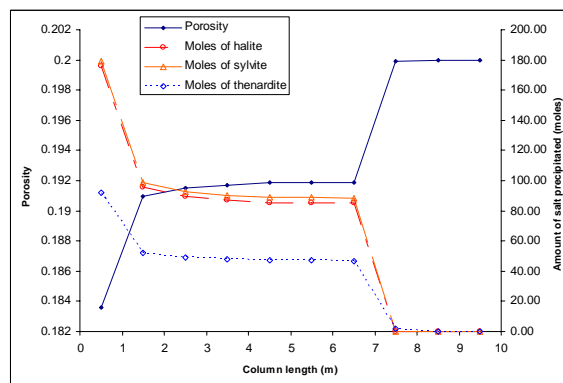


Figure 12. Total amount of salts precipitated (halite, sylvite and thenardite) and variations in porosity within the entire column after a CO_2 injection period of one day. Initial solution contains $(\text{Na} + \text{K} + \text{Cl} + \text{SO}_4)$.

DISCUSSION AND CONCLUSIONS

A numerical modeling approach coupling hydraulic and chemical processes was carried out to calculate the evolution of liquid and gas saturations in space and time during the injection of dry supercritical CO₂. A fine discretization of the plug allows us to capture the variations in water and gas profiles within the porous medium and to estimate the salt deposits according to water salinity.

This study emphasizes that the precipitation of salts is a process that must be considered in the simulations of CO₂ injection. Different investigators have worked on this topic, and they have developed some TOUGH modules that simulate the precipitation of NaCl in porous media (Battistelli et al., 1997; Carpita et al., 2006; Giorgis et al., 2007). But for the most part, the salinity of the investigated solutions is expressed in equivalent NaCl. In this study, we go further, demonstrating that the impacts on rock porosity and permeability are highly dependent on the nature of salts. We demonstrate that the precipitation of a Na-SO₄ brine will have more impact on the porosity of a porous medium than the precipitation of a Na-Cl brine. Moreover, besides the nature of the fluid, temperature is also a key factor in the amount of precipitated salt.

This study constitutes just a first step, and many other parameters have to be studied in detail. For instance, up to now all these simulations are performed with a cubic law to represent the relationship between porosity and permeability. This point has not been discussed in this paper but it is a key point in the evolution of the injectivity index. According to the selected relationship (cubic law, Kozeny-Carman, Verma-Pruess), the impact on permeability due to salt precipitation can be under- or overestimated. The particular location of salt precipitation can greatly impact the global permeability of the system, with a possible clogging of the system.

Moreover, from a chemical point of view, these simulations were done with the released version of TOUGHREACT, which uses only the extended Debye-Hückel approach. More accurate predictions of salt formation could be obtained by using a Pitzer formalism.

ACKNOWLEDGMENT

This work has been carried out within the framework of the “Proche Puits” project, co-funded by the French National Agency for Research (ANR).

REFERENCES

- André L., Audigane P., Azaroual M., Menjoz A., Numerical modeling of fluid-rock chemical interactions at the supercritical CO₂-liquid interface during supercritical carbon dioxide injection into a carbonated reservoir, the Dogger aquifer (Paris Basin, France). *Energy Convers. Manag.* 48, 1782-1797, 2007.
- Azaroual M., Kervévan C., Durance M.V., Brochot S., Durst P., SCALE2000 (V3.1), Logiciel de calculs thermodynamiques et cinétiques applicables aux saumures pétrolières, hydrothermales et industrielles (*User's Manual in French*). BRGM, ISBN 2-7159-0939-X, 2004.
- Battistelli A., Calore C., Pruess K., The simulator TOUGH2/EWASG for modelling geothermal reservoirs with brines and a non-condensable gas. *Geothermics*, 26(4), 437-464, 1997
- Carpita M., Giorgis T., Battistelli A., Modeling CO₂ injection with halite precipitation using an extended Verma & Pruess porosity-permeability model. *Proceedings TOUGH symposium 2006*, Berkeley, CA (USA), May 15-17, 2006.
- Giorgis T., Carpita M., Battistelli A., 2D modeling of salt precipitation during the injection of dry CO₂ in a depleted gas reservoir. *Energy Convers. Manag.*, 48, 1816-1826, 2007.
- Helgeson H.C., Kirkham D.H., Flowers G.C., Theoretical prediction of the thermodynamic behaviour of aqueous electrolytes at high pressures and temperatures. 4. Calculation of activity coefficients, osmotic coefficients, and apparent molal and standard and relative partial molal properties to 600 °C and 5 kb. *Am. J. Sci.*, 281, 1249-1516, 1981.
- Kaszuba J.P., Janecky D.R., Snow M.G., Carbon dioxide reaction processes in a model brine aquifer at 200 °C and 200 bars: implications for geologic sequestration of carbon. *Appl. Geochem.*, 18, 1065-1080, 2003.
- Kleinitz W., Dietzsch G., Köhler M., Halite scale formation in gas-producing wells. *Trans IChemE*, 81, Part A, 352-358, 2003
- Mahadevan J., Flow-through drying of porous media. PhD Dissertation. The University of Texas at Austin, August 2005.
- Mahadevan J., Sharma M.M., Yortsos Y.C., Water removal from porous media by gas injection: experiments and simulation. *Transp. Porous Med.*, 66, 287-309, 2007.

- Pettenati M., Mercury L., Azaroual M.: Capillary geochemistry in non-saturated zone of soils. Water content and geochemical signatures. *Appl. Geochem.*, 23, 3799-3818, 2008.
- Piantone P., Nowak C., Blanc P., Lassin A., Burnol A., THERMODDEM : THERmodynamique et MOdélisation de la Dégradation des DEchets Minéraux. Report BRGM/RP- 54547-FR, 2006.
- Pruess K., Oldenburg C., Moridis G., *TOUGH2 User's Guide, Version 2.0*. Report LBNL-43134, Lawrence Berkeley National Laboratory, Berkeley, CA (USA), 1999.
- Pruess K., ECO2N: a TOUGH2 fluid property module for mixtures of water, NaCl and CO₂. Report LBNL-57952, Lawrence Berkeley National Laboratory, Berkeley, CA (USA), 2005.
- Rosenbauer R.J., Koksalan T., Palandri J.L., Experimental investigation of CO₂-brine-rock interactions at elevated temperature and pressure: implications for CO₂ sequestration in deep-saline aquifers. *Fuel Proc. Technol.*, 86, 1581-1597, 2005.
- Rossi C., Nimmo J.R., Modeling of soil water retention from saturation to oven dryness. *Water Resour. Res.*, 30, 701-708, 1994.
- Xu T., Pruess K., Modeling multiphase non-isothermal fluid flow and reactive geochemical transport in variably saturated fractured rocks: 1. Methodology. *Am. J. Sci.*, 301, 16-33, 2001.

REACTIVE GEOCHEMICAL TRANSPORT MODELING TO STUDY CONTRIBUTION OF CHEMICAL TRAPPING MECHANISM IN THE LONG-TERM STORAGE OF CARBON DIOXIDE IN A SALINE AQUIFER

Chitoshi Akasaka¹, Norifumi Todaka², Shuji Ajima¹, and Nakanishi Shigetaka¹

¹Electric Power Development Co., Ltd.
15-1, Ginza 6-Chome, Chuo-ku,
Tokyo 104-8165, Japan
e-mail: chitoshi_akasaka@jpower.co.jp

²Japan CCS Co., Ltd.
7-12, Marunouchi 1-Chome, Chiyoda-ku,
Tokyo 100-0005, Japan
e-mail: norifumi.todaka@japanccs.com

ABSTRACT

Two-dimensional numerical modeling was performed using the reactive geochemical transport code TOUGHREACT to understand the contribution of chemical trapping mechanisms in a saline aquifer. The simulation was carried out for 10,000 years after CO₂ injection ceased, to study the geochemical behavior within long-term CO₂ storage. The geological setting of the model was based on a typical sedimentary basin in Japan. Supercritical CO₂ injected into a reservoir moved upward towards the cap rock because of buoyant forces, but then changed its migrating direction to lateral, along the bottom of the cap rock. In the upper front portion of the migration, CO₂ dissolved into the groundwater. In the CO₂ plume, water pH drops from 7.8 (initial) to 4.9 by dissolution and dissociation of CO₂. The acidified water induces mineral dissolution and complexing with dissolved ions, and then moves downward to the bottom of the reservoir due to density increase. This process caused convective mixing and enhanced CO₂ solubility trapping. Mineral dissolution contributes to solubility acceleration in the evolving early-solubility-trapping period. In the peripheral zone of the CO₂ plume, the acidified water comes in contact with fresh reservoir water and calcite (and siderite, in lesser amount) precipitates. The precipitation of carbonate minerals might form a low-permeability barrier in the peripheral zone and increase the storage security with time. Calcite is the dominant carbonate precipitate for this long-term condition. Dawsonite, which is occasionally considered as an important trapping carbonate in the saline aquifer storage, is found to have limited stability under high CO₂ pressure in the model. While the total amount of CO₂ trapped by mineralization gradually increased with time in long-term storage, solubility trapping was dominated in the early period of storage by mineral dissolution. In the case of this model, injected CO₂ was rapidly dissolved into the groundwater in hundreds of years, then gradually continued to dissolve and finally 33% was trapped by solubility trapping after 10,000 years. Mineral trapping

becomes predominant after 1,000 years, and 9% of the CO₂ is trapped after 10,000 years.

INTRODUCTION

Deep saline aquifers are thought to be potentially one of the important reservoirs for geological sequestration of carbon dioxide, because these aquifers are likely to have the largest storage capacity of all classes of potential geological storage sites. A large amount of storage capacity in saline aquifers is also expected to be found in the coastal area of Japan (Nakanishi et al., 2008).

Evaluation of the CO₂ storage capacity in deep saline aquifers is complex because several trapping mechanisms progress simultaneously. Two trapping processes are known by which CO₂ can become trapped in deep saline aquifers (Bachu et al., 2007) (1) physical trapping (static, residual-saturation and hydrodynamic), and (2) chemical trapping (dissolution and mineralization). Chemical trapping occurs when CO₂ dissolves in subsurface fluids, and may be involved in chemical reactions with the rock matrix (mineral trapping) or become adsorbed onto mineral surfaces. Because the time scale of chemical trapping tends to be long (especially mineral trapping), investigators often turn to numerical modeling, which can be useful in studying the chemical trapping contribution to long-term storage of CO₂. Consequently, we performed numerical modeling using the reactive geochemical transport code TOUGHREACT, to understand the contribution of the chemical trapping mechanism within deep saline aquifers.

NUMERICAL MODELING METHOD

Modeling of reactive geochemical transport within a typical saline aquifer in Japan was performed using the reactive transport computer code TOUGHREACT (Xu and Pruess, 2001; Xu et al., 2006). The code uses a sequential iteration approach (similar to Yeh and Tripathi, 1991; Walter et al.

(1994); and Xu et al., 1999) that solves the transport and reaction equations separately. Flow and transport are based on space discretization by means of integral finite differences (Narasimhan and Witherspoon, 1976). An implicit time-weighting scheme is used for the individual components of the model, consisting of flow, transport, and kinetic geochemical reactions. The chemical transport equations are solved independently for each component, whereas the reaction equations are solved on a gridblock basis using Newton-Raphson iteration. Full details of the code are given in Xu and Pruess (2001). Because CO_2 geological storage in a deep saline aquifer has to treat supercritical CO_2 , the TOUGHREACT ECO2N module (Pruess, 2005) was used for the simulation.

HYDROGEOLOGICAL AND GEOCHEMICAL CONDITIONS

Hydrogeological conditions

At depths greater than ~ 800 m (depending on temperature and pressure profiles), a supercritical pressure regime could be sustained. Thick alternations of sandstone and mudstone, called the Kazusa Group, occur at depth under the Tokyo Bay region in Japan. The Kazusa Group consists of turbidite domain alternation of sandstone and mudstone. The sandstone has high porosity and permeability, and the mudstone has low permeability, characteristics well suited for geological storage of CO_2 . In this simulation study, sandstone (the Umegase Formation) was assumed to be the reservoir, and the mudstone (the Kokumoto Formation) overlaying the sandstone was assumed to be the cap rock.

The simulation model is shown in Figure 1. Model dimensions are 5,000 m (horizontal) \times 400 m (vertical) \times 1,000 m (thick), with a 300 m thick sandstone formation underlying the 100 m thick mudstone (cap rock) in the 2-D aquifer model. The study region is subdivided into 1,100 gridblocks (55 \times 20) for computational purposes (Figure 2). The size of a gridblock was basically 100 m \times 20 m \times 1000 m. Half-size blocks were set near the injecting blocks (from 0 m to 500 m in horizontal). Injecting blocks are set at the left end of the model. From these, pure CO_2 gas is injected at a rate of 7.922 kg/s for 50 years. The total amount of CO_2 injected is 12.5 million metric tons (in other words 25 million tons, considering model symmetry). The properties of injected CO_2 and subsequent reaction of the system was calculated for the 10,000 years after ceasing injection.

The top plane of the cap rock is 1,000 m deep—the permeable region extends from 1,300 to 1,600 m. The left sides and bottom of the computing region are considered impermeable and insulated. The right side and top are considered permeable and a constant

pressure boundary. Temperature is uniform at 40°C , and fluid pressure at the top of the cap rock is equal to 100 bars. The initial pressure distribution with depth is hydrostatic.

Figure 3 shows the relative permeability function used in the simulations. Corey-type (Corey, 1954) relative permeability descriptions shown in Figure 3 are used for the gas phase, and van Genuchten-type (van Genuchten, 1980) descriptions are used for the aqueous phase.

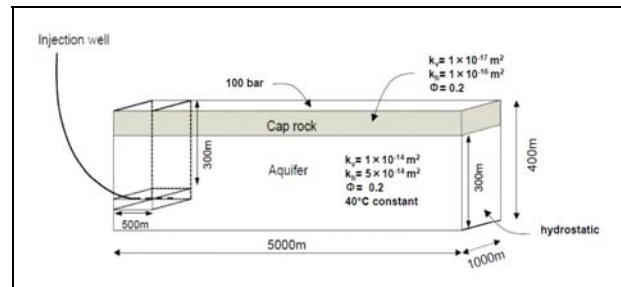


Figure 1. Outline of numerical CO_2 injection model

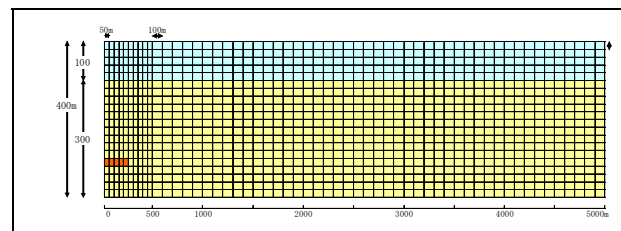


Figure 2. Grid division of the model

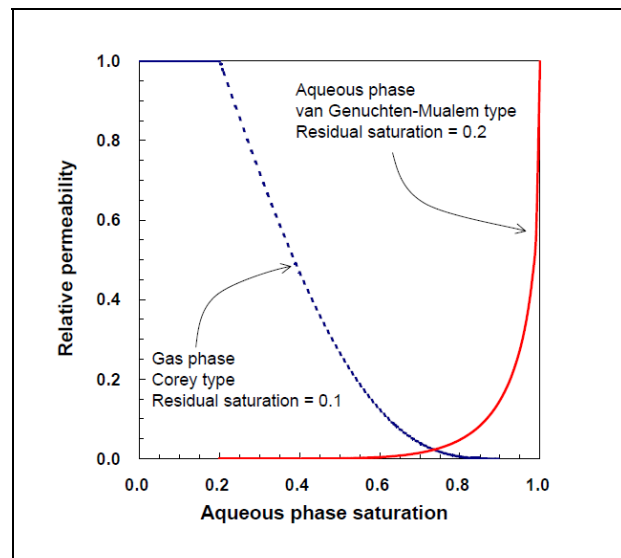


Figure 3. Relative permeability curve used for the simulation

Geochemical conditions

Chemical components of the Kameido Hot Spring were used for simulating water chemistry, as shown in Table 1. This water, representing deep saline formation water, has average salinity and good ionic balance. Chemical components of the rock matrix are indicated in Table 2. Mineral species used for the simulation are those found in the rock and others added from previous references (e.g., Xu and Pruess, 2001; Xu et al., 2006). Chemical species used in the simulation consist of 13 primary and 46 secondary species, as indicated in Table 3 (next page). Parameters for reaction kinetics were taken from Xu et al. (2006), and equilibrium constants from the EQ3/6 V7.2b database.

Table 1. Water chemistry used for the simulation

Component		Initial water
pH	-	7.8
Na ⁺	mg/l	5569.09
K ⁺	mg/l	271.530
Ca ²⁺	mg/l	118.650
Mg ²⁺	mg/l	127.970
Fe ²⁺	mg/l	5.350
Al ³⁺	mg/l	28.170
HCO ₃ ⁻	mg/l	1439.190
Cl ⁻	mg/l	8793.08
SO ₄ ²⁻	mg/l	15.060
SiO ₂ (aq)	mg/l	31.40

Kameido hot spring water (data from Ministry of Health, Labor and Welfare)

Depth: 1100m

Sampling temperature: 29.5°C

SiO₂(aq) concentration is estimated using chalcedony geothermometer.

Table 2. Rock chemistry in volume fraction used for the simulation

Minerals		Umegase Formation	Kokumoto Formation*
Quartz	SiO ₂	0.300	0.330
Oligoclase	Na ₄ CaAl ₆ Si ₁₄ O ₄₀	0.219	0.216
K-feldspar	KAlSi ₃ O ₈	0.011	-
Diopside	CaMgSi ₂ O ₆	0.030	-
Illite	K _{0.6} Mg _{0.26} Al _{2.3} Si _{3.5} O ₁₀ (OH) ₂	0.085	0.158
Na-smectite	Na _{0.33} Mg _{0.33} Al _{1.67} Si _{4.00} O ₁₀ (OH) ₂	0.040	0.121
Ca-smectite	Ca _{0.165} Mg _{0.33} Al _{1.67} Si _{4.00} O ₁₀ (OH) ₂	0.040	0.121
Chlorite	Fe _{2.5} Mg _{2.5} Al ₂ Si ₃ O ₁₀ (OH) ₈	0.021	0.019
Calcite	CaCO ₃	0.001	0.042
Dolomite	CaMg(CO ₃) ₂	-	-
Magnesite	MgCO ₃	-	-
Siderite	FeCO ₃	-	-
Ankerite	CaMg _{0.7} Fe _{0.3} (CO ₃) ₂	-	-
Dawsonite	NaAl(CO ₃)(OH) ₂	-	-
Albite-low	NaAlSi ₃ O ₈	-	-
Kaolinite	Al ₂ Si ₂ O ₅ (OH) ₄	-	-
Goethite	FeO(OH)	-	0.053
Magnetite	Fe ₃ O ₄	0.022	-
Pyrite	FeS ₂	0.006	0.001

*: Estimation by clay mineral norm calculation (Igarashi, 1984)

RESULTS AND DISCUSSION

CO₂ migration

In the simulation, CO₂ injected into the storage reservoir migrated upward towards the cap rock because of buoyant force. In the upper portion of the reservoir, water pH dropped from 7.8 (initial) to 4.9 due to CO₂ dissolution. The acidic condition induces mineral dissolution and complexing with dissolved ions such as Na⁺, Ca²⁺, Mg²⁺ and Fe²⁺ forming NaHCO₃, CaHCO₃⁺, MgHCO₃⁺, and FeHCO₃⁺. Over time, these dissolution and complexing processes increase CO₂ solubility and increase the density of the aqueous phase. That aqueous phase then moves downward due to gravity, giving rise to “convective mixing,” as shown in Figure 4, and CO₂ solubility trapping enhancement. The resulting solubility trapping enhancement due to these processes is consistent with the conclusion of Xu and Pruess (2007).

Mineral dissolution and precipitation

Initially, calcite dissolves in the two-phase region due to induced low pH by CO₂ gas dissolution, whereas calcite and siderite precipitate in the periphery zone of the single aqueous phase—especially just below the mushroom structure of the CO₂ gas migration path (Figure 5). The precipitation of carbonate minerals may form a low-permeability barrier in the periphery zone and increase the storage security over time.

Calcite dissolves and dawsonite precipitates in the two-phase region after 100 years. After several thousand years, calcite changes from dissolution to precipitation, but dawsonite changes from precipitation to dissolution. The changed pattern of dawsonite is related to dissolution of the plagioclase (oligoclase)

and precipitation of kaolinite. Dawsonite is a stable phase only under high CO_2 pressure. Early-formed dawsonite starts to dissolve when the CO_2 pressure decreases out of its stability field, leading to kaolinite precipitation.

Table 3. Chemical species used for the simulation

Primary species: 13
H_2O , H^+ , Na^+ , K^+ , Ca^{2+} , Mg^{2+} , AlO_2^- , Fe^{2+} , Cl^- , HCO_3^- , SO_4^{2-} , $\text{SiO}_2(\text{aq})$, $\text{O}_2(\text{aq})$
Secondary species: 46
OH^- , $\text{HAlO}_2^-(\text{aq})$, $\text{NaAlO}_2(\text{aq})$, $\text{Al}(\text{OH})_2^+$, AlOH^{2+} , Al^{3+} , $\text{CO}_2(\text{aq})$, $\text{NaHCO}_3(\text{aq})$, MgHCO_3^+ , CaHCO_3^+ , FeHCO_3^+ , $\text{CaCO}_3(\text{aq})$, CO_3^{2-} , $\text{MgCO}_3(\text{aq})$, NaCO_3^- , $\text{FeCO}_3(\text{aq})$, CaCl^+ , $\text{CaCl}_2(\text{aq})$, $\text{CaSO}_4(\text{aq})$, CaOH^+ , $\text{NaCl}(\text{aq})$, MgCl^+ , $\text{KCl}(\text{aq})$, FeCl^+ , $\text{HCl}(\text{aq})$, $\text{FeCl}_2(\text{aq})$, FeCl_4^{2-} , $\text{FeSO}_4(\text{aq})$, FeOH^+ , $\text{Fe}(\text{OH})_3(\text{aq})$, $\text{Fe}(\text{OH})_2^+$, $\text{Fe}(\text{OH})_4^-$, FeOH^{2+} , FeCO_3^+ , Fe^{3+} , $\text{H}_2(\text{aq})$, KSO_4^- , $\text{KOH}(\text{aq})$, $\text{MgSO}_4(\text{aq})$, NaSO_4^- , $\text{NaHSiO}_3(\text{aq})$, $\text{NaOH}(\text{aq})$, HS^- , $\text{H}_2\text{S}(\text{aq})$, HSO_4^- , HSiO_3^-

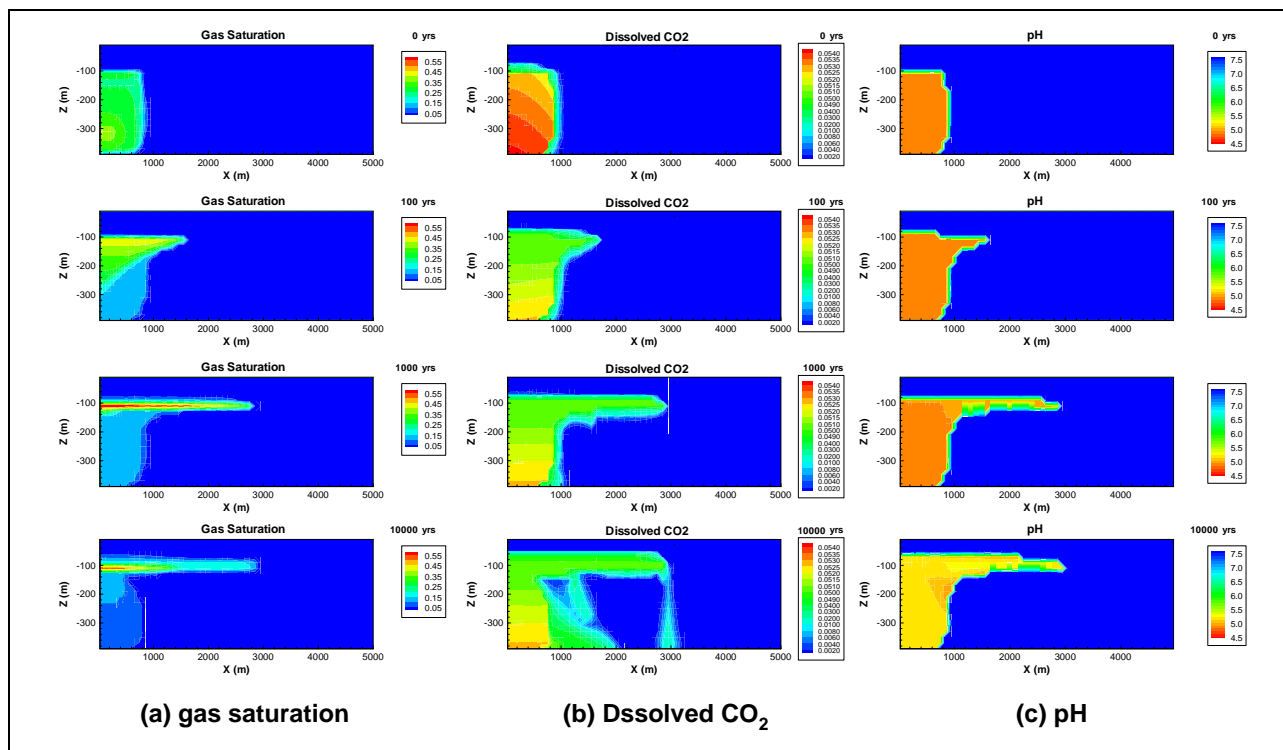


Figure 4. Distribution of gas saturation, dissolved CO_2 , and pH calcite after 0 year, 100 years, 1,000 years and 10,000 years since ceasing CO_2 injection

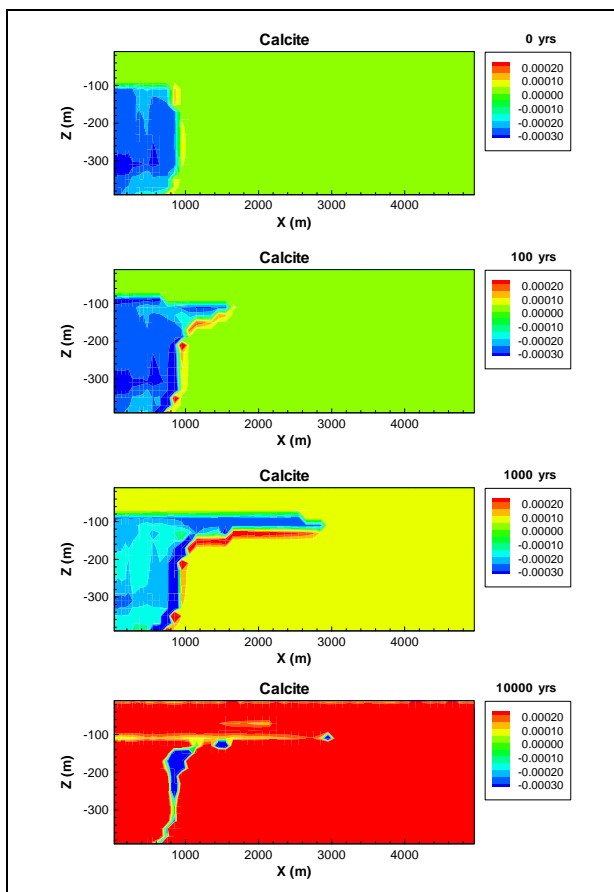


Figure 5. Distribution of calcite after 0 year, 100 years, 1,000 years and 10,000 years since ceasing CO_2 injection

After 10,000 years since ceasing CO_2 injection (Figure 6), pH increases to 5.5 in the two-phase region. Calcite is the dominant carbonate precipitate. The larger mineral-trapping capability is because of the high abundance of plagioclase initially present in the storage formation, whose dissolution provides Ca for calcite precipitation.

Dawsonite is a relatively rare mineral that could form to trap CO_2 under conditions of geological sequestration (high CO_2 partial pressure). Dawsonite could be an important CO_2 trapping mineral according to the reactive transport modeling of Xu et al. (2004), using a U.S. Gulf Coast sandstone.

The kinetic-rate constant (k_{25}) of dawsonite is not well known. Rate constants for aluminosilicate minerals such as plagioclase and K-feldspar used in the modeling are several orders of magnitude smaller than that of carbonate minerals. Therefore, dawsonite precipitation might be controlled by plagioclase dissolution kinetics rather than dawsonite kinetics, because the needed Al^{3+} ion is provided by the dissolution of aluminosilicate minerals.

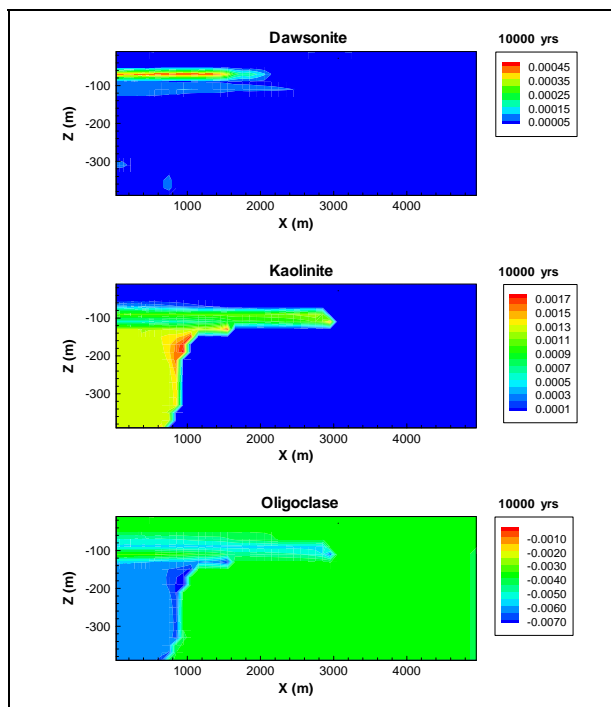
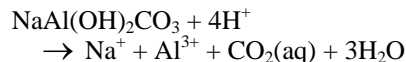


Figure 6. Changes in mineral dissolution or precipitation in volume fraction after 10,000 years since ceasing injection

The kinetic-rate constant (k_{25}) of dawsonite is not well known. Rate constants for aluminosilicate minerals such as plagioclase and K-feldspar used in the modeling are several orders of magnitude smaller than that of carbonate minerals. Therefore, dawsonite precipitation might be controlled by plagioclase dissolution kinetics rather than dawsonite kinetics, because the needed Al^{3+} ion is provided by the dissolution of aluminosilicate minerals.

Dawsonite dissolution would be affected by CO_2 partial pressure as well as Al concentration.



The geochemical behavior of the Al^{3+} ion would be a key in determining the potential of dawsonite to sequester carbon. It is important to understand the dissolution rate of plagioclase as a source of Al^{3+} ion. AIST is carrying out experiments on the dissolution rate of plagioclase (Ca-rich feldspar), under a supercritical CO_2 -water system using a phase-shift interferometer (Sorai et al., 2008). We will compare numerical simulations with natural analogues to understand whether dawsonite is stable during CO_2 sequestration. Note that results are sensitive to many parameters, such as initial mineral composition and reaction kinetics.

Contribution of chemical trapping

Figure 7 shows the contribution of trapping mechanisms to CO₂ geological storage over time. Physical trapping has the higher percentage of total trapping mechanisms over the entire period. Note that it is difficult to distinguish residual trapping from hydrodynamic trapping.

Solubility trapping occurs from the beginning of CO₂ injection, because the injected supercritical CO₂ dissolves in formation water at the contact between CO₂ and water, based on the solubility of CO₂ determined by pressure and temperature.

Mineral trapping becomes predominant 1000 years after ceasing injection. Mineral dissolution into the water dominates at early times, because the acidic condition induces mineral dissolution and complexing, thus mineral precipitation tends to increase.

In this study, 10,000 years after ceasing injection, 9% of injected CO₂ is trapped via mineral trapping and 33% is trapped via solubility trapping.

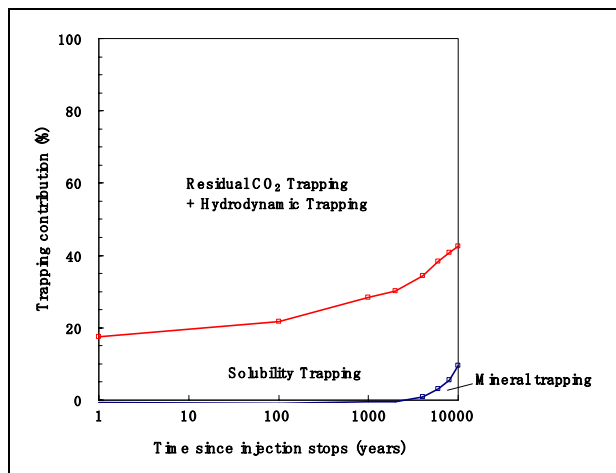


Figure 7. Contribution of CO₂ geochemical storage mechanisms

CONCLUSIONS

Two-dimensional reactive transport simulation is conducted for a deep saline aquifer using TOUGHREACT/ECO2N. The simulation results described here provide useful insight into geological storage mechanisms and their contribution over time. In the resulting simulation, calcite is shown to be the dominant carbonate precipitate under long-term conditions, whereas Dawsonite is found to have limited stability under high CO₂ pressure.

Injected CO₂ rapidly dissolves into the groundwater at early times, then gradually continues to dissolve and finally 33% is trapped as solubility trapping after

10,000 years. Mineral trapping becomes predominant after 1,000 years, with 9% CO₂ trapped at 10,000 years after ceasing injection.

ACKNOWLEDGMENT

The base model of this simulation study was made under contract with Yasuko Okuyama and the CO₂ storage group of the National Institute of Advanced Industrial Science and Technology (AIST).

REFERENCES

- Bachu, S., D. Bonijoly, J. Bradshaw, R. Burruss, N. P. Christesen, S. Holloway and O. Mathiassen, *Estimation of CO₂ Storage Capacity in Geological Media –Phase 2-*, CSLF-T-2007-04, 2007.
- Corey, A.T., The interrelation between gas and oil relative permeabilities. *Producers Monthly*, 38-41, 1954.
- Greenhouse Gas Control Technologies 9, Proceedings of the 9th International Conference on Greenhouse Gas Control Technologies (GHGT-9), Washington DC, 2008.
- Igarashi, T., Calculation of the clay mineral norm (N88 basic program), *geology news*, 352, 37-47 (in Japanese), 1984.
- Intergovernmental Panel on Climate Change, Special report on carbon dioxide capture and storage. Contribution of Working Group III of the Intergovernmental Panel on Climate Change (Metz, B., Davidson, O., Coninck, H., Loos, M. and Meyer, L., Eds.). pp.431, Cambridge University Press, Cambridge, U.K. and New York, N.Y., U.S.A., 2005.
- Nakanishi, S., M. Yasunobu, T. Okumura, H. Miida, T. Shidahara, and S. Hiratsuma, Methodology of CO₂ aquifer storage capacity assessment in Japan and overview of the project, 2639–2646, 2008.
- Narasimhan, T. N. and P. A. Witherspoon, “An integrated finite difference method for analyzing fluid flow in porous media”, *Water Resour. Res.*, 12, 57-64, 1976.
- Okuyama, Y., M. Sasaki, M. Sorai, N. Kaneko, H. Muraoka, N. Yanagisawa and T. Tosha, Formation-water database on saline aquifers in Japan: Toward geochemical modeling in underground sequestration of CO₂. In T. Bullen and Z. Wang (eds.), *Proc. 12th Water-Rock interaction*, 1, 633-636, 2007.
- Pruess, K., C. Oldenburg, and G. Moridis, *TOUGH2 User's Guide, Version 2.0*, Report LBNL-43134, Lawrence Berkeley National Laboratory, Berkeley, Calif., 1999.

- Pruess, K., *ECO2N: A TOUGH2 Fluid Property Module for Mixtures of Water, NaCl, and CO₂*. Lawrence Berkeley National Laboratory Report LBNL-57952, Berkeley, California, August 2005, pp.66, 2005.
- Sorai, M., M. Sasaki, Y. Okuyama And T. Tosha, Dissolution kinetics of Ca-rich feldspar under supercritical CO₂-water system. Abstr. 33rd IGC, COC02610L, Oslo(Norway), 2008.
- van Genuchten, M. T., A closed-form equation for predicting the hydraulic conductivity of unsaturated soils. Soil Sci. Soc. Am. J., 44, 892-898, 1980.
- Walter, A. L., E. O. Frind, D. W. Blowes, C. J. Ptacek, J. W. Molson, "Modeling of multicomponent reactive transport in groundwater: 1, Model development and evaluation", Water Resour. Res., 30, 3137-3148, 1994.
- Xu, T., J. A. Apps, and K. Pruess, Numerical simulation of CO₂ disposal by mineral trapping in deep aquifer. Appl. Geochem. 19, 917-936, 2004.
- Xu, T., J. Samper, C. Ayora, M. Manzano and E. Custodio, "Modeling of non-isothermal multi-component reactive transport in field-scale porous media flow system", Jour. Hydrol., 214, 144-164, 1999.
- Xu, T. and K. Pruess, Modeling multiphase non-isothermal fluid flow and reactive geochemical transport in variably saturated fractured rocks: 1 Methodology. Am. J. Sci. 301, 16-33, 2001.
- Xu, T. and K. Pruess, Mineral Dissolution, Enhanced CO₂ Solubility Trapping and Convective Mixing. AGU Fall Meeting, H13F-1647, 2007.
- Xu, T., E. Sonnenthal, N. Spycher and P K. Pruess, TOUGHREACT: a simulation program for non-isothermal multiphase reactive geochemical transport in variably saturated geologic media. Comput. Geosci. 32, 145-165, 2006.
- Yeh, G. T. and V. S. Tripathi, "A model for simulating transport of reactive multispecies components: model development and demonstration," Water Resour. Res., 27, 3075-3094, 1991.

GEOCHEMICAL MODELING OF CHANGES IN SHALLOW GROUNDWATER CHEMISTRY OBSERVED DURING THE MSU-ZERT CO₂ INJECTION EXPERIMENT

¹Liange Zheng, ¹John A. Apps, ¹Nicolas, Spycher, ¹Jens T. Birkholzer, ²Yousif Kharaka, ²James Thordsen,
²Evangelos Kakouros and ³Robert Trautz

¹Lawrence Berkeley National Laboratory, Berkeley, CA 94720, USA
2 U.S Geological Survey, Menlo Park, CA 94205, USA
³ EPRI, Palo Alto, CA 94304, USA
e-mail: lzheng@lbl.gov

ABSTRACT

Food-grade CO₂ was injected into a shallow aquifer through a perforated pipe placed horizontally 2–2.3 m deep at the Montana State University Zero Emission Research and Technology (MSU-ZERT) field site at Bozeman, Montana. The possible impact of elevated CO₂ levels on groundwater quality was investigated by analyzing 80 water samples taken before, during, and following CO₂ injection from 10 shallow observation wells (1.5 or 3.0 m deep) located 1–6 m from the injection pipe, and from two distant monitoring wells. Field determinations and laboratory analyses suggest rapid and systematic changes in pH, alkalinity, and conductance, as well as increases in the aqueous concentrations of trace element species.

A single-cell geochemical model was created to simulate the processes likely to be responsible for the observed increases in the concentrations of dissolved constituents, e.g., the dissolution of carbonate minerals and/or desorption or ion exchange resulting from lowered pH values. Modeling was conducted using an enhanced version of TOUGHREACT with the capability of calculating the distribution of adsorbed aqueous species using a surface complexation model. Reasonable matches between measured data and model results suggest that: (1) calcite dissolution is the primary pH buffer, (2) increases in the concentrations of most major and trace metal cations except Fe could be explained by Ca⁺²-driven exchange reactions, (3) the release of anions from adsorption sites due to competitive adsorption of carbonate could explain the observed trends of most anions, and (4) siderite dissolution might explain the observed increase in Fe concentration.

INTRODUCTION

One promising approach to mitigating the potential adverse effects of increasing CO₂ in the atmosphere is its storage in deep subsurface reservoirs (Bachu, 2000; White et al., 2005). With proper site selection

and management of CO₂ storage projects, the risks to human health and the environment could be minimal. However, the stored CO₂ could leak from a deep formation into overlying shallow groundwater resources that are used for potable or agricultural purposes. The dissolution of leaking CO₂ in a freshwater aquifer would increase the total concentration of dissolved carbonate and thus increase the acidity. This increased acidity could in turn increase the concentrations of hazardous trace elements, detrimentally impacting groundwater quality.

The mobilization of hazardous trace elements in response to CO₂ intrusion has been reported in laboratory experiments (McGrath et al., 2007; Smyth et al., 2008; Carroll et al., 2009) and field tests (Kharaka et al., 2009a, submitted), and studied using numerical models (Carroll et al., 2008; Apps et al., 2009; Wang and Jaffe, 2004; Zheng et al., 2009a). The chemical processes responsible for the mobilization of trace elements include the dissolution of carbonates (Birkholzer et al., 2008; McGrath et al., 2007), sulfides (Apps et al., 2009; Zheng et al., 2009a) and iron oxyhydroxide minerals (Kharaka et al., 2009b), and surface reactions such as adsorption/desorption and ion exchange (Apps et al., 2009; Zheng et al., 2009a).

In a generic study of groundwater quality changes in response to CO₂ leakage (Apps et al., 2009; Zheng et al., 2009a), reactive transport modeling suggests that substantial increases in aqueous lead and arsenic concentrations could occur as a result of CO₂ intrusion, and the predicted As concentration could locally and incrementally exceed the Maximum Contaminant Level (MCL) mandated by U.S. Environmental Protection Agency (EPA) (U.S. Environmental Protection Agency, 2004). The study also indicated that adsorption/desorption could be very important in mobilizing hazardous elements during CO₂ intrusion. However, as also noted by Apps et al. (2009), both the specific processes leading to mobilization of hazardous constituents and

the magnitude of the effect is determined by site-specific conditions, and field tests accompanied by geochemical model development and interpretation are necessary to confirm the validity of the postulated processes. The CO₂ leakage test at the Montana State University Zero Emission Research and Technology (MSU-ZERT) field site, located at Bozeman, Montana, provides just such an opportunity.

At the MSU-ZERT field site, CO₂ was injected into a shallow aquifer (Spangler et al., 2009). The possible impact of elevated CO₂ levels on groundwater quality was investigated by sampling and analyzing groundwaters before, during and following CO₂ injection (Kharaka et al., 2009b). Increases in the concentrations of major and trace chemical constituents were observed following injection of CO₂. The principal objective of this study is to identify the geochemical processes responsible for the observed changes in the chemical composition of the groundwater in response to elevated partial pressures of CO₂.

In the following sections, we provide a brief description of the ZERT field test. We then describe the setup of a numerical model to simulate the observed geochemical response to CO₂ leakage. The model results are then compared with field observations. The paper concludes with a discussion of the results, some tentative conclusions, and cautionary notes regarding still to be resolved uncertainties relating to the present modeling.

MSU-ZERT FIELD TEST

The ZERT field site is located on a relatively flat 12-hectare agricultural plot at the western edge of the MSU-Bozeman campus (Spangler et al., 2009). The overall goal of this research project is to evaluate atmospheric and near-surface monitoring and detection techniques applicable to the subsurface storage and potential leakage of CO₂ (<http://www.montana.edu/zert/home.php>). Details of regional setting, test methods, geology and hydrologic conditions of the test area are given in Spangler et al. (2009).

Between July 9 and August 7, 2008, approximately 300 kg/day of food-grade CO₂ was injected into a shallow aquifer through a perforated pipe placed horizontally 2-2.3 m deep, the average depth to the water table being approximately 0.75 m. As part of the project, United States Geological Survey (USGS) staff collected approximately 80 water samples from 10 observation wells (1.5 or 3.0 m deep) located 1-6 m from the injection pipe, and from two distant monitoring wells (Kharaka et al., 2009). The samples were collected before, during and following CO₂

injection. Detailed chemical analyses were conducted on over 60 groundwater samples collected from the ZERT wells during July and August 2008 (Kharaka et al., 2009). Thirty chemical constituents, T, EC, pH, TDS and total cation and anion concentrations were also measured. Rapid and systematic changes following CO₂ injection were observed in chemical parameters measured at the site, including pH, alkalinity, electrical conductance and the concentrations of major and trace chemical constituents.

GEOCHEMICAL MODEL

Geochemical data analysis

As a preliminary step in developing a geochemical model, the measured geochemical data were subjected to a principal component analysis (PCA) to establish correlations between the chemical constituents and tentatively identify thermodynamic controls. Given that the groundwater at the ZERT site is very shallow and easily perturbed by atmospheric precipitation, the dataset used in the geochemical evaluation was restricted to 21 complete analyses of groundwaters taken between July 7, and July 17, 2008, before the first significant rainfall after CO₂ injection had started. The PCA results were interpreted in conjunction with preliminary results of mineralogical studies of core material and used as a basis for hypothesizing some of the principal chemical processes that might be operative. The PCA findings are as follows:

- A strong correlation between alkali metals (Li, Na, K), alkali earths (Mg, Ca, Sr, Ba), B, Al, Cr, SiO₂(aq), Cd, and Pb, and an inverse relationship to pH is observed, suggesting ion exchange, most likely on smectite.
- F, As, Se and Mo are correlated, suggesting possible adsorption of anionic species on secondary iron oxides or anionic clays.
- NO₃ is negatively correlated with Mn, Fe, and Co, and positively correlated with As, suggesting that NO₃ is acting as an oxidizing agent, leading respectively to secondary precipitation or co-precipitation of Mn, Fe and Co, or oxidative mobilization of As.
- PO₄ is negatively correlated with Mn, Fe, and Co, suggesting some precipitation/dissolution mechanism may be operative.
- Cl, Br, and SO₄⁻² are correlated and appear to be related to atmospheric precipitation.
- U and Zn are outliers, whose chemical behavior is not presently understood.

Model setup

To evaluate whether adsorption/desorption and cation exchange can explain the observed evolution of aqueous constituents, a single-cell geochemical model was set up using the reactive transport simulator TOUGHREACT. The capabilities of this code were enhanced through incorporation of a surface complexation model to compute the distribution of adsorbed chemical species on mineral surfaces (Zheng et al., 2009a).

The measured CO₂ volume fractions in the monitoring well headspace at the ZERT site increase up to 90%, which indicates that the partial pressure of CO₂ in contact with groundwater increases to about 1 bar at the water table, and in excess of 1 bar at the point of injection. We therefore assume in the model that CO₂ is injected continually into the cell, so that the fugacity of CO₂ eventually attains 1.5 bars while the pH falls concomitantly to about 5.8 due to an assumed instantaneous equilibration of gaseous CO₂ with the aqueous phase. The elements of the model are described below.

Initial conditions

Table 1. Primary species and their initial concentration

Species	Concentration (mol/L)	Species	Concentration (mol/L)
pH	7.1	Ba ⁺²	7.9E-07
Ca ⁺²	1.9E-03	Cd ⁺²	2.0E-09
Mg ⁺²	9.8E-04	Co ⁺²	4.2E-09
Na ⁺	3.3E-04	Cu ⁺²	2.4E-08
K ⁺	1.4E-04	H ₂ AsO ₄ ⁻	1.3E-08
Fe ⁺²	1.8E-09	Mn ⁺²	1.8E-08
AlO ₂ ⁻	1.2E-07	Sr ⁺²	3.0E-06
SiO ₂ (aq)	5.3E-04	Zn ⁺²	4.6E-08
Cl ⁻	1.3E-04	HSeO ₃ ⁻	4.9E-08
HCO ₃ ⁻	6.3E-03	MO ₄ ⁻²	4.6E-09
SO ₄ ⁻²	7.7E-05	UO ₂ ⁺²	1.7E-08
NO ₃ ⁻	9.6E-06	Cr(OH) ₂ ⁺	2.2E-07
O ₂ (aq)	1.2E-51	HPO ₄ ⁻²	1.8E-06
Pb ⁺²	2.4E-10	Li ⁺	7.7E-07

Five samples were taken before the release of CO₂. The initial chemical composition (Table 1) was taken from sample 08ZERT-107, with pH adjusted slightly from 6.7 to 7.1 so that our calculation covers the pH range of all samples considered in this study. Aqueous speciation was conducted with EQ3 (Wolery, 1993) to identify the primary species. The initial partial pressure of CO₂ in the groundwater is calculated to be 2.5×10⁻² bars. Furthermore, calcite is close to saturation, i.e., SI(calcite) ≈ -0.1.

Mineralogy

Kharaka et al. (2009) describe the geology at the MSU-ZERT site. However, detailed mineralogical characterization of core material is still under way. Preliminary mineralogical analyses of cored sections to a depth of approximately 3 m showed that sediments in the saturated zone were composed predominantly of a matrix of cobble-sized rounded fragments, consisting primarily of andesitic volcanic rocks with predominant plagioclase, quartz-biotite-amphibole gneiss, and red granite/gneiss. The mafic volcanic rock fragments were very high in magnetic iron. Minor limestone and occasional dolomite fragments were also observed in the matrix. Unspecified Fe oxides appear in a <0.25 mm fraction as “powdery orange blebs.” Secondary carbonate coatings were found throughout the core, and a caliche zone was present in the overlying unsaturated zone. Small quantities of clay (~1 wt%), believed to consist of smectite and minor kaolinite were also found in the saturated zone. Table 2 lists the minerals considered in the model as proxies for the mineralogy of the sediment matrix. Arbitrary volume fractions are assigned to each mineral, which are roughly consistent with the preliminary mineralogy analyses. It should be noted that in the time frame of the simulation described in this paper, most of the listed rock-forming minerals are essentially inert, i.e., they are unreactive.

Table 2. Minerals considered in the model.

Primary Mineral	Volume fraction	Primary Mineral	Volume fraction
Quartz	0.45	Ferrihydrite	0.01
K-feldspar	0.1	Magnetite	0.02
Oligoclase	0.34	Goethite	0.001
Smectite	0.01	Siderite	0.001
Dolomite	0.02	Calcite	0.05

Chemical reactions

Chemical reactions considered in the model include aqueous complexation, cation exchange, adsorption/desorption and mineral dissolution/precipitation. Of these, cation exchange and adsorption/desorption reactions are believed to predominate. Table 3 lists the cation exchange reactions and the selectivity coefficients. Gaines-Thomas convention is used here. The selectivity coefficient for exchangeable H⁺ is taken from Charlet and Tournassat (2005), and those for the remainder of the exchangeable cations are taken from Appelo and Postma (1994). The cation exchange capacity (CEC) is the key parameter for the calculation of cation exchange. Because the measured CEC for the sediments at MSU-ZERT site is not currently available, we used the measured the CEC of

around 12 meq/100g for Hanford sediments (Steeffel et al., 2003), which has similar composition to the sediments at the MSU-ZERT site. A nonelectrostatic surface complexation model calculates adsorption/desorption, which involves most anions and H^+ . Table 4 lists the surface complexation reactions. Surface complexation constants are taken from Dzombak and Morel (1990). Hydrated ferric iron oxide (HFO) is assumed to be the only adsorbent. The site density for the strong site is assumed to be 1.76×10^{-6} mol/m², and that for weak sites is assumed to be 3.22×10^{-6} mol/m² (Muller and Sigg, 1991). The specific surface area is assumed to be 14.7 m²/g (Muller and Sigg, 1991).

Table 3. Cation exchange reactions and selectivity coefficients.

Cation exchange reaction	$K_{Na/M}$
$Na^+ + X-H = X-Na + H^+$	1
$Na^+ + X-K = X-Na + K^+$	0.2
$Na^+ + 0.5X-Ca = X-Na + 0.5Ca^{+2}$	0.4
$Na^+ + 0.5X-Mg = X-Na + 0.5Mg^{+2}$	0.45
$Na^+ + 0.5X-Pb = X-Na + 0.5Pb^{+2}$	0.4
$Na^+ + 0.5X-Ba = X-Na + 0.5Ba^{+2}$	0.35
$Na^+ + 0.5X-Cd = X-Na + 0.5Cd^{+2}$	0.4
$Na^+ + 0.5X-Co = X-Na + 0.5Co^{+2}$	0.6
$Na^+ + 0.5X-Cu = X-Na + 0.5Cu^{+2}$	0.5
$Na^+ + 0.5X-Mn = X-Na + 0.5Mn^{+2}$	0.55
$Na^+ + 0.5X-Sr = X-Na + 0.5Sr^{+2}$	0.35
$Na^+ + 0.5X-Zn = X-Na + 0.5Zn^{+2}$	0.4
$Na^+ + 0.5X-Fe = X-Na + 0.5Fe^{+2}$	0.6

Mineral dissolution/precipitation reactions are written in terms of the primary species listed in Table 1. Table 5 lists their solubility products, which, except for siderite, are based on the database, Data0.dat.YMP.R4 qualified by the U.S. Department of Energy for the Yucca Mountain Project and used with EQ3.V7.2b (Wolery, 1993). The solubility product of siderite is that recommended by Preis and Gamsjager (2002), which differs slightly from that adopted in Data0.dat.YMP.R4. Kinetic rate constants of mineral dissolution are important only for those minerals that dissolve rapidly under the conditions and duration-selected interval of the MSU-ZERT test, such as calcite and siderite. Currently, TOUGHREACT (Xu et al., 2006) uses a general form of rate expression based on transition state theory (TST) (Lasaga et al., 1994; Steefel and Lasaga, 1994):

$$r = kA \left[1 - (Q/K)^\theta \right]^\eta \quad (1)$$

where r is the kinetic rate (positive values indicate dissolution, negative values precipitation), k is the rate constant (moles per unit mineral surface area and unit time), which is temperature dependent, A is the specific reactive surface area per kg H₂O, K is the equilibrium constant for the mineral–water reaction written for the destruction of one mole of mineral, and Q is the reaction quotient. The parameters θ and η should be determined by experiments, but are commonly set equal to unity when experimental quantification is unavailable. For further details concerning the kinetics of mineral dissolution/precipitation, the reader is referred to Xu et al. (2006).

Table 4. Surface complexation reactions and surface complexation constants (logK) on HFO

Surface complexation	logK
$HFO_sOH_2^+ = HFO_sOH + H^+$	-7.29
$HFO_wOH_2^+ = HFO_wOH + H^+$	-7.29
$HFO_sO^- + H^+ = HFO_sOH$	8.93
$HFO_wO^- + H^+ = HFO_wOH$	8.93
$HFO_sOHSO_4^{-2} = HFO_sOH + SO_4^{-2}$	-0.79
$HFO_wOHSO_4^{-2} = HFO_wOH + SO_4^{-2}$	-0.79
$HFO_sSO_4^- + H_2O = HFO_sOH + SO_4^{-2} + H^+$	-7.78
$HFO_wSO_4^- + H_2O = HFO_wOH + SO_4^{-2} + H^+$	-7.78
$HFO_sSeO_3^- + H_2O = HFO_sOH + HSeO_3^-$	-4.29
$HFO_wSeO_3^- + H_2O = HFO_wOH + HSeO_3^-$	-4.29
$HFO_sMoO_4^- + H_2O = HFO_sOH + MoO_4^{-2} + H^+$	-9.5
$HFO_wMoO_4^- + H_2O = HFO_wOH + MoO_4^{-2} + H^+$	-9.5
$HFO_sOHMoO_4^{-2} = HFO_sOH + MoO_4^{-2}$	-2.4
$HFO_wOHMoO_4^{-2} = HFO_wOH + MoO_4^{-2}$	-2.4
$HFO_sH_2AsO_4 + H_2O = HFO_sOH + H_2AsO_4^- + H^+$	-10.17
$HFO_wH_2AsO_4 + H_2O = HFO_wOH + H_2AsO_4^- + H^+$	-10.17
$HFO_sHAsO_4^- + H_2O = HFO_sOH + H_2AsO_4^-$	0.35
$HFO_wHAsO_4^- + H_2O = HFO_wOH + H_2AsO_4^-$	0.35
$HFO_sH_2PO_4 + H_2O = HFO_sOH + HPO_4^{-2} + 2H^+$	-18.9
$HFO_wH_2PO_4 + H_2O = HFO_wOH + HPO_4^{-2} + 2H^+$	-18.9
$HFO_sPO_4^{-2} + H_2O = HFO_sOH + HPO_4^{-2}$	-5.4
$HFO_wPO_4^{-2} + H_2O = HFO_wOH + HPO_4^{-2}$	-5.4
$HFO_wCO_2^- + H_2O = HFO_sOH + HCO_3^-$	-2.45
$HFO_wCO_2H + H_2O = HFO_sOH + HCO_3^- + H^+$	-2.45

Table 5. Solubility production of minerals

Primary Mineral	Solubility product	Primary Mineral	Solubility product
Quartz	-3.75	Ferrihydrite	-63.24
K-feldspar	-22.91	Magnetite	-6.505
Oligoclase	-97.78	Goethite	-8.12
Smectite	-39.51	Siderite	-0.251
Dolomite	2.524	Calcite	1.85

RESULTS AND DISCUSSION

Earlier generic studies of CO₂ leakage into potable groundwater aquifers (Birkholzer et al., 2008; Wang and Jaffe, 2004; Zheng et al., 2009a) indicated that the dissolution of carbonate minerals (mainly calcite) can significantly buffer pH through the dissociation of carbonic acid. Clay ion exchangers, when present in significant amounts in an aquifer host rock or sediment, can also strongly buffer pH through exchange of H⁺ with the groundwater (Bradbury and Baeyens, 1997; Samper et al., 2008; Zheng and Samper, 2009; Zheng et al., 2009b). In the present model, the dissolution of calcite, dolomite and siderite and H⁺ buffering through cation exchange and surface complexation could all contribute to buffering pH. Figure 1 shows the calculated pH by different combinations of these chemical equilibria. A simulation without carbonate minerals leads to a lower pH than the base case where the presence of carbonates is assumed, but is only marginally higher than the simulation without any buffering. This suggests that at the MSU-ZERT site, dissolution of carbonate minerals is the principal pH buffering process, whereas the H⁺ exchange by clays does not affect pH significantly, because the shallow saturated zone at the MSU-ZERT site soil does not contain large amounts of clay minerals.

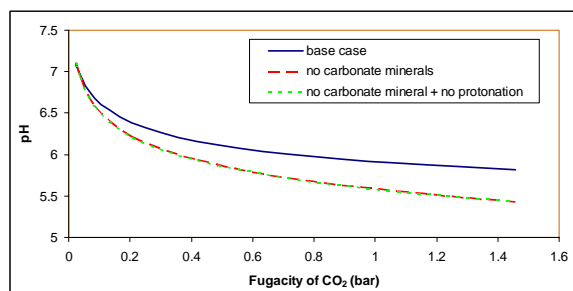


Figure 1. Calculated pH with different combination of chemical reactions

The groundwater at the MSU-ZERT site responds promptly to the release of CO₂, as the pH falls within 1 or 2 days, and a significant increase in major cations and trace metals are observed before the first rainfall occurs about 10 days later. In such a short-

duration test, only the dissolution kinetic rates for rapidly dissolving minerals such as calcite are important. The dissolution rate of calcite is particularly critical, because the resulting increase of Ca⁺² induces cation exchange, which is responsible for the increases in major cations and most trace metals except for Fe and possibly Mn and Co. Depending on the level of undersaturation, according to Kaufmann and Dreybrodt (2007), the dissolution of calcite can be described by a fast and a slow rate law. The fast and slow rate laws are discriminated by the ratio of calcium concentration in the solution to the calcium concentration in equilibrium with calcite (C/Ceq) at a given CO₂ partial pressure. Kaufmann and Dreybrodt (2007) reported that when the ratio (C/Ceq) is <0.3, the fast rate law applies, whereas when C/Ceq > 0.3, the slow rate law applies. In the current simulation, C/Ceq is about 0.4–0.5 and thus the slow rate law is adopted where the rate constant *k* in Equation (1) is 1.6×10⁻⁶ mol/m²/s. Svensson and Dreybrodt (1992) investigated the dissolution kinetics of calcite in CO₂-water systems approaching calcite equilibrium and gave a rate constant *k* of 1.6×10⁻⁶ – 2.2×10⁻⁶ mol/m²/s, although they indicated that C/Ceq should be around 0.6–0.8. Gledhill and Morse (2006) reported that the dissolution rate depends on brine composition, pCO₂ (0.1–1 bar), and temperature and the rate constant (*k*) can be estimated from a multiple regression model. Applying their regression model to our simulation conditions, the rate constant is from 1.6×10⁻⁶ to 2.2×10⁻⁵ mol/m²/s. Jordan and Rammensee (1998) gave a dissolution rate of 1.6×10⁻⁶ mol/m²/s on the calcite surface obtained by scanning force microscopy, which corresponds well to the rates obtained from batch experiments. Pokrovsky et al. (2005) measured the dissolution rate of calcite at high pressure, which is more relevant to deep CO₂ geological storage than CO₂ releases at the MSU-ZERT site. In summary, the published dissolution rates for calcite at lower levels of undersaturation are quite consistent. The value adopted in this study falls within the lower range of published values and correlates well with measured changes in calcium concentration observed in the field (Figure 2). If a higher calcite dissolution rate is used, such as that given by Gledhill and Morse (2006), i.e., 2.2×10⁻⁵ mol/m²/s, the computed calcium concentration overestimates the measured data (Figure 2).

With a decrease in pH, calcite dissolves and releases Ca⁺² into the aqueous phase. Aqueous Ca⁺² in turn exchanges with the exchangeable cations on the cation exchanger, tentatively assumed to be smectite. As a result, the concentrations of the major cations increase in solution. Figures 3 and 4 show the calculated sodium and magnesium concentration

versus pH. The close fits between calculated and measured concentrations support the hypothesis that cation exchange could dominate the evolution of major cations in response to the CO₂ leakage at the MSU-ZERT site. Figures 5–8 show the calculated lead, cadmium, copper, and zinc. With the exception of Zn, which PCA shows to behave anomalously, reasonable matches between calculated and measured concentrations again suggest that the calcium-driven cation exchange could explain the observed trace metal response to CO₂ leakage.

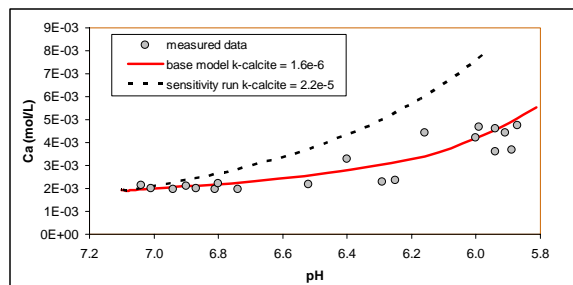


Figure 2. Calculated calcium concentration vs pH with different calcite dissolution rate.

A simulation that considers only cation exchange for iron leads to a significant underestimation of measured iron concentrations (see Figure 9). This finding is consistent with the PCA, which indicates that its behavior is not identified with the component associated with ion exchange. We therefore decided, for the sake of argument, to test the assumption that siderite dissolution might be contributing to the increase in aqueous iron concentration, even though it is initially undersaturated ($SI(\text{siderite}) \approx -2.5$). Although the predicted iron concentrations are still lower than those actually measured, a better fit is obtained. Note that the calculated iron concentration is highly sensitive to the rate of siderite dissolution. In the present study, the kinetic rate reported by Duckworth and Martin (2004) is adopted. These investigators studied the dissolution of siderite under both oxic and anoxic conditions at 298 K, and fitted their measured data to a mechanistic kinetic equation similar to that employed in TOUGHREACT. The rate constant is given for both neutral and acid dissolution mechanisms:

$$k = k_n[\text{H}_2\text{O}] + k_H[\text{H}^+] \quad (2)$$

with $k_n = 10^{-8.65}$ mol/m²/s and $k_H = 10^{-4.6}$ mol/m²/s, respectively. The dissolution rate is dominated by the neutral mechanism when $\text{pH} > 5.5$, whereas the acid mechanism becomes important when $\text{pH} < 5.5$. Testemale et al. (2009) confirmed that the dissolution

rate constant of siderite at acid condition ($\text{pH} < 4$) can be expressed as:

$$k = k_H[\text{H}^+] \quad (3)$$

with $k_H = 10^{-9.3}$ mol/cm²/s ($k_H = 10^{-5.3}$ mol/m²/s) which is close to the k_H given by Duckworth and Martin (2004). Testemale et al. (2009) compared their findings with other data (Braun, 1991; Golubev et al., in press) and concluded that published kinetic rates for siderite dissolution are generally in good agreement. Duckworth and Martin (2004) also mentioned that the dissolution of siderite is retarded under oxic conditions. At the MSU-ZERT site, the existence of dissolved oxygen in the saturated zone cannot be discounted, since the water table is close to the surface, and the observed presence of secondary ferric oxy-hydroxides is at least indicative of transient oxidative conditions. The dissolution rate of the postulated siderite used in current model thus might be higher than actually occurs, although the calculated iron concentration is lower than measured data. Model results suggest the dissolution of ferrihydrite ($\text{Fe}_2\text{O}_3 \cdot 13\text{H}_2\text{O}$) favors goethite precipitation, but this process would barely contribute to the observed increase in total aqueous iron.

Table 6. Initial (C^i) and final (C^f) adsorbed concentration and their difference $C^f - C^i$

Adsorbed species	C^i	C^f	$C^f - C^i$
s_H ⁺	1.7E-03	2.0E-03	3.0E-04
s_SO ₄ ⁻²	5.2E-07	2.1E-07	-3.1E-07
s_HSeO ₃ ⁻	9.4E-07	5.2E-07	-4.2E-07
s_MoO ₄ ⁻²	1.7E-09	1.0E-09	-7.1E-10
S_HCO ₃ ⁻	2.3E-03	3.0E-03	7.2E-04
s_H ₂ AsO ₄ ⁻	8.5E-08	6.7E-08	-1.9E-08
s_HPO ₄ ⁻	2.3E-04	2.3E-04	7.4E-07

Another effect of increasing dissolution of CO₂ in the groundwater is the increase of aqueous bicarbonate (HCO₃⁻) concentration (Figure 10). This increase modifies the distribution of adsorbed anionic species on HFO. Table 6 lists the adsorbed concentrations associated with those ions considered in the surface complexation reactions on HFO, as listed in Table 4. Desorption and adsorption constitutes the net effects of decreasing and increasing the concentrations for all relevant surface complexes. For example, the desorption/adsorption of As(V) can be represented by all relevant surface complexes including HFO_sH₂AsO₄, HFO_wH₂AsO₄, HFO_sHAsO₄⁻ and HFO_wHAsO₄⁻ (see Table 4). The total adsorbed concentration (represented as s_H₂AsO₄⁻ in Table 6) is the summation of the concentrations for all four

complexes. Table 6 shows the initial (C^i) and final (C^f) adsorbed concentrations and their difference $C^f - C^i$. Negative values of $C^f - C^i$ indicate desorption, while positive values indicate adsorption. Initially, adsorbed carbonate occupies a large portion of the sorption sites (about 55%). The increase in HCO_3^- due to the dissolution of CO_2 leads correspondingly to increased adsorption of carbonate on the HFO surface. As a result, some anionic species are displaced into the aqueous phase. Figure 11 shows the aqueous concentration of arsenic. The good agreement between computed and measured As concentrations supports carbonate-initiated desorption as a controlling process for As(V). It should be noted, however, that our model has ignored adsorption due to As(III) species, and these could influence the distribution of total As between adsorption sites and the aqueous solution. However, a preliminary evaluation of the distributions of aqueous species in MSU-ZERT groundwater samples using EQ3 indicates that As(V) oxy-fluoride complexes species predominate in solution. Whether such species might also adsorb remains an open question.

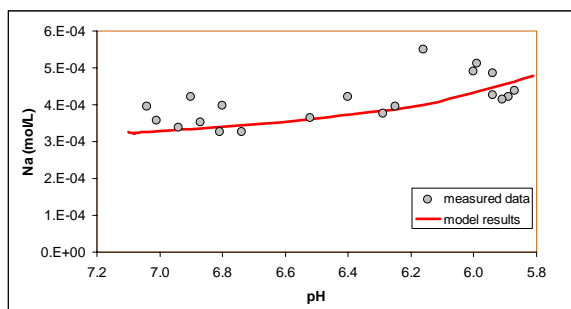


Figure 3. Calculated sodium concentration vs pH.

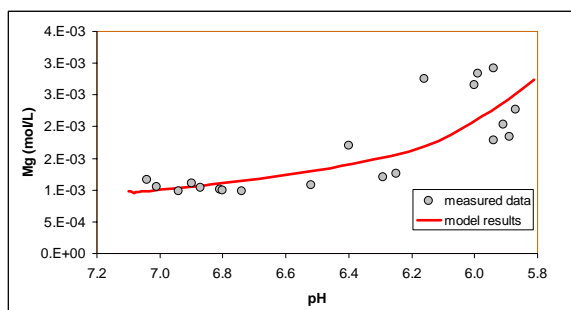


Figure 4. Calculated magnesium concentration vs pH.

The computed aqueous concentrations of selenium overestimate the measured concentrations (Figure 12), possibly attributable either to uncertainties in the selenite surface-complexation constant, or to the omission of adsorbed selenate or selenide species. Preliminary EQ3 distribution of species modeling

suggests that oligomeric neutral selenide complexes of Fe and Zn may predominate in solution, although such a distribution is highly dependent on a correct estimate of the redox state of the groundwater, and the unlikely assumption that homogeneous equilibrium with respect participating redox species has been attained. The concentration of aqueous phosphate (Figure 13) decreases with the decrease in pH, because anionic adsorption occurs. Although the concentrations of adsorbed HFO_sPO_4^{-2} and HFO_wPO_4^{-2} tend to decrease as carbonate species adsorb, the concentrations of $\text{HFO_sH}_2\text{PO}_4$ and $\text{HFO_wH}_2\text{PO}_4$ increase as the pH falls, the incremental increase more than compensating for the decrease in HFO_sPO_4^{-2} and HFO_wPO_4^{-2} . Adsorption thus occurs, and the concentration of phosphate in the groundwater falls.

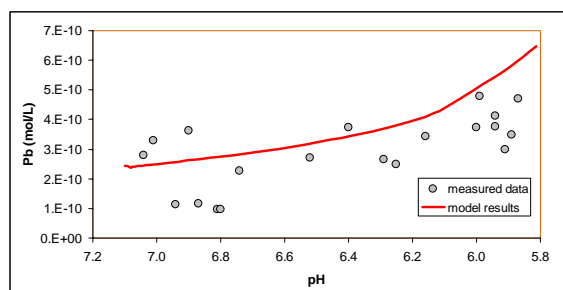


Figure 5. Calculated lead concentration vs pH

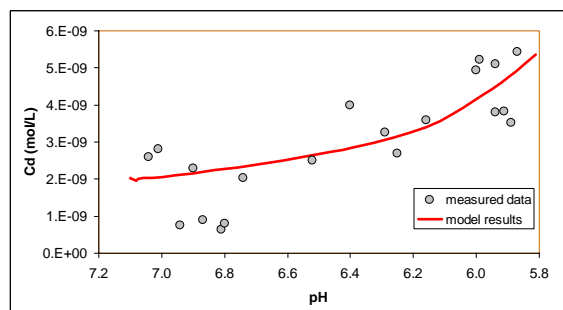


Figure 6. Calculated cadmium concentration vs pH

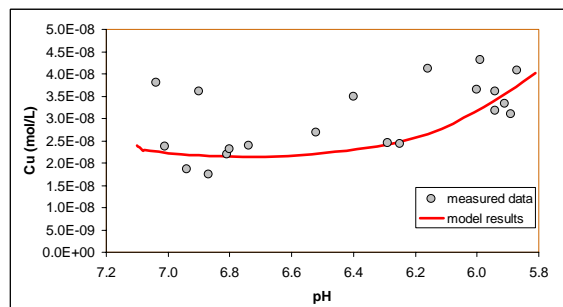


Figure 7. Calculated copper concentration vs pH

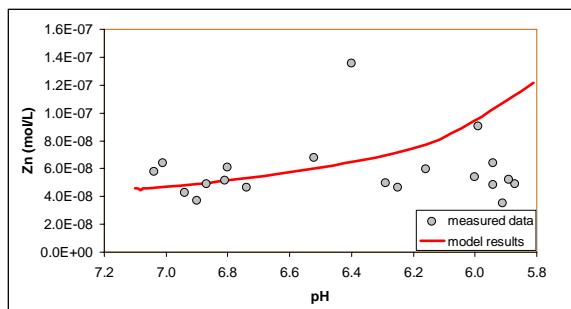


Figure 8. Calculated zinc concentration vs pH

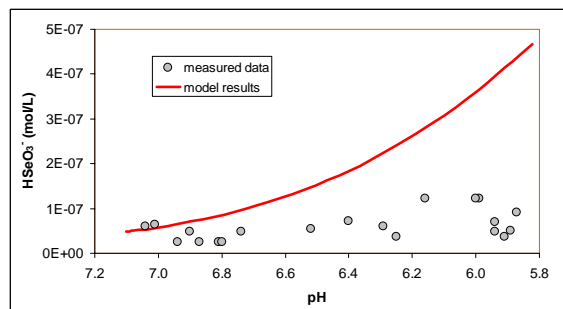


Figure 12. Calculated selenium concentration vs pH

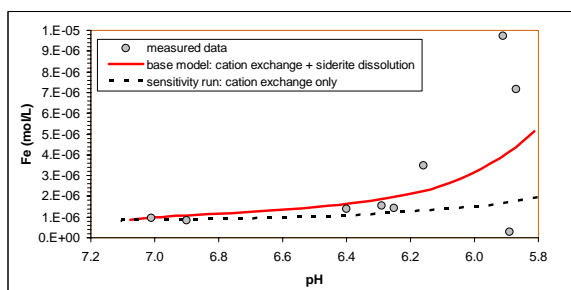


Figure 9. Calculated iron concentration vs pH in the base model, in which both cation exchange and siderite dissolution are considered and a sensitivity run in which only cation exchange is considered

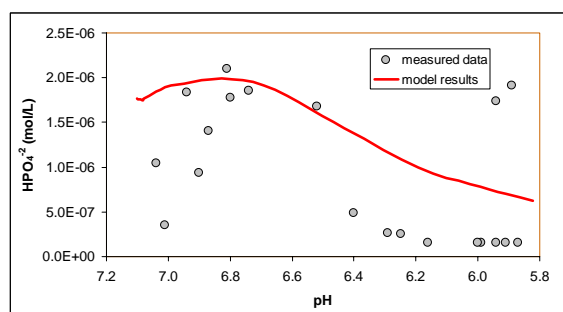


Figure 13. Calculated phosphate concentration vs pH

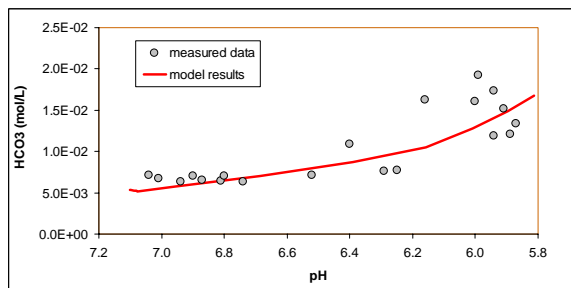


Figure 10. Calculated bicarbonate concentration vs pH

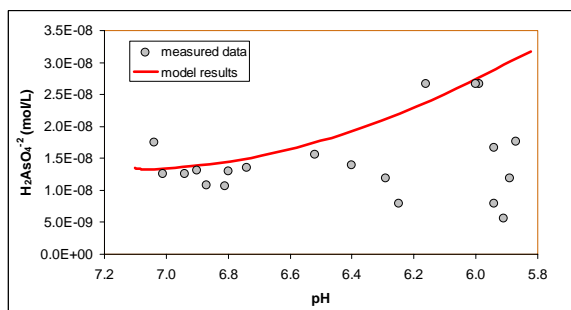


Figure 11. Calculated arsenic concentration vs pH

CONCLUDING REMARKS

Rapid and systematic increases in major and trace elements were observed at the MSU-ZERT field test (Kharaka, et al., 2009b), which has been interpreted with a single-cell geochemical model in which hypothesized chemical processes were tested. Measured data before the first rainfall after the start of the test were used for comparison with model results, in an attempt to eliminate complex interactions resulting from mixing of infiltrating rainwater with the groundwater. Reasonable matches between measured data and model results suggest that (1) calcite dissolution could be the primary process buffering pH, (2) the increase in the concentrations of major cations and trace metals except Fe could be explained by Ca^{+2} -driven exchange reactions, (3) the release of anions from adsorption sites due to competing adsorption of bicarbonate could explain the concentration trends of most anions and (4) siderite dissolution might explain the increase in total Fe concentration.

Because of the lack of key parameters such as the cation exchange capacity, smectite and iron oxyhydroxide content, current model interpretation of measured data depends largely on hypothetical values for those critical parameters. Consequently, the observed correlation between measured data and our model is not conclusive. Furthermore, secondary precipitates whose concentrations are too low to be

detected by conventional mineralogical methods of analysis might control the aqueous concentrations of some trace elements. Finally, many of the trace elements might be presenting different oxidation states than assumed. Because characterization of the redox state of the groundwater at the MSU-ZERT site has not yet been successful, and there is ample evidence to suggest that a state of disequilibrium exists in the groundwater with respect to redox species, our modeling does not capture this condition, and the redox state of some of the trace element species may have been misidentified. Thus, the model results presented here represent work in progress rather than the final word. More precise modeling will be conducted as further mineralogical and chemical characterization studies are completed, and the system is better characterized.

ACKNOWLEDGMENT

This research was conducted within the MSU-ZERT project directed by Lee Spangler and managed by Laura Dobeck, MSU, Bozeman, MT. We thank the entire MSU-ZERT team and participating organizations for creating a supportive and exciting research environment. This research was funded primarily by the Electric Power Research Institute, EPRI.

REFERENCES

- Appelo, C.J.A. and D. Postma, *Geochemistry, groundwater and pollution*. A.A.Balkema, Rotterdam, Netherlands, 1994.
- Apps, J.A., L. Zheng, Y. Zhang, T. Xu and J.T. Birkholzer, Evaluation of Groundwater Quality Changes in Response to CO₂ Leakage from Deep Geological Storage. *Transport in Porous Media*, submitted, 2009.
- Bachu, S., Sequestration of CO₂ in geological media: criteria and approach for site selection in response to climate change, *Energy Conv. Manag.*, 42, 953–970, 2000.
- Birkholzer, J.T., J.A. Apps, L. Zheng, Y. Zhang, T. Xu and C.-F. Tsang, *Research Project on CO₂ Geological Storage and Groundwater Resources: Water Quality Effects Caused by CO₂ Intrusion into Shallow Groundwater*. Technical Report LBNL-1251E, Lawrence Berkeley National Laboratory, Berkeley, CA, 2008.
- Bradbury, M.H. and B. Baeyens, A mechanistic description of Ni and Zn sorption on Namontmorillonite, part II: modelling. *J. Contaminant Hydrology*, 27, 223-248, 1997.
- Braun, R.D., Solubility of iron(II) carbonate at temperature between 30 and 80°, *Talanta*, 38(2), 205-211, 1991.
- Carroll, S., Trace metal release from Frio Sandstone reacted with CO₂ and 1.5N NaCl brine at 60 °C, Eighth Annual Carbon Capture & Sequestration Conference, May 4-7, Pittsburgh, PA, 2009.
- Carroll, S., Y. Hao, and R. Aines. Transport and detection of carbon dioxide in dilute aquifers, Proceedings 9th International Conference on Greenhouse Gas Control Technologies, November 2008, Washington, D.C., 2008.
- Charlet, L. and C. Tournassat, Fe(II)–Na(I)–Ca(II) Cation Exchange on Montmorillonite in Chloride Medium: Evidence for Preferential Clay Adsorption of Chloride – Metal Ion Pairs in Seawater, *Aquatic Geochemistry*, 11, 115-137, 2005.
- Duckworth, O.W. and S.T. Martin, Role of molecular oxygen in the dissolution of siderite and rhodochrosite. *Geochimica et Cosmochimica Acta*, 68(3), 607-621, 2004.
- Dzombak, D.A. and F.M.M. Morel, *Surface complexation modeling-hydrous ferric oxide*, John Wiley & sons, New York, 393 pp. 1990.
- Gledhill, D.K. and J.W. Morse, Calcite dissolution kinetics in Na–Ca–Mg–Cl brines, *Geochimica et Cosmochimica Acta*, 70: 5802-5813, 2006.
- Golubev, S.V., P. Bénézech, J. Schott, J.-L. Dandurand and A. Castillo, Siderite dissolution kinetics in acidic aqueous solutions from 25 to 100 °C and 0 to 50 atm pCO₂. *Chemical Geology*, Special Issue on CO₂ geological sequestration, in press.
- Jordan, G. and W. Rammensee, Dissolution rates of calcite (1014) obtained by scanning force microscopy: Microtopography-based dissolution kinetics on surfaces with anisotropic step velocities, *Geochimica et Cosmochimica Acta*, 62, 941-947, 1998.
- Kaufmann, G. and W. Dreybrodt, Calcite dissolution kinetics in the system CaCO₃–H₂O–CO₂ at high undersaturation, *Geochimica et Cosmochimica Acta*, 71, 1398-1410, 2007.
- Kharaka, Y., D.R. Cole, S.S. Hovorka, W.D. Gunther, K.G. Knauss, and B.M. Freifeld, Gas-water-rock interactions in Frio formation following CO₂ injection: implications for the storage of greenhouse gases in sedimentary basins, *Geology*, 34, 577–580, 2006.

- Kharaka, Y.K., J.J. Thordsen, S.D. Hovorka, H.S. Nance, D.R. Cole, T.J. Phelps and K.G. Knauss, Potential environmental issues of CO₂ storage in deep saline aquifers: Geochemical results from the Frio-I Brine Pilot test, Texas, USA, *Applied Geochemistry*, 24, 1106-1112, 2009.
- Kharaka Y.K., J. Thordsen, E. Kakouros, G. Ambats, W. N. Herkelrath, J.T. Birkholzer, J.A. Apps, N.F. Spycher, L. Zheng, R. C. Trautz, H.W. Rauch, K.S. Gullickson. Changes in the Chemistry of Shallow Groundwater Related to the 2008 Injection of CO₂ at the ZERT Field Site, Bozeman, Montana, *Environmental Geology*, Submitted.
- Lasaga, A.C., J.M. Soler, J. Ganor, T.E. Burch and K.L. Nagy, Chemical weathering rate laws and global geochemical cycles, *Geochimica et Cosmochimica Acta*, 58, 2361-2368, 1994.
- McGrath, A.E., G.L. Upson, and M.D. Caldwell (2007), Evaluation and mitigation of landfill gas impacts on cadmium leaching from native soils, *Ground Water Monitoring & Remediation*, 27, 99-109.
- Muller, B. and L. Sigg, Adsorption of lead(II) on the goethite surface: voltammetric evaluation of surface complexation parameters, *Journal of Colloid and Interface Science*, 148(2), 517-532, 1991.
- Pokrovsky, O.S., S.V. Golubev and J. Schott, Dissolution kinetics of calcite, dolomite and magnesite at 25 °C and 0 to 50 atm pCO₂, *Chemical Geology*, 217, 239-255, 2005.
- Preis, W. and H. Gamsjager, Critical evaluation of solubility data: enthalpy of formation of siderite, *Phys. Chem. Chem. Phys.*, 4, 4014-4019, 2002.
- Samper, J., L. Zheng, A.M. Fernández and L. Montenegro, Inverse modeling of multicomponent reactive transport through single and dual porosity media. *Journal of Contaminant Hydrology*, 98(3-4), 115-127, 2008.
- Smyth, R.C., S.D. Hovorka, J. Lu, K.D. Romanak, J.W. Partin, and C. Wong, Assessing risk to fresh water resources from long term CO₂ injection – laboratory and field studies, Proceedings 9th International Conference on Greenhouse Gas Control Technologies, November 2008, Washington, D.C., 2008.
- Spangler LH, Dobeck LM, A controlled field pilot in Bozeman, Montana, USA, for testing near surface CO₂ detection techniques and transport models, *Environmental Geol.*, Submitted, 2009.
- Steeffel, C.I., S. Carroll, P. Zhao and S. Roberts, Cesium migration in Hanford sediment: a multisite cation exchange model based on laboratory transport experiments, *Journal of Contaminant Hydrology*, 67(1-4), 219-246, 2003.
- Steeffel, C.I. and A.C. Lasaga, A coupled model for transport of multiple chemical species and kinetic precipitation/dissolution reactions with applications to reactive flow in single phase hydrothermal system, *Am. J. Sci*, 294, 529-592, 1994.
- Svensson, U. and W. Dreybrodt, Dissolution kinetics of natural calcite minerals in CO₂-water systems approaching calcite equilibrium. *Chemical Geology*, 100, 129-145, 1992.
- Testemale, D., F. Dufaud, I. Martinez, P. Bénézeth, J.-L. Hazemann, J. Schott and F. Guyot, An X-ray absorption study of the dissolution of siderite at 300 bar between 50 °C and 100 °C, *Chemical Geology*, 259, 8-16, 2009.
- Wang, S. and P.R. Jaffe, Dissolution of a mineral phase in potable aquifers due to CO₂ releases from deep formations; effect of dissolution kinetics, *Energy Conversion and Management*, 45, 2833-2848, 2004.
- White, C.M., D.H. Smith, K.L. Jones, A.L. Goodman, R.B. LaCount, S.B. DuBose, E. Zdemir, B.I. Morsi and K.T. Schroeder, Sequestration of carbon dioxide in coal with enhanced coalbed methane recovery—A review, *Energy Fuels*, 19, 659-724, 2005.
- Wolery, T.J., EQ3/6, A software package for geochemical modelling of aqueous systems (Version 7.2). UCRL-MA 110662, Lawrence Livermore National Laboratory. 1993.
- Xu, T., E. Sonnenthal, N. Spycher and K. Pruess, TOUGHREACT: A Simulation Program for Non-isothermal Multiphase Reactive Geochemical Transport in Variably Saturated Geologic Media. *Computers and Geosciences*, 32: 145-165, 2006.
- Zheng, L., J.A. Apps, Y. Zhang, T. Xu and J.T. Birkholzer, On mobilization of lead and arsenic in groundwater in response to CO₂ leakage from deep geological storage, *Chemical Geology*, 2009a.
- Zheng, L. and J. Samper, A coupled THMC model of FEBEX mock-up test. *Physics and Chemistry of the Earth*, 33, S486-S498, 2009.
- Zheng, L., J. Samper, L. Montenegro and A.M. Fernández, A coupled THMC model of a heating and hydration laboratory experiment in unsaturated compacted FEBEX bentonite, *Journal of hydrology*, submitted, 2009b

ENVIRONMENTAL ENGINEERING

MODELING THE MULTIPHASE DIFFUSIVE PROCESSES OF TRITIUM IN AN UNDERGROUND ACCELERATOR FACILITY

Quanlin Zhou^{a*}, Lehua Pan^a, James Hylan^c, Byron G. Lundberg^b,
Robert K. Plunkett^b, Stephen H. Pordes^b, and Stefan Finsterle^a

^aEarth Sciences Division, Lawrence Berkeley National Laboratory, Berkeley, CA 94720

^bParticle Physics Division, Fermi National Accelerator Laboratory, Batavia, IL 60510

^cAccelerator Division, Fermi National Accelerator Laboratory, Batavia, IL 60510

e-mail: qzhou@lbl.gov

ABSTRACT

Tritium is generated by neutrino experiments in the underground NuMI facility at Fermilab, Illinois. Detailed measurements have shown that tritium is (1) generated in steel and concrete shielding, as well as in surrounding fractured rock, (2) transported through the facility mainly as tritiated water-vapor along with ventilated air through a tunnel, and (3) locally transferred into liquid water, which (a) seeps into the tunnel and is collected by a drainage system, or (b) is imbibed into surrounding concrete and fractured rock. Mitigation measures have been taken, and tritium concentrations have been reduced. To understand the transport of tritium in the variably saturated engineered and earth materials, we developed a three-dimensional flow and transport model using TOUGH2. The model focuses on a 670 m section of the facility (fractured rock, concrete shielding, a tunnel, and a drainage system) and accounts for variably saturated water flow from saturated rock to the drainage system. Steady-state flow conditions were calibrated against multipoint flow-rate observations. The transport model was developed to account for advection and diffusion of tritium in the tunnel, concrete, and fractured rock, as well as diffusive mass transfer among these three elements of the facility. The diffusion coefficient of tritium in fully saturated and unsaturated concrete samples was measured experimentally (indicating that the effective diffusion coefficient linearly depends on water saturation) and used directly for our numerical modeling. Modeling results indicate that the tritium mass generated during the facility's lifetime accumulates in the concrete shielding, and then is slowly transported, advectively and diffusively, into the drainage system surrounding the concrete shielding—which is consistent with the observation of tritium concentrations and mass collected during the first 4 years of the project operation.

1. SITE DESCRIPTION

Fermi National Accelerator Laboratory (Fermilab) operates the Neutrino at the Main Injector (NuMI) beamline for experimental studies in physics. NuMI is an ~1,300 m long underground facility, consisting of a pre-target tunnel, a target pile within a target

hall, a decay pipe, a passageway running parallel to the decay pipe, an absorber hall, the MINOS Hall, several ventilation shafts, and various surface facilities (Figure 1). The slope of the decay pipe is ~5.8%; the depth of the sump is ~100 m below land surface. The facility has been excavated in Silurian-age Niagaran and Alexandrian dolomite, and Ordovician-age Maquoketa Shale overlain by glacial till. Airflow through NuMI is controlled by two engineered ventilation systems, and the exhaust air is discharged to the atmosphere at four locations. Water entering the facility is collected in a drainage system and pumped to surface holding tanks.

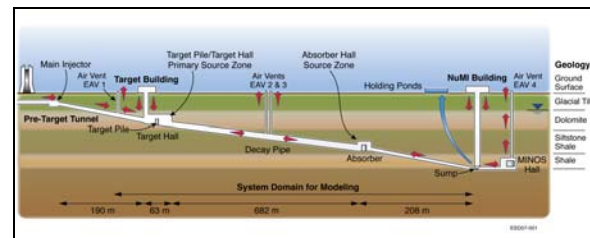


Figure 1. Schematic of the NuMI facility (not to scale)

The NuMI beamline produces (among other radionuclides) tritium as a byproduct. This tritium production occurs predominantly in the target pile within the target hall, but also in the absorber hall, in the concrete along the decay pipe, and in the surrounding rock formation. Tritium may be generated in the gas phase, in pore water, and in the solid components of the surrounding engineered and earth materials. Once the tritium is generated, it may be contained at the source location or migrate to other parts of the facility, with the possibility of being released to the surrounding environment. To monitor the fate of tritium, samples of water, concrete, and rock have been collected at multiple locations within the facility to infer tritium concentrations in the vapor phase, pore water, drainage water, condensate, and solid materials. Figure 2 shows the tritium concentration of the drainage water (pumped from the tunnel sump) in the surface holding tank, as well as the beam intensity in terms of the amount of protons on the target (pot) for the physics experiments. There are significant variations in

tritium concentrations caused by switching of many operation components (e.g., ventilation on/off, dehumidifier addition, and conditions for the target pile sealing and air flow recirculation). These operation conditions mainly affect the air-flow flux and the tritiated water concentrations in the air flow, both of which in turn affect the mass transfer between the air flow and seeping water in the tunnel. In spite of the variations in the tritium concentration, there has been no systematic trend of minimum concentration increase with time during the 4-year operation of the facility. This indicates that the tritium collected in the drainage system mainly comes from the mass transfer from tritiated-water-vapor-containing air flow through the tunnel to the seeping water on the tunnel walls; the direct release of tritium generated in the concrete shielding contributes little to the tritium mass collected at the sump. Additional evidence in support of this conclusion is that there is no apparent correlation between the tritium concentrations in the sump and the beam intensity, which determines the rate of tritium production in the concrete and fractured rock.

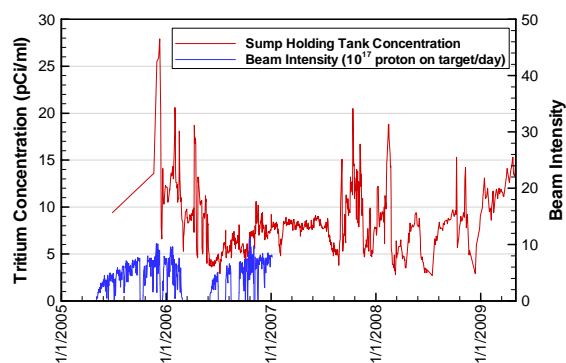


Figure 2. Tritium concentrations in the surface holding-tank water pumped from the sump of the drainage system, and beam intensity

Since most of the measured tritium concentrations in the drainage water are less than the EPA standard of 20 pCi/ml for drinking water, there is no direct environmental concern about tritium contamination in the drainage water and groundwater in the vicinity of the facility. This research addresses the long-term fate of tritium produced in the decay-pipe concrete shielding, including advection and diffusion in the unsaturated concrete, and the slow release into the drainage system during NuMI operation time (2006 through 2019) and after the site is decommissioned.

2. RELEVANT TRANSPORT PROCESSES

2.1. Transport Processes

In this modeling study, we focused on the 670 m long decay-pipe region, a cross section of which is shown

in Figure 3. The cross section consists of the concrete shielding, the walkway tunnel, the drainage system (the “dimple mat” between fractured rock and the concrete shielding, grates, and the main drain), and surrounding fractured rock. The radial part of the cross section consists of four concentric zones: (1) the vacuum tube ($r < 1$ m), (2) the decay-pipe concrete ($1 \text{ m} < r < 3.3$ m), (3) the tritium-producing zone of the fractured rock ($3.3 \text{ m} < r < 6$ m), and (4) an outer, tritium-free region ($6 \text{ m} < r < 15$ m).

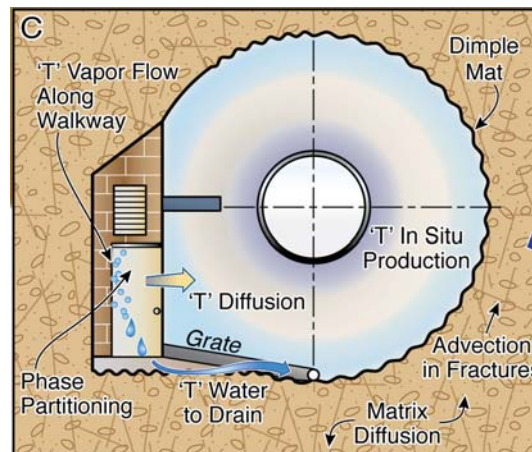


Figure 3. Schematic of tritium production and transport in a vertical cross section

For the representative cross section of the decay pipe, there are various processes involved in transporting the tritium generated in the facility. Globally, tritium is transported with ventilated air flow from the source region in the Target Pipe and Hall and from the source region in the Absorber Hall. Locally, the tritiated water vapor is mass-transferred into the water seeping around the walls of the walkway tunnel, while the seeping water with relatively high concentrations is collected through 11 grates into the main drain, and then mixed with the low-concentration water flowing through the dimple mat. The low tritium concentration results from advective transport through fractures and diffusion in the matrix of the tritium generated in the fractured rock. A much higher tritium mass, generated in the concrete, is transported advectively and diffusively to the dimple mat. Advective transport within the unsaturated concrete depends on the intrinsic permeability and relative permeability, which are a function of the concrete water saturation. Diffusive transport in the unsaturated concrete depends on water saturation (Pruess et al., 1999). In the modeling effort, we neglected the global air flow and its mass transfer with seeping water around tunnel walls. We focused on the fate and transport of tritium generated in the unsaturated concrete.

2.2. Tritium Production

The tritium mass produced in the concrete shielding of the decay pipe was simulated using the MARS model (Lundberg, 2006). The model was used to calculate the spatially varying star density by

$$S_C = A_0 \exp(Az) [A_1 \exp(B_1 r + D_1) + \exp(B_2 r + D_2)] \quad (1)$$

where S_C (star/cm³ pot) is the star density (defined as a hadronic interaction vertex with at least one secondary particle that has a kinetic energy higher than a cut-off value (e.g., 30 MeV)) per unit volume of concrete per proton on target, r (cm) is the radius from the center of the vacuum tube, z (cm) is the longitudinal distance from the start of the target pile, and the parameter values are $A_0 = 2.73 \times 10^{-7}$, $A_1 = 0.14$, $A = -4.49 \times 10^{-5}$, $B_1 = -0.032$, $D_1 = 2.91$, $B_2 = -0.082$, and $D_2 = 7.462$. These model parameters were obtained through calibrating the MARS model against the measured concrete concentration (see Figure 4).

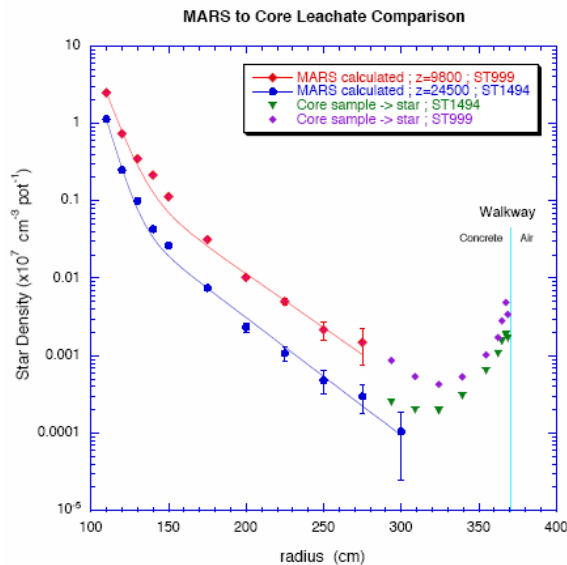


Figure 4. Fitting of star density values (symbols) calculated using the MARS model by exponential functions (solid line), with converted star density values (symbols) from tritium concentration measured in concrete cores (Lundberg, 2006)

In the MARS model, the decay pipe starts at $\sim z = 5,100$ cm and ends at $z = 72,000$ cm, based on the reference point for the coordinate z ($z = 9,300$ cm for STA 9+84). The number of stars (N_S) generated per pot within a given concrete element of

volume (r_{\min}, r_{\max}) by (z_{\min}, z_{\max}) in the 2D radial system can be calculated easily by integration. The non-uniform distribution of tritium mass is calculated using (1) the stars for a given gridblock and (2) the cumulative total number of protons on target during this period. The tritium activity (M) generated within a given volume is calculated as

$$M = N_S \times K_p \times W_m \times M_n \times SA \times N_P \quad (2)$$

where N_S (star/pot) is the number of stars, K_p (³H/star) is the tritium production rate per star, W_m (= 20 mole/atom) is the molar weight of the tritiated water (HTO), M_n (1.67×10^{-24} g/mole) is the mass of HTO per nuclei, SA (1520 Ci/g) is the specific activity of HTO, and N_P (pot) is the total number of protons on target for a given time period. Based on the parameter values provided above (Lundberg, 2006), the tritium activity in the concrete is calculated to be:

$$M_C = 3.72 \times 10^{-21} N_S N_P \text{ (Ci)} \quad (3)$$

where a value of $K_p = 0.0732$ ³H/star is used for the concrete, and M_C is the tritium activity in the concrete. The annual beam intensity for the lifetime operation of the facility varies from 1.5×10^{20} pot to 8.0×10^{20} pot, with a total of 48×10^{20} pot. Considering the slight difference in the MARS model parameters for the medium- and (later) low-energy physics experiments, the total tritium mass-generated in the concrete is 1161.8 Ci for 2006 through 2019.

3. MODEL DEVELOPMENT

3.1. Mesh Generation

Figure 5 show the 2D mesh for a cross section. The 2D mesh consists of a radial-gridblock region, and a rectangular-gridblock region. The radial-gridblock region includes 33 rows (having the same radius), each having 40 gridblocks and a radian of 0.05π . Normal to the row, discretization varies from 0.01 m to 0.2 m for the concrete ($1 \text{ m} < r < 3.3 \text{ m}$) and 0.25 to 0.4 m for the tritium-producing zone of the fractured rock ($3.3 \text{ m} < r < 6 \text{ m}$), and 2.0 m to 3.0 m for the tritium-free zone of the fractured rock ($6 \text{ m} < r < 15 \text{ m}$). The rectangular-gridblock region is embedded within the radial-shaped region in the vicinity of the walkway, including part of the concrete, the entire walkway, and part of the fractured rock. Different refinement of the rectangular gridblocks is used to capture the seepage along the tunnel walls and the sharp change in water saturation. A thin (0.05 m) ring of high-permeability

elements at $r = 3.3$ m represents the dimple mat. For the entire 3D model domain, 49 model layers along the decay pipe were employed, honoring the geometric feature of the decay pipe. Gridblocks of the 11 grates were added to account for gravity drainage, and a column of 49 gridblocks were added to represent the main drain, which was connected to the grate gridblocks and dimple-mat gridblocks.

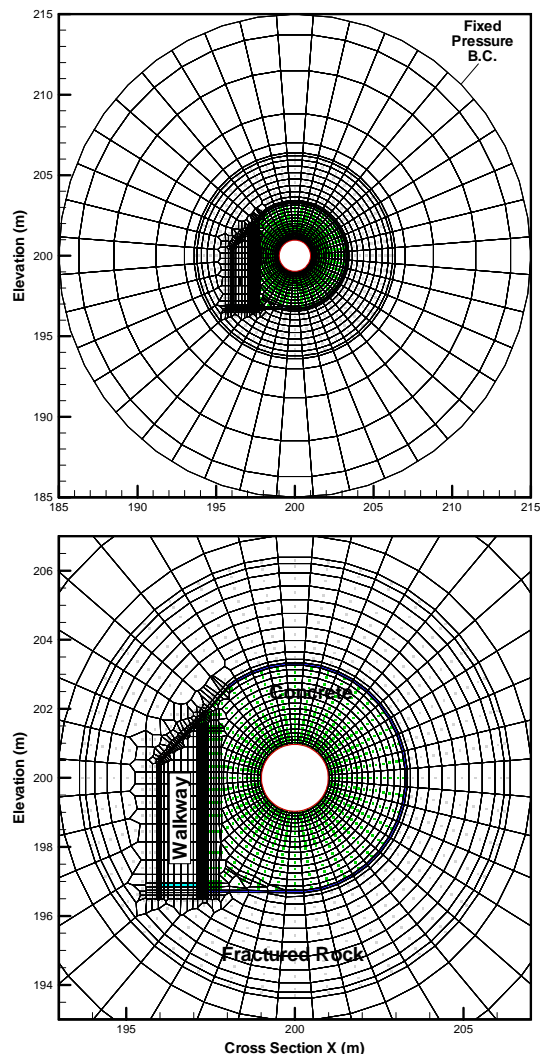


Figure 5. Model domain, computational TOUGH2 mesh, and boundary conditions for a reference cross section centered at (200 m, 200 m)

A methodology was used to deform the base cross section 2D mesh along the decay pipe to account for the geometric changes of the walkway and the vacuum tube relative to the concrete. For each cross section, the number of gridblocks was kept unchanged; the nodes used for defining the boundary of each gridblock were used to track the geometric changes. For a deformed model layer, the volume and connection properties (distances, interface area) were

accordingly changed for all gridblocks located within a region enveloped by fixed-coordinate nodes. In total, there were ~95,000 3D gridblocks.

3.2. Rock and Concrete Properties

The model domain is located within four geologic layers: (in order from the top) the Kankakee Formation of dolomite, the Elwood Formation of dolomite, the Brainard Formation of dolomite, siltstone, and shale, and the Scales Formation of shale and mudstone. Their permeability assigned to the model is 1.44×10^{-14} , 1.44×10^{-14} , 2.88×10^{-15} and 1.44×10^{-16} m², respectively. For the concrete (using the recipe provided by Fremilab), the absolute permeability and porosity measured on the fabricated decay pipe are 5.7×10^{-15} m², and 0.218, respectively. The concrete diffusion coefficient was also measured on a different fabricated decay-pipe concrete using through-diffusion laboratory experiments. The measured diffusion coefficient is 2.4×10^{-10} m²/s for fully saturated samples, while the measured value is smaller for the same samples with a water saturation of 0.6. The porosity of this fabricated concrete sample is 0.23, close to the samples for measuring absolute permeability. Permeability for the drainage system (the dimple mat, grates, and main drain) is set to be an arbitrarily high value.

3.3. Boundary Conditions

Considering that the convergent flow to the drainage system is dominant over regional groundwater flow, we assumed that the water table is constant in the area of the NuMI facility; only the local water flow converging towards the NuMI drainage system (i.e., dimple mat, grates in passageway, and main drain) was simulated. The convergent water flow was assumed to be at steady state. Water pressure at the outer radial boundary was specified assuming hydrostatic conditions with a water level of 210.30 m (690 feet). The walkway was connected to EAV 2 and EAV 3, which were at atmospheric pressure. The main drain was also at atmospheric pressure with an open-channel flow.

For the transport simulation, initially there was no tritium concentration in the entire model domain. Tritium mass is introduced into the system via a source term for the concrete gridblocks. The mass influx for each concrete gridblock is calculated using Eq. (1) and the beam intensity.

4 MODELING RESULTS AND DISCUSSION

4.2. Quasi-Steady-State Flow

The entire NuMI facility is under the water table. The passageway is connected to EAV 2 and EAV 3, which are at atmospheric pressure. The main drain is also at atmospheric pressure. Figure 6a shows the pressure distribution in an upstream cross section,

with the center of the decay pipe shifted from 184.17 m to 200 m. The concrete, the walkway tunnel, and the immediate surrounding fractured rock are unsaturated, with water saturation close to zero in the tunnel and 0.5 in the concrete, while most of the fractured rock is fully saturated. The flow is from out of the model domain to the drainage system, and water is collected through the dimple mat and tunnel through grates to the main drain. The flow rate for the entire decay pipe region is about 6.3 L/s (100 gallons/minute). The calibrated fractured rock permeability for the upper two hydrogeologic layers is $1.44 \times 10^{-14} \text{ m}^2$.

The saturation of the concrete was initially very low, and the dimple mat around the concrete reduces the interface area, so that the concrete saturation might slowly increase with time as a result of capillary imbibition. There were no saturation measurements available; however, the saturation was calibrated through the transport simulation. The measured tritium concentration in the drainage water was not affected by the release of tritium generated in the concrete during the first four years of operation. The measured absolute permeability was $5.7 \times 10^{-15} \text{ m}^2$, and the advective transport in the concrete was negligible. As a result, the relative permeability of the aqueous phase was small. The calibrated concrete saturation was ~ 0.5 .

4.2. Transient Transport

For the transient transport simulation, we assumed that the flow was steady state, with very slow water flow into the concrete from the dimple mat. Initially, we assumed that the entire domain was free of tritium, and that tritium was generated in the concrete at a total rate of 57.12 Ci/year for 10 years. The non-uniform distribution of the tritium mass generated was generated using Equations (1) and (2). Transport mechanisms include advection, diffusion, and decay, and the half life of tritium is 12.4 years. The unsaturated diffusion coefficient depends on the tritium diffusion coefficient in water ($1.0 \times 10^{-9} \text{ m}^2$), medium's tortuosity (0.218), and the effective tortuosity related to water saturation (0.5) (Pruess et al., 1999).

4.1. Steady-State Flow

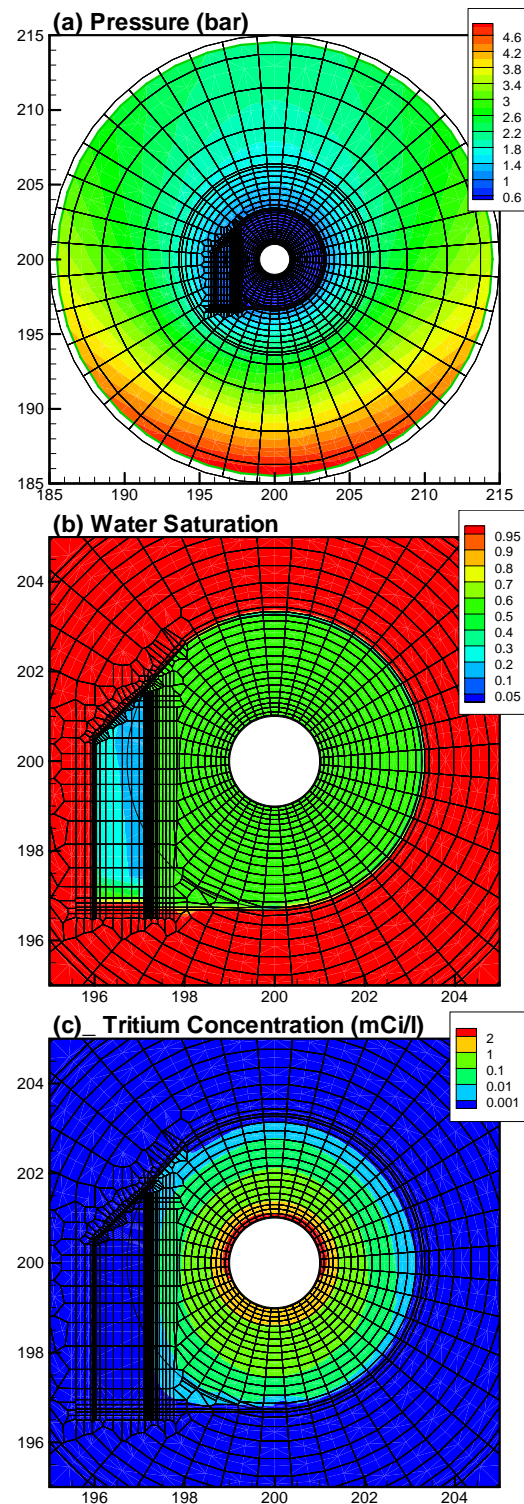


Figure 6. Pressure, water saturation, and tritium concentration simulated at 10 yrs in a representative cross section of the decay pipe, with reference center (200 m, 200 m)

Figure 6c shows the tritium concentration in the concrete. Overall, the contour of the tritium concentration at 10 years shows the signature of the tritium mass generated in the concrete: higher concentration close to the vacuum pipe of the decay pipe, and lower concentrations in the outer region of the concrete. Figure 6c also shows the impact of advective and diffusive transport on the concentration contour. Transport makes the concentration contour different from the concentric pattern of tritium mass generated. The release of tritium from the concrete to the drainage system in the 10 years of simulation period was negligible. Note that the water saturation in this case is calibrated using the measured tritium concentration in the drainage water. For the sensitivity analysis of tritium release on water saturation, we also simulated cases with saturation of 0.4, 0.6, and 0.7, and found that for the case of 0.7 saturation, the remaining tritium mass in the concrete was 31.26 Ci, indicating that more than 12.3 Ci tritium was released into the drainage system over the 10 years. In comparison, the total tritium mass collected in the drainage system was about 4 Ci/year, which can be attributed to the mass transfer between globally transported tritiated vapor and seeping water. Although the calibrated water saturation was in a range between 0.2 and 0.6, the value of 0.5 was used to represent the most likely scenario of tritium transport.

SUMMARY AND CONCLUSIONS

A three-dimensional numerical model was developed to simulate the steady-state flow and transient transport of tritium in the NuMI facility. The steady-state flow was induced by the subsurface facility located below the water table, and by the unsaturated walkway tunnel connected to the atmosphere. Tritium was generated within steel and concrete shielding in the target pipe and target hall, steel and concrete shielding in the absorber hall, and concrete shielding

in the decay pipe, as well as in the surrounding fractured rock. Our modeling was focused on the 670 m long decay pipe region, where the majority of tritium mass was generated in the concrete. To account for the non-uniform distribution of tritium mass simulated using the MARS model, we generated an irregular base cross section mesh. A mesh deformation was performed to account for the changes in geometries and location of the facility components (e.g., walkway). Simulation results showed that concrete saturation had been at a low value (~0.5), calibrated using the fact that tritium release from concrete into the drainage system would be small in the first 4 years of facility operation. This low saturation stems from (1) a small initial saturation condition, and (2) a reduced connection area between saturated fractured rock and unsaturated concrete by dimple mat. The tritium generated in the concrete is redistributed slowly by advection, diffusion, and decay, and after 100 years, the total tritium mass has essentially migrated out of the model domain.

ACKNOWLEDGMENT

This work was supported by the Fermi National Accelerator Laboratory (Fermilab). The support is provided to Berkeley Lab through the U.S. Department of Energy Contract No. DE-AC02-05CH11231.

REFERENCES

- Pruess, K., C. Oldenburg, and G. Moridis, *TOUGH2 User's Guide, Version 2.0*, Report LBNL-43134, Lawrence Berkeley National Laboratory, Berkeley, Calif., 1999.
- Lundberg, B., Tritiated water in the decay region: model comparisons to data, Projects Document 136-v3, Fermilab Report, December 2006.

MODELING OF DENSE NON-AQUEOUS-PHASE LIQUID ENTRAPMENT AND DISSOLUTION IN VARIABLE APERTURE FRACTURES

Zhibing Yang¹, Auli Niemi¹, Fritjof Fagerlund¹ and Tissa Illangasekare²

¹Department of Earth Sciences, Uppsala University
Villavägen 16
Uppsala, 75236, Sweden
e-mail: zhibing.yang@hyd.uu.se

²Colorado School of Mines
Center for Experimental Study of Subsurface Environmental Processes
Golden, CO 80401, U.S.A

ABSTRACT

This study investigates dense non-aqueous phase liquid (DNAPL) entrapment and dissolution in single, variable-aperture fractures. Log-normally distributed aperture fields with local permeabilities following the cubic law are assumed. Special attention is given to the capillary pressure-liquid saturation function to account for the specific drainage and wetting characteristics of fractures. DNAPL migration and immobilization is modeled by using the iTOUGH2/T2VOC models, and dissolution is simulated using the TMVOC model. Multiple realizations with different sets of aperture statistics and fracture inclination angles are analyzed.

The results suggest that the entrapment geometry of DNAPL in a heterogeneous fracture is highly sensitive to the aperture statistics. Larger correlation length or standard deviation produces a wider range of total entrapped DNAPL volume. Modeling of different fracture inclination angles reveals that gravity force plays an important role as well. Subsequent dissolution modeling shows that mass transfer will also be strongly influenced by the different DNAPL entrapment architectures corresponding to the different aperture correlation lengths and standard deviations.

INTRODUCTION

Dense non-aqueous phase liquids (DNAPLs) released into the subsurface can migrate rapidly through fracture networks under the influence of gravitational, viscous, and capillary forces, until they get trapped in dead-end fractures or as residual ganglia in the pathways. Entrapped DNAPLs will act as long-term contamination sources as they dissolve into the surrounding aqueous phase.

The complex heterogeneity of fractured media, both at the level of individual fractures and at the level of fracture networks, makes the effective remediation of these media extremely difficult. An improved under-

standing of DNAPL spreading, immobilization and dissolution behavior in fractured rocks is therefore needed. Addressing this behavior in complex field-scale fracture networks requires a solid understanding of the behavior in individual fractures that form the building blocks of the fracture networks.

How a DNAPL infiltrates and becomes entrapped within a discrete single fracture of a fracture network affects the subsequent dissolution and the longevity of the DNAPL. Predicting the dissolved mass flux generation from entrapped DNAPLs requires the modeling of both the entrapment of the DNAPL and its dissolution. DNAPL dissolution in single fractures has been experimentally and numerically studied by several researchers. Detwiler et. al. (2001) presented a variable-aperture pore-scale entrapped DNAPL dissolution model that explicitly incorporates the geometry of individual blobs and thus does not rely on empirical mass-transfer correlations. Based on experimental and simulation results, Detwiler et. al. (2001) then used a simple exponential relation to model the DNAPL saturation depletion at a fracture scale. Dickson and Thomson (2003) developed a Sherwood-type empirical correlation based on eight dissolution experiments using natural rock fractures. In their Sherwood number correlation, Dickson and Thomson (2003) chose tracer aperture ratio as an indirect measure of the initial trapped DNAPL configuration, although the actual architecture was not known.

Depending on the fracture aperture variability, dipping angle and boundary characteristics, DNAPL entrapment morphology can be complicated, exhibiting a wide range of blob sizes at various locations. For such different entrapment morphologies, different dissolution behavior can be expected as well. This work investigates the effects of different sets of fracture characteristics on DNAPL entrapment and dissolution by means of numerical simulation.

MODELING APPROACH

Variable aperture field

To take into account the heterogeneity within the rough-walled fracture, variable apertures are assigned to a two-dimensional fracture plane. Gridblock volume and connection areas are assigned accordingly. Log-normally distributed aperture values are generated using a random field generator available in Processing Modflow for Windows (Chiang and Kinzelbach, 2001), which uses an exponential correlation function with assigned correlation lengths. The mean aperture is set at 300 μm , which is on the order of laboratory measurements (Hakami and Larsson, 1996) of natural granite fractures at low confining stress (< 0.5 MPa). Correlation length and aperture standard deviation are two of the factors expected to affect DNAPL entrapment and dissolution, and are allowed to vary from 1 to 3 cm and from 0.25 to 0.5 (log10), respectively. Permeability k of each gridblock is related to aperture b by the equation $k = b^2/12$.

Infiltration and immobilization

Two-phase flow in single fractures has been simulated using invasion percolation (IP) model (Pyrak-Nolte et al., 1992), modified invasion percolation (MIP) model (Glass et al., 1998) and pore network model (Hughes and Blunt, 2001). In this study, we use a continuum-based approach to model DNAPL migration in fractures where gravity force also plays a role (i.e., nonhorizontal fracture). A unique ‘flat’ capillary pressure-saturation function (see Figure 1) is defined for each of the gridblocks with variable apertures. This form of the function allows a rapid drainage of the fracture location once the nonwetting phase entry pressure corresponding to the fracture opening at that location is reached. The entry pressure is allowed to vary according to the variable aperture and is linked to it as follows.

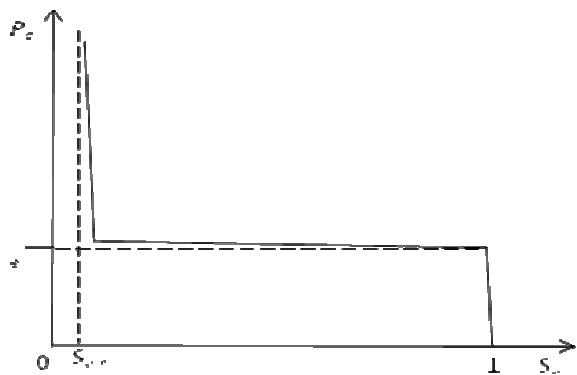


Figure 1. Illustration of capillary pressure-saturation used in the fracture-DNAPL modeling

Nonwetting phase entry pressure P_e can be calculated using the Young-Laplace equation:

$$P_e = \gamma \left(\frac{1}{r_1} + \frac{1}{r_2} \right) \quad (1)$$

where γ is the interfacial tension, r_1 is the principal radius of the curvature perpendicular to the fracture plane, and r_2 is the principal radius of the curvature of in-plane fluid interface. Considering in our case that the aperture correlation length is much larger than the mean aperture, which indicates a very small dimensionless curvature number C (C is equal to the ratio of mean aperture and correlation length multiplied by absolute value of the cosine of the contact angle, as defined by Glass et al. (1998)), we can then use the approximation of $P_e \approx \gamma/r_1 = 2\gamma\cos\theta/b$, where θ is the contact angle and b is the aperture. In essence, the ‘flat’ capillary pressure-saturation function makes the model similar to an invasion percolation model. This is implemented into iTOUGH2 (Finsterle, 2000) with T2VOC (Falta et al., 1995) module.

DNAPL dissolution

Since the time scale for DNAPL entrapment can be orders of magnitude smaller than that for dissolution processes, we can model migration and dissolution in a stepwise manner. Although local equilibrium assumption (LEA) is generally believed to underestimate the time for DNAPL removal, in this preliminary study we use this assumption based on the following considerations. First, our work has a focus on the effect of heterogeneity on DNAPL dissolution at a scale of a fracture much larger than the computational gridblock scale, so the local rate-limited dissolution behavior may be of secondary importance. Second, the average water flow velocity is very small, on the order of 10^{-5} m/s, as dissolution in the presence of natural groundwater gradient of 0.001 is modeled instead of (for example) any remediation activity. Temporal variation of local aqueous phase relative permeability (i.e., increase with the ongoing dissolution process that reduced DNAPL saturation) is taken into account by using a simple power function of water saturation with an exponent of 1.5. This is a preliminary value, and the effect of heterogeneity on DNAPL dissolution should not be affected, since the same value is used for all the different cases. TMVOC code (Pruess and Battistelli, 2002) is used for the dissolution modeling.

Modeling scenario

The modeling scenario consists of trichloroethylene (TCE) source (specified pressure) on the entire top boundary, no-flow boundary at the bottom, and constant head at left- and right-hand side boundaries. This represents a fracture with no intersection at the bottom. When the DNAPL migration through the

domain has reached a steady state, the DNAPL source at the top boundary is turned off, and the DNAPL is allowed to immobilize. After DNAPL immobilization dissolution modeling continues. The 30×30 cm² fracture plane is discretized into 60×60 gridblocks. Multiple realizations with different sets of aperture statistics and fracture inclination angles are simulated. An example realization of the aperture field is shown in Figure 2.

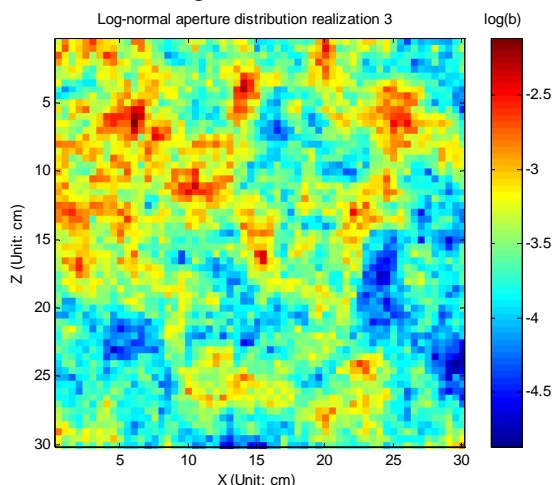


Figure 2. An example realization of the aperture field with a correlation length of 2 cm and a standard deviation 0.4 (log10)

RESULTS AND DISCUSSION

Entrapped DNAPL volumes for different sets of correlation lengths and aperture standard deviations, as well as different fracture inclination angles, can be analyzed from the results. An example of DNAPL entrapment for the vertical fracture with the aperture field in Figure 2 is shown in Figure 3. Most entrapment morphologies resulting from the simulations showed similar tendencies as the result in Figure 3, with entrapped DNAPL in small, sparse blobs, as well as in large blobs in the vicinity of the closed bottom boundary.

Entrapment of DNAPL

Volumetric DNAPL content (S_n) is defined as the ratio between total trapped DNAPL volume and fracture void volume. As can be seen in Figure 4(a), when the correlation length is longer (log aperture standard deviation is fixed at 0.4), the trapped DNAPL volume becomes smaller, and at the same time varies more between different realizations. This is not surprising, because longer correlation length means more chances of getting pathways through the domain. If more pathways lead to the bottom, which is closed, then relatively large NAPL entrapment in the fracture plane results; while if more pathways lead to the open sides, relatively small amounts of trapped NAPL are obtained.

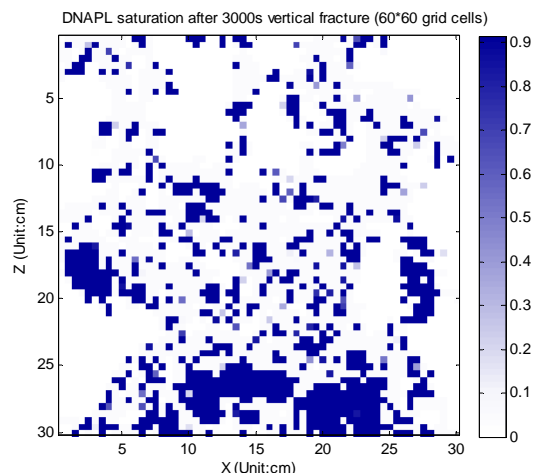


Figure 3. DNAPL entrapment for a vertical fracture with the aperture field shown in Figure 2

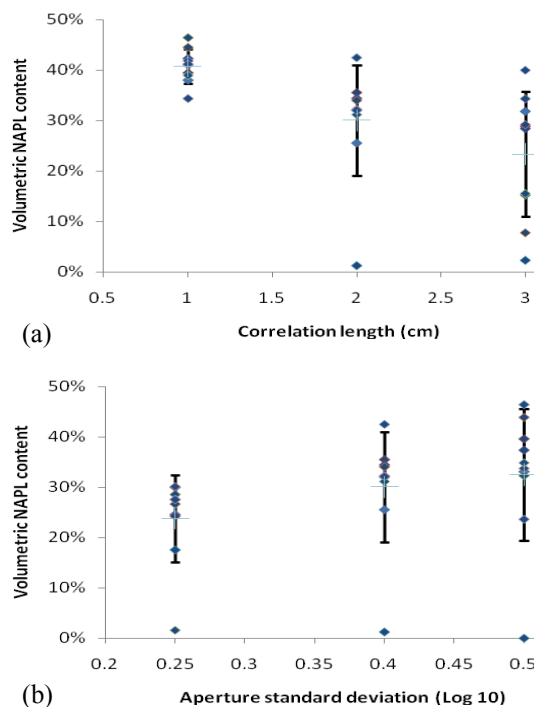


Figure 4. Effect of correlation length (a) and aperture standard deviation (b) on total DNAPL entrapment volume. The cross and bar show the mean and standard deviation of DNAPL entrapment volume for different realizations, the symbols correspond to individual realizations.

As shown in Figure 4(b), on average, the larger the aperture standard deviation (correlation length is constant 2 cm), the more trapped DNAPL. This is because larger standard deviation of apertures produces more distinct contrasts between small and

big aperture regions. In each group, there is also one realization with almost zero entrapment. The reason for this is that these realizations have very small apertures on the top of the fracture, and DNAPL source pressure is not sufficient to overcome the capillary barrier to enter these regions.

Fracture inclination angle is an important parameter affecting DNAPL entrapment. Different angles give different Bond numbers (Bo, ratio of gravity force and capillary force). It can be seen from Figure 5a that a fracture inclination angle of 30° can result in a wide range of DNAPL entrapment, from 3% to 45%. This means that the gravity force and capillary force both come into play and interact with the aperture field geometries, resulting in strikingly different initial entrapment morphologies. Figure 5b shows the same results in terms of center of DNAPL mass in the Z direction along the fracture plane.

It can be seen and should be noted that fracture boundary conditions surely influence the DNAPL entrapment. In some cases, for instance a dead-end fracture, trapping by the boundaries can be dominant over trapping in the fracture plane along migration pathways. So, for different boundary scenarios, different entrapment behaviors should be expected, an issue that needs to be addressed in future studies.

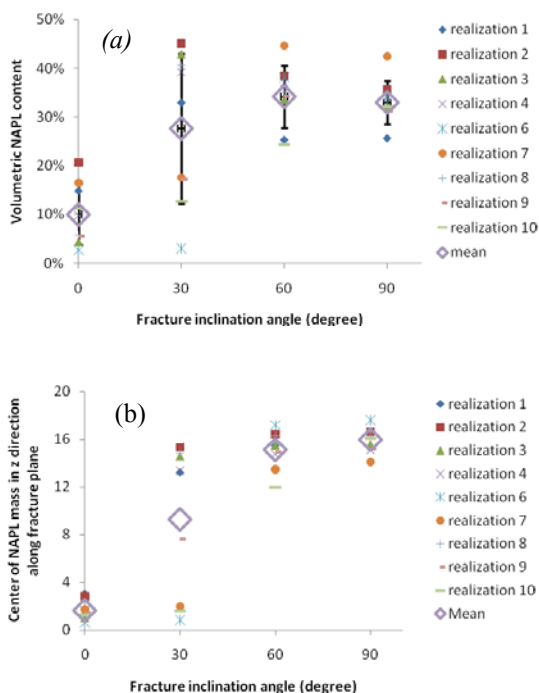


Figure 5. Effect of fracture inclination angle on DNAPL entrapment. 90 degree indicates a vertical fracture.

Dissolution of DNAPL

To describe the DNAPL dissolution process, we use the temporal evolution of the normalized TCE concentration in the aqueous phase C_{out}/C_{eq} (flow-averaged concentration at the outlet boundary divided by equilibrium concentration) and of the normalized DNAPL content S_n/S_{ni} (volumetric DNAPL content normalized to the initial DNAPL content in the fracture at the end of the immobilization phase). Considering an influent concentration of zero, we may use C_{out}/C_{eq} as a measure of effective mass transfer coefficient for the fracture scale.

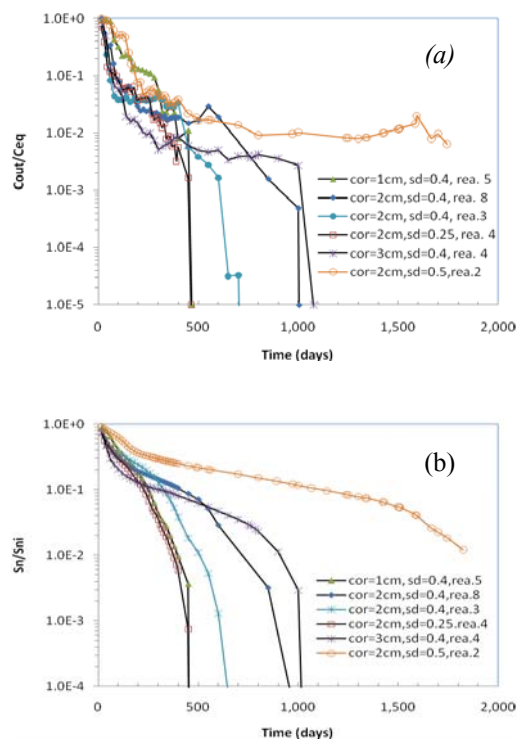


Figure 6. Effect of fracture in-plane heterogeneity on trapped DNAPL dissolution. (a) flow-averaged outflow concentration. (b) relative volumetric DNAPL content in fracture plane.

Only one or two realizations from each set of correlation length and aperture standard deviation are selected for dissolution modeling, but these are selected to have a S_n close to the mean S_n of the group. It can be seen from Figure 6(a) that solute concentration C_{out}/C_{eq} usually quickly drops to below 0.1, indicating that the effective mass-transfer rate reduces fast. It can also be observed that both an increase in permeability correlation length and in permeability standard deviation lead to longer DNAPL removal times. For the highest standard deviation case (correlation length 2 cm and standard deviation 0.5), a complete removal of DNAPL is not simulated, but the estimated removal time is about

2000 days. Visual inspection of DNAPL entrapment geometries from figures like that in Figure 3 indicates that generally the entrapment blob or cluster size increases with correlation length and standard deviation, though quantitative analyses have not been carried out yet. Large clusters are usually correlated with small interfacial areas per unit NAPL volume, and thereby with less contact area for dissolution to take place.

Figure 6(b) shows the DNAPL depletion as dissolution proceeds. If we compare two curves (correlation lengths of 1 cm and 3 cm, both with standard deviation 0.4), we can see that the case with correlation length 3 cm dissolves much slower than the one with 1 cm, even though the latter case has an initial S_n higher than the former one. So the initial S_n is a factor, but some other factors, such as entrapment morphology or interfacial area, and groundwater flow accessibility for the big blobs, may be more important in terms of dissolution kinetics.

Figure 7 shows the temporal change of first and second spatial moments of NAPL mass for one example realization (correlation length of 2 cm, standard deviation 0.4) as dissolution proceeds. It can be observed that the second moment in Z direction drops fast in the first 200 days, indicating that the small, sparse entrapped blobs above the pool at the bottom have been removed by dissolution during this period. The DNAPL pools or clusters remain for a much longer time. In this sense, longevity of DNAPL in the fracture is controlled by these clusters.

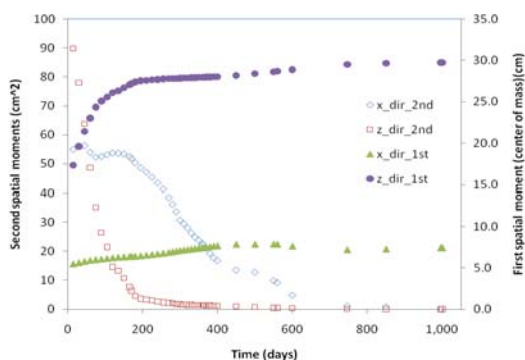


Figure 7. Temporal change of spatial moments with dissolution process (correlation length 2 cm, standard deviation 0.4, realization 8).

CONCLUDING REMARKS

DNAPL entrapment and dissolution in a single variable aperture fracture has been studied. Preliminary results show that aperture statistics (standard deviation and correlation length) as well as fracture inclination angle affect the amount of DNAPL trapped, as well as the entrapment architecture. This

initial entrapment architecture, together with the heterogeneous aperture field, will then strongly control the flow and transport during the dissolution process. Generally, a more heterogeneous aperture field results in an initial entrapment architecture that contributes to a slower mass transfer.

These preliminary results show the significant effect the boundary conditions have on DNAPL entrapment architecture. In field-scale fracture networks, a number of different boundary conditions can be encountered, depending on fracture termination and connectivity as well as connection type with other fractures. Therefore, a number of different boundary condition scenarios need to be considered to be able to address the field-scale fracture-network problems. These are the topic of further studies. It should also be pointed out that the simulations presented in this work are carried out with a relatively coarse discretization. The effect of using a more refined mesh is also considered in future work.

ACKNOWLEDGMENT

Funding support for the project by the Swedish National Research Council (Vetenskapsrådet) is gratefully acknowledged. The authors also wish to thank Dr Yvonne Tsang from Lawrence Berkeley National Laboratory and Imperial College for stimulating discussions.

REFERENCES

- Chiang, W. H. and W. Kinzelbach, *3-D groundwater modelling with Processing MODFLOW for Windows*, Springer, 2001.
- Detwiler, R. L., H. Rajaram and R. J. Glass, Nonaqueous-phase-liquid dissolution in variable-aperture fractures: Development of a depth-averaged computational model with comparison to a physical experiment. *Water Resour. Res.*, 37(12), 3115–3129, 2001.
- Dickson, S. E. and N. R. Thomson, Dissolution of entrapped DNAPLs in variable aperture fractures: experiments and empirical model development. *Environ. Sci. Technol.* 37, 4128–4137, 2003.
- Falta, R.W., K. Pruess, S. Finsterle and A. Battistelli., *T2VOC User's Guide*, Report LBL-36400, UC-400, Lawrence Berkeley National Laboratory, Berkeley, Calif., 1995.
- Finsterle, S., *iTOUGH2 User's guide*, Report LNBL-40040, 2nd rev., Lawrence Berkeley National Laboratory, Berkeley, Calif., 2000.
- Glass R. J., M. J. Nicholl, and L. Yarrington, A modified invasion percolation model for low-capillary number immiscible displacements in horizontal rough walled fractures: influence of

- local in-plane curvature, *Water Resour. Res.*, 34(12), 3215–3234, 1998.
- Hakami, E. and E. Larsson, Aperture measurements and flow experiments on a single natural fracture, *Int. J. Rock Mech. Min. Sci. & Geomech. Abstr.* 33 (4), 395–404, 1996.
- Hughes, R. G. and M. J. Blunt, Network modeling of multiphase flow in fractures, *Adv. Water Resour.*, 24, 409–421, 2001.
- Pyrak-Nolte, L. J., D. Helgeson, G. M. Haley and J. W. Morris, *Immiscible fluid flow in a fracture*. In: Tillerson J. R., Wawersik W. R., Editors, *Rock mechanics, Proceedings of the 33rd US Symposium*, Rotterdam, Netherlands: A.A. Balkema, 571–578, 1992.
- Pruess K., and A. Battistelli. *TMVOC, A Numerical Simulator for Three-Phase Non-isothermal Flows of Multicomponent Hydrocarbon Mixtures in Saturated-Unsaturated Heterogeneous Media*. Report LBNL-49375, Lawrence Berkeley National Laboratory, Berkeley, Calif., 2002.

APPLICATION OF TOUGHREACT V2.0 TO ENVIRONMENTAL SYSTEMS

N. Spycher¹, G. Zhang¹, S. Sengor², M. Issarangkun², T. Barkouki², T. Ginn², Y. Wu¹, R. Smith³, S. Hubbard¹,
Y. Fujita⁴, R. Sani⁵, and B. Peyton⁶

¹Lawrence Berkeley National Laboratory, Earth Sciences Division, Berkeley, CA 94720

²University of California Davis, Department of Civil and Environmental Engineering, Davis, CA 95616

³University of Idaho, Idaho Falls, ID 83402

⁴Idaho National Laboratory, Idaho Falls, ID 83415

⁵South Dakota School of Mines and Technology, Chemical and Biological Engineering, Rapid City, SD 57701

⁶Montana State University, Chemical and Biological Engineering Department, Bozeman, MT 59717

e-mail: nspycher@lbl.gov

ABSTRACT

Three example applications of TOUGHREACT to environmental systems are presented. In each example, the simulated biogeochemical processes differ significantly, illustrating a range of code applicability. The first study involves metal cycling in iron-rich lake sediments impacted by mining activities. The mobilization of metals by both biotic and abiotic reductive dissolution of iron hydroxides is assessed, and compared to the effect of dissolution of primary sulfide (detrital) ore minerals. In a second example, the precipitation of calcite induced by urea hydrolysis (ureolysis) is modeled to assess the remediation of ⁹⁰Sr contamination in saturated sediments. A ureolysis column experiment is simulated, with results compared to experimental data. In the last example, TOUGHREACT is used to investigate thermodynamic and kinetic constraints affecting the biogenic precipitation of uraninite and its reoxidation by iron hydroxides.

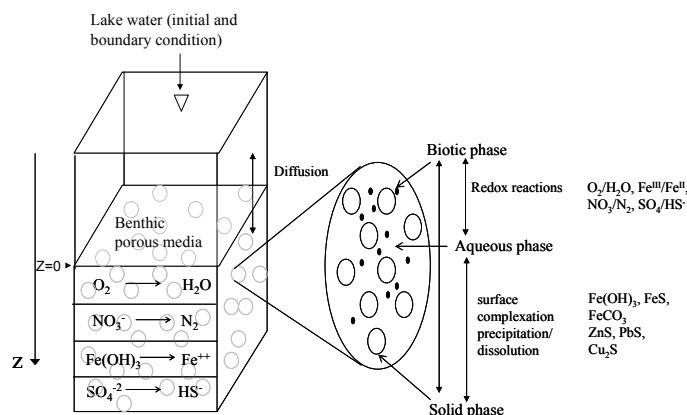
INTRODUCTION

TOUGHREACT has been widely applied to simulate coupled thermal, hydrological, and chemical processes related to nuclear waste storage, geothermal systems, CO₂ sequestration, and water-gas-rock interactions in deep reservoirs. Here, building on recent code enhancements (Xu et al., these proceedings), TOUGHREACT is applied to three different problems related to shallow environmental systems: the cycling of metals in contaminated lake sediments, calcite precipitation induced by urea hydrolysis, and the biogenic precipitation and reoxidation of uraninite. These examples cover a range of biotic and abiotic geochemical processes typically encountered in shallow subsurface environments, such as redox disequilibrium, reductive dissolution, sorption, desorption, co-precipitation, and ion exchange. These three examples reflect recent projects with modeling components born primarily from collaborative research between LBNL and U.C. Davis. The modeling work presented here draws partly on previously published work as well as

ongoing investigations, as detailed below and in references therein.

METAL CYCLING IN LAKE SEDIMENTS

This study investigates the cycling of iron and heavy metals (Zn, Pb, Cu) in sediments of Lake Coeur d'Alene, Idaho, which have been heavily impacted by mining activities. As a result, these sediments contain elevated concentrations of iron and heavy metals. The sediments consist primarily of quartz, siderite, and iron hydroxides (primarily ferrihydrite; Toevs et al., 2006; Moberly et al. 2009). The microbial reductive dissolution of iron hydroxides in the sediments leads to the release of metals sorbed onto these mineral phases, generating benthic fluxes of metals from the sediments to the lake water. Deeper into the sediments, metals mobilized by reductive dissolution become immobilized by reaction with biogenic sulfide to form sulfide minerals. The abiotic reductive dissolution of iron hydroxides by biogenic sulfide and the oxidation of native (detrital) sulfide ore minerals also affect the geochemical behavior of metals in the sediments. These coupled processes are simulated for a 1D sediment column under redox disequilibrium conditions (Figure 1), building on work previously published by Sengor et al. (2007a,b)



and expanded by Spycher et al. (2008).

Figure 1. Conceptual 1D diffusive biogeochemical model (Sengor et al, 2007a)

Biogeochemical Model

The setup and input data for the basic TOUGHREACT model are unchanged from the model presented earlier (Sengor et al. 2007a), which was built using PHREEQC (Parkhurst and Appelo, 1999). The model incorporates a multicomponent biotic reaction network with multiple terminal electron acceptors (Table 1), diffusive transport, mineral precipitation and dissolution, and surface complexation. We have added to this model the effect of sedimentation, approximated by advecting sediment solids and pore water downward at a rate decreasing with depth to mimic compaction. In addition to species originally considered for sorption onto Fe hydroxides (Zn^{+2} , $Cu^{+2/+1}$, Pb^{+2} , H^+ , Ca^{+2} , Mg^{+2} , SO_4^{-2} ; Dzombak and Morel, 1990), Fe^{+2} surface complexation (Liger et al., 1999) was also added to the original model. Note that for all cases discussed below, kinetic reactions potentially reaching equilibrium are implemented with a thermodynamic affinity term that effectively shuts down the reaction if equilibrium is reached.

The top model boundary is at the lake water-sediment interface. It is set at a fixed composition equal to the (measured) composition of lake water equilibrated with sorption sites on ferrihydrite. It is also set with a fixed mineralogy identical to the initial mineralogy specified for the entire sediment column (described below for each case considered). Transport is entirely diffusive, with a closed bottom model boundary.

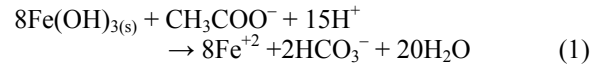
The simulated 1D sediment column is 45 cm long, with a grid spacing of 0.5 cm for the first top 8 cells, then increasing to 1 cm through the remainder of the column. The sedimentation rate is set at 2 cm/yr at the top of the column (Horowitz et al., 1995), and linearly decreasing to zero at the base of the column. The diffusion coefficient is low ($\sim 4 \times 10^{-6}$ cm²/s), reflecting very fine-grained sediments (Ballistreri, 1998). Simulations are carried out with time steps up to 0.5 days, for a simulated period of about 5 years, after which nearly steady conditions prevail.

Simulated Cases

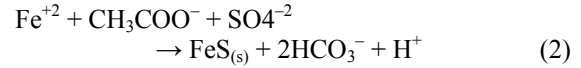
Simulations are run for three cases, each selected to represent processes that are likely to take place in the sediments of Lake Coeur d'Alene. Each case is modeled separately to assess individual effects. However, it is likely that the processes modeled for all three cases operate simultaneously, at least to some extent, depending on seasonality and location.

Case 1: Biotic reductive dissolution (base case)

This is the reaction network modeled by Sengor et al. (2007a). Higher in the sediment column, iron-reducing bacteria reduce iron hydroxides:



This reaction leads to the release of sorbed metals (Zn, Cu, Pb). At depth, sulfate reducing bacteria produce sulfide, which can react with Fe(II) and other metals to form precipitates:



Reactions (1) and (2) proceed through the coupling of the reaction network shown in Table 1 with ferrihydrite (modeled as $Fe(OH)_3$) and mackinawite (FeS , disordered) reacting at equilibrium. Sphalerite (ZnS), galena (PbS) and chalcocite (Cu_2S) are included as “proxy” phases precipitating under kinetic constraints to provide a sink for heavy metals. Siderite ($FeCO_3$) is also included as a phase reacting under kinetic constraints. The only minerals initially present in the modeled column consist of ferrihydrite and siderite, which are observed throughout the lake sediments in significant amounts (Toevs et al., 2006), likely from both detrital and diagenetic origins.

The model is started with (oxic) lake water initially throughout the column. A redox stratification eventually develops through the microbial reaction network (Table 1), from oxic lake-water conditions at the top of the column to sulfate-reducing conditions at the bottom of the column. Kinetic reaction parameters are initially obtained from the literature, then are adjusted as necessary to best match the model results to field data (Winowiecki, 2002) (Figure 2). Note that the electron donor (taken as acetate) is reported in pore water at ~ 150 μ M and is assumed un-limiting.

Table 1. Microbial reactions and rate laws (from Sengor et al., 2007).

<i>Microbially mediated reactions:</i>	
$CH_3COO^- + 2O_2 \rightarrow 2CO_3^{-2} + 3H^+$	R_{O_2}
$CH_3COO^- + 1.6NO_3^- \rightarrow 2CO_3^{-2} + 0.8N_2 + 1.4H^+ + 0.8H_2O$	R_{NO_3}
$CH_3COO^- + 8Fe^{+3} + 4H_2O \rightarrow 8Fe^{+2} + 2CO_3^{-2} + 11H^+$	R_{Fe+3}
$CH_3COO^- + SO_4^{-2} \rightarrow 2CO_3^{-2} + HS^- + 2H^+$	R_{SO_4-2}
<i>Kinetic rate laws:</i>	
$R_{O_2} = V_m^{O_2} \frac{[O_2]}{[O_2] + K_s^{O_2}}$	
$R_{NO_3} = V_m^{NO_3} \frac{[NO_3^-]}{[NO_3^-] + K_s^{NO_3}} \frac{K_{O_2}^{in}}{K_{O_2}^{in} + [O_2]}$	
$R_{Fe+3}^{(*)} = V_m^{Fe} \frac{K_{O_2}^{in}}{K_{O_2}^{in} + [O_2]} \frac{K_{NO_3}^{in}}{K_{NO_3}^{in} + [NO_3^-]}$	
$R_{SO_4-2} = V_m^{SO_4} \frac{[SO_4^{-2}]}{[SO_4^{-2}] + K_s^{SO_4}} \frac{K_{O_2}^{in}}{K_{O_2}^{in} + [O_2]} \frac{K_{NO_3}^{in}}{K_{NO_3}^{in} + [NO_3^-]} \frac{K_{Fe}^{in}}{K_{Fe}^{in} + [Fe^{+3}]}$	

V_m^i Maximum substrate utilization rate constant

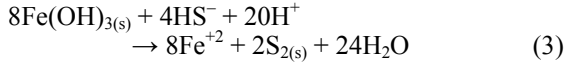
K_s^i Half saturation constant

K^{in} Inhibition constants

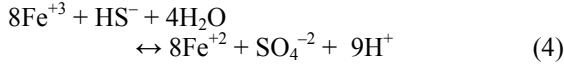
(*) Assumes unlimited Fe^{+3} supply from abundant solid Fe hydroxides

Case 2: Abiotic reductive dissolution by sulfide

In this case, the same setup and input parameters are taken as in Case 1, except that the microbial reductive dissolution of ferrihydrite is replaced by abiotic reduction by sulfide (Poulton et al., 2004):

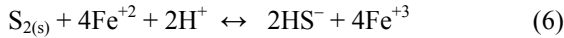


This reaction pathway is implemented in the model with the following reaction:



$$R_{\text{Fe}^{+3} \rightarrow \text{Fe}^{+2}} = k_4 [\text{H}_2\text{S}_{(\text{aq})}]^{0.5} \quad (5)$$

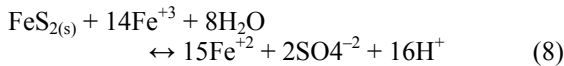
and including sulfur as a potentially forming solid phase reacting at equilibrium with Fe(II)/(III):



The rate constant ($k_4 = 10^{-3} \text{ mol}^{0.5} \text{ L}^{-0.5} \text{ m}^2 \text{ s}^{-1}$) is taken in the range of values reported by Poulton et al. (2004), taking into account H_2S dissociation as a function of pH. Note that even though Reaction (3) is abiotic, the sulfide itself is still biogenic.

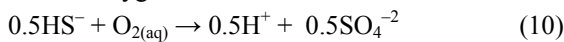
Case 3: Oxidation of primary ore minerals

This case is quite different from the previous cases, in that it assumes (hypothetically) that the sediments initially contain sulfide minerals (pyrite, FeS_2 ; chalcopyrite, CuFeS_2 ; sphalerite, ZnS ; and galena, PbS), presumably as detrital ore minerals. As previously, siderite is included in the initial mineral assemblage, but ferrihydrite is not. The latter is allowed to form through the oxidation of pyrite. The microbial reaction network (Table 1) is no longer considered and replaced with reactions for the abiotic oxidation of ferrous iron and aqueous sulfide. Following the approach presented by Steefel (2000), we implement rate laws for abiotic ferrous iron oxidation (Wehrli, 1990), and parallel rate laws for the pyrite oxidation (Williamson and Rimstidt, 1994):



$$R_{\text{pyrite-ox}} = k_7 \frac{[\text{O}_2]^{0.5}}{[\text{H}^+]^{0.11}} + k_8 \frac{[\text{Fe}^{+3}]^{0.3}}{[\text{Fe}^{+2}]^{0.47} [\text{H}^+]^{0.32}} \quad (9)$$

with $k_7 = 10^{-8.1}$ and $k_8 = 10^{-8.58} \text{ mol m}^{-2} \text{ s}^{-1}$. In addition, the rate law of Nielsen et al. (2003) is implemented for the oxidation of aqueous sulfide by dissolved oxygen:



$$R = k_{10} [\text{S}^{(-2)}_{\text{total}}]^{0.82} [\text{O}_{2(\text{aq})}]^{0.2} \quad (11)$$

with $k_{10} \sim 2.4 \text{ mol L}^{-1} \text{ s}^{-1}$. As for Case 1 and Case 2, the simulation is started with oxic lake water throughout the modeled column. However, in this case, the initial mineral assemblage reflects sulfate-

reducing conditions. As oxygen and ferric iron are consumed by sulfide oxidation, a gradient develops from oxic conditions at the top of the column to reduced conditions deeper into the column.

Biogeochemical Model Results

In Case 1 and Case 2, modeled concentrations trends for key species are generally consistent with measured data (Figure 2). The main difference is the higher sulfate concentration resulting from sulfide oxidation (Reaction 4). These higher concentrations feed back on microbial sulfate reduction (i.e., recycling of SO_4^{-2}), which generates higher alkalinity values (last reaction in Table 1) despite the fact that Case 2 includes one less microbial reaction than Case 1 (i.e., no microbial Fe reduction).

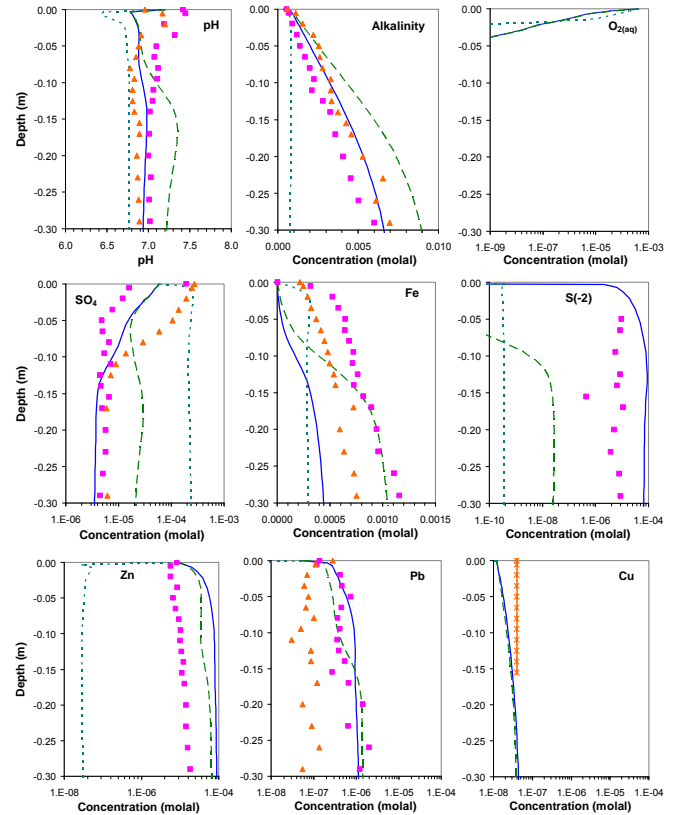


Figure 2. Concentrations of key parameters, redox species, and metals with depth from the top of the sediment column. Lines show computed values (Case 1, solid; Case 2, dashed; Case 3, dotted). Symbols are measured values by Winowiecki (2003) (Summer/Fall 2001), except for Cu (average over interval shown, from Sengor et al. 2007a).

Although FeS is predicted to form in Case 1, it is not in Case 2 because the system becomes more depleted in sulfide. Sulfur (Reaction 6) does not form in Case 2, although it was predicted to form in some cases

with slower sulfide oxidation rates. In Case 2, the increased iron reduction by biogenic sulfide at depth results in more ferrihydrite dissolution (Figure 3).

The behavior of heavy metals is primarily driven by sorption. In Case 1, reductive dissolution releases metals. In Case 3, ferrihydrite forms by oxidation of siderite and pyrite at the top of the column (Figure 3) and sorbs the metals released by the dissolution of sulfides (Cu and Pb fall below the range shown in Figure 2). In these simulations, siderite oxidizes somewhat more than pyrite (Figure 3). However, the amount of pyrite oxidation is highly dependent on the relative dissolution rates of these two minerals. As expected, oxidation of sulfide minerals in Case 3 generates elevated sulfate concentrations not representative of existing conditions at depth within the column.

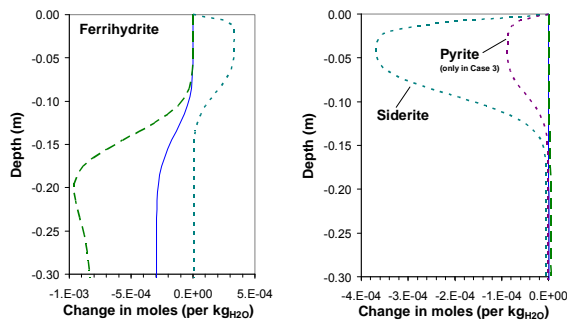
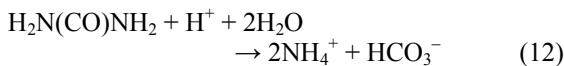


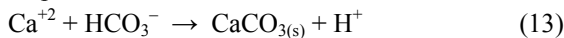
Figure 3. Computed change in abundance of Fe minerals (Case 1, solid line; Case 2, dashed line; Case 3, dotted line)

UREOLYTIC CALCITE PRECIPITATION

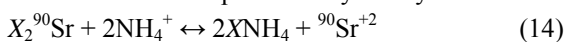
In this example, TOUGHREACT is applied to simulate urea hydrolysis (ureolysis) as a means to remediate ^{90}Sr contamination in the saturated zone (Fujita et al., 2000 and 2004; Mitchell and Ferris, 2005). Ureolysis consumes hydrogen ions and produces ammonium and bicarbonate ions:



Therefore, the injection of urea into groundwater causes pH and alkalinity to increase, driving calcite precipitation:

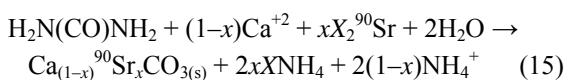


^{90}Sr , which strongly partitions into soils, exchanges with ammonium ions produced by ureolysis:



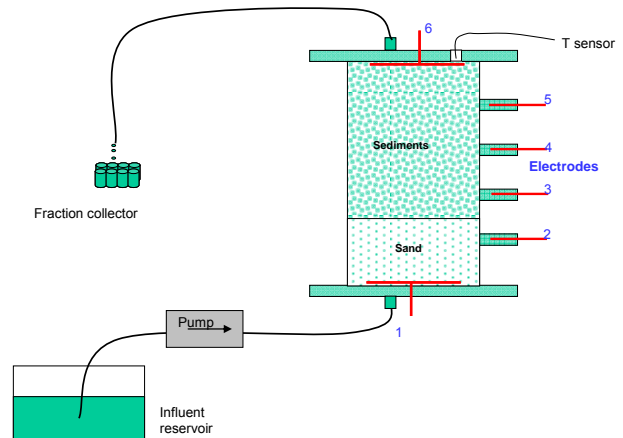
(with X denoting exchange sites). The exchanged ^{90}Sr then precipitates with calcite.

The overall reaction can be written as:



where x is the mole fraction of strontium incorporated into calcite.

This reaction network was simulated for a column experiment (at room temperature) designed to investigate geo-electrical signatures of ureolysis, calcite precipitation and increased conductivity of the solution at outlet (Wu et al., in prep.) The column (Figure 4) was packed and saturated with groundwater and sediments from the Idaho National Laboratory Vadose Zone Research Park (VZRP). It was then flushed with site groundwater for ~15 days, after which time a relatively steady water composition was obtained at the outlet. Injection was then continued for about another 15 days with added urea at a concentration of 10 mM. Prior to urea injection, molasses was added to the injected solution for a short period of time, to stimulate ureolytic activity in the column.



Column Dimensions	Injection Data	Hydraulic Properties
Length: 0.14 m sediments 0.06 m sand	Flow rate = 0.21 ml/min $V_{\text{pore}} = 1.9 \times 10^{-6}$ m/s	$K_{\text{Hydr}} = 1.2 \times 10^{-5}$ m/s Porosity = 0.4
Diameter (inner): 0.076 m		

Figure 4. Ureolysis flow-through experiment (Wu et al., in prep.)

Ureolysis Kinetic Rate Law

Ureolysis is modeled as an enzymatic reaction, with a rate law taking into account the effect of pH on the enzyme (urease) protonation and deprotonation (Fidaleo and Lavecchia, 2003):

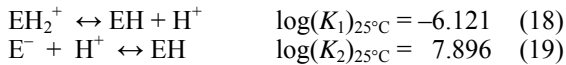
$$R = k \frac{[\text{EH}][\text{Urea}]}{(K_M + [\text{Urea}]) \left(1 + \frac{[\text{NH}_4^+]}{K_P}\right) \left(1 + \frac{10^{-\text{pH}}}{K_1} + \frac{K_2}{10^{-\text{pH}}}\right)} \quad (16)$$

In this equation, brackets indicate concentrations, EH represents the enzyme driving the hydrolysis of urea, K_M and K_P are the half-saturation and inhibition constants, respectively, and k is the rate constant. K_1 and K_2 are dissociation constants to represent the enzyme protonation and de-protonation reactions.

This rate law is implemented into TOUGHREACT using a standard Michaelis-Menten rate law with an inhibition term:

$$R = k[\text{EH}] \frac{[\text{Urea}]}{K_M + [\text{Urea}]} \frac{K_p}{K_p + [\text{NH}_4^+]} \quad (17)$$

and adding into the input thermodynamic database a primary species, EH, to represent the enzyme, and two additional secondary species, EH_2^+ and E^- , expressing the protonated and deprotonated enzyme:



It can be shown that this approach is a mathematical equivalent to using Equation (16). Values of K_1 and K_2 are taken from Fidaleo and Lavecchia (2003). Other rate law parameters are taken from the same authors as follows (25°C, with k re-expressed using molar concentrations):

$$\begin{aligned} K_p &= 1.22 \times 10^{-2} \text{ mol/L} \\ K_M &= 3.21 \times 10^{-3} \text{ mol/L} \\ k &= 146.4 (\text{mol urea})(\text{mol urease})^{-1}\text{s}^{-1} \end{aligned}$$

Model Setup and Approach

A 15-day period starting at the time of urea injection is simulated. The initial sediment pore water is taken as the measured water composition at the column outlet after the initial equilibration period, prior to urea injection (pH ~8.5). The composition of injected water is slightly altered from measured data to reflect equilibration of calcite in the influent reservoir under near atmospheric P_{CO_2} (pH ~7.8). Geochemical processes considered in the simulations include ureolysis, as described above, together with calcite precipitation, ion exchange, and NH_4^+ oxidation, as further discussed below. The effect of dissolution and precipitation of other minerals in the sediment is assumed to be negligible during the relatively short time frame of this experiment, and the sand pack of the column is assumed unreactive.

The model domain is set as a 1D cylindrical column with dimensions and properties shown on Figure 4. A fixed influx rate (0.21 mL/min) is applied at the modeled column inlet. The column is discretized into 205 gridblocks at regularly spaced intervals of 1 mm. A sequential-iterative (transport/reaction) method is implemented, using a maximum time step of 500 s (~1 x Courant). Tests using finer time and space intervals indicate that this set of parameters yields a reasonable compromise between speed and accuracy.

The model is run using EH (in Equation 17) as the main calibration parameter. The model is first run without considering ion exchange or NH_4^+ oxidation. These processes are then added to the simulations using data from the literature. Final model results are refined by calibrating other parameters (biomass for

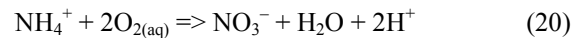
nitrification, and ion selectivity coefficients), as discussed below. Automatic calibration is performed using PPEST (Doherty, 2008) on a Unix cluster.

Calcite precipitation

Calcite (CaCO_3) is allowed to form as an ideal solid solution with strontianite (SrCO_3) (i.e., assuming activity = mole fraction). The solid solution is set to precipitate under kinetic constraint with a rate constant estimated ($10^{-7} \text{ mol m}^{-2}\text{s}^{-1}$) within a range of published data. A standard rate law derived from Transition State Theory (TST) is implemented, in which the rate is proportional to $A \times (1-Q/K)$, with A representing the reactive surface area and Q/K the solid-phase saturation index. (Note that for an ideal solid solution at equilibrium, it can be shown that Q/K equals the sum of the Q/K 's of each individual end-members.) Nucleation is not specifically modeled, and initial calcite precipitation is assumed to occur via a precursor surface with an area calculated from an assumed calcite precursor volume fraction (10^{-6}). This approach is approximate but yields reasonable results, keeping in mind that the uncertainty of the calcite precipitation rate is large and partly carried through the calibration of other parameters.

Ammonium oxidation

The oxidation of NH_4^+ is considered in the simulations to account for a significant increase in nitrate concentrations observed at the onset of ureolysis. Here, NH_4^+ oxidation is attributed to nitrification, which is approximated by the following overall reaction (assuming no NO_2^- buildup):



The overall rate is described using Monod kinetics:

$$R_{\text{NH}_4^+} = \frac{\mu_{\text{max}}}{Y_{\text{bio}}} C_{\text{bio}} \frac{C_{\text{NH}_4^+}}{K_{\text{NH}_4^+} + C_{\text{NH}_4^+}} \frac{C_{\text{O}_{2(\text{aq})}}}{K_{\text{O}_{2(\text{aq})}} + C_{\text{O}_{2(\text{aq})}}} \quad (21)$$

Half-saturation constants $K_{\text{NH}_4^+}$ ($1.48 \times 10^{-5} \text{ mol/L}$) and $K_{\text{O}_{2(\text{aq})}}$ ($2.41 \times 10^{-5} \text{ mol/L}$), the rate μ_{max} ($9.53 \times 10^{-6} \text{ s}^{-1}$), and the yield Y_{bio} ($2 \times 10^4 \text{ mg/mol}$) are taken from the literature (Maggi et al., 2008). The concentration of the biomass, C_{bio} , is assumed constant and is calibrated.

Ion exchange

Ion exchange is implemented for Na^+ , K^+ , NH_4^+ , Ca^{+2} , Mg^{+2} , and Sr^{+2} , using a generic exchanger (i.e., no specific minerals are associated with exchange) and the measured sediment cation exchange capacity (21 cmol/kg). The Gaines-Thomas convention is used, with Na^+ as the reference cation, and selectivity coefficients calibrated starting from (and within the magnitude of) published data currently in the PHREEQC v2.12 thermodynamic database (K^+ , 0.15; NH_4^+ , 0.3; Ca^{+2} , 0.21; Mg^{+2} , 0.20; and Sr^{+2} , 0.1; for one Na^+ in each exchange reaction). Note that site-

specific data are currently being measured for future modeling work.

Ureolysis Model Results

The expected trends of key constituents, including sharp increases in NH_4^+ from ureolysis (Reaction 12) and NO_3^- from NH_4^+ oxidation (Reaction 20), are well captured by the experimental measurements and model results (Figure 5). Note that the sharp fronts could only be modeled by iterating between transport and reaction. The expected pH increase (Reaction 12) is buffered by calcite precipitation (Reaction 15). The amount of calcite forming in the column is calculated to be quite small, in part because this mineral precipitates from the solution prior to injection. Ion exchange contributes to smoothing the NH_4^+ profile and raising the Sr^{+2} concentrations. Early effects of ion exchange are not reproduced well, however, likely because of sediment heterogeneities and uncertainty regarding selectivity coefficients.

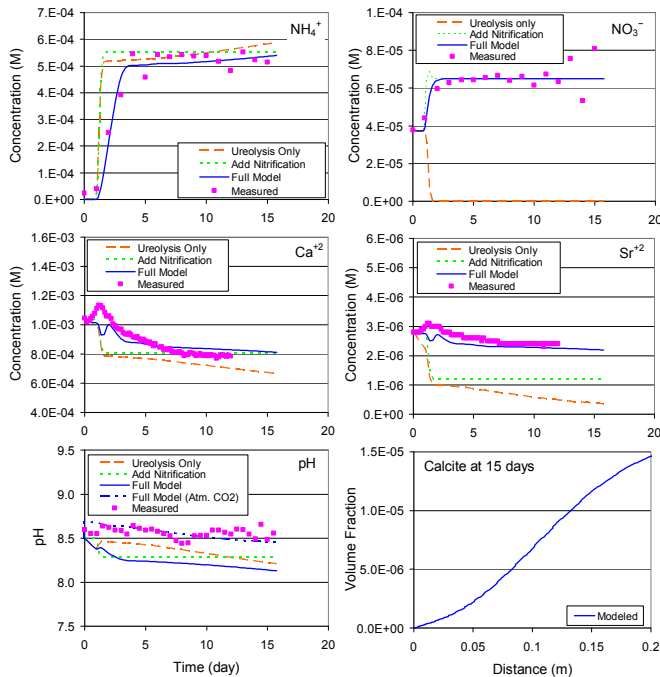


Figure 5. Observed and modeled profiles of key constituents through time at the column outlet (aqueous species) and along the column length (calcite)

UO₂ BIOREDUCTION AND REOXIDATION

In this last example, we investigate the reoxidation of biogenically produced UO_2 in the presence of iron hydroxides. Such reoxidation may impede cleanup efforts where U(VI)-contaminated groundwater is remediated using organic electron donors to reduce U(VI) and precipitate U(IV) as $\text{UO}_2(\text{s})$. We focus here on batch experiments conducted by Sani et al. (2004, 2005). In these experiments, biogenic UO_2 was precipitated from initially oxidized U(VI) solutions

using sulfate-reducing bacteria. Some of these experiments were conducted in the presence of hematite, using lactate as an electron donor, at a PIPES-buffered pH ~ 7 . Under lactate-limited conditions, it was observed that once lactate ran out, UO_2 reoxidized even though conditions remained reducing (sulfide was still present). The modeling objective is to understand the thermodynamic and kinetic constraints at play in these experiments.

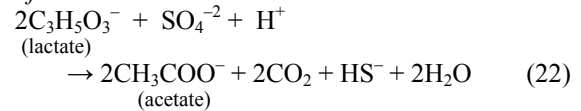
Modeling Approach

TOUGHREACT is used in “batch” mode (i.e., no transport) to investigate a set of potential redox reactions. The initial goal is to reproduce general trends of UO_2 precipitation and reoxidation under conditions similar to those in Sani et al. (2005). We first establish a set of potential reactions, then simulate these reactions and vary key kinetic parameters. All reactions are constrained by their thermodynamic affinity, calculated from most recent published data (e.g., Guillaumont et al., 2003, Dong and Brooks, 2007). The solubility of UO_2 is increased from that of uraninite to account for observed nm-sized particles. It is calculated for 3 nm particles, and is very close to the solubility given by Guillaumont et al. (2003) for $\text{UO}_2(\text{am})$ (Spycher et al., in prep.)

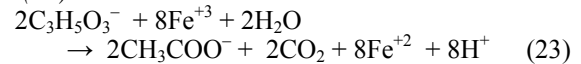
Reaction network

Based on experimental results (Sani et al., 2005), the following reaction network is postulated:

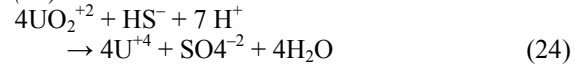
Sulfate reduction



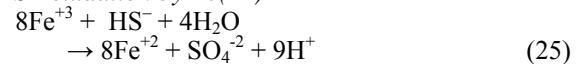
Fe(III) reduction



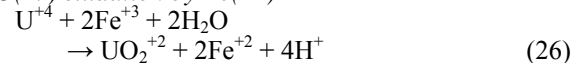
U(VI) reduction



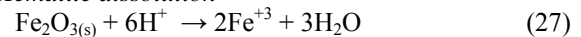
HS⁻ oxidation by Fe(III)



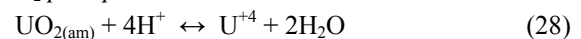
U(IV) oxidation by Fe(III)



Hematite dissolution



UO₂ precipitation/dissolution



The sulfate and initial iron reduction (Reactions 22 and 23) is biotic, with reaction rates modeled using a dual-Monod rate law similar to Equation (21), but with biomass growth. The U(VI) reduction (Reaction 24) was initially tested using a fast (nonlimiting) rate, thus allowing this reaction to proceed at a rate limited

only by the rate of Reaction (22). However, in doing so, modeled U(VI) concentrations decreased much faster than observed values (relative to lactate depletion), and UO_2 did not reoxidize once lactate ran out. Model results consistent with experiments were obtained only by setting the U(VI) reduction to be lactate-limited, with a rate slower than the rate of Reaction (22). This was done by introducing a lactate Monod term in the rate law for Reaction (24) and adjusting its half-saturation constant to reproduce observed trends. In contrast, the oxidation of U(IV) and HS^- by Fe(III) (Reactions 25 and 26) is considered abiotic with reversible rates.

The dissolution/precipitation reactions for UO_2 and hematite (Reactions 27 and 28) are set to proceed at equilibrium. In doing so, dissolution/precipitation rates are indirectly limited by the rate of the redox reactions coupling UO_2^{+2} to U^{+4} and Fe^{+3} to Fe^{+2} . The simulations discussed here do not include the precipitation of sulfur and sulfide phases, although it is considered in ongoing modeling work.

Initial solution composition

The composition of the initial solution is based on experimental conditions (Sani et al., 2005): 5 mmol hematite, 90 μmol U(VI), 20 mmol SO_4^{2-} , 30 mmol lactate, and 30 mmol PIPES buffering the pH at ~ 7 . The bicarbonate concentration is set to reflect equilibrium with atmospheric CO_2 (~ 0.12 mmol), and Na is included for charge balance.

UO_2 Reoxidation Simulations and Results

The batch model is run for a simulated period (~ 50 days) covering the length of experiments. Kinetic parameters are adjusted to roughly capture observed trends and magnitudes of lactate, HS^- , and U(VI) concentrations (Figure 6). Model results and additional thermodynamic analyses show oxidation of HS^- by Fe(III) (Reactions 25+27) directly competing with UO_2 reoxidation (Reactions 26+28), because Fe(III) oxidizes HS^- preferentially to biogenic UO_2 (thermodynamically). Thus, the relative rates of Reactions (25) and (26) determine whether UO_2 reoxidizes. When Reaction (25) shuts down, UO_2 reoxidation is favored once lactate runs out (Figure 6, top). However, when the Reaction (25) rate is increased and eventually exceeds that of Reaction (26), UO_2 reoxidizes to a lesser extent and eventually reprecipitates (Figure 6, bottom).

CONCLUSIONS

Three quite different examples of code application to environmental systems were presented. These examples illustrate the complex interplays and couplings at work in these biogeochemical systems. It is clear that the value of the modeling is more in helping understand potential mechanisms at play than

in providing truly predictive work. This is because the number of uncertain or unknown parameters in these complex systems is large, making long-term predictive work highly uncertain if not futile, at least with current models. Nevertheless, when carefully integrated with field and laboratory measurements, numerical simulations such as those presented here are an invaluable tool to help understand complex systems, including unintuitive feedbacks that often create delicate balances between various reactive and transport processes. At contaminated sites, this gained understanding feeds into, and greatly benefits, decision making regarding long-term stewardship.

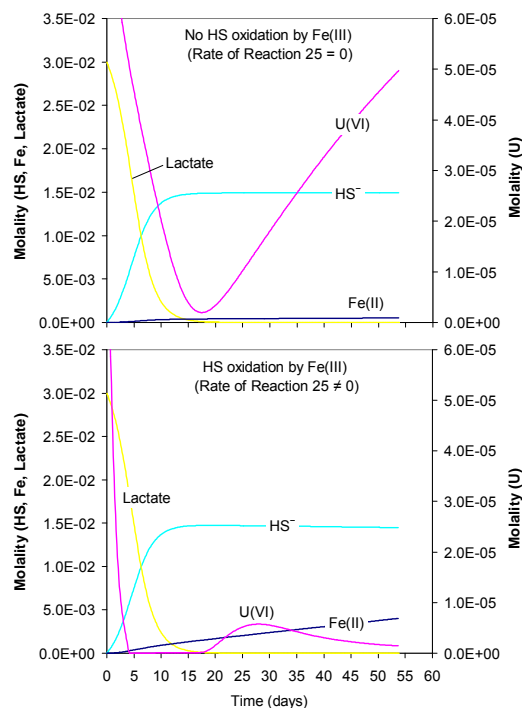


Figure 6. Simulation of biogenic UO_2 precipitation followed by UO_2 reoxidation in the presence of hematite (see text)

ACKNOWLEDGMENT

These studies were funded by the U.S. Department of Energy Environmental Remediation Science Program and by the National Science Foundation.

REFERENCES

- Balistreri, L.S., Preliminary estimates of benthic fluxes of dissolved metals in Coeur d'Alene Lake, Idaho. U.S.G.S. Open File Report 98-793, 1998.
- Doherty, J.: PEST - Model-Independent Parameter Estimation. Watermark Numerical Computing, Corinda 4075, Brisbane, Australia (2008) <http://www.sspa.com/pest/>
- Dong, W., Brooks, S.C., Determination of the formation constants of ternary complexes of

- uranyl and carbonate with alkaline earth metals (Mg^{2+} , Ca^{2+} , Sr^{2+} , and Ba^{2+}) using anion exchange method. *Environ. Sci. Technol.* 40, 4689-4695, 2006.
- Dzombak, D. A., Morel, F. M. M., urface complexation modeling hydrous ferric oxide. John Wiley & Sons, New York, 1990.
- Fidaleo, M., Lavecchia, R., Kinetic study of enzymatic urea hydrolysis in the pH range 4–9. *Chem. Biochem. Eng. Q.* 17 (4) 311–318, 2003.
- Fujita, Y., Redden, G.D., Ingram, J.C., Cortez, M.M., Ferris, F.G., Smith R.W., Strontium incorporation into calcite generated by bacterial ureolysis. *Geochim. Cosmochim Acta* 68, 3261–3270, 2004.
- Fujita, Y., Ferris, F.G., Lawson, R.D., Colwell, F.S., Smith, R.W., Calcium carbonate precipitation by ureolytic subsurface bacteria. *Geomicrobiology Journal*, 17:305–318, 2000.
- Guillaumont, R., T. Fanghanel, J. Fuger, I. Grenthe, V. Neck, D.A. Palmer, M.H. Rand, F.J. Mompean, M. Illemassene, Domenechi-Orti, C., Update on the chemical thermodynamics of uranium, neptunium, plutonium, americium, and technicium. Elsevier: Amsterdam, 2003.
- Horowitz, A.J., Elrick, K.A., Robbins, J.A., and Cook, R.B., Effect of mining and related activities on sediment trace element geochemistry of Lake Coeur D'Alene, Idaho, USA Part II. Subsurface sediments: *Hydrol. Process.* 9, 35-54, 1995.
- Liger, E., Charlet L., Van Cappellen, P., Surface catalysis of U(VI) reduction by Fe(II). *Geochim. Cosmochim. Acta*, 63, 2939–2955, 1999.
- Mitchell, A.C., Ferris, F.G., The coprecipitation of Sr into calcite precipitates induced by bacterial ureolysis in artificial groundwater: Temperature and kinetic dependence. *Geochim. Cosmochim. Acta* 69, 4199–4210, 2005.
- Moberly, J.G., Borch T., Sani R.K., Spycher N.F., Şengör S.S., Ginn T.R., and Peyton B.M., Heavy metal-mineral associations in Coeur d'Alene river sediments: A synchrotron-based analysis. *Water, Air, and Soil Pollution.* 200: 195-208, 2009.
- Maggi, F., C. Gu, W.J. Riley, G.M. Hornberger, R.T. Venterea, T. Xu, N. Spycher, C. Steefel, N.L. Miller, and C.M. Oldenburg, A mechanistic treatment of the dominant soil nitrogen cycling processes: Model development, testing, and application, *J. Geophys. Res. Biogeosciences*, 113, G02016, 2008.
- Nielsen, A.H., Vollertsen, J., Hvitved-Jacobsen, T., Determination of kinetics and stoichiometry of chemical sulfide oxidation in wastewater of sewer networks. *Environ. Sci. Technol.* 37, 3853-3858, 2003.
- Parkhurst, D. L., Appelo, C. A. J., User's Guide to PHREEQC (V2). Water-Resources Investigations Report 99-4259; U.S.G.S., Denver, CO, 1999.
- Poulton, S., Krom, M., Raiswell, R., A revised scheme for the reactivity of iron (oxyhydr)oxide minerals towards dissolved sulfide. *Geochim. Cosmochim. Acta*, 68, 3703-3715, 2004.
- Sani, R.K., Peyton, B.M., Amonette, J.E., Dohnalkova, A, Reoxidation of uranium in the presence of iron (III)-(hydr)oxides under sulfate-reducing conditions. *Environ. Sci. Technol.* 39: 2059-2066, 2005.
- Sani, R.K., Peyton, B.M., Amonette J.E., Geesey, G.G., Reduction of U(VI) under sulfate reducing conditions in the presence of Fe(III)-(hydr)oxides. *Geochim. Cosmochim. Acta* 68: 2639-2648, 2004.
- Sengör, S.S., Spycher N., Ginn T.R., Sani R.K., Peyton B., Biogeochemical reactive-diffusive transport of heavy metals in Lake Coeur d'Alene sediments, *Applied Geochem.* 22, 2569-25, 2007a.
- Sengör, S.S., Spycher, N.F., Ginn, T.R., Moberly, J., Peyton, B., & Sani, R.K., Reductive dissolution and metal transport in Lake Coeur d'Alene sediments. In *Water-Rock Interaction, WRI-12* (Bullen T. and Wang Y., eds.), Taylor & Francis, New York, Vol. 2, 895-899, 2007b.
- Steefel, C., New directions in hydro-geochemical transport modeling: Incorporating multiple kinetic and equilibrium reaction pathways. *Proceedings, Comp. Methods Water Res., CMWR VIII*, June 25-29, Calgary, Canada, 2000.
- Spycher, N., Sengor, S., Ginn, T., Peyton, B., Sani, R., Moberly, J., Modeling iron (hydr)oxide reductive dissolution and metal transport in mining-impacted riverine and lacustrine sediments. *Comp. Methods Water Res., CMWR XVII*, July 6-10, San Francisco, California, 2008.
- Toevs, G.R., Morra, M.J., Polizzotto, M.L., Strawn, D.G., Bostick, B.C., Fendorf, S., Metal(loid) diagenesis in mine-impacted sediments of Lake Coeur d'Alene, Idaho. *Environ. Sci. Technol.* 40, 2537–2543, 2006.
- Wehrli, B., Redox reactions of metal ions at mineral surfaces. In W. Stumm (ed.) *Aquatic chemical kinetics. Reaction rates of processes in natural waters.* Wiley-Interscience, 1990.
- Williamson, M.A., Rimstidt, J.D., The kinetics and electrochemical rate-determining step of aqueous pyrite oxidation. *Geochim. Cosmochim. Acta* 58: 5443-5454, 1994.
- Winowiecki, L., Geochemical cycling of heavy metals in the sediment of Lake Coeur d'Alene, Idaho. Masters Thesis, University of Idaho, Moscow, Idaho, 2002.

MODELING ACID ROCK DRAINAGE IN A MINE ROCK PILE USING A MODIFIED VERSION OF TOUGHREACT

Marcin Niewiadomski, Edward Trujillo, You Li, Surya Prakash Sunkavalli
University of Utah, Department of Chemical Engineering
50 S. Central Campus Drive - 3290 MEB
Salt Lake City, UT 84112 U.S.A.
edward.trujillo@utah.edu

ABSTRACT

Acid rock drainage (ARD) is a serious environmental problem affecting the mining industry. It includes mineralogical, geochemical, physical and biological changes in a complex geological system, and all three phases—solid, liquid, and gas. Various models have been proposed over the years to simulate this phenomenon, but few have included all the important mechanisms that result in the formation of *in situ* convective air currents as well as the changes in the mineralogical composition and water chemistry over time. ARD has been previously simulated by Lefebvre et al., with a modified TOUGH code, called TOUGH-AMD and more recently by Xu et al. using TOUGHREACT.

In our study, TOUGHREACT v. 1.2 was selected to model temperature, fluid flows and mineralogical changes in a mine rock pile over time. The model includes 15 minerals, over 50 secondary species, and carbon dioxide and oxygen in the gas phase. The rock pile consists of several layers with various physical and chemical properties. It was found that preparation of the computational mesh was difficult due to the existence of many thin and distinct layers; therefore, not only a regular but also an irregular mesh was tested. The existing TOUGHREACT code was modified to accommodate the complex processes required to successfully simulate ARD in a rock pile. Code parallelization with OpenMP was accomplished, heats of reaction were implemented for dissolving or precipitating minerals, and the iron (+2) and iron (+3) species were decoupled to allow both iron forms to be in the primary species list, thus allowing two different reactions with pyrite as well as the aqueous oxidation of iron (+2) to iron (+3). In addition, bacteria was included on the primary species list, with a kinetic growth-rate expression and a death rate for the bacterially catalyzed iron oxidation reaction. An overall view of the study will be presented, as well as a discussion of the process to be used for validation and verification. Evaluation of the code modifications for ARD modeling will also be presented.

INTRODUCTION

Acid rock drainage (ARD) occurs in rock piles and tailings when sulfide minerals oxidize in the presence of water and air to produce sulfuric acid. The acid leaches through the rock material, reacts with other minerals, and can contaminate nearby streams and lakes. There have been numerous mathematical models of weathering and acid rock drainage (ARD) over the last few decades, starting with rather simple models to very complicated coupled models. The objective of most is to predict water quality after mine closure for a number of years. The problem is that ARD is a very complex process, involving not only mineralogical and geochemical changes but physical and biological changes as well. Most rock piles are heterogeneous in terms of mineralogy and flow properties, and the ARD process involves all three phases—solid, liquid, and gas. In addition, due to heats of reaction, there is an energy component that can produce natural convective air currents in unsaturated, highly permeable rock piles.

TOUGH2 was modified by Lefebvre [Lefebvre, 1994; Lefebvre, 2001ab] to include a limited number of geochemical reactions and was developed as part of a MEND project (project number 1.14.2). Lefebvre refers to this model as TOUGH-AMD. Subsequently, the TOUGHREACT model developed at Lawrence Berkeley National Laboratory (LBNL) included chemical reactions, and coupled the TOUGH2 transport code with the EQ3/6 geochemical equilibrium code [Xu, 1999; Xu, 2000; Xu, 2008]. LBNL also developed a model called TOUGH2-CHEM that can be applied to ARD, but uses a different solution algorithm than TOUGHREACT and is much more convoluted computationally.

We have been working with the TOUGHREACT code, version 1.2, and found that we needed to make several code modifications to properly simulate most of the principal mechanisms involved in ARD and to improve the amount of time it takes to run the code. These are described in the following sections.

TOUGHREACT MODIFICATIONS

Parallelization

In order to improve the overall speed of the TOUGHREACT program, we have developed parallelized code to run on systems with multiple processors.

As seen in the figure above, the idea of parallelization is to divide the workload into multiple portions depending on the number of processors available, and each portion is sent to a thread. After each thread completes its share, the results are sent back to the master thread and combined together, then synchronized among all the threads. The following techniques are used to achieve the speed improvement.

Preliminary Optimization

A significant speed improvement has been accomplished in operations of string variable comparison, where strings are element names, species names, etc. String comparison is an expensive operation to perform, and consequently it has been replaced with integer comparison, a much faster operation. All subject to comparison strings have been assigned a unique integer ID for this purpose.

Parallelization with Message Passing Interface (MPI)

Message Passing Interface (MPI), a language-independent communication protocol, allows communication between many computers over the network. It is commonly used in computer clusters and supercomputers, working in distributed memory system architecture.

However, a version of MPI-enabled TOUGHREACT, developed to run on clusters of the University of Utah's Center for High Performance Computing (CHPC), revealed compatibility problems between the MPI library and the compiler. Further development was thus directed to Open Multi-Processing (OpenMP) instead.

Parallelization with Open Multi-Processing (OpenMP)

OpenMP, in contrast to MPI, works in a shared-memory computer architecture. The synchronization of data taking place in the same memory system is much faster. However, there are limitations to how many processors can be utilized since it is difficult to build a shared-memory system with large number of processors.

One advantage of OpenMP is its simplicity. All the modifications are done with compiler directives. If a given compiler does not support OpenMP, it simply ignores the directives and generates a single-threaded executable program. The process of parallelization involves the following steps:

1. Identification of loops that can be parallelized
2. Identification of variables that need to be synchronized
3. Insertion of necessary OpenMP directives to distribute the work and synchronize the data

New Server and Intel Compiler

An eight-core server consisting of two quad-core Intel Xeon processors was built to run the Open-MP-enabled TOUGHREACT program. Previously, a dual-processor AMD Opteron server was used. The benefit of using both the Intel processor system and compiler was that they were designed to work together. Comparison of experimental runs showed a 10% to 15% speed increase in the case of the Intel system over the AMD system with The Portland Group compiler.

Parallelization has been introduced to the CS_CP and CR_CP subroutines. However, recent testing indicates that the parallel overhead was comparable with computation time gain; thus the net time advantage was not very significant. Further parallelization and consideration of parallelizing individual loops is planned.

Heats of Reactions

Heats of reactions were added to the code for mineral dissolution and precipitation reactions. Values were declared in the chemical.inp file in units of J/mol, corresponding to heat effects per one mole of a given mineral dissolving according to the reaction specified in the database. After the amount of mineral either dissolving or precipitating in a given time step was determined, the amount of heat was calculated and stored in an array variable. During the subsequent time step, while solving the flow distribution, the calculated heat was added to the heat-balance equation as an arbitrary amount of heat would be added from a GENER record. In the investigated model, heats of reaction were set for two pyrite dissolution reactions (-1,409.0 kJ/mol for pyrite dissolution by the oxygen mechanism, and -11.5 kJ/mol by the acid mechanism [iron +3, value calculated theoretically from CRC online data])—and -35.13 kJ/mol for calcite dissolution.

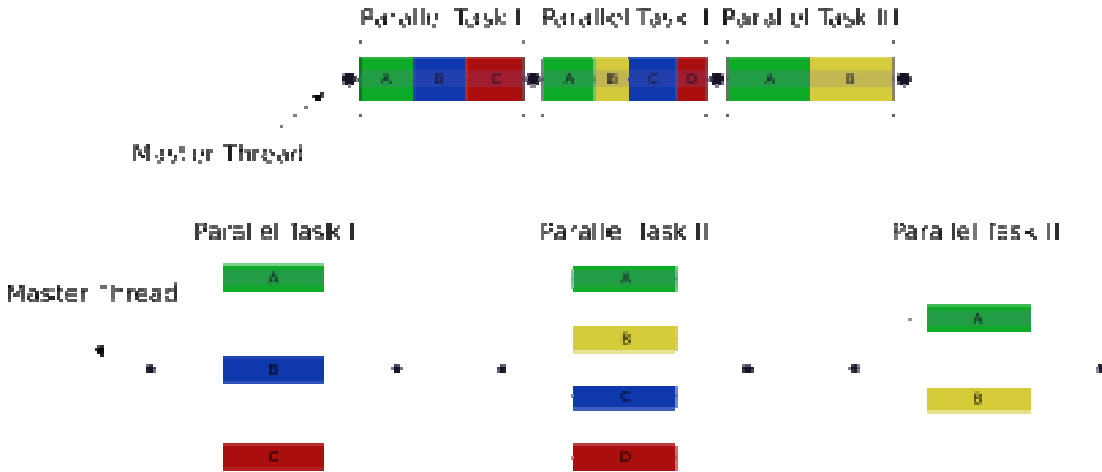
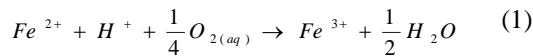


Figure 1. An illustration of multithreading where the master thread forks off a number of threads which execute blocks of code in parallel

Iron Oxidation Reaction

The proposed ARD model required the presence of minerals containing iron in two oxidation states (+2 and +3), which required them to be at disequilibrium. Both irons were placed in a primary species list. Iron oxidation from +2 to +3 has been implemented as a kinetic reaction in bulk solution by using the kinetic mineral reaction mechanism. A “virtual mineral” (called Fe handler in the database) has been declared that by precipitation was consuming iron (+2) and releasing iron (+3) to the solution. The following reaction has been implemented:



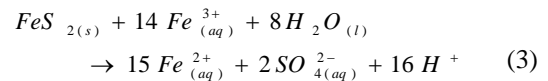
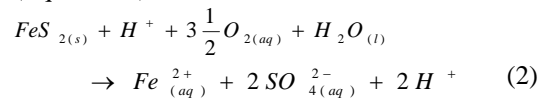
The virtual mineral was allowed only to precipitate, which allowed iron (+2) only to oxidize to iron (+3). Fe_handler, while included in the database reaction on the right side of Equation (1), was not included in the stoichiometry. Also, the virtual mineral volume was set very small (0.00001 cm³/mol), which ensured that changes in solid phase volume were negligible when precipitation occurred.

The neutral mechanism (in pure water) rate constant for Fe_handler was set to zero. The actual reaction rate was calculated using the feature of additional mechanisms. Three such mechanisms were declared. The first mechanism included the effect of bacteria concentration on the oxidation reaction according to Pesic *et al.* (1989). Code modification was required to make this mechanism independent from the hydrogen ion concentration at pH values lower than

2.2. The last two mechanisms represented the abiotic oxidation rate and could be implemented without code modification. They represented pH-dependent and independent regions as given by Singer and Stumm (1970).

Pyrite Dissolution Reactions

The ARD model also required two pyrite dissolution mechanisms that would be included in the mass balance. This was achieved by declaring two pyrite minerals “a” and “b” (pyrite-2a, pyrite-2b) for oxidation by oxygen (Equation 2) and oxidation by Fe³⁺ (Equation 3).

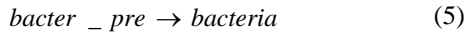
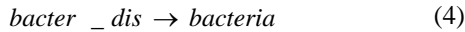


Appropriate changes were made in the code. Calculations of overall available mineral reactive surfaces for two pyrites were taking into account by adding amounts of both minerals.

Bacteria Growth and Death

The growth and death of the *Acidothiobacillus ferrooxidans* bacteria has been included in the model, since this bacteria serves as a catalyst in the iron oxidation reaction. Bacteria were declared as a primary species with zero charge. The same technique of using a virtual mineral was applied with two such minerals, one for bacterial growth, allowed only to dissolve; and one for bacterial death, allowed

only to precipitate. This gave an effect of simultaneous bacterial growth and death under kinetic constraints. The two reactions/processes were described in the database as follows:



The neutral mechanism rate constants were set to zero in both cases, and similarly to the case of Fe_handler, the reaction rate was controlled by the feature of additional mechanisms. The rate expression (6) has been hardcoded for bacterial growth, and the rate expression (7) for bacterial death rate could be used without code modification (Shrihari and Kumar, 1990):

$$\frac{d[bacteria]}{dt} = A \cdot [bacteria] \cdot \left\{ \frac{[H^+]}{B + [H^+]} \right\} \cdot \left\{ \frac{[Fe^{2+}] \cdot M_{Fe}}{[Fe^{2+}] + C \cdot (1 + D \cdot [Fe^{3+}] \cdot M_{Fe})} \right\} \quad (6)$$

$$\frac{d[bacteria]}{dt} = -E \cdot [bacteria] \quad (7)$$

where:

- M_{Fe} - iron molar mass, g/mol
- bacteria - concentration in solution, g/L
- A,B,C,D,E - constants

Additional Functions

Additional functions such as relative permeability and capillary pressure relationships (soil water characteristic curve, SWCC) were added. The Modified Campbell relative permeability function was coded into TOUGHREACT (Campbell, 1974) and the Fredlund and Xing soil water characteristic curve has been applied (Fredlund and Xing, 1994). The SWCC has been implemented as a discretized relationship, owing to the difficulty in

mathematically converting the Fredlund and Xing formula from liquid saturation as a function of capillary pressure, $S_L(P_C)$, to capillary pressure as a function of liquid saturation, $P_c(S_L)$. These functions have been found to best represent unsaturated liquid flow in rock piles associated with ARD.

Testing of TOUGHREACT Code Changes

The heats of reaction in the modified TOUGHREACT code were tested by inspecting heat values recorded in an output log file and comparing them with published field models for similar geometries. Additional tests are intended.

The kinetic iron oxidation reaction has been tested using a one-element model in TOUGHREACT and compared to a similar PHREEQC batch model, both containing only Fe^{2+} , Fe^{3+} , $Fe(OH)^+$ and $Fe(OH)_2^+$ ions. Figure 2 shows a comparison of Fe^{2+} concentrations in both simulations. Initial conditions were set the same, and the slight differences are expected because of the slightly different ways of initializing calculations for both simulators.

Coupling of the two pyrite reactions was tested by performing a short simulation with 3 time steps, in which pyrite-2a was in amount of 1.5% and pyrite-2b was in amount of 0.5%. The modified TOUGHREACT code properly dissolved both pyrites as if 2.0% were present in the system, which was confirmed by inspecting recorded values in the chdump.out file. The bacterial growth and death has not been tested yet, but simulations were performed using this feature. Since bacterial measurements of rock piles are rarely done, it would be difficult to validate this aspect of the model.

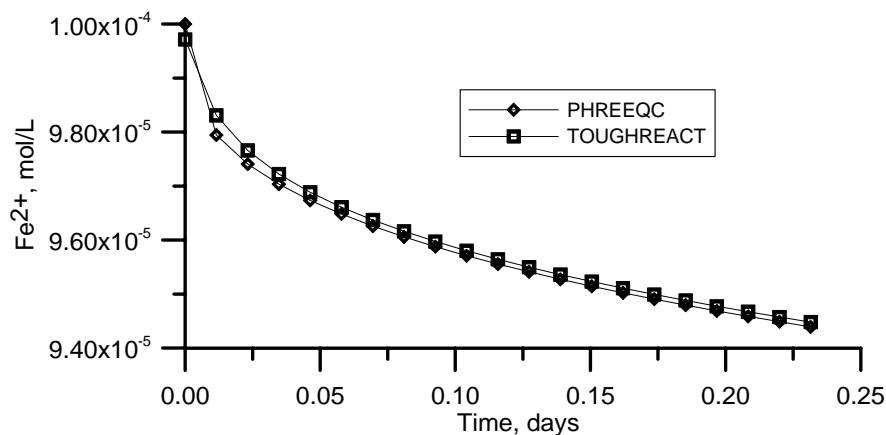


Figure 2. Comparison of Fe^{2+} concentrations in the kinetic oxidation reaction of pyrite calculated in our modified TOUGHREACT code compared to PHREEQC calculations.

ROCK PILE MODEL

A model of a hypothetical rock pile has been constructed. Both regular rectangular and irregular meshes were attempted. The irregular mesh was a better reflection of the geometry of the rock pile without the addition of a large number of small elements. The model consists of 34 model layers, from which 26 are geochemical layers having distinct initial material properties and chemical compositions. However, hydrological layers are separated into just

4, with four hydrological properties (fine, medium, coarse, and colluvium). The regular and irregular meshes are presented in Figures 3 and 4, respectively. The chemical composition of the system consists of 15 primary species including bacteria, 55 secondary species, and 19 minerals, including 2 pyrites and 3 virtual minerals. Table 1 presents species that were used in the rock pile field model.

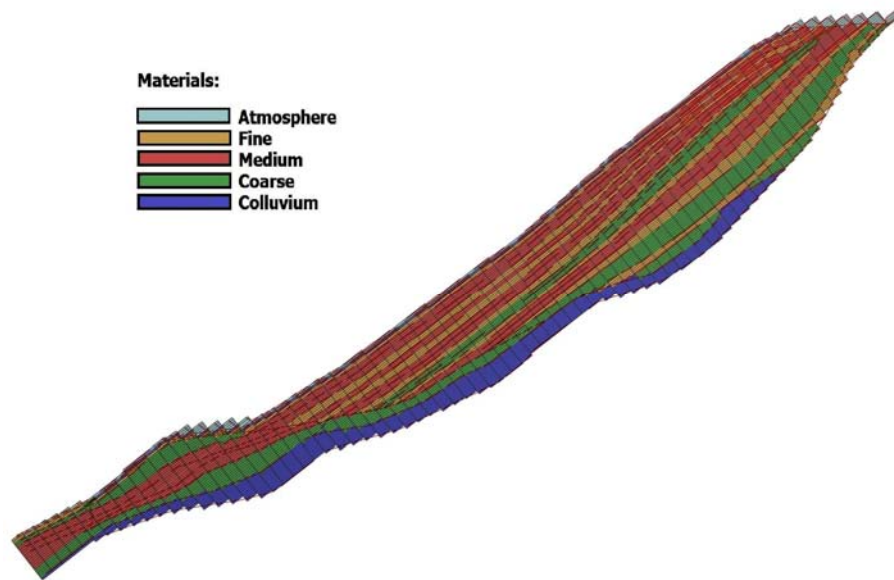


Figure 3. Regular mesh of rock pile field model.

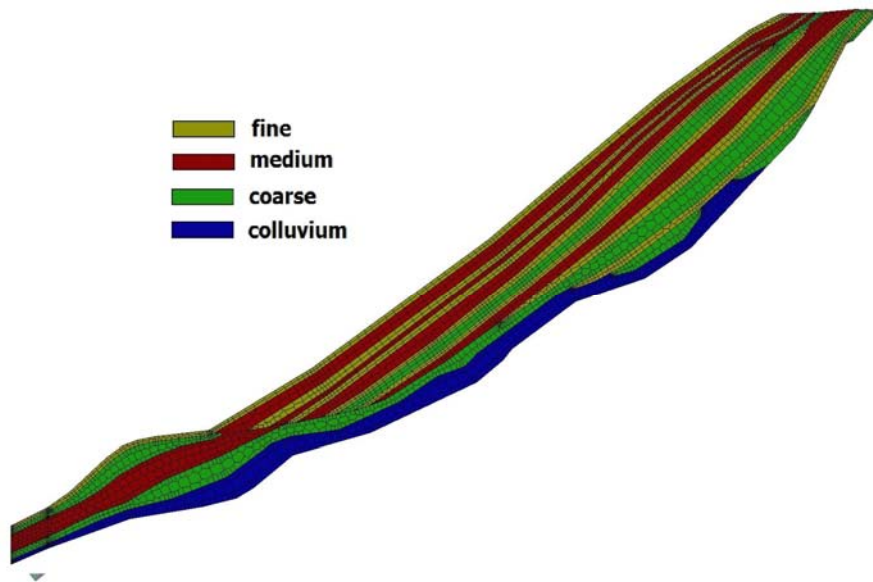


Figure 4. Irregular mesh of rock pile field model.

Table 1. Species used in the rock pile field model in TOUGHREACT 1.2.

Primary Aqueous Species	Aqueous Complexes			Minerals	Gases
'h2o'	'oh-'	'fe(oh)2(aq)'	'nahsio3(aq)'	'calcite'	'co2(g)'
'h+'	'al+3'	'fe(oh)2+'	'naf(aq)'	'pyrite-2a'	'o2(g)'
'ca+2'	'aloh+2'	'fe(oh)3(aq)'	'naso4-'	'pyrite-2b'	
'mg+2'	'al(oh)2+'	'fe(oh)3-'	'co2(aq)'	'gypsum'	
'na+'	'al(oh)3(aq)'	'fe(oh)4-'	'co3-2'	'kaolinite'	
'k+'	'al(oh)4-'	'feco3+'	'mgso4(aq)'	'illite'	
'fe+2'	'al(so4)2-'	'fef+'	'mgco3(aq)'	'k-feldspar'	
'fe+3'	'alf+2'	'fef+2'	'mgf+'	'chlorite'	
'sio2(aq)'	'alf2+'	'fef2+'	'mghco3+'	'smectite-ca'	
'hco3-'	'alf3(aq)'	'fehso4+2'	'mgoh+'	'albite~low'	
'so4-2'	'alf4-'	'feoh+'	'kso4-'	'anorthite-a1'	
'alo2-'	'also4+'	'feoh+2'	'khso4(aq)'	'fluorite'	
'f-'	'caso4(aq)'	'feso4(aq)'	'koh(aq)'	'goethite'	
'o2(aq)'	'cahco3+'	'feso4+'	'hso4-'	'epidote'	
'bacteria'	'caco3(aq)'	'nahco3(aq)'	'hf(aq)'	'jarosite'	
	'caoh+'	'naalo2(aq)'	'hf2-'	'fe(oh)3'	
	'caf+'	'naoh(aq)'	'halo2(aq)'	'fe_handler'	
	'fehco3+'	'naco3-'	'h3sio4-'	'bacter_dis'	
	'feco3(aq)'			'bacter_pre'	

RESULTS

One Element Chemical Reaction Tests.

To test all the implemented code changes, we set up a simple model that consisted of a single rock element connected to a large atmospheric element. The simulation covered 100 years. Selected results are presented in Figure 5. Temperatures of the element increased from 20°C to over 35°C, which appears to be correct for pyrite oxidation in a rock pile. The pH did not change significantly during the simulated time, which can be explained by an excess of calcite that could neutralize, produced acidity. The middle graphs, upper and lower, present Fe^{2+} and Fe^{3+} concentrations respectively. The Fe^{2+} concentration continuously increased, whereas the Fe^{3+} concentration initially decreased, but after approximately 50 years started to increase. Pyrite volumetric content in the solid phase pertains to both reactions (pyrite-2a and pyrite-2b) and its overall rate

of dissolution increased. Calcite was not exhausted within 100 years.

Field Model Rock Pile Results

Flow without chemical reactions for the rock pile field model, simulated in the regular mesh for 100 years, is presented in Figure 6. The color scale represents water velocities that range from 1.0×10^{-7} m/s to 17.0×10^{-6} m/s. Velocities below 1.0×10^{-7} m/s are not represented by arrows to better show the main water flow patterns. Recharge flow was injected only into the crust layers of the slope and toe sections. The majority of flow permeated into the colluvium at the toe section. The toe extension was considered outside of the system. Discharge was applied using a constant pressure boundary, which in fact turned out to recharge the toe extension. (Correction of the boundary condition is planned in the future.)

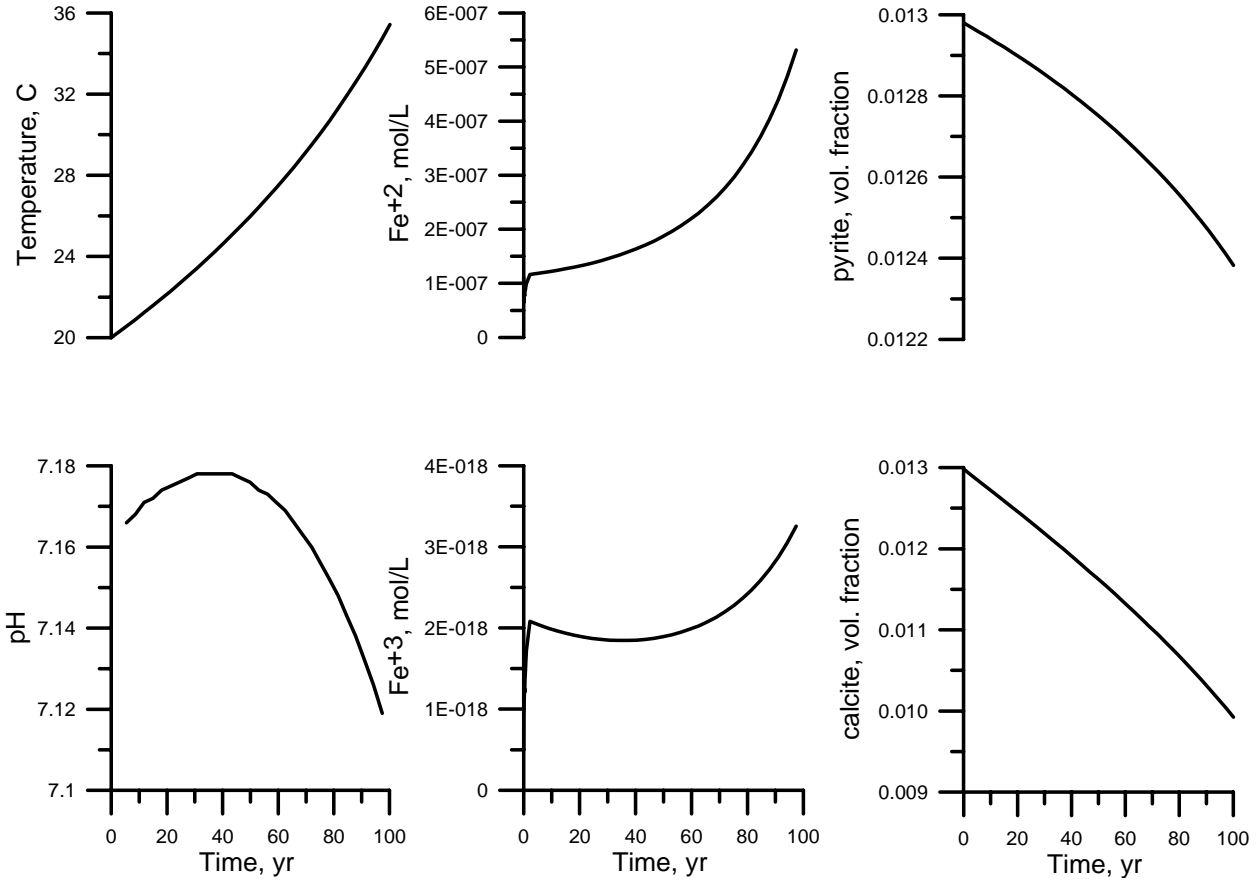


Figure 5. Single element rock pile simulation for 100 year showing the results for some of the parameters

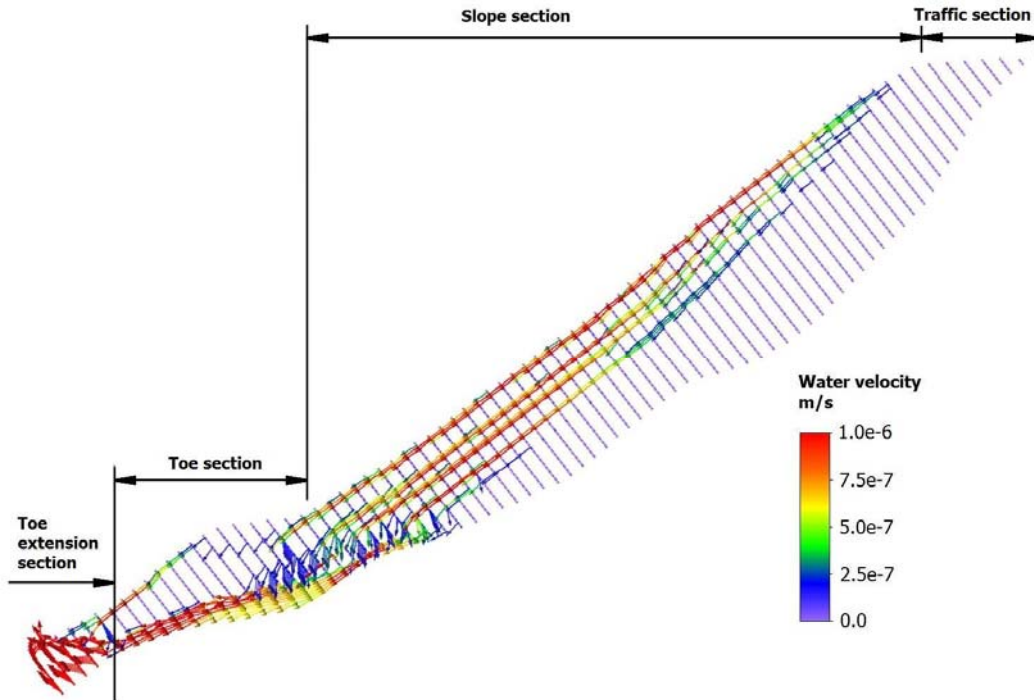


Figure 6. Flow results at 100 years using the regular mesh

CONCLUSIONS

The TOUGHREACT v.1.2 simulator was successfully used to model the ARD chemical processes on the small scale of one rock element, with several changes to existing code and a few new features. Presently, simulation of both chemical reactions with flow for 100 years for all 26 layers is planned.

ACKNOWLEDGMENTS

This project was funded by Chevron Mining Inc. (formerly Molycorp, Inc.) for which we are grateful. We would also like to thank everyone on the large multidisciplinary team associated with this project for their helpful suggestions and comments during the development of these models.

REFERENCES

Campbell, G. S., A simple method for determining unsaturated conductivity from moisture retention data, *Soil Science*, 117(6), (June), 311-314, 1974.

Fredlund, D. G. and A. Xing, Equations for the soil-water characteristic curve, *Canadian Geotechnical Journal*, 31(3), 521-532, 1994.

Lefebvre, R., and D. Hockley, et al., Multiphase transfer processes in waste rock piles producing acid mine drainage: 2. Applications of numerical simulation, *Journal of Contaminant Hydrology* (52), 165-186, 2001a.

Lefebvre, R. and A. Lamontagne, *Numerical Simulations of Acid Rock Drainage in the Questa Mine Rock Piles, New Mexico*. Report No 2001-01 submitted to Chris Wels, Robertson Geoconsultants Inc., Vancourver, January 31, 1-42, 2001b.

Lefebvre, R., A. Lamontagne, et al. (2002). ARD Production and Water Vapor Transport at the Questa Mine, Tailings and Mine Waste 2002, proceedings of the Ninth International Conference on Tailings and Mine Waste, Fort Collins, Colorado, USA, January 27-30, 479-488, 2002.

Pesic, B., D. J. Oliver and P. Wichlacz, An electrochemical Method of Measuring the Oxidation Rate of Ferrous to Ferric Iron with Oxygen in the Presence of *Thiobacillus ferrooxidans*. *Biotechnology and Bioengineering*, 33, 428-439, 1989.

Shrihari, K., S. Gandhi and R. Kumar, Modeling of ferrous oxidation by *Thiobacillus ferrooxidans*, *Appl. Microbiol. and Biotech.*, 33, 524-528, 1990.

Singer, P. C. and W. Stumm, Acidic Mine Drainage: The Rate-Determining Step, *Science*, 167(3921), (Feb. 20), 1121-1123, 1970.

Xu, T., K. Pruess, et al., An improved equilibrium-kinetics speciation algorithm for redox reactions in variably saturated subsurface flow systems. *Computers & Geosciences*, 25(6), 655-666, 1999.

Xu, T., S. P. White, et al., Modeling of Pyrite Oxidation in Saturated and Unsaturated Subsurface Flow Systems, *Transport in Porous Media*, 39, 25-56, 2000.

Xu, T., Incorporating Aqueous Reaction Kinetics and Biodegradation into TOUGHREACT: Applying a Multiregion Model to Hydrobiogeochemical Transport of Denitrification and Sulfate Reduction, *Vadose Zone Journal*, 7(1), 305-315, 2008.

BEHAVIOR OF CONTAMINANT MIGRATION THROUGH SOIL CEMENT BARRIERS USING THE TMVOC SIMULATOR

C. Kererat¹ and S. Soralump²

¹Lecturer, Department of Civil Engineering, Rajamangala University of Technology Rattanakosin, Thailand

²Assistant Professor, Department of Civil Engineering, Kasetsart University, Thailand

Email: kererat_kkw@hotmail.com, fengsus@ku.ac.th

ABSTRACT

The spill of hydrocarbons from industrial plants is a significant problem for groundwater. Through advection and diffusion, contaminant migration can spread widely in the subsurface. The effect of contaminated groundwater can become still more serious if contamination occurs in sandy soil. This paper focuses on the study of LNAPL migration in soil and through a containment barrier. The simulation study of contaminant migration considers two scenarios, as follows: (1) without groundwater flow and (2) with groundwater flow, with a hydraulic gradient of 0.017. The wall, 5 m deep and 1 m thick, was modeled as a containment system. The NAPL spill was modeled with a constant-rate release lasting 2 years. The study found that the permeability of soil and the hydraulic gradient of the aquifer were the factors that affected contaminant migration. The results obtained could be used as a guide for the design of impervious wall dimensions and properties to properly contain contaminant migration.

INTRODUCTION

Subsurface contamination problems due to the release of toxic substances, such as inorganic and organic compounds including hydrocarbon volatile organic compounds (VOCs), may affect the environment and the life cycle of natural animals and humans.

The spill of light nonaqueous phase liquid (LNAPL), such as gasoline, into the vadose zone is more risky than the spill of heavy contaminants (DNAPL), because LNAPL can spread quickly, especially in the presence of high-permeability soil. For these reasons, this paper focuses on the benzene (STD) migration behavior through a soil cement barrier. Benzene is an aromatic hydrocarbon having a high solubility in water and a non-negligible vapor pressure. When spilled into the subsurface, it migrates, giving rise to multiphase flow processes.

In this study, the simulations took into account different barrier materials and different aquifer hydraulic gradients. The TMVOC simulator was used within the PetraSim 4.2 pre- and postprocessing

interface. PetraSim is one of the graphical interface available for the TOUGH2 family of reservoir simulators developed at Lawrence Berkeley National Laboratory (USA). TOUGH2 and its derivatives were recognized for their broad range of subsurface simulation capabilities, including heat and multiphase flow and reactive transport. In the past, modeling of multiphase organic contaminant migration was performed by several authors, such as Abriola and Pinder (1985), Kaluarachchi and Parker (1989), Falta et al. (1995), Soga et al. (2003), Pruess and Battistelli (2003), Fagerlund and Niemi (2003), Dunn (2005), and Battistelli (2008).

SOIL CEMENT COLUMN BARRIER

Soil-cement walls are structures often used to improve the geotechnical properties of soft soil. They can be constructed by two methods: (1) a rotary mixed method, the technique preferred for cohesive soil, with a widespread use in Japan; and (2) a jet grouting method, a technique for both cohesive soil and cohesionless soil. The latter method can be especially useful for sandy soil, where the injection of cement slurry is more effective than in clay. This approach offers the advantage of building wall columns in both a vertical and inclined direction by cement-based grout. The construction of soil-cement columns by means of jet grouting can be depicted step-by-step as shown in Figure 1.

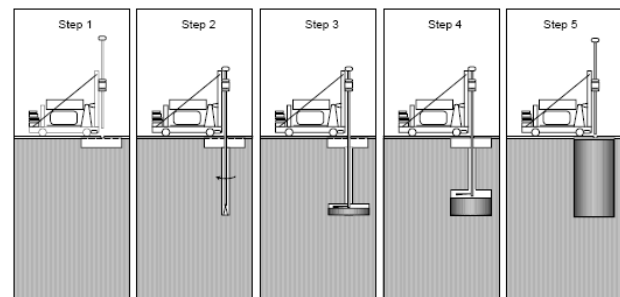


Figure 1. Step-by-step construction of soil cements columns by means of jet grouting technique.

In Thailand, soil-cement columns are often used for improvement of soft soil. The main objective is to decrease settlement and increase the bearing capacity of soft soil. In addition, they can also reduce the permeability of sandy soil. Therefore, soil-cement columns can also be used as physical barriers to contain the migration of contaminants in the subsurface.

MODELING APPROACH

Model Characteristics and Material Properties

The conceptual models used in the study are shown in Figure 2. They are two dimensional sections 60.2 m long, 15.1 m thick and 1 m wide. The characteristics of the four models are: (1) no groundwater flow (hydraulic gradient equal to zero), (2) groundwater flow with a hydraulic gradient of 0.017 (water table difference of 1 m along a distance of 60 m (1/60)), (3) no groundwater flow with containment (hydraulic gradient equal to zero), and (4) ground water flow with a hydraulic gradient of 0.017 with containment. The spill point of the benzene is located in the unsaturated zone at a distance from the left side of 29.6 m for Models 1 and 3, and 19.6 m for Models 2 and 4. The groundwater table is 2 m below the ground surface for Models 1 and 3, while for Models 2 and 4, it is 2 m and 3 m deep at the left and right boundaries, respectively. The containment system is 1 m thick, 5 m deep and is located at 1.5 m from the spill point in the both left and right directions.

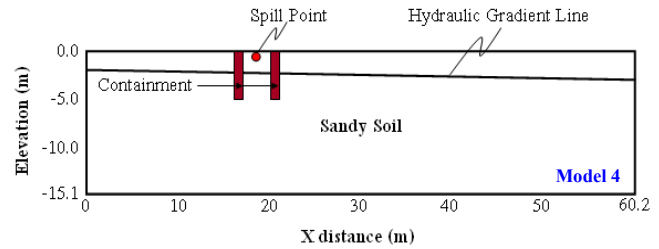
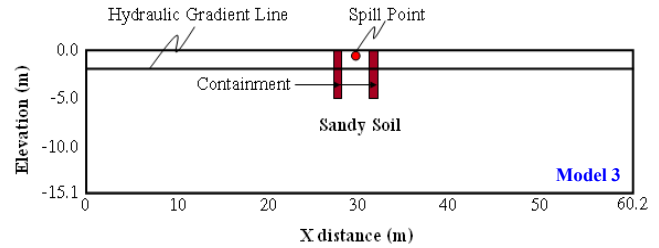


Figure 2. Conceptual models 1, 2, 3 and 4 (Con.)

We studied the effect of intrinsic permeability. Three intrinsic permeability values of soil were used: 10^{-9} m^2 , 10^{-10} m^2 and 10^{-11} m^2 . Three intrinsic permeability values of the barrier were also used: 10^{-13} m^2 , 10^{-14} m^2 and 10^{-15} m^2 . This study considers a total of 24 different cases; basic petrophysical properties are listed in Table 1. The relative permeability and capillary pressure curves for three-phase systems are described according to the Stone (1970) and Parker et al. (1987) models, respectively. The corresponding parameters are summarized in Tables 2 and 3 for the relative permeability and the capillary pressure, respectively. The simulations are performed at a constant temperature of 20°C. The atmospheric boundary conditions are fixed at the grid top and specified as a constant absolute pressure of $1.01 \times 10^5 \text{ Pa}$.

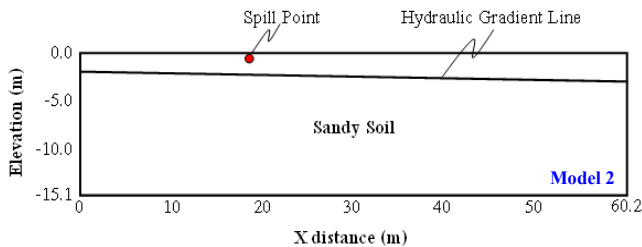
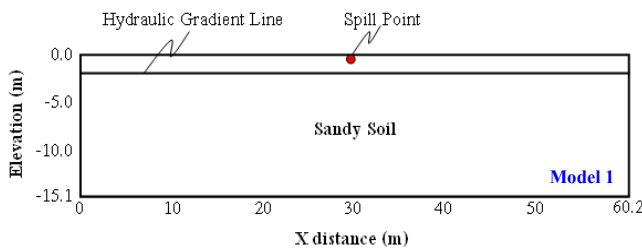


Figure 2. Conceptual models 1, 2, 3, and 4

Table 1. Main petrophysical properties of rock domains

Soil criteria	Rock grain density kg m ⁻³	Porosity	Horizontal permeability m ²	Vertical permeability m ²
ATMOS	2600	0.35	1×10^{-8}	1×10^{-8}
Soil 1	2600	0.31	1×10^{-9}	1×10^{-9}
Soil 2	2600	0.35	1×10^{-10}	1×10^{-10}
Soil 3	2600	0.39	1×10^{-11}	1×10^{-11}
Wall 1	2600	0.43	1×10^{-13}	1×10^{-13}
Wall 2	2600	0.47	1×10^{-14}	1×10^{-14}
Wall 3	2600	0.51	1×10^{-15}	1×10^{-15}

Table 2. Relative permeability parameters of different rock domains (first Stone's modified model)

Soil criteria	Swr	Snr	Sgr	n exponent
ATMOS	0.15	0.05	0.05	3
Soil1, Wall1	0.15	0.05	0.05	3
Soil2, Wall2	0.15	0.05	0.05	3
Soil3, Wall3	0.15	0.05	0.05	3

Remarks: Swr = irreducible aqueous phase saturation, Snr = irreducible NAPL saturation, Sgr = irreducible gas phase saturation, NAPL = non aqueous liquid

Table 3. Capillary pressure parameters of different rock domains (Parker's model)

Soil criteria	Sm	α_{gn}	α_{nw}	n exponent
ATMOS		no capillary		
Soil 1	0	100	110	1.84
Soil 2	0	30	33	1.84
Soil 3	0	10	11	1.84
Wall 1	0	1	1.1	1.84
Wall 2	0	3	3.3	1.84
Wall 3	0	0.1	0.11	1.84

Remarks: Sm = limiting saturation, α_{gn} = strength parameter for gas-NAPL, α_{nw} = strength parameter for NAPL-aqueous phase liquid

The applied boundary conditions are shown in Table 4. For this application, the formation of heterogeneities, the seasonal water table fluctuations, and the water infiltration have been neglected.

Table 4. Boundary conditions applied to simulation

Boundary	Pressure	Condition
Hydraulic Gradient, $i = 0$		
Top	1.01×10^5	Gas Only
Left ($x = 0$ m)	1.01×10^5 $1.01 \times 10^5 + 9789z$	Gas and Water, Above Water Table ($z \leq 2.1$ m, water sat. = 0.20) Water Only, Below Water Table ($z > 2.1$ m)
Right ($x = 60.2$ m)	1.01×10^5 $1.01 \times 10^5 + 9789z$	Gas and Water, Above Water Table ($z \leq 2.1$ m) Water Only, Below Water Table ($z > 2.1$ m)

Table 4. Boundary conditions applied to simulation (Cont.)

Boundary	Pressure	Condition
Hydraulic Gradient, $i = 0.017$		
Top	1.01×10^5	Gas Only
Left ($x = 0$ m)	1.01×10^5 $1.01 \times 10^5 + 9789z$	Gas and Water, Above Water Table ($z \leq 2.1$ m, water sat. = 0.20) Water Only, Below Water Table ($z > 2.1$ m)
Right ($x = 60.2$ m)	1.01×10^5 $1.01 \times 10^5 + 9789z$	Gas and Water, Above Water Table ($z \leq 3.1$ m) Water Only, Below Water Table ($z > 3.1$ m)

Model Characteristics and Material Properties

The modeling is discretized with 16 layers and 62 columns for a total of 992 elements. The vertical and horizontal spacing is 1×1 m, except the elements of top row which are 1×0.1 m; left and right boundary columns have the spacing of 0.1×1 m. The simulations are divided into several steps, as follows: (1) setting up the initial conditions at left and right boundary columns; (2) running to steady state controlled by gravity and capillary forces and subjected to the boundary conditions at lateral and top grid sides specified for each case; and (3) modeling of spill for 2 years, starting from the steady-state conditions obtained in Step 2. The LNAPL spill has been modeled assuming a constant rate of 1.154×10^{-5} kg/s, equivalent to 1 kg/day. In this study, the effectiveness of the barrier is analyzed, looking at the effects of aquifer permeability and hydraulic gradient.

RESULTS

Modeling of steady state

The initial conditions for modeling the spill scenarios were obtained running the system to steady state, governed by gravity and capillary forces under the boundary conditions specified for each case. The steady-state pressure distribution is shown in Figure 3. In case of $i = 0$, the LNAPL plume spreads symmetrically over the water table, while in the case of aquifer flow, the LNAPL plume moves preferentially following the water table slope.

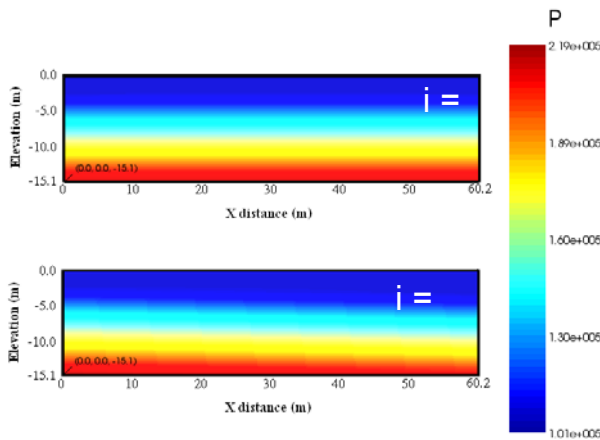


Figure 3. Pressure distribution at steady state conditions.

Migration of LNAPL into subsurface

The spill of benzene was modeled at a constant rate of 1 kg/day into the vadose zone for 2 years. The simulations were performed under isothermal conditions. In this study, the standard benzene properties (STD) supplied by Petrasim have been used. The diffusion coefficients of mass components in the different phases are summarized in Table 5.

Table 5. Molecular diffusion coefficients of mass components.

	GAS	AQUEOUS	NAPL
Air	2.0×10^{-5}	6.0×10^{-10}	6.0×10^{-10}
Water	2.0×10^{-5}	6.0×10^{-10}	6.0×10^{-10}
Benzene	7.7×10^{-6}	6.0×10^{-10}	6.0×10^{-10}

The simulation results relative to the total mass fraction of benzene in the aqueous liquid (XVOCW) can be described as follows:

- (1) Case $i = 0$: the benzene moves downward according to gravity; then the LNAPL plume floats on the water table and spreads out laterally. The depth reached by the dissolved benzene plume below the water table is about 1.5 m, and the distance of the benzene migration decreases with the soil permeability. In the presence of the containment wall, the dissolved benzene is contained by the barrier and cannot migrate beyond the containment.
- (2) Case of $i = 0.017$: once it reaches the water table, the LNAPL plume migrates preferentially in the direction of water table gradient. The shape of the dissolved benzene plume changes, depending on the soil permeability. The result of the model scenario without containment shows that if the permeability of soil decreases, the LNAPL plume could migrate to longer distances. Higher soil permeability allows a greater evaporation of benzene. The results of the

model scenario with wall containment show that the benzene migration is reduced by the containment. The dissolved benzene plume moves downward along the barrier, and some benzene can flow under the wall base when the soil has lower permeability, as shown in Figure 4 and 5.

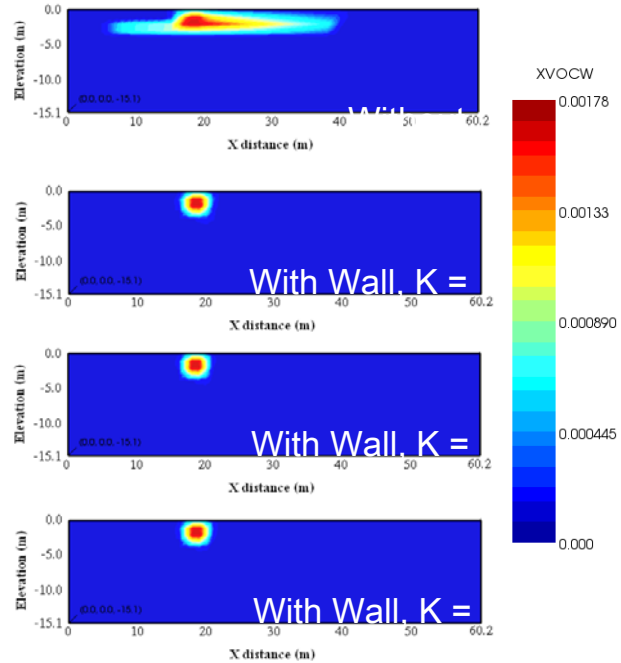


Figure 4. Total mass fraction of VOCs in aqueous phase in sandy soil with $K = 1 \times 10^{-9} \text{ m}^2$ and $i = 0.017$.

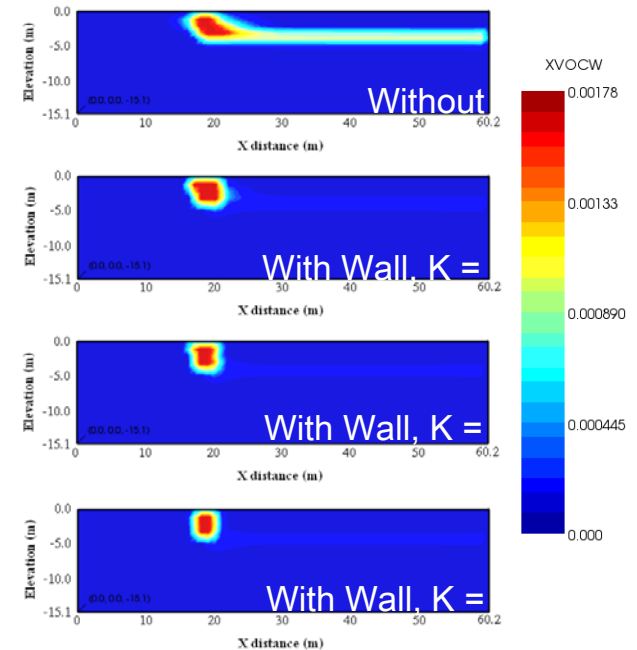


Figure 5. Total mass fraction of VOCs in aqueous phase in sandy soil with $K = 1 \times 10^{-11} \text{ m}^2$ and $i = 0.017$.

The total mass fraction of VOCs dissolved in the aqueous phase outside the containment zone, at depth of 1–6 m below the ground surface in the case of $i = 0$ with containment, is reduced close to zero, as shown in Figures 6–8. For the case of $i = 0.017$, the concentration of the benzene increases at the end of the barrier in concert with the permeability decrease, due to the effect of groundwater flow, as shown in Figures 9–11.

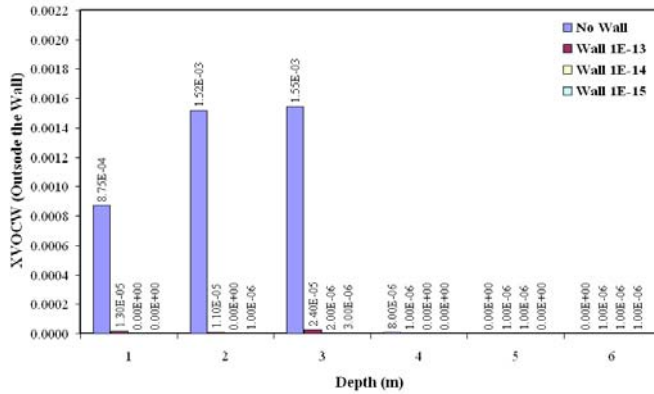


Figure 6. Comparison of total mass fraction of VOCs in aqueous phase outside the wall for sandy soil layer with $K = 1 \times 10^{-9} \text{ m}^2$ and $i = 0$.

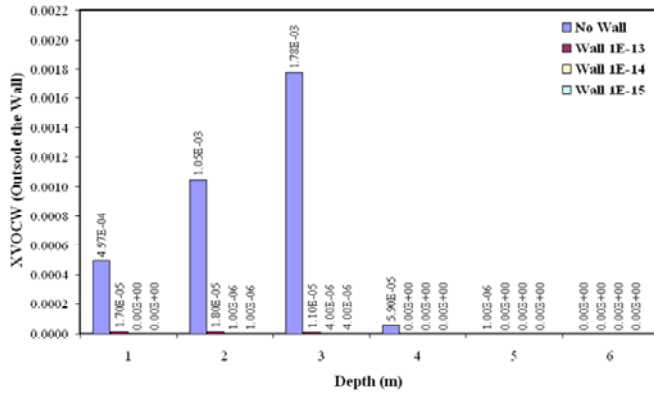


Figure 7. Comparison of total mass fraction of VOCs in aqueous phase outside the wall for sandy soil layer with $K = 1 \times 10^{-10} \text{ m}^2$ and $i = 0$.

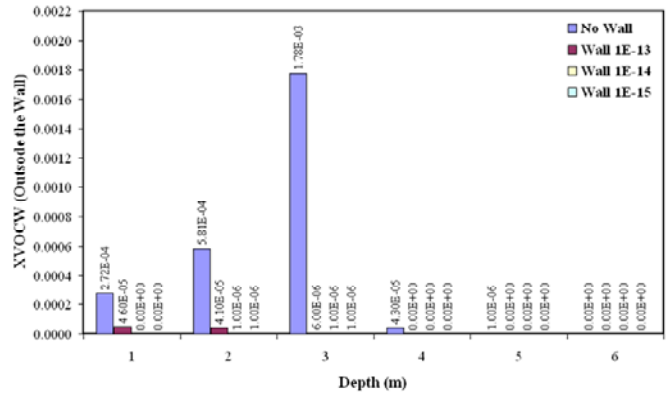


Figure 8. Comparison of total mass fraction of VOCs in aqueous phase outside the wall for sandy soil layer with $K = 1 \times 10^{-11} \text{ m}^2$ and $i = 0$.

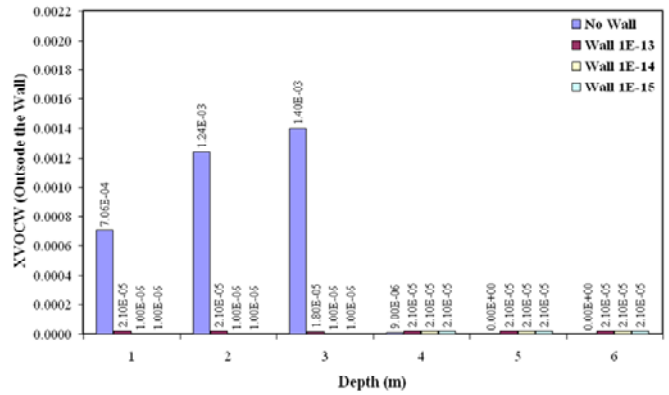


Figure 9. Comparison of total mass fraction of VOCs in aqueous phase outside the wall for sandy soil layer with $K = 1 \times 10^{-9} \text{ m}^2$ and $i = 0.017$.

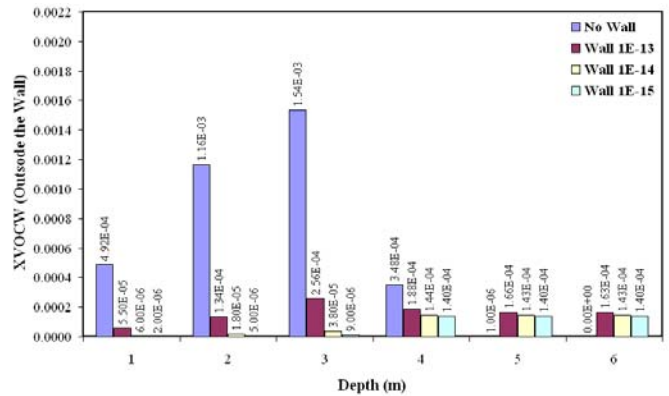


Figure 10. Comparison of total mass fraction of VOCs in aqueous phase outside the wall for sandy soil layer with $K = 1 \times 10^{-10} \text{ m}^2$ and $i = 0.017$.

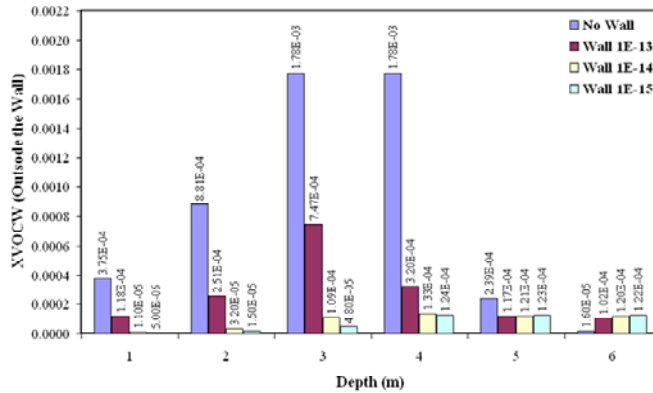


Figure 11. Comparison of total mass fraction of VOCs in aqueous phase outside the wall for sandy soil layer with $K = 1 \times 10^{-11} \text{ m}^2$ and $i = 0.017$.

CONCLUSIONS

This paper presents simulation of benzene migration in the subsurface as a consequence of a constant-rate spill in the unsaturated zone. Several scenarios have been modeled with a phreatic aquifer in a sandy soil of varying permeability, with different hydraulic gradients, and with or without the presence of a vertical containment wall. Simulations results reveal that the soil-cement barrier can reduce the contamination of the benzene and show that soil permeability and water table hydraulic gradient are the significant factors.

The benzene migration in the case of $i = 0$, occurs only by a gravity-driven NAPL plume flow and diffusion of dissolved benzene in the groundwater. In the presence of aquifer flow, dissolved benzene may be transported over long distances by advective flow. Without the groundwater flow, the contaminant migration is contained by the soil-cement barrier in the vadose zone; the dissolved benzene plume reaches less than 2 m below the water table. Consequently, the depth of the soil-cement wall should be more than 2 m below the groundwater level. With groundwater flow, the concentration of contamination depends on the hydraulic gradient, which enhances the transport processes. The hydraulic gradient has an impact on the depth of contaminant migration outside the wall. From the scenarios simulated, it can be concluded that soil-cement barriers can be used to limit the spread of benzene spilled in the unsaturated zone. Modeling studies such as those described may help in the design of containment operations and in risk assessment studies.

Note that presented herein is a preliminary study dealing with the processes controlling the migration of VOCs spilled in the vadose zone in the presence of vertical containment walls in sandy aquifers. The properties of the soil-cement used in these simulations are derived from bibliographic sources. Experimentally derived properties will be considered in future simulation works.

ACKNOWLEDGMENT

The authors would like to thank the Commission on Higher Education of Thailand for support given through a grant fund under the Strategic Scholarships for Frontier Research Network for the Joint Ph.D. Program, Thai Doctoral degree. Thanks are due to Alfredo Battistelli for information about the TMVOC simulator and for valuable suggestions.

REFERENCES

- Battistelli, A., 2008. Modeling Multiphase Organic Spills in Coastal Sites with TMVOC V2.0. *Vadose Zone Journal*, Vol.7, No.1., 316-324, 2008
- Falta, R. W., K. Pruess, S. Finsterle, and A. Battistelli, *T2VOC User's Guide*. Report LBL-36400, Lawrence Berkley National Laboratory. Berkeley, Calif. 1995.
- Pruess K., and A. Battistelli, *TMVOC, A Numerical Simulator for Three-Phase Non-Isothermal Flows of Multicomponent Hydrocarbon Mixtures in Saturated-Unsaturated Heterogeneous Media*. Report LBNL-49375, Lawrence Berkley National Laboratory. Berkeley, Calif., 2002.
- Thunderhead Engineering, *PetraSim User Manual*, Manhattan, 2008.

ESTIMATION OF LANDFILL GAS GENERATION RATES AND GAS PERMEABILITY FIELD OF REFUSE USING INVERSE MODELING

Yoojin Jung¹, Paul Imhoff¹, and Stefan Finsterle²

¹Department of Civil and Environmental Engineering, University of Delaware
Newark, DE 19716, USA

²Earth Sciences Division, Lawrence Berkeley National Laboratory
Berkeley, CA 94720, USA

e-mail: yjjung@udel.edu

ABSTRACT

Landfill methane must be captured to reduce emissions of greenhouse gases and to use as an alternative energy source. However, despite the widespread use of landfill gas collection systems for over two decades, little information about their capture efficiency is available, because landfill gas (LFG) generation rates usually remain unknown. Therefore, to assess the efficiency of greenhouse gas capture and the amount of fugitive emissions, LFG production rates should be properly determined. In addition, to improve the capture efficiency of methane while minimizing air intrusion from the atmosphere, it is important to quantify gas flow patterns within landfills. In this study, a methodology to quantify methane generation rates and estimate the gas permeability field was examined using inverse modeling. To take account of the heterogeneous, but spatially correlated structure of refuse, a geostatistical approach combined with the pilot point method was used. Synthetic observation data were generated from forward simulations for a pumping test and a baro-pneumatic test, and these data were used to test the inversion procedure. The inverse model was able to reproduce the spatial permeability distribution using the transient pressure changes in response to the withdrawal of LFG during the pumping test. The LFG production rate was also successfully estimated using the data from the baro-pneumatic test with 97% accuracy. Note that while this methodology was developed using synthetic data, it will be tested in the future using field data from the bioreactor test cells at the Yolo County Central Landfill, CA.

INTRODUCTION

Landfill gas collection systems have been widely used to minimize the environmental impacts of landfill gas (LFG). Methane, which accounts for 50–60% of LFG, is a potent greenhouse gas: its global warming potential is 23 times greater than that of carbon dioxide (IPCC, 2001). To reduce methane emissions, the LFG collected is sometimes simply flared to destroy its methane. The emissions of other

air pollutants in LFG, such as nonmethane organic compounds, should also be controlled and reduced. When operating landfills as bioreactors, capturing LFG is even more important, due to the rapid degradation of organic waste.

Collected landfill methane is increasingly used for electricity generation. Using the landfill methane as an alternative energy source works to offset the use of nonrenewable fossil fuels, in addition to providing an economic benefit to landfill owners. Concerns about the energy crisis reinforce the importance of intelligent LFG collection systems to improve methane capture efficiency.

However, despite the widespread use of landfill gas collection systems for over two decades, little information on their capture efficiency is available, because LFG (or methane) generation rates usually remain unknown. Methods currently used suffer significant limitations: the most common methods are technically flawed (Pierce et al., 2004; Walter, 2003) and result in estimates that are in error by as much as an order of magnitude (Scharff and Jacobs, 2006). Furthermore, they provide little information for quantitative understanding of LFG flow that could aid in the design of LFG collection systems specific to each landfill. Therefore, to assess the efficiency of greenhouse gas capture and the amount of fugitive emissions, LFG (or methane) production rates should be properly determined. In addition, to improve the capture efficiency of methane while minimizing air intrusion from the atmosphere, it is important to quantify gas flow patterns within landfills.

The baro-pneumatic method is a newly proposed technique for quantifying LFG generation rates and estimating the gas permeability field within landfills (Bentley et al., 2003). In contrast to other methods currently in use, the baro-pneumatic method employs the complete equations for LFG generation and flow, and thus avoids the technical flaws common in simplified approaches. While a limited number of field applications have shown that the method

produces estimates of LFG generation rates independently (Bentley et al., 2005), the method has not been rigorously evaluated, particularly for heterogeneous waste.

The permeability of refuse commonly varies several orders of magnitude within any given landfill, and this heterogeneity can cause unexpected and undesirable operational conditions (Reinhart, 1996; Reinhart et al., 2002): the spatial variation of gas permeabilities likely affects the efficiency of LFG collection and the control of methane emissions. In this study, a methodology to quantify LFG generation rates and to estimate the gas permeability field was examined using inverse modeling. Geostatistical simulation was used to capture the heterogeneous, spatially correlated structure of refuse, and the pilot point method (RamaRao et al., 1995) was used to condition this random structure on site-specific conditions as part of the inversion. Synthetic observation data were generated from forward simulations for a pumping test and a baro-pneumatic test, and these data were used to test the inverse modeling approach.

BARO-PNEUMATIC METHOD

In a porous medium with no *in situ* gas generation, gas pressures in the subsurface change in response to the variation of barometric pressure at the surface. As the surface pressure signal propagates into the subsurface, the responses are delayed and attenuated as a function of depth and pneumatic diffusivity, which is defined as

$$D_g = \frac{kP_g}{n_g \mu}$$

where D_g is pneumatic diffusivity, k is the gas permeability, P_g is the mean pressure, n_g is the gas-filled porosity, and μ is the dynamic viscosity of the gas. For this situation, time-varying pneumatic pressure data collected *in situ* can be used to estimate the pneumatic diffusivity. In the past, pneumatic pressure data have been used to determine the vertical permeability of unsaturated soils (Shan, 1995; Weeks, 1978).

The same concept was first applied to landfills by Hydro Geo Chem, Inc. to estimate the gas permeability of refuse and the LFG generation rate (Bentley et al., 2005). With this approach, gas pressures within a landfill and at the landfill surface are monitored simultaneously. The LFG generation rate is estimated by attributing the difference between the mean absolute gas pressure in the landfill and the barometric pressure to LFG generation, while the lag

in gas pressures measured *in situ* with those measured at the landfill surface is used to infer the ratio of vertical gas permeability and porosity (the pneumatic diffusivity). To support the baro-pneumatic data, which are not sensitive to the horizontal gas permeability, pneumatic pumping tests are also conducted so that the gas porosity and the horizontal gas permeability of the refuse are independently measured. The baro-pneumatic method thus includes the simultaneous measurement of gas pressures at the landfill surface and with depth during nonpumping or constant pumping periods—the baro-pneumatic test—and a few pneumatic pump tests.

One advantage of using the baro-pneumatic method for estimating LFG generation rates is that the method is site-specific. A gas flow model is calibrated to each landfill by varying gas permeabilities and LFG generation rates to provide a best match to the available field data. This LFG generation and flow model can be used to improve the design of LFG collection systems and LFG capture efficiency. While the baro-pneumatic method shows much promise, the efficacy of the approach in heterogeneous waste has not been carefully evaluated.

MODELING APPROACH

To evaluate the efficacy of the baro-pneumatic method in heterogeneous waste, a two-dimensional vertical model was developed with a gas extraction well at the center of the landfill cell. Figure 1 shows a schematic of the model domain. The shape and size of the model was patterned after a bioreactor landfill cell at Yolo County Central Landfill, Woodland, California, which will be used in the future to collect field data and test the methodology. The model domain was discretized into gridblocks of size $\Delta X \times \Delta Y \times \Delta Z = 1.0 \times 1.0 \times 0.48$ m. Because waste dumped in landfills is packed over time and compressed by overlying material, the domain for the refuse was divided into five layers, and the mean permeability of each layer was specified assuming that the permeability of the waste decreased exponentially with depth. The ratio of the horizontal to vertical permeability of refuse was assumed to be 10. The horizontal gas permeabilities, the porosity, and the LFG generation rate used for forward simulations are given in Table 1. The LFG was assumed to be 55% methane and 45% carbon dioxide. Details of the other assumed parameters in the model are given elsewhere (Jung et al., 2009).

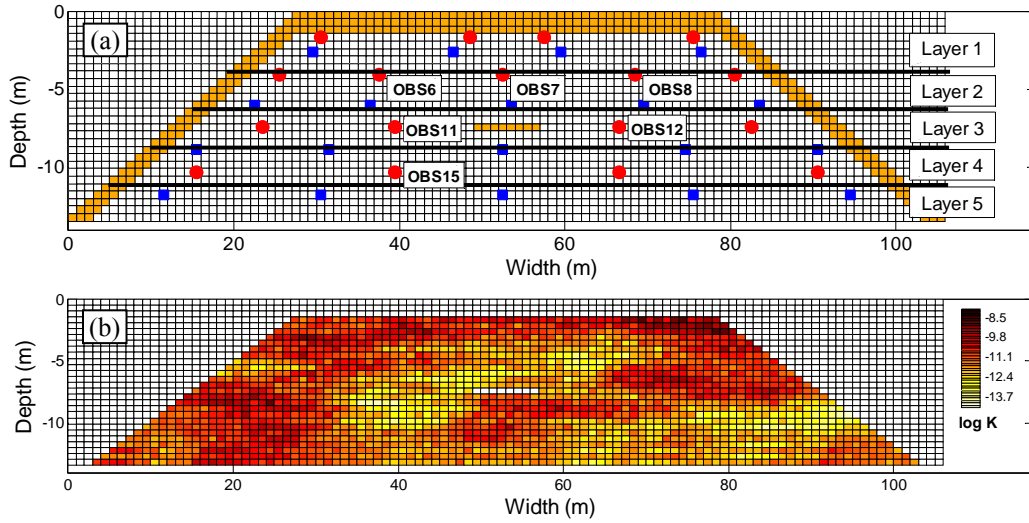


Figure 1. Schematic of the model domain. (a) Geometry of observation (red circles) and pilot points (blue squares) and (b) the true permeability distribution used.

To create a heterogeneous gas permeability field, the sequential Gaussian simulation technique was used (Deutsch and Journel, 1992). Since no study has been conducted to statistically describe the heterogeneous structure of landfilled waste, the spatial correlation of the log-permeability field was assumed to follow a spherical semivariogram, with a nugget effect of 0.1, a correlation length of 4.0 m, and a sill value of 1.0. One realization of the resulting log-permeability field was presumed the actual permeability field and is shown in Figure 1b.

Barometric pressure data collected for four days at the bioreactor landfill cell at the Yolo County Central Landfill were used for a time-varying surface boundary condition, and a no-flux boundary was assumed for the bottom border of the simulation domain to capture the effect of the landfill liner. Unless the gas extraction well is newly installed for the pumping test, the gas collection well should be in continuous operation to mitigate methane emissions. Stopping the operation for several days to conduct the baro-pneumatic test may not be recommended, which is the case at the Yolo County Central Landfill. Therefore, in the simulations, the flow rate at the gas collection well was typically set equal to 80% of the total LFG generation rate: gas collection rates in landfills with intermediate covers are believed to be less than LFG generation rates to avoid significant intrusion of air from the landfill surface into the refuse. Since the gas pumping rate was constant during these periods, gas pressures within the refuse fluctuated in response to barometric pressure change alone. For the pneumatic pump test, the gas extraction rate at the well was quintupled to generate short-term transient pump data. The

atmospheric pressure changes for the first day and the pumping schedule of the gas collection well are shown in Figure 2. Transient pressure responses resulting from the barometric pressure changes were collected every 30 min. During the pumping test, data were collected at 10 min intervals to capture pressure changes. Monitoring points for collecting gas-pressure data are shown in Figure 1a and illustrate gas sampling probes installed in the bioreactor landfill cell at Yolo County Central Landfill.

Table 1. Summary of conditions used in forward simulation.

		Horizontal gas permeability (m ²)	Effective gas porosity	LFG generation rate (m ³ /yr/m ³) ^a
Refuse	Layer 1	1.95e-11	0.16	15.8
	Layer 2	1.39e-11	0.15	16.8
	Layer 3	1.05e-11	0.135	17.8
	Layer 4	8.1e-12	0.12	18.6
	Layer 5	6.4e-12	0.11	19.4
Soil cover		1.0e-12	0.35	
Pumping well		3.0e-8	0.50	

^a Calculated for a unit volume (1 m³) of refuse.

For inverse modeling, the gas permeability field and the LFG generation rate were estimated sequentially using independent data sets: the pumping test data for the permeability field and the baro-pneumatic test data for the LFG generation rate. At the first stage of inversion using the pump test data, a log-permeability modifier was selected as the targeted parameter field. Since the permeability of refuse could vary over a

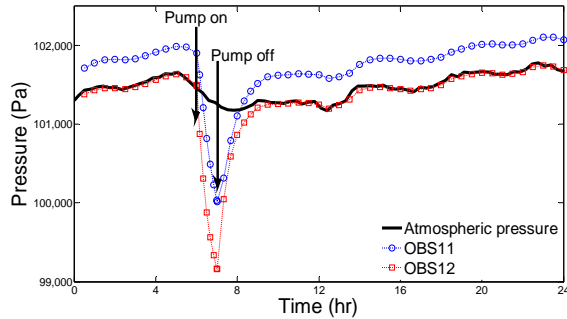


Figure 2. Variation of atmospheric pressures and the corresponding pressure responses at observation points OBS11 and OBS12 for the first day of the test. The pumping schedule is also shown, where “Pump on” is when the gas extraction rate was increased by a factor of five and “Pump off” is when the gas extraction rate returned to 80% of the LFG generation rate of the landfill.

wide range, estimating the logarithm of the permeability rather than the permeability itself made the inverse problem more linear. The use of the pilot point method reduced the number of parameters; only the horizontal and vertical permeabilities at the pilot points were estimated instead of the log-permeability modifier of each gridblock. The pilot points were distributed over the model domain (see Figure 1a), and the heterogeneous permeability field was automatically modified during the inversion to improve the match to the measured pressure data in response to the change in pumping rate. Since no point measurements of the log permeability were available, all pilot points were initially assumed to have the same log permeability as the mean value specified in Table 1. To simplify the test conditions, the porosity and the geostatistical parameters were assumed to be known from other measurements.

Here, it should be noted that the semivariogram parameters were considered as a tool to quantitatively represent the heterogeneous structure of waste with a small number of parameters. Once estimated, the permeability field was considered to be known, and the gas generation rates were estimated by calibrating the model simulations against the baro-pneumatic test data. The assumed parameters for the permeability field and the LFG generation rate are listed in Table 2. These parameters were fixed during the inversion.

To model transport of multiple gas constituents (methane, carbon dioxide, oxygen, and nitrogen), TMVOC (Pruess and Battistelli, 2002) was used for forward simulations. The utility of using the gas

composition data in addition to gas pressure data for inverse modeling will be evaluated in the future. For this study, TMVOC was coupled with iTOUGH2 (Finsterle, 1999) for inverse simulations. The pilot point method used as an inversion scheme is implemented in iTOUGH2 (Finsterle and Kowalsky, 2007).

MODELING RESULTS

Influence of Heterogeneous Gas Permeabilities

Even though the heterogeneous characteristic of refuse is well acknowledged, this feature is typically neglected when designing LFG collection systems. In previous applications of the baro-pneumatic method, the horizontal permeability of the system was assumed uniform and inferred from the pneumatic drawdown data at the gas extraction well. While this approach is acceptable for an approximate estimate of the average gas permeability within the influence of the pumping well, it may not be sufficient to determine the spatial variability of permeability of refuse and its impact on LFG collection systems.

To evaluate the benefit of characterizing the heterogeneous permeability field, inverse modeling of the pneumatic pump test data was first conducted assuming the gas permeability to be homogeneous throughout the landfill. Figure 3a illustrates the results from this effort, where an excellent match was achieved between the observation data and the simulation results at the pumping well. However, the pressure response at other observation points could not be simulated with the best-fit permeability (see Figure 3b–d). This means that the actual pattern of gas flows would likely be different from that predicted using a gas flow model that assumed permeability homogeneity, which might result in suboptimal LFG collection if this gas flow model was used for design of the LFG collection system. Therefore, it is important to characterize the heterogeneity of gas permeabilities to improve LFG capture efficiency.

Table 2. Assigned parameters for inverse simulation

Parameter	Value
Porosity	0.15
Nugget Effect	0.01
Sill Value	0.9
Correlation Length (m)	15.0
Anisotropy Ratio	10.0
LFG generation rate ($\text{m}^3/\text{yr}/\text{m}^3$) ^a	80% of the true LFG generation rate

^a The LFG generation rate was fixed only when the permeability field was estimated.

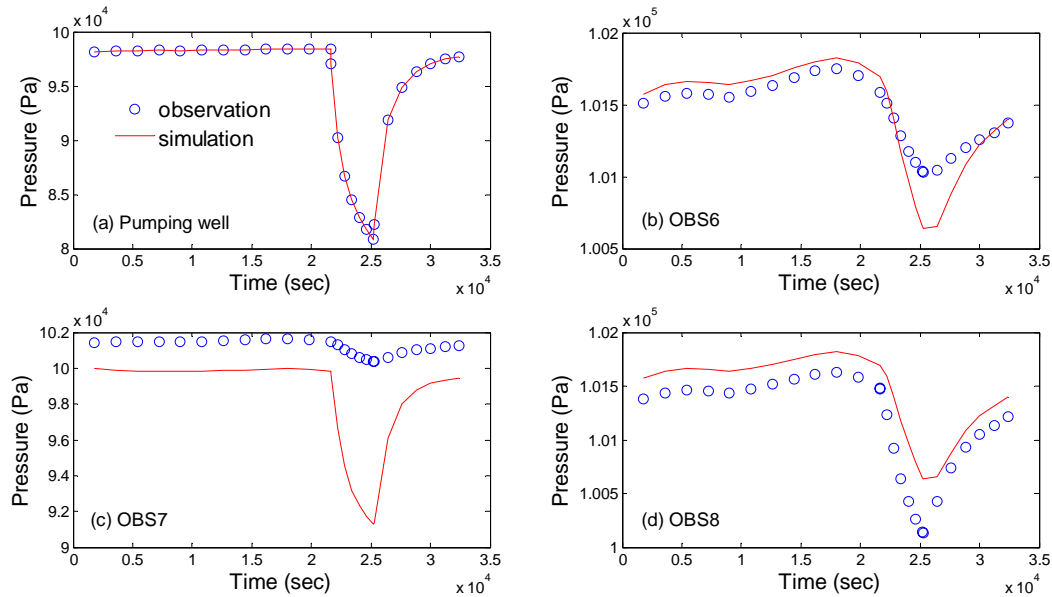


Figure 3. Pressure response at the extraction well (a) and at other observation points ((b) OBS6, (c) OBS7, and (d) OBS8)

Impact of Systematic Errors on Estimation of the Permeability Field

When estimating the permeability field using the pumping test data, the gas generation rate was fixed and not subjected to the inversion procedure. However, if a gas generation rate with error is assigned, the static pressure at a given location will not be accurately reproduced by the model. This systematic error leads to biased estimates of the permeability field, because the inversion scheme attempts to minimize the differences in the mean pressure rather than match the time lag and attenuation of the pressure fluctuation.

To resolve this issue and improve the fit, the pressure offset between the measured and simulated data at each observation point during the pumping test was parameterized. The simulated pressure data were shifted by an unknown constant value to match the measured mean pressure data. Using a constant shift of the pressure seemed appropriate, since the LFG generation rates would not vary during the short-term pumping test period.

The results obtained from inverse modeling with and without parameterizing the pressure offset were compared. While most of the data looked reasonably well matched in both cases, the benefit of using a pressure offset was observed. When a pressure offset was not included in the inverse modeling, the pressure data before and after the pumping test were underpredicted, and the pressure data during the pumping test were overpredicted. To better illustrate

this systematic error, the residuals are plotted as a function of time in Figure 4. By including the pressure offset parameter, the overall residuals were reduced and the mismatch in pressures at the beginning and end of the pumping test was reduced. The impact of including the pressure offset parameter in inverse modeling became more significant as the error in the assumed LFG generation increased. For instance, when the LFG generation rate was 50% of the actual generation rate, the systematic errors from inverse modeling without the pressure offset resulted in the poor match shown in Figure 5. The fit was clearly improved with the consideration of the pressure offset, also shown in Figure 5.

However, adding the pressure offset parameter could lead to overparameterization in some cases, causing higher parameter correlation and estimation uncertainty. Therefore, care should be exercised when deciding whether to include this additional model parameter.

Parameter Estimation

Permeability field estimation using pumping test data

A good match between observation data and simulation results is not sufficient to guarantee that the parameters estimated are physically reasonable. In this section, the average of the estimated permeability fields was compared with the actual permeability field. In addition, parameters considered as unknowns were expanded to test whether the

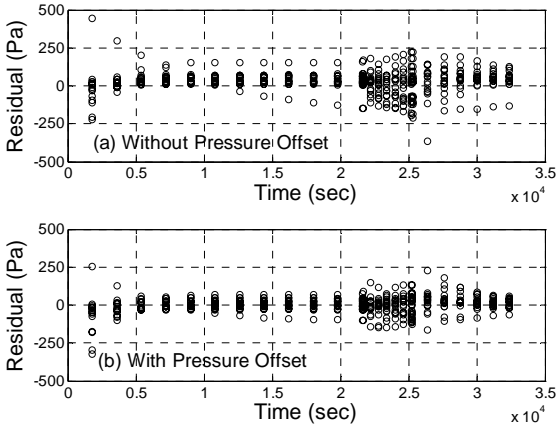


Figure 4. Residuals as a function of time, (a) without and (b) with considering the pressure offset parameter

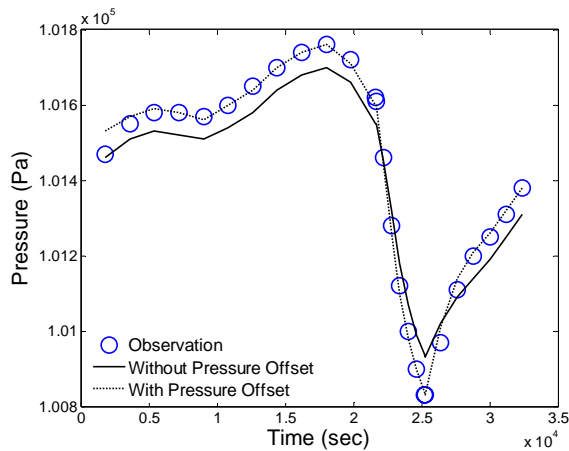


Figure 5. Comparison between the measured and the calculated pressures at the observation point OBS7 for inverse modeling with and without the pressure offset

additional parameters could be estimated jointly with the permeability distribution. For comparison, at first only the permeability field was estimated using the pneumatic pump test data (Case 1), which was the case described in the modeling method section, and then the porosity (Case 2) and the semivariogram parameters (Case 3) were added serially to the parameter set to be estimated. Inversions on five different realizations were performed for each case.

Figure 6 shows the average permeability field of Case 1 in a logarithmic scale. The estimated permeability field was not exactly the same as the actual permeability field shown in Figure 1b. The local heterogeneity was smoothed out, which was expected since a higher correlation length and a smaller nugget effect than the true model were assumed (see Table 2). In reality, information about

the variogram parameters is highly uncertain. In addition, the permeability was significantly different from the true value in the region where no observation data were available and no pilot points were placed. However, the major spatial structure of the permeability field was captured well: the relatively low permeability zone on the west side of the pumping well and the relative high permeability zone on the east side of the well were matched. Thus, the major heterogeneities in the gas permeability field that influence gas flow patterns were captured by the inverse modeling.

When porosity was added as one of the unknown parameters, the estimated permeability field was almost identical to that determined for Case 1 (results not shown). The porosity assumed in Case 1 was 0.15, which is relatively close to the true value (11% higher than the average of the true porosities, see Table 1). As a result, the advantage of estimating the porosity together with the gas permeability field was insignificant, and no improvement in model-fitted gas permeabilities was observed. The porosity estimated for Case 2 was 0.09, which is 33% smaller than the average of the porosities used for forward simulations. This poor estimation might be explained by the correlation between parameters. While the use of the pilot point method enabled the model to explain the heterogeneous gas permeability field well, it increased the correlation between the parameters and made estimation uncertainty higher. Performing a pumping test at different pressure levels might help to resolve the strong correlation between the parameters.

The geostatistical parameters and porosity were included with the gas permeabilities in the unknown parameter set for Case 3. The estimated permeability field was again very similar to the permeability field of Case 1 (results not shown). However, the estimated variogram parameters greatly varied for each inversion. For instance, the standard deviation of the sill value was 0.91 when the average of five equally probable realizations was 1.14. This result might be due to low sensitivity of the geostatistical parameters or high correlation with the other parameters. The sensitivity coefficient of the variogram parameters was almost two orders of magnitude smaller than the sensitivity of the flow parameters. This means that the geostatistical parameters may not be estimated accurately with the permeability field from inversion of a single pneumatic pump test, and other types of data may be required to improve the determination of these parameters—perhaps additional pump tests conducted in different regions of the landfill.

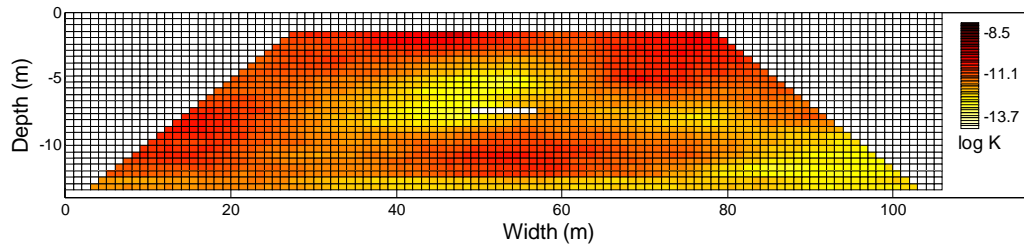


Figure 6. Estimated permeability field when the log permeability was the only unknown parameter

LFG generation rate estimation using baro-pneumatic test data

In this section, the LFG generation rate was estimated using the baro-pneumatic test data—those data in Figure 2 that lie outside the pumping test period. Here, the permeability field estimated using the pumping test data was considered known, and the LFG generation rate was treated as the only unknown parameter. This sequential estimation procedure was selected since concurrent estimation of the gas permeability field and the LFG generation rate might result in non-unique solutions. The overall fit between the observation and the simulation data was excellent, as shown in Figure 7. Note that the average pressure at the shallow observation point (OBS6) is higher than those at the deeper observation points (OBS11 and OBS15), due to the constant pumping at the extraction well, but the fluctuation of the pressures exactly follows the variation of the barometric pressure. The estimated LFG generation rate was 97% of the true value, demonstrating the capability of the estimated permeability field to capture the gas flow pattern and the subsequent pressure distribution.

CONCLUSIONS

Landfill gas collection systems have been used to reduce methane emissions and generate electric power from the methane collected. However, the efficiency of LFG collection systems is largely unknown, because these systems have been designed and operated without careful assessment of LFG generation rates. In addition, a poor understanding of gas flow patterns in refuse hinders optimal LFG collection practices.

The baro-pneumatic method is a promising technique for estimating LFG generation rates. It involves pneumatic pump tests and baro-pneumatic tests. The method can be used to create a gas flow model for individual landfills, which may be used to design or improve existing LFG collection systems. While the method holds much promise, there is considerable uncertainty about its utility in heterogeneous refuse, where the gas permeability field varies significantly

in space. Using the simple example in this study, if the gas permeability field is assumed homogeneous, the gas permeability field estimated from the baro-pneumatic method was not sufficient to reproduce the gas pressure field. Thus, the simplifying assumption of homogeneous conditions in the near-well regions for the baro-pneumatic method may not be sufficient to characterize gas flow patterns in heterogeneous landfills.

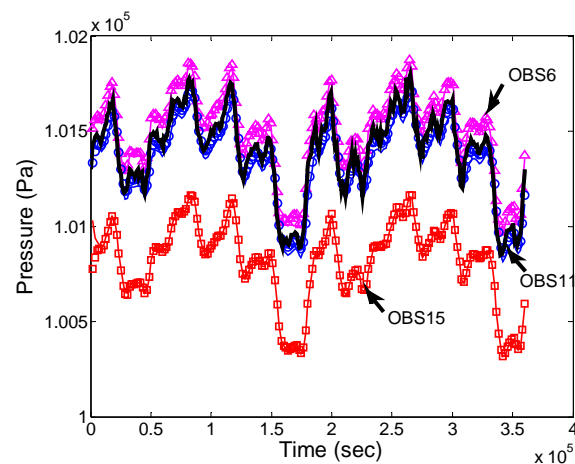


Figure 7. Match of pneumatic pressures at different locations. Barometric pressure data are shown as a black bold line. Observation data are shown as triangles (OBS6), circles (OBS11), and squares (OBS15). Simulation results based on the estimated parameter are shown as solid lines.

To apply the method to heterogeneous refuse, an inversion approach using the pilot point method was evaluated. Observation data were generated for synthetic experiments, which consisted of a pumping test and a baro-pneumatic test, and used for parameter estimation. The gas permeability field was first estimated using the pumping test data, and then the gas generation rate was estimated using the baro-pneumatic test data.

The heterogeneous structure of the gas permeabilities was captured well using the pilot point method and

pneumatic pump test data. The systematic error resulting from the use of an erroneous LFG generation rate in fitting the pneumatic pump test data was resolved by parameterizing the pressure offsets, and an excellent match between the observed and the simulated data was achieved. The LFG generation rate was also successfully calculated when the gas permeability field was first determined from the pneumatic pump test.

Despite the promising results from this work, the use of the pilot point method resulted in model overparameterization, particularly when the porosity and variogram parameters describing the gas permeability field were fitted along with log permeabilities. Further study is required to reduce the uncertainty in estimating these parameters, perhaps by using additional data collected from pneumatic pump tests at different locations, or different types of data that are affected by the gas flow field, e.g., gas composition data.

ACKNOWLEDGMENT

The authors thank Dr. Herold Bentley and Mr. Stewart Smith for helpful discussions on estimating gas permeability and LFG generation rates using the baro-pneumatic method. Financial support for this study was provided by the US Department of Energy under Cooperative Agreement DE-FC26-05NT42432 and the California Energy Commission.

REFERENCES

- Bentley, H. W., S. J. Smith and T. Schrauf, Baro-pneumatic estimation of landfill gas generation rates at four operating landfills, *Proceedings, SWANA's 28th Annual Landfill Gas Symposium*, San Diego, CA, March 7-10, 2005.
- Bentley, H. W., S. J. Smith, J. Tang and G. R. Walter, A method for estimating the rate of landfill gas generation by measurement and analysis of barometric pressure waves, *Proceedings of the 18th International Conference on Solid Waste Technology and Management*, Philadelphia, PA, March 23-26, 2003.
- Deutsch, C. V. and A. G. Journel, *GSLIB Geostatistical software library and user's guide*, Oxford University Press, New York, 1992.
- Finsterle, S., *iTOUGH2 User's Guide*, Report LBNL-40040, Lawrence Berkeley National Laboratory, Berkeley, CA, 1999.
- Finsterle, S. and M. B. Kowalsky, *iTOUGH2-GSLIB User's Guide*, Report LBNL/PUB-3191, Lawrence Berkeley National Laboratory, Berkeley, CA, 2007.
- IPCC, *Intergovernmental Panel on Climate Change, Climate Change 2001: The Scientific Basis*, Cambridge University Press, United Kingdom, 2001.
- Jung, Y., P. T. Imhoff, D. C. Augenstein and R. Yazdani, Influence of high-permeability layers for enhancing landfill gas capture and reducing fugitive methane emissions from landfills, *J. Environ. Eng.*, 135 (3), 138-146, 2009.
- Pierce, J., L. LaFountain and R. Huitric, *LFG generation and modeling manual of practice*, Solid Waste Association of North America (SWANA), 2004.
- Pruess, K. and A. Battistelli, *TMVOC, A numerical simulator for three-phase non-isothermal flows of multicomponent hydrocarbon mixtures in saturated-unsaturated heterogeneous media*, Report LBNL-49375, Lawrence Berkeley National Laboratory, Berkeley, CA, 2002.
- RamaRao, B. S., M. Lavenue, G. de Marsily and M. G. Marietta, Pilot point methodology for automated calibration of an ensemble of conditionally simulated transmissivity fields 1. Theory and computational experiments, *Water Resour. Res.*, 31 (3), 475-493, 1995.
- Reinhart, D. R., Full scale experiences with leachate recirculating landfills: case studies, *Waste Manage. Res.*, 14 347-365, 1996.
- Reinhart, D. R., P. T. McCreanor and T. G. Townsend, The bioreactor landfill: its status and future, *Waste Manage. Res.*, 20 172-186, 2002.
- Scharff, H. and J. Jacobs, Applying guidance for methane emission estimation for landfills, *Waste Manage.*, 26 417-429, 2006.
- Shan, C., Analytical solutions for determining vertical air permeability in unsaturated soils, *Water Resour. Res.*, 31 (9), 2193-2200, 1995.
- Walter, G. R., Fatal flaws in measuring landfill gas generation rates by empirical well testing, *J. Air & Waste Manage. Assoc.*, 53 (4), 461-468, 2003.
- Weeks, E. P., *Field determination of vertical permeability to air in the unsaturated zone*, U.S. Geological Survey Professional Paper 1051, US Geological Survey, Denver, CO, 1978.

COMPARISON OF SINGLE AND TWO-PHASE FLOW MODELING IN THE ASSESSMENT OF CONTAMINATION

Kuo-Chin Hsu and Kuan-Chih Chen

Department of Resources Engineering, National Cheng-Kung University
Tainan, Taiwan 70101, R. O. C.

e-mail: kchsu@mail.ncku.edu.tw

ABSTRACT

A physically motivated model is indispensable for a successful analysis of the impact of leaching from nuclear waste storage sites on the environment and public health. While most analyses use the single-phase flow model for modeling unsaturated flow and solute transport, the two-phase flow model considering the resistance of gas to water flow is a more realistic one. Here, in this study, we first theoretically investigate the effect of the two-phase flow model on water content. Then, by combining a geostatistical generator using the turning bands method and the multiphase transport code TOUGH2, an automatic process is used for Monte Carlo simulation of solute transport. This stochastic approach is applied to a site that potentially may be polluted by low-level nuclear waste in Taiwan. In the simulation, the saturated hydraulic conductivity is treated as a random variable. The stochastic approach provides a probabilistic assessment of contamination. Results show that even though water content from the two-phase flow model is only 1.5% less than that from the single-phase flow model, the two-phase flow causes a slower movement but a wider lateral spreading of the plume in the unsaturated zone. The stochastic approach provides useful probability information not available from the deterministic approach. The probability assessment of groundwater contamination provides the basis for more informed waste management, better environmental assessment, and improved evaluation of public health impact.

1. INTRODUCTION

Probabilistic assessment of contamination is important in nuclear waste management. It can be used for risk analysis and provides essential information for evaluating the impact of leaching from nuclear waste storage sites on the environment and public health. To predict the contaminant movement in the field, an appropriate model is indispensable.

Recent studies on hydrogeology have shown that the hydraulic properties of natural porous media often display high spatial variability (Gelhar, 1986). Theoretical analyses (Dagan, 1982, 1989;

Gelhar and Axness, 1983; Gelhar, 1992) and field experiments (Freyberg, 1986; Ellsworth *et al.*, 1991; Garabedian *et al.*, 1991) indicate that this spatial variability dominates the behavior of flow and solute transport in an aquifer. Other research has shown that among all hydraulic properties, hydraulic conductivity shows the most spatial variance and significantly affects flow and solute transport (van der Zee and Boesten, 1991; Franke and Teutsch, 1994).

The classical deterministic approach has difficulty in treating spatial variability, due to the inherent randomness of the medium and scarcity of available data (Nielsen *et al.*, 1973; Russo and Bresler, 1981). Conversely, the stochastic approach treats the soil properties as random variables and is able to take spatial variability and uncertainty into account in an analysis. In particular, the stochastic approach is useful for the probabilistic assessment of groundwater contamination problems and is therefore used in risk analysis.

Despite significant progress in the development of stochastic approaches, applications of stochastic theory to real-world problems are still limited (Zhang and Zhang, 2004). This situation is likely to change however, since further development of stochastic theory and application of stochastic approaches in hydrogeologic investigations and modeling could lead to a better understanding of natural subsurface hydrological systems (Neuman, 2004; Winter, 2004; Christakos, 2004; Molz, 2004). For example, Lo *et al.* (1999) performed a risk assessment of landfill systems using Monte Carlo simulations to predict the contamination issues underneath a landfill clay liner. Maxwell and Kastenber (1999) also performed a stochastic environmental risk analysis to predict cancer risk due to contaminated groundwater, by considering the effects of uncertainty and variability of numerous processes. Kovscek and Cakici (2005) applied a stochastic approach to geologic sequestration with enhanced oil recovery to evaluate the influence of geologic uncertainty.

In this study, a stochastic approach is proposed to investigate the effect of heterogeneous porous media on groundwater flow and solute transport in both

saturated and unsaturated zones. We first investigate the effect of the two-phase flow model on the unsaturated flow. Then, we perform a Monte Carlo simulation of solute transport for a potentially polluted site in Taiwan by combining the geostatistical method and the multiphase transport code TOUGH2 (Pruess, 1991). Because of the high spatial variability of the saturated hydraulic conductivity, we treat it as a random variable and assume other spatial variables as deterministic in the geostatistical model. The effect of two-phase flow on solute transport is investigated, and the stochastic result is also compared to the deterministic approach. Finally, the probabilistic assessment of contamination is addressed, based on our stochastic results.

2. THE EFFECT OF THE TWO-PHASE FLOW ON TRANSPORT

The two-phase flow model considers the movement of both gas and aqueous phases in the porous medium, whereas the single-phase flow model only takes account of water and treats the soil gas as providing no resistance to water flow (Kutilek and Nielsen, 1994). We explore the effect of the gas-phase on flow by considering the *van Genuchten-Mualem* model for relative hydraulic conductivity (van Genuchten, 1980).

$$K_{rl} = \begin{cases} \sqrt{S^*} \left\{ 1 - \left(1 - [S^*]^{1/\lambda} \right)^\lambda \right\}^2 & \text{if } \theta_l < \theta_{ls} \\ 1 & \text{if } \theta_l \geq \theta_{ls} \end{cases} \quad (1)$$

where K_{rl} is liquid relative permeability, S^* is the effective saturation, the definition of which depends on the flow model (it is $\frac{\theta_l - \theta_{lr}}{\theta_{ls} - \theta_{lr}}$ for the single-phase flow model and $\frac{\theta_l - \theta_{lr}}{\theta_{ls} - \theta_{lr} - \theta_{gr}}$ for the two-phase flow model); θ_l , θ_{lr} , θ_{ls} and θ_{gr} are water content, residual water content, saturated water content, and residual gas content, respectively, and λ is an empirical parameter of the retention model of van Genuchten (1980). In the single-phase flow model, the soil gas content is not considered, due to the great fluidity of soil gas, and the water content in soil is obtained as

$$\theta_{l1} = \theta_{lr} + S_1^* (\theta_{ls} - \theta_{lr}) \quad (2)$$

where θ_{l1} and S_1^* are water content and effective saturation in the single phase. In the two-phase flow

model, gas content is included in calculating the associated water content. The water content becomes

$$\theta_{l2} = \theta_{lr} + S_2^* (\theta_{ls} - \theta_{lr} - \theta_{gr}) \quad (3)$$

where θ_{l2} and S_2^* are for the two-phase situation.

When steady precipitation is smaller than the saturated hydraulic conductivity K_S of the soil, the flux density q will be equal to $K_S K_{rl} \frac{dH}{dz}$, according

to Darcy-Buckingham's equation, where K_S is the saturated hydraulic conductivity. Here, we denote $\left(\frac{dH}{dz}\right)_1$ and $\left(\frac{dH}{dz}\right)_2$ as the hydraulic gradients in the

single-phase and two-phase models, respectively. The water contents of the single-phase and two-phase models will depend on the relation between $\left(\frac{dH}{dz}\right)_1$

and $\left(\frac{dH}{dz}\right)_2$. Case 1 is for $\left(\frac{dH}{dz}\right)_1 = \left(\frac{dH}{dz}\right)_2$. In this

case, the infiltration rate will be equal to $K_S \times K_{rl}$ with associated S^* in the unsaturated zone. Since S_1^* has to be equal to S_2^* to satisfy the steady flow condition, it can be immediately seen from Equations (2) and (3) that the water content θ_{l2} for the two-phase flow model will be less than θ_{l1} for the single-

phase flow model. Case 2 is for $\left(\frac{dH}{dz}\right)_1 < \left(\frac{dH}{dz}\right)_2$.

In this case, the liquid relative permeability in the single-phase model will be greater than that in the two-phase model with associated S^* . According to Equations (2) and (3), the water content θ_{l2} will be

less than θ_{l1} . Case 3 is for $\left(\frac{dH}{dz}\right)_1 > \left(\frac{dH}{dz}\right)_2$. In this

case, the liquid relative permeability in the single-phase model will be less than the one in the two-phase model with associated S^* . According to the Equations (2) and (3), S_1^* has to be less than S_2^* , and θ_{l1} and θ_{l2} are functions of θ_{gr} , S_1^* and $\Delta S (= S_2^* - S_1^*)$. Figure 1 shows (a) a three-dimensional diagram and (b) a fence diagram to

illustrate the relation between θ_{l1} and θ_{l2} , which depends on θ_{gr} , S_1^* and ΔS for the clay material used in this study with $\theta_{ls} = 0.465$ and $\theta_{lr} = 0.292$.

When the combination of θ_{gr} , S_1^* and ΔS fall in

the region of light color, the water content θ_{l2} will be less than θ_{l1} . Otherwise, θ_{l2} will be larger than θ_{l1} . Figure 1 indicates that the region for the water content θ_{l2} produced by the two-phase model is less than θ_{l1} from the single-phase model. The simulations shown in the next section fall into this region. Other research has shown that a larger macrodispersivity is associated with an unsaturated soil having a smaller water content (Russo, 1993, 1998; Yang et al., 1996; Harter and Zhang, 1999). Laboratory results also show that at lower water content, the porous medium has higher dispersion (Padilla et al., 1999). Therefore, the size of the contaminant plume may be underestimated in the unsaturated zone if the single-phase flow model is adopted.

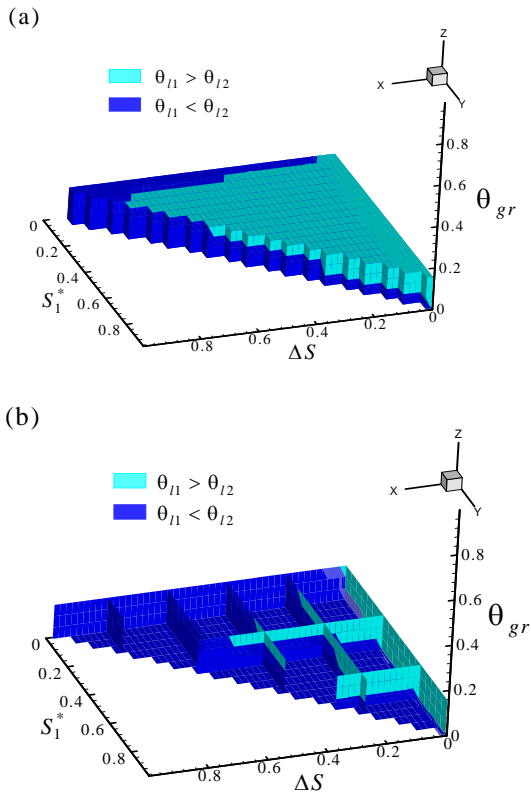


Figure 1. The relation between θ_{l1} , θ_{l2} , θ_{gr} , S_1^* and ΔS : (a) three dimension diagram and (b) fence diagram

3. SITE APPLICATION

The stochastic approach using the Monte Carlo method is applied to a temporary low-level nuclear waste storage site in Taiwan for the probabilistic assessment of contamination. The realizations of the hydraulic conductivity field are generated from the mean, variance, and covariance function by a

geostatistical program, using the turning bands method (Matheron, 1973; Mantoglou and Wilson, 1982). Then, the realizations are solved by TOUGH2 for two-phase flow and solute transport. In this study, a total of 1,000 realizations are generated and simulated, and the probabilistic assessment is based on the results of those realizations. To increase the applicability of the stochastic approach, an automatic process is established.

The potentially polluted site is located in Tao-Yuan, Taiwan, and is used for temporary storage of low-level nuclear waste on the ground surface. If a leak occurs, the contaminant will penetrate through the vadose zone and pollute the regional groundwater. The water level is about 8.0 m below the ground surface at this area. The recorded annual precipitation and estimated annual evaporation are 2,541.2 mm/yr and 841.9 mm/yr, respectively. The groundwater flow direction is from northwest to southeast, with an average hydraulic gradient of 0.016. According to a few borehole data, there are two horizontal layers below the ground surface, clay on top and a gravel layer below it. The average thickness of the clay and gravel layers are about 2.0 and 14.0 m, respectively. A total of 39 samples are taken from the ground surface and are measured for hydraulic conductivity by using a constant-head permeameter in the laboratory (Yeh, 2001).

The locations of the sample sites are shown in Figure 2. Only six hydraulic conductivities of gravel are measured, using pumping tests, slug tests, or determined by constant-head permeameter (Ji and Song, 1994). To obtain the unsaturated hydraulic properties, the capillary pressures are measured by the centrifuge method, and water contents are obtained by the classical soil physical method. Then, the water retention data is fitted with the van Genuchten model (Yeh, 2001). Table 1 shows the soil properties within the site that are used in the numerical modeling. Since data are scarce in the gravel layer, the variance and correlation scale estimates are based on the information from the Cape Cod site (Leblanc et al., 1991), because of their similarity in soil type. The residual gas saturation is assumed to be 0.1.

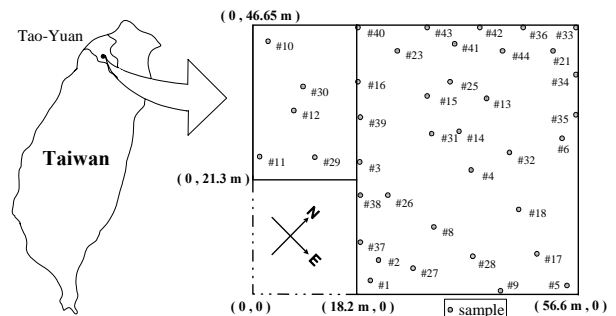


Figure 2. The sampling locations in the study site of Tao-Yuan, Taiwan

3. NUMERICAL SIMULATION

We model the possible solute transport within the site with a two-dimensional vertical cross section including both saturated and unsaturated zones. The modeling domain and boundary conditions are shown in Figure 3.

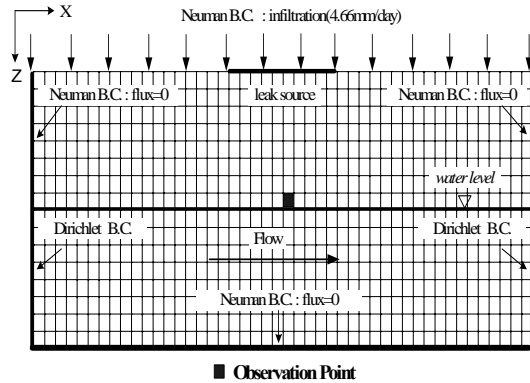


Figure 3. Domain and boundary conditions for the study site. A uniformly fixed infiltration rate is applied to the top of the domain. No-flow boundaries are applied to the bottom and two sides of the unsaturated zone. Dirichlet boundaries of 8.0m and 8.75m are applied to the left and right side of the saturated zone, respectively.

Domain size is 46 m×16 m and is discretized by uniform grids of 1 m×1 m, 46 grids in the horizontal direction, and 16 in the vertical direction. Clay material is assigned to the top two meters and gravel material is assigned to the rest of the area. Water level is set at 8.0 m below the ground surface. Assuming no surface runoff, a uniformly fixed infiltration rate of 1699.3 mm/yr is applied to the top of the domain. No-flow boundaries are applied to two sides of the unsaturated zone. Dirichlet boundaries of 8.0 m and 8.75 m are applied to the left and right side of the saturated zone, respectively. The Dirichlet boundary condition creates a hydraulic gradient of 0.016 in the saturated zone. The bottom of the domain is a no-flow boundary. In the transport simulation, contamination is applied to 10 m of the center area at the top of the domain to simulate a leaching event. A total of 1,000 simulations are done for the probabilistic assessment. Realizations of the hydraulic conductivity field are generated by the turning bands method. Since the spatial variation in the hydraulic conductivity causes several orders of magnitude variation in capillary pressure parameters (porosity, α , and n) and the hydraulic conductivity is assumed to be the most important factor affecting flow and transport [Chen and Lee, 2003], only the hydraulic conductivity is treated as a random variable in the analysis. An isotropic exponential correlation function of hydraulic conductivity, with the parameters shown in Table 1, is assumed for gravel,

because the hydraulic conductivities were measured at a local scale (pumping test, slug test and permeameter). An anisotropic exponential correlation function is used for clay material. A horizontal correlation length is assumed, as shown in Table 1, along with an infinite vertical correlation length (due to lack of data for this direction). Due to the limited number of soil types in TOUGH2, the hydraulic conductivities are divided into eight classes for clay and 16 classes for gravel. The variograms of clay and gravel in the horizontal direction before and after the classification are compared in Figure 4.

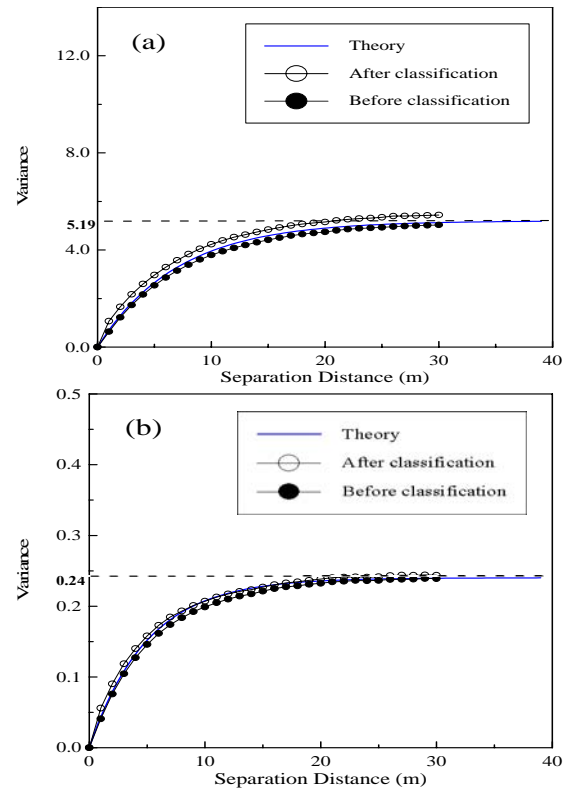


Figure 4. The variograms of (a) clay and (b) gravel in the horizontal direction before and after the classification

The figure shows that with a limited number of soil types in clay and gravel, a theoretical variogram can be modeled reasonably. Each realization is used to simulate steady-state flow conditions; then the resultant flow field is used for the transport simulation.

The low-level nuclear contaminant is simulated by using the nonabsorptive solute chlorite and the EOS7 module in TOUGH2. The chlorite is assumed to uniformly leak from the subsurface (19~28 m on the x-axis; see Figure 3) with an initial concentration C_o of 1,700 milligrams per liter (mg/L). A total of 1,000 realizations are utilized in the Monte Carlo simulation. By collecting the chlorite concentrations at each grid from all simulations, the probability for a

concentration greater than a certain threshold can be assessed. Given an environmental protection criterion, the probabilistic assessment of contamination can be performed.

5. RESULTS AND DISCUSSION

The effect of the two-phase flow model on flow is investigated by comparing the results with those of the single-phase flow model. The single-phase flow condition is approximated by assigning $\theta_{gr} = 0$ in the EOS7 module. When aqueous-gas-phase flow is considered, the mean value of unsaturated water content in the unsaturated zone is about 0.261—only slightly smaller than 0.265 for the single-phase flow model, but still consistent with the two-phase model producing smaller water content.

5.1 Comparing The Results Of Solute Transport From Single-Phase And Two-Phase Models

An observation point near the water table and on the path of the plume center was set in the unsaturated zone, as shown in Figure 3, to observe the breakthrough curve of the solute transport. Figure 5 shows the dimensionless concentration breakthrough curves at the observation point for both single-phase model and two-phase model.

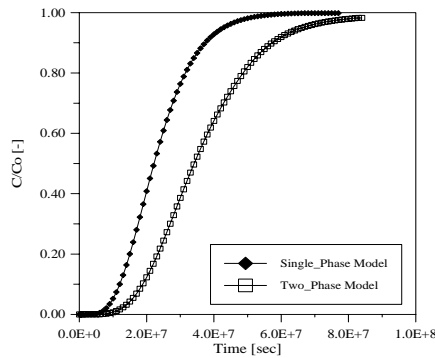


Figure 5. The dimensionless concentration breakthrough curves at the observation point for both (a) single-phase model and (b) two-phase model

The plume moves slower in the longitudinal flow direction within the unsaturated zone in the two-phase model than in the single-phase model. Figure 6 shows a snapshot of mean concentration contours of 1,000 realizations for the single-phase and two-phase models on the 365th day. The results not only confirm the slower movement of the plume in the unsaturated zone, but also show a wider lateral spreading of the plume produced by the two-phase model. The slower movement of the plume in the unsaturated zone for the two-phase model indicates a smaller polluted area in the saturated zone.

According to the environmental protection criteria of Taiwan, chlorite in groundwater must not exceed the

maximum concentration limit (MCL) of 250 mg/L; that is, 14.7% of the leaking source. Our probabilistic assessment is performed based on this criterion.

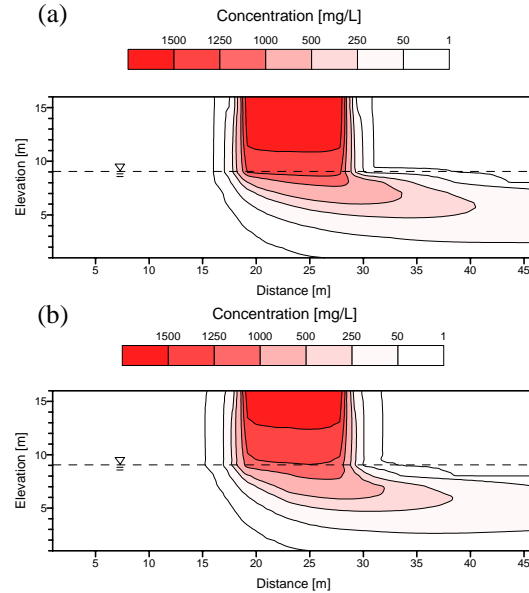


Figure 6. The mean concentration contours of 1000 realizations of (a) the single-phase and (b) two-phase model on 365th day

Figure 7 shows the probability of exceeding the MCL on the 365th day. When the single-phase model is considered, the probability of exceeding MCL will be overestimated in the saturated zone, while it will be underestimated in unsaturated zone. Although the water content from the two-phase flow model is only 1.5% less than that in the single-phase flow model, the effect of the two-phase flow model on the probabilistic assessment is significant.

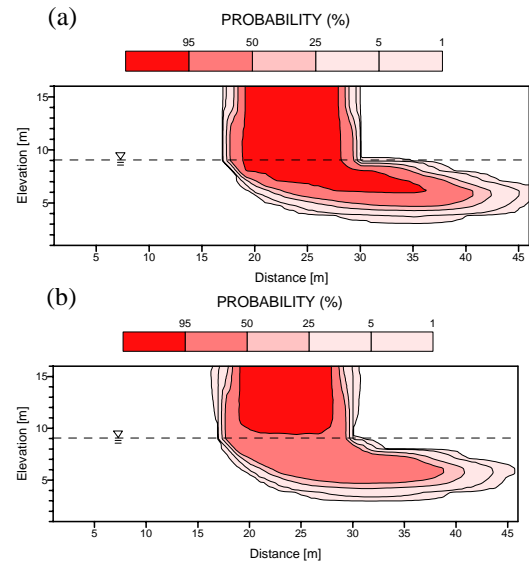


Figure 7. Probability distribution contour of chlorite for both (a) single-phase model and (b) two-phase model on 365th day

5.2 Comparing The Results Of Solute Transport From Deterministic And Stochastic Models

To demonstrate the utility of the stochastic approach, we also perform a deterministic simulation using the average soil properties shown in Table 1.

Table 1. Parameter information (Ji and Song, 1994; Yeh, 2001)

Parameter	Value	
	Clay layer	Gravel layer
Hydraulic conductivity, K (m sec ⁻¹)	9.9×10^{-7}	1.45×10^{-5}
Porosity, ϕ	0.465	0.41
Bulk density (kg m ⁻³), ρ_b	2700	2800
Mean of $\ln K$, Y	-9.22	-6.54
Variance of $\ln K$, σ^2	5.19	0.24*
Correlation scale (m), λ	7.0	5.0*
α (m ⁻¹)	107	7.5
n	1.84	1.89
Saturated water content, θ_s	0.465	0.41
Residual water content, θ_{lr}	0.292	0.065
Residual gas content, θ_{gr}	0.0465**	0.041**

* from the Cape Cod Site (Leblanc et al., 1991)

**assume $S_{gr} = 0.1$

The stochastic result for the probability of exceeding MCL on the 104th day and the deterministic result for the concentration contour of MCL on the same day are shown in Figure 8.

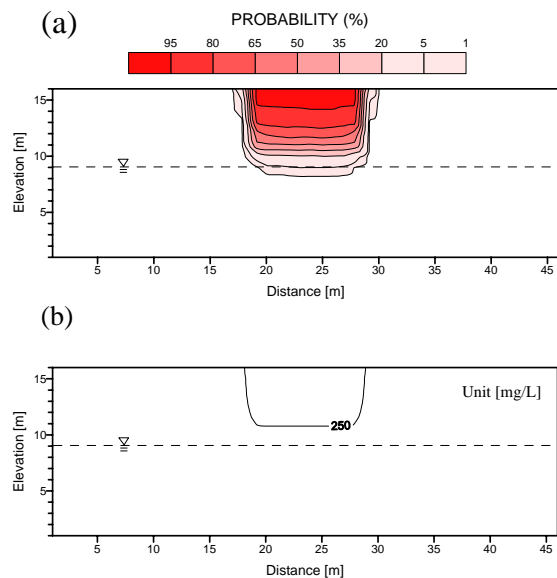


Figure 8. (a) Probability distribution contour of chlorite from stochastic analysis and (b) the contaminant front of the MCL from deterministic approach on 104th day

Figure 8(a) indicates that the plume in the unsaturated zone is symmetric about the source area and the regional groundwater may be polluted on the 104th day with a probability of 0.05. Figure 8(b) shows the result for the deterministic case. In the deterministic approach the contaminant front of the MCL will not reach the regional groundwater while the stochastic result shows a possibility of pollution in groundwater at the same time.

Figures 9(a) and (b) show the results for the stochastic and the deterministic approaches on the 365th day, respectively. Both approaches show that both saturated and unsaturated zones are polluted at this time. The stochastic approach provides additional information on the probability distribution of the contaminant. The region with highest pollution probability (probability greater than 0.95) is from subsurface to about 8 m depth. The deterministic result in Figure 9(b) shows that the contaminant still does not reach the boundary at this time, but the stochastic result shows that there exists possible pollution, with a probability of 0.005. Although the deterministic approach requires less labor, it doesn't provide information on prediction uncertainty. Conversely, the stochastic approach provides a probability distribution that is useful for contamination risk assessment.

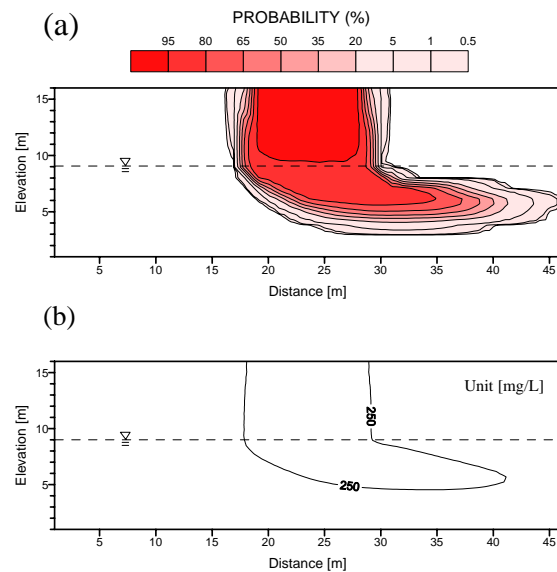


Figure 9. (a) Probability distribution contour of chlorite from stochastic analysis and (b) the contaminant front of the MCL from deterministic approach on 365th day

6. CONCLUSIONS

Our results lead to the following conclusions:

1. Although the difference in soil water content between the single-phase and the two-phase model may be small, the two-phase flow model

provides a significantly different assessment of contamination risks.

2. When applied to a potentially polluted site in Taiwan, the stochastic approach provides useful probability information not available from the deterministic approach.
3. The probabilistic assessment of groundwater contamination is important, in that it provides the basis for more informed waste management, better environmental assessment, and improved evaluation of impact on public health.

REFERENCES

- Chen, J. F. and Lee, C. H. (2003) An analytical solution on water budget model in unsaturated zone, *Journal of Chinese Institute of Engineers*, 23(3), 321-332.
- Christakos, G. (2004), A sociological approach to the state of stochastic hydrogeology, *Stoch. Envir. Res. and Risk Ass.* 18, 274-277.
- Dagan, G. (1982) Stochastic modeling of groundwater flow by unconditional and conditional probabilities, 2, The solute transport, *Water Resource Research* 18, 835-848.
- Dagan, G. (1989) Flow and Transport in Porous Formations, Springer-Verlag, New York.
- Ellsworth, T. R., Jury, W. A., Ernst, F. F. & Shouse, P. J. (1991) A three-dimensional field study of solute transport through unsaturated, layered, porous media, 1, Methodology, mass recovery, and mean transport, *Water Resource Research* 27, 951-965.
- Franke, H. J. & Teutsch, G. (1994) Stochastic Simulation of the Regional Pesticide Transport Including the Unsaturated and the Saturated Zone, *ECOLOGICAL MODELLING* 75,529-539.
- Freyberg, D. L. (1986) A natural gradient experiment on solute transport in a sand and gravel aquifer, 2, Spatial moments and the advection and dispersion of nonreactive tracers, *Water Resource Research* 22, 2031-2046.
- Garabedian, S. P., LeBlanc, D. R., Gelhar, L. W. & Celia, M. A. (1991) Large-scale natural gradient tracer test in sand and gravel, Cape Cod, Massachusetts, 2, Analysis of spatial moments for a nonreactive tracer, *Water Resource Research* 27, 911-924.
- Gelhar, L. W. & Axness, C. L. (1983) Three-dimensional stochastic analysis of macrodispersion in aquifers, *Water Resource Research* 19, 161-180.
- Gelhar, L. W. (1986) Stochastic subsurface hydrology from theory to applications, *Water Resource Research* 22, 135-145.
- Gelhar, L. W. (1992) Stochastic Subsurface Hydrology, Prentice-Hall, Englewood Cliffs, N. J..
- Harter, T. & Zhang, D. (1999) Water flow and solute spreading in heterogeneous soils with spatially variable water content, *Water Resource Research* 35, 415-426.
- Ji, L. M. & Song G. L. (1994) Geology of the district of the Institute of Nuclear Energy Research, Report of the district of the Institute of Nuclear Energy Research, INER-T2020.
- Kovscek, A. R. & Cakici, M. D. (2005) Geologic storage of carbon dioxide and enhanced oil recovery: II. Co-optimization of storage and recovery, *Energy Convers. Manage* 46, 1941-1956.
- Kutilek, M. & Nielsen, D. R. (1994) Soil Hydrology, Catena Verlag.
- Leblanc, D. R., Garabedian, S. P., Hess, K. M., Gelhar, L. W., Quadri, R. D., Stollenwerk, K. G. & Wood, W. W. (1991) Large-scale natural gradient tracer test in Sand and gravel, Cape Cod, Massachusetts, *Water Resource Research* 27, 895-910.
- Lo, I. M. C., Law, W. K. W. & Shen, H. M. (1999) Risk assessment using stochastic modeling of pollutant transport in landfill clay liners, *Water Science and Technology* 39, 337-341.
- Matheron, G. (1973) Intrinsic random functions and their applications, *Advances in Applied Probability* 5, 439-468.
- Mantoglou, A. & Wilson, J. L. (1982) The turning bands method for simulation of random fields using line generation by a spectral method, *Water Resource Research* 18, 1379-1394.
- Maxwell, R. M. & Kastenber, W. E (1999) Stochastic environmental risk analysis-an integrated methodology for predicting cancer risk from contaminant groundwater, *Stochastic Environmental Research and Risk Assessment* 13, 22-47.
- Molz, F. J., Rajaram, H. & Lu, S. (2004), Stochastic fractal-based models of heterogeneity in subsurface hydrology: origins, applications, limitations, and future research questions, *Rev. Geophys.*, 42, RG1002, doi:10.1029/2003RG000126, 2004.

- Neuman, S. P. (2004), Stochastic groundwater models in practice, *Stoch. Envir. Res. and Risk Ass.* 18, 268-270.
- Nielsen, D. R., Biggar, J. W. & Erh, K. T. (1973) Spatial variability of field-measured soil-water properties, *Hilgardia* 42, 215-260.
- Padilla, I. Y, Yeh, T.-C. J. and Conklin, M. H. (1999) The effect of water content on solute transport in unsaturated porous media, *Water Resource Research* 35, 3303-3313.
- Pruess, K. (1991) EOS7, an equation-of-state module for the TOUGH2 simulator for two-phase flow of saline water and air, *Rep. LBL-31114*, Lawrence Berkeley Lab., Berkeley, Calif.
- Russo, D. (1993) Stochastic modeling of macrodispersion for solute transport in a heterogeneous unsaturated porous formation, *Water Resource Research* 29, 383-397.
- Russo, D. (1998) Stochastic analysis of flow and transport in unsaturated heterogeneous porous formation : Effect of variability in water saturation, *Water Resource Research* 34, 569-581.
- Russo, D. & Bresler, E. (1981) Soil hydraulic properties as stochastic processes, I, An analysis of field spatial variability, *Soil Science Society of America Journal* 45, 682-687.
- van Genuchten, M. T. (1980) A closed-form equation for predicting the hydraulic conductivity of unsaturated soils, *Soil Science Society of America Journal* 44, 892-898.
- vanderZee, S. & Boesten, T. (1991) Effects of Soil Heterogeneity on Pesticide Leaching to Groundwater, *Water Resource Research* 27, 3051-3063.
- Winter, C. L. (2004), Stochastic hydrology: practical alternatives exist, *Stoch. Envir. Res. and Risk Ass.* 18, 271-273.
- Yang, J., Zhang, R. & Wu, J. (1996) Stochastic analysis of adsorbing solute transport in two-dimensional unsaturated soils, *Water Resource Research* 32, 2747-2756.
- Yeh, Y. J. (2001) Effect of groundwater flow on solute transport in saturated and unsaturated soils - A case study in INER test site, Ph D. Dissertation. National Cheng Kung University, Tainan, Taiwan.
- Zhang, Y.-K. and D. Zhang (2004), Forum: the state of stochastic hydrology, *Stoch. Envir. Res. and Risk Ass.* 18, 265.

DISSOLUTION OF A SPATIALLY VARIABLE NON-AQUEOUS PHASE LIQUID SOURCE: EXPERIMENTAL STUDY AND MODEL DEVELOPMENT

Fritjof Fagerlund^{1,2}
Menka Mittal²
Tissa H. Illangasekare²
Tanapon Phenrat³
Hye-Jin Kim³
Gregory V. Lowry³

¹⁾ Uppsala University, Dept. of Earth Sciences, Villavägen 16, 75236 Uppsala, Sweden

²⁾ Centre for Experimental Study of Subsurface Environmental Processes (CESEP),
Env. Sci. and Eng., Colorado School of Mines, Golden, CO 80401-1887, USA

³⁾ Civil and Environmental Engineering Division, Carnegie Mellon University, Pittsburgh, PA 15213

e-mail: Fritjof.Fagerlund@geo.uu.se

ABSTRACT

Mass transfer from subsurface occurrences of non-aqueous phase liquids (NAPLs) to the surrounding groundwater is a key process, both for persistent contamination problems originating from organic liquid sources, and for dissolution trapping in geological CO₂ sequestration. While the dissolution typically is governed by processes that occur on very small scales (i.e., the pore scale), there is a need to model the mass transfer coupled to transport of dissolved chemical components over field scales that are several orders of magnitude larger. Upscaled models, linking the small-scale characteristics to the total mass transfer from sources of dissolved chemicals, are therefore needed. Well-controlled laboratory experiments conducted in test cells allow for the generation of accurate data to validate such upscaling methods before applying them to much more complex field systems.

Following this approach, a set of experiments were conducted in a two-dimensional sand tank, where the dissolution of a spatially variable, 5 cm by 5 cm DNAPL tetrachloroethene (PCE) source was carefully monitored in space and time. With a resolution of 0.2×0.2 cm, NAPL saturations were measured using x-ray attenuation techniques at approximately 1,000 individual pixels in the source zone. By continuously measuring the NAPL saturations, the temporal evolution of DNAPL mass loss by dissolution to groundwater could be measured at each pixel. The rate of dissolution varied spatially and temporally within the source, and was found to be correlated to NAPL morphology, groundwater flow velocity, and position within the source. The dissolution process was modeled using iTOUGH2/T2VOC under assumption of local equilibrium (LE) between the DNAPL and dissolved PCE. A preliminary model of rate-limited (RL) dissolution, based on a Gilland-

Sherwood type relation implemented in MODFLOW/RT3D, was also tested. It was found that the LE model could not capture the observed dissolution patterns, although it predicted the total rate of mass transfer well for the given source conditions. The RL model showed potential to better capture the dissolution pattern after further model development. Ongoing work is aimed at addressing these issues by correlating the detailed measurements of NAPL entrapment morphology and local dissolution rates, with the final goal of developing an upscaled model of the total mass transfer from the source zone.

INTRODUCTION

Dense non-aqueous phase liquids (DNAPLs) constitute a widespread problem of severe groundwater contamination. DNAPLs are heavier than water, and many, such as tetrachloroethene (PCE) and trichloroethene (TCE) also have comparatively low viscosities, making them highly mobile. When released to the subsurface, the DNAPL can penetrate below the water table, and the high mobility in combination with geological heterogeneity typically produces a complicated migration pattern as well as a complex architecture of trapped and immobilized DNAPL (Mercer and Cohen, 1990; Illangasekare et al., 1995; Fagerlund et al. 2007b, 2008). While the dissolution of DNAPLs in groundwater tends to be slow, many (e.g., chlorinated ethenes) are harmful already at very low aqueous concentrations. Therefore, occurrences of DNAPLs in the subsurface constitute long-term sources of groundwater contamination, and the process of DNAPL migration and subsequent immobilization is fast compared to the lifetime of the DNAPL and groundwater contaminants originating from it. The zone of the aquifer where entrapped DNAPL exists is referred to as the DNAPL source zone.

The mass transfer of contaminants from the DNAPL to the groundwater is a key process for the assessment of the source and the design of efficient actions of remediation and risk management. The dissolution process depends on several factors, including the aqueous solubility of the DNAPL constituents, the groundwater flow through the source zone and the interfaces between DNAPL and the aqueous phase in relation to the groundwater flow field. While dissolution originates from pore-scale processes at NAPL-water interfaces in the pores or pore throats of the medium, for practical reasons, there is a need to model dissolution at much larger scales which require upscaled models. While upscaled dissolution models remain scarce, developments have been done by (for example) Parker and Park (2004) and Saenton and Illangasekare (2007).

Experimental studies on DNAPL dissolution have mainly been performed in one-dimensional columns (Miller et al., 1990; Mackay et al., 1991; Powers et al., 1992; Geller and Hunt, 1993; Imhoff et al., 1993; Powers et al., 1994) and to a lesser extent in two-dimensional bench-scale flumes (Imhoff et al., 1996, including also one three-dimensional experiment; Powers et al., 1998; Nambi and Powers, 2000; Saba and Illangasekare, 2000). However, in the 1D experiments, it is not possible to quantify effects of variations in the spatial distribution of the DNAPL, and in the abovementioned 2D (and 3D) experiments detailed measurements of the DNAPL spatial distribution are lacking, with exception of one experiment presented by Imhoff et al. (1996). Here, in a series of two-dimensional experiments Imhoff et al. (1996) investigated the formation of dissolution fingers in a (0.64×12×20) cm flow cell. In one of these experiments the flow was stopped three times during the experiment, and the spatial distribution of the DNAPL was measured using an x-ray attenuation technique at 5 mm×5 mm resolution. To understand how the DNAPL architecture in the source zone affects the dissolution patterns in space and time more such data sets for variable DNAPL saturation conditions are needed.

Here, we present a 2D study in which the DNAPL saturation is continuously measured in space and time, using x-ray attenuation measurements and applying a methodology similar to that of Fagerlund et al. (2007a). The objectives were (i) to generate a detailed data set on the spatial and temporal evolution of DNAPL saturations during dissolution to flowing groundwater, thereby characterizing the spatially varying local dissolution rates; and (ii) to test existing dissolution models against this data and identify source characteristics essential to the dissolution process. The latter is the first step in an attempt to develop an upscaled model that accounts for spatially varying DNAPL saturations (architecture) and dissolution patterns produced by such heterogeneous

DNAPL source zones. In this paper, modeling using a local equilibrium assumption (LE) is presented, together with a very preliminary rate-limited (RL) approach. A more rigorous RL model will be presented in future work.

EXPERIMENTAL METHODS

The experimental flow setup consisted of a 2D flow cell connected to a peristaltic pump on the inflow side and to a constant head effluent collection system on the outflow side. The custom made flow cell, shown in Figure 1, has inner dimensions 27×17×2.8 cm. It has an aluminum frame, a glass front plate, and an aluminum back plate with numerous sampling ports. The top plate can be removed, allowing controlled packing of the tank. The tank was packed wet using de-aired, de-ionized water and three different sands. To achieve uniform flow conditions at the inflow and outflow boundaries, a 2.5 cm wide vertical section was packed with a very coarse sand (Unimin sand # 8), and the flow to and from the tank was evenly distributed through three ports at different heights. The rest of the tank constituted the experimental domain and had dimensions 22.9×14.6×2.8 cm. It was packed with a fine sand (Unimin # 50) and a coarse sand (Unimin # 16) creating a 5×5 cm source zone of coarse sand where the DNAPL could be trapped by capillary forces. The permeability (k), porosity (Φ), pore-size distribution index λ (as defined by Brooks and Corey, 1964) and residual water saturation (S_{wr}) for these two sands are given in Table 1.



Figure 1. Two-dimensional flow cell used in the experiments. The total length of tank is approximately 30 cm and the DNAPL source zone (red) is 5x5 cm.

Table 1. Sand properties, measured by Sakaki et al. (2007).

Sand	k (m ²)	ϕ	λ	S_{wr}
Unimin 16	5.63E-10	0.407	3.01	0.022
Unimin 50	3.38E-11	0.426	4.729	0.035

The DNAPL used in the experiment was tetrachloroethene (PCE) colored red using Sudan IV. To achieve an average NAPL saturation of approximately 0.4, but also distribute the PCE over the entire source zone, the PCE was first injected to an average saturation of approximately 80% and then withdrawn until a saturation of 40% remained. The colored PCE was injected and withdrawn at a rate of 0.25 mL/minute through two ports in the back of the tank. The source was then allowed to stabilize (redistribute until immobile) for 2 days before the water flow was turned on and the dissolution of DNAPL started. The water flow was maintained constant using an inflow pump rate of 1.5 mL/minute, which corresponds to an average Darcy velocity of approximately 0.52 m/day. The outflow boundary was maintained at constant head as the effluent water was collected in a gas-tight Teflon bag.

Both before the water flow started and continuously throughout the experiment, the spatial distribution of NAPL saturations in the source zone was measured using an x-ray attenuation technique. The x-ray measurement system used an x-ray tube from which a beam of photons within the x-ray energy spectrum was shot through the 2D flow cell. On the other side of the flow cell, a detector counted the number of photons that passed through the sample unattenuated within each of 1500 energy intervals. Thereby the saturation of water and NAPL could be determined in the volume that the photon beam travelled through. The tube and detector were mounted on a moving frame and could be moved in synchronization from point to point in a fully automated manner, using high-precision motors. The collimated photon beam had a diameter of 2 mm, which thus was the maximum resolution of the measurements. Moving the tube and detector around, the fluid saturations were continuously scanned taking measurements at 2 mm spacing in a 74×74 mm square overlapping the source zone (total of 1369 points of measurement). By returning to measure the same points, the behavior with time at each point in space was recorded, which allowed interpolation to any given time at all points (see Fagerlund et al., 2007a for more details). These measurements provided a high-precision, high-resolution monitoring of the spatial and temporal distributions of fluid saturations, as well as the patterns of dissolution. The theory behind these methods has also been described in more detail by Hill (2001), Hill et al. (2002), and Ferre et al. (2005).

MODELING METHODS

Local Equilibrium Approach

Modeling of the DNAPL dissolution process under an assumption of local equilibrium (LE) was done using iTOUGH2/T2VOC (Finsterle, 2000; Falta et al., 1995). iTOUGH2 (Finsterle, 2000) adds inverse modeling capability to the TOUGH2 equation of state

module T2VOC (Falta et al., 1995), which is a numerical simulator for multiphase flow and transport of a single component volatile organic chemical (VOC), water and air. Here, only VOC (PCE) and water were present, and water was the only mobile fluid phase. However, as immobile DNAPL dissolves, the relative permeability to water increases and the groundwater flow field changes. The Brooks and Corey (1964)–Burdine (1953) (BCB) equation was used to calculate aqueous-phase relative permeability (k_{rw}):

$$k_{rw} = \bar{S}_w^{(3+2/\lambda)} \quad (1)$$

$$\bar{S}_w = \frac{S_w - S_{wr}}{1 - S_{wr}} \quad (2)$$

Here S_{\square_w} is the effective water saturation, λ is the pore-size distribution index and S_{wr} is the residual water saturation. Molecular diffusion in liquid phases is not implemented in T2VOC, but a comparative simulation of part of the experiment using TMVOC (Pruess and Battistelli, 1999) including dissolution, showed that advective transport of dissolved components dominated over diffusion, which in comparison was very small for the flow conditions in this experiment.

Rate Limited Approach

Rate limited (RL) mass transfer between the DNAPL and the aqueous phase was described by a linear driving force model where the PCE mass flux J from the DNAPL to the aqueous phase, is proportional to the difference between its aqueous concentration in thermodynamic equilibrium with the DNAPL (effective aqueous solubility) C_{PCE}^* and its actual concentration C_{PCE} in the aqueous phase (Miller et al. 1990):

$$J = K_L (C_{PCE}^* - C_{PCE}) \quad (3)$$

Here, K_L is the lumped mass-transfer coefficient over the DNAPL-water interface. K_L is contained in a modified Sherwood number $Sh' = K_L d_{50}^2 D_m^{-1}$, where d_{50} is the median grain size and D_m is the molecular diffusion coefficient of PCE in water. Several mass-transfer models have been developed that relate the Sherwood number to other dimensionless groups, including the Reynolds number Re , Schmidt number Sc , and parameters related to the porous medium and DNAPL morphology (e.g., Miller et al., 1990, Powers et al., 1992, Geller and Hunt, 1993, Imhoff et al., 1994, Powers et al., 1994). Here a simplified model is tested assuming that Sh' is a function of only Re and Sc , and furthermore, following Miller et al. (1990), assuming that the dependence on Re and Sc can be described by power functions so that $Sh' = a_0 Re^{a_1} Sc^{a_2}$, where a_0, a_1 are

empirical constants and $a_2 = 0.5$. For isothermal conditions where $Sc = \mu_a \rho_a^{-1} D_m^{-1}$ does not change, Sc^{a_2} is a constant and can be lumped together with a_0 , so that $Sh^* = a_0 Re^{a_1}$, i.e.:

$$\frac{K_L d_{50}^2}{D_m} = a_0 Re^{a_1} \quad (4)$$

Here, $Re = v_a \rho_a d_{50} \mu_a^{-1}$ is the Reynolds number for the aqueous phase; μ_a , ρ_a and v_a are the aqueous-phase viscosity, density, and mean pore-water velocity, respectively.

Equations (3) and (4) were implemented to the reaction module RT3D (Clement, 1997) which simulates reactive transport when the groundwater flow has first been solved for using the groundwater modeling software MODFLOW (Harbaugh et al., 2000). In the MODFLOW simulations, relative permeability to the aqueous phase was accounted for using Equations (1) and (2). However, an iterative updating scheme was not yet in place, meaning that changes in k_{rw} could not be accounted for in an automated manner. Results from this preliminary model are therefore valid only as long as changes in NAPL saturations are relatively insignificant to groundwater flow, which in this case corresponds to a time period on the order of a couple of days. Therefore, only very brief RL results are presented here. This preliminary RL simulation used uncalibrated values for a_0 and a_1 taken from different ongoing work. These values were $a_0 = 8.8$ and $a_1 = 0.837$. $D_m(\text{PCE})$ was $8.18\text{E-}10 \text{ m}^2/\text{s}$, and d_{50} was 0.974 mm , and 0.303 mm for # 16 and # 50 sand, respectively (Sakaki et al., 2007).

Discretization, Initial and Boundary Conditions

The experiment domain consisting of Unimin sands # 50 and # 16 (see Figure 1) was discretized into 54 by 46 rectangular gridblocks in the horizontal and vertical directions, respectively, yielding a total of 2484 blocks. The discretization was finer in the vicinity of the source zone, where the spacing was $2 \times 2 \text{ mm}$. Further away from the source, the maximum block length was 10 mm and 8 mm in the x- and z-direction, respectively. Inflow to the tank was modeled as a constant generation rate of water to the leftmost vertical column of blocks, corresponding to the total pump rate of 1.5 mL/minute . The outflow boundary on the right was assigned constant head using inactive gridblocks. Other boundaries were no-flow. The initial NAPL saturation, as measured at $2 \text{ mm} \times 2 \text{ mm}$ resolution using x-ray attenuation, was assigned to the initial conditions for the corresponding gridblocks in the source zone. The initial conditions and block discretization are shown in Figure 2. Because the DNAPL had become immobile, the relative permeability to NAPL was set to zero in the T2VOC simulations.

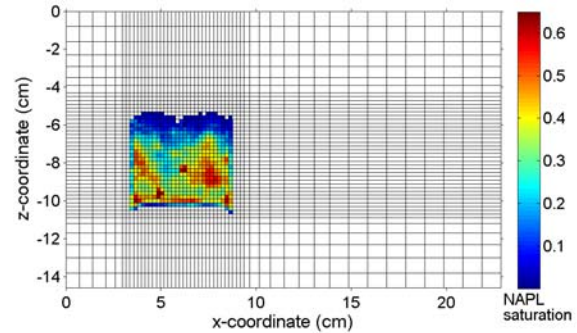


Figure 2. Block discretization and initial DNAPL saturation used in the simulations

RESULTS AND DISCUSSION

Figure 3 shows the initial spatial distribution of NAPL saturation (S_n) in the source zone as measured using x-ray attenuation techniques. The average NAPL saturation in the entire source zone was approximately 0.4, but as can be seen, there were relatively large variations in S_n although the source zone consisted of relatively uniform # 16 sand. The non-uniform DNAPL entrapment architecture can be explained by small variations in capillarity (entry pressures), which produced spatially heterogeneous entrapment.

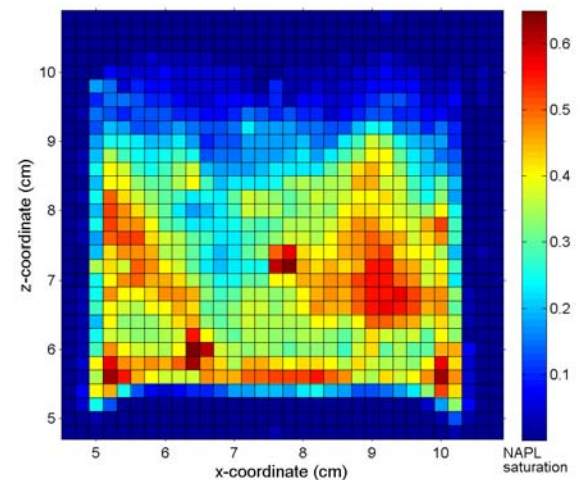


Figure 3. Measured initial NAPL saturations

The continuous scanning of NAPL saturations in the source zone provided measurements of the NAPL saturations during the dissolution process. As an example, the S_n distribution after 9 days of water flow through the tank is shown in Figure 4.

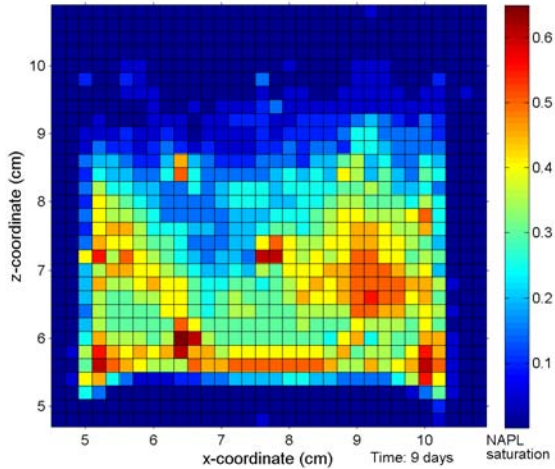


Figure 4. Measured NAPL saturations after 9 days of dissolution.

Comparison between the initial NAPL saturation, $S_{n,initial}$, (Figure 3) and NAPL saturation at a time t during dissolution, $S_n(t)$, (e.g., Figure 4) revealed the dissolution patterns in the source zone. This is illustrated in Figure 5, which shows the spatial variation in quantity of NAPL that has been dissolved at a given time after the start of dissolution. This is expressed as $S_{n,initial} - S_n(t)$, and referred to as dissolved S_n .

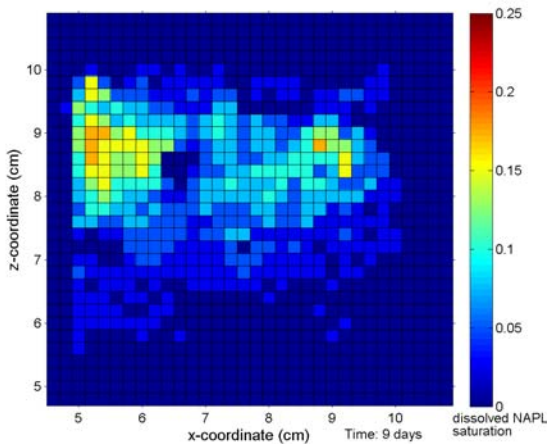


Figure 5. Measured dissolved S_n after 9 days

From Figure 5, it can be concluded that for the time period 0 to 9 days, the dissolution occurred mainly in the upper part of the source zone. As can be seen in Figures 3 and 4, representing the two limits for this time period, the NAPL saturations were on average lower in this zone compared to the lower parts of the source. Therefore, the relative permeability to water (k_{rw}) was higher, leading to more water flow passing through this zone. Significantly more water flow passing through the upper source zone than the lower

would promote the observed dissolution pattern. However, other factors, such as the possibly larger NAPL-water interfacial area contacting the flowing water in the low S_n regions, could also contribute.

It can also be noted that the dissolution was relatively evenly distributed in the horizontal direction, parallel to the general direction of water flow. This indicates that the water passing through the source zone did not immediately become saturated with dissolved PCE, but rather was able to pick up more dissolved components on its way through the source.

Figure 6 shows the simulated dissolved S_n after 9 days of dissolution, using T2VOC (Falta et al., 1995). Here, local equilibrium (LE) between the NAPL and the dissolved PCE in each gridblock was assumed. The LE assumption meant that the groundwater that flowed into the source zone was assumed to become saturated with dissolved PCE the first time it encountered NAPL. As a result, this groundwater could not dissolve any more NAPL on its way through the source zone, and hence, the NAPL source was predicted to dissolve from its upstream edges in a stepwise manner. The predicted dissolution was therefore concentrated on the leftmost side of the source zone where the groundwater entered. Comparing Figures 5 and 6, it is clear that the LE simulation could not predict the observed dissolution pattern.

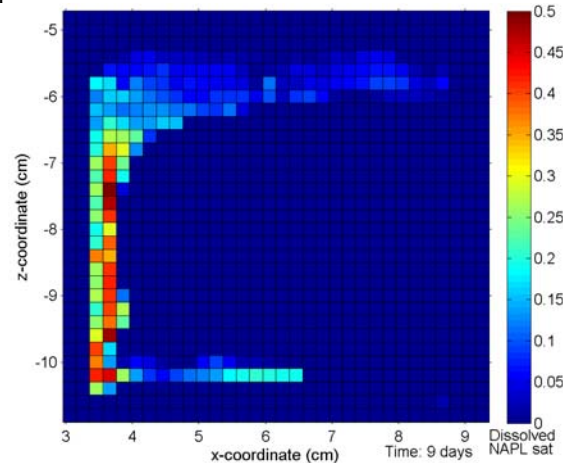


Figure 6. LE simulated dissolved S_n after 9 days

In this work, only a very preliminary RL simulation is included. The simulation, which extends only up to 2 days of dissolution, was done using MODFLOW (Harbaugh et al., 2000) and a modified version of RT3D (Clement, 1997) implementing Equations (3) and (4). The predicted pattern of dissolved S_n after 2 days of flow is shown in Figure 7. As will be shown below, this RL model underestimated the total amount of NAPL that dissolved. However, the pattern of dissolution was in a general sense similar to the measured one. The NAPL was predicted to

first dissolve in its upper parts, and this dissolution was relatively evenly distributed horizontally over the source zone. Although this is a very preliminary observation, it seems likely that a more rigorous RL model than one used here can capture the measured dissolution patterns to greater extent than the LE model.

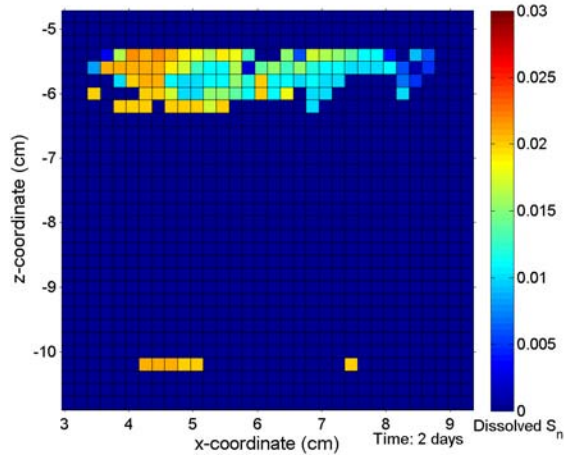


Figure 7. Dissolved S_n after 2 days as predicted by the preliminary rate-limited model

Figure 8 shows the normalized total NAPL volume V_m remaining in the flow cell at different times during dissolution:

$$\bar{V}_m = \frac{V_m(t)}{V_{m,initial}} \quad (3)$$

$V_m(t)$ is the total NAPL volume in the source zone at time t , and $V_{m,initial}$ is the total initial NAPL volume.

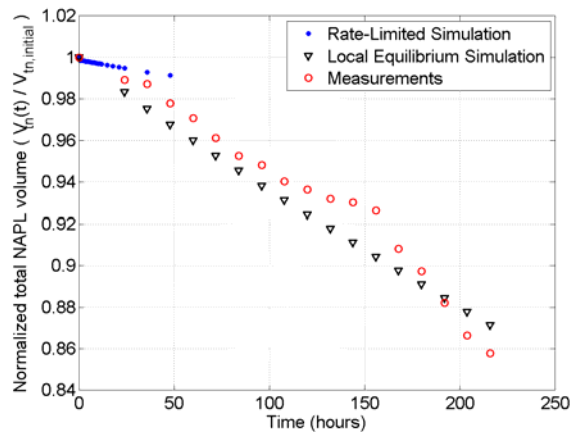


Figure 8. Normalized total NAPL volume remaining in the flow cell as a function of time

In Figure 8, observations based on x-ray measurements as well as results from the LE simulation are presented for times up to 9 days after the start of water flow, when approximately 15% of the total

NAPL in the source zone had dissolved. At this point, because of problems with the x-ray measurement system, further measurements of S_n covering the later stages of the dissolution process are not available. As can be seen, the LE simulation predicted the average total dissolution rate well for this time period. However, because the LE model could not predict the pattern of dissolution, it is unlikely that it could correctly predict the total rate of dissolution for long time periods, when the NAPL saturation distribution changes significantly as a result of dissolution. The two days of data from the preliminary RL simulation show that this model underestimated the total rate of dissolution.

CONCLUDING REMARKS

The detailed measurements of NAPL saturations in space and time during dissolution to flowing groundwater show that the patterns of dissolution are strongly correlated to the entrapped NAPL morphology, referred to as NAPL architecture. Dissolution is markedly faster in the upper part of the source zone where NAPL saturations are generally lower compared to the lower parts of the source. This can be attributed to the preferential flow of groundwater occurring in the upper zone due to higher relative permeability, but may also be correlated to NAPL-water interfacial area, which is also a function of S_n . The relatively even dissolution over the length of the source zone in the direction of flow indicates that equilibrium between NAPL and dissolved PCE was not reached, and mass transfer was rate limited.

Even so, the LE simulations presented here showed that the average total rate of mass transfer from the DNAPL source zone could be correctly predicted under the LE assumption for the time period and experimental conditions studied. At the same time, the pattern of dissolution obtained with the LE simulation was clearly different from the measured one. The first of these two observations indicate that an LE approach can work for upscaling the mass-transfer from source zones having certain architecture characteristics (such as the one presented here). However, the second observation shows that an LE approach will not work for all architectures and cannot correctly predict how architecture changes over time. The situations where LE models can capture the total mass transfer from a source zone are likely related to conditions in which the residence time of the flowing groundwater in the source zone is long enough for it to become saturated with dissolved components. In such cases, the total mass transfer from the source (but not the dissolution pattern) is the same for LE and RL models.

Even though the time period for which x-ray data on NAPL saturations exist is only 9 days (in fact, up to 13 days will be available after additional data

processing), the existing data is very detailed, and of high precision. The data also cover a wide range of NAPL saturations, variations in aqueous relative permeability, and variations in the groundwater flow field.

Ongoing work is aimed at building a rigorous model of NAPL dissolution, taking into account the measured NAPL architecture and its effects on relative permeability and the groundwater flow field. Correlations between local dissolution rates and parameters related to entrapment architecture will be investigated using the data presented. Once these correlations have been rigorously investigated, ways of developing an upscaled model that can correctly predict the total mass-transfer from a source zone or part of a source zone will be sought.

ACKNOWLEDGMENTS

The US Strategic Environmental Research and Development Program (SERDP), project number ER-1485, and the Swedish Research Council for Environment, Agricultural Sciences and Spatial Planning (FORMAS), project number 214-2008-1032, are acknowledged for providing funding for this research.

REFERENCES

- Brooks, R. H. and A. T. Corey, *Hydraulic properties of porous media*, Hydrology paper 3, Colorado State University, Fort Collins, Colorado, 1964.
- Burdine, N. T., Relative permeability calculations from pore size distribution data. *Trans. Am. Inst. of Mining and Met. Engineers*, 198, 71-78, 1953.
- Clement, T.P., *RT3D A modular computer code for simulating reactive multi-species transport in 3-dimensional groundwater systems*, Pacific Northwest National Laboratory, Report PNNL-11720, Richland, WA, U.S.A., 1997.
- Fagerlund, F., T.H. Illangasekare and A. Niemi, Nonaqueous-phase liquid infiltration and immobilization in heterogeneous media: 1. Experimental methods and two-layered reference case. *Vadose Zone J.*, 6, 471-482. doi:10.2136/vzj2006.0171, 2007a.
- Fagerlund, F., T.H. Illangasekare and A. Niemi, Nonaqueous-phase liquid infiltration and immobilization in heterogeneous media: 2. Application to stochastically heterogeneous formations. *Vadose Zone J.*, 6, 483-495, doi:10.2136/vzj2006.0172, 2007b.
- Fagerlund, F., A. Niemi, and T.H. Illangasekare, Modeling of NAPL migration in heterogeneous saturated media: Effects of hysteresis and fluid immobility in constitutive relations, *Water Resour. Res.*, 44, W03409, doi:10.1029/2007WR005974, 2008.
- Falta, R.W., K. Pruess, S. Finsterle and A. Battistelli, *T2VOC User's Guide*. Report LBL-36400, UC-400, Lawrence Berkeley National Laboratory, Berkeley, Calif., 1995.
- Ferré, T.P.A., A. Binley, J. Geller, E. Hill and T.H. Illangasekare, Hydrogeophysical methods at the laboratory scale. Chapter 15: p. 441-463. In Rubin, Y. and S.S. Hubbard (eds.) *Hydrogeophysics*. Springer, Dordrecht, The Netherlands, 2005.
- Finsterle, S., *iTOUGH2 User's Guide*, Report LNBL-40040, 2nd rev., Lawrence Berkeley National Laboratory, Univ. Calif., Berkeley, Calif., 2000.
- Geller, J.T., and J.R. Hunt, Mass transfer from nonaqueous phase organic liquids in water-saturated porous media. *Water Resour. Res.*, 29(4), 833-845, 1993.
- Harbaugh, A.W., Banta, E.R., Hill, M.C., McDonald, M.G., *MODFLOW-2000, the U.S. Geological Survey modular ground-water model – user guide to modularization concepts and the ground-water flow process*, U.S. Geological Survey, Open-File Report 00-92, Reston, VA, U.S.A., 2000.
- Hill, E. H. III, L. L. Kupper and C. T. Miller, Evaluation of path-length estimators for characterizing multiphase systems using polyenergetic x-ray absorptiometry, *Soil Sci.*, 167(11), 703-719, 2002.
- Hill, E. H. III, *User's Manual for V2.0 of the CMR X-ray Attenuation Analysis Programs*, Unpublished Report, Center for Multiph. Res., Dept., Env. Sci. Eng., Univ. N. Carolina, Chapel Hill, NC, 2001.
- Illangasekare, T. H., J. L. Ramsey Jr., K. H. Jensen and M. B. Butts, Experimental study of movement and distribution of dense organic contaminants in heterogeneous aquifers, *J. Contam. Hydrol.*, 20, 1-25 1995.
- Imhoff, P.T., P.R. Jaffe, and G.F. Pinder, An experimental study of complete dissolution of a nonaqueous phase liquid in saturated porous media, *Water Resour. Res.*, 30(2), 307-320, 1993.
- Imhoff, P.T., G.P. Thyrum, and C.T. Miller, Dissolution fingering during the solubilization of nonaqueous phase liquids in saturated porous media 2. Experimental observations, *Water Resour. Res.*, 32(7), 1929-1942, 1996.

- Mackay, D., W.Y. Shiu, A. Maijanen, and S. Feenstra, Dissolution of non-aqueous phase liquids in groundwater, *J. Contam. Hydrol.*, 8, 23-42, 1991.
- Mercer J.W., and R.M. Cohen, A review of immiscible fluids in the subsurface: properties, models, characterization and remediation, *J. Contam. Hydrol.*, 6, 107-63, 1990.
- Miller, C.T., M.M. Poirer-McNeill, and A.S. Mayer, Dissolution of trapped nonaqueous phase liquids: Mass transfer characteristics. *Water Resour. Res.*, 26(11), 2783-2796, 1990.
- Nambi, I.M., and S.E. Powers, NAPL dissolution in heterogeneous systems: an experimental investigation in a simple heterogeneous system. *J. Contam. Hydrol.*, 44, 161-184, 2000.
- Parker, J.C., and E. Park, Modeling field-scale dense nonaqueous phase liquid dissolution kinetics in heterogeneous aquifers, *Water Resour. Res.*, 40, W05109, doi:10.1029/2003WR002807, 2004.
- Powers, S.E., L.M. Abriola, and W.J. Weber Jr., An experimental investigation of nonaqueous phase liquid dissolution in saturated subsurface systems: Steady state mass transfer rates, *Water Resour. Res.*, 28(10), 2691-2705, 1992.
- Powers, S.E., L.M. Abriola, and W.J. Weber Jr., An experimental investigation of nonaqueous phase liquid dissolution in saturated subsurface systems: Transient mass transfer rates, *Water Resour. Res.*, 30(2), 321-332, 1994.
- Powers, S.E., I.M. Nambi, and G.W. Curry Jr., Non-aqueous phase liquid dissolution in heterogeneous systems: Mechanisms and a local equilibrium modeling approach, *Water Resour. Res.*, 34(12) 3293-3302, 1998.
- Pruess, K., and A. Battistelli, *TMVOC, a numerical simulator for three-phase non-isothermal flows of multicomponent hydrocarbon mixtures in saturated-unsaturated heterogeneous media*, Report LBNL-49375, Lawrence Berkeley National Laboratory, Berkeley, CA, 2002.
- Saba, T. And T.H. Illangasekare, Effect of groundwater flow dimensionality on mass transfer from entrapped nonaqueous phase liquid contaminants. *Water Resour. Res.*, 36(4), 971-979, 2000.
- Saenton, S., and T.H. Illangasekare, Upscaling of mass transfer rate coefficient for the numerical simulation of dense nonaqueous phase liquid dissolution in heterogeneous aquifers, *Water Resour. Res.*, 43, W02428, doi:10.1029/2005WR004274, 2007.
- Sakaki, T., M. Komatsu, and A. Limsuwat, *Physical and hydraulic properties of silica sands for laboratory experiment, Version 3.1 (4/3/2007)*, Unpublished Report, Center for Experimental Study of Subsurface Environmental Processes (CESEP), Colorado School of Mines, Golden, CO, 2007.

SIMULATION OF DNAPL INFILTRATION INTO GROUNDWATER WITH DIFFERING FLOW VELOCITIES USING TMVOC COMBINED WITH PETRASIM

Katharina Erning¹, Dirk Schäfer¹, Andreas Dahmke¹, Antonella Luciano², Paolo Viotti², Marco Petrangeli Papini³

¹Christian-Albrechts-University of Kiel, Department of Applied Geology
Ludewig-Meyn-Strasse 10, D-24118 Kiel, Germany
e-mail: erning@gpi.uni-kiel.de

²Sapienza University of Rome, Department of Hydraulics, Transportations and Roads
Via Eudossiana 18, I-00184 Rome, Italy
e-mail: antonella.luciano@uniroma2.it

³Sapienza University of Rome, Department of Chemistry
P. le Aldo Moro 8, I-00185 Rome, Italy

ABSTRACT

The aim of this work is to simulate the infiltration of DNAPL into fully water saturated media with differing groundwater flow velocities. A 2D-model, $5.00 \times 0.12 \times 0.50 \text{ m}^3$, (LxWxH) was created using TMVOC (Pruess and Battistelli, 2002) combined with PetraSim 4.2 (Thunderhead Engineering, 1999–2008). Three laboratory experiments were conducted in order to calibrate the model regarding capillary pressure and relative permeabilities. At flow velocities ranging from 0 m/s to 4.73×10^{-4} m/s two litres of the DNAPL HFE-7100 were infiltrated within 6000s and monitored over a total time of 24,000 s. In all three simulations, the DNAPL forms a pool on top of the impermeable layer, but the traveling time to reach the layer, as well as the position of the pool in relation to the infiltration point, differs with increasing flow velocities. Moreover, maximum DNAPL saturations within the pool decrease with increasing water flow.

The results from this work indicate that high groundwater flow velocities can influence the distribution of DNAPLs with respect to position and size—which can have a huge impact on source zone architecture, exploration strategies for contaminant sources, and remediation of contaminated industrial sites.

INTRODUCTION

Chlorinated solvents like trichloroethylene (TCE) and tetrachloroethylene (PCE) are among the most widespread groundwater contaminants worldwide. Due to their physicochemical properties (low viscosity, low water solubility, high density, and high toxic potential), they pose a significant threat to the environment. When TCE or PCE are released into the subsoil, they preferentially move downwards through the vadose zone as a distinct phase. When reaching the water table, the DNAPL accumulates until it exceeds the entry pressure and continues (under average flow conditions) its downward motion until it reaches an impermeable layer, on which it will spread according

to the inclination. However, in gravel-sandy aquifers in the foothills of mountain ranges, or in aquifers influenced by, for example, active pump and treat remediation actions, average groundwater flow velocities of 1 m/day can be exceeded.

Although a great deal of research has focused on the subject of DNAPL migration in the saturated zone with respect to large- and small-scale heterogeneities (Bradford et al., 2003; Broholm et al., 2005; Fagerlund, 2006; Illangasekare et al., 1995; Jawitz et al., 2005; Kueper and Frind, 1988; Page et al., 2007; Saenton et al., 2002), dissolution (Falta, 2003; Falta et al., 2005; Fure et al., 2006; Zhu and Sykes, 2000) and mass flux (Illangasekare et al., 2006; Jellali et al., 2003; Soga et al., 2004), there has not yet, as far as the authors know, been a distinct focus on the behavior of DNAPLs under different and/or high flow velocities. According to Sale and McWhorter (2001), who analyzed analytically and numerically the sensitive parameters for mass transfer of a DNAPL source zone, one of the key parameters is the geometry and orientation of the DNAPL source zone within the water flow, which determine its persistence. Therefore, we want to analyze to what extent the geometry and the position of a DNAPL source zone depends on groundwater flow velocities.

The work presented here is the first one in a series of experiments and simulations that deal with the spreading behavior of DNAPL under high groundwater flow velocities. Three small-scale ($<1 \text{ m}^2$) laboratory experiments were performed to provide the primary dataset to calibrate the multiphase flow model in TMVOC (combined with PetraSim) on a small scale. Furthermore, based on these first experiments and simulations, the model was extrapolated to a slightly larger scale (3 m^2) to observe the spreading behavior of the DNAPL on an impermeable horizontal layer as a result of high groundwater flow velocities. The laboratory experiments were conducted at the La Sapienza University of Rome, Italy; the modeling was performed at the Christian-Albrechts-University of Kiel, Germany.

METHODS

Experimental Setup

Luciano et al. (2009, submitted) performed three 2D-laboratory experiments. The size of the tank used in the experiment was 1.33 m x 0.12 m x 0.70 m (L x W x H), with in- and outflow chambers at both sides, separated by filter gravel and stainless steel meshes from the porous media to provide constant hydraulic gradients.

The tank (Figure 1) was filled with coarse glass beads (Table 1) to a height of 0.60 m. Two low permeable lenses of finer glass beads 0.03 m heights are installed at heights 0.19 m and 0.30 m, respectively. The infiltration point was set at 0.14 m below the water table, at an offset of 0.40 m from the inflow.

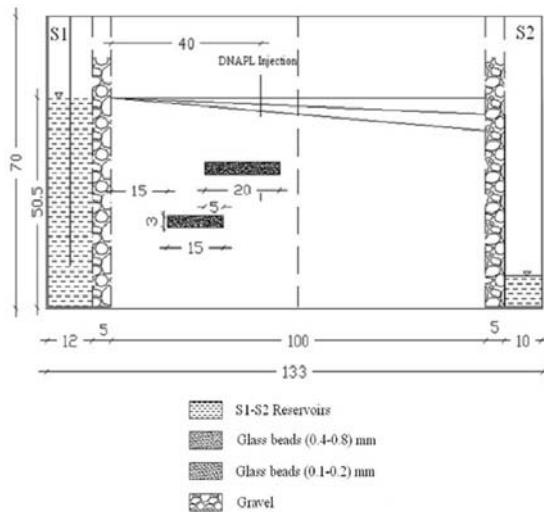


Figure 1. Experimental setup (Luciano et al., 2009)

Table 1. Material parameters of the artificial porous media

	Glass beads 1	Glass beads 2
Size [mm]	0.4-0.8	0.1-0.2
Porosity	0.388	0.373
Specific weight [kg/m ³]	2500	2500
Bulk density [kg/m ³]	1530	1570
Intrinsic permeability, horizontal [m ²]	2.4*10 ^{-10*}	(8.5*10 ^{-15**})
Intrinsic permeability, vertical [m ²]	1.94*10 ^{-10*}	(8.5*10 ^{-15**})

*calculated

** defined as impermeable for simulations

Within each experiment, the chosen water level and hydraulic gradient were kept constant by fixed hydraulic heads, using a constant inflow-water level and a weir at the outflow. The different flow regimes were installed prior to DNAPL infiltration, and steady-state conditions were controlled by a flow

meter attached to the outflow of the tank. The pore velocities (v_{water}) are listed in Table 2. The front side of the tank was made of glass for enabling an image-analysis visualisation of the dyed DNAPL migration.

Table 2. Pore velocities of water (v_{water}) of Experiments 1-3

	v_{water} [m/s]	v_{water} [m/d]
Experiment 1	0	0
Experiment 2	2.46*10 ⁻⁴	21.25
Experiment 3	4.73*10 ⁻⁴	40.86

Infiltrated DNAPL

Due to the toxic properties of TCE (carcinogenic, narcotic, damage to the nervous system (European Commission-European Chemicals Bureau, 2000)) the nontoxic substitute hydrofluorether HFE-7100 (3M, 2005), featuring similar physico-chemical properties as TCE, was used. HFE-7100, a colourless liquid, was dyed with sudane blue to allow visualisation, resulting in a slightly altered density of 1,480 kg/m³ instead of 1,500 kg/m³ of the pure component HFE-7100. As can be seen in Table 3, density, viscosity and the interfacial tension of HFE 7100 reflects the physical properties of TCE appropriately.

Table 3. Physico-chemical properties of HFE-7100 compared to TCE

Property	HFE-7100	TCE
Chemical formula	C ₄ F ₉ OCH ₃	C ₂ HCl ₃
Relative density [kg/m ³]	1500 / 1480 (dyed)	1464
Relative viscosity [cP]	0.6	0.59
Surface tension [mN/m]	13.60	29.30
Interfacial tension [mN/m]	35.59	34.50
Vapour Pressure [kPa]	28.00	7.73
Water solubility [ppm]	12	1100

Differences in vapor pressure and water solubility can be neglected in the chosen experimental setup.

Infiltration procedure

Infiltration took place through a glass tube installed at a depth of 0.14 m below the water table. The tube was equipped with a spill in order to infiltrate with constant hydraulic head. It was connected via a peristaltic pump with a storage tank, containing 2 liters HFE-7100, keeping the tube constantly filled to the spill point. Thus, the hydrostatic head of the infiltrated DNAPL was kept constant, resulting in an inactive infiltration process without additional pressure, and thus resembling a natural seepage process. The time needed to infiltrate the total volume of 2 liters changed significantly from Experiment 1 to 2 and 3, because the higher the hydraulic gradient within the porous media, the

higher the speed of natural seepage into the water saturated media—that is, the advective flow of the water promoted the lateral and vertical spreading of the DNAPL). Table 4 lists the seepage times and the overall times of the experiments.

Table 4: Infiltration and spreading times

Experiment	1	2	3
Seepage time [s]	5905	3690	1580
Spreading time [s]	10217	1890	4325
Total time [s]	16122	5580	5905
Total time [h]	4.48	1.55	1.64

Image analysis procedure

The tank was kept at constant illumination, and every 5 seconds a photo was taken from a fixed position. Thus, it was possible to track the spatial and temporal distribution of the DNAPL during infiltration and redistribution processes. Documentation ended when there was no visible change in the DNAPL distribution over a period of 10 consecutive pictures. Details of the image analysis procedure will be presented by Luciano et al. (2009, submitted).

Conceptual model and calibration procedure

The size of the calibration model was $1.00 \text{ m} \times 0.12 \text{ m} \times 0.60 \text{ m}$ ($L \times W \times H = x, y, z$) with a resolution of 75 cells in x -, 1 cell in y -, and 44 cells in z -direction, creating a 2D – model domain of 3,300 cells, with a high resolution (1 cm^2) zone in the surrounding of infiltration point and lenses, and low resolution (max. 4 cm^2) at the margins (Figure 2). Based on the simulation results, the geometrical configuration of the laboratory experiments was modified from its original design. The physical properties of the glass beads were used in the simulations (see Table 1).

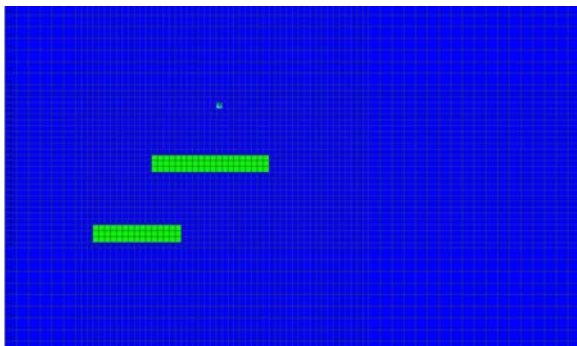


Figure 2: Model domain and discretization in TMVOC, impermeable lenses in green, injection point in light blue

The model was initialized as a fully water-saturated media without an unsaturated zone. First-order boundary conditions with constant water pressure and water saturation were chosen for the in- and outflow of the model domain. The upper side of the model was defined as a no-flow boundary, as well as the

bottom of the domain, thus representing a confined aquifer, although the aquifer in the laboratory experiments was unconfined. This simplification was chosen because infiltration in the laboratory experiments took place below water level, and the simulation of a capillary fringe on cm^2 scale would be excessively runtime consuming and of no interest for this investigation.

Different sets for capillary pressure and relative permeability were tested during the calibration process. The parameters for capillary pressure and relative permeability were chosen according to Parker's three-phase formulation for capillary pressure (Parker and Lenhard, 1987; Pruess and Battistelli, 2002) and Stone's three-phase formulation for relative permeability (Stone, 1970), because spreading behavior could be reproduced best by this set.

Extrapolation to 5 m scale

Based on the calibration, the model domain and setup were adapted to assess DNAPL spreading behavior in a horizontal impermeable layer on a larger spatial and temporal scale, due to high flow velocities.

The domain was elongated to a total length of 5.00 m. The resolution was 90 cells in length ($20 \times 0.10 \text{ m}$, $50 \times 0.02 \text{ m}$, $20 \times 0.10 \text{ m}$), 1 cell in width and 30 cells ($30 \times 0.10 \text{ m}$) in height, resulting in a high-resolution zone in the center of the model. The porous media was defined as homogeneous without lower permeable lenses, corresponding to the coarse glass beads of the laboratory experiment 1 (see. Table 1). The hydraulic gradients, identically to Experiments 1–3, were kept constant via first-order boundary conditions at the left and right model domain for each simulation run, resulting in the same water pore velocities as in Experiments 1–3 (see Table 2). The injection point for the DNAPL HFE-7100 was set at 2.50 m from the inflow, 0.17 m below the water table.

Over a period of 6000 s (1.67 h), a total volume of 3.05 liters HFE-7100 was infiltrated, corresponding to an infiltration rate of $5.08 \times 10^{-4} \text{ kg/s}$. After injection, the simulation was run for an additional 5 hours' simulation time to observe the spreading behavior on the bottom of the aquifer, resulting in an overall simulation time of 6.67 hrs.

RESULTS

Calibration

The chosen formulations for relative permeability (Stone's 3-Phase) and for capillary pressure (Parker's 3-Phase) were adapted manually to fit the photo-documented spreading behavior. Thus, the one set of parameters fitted the temporal behavior of all three

experiments, i.e., it was valid for the flow velocity range from 0 m/s up to 4.73×10^{-4} m/s. The fitted parameters are listed in Table 5, with S_{wr} being the residual water saturation, S_{nr} residual NAPL saturation, S_{gr} residual gas saturation, with n , α_{gn} and α_{nw} as scaling factors.

Table 5. Determined parameters for capillary pressure and relative permeability

	Relative permeability (Stone's 3-Phase)	Capillary pressure (Parker's 3-Phase)
S_{wr}	0.1	-
S_{nr}	0.1	-
S_{gr}	0.0	-
n	2.5	2.5
S_m	-	0.1
α_{gn}	-	100
α_{nw}	-	50

Calibration results were crosschecked with every documented time step for all three experiments and are shown as examples in Figure 3 for Experiment 2 (pore velocity 2.46×10^{-4} m/s) at $T=3690$ s.

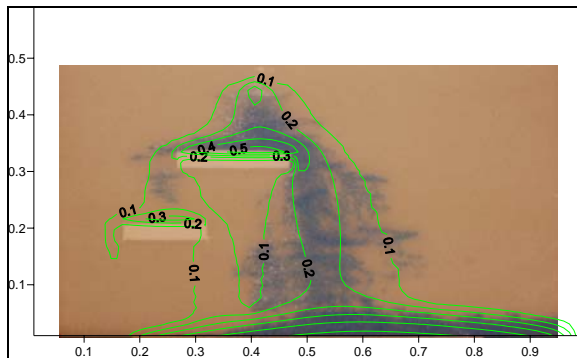


Figure 3. Area of interest of laboratory experiment 2 overlaid by results of model calibration (isolines showing modeled DNAPL saturation) at $T=3690$ s

Extrapolation 5 m scale: Simulation 1–no flow

Under no-flow conditions, the DNAPL moves down vertically without distortion within the homogeneous medium. At 1,800 s, it reaches the bottom of the model domain. Saturation ranges from 0.05 at the margins to 0.25 around the infiltration point. It starts to accumulate on top of the aquitard, reaching DNAPL saturations of $SO=0.25$ at 2100 s (Figure 4a).

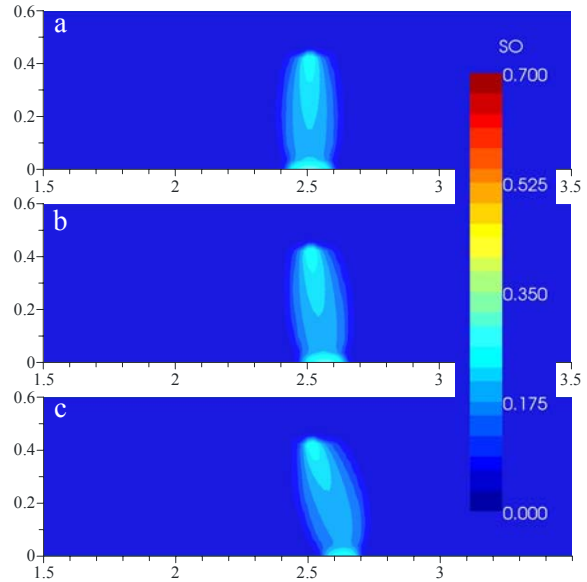


Figure 4. DNAPL saturation (SO) after 2100s for simulation 1-3 (a-c), scale in [m]

Within the percolation zone, the DNAPL saturation is below 15%, while a pool forms at the bottom. At 3,000 s, the pool reaches an overall length of 0.50 m with saturation up to 50%, spreading symmetrically below the infiltration point.

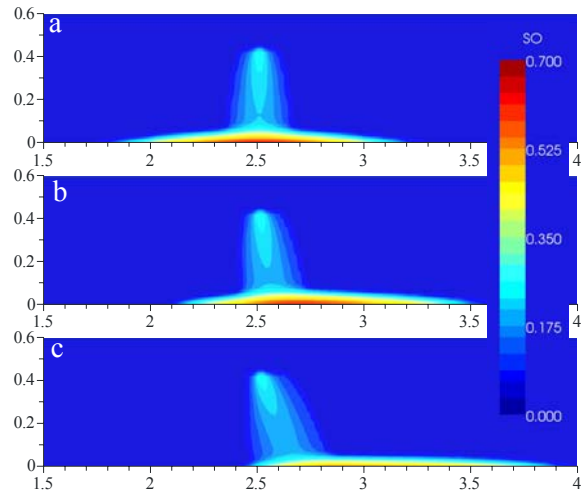


Figure 5. DNAPL saturation (SO) after 6000s for Simulations 1–3 (a-c), scale in [m]

After 6000 s (Figure 5a) the maximum DNAPL concentration of 66% is reached in the center of the pool, which spreads over a total length of 1.38 m.

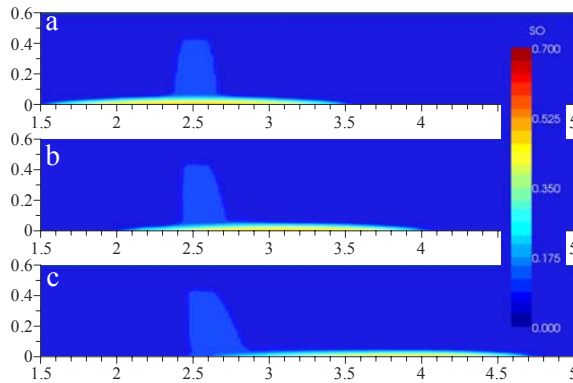


Figure 6: DNAPL saturation (SO) after 9000s for simulation 1-3 (a-c), scale in [m]

After the end of infiltration at $T=6000$ s, the DNAPL spreads further on the bottom (Figure 6a) due to gravitation and capillary pressure, thus elongating and reducing its saturation. The trend continues until the pool obtains its maximum length of 3.28 m at 24,000 s with a maximum saturation of $SO=0.42$. The flow path below the infiltration point remains at a residual saturation of $SO = 0.05-0.10$.

Extrapolation 5 m scale: Simulation 2—pore velocity 2.46×10^{-4} m/s

In the intermediate flow field scenario (2.46×10^{-4} m/s = 21.25 m/day), the DNAPL reaches the bottom of the model domain within the first 1800 s. Compared to Simulation 1, it is distorted by $\sim 10^\circ$ of the strict vertical movement, which was observed under no-flow conditions. The distribution of saturation ranges at $T=2100$ s between $SO = 0.30$ in the center of the beginning pool and $SO = 0.05$ at the outer margins (Figure 4b).

At $T=3000$ s, the center of DNAPL pool with $SO_{\max}=0.50$ has a downstream offset of 0.06 m compared to Simulation 1. Maximum saturations of $SO=64\%$ are reached at the end of infiltration at $T=6000$ s (Figure 5b), while the pool spreads over a length of 1.45 m. During the ongoing spreading under steady flow field (Figure 6b), the DNAPL reaches the right-side boundary with flow velocities of $v_{\text{DNAPL}}=6.67 \times 10^{-5}$ m/s at $T=18,000$ s, thus it is not further possible to assess the complete length. At this time, the DNAPL forms a pool of $L=3.05$ m with $SO_{\max}=0.35$. Compared to Simulation 1, the pool has a downstream offset of 0.88 m. During the next 6000 s simulation time, there is no change in the spatial distribution, only in the degree of saturation, dropping from 35% to 25% until $T=24,000$ s.

Extrapolation 5 m scale: Simulation 3—pore velocity 4.73×10^{-4} m/s

In the third simulation, high pore velocities of 4.73×10^{-4} m/s (40.87 m/day) were incorporated. During infiltration, the DNAPL gets deflected by 15°

compared to Simulation 1. After 1800 s, it achieves a vertical travel distance of 0.41 m compared to 0.43 m in Simulations 1 and 2. Domain bottom is reached within the next 300 s, thus starting to form a pool at $T=2100$ s (Figure 4c). The pool has a downstream offset of 0.16 m compared to Simulation 1 and of 0.08 m compared to Simulation 2, respectively. Saturation increases to 32% in the center of the pool. At $T=3000$ s the pool reaches a length of 0.54 m and maximum DNAPL saturation of 45%.

At the end of the infiltration process, maximum DNAPL concentrations of $SO=0.58$ are reached. At $T=6000$ s (Figure 5c), the lateral extension of the pool is 1.55 m, thus 10 cm longer than the pool in Simulation 2 and 17 cm longer than in Simulation 1 at the same time. During the time after the infiltration, the DNAPL moves downstream (Figure 6c) with mean DNAPL-flow velocities of $v_{\text{DNAPL}}=1.05 \times 10^{-4}$ m/s.

The end of the model domain is reached at $T=12,000$ s, and the DNAPL obtains its maximum assessable elongation of 2.63 m. Within the next 12,000 s, there is no change in the lateral distribution of the NAPL, but the center of highest saturation within the pool moves downstream.

DISCUSSION

Calibration

Calibration showed that at given material and hydraulic properties, two key parameters for the spreading behavior of the DNAPL exist: (1) the intrinsic permeability and (2) the relative permeability-saturation formulation. While the first one can be measured experimentally and recalculated from the Darcy flow of water, respectively, the relative permeability function is harder to obtain. The capillary pressure function has to be adapted in the following, after the fitting of the relative permeability.

As can be seen in Figure 3, there are small differences between the results of the laboratory experiment and the model calibration. For example, the DNAPL of the simulation passes the first lense in larger amounts on the upstream side, thus resulting in lower DNAPL concentration in the downstream area. This can be explained mainly by the fact that the porosity and permeability of the coarse sand are homogeneously distributed in the model, while in reality there are always small-scale heterogeneities due to the filling process of the tank, creating preferential flow paths within the medium. Secondly, between experiment and simulation, there are small differences in the geometry of infiltration point and fine sand lenses, due to the discretization of the model, influencing the distribution of the DNAPL.

Thirdly, it is possible that the DNAPL within the laboratory experiments are distributed irregularly over the tank width, while in the 2D model there is no distribution in depth. However, considering all other time steps and experimental setups, there is a good agreement between observation and simulation results.

5 m scale: Simulations 1–3

As can be seen in Figures 4–6, there are broad differences in the spreading behavior of a DNAPL under different flow velocities. Table 6 shows a summary of the main differences.

The major aspect is the distortion within the percolation zone from the strict vertical movement. This downstream offset is further enhanced by the DNAPL flow velocities, which show a clear dependence on water flow velocities. In Simulation 2, the DNAPL flow velocities increase by a factor of 1.7, in Simulation 3 by a factor of 2.7, in comparison to the case scenario of Simulation 1. The maximum lateral extension of the DNAPL pool cannot be obtained for the different simulations, because the length of the model domain restricts the assessment. However, the drop in maximum DNAPL saturation from Simulation 1 to 3 implies an increasing pool length by increasing water flow velocities.

Table 5: Main differences between Simulations 1-3

Simulation	1	2	3
V_{water} [m/s]	0	$2.46 \cdot 10^{-4}$	$4.73 \cdot 10^{-4}$
V_{DNAPL} [m/s]	$3.88 \cdot 10^{-5}$	$6.68 \cdot 10^{-5}$	$1.05 \cdot 10^{-4}$
Distortion	0°	10°	15°
Downstream offset at T=6000s [m]	0	0.06	0.16
Downstream offset at T=24000s [m]	0	1.08	1.50
Pool length [m]	3.28	(> 3.05)	(> 2.63)
Max. DNAPL saturation	0.66	0.64	0.58

The limitations of the simulations lie in the simplification of the stratum, the small scale of the model domain, and the specific end-time of the simulations instead of conducted steady-state simulations as well as in the very high water flow velocities up to 40.87 m/day. However, the results imply that in a real case, scenario changes in spatial distribution, DNAPL saturation, and geometry of the source zone should be expected.

CONCLUSION

The results show the influence of high groundwater flow velocities on the distribution of DNAPLs in the saturated zone. The effects of distortion during infiltration seem to be small within these simulations, resulting in a downstream offset of 0.06 m and 0.16 m, respectively. However, these effects will be of greater importance in a real case scenario with an aquifer thickness of, for example, 50 m, resulting in a downstream offset of ~15 m. One potential impact for remediation would be that a larger area must be investigated to detect the DNAPL source zone. In case of a direct chemical oxidation method, heat treatment, or excavation used for remediation, a larger contaminated aquifer volume has to be treated. Moreover it is possible that pump and treat or reactive barrier installation are passed by DNAPLs as a distinct phase.

Further research will focus on realistic aquifer geometries, the physical properties concerning heterogeneous permeabilities, and mass flux rates from the source zone in relation to groundwater flow velocities.

ACKNOWLEDGEMENT

The research leading to these results has received funding from the European Community's Seventh Framework Programme (FP7/2007-2011) under grant agreement n 213161 (ModelPROBE).

REFERENCES

- 3M, *3M NOVEC TM 7100 - Engineered fluid. Product information*, St. Paul, MN, USA, 2005.
- Bradford, S. A., K. M. Rathfelder, J. Lang and L. M. Abriola, Entrapment and dissolution of DNAPLs in heterogeneous porous media, *Journal of Contaminant Hydrology*, 67, 133-157, 2003.
- Broholm, K., S. Feenstra and J. A. Cherry, Solvent release into a sandy aquifer. 2. Estimation of DNAPL mass based on a multiple-component dissolution model, *Environ. Sci. Technol.*, 39(1), 317-324, 2005.
- European Commission - European Chemicals Bureau, *IUCALID DATASET: SUBSTANCE ID: 79-01-6: Trichloroethylene*, European Commission - European Chemicals Bureau, European Commission, 2000.
- Fagerlund, F., *Experimental and modelling studies on the spreading of non-aqueous phase liquids in heterogeneous media*, Dissertation, Uppsala Universitet, Uppsala, 2006.

- Falta, R. W., *Simulation of subgridblock scale DNAPL pool dissolution using a dual domain approach*, Lawrence Berkeley National Laboratory, Berkeley, California, 2003.
- Falta, R. W., N. Basu and P. S. Rao, Assessing impacts of partial mass depletion in DNAPL source zones: II. Coupling source strength functions to plume evolution, *Journal of Contaminant Hydrology*, 79(1-2), 45-66, 2005.
- Fure, A. D., J. W. Jawitz and M. D. Annable, DNAPL source depletion: Linking architecture and flux response, *Journal of Contaminant Hydrology*, 85(3-4), 118-140, 2006.
- Illangasekare, T. H., J. Munakata Marr, R. L. Siegrist, K. Soga, K. C. Glover, E. Moreno-Barbero, J. L. Heiderscheidt, S. Saenton, M. Matthew, A. R. Kaplan, Y. Kim, D. Dai and J. W. E. Page, *Mass transfer from entrapped DNAPL sources undergoing remediation: Characterization methods and prediction tools*, SERD Project No. CU-1294, Colorado School of Mines, 2006.
- Illangasekare, T. H., J. L. Ramsey, K. H. Jensen and M. B. Butts, Experimental study of movement and distribution of dense organic contaminants in heterogeneous aquifers, *Journal of Contaminant Hydrology*, 20(1-2), 1-25, 1995.
- Jawitz, J. W., A. D. Fure, G. G. Demmy, S. Berglund and P. S. C. Rao, Groundwater contaminant flux reduction resulting from nonaqueous phase liquid mass reduction, *Water Resour. Res.*, 41, 2005.
- Jellali, S., H. Benremita, P. Muntzer, O. Razakarisoa and G. Schäfer, A large-scale experiment on mass transfer of trichloroethylene from the unsaturated zone of a sandy aquifer to its interfaces, *Journal of Contaminant Hydrology*, 60(1-2), 31-53, 2003.
- Kueper, B. H. and E. O. Frind, An overview of immiscible fingering in porous media, *Journal of Contaminant Hydrology*, 2(2), 95-110, 1988.
- Luciano, A., P. Viotti and M. Petrangeli Papini, Laboratory investigation of DNAPL migration in porous media, *submitted to Journal of Hazardous Material*, 2009.
- Page, J. W. E., K. Soga and T. Illangasekare, The significance of heterogeneity on mass flux from DNAPL source zones: An experimental investigation, *Journal of Contaminant Hydrology*, 94(3-4), 215-234, 2007.
- Parker, J. C. and R. J. Lenhard, A model for hysteretic constitutive relations governing multiphase flow in porous media. 1. Saturation-pressure relations, *Water Resources Research*, 23(12), 2187-2196, 1987.
- Pruess, K. and A. Battistelli, *TMVOC, a numerical simulator for three-phase non-isothermal flows of multicomponent hydrocarbon mixtures in saturated-unsaturated heterogeneous media*, Report LBNL-49375, Lawrence Berkeley National Laboratory, Berkeley, California, 2002.
- Saenton, S., T. H. Illangasekare, K. Soga and T. A. Saba, Effects of source zone heterogeneity on surfactant-enhanced NAPL dissolution and resulting remediation end-points, *Journal of Contaminant Hydrology*, 59(1-2), 27-44, 2002.
- Sale, T. C. and D. B. McWhorter, Steady state mass transfer from single-component dense nonaqueous phase liquids in uniform flow fields, *Water Resour. Res.*, 37, 2001.
- Soga, K., J. W. E. Page and T. H. Illangasekare, A review of NAPL source zone remediation efficiency and the mass flux approach, *Journal of Hazardous Materials*, 110(1-3), 13-27, 2004.
- Stone, H. L., Probability model for estimating three-phase relative permeability, *Trans. SPE of AIME*, 249, 214-218, 1970.
- Thunderhead Engineering, *PetraSim-Interactive model creation for advanced flow, transport and heat transfer models*, Manhattan, 1999-2008.
- Zhu, J. and J. F. Sykes, The influence of napl dissolution characteristics on field-scale contaminant transport in subsurface, *Journal of Contaminant Hydrology*, 41(1-2), 133-154, 2000.

TMVOC MODELING OF H₂O₂ INJECTION AT AN ISCO PILOT TEST SITE

Michele Carpita^[1], Ivan Innocenti^[2], Nardella Alessandro^[2], Guido Giulia^[1], Alfredo Battistelli^[1]

[1] Environmental Engineering Unit, Saipem SpA, Via Toniolo 1, Fano (PU), 61032, Italy.

[2] Refining & Marketing Division, ENI Spa, Via Ramarini 32, Monterotondo (Roma), 00016, Italy.

e-mail: michele.carpita@saipem.eni.it, ivan.innocenti@eni.it, alessandro.nardella@eni.it,
giulia.guido@saipem.eni.it, alfredo.battistelli@saipem.eni.it

ABSTRACT

TMVOC V.2 was used to predict the performance of a planned pilot soil decontamination test by means of *in situ* chemical oxidation (ISCO) through the injection of an aqueous solution of hydrogen peroxide (H₂O₂). Simulated phenomena include: injection of the hydrogen peroxide aqueous solution in a sandy phreatic aquifer with a thin unsaturated zone; decomposition of H₂O₂; oxygen generation from H₂O₂ decomposition; stripping of VOCs adsorbed onto the soil matrix; containment of the reactive zone with aqueous-phase extraction by means of pumping wells and gas-phase capture through vacuum extraction trenches.

INTRODUCTION

The pilot test site is made of a square flat surface of approximately 100 m² where 12 existing wells are placed along a regular grid, as shown in Figure 1.

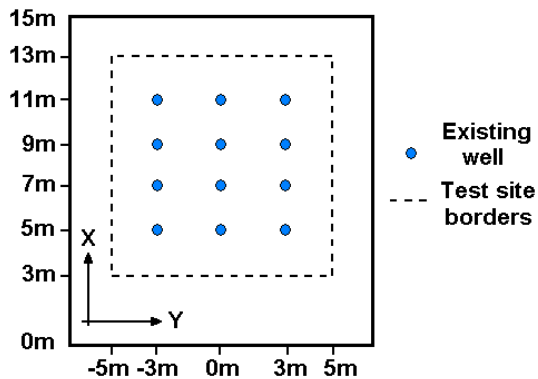
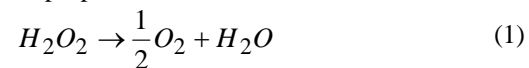


Figure 1. Top view of test site existing elements.

A thin unsaturated zone is present in the first 0.5–0.9 m, depending on the seasonal variations in the water table, and acts as a preferential layer for gas flows inside the formation. The pilot test will be performed by injecting a H₂O/H₂O₂ aqueous solution in a row of three wells in the lower part of the field (bottom in Figure 1), while extracting fluid in the upper (top) part of it from another three-well row. Extraction wells are necessary to control the pressure increase inside the formation, where the natural hydraulic gradient is negligible. A set of vacuum drainage trenches will be arranged around the test field perimeter in order to intercept gases flowing in the unsaturated zone. To avoid gas leakages to the

atmosphere, an impermeable capping will be placed aboveground around the injection wells up to the perimeter trenches. The optimal pattern of injection and extraction wells and drainage trenches is strongly dependent on the amount of gas generated in the lower formation levels, where the hydrogen peroxide solution is preferentially injected. Such a gas phase will mostly be made of O₂ generated from the H₂O₂ disproportionation reaction below:



which is an exothermal reaction, with a heat of reaction of 98.3 kJ/mol. The O₂ generation rate will be clearly dependent on the H₂O₂ injected rate.

This system was modeled with TMVOC (Pruess and Battistelli, 2001; Battistelli, 2008), a numerical simulator belonging to the TOUGH2 family (Pruess et al., 1999). Modeling was basically aimed to evaluate the maximum injection rate of hydrogen peroxide solution so as not to increase the water table elevation above ground level. The evolution of gas fluxes produced by the hydrogen peroxide decomposition and VOC stripping was also modeled until the gas flows became negligible.

A preliminary set of simulations was performed to reproduce available experimental results for the H₂O₂ kinetic decomposition constant and H₂O₂/O₂ flows measured in column tests. The experimental data were used to validate the reliability of TMVOC in handling the gas generation from the H₂O₂ disproportionation. These numerical tests were then followed by a set of simulations in 2D radial and 3D Cartesian geometries to evaluate the maximum injection rate and the extent of aqueous and gaseous fronts that will develop within the planned pilot test site.

FIRST-ORDER KINETIC DEGRADATION

The hydrogen peroxide degradation constant was measured by a set of experimental batch tests. An H₂O/H₂O₂ solution of ~8.5% mass concentration was placed in a sealed container, and the peroxide concentration was periodically measured for approximately three days. Results show an exponential decay in H₂O₂ concentration. Selected results from two different tests (Bacocchi et al., 2008) are shown in Figure 2.

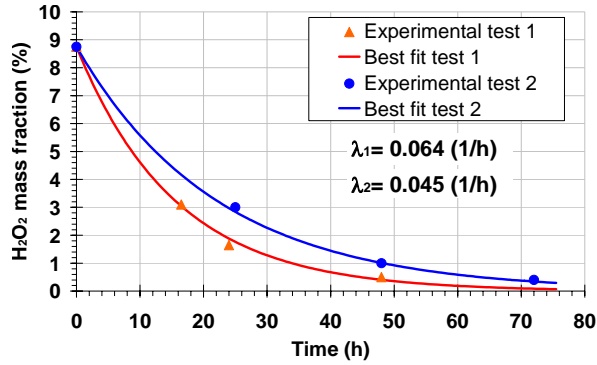


Figure 2. Experimental H_2O_2 degradation batch tests

Such a decay suggests a first-order degradation of the hydrogen peroxide with an average half-life constant of $\lambda_{(1-2)} = 0.057h^{-1} = 1,58 \times 10^{-5} s^{-1}$, which is the value used for the whole set of simulations. Such a value was also confirmed by further batch tests. An additional estimate was performed by using column test values, obtaining a good agreement with the abovementioned experimental values.

Temporal evolution of solute concentration profile

Monod's biodegradation model, already implemented into TMVOC V.2 (Battistelli, 2004), is used to describe the H_2O_2 decomposition reaction. The basic kinetic-rate equation for a solute of concentration C subjected to biodegradation through a bacterial species of concentration B , with no inhibition factors and no electron acceptors, is given by:

$$\frac{dC}{dt} = -\mu_{\max} \frac{C}{K_S + C} B \quad (2)$$

where μ_{\max} is the maximum specific substrate utilization rate. It is possible to describe a first-order degradation process by assuming the emisation constant $K_S \gg C$. Under this hypothesis, Equation (2) becomes:

$$\frac{dC}{dt} = -\frac{\mu_{\max} B}{K_S} C = -\lambda C \quad (3)$$

which can be easily integrated, giving an exponential decay for solute concentration where the first-order degradation constant is defined as:

$$\lambda = \frac{\mu_{\max} B}{K_S} \quad (4)$$

Equation (3) is used to simulate the H_2O_2 decomposition process observed in the lab experiments.

COLUMN TESTS

A set of experimental column tests was performed to study the behavior of the H_2O/H_2O_2 solution when injected into an initial water-saturated porous medium, and to quantify the gas production rate over time. TMVOC was used to perform a set of simulations aimed to reproduce the laboratory results by evaluating petrophysical and reaction parameters controlling the observed processes.

Experimental setup

Four different column tests were performed. In each test, a different packed sandy soil sample (10 cm long and 4.3 cm in diameter) is inserted between two synthetic porous medium layers into a 27 cm long column, as shown in Figure 3.

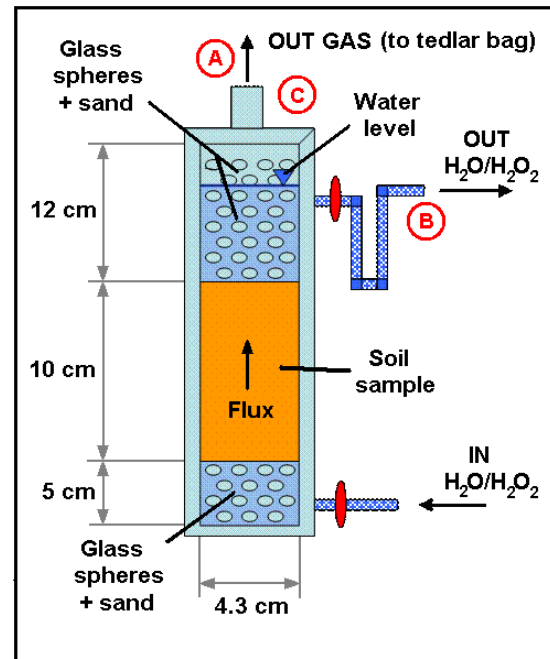


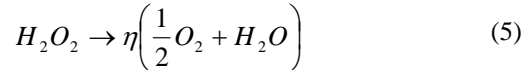
Figure 3. Experimental setup for column tests. H_2O/H_2O_2 solution is injected at the bottom of the column.

The synthetic layers were made of a mix of coarse sand (about 1 mm grain diameter) and glass spheres (1–4 mm in diameter). The column was then filled with water as shown in Figure 3. A Tedlar bag was placed on the top of the column to collect the gases produced during sand pack flooding. The H_2O/H_2O_2 solution was injected from the bottom of the column and was collected at the lateral outlet near the top. In several tests, the injected hydrogen peroxide concentration varied with time, as shown in Table 1 below.

Table 1. Experimental injected flow rates and H_2O_2 concentrations

Test name	Injection rate (mL/min)	H_2O_2 concentration (by mass)	Duration of injection (hours)
Column 1	360	9.0 %	26.5
Column 2	180	5.0 %	1
		7.0 %	1
		9.0 %	24
Column 3	36	1.0 %	1
		3.0 %	4
		6.0 %	20
Column 4	24	2.0 %	7
		4.4 %	16

Experimental data showed that just a fraction of the depleted H_2O_2 actually turned into O_2 , the rest being lost in other chemical reactions. As we focused only on molecular oxygen generation, it was necessary to introduce an O_2 generation efficiency parameter η . As a first-order approximation: (a) we supposed that there was no O_2 generation other than what was produced by the main reaction, and (b) we neglected the heat of reaction associated with other reactions consuming H_2O_2 . Those assumptions turned into the following reaction:



with a heat generation of $\eta 98.3 \text{ kJ/mol}$. Table 2 below lists the experimental evaluated values for the reaction efficiency η .

Table 2. Measured O_2 generation efficiency

Test name	Total gas collected (mL)	O_2 (volume fraction)	O_2 generation efficiency
Column 1	4480	70.3 %	16 %
Column 2	2632	44.0 %	6 %
Column 3	4032	78.6 %	37 %
Column 4	3360	76.6 %	40 %

Column test results and TMVOC simulations

TMVOC simulations were aimed to replicate three main experimental data provided by the tests, namely:

- Cumulative gas volume produced in the sample (“A” in Figure 3). Tedlar bag gas volume was measured from the beginning of the test to about 4 days after the end of the injection phase, so as to collect gases produced by the decomposition of residual H_2O_2 inside the column;

- H_2O_2 concentration profile at the outlet for the whole duration of the injection phase (“B” in Figure 3). Steady-state conditions were reached early after each injected concentration change: TMVOC simulations aimed especially to replicate the average peroxide concentration during such a steady-state phase;
- Time profile of O_2 rate flowing from the column into the Tedlar bag (“C” in Figure 3). The molecular oxygen contribution was calculated by scaling down the whole measured gas rate (which included gases other than O_2) by the O_2 total volume contribution in the Tedlar bag at the end of the test. Such a calculation is nevertheless an approximation, because it is implicitly assumed that O_2 is produced with a constant ratio compared to the other gases for the whole duration of the test. This could not be always true, especially in the first hours of fluxing, as shown in detail below.

The simulations were performed with a 1D vertical grid replicating the experimental apparatus of Figure 3. It must be remembered that only H_2O_2 degradation in O_2 and water is simulated. Injection rate and O_2 generation efficiency were mostly set according to the results of Tables 1 and 2.

Soil petrophysical properties were as follows: effective porosity was estimated to be around $\phi=0.25$, average permeability was measured as approximately $K=1,73 \times 10^{-11} \text{ m}^2$. Irreducible gas and water saturation were estimated to be around $S_{wr}=0.20$ and $S_{gr}=0.04$ respectively, based on analogous soil rock properties. The relative permeability curve for the aqueous phase was described according to van Genuchten’s model, with exponent $m=0.520$, while Corey’s model (Corey, 1954) was used for the gas phase. The capillary pressure was also described with a van Genuchten’s model (van Genuchten et al., 1980) whose parameters are $\lambda=0.532$, $S_{wr}=0.0738$, $P_{c0}=693.0 \text{ Pa}$.

The synthetic soil hydraulic properties were estimated from grain-size distribution by means of the RETC code (van Genuchten et al., 1991). Parameters similar to those of a coarse sand were initially estimated, namely $m=0.80$, $S_{wr}=0.10$, $\phi=0.30$ and permeability $K=4.0 \times 10^{-11} \text{ m}^2$. Given the fact that each artificial soil was different in every column test, such average initial values were slightly changed for each TMVOC simulation.

Experimental and simulated data showed an acceptable agreement, as can be seen in Figure 4, which represents some selected results.

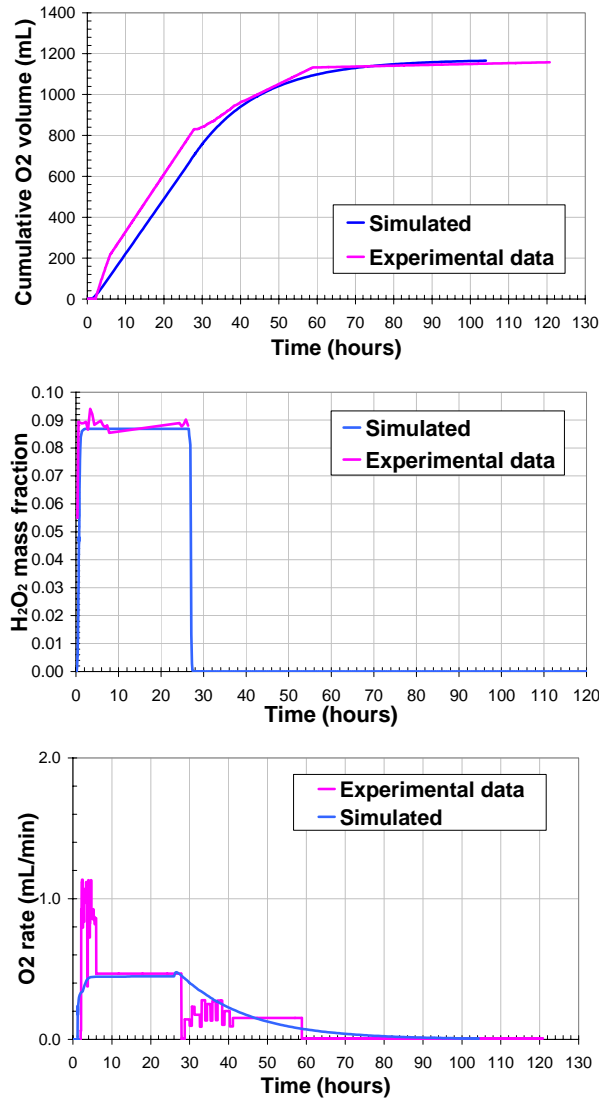


Figure 4. Selected comparisons between experimental and simulated data. From top to bottom: a) Cumulative collected O₂; b) H₂O₂ concentration in the aqueous phase at column outlet; c) O₂ rate profile entering the tedlar bag.

It must be noted that the simulated gas rate shown in Figure 4c does not replicate the large gas spike observed in all the experimental tests in the first 3–6 hours of fluxing. The spike is likely due to O₂ and other gases generated by a secondary H₂O₂ degradation process whose identification is still ongoing. Such a spiked shape at the beginning of injection also suggests the depletion of a reagent inside the sample. Because of the complications involved in simulating such a process, and because of the fact that such a spike does not significantly contribute to the total gas amount at the end of the test (see Figure 4a), the replication of the gas spike was neglected.

The general expression for the transport equation of a solute moving along a 1D path is:

$$R \frac{\partial C}{\partial t} = D \frac{\partial^2 C}{\partial x^2} - v \frac{\partial C}{\partial x} - R \lambda_n C - \mu_{\max} \left(\frac{C}{K_s + C} \right) B \quad (6)$$

If we assume stationary conditions $\frac{\partial C}{\partial t} = 0$, no hydrodynamic dispersion ($D = 0$), no adsorption ($R = 1$), no biomass growth ($B = 1$) and no natural decay ($\lambda_n = 0$), the expression above becomes:

$$-v \frac{\partial C}{\partial x} - \mu_{\max} \left(\frac{C}{K_s + C} \right) = 0 \quad (7)$$

which describes the 1D transport of a solute affected only by biomass-degradation. By assuming again $K_s \gg C$ and integrating with the condition $C = C_0$ for $x = 0$, we get a simplified form of the analytical solution of Parlange et al. (1984):

$$x = \frac{v}{\mu_{\max}} K_s \ln \left(\frac{C}{C_0} \right) \quad (8)$$

which can also be written as:

$$C = C_0 e^{-\frac{\lambda}{v} x} \quad (9)$$

where, in two-phase steady-state conditions, fluid velocity v can be estimated assuming an average value of the aqueous-phase saturation:

$$v = \frac{q}{A \phi S_w} \quad (10)$$

where q is the injected volumetric rate, A is the column cross section, and S_w is the average water saturation inside the column evaluated with the column tests simulation. By using Equation (10), it is possible to obtain an estimate of the expected H₂O₂ mass fraction at the column outlet. A comparison among the expected values and the measured and simulated ones is shown in Table 3.

Table 3. Comparison among theoretical, experimental, and simulated H₂O₂ concentration at the column outlet.

Test name	H ₂ O ₂ mass fraction at the column outlet		
	Theoretical (Parlange)	Simulated (TMVOC)	Measured
Column 1	8.87 %	8.65 %	8.70 %
Column 2	9.72 %	8.80 %	9.40 %
Column 3	5.24 %	4.95 %	4.80 %
Column 4	4.23 %	3.85 %	3.80 %

Assuming an average constant value for water saturation inside the column it is possible to use equation

(8) to get an additional estimate of λ by using measured H_2O_2 concentrations at the column inlet and outlet when in steady-state conditions. All four column tests give similar values whose average is $\bar{\lambda}_{\text{column}} = 1.628 \times 10^{-5} \text{ s}^{-1}$, which is in agreement with $\lambda_{(1-2)}$ from the experimental batch tests.

2D RADIAL SIMULATIONS

Column test results provided confidence in using TMVOC to predict the performances of the pilot test plant. Preliminary 2D radial simulations were then performed to obtain a sensitivity analysis of pressure buildup around a single injection well. Pressure increase depends on the injected rate of the $\text{H}_2\text{O}/\text{H}_2\text{O}_2$ solution, and it is due to both the higher liquid rate and gas generation. The 2D radial mesh is shown in Figure 5 below.

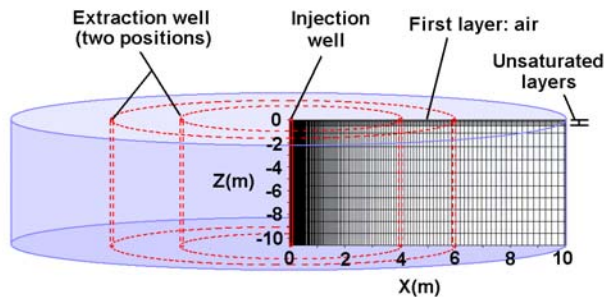


Figure 5. Geometrical model of 2D simulations. The well location and the thin unsaturated zone are highlighted.

The injection well is along the Z axis of the 2D radial grid. Injection is performed between $Z = -0.30 \text{ m}$ and $Z = -5.0 \text{ m}$, according to the actual well completion used. Constant conditions are maintained at the lateral boundary at $X = 10 \text{ m}$. The topmost layer of the formation is maintained at constant atmospheric conditions, assuming pure N_2 instead of air. Initial O_2 concentration was purposely removed from the simulation grid to better evaluate the oxygen generation in the lower layers. Below the atmospheric boundary, the first layers represent the unsaturated zone and are set in two-phase conditions. Below them, fully water-saturated layers represent the phreatic aquifer down to 10 m of depth.

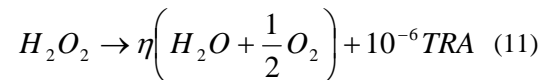
The presence of an extraction well is modelled in an approximate way by placing a constant mass extraction at some distance from the injection well to provide the necessary pressure gradient in the formation. Due to actual test plant constraints, only two possible distances for the injection well were suitable, at $X = 4 \text{ m}$ or $X = 6 \text{ m}$. Extraction elements are placed between $Z = -2.0 \text{ m}$ and $Z = -5.0 \text{ m}$ elevations, according to actual well completions. $\text{H}_2\text{O}/\text{H}_2\text{O}_2$

concentration was set to a constant value of 10% in all 2D simulations, as planned for the pilot test. O_2 generation efficiency was set to $\eta = 20\%$ by averaging the values shown in Table 2.

Soil properties for the whole formation are similar to those already listed for the column test soil samples. Horizontal absolute permeability was the same as for soil samples, while vertical permeability was assumed to be half of this value. Initial water saturation in the unsaturated zone was determined by running the model to capillary-gravity equilibrium.

A preliminary analysis of trench effects was also included in the 2D simulations. A single element at $X = 8 \text{ m}$ on the topmost unsaturated layer is held at constant pressure of $P = 99000 \text{ Pa}$, in order to simulate the draining effect of the extraction trench. The pressure value was chosen to avoid the inflow of the aqueous phase from the fully saturated layers.

The generation and transport of a tracer was also modeled. The tracer is a fictitious product of H_2O_2 decomposition, it has the same molecular weight of water; it is generated in very small concentrations, and it does not partition into the gas phase. The tracer was added by modifying H_2O_2 disproportionation (5) as follows:



The tracer was monitored in order to investigate the area affected by the transport of potential aqueous H_2O_2 reaction by-products.

A sensitivity analysis was performed by varying the injection rate, the extraction rate, and the distance of the extraction wells (both possible extraction well positions were considered), to define the best injection procedures that would prevent the water table from rising to the surface. The thickness of the unsaturated area was modified by changing water table elevation between the highest ($Z = -0.5 \text{ m}$) and the lowest ($Z = -0.9 \text{ m}$) value, according to the seasonal change observed at the pilot test site. In every simulation, the injection phase lasted 27 hours, followed by 72 hours of free evolution, to assure that H_2O_2 was depleted before the end of the run.

Simulation results suggested restricting the maximum injection rate to $q_{\text{inj}} = 15\text{-}20 \text{ m}^3/\text{day}$ when the initial water table level was $Z = -0.9 \text{ m}$, and to $q_{\text{inj}} = 10\text{-}15 \text{ m}^3/\text{day}$ when the initial water table level was $Z = -0.5 \text{ m}$. The lower end of the two above-mentioned ranges is necessary when the extraction well is nearer to the injection point. Figure 6 shows a selected optimum case with an initial water table level of $Z = -0.5 \text{ m}$. The injected rate is $10 \text{ m}^3/\text{day}$ and the extracted rate is $20 \text{ m}^3/\text{day}$, with an extraction well at 6 m from the injection well. This figure shows

the most significant variables plotted at the end of the injection phase (27 hours). In every picture, the red rectangle represents the extraction well, while the small blue rectangle in the top-left corner represents the trench. Dimensions are to scale.

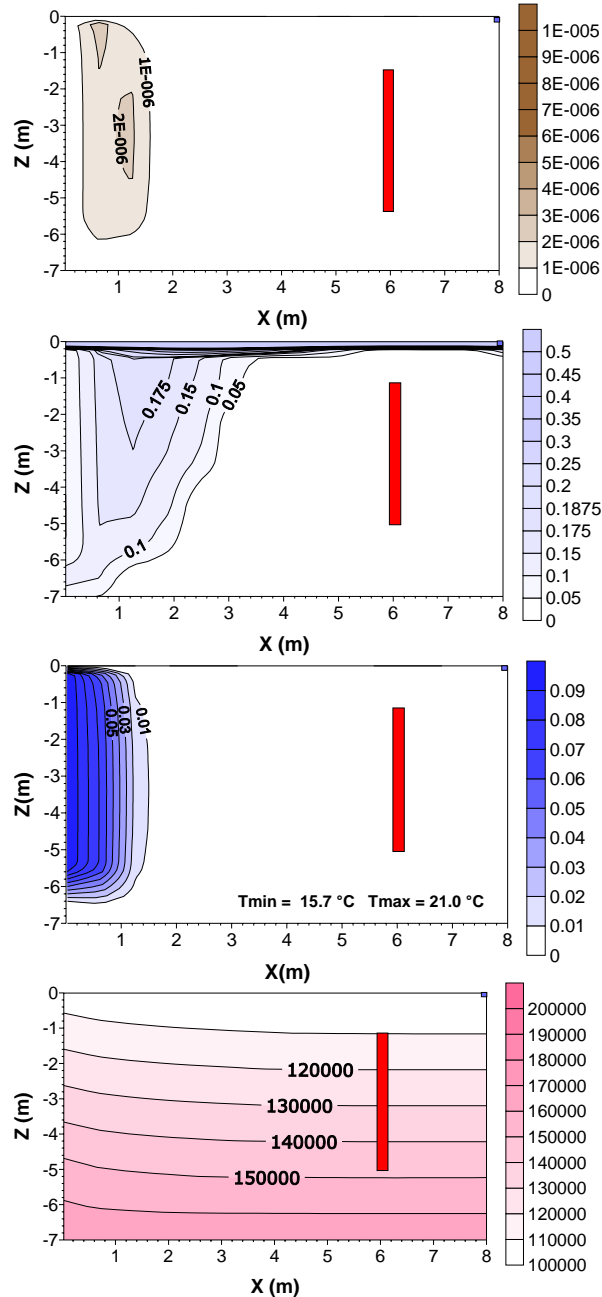


Figure 6. Selected 2D simulation plot with optimum injection and extraction rates. Initial water table level is $Z = -0.5\text{m}$, extraction well is at $X = 6.0\text{m}$. From top to bottom: a) tracer mass fraction; b) O_2 gas saturation; c) H_2O_2 mass fraction; d) pressure (Pa).

Two-dimensional simulations also showed other important results:

- The best distance between injection and extraction wells is 4 m;
- Maximum extraction rate should be limited to $20\text{ m}^3/\text{day}$ for a single extraction well;
- Vacuum trenches should not be placed nearer than 4 m from the injection well in order to optimize gas capture from the lower layers (see Figure 7b);
- Tracer front is mostly coincident with aqueous H_2O_2 front;
- Maximum temperature increase inside the formation due to exothermic H_2O_2 decomposition is limited to $5\text{--}7^\circ\text{C}$. This is also in agreement with the experimental results of the column tests.

3D SIMULATIONS

Results obtained with 2D simulations were implemented in a 3D Cartesian layout whose outline was more similar to the actual pilot site. A set of simulations was then performed. The aim of these 3D simulations was to give an estimate of the temporal and spatial gas evolution inside the formation, and to evaluate the maximum effectiveness range of the water-dissolved H_2O_2 front. In 3D geometry, the problem is symmetrical along the vertical plane, through the X axis along the middle row of wells, so only half of the test area was simulated. The 3D X-Z cross section of the simulation grid is similar to the 2D cross section previously described, while on the horizontal plane, the 3D mesh is thickened close to the injection and extraction wells.

Field dimensions and well positions were set according to the planned pilot test shown in Figure 1, while perimeter vacuum trenches were set according to 2D simulation results. A schematic layout of this 3D mesh is shown in Figure 7. Coloured planes represent the most significant sections from which data are extracted to document different 3D simulation results.

The approach used for 3D simulations was analogous to that used for the 2D radial simulations described above. Soil properties, well completions, layer thickness and initial conditions, duration of injection, and injected fluid composition are the same as the 2D runs, except for the tracer modeling, which was removed. The extraction rate was set to $20\text{ m}^3/\text{day}$; the injection/extraction-well distance to 4 m, and vacuum trenches were placed along the external pilot area perimeter. The presence of n-heptane, mainly adsorbed on the rock matrix, was added to estimate the effects of possible VOC stripping processes induced by O_2 fluxes. N-heptane concentration was constant and set to 7200 ppm with respect to dry rock matrix mass, according to the field data.

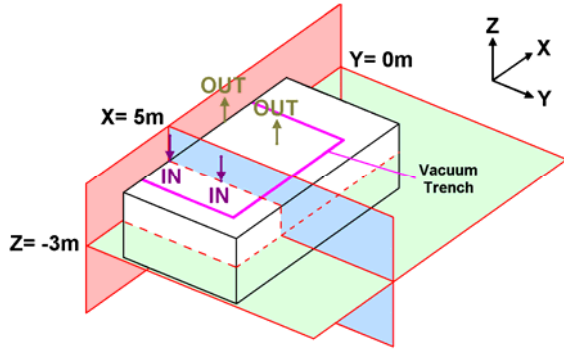


Figure 7. Scheme of 3D simulated half-field. Planes highlight the most significant simulation sections.

A refined sensitivity analysis was then performed by slightly changing the injection and extraction values around the optimum values found in 2D simulations. The 3D results suggested further lowering the optimal injection rates to a maximum of 15 m³/day if the initial water table level was Z= -0.9 m, and 10 m³/day if the water table was Z= -0.5 m.

Figure 8 shows relevant parameters distribution at the end of the injection phase (27 hours) along the central section (red plane Y= 0 m on Figure 7) for the optimized 3D simulation with initial water table level of Z= -0.9 m. In every picture, the grey rectangle represents the injection well, while the red rectangle is the extraction well. Dimensions are to scale.

A top view of the same simulation along the quote of maximum H₂O₂ progression (Z= -3m) is depicted in Figure 9. It corresponds to the green plane section of Figure 7.

Further investigation with a 3D simulation run where O₂ generation was switched off showed that H₂O₂ plume distribution was in good agreement with a set of simulations of H₂O₂ injection and decomposition performed with the FEFLOW numerical code (Baciocchi et al 2008).

The suggested final configuration for the pilot site is shown in Figure 10.

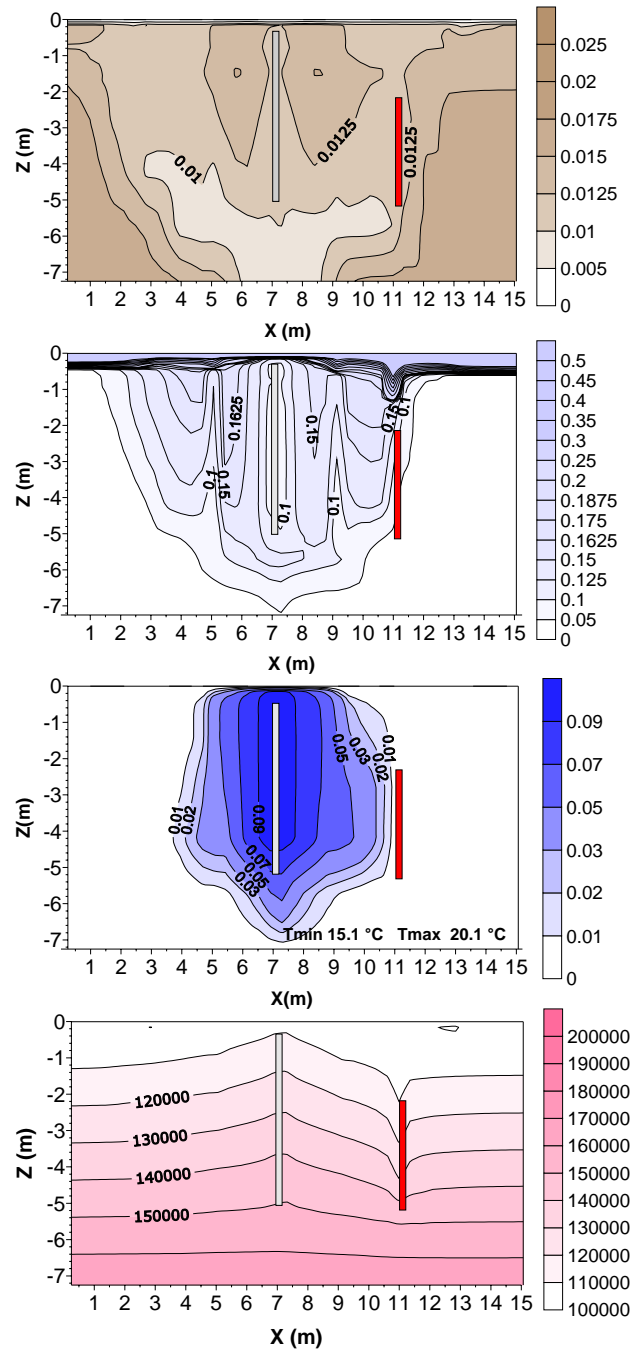


Figure 8. Selected 3D simulation plot with optimum injection and extraction rates. Initial water table level is Z=-0.9m. From top to bottom: a) n-heptane mass fraction in gaseous phase; b) O₂ gas saturation; c) H₂O₂ mass fraction; d) pressure (Pa).

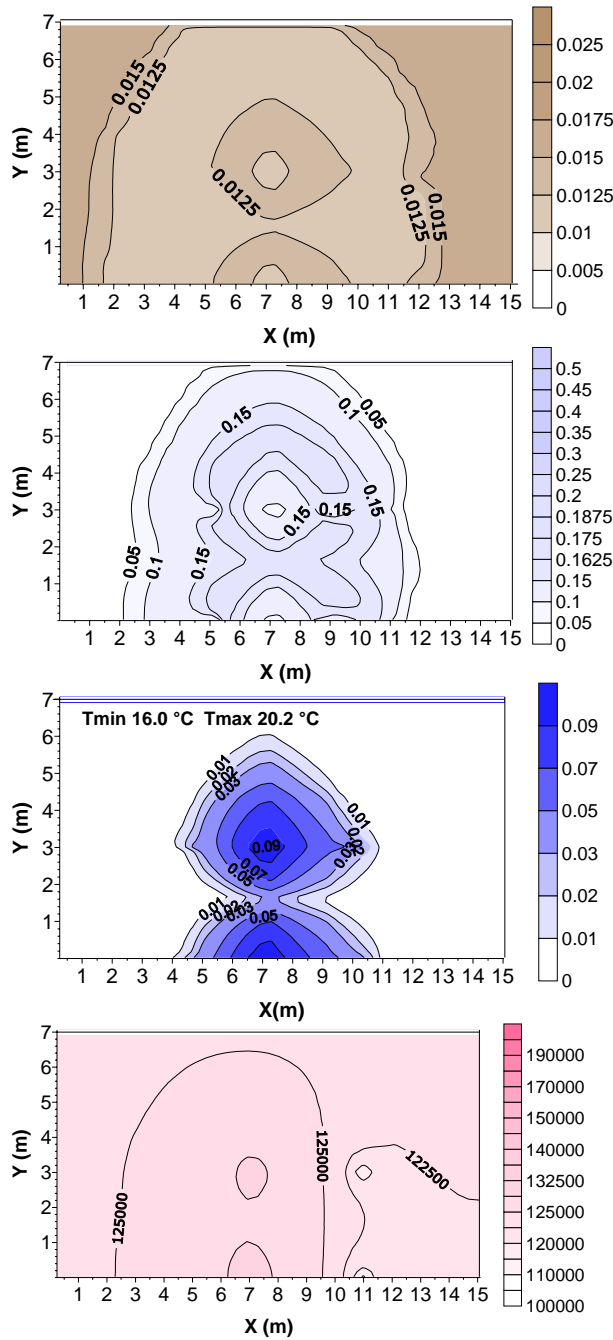


Figure 9. Top view of the same 3D simulation results shown in Figure 7. The same variables are plotted.

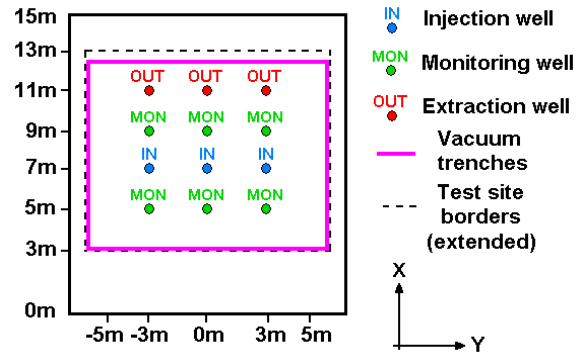


Figure 10. Final configuration for the pilot test site

CONCLUSIONS

This work suggests that TMVOC V.2 is able to effectively simulate prominent transport processes in aqueous and gaseous phases driven by the decomposition of H₂O₂ injected into the subsurface as an aqueous solution. Simulations were performed following a systematic approach in order to progressively narrow down the possible range of variation of relevant parameters. The first set of simulations reproduced with reasonable agreement the available laboratory experimental results regarding the H₂O₂ kinetic decomposition rate and the H₂O₂ to O₂ conversion ratio.

Increasingly complex 2D and 3D simulations of the planned ISCO pilot test were performed to evaluate the maximum injection rate preventing aqueous phase surfacing. Along with this parameter, a set of ancillary variables were estimated, to define a reliable well configuration and operational procedures for the pilot test. The results obtained with the 3D models will be validated as soon as the pilot site becomes operational and the monitoring data available.

ACKNOWLEDGMENTS

The authors would like to thank Prof. Renato Baciocchi, Roma Tre University, for providing the experimental data regarding H₂O₂ solution batch tests. The management of Eni R&M Division is also warmly acknowledged for the permission to publish the results of the simulation study.

REFERENCES

- Baciocchi, R., C. Ciotti, G. Capotorti, I. Innocenti, and A. Nardella, Pilot scale in situ chemical oxidation treatment of a former refinery site. *ConSoil 2008, 10th Intl UFZ/TNO Conference on Soil-Water Systems*, 3-6 June 2008, Milano, Italy, 2008.
- Battistelli, A., Modelling biodegradation of organic contaminants under multiphase conditions with TMVOCBio. *Vadose Zone Journal*, Vol. 3, n.3, 875-883, 2004.
- Battistelli, A., Modelling multiphase organic spills in coastal sites with TMVOC V.2.0. *Vadose Zone Journal*, Vol.7, 316-324, 2008.
- Corey, A.T., The Interrelation Between Gas and Oil Relative Permeabilities. *Producers Monthly*, 38-41, 1954.
- Parlange, J.Y., J.L. Starr, D.A. Barry, and R.D. Braddock, Some approximate solutions of the transport equation with irreversible reactions. *Soil Science Soc. of America J.*, Vol. 137, N. 6, 434-442, 1984.
- Pruess, K., C. Oldenburg, and G. Moridis, TOUGH2 User's Guide, Version 2.0. Report LBNL-43134, Lawrence Berkeley National Laboratory, Berkeley, CA, 1999.
- Pruess, K. and A. Battistelli, TMVOC, A Numerical Simulator for Three-Phase Non-isothermal Flows of Multicomponent Hydrocarbon Mixtures in Saturated-Unsaturated Heterogeneous Media. Report LBNL-49375, Lawrence Berkeley National Laboratory, Berkeley, CA, 2002.
- Van Genuchten, M.Th., A Closed-Form Equation for Predicting the Hydraulic Conductivity of Unsaturated Soils. *Soil Sci. Soc.* 44, 892-898, 1980.
- Van Genuchten, M. TH., F.J. Leiji, and S.R. Yates, The RETC code for quantifying the Hydraulic Functions of Unsaturated Soils. US Department of Agriculture. EPA 600/2-91/065, 1991.

USING A MODFLOW GRID, GENERATED WITH GMS, TO SOLVE A TRANSPORT PROBLEM APPLYING TOUGH2 TO COMPLEX GEOLOGICAL ENVIRONMENTS: THE INTERTIDAL DEPOSITS OF THE VENETIAN LAGOON.

Borgia A.^{1,6}, Cattaneo L.^{1,6}, Marconi D.¹, Delcroix C.², Rossi E.L.², Clemente G.²,
Amoroso C.G.³, Lo Re F.⁴, Tozzato E.⁵

EDRA
Via di Fioranello 31, 00134 Roma, ITALIA
e-mail: andrea@borgia.net

1. *EDRA, via di Fioranello 31, 00134 Roma, Italia*
2. *IGEAM, via della Maglianella 65/T, 00166 Roma, Italia*
3. *Altieri spa, via Colleoni 50, 36016 Thiene (VI), Italia*
4. *Mantovani spa, via Belgio 26, 35127 Padova, Italia*
5. *Consorzio Venezia Nuova, Palazzo Morosini, San Marco 2803, 30124 Venezia, Italia*
6. *Università degli Studi di Milano, Dip. Scienze della Terra, via Botticelli 23, 20133 Milano, Italia*

ABSTRACT

The tides of the Venetian Lagoon generally vary between -0.5 and +0.7 m a.s.l. Occasionally, they may reach maximums of 1.5 m (acqua alta) and minimums of -0.8 m a.s.l. (acqua bassa). Intertidal areas, called “barene,” exist all along the coast of the Lagoon. These areas are characterized by canals that concentrate the flow of water during the rising and waning of the tide, and drain the vegetated areas (inundated during high tides) found between canals. Therefore, because of the different energies of the water flow, sands are deposited in the canals, while organic-rich clayey deposits form in the vegetated areas. Since vegetation stabilizes the clayey areas, the same canal network tends to last for long periods of time until a “catastrophic” event (such as an inundation) occurs, rearranging the network. As a consequence, during subsidence, relatively thick sand-dikes (the original canals) become juxtaposed to clayey-dikes. However, these sand deposits form a continuous network, quite similar to that of a vascular system, that effectively drains all the “barena” deposits.

To be effective, measures for monitoring, confining, or remediating the transport of pollutants through these kinds of environments must explicitly take into account their complexity. The same complexity must be included in the numerical models that support remediation efforts. At the moment, there appear to be no off-the-shelf graphical interfaces for TOUGH2 able to manage such complexity. To attempt to solve this problem we have used a calibrated USGS-MODFLOW model for the “barena” of “Passo a Campalto” in the Venetian Lagoon, developed with the GMS™ graphical interface. This model is composed of 42 layers, which, apart from the first layers, are 0.5 m thick, with the first layers following the geometry of a dump found on top of the Barena deposit. Each layer consists of 100×60 square cells, for a total of 252,000 cells, of which only half are active. We have translated this grid, with all hydrogeologic

boundary conditions, into a TOUGH2 input file, providing additional necessary information. The first results of this experiment are promising, since we were easily able to produce TOUGH2 grids with very complex geology and run the models with success. The results can be imported back into GMS™ for visualization or plotted with any plotting software. Developing conceptual and numerical models with an elaborate graphical interface such as GMS™ permits effective construction of complex problems, allowing the modeler to concentrate on physics.

INTRODUCTION

Measures for monitoring, confining, and remediating the transport of pollutants in groundwater systems are often supported by elaborated numerical models of the mechanical, thermal, and chemical behavior of the various phases present in the porous/fractured media. One of the most reliable codes for this modeling, even if not widely used, is LBNL-TOUGH2 (Pruess and Oldenburg, 1995). While this code is relatively straightforward for the TOUGH2 expert, it is quite unfriendly for hydrogeologists unfamiliar with it.

Perhaps the most commonly used graphical user-interface for TOUGH2 is PETRASIM™. Despite this interface’s value, particularly for learning TOUGH2 and solving simple transport models in porous media, it is harder to use with complex geological systems—such as the ones found in the intertidal deposits of the Venetian Lagoon. In these deposits, the aerial juxtaposition of hydrostratigraphic units with widely different flow properties inhibits any attempt at creating layers or volumes of homogeneous properties. However, GMS™ (Groundwater Modeling System) has a quite versatile conceptual-model-oriented graphic user interface for the USGS groundwater flow model MODFLOW and associated codes, which allows “non-standard”

approaches to stratigraphic modeling of complex geological systems.

In this paper, we show that it is relatively straightforward, running in batch under any operating system, to translate a MODFLOW grid, created with the GMS™ conceptual model of the Venetian Lagoon intertidal deposits, to a TOUGH2 input file. The results of the simulations can either be translated back into GMS™ as “3D-scatter point” text file, or plotted with any adequate graphical software.

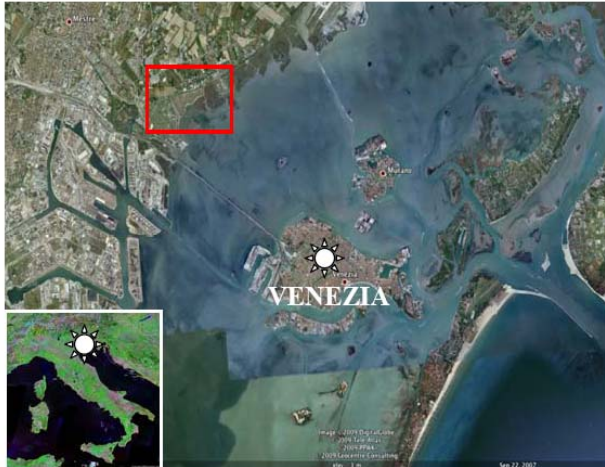


Figure 1. Google™ view of the Venezia Lagoon. Red box is the studied area.

THE GEOLOGIC COMPLEXITY OF THE “BARENA” DEPOSITS

The dump of Passo a Campalto is located on the shore of the Venezia Lagoon northeast of the city. It is about 1000 m×600 m, with the major dimension oriented ENE-WSW. To the north and west, it is bounded respectively by the Osellino and Rotte canals, to the east and south, by the Lagoon. The upper few tens of meters of the stratigraphic sequence are characterized by Pleistocene to Olocene intertidal deposits originated in the “barena” of the Venetian Lagoon. The main characteristic of these deposits is the extreme horizontal variability of the stratigraphy, in which sands are juxtaposed to clays, frequently showing even vertical contacts (Figure 2). This is due to the stability of canals (where sands are deposited) and vegetated areas (where clayey sediments are emplaced) during subsidence. The topological complexity of the barena deposits is such that it inhibits the creation of any reasonable geologic modeling based on standard approaches, such as correlating the stratigraphy of adjacent boreholes (Figure 2d). Also, the statistical analysis of lithological distribution using the Markov approach (Carle, 1999) cannot be applied, because vertical variability is not correlated to horizontal lithological distribution. In fact, etheropic facies formed

in the barena depositional environment do not follow the simple processes of sedimentary progradation: Walther’s law, which states that the vertical succession of facies is correlated to the lateral succession of deposition environments, is not applicable. For these reasons, we have applied a method for creating a geologic model based on a palinspastic reconstruction of the barena’s depositional environments.

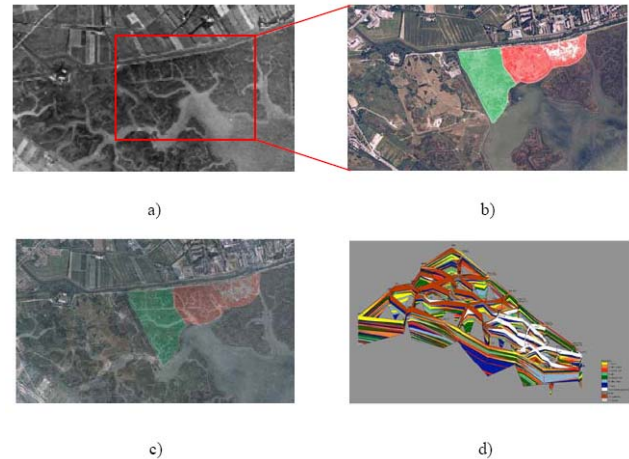


Figure 2. Images of the Barena of Passo a Campalto in the Lagoon of Venezia as it appeared in a 1950 (a) and (b) 1995 aerial photos; note the light areas that form the canals and the darker grey areas that are the vegetated areas that become inundated during high-tides. (c) Is the superposition of the two photos in a) and b) to show that tidal canals have not changed at all since 1950, in spite of the large 1966 flooding event. The dump area is highlighted in green (toxic waste) and red (phosphogypsum). (d) Shows the extremely complex stratigraphy characteristic of the barena (Legend: yellow-sand; orange-silty sand; red-sandy silt; light green-silt; green-clayey silt; light blue-silty clay; blue-clay; white-phosphogypsum; grey-bitumes; brown-wastes debris; beige-cover; light grey-blank).

THE PALINSPASTIC APPROACH

We approach the problem of creating an adequate geologic model pragmatically, starting from the numerical grid. We observe that for describing the actual geology, our model does not need to be more accurate than what can be effectively represented in a grid adequate for the numerical computation. As a consequence, our 3D grid is 1000 m×600 m in areal extent and 30 m in the vertical direction (5 m a.s.l., to include the dump, and 25 m b.s.l. in the barena deposits). Grid cells are 10×10 m² on the horizontal plane and 0.5 m in thickness, for a total of 360,000 cells. These dimensions result from a compromise function of:

- 1) The necessity to confine the number of cells to a minimum to make the numerical problem approachable;

- 2) The reliability, density and depth of stratigraphic boreholes;
- 3) The need to represent the actual materials of the dump and of the complex geology of the “barena” deposits under the dump with adequate detail.

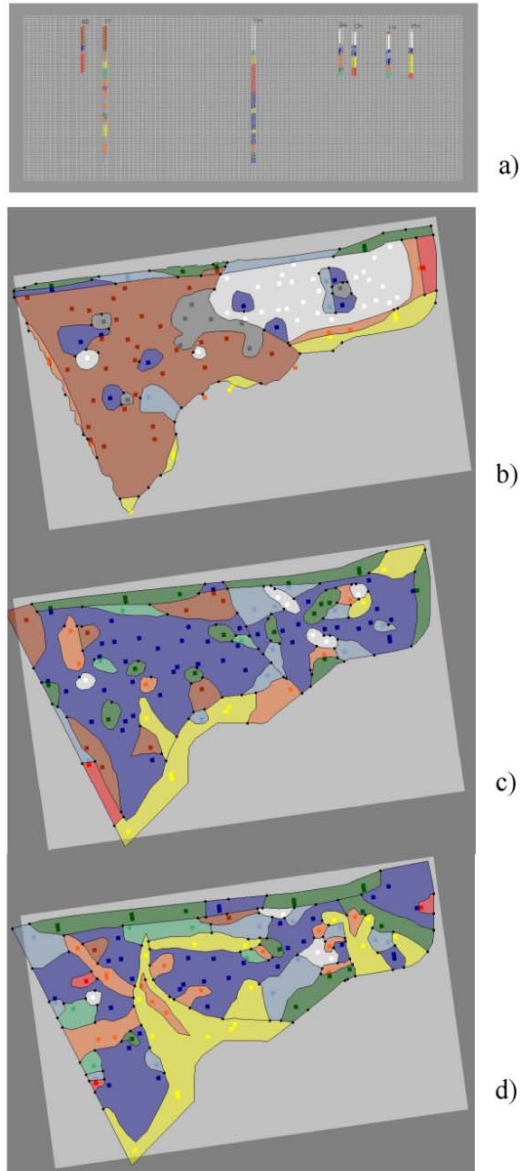


Figure 3. The palinspastic reconstruction of depositional environments of the Passo a Campalto barena: a) WSW-ENE cross-section of the 3D numerical grid with the boreholes hydrogeologic units transferred to it. b) The reconstruction of the dump materials (+0.25 m); note the clayey diapirs (blue) that rise into dump do to differential loading of the dump onto the barena. c) The clayey “Caranto” paleosoil below the dump (-0.75 m); note the “anchors” of phosphogypsum (white) that sink into the layer. d) Palinspastic reconstruction of a paleobarena environment (now at -1.25 m); note the canals (yellow/orange) and the flooding areas (blue/light blue).

Then, we attribute the lithologic units occurring in each borehole to the corresponding vertical column cells using three approximations (Figure 3a)

Since boreholes stratigraphies were made by different workers, they inherit an error in lithological identification that is a function of worker biased judgments, and it is impossible to remove. Therefore, we identify seven different hydrogeologic units, used to represent the lithologies found in the boreholes, trying to keep a similar degree of approximation. These are: (1) sands, (2) silty-sands, (3) sandy-silts, (4) silts, (5) clayey-silts, (6) silty-clays, and (7) clays. In addition, the materials occurring in the dump are further subdivided into: (8) phosphogypsum, (9) bitumes, and (10) waste detritus.

A borehole hydrogeologic unit is assigned to a cell: (1) if it is the most representative unit inside the cell itself; or (2) if, in relation to the materials present above and below, that unit has the greatest “impact” on the flow of fluids through the cell.

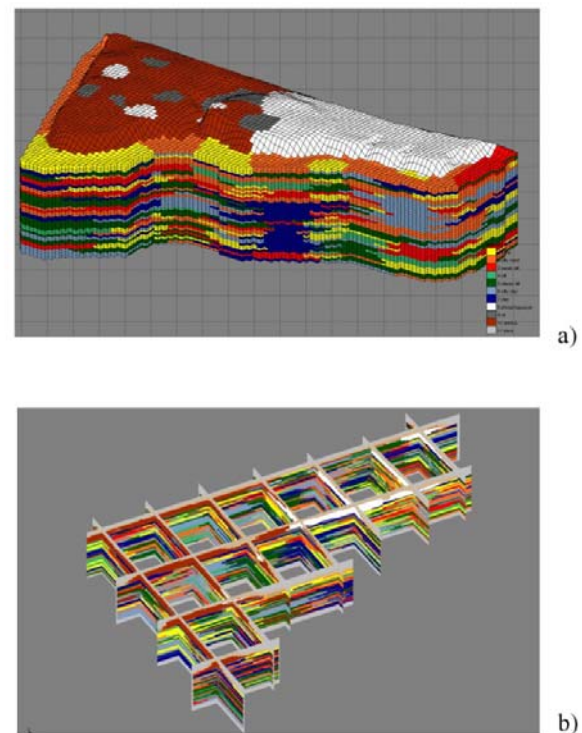


Figure 4. The geologic model; note how the complex relations among hydrogeologic units is accurately reflected in the model. a) 3D view of the model created for the Passo a Campalto dump and underlying barena deposits. b) Box cross-section of the model.

The hydrogeologic units found in boreholes, which have a diameter of 0.1 m, are extrapolated to cells that are 10^4 times wider.

Finally, based on the topological distribution of units present in each layer of the grid, we reconstruct the

paleo-depositional environment (Lanzoni et al., 2002; Critto et al., 2003; D’Alpaos et al., 2005; EDRA, 2006; Defina et al., 2007; Carniello et al., 2008; Marani et al., 2008) according to the following sedimentologic and statistic criteria: (1) the distribution of materials in the dump should reflect the actual procedure of dump creation (Figure 3b); (2) the distribution of the materials in the barena under the dump should reflect that indicated by the 1950 aerial photo; (3) the first nonconductive layer, a continental paleosoil called “Caranto” under the barena, tends to be continuous (Figure 3c); (4) the layer underlying the “Caranto” is an intertidal deposit that reflects the barena environment, characterized by channels and vegetated flooding zones (Figure 3d); (5) the first conductive level of sands under the Caranto, owing to extension, thickness, and degree of sorting, is assumed to be a sand-dune deposit; (6) the boundary between areas with different hydrogeologic units is set to be equidistant from them; (7) the materials present in boreholes are effectively extrapolated to areas that, on average, are 6×10^6 times larger than the boreholes.

The reliability of our geologic model (Figure 4), is tested against 8 stratigraphic boreholes made in the areas where the model had the largest approximation (Figure 5). We consider the fit between predicted and actual stratigraphy very good. Thus, we believe that the final model, which includes the corrections made with these latest boreholes, is statistically a reliable approximation of the actual stratigraphic complexity within this specific barena environment.

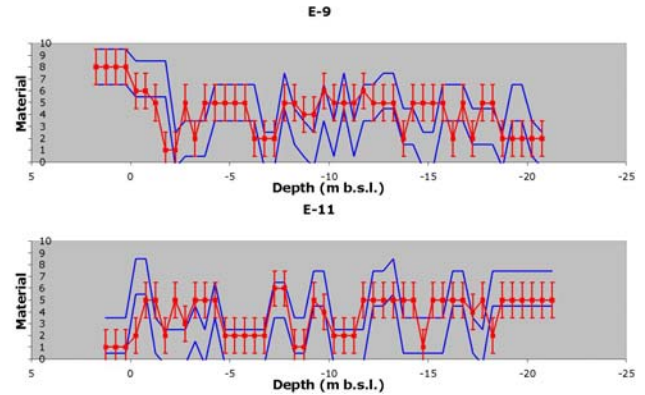


Figure 5. Comparison between actual stratigraphic units (red line with error bars) and confidence intervals predicted by our geological model (blue lines) of two stratigraphic boreholes (E-9 and E-11) made in the most uncertain areas. Note that, in spite of the complex topology found in the barena deposits (Fig. 4), the predicted stratigraphy adequately reflects the actual pattern found in the boreholes.

TRANSLATING A G MS-MODFLOW GRID INTO A TOUGH2 GRID

We wrote a FORTRAN code, called TMT (Translating MODFLOW to TOUGH2), to translate GMS-MODFLOW input files in TOUGH2 input files, adding all information needed in TOUGH2 not included in the MODFLOW code.

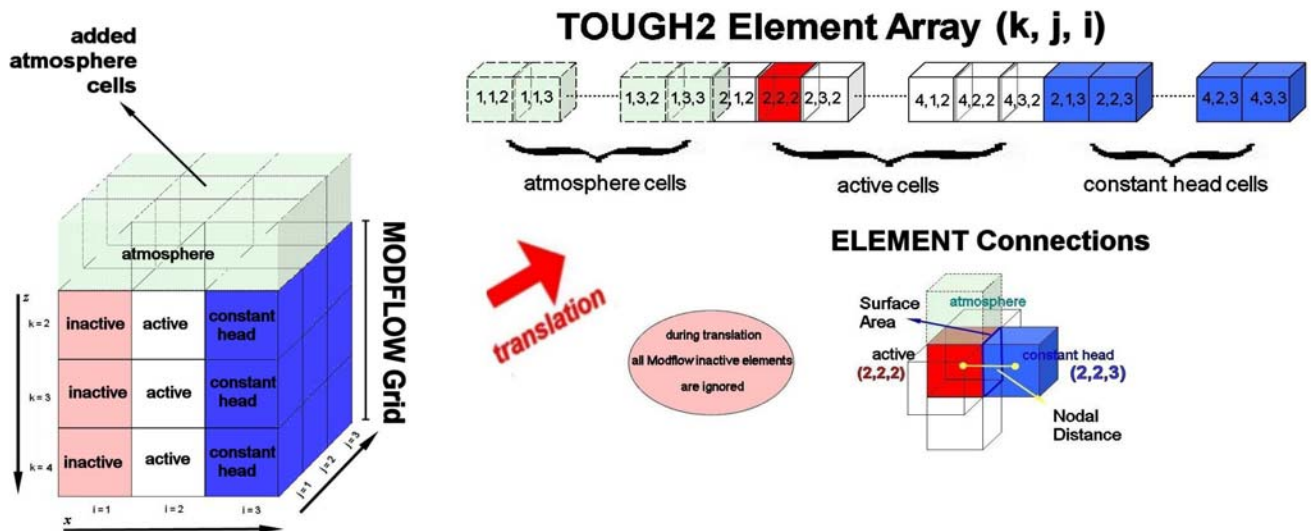


Figure 6. MODFLOW input files are used to create TOUGH2 input files: only active elements of the regular MODFLOW grid are ordered in a 1D array where constant head elements are inserted at the end. It is not necessary that consecutive elements of the array be actually interconnected. Connections between elements are given by elements pairs, surface area of contact, nodal distance and the angle between the nodal distance and the gravity acceleration vectors. All MODFLOW inactive elements are ignored.

In practice, MODFLOW creates a discrete domain, made by rectangular cells, each identified by a three-index code (i, j, k). In addition, the IBOUND matrix identifies which cells are active (value = 1) or inactive (value = 0). Our TMT Code reads grid information from MODFLOW input files and calculates active cells nodes coordinates (Figure 6). In addition, for adjacent cells it computes connections, interfaces surface area, distances of interfaces along nodal directions, and the angle between nodal directions and the gravity acceleration vector.

The MODFLOW hydraulic conductivity tensor (K_i) (Table 1) is translated into the intrinsic permeability tensor (k_i), used in TOUGH2, using the common relation:

$$K_i = \frac{\rho g k_i}{\mu} \quad (1),$$

where ρ and μ are respectively fluid density and viscosity, and g gravity. Porosity, has no need to be translated, while other thermophysical variables, needed in TOUGH2, such as rock-grain density, heat conductivity, and specific heat must be added to the input file. Then, in our specific case, cells defined in MODFLOW as “constant head” are transformed into TOUGH2 as constant pressure cells, following

$$p = p_0 + \rho g h \quad (2),$$

in which h is calculated at the TOUGH2 cell nodes and p_0 is the atmospheric pressure assumed as constant at 10^5 Pa.

Furthermore, to simulate recharge, we translated the MODFLOW Recharge Package, in which a recharge (R) is given in length/time into a source term (S), given in mass/time, for each cell at the top of the morphology.

$$S = RA\rho \quad (3).$$

Table 1. Conductivity and porosity values assigned to materials

	Horizontal Hydraulic Conductivity (m/s)	Vertical Hydraulic Conductivity (m/s)	Porosity	Font
Sand	$5,0 * 10^{-6}$	$5,0 * 10^{-6}$	0,3	Lefranc Experimental Tests
Silty Sand	$1,0 * 10^{-6}$	$0,5 * 10^{-6}$	0,3	Lefranc Experimental Tests
Sandy Silt	$5,0 * 10^{-7}$	$2,5 * 10^{-7}$	0,3	Extrapolated
Silt	$1,0 * 10^{-7}$	$3,3 * 10^{-8}$	0,3	Extrapolated
Clayey Silt	$5,0 * 10^{-8}$	$1,67 * 10^{-8}$	0,3	Extrapolated
Silty Clay	$1,0 * 10^{-8}$	$2,0 * 10^{-9}$	0,3	Extrapolated
Clay	$5,0 * 10^{-9}$	$5,0 * 10^{-10}$	0,3	Laboratory Tests
Phosphogypsum	$1,0 * 10^{-6}$	$0,5 * 10^{-6}$	0,3	C.V.N. Technical Report
Wastes Detritus, Bitumes	$5,0 * 10^{-6}$	$2,5 * 10^{-6}$	0,3	Extrapolated

Finally, to simulate the atmosphere, we added an additional layer of cells above the upper MODFLOW layer. We force these cells to have constant thermo-physical values by making their volumes and intrinsic permeability “infinite” and their porosity equal to 1.

RUNNING THE TOUGH2 SIMULATION

To achieve a numerical solution, while running TOUGH2 on a PC, in a reasonable amount of time, we had to reduce the number of grid cells from the original grid. We merged the 10×10 m² cells used in the MODFLOW simulations into 40×40 m² cells, obtaining a computation grid made of 10,535 active cells distributed in 43 layers (Figure 7). Each cell has a volume of 800 m³, except for the elements of the upper layer, which, as stated, have “infinite” volumes.

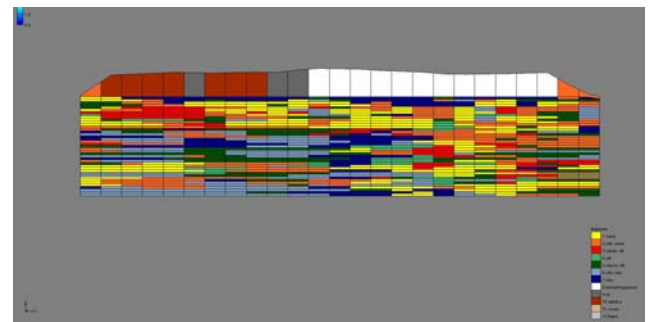


Figure 7. WSW-ENE cross section through the model grid at 150 m south of Osellino canal. Note the toxic waste (brown and gray colors in the top-left of the model) and the phosphogypsum (white color in the top-right of the model) sections of the Barena. Comparing this to Figure 3 indicates that the TOUGH2 model grid maintains the topological complexity observed in the MODFLOW geologic model grid. In the TOUGH2 simulation, all toxic waste has the same hydrogeologic properties. The materials of the legend dump “cover” and “blank” (the atmosphere) are not represented.

We ran TOUGH2 with the EOS7 module, which provides the thermophysical properties of air, pure water, and a brine. The salinity of the aqueous phase is calculated using the brine mass fraction, X_b ; the density and viscosity are interpolated from the values for the water and the brine end-members relative concentrations using specific equations. (Pruess et al., 1999).

We ignore heat fluxes, considering the system as isothermal, because the recorded temperature changes seasonally only a few degrees. We run the model at 25°C; our choice of a temperature slightly higher than the maximum recorded temperature (18°C) is conservative. In fact, to a higher temperature corresponds a larger hydraulic conductivity, because the decrease in viscosity

overwhelms the decrease in density, facilitating the downward percolation of pollutants. Therefore, temperature wise, we tend to reproduce a worst-case scenario.

As inherited from the MODFLOW model, we have set constant head boundaries at sea level in all cells around the model, which reflect the presence of the lagoon to the south and east, the Rotte canal to the west, and the Osellino canal to the north. Also, the bottom-layer cells are set at the same constant head. The pressure related to the sea-level water head is calculated assuming a salinity of 35‰, which is approximately the average largest salinity recorded during the monitoring program in the underground waters of the Barena at Passo a Campalto.

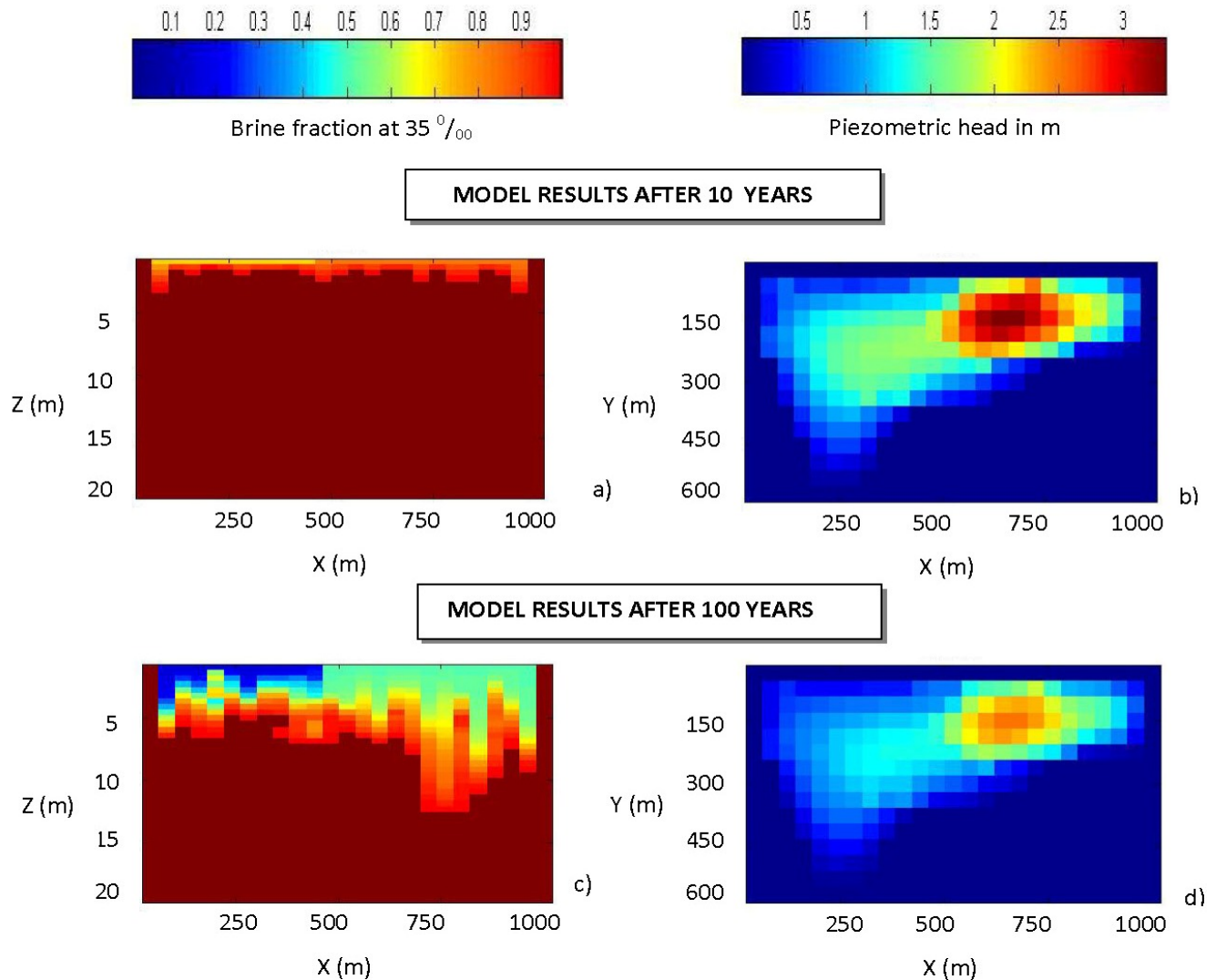


Figure 8. Brine mass fraction (a, c) and piezometric heads (b, d) computed by the TOUGH2 model on the cross section shown in Figure 7. Results the of the model are displayed after 10 years (a, b) and 100 years (c, d) from the start of the simulation. The changing brine mass fraction over time, shows the downward migration of dump percolates that displace the salty water. Note that the clayey layers below the toxic-waste section of the dump (left) effectively reduce the downward propagation of pollutants relative to the phosphogypsum section (right). Note that the water table decreases in time to reach a steady state condition.

We compute our starting condition for the TOUGH2 simulation by letting the model equilibrate at sea level with no recharge. Then we introduce the recharge and let the model run for many hundreds of years. The recharge is modeled with a water-source term on the first layer of cells below the atmosphere. From the monitoring data, we observe that the groundwater of the phosphogypsum section of the dump has a salinity that ranges between 4 and 12‰, while in the toxic-waste section of the dump, the groundwater has a salinity around 4–7‰. Therefore, we have simulated a recharge with two different salinities that reflect a possible extreme scenario, in which the percolates from the toxic side of the dump have a salinity of 5‰, while those from the phosphogypsum side have a salinity of 15‰. The different recharge salinities were modeled using the appropriate mixture of two source terms, pure water (S_w) and brine (S_b), calculated with:

$$S_w(1 - X) + S_b X = S_m \quad (4),$$

where S_m is the salinity of the recharge mixture and X is the brine volume fraction of total recharge volume. The recharge 70 (mm/a) is calibrated so that the hydraulic heads calculated during the simulation are reasonably similar to the heads actually measured during the monitoring program. To show the importance for any remediation effort to reduce the recharge, we have also run a simulation with a recharge of 10 (mm/a).

DISPLAYING THE RESULTS

Our 3D model shows the downward percolation of the recharge fluids (70 mm/a) that have a salinity of 5‰ in the toxic-waste section of the dump, and a salinity of 15‰ in the phosphogypsum section. As time passes, the less salty recharge water displaces the salty water (35‰), downward, which fills the porous medium at the beginning of the simulation from sea level downward (Figures 8 and 9). The presence of more impermeable layers at depths of 7–10 m (Figure 7) on the toxic-waste side of the model clearly inhibits the percolation. On the other hand, the percolates from the phosphogypsum section of the dump reach depths of -14 m a.s.l. in about 100 years, perhaps becoming a threat for the superficial groundwater. The results show that the water table decreases exponentially with time by about 10% to reach a steady-state value after many decades.

To test the effect of the recharge waters on the rate of downward percolation, we have, in a second simulation, reduced the recharge by 1/7 (10 mm/a). The results show that the downward penetration of the less salty plume of water is confined to only -5 to -6 m a.s.l. (Figure 9). This is an additional proof of the commonly used remediation measure, based on the drastic reduction of the recharge into a dump.

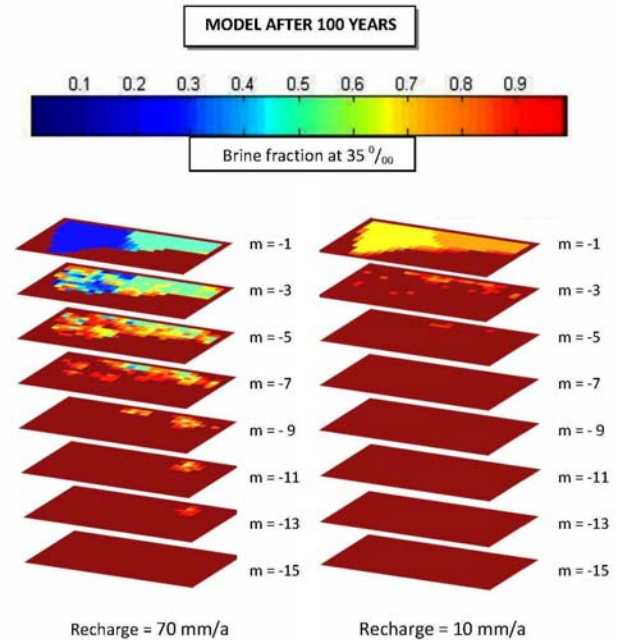


Figure 9. Brine mass fraction distribution in eight consecutive horizontal (x,y) sections underlying the dump after about 100 years from the beginning of the simulation. The recharge rate is 70 mm/a on the left side, 10 mm/a on the right. Note the much deeper penetration of the plume originating in the dump for the larger recharge.

CONCLUSIONS

Using the GMS™ conceptual-model-oriented graphic user interface, used for the USGS MODFLOW, we succeeded in making a 3D model of the highly complex geologic environment that characterizes the intertidal deposits found below the dump of Passo a Campalto (Venezia). This depositional environment, combined to subsidence, creates a dendritic pattern of sand dykes (the original tidal canals) that tend to drain the clayey rock volumes (the original tidal flooding areas). The complexity is such that it cannot be easily discretized using standard geologic-modeling tools used in many graphic user interfaces.

In response to this complexity, we translated the MODFLOW grid into a TOUGH2 input file and ran the model with the EOS7 package in isothermal mode. We approached model calibration with a direct procedure using the salinity and the water table measured during a many-years-long monitoring program of the dump site. The TOUGH2 results, obtained with two different recharge rates (70 mm/a and 10 mm/a), show the downward percolation of dump fluids and, as expected, the drastic reduction in the amount of percolation for the smaller recharge rate. For visualization purposes, the results can be easily translated back to GMS™ or plotted with any adequate graphical software package.

As a consequence of our positive effort, we strongly encourage future attempts in building adequate graphical user interfaces for the TOUGH series of codes. Many hydrogeologists, especially those who need to concentrate on modeling complex stratigraphies before actually solving the porous/fractured media flow problem, would substantially benefit from being able to use the power of the TOUGH codes.

ACKNOWLEDGMENT

We thank Curtis Oldenburg and Giovanni Grieco for continuous intellectual and logistic support. This project received financial support by the Magistrato delle Acque di Venezia.

REFERENCES

- Carle S.F., T-PROGS: Transitional Probability Geostatistical Software, version 2.1. University of California, Davis, 1999.
- Carniello L., L. D'Alpaos, A. Defina and S. Fagherazzi, A conceptual model for the long term evolution of tidal flats in the Venice lagoon, *River, Coastal and Estuarine Morphodynamics: RCEM 200*, 137-144, 2008.
- Critto A., C. Carbon and A. Marcomini, Characterization of contaminated soil and groundwater surrounding an illegal landfill (S. Giuliano, Venice, Italy) by principal component analysis and kriging, *Environmental Pollution*, 122(2), 235-244, 2003.

- D'Alpaos A., S. Lanzoni and M. Marani, S. Fagherazzi, A. Rinaldo, Tidal network ontogeny: Channel initiation and early development, *Journal of geophysical research*, Vol. 110 F02001, 1-14, 2005.
- Defina A., L. Carniello, S. Fagherazzi and L. D'Alpaos, Self-organization of shallow basins in tidal flats and salt marshes, *Journal of geophysical research*, Vol. 112 F03001, 1-11, 2007.
- EDRA, 2006. Modello idrogeologico della discarica di Passo a Campalto – Fase 0 – attività preliminari (1° anno). Magistrato delle Acque di Venezia, pp. 98.
- Lanzoni S., G. Seminara, Long-term evolution and morphodynamic equilibrium of tidal channels, *Journal of geophysical research*, Vol. 107 NO. C1, 1-13, 2002.
- Marani M., A. D'Alpaos, S. Lanzoni, L. Carniello and A. Rinaldo, Multiple equilibria in tidal geomorphology, *River, Coastal and Estuarine Morphodynamics: RCEM 2007*, 263-269, 2008.
- Pruess K., A. Simmons, Y.S. Wu and G. Moridis, 1996. TOUGH2 Software Qualification, Lawrence Berkeley National Laboratory Report LBL-38383.
- Pruess, K., C. Oldenburg, and G. Moridis, *TOUGH2 User's Guide, Version 2.0*, Report LBNL-43134, Lawrence Berkeley National Laboratory, Berkeley, Calif., 1999.

FORWARD AND INVERSE BIO-GEOCHEMICAL MODELING OF MICROBially INDUCED PRECIPITATION IN 0.5M COLUMNAR EXPERIMENTS

T. Barkouki¹, B. Martinez¹, B. Mortensen¹, T. Weathers¹, J. DeJong¹, N. Spycher², T. Ginn¹,
Y. Fujita³, and R. Smith⁴

¹University of California Davis, Department of Civil and Environmental Engineering, Davis, CA 95616

²Lawrence Berkeley National Laboratory, Earth Sciences Division, Berkeley, CA 94720

³Idaho National Laboratory, Idaho Falls, ID 83415

⁴University of Idaho, Idaho Falls, ID 83402

e-mail: tbarkouki@ucdavis.edu

ABSTRACT

Microbial ureolysis-induced calcite precipitation may offer an *in situ* remediation for heavy metal and radionuclide contamination, as well as an alternative to traditional soil strengthening techniques. A microbially mediated calcite precipitation model was built in TOUGHREACT v2 and calibrated to batch and columnar experimental data. Kinetic ureolysis and calcite precipitation-rate expressions were parameterized by coupling TOUCHREACT with UCODE.

INTRODUCTION

Techniques for soil stabilization (e.g., grouting) are energy-intensive and pose risks from toxic chemicals. Subsurface contamination by metals threatens water supplies and ecosystem health at sites worldwide. These seemingly unrelated challenges share a common solution: microbially mediated ureolysis can be induced *in situ* to drive calcite precipitation. Specifically, immobile aerobic biophases (cells or enzymes) mediate ureolysis, converting urea to ammonium and carbonate, raising pH. *Stable* calcite precipitation results when resident and injected solutions are near calcite saturation (Fujita et al., 2000). Divalent species such as strontium co-precipitate on surfaces, resulting in *in situ* immobilization. Calcite precipitation also enables control of mechanical properties through the cementation of particles, thus increasing the shear strength and stiffness, while decreasing the permeability and compressibility of the medium (DeJong et al., 2009; Figure 1). Challenges in application include: design of the injectate aqueous chemistry (e.g., calcium, carbonate, urea, pH buffer, microbial nutrients) and injection rates to control the timing and rate of calcite precipitation, to generate the desired spatial distribution. Both applications rely on the supply of organics for ureolytic agents to oxidize during ureolysis. Ureolytic agents may be augmented, or native species may be enlisted, but in all applications, wells are used to control hydraulics and inject reactants. Consequently, modeling ultimately requires incorporation of comprehensive reaction networks into transport simulators for non-uniform flow with radial components.

To develop and validate the reaction network for use in both applications, both TOUGHREACT (Xu et al., 2006) and PHREEQCII (Parkhurst and Appelo, 1999) are being applied in comparative modeling of laboratory batch and columnar data, as well as in preliminary predictive modeling of reactive transport in radial flow. Data from both published and ongoing experiments are used. The original reaction network was created and validated in PHREEQCII against published batch data involving ureolysis by urease enzyme (Fidaleo and Lavecchia, 2003). This reaction network was then converted to TOUGHREACT for application to ongoing batch and pulsed-flow column (0.5 m) experiments at UC Davis involving *Sporosarcina pasteurii*, and incorporated into a streamtube-ensemble context within PHREEQCII for application to radial injection problems *in situ*, relying on native organisms.

Column experiments included continuous and repeat pulse-flows, with mass flux equal in both cases. Aqueous chemistry and calcite distribution were monitored, as well as seismic shear waves that correlate to the stiffness of the column. TOUGHREACT was coupled with the inversion code UCODE (Hill and Tiedeman, 2006) to invert on observed pH data to determine the effective urease concentration that drives the ureolysis rate in batch. The calibrated model was then applied to the column experiments to determine calcite precipitation amounts and to establish a correlation between observed shear wave velocity and calcite abundance, with good results. Separately, calcite precipitation between an injection/extraction well triplet at the Vadose Zone Research Park (VZRP) in Idaho Falls, Idaho, is modeled via a streamtube ensemble with travel times derived from *in situ* tracer tests. Each streamtube is represented in PHREEQCII, and arrivals at the production well are modeled as solute-flux averages. In future work, model cross-validation will involve comparison with results from the TOUGHREACT simulations that implement the same conditions and reaction network expressed in Eulerian form for the VZRP non-uniform flow field.

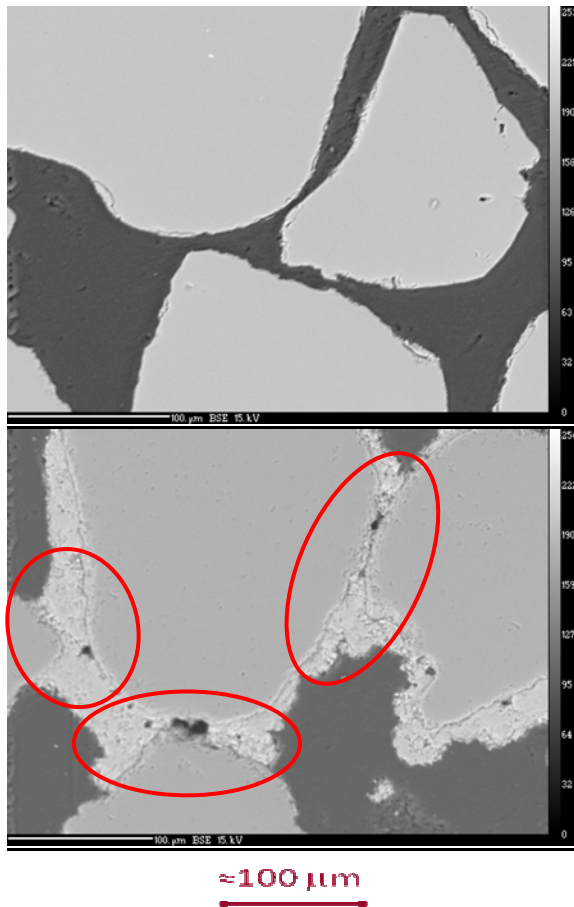


Figure 1. SEM images show sand grains before (top) and after (bottom) calcite precipitation around sand grains and at grain interfaces. Calcite “bridges” (red circles) between sand grains increase the stiffness properties of soil.

OVERVIEW OF EXPERIMENTS

Laboratory experiments were performed at the Soil Interactions Laboratory at UC Davis to study the physical, chemical, and biological aspects of the ureolytic calcite-precipitation treatment. Data from these batch and column “treatment optimization” experiments were used to calibrate ureolysis and calcite precipitation kinetics in TOUGHREACT. These batch and column experiments provided data on the physical, chemical, and biological aspects of the ureolytic calcite-precipitation treatment process. The two major types of variables investigated were aqueous compositions and flow schedule of the treatment fluid.

Batch Experiments

The batch experiments contained aqueous concentrations of a urea-based nutrient broth, sodium bicarbonate, ammonium chloride, and 10^7 cells/mL of *Sporosarcina pasteurii*. Aqueous concentrations are shown in Table 1. The bacteria were grown in ammonium-yeast extract growth media and inoculated after storage at 4°C . The pH was measured every 15 minutes for 150 data points. Six concentrations of ammonium chloride were tested in triplicate. Results are plotted in Figure 3.

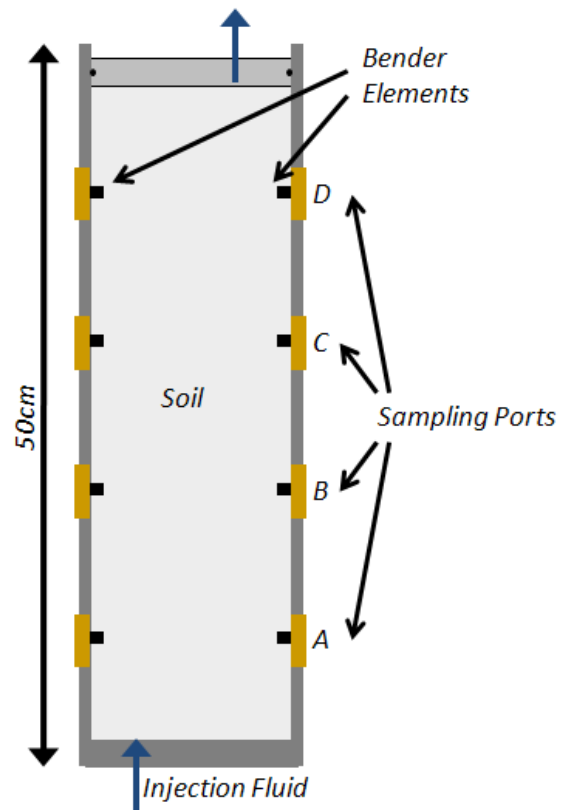


Figure 2. This schematic shows the experimental setup for column experiments. Bender elements measured shear wave velocity to determine soil stiffness. Aqueous samples were extracted from ports on the side of the column and analyzed for pH and ion concentrations.

Column Experiments

Two column experiments were run simultaneously to explore the use of pulse-flow versus continuous injection of the calcium-urea treatment solution. The 42.5 cm long, 2.5 cm radius acrylic columns (Figure 2) were filled with Ottawa 50-70 sand at a porosity of

0.36–0.37. A bacterial solution with a urea-based nutrient broth was injected initially from the top of the column and given a no-flow period of eight hours to allow bacteria to attach to sand grains. A cementation solution (Table 1, “Boundary Solution”) was then injected from the bottom of the columns via a peristaltic pump. The continuous column was pumped at a flow rate of 2 mL/min, while the pulsed-flow column was pumped at 10 mL/min for roughly 40 minutes at repeated intervals every three hours (for the 50-hour experiment). Aqueous samples, taken from the column effluent line and through four sampling ports located along the length of the column (Figure 2), were analyzed for ion concentrations and pH. Four pairs of piezoelectric bender elements measured shear wave velocity through the soil matrix to determine soil stiffness and as an indirect measure of precipitated calcite abundance. The sand columns were extruded after the experiment, and calcite abundance was determined gravimetrically.

Table 1. Aqueous concentrations for batch and column experiments and models (mmol)

Component	Batch Initial	Column Initial	Column Boundary
pH	7.5	9.0	7.5
Na ⁺	25.2	25.2	25.2
Ca ⁺²	0*	0*	100
Cl ⁻	(a)	374	474
CO ₃ ⁻²	25.2	194	25.2
NH ₄ ⁺	(a)	711	374
NO ₃ ⁻²	0*	0*	0*
Urea	333	165	333
O _{2(aq)}	(b)	(b)	(b)
ZH (urease)	(c)	(c)	(c)

(a) 6 beakers with [NH₄Cl] = 0, 62.3, 125, 187, 380 & 374

(b) In equilibrium with O_{2(g)} at log(fugacity/bar) = -0.82

(c) Estimated by regression in UCODE

* Zero concentrations were modeled as 10⁻²² millimolal

TOUGHREACT MODEL

TOUGHREACT v2 was used in batch mode (single gridblock) and for 1D simulations of column experiments, respectively. Longitudinal dispersivity of the columns was determined from analysis of tracer breakthrough to determine the grid discretization required to match real dispersion with the appropriate level of numerical dispersion. The “equation-of-state” (EOS1) module in isothermal mode, at 25°C, was used for all simulations.

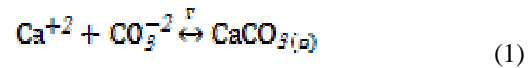
Chemical Model

The chemical system was defined by the components H₂O, H⁺, Na⁺, Ca⁺², Cl⁻, CO₃⁻², NO₃⁻, NH₄⁺, O_{2(aq)},

urea, and ZH (urease). The model included CO_{2(g)} and O_{2(g)} (bystanders) dissolution/exsolution, kinetic calcite mineral precipitation/dissolution and ureolysis following the rate law of Fidaleo and Lavecchia (2003). The PHREEQC minteq v4 thermodynamic database was employed, with the addition of the component ZH and other modifications explained below.

Calcite Precipitation

The calcite precipitation reaction and rate expression are:

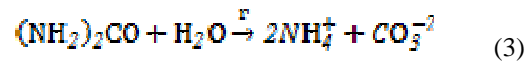


$$r = \pm k_c A_c \left| 1 - \frac{(\text{Ca}^{+2})(\text{CO}_3^{-2})}{K_{sp}} \right| \quad (2)$$

with k_c , A_c , and K_{sp} are the forward rate constant, mineral reactive surface area, and equilibrium constant for calcite. (Ca^{+2}) and (CO_3^{-2}) denote aqueous activities of the two reactant species. k_c and K_{sp} are fixed inputs, while A_c is calculated from the mineral amount, molecular weight and molar volume, which for calcite are 100.089 g/mol and 36.933 cm³/mol, respectively. Since A_c equals zero when there is no calcite in the system (initial conditions), we use an effective reactive surface area (AMIN) to produce a positive reaction rate and initiate precipitation. AMIN may represent any type of (assumed immobile) nucleation point in the system—and is unknown and therefore a fitting parameter. The solubility product value (K_{sp}) for calcite found in the minteq v4 database is -8.48, while the forward rate constant (k_c) was considered from several authors (Nilsson and Sternbeck 1999, Ferris et al. 2003), and 1.0×10⁻⁸ mol/m²/sec was selected.

Ureolysis

The ureolysis reaction equation and rate expression are:



$$r = v_{max} [\text{ZH}] \frac{1}{K_M + [\text{S}] \frac{K_P}{K_P + [\text{P}]} } \quad (4)$$

with v_{max} the maximum forward rate constant, [ZH] the effective urease concentration, K_M the Monod constant, and K_P the product (NH_4^+) inhibition constant. Fidaleo and Lavecchia (2003) reported the maximum rate constant $v_{max} = 1.83 \times 10^2$ mol/g/min = 146.4 mol/L/sec, and half saturation constants $K_M = 3.21 \times 10^{-3}$ mol/L and $K_P = 1.22 \times 10^{-2}$ mol/L. The effect of pH and urease - NH₄⁺ complexation on reactive urase activity (ZH) was accounted for in the TOUGHREACT model by adding the following

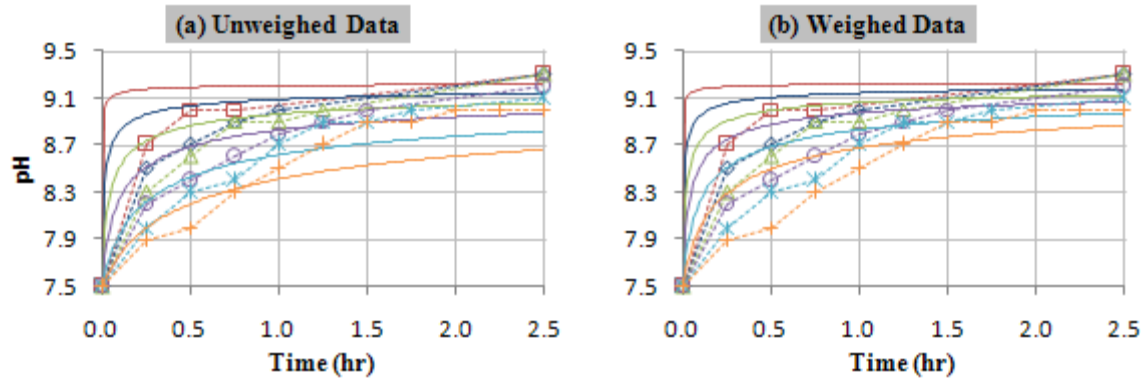
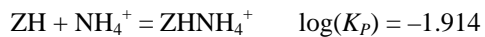


Figure 3. Simulated (solid lines) and experimental (dashed lines with symbols) pH vs time plots showing the effect of $[\text{NH}_4^+]$ on ureolysis rate: (a) regression with equal weights on pH data, (b) weighs the latter half of the pH values more than the early half to capture asymptotic pH value within experimental retention times. Lowest lines (yellow, slowest ureolysis) correspond to highest NH_4^+ concentrations (374 mmol), highest lines (red, fastest ureolysis) correspond to no initial NH_4^+ present (see Table 1, note a).

equilibrium protonation/deprotonation/complexation reactions to the thermodynamic database:



Batch Experiment Model

The beaker experiments conducted to determine the effect of ammonium inhibitor concentration on ureolysis rate were modeled as batch reactors, or single gridblock models.

Initial Conditions

Initial aqueous concentrations are shown in Table 1.

Inverse Modeling of Batch Experiments

The initial concentration of urease component [ZH] was estimated by optimizing the TOUGHREACT model with UCODE, using pH data from the batch experiments. The regression was performed with no prior information or constraints on [ZH], and all the pH data from the batch tests were initially equally weighted. A template of the chemical.inp TOUGHREACT input file was created as an input for UCODE, to perturb and estimate [ZH] for all the batches and to perform regression. Simulated pH values corresponding to the experimental pH data were extracted from the TOUGHREACT output file by UCODE.

Column Experiment Model

The column experiments were modeled as 1D meshes with flux boundary conditions at either end. A tracer test was performed in the laboratory on a 50 cm sand

column with 50 ppm NaBr pumped at 4.5 mL/min to determine the spatial discretization needed to simulate hydrodynamic dispersion. The simulated breakthrough curves of a passive chemical component from models of different grid sizes were compared to the tracer test breakthrough data. Figure 4 shows that the 100-gridblock implicit model exhibits more numerical dispersion than the hydrodynamic dispersion shown by the tracer data.

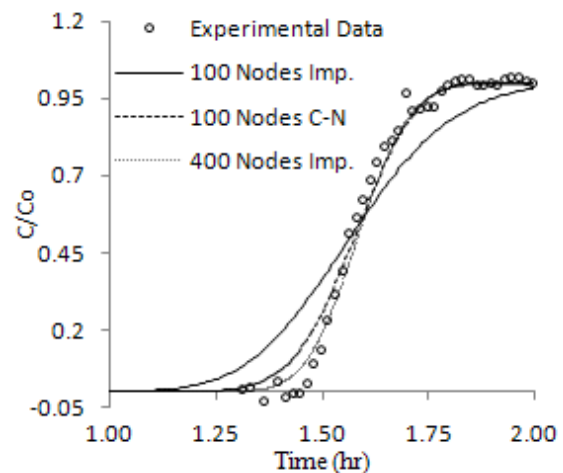


Figure 4. Tracer test data and simulated breakthrough curves with 100 and 400 gridblocks using fully implicit schemes and a 400-gridblock mesh using a Crank Nicholson scheme

The 100-gridblock Crank-Nicholson and 400-gridblock implicit models produce less numerical dispersion and match the experimental data well. The 100-gridblock Crank Nicholson model was coupled to UCODE for inversion, and then the calibrated model was rerun in implicit 100- and 400-gridblock

models to compare the effects of grid discretization and time stepping scheme on the geochemical results.

Initial/Boundary Conditions

Initial and boundary solution component concentrations are shown in Table 1. The boundary solution was assigned to the first block of the two columns, which had sink/source pairs corresponding to the pumping via the peristaltic pump used in the experiments. The continuous column sink/source pair had a constant generation rate of 3.33×10^{-5} kg/s (= 2 g/min = 2 mL/min) while the pulsed-flow column was given a variable generation rate of 1.67×10^{-4} kg/s (= 10 mL/min) at roughly 40-minute intervals, followed by no flow for the remainder of each three-hour injection cycle.

Inverse Modeling of Column Experiments

The pH and calcite data were formatted into UCODE input files and run with the TOUGHREACT model to parameterize the kinetic calcite precipitation rate expression and the mineral zone parameters for calcite. UCODE was instructed to extract the pH values of the last gridblock of the 1D grids at the simulation times corresponding to the effluent sampling times during the experiment.

The calcite content of the sand columns was determined by extruding the sand from the acrylic columns, cutting them into four sections, and measuring the calcite gravimetrically by dissolving the calcite with HCl. This determined the averaged calcite content of each of the four sections containing roughly $\frac{1}{4}$ of the total calcified sand matrix in units of mols CaCO_3 /volume of solid medium. This meant that to accurately compare the calcite data to the simulated outputs, UCODE was instructed to average the calcite abundances in the corresponding grid blocks and compare those averaged values to the experimental data for regression. Effluent pH data was also used to calibrate the model. The estimated parameters were [ZH] (reactive urease initial concentration) and AMIN (minimum reactive surface area to compute initial calcite precipitation rate). Sensitivity analysis showed that these two parameters were uncorrelated and had composite-scaled sensitivities within an order of magnitude of each other, meaning both could be calibrated to determine a locally unique solution. Four regressions were performed with different initial guess values, to test the global uniqueness of the solution by “sweeping” for local minima in the error function.

RESULTS AND DISCUSSION

The experimental and simulated pH data from the batch experiments are plotted in Figure 3a. It can be seen that the model overestimates the rate at early

time and then underestimates at later time. Temperature effects on enzymatic activity may have contributed to the discrepancy between experimental and simulated pH trends, since the batch experiments were inoculated with bacteria stored at 4°C, which manifested as a slow initial rate of reaction that the model is unable to capture with temperature-independent formulation. Future work will include experiments where the bacteria are allowed to acclimate to room temperature and begin ureolysis to develop metabolic pathways before being added to the urea batch to test this hypothesis. Alternatively, the model may be augmented to include bacterial growth and metabolism kinetics capable of capturing more complex microbiological processes, which will require data from beaker tests at various temperatures. It is assumed that the bacteria are acclimated to the 25°C environment and have established stable enzymatic activity by the second half of the experiment. A second regression was performed with the pH data from 1.25 hrs to 2.5 hours weighed an order of magnitude higher than the earlier pH data. The results of this run are shown in Figure 4b and show a tighter fit of the asymptotic pH values, but more discrepancy at early time. Finally, we determined that ureolysis with the *Sporosarcina pasteurii* system can be adequately modeled in TOUGHREACT v2 with the Fidaleo and Lavecchia (2003) kinetic model, with reactive urease concentration [ZH] as a fitting parameter.

Columnar experimental data and TOUGHREACT simulations show that repeated pulsed-flow injections of cementation fluid result in more uniform distribution of calcite as compared to continuous injection (Figure 5). The experimental calcite profiles reveal the formation of a “puck” of high calcite content in the section of the continuous flow column closest to the injection port, then steadily decreasing calcite downstream to virtually no calcite near the extraction port. Conversely, the pulsed-flow column shows very uniform calcite throughout the length of the column. In fact, the data shows highest calcite content at the downstream end of the column, possibly explained by higher microbe densities, because they were introduced from the opposite end of the column than the cementation solution. This effect may have been augmented in the pulsed-flow column, whereby the faster pulses induce enough shear forces to dislodge and transport the microbes downstream. Future modeling work will explore calibrating the model with spatially variable urease activities to account for non-uniform distributions of bacteria.

Figure 6 shows temporal changes in shear wave velocity and simulated calcite abundances at four bender element pair locations in the continuous and pulsed-flow columns. The similarity in the trends suggests that there is a strong relationship between

shear wave velocity (an indirect measure of stiffness) and calcite abundance. Furthermore, the trends show that pulsed-flow produces calcite abundance and stiffness within half an order of magnitude throughout the column, while continuous injection produces calcite abundance and stiffness that spans two orders of magnitude along the column length. The regression on [ZH] and AMIN reveals several local minima with much higher objective function values than the adopted solution. This highlights the importance of picking good initial guesses and testing several initial guess sets to rule out local minima.

Regression in UCODE requires $N + 1$ model runs (N = number of parameters) per iteration and sometimes dozens of iterations. The 400-gridblock model had a run time of over 2.5 hours, while the 100-gridblock models ran in less than 0.5 hours, making it attractive to reduce numerical dispersion using methods other than grid refinement when running an inverse model. Other questions exist when considering grid size, such as the existence of the representative elementary volume in a 400-gridblock 1D model of a 50 cm column (gridblock thickness ~ 1 mm) with sand having an average particle diameter of 0.15 mm.

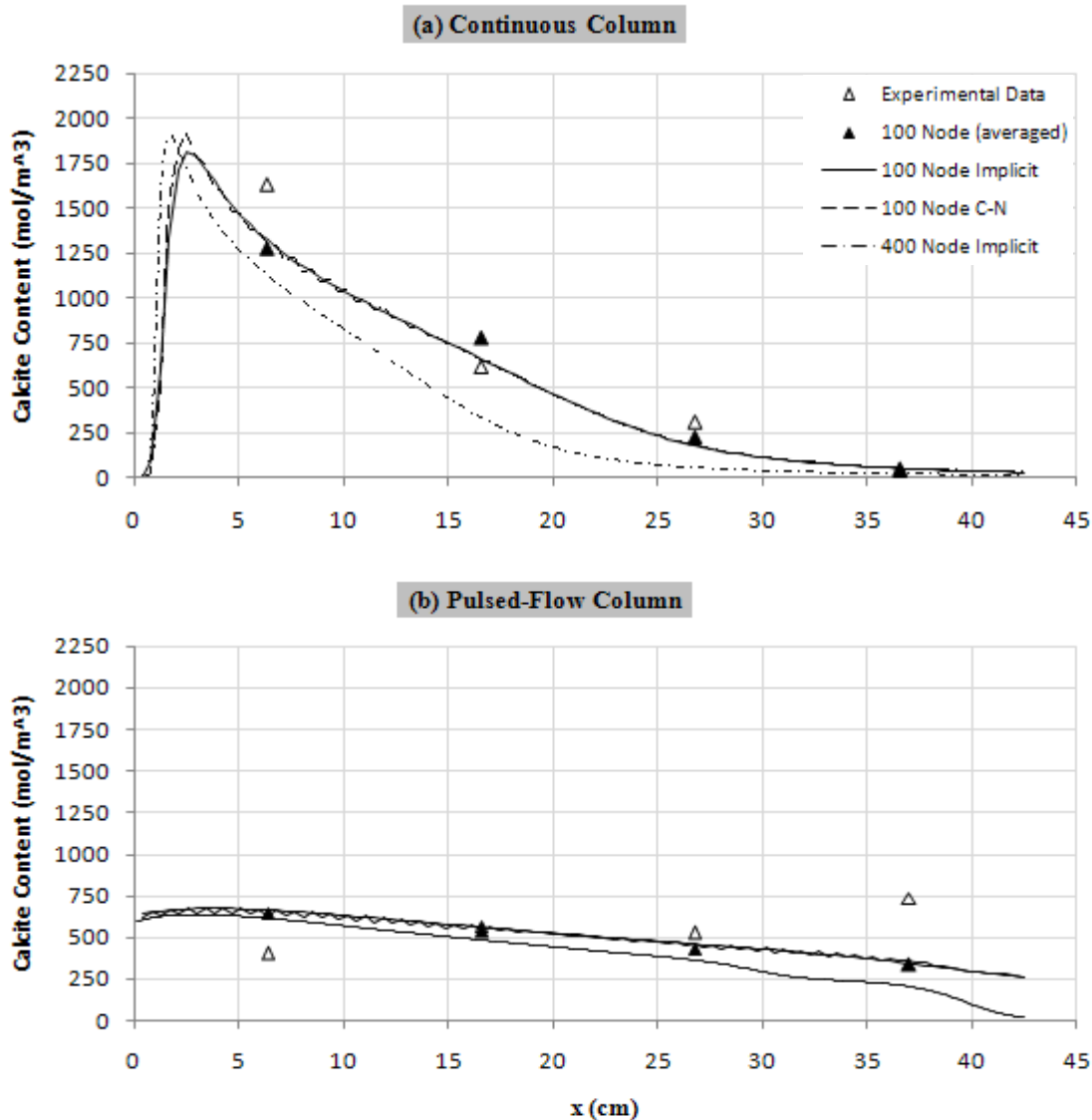


Figure 5. Simulated results and experimental data from continuous injection (a) and pulsed-flow injection (b) column conditions. Several numerical configurations (grid size and time stepping scheme) were tested to explore their effects on modeling results. Model parameters were calibrated in the 100-gridblock, Crank-Nicholson model which exhibited some instability (the "saw-tooth" trend).

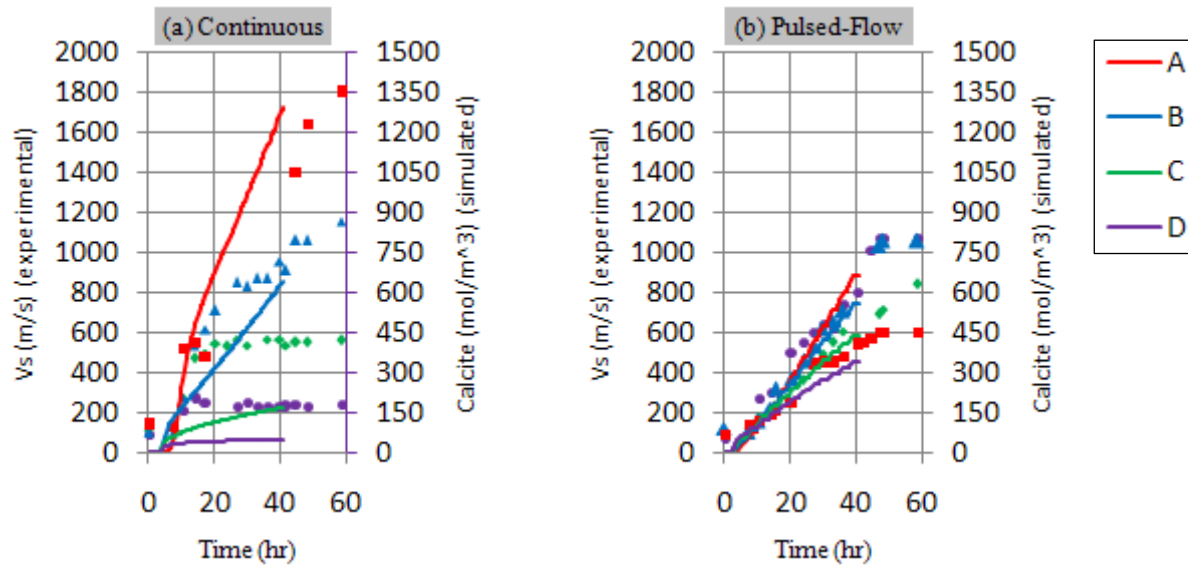


Figure 6. Left vertical axis shows experimental shear wave velocity measured from piezoelectric bender elements and right vertical axis shows simulated calcite growth at four locations in continuous (a) and pulsed-flow (b) injection columns. Location A is at the bottom (injection end) of the column while D is at the top (extraction end) of the columns (see Figure 2).

COMPARATIVE MODELING

TOUGHREACT will also be used to validate a model for *in situ* immobilization of strontium by co-precipitation with calcite. The original reaction network incorporates cation exchange, solid solutions, ureolysis kinetics, and transport via a streamtube ensemble to simulate an injection/extraction well triplet at the Vadose Zone Research Park (VZRP) in Idaho Falls, Idaho. The streamtube ensemble is created as multiple paths each modeled with PHREEQCII's 1D advective-dispersive transport and their respective breakthrough curves weighted by the path-respective flux fractions (of total fraction) to obtain the flux-average of flow contributions to the observation well. The flux fraction of a given path is the flux associated with that path's travel time. Deconvolution using solute flux averaging of tracer test data from experiments performed at the VZRP resulted in a travel-time distribution specific to the experimental site. The ensemble was parameterized from tracer test analyses; thus, the travel time distribution should inherently reflect regional gradients and hydrogeologic/hydraulic characteristics of the site.

In radial flow, the velocity within any given streamtube is variable in space, being highest at the input and output wells and approaching a minimum at the midpoint between the wells. This velocity variability (valid only in the absence of a regional gradient and in homogeneous conditions, thus termed here "idealized") is of significance if kinetic reactions

are velocity dependent, if they are heterogeneous, and/or if they impact physical characteristics, as does ureolytic calcite precipitation. To approximate this idealized non-uniform velocity, we implement a non-uniform spatial discretization within each streamtube that honors that streamtube's travel time as specified from the tracer tests. To achieve this within a code that uses a constant ("shift") velocity, each streamtube is separated into a specified number of cells, and non-uniform velocities within the streamtube are defined by varying the length of each cell while keeping the time spent within each cell constant. The overall travel time for that streamtube is equal to the summation of the time spent in each cell; similarly, the summation of each cell's length approximates the actual length of the streamtube. The use of PHREEQCII's transport function is convenient, because it treats each increment as a shift and allows different cell sizes (and thus freedom from local mass balance of water) within shifts. The mass-balance constraint is met overall, however, as long as total travel times are honored.

An alternate method for developing cell lengths is to utilize particle tracking simulators based on the solution to equations for groundwater flow analyzed via codes such as PUMPIT 4.0 (AquaLogic, 1995). Application of the tracer test data in PUMPIT will provide particle locations over time that can be used to develop a customized velocity function that reflects specific site characteristics. These site characteristics can also be addressed with this same streamtube ensemble approach, but reflect more site-

specific aspects of the paths, such as distribution of path lengths, and nonideal non-uniform velocities.

The reaction network for this application within PHREEQCII is largely the same as that applied to the column simulations currently modeled with TOUGHREACT. Thus, TOUGHREACT's Eulerian formulation can be utilized for verification of the PHREEQCII and streamtube ensemble simulation, which is Lagrangian. Conversely, PHREEQCII could be used to validate results produced by TOUGHREACT's columnar modeling. Ideally, comparison between the models, regardless of application, should yield similar results.

CONCLUSIONS

Microbial ureolytic calcite precipitation in batch and in 0.5 m column experiments was modeled in 1D with TOUGHREACT v2, using equilibrium and kinetic aqueous speciation and kinetic mineral precipitation. The model was calibrated with pH and calcite abundance data from the experiments, and inverted with UCODE. The data and model show that product inhibition and pulsed-flow injection produce relatively uniform calcite distribution in 0.5 m columns compared to continuous injection. The model reveals the importance of acquiring spatial calcite precipitation data, and ongoing and future bench- and pilot-scale experiments will aim to characterize calcite distributions in detail, to improve model calibration with inverse modeling. Furthermore, the model will be used in the forward sense to investigate flow rates and pump schedules that will influence future experiments.

Different grid discretizations and time stepping schemes were explored to understand their effects on geochemical modeling. Although the 100-gridblock fully implicit model showed more numerical dispersion than the 100-gridblock Crank-Nicholson and 400-gridblock fully implicit models, the two 100-gridblock models produced the same geochemical results. The Crank-Nicholson scheme showed some instability, which usually counter-indicates its utilization in TOUGHREACT. However, the 400-gridblock model may violate assumptions for Darcy flow based on a representative elementary volume. Since an analytical solution does not exist for this reactive transport system, careful convergence and sensitivity analysis must be performed to gain confidence in modeling results.

ACKNOWLEDGMENT

This research has been supported in part by the DOE ERSP project "Field Investigation of Microbially Facilitated Calcite Precipitation for Immobilization of Strontium-90 and Other Trace Metals in the Subsurface" and by NSF CMMI #0628782 project "Bio-Mediated Improvement of Soil and Soil-Structure Interface Behavior."

REFERENCES

- AquaLogic, *PUMPIT 4.0 User Manual*, AquaLogic, Berkeley, Calif., 1995.
- DeJong, J. T., B. M. Mortensen, B. C. Martinez, and D. C. Nelson, Bio-Mediated Soil Improvement, *Eco. Eng., Article in Press*, 2009.
- Fidaleo, M. and R. Lavecchia, Kinetic Study of Enzymatic Urea Hydrolysis in the pH Range 4-9, *Chem. Biochem. Eng., 17(4)*, 311-318, 2003.
- Fujita, Y., F. G. Ferris, R. D. Lawson, F. S. Colwell, and R. W. Smith, Calcium Carbonate Precipitation by Ureolytic Subsurface Bacteria, *Geomicrobiol. J., 17*, 305-318, 2000.
- Parkhurst, D., and C. Appelo. *User's guide to PHREEQC (Version 2) – A computer program for speciation, batch-reaction, one-dimensional transport, and inverse geochemical calculations*, Water-Resources Investigations Report 99-4259, Denver, CO, 1999.
- Poeter, E. P., M. C. Hill, E. R. Banta, S. Mehl, and S. Christensen, *UCODE_2005 and Six Other Computer Codes for Universal Sensitivity Analysis, Calibration, and Uncertainty Evaluation*, Techniques and Methods 6-A11, U.S. Geological Survey, Reston, Virginia, 2005.
- Xu, T., E. Sonnenthal, N. Spycher, and K. Pruess, *TOUGHREACT User's Guide: A Simulation Program for Non-isothermal Multiphase Reactive Geochemical Transport in Variably Saturated Geologic Media*, Report LBNL-55460, Earth Sciences Division, Lawrence Berkeley National Laboratory, University of California, Berkeley, 2004.

GENERAL

MODELING THE INTERACTION BETWEEN COMPACTED BENTONITE CLAY AND HYPERALKALINE SOLUTION

Merja Tanhua-Tyrkkö (*), Markus Olin (*) and Jarmo Lehtikoinen (**)

(*) VTT Technical Research Centre of Finland
P.O. Box 1000
FI-02044 VTT, Finland

(**) B+Tech Oy
Laulukuja 4
FI-00400, Helsinki, Finland

e-mail: merja.tanhua-tyrkk@vtt.fi

ABSTRACT

Spent nuclear fuel is planned to be disposed of in deep underground repositories in many countries, including Finland. An essential part of the Finnish final repository concept is a compacted bentonite buffer. Unfortunately, experimental work is only of limited use when predicting the long-term stability of bentonite in repository conditions, and therefore complementary modeling tools and method development are needed to gain confidence in the safety of the disposal. This work involves the modeling of the chemical interaction between inflowing hyperalkaline solution—envisaged to constitute a risk to the long-term chemical stability of the buffer—and bentonite clay in a column filled with crushed rock and compacted bentonite. The main interest was in the cation-exchange equilibria and mineral alterations in bentonite. TOUGHREACT was found to be a useful modeling tool in stability studies of the bentonite. Especially good results were gained for the cation-exchanger composition.

INTRODUCTION

In Finland, spent nuclear fuel is planned to be disposed of in a repository excavated deep (400–700 m) in the crystalline bedrock at the Olkiluoto site. The disposal is based on an engineered-barrier system (*Figure 1*), which contains and isolates, and retards the migration of radionuclides in the spent fuel. Details on the safety functions of the KBS-3 repository concept can be found from Pastina and Hellä (2008).

In the disposal method, the bentonite clay surrounding the spent fuel canister has an important role in providing a buffer against minor rock movements, keeping the canister in place, and conducting heat from the canister to the rock. It has a high adsorption capacity, and solute transport within it is governed by diffusion, which effectively retards the migration of released radionuclides.

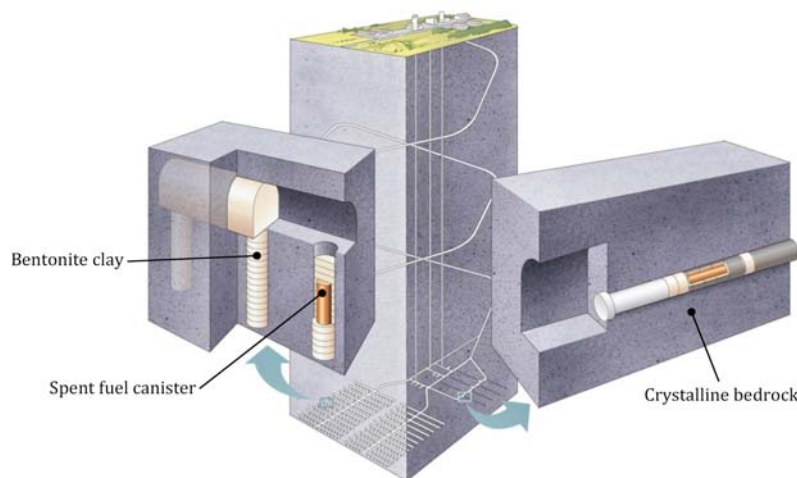


Figure 1. The KBS-3V (left) and KBS-3H (right) alternative realizations of the KBS-3 spent fuel disposal method. KBS-3V is the reference variant.

A possible risk for the long-term chemical stability of bentonite clay is posed by cementitious materials used in the construction and operation of the repository. The chemical degradation of these materials may produce a highly alkaline leachate. If this high-pH solution comes into contact with bentonite, the beneficial properties of bentonite may be impaired (Figure 2). The long-term safety concerns include a loss of bentonite swelling pressure, increased hydraulic conductivity, and possibly fracturing of bentonite due to cementation.

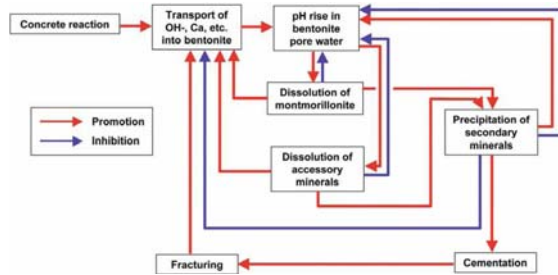


Figure 2. Dynamic nature of bentonite-cement interaction (Takase, 2004). Promoting and inhibiting effects are denoted by red and blue arrows, respectively.

GOAL

The modelling was based on the experimental work reported in Vuorinen et al. (2006), where the interest was in the effect of hyperalkaline water (pH 12.5) on the cation exchange, mineral alterations, and the pH-buffering in compacted bentonite. In the present modeling exercise, the main interest was in the first two. The cation form of the bentonite buffer has implications for material behavior and may hence affect the long-term performance of the buffer in the repository.

EXPERIMENTAL

The experimental set-up in Vuorinen et al. (2006) consisted of an 11 cm long cylindrical column, with a diameter of 5 cm. One half of the column was filled with compacted bentonite, the other half with crushed rock (Figure 3). The rock was from the Olkiluoto site and crushed to a grain size of 1.5 mm.

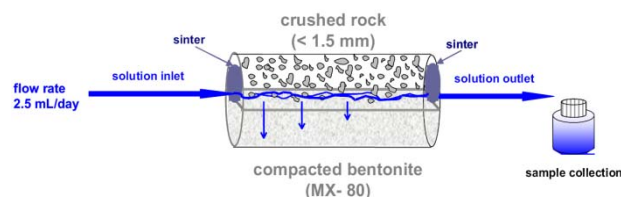


Figure 3. The experimental setup used in Vuorinen et al. (2006)

The clay material was compacted Volclay MX-80 bentonite (dry density $\sim 1600 \text{ kg/m}^3$); its mineralogical composition is shown in Table 1.

Table 1. Mineral composition of MX-80 bentonite (Vuorinen et al., 2006)

Mineral	Volume fraction
Montmorillonite (cation exchanger)	0.82
Albite	0.07
Quartz	0.05
Cristobalite	0.04
Gypsum	0.01
Muscovite	0.01

The hyperalkaline solution (Table 2) was injected into the crushed rock from the left end of the column and effluent samples were collected from the right end of the column (see Figure 3).

Table 2. Chemical composition of the inflow water (Vuorinen et al., 2006)

Aqueous component	Total dissolved concentration (mol/l)
Na^+	0.428
Ca^{2+}	0.018
Cl^-	0.462
pH	12.5

NOTE: Concentrations of other component species (Al^{3+} , K^+ , Mg^{2+} , $\text{H}_4\text{SiO}_4(\text{aq})$, SO_4^{2-}) in the inflow solution were at trace level.

The flow rate through the column was 2.5 ml/d ($\sim 1 \text{ l/a}$), which is comparable with the flow rate in a deep repository.

Two parallel experiments were performed, one for 360 days and the other for 560 days of interaction.

MODELING

Transport

The model considered diffusion in the compacted bentonite and flow in the crushed rock (hydraulic properties of the two materials in Table 3).

Table 3. Properties of bentonite and crushed rock.

Parameter	Bentonite	Crushed rock
Density (kg/m ³) ⁽ⁱ⁾	2750	2650
Porosity (-)	0.438	0.285
Permeability (x, y and z) (m ²)	1.0E-21 ⁽ⁱⁱ⁾	5.0E-11 ^(iv)
Tortuosity (-)	0.13 ⁽ⁱⁱⁱ⁾	0.53 ^(v)

⁽ⁱ⁾ (Vuorinen et al., 2006)

⁽ⁱⁱ⁾ (Harrington and Horseman, 2003), (Jussila, 2007)

⁽ⁱⁱⁱ⁾ Calculated from the empirical relation for the effective diffusion coefficient of tritiated water (Ochs and Talerico, 2004)

^(iv) (Odong, 2007)

^(v) From the Bruggeman equation

A molecular diffusivity of 10⁻⁹ m²/s was assigned for all aqueous species.

Chemistry

The Gaines-Thomas cation-exchange selectivities in MX-80 bentonite are given in Table 4.

Table 4. Gaines-Thomas cation-exchange selectivities for MX-80 bentonite (Bradbury and Baeyens, 2003)

Reaction	log K
$\text{Na}^+ + \text{K-X} = \text{Na-X} + \text{K}^+$	0.6
$\text{Na}^+ + \frac{1}{2}\text{Ca-X}_2 = \text{Na-X} + \frac{1}{2}\text{Ca}^{2+}$	0.41
$\text{Na}^+ + \frac{1}{2}\text{Mg-X}_2 = \text{Na-X} + \frac{1}{2}\text{Mg}^{2+}$	0.34

The cation-exchange capacity (CEC) of MX-80 bentonite is 71.7 meq/100 g (Vuorinen et al., 2006). For TOUGHREACT, the initial water composition was formulated to reproduce the experimentally found equivalent fractions in the exchanger phase (Table 5) and to represent a very dilute solution with a pH of 7. The concentrations for the exchangeable cations in the initial water were calculated according to Tournassat et al. (2007). Isothermal conditions (25°C) were assumed throughout.

Table 5. Initial equivalent fractions of exchangeable cations.

	eq/100g in bentonite	Equivalent fraction
Na ⁺	0.552	0.770
Ca ²⁺	0.106	0.148
K ⁺	0.0086	0.012
Mg ²⁺	0.0502	0.07

In addition to cation exchange, mineral alterations in bentonite were of interest. Except for

montmorillonite, which was taken as an inert cation exchanger, mineral reactions were kinetically controlled. Consequently, kinetic parameters for the primary and secondary minerals needed to be defined (Table 6). The precipitation rates of minerals were taken to be identical to their dissolution rates. To simplify calculations, the crushed rock was assumed chemically inert; that is, no reactions involving its constituent minerals were considered in the calculations. Also, no feedback from mineral dissolution/precipitation reactions to the hydraulic properties of the materials was taken into account.

The thermodynamic database adopted for aqueous and mineral equilibria was THERMOTDEM (Blanc et al., 2008). The thermodynamic data for K-feldspar and calcium silicate hydrate (CSH) gels were taken from the default TOUGHREACT database (ThermXu.dat) and from Montori et al., 2008, respectively.

RESULTS

To enable comparing predicted and experimental results, the column was sectioned as in Figure 4.

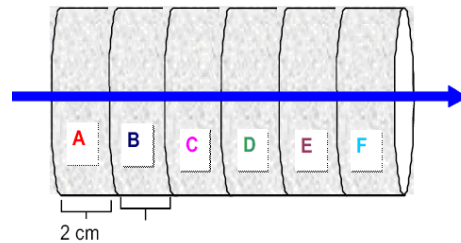


Figure 4. Labelling of the column sections in the bentonite half taken for chemical analyses. The blue arrow indicates the direction of the flow.

The results for the cation exchange are presented in Figure 6 for Ca and Na and in Figure 7 for K and Mg. The initially Na-rich montmorillonite would not convert to a Ca-rich form, because the concentration of sodium in the inflowing water is relatively high. The experimentally observed increase in potassium content is also clearly seen in model results.

Table 6. Dissolution and precipitation parameters for the primary and secondary species. The kinetic rate constants (k_{25}) ($\text{mol/m}^2/\text{s}$) are from Palandri and Kharaka (2004) unless noted otherwise.

Mineral Dissolution/pr	Precipitation parameters						
	Neutral mechanism	Acid mechanism		Base mechanism		Surface area	Grain radius
	k_{25}	k_{25}	$n(H^+)$	k_{25}	$n(H^+)$	(cm^2/g)	(m)
<i>Primary minerals</i>							
Albite	2.8E-13	6.9E-11	0.317	2.5E-16	-0.471	9.8	0.001
Cristobalite	4.9E-13					9.8	0.001
Gypsum	2.0E-3	No additional mechanisms				9.8	0.001
Muscovite	3.0E-14	1.41E-12	0.37	2.82E-15	-0.22	151.6	0.001
Quartz	1.0E-14	Not available		5.0E-17	-0.5	9.8	0.001
<i>Secondary minerals</i>							
Brucite	5.75E-9	1.86E-5	0.5	Not available		5.0E4	0.001
Gibbsite	3.16E-12	2.24E-8	0.992	2.0E-17	-0.784	5.0E4	0.001
K-feldspar	3.9E-13	8.7E-11	0.5	6.31E-12	-0.823	5.0E4	0.001
Ettringite, Friedel_Salt, Hydrotalcite, Katoite, Monosulfoaluminate, Portlandite, Straetlingite, Tobermorite_11A, Tobermorite_14A	1.0E-10 ⁽ⁱ⁾	No additional mechanisms				5.0E4	0.001
Hydrogarnet, CSH_0.0 ⁽ⁱⁱ⁾ , CSH_0.4, CSH_0.8, CSH_1.2, CSH_1.667	Assumed at equilibrium						
⁽ⁱ⁾ Set arbitrarily.							
⁽ⁱⁱ⁾ CSH_x, where x is the calcium-to-silica ratio.							

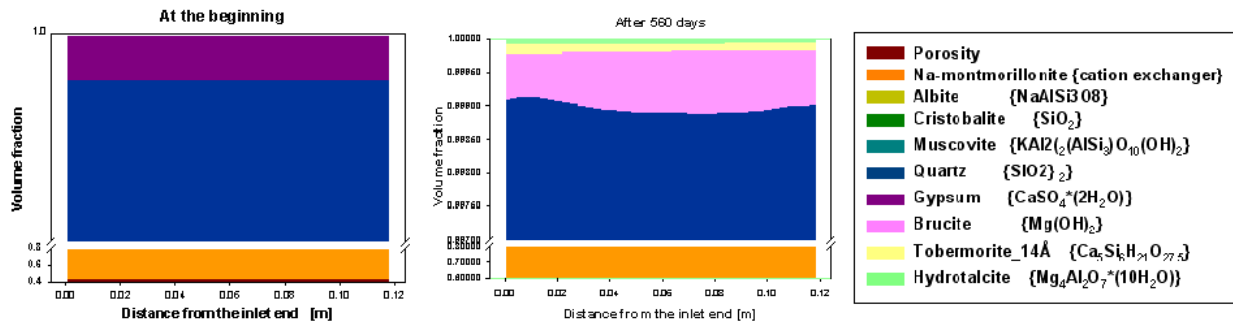


Figure 5. Mineralogical composition of bentonite at the beginning of the experiment (left) and after 560 days (right). The changes in volume fraction are seen to be quite small. Note the scale on the y axis.

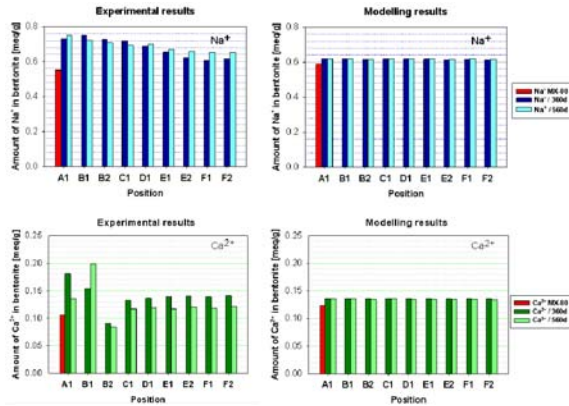


Figure 6. Experimental (left) and calculated (right) exchangeable calcium (top) and sodium (bottom) in the column (see Figure 4 for the legend).

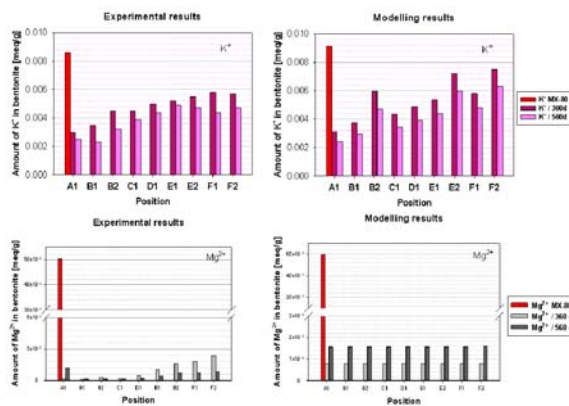


Figure 7. Experimental (left) and calculated (right) exchangeable potassium (top) and magnesium (bottom) in the column (see Figure 4 for the legend).

The mineralogical composition of the bentonite at the onset of the experiment and after 560 days of interaction is presented in Figure 5.

DISCUSSION

The spatial and temporal match between experimental and predicted exchangeable cations in the exchanger phase (i.e., montmorillonite) was found to be fairly good, except for magnesium. Consequently, this supports the conception that the dissolution rate of montmorillonite is slow enough not to invalidate our model assumption on the chemical inertness of montmorillonite within the experimental time.

From Figure 5, the change in the mineral composition of bentonite is seen to be insignificant. This is not surprising, given the short duration of the experiment and the assumed inertness of montmorillonite, which

has, by and large, the greatest volume fraction in bentonite (see Table 1).

CONCLUSIONS

The modeling of the cation-exchange equilibria from the flow-through experiment reported in Vuorinen et al. (2006) with TOUGHREACT was successful. In addition, some minor mineral alterations in bentonite, due to the hyperalkaline solution, were calculated.

The interaction of cementitious material with bentonite needs to be studied in highly variable and challenging systems, such as that formed by a spent-fuel repository. Theoretical model development and its successful implementation into TOUGHREACT, as realized in this work, will form the essential know-how for future studies

ACKNOWLEDGMENT

This work was jointly funded by VTT (Technical Research Centre of Finland) and Posiva Oy.

REFERENCES

- Blanc, P., A. Lassin and P. Piantone, THERMODDEM a database devoted to waste minerals, BRGM - Bureau de Recherches Géologiques et Minières, Orléans, France, 2008, <http://thermoddem.brgm.fr/>,
- Bradbury, M. H. and B. Baeyens, Porewater chemistry in compacted re-saturated MX-80 bentonite, *Journal of Contaminant Hydrology*, 61(1-4), 329-338, 2003.
- Harrington, J. F. and S. T. Horseman, *Gas migration in KBS-3 buffer bentonite. Sensitivity of test parameters to experimental boundary conditions*. SKB-TR-03-02, SKB, Svensk Kärnbränslehantering AB, Stockholm, Sweden, 2003.
- Jussila, P., *Thermomechanics of swelling unsaturated porous media Compacted bentonite clay in spent fuel disposal*, Report STUK-A223, Yliopistopaino, Helsinki, Finland, 2007.
- Montori, J., J. M. Soler and M. W. Saaltink, *Reactive transport modeling of the effect of hyperalkaline solutions along a fracture at the ONKALO site*, Posiva-WR 2008-14, Posiva Oy, Olkiluoto, Finland, 2008.
- Ochs, M. and C. Talerico, *SR-Can Data and uncertainty assessment Migration parameters for the bentonite buffer in the KBS-3 concept*, SKB-TR-04-18, SKB, Svensk Kärnbränslehantering AB, Stockholm, Sweden, 2004.

- Odong, J., Evaluation of empirical formulae for determination of hydraulic conductivity based on grain-size analysis, *Journal of American Science*, 3(3), 54-60, 2007.
- Palandri, J. L. and Y. K. Kharaka, *A compilation of rate parameters of water-mineral interaction kinetics for application to geochemical modeling*, Open File Report 2004-1068, U.S. Geological Survey, Menlo Park, California, USA, 2004.
- Pastina, B. and P. Hellä, *Expected evolution of a spent nuclear fuel repository at Olkiluoto (revised)*, Posiva-2006-05, Posiva Oy, Olkiluoto, Finland, 2008.
- Takase, H., *Discussion on PA model development for bentonite barriers affected by chemical interaction with concrete: Do we have enough evidence to support bentonite stability*, WR 2004-25, Posiva Oy, Olkiluoto, Finland, 2004.
- Tournassat, C., H. Gailhanou, C. Crouzet, Two cation exchange models for direct and inverse modelling of solution major cation composition in equilibrium with illite surfaces, *Geochimica et Cosmochimica Acta*, 71(5), 1098-1114, 2007.
- Vuorinen, U., J. Lehtikoinen, A. Luukkonen and H. Ervanne, *Effects of salinity and high pH on crushed rock and bentonite - Experimental work and modelling*, Posiva-2006-01, Posiva Oy, Olkiluoto, Finland, 2006.

IMPLEMENTING THE BARCELONA BASIC MODEL INTO TOUGH-FLAC FOR ANALYSIS OF THE GEOMECHANICAL BEHAVIOR OF UNSATURATED SOILS

Jonny Rutqvist¹, Yuji Ijiri², and Hajime Yamamoto²

¹Lawrence Berkeley National Laboratory, Berkeley, USA
e-mail: jrutqvist@lbl.gov

²Taisei Corporation, Tokyo, Japan
e-mail: ijiri@ce.taisei.co.jp, hajime.yamamoto@sakura.taisei.co.jp

ABSTRACT

This paper presents the implementation of the Barcelona Basic Model (BBM) into the TOUGH-FLAC simulator for analysis of geomechanical behavior of unsaturated soils. We implemented the BBM model into TOUGH-FLAC by (1) extending the existing Modified Cam-Clay (MCC) model in FLAC3D using the FLAC3D User Defined constitutive Model (UDM) option, and (2) by adding routines for suction-dependent strain and net stress (referring to total stress less gas pressure) for unsaturated soils. We implemented a thermo-elastoplastic version of the BBM in which the soil strength not only depends on suction, but also on temperature. The model and its implementation were verified and tested against several examples of laboratory and independent numerical solutions of coupled thermal-hydrological-mechanical behavior of unsaturated soils.

INTRODUCTION

The Barcelona Basic Model (BBM) is a geomechanical constitutive model for the elasto-plastic behavior of soils under unsaturated conditions. The model was first developed and presented in the early 1990s as an extension of the classical Modified Cam Clay (MCC) model from saturated to unsaturated soil conditions (Alonso et al., 1990). The model can describe many typical features of unsaturated-soil mechanical behavior, including wetting-induced swelling or collapse strains depending on the magnitude of applied stress, the increase in shear strength, and apparent preconsolidation stress with suction (Gens et al., 2006).

In this paper, we present the implementation of the BBM into the TOUGH-FLAC simulator (Rutqvist et al., 2002, 2003). We implement a thermo-elastoplastic version of the BBM in which the soil strength not only depends on suction, but also on temperature and includes features for expansive (swelling) clay. This constitutive model, denoted herein as BBM-TEPU, is also implemented in the CODE-BRIGHT finite element code at the University of Cataluña, Barcelona (CIMNE, 2002), and was recently applied to model the FEBEX *in situ* heater test at the Grimsel Test Site in Switzerland (Gens et al., 2009). We verified and tested the implemented constitutive model by com-

parison to published laboratory data on unsaturated soils, including swelling and triaxial loading of MX-80 bentonite.

THE BBM-TEPU MODEL

This section presents an overview of the BBM-TEPU constitutive model and its relation to the original BBM and MCC models. The description of the BBM-TEPU model is in part similar to that of Kristensson and Åkesson (2008), but with the inclusion of temperature effects.

Stress State and Failure Surface

In soil mechanics, the mechanical behavior and mechanical constitutive laws are frequently expressed in terms of effective mean pressure, P' and deviatoric stress q . The effective mean pressure is equivalent to the mean of effective normal stresses, defined as:

$$P' = \frac{1}{3}(\sigma'_1 + \sigma'_2 + \sigma'_3) = P - P^p \quad (1)$$

where P is total mean stress and P^p is pore pressure.

The deviatoric stress, a measure of shear stress, is defined as:

$$q = \sqrt{\frac{(\sigma'_1 - \sigma'_2)^2 + (\sigma'_2 - \sigma'_3)^2 + (\sigma'_1 - \sigma'_3)^2}{2}} \quad (2)$$

The original MCC model is expressed in terms of P' and q where P' is the conventional effective mean stress under saturated conditions, defined as

$$P' = \sigma'_m = \sigma_m - P^p \quad (3)$$

where σ_m is the total mean stress and P^p is the pore pressure. However, in the BBM, the strains are related to changes in the two independent stress variables, namely the net stress P' , defined as

$$P' = \sigma'_m = \sigma_m - P^g \quad (4)$$

and suction, s , defined as

$$s = P^g - P^l \quad (5)$$

where P^g and P^l are gas and liquid phase pressures.

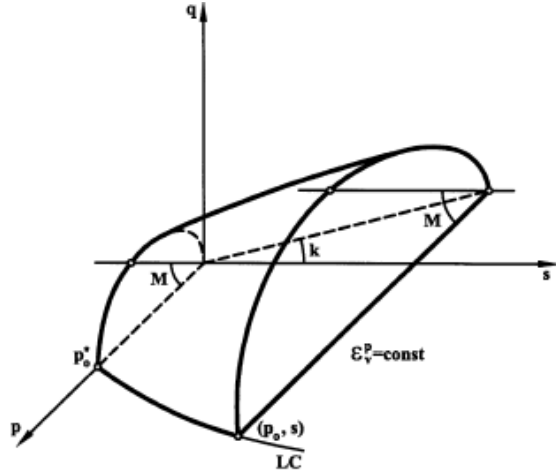


Figure 1. Three-dimensional representation of the yield surface in the BBM (Gens et al., 2006).

The original BBM model is summarized in Figure 1, where the three-dimensional yield surface in p-q-s space is depicted (Gens et al., 2006). Under saturated conditions ($s = 0$), the yield surface corresponds to the MCC ellipse (Roscoe and Burgland, 1968), and the size of the elastic domain increases as suction increases. The rate of increase, represented by the loading-collapse (LC), is one of the fundamental characteristics of the BBM.

Five parameters are required to define the MCC model, and 7 additional parameters are required for the BBM model. That is, 12 parameters need to be determined from well-controlled laboratory experiments to apply the BBM model. In the BBM-TEPU model, the failure surface also depends on the temperature. Twenty-one material parameters are needed to completely define this model.

In these soil mechanics models, the concepts of specific volume, v , and void ratio, e , are used, which in turn can be related to porosity, ϕ , according to:

$$\phi = \frac{v-1}{v} = \frac{e}{1+e} \quad (6)$$

The evolution of void ratio is calculated from the evolution of volumetric strain.

Strains due to stress, and temperature and suction changes

In the TEPU model, the strain tensor, $\boldsymbol{\varepsilon}$, is related to P' , q and s . We may partition the total strain into mechanical elastic, mechanical plastic, hydraulic, and thermal strain:

$$\boldsymbol{\varepsilon} = \boldsymbol{\varepsilon}^e + \boldsymbol{\varepsilon}^p + \boldsymbol{\varepsilon}^s + \boldsymbol{\varepsilon}^T \quad (7)$$

where the hydraulic strain represents the strain associated with changes in suction.

Mechanical Elastic Strain

The mechanical volumetric elastic volumetric strain increment is defined as

$$d\varepsilon_v^e = \frac{1}{K^m} dP' \quad (8)$$

where the mechanical bulk modulus is defined as

$$K^m = \frac{(1+e)P'}{\kappa_i(s)} \quad (9)$$

The elastic modulus function $\kappa_{PS}(s)$ is defined as

$$\kappa_{PS} = \kappa_{PS0} [1 + s\alpha_{PS}] \quad (10)$$

The deviatoric mechanical strain increments are defined as

$$de^e = \frac{1}{2G} ds \quad (11)$$

where G is obtained using a constant Poisson's ratio ν in

$$G = \frac{3(1-2\nu)}{2(1+\nu)} K^m \quad (12)$$

Mechanical Plastic Strain

The elastic region is bounded by the yield surface

$$f = \frac{q^2}{g_y(\theta)^2} - \frac{M^2}{g_y(\theta=0)^2} (p' + p_s(s, T))(P_0^*(p_0^*, s)) - p' = 0 \quad (13)$$

where θ is the stress invariant called Lode's angle, and the function $g_y(\theta)$ describes the shape of the yield surface in the deviatoric plane. The shape function is assumed to be equal to unity in this work (von Mises). M is the constant slope of the critical state line defining the current maximum deviatoric, or shear, strength. The function

$$P_s(s, T) = P_{S0} + k_s s \exp[-\rho_s (T - T_{ref})] \quad (14)$$

describes the yield surface at hydrostatic tension as a function of suction and temperature change by increasing the cohesion.

$P_0^*(P_{0T}^*(T), \lambda(s))$ is the yield stress at hydrostatic compression, expressed as

$$P_0(s, T) = p^c \left(\frac{P_{0T}^*(T)}{P^c} \right)^{[\lambda(0) - \kappa_{i0}][\lambda(s) - \kappa_{i0}]} \quad (15)$$

where $P_{0T}^*(T) = P_0^* + 2(\alpha_1 \Delta T + \alpha_3 \Delta T |\Delta T|)$ is the yield stress at hydrostatic compression conditions at full saturation, containing $P_0^* = P_{0T}^*(T_0)$, which is a hardening parameter having the evolutionary law

$$dP_0^* = \frac{1+e}{\lambda_0 - \kappa_{i0}} P_0^* d\varepsilon_v^p \quad (16)$$

$\lambda(s)$ is a parameter describing the soil stiffness; $\lambda(s)$ appears in the expression for the description of the specific volume $v = N(s) - \lambda(s) \ln(p'/p^c)$, where p^c is a reference pressure, and $N(s)$ is the specific volume at $p = p^c$. $\lambda_{PS}(s)$ is taken as

$$\lambda_{PS}(s) = \lambda_{PS0} \left((1 - r_\lambda) \exp(-\beta_\lambda s) + r_\lambda \right) \quad (17)$$

when the stress state is on the yield surface the plastic strains are obtained from the yield rule

$$d\varepsilon^p = d\Lambda \frac{\partial g}{\partial \sigma} \quad (18)$$

where $d\Lambda$ is the plastic multiplier obtained from the consistency condition $df = 0$ and g is the plastic potential defined by

$$g = \frac{\alpha_a q^2}{g_y(\theta)^2} - \frac{M^2}{g_y(\theta=0)^2} (p' + p_s(s, T)) (P_0(P_0^*, s)) - p' \quad (19)$$

where α is the parameter that gives rise to the nonassociative model, i.e. $g \neq f$.

Thermal Strain

Thermally induced strains are purely volumetric:

$$d\varepsilon_v^t = (\alpha_0 + 2\alpha_2 \Delta T) dT \quad (20)$$

where α_0 and α_2 are material parameters defining the temperature-dependent volumetric thermal expansion coefficient.

Hydraulic Strain

In analogy with thermally induced strains, the hydraulic (or suction) strains are purely volumetric:

$$d\varepsilon_v^h = \frac{1}{K^h} ds \quad (21)$$

where the hydraulic bulk modulus is defined.

$$K^h = \frac{(1+e)(s + p_{am})}{\kappa_{SP}(p', s)} \quad (22)$$

κ_{SP} is a hydraulic elastic modulus function defined as

$$\kappa_{SP}(p', s) = \kappa_{SP0} \left(1 + \alpha_{SP} \ln \frac{p'}{P_{ref}} \right) \exp(\alpha_{SS} s) \quad (23)$$

IMPLEMENTATION OF BBM-TEPU MODEL IN TOUGH-FLAC

The implementation of the BBM-TEPU model was conducted by adding a new constitutive model to the FLAC3D, using the option of User Defined Models (UDM). In addition to developing and implementing the BBM-TEPU model, hydraulic (or suction induced) volumetric strain had to be added.

Suction and effective pore pressure

For the implementation of the BBM-TEPU model into TOUGH-FLAC, suction, as well as gas pressure in the pores, is needed. In this implementation, it is assumed that

$$s = -P^c \quad (23)$$

where P^c is the capillary pressure.

Moreover, in TOUGH-FLAC, the concept of net pressure for unsaturated soils is implemented by

transferring the maximum of the gas or liquid pressure from TOUGH to FLAC3D according to

$$P^P = \text{MAX}(P^l, P^g) \quad (24)$$

This approach enables simulation of both saturated and unsaturated soils. In TOUGH-FLAC, this is done by always transferring the first primary TOUGH2 variable of pressure from TOUGH to FLAC. In single-fluid phase conditions, the first primary variable is P^g for single gas phase or P^l for single liquid phase. For two fluid phase conditions, the primary variable is gas pressure, which is greater than the liquid pressure.

Then, for fully liquid saturated conditions, the conventional effective stress applies according to Equation (3), whereas for unsaturated conditions, the mechanical behavior depends on the two stress variables net stress and suction, defined in Equations (4) and (5).

Hydraulic strain

Hydraulic strain is added to the TOUGH-FLAC in an analogous manner to treatment of thermal strain in FLAC3D. The hydraulic strain is defined as

$$d\varepsilon_v^h = \frac{1}{K^h} ds \quad (25)$$

where s is changes in suction and K^h is denoted as the hydraulic modulus, as suggested by Kristensson and Åkesson (2008). The hydraulic strain is considered by adding an equivalent mean stress increment according to

$$d\sigma_m^h = K^m d\varepsilon_v^h = \frac{K^m}{K^h} ds \quad (26)$$

This is implemented in FLAC3D by adding increments to the normal stresses:

$$d\sigma_{xx}^h = \frac{K^m}{K^h} ds \quad (27a)$$

$$d\sigma_{yy}^h = \frac{K^m}{K^h} ds \quad (27b)$$

$$d\sigma_{zz}^h = \frac{K^m}{K^h} ds \quad (27c)$$

Both K^m and K^h are dependent on suction and mean net stress and are calculated within the constitutive TEPU model, whereas the stress increments are added in a routine using FISH, which is a programming capability attached to FLAC3D

BBM-TEPU UDM constitutive mode

The BBM+TEPU constitutive model was programmed in C++ and compiled as a DLL file (dynamic link library) that can be loaded whenever needed. The new C++ program module was developed by modifying an existing C++ program module for the FLAC3D MCC model. Whereas the MCC model depends on five material parameters, the

BBM-TEPU model depends on 21 material parameters to be fully defined. The BBM-TEPU model was developed from the existing MCC model by adding suction and temperature dependency to the failure surface and yield function. Moreover, the formulation was extended from associative to nonassociative plasticity. The calculation of plastic multiplier Λ was modified to consider suction and temperature-dependent P_s and P_0 , and the nonassociativity parameter, α_a . The final C++ code was compiled as a DLL, resulting in the file `bbmtepu.dll`. The `bbmtepu.dll` file should be added to the `exe32` directory under `FLAC3D` and can be invoked when the `FLAC3D` is configured for UDM.

SIMULATION TESTS OF THE IMPLEMENTED BBM-TEPU MODEL

The newly implemented geomechanical constitutive model was tested by running a number of simulation test examples listed in Table 1. The performance of the newly implemented model was confirmed by comparison to results published in Alonso et al. (1990) and Kristensson and Åkesson (2008). The three test examples K&A1, K&A2 and K&A3 are particularly useful in this context, as these enable comparison to actual experimental data on MX-80 bentonite material.

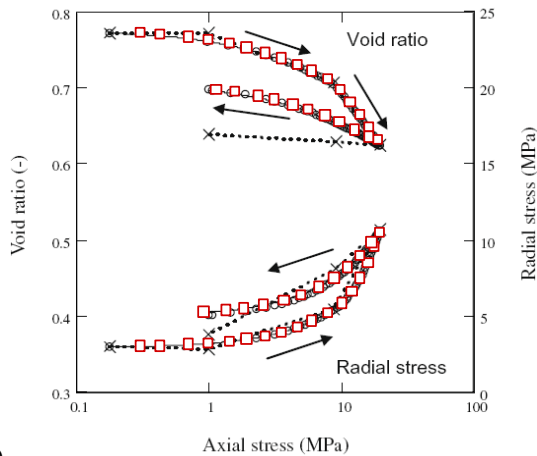
Table 1. Simulation tests of the implemented BBM-TEPU implemented in TOUGH-FLAC.

Test	Processes	Reference
AGJ1	Volumetric deformation induced by wetting at increasing confining stress	Alonso et al. (1990)
AGJ2	Effect of alternate application of load and suction.	Alonso et al. (1990)
AGJ4	Shear tests for different suction.	Alonso et al. (1990)
AGJ6	Shear tests on partially saturated Kaoline	Alonso et al. (1990)
K&A1	Compression test of MX80 bentonite with constant suction	Kristensson and Åkesson (2008)
K&A2	Elastoplastic behavior of during a swelling test of MX-80 bentonite	Kristensson and Åkesson (2008)
K&A3	Triaxial compression of MX-80 bentonite	Kristensson and Åkesson (2008)

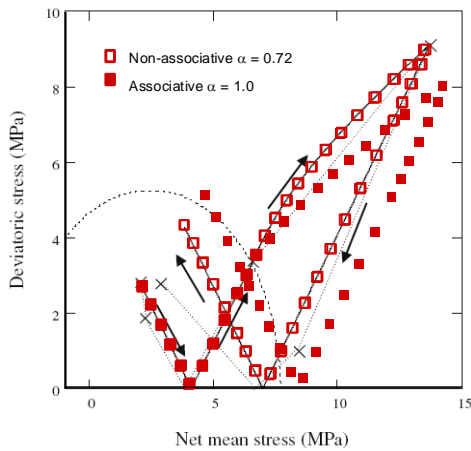
Table 2. BBM-TEPU model parameters for simulation test K&A1.

Parameter	Value	Description
κ_{PS0}	0.057	Initial (zero suction) elastic slope for v-p'
κ_{SP0}	0.0	Initial (zero suction) elastic slope for v-s
ν	0.224	Poisson's ratio
α_{SS}	0.0	Parameter for s (only for expansive material)
α_{PS}	0.0	Parameter for i (only for expansive material)
α_{SP}	0.0	Parameter for s (only for expansive material)
P_{ref}	0.0	Reference mean stress (only for expansive material)
α_0	0.0	Basic volumetric thermal expansion coefficient at reference temperature
α_2	0.0	Parameter for temperature dependency of thermal expansion coefficient
λ_{PS0}	0.101	Slope of void ratio—mean stress curve at zero suction
r_λ	0.0	Parameter defining the maximum soil stiffness
β_λ	0.0	Parameter for increase of soil stiffness with suction
ρ_s	0.0	Parameter for decrease of tensile strength due to T
k_s	0.1	Parameter for increase of tensile strength due to s.
P_{S0}	0.0	Tensile strength in saturated conditions
P^C	0.1 MPa	Reference pressure
M	1.0	Critical state line parameter
α_a	0.72	Non-associativity parameter
v_L	3.535	Initial specific volume
P_0^*	7.7 MPa	Initial preconsolidation mean stress for saturated soil
T_0	NA	Reference temperature

In this section, the K&A1 test example is presented in more detail. The K&A1 is a test example involving a compression test at constant suction with comparison to experimental data of MX-80 bentonite, as presented by Kristensson and Åkesson (2008). The input parameters taken from Kristensson and Åkesson (2008) are presented in Table 2. The experiment involves axial loading with compressive stress from 0.18 MPa to 19.77 MPa, and subsequent unloading to 1.0 MPa. The loading and unloading was performed under a constant confining compressive stress of 2.97 MPa and a constant suction of 28 MPa. Both the experimental and numerical results show a significant irreversible volumetric deformation as a result of plastic collapsing soils (Figure 2).



(a)



(b)

Figure 2. Comparison of TOUGH-FLAC results using BBM-TEPU model with results presented in Kristensson and Åkesson (2008) for MX-80 bentonite. The FLAC3D BBM-TEPU results are the red squares.

Figure 2 shows a perfect agreement between the FLAC3D TEPU and the calculation results published in Kristensson and Åkesson (2008). Moreover, Figure 2b shows a comparison of FLAC3D TEPU

results for associative plasticity ($\alpha = 1.0$) and nonassociative plasticity ($\alpha = 0.72$). It is very important to consider nonassociative plasticity to replicate the stress-strain behavior observed in the laboratory, which necessitated the implementation of the nonassociative plasticity model.

SIMULATION TESTS OF TOUGH-FLAC WITH BBM-TEPU CONSTITUTIVE MODEL AND SWELLING

The interaction of the TOUGH-FLAC simulator with the newly implemented TEPU model and the new implementation of swelling (or hydraulic strain) are tested using two example problems:

- 1) A laboratory swelling stress experiment.
- 2) A horizontal nuclear waste emplacement tunnel at 500 m depth.

The two examples are simulated using two options:

- 1) Simple swelling model using a linear elastic model and swelling strain linearly dependent on saturation changes.
- 2) A full BBM-TEPU model with suction-dependent swelling.

The input parameters for the BBM-TEPU model were extracted from Gens et al. (2009) and represent material parameters for the bentonite buffer to model the FEBEX experiment at Grimsel test site in Switzerland.

TOUGH-FLAC simulation of a swelling stress experiment

Swelling pressure tests are conducted on fully confined samples wetted to full saturation. In this case, the experiments were conducted on bentonite material used in the FEBEX *in situ* experiment and part of the international collaborative project DECOVALEX III (Alonso et al., 2005). For a dry-density of 1.6 g/cm^3 , a swelling pressure of about 5 MPa was developed in the swelling experiments.

For the simple swelling model, the model input parameters can be determined analytically to achieve a maximum swelling stress of 5 MPa. In such a case, the bentonite is assumed to behave elastically with a volumetric swelling and a swelling stress that depends on the changes in water saturation, ΔS_1 , according to:

$$\Delta\sigma' = 3K_D\Delta\varepsilon_{sw} = K_D\Delta S_1\beta_{sw} \quad (28)$$

where $\Delta\sigma'$ is the induced swelling stress (an effective stress), K_D is the bulk modulus, and β_{sw} is the moisture swelling coefficient.

The swelling strain model is designed to produce a swelling stress of 5 MPa at full saturation. An average bulk modulus of about 20 MPa is assumed for the bentonite. The initial saturation is 65%, and

therefore ΔS_l to full saturation is 0.35 (1–0.65). Using this information, the appropriate moisture swelling coefficient can be calculated using Equation (28) as:

$$\beta_{sw} = \frac{\Delta\sigma'}{3K_D\Delta S_l} = \frac{5 \cdot 10^6}{3 \cdot 20 \cdot 10^6 \cdot 0.35} = 0.238 \quad (29)$$

The swelling stress experiments is simulated using a 3D 20×20×20 mm model with 20 element in the vertical direction (Figure 3). The model boundaries are fixed for displacement normal to the boundaries, which means that the model is fully confined from a mechanical viewpoint. The model is also hydraulically confined (no flow across boundaries) except at the bottom (water inlet) where a fully saturated condition is applied. The simulation is conducted for about 10 days under isothermal conditions at a temperature of 25°C. Figure 3 shows a plot of the saturation distribution after about 4 days.

In the simulation, the soil sample becomes practically fully saturated in about 10 days (Figure 4a). The compressive stress increases proportionally to the saturation, but does achieve a maximum value of about 5.56 MPa, which is higher than the expected 5 MPa (Figure 5 solid lines). The reason for this is that gas is trapped and gas pressure increases by about 0.5 MPa, creating an additional stress increase of about 0.5 MPa (Figure 4b). The effect of gas pressure on stress can be eliminated by setting Biot's constant to a very small number (e.g. 1e-10). In such a case, the final stress is 5.12 MPa, i.e., exactly 5 MPa above the initial stress of 0.12 MPa (Figure 5a dashed line). This shows that the implemented approach for hydraulic strain works as intended.

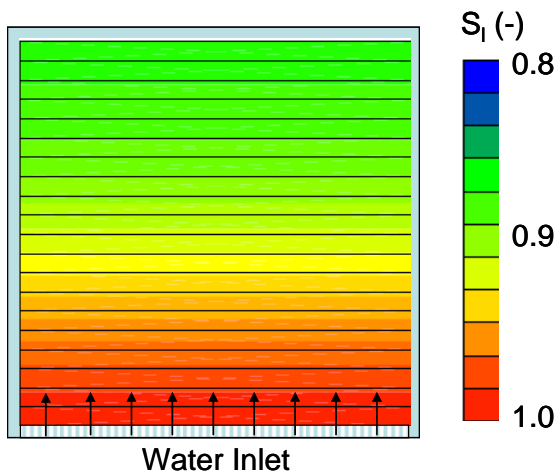


Figure 3. TOUGH-FLAC model of a swelling stress experiment and results of liquid saturation after 4 days of water infiltration.

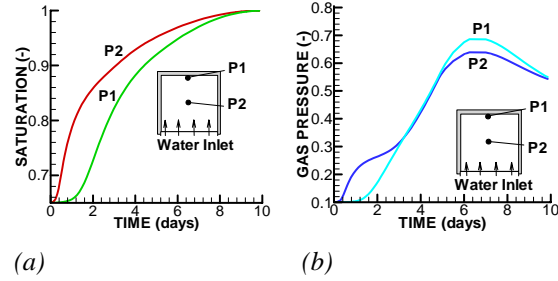


Figure 4. Simulated time evolution of (a) saturation, and (b) gas pressure at the upper end of the model.

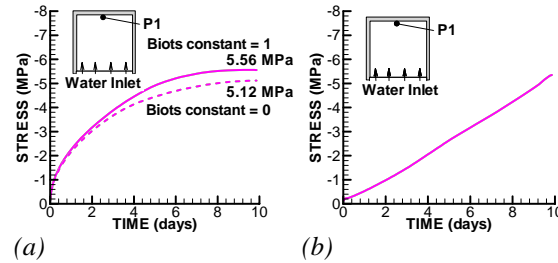


Figure 5. Simulated time evolution of compressive stress for (a) simple swelling model and (b) full BBM-TEPU model.

TOUGH-FLAC modeling of a horizontal nuclear waste emplacement tunnel

This modeling example is taken from the DECOVALEX IV project involving a horizontal nuclear waste emplacement tunnel at 500 m depth in granitic rock (Figure 6) (Rutqvist et al., 2009). The problem has been simulated by a number of teams in the DECOVALEX project using simplified models of the bentonite behavior. Simplified bentonite models were used in the DECOVALEX project, which was focused on the behavior of the fractured rock surrounding the emplacement drift, rather than the behavior of the bentonite itself. The problem was also simulated within the DECOVALEX using TOUGH2 only for a TH analysis (no geomechanical coupling). A full TOUGH-FLAC analysis was not conducted because the bentonite swelling had not been implemented into TOUGH-FLAC at that time.

The model simulation was conducted in a nonisothermal mode with a time-dependent heat power input. The simulation was conducted for 100,000 years. On a standard PC, the TOUGH2 simulation took about 9 minutes to run, whereas the coupled TOUGH-FLAC simulation took about 3 to 4 times longer to complete.

Figure 7 presents the calculated evolution of temperature, saturation, fluid pressure within the buffer, and vertical uplift of the ground surface. The evolution of temperature, saturation, fluid pressure and displacement has already been compared to the

results of other simulation codes within the DECOVALEX project, showing a good agreement (Rutqvist et al., 2009). The 30 cm ground uplift is a result of rock-mass thermal expansion.

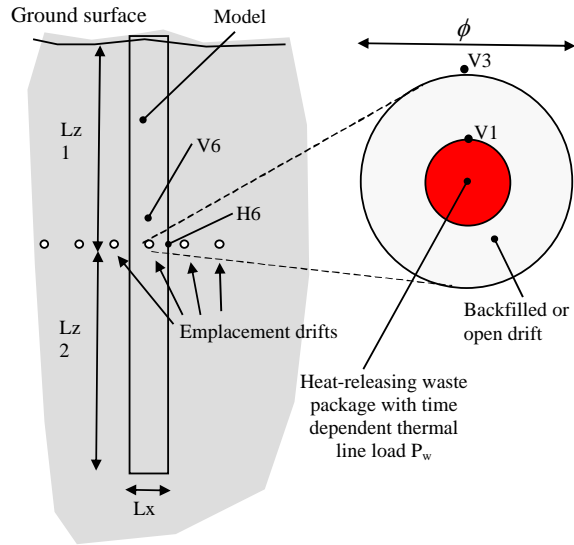


Figure 6. Model domain for a TOUGH-FLAC test example of a bentonite back-filled horizontal emplacement drift at 500 m (Rutqvist et al., 2009).

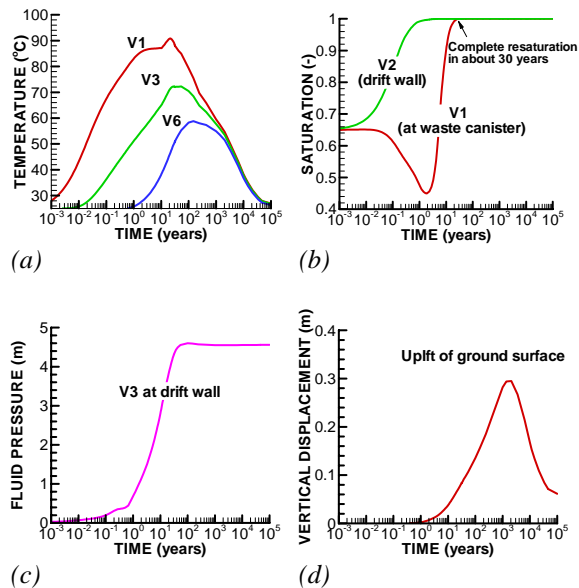


Figure 7. Simulated evolution of (a) temperature, (b) liquid saturation, (c) fluid pressure, and (d) vertical displacement.

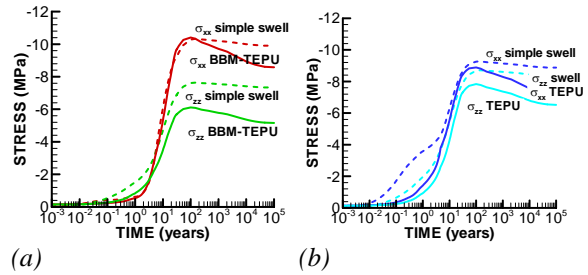


Figure 8. Simulated evolution of stress within the bentonite (a) at the canister, and (b) at the drift wall. Dashed lines are calculated with the simple swell model whereas solid lines are calculated with the fill BBM-TEPU model.

The stress evolution in Figure 8 is presented for both the simple swelling model and the full BBM-TEPU model. The final compressive stress achieved in the bentonite buffer at 100,000 years is caused by the swelling of the bentonite resulting from changes in fluid pressure. The saturation and suction induced swelling may cause a stress increase of about 5 MPa, whereas the fluid pressure may cause another 4.5 MPa increase in compressive stress, leading to final stress increases of a maximum 9.5 MPa. These results are reasonable and comparable with results achieved by other models within the DECOVALEX project. However, there is a marked difference in the stress evolution calculated with the simple swelling model and the full BBM-TEPU model. In the case of the full BBM-TEPU model, the stresses are partly relaxed after the peak thermal load. This relaxation is caused by a shear failure that occurred in the buffer near the canister (Figure 9). A plot of the specific volume at the canister reveals that a permanent pore collapse has occurred near the canister. The porosity has decreased from the initial 40% to 20%.

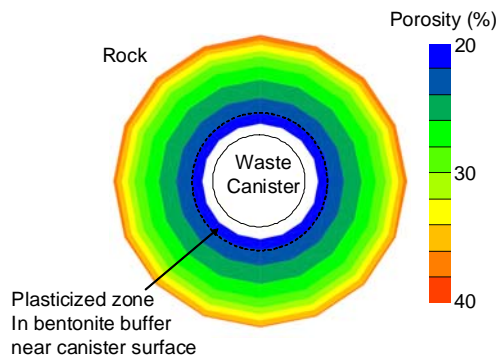


Figure 9. Calculated porosity distribution in the buffer at the 100,000 years showing a permanent pore collapse near the canister induced by drying shrinkage and shear failure.

CONCLUDING REMARKS

A thermoelastoplastic constitutive model based on the Barcelona Basic Model for mechanical behavior of unsaturated soils has been implemented into TOUGH-FLAC. The model has been tested using a number of simulations, both in terms of the newly implemented constitutive model and in terms of the TOUGH-FLAC simulations of suction-induced swelling of unsaturated soils. The constitutive model is provided in a .dll file for linkage to FLAC3D using the user-defined model option. The model is now fully functional and ready to be applied to problems related to nuclear waste disposal and other scientific and engineering problems related to geomechanical behavior of unsaturated soils.

ACKNOWLEDGMENTS

This work was supported by the Taisei Corporation, Tokyo, Japan, through the U.S. Department of Energy Contract No. DE-AC02-05CH11231. We are grateful for reviews by Kenzi Karasaki and Dan Hawkes at the Lawrence Berkeley National Laboratory. We also wish to thank Antonio Gens at the University of Cataluña, Barcelona, and Ola Kristensson at Clay Technology, Sweden, for useful discussions and clarifications about the Barcelona Basic Model.

REFERENCES

- Alonso EE, Gens A, Josa A. A constitutive model for partially saturated soils. *Geotechnique* 40: 405–430, 1990.
- Alonso E.E., et al. (26 co-authors) The FEBEX Bechmark test. Case Definition and comparison of modelling approaches. *Int. J. Rock Mech. & Min. Sci.* 42, 611-638, 2005.
- CIMNE, Code_Bright user's guide, Departamento de Ingeniería del Terreno, Universidad Politécnica de Cataluña, 2002.
- Gens A., Sanchez M., Do L., Guimaraes N., Alonso E., Lloret A., Olivella S., Villar M.V., Huertas F. A full-scale in situ heating test for high-level nuclear waste disposal: observations, analysis and interpretation. *Geotechnique* 59, 1–23, 2009.
- Gens A., Sanchez M., and Sheng D. On constitutive modelling of unsaturated soils. *Acta Geotechnica*, 1, 137–147, 2006.
- Itasca Consulting Group. Flac 3d, Fast Lagrangian analysis of continua in 3 dimensions, Minneapolis, Minnesota, 2002.
- Kristensson O., Åkesson M. Mechanical modeling of MX-80 – Quick tools for BBM parameter analysis. *Physics and Chemistry of the Earth* 33, S508–S515, 2008.
- Pruess, K., C. Oldenburg, and G. Moridis, TOUGH2 User's Guide, Version 2.0, Report LBNL-43134, Lawrence Berkeley National Laboratory, Berkeley, Calif., 1999.
- Roscoe, K.H., Burland, J.B. On the generalized stress-strain behaviour of the 'wet' clay. In: Heyman, J., Leckic, F.A. (Eds.), *Engineering Plasticity*. Cambridge University Press, Cambridge, pp. 535-609, 1968.
- Rutqvist, J, Y-S. Wu, C-F Tsang and G. Bodvarsson. A modeling approach for analysis of coupled multiphase fluid flow, heat transfer, and deformation in fractured porous rock, *Int. J. Rock Mech. Min. Sci.* 39, 429-442, 2002.
- Rutqvist J., Barr D., Birkholzer J.T., Fujisaki K., Kolditz O., Liu Q-S, Fujita T., Wang W., Zhang C.-Y. A comparative simulation study of coupled THM processes and their effect on fractured rock permeability around nuclear waste repositories. *Environ Geol.* 57:1347–1360, 2009.

PRELIMINARY MODELING OF ROCK WETTABILITY ALTERATION DURING LOW-SALINITY WATERFLOODING USING TOUGH2-TMGAS

Marica Marcolini⁽¹⁾, Franco Masserano⁽²⁾, Alfredo Battistelli⁽¹⁾

(1) RISAMB Dept., Environmental Engineering Unit, Saipem SpA (Eni Group), 61032 Fano (PU), Italy

(2) TEOR Dept., E&P Division, Eni SpA, 20097 San Donato Milanese (MI), Italy

e-mail: marica.marcolini@saipem.eni.it, franco.masserano@eni.it, alfredo.battistelli@saipem.eni.it

ABSTRACT

Laboratory experiments and field tests suggest that under proper conditions, the injection of low-salinity water (instead of high-salinity brine) may improve oil recovery during waterflooding. Even though the exact EOR mechanisms are not fully understood, the change of rock wettability from Oil-Wet (OW) or Mixed-Wet (MW) towards Water-Wet (WW) conditions has been invoked to explain the increased oil recovery with low salinity waterflooding. From a modeling point of view, the wettability alteration has been tentatively described by a change from oil-wet to water-wet relative characteristic curves linked to the local salt content of the aqueous phase.

Within a R&D project aimed to investigate low-salinity waterflooding as an improved oil recovery method, the advanced modeling capabilities required to simulate the involved processes have been coded into the TMGAS EOS module of TOUGH2 reservoir simulator. The new features include (i) the treatment of OW and MW domains in addition to the WW conditions conventionally assumed by TOUGH2; (ii) the switching from OW or MW to WW relative permeability and capillary pressure curves, depending on the local sodium chloride concentration.

INTRODUCTION

Waterflooding is the most widely applied technique to sustain oil production affected by reservoir pressure depletion. It allows pressure maintenance and oil displacement towards the production wells. Enhanced Oil Recovery (EOR) processes involve the injection of fluids into the reservoir, whereupon the injected fluid interacts with the reservoir rock/oil system to create conditions favorable for oil recovery (Green and Willhite, 1998). The main physical and chemical mechanisms leading to an improvement in oil displacement efficiency can act throughout oil viscosity reduction, oil swelling, mass transfer between oil and solvent, interfacial tension (IFT) reduction, wettability modifications, or favorable phase behavior.

Low-salinity waterflooding is an EOR method presently under evaluation, consisting of the injection of low-salinity brine to improve oil recovery over

conventional higher salinity waterflooding. The availability and the assurance that it does not affect formation injectivity are traditionally the main factors affecting the choice of the waterflooding brine. Less attention has been placed so far on how brine composition affects displacement efficiency. Laboratory experiments indicate that injection of low-salinity brine can provide a marked increase in oil recovery (Tang and Morrow, 1997, 1999; Webb et al., 2004, 2005; McGuire et al., 2005; Zhang and Morrow, 2006; Lager et al., 2006, 2008) compared to injection of seawater or high-salinity produced water. Due to the complexity of the crude oil/brine/rock interactions, discussion of the mechanisms by which oil recovery is improved due to low-salinity waterflooding is still open. The formulated hypotheses include increasing pH leading to *in situ* saponification and IFT reduction, emulsion formation, clay migration, multi-component ion exchange (MIE), and wettability alterations.

Regardless of the mechanism, the reservoir rock and fluids need to satisfy certain requirements for low-salinity waterflooding to be successful (Jerauld et al., 2006): connate water must be present, reservoir oil must contain polar components, and reservoir rock must contain minerals with cation exchange capacity as clay minerals (Lager et al., 2006). Most of the proposed theories that explain the increase in oil recovery with a change in injected brine salinity are consistent with the results of Tang and Morrow (1997). They suggest that the complexity of oil-brine-reservoir interactions controls the wettability by a variety of possible mechanisms and, moreover, that changes from OW or MW conditions toward WW occur with a decrease in salinity, together with oil recovery by spontaneous imbibition and oil recovery by waterflooding.

THE TOUGH2-TMGAS SIMULATOR

TMGAS (Battistelli and Marcolini, 2009) is an EOS module specifically designed for the TOUGH2 reservoir simulator (Pruess et al., 1999), able to model the two-phase flow of an aqueous (Aq) and a nonaqueous (NA) phase in deep geological structures. TMGAS can simulate the two-phase behavior of NaCl-dominated brines in equilibrium with a NA mixture containing hydrocarbons (pure as well as pseudo-components) and inorganic gases. The

NA phase can be either in gas, supercritical, or liquid (condensed) conditions, with the limitation that such conditions cannot coexist within the same grid element. The PR cubic EOS (Peng and Robinson, 1976), with the modifications suggested by Soreide and Whitson (1992), is used for phase-equilibria calculations.

NA phase density is computed using the PR EOS, accounting for conventional volume shift correction, whereas departure enthalpy and dynamic viscosity are computed using the LK EOS (Lee and Kesler, 1975) and the Friction Theory Model (Quinones-Cisneros et al., 2001), respectively. The most accurate Friction Theory Model with seven adjustable parameters was calibrated for all the pure components covered by the internal database of TMGAS against the NIST Web Database REFPROP7 (Lemmon et al., 2002). In addition, the general one-parameter Friction Theory Model is available in the code, specifically implemented for pseudo-components and species not already supported by the internal database. This can be very useful when dealing with ordinary petroleum mixtures generally described by means of both pure components and pseudo-components. Brine properties are evaluated using updated versions of the correlations implemented in the EWASG EOS module (Battistelli et al., 1997) for water and sodium chloride mixtures. For a detailed description of TMGAS, refer to Battistelli and Marcolini (2009).

WETTABILITY ALTERATION MODEL

A model was developed to describe the wettability alteration from OW or MW conditions to WW, consequent to the low-salinity brine injection into the reservoir. The model is inspired by the work of Delshad et al. (2006) for the reservoir simulator UTCHEM (University of Texas, 2000) concerning rock wettability changes induced by the injection of an aqueous solution containing a specific polymer. It is based on the introduction of two sets of relative permeability and capillary pressure curves corresponding to the “initial” wettability conditions (OW or MW) and final wettability conditions (WW). The property value is obtained by linear interpolation between initial and final conditions:

$$k_{r\beta} = \omega k_{r\beta}^{initial} + (1 - \omega) k_{r\beta}^{final} \quad (1)$$

$$P_c = \omega P_c^{initial} + (1 - \omega) P_c^{final} \quad (2)$$

where $k_{r\beta}$ indicates the relative permeability to the phase β and P_c is the capillary pressure. The interpolation parameter ω is correlated to the normalized concentration of salt in the two component water–sodium chloride system, as given by Equation (3), where X indicates the mass fraction in the Aq phase.

$$\overline{X_{Aq}^{NaCl}} = \frac{X_{Aq}^{NaCl}}{X_{Aq}^{NaCl} + X_{Aq}^{H_2O}} \quad (3)$$

Analogously to Jerauld et al. (2006), two threshold values for the normalized sodium chloride concentration, X_{max}^{wet} and X_{min}^{wet} , are assumed. During the dilution process, when the normalized NaCl mass fraction reaches the upper bound, the transition from initial to final wettability conditions begins. Until the salt concentration is comprised between the two concentration thresholds, relative permeabilities and capillary pressure are calculated as indicated by Equations (1) and (2). The wettability alteration process toward WW conditions is completed when the salt concentration becomes lower than the lower threshold value.

The proposed modeling approach requires that the interpolation parameter ω assumes the following values outside the interpolation interval:

$$\omega = 1 \quad \text{if} \quad \overline{X_{Aq}^{NaCl}} \geq X_{max}^{wet} \quad (4)$$

$$\omega = 0 \quad \text{if} \quad \overline{X_{Aq}^{NaCl}} \leq X_{min}^{wet} \quad (5)$$

For intermediate sodium chloride concentrations, a specific interpolation function is needed. TOUGH2-TMGAS implements three different formulations, based on linear and trigonometric functions.

TOUGH2 assumes the porous medium is always under WW conditions; since the NA phase pressure is the reference pressure, the capillary pressure is always negative. This limitation is removed in order to implement the wettability alteration model by introducing the wettability index IOW, defined for each gridblock. IOW assumes the following values:

- 0 in WW conditions (default)
- 1 in OW conditions
- 2 in MW conditions

In the present formulation, wettability conditions other than WW are available only by selecting the Corey characteristic curves for phase relative permeability and capillary pressure. The Corey model for strongly WW or strongly OW conditions is defined as follows:

$$k_{r\beta} = k_{r\beta}^o S_{n\beta}^{E\beta} \quad (6)$$

$$P_c = C_{Pc} \sqrt{\frac{\Phi}{k}} (1 - S_{n\beta})^{E_{Pc}} \quad (7)$$

where Φ and k are porosity and absolute permeability, respectively; the relative permeability end point $k_{r\beta}^o$ and the exponent E_β depend on phase

β , and C_{Pc} and E_{Pc} are constants. To satisfy the TOUGH2 convention, C_{Pc} is negative for WW

conditions and positive for OW conditions. The normalized saturation $S_{n\beta}$ is given by:

$$S_{n\beta} = \min \left[1, \max \left(0, \frac{S_{\beta} - S_{\beta r}}{1 - S_{wr} - S_{or}} \right) \right] \quad (8)$$

For a MW porous medium, Corey's model for relative permeability is unchanged, whereas the capillary pressure needs substantial variations. The curve is subdivided into a positive and negative branch, and the capillary pressure cancels out if the Aq phase saturation is equal to a specific S^* . If $S_w \leq S^*$:

$$S_{nw} = \min \left[1, \max \left(0, \frac{S^* - S_w}{S^* - S_{wr}} \right) \right] \quad (9)$$

$$P_{cw} = C_{Pcw} \sqrt{\frac{\Phi}{k}} S_{nw} e^{P_{cw}} \quad (10)$$

while if $S_w \geq S^*$:

$$S_{no} = \min \left[1, \max \left(0, \frac{S_w - S^*}{1 - S_{or} - S^*} \right) \right] \quad (11)$$

$$P_{co} = C_{Pco} \sqrt{\frac{\Phi}{k}} S_{no} e^{P_{co}} \quad (12)$$

New necessary parameters are supplied throughout the ROCKS and SELEC data blocks. The estimation of the interpolation parameter ω is performed in the two-phase section of the EOS module. Regardless of the salt concentration, WW conditions cannot be changed and ω is set at zero. Only if IOW is not equal to zero, then ω assumes a unit value or is calculated on the basis of previously introduced functional forms.

1D LINEAR SIMULATIONS

The constant injection rate of low-salinity brine in a homogeneous and isotropic reservoir of 1000 m length is modeled using a 1D Cartesian grid. The system is discretized into 100 elements of 10 m length and constant cross area of 100 m². The system is initially in OW conditions and at residual saturation of the aqueous phase. Brine is injected on one side of the grid while, on the opposite side, constant conditions equal to initial conditions are maintained. The salinity of the injected brine is lower than the salinity of the reservoir connate brine and low enough to start a rock wettability alteration process. The upper threshold value of normalized sodium chloride concentrations is set equal to 10,000 ppm, while the lower threshold limit is set equal to 2000 ppm. The sinusoidal functional form for the interpolation parameter ω was adopted for every simulation. The main petrophysical properties of the

reservoir and thermophysical parameters of fluid phases are listed in Table 1. Except for a negligible amount of water imposed by the two-phase equilibrium with the Aq phase, it is assumed that the NA phase is composed of just one component, described by means of the pseudo-component approach. The Friction Theory Model and the Peneloux volume shift have been used to reproduce, respectively, the oil viscosity and density specified in Table 1. The parameters of the relative permeability and capillary pressure curves specific of initial OW and final WW conditions are listed in Table 2.

Table 1. Main petrophysical properties of the reservoir and thermophysical properties of the fluid phases.

Initial pressure (Pa)	100×10 ⁵
Constant temperature (°C)	40
Initial salinity (molal)	0.9
Absolute permeability (m ²)	5.0×10 ⁻¹²
Porosity	0.20
Initial brine density (kg/m ³)	997.25
Initial oil density (kg/m ³)	637.35
Initial brine viscosity (Pa s)	0.6550×10 ⁻³
Initial oil viscosity (Pa s)	4.4856×10 ⁻³
Brine injection rate (kg/s/m ²)	1.002E-2
Mobility ratio ¹ (OW)	11.98
Mobility ratio (WW)	2.74

Table 2. Parameters of initial (OW) and final (WW) relative permeability and capillary pressure curves.

	Oil-Wet	Water-Wet
S_{wr}	0.35	0.40
S_{or}	0.35	0.10
$K_{rw,0}$	0.7	0.4
$K_{ro,0}$	0.4	1
E_{kw}	2	2
E_{ko}	2	2
C_{pc}	0.51371	-0.51371
E_{pc}	6.2	4

Continuous injection of low-salinity brine

An aqueous solution with NaCl concentration of 1000 ppm is injected for 1 year. Relative permeability and capillary pressure evolution in a grid element close to the boundary opposite to the injection is shown in Figure 2. Figure 1 and 2 show that, initially, both relative permeabilities and capillary pressure follow the OW characteristic curves. When the concentration in the gridblock

¹ Mobility ratio definition by Green and Willhite (1998):

$$M = \left(\frac{k_{rw}}{\mu_w} \right)_{S_{or}} \left(\frac{\mu_o}{k_{ro}} \right)_{S_{wr}}$$

reaches the upper salinity limit, the linear interpolation process between OW and WW curves starts and continues until the lower salinity threshold is achieved. From that point on, the WW characteristic curves are maintained.

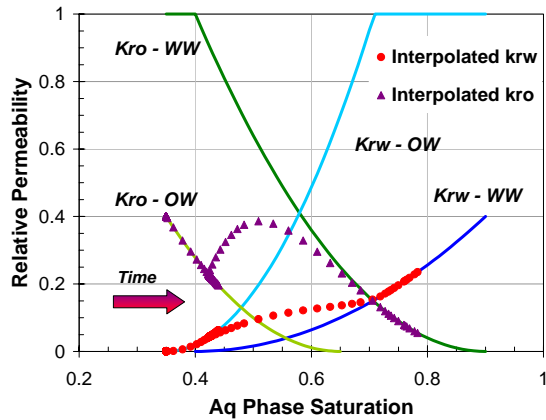


Figure 1. OW and WW relative permeabilities as functions of Aq phase saturation and calculated relative permeabilities at the end of the 1D grid as time increases.

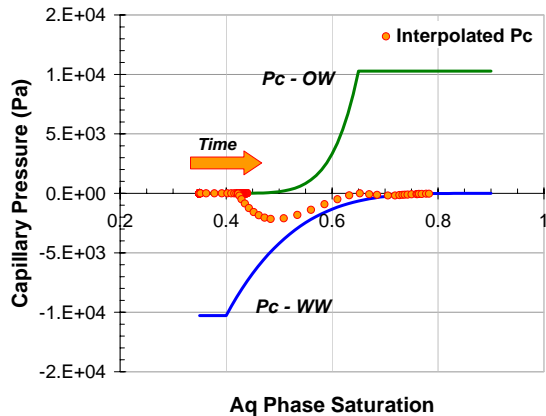


Figure 2. OW and WW capillary pressures as functions of Aq phase saturation and calculated capillary pressure in an observation grid element as time increases.

Figure 3 shows, at fixed simulation times, the profiles of Aq phase saturation and NaCl mass fraction as a function of the distance from the injection well. The injected brine displaces the reservoir oil, so the Aq phase saturation increases with time, whereas the Aq phase salinity decreases. As shown in Figure 5, after 1 month of injection, the final WW conditions have been established only in the first few gridblocks. However, after 9 months, the salt concentration drops below the lower boundary of 2000 ppm over the entire system, and the rock domain becomes completely WW.

As can be seen in Figure 3, at great distances the Aq phase saturation takes on a value slightly greater than the residual brine saturation. This is due to the formation of a “connate water bank” more evident in Figure 5 relative to a fairly short simulation time of 1.5×10^6 s. Initially the injected brine displaces the connate brine that accumulates ahead of the oil displacement front, denoted by a vertical dotted line for both low- and high-salinity injection cases. As time increases, in a growing number of grid elements, the wettability alteration process toward WW conditions takes place: oil phase mobility increases, together with the volume accessible to the aqueous phase. In Figure 5, the distance covered by the final WW conditions is highlighted by a vertical black dotted line.

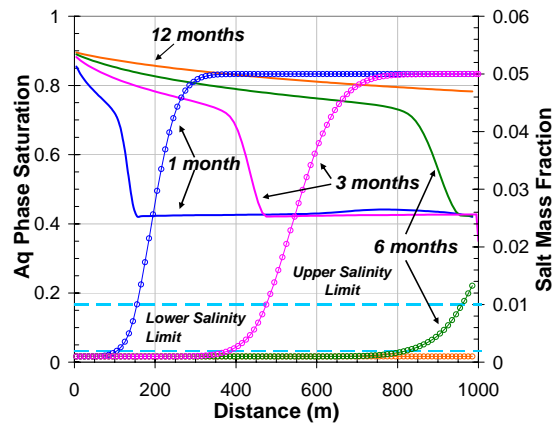


Figure 3. Continuous injection of low salinity brine: Aq phase saturation (continuous line) and NaCl concentration (line plus symbols) at four different times.

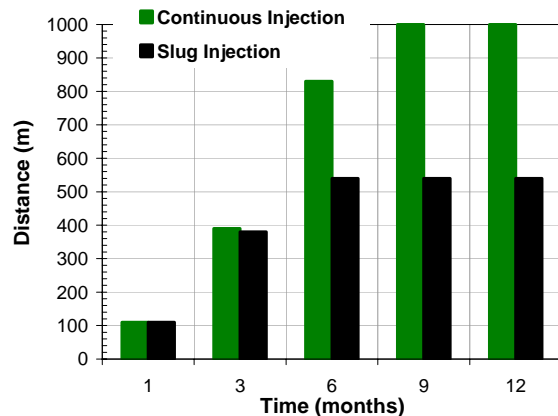


Figure 4. Continuous injection of low salinity brine vs. slug injection: location of wettability change front from OW to WW conditions at fixed simulation times.

Slug injection of low salinity brine

If low-salinity brine must be provided by treating higher salinity brines, it could be more convenient to inject limited amounts of low-salinity brine, followed by the conventional waterflooding process.

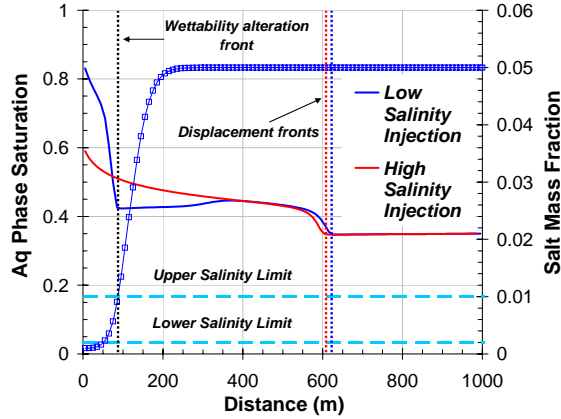


Figure 5. Comparison between Aq phase saturation profiles (continuous line) resulting from high and low salinity injection and NaCl concentration profile (line plus symbol) at a short time ($t=17.36$ days).

Leaving the same total simulation time, first we inject low-salinity brine for two months and brine with the same connate brine composition for the residual time (referred to from here on as “high salinity brine”). As shown in Figure 4, after 6 months the wettability alteration process is completely arrested, and water wet conditions have been established in the first 520 m of the system. Oil mobilized in these gridblocks accumulates downstream, generating an “oil bank” (Figure 6) that is slowly displaced as time increases.

The NaCl concentration profiles reported in Figure 7 show that high-salinity injection interrupts dilution. The salt mass fraction again rises over the upper salinity threshold, limiting the wettability alteration process to a small region of the system.

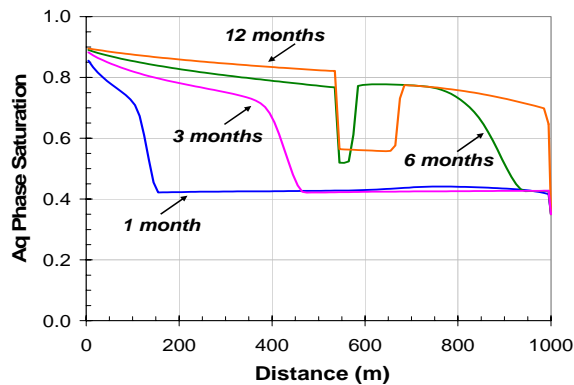


Figure 6. Slug injection of low salinity brine: Aq phase saturation profiles at four different times.

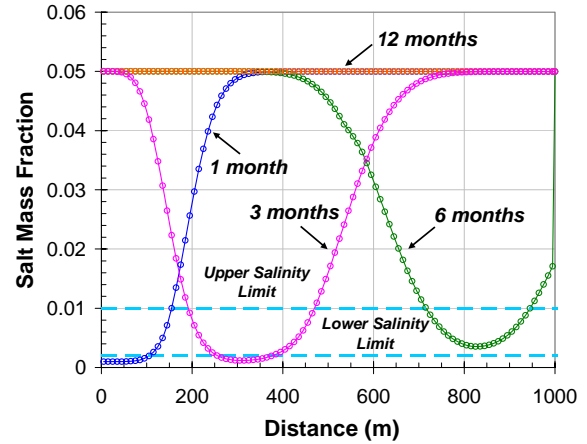


Figure 7. Slug injection of low salinity brine: NaCl concentration profiles at four different times.

In Figure 8, the cumulative oil recovery relative to the previously described cases can be analyzed, together with the upper and lower bounds of achievable oil recovery, represented by the waterflooding in a WW domain (independent on brine salinity) and by the injection of the high salinity brine, respectively. All simulations are performed at the same initial conditions. Then, if the rock-domain is WW, the aqueous phase saturation of 0.35 is less than the WW irreducible water saturation equal to 0.40. Fig. 8 shows that the change in slope indicative of the water breakthrough is delayed for a WW domain, due to the higher AQ phase irreducible saturation of the WW domain compared to the cases characterized by an initial OW domain. In the three examined OW scenarios the aqueous phase breakthrough takes place at the same injection time since it occurs so rapidly as to anticipate the beginning of wettability alteration process.

The oil recovery factor is strongly affected by the residual oil saturation specific of the final wettability status reached in the reservoir. In general, compared with an OW domain, a WW domain is characterized by lower residual oil saturation since it tends to retain water. Regardless of the speed, the maximum achievable oil recovery is that obtainable if WW conditions are established in all grid-block elements. On the other hand, if OW conditions persist all over the system the oil recovery is minimum. While intermediate amounts of produced oil correspond to those situations wherein the wettability alteration process is completed only in a section of the total domain.

Concerning the two cases described above, the continuous injection of low-salinity brine seems to add minor increments to the recovery factor compared to the 2 months of slug injection.

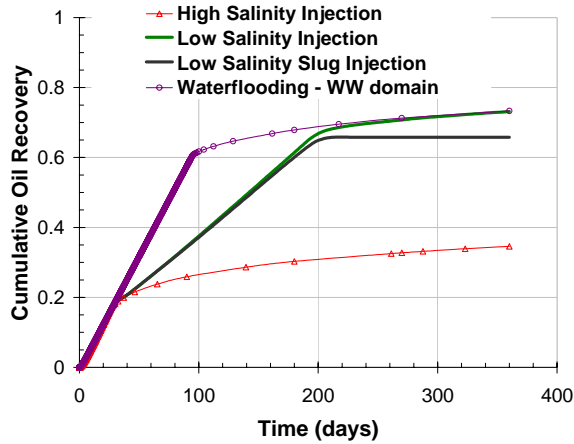


Figure 8. Comparison among the cumulative oil recovery obtained with waterflooding of a WW domain and an OW domain with high salinity brine and with continuous and slug low salinity injection.

5-SPOT WELL PATTERN SIMULATIONS

The slug injection of low-salinity brine is also modeled by using a 5-spot well pattern approach. The 2D Cartesian grid was generated with the PATTY code (Fuller e Pruess, 1985) developed at LBNL for simulators of the TOUGH2 family. Since simulation results can be affected by grid orientation effects, a 9-point differencing scheme was adopted with a parallel grid. Due to the symmetry of the system, the simulations are limited to 1/8 sector of a 5-spot well pattern. The horizontal layer is discretized into 121 elements, for a total surface area of 20,240 m², with the injector-producer spacing equal to 284.5 m. The parameters of relative permeabilities and capillary pressure curves specific for initial OW and final WW conditions are in Table 3.

Table 3. Parameters of initial (OW) and final (WW) relative permeability and capillary pressure curves.

	Oil-Wet	Water-Wet
<i>S_{wr}</i>	0.15	0.20
<i>S_{or}</i>	0.35	0.20
<i>K_{rw,0}</i>	0.6	0.2
<i>K_{ro,0}</i>	0.4	1
<i>E_{kw}</i>	2	5
<i>E_{ko}</i>	6	2
<i>C_{pc}</i>	0.7	-0.7
<i>E_{pc}</i>	3	3

Both the continuous (Case A) and the 0.25 PV slug (Case B) injection of low-salinity brine have been simulated. The system initially has a brine phase at irreducible saturation with a 0.9 molal NaCl concentration. Initial pressure and temperature are, respectively, 136.2 bar abs and 39.44°C. Porosity, absolute permeability, oil properties, and the

wettability alteration model used for the 1D simulation have been preserved. Brine is injected at a constant rate of 0.0255 kg·s⁻¹·m⁻¹, and production occurs with a well on deliverability at a constant bottomhole pressure of 130 bar abs.

Figure 9 shows the Aq phase saturation and NaCl mass fraction profiles in the production well block for both cases A and B. Since oil displacement occurs preferentially along the connection between injection and production wells, the Aq phase breakthrough takes place just after 0.15 injected PV, as attested by the early increment of the Aq phase saturation.

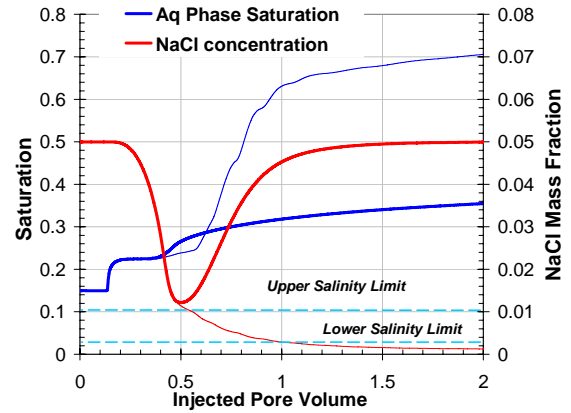


Figure 9. Case A (thin line) and B (thick line): Aq phase saturation and NaCl concentration as function of injected PV.

The Aq phase saturation remains stable until the transit of the connate water bank is completed, and then it starts increasing again while the wettability alteration process advances toward WW conditions. Figures 10 and 11 show the NA-phase saturation distribution for cases A and B, respectively, corresponding to four subsequent simulation times.

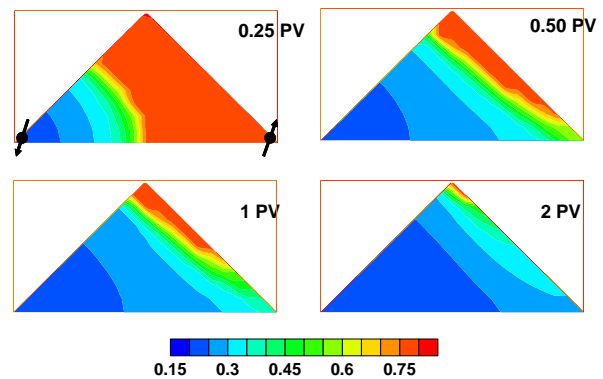


Figure 10. Case A: NA phase saturation distribution at different injected pore volumes.

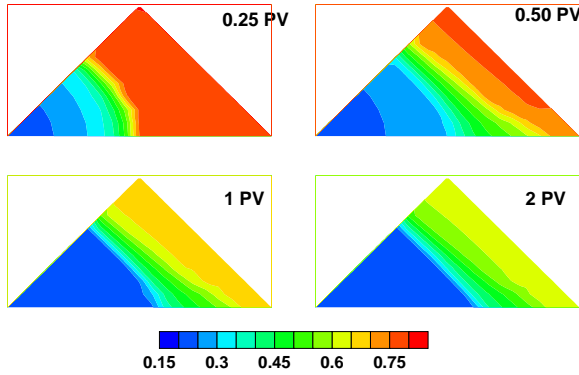


Figure 11. Case B: NA phase saturation distribution at different injected pore volumes.

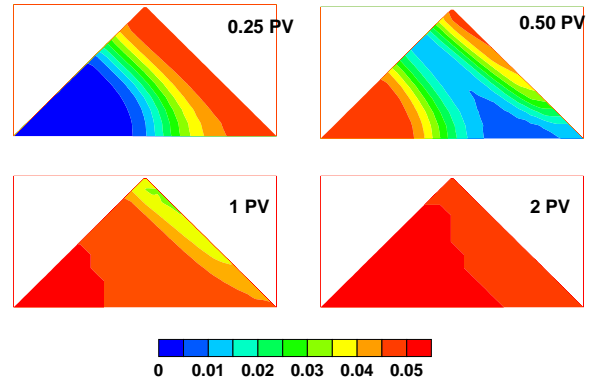


Figure 14. Case B: NaCl mass fraction distribution at different injected pore volumes.

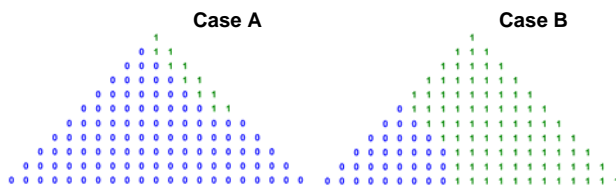


Figure 12. Case A and B: WW conditions distribution at final simulation time (0= WW, 1=OW).

At final simulation time, Case A oil saturation is close to the WW residual saturation almost everywhere over the domain, while in the other scenario, the preservation of OW conditions in a large number of the gridblocks (Figure 12) prevents an increase in oil-phase mobility.

The NaCl concentration evolution is shown in Figures 13 and 14. Moving away from the injection well, the low-salinity slug mixes with the connate brine, while the high-salinity brine injected upstream and the resulting NaCl concentration do not favor a consistent WW-condition advancement. At final simulation time, the initial salt mass fraction is almost fully restored over the entire domain.

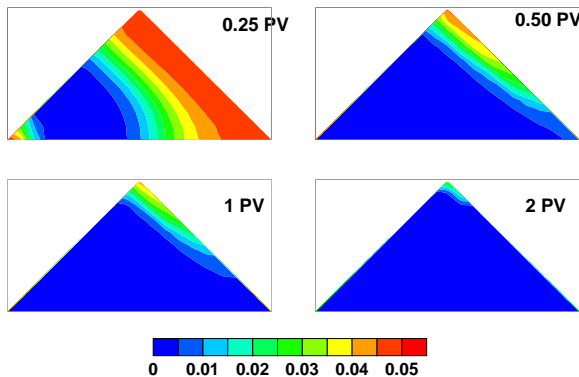


Figure 13. Case A: NaCl mass fractions distribution at different injected pore volumes.

Figure 15 shows a comparison between the oil recovery curves in the two considered scenarios. In Case A, the final oil recovery is ~70% of the Original Oil In Place (OOIP), while it decreases to 50% if only a low-salinity brine slug is injected—it is strongly dependent on the advancement of the WW-conditions front and, then, on slug size. Note that a 20% increment of oil recovery requires injecting a low-salinity volume eight times that of the slug.

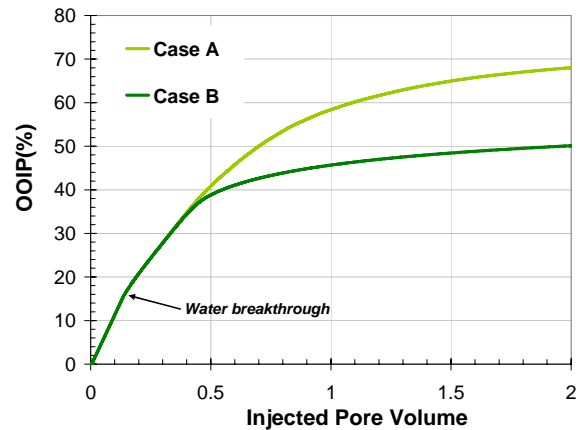


Figure 15. Case A and B: OOIP(%) as function of injected pore volumes.

CONCLUSIONS

Although experimental results and field tests seem to confirm the effectiveness of low-salinity waterflooding, the exact mechanisms responsible for the oil recovery increase are still to be understood. Among the modeling solutions proposed to simulate the observed EOR phenomena by Jerauld et al. (2006), the most important is the alteration of rock wettability conditions as a function of Aq phase salinity in the reservoir.

The effects of salt concentration on relative permeability and capillary pressure characteristic curves were treated with a simplified approach, similar to that used by Delshad et al. (2006) concerning the

wettability alteration induced by surfactant and/or polymer injection. The formulated model consists substantially in the introduction of two sets of characteristic curves, specific of initial (OW or MW) and final (WW) rock wettability conditions. The relative permeability and capillary pressure values are the result of linear interpolations depending on parameter ω , strongly correlated to the local salt concentration. Parameter ω can vary from 1 to 0 according to different functional forms. The model was implemented in the TMGAS EOS module (Battistelli and Marcolini, 2009) of the TOUGH2 reservoir simulator (Pruess et al., 1999).

To verify the performances of the wettability alteration model and analyze related processes during waterflooding, different simulations have been presented. A 1D Cartesian grid and a 2D 5-spot well pattern have been used. Both continuous and slug injection of low-salinity brine have been simulated, evaluating the additional reservoir oil recovery of low-salinity injection compared with the high-salinity injection. The formation of a connate water bank, as described in Jerauld et al. (2006), has been observed. Numerical simulation seems to be a promising tool for analyzing laboratory and field tests and optimizing low salinity waterflooding operations.

ACKNOWLEDGMENTS

This work was performed within the EFIP R&D project sponsored and coordinated by the Eni E&P Division. The authors would like to thank the E&P Division for permission to publish this paper.

REFERENCES

- Battistelli A. and M. Marcolini, TMGAS: a new TOUGH2 EOS module for the numerical simulation of gas mixtures injection in geological structures, *Intl. J. Greenhouse Gas Control*, 3, 481-493, 2009.
- Battistelli A., Calore C. and K. Pruess, The simulator TOUGH2/EWASG for modelling geothermal reservoirs with brines and a non-condensable gas. *Geothermics*, 26, 4437-464, 1997.
- Corey A. T., The interrelation between gas and oil relative permeabilities. *Producers Monthly*, 38-41, November, 1954.
- Delshad M., Najafabadi N.F., Anderson G.A, Pope G.A. and K. Sepehrnoori, Modeling Wettability Alteration in Naturally Fractured Reservoirs. SPE 100081 Paper presented at SPE/DOE Symposium on Improved Oil Recovery held in Tulsa, Oklahoma, U.S.A, 22-26 April, 2006.
- Fuller P. and K. Pruess, PATTY – A mesh generator for simulations of five-, seven-, and nine-spot floods, Report LBNL-20739, Lawrence Berkeley National Laboratory, Berkeley, Calif., 1985.
- Green D.W. and G.P. Willhite, *Enhanced Oil Recovery*, Henry L. Doherty Memorial Fund of AIME, Society of Petroleum Engineers, Richardson, Texas, 1998.
- Jerauld G.R., Lin C.Y., Webb K.J. and J.C. Secombe, Modeling low-salinity waterflooding. SPE 102239, 2006.
- Lager A., Webb K.J., Black C.J.J., Singleton M. and K.S. Sorbie, Low salinity oil recovery – An experimental investigation. Paper SCA 2006-36 (Intl. Symp. Society of Core Analysts), 2006.
- Lager A., Webb K.J., Collins I.R. and D.M. Richmond, LoSal™ Enhanced Oil Recovery: Evidence of Enhanced Oil Recovery at the Reservoir Scale, SPE 113976, 2008.
- Lee B.I. and M.G. Kesler, A generalized thermodynamic correlation based on three-parameter corresponding states, *AICHE J.*, 21, 3, 510-527, 1975.
- Lemmon E.W., McLinden M.O., Huber M.L., *Reference Fluid Thermodynamic and Transport Properties*, NIST Standard Reference Database 23, Version 7.0, 2002.
- McGuire P.L., Chatam J.R., Paskvan F.K., Sommer D.M. and F.H. Carini, Low salinity oil recovery: an exciting opportunity for Alaska's North Slope. SPE 93903, Western Regional Meeting, Irvin, CA, 30 March-1 April, 2005.
- Peng D.Y. and D.B. Robinson, A New Two-Constant Equation of State. *Ind. Eng. Chem. Fund.* 15, 59-64, 1976.
- Pruess K., C. Oldenburg, and G. Moridis, *TOUGH2 User's Guide, Version 2.0*, Report LBNL-43134, Lawrence Berkeley National Laboratory, Berkeley, CA, 1999.
- Soreide I. and C.H. Whitson, Peng-Robinson predictions for hydrocarbons, CO₂, N₂, and H₂S with pure water and NaCl brine, *Fluid Phase Equilibria*, 77, 217-240, 1992.
- Tang G.Q. and N.R. Morrow, Salinity, temperature, oil composition, and oil recovery by waterflooding, *SPE Reservoir Engineering* 33680, 1997.
- Tang G.Q. and N.R. Morrow, Influence of brine composition and fines migration on crude oil/brine/rock interactions and oil recovery. *J. of Petroleum Science and Eng.*, 24, 99-111, 1999.
- University of Texas, *User's Guide for UTCHEM-9.0: A Three-dimensional Chemical Flood Simulator*. Reservoir Engineering Research Program Center for Petroleum and Geosystems Engineering, The University of Texas at Austin, Texas, 78712, 2000.
- Webb K.J., Black C.J.J. and H. Al-Jeel, Low Salinity oil recovery – log inject log, SPE 89379, 2004.
- Webb K.J., Black C.J.J. and I.J. Edmonds, Low salinity oil recovery – the role of reservoir condition corefloods, EAGE conference, Budapest, Hungary, 2005.
- Zhang Y. and N.R. Morrow, Waterflood performance by injection of brine with different salinity of reservoir cores, SPE 109849, 2007.

HYDROGEOPHYSICAL APPROACHES WITH THE TOUGH FAMILY OF CODES

M. B. Kowalsky, S. Finsterle, E. Gasperikova, G. Moridis, and S. S. Hubbard

Lawrence Berkeley National Laboratory
1 Cyclotron Road
Berkeley, CA, 94705, U.S.A
e-mail: mbkowsky@lbl.gov

ABSTRACT

We describe three hydrogeophysical approaches for improving characterization of subsurface flow and transport by integrated simulation of geophysical and hydrogeochemical processes and measurements. Each approach is presented with an example that benefits from recent advances in the TOUGH family of codes. The first example considers the coupled simulation of time-lapse electrical resistivity data (ERT) and hydrogeochemical data to evaluate the impact of recharge on subsurface contamination at the DOE Oak Ridge Integrated Field Challenge site. The second example involves the combination of multiscale hydrogeophysical data integration and dual-domain transport modeling to enable long-term transport prediction at a contaminated site within the DOE Savannah River Site. The third example, based on a site in the Gulf of Mexico, demonstrates how the coupled simulation of gas production and time-lapse seismic surveys can help monitor the evolution of subsurface properties, and thus manage production from a gas hydrate accumulation. While the approaches considered in these examples are entirely different from one another, they share the common goal of improving subsurface characterization by taking advantage of the sensitivity of geophysical data to subsurface fluid distributions and properties that govern flow and transport. This work reflects the substantial progress made in developing approaches for integrating geophysical and hydrogeochemical data in the TOUGH family of codes, in applications ranging from environmental remediation to nuclear waste storage to oil and gas production.

INTRODUCTION

The use of geophysical data for hydrological investigations—broadly referred to as the field of hydrogeophysics—is increasingly popular, due to the sensitivity of geophysical measurements to properties that are (directly or indirectly) related to hydrological processes. The challenge is in extracting information from geophysical data at a relevant scale that can be used quantitatively to inform hydrological models.

A powerful recently developed hydrogeophysical approach involves the coupled modeling of hydrological and geophysical processes, such that simulated geophysical measurements become a

function of the hydrological processes. This modeling approach, sometimes referred to as coupled hydrogeophysical modeling, can be used in “inverse mode,” wherein hydrological parameters are estimated by minimizing the difference between measured and simulated geophysical and hydrological data using an optimization algorithm. Coupled hydrogeophysical modeling is also useful in “forward mode,” for example, to evaluate the sensitivity of different geophysical measurements for monitoring purposes or experimental design.

The TOUGH family of codes has been used for a variety of coupled hydrogeophysical modeling applications. For example, an approach involving time-lapse ground-penetrating radar measurements (Kowalsky et al., 2004; Finsterle and Kowalsky, 2008) was applied to an infiltration experiment at the DOE Hanford site (Kowalsky et al., 2005) and to a drift-scale experiment at the proposed site for nuclear waste disposal at Yucca Mountain (Kowalsky et al., 2008). The use of electrical resistance tomography (ERT) data was also considered (Lehikoinen et al., 2009a; 2009b). Such approaches are applicable when physical properties in the system (e.g., aqueous- or gas-phase saturation, solute concentration, pressure, temperature) are undergoing transient changes, and time-lapse geophysical measurements are available that are sensitive to such changes. These were also local-scale studies, limited to relatively small regions in the vicinity of boreholes.

For studies involving much larger scales, such as the plume scale, time-lapse geophysical data are not always applicable or available for aquifer characterization, and different techniques are needed for integrating hydrogeophysical measurements. While it is impractical to collect high-resolution characterization data over the entire aquifer, various types of hydrogeophysical data are commonly collected that cover a range of scales: from regional-scale surface geophysical data, to local-scale crosshole geophysical data, to well logging and core data. Such data may be accommodated using a multiscale hydrogeophysical data integration framework (Kowalsky et al., 2007) to provide useful information that can be integrated directly into a hydrological model.

Here we describe three examples of recent studies involving the TOUGH family of codes that reflect a

variety of hydrogeophysical approaches: coupled hydrogeophysical modeling of time-lapse electrical resistivity data and hydrogeochemical data to evaluate the impact of recharge on subsurface contamination at the DOE Oak Ridge Integrated Field Challenge site (Example 1); combined multiscale hydrogeophysical data integration and dual-domain transport modeling to enable long-term transport prediction at a contaminated site at the DOE Savannah River Site (Example 2); and examining the feasibility of seismic methods for monitoring a gas hydrate accumulation undergoing production (Example 3).

EXAMPLE 1: COUPLED MODELING OF ELECTRICAL RESISTIVITY DATA AND HYDROGEOCHEMICAL DATA

Here we describe an approach that will be used to help understand the impact of recharge on subsurface contamination at the southern-most corner of the S-3 ponds at the Oak Ridge Integrated Field Research Challenge (IFRC) site in eastern Tennessee. The approach involves the coupled modeling of time-lapse electrical resistivity (ERT) voltage data and hydrogeochemical data, including water level and solute concentration data. Details of the work may be found in Kowalsky et al. (2009a).

At the study site, recharge to groundwater is substantial and highly variable, exerting a major influence on local hydrological processes. Recharge from precipitation fluctuates not only seasonally and annually, but also varies rapidly in response to individual storm events. A related source of recharge—runoff from the S-3 parking lot—enters the formation through intermittent standing water in a drainage ditch. The formation of perched water zones is commonly observed at shallow depths, also affecting local recharge. Heterogeneity at the S-3 site—resulting from a complex mixture of soil, saprolite, and fractured sedimentary rocks—along with preferential flow paths, and a rapid aquifer response to fluctuations in recharge, all lead to spatial and temporal variability of groundwater chemistry and contaminant transport (Van de Hoven, 2005), necessitating the development of new approaches to interpret data and understand hydrological processes at the site.

We developed a coupled hydrogeophysical modeling approach for the site using iTOUGH2 (Finsterle, 2004), which provides forward and inverse modeling capabilities for a variety of hydrogeochemical and geophysical data. The approach integrates a hydrogeochemical forward model (HM) and a geophysical forward model (GM). The HM is TOUGH2 (Pruess et al., 1999), which simulates fluid flow and solute transport, and the corresponding hydrogeochemical measurements. The GM is an electrical resistivity model called CRMOD (Kemna

et al., 2002), which simulates electrical current in the subsurface and the corresponding resistivity measurements.

The coupled hydrogeophysical modeling approach (Figure 1) can be used to perform inverse modeling, as follows: (1) a set of hydrogeochemical and geophysical parameters is specified; (2) a hydrogeochemical simulation is performed with the HM, producing the simulated hydrogeochemical data and the information used as input for the GM; (3) a petrophysical model translates the HM output (e.g., water saturation, solute concentration, and porosity) into the relevant geophysical property (e.g., electrical resistivity); (4) the geophysical data are simulated with the GM at the specified geophysical survey times; (5) an objective function is evaluated to measure the dissimilarity between the measured and simulated hydrogeochemical and geophysical data; (6) a new set of hydrological and geophysical parameters are obtained through an optimization algorithm (or a nongradient-based optimization algorithm); and (7) the process is repeated starting at (2), until a set of parameters that sufficiently minimizes the objective function is found, at which point the inversion is complete.

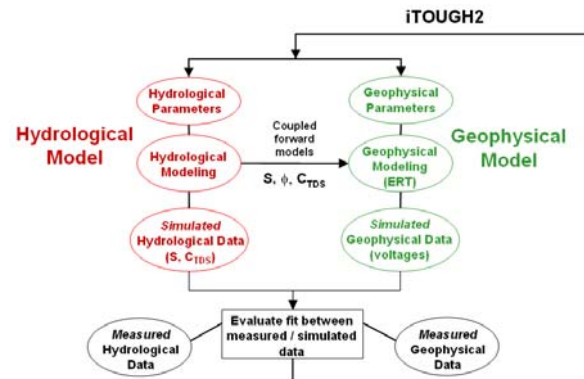


Figure 1. Approach for coupled hydrogeophysical inverse modeling.

For this study, we constructed a local-scale hydrogeochemical model based on field data collected near the S-3 ponds site at Oak Ridge in late 2008 during high precipitation and recharge events. Time-varying infiltration due to rainfall and a drainage ditch drives the system and is implemented based on measured data. As a first step, we consider at present a vertical 1D model (Figure 2); its use makes the implicit assumption that lateral flow is less significant than vertical flow (this assumption will be relaxed in future work). An atmospheric boundary is at the top surface of the model, and a semi-confining layer is at the bottom.

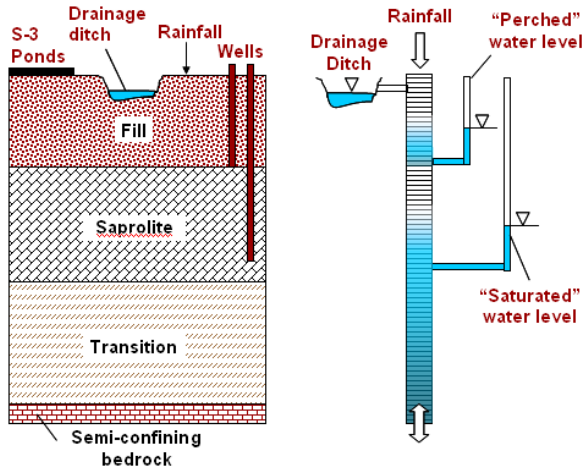


Figure 2. Conceptual model (left), and schematic of 1-D hydrological model (right).

The model is calibrated to water level data measured in wells within the saturated zone and a zone with an intermittently perched water table, and to nitrate concentration data collected from a multilevel sampling well. In Figure 3, preliminarily simulated hydrogeochemical data are compared with measured data.

The 1D hydrogeochemical model described above is coupled to a 2D electrical resistivity model. That is, output from the vertical 1D hydrological grid is projected onto the 2D ERT grid (Figure 4), giving an ERT model with time-varying vertical heterogeneity.

In this study, we consider a subset of the ERT electrode configurations used in the field experiment. The chosen subset is sensitive to vertical variations in properties and time-varying changes thereof, and thus is well suited to the hydrological model. In particular, the subset of measurements includes current dipoles formed with electrodes in opposing boreholes, and potential dipoles formed by receivers in individual boreholes (and only the electrodes that stay below the fluctuating water table are considered). One of the current dipoles and its corresponding measurement dipoles are depicted in Figure 4.

The ERT voltages simulated at four survey times for all current and measurement dipole combinations considered in this study are shown in Figure 5. Note that changes from the first to the second survey are minor, but significant changes from the first to the third and fourth surveys are substantial, indicating good sensitivity of ERT data to the hydrogeochemical processes. In ongoing work, we are performing the coupled hydrogeophysical inversion of these data sets (Figure 3 and 5).

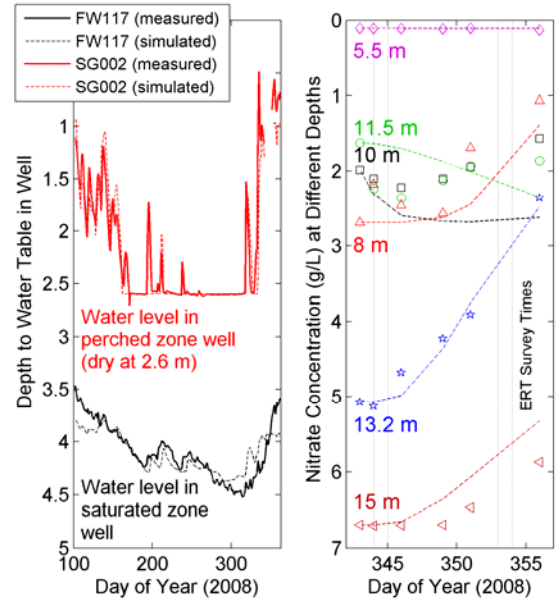


Figure 3. Measured and simulated (left) water level data in the perched and saturated zone wells, and (right) nitrate concentrations at noted depths in a multilevel sampling well. Depths less than 2.6 m indicate the presence of water in the perched zone well.

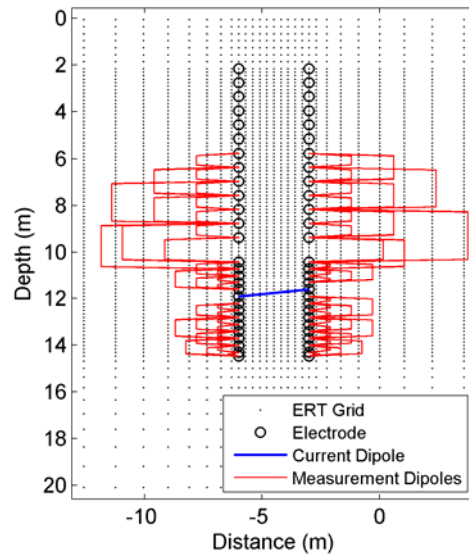


Figure 4. Numerical grid for ERT showing the electrodes for a current dipole (blue line) and the corresponding 67 measurement dipoles (red lines). An additional 20 current dipoles at different depths are also included, each with a different set of measurement dipoles, giving 1,442 measurements per survey. We consider four surveys in all from December 2008.

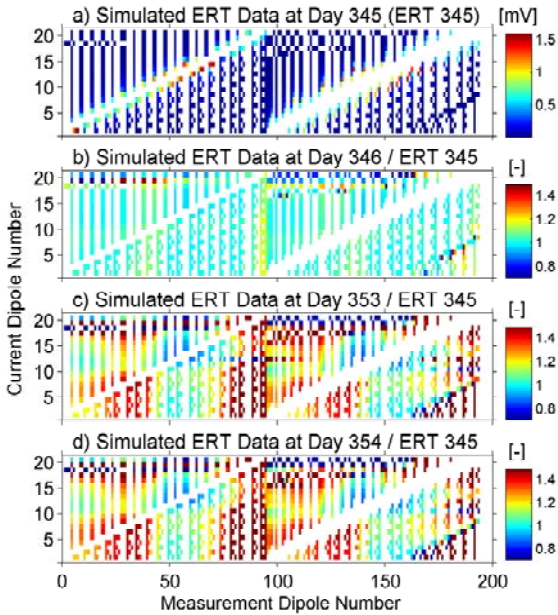


Figure 5. Simulated ERT data as a function of measurement dipole (x-axis) and current dipole (y-axis) for four survey times. Voltages are shown in (a) for the first survey time (Day 343), while voltages for later survey times (Days 344, 353, 354), in (b)–(d), respectively, are normalized by values of the first survey time.

The overall goals in this study are to evaluate the sensitivity of the approach for discerning the hydrogeochemical processes of interest and to evaluate the sensitivity of the electrical resistivity datasets for monitoring freshwater recharge and associated contaminant dilution effects. The insight gained is expected to help guide site-wide efforts examining the influence of recharge on contaminant concentrations and natural attenuation mechanisms. Future work will involve the incorporation of increasingly complex processes (e.g., fracture-matrix interactions), additional hydrogeochemical data types (e.g., isotopic data), and additional geophysical data types (e.g., surface-based ERT, self potential or SP, and surface seismic) into the modeling framework.

EXAMPLE 2: COMBINED HYDROGEOPHYSICAL DATA INTEGRATION AND DUAL-DOMAIN TRANSPORT MODELING

Predicting the long-term behavior of contaminant plumes using conventional characterization and modeling approaches is not reliably accurate for guiding environmental remediation strategies. The deficiency evidently results from an inability to collect high-resolution characterization data over the plume scale, and from the computational burden of high-resolution plume-scale transport simulations. In

this example, we discuss an approach that enables more reliable and computationally efficient contaminant transport prediction, through the combination of multiscale hydrogeophysical data integration and dual-domain transport modeling. Details of this work will be provided in a publication that is in preparation; an earlier version was presented by Kowalsky et al. (2007).

Because the approach is developed within the context of a contaminated site (the P-Area) at the DOE Savannah River Site, we assume the aquifer of interest is composed of two dominant facies: one mobile and one immobile (or less mobile). Contaminant interactions between the mobile and immobile facies are expected to play a key role in long-term behavior at the plume scale; such interactions can be accounted for using a dual-domain model (DDM), provided that the necessary parameters are obtainable from characterization data. Accordingly, the approach we developed combines (1) a DDM that relies on field-measurable attributes; and (2) a facies-based multiscale characterization procedure that incorporates different types of hydrological and geophysical data (e.g., seismic and electrical resistivity) collected at various scales (i.e., surface, crosshole, and core scale), as guided by parameterization needs of the DDM.

The progression of the approach is depicted in Figure 6, with the hydrogeophysical data as the first component. The surface-based geophysical data provide information over large regions but with relatively low resolution, while the crosshole data provide higher resolution information but at limited locations. The crosshole data may be useful for mapping the distribution of sand or clay facies, for example, between two wells; lower resolution surface data provide larger-scale (regional) information, such as the average proportion of sand or clay facies within a depositional unit throughout the aquifer. Core data provide point measurements that help to interpret crosshole geophysical data and link them to surface data.

Hydrogeophysical data integration is the second component of the approach (Figure 6). It is performed using a Bayesian statistical model, similar to that developed by Chen et al. (2004), in which the unknowns, cast as random variables, are framed as a joint conditional probability density function (pdf). By sampling the pdf, the regional-scale volume fraction is estimated throughout the aquifer, based on the surface-based geophysical data, while being conditioned to the core data and crosshole geophysical data at a smaller scale. Figure 7 depicts the various scales of data and the unknowns.

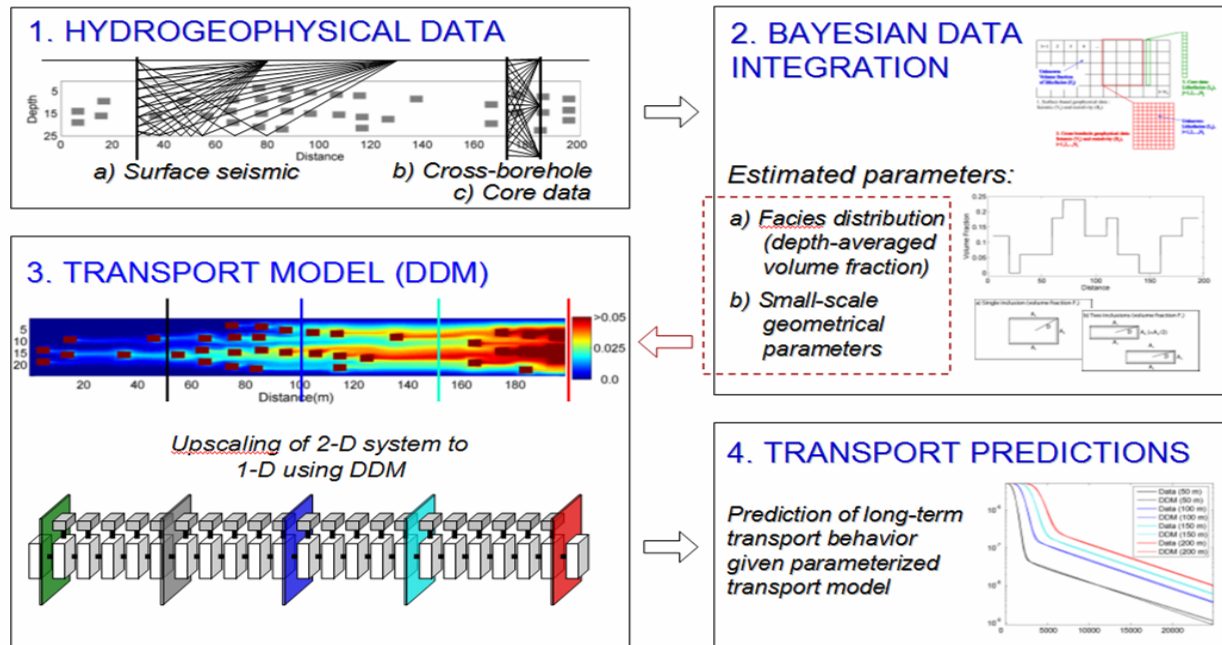


Figure 6. Approach for combined hydrogeophysical data integration and dual-domain transport modeling.

For the transport model (the third component of the approach, as depicted in Figure 6), we employ a 1D DDM with the assumption that it can adequately reproduce the transport behavior of a 2D aquifer containing low-permeability inclusions. Transport between the mobile domain (i.e., high-permeability regions) and the immobile domain (i.e., low-permeability regions) is explicitly accounted for using geometrical features inferred in the data integration approach. Specifically, the transport model requires characterization of the inclusion geometry, the spatially varying volume fraction of each facies, and a mass-transfer parameter.

The last step entails hydrological predictions, such as contaminant breakthrough curves at wells that are downgradient from the contaminant source, using the DDM parameterized with data from the hydrogeophysical data integration (fourth component in Figure 6).

We performed a synthetic study to explore links between the geophysical data and the DDM parameters, and to test the overall feasibility of the approach. iTOUGH2 was used to (1) develop a high-resolution transport model for generating the “real” data, (2) develop the DDM and incorporate output from the hydrogeophysical data integration, and (3) make transport predictions. An example of the synthetic data is shown in Figure 8.

In summary, we have developed a linked data integration-transport modeling approach for long-

term contaminant transport predictions and collected a variety of field-scale hydrogeophysical data at the P-Area to test the approach. We are using a simplified transport model that can be parameterized mechanistically with multiscale characterization data. Currently, the approach is being applied to prediction of trichloroethylene plume behavior at the Savannah River Site.

EXAMPLE 3: MONITORING GAS HYDRATE PRODUCTION WITH SEISMIC DATA

Many studies involving the application of geophysical methods in the field of gas hydrates have focused on determining rock-physics relationships for hydrate-bearing sediments, with the goal of using remote-sensing techniques to delineate boundaries of gas hydrate accumulations, and to estimate the quantities of gas hydrate within such accumulations. However, the potential for using time-lapse geophysical methods to monitor the evolution of hydrate accumulations during production has not been investigated. In this study, we begin to examine the feasibility of using time-lapse seismic methods, vertical seismic profiling (VSP) in particular, for monitoring changes in hydrate accumulations predicted to occur during production of natural gas. This is made possible through a numerical simulation tool we developed for the coupled simulation of (1) large-scale production in hydrate accumulations and (2) time-lapse geophysical surveys. While details of the study have been submitted for publication (Kowalsky et al., 2009b), a brief overview follows.

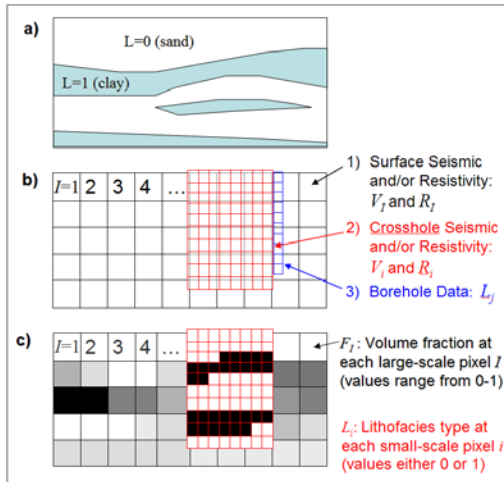


Figure 7. Depiction of data types and scales. Hydrogeophysical data: a) conceptual model, b) data sets at two scales (schematic), c) unknown parameters to be estimated.

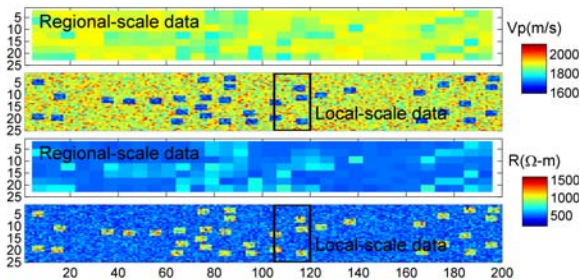


Figure 8. Example of synthetic hydrogeophysical data: regional-scale (surface-based) and local-scale (cross-borehole). The top subplots show seismic; the bottom show resistivity.

We consider a hydrate accumulation in the Gulf of Mexico that represents a promising target for production. The overall goals of the work are to examine the sensitivity of geophysical attributes and parameters to the changing conditions in hydrate accumulations, and to determine optimal sampling strategies (e.g., source frequency, time interval for data acquisition) and measurement configurations (e.g., source and receiver spacing for vertical seismic profiling), while taking into account uncertainties in rock-physics relationships. The study focuses on the use of seismic measurements, but the approach can easily be extended to consider additional geophysical data, such as electromagnetic measurements.

TOUGH+HYDRATE is the code used in this study for simulating gas production from a hydrate accumulation. This code, the successor to an earlier version called TOUGH-Fx/HYDRATE (Moridis et

al., 2005), models the nonisothermal hydration reaction, phase behavior, and flow of fluids and heat under conditions typical of natural methane-hydrate deposits in complex geological formations. It includes both equilibrium and kinetic models of hydrate formation and dissociation, and can handle any combination of hydrate dissociation mechanisms, such as depressurization and thermal stimulation. It accounts for heat and up to four mass components (i.e., water, CH₄, hydrate, and water-soluble inhibitors such as salts or alcohols) that are partitioned among four possible phases (gas, liquid, ice or hydrate phases, existing individually or in any of 12 possible combinations).

To simulate seismic measurements within a TOUGH+HYDRATE production simulation, we implemented a code that numerically solves the wave equations for an isotropic linear viscoelastic medium in 2D using a time-domain staggered-grid finite difference formulation. The input for the seismic simulations includes bulk density, and the bulk and shear moduli. The bulk density is a function of the density of the aqueous, gas, and hydrate phases, calculated in TOUGH+HYDRATE as a function of pressure and temperature. The bulk and shear moduli are determined using a rock-physics model.

The numerical grids used for simulating production of natural gas from a hydrate-bearing layer (HBL), as well as the overlapping grid used to simulate the time-lapse seismic surveys, are shown in Figure 9. Seismic properties, calculated using output from the TOUGH+HYDRATE grid, are mapped onto the seismic grid by interpolation.

Evolution of the hydrate and gas saturation is depicted in Figure 10, revealing the occurrence of three moving dissociation fronts within the HBL: the first moving in the radial direction, confined to relatively small distances from the wellbore; the second descending at the upper boundary of the entire HBL; and the third ascending at the lower boundary of the entire HBL. As the HBL undergoes dissociation, hydrate saturation decreases, while gas and water saturation increase. The largest accumulation of gas occurs just above the top of the HBL, but gas is also seen to increase below and within the HBL. A description of the production model and comprehensive analysis of the system behavior are given in Moridis and Reagan (2007).

The changes in physical properties within the HBL described above may be detectable using geophysical monitoring techniques. Using the coupled production-seismic model described above, we simulate vertical seismic profile (VSP) surveys at various times during production. We achieve different angles of VSP measurements by modeling the source as an

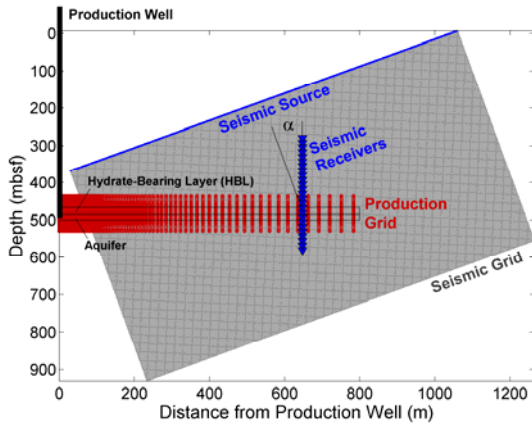


Figure 9. Numerical grids for simulating production of natural gas from a hydrate-bearing layer (red grid) and corresponding time-lapse seismic surveys (gray grid). The seismic source and receivers are shown in blue.

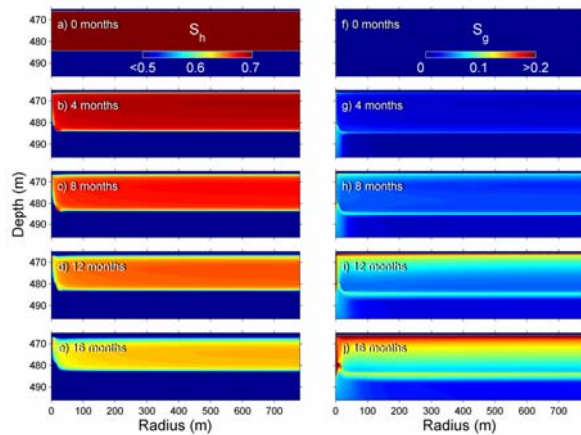


Figure 10. Distributions of simulated gas hydrate saturation (left column) and gas saturation (right column) for increasing times during production (0, 4, 8, 12, and 16 months, respectively). The color scales for S_h and S_g are clipped below 0.5 and above 0.2, respectively, to improve visualization.

incoming plane wave with the desired angle of incidence to the hydrate-bearing layer (the geophysical grid is rotated accordingly to minimize boundary effects). The simulated waveforms are recorded at a string of receivers spanning from above the hydrate-bearing layer to below for each survey.

An example of the simulated seismic response for a receiver located above the HBL at a depth of 355 m is shown in Figure 11. Waveforms are shown at six survey times, up to 20 months after the start of production, for four feasible rock physics models.

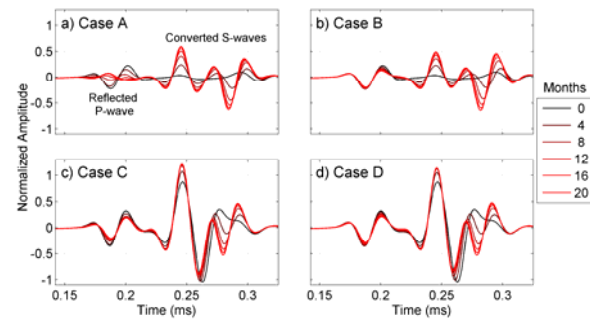


Figure 11. Seismic response during production. Seismic signal recorded above the HBL at a depth of 355 m. Waveforms are shown at six survey times (0, 4, 8, 12, 16, and 20 months after the start of production) for four rock physics models (a–d).

The initial arrival is the reflected P-wave, as labeled in the figure, followed closely by the converted S-wave arrivals. The converted S-wave evidently provides a good indicator of changes in the HBL during production, but it is important to note that the choice of rock physics model greatly affects the magnitude of change and the shape of the signal in general. In addition, we observed that converted transmitted S-waves recorded below the HBL (not shown) are especially well suited to detect changes occurring in the HBL.

In summary, the application of VSP measurements for monitoring production appears promising, but it is important to accurately determine the rock-physics models and consider uncertainty in the associated parameters.

The numerical simulation tool being developed can provide a means for designing cost-effective geophysical surveys that successfully track the evolution of hydrate properties. This work also serves as a basis for developing a comprehensive method for monitoring production and integrating multiple types of geophysical and hydrological data.

SUMMARY

While the approaches considered in the preceding examples are entirely different from one another, they share the common goal of improving subsurface characterization, by taking advantage of the sensitivity of geophysical data to subsurface fluid distributions and the properties that govern flow and transport. This work reflects the substantial progress made in developing approaches for integrating geophysical and hydrogeochemical data in the TOUGH family of codes in applications ranging from environmental remediation, to nuclear waste storage, to oil and gas production.

ACKNOWLEDGMENT

This work was supported by the U.S. Department of Energy, Contract No. DE-AC02-05CH11231.

REFERENCES

- Chen, J., S. Hubbard, Y. Rubin, C. Murray, E. Roden, and E. Majer, 2004. Geochemical characterization using geophysical data and Markov chain Monte Carlo methods: a case study at the South Oyster Bacterial Transport Site in Virginia, *Water Resour. Res.*, 40(12), W12412.
- Finsterle, S., 2004. Multiphase inverse modeling: Review and iTOUGH2 applications, *Vadose Zone J.*, 3: 747–762.
- Finsterle, S., C. Doughty, M. B. Kowalsky, G. J. Moridis, L. Pan, T. Xu, Y. Zhang, and K. Pruess, 2008. Advanced vadose zone simulation using TOUGH, *Vadose Zone Journal*, 7, 601-609.
- Finsterle, S., and M. B. Kowalsky, 2008. Joint hydrological-geophysical inversion for soil structure identification, *Vadose Zone Journal*, 7, 287–293.
- Kemna, A., J. Vanderborght, B. Kulesa and H. Vereecken, 2002. Imaging and characterization of subsurface solute transport using electrical resistivity tomography (ERT) and equivalent transport models, *Journal of Hydrology*, 267(3-4), 125-146.
- Kowalsky, M. B., J. Birkholzer, J. Peterson, S. Finsterle, S. Mukhopadhyay, and Y. Tsang, 2008. Sensitivity analysis for joint inversion of GPR and thermal-hydrological data from a large-scale underground heater test, *Nuclear Technology*, 164(2), 196-206.
- Kowalsky, M. B., S. Finsterle, J. Peterson, S. Hubbard, Y. Rubin, E. Majer, A. Ward, and G. Gee, 2005. Estimation of field-scale soil hydraulic and dielectric parameters through joint inversion of GPR and hydrological data, *Water Resour. Res.*, 41, W11425.
- Kowalsky, M. B., S. Finsterle, and Y. Rubin, 2004. Estimating flow parameter distributions using ground-penetrating radar and hydrological measurements during transient flow in the vadose zone, *Adv. in Water Res.*, 27(6), 583-599.
- Kowalsky, M. B., E. Gasperikova, S. Finsterle, D. Watson, S. S. Hubbard, 2009a (submitted). Coupled modeling of hydrogeochemical and electrical resistivity data for exploring the impact of recharge on subsurface contamination, *Geophysics*.
- Kowalsky, M. B., S. S. Hubbard, J. Chen, J. E. Peterson, G. P. Flach, 2007. Multiscale hydro-geophysical data integration for parameterization of transport model at Savannah River Site, *EOS Trans. AGU*, 88(52), Fall Meet. Suppl., Abs. H14C-01.
- Kowalsky, M. B., S. Nakagawa, and G. Moridis, 2009b (submitted). Feasibility of Monitoring Gas Hydrate Production with Geophysical Methods, *SPE Journal*.
- Kowalsky, M. B., and G. J. Moridis, 2007. Comparison of kinetic and equilibrium reactions in simulating the behavior of gas hydrates. *Energy Conversion and Management*, 48, 1850–1863.
- Lehikoinen, A., S. Finsterle, A. Voutilainen, M. B. Kowalsky, J. P. Kaipio, 2009a. Dynamical inversion of geophysical ERT data: state estimation in the vadose zone, *Inverse Problems in Sci. and Eng.*, 17(6), 715-736..
- Lehikoinen, A., J. M. Huttunen, S. Finsterle, M. B. Kowalsky, J. P. Kaipio, 2009b (submitted). Dynamic inversion for hydrological process monitoring under model uncertainties, *Water Resources Res.*
- Moridis, G. J., Kowalsky, M. B. Pruess, K. 2005. TOUGH-Fx/HYDRATE v1.0 User's Manual: A code for the Simulation of System Behavior in Hydrate-Bearing Geologic Media, Report LBNL/PUB 3185, Lawrence Berkeley National Laboratory.
- Moridis, G. J., M. T. Reagan, 2007. Gas Production From Oceanic Class 2 Hydrate Accumulations. Paper OTC 18866 presented at the 2007 Offshore Technology Conference, Houston, Texas, April 30–May 3, 2007.
- Pruess, K., C. Oldenburg, and G. Moridis, 1999. *TOUGH2 User's Guide, Version 2.0*, Report LBNL-43134, Lawrence Berkeley National Laboratory, Berkeley, Calif.
- van de Hoven, S. J., D. K. Solomon, and G. R. Moline, 2005. Natural spatial and temporal variations in groundwater chemistry in fractured, sedimentary rocks: scale and implications for solute transport, *Applied Geochemistry*, 20, 861-873.

CONCEPTUAL MODELING OF A DEEP SEATED NAPL DEPOSIT IN VOLCANOGENIC ROCKS

Alexey V. Kiryukhin

Institute of Volcanology and Seismology FEB RAS
Piip-9

Petropavlovsk-Kamchatsky, Russia
e-mail: avk2@kscnet.ru

ABSTRACT

A NAPL-bearing volcanogenic reservoir exists in West Siberia, hosted in Triassic age rocks (rhyolite tuffs) at a depth between 2.5 and 2.8 km, overlaid by low-permeable clay-argillite formations. Reservoir temperatures range from 120 to 130°C, and pressures from 290 to 310 bars. Integrated analysis of the geological and geophysical data shows circulation patterns, where upflow zones can be identified by positive temperature and pressure anomalies, while downflows lead to negative anomalies. These circulation patterns coincide with the former Triassic volcano vents, which are related to volcanic breccias.

Conceptual TOUGH modeling was used to verify the possibility of a NAPL deposit accumulation in the clay overlaying the Triassic rhyolite tuff reservoir. This deposit is fed by NAPL bearing upflows from buried volcanic vents. In a first step, a 3D numerical model of the reservoir was developed, covering $10 \times 8 \times 3 \text{ km}^3$, and discretized by rectangular $10 \times 8 \times 30$ grid. Inverse iTOUGH2-EOS1 modeling was used to estimate heat and mass flows as well as permeabilities. Next, forward T2VOC modeling was used to reproduce the NAPL distribution in the volcanogenic reservoir. NAPL phase saturations matched the reservoir exploration data. In parallel to conceptual modeling, iTOUGH2-EOS3 was used to estimate thermal properties of reservoir rocks (heat conductivity and specific heat) based on laboratory heat test data performed on rock samples.

INTRODUCTION

Papers presented at the World Geothermal Congress in 2005 and previous publications show that most of the high-temperature geothermal fields occur in various hydrogeological structures of recent volcanic areas: 1. Basins of the Quaternary stratovolcanoes and shield volcanoes (15% of the world geothermal electricity production); 2. Contact zones of the Quaternary intrusions and dyke swarms hosted in Neogene-Quaternary volcanogenic basins (19%); 3. Artesian volcanogenic basins of the Neogene-Quaternary age (8%); 4. Contact zones of the Quaternary intrusions hosted in sedimentary basins (48%); 5. Fault systems in basement rocks (10%).

Hydrothermal reservoirs in Neogene-Quaternary volcanogenic formations include: 1. Single Fault or Multiple Faults Systems (Ogiri, Hatchubaru, Sumikawa, Okuadzu, Mutnovsky (Dachny), Momotombo, Lihir, Nevada Basins and Ranges); 2. Semi-permeable Faults (Dykes) (Mac-Ban (Bulalo), Tiwi); 3. Intrusions External Contact Zones (Matsukawa, Kakkonda, Uenotai, Fushime, Tongonan, Palinpinon, Krafla, Svartsengi, Nesjavellir, Hellisheidi); 4. Volcano Conduit Zones (Hatchijo-Jima, Darajat); 5. Nonwelded Tuffs and Lavas Stratigraphic Contact Zones (Yellowstone, Los-Azufres, Ahuachapan, Miravalles, El-Tatio, Olkaria, Oguni, Takigami, Wairakei, Casa-Diablo, Pauzhetsky); 6. Lava Formations (Kamojang).

The examples of the Pauzhetsky field (Kiryukhin et al., 2004, 2008) and Mutnovsky field (Kiryukhin et al., 2009) show that high-temperature upflows and recharge downflows coincide with faults or channels, which are main conduits also for magma extrusions and volcanoes (see Figures 1 and 2). This is probably a typical case for many geothermal fields.

Geothermal field exploration and modeling experience may apply to the NAPL-bearing volcanogenic Rogozhnikovsky reservoir in West Siberia, hosted in Triassic rocks, which also shows multiple single faults and deep roots (Kiryukhin et al., 2008) (Figure 3).

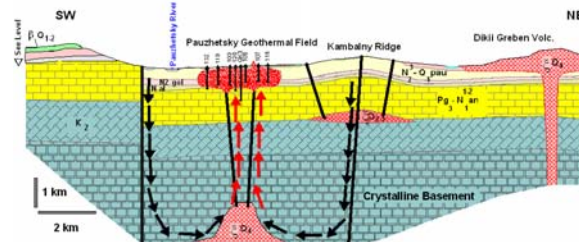


Figure 1 . Conceptual hydrogeological model of the Pauzhetsky geothermal system (Kiryukhin et al., 2008). Lithologic units: K_2 – metamorphic basement, $Pg_3-N_1^{1-2}$ an – Miocene sandstones, N_{1al} – Neogene andesite tuffs and lavas, $N_2\text{gol}$ – Golyginsky Layer, $N_2^3-Q_{1pau}$ – Pauzhetka Tuff, βQ_{1-2} – andesites, ζQ_{2-3} , ζQ_4 – Dacite Extrusive Complex. Black arrows: cold-water (meteoric) recharge; red arrows: upflow of hot fluids; black lines: faults; short vertical black lines: geothermal wells.

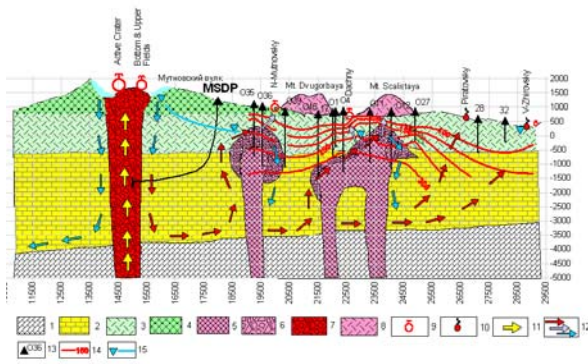


Figure 2. Conceptual model of Mutnovsky volcano - hydrothermal system: 1: crystalline basement, 2: Cretaceous basement and Neogene sandstones, 3: Neogene volcanogenic-sedimentary rocks, 4: Mutnovsky stratovolcano (Q_3-Q_4), 5: diorite intrusions, 6: diorite intrusion contact zone, 7: Mutnovsky volcano magma feed system, 8: rhyolite and dacite extrusions (Q_3-Q_4), 9: fumarole fields, 10: hot springs, 11: magma and magmatic fluids, 12: hydrothermal fluids, 13: geothermal wells, 14: temperature distributions, 15: water level surface in reservoir. MSDP: proposed position of Mutnovsky Scientific Drilling Well.

INPUT DATA FOR NAPL DEPOSIT NUMERICAL MODEL

Geological Setting

Triassic volcanism in the Rogozhnikovsky area took place 242 to 258 million years ago (U-Pb dating; Korovina, 2008). Adjacent Pre-Jurassic rhyolites units penetrated by wells cover a vast area around $500 \times 250 \text{ km}^2$ (Bochkarev et al., 2008), which indicates either significant arc volcanism or intra-plate rifting conditions at that time. As a result of this, arc and rift fracture systems maintain active fluid circulation in the West Siberian basin, which cause significant vertical disturbance of brine concentration (heavy brine upflows and diluted fluid downflow zones), thermal anomalies, and fluid pressure anomalies (low and above hydrostatic pressure zones) (Matusevich et al., 2005).

A NAPL-bearing volcanogenic reservoir exists in West Siberia, hosted in Triassic rocks (rhyolite tuffs) at a depth between 2.5 and 2.8 km, overlaid by low-permeability clay-argillite formations. Reservoir temperatures range from 120 to 130°C , and pressures from 290 to 310 bars.

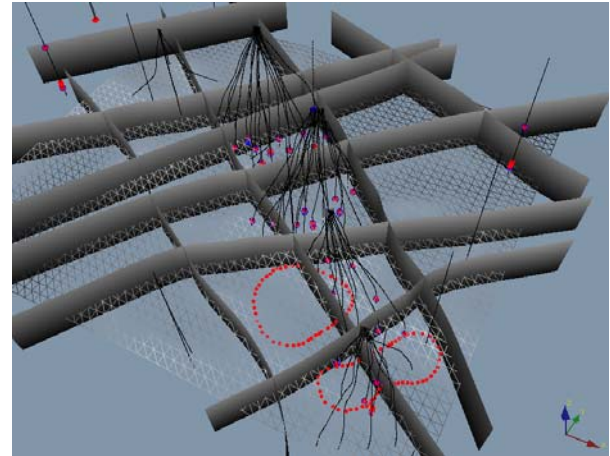


Figure 3. 3D view of Rogozhnikovsky (from Kiryukhin et al., 2008). Fractures are inferred from seismo tomography data; red dotted lines: geoisotherms 120°C at -2500 m.a.s.l. , circles: production zones: circles (red: NAPL; blue: water; purple: NAPL above 25%+water). Grid: roof of the Triassic volcanogenic reservoir.

Integrated analysis of the geological and geophysical data shows circulation patterns, where upflow zones are identified by positive temperature and pressure anomalies, while downflow zones are identified by negative anomalies. Those circulation patterns do not clearly fit the fracture system inferred from 3D seismotomographic data (Figure 3), while more closely coincide with the former Triassic volcano vents, detected by volcanic breccias penetrated by drill holes (Figure 4).

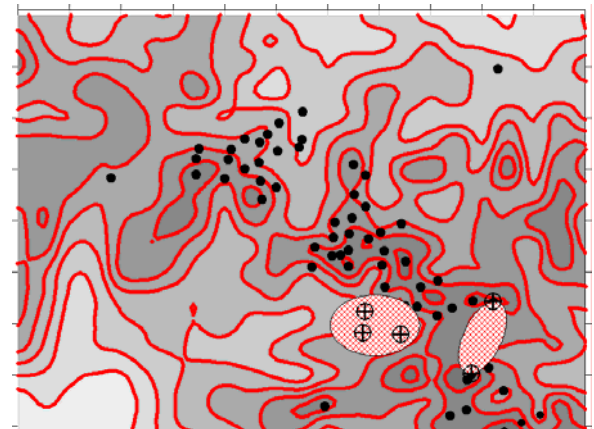


Figure 4. Surface of the volcanogenic unit (filled color, 50 m interval contours, darker at higher elevations); potential volcanic vents shown by crossed-hatched areas; filled circles: wells; crossed circles: wells penetrating breccias; grid size: 1 km.

Thermal Properties of the Reservoir Rocks Estimate

Heat test setup

Heat properties of reservoir rocks were estimated based on experiments with cylindrical rock samples of 50 mm diameter and 50 mm height. The laboratory experimental setup includes a heat source (12 W) at the bottom of the cylindrical sample, a zond type temperature logger installed 10 mm from the top of the thermally insulated sample in a hole with 2.4 mm diameter (see Figure 5). KIIT-8 paste was used to improve the thermal contact between logger and sample. A Hioki 3447-01 temperature logger was employed to register transient temperature changes (accuracy of measurements: 0.1°C). All measurements took place in an underground facility with stable temperature conditions after 24 hr of delay time to reach constant initial conditions in the sample. Observational data include transient temperature records at 10 sec intervals during 5 min after beginning of heating .

Inverse iTOUGH2-EOS3 modeling of the Heat Tests

A cylindrical grid was used to represent the rock sample in the model (Figure 5). The grid includes 26 2-mm thick layers and 12 radial zones with logarithmically increasing radii (increment rate 1.165), where the first radius corresponds to the zond diameter of 1.2 mm; the thickness of the last cylindrical element is 25 mm. Model elements are named as AI_K, where I is the layer number (from above), and K is the radial zone number (from the center). Subsequently, two domains were assigned: rock sample domain and zond domain (elements AI_1, where I=1, ... , 5 up to depth 10 mm).

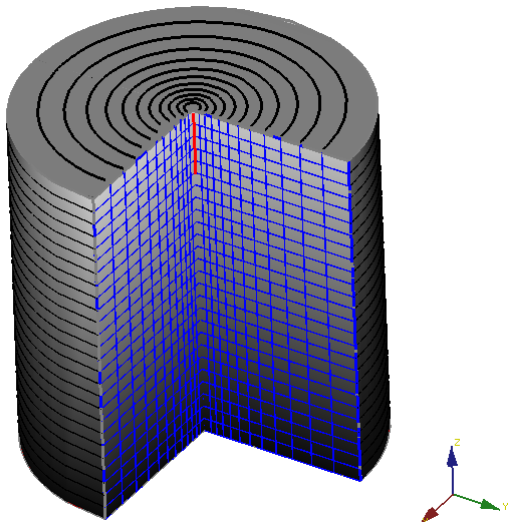


Figure 5. Numerical grid used to represent the cylindrical rock sample. The temperature logger is inserted at the top of the sample to a depth of 10 mm. The heat source is located at the bottom.

Grain density, porosity, and permeability were assigned as known petrophysical parameters. Since 99% of the pore volume in the rock samples were occupied by air, the EOS3 module for water and air was used. Correspondingly, three primary variables were used: gas phase pressure P, gas saturation S_g , and temperature T. Initial values were assigned as $P = 10^5$ Pa and $S_g = 0.999$ (dry samples). A linear function was used for the heat conductivity λ as a function of water saturation S_w , $\lambda = \lambda_r + (\lambda_w - \lambda_r) S_w$, where λ_w is the heat conductivity of the wet rock, and λ_r is the heat conductivity of the dry rock. The heat source was assigned to a single element B_1, which is connected to the bottom elements A_QI (I=1, ..., 12) with volume-proportional contact areas. The measured, transient calibration data were compared to the calculated temperature at the zond hole center (Element A3_1).

Model parameters to be estimated include heat conductivity (dry) λ_r , specific heat C_r , initial rock sample temperature T_0 and heat source rate W. Initial temperature T_0 and heating rate W were added to the parameter list, because (although measured during the experiment) small variations in T_0 and W have a large impact on the predicted temperatures.

The output results of iTOUGH2-EOS3 inversions include tables of sensitivity coefficients, correlation charts, residuals, best estimates and their standard deviations. The example below shows an excerpt from the inverse modeling outputs for the 18th of 38 laboratory experiments analyzed by iTOUGH2.

Standard Deviations						
PARAMETER	BEST ESTIMATE	A PRIORI	CONDITIONAL	MARGINAL	C/E	1-3/P
Initial Tempera	0.1891069E+02	N/A	0.6382464E-02	0.1021403E-01	0.623	1.000
HEAT-CAP-ROCK1	0.9082472E+03	N/A	0.1329833E+01	0.1838944E+02	0.072	1.000
HEAT FLOW	0.1418097E+01	N/A	0.8870081E-03	0.1419115E+00	0.065	1.000
HEAT-COND-DRY	0.1799866E+01	N/A	0.4231720E-02	0.7494515E-01	0.056	1.000

Correlation Chart							
-1.0 -0.8 -0.6 -0.4 -0.2 0.0 0.2 0.4 0.6 0.8 1.0							
PARAMETER							
Initial Tempera		HEAT-CAP-ROCK1		HEAT FLOW		HEAT-COND-DRY	

A four-parameter inversion shows acceptable correlations between the estimated parameters, which allows us to get sufficiently accurate estimates of heat conductivity (dry) (standard deviation: 0.1 W/(m °C)) and specific heat (standard deviation: 20 kJ/(kg °C)).

Figure 6 shows the comparison between measured and calculated temperatures after calibration.

Based on the inversion of 38 laboratory experiments on rock samples from a well that penetrated the volcanogenic reservoir at a depth between 2580 and 2795 m, an average value of heat conductivity (dry) of 1.44 W/(m °C), and an average specific heat of 850 kJ/(kg °C) was obtained. According to the Rautman

function, the saturated rock has a thermal conductivity of about 1.88 W/(m °C) (1.44 dry rock + 0.44 water contribution).

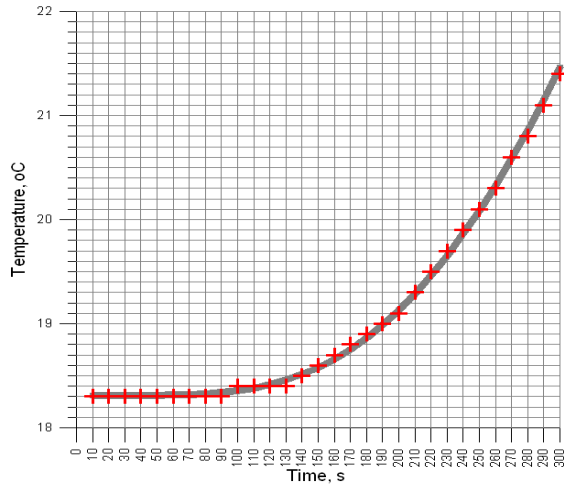


Figure 6. Comparison between measured and calculated temperatures after iTOUGH2-EOS3 calibration of the heat test: crosses: observational data (laboratory test #18); line: calculated temperatures.

Relative Permeabilities and Capillary Pressures

Laboratory measurements of relative permeabilities of five Triassic volcanogenic reservoir rock samples suggest that the van Genuchten model is appropriate for the water phase, with a residual water saturation between 0.2 and 0.5, whereas Corey’s model can be conveniently used to describe the NAPL relative permeability with residual NAPL saturation between 0.3 and 0.4 (see Figure 7).

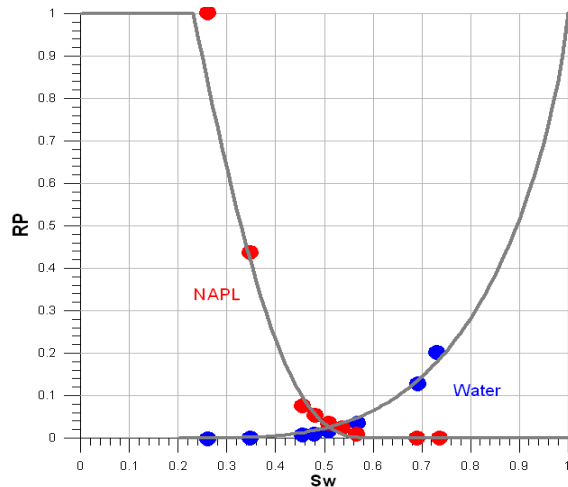


Figure 7. Experimental data (filled circles) and van Genuchten fits of NAPL and water relative permeabilities vs. water saturation S_w of rock samples from the volcanogenic reservoir (depth of sampling: 2640 m). Van Genuchten and Corey parameters: $IRP=7$, $RP1=0.76$ (λ), $RP2=0.23$ (residual water saturation), $RP3=1$, $RP4=0.4$ (residual NAPL saturation)).

Laboratory measurements of capillary pressures of 126 Triassic volcanogenic reservoir rock samples suggest that the van Genuchten model ($ICP=7$, $CP1=0.4438$, $CP2=S_{lr}=0.22$, $CP3=1/P_0=1.50E-05$, $CP4=P_{max}=50$ bar, $CP5=S_{ls}=1.0$) can reasonably match the experimental data (Figure 8).

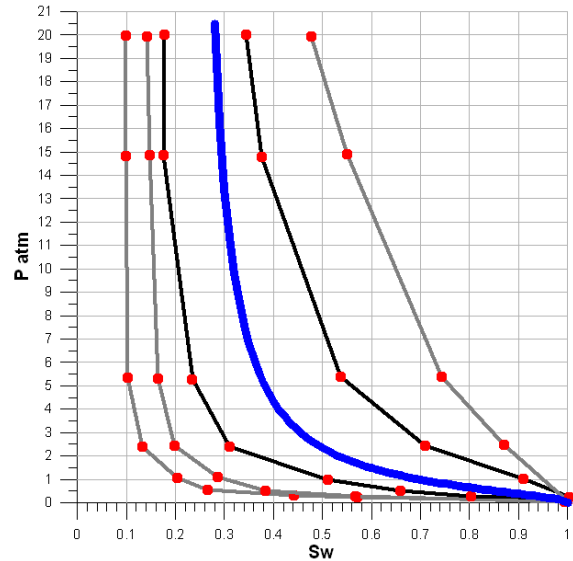


Figure 8. Experimental data (filled circles) and van Genuchten approximation (thick blue line) of capillary pressures laboratory tests of rock samples from Triassic volcanogenic reservoir. Van Genuchten parameters: $ICP=7$, $CP1=0.4438$, $CP2=S_{lr}=0.22$, $CP3=1/P_0=1.50E-05$, $CP4=P_{max}=50$ bar, $CP5=S_{ls}=1.0$.

A laboratory study shows a strong relationship between the initial and residual NAPL saturation.

Note that West Siberian reservoirs are generally characterized by hydrophobic properties, caused by high feldspar fractions of the minerals (Matusevich et al., 2005). This means that positive oil/water capillary pressures ($P_c(o-w) = P_c(g-w) - P_c(o-w) > 0$) keep the reservoir oil-wet. According to Matusevich et al. (2005), positive capillary pressures may reach 5.6 bars under some reservoir conditions, reducing the efficiency of oil recovery from the matrix by water flooding.

NUMERICAL MODELING OF NAPL DEPOSIT FORMATION IN VOLCANOGENIC ROCKS

Model Setup

TOUGH-based numerical modeling was used to understand NAPL formation and distribution in the reservoir. First, a 3D numerical model of the reservoir was developed, covering a volume of $10 \times 8 \times 3$ km³, discretized by a rectangular $10 \times 8 \times 30$ grid. This model covers the area shown on Figure 4.

The uppermost layer of the model (#30) was assigned at fixed state condition (10 bars, 5°C), which corresponds to conditions approximately 100 m below land surface, where mean annual pressures and temperatures are maintained. The bottom layer of the model (#1) includes sources (potential upflow zones, where positive mass flow rate and enthalpy are assigned), sinks (potential downflow zones, where negative mass flow rates are assigned), and conductive heat flow sources in all elements of the bottom layer.

Regional lithologic characteristics used as input data for the numerical model are summarized in Table 1. These data were obtained based on core studies and correspond to matrix properties of the reservoirs. The model zonation is illustrated in Table 2.

The volcanogenic reservoir is characterized by double-porosity properties identified based on the Fracture Micro Images (FMI) study, with an average vertical fracture spacing of FS=26 m, average fracture aperture of 0.3 mm (range 0.17–0.5), and a fracture volume fraction of $FV=3.17 \times 10^{-5}$. Corresponding fracture permeability ranges from 0.23 to 1.59 darcy (assuming a parallel plate model). Nevertheless, a single-porosity model based on matrix properties was used as a first modeling approach.

Table 1. Regional lithologic characteristics: ρ : grain density, ϕ : porosity, k : permeability, λ : heat conductivity, SH : specific heat.

Geological index	ρ kg/m ³	ϕ	k mD	λ W/m/ °C	SH kJ/kg/ °C
K ₂ -Q caprock	2700	0.35	0.1	1.1	800
K ₁₋₂ aquifer J-K ₁ caprock J aquifer	2700	0.20	0.19	1.2	900
Tr volcanogenic reservoir	2620	0.16	1.0	1.8	1000
Base layer	2800	0.02	0.1	2.1	1000

Table 2. Model zonation.

Geological index	Lithology	Model layers	Elevations m.a.s.l.	Domain ##
K ₂ -Q caprock	aleurite, clays	26-40	-1450, -50	K2Q_1
K ₁₋₂ aquifer J-K ₁ caprock J aquifer	Sand-aleurite	14-26	-2650, -1450	JK_1
Tr volcanogenic aquifer	Lavas, clastolavas tuffs and breccias	11-16	-2950, -2450	TR_
Basement		1-10	-3950, -2650	BASE1

Inverse iTOUGH2-EOS1 Modeling

Inverse iTOUGH2-EOS1 modeling was used to estimate heat and mass flows and permeabilities (base conductive heat flow, permeabilities of J-K₁ and K₂-Q units, upflow rate and enthalpy, and downflow rate). Model calibration was based on 41 temperature and 20 pressure calibration points. A natural-state run was performed for 10⁶ years. Modeled and measured data matched relatively well, with a mean temperature deviation (bias) of -0.3°C, a temperature standard deviation of 5.6°C, and a mean pressure deviation of -0.03 bar, a pressure standard deviation of 8.9 bar (3% of absolute value). The uncertainty of some parameter estimates is rather high, most likely due to over-parameterization, which leads to strong correlations, specifically between mass flows and the permeability of the K₂-Q unit. The best estimates values are: base conductive heat flow: 50.2 mW/m²; permeabilities of the J-K₁ and K₂-Q units: 0.19 mD and 0.0011 mD, respectively; total upflow rate: 3.6 kg/s with enthalpy of 558 kJ/kg; downflow rate: 3.6 kg/s.

Figure 9 shows the corresponding pressure and temperature distributions at -2550 m.a.s.l. Upflow and downflow in the model are the same, indicating that a circulation pattern exists in the basement of the volcanogenic reservoir, despite of recharge boundaries specified on the top of the reservoir.

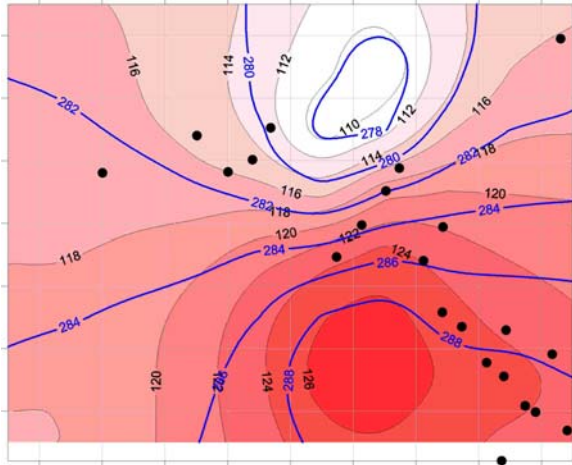


Figure 9. iTOUGH2-EOS1 natural-state modeling: temperature and pressure distributions at -2550 m.a.s.l. Black filled circles indicate wells; grid size is 1 km.

T2VOC (direct iTOUGH2 -EOS10) Nat ural-State Modeling

Model Setup

T2VOC (forward iTOUGH2-EOS10) modeling was used to reproduce the NAPL distribution in the volcanogenic reservoir, based on initial conditions obtained by the previous iTOUGH2-EOS1 modeling. The following scenario was used: 75.6×10^9 kg (0.24 kg/s during 10,000 years) of NAPL was injected into the reservoir through the base upflow zones, following 90,000 years of water upflow.

Van Genuchten relative permeability and capillary pressure functions were used with the parameters values above mentioned. Oil-wet positive capillary pressures were assigned directly in T2VOC by adding one line in the code: PC = -PC at the end of the van Genuchten part of SUBROUTINE PCAP.

Modeling Results

NAPL phase saturations vs. reservoir exploration data are shown in Figure 10. The modeled NAPL distribution appears as a region with an S_o range from 0.05 to 0.35 inside the zone of 45–55% NAPL phase saturation revealed by exploration. Low NAPL-phase concentrations are seen in the north-east of the modeling area, which corresponds to the downflow zone.

Although this modeling example is probably not a real history of NAPL accumulation under specific reservoir conditions, nevertheless it shows the conceptual possibility of NAPL deposit accumulation in clays overlaying a Triassic rhyolite tuff reservoir fed by NAPL bearing upflows from buried volcanic vents (Figure 11).

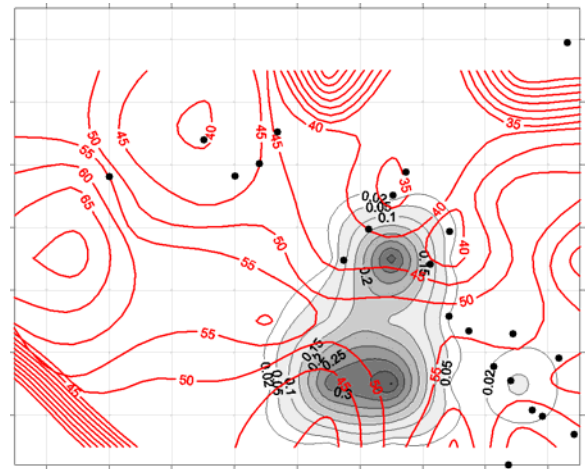


Figure 10. iTOUGH2-EOS10 natural-state modeling vs. exploration data at -2550 m.a.s.l: modeled NAPL phase concentrations are shown as filled grey contours; exploration data NAPL phase concentrations (in %) are shown as red line;. grid size is 1 km.

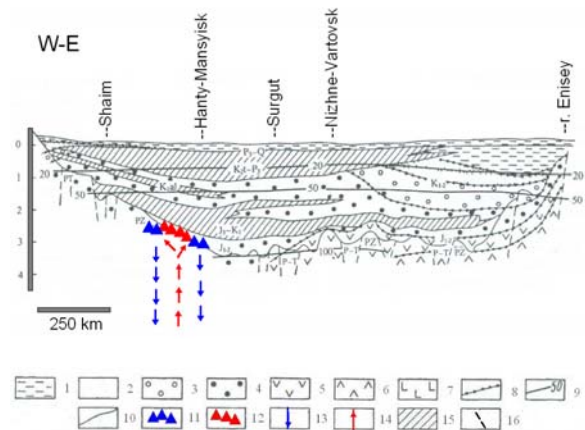


Figure 11. Cross section of the West Siberian basin (from V.A. Kiryukhin, 2005) with added schematic indication of Triassic volcanogenic reservoir and possible circulation patterns along former volcano vents. 1–7: hydrogeochemical zonation: mineralization < 1 g/l (1), 1–3 g/l (2), 3–10 g/l (3), 10–35 g/l (4), 35–70 g/l (5), 70–150 g/l (6), 150–375 g/l (7); 8: hydrogeochemical zone boundaries; 9: geoisotherms, °C; 10: lithological boundaries; 11: water filled volcanogenic reservoir; 12: NAPL filled volcanogenic reservoir; 13: separated water downflow channels; 14: NAPL bearing ascending fluid channels; 15: clay caprock units; 16: faults.

Future Study

We plan to extend the model domain to include the entire field, making a short-term study of the natural state conditions of the Rogozhnikovsky reservoir to understand the existing NAPL body dynamics under

the current temperature distributions and upflow-downflow conditions.

In parallel to this, a more detailed model approach for different exploitation scenarios is needed. This study should include well-by-well grid generation, taking into account double-porosity properties, spatial distributions of reservoir parameters (such as matrix porosity, permeability, initial NAPL saturations) as confirmed by extensive geophysics well logging, seismo tomography and FMI, as well as extensive core petrophysical studies. NAPL production and water production history matching is also planned. It would be necessary to consider in a more rigorous way the effects of brine properties (density, viscosity) that are functions of salt concentration. Future drilling locations and how to improve the efficiency of NAPL recovery from oil-wet volcanogenic reservoir conditions remain the primary challenge.

CONCLUSIONS

1. Based on analyses of hydrothermal reservoirs in recent volcanic areas, a conceptual model of NAPL reservoir formation in old volcanogenic formations was hypothesized. It was assumed that these reservoirs may use former volcano vents buried under sedimentary basins as channels of ascending NAPL-bearing fluids.

2. iTOUGH2-EOS3 modeling was used to estimate heat properties of the volcanogenic formation based on laboratory heat tests on 38 rock samples. iTOUGH2 inversions show the possibility of simultaneously estimating heat conductivity (dry) and specific heat with reasonable accuracy. Mean heat conductivity (dry) of 1.4 W/m°C and specific heat of 850 kJ/kg °C were obtained.

3. Conceptual iTOUGH2-EOS1 natural-state modeling based on measured pressure-temperature calibration data is an effective way to verify deep seated circulated mass flow conditions, base conductive heat flow and permeabilities. However, just three of the six estimated parameters are independent enough for accurate estimation. The best estimates are: base conductive heat flow: 50.2 mW/m²; permeabilities of the J-K₁ and K₂-Q: 0.19 mD and 0.0011 mD, respectively; total upflow rate: 3.6 kg/s with an enthalpy of 558 kJ/kg; downflow rate: 3.6 kg/s.

4. Conceptual T2VOC (forward iTOUGH2-EOS10) modeling was used to demonstrate the possibility that oil deposits accumulate in clay overlaying Triassic volcanogenic reservoirs, fed by NAPL-bearing upflows from buried volcanic vents.

ACKNOWLEDGMENTS

The author expresses gratitude to Dr. A. Battistelli and Dr. S. Finsterle for their helpful comments and suggestions. This work was supported by RFBR project 09-05-00605-a.

REFERENCES

- Bochkarev V.S., Brekhuntsov V.M., Lukomskaya K.G. On the Issue of the Permian-Triassic in Western Siberia, *Gornye Vedomosti* 2, p. 7-17 (in Russian), 2009.
- Falta R., Pruess K., Finsterle S., Battistelli A. T2VOC User's Guide LBNL-36400, 1995.
- Finsterle S. iTOUGH2 User's Guide, LBNL-40040, 1999.
- Kiryukhin A.V., Yampolsky V.A., Modeling Study of the Pauzhetsky Geothermal Field, Kamchatka, Russia, *Geothermics*, v.33, No.4, p. 421-441, 2004.
- Kiryukhin A.V. Modeling of the Dachny Site Mutnovsky Geothermal Field (Kamchatka, Russia) in Connection with the Problem of Steam Supply for 50 MWe Power Plant, *Proceedings World Geothermal Congress 2005 Antalya, Turkey*, 24-29 April 2005, 12 p.
- Kiryukhin A.V., Nikolaeva E.V., Baturin A.Y. Comparative Analysis Geological and Thermohydrodynamic Models of Oil and Geothermal Deposits Hosted in Volcanogenic Rocks of Different Age, *Proc. All Russia Conference "Earth Degassing: Geodynamics, Geofluids, Gas and their Para genesis"* Moscow, p. 204-206 (in Russian), 2008.
- Kiryukhin A.V., Asaulova N.P., Finsterle S. Inverse modeling and forecasting for the exploitation of the Pauzhetsky geothermal field, Kamchatka, Russia, *Geothermics*, V. 37, p. 540-562, 2008.
- Kiryukhin A.V., Kiryukhin V.A. Manukhin Y.F. Hydrogeology of Volcanogenic Areas, S-Petersburg, Nauka Publ., 396 p. (in Russian), 2009.
- Kiryukhin V.A. Regional Hydrogeology, S-Petersburg Mining Inst., 343 p, 2005.
- Matusevich V.M., Rylkov A.V., Ushatinsky I.N. Geofluid Systems and Problems of Oil and Gas Deposits Distributions in West Siberia Megabasin, Tumen State Oil University, 224 p. , 2005
- Pruess, K., Oldenburg, C., Moridis, G., TOUGH2 User's Guide, Version 2.0. Lawrence Berkeley National Laboratory report LBNL-43134, Berkeley, CA, USA, 198 pp, 1999.

UNCERTAINTY REDUCTION OF HYDROLOGIC MODELS USING DATA FROM SURFACE-BASED INVESTIGATION

Kenzi Karasaki¹, Kazumasa Ito², Yu-Shu Wu³, Michito Shimo⁴, Atsushi Sawada⁵,
Keisuke Maekawa⁵ and Koichiro Hatanaka⁵

¹Lawrence Berkeley National Laboratory
Berkeley, CA, 94720, USA
kkarasaki@lbl.gov

²National Institute of Advanced Industrial Science and Technology

³Colorado School of Mines

⁴Taisei Corporation

⁵Japan Atomic Energy Agency

ABSTRACT

Geohydrologic model uncertainties include permeability, boundary, and initial conditions. We present some examples of using information other than pressure data to constrain a geohydrologic model. The initial model was constructed using information from surface geology and a few boreholes. Inversion analysis of pressure data implied the existence of a low-permeability cap rock. We then used river flow data and temperature data from a hot spring as a basis for estimating the recharge flux, which suggested that the overall permeability of the modeled area could be one order of magnitude larger than that of the base model. Next, we simulated a saltwater washout process and compared the simulated salinity distribution with the salinity data from a borehole. We found that a better match to the salinity data is obtained if the increase in permeability is taken up by the fault zone rather than uniformly by the entire model. A smaller-scale match to the temperature, pressure, and density profiles from two boreholes indicated that there was a low-permeability fault in between the two boreholes.

1. INTRODUCTION

It is very difficult to characterize a large body of heterogeneous rock sufficiently, and to build a reliable groundwater flow model, particularly when the rock is fractured, which is most often the case. Available hydrological data are often limited and insufficient, both spatially and temporally. It is extremely challenging to scale-up detailed small-scale measurements and to predict and verify large-scale behavior. Unless there is an underlying known property that extends over scales, measurements conducted at a certain scale can only be used to describe the processes at the same scale. Some geostatistical tools may be used to predict the range of the model outcome. However, the more heterogeneous the rock is, the larger the uncertainty becomes.

Building a geohydrologic model of a large area involves many uncertainties from various sources, from the conceptual model to the input parameters. Model uncertainties include material parameters such as permeability and porosity. Often overlooked are boundary conditions and initial conditions. The most important element of a reliable model is the correct conceptual understanding of the geohydrologic processes within the area, which comes only after a long progression of model building, with much trial and error. Although model uncertainties originating from different modeling approaches have been addressed (e.g., Ijiri et al., 2009), uncertainty studies applied to actual field sites are limited. Most numerical models have implicit limitations that may lead to uncertainties that are inconspicuous and are seldom discussed. Many numerical models do not consider all the physical processes involved, which may or may not be necessary. A complete THMC (thermal, hydrological, mechanical, and chemical) simulation is very challenging and a subject of intense research at present. There are multiple reasons for this, including the difficulty in estimating the initial conditions and specifying the constitutive equations (such as the porosity-permeability relationship) that are applicable at a practical scale, in addition to the scarcity of relevant data.

The conditions at the outer boundaries of numerical models need to be specified all around, although they are usually immeasurable in practice. Therefore, they are often chosen for the convenience of modeling. The surface boundary conditions are often set to be a constant flux condition. Observations that can be made in the field are often severely limited in type, space, and time. One type that can be relatively easily observed is pressure, which can involve uncertainties of its own, such as gauge drift and borehole short-circuiting due to packer leak. To measure pressure at depth, we need to drill deep boreholes, which is very expensive. As a consequence, only a limited number of boreholes are drilled. Furthermore, the locations

where boreholes can be drilled are often limited for reasons such as physical accessibility.

Ideally, tests should be designed to directly stress the system at the scale of interest, so that the observed response is the result of the averaging of the inherent properties up to that scale. However, this is difficult if the scale is over a kilometer or more. Moreover, in a very active tectonic environment like that of Japan, faults exist ubiquitously, which greatly affect the hydrology around their vicinity. Correct characterization of large faults is crucial in building a reliable geohydrologic model.

Large-scale groundwater flow models are typically calibrated to the steady-state pressure head data. An inversion scheme can be used to search for optimum parameters. However, we rarely have enough head data, and furthermore, head data alone are not sufficient for building a reliable model. Therefore, it

is very important to utilize all available relevant data to constrain model uncertainties. In this paper, we

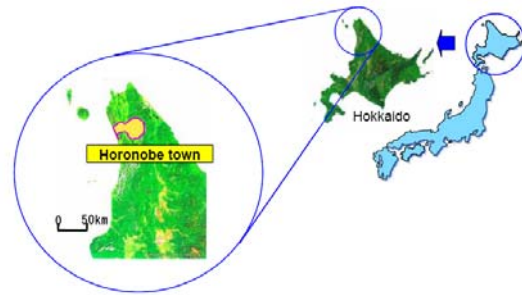


Figure 1. Location of Horonobe Town (after Yamasaki et al., 2004)

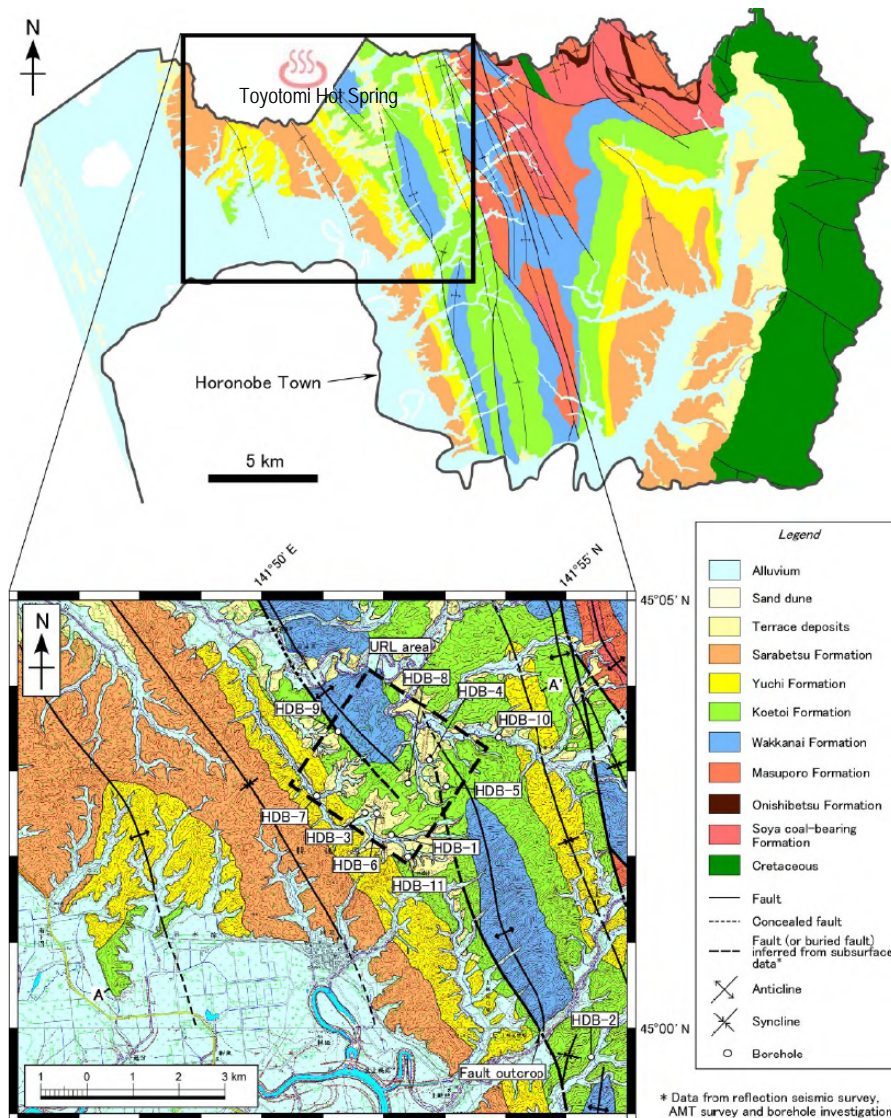


Figure 2. Horonobe Town (top, the yellow area in Figure 1) and the Horonobe URL area (below, broken square). Also shown are the borehole locations and the geology (after Ota et al., 2007).

show a progressive model improvement, in which information other than pressure data, such as temperature and salinity data, are used to constrain a hydrologic model to help reduce uncertainties in the conceptualization of a large heterogeneous rock formation, using the data from the Horonobe Underground Research Laboratory in Japan during the ground-surface-based initial investigation phase.

2. HORONOBE SITE

The Japan Atomic Energy Agency (JAEA) is constructing an underground research laboratory (URL) in Horonobe Cho, Hokkaido (Figure 1), to study physical and chemical processes deep underground and to develop technologies that may be applied to future geologic disposal of high-level radioactive waste elsewhere in Japan (Ota et al., 2007). At the Horonobe URL, eleven deep boreholes (HDB-1 to HDB-11) have been drilled, with depths ranging from 470 m to 1020 m (Figure 2). After various investigations, loggings, and pressure tests were conducted, each borehole was isolated by packers into several intervals, and the pressure was monitored.

3. GEOHYDROLOGIC MODEL

Groundwater in the Horonobe area in general is expected to flow from the higher hills in the east to the Japan Sea in the west. Based on the information obtained from early boreholes, geologic, and geophysical surveys, Imai et al. (2002) constructed a hydrogeologic model of the Horonobe area. The original mesh of Imai et al.'s model was in a finite element model (FEM) format, which was converted to that of integrated finite difference (IFDM) for simulations using TOUGH2 (Pruess et al., 1999). Figure 3 shows the geohydrological model used for the simulations. Heads observed in the boreholes show an increase with depth, which can be caused by several sources, including the topography, geostatic load or gas generation. The initial version of the Imai et al. model shown in Figure 3 failed to reproduce the observed head data.

3.1 Static head inversion

Ito et al. (2004) attempted to assess whether the topography and permeability structure alone can explain the high heads at depth, by changing the input permeabilities. To match model predictions to observed data, modelers often employ a trial and error approach, in which forward model runs are repeated numerous times by adjusting input

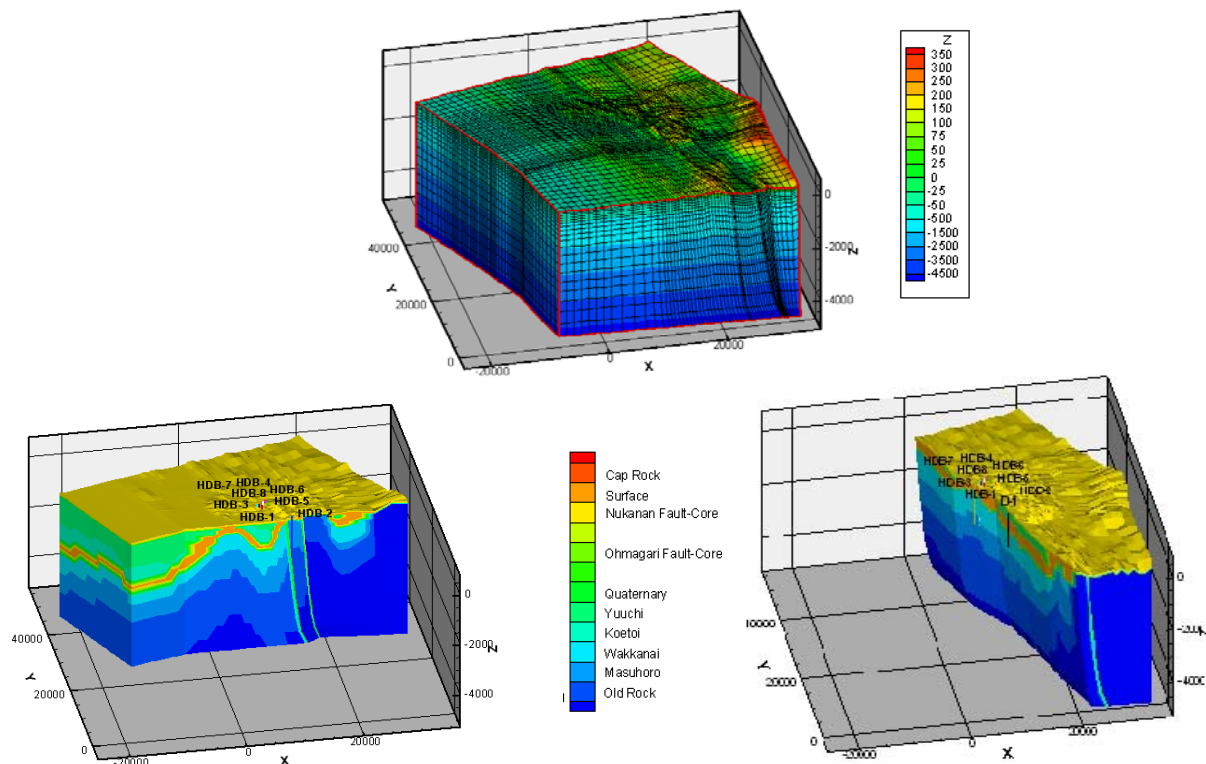


Figure 3. Numerical grid (top), EW (left) and NS (right) cross section of the geohydrological model of the Horonobe area showing the borehole locations, surface elevation (top plot), and geological formations (bottom plots). The model is 40km×40km×5km centered on the Horonobe URL area shown in Figure 2.

parameters. This approach is often useful, because it gives the modeler insights into which parameters are more important relative to one another. However, it is often very tedious and difficult to conduct in a systematic manner. Ito et al. (2004) used iTOUGH2 (Finsterle, 1998; 2008), which solves the inverse problem by automatically calibrating a TOUGH2 model against observed data.

By assuming the existence of a low-permeability cap rock, Ito et al. (2004) showed that the high heads at depth can be explained. They also examined the influence of fault properties on the observed data. In one model, the fault is assumed to have a sandwich structure, with a low-permeability core and high-permeability damaged zones on both sides. In another model, the fault was assumed to be a simple low-permeability structure (base case). The head at greater depth diverged between the two fault models

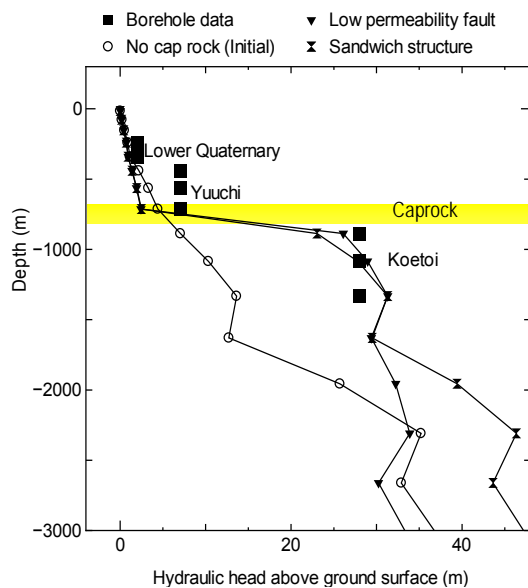


Figure 4. Head inversion results for two different structures of fault

(Figure 4). Because there were no data available from the depth, the results were inconclusive regarding the structure of the fault. Table 1 shows the calibrated values of permeabilities, which we call the base case.

3.2 Use of River Flow Data

One of the important but very difficult parameters to estimate for a geohydrologic model is the surface boundary condition. This is especially true when the model area is very large, i.e., several tens of square kilometers. One approach is to use river flow data, if there is a river that runs across the area of interest, preferably forming a basin. Ito et al. (2004) used the data from the Teshio River, which flows from east to west within the modeled area, to estimate the recharge rate, by taking the difference of the average monthly flow rate between two measurement locations that are approximately at the east and west end of the area.

Table 1. Permeability values of the base case

Geological Period	Epoch	Model Units	Hydraulic Conductivity (m/s)
		Surface	2.0E-06
Quaternary		Quaternary Sediments	1.0E-06
Neogene	Pliocene	Yuuchi F.	1.0E-07
		Low permeability zone	6.3E-11
	Miocene	Koetoi F.	1.0E-09
		Wakkanai F.	1.0E-10
		Masuhoro F.	5.0E-10
Cretaceous		Cretaceous rock	1.0E-11
Faults		Oomagari Fault core	1.0E-10
		Nukanan Fault core	1.0E-10

Figure 5 shows the calculated difference between the two locations for flow rates less than $50 \text{ m}^3/\text{s}$, which is assumed to be the maximum base flow rate. Based on the figure, the flow-rate difference is approximately $5 \text{ m}^3/\text{s}$, considered to be closely related to the recharge rate in the area. However, note that the variance is very large; thus, it should only be considered as approximate. The $5 \text{ m}^3/\text{s}$ recharge rate for the area translates to roughly $80 \text{ mm}/\text{year}$ of recharge for the entire area. Using data from much smaller sub-basins in the area, Kurikami et al. (2008) estimated the recharge rate to be from $64 \text{ mm}/\text{year}$ to $283 \text{ mm}/\text{year}$, or approximately from 5% to 20% of the annual average rainfall of $1,400 \text{ mm}/\text{year}$.

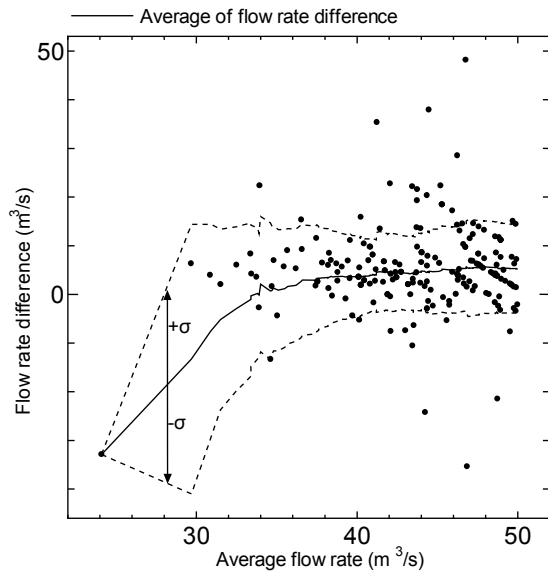


Figure 5. Flow-rate difference between two points of the Teshio River. Broken lines indicate one standard deviation.

The model calibrated to the measured heads described in the previous section calculates only 8 mm/year of recharge. Calibration to head values alone is only sensitive to the relative contrast (ratio) of the permeability of each layer and not to the absolute values of permeability. Therefore, permeability values can be multiplied by a constant value for all layers and still maintain the same goodness of fit for the steady-state head analysis.

3.3 Hot Spring Data

Adjacent to the north of Horonobe Town is Toyotomi Onsen, a hot spring (see Figure 2). Hot spring water has been produced since the 1920s from a depth of ~800–900 m. The water temperature is reportedly around 42°C (Toyotomi Onsen, 2009). We use TOUGH2 with the EOS3 module to simulate coupled heat and fluid flow. The bottom boundary condition is set at a constant heat flux of 20 mW/m² with no fluid flow. The top boundary condition is set at atmospheric pressure with 10°C, the annual average temperature of the area.

Figure 6 shows a comparison of the steady-state temperature profiles when the permeability of each layer in the model is multiplied by a constant value. Also shown in the figure is the approximate depth and temperature of the hot-water production zone for the hot spring (double-headed arrow). As can be seen from the figure, the case with ten to twenty times the permeability of the base-case model matches the temperature of the production zone best.

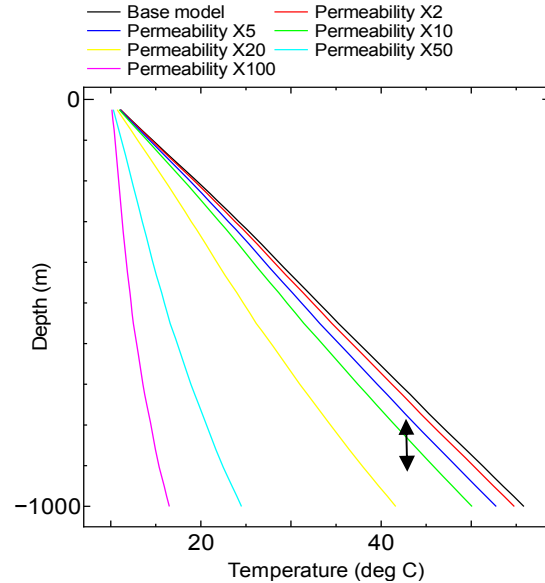


Figure 6. Modeled temperature profile at Toyotomi Hot Spring for various permeability multipliers. The arrow indicates approximate temperature and depth of the source of Toyotomi Hot Spring.

3.4 Use of Salinity Data

Salinity distribution in groundwater may yield some clues as to how the groundwater has evolved. High-salinity water is encountered at depths in HDB boreholes. It is believed that the study area was once under the sea before it rose to its present state. The land mass was initially saturated with saltwater, but as a result of rainfall, which recharges fresh water into the ground, the saltwater has been gradually washed out, particularly near the surface. We model the saltwater washout process by using TOUGH2 with the EOS7 module to simulate nonisothermal, density-driven, single-phase flow. As the initial condition for the salt concentration, we assume that the entire model is saturated with seawater (3.2% salt concentration). By setting the top boundary condition at atmospheric, recharge of fresh water takes place from the surface. The boundary conditions are much the same as in the previous case, with the strength and pattern of freshwater recharge a function of permeability and topography.

Figure 7 shows the simulation results after 2.5 Ma: (a) the case with 10 times larger permeability than the base case, and (b) the case in which the permeability of the fault zone is 100 times larger than the base case, while the rest of the permeabilities are kept the same as the base case. The latter still allows a similar amount of total recharge (~50 mm/year), but the flow is localized to the fault zone. The high-permeability fault model is consistent with the finding by Ishii et

al. (2006), who suggested deep intrusions of fresh water along the Omagari Fault based on the AMT (audio-frequency magnetotelluric) surveys.

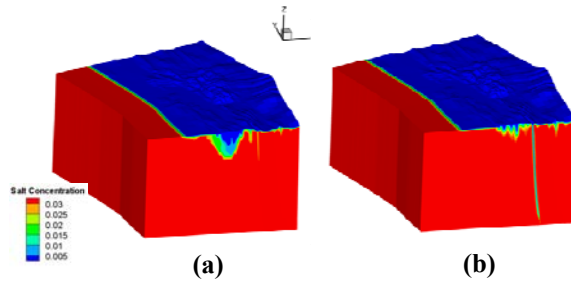


Figure 7. Salt concentration distribution after 2.5 Ma for the cases: (a) ten times the base case permeability, and (b) high permeability fault. Fresh water intrudes deeply along the faults.

Figure 8 shows a comparison of the salt concentration and the temperature data from HDB-1 with the simulation results. It should be noted that the data were collected shortly after the drilling and may not reflect true *in situ* conditions. The model with 10 times larger permeability than the base case matches reasonably well with the temperature data after 2.5 Ma, but does poorly against the salt concentration data. The permeability appears to be too large, and the freshwater washes out the salt too quickly. The high-permeability-fault case matches reasonably well with the temperature and salt concentration data. Note that 2.5 Ma is approximately the age of the study area.

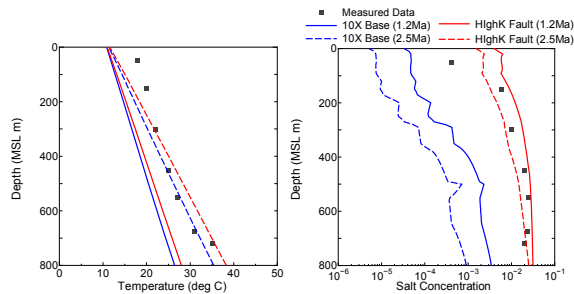


Figure 8. Saltwater washout simulation results. Markers denote measured data along HDB-1. Blue colored lines are for the case with 10 times the base permeability. Red lines are for the high permeability fault case.

4. FAULT ZONE CHARACTERIZATION

Geothermal gradients or temperature profiles are very sensitive to, and thus useful in, estimating water percolation fluxes in the subsurface (e.g., Wu et al.

2004; 2007). In particular, temperature profiles near a fault are often used to assess fault properties (Fairley and Hinds, 2004a, 2004b; Heffner and Fairley, 2006; Doan, 2007). Wu and Karasaki (2009) used the measured temperature data to estimate both flow rate and flow directions in two HDB boreholes at Horonobe (Figure 1). It is suspected that a fault or a set of faults exist at the Horonobe site, one of which is the Omagari Fault as shown in Figure 3. The HDB boreholes at the site are packed off into several monitoring intervals using packers. Pressure and temperature are monitored in each interval. Figure 9 shows the temperature profiles along the HDB boreholes. As the figure shows, the temperature profile along HDB-7 is different from that of other boreholes—slightly concave upward, generally indicating colder groundwater flowing downward. The other profiles are all concave downward, indicating that warm groundwater may be flowing upward.

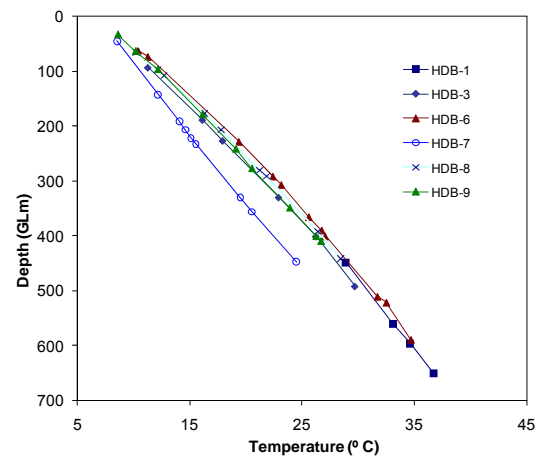


Figure 9. Temperature profile along HDB boreholes. The blue line is the temperature profile along HDB-7.

Wu and Karasaki (2009) used the TOUGH2 code with the modified EOS3 module to simulate nonisothermal flow of single-phase water with density dependence on mineral compositions, in addition to pressure and temperature in the two wells, HDB-7 and HDB-8. For each layer, the most recent permeability value based on borehole tests was used. The basic assumption was that the system is at steady-state conditions for water flow, solute transport, and heat flow. Aqueous mineral concentration distribution was assumed at steady state as a function of depth only for each well. The water density is correlated to mineral compositions by extrapolating and interpolating the measured

mineral compositional data from the two wells, and its dependence on pressure and temperature.

Figure 10 shows the simulated temperature profile. A downward flow of 3 mm/year matches the HDB-7 data, and an upward flow of 6 mm/year matches HDB-8 data. Note that the two wells, HDB-7 and HDB-8, are close to each other, with HDB-8 further inland. Head values in HDB-8 are ~10 m higher than those in HDB-7. Comparing the simulation results with the data indicates different flow directions, i.e., flow at HDB-8 is upwards (discharge) and flow at HDB-7 is downwards (recharge). This finding indicates a likely fault separating the two boreholes, with the fault behaving as a closed boundary or low-permeability barrier to flow across it. Figure 11 shows a conceptual model of groundwater flow crossing a fault zone. A similar model was proposed by Bense and Kooi (2004) for Peel Boundary Fault in The Netherlands. The Figure 11 model most likely applies to the Omagari Fault zone: upward flow along the damage zone east of the fault (HDB-8) and downward flow along the damage zone to the west

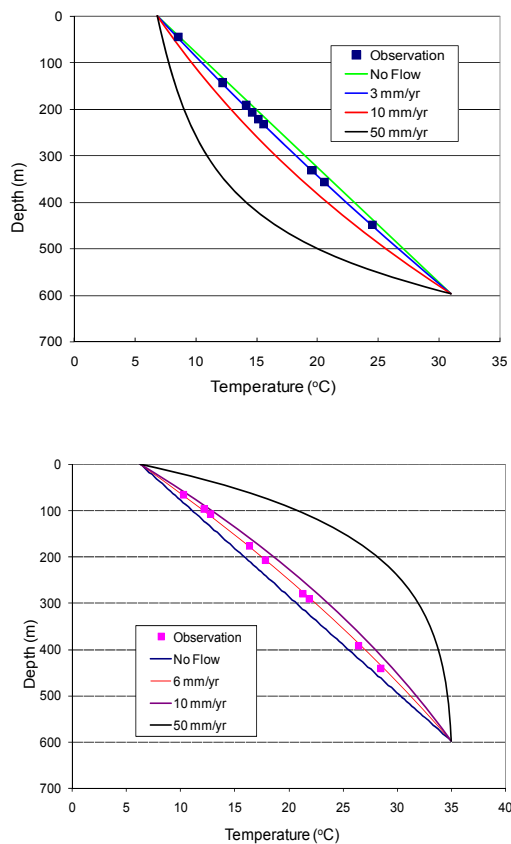


Figure 10. Simulated temperature profile along HDB-7(top) and HDB-8(bottom) for various downward (top) and upward (bottom) flow rates

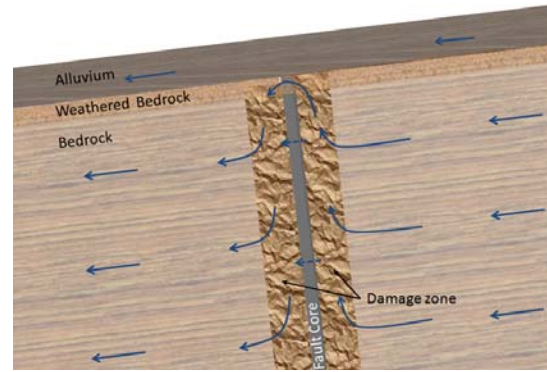


Figure 11. Conceptual model of fault zone flow

(HDB-7)—and overall higher head in HDB-8 than in HDB-7.

5. SUMMARY AND DISCUSSION

In this paper, we presented (through some examples) the use of information other than pressure data to constrain a geohydrologic model. The initial model was constructed using information on surface geology and from a limited number of boreholes. The inversion analysis of pressure implied the existence of a low-permeability cap rock. We then used river flow data and temperature data from a hot spring for estimating the recharge rate. The estimated recharge rate was ten times larger than the original model had calculated, which suggested that the overall permeability of the model may be one order of magnitude larger than that of the base model. Next, we simulated the saltwater washout process and compared it with salinity data from a borehole. We found that a better match to the salinity data is obtained if the increase in permeability were taken up by the fault zone rather than assigning larger permeability uniformly to the entire model. At a smaller scale, we conducted a 1D simulation and matched the temperature, pressure, and density profiles from two boreholes. We found that there may be a low-permeability fault in between the two boreholes. A conceptual flow model across a fault is proposed. Table 2 summarizes the model evolution.

Inclusion of additional processes in a geohydrologic model, such as heat and salt transport, requires additional parameters and may actually increase uncertainty. For example, heat-conductivity and heat-flux data are needed, in addition to the usual hydrologic parameters. Although the initial saltwater distribution is unknown, the model assumes that the rise and formation of the present-day Hokkaido Island happened instantaneously. However, when a model successfully matches temperature and salinity

data in addition to pressure data, the model may be deemed more reliable than a model constructed by simply extrapolating or upscaling small-scale observations. This is because pressure, temperature, and salinity data reflect the results of the natural averaging process that takes place at a large scale and over a long time duration. Thus, we believe that we now have more enhanced understanding of the large-scale geohydrologic processes at the Horonobe Site.

Table 2. Summary of geohydrologic model evolution

Section No.	Data Used (Additional)	Processes Modeled	Findings
3.1	Hydraulic head	Groundwater flow	Low permeability layer
3.2	River flow rate	Groundwater flow	Larger recharge rate
3.3	Hot spring data	Groundwater and heat flow	10× larger overall permeability
3.4	Fluid salinity, temperature profiles	Groundwater, brine, and heat flow	Localized fault zone permeability
4	Pressure, temperature, salinity profiles	Groundwater flow, heat, mineral composition	Flow direction and flux in fault zone

ACKNOWLEDGMENT

This work was supported by the Japan Atomic Energy Agency (JAEA) and performed under the US Department of Energy Contract #DE-AC02-05CH11231. The authors would like to thank Dr. Christine Doughty of LBNL and Dr. Kaname Miyahara of JAEA for their kind and constructive review.

REFERENCES

Bense, V. F. and H. Kooi, Temporal and spatial variations of shallow subsurface temperature as a record of lateral variations in groundwater flow, *Journal of Geophysical Research*, Vol. 109, B04103, doi:10.1029/2003JB002782, 2004.

Doan, M. L., and F. H. Cornet, Thermal anomaly near the Aigio fault, Gulf of Corinth, Greece, maybe due to convection below the fault, *Geophys. Res. Lett.*, 34, L06314, doi:10.1029/2006GL028931, 2007.

Fairley, Jerry P. and Jennifer J. Hinds, Field observation of fluid circulation patterns in a normal fault system, *Geophysical Research*

Letters, Vol. 31, L19502, doi:10.1029/2004GL020812, 2004a.

Fairley, Jerry P. and Jennifer J. Hinds, Rapid transport pathways for geothermal fluids in an active Great Basin fault zone, *Geology*, Vol. 32, No. 9, 825-828, 2004b.

Finsterle, S., <http://www-esd.lbl.gov/iTOUGH2>, 2008.

Finsterle, S., and J. Najita, (1998): Robust Estimation of Hydrogeologic Model Parameters, *Water Resources Research*, Vol.34(11), pp.2939-2947.

Heffner, James and Jerry Fairley, Using surface characteristics to infer the permeability structure of an active fault zone, *Sedimentary Geology* 184, 255–265, 2006.

Imai, H., N. Maeda, I. Shiozaki, K. Amamiya, and M. Chijimatsu, Groundwater flow analysis for the Horonobe Underground Rock Laboratory Project, JNC Report, JNC TJ1410 2002-004, 2002

Ishii, E., K. Yasue, T. Tanaka, R. Tsukuwi, K. Matsuo, K. Sugiyama, and S. Matsuo, Three-dimensional distribution and hydrogeological properties of the Omagari Fault in the Horonobe area, northern Hokkaido, Japan, *Journal of the Geological Society of Japan*, 112(5), 2006.

Ito, K., K. Karasaki, K. Hatanaka and M. Uchida, Hydrogeological Characterization of Sedimentary Rocks with Numerical Inversion using Vertical Hydraulic Head Distribution : An Application to Horonobe Site, *Journal of the Japan Society of Engineering Geology*, 45(3), 125-134, 2004.

Kurikami, H., R. Takeuchi and S. Yabuuchi, Scale effect and heterogeneity of hydraulic conductivity of sedimentary rocks at Horonobe URL site, *Physics and Chemistry of the Earth*, 33, 2008.

Kurikami, H., R. Takeuchi, S. Yabuuchi, S. Seno, G. Tomura, K. Shibano, M. Hara and T. Kunimaru, Hydrological investigations of surface-based investigation phase of Horonobe URL Project, *Journal of the Japan Society of Civil Engineers C*, 64(3), 2008.

Ota, K., H. Abe, T. Yamaguchi, T. Kunimaru, E. Ishii, H. Kurikami, G. Tomura, K. Shibano, K. Hama, H. Matsui, T. Niizato, K. Takahashi, S. Niunoya, H. Ohara, K. Asamori, H. Morioka, H. Fukai, N. Shigeta and T. Fukushima, Horonobe Underground Research Laboratory Project Synthesis of Phase I Investigations 2001 – 2005,

- Volume "Geoscientific Research", JAEA-Research 2007-044, 2007.
- Pruess, K., C. Oldenburg, G. and Moridis, TOUGH2 User's Guide, Version 2.0, LBL Report, LBNL-43134, 1999.
- Toyotomi Onsen, <http://www.toyotomi-onsen.com/index.php?itemid=2>, 2009
- Vasco, D. W., Karasaki, K. and Kishida, K., A coupled inversion of pressure and surface displacement, *Water Resour. Res.*, 37(12), 3071-3089, 2001.
- Vasco, D. W., Wicks, C., Karasaki, K. and Osni Marques, Geodetic imaging: High resolution reservoir monitoring using satellite interferometry, *Geophys. J. Int.*, 149, 555-571, 2002(a).
- Vasco, D. W., Karasaki, K. and Nakagome, O., Monitoring reservoir production using surface deformation at the Hijiori test site and the Okuaizu geothermal field, Japan, *Geothermics*, 31 (3), 303-342, 2002(b).
- Wu, Y. S., G. Lu, K. Zhang, and G. S. Bodvarsson, A Mountain-Scale Model for Characterizing Unsaturated flow and Transport in Fractured Tuffs of Yucca Mountain, LBNL-52524, *Vadose Zone Journal*, Vol. 3, pp.796-805, 2004.
- Wu, Y.-S., Guoping Lu, Keni Zhang, L. Pan, and G. S. Bodvarsson, Analyzing Unsaturated Flow Patterns in Fractured Rock Using an Integrated Modeling Approach, LBNL-54006, *Hydrogeology Journal*, Vol. 15, pp.553-572, 2007.
- Wu, Y.S. and K. Karasaki, Conceptualization and Modeling of Flow and Transport Through Fault Zones, SPE 122456, in proceedings, 2009 SPE Latin American and Caribbean Petroleum Engineering Conference, Cartagena, Colombia, 31 May-3 June 2009.
- Yamasaki, S., H. Matsui, K. Hama, H. Morioka, K. Hatanaka, and T. Fukushima, International Workshop on Horonobe Underground Research Laboratory Project, JNC TN5400 2004-004, 2004.

A NUMERICAL STUDY OF MICROSCALE FLOW BEHAVIOR IN TIGHT GAS AND SHALE GAS RESERVOIR SYSTEMS

C.M. Freeman, G.J. Moridis, T.A. Blasingame

Dept. of Petroleum Eng/Texas A&M University
3116 TAMU
College Station, TX, 77845-3116, U.S.A.
e-mail: matt.freeman@pe.tamu.edu

ABSTRACT

Various attempts have been made to model flow in tight gas and shale gas systems. However, there is currently little consensus regarding the impact of molecular diffusion on flow behavior over time in such systems.

The composition of gas produced from tight gas and shale gas reservoirs varies with time. The main driver behind this phenomenon is the selective desorption of gases from the surface of the kerogen in the case of shale.

However, a secondary but important driver is the fractionating effect of the reservoir rock itself. Pore throat diameters on the order of molecular mean free path lengths will create an exaggerated slip-flow-like condition. When this condition prevails, Darcy's law can no longer be used without adjustment. Florence et al. (2007) proposed a 'microflow' model for effective permeability correction that correctly represents flow in the Knudsen and transitional flow regimes.

In this study, we implement the microflow model into a fluid flow modeling tool based on the TOUGH+ family of codes. We examine the behavior of the microflow correction on gas composition in ultra-tight rock. We show that for very small average pore throat diameters, lighter gases are preferentially produced at concentrations as high as double what would otherwise be expected.

Our contributions include a new, fit-for-purpose numerical model, based on the TOUGH+ code, capable of characterizing flow behavior in hydraulically fractured horizontal wells. This model includes a demonstration of a "microflow" model for fluid flow in micro- and nanoscale porous media.

INTRODUCTION

Background

The composition of gas produced from wells in ultra-tight gas reservoirs varies with time. In shale gas reservoirs possessing high organic content, the

gradual change in produced gas composition is attributed to preferential desorption of different gas species at different rates. For example, carbon dioxide will desorb from kerogen more readily than methane, so at earlier times the concentration of carbon dioxide in the produced gas will be higher, and will gradually taper off (Gao et al., 1994).

However, this is not the only explanation for the change in gas composition. Shale gas and tight gas reservoirs can possess a high degree of heterogeneity and widely varying porosity distributions. The kerogen content in shale can be considered to provide an entirely separate porosity system (Clarkson et al., 1999).

The pore throat dimensions of these porosity systems can vary widely, potentially ranging from 10 nm to 50 μm . The distribution of pore throat sizes will vary reservoir by reservoir.

According to the theory of gas kinetics, the mean free path is defined as the mean distance a molecule in a gas will travel before interacting with another gas molecule. When the mean free path is comparable to the pore throat size, a continuum flow assumption is no longer fully valid, and Darcy's law cannot be used without modification.

The ratio of the mean free path over the feature length, in this case the pore throat diameter, is expressed as the Knudsen number,

$$K_n = \frac{\lambda}{L_{char}} \dots\dots\dots(1)$$

For Knudsen numbers less than 0.001, Darcy's law remains valid. For Knudsen numbers more than this value, an effective permeability must be computed that corrects for the "microflow" effect.

In this work, we implement the "microflow" model proposed by Florence et al. (2007) into a numerical model based on the TOUGH+ family of reservoir simulators to examine the effect of microflow phenomena on multicomponent gas flow.

Mathematical Development

The flow regime of Knudsen flow, similar to the idea of gas slippage, occurs when the mean free path of the gas molecules is on the order of the average pore throat radii. The mean free path of a molecule in a single-component gas can be computed by

$$\bar{\lambda}(\bar{p}, T) = \sqrt{\pi/2} \frac{1}{\bar{p}} \mu \sqrt{\frac{RT}{M}} \dots\dots\dots(2)$$

Figure 1 demonstrates the effect of pressure on mean free path for various gases.

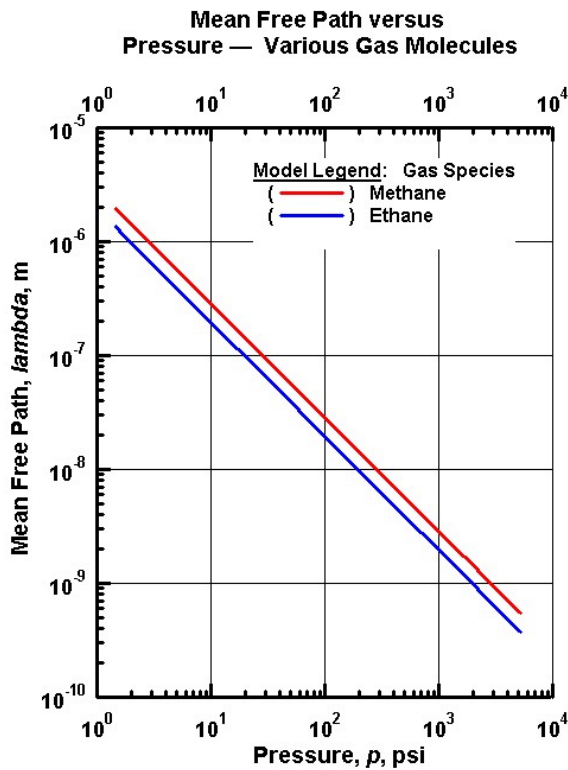


Figure 1. Effect of pressure on mean free path of various gases.

This is how the mean velocity of the molecule is computed. The mean free path of a molecule in a single-component gas is conceptually the ratio of the distance traveled divided by the volume of interaction,

$$\bar{\lambda} = \frac{\text{distance traveled}}{\text{volume of interaction}} = \frac{\bar{v}t}{\pi d^2 \bar{v} t n_v} \dots\dots(3)$$

However, this method of computing the mean free path leaves out the important consequences of gas

mixtures. The average velocity of a molecule in a gas is

$$\bar{v} = \sqrt{\frac{8RT}{\pi M}} \dots\dots\dots(4)$$

The use of a single average velocity is inappropriate for a gas mixture, where each species in the gas possesses a different average velocity as a function of molar mass. Therefore, we must compute the average velocity of a gas molecule in a gas mixture.

The relative velocity between two gas particles is expressed as

$$v_{rel} = \sqrt{\bar{v}_{rel} \cdot \bar{v}_{rel}} \dots\dots\dots(5)$$

where

$$\bar{v}_{rel} = \bar{v}_1 - \bar{v}_2 \dots\dots\dots(6)$$

So, taking the magnitude of the relative velocity vector,

$$v_{rel} = \sqrt{(\bar{v}_1 - \bar{v}_2) \cdot (\bar{v}_1 - \bar{v}_2)} \dots\dots\dots(7)$$

algebraically rearranged,

$$v_{rel} = \sqrt{\bar{v}_1 \cdot \bar{v}_1 - 2\bar{v}_1 \cdot \bar{v}_2 + \bar{v}_2 \cdot \bar{v}_2} \dots\dots\dots(8)$$

Since we are not truly examining individual molecules but rather the average properties of the statistical ensemble of the gas, we take the averages of the terms:

$$\overline{v_{rel}} = \sqrt{\overline{\bar{v}_1 \cdot \bar{v}_1} - 2\overline{\bar{v}_1 \cdot \bar{v}_2} + \overline{\bar{v}_2 \cdot \bar{v}_2}} \dots\dots\dots(9)$$

Since \bar{v}_1 and \bar{v}_2 (the average velocity vectors for two different gas particles) are random and uncorrelated, their dot product equals zero. Thus, the formula for average velocity reduces to simply

$$\overline{v_{rel}} = \sqrt{\overline{v_1^2} + \overline{v_2^2}} \dots\dots\dots(10)$$

where the average velocities of the two species are in fact different, computed from Equation (4).

For one gas species in a multicomponent gas mixture, the “volume of interaction” term of the expression is modified to

$$\bar{\lambda}_1 = \frac{\bar{v}_1}{\sum_{i=1,n} \pi d_1 d_i \sqrt{v_1^{-2} + v_i^{-2}} n_{vi}} \dots\dots\dots(11)$$

The n_{vi} term can be modified by a perfect gas law approximation,

$$\bar{\lambda}_1 = \frac{\bar{v}_1}{\sum_{i=1,n} \pi d_1 d_i \sqrt{v_1^{-2} + v_i^{-2}} \frac{N_A P_i}{RT}} \dots\dots\dots(12)$$

Rather than relying on a perfect gas assumption, we can use the more accurate density computation for density of a gas from an equation of state already intrinsic to our numerical implementation,

$$\bar{\lambda}_1 = \frac{\bar{v}_1}{\sum_{i=1,n} \pi d_1 d_i \sqrt{v_1^{-2} + v_i^{-2}} \frac{N_A \rho X_i}{M_i}} \dots\dots\dots(13)$$

We now have a method by which to characterize the mean free path of a single gas species in the multicomponent gas within our system. Thus, we can now examine the ramifications of different mean free paths on gas flow in porous media with microscale features. The dimensionless Knudsen number will identify the severity of the non-Darcy “slippage” effect.

$$K_n = \frac{\bar{\lambda}}{L_{char}} \dots\dots\dots(14)$$

For Knudsen numbers smaller than 0.01, the assumption of “continuum flow” is valid and Darcy’s law can be used unmodified. Knudsen numbers in the realm of 0.1 qualify as slip flow and can be characterized by the Klinkenberg correction to acceptable accuracy. Kn of around 1.0 qualify as transitional flow, which is less strongly characterized by the Klinkenberg correction, and Kn greater than 10 exhibit free molecular flow, which is dominated by diffusion effects (i.e., any parameterization by “viscosity” and “permeability” no longer has a meaningful physical interpretation). Figure 2 shows the impact of pressure on Knudsen number for various pore throat sizes.

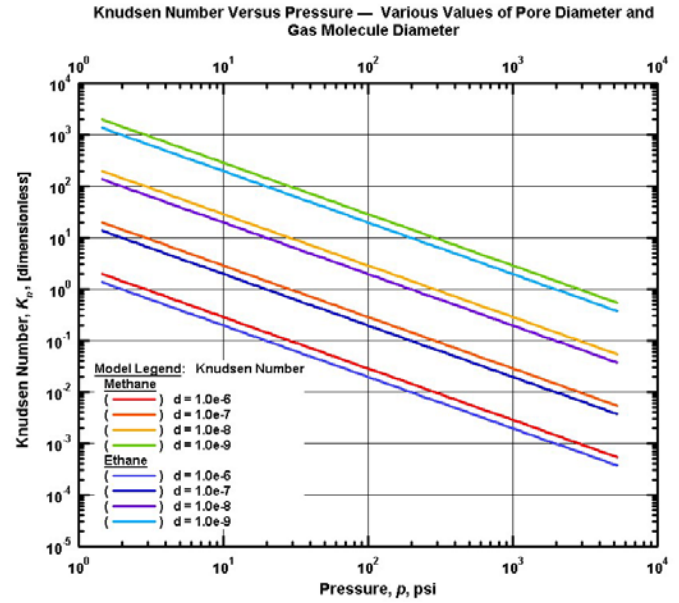


Figure 2. Effect of pressure on Knudsen number for various pore throat sizes and gases

In fact, it is likely that flow through shale will exhibit all of the above regimes and Knudsen numbers.

Klinkenberg demonstrated the approximately linear relationship between measured permeability and inverse pressure:

$$k_a = k_\infty \left[1 + \frac{b_K}{p} \right] \dots\dots\dots(15)$$

The gas slippage factor is regarded as constant in the flow regime where the Klinkenberg approximation is valid, and is related to the mean free path

$$\frac{b_K}{p} = \frac{4c\lambda}{r} \dots\dots\dots(16)$$

This gas slippage factor is related to the beta term via

$$b_K = \beta \left[\frac{k_\infty}{\phi} \right]^{-0.5} \dots\dots\dots(17)$$

While this beta-form of the Klinkenberg approximation is simple and convenient for the purposes of numerical simulation due to its computational simplicity, a more robust, rigorously developed “microflow” model has been proposed by Florence, et al. (2007), which is valid for all flow regimes in porous media, from free-molecular flow through continuum flow, though not verified and probably invalid in high-rate inertial (Forchheimer)

flow regimes. The basis of this model is to adjust the theoretical permeability to an “effective” permeability through use of the Knudsen number:

$$k_a = k_\infty \left[1 + \alpha(Kn)Kn \right] \left[1 + \frac{4Kn}{1 + Kn} \right] \dots\dots\dots(18)$$

The function α is a rarefaction coefficient parameter, a dimensionless adjustment parameter of the form

$$\alpha(Kn) = \alpha_0 \frac{2}{\pi} \tan^{-1} [c_1 Kn^{c_2}] \dots\dots\dots(19)$$

This formula, Equation (18), will vary the “effective” permeability experienced by each individual gas species, due to the fact that each gas species in the mixture will have a different mean free path and thus a different Knudsen number. Implementation of this theory will enable modeling of the “fractionating” effect of reservoirs with extremely small pores, wherein smaller molecules flow preferentially faster than larger ones. Figure 3 shows the impact of various pore throat dimensions on adjusted permeability for various gases.

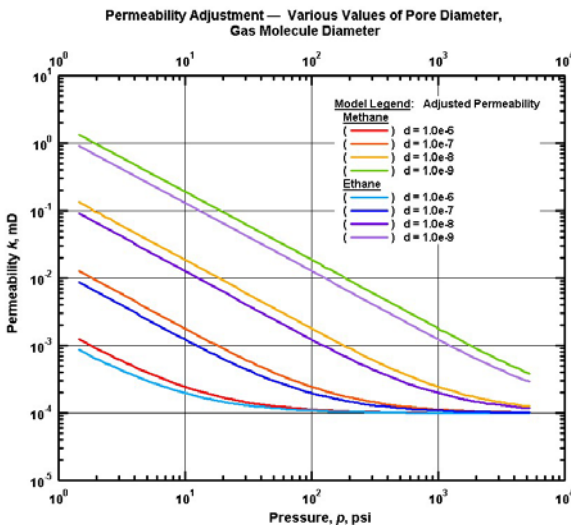


Figure 3. Effect of various pore throat dimensions on adjusted permeability for various gases at varying pressure

MODEL DESCRIPTION

The vast majority of shale gas and tight gas wells are stimulated via hydraulic fracturing. Typical completion strategies for these reservoirs involve either a vertical well with a vertical bi-wing hydraulic fracture, or a horizontal well with multiple transverse hydraulic fractures. At early times, the flow character is dominated by linear inflow into the fractures. Gradually, the flow regime passes through transition stages into an elliptical flow regime. To capture the character of the early and late end-member behaviors, linear grids and radial grids are employed.

A Peng-Robinson equation of state is used to model the gas density as a function of pressure. Gas viscosity is modeled by the Chung et al. (1988) method. Isothermal conditions are assumed because with a very low flow rate of gas, the effect of Joule-Thompson cooling will be minimal.

For all cases, flow from a fracture face was simulated for a period of 2 days through 1 μ D rock. The molar initial composition of each gas component is equal, i.e., all molar gas compositions are initially one-third. The initial reservoir pressure was 145 psia, and the fracture-face pressure was 14 psia. Porosity is 10%. A sensitivity analysis was performed on the pore throat radius.

Table 1. Sensitivity parameters.

	Initial Reservoir Pressure (psia)	Fracture Face Pressure (psia)	Pore Throat Radius (m)
Case 1	145	14.5	5.00E-06
Case 2	145	14.5	5.00E-07
Case 3	145	14.5	5.00E-08
Case 4	145	14.5	5.00E-09

RESULTS

The pressure transient progresses less than 0.8 meters in any given case, as shown via the purple line in Figure 4. According to these sensitivities, the gas deviation from the expected (initial) gas composition is plotted in Figure 4.

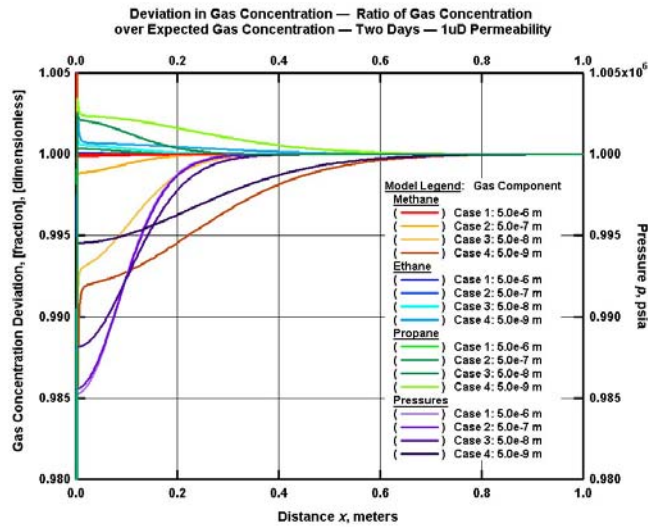


Figure 4. Results of sensitivity analysis; deviation of gas composition from initial gas composition, with pressure transient

These results satisfy our expectation that methane will flow more quickly than propane and ethane with decreasing pore throat diameter. In the 10 nm pore throat diameter case (corresponding to a pore radius of 5.0e-9m), the methane composition at the fracture face is 1% less than expected, since this region has already been evacuated of methane while the relative concentration of ethane and propane remains high.

The shape of the pressure transient is strongly impacted and somewhat distorted by the small pore throat effects. This nonlinearity presents obstacles to numerical convergence. Furthermore, this sharper pressure transient and may explain the sharp decline in production rate seen at early times in ultratight gas reservoirs.

Through the short duration of production simulated, the gas composition in the produced gas stream remains relatively constant in a given case. The simulation time in these cases has not progressed long enough to demonstrate a strong change in gas concentrations over time in a given case. However, between cases, the composition of the produced gas varies dramatically. Figure 5 shows the variation of gas composition in the gas produced from each of the sensitivity cases.

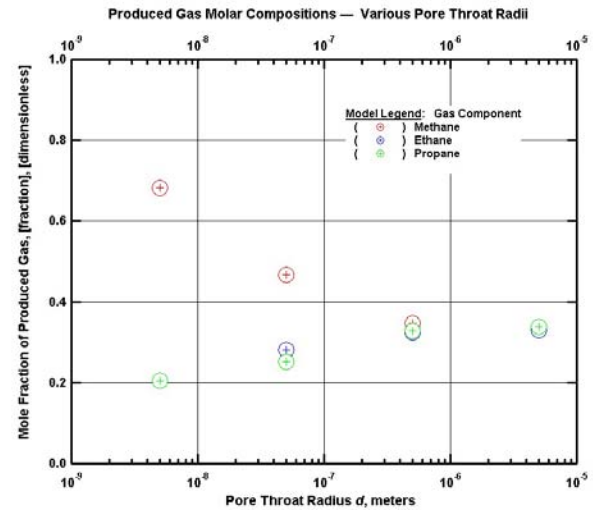


Figure 5. Variation of produced gas mole fraction with pore throat radius

With the very small pore throat sizes, the composition of methane in the produced gas stream is as high as 68% by mole, despite the fact that only 33% by mole of the gas in the pores is methane. If this concept is scaled up to examine reservoir-scale behavior, it becomes clear why only methane is produced from ultratight reservoirs—the other gas species are left behind.

CONCLUSIONS

Decreasing pore throat size is shown to accelerate production of lighter, smaller gases at the expense of heavier ones. Pore throats of 10 nm diameter cause the produced gas to contain more than twice the concentration of methane than would be expected without microflow adjustment.

The lighter gases are shown to deplete from the near-fracture region more quickly than heavier gas species. Correspondingly, the rate and degree of propagation of the pressure transient into the reservoir is increased by the microflow adjustment caused by smaller pore throats.

Implementation of the microflow permeability adjustment model into a robust fluid flow modeling tool demonstrates (a) promise for future work in predicting compositional change with time in ultratight reservoirs and (b) potential utility in sampling changes in gas composition with time in these reservoirs, in order to better characterize the rock properties.

This model provides a strong basis for future work, such as to incorporate a desorption model and simultaneously model multicomponent desorption and multicomponent microflow-adjusted gas flow.

SYMBOLS AND ABBREVIATIONS

$\bar{\lambda}$	mean free path
\bar{p}	average pressure
T	temperature
μ	viscosity
R	ideal gas constant
\bar{M}	molecular mass of gas molecule
\bar{v}	mean velocity of a molecule in a gas
d	effective molecule diameter
t	time of flight
n_v	number of molecules per unit volume
v_1	the average v_{rms} of component number 1
$\bar{\lambda}_1$	the mean free path of component number 1
\bar{v}_i	the average v_{rms} of the i th component
d_i	the molecular diameter of the i th component
N_A	Avogadro's number, 6.02e23
X_i	mass fraction of component i in the gas mixture
ρ	total density of the gas mixture
ρ_i	partial density of the gas mixture
n	the total number of present gas components
i	the gas component index
K_n	Knudsen number
L_{char}	characteristic length of flow geometry (average pore throat diameter)
k_∞	permeability to liquid
k_a	measured permeability
b_K	gas slippage factor
c	approximately 1
r	effective pore radius
α	rarefaction coefficient parameter, dimensionless
c_1	a constant valued at 4.0
c_2	a constant valued at 0.4
α_0	a constant valued at $\frac{64}{15\pi}$

ACKNOWLEDGMENT

This work was supported by RPSEA (Contract No. 07122-23) through the Ultra-Deepwater and Unconventional Natural Gas and Other Petroleum Resources Research and Development Program as authorized by the US Energy Policy Act (EPA) of 2005. The authors are indebted to Dan Hawkes for his careful review.

REFERENCES

- Chung, T.H., Ajlan, M., Lee, L.L., and Starling, K.E., Generalized Multiparameter Correlation for Nonpolar and Polar Fluid Transport-Properties, *Industrial & Engineering Chemistry Research* 27, 671-679, 1988.
- Clarkson, C.R. and Bustin, R.M., Binary gas adsorption/desorption isotherms: effect of moisture and coal composition upon carbon dioxide selectivity over methane. *International J. of Coal Geology*. 42(2000) 241-271, 1999.
- Florence, F.A., Rushing, J.A., Newsham, K.E., and Blasingame, T.A., Improved Permeability Prediction Relations for Low-Permeability Sands. SPE paper presented at the SPE Rocky Mountain Oil & Gas Technology Symposium held in Denver, Colorado, 16-18 April 2007.
- Gao, C., Lee, J.W., Spivey, J.P., and Semmelbeck, M.E., Modeling Multilayer Gas Reservoirs Including Sorption Effects. SPE paper 29173 presented at the SPE Eastern Regional Conference & Exhibition, Charleston, West Virginia, 8-10 November 1994.
- Hill, D.G., and Nelson, C.R., Gas Productive Fractured Shales: An Overview and Update. *Gas TIPS* 6 (3): 4-13, 2000.
- Javadpour, F., Fisher, D., and Unsworth, M., Nanoscale Gas Flow in Shale Gas Sediments. *JCPT*. 46 (10): 55-61, 2007.
- Mattar, L., Gault, B., Morad, K., Clarkson, C.R., Freeman, C.M., Ilk, D., and Blasingame, T.A., Production Analysis and Forecasting of Shale Gas Reservoirs: Case History-Based Approach. SPE paper 119897 presented at the SPE Shale Gas Production Conference, Fort Worth, TX, 16-18 Nov. 2008.
- Medeiros, F., Ozkan, E., and Kazemi, H., Productivity and Drainage Area of Fractured Horizontal Wells in Tight Gas Reservoirs. SPE paper 108110 presented at the Rocky Mountain Oil & Gas Technology Symposium held in Denver, Colorado, 16-18 April 2007.
- Medeiros, F., Ozkan, E., and Kazemi, H., A Semianalytical, Pressure-Transient Model for Horizontal and Multilateral Wells in Composite, Layered, and Compartmentalized Reservoirs. SPE paper 102834 presented at the SPE Annual Technical Conference and Exhibition held in San Antonio, Texas, 24-27 September 2006.
- Raghavan, R.S., Chen, C., and Agarwal, B., An Analysis of Horizontal Wells Intercepted by Multiple Fractures. SPE paper 27652 presented at the SPE Permian Basin Oil and Gas Recovery

Conference held in Midland, Texas, 16-18 March 1997.

Schettler, P.D., and Parmely, C.R., Contributions to Total Storage Capacity in Devonian Shales. SPE paper 23422 presented at the SPE Eastern Regional Meeting held in Lexington, Kentucky, 22-25 October 1991.

EVALUATING MODEL PREDICTIONS AND CHARACTERIZATION METHODS APPLIED TO THE DEEP VADOSE ZONE AT SAN GORGONIO PASS, CALIFORNIA: LESSONS LEARNED AFTER 5 YEARS OF ARTIFICIAL RECHARGE

Alan L. Flint¹, Kevin M. Ellett¹, Allen H. Christensen², and Peter Martin²

U.S. Geological Survey, Water Resources Discipline
¹Placer Hall, 6000 J St., Sacramento, CA 95819 USA
²4165 Spruance Rd., San Diego, CA 92101-0812 USA
e-mail: aflint@usgs.gov

ABSTRACT

Over a five-year period (2003–2007), water from the California State Water Project was applied at a selected site through surface spreading in an attempt to recharge the underlying aquifer in the San Gorgonio Pass area in southern California. Prior to long-term application of water, a study was conducted (1997–2003) by the U.S. Geological Survey to determine the suitability of the site for artificial recharge. The hydrogeology of the unsaturated zone was characterized and conceptualized by integrating results from surface geophysics, borehole instrumentation, and laboratory analyses of core and cuttings. In 2004, a modeling study was published that predicted artificial recharge would not occur in the aquifer for more than 5 years, due to the existence of a perching layer that would impede the downward flow of water, causing lateral flow and loss of water downgradient to a permeable fault system at the model boundary. Continuous monitoring of the water level in the perched zone showed rising and falling water levels corresponding to increases and decreases of surface-applied water. Near-continuous monitoring of the water level at the water table showed a water table rise at between 3.75 years and 4.5 years since the initiation of surface application of water. Using the known application rate, the rise and fall of the water level at the perched layer and the approximate arrival time to the water table, the hydrologic properties in the existing 3D TOUGH2 model were modified to best match the new data. The only required changes were to increase the permeability of the perching layer by about 60%, and add a specific gravel layer above the perching layer to limit the rise of the perched water observed in the field data. The resultant increase in permeability reduced the overall flow of water downgradient from the original model, so that all applied water recharged the aquifer within the modeling domain.

INTRODUCTION

Artificial recharge using water from the California State Water Project by surface spreading is being applied in the San Gorgonio Pass area of southern California, which is about 137 km east of Los Angeles (Figure 1). In the early 1990s, the San

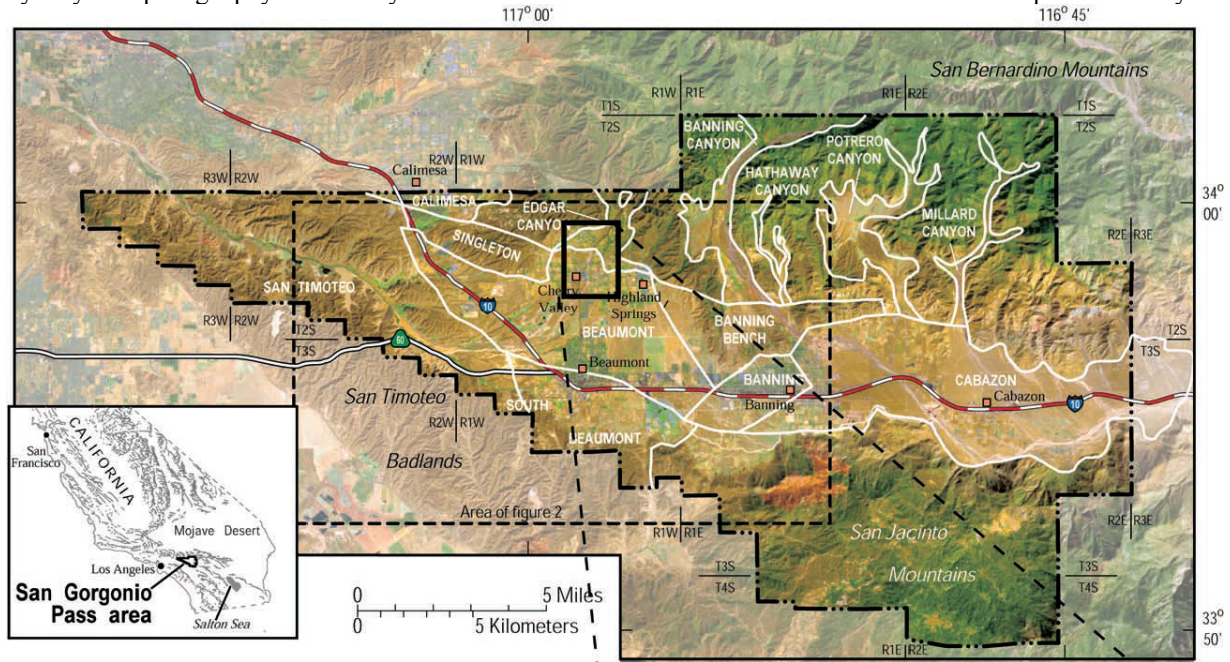
Gorgonio Pass Water Agency (SGPWA) constructed spreading ponds near Little San Gorgonio Creek (Figure 1, inset) for the purpose of recharging the underlying aquifer using water from the California State Water Project. By 1995, the SGPWA had conducted its first feasibility study by applying local water for 50 days to determine infiltration rates and percolation rates through the unsaturated zone (Boyle Engineering Corporation, 1992; Shaikh, 1995). Prior to long-term application of water, a study was conducted (1997–2003) by the U.S. Geological Survey in cooperation with SGPWA to determine the suitability of the site for artificial recharge (Flint and Ellett, 2004). Since 2003, water from the California State Water Project has been applied at the site at various rates to recharge the underlying aquifer. (This report uses data from November 2002, when a small prewetting experiment was conducted, through December, 2007.)

The hydrogeology of the area has been described in previous studies by Bloyd (1971), Boyle Engineering Corporation (1990, 1992, 1993a, 1993b), and Rewis, and others (2005). The site is bound to the north by the Banning fault and to the south by the Cherry Valley fault zone (Figure 2). Underlying the site is a series of Quaternary alluvium layers dipping 5 degrees to the south, with a restrictive zone at approximately 70 m that perches water from natural recharge occurring under Little San Gorgonio Creek (Figure 1, inset). The regional water table is ~185 m deep. Alluvial deposits that comprise the unsaturated zone underlying the spreading basins include younger surficial deposits (Qy), older surficial deposits (Qo), very old surficial deposits (Qvo), and the upper member of the San Timoteo beds (Qsu) (Figure 2). In general, the surficial sedimentary materials (Qy, Qo, and Qvo) within the study area consist of interlayered sand and gravel deposits, with intermittent layers of clay, silt, and fine sand that become more compacted with depth. Unit Qsu consists of sand and gravel layers that are locally cemented into beds of sandstone and conglomerate.

In the original modeling study of Flint and Ellett (2004), the unsaturated zone hydrogeologic system was characterized and conceptualized by integrating results from surface geophysics, borehole

instrumentation, and laboratory analyses of core and cuttings samples. Details of the integrated approach are provided in Ellett (2002) and are mentioned only briefly here. In addition to characterization, this approach was designed to allow an efficient transition to monitoring the effects of artificial recharge (AR) by way of repeat geophysical surveys and continuous

observations from the borehole instrumentation. Repeat geophysical surveys are ongoing and are still being analyzed to determine whether they are clearly effective in resolving changes in subsurface water storage. The focus of this paper is to evaluate the long-term performance of the borehole instrumentation collected subsequent to analysis by



EXPLANATION

- Study area boundary
 - San Gorgonio Pass Water Agency boundary
 - Approximate storage unit boundary*
 - BEAUMONT**
□ Name of storage unit
 - Banning**
□ Town or community and name
- *Adapted from the USGS Water-Supply Paper 1999-D



Figure 1. Landsat image of the San Gorgonio Pass Water Agency boundary area. Delineations of ground water storage unites are defined by Bloyd (1971). The area used for artificial recharge (satellite photograph show in inset) lies along the northern boundary of the Beaumont storage unit near Edgar Canyon.

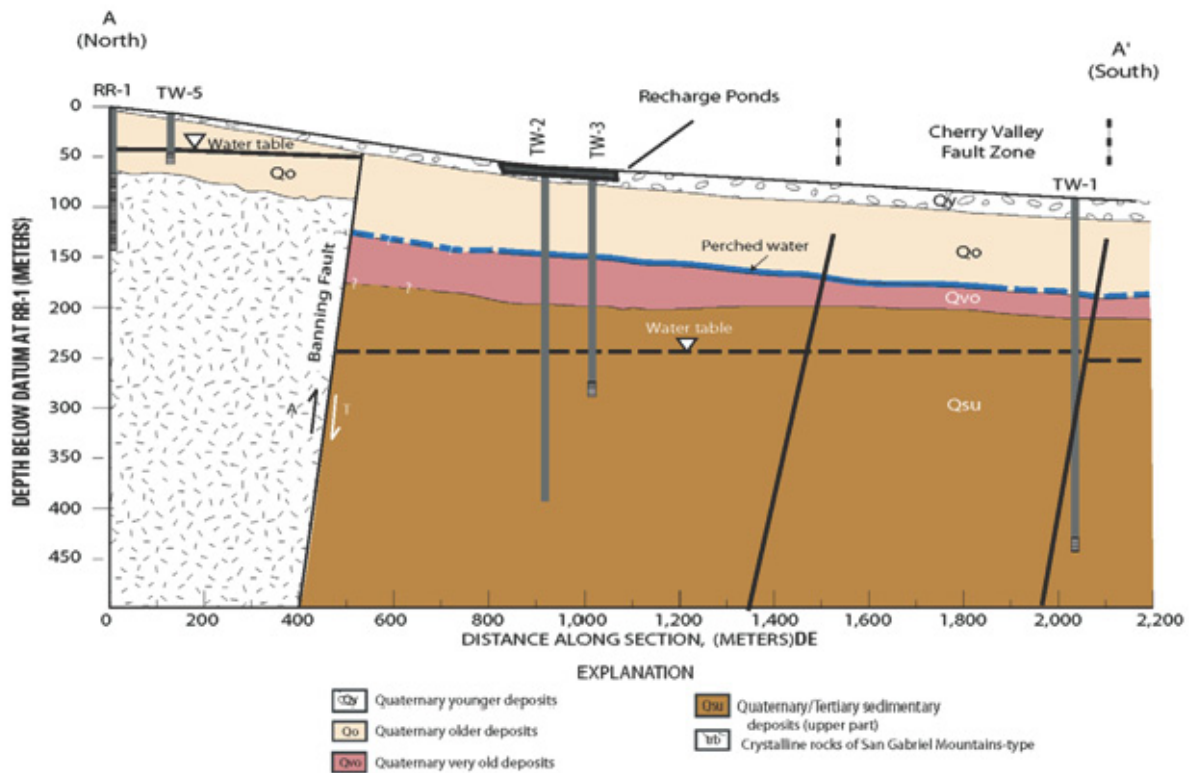


Figure 2. Conceptual cross section of the layered stratigraphy, a fault, and the relative location of the cross-section (A-A', Fig. 1) and near-surface recharge ponds to features of the San Geronio Pass area, California.

Ellett (2002) and update our analysis of the observations to assess the performance of the original unsaturated zone model of Flint and Ellett (2004) in predicting the effects of artificial recharge.

EVALUATION OF THE CHARACTERIZATION AND MONITORING APPROACH

Borehole instrumentation at two locations proved particularly useful in this analysis: Test Well #3, located directly at the spreading pond area; and Test Well #5, located near the channel of Little San Geronio Creek north of the Banning Fault (Fig. 1 and 2). Test Well #3 provides observations on changes in soil-matric potential and temperature below the spreading ponds (Figure 3; Pond 1 at the bottom through Pond 5 at the top of the figure) using heat dissipation probes (HDP; Flint and others, 2002) and advanced tensiometers (AT; Hubbell and Sisson, 1998). Test Well #5 yields data on natural recharge derived from ephemeral stream flow in Little San Geronio Creek. Figure 4a-d shows the time series of soil-matric potential, and Figure 5 shows temperature from select depths, both at Test Well #3. Measurements from AT have proven to be reliable and robust over the 9 years of



Figure 3. Satellite image of the San Geronio Pass Water Agency ponds being recharged. TW3 is just above and left of the lowest pond.

continuous operation (gaps in data sometimes occurred from loss of data logger power). Some HDP heating elements have failed, however, leading to loss of soil-matric potential measurements at various depths over time. Despite problems with some of

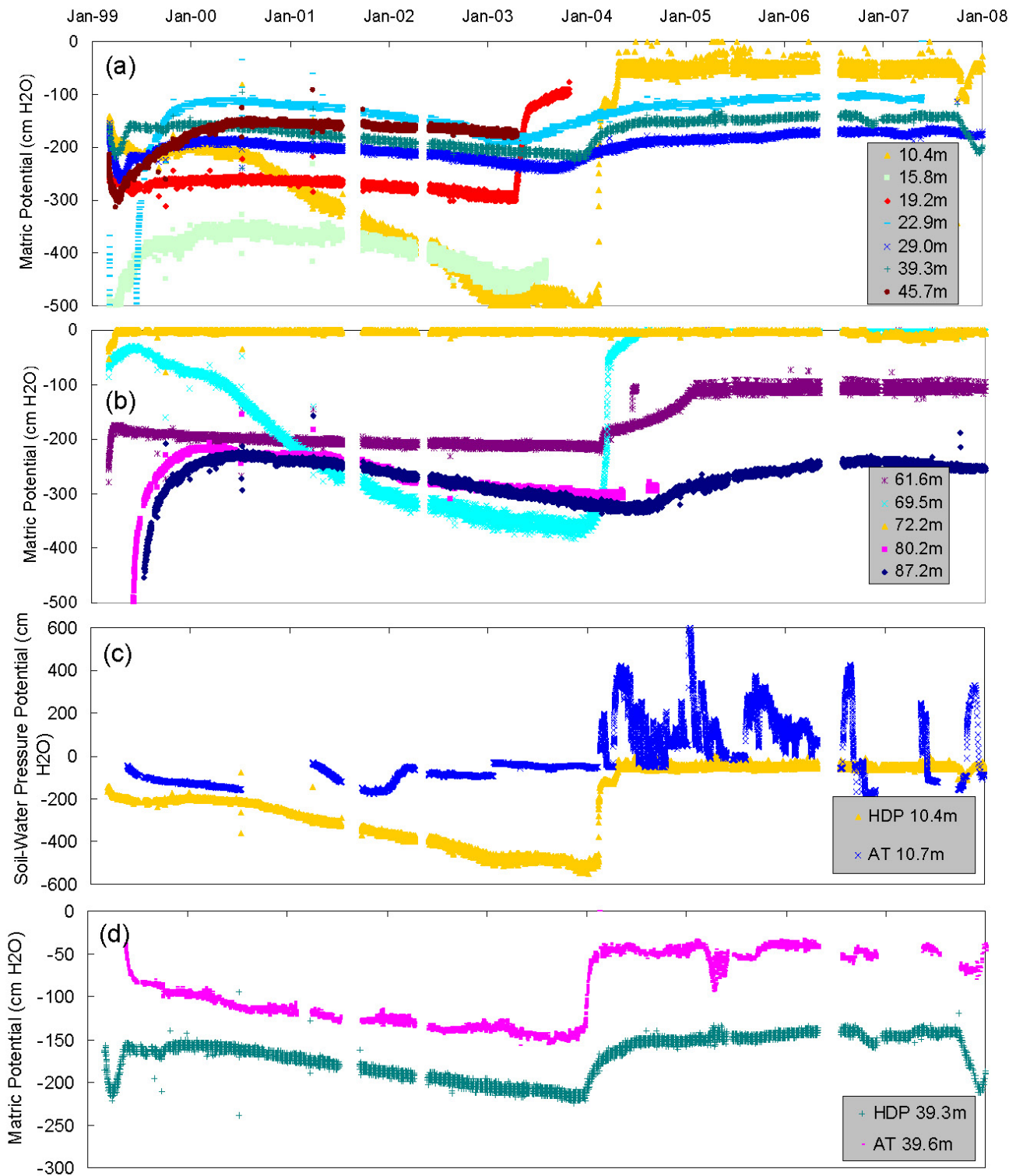


Figure 4. Measurements from borehole instrumentation at Test Well #3. Soil-water potential from HDPs at (a) shallower depths and (b) deeper depths, and comparison of HDPs and ATs at (c) shallower depths and (d) deeper depths.

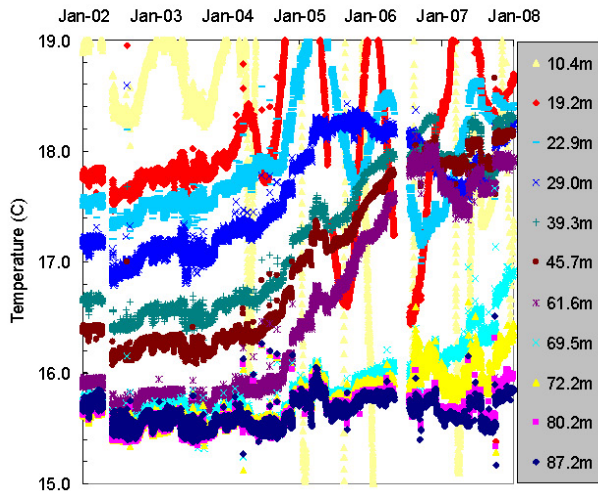


Figure 5. Measurements of soil temperature from HDPs in Test Well #3.

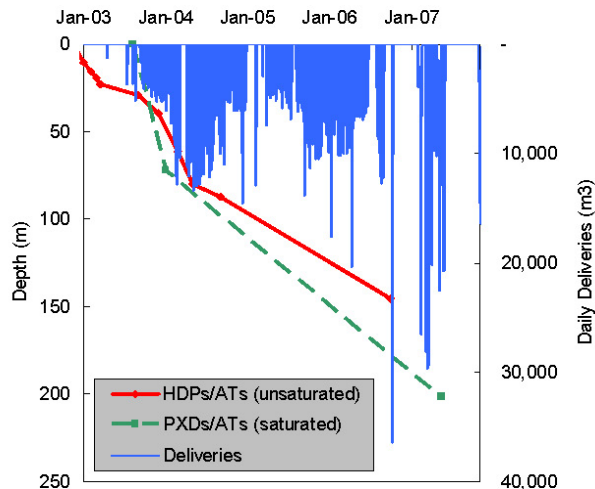


Figure 6. Migration of the infiltration front estimated from HDPs and ATs and water deliveries to the spreading ponds.

the heating elements, the HDP thermocouple measurements of soil temperature have all performed well during this study. The agreement between the HDPs and ATs are relatively good and track reasonably well, but differ slightly (Figure 4c, d), likely due to calibration errors and hysteresis of the matrix material in the HDPs. One advantage of the ATs is their ability to show positive head in the formation when it does occur (Figure 4c).

The migration of the AR wetting front is depicted in Figure 6, based on the arrival time observed by the HDPs and ATs at various depths. A small volume of 7,400 m³ was applied to the ponds in November 2002 to provide an initial wetting of the system. The infiltration of this pulse was tracked by the

instruments throughout 2003 with a vertical pore-water velocity of ~ 4 m month⁻¹. Cumulative AR volumes began in earnest in August 2003 (Figure 6), and a clear response in the perched water level was observed in the AT at 72 m depth by January 2004, leading to a velocity of approximately 15 m month⁻¹. A comparison of water-level variability in Pond 2 versus changes in water level of the perched system indicates that the system now responds quickly, with a lag time of only ~ 1 month between land surface and the perched aquifer (Figure 7). The lack of water level in Pond 2 in the first four months is caused by the water being delivered exclusively to Pond 1 (Figure 3) rather than being distributed evenly over the five ponds, which was done for the remainder of the recharge application.

The observed wetting-front arrival below the perching layer at the 80 and 87 m depth below land surface (bls) HDPs indicates that the pore-water velocity has been reduced significantly to ~ 2 m month⁻¹, due to the low hydraulic conductivity of the perching layer. Arrival at the 145 m depth bls AT in October 2006 also indicates a vertical velocity of ~ 2 m month⁻¹. The effect of a reduced water flux below the perching layer can also be seen in the temperature data (Figure 5) where the deeper instruments have not been warmed by the convective transport of heat through the perching layer. (Note that small shifts are artificial effects caused by changes in the data logger power supply.)

Water-level variability was measured in the perched aquifer system relative to the regional aquifer system

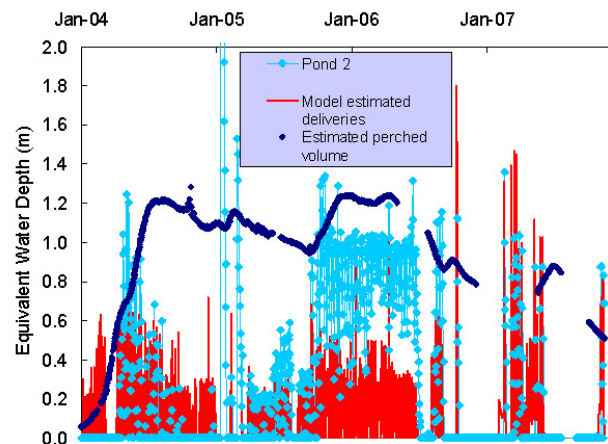


Figure 7. Water-level measured in Pond 2 versus equivalent water depth estimated for storage in the perched water body and daily deliveries used in the model.

at Test Well #3, which showed a general decline (Figure 8) from January 1999 to September 2006, but

showed significant rise by May 2007 (power to the transducer was unintentionally off between September 2006 and May 2007). Arrival of the AR wetting front at the water table was estimated to have occurred in January 2007 (based on extrapolation, because the AT pressure transducers had lost power during that time span). The arrival time observed by the water-level pressure transducer led to a calculated pore-water velocity below the perched layer roughly twice as fast as the velocity calculated from the HDPs (i.e., the greater slope shown in Figure 6). The discrepancy between these rates is attributable to a number of factors. First, since water pressure fronts are sensed over long ranges, the water-level rise observed at Test Well #3 does not have to correspond to an arrival of recharge water at that specific location. The variability in water volumes applied to specific ponds and subsurface heterogeneity would contribute to this effect. Second, the emplacement of HDPs down the borehole requires a backfill material, and this has previously been shown to cause a lag in the instrument response, owing to the fact that water must flow from the formation through the backfill material before the sensor can observe any changes (Ellett, 2002). Finally, a major runoff event occurred in January 2005 that contributed natural recharge below the stream channel. Measurements at Test Well #3 are sensitive to such events, even though the borehole is located some distance away from the channel (Ellett, 2002). Observations from Test Well #5 showed small changes in matric potential with increasing depth (Figure 9a) and a small change in slope when water level was rising at about 37 m (Figure 9b), indicating that the natural recharge pulse is apparently far smaller in magnitude than the observed response at Test Well #3 (Figure 8).

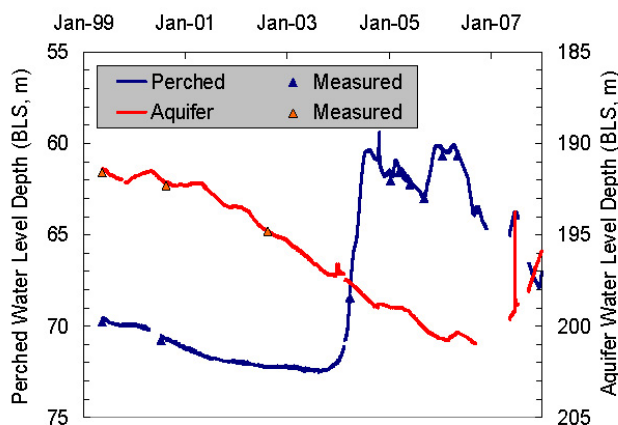


Figure 8. Hydrographs of the perched and regional aquifers at TW3 and field verified water levels.

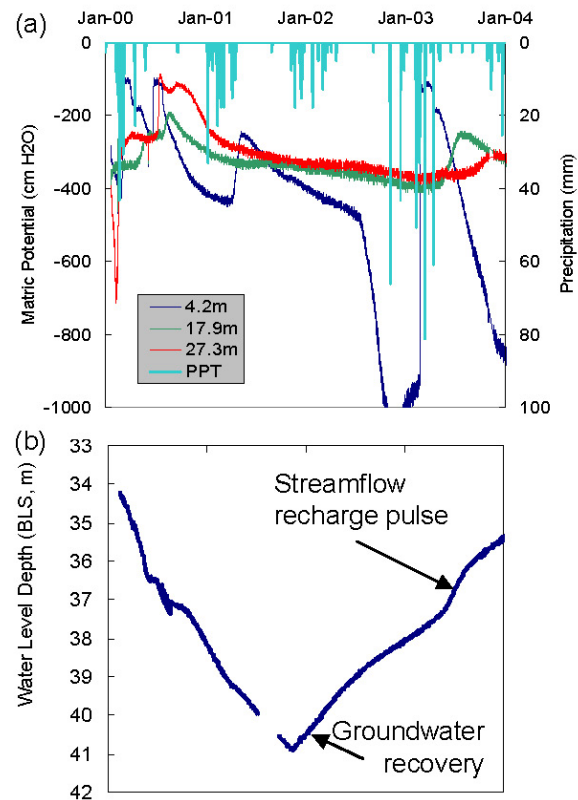


Figure 9. Natural recharge from streamflow events in Little San Gorgonio Creek, (a) matric potential at selected depths in TW5 and precipitation (PPT) at Beaumont, and (b) water table hydrograph.

Estimating Recharge Flux and Conductivity of the Perching Layer

Moisture content measurements from core samples and moisture retention characteristics reported in Ellett (2002) provided an estimate of $0.15 \text{ m}^3 \text{ m}^{-3}$ for the mean volumetric water content of the profile at Test Well #3. Using this estimate, we converted the 2 m month^{-1} pore-water velocity into an estimate of 0.3 m month^{-1} for the water flux below the perching layer. Another method for estimating the drainage flux through the perching layer involves the rate of decline in the water level of the perched system during periods of minimal infiltration. This decline is caused by a combination of vertical drainage and lateral flow; therefore, this method provides an estimate of the upper bound of the drainage flux. From Figure 8, the rate of decline in water level over such periods is generally around 1 m month^{-1} . Assuming a specific yield of 0.25 results in a calculated water-flux estimate of $0.25 \text{ m month}^{-1}$; notably consistent with the estimate based on the wetting-front migration.

In the original study from 1999 to 2002, water flux below the perching layer was estimated by three separate methods to be ~ 0.03 m per month⁻¹. The corresponding hydraulic conductivity of the perching layer was calculated from Darcy's law using a mean hydraulic gradient of 2 m m⁻¹ across the perching layer (0.015 m month⁻¹). With the rise in the perched water level from 2 m above the perching layer (at 74.5 m) to almost 12 m (Figure 8), the mean hydraulic gradient during the period of 2004–2007 was increased by a factor of 6 relative to the earlier period (12 m m⁻¹ versus 2 m m⁻¹). Thus, if the earlier analysis were correct, we would expect the flux estimates in the current study to be roughly 6 times the estimates from the 1999–2002 period, or ~ 0.18 m month⁻¹. Instead, we have obtained estimates of 0.25 – 0.3 m month⁻¹, indicating that the vertical hydraulic conductivity of the perching layer in the UZ model will likely need to be increased by a factor of around 1.5 to match the new observations now available.

ARTIFICIAL RECHARGE MODELING

The numerical model used in this and the prior study (Flint and Ellett, 2004) was developed using TOUGH2, an integrated finite-difference numerical code (Pruess et al., 1999). The prior study used the equation-of-state model EWASG (Battistelli et al., 1997) to simulate the flow of heat, air, water, and dissolved components (NO₃, which is associated with septic tank leach fields in the area). To simplify the modeling approach, the equation-of-state module EWASG was replaced with EOS9, which only calculates the saturated and unsaturated flow of water. The increase in computing speed allowed us to do multiple simulations for relatively small cost and allowed faster automatic calibration of the TOUGH2 model through inverse modeling using iTOUGH2 (inverse TOUGH2; Finsterle, 2007). The geometry of

the site requires a three-dimensional recharged water through the alluvial fan deposits (north to south), as well as lateral flow of natural recharge (generally east to west) from the nearby approach because of down-dip migration of stream. The modeling domain is ~ 2.5 km (east to west) by 1.25 km by 185 m and contains more than 50,000 grid elements. Vertically, the model was divided into seven layers (Table 1). Layer 1 represents Qy, Layers 2 through 4 represent Qo, and Layer 5 represents the perching layer at the top of Qsu (Table 1). The north and south lateral contact of Qo and Qvo, Layers 5 and 6 represent Qvo, and Layer 7 represents the bottom of Qvo, and boundaries of the model are located along faults and are assumed no-flow boundaries. The east and west boundaries represent the edges of the alluvial basin where they encounter the mountain block. The bottom boundary is the water table, the upper boundary is specified flux. The surface flux is temporally and spatially variable, depending on the artificial recharge scenario, and the location and amount of streamflow, septic tank return flow, and natural recharge from precipitation.

The model was developed using hydrologic properties measured in the laboratory or estimated from laboratory data (Table 1; Ellett, 2002). Model parameters were further refined to better simulate field data of temperature, matric potential, and perched water levels. The details of the calibration and applications are presented in detail by Flint and Ellett (2004) and will not be presented here. It should be noted that in the original paper, Flint and Ellett (2004), assumed the perching layer to be 2 m thick with a hydraulic gradient of 2 m m⁻¹, which yielded a hydraulic conductivity of 0.35 m yr⁻¹ that calibrated well to the other borehole data. A revised estimate based on reanalysis of the historic data using

Table 1. Alluvial deposits and corresponding layers and properties used in unsaturated zone model.

Alluvial Deposit [†]	Model layer	Depth Interval	Porosity	Saturated Hydraulic Conductivity	van Genuchten Parameters	
					m	α
		(meters)		(m d ⁻¹)		(1 Pa ⁻¹)
Qy	1	0 - 24	0.345	1.01E+00	0.270	1.84E-04
Qo	2	24 - 36	0.278	1.63E+00	0.367	1.84E-04
Qo	3	36 - 39	0.278	9.83E-01	0.245	1.84E-04
Qo	4	39 - 73	0.278	2.33E+00	0.440	1.84E-04
Qvo [‡]	5	73 - 74	0.350	1.53E-03	0.130	1.03E-04
Qvo	6	74 - 106	0.350	6.78E-01	0.398	1.69E-04
Qvo-Qsu	7	106 - 198	0.304	5.93E-02	0.301	1.63E-04

[†] See Fig. 2.

[‡] In the original model this unit layer was 2 m thick; it is now 1 m thick and was moved 2 m deeper in the profile. (Model Layer 4 was extended by 2 m and the start of Layer 6 was moved 1 m deeper, and the original saturated hydraulic conductivity was $9.57E-4$ m d⁻¹.)

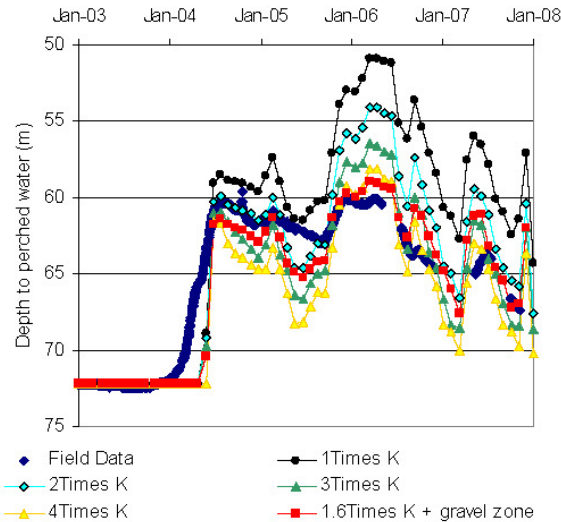


Figure 10. Measured perched water levels compared to simulated perched water level using the perching layers with original estimated permeability and increases in permeability of two, three, and four times the original, plus addition of gravel zone..

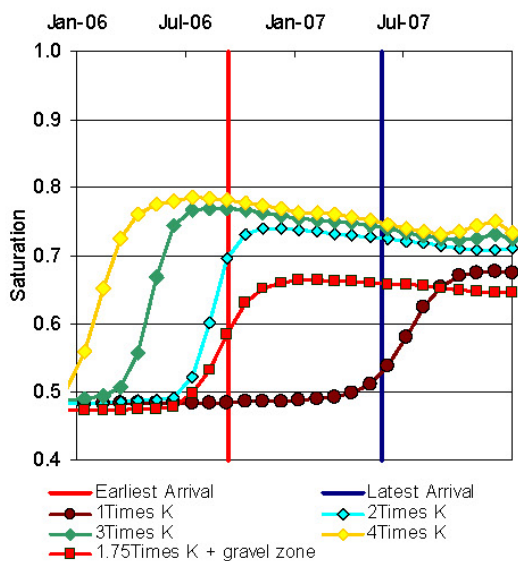


Figure 11. Estimates of the earliest and latest arrival time of the wetting front to the regional aquifer and simulated arrival time using the perching layers with original estimated permeability and increases in permeability of two, three, and four times the original, plus addition of gravel zone.

hydraulic conductivity cannot be known, but needs to be consistent with the thickness of the perching layer used in the model and calibration to additional data collected since the original study was published. The new model discussed in this paper uses the revised lower permeability and thinner layer thickness to maintain the match to the estimated 0.35 m yr^{-1} fluxes determined in the earlier study (Ellett, 2002; Flint and Ellett, 2004).

The application rate of water in the recharge ponds was used as a specified flux at the surface—starting with the original archived model, modified with the corrected perching layer thickness of 1 m (reduced from 2 m) and a corrected saturated hydraulic conductivity of $0.092 \text{ m yr}^{-1} \text{ m}$ (reduced from 0.35). The time of simulation was for an equivalent time period of November 2002 through December 2007 (Figure 6) using monthly time steps. The modified conditions (although equivalent hydrologically for the base conditions) resulted in a higher increase in the rise of the perched water than was measured in the field (Figure 10). The permeability of the perching layer was increased by a factor of two, three, and four times the original permeability, showing less rise in the height of the perched water (Fig. 10) matching the field-measured water levels better than the original model.

As noted earlier, the arrival of the wetting front to the water table and subsequent rise of the water was not detected by field instrumentation. However, the field data gives us a window of when the water would have reached the water table (Figure 8; water table rise started between September 2006, when the transducer lost power, and May 2007, when the transducer power was restored). The original model reached steady-state recharge at the water table after September 2007, well after water table rise was under way (Fig. 8 and 11). The change in permeability of the perching layer also resulted in earlier arrival times at the water table (Figure 11).

Doubling the permeability of the perching layer resulted in steady-state recharge to the water table around mid-October 2006, which is consistent with the estimated arrival time between September 2006 and May 2007. Three times and four times the original permeability resulted in a steady-state

a 1 m thick perching layer and the 2.0 m hydraulic gradients provided an estimate of $\sim 0.15 \text{ m yr}^{-1}$. This difference is indistinguishable compared to the earlier estimate using the limited field data available for the original study. Because the actual thickness of the perching layer is unknown, the absolute value of

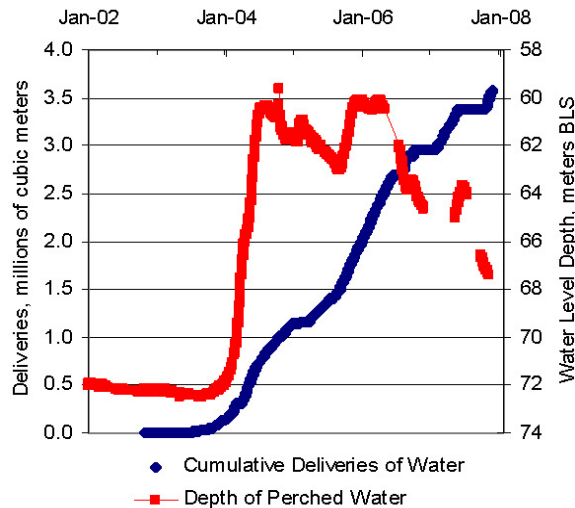


Figure 12. Cumulative deliveries to the spreading ponds and corresponding water level depth of perched zone.

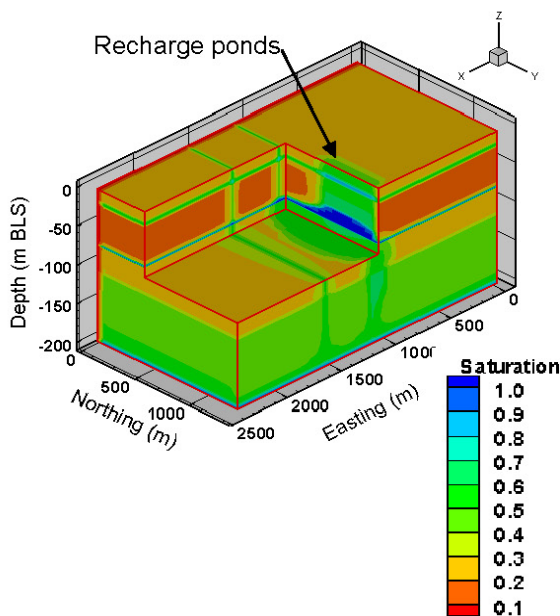


Figure 13. Cut away from the 3-D model showing the lateral and down gradient flow of water from the recharge ponds.

recharge to the water table in April 2006 and June 2006, respectively, several months earlier than our best estimate. Measurement of water table rises associated with artificial recharge may be delayed if the point or area of recharge is somewhat removed from the instrumentation. Based on this possibility, and the height of the perched water, our best estimate of the permeability of the perching layers is about 60 percent higher than the original model. A new concept is now being developed after doing a more detailed analysis of the cumulative application of

water that was compared to the height rise of the perched water (Fig. 12). The analysis shows an apparent limit to the rise of the water at about 60 m bls. There was a fairly steady application rate between January 2004 and July 2004, and October 2005 and August 2006, with a consistent rise of the perched water until March 2004 and January 2006, respectively, when it flattened out within 60 m of land surface. An evaluation of the textural data shows an apparent sand and gravel layer at this location (60 m bls). This layer was contained in Model Layer 4 (Table 1), because it was not considered a major factor to the downward migration of water. When that layer was explicitly incorporated into the model, (although preliminary and not included in the table), it had the effect of limiting the height rise of the perched water by allowing lateral spreading to occur and re-infiltrate the underlying layer when the perched water reached that height. The saturated hydraulic conductivity of the perching layer was increased to 1.6 times the original conductivity to provide the best match between the simulated height of the perched water level and the measured data (labeled as 1.6Times K + gravel zone; Figure 12), as well as reaching the water table within the prescribed time (Figure 11). Additional data are continuing to be collected at the site and will be analyzed with this concept in mind over the next year.

The perching layer caused the wetting front to spread out and move downgradient (Figure 13); however, all of the water applied to the surface is either still in the unsaturated zone in the modeling domain or has reached the water table. The application rate over the period of study (2003–2007) was $\sim 2,200 \text{ m}^3 \text{ day}^{-1}$, or an average of 0.11 m day^{-1} over 12 ha. The recharge at the water table is $\sim 0.011 \text{ m day}^{-1}$ over 120 ha, or about a 10:1 spreading due to the perched layer (and other minor restrictive layers in the profile).

SUMMARY AND CONCLUSIONS

Over a five-year period (2003–2007), 3.5 million cubic meters of water from the California State Water Project was applied through surface spreading to recharge the underlying aquifer in the San Geronio Pass area in southern California. Travel through the unsaturated zone was impeded by a low-permeability perching layer that delayed the recharge to the aquifer. Near-continuous monitoring of the water level at the water table showed a water table rise at between 3.75 years and 4.5 years since the initiation of surface application of water. Using the known application rate, the rise and fall of the water level at the perched layer and the approximate arrival time to the water table, the hydrologic properties in the existing 3-D TOUGH2 model were modified to best match the new data. The only required changes were to increase the permeability of the perching layer by 60% and add a higher permeability gravel layer

above the perching layer to limit the rise of the perched water. Due to the presence of the restrictive layer, the original model predicted that over ten percent of the applied water would be lost down gradient and not recharge the underlying aquifer. The resultant increase in permeability from this analysis reduced the overall flow of water down-gradient, so that all applied water recharged the aquifer within the modeling domain.

ACKNOWLEDGMENTS

The San Gorgonio Pass Water Agency and Jeff Davis, General Manager, supported this work and provided the water application data used in the numerical simulation.

REFERENCES

- Falta, R. W., K. Pruess, I. Javandel, and P. A. Witherspoon, Density-driven flow of gas in the unsaturated zone due to the evaporation of volatile organic compounds, *Water Resour. Res.*, 25(10), 2159–2169, 1989.
- Bloyd, R.M., Underground storage of imported water in the San Gorgonio Pass area, southern California, *USGS Water-Supply Paper 1999-D*, U.S. Geological Survey, Washington, D.C., 1971.
- Ellett, K.M., Hydrologic characterization of the deep vadose zone of the San Gorgonio Pass area for artificial and natural recharge analysis, *M.S. Thesis*, University of California, Davis, 138 p., 2002.
- Finsterle, S.. *iTOUGH2 User's Guide*, Rep. LBNL-40040, Lawrence Berkeley Natl. Lab., Berkeley, CA., 2007.
- Flint, A.L., G.S. Campbell, K.M. Ellett, and C. Calissendorff, Calibration and temperature correction of heat dissipation matric potential sensors, *Soil Science Society of America Journal*, 66:1439-1445, 2002.
- Flint, A.L. and K.M. Ellett, The role of the unsaturated zone in artificial recharge at San Gorgonio Pass, California, *Vadose Zone Journal* 3:763-774, 2004.
- Hubbell, J.M. and J.B. Sisson, Advanced tensiometer for shallow or deep soil water potential measurements, *Soil Science* 163(4):271-277, 1998.
- Pruess, K., C. Oldenburg, and G. Moridis, *TOUGH2 User's Guide, Version 2.0*, Report LBNL-43134, Lawrence Berkeley Natl. Lab., Berkeley, CA., 1999.
- Rewis, D.L., A.H. Christensen, J.C. Matti, J.A. Hevesi, T. Nishikawa, and P. Martin, *Geology, ground-water hydrology, geochemistry, and ground-water simulation of the Beaumont and Banning storage units, San Gorgonio Pass area, Riverside County, California*, U.S. Geological Survey Scientific Investigations Report 2006-5026, 173 p., 2006.
- Shaikh, A., R.B. Bell, M.E. Ford, and S.P. Stockton, *Feasibility of recharge by surface spreading, vol. II* in A.I. Johnson and R.D. Pyne, eds., *Artificial recharge of ground water*: American Society of Civil Engineers, New York, p. 159-167, 1995.

TOUGH2 SIMULATION OF CAVERN CREATION USING ACID DISSOLUTION OF LIMESTONE

Ron Falta, Department of Environmental Engineering and Earth Sciences, Clemson University
Geoff Chambers, Department of Environmental Engineering and Earth Sciences, Clemson University

ABSTRACT

The seasonal nature of natural gas demand results in a cyclical variation in natural gas prices, and occasional shortages. Natural gas is normally delivered to consumers through pipelines with very little storage capacity. Increasing the capacity to store natural gas can improve both the economics and the deliverability of the product. Current natural gas storage facilities primarily consist of deep saline aquifers and mined caverns in salt domes. An alternative storage method could involve the creation of large (~60,000 m³) caverns in low-permeability limestone formations using acid mining. The fact that large parts of the Northeastern and Midwestern US are underlain by these types of formations at depths of 1,000 to 3,000 m makes this idea potentially attractive.

We developed a fully coupled, implicit TOUGH2 module to simulate cavern creation in limestone formations using hydrochloric acid (HCl) injection. The reaction between the HCl and the limestone produces calcium chloride (CaCl₂), water, and carbon dioxide.



As the reaction proceeds, CaCl₂ dissolves in water to form a dense brine, while the CO₂ will either dissolve in the brine or exist as a separate supercritical phase. To develop the TOUGH2 module for this process, we modified the ECO2 version of EWASG (Pruess and Garcia, 2002). The key modifications consist of replacing the NaCl component in ECO2 with CaCO₃, adding HCl and CaCl₂ as additional mass components, and including the equilibrium acid limestone

dissolution reaction. The reaction between the acid and the limestone in each gridblock is assumed to be instantaneous and complete.

Because the limestone replaces NaCl in ECO2, the model porosity is initially set equal to 1, and the limestone porosity becomes one minus the solid phase saturation. In this way, as the limestone dissolves, the solid saturation decreases, and an open cavern forms. Fluid flow in the open cavern is approximated by Darcy's law, using a very large intrinsic background permeability. The permeability reduction factor is specified to be a power function of the apparent porosity, so that at high solid saturations (~.9 to .99), realistic limestone intrinsic permeabilities are present. Mass transfer between the open cavern and the cavern walls is approximated by a first-order mass-transfer reaction using a diffusion-like conductance term and the concentration difference between the rock and the cavern. A nonreactive version of this mass-transfer approach was used to successfully simulate a large salt cavern dissolution experiment.

The acid dissolution model was used to explore different strategies for creating caverns using a single borehole. These strategies involved injection of HCl at one depth, with production of the CaCl₂ brine and CO₂ at other depths. Two approaches appear to be feasible: one in which low strength acid is injected, and in which the resulting CO₂ is dissolved in the brine; and one in which high-strength acid is injected, and a separate supercritical CO₂ phase is produced.

INVESTIGATION OF STRONTIUM ISOTOPIC EXCHANGE IN SINGLE AND DUAL CONTINUA USING TOUGHREACT

Jennifer Druhan, Eric Sonnenthal, and Don DePaolo

University of California Berkeley & Lawrence Berkeley National Laboratory
307 McCone Hall MC 4767
Berkeley, CA 94720 USA
e-mail: jennydruhan@berkeley.edu

ABSTRACT

Isotopic measurements are a commonly employed tool in the characterization of groundwater flow paths, residence times, and water-rock interactions in a variety of systems (e.g., Johnson et al., 2000). For example, many soluble species are unevenly distributed between solid and liquid phases of unique isotopic compositions, resulting in detectable shifts in the isotopic ratios as a result of minor amounts of dissolution. Analytical models have been applied to treat isotopic ratios under a variety of reactive transport regimes (e.g., Johnson and DePaolo, 1994; 1996; 1997a). While these models are capable of identifying important constraints on the physical and chemical properties of hydrologic systems, they are fundamentally limited by simplifying assumptions that neglect the relationships between specific mineral assemblages, reactive surface areas, reaction rates, and flow field characteristics. Treatment of isotopes within reactive transport modeling has been shown to improve upon existing analytical models and expands our ability to infer hydrologic processes (e.g., Singleton et al., 2004).

Using TOUGHREACT (Xu et al., 2006) we evaluate further the isotopic exchange and water-rock interaction of strontium in fractured rock that was investigated by DePaolo (2006) using analytical solutions. Strontium isotopes are treated as explicit constituents in the fluid and mineral phases, as well as considering advective and diffusive transport. Initial flow model and chemical input parameters are based on DePaolo (2006). A single porosity flow field serves as a reference model for the dual porosity case, in which advective flow is confined to fractures evenly spaced between blocks of porous material. Exchange between the fluid in the fracture and fluid in the matrix pores is limited to diffusive transport, offering the opportunity to demonstrate the relationship between element-specific diffusive reaction lengths, reaction rates, and fracture spacing in comparison with the analytical solution presented by DePaolo (2006). Results indicate proper implementation of the isotopic constituents in TOUGHREACT and illustrate more realistic treatment in comparison with the analytical solution. Results provide valuable information on subsurface hydrologic and geochemical characteristics such as

fracture spacing and reaction rates, and further demonstrate the utility of incorporating isotope ratios into a time-dependent, multicomponent reactive transport model.

INTRODUCTION

Explicit treatment of multiple isotopes in a reactive transport model presents a novel means of chemical and hydrologic analysis. Isotopic ratios for a given mineral, aqueous, or gaseous species incorporate information about the sources and process history of that phase associated with, but distinct from, species concentration. For example, many soluble species are unevenly distributed between solid and liquid phases of unique isotopic composition, resulting in detectable shifts in the isotopic ratios as a result of minor amounts of dissolution or precipitation. Isotopic characteristics such as sensitivity to minor exchange rates and individual signatures of unique isotopic sources have been applied to characterization of flow paths, advective and diffusive transport, mineral dissolution and precipitation rates, ion exchange, evaporation/condensation rates, biological activity, and available mineral surface areas (Lasaga, 1984; Blattner and Lassey, 1989; Bickle et al., 1995, 1997; Johnson and DePaolo, 1997a, 1997b, Johnson et al., 2000; Massmann et al., 2003; Conrad and DePaolo, 2004; Maher et al., 2006; Singleton et al., 2006). However, the majority of such analyses have required the assumption of a single porosity system in order to quantify residence times, transport rates, and reaction rates from isotopic data. Often this assumption represents the single largest source of error in the estimate (Manning and Solomon, 2004) or conversely, when unreasonable values are obtained, is cited as evidence for a more complex permeability distribution (Thomas et al., 1996; Scanlon, 2004).

Interpretation of isotopic data using a single porosity assumption incorporates errors both in the estimated value of porosity and in the difference in isotopic effects anticipated under more complex flow regimes. In a dual porosity system, the contrast in transport and residence times between fast flow path and pore waters may result in differences in their associated isotopic ratios and the mixing between them. DePaolo (2006) presents a simplified analytical

solution to the effects of single and dual porosity systems on isotopic ratios of Sr and O in a fractured media. Our research further evaluates these effects using TOUGHREACT to include the influence of specific mineral assemblages and associated time-evolving reaction rates and reactive surface areas in both single and dual porosity systems. The study also serves to verify proper incorporation of isotopes in the TOUGHREACT code against an analytical solution.

PROBLEM DESCRIPTION

DePaolo (2006) presents a steady-state solution for isotopic effects in a saturated, advective system with unique water and matrix isotopic ratios. A single porosity reference model is compared to a simplified dual porosity system consisting of parallel fractures evenly spaced between blocks of porous matrix (Figure 1). The isotopic ratios of the pore fluid are a function of the reaction rate with the host media (R) and diffusion of fracture fluid along the walls of the block. Fracture water-isotopic ratios are influenced by advection, dispersion, and diffusion of pore fluid along the walls of the fracture. Diffusion along fracture walls is the only mechanism by which fracture and pore fluid communicate.

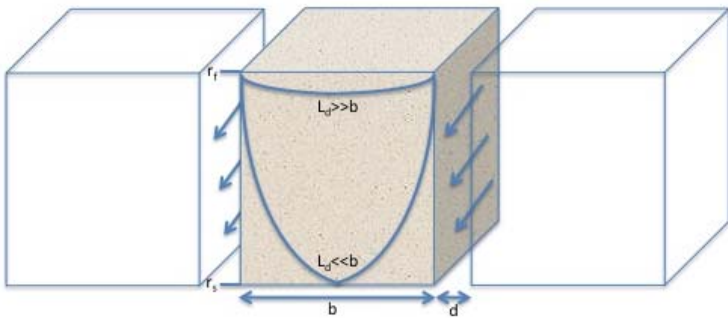


Figure 1. Conceptual model of simplified dual porosity system. Fluid flows along parallel fractures of width d evenly spaced between blocks of porous media of width b . The starting fluid and pore water isotopic ratios are r_f and r_s , respectively. The central media block illustrates two potential distributions of isotopic ratios in the pore water with distance away from the fracture.

Thus, the characteristic length scale for diffusive mixing in the pore fluid is defined as (DePaolo, 2006):

$$L_d = \left(\frac{D_i}{R_m M K_i} \right)^{1/2} \quad (1)$$

where D_i is the aqueous diffusivity of element i , R_m is the bulk reaction rate for the solid phase, M is the mass ratio of solid to fluid, and K_i is the distribution coefficient of solid to fluid for element i . The distribution of isotopic ratios in the pore fluid is a function of the ratio between L_d for a given element and b , the spacing between fractures. When this ratio is large, the difference between fracture and pore fluids is minimal, while small values indicate the reaction rate between the solid and pore fluid is fast in comparison to diffusion from the fracture wall, creating a larger gradient in isotopic ratios with distance into the block (Figure 1).

There are multiple simplifying assumptions incorporated into the analytical solution. First, the system is assumed to have evolved to steady state, with unique isotopic compositions in the incoming fracture water and pore fluid. Similarly, the isotopic composition of the solid phase does not evolve with time. Second, the porous media is treated as monomineralic and equal in rates of dissolution and precipitation with the pore fluid, such that no net change in porosity occurs. This assumption also implies that the concentration of a given element in the pore fluid does not vary as a result of interaction with the host rock. Third, the effects of dispersion in the fracture fluid are ignored, so that the only factors influencing variation in the fracture-fluid isotopic ratio are advective transport and diffusion along the fracture walls.

MODEL DESCRIPTION

Simulations were performed using the TOUGHREACT nonisothermal multiphase geochemical reactive transport program (Xu et al., 2006). Input parameters for both the single and dual porosity models were taken directly or adapted from DePaolo (2006) (Table 1). For the single porosity reference model, both a monomineralic and a multimineraleic system were considered. In the monomineralic case, the porous media was composed of an anorthite with a mole fraction of 0.4% Sr substituting for Ca. In the multimineraleic version, the initial solid phase was composed of 13.2% volume fraction potassium feldspar, 29.9% albite, 34.3% quartz, and 10% anorthite with the same mole fraction of Sr as the monomineralic model.

The single porosity models were run over a 200 m long grid composed of 1 m^3 blocks. Fluid velocity was established by setting constant pressure heads at the boundaries. The dual porosity model was constructed as a 50 m long grid.

Table 1. Parameter values

Parameter	Value	Units
Temperature	25	°C
Fluid velocity	1	m/yr
K dist. coeff.	35	
Solid/fluid density	2.6	
Matrix porosity	0.01	
Permeability	6.51×10^{-12}	m^2
Disp. Coeff.	0.01	m^2/yr
Solid bulk reaction rate	2.5×10^{-5}	yr^{-1}
Initial $^{87}\text{Sr}/^{86}\text{Sr}$ of fluid	0.7092	
Initial $^{87}\text{Sr}/^{86}\text{Sr}$ of the solid	0.7032	

One-cubic-meter gridblocks were subdivided based on the multiple interacting continua (MINC) process. Flow was confined to a 0.1 m width, while the rest of the block was divided into nested gridblocks, with the largest volume at the center and progressively smaller shells extending to the fracture. This subdivision allowed for analysis of the pore fluid chemistry with distance from the fracture wall. Pressure heads were set at both ends as in the single porosity model, and the system was run with no reactive transport to initialize the pressure distribution throughout the nested grid system prior to starting the geochemical simulation.

Each simulation was run for 200 years to establish a steady-state solution for comparison to the DePaolo (2006) solution. A no-flow simulation was conducted to determine the equilibrium chemical composition of pore water in the host media. Inlet water chemistry was set equal to that of the pore fluid, except for adjustment to the Sr values, to establish a unique isotopic ratio (Table 2). Sr isotopes were defined explicitly in the thermodynamic database, such that fluid phase and anorthite Sr were divided into ^{87}Sr and Sr' , which accounted for the remainder of the Sr isotopes. Using this method, the isotopic components summed to the total concentration of Sr, thus preserving stoichiometry in the mineral assemblage. Strontium-86 was back-calculated from Sr' , based on the natural abundances of ^{84}Sr , ^{86}Sr and ^{88}Sr . From this, the appropriate ratio of ^{87}Sr to Sr' could be calculated to establish a required $^{87}\text{Sr}/^{86}\text{Sr}$ ratio for a given total concentration of Sr

Table 2. Initial fluid concentrations

Aqueous species	Concentration (mol kg^{-1})
H^+	2.6×10^{-6}
Ca^{2+}	1×10^{-10}
Na^+	1×10^{-10}
$\text{SiO}_{2(\text{aq})}$	1×10^{-10}
K^+	1×10^{-10}
AlO_2^-	1×10^{-10}
Sr' (pore water)	6.06559×10^{-5}
^{87}Sr (pore water)	4.56075×10^{-6}
Sr' (inlet water)	6.06918×10^{-5}
^{87}Sr (inlet water)	4.52484×10^{-6}

In order to match the assumptions of the DePaolo (2006) analytical model as closely as possible, porosity was set as a constant, regardless of dissolution and precipitation reactions. The kinetic rate constant and specific surface area of anorthite were calculated to match the reaction time constant specified in the analytical model.

RESULTS AND DISCUSSION

Single Porosity Model

The monomineralic simulation consisting of a pure anorthite porous media equilibrated rapidly and showed no appreciable adjustment in the Sr isotopic ratio of the fluid away from 0.7092. The model was adjusted to allow kaolinite precipitation in an attempt to keep the fluid undersaturated with respect to the anorthite, but this made no appreciable difference. It was concluded that a multiminerale system was required to maintain anorthite dissolution as is assumed in the DePaolo (2006) analytical model.

The multiminerale single porosity system showed evolution to a steady-state profile similar to that of the DePaolo (2006) analytical model (Figure 2). Multiple secondary species were allowed to form in the simulation. This resulted in the precipitation of predominantly Si and Al species, keeping the saturation with respect to anorthite low and allowing the solid phase $^{87}\text{Sr}/^{86}\text{Sr}$ ratio to influence the fluid isotopic composition.

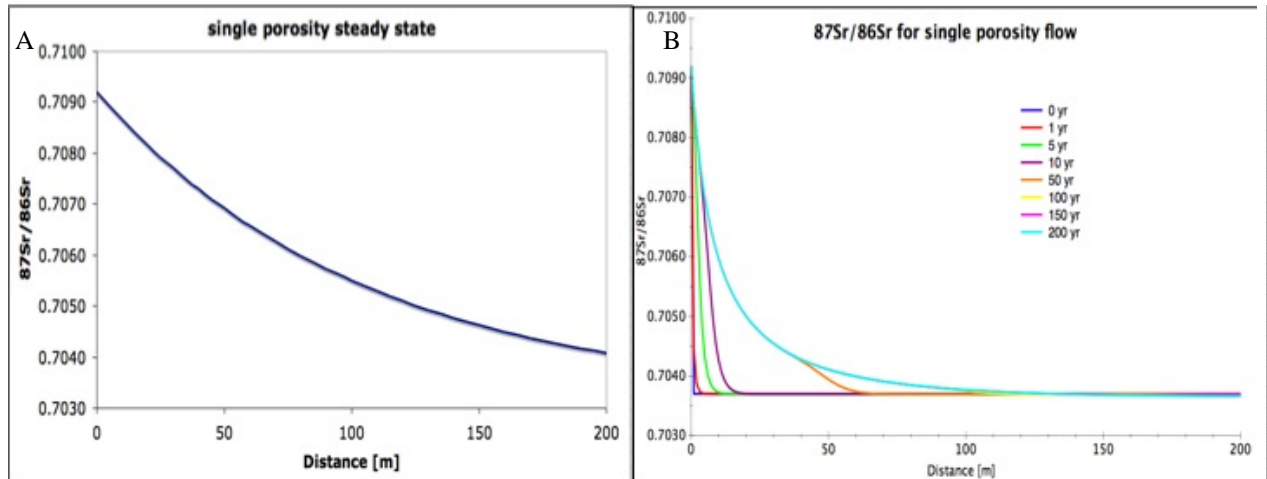


Figure 2. Single porosity models: (A) DePaolo (2006) analytical solution and (B) the TOUGHREACT solution including evolution to the steady-state profile

The final $^{87}\text{Sr}/^{86}\text{Sr}$ value of the fluid phase at the end of the 200 m grid was 0.7038, as opposed to a value of 0.7041 in the DePaolo (2006) model. The steady-state profile generated by the TOUGHREACT simulation shows a sharper drop to the final fluid isotopic value than the analytical solution. This difference is attributed to the change in fluid Sr concentration and associated decrease in volume fraction anorthite over the course of the TOUGHREACT simulation (Figure 3). In the analytical solution, the distribution coefficient between fluid and solid Sr concentrations is constant, and under the assumption that solid phase Sr does not change, this constraint leads to a constant fluid phase Sr concentration.

In the TOUGHREACT simulation, the concentration of Sr in the fluid increases by a factor of roughly 7 times, with the most pronounced increase occurring at early time. As the simulation proceeds, the amount of anorthite per unit volume decreases due to dissolution, and the increase in aqueous Sr becomes more gradual across the domain. This increase in aqueous Sr from mineral dissolution serves to partially swamp the influent aqueous $^{87}\text{Sr}/^{86}\text{Sr}$ value, leading to a final fluid $^{87}\text{Sr}/^{86}\text{Sr}$ value closer to the mineral ratio than the analytical solution, and also decreasing the distance along the flow path required to reach this value.

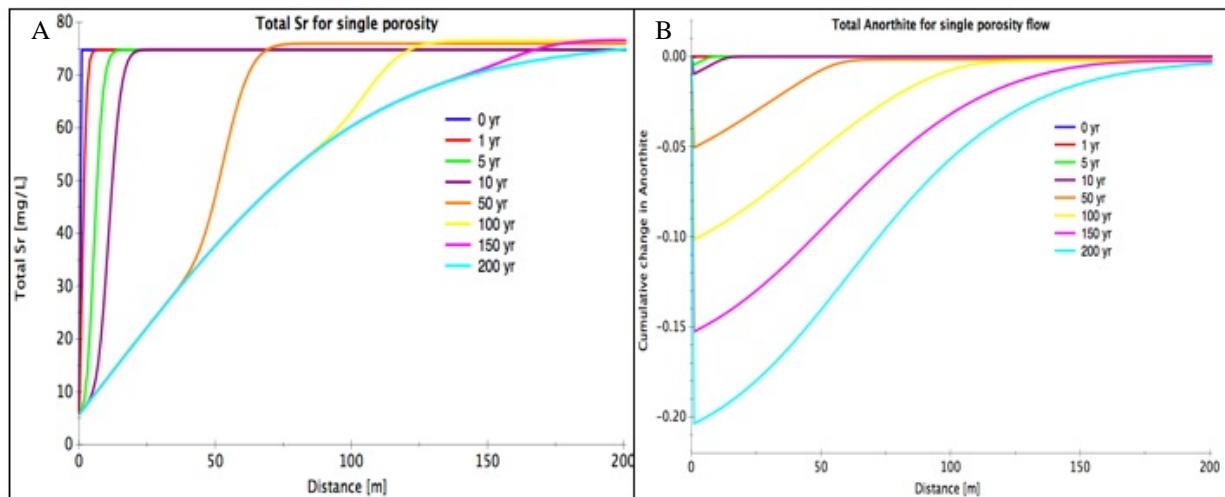


Figure 3. Single porosity multiminerale simulation (A) total Sr (mol L^{-1}) in the fluid phase (B) cumulative change in anorthite (mol/m^3)

A potential means of bringing the TOUGHREACT solution closer to that of the analytical solution is adjustment of the fluid chemistry and addition of specific minerals, to set up a system in which excess Sr is “scrubbed” from the fluid through precipitation. While this may be an instructive exercise, the simulation presented here represents a more realistic situation and emphasizes the fact that under appropriate conditions, the analytical solution underestimates the influence of the solid-phase isotopic ratio due to the assumption of constant concentration. Furthermore, despite the decrease with time, the overall depletion in the anorthite reactive surface area is minimal, indicating that the amount dissolved is small and thus the reaction rate is staying approximately constant during the simulation, in accordance with the analytical model.

Dual Porosity Model

The 200-year steady-state results of the dual porosity simulation are plotted to show variation in the pore fluid isotopic ratio with distance away from the fracture (Figure 4). The final $^{87}\text{Sr}/^{86}\text{Sr}$ ratio at the end of the 50 m domain in the fracture fluid is 0.7062, as compared with a value of 0.7035 in the analytical solution under these conditions. The ratio of L_d (Equation 1) to b (the spacing between fractures) is 0.2. Under this flow regime, the same final fluid $^{87}\text{Sr}/^{86}\text{Sr}$ ratio as the single porosity system would

require a much larger reaction rate, because the fluid in the fracture is in contact with a much smaller amount of the solid, and obtains the majority of influence from the solid-phase $^{87}\text{Sr}/^{86}\text{Sr}$ through diffusion in the pore fluid. Within the porous medium, fluid does not advect and correspondingly takes on an isotopic ratio closer to the solid phase.

In this system, the influence of increased Sr concentrations in the fluid is partially offset by the decreased contact between advecting fluid and the solid phase, as well as establishment of a mixing zone in the pore water close to the fracture. At the inlet, the $^{87}\text{Sr}/^{86}\text{Sr}$ values of the fluid with distance into the porous matrix are quite comparable between the TOUGHREACT and analytical models; however, the final $^{87}\text{Sr}/^{86}\text{Sr}$ of the fracture fluid is closer to the influent value in the TOUGHREACT simulation. Just as the fracture fluid is exposed to less anorthite per unit area than the single porosity model, the fast advection and limited surface area also impede the precipitation of secondary minerals, bringing the fracture fluid closer to saturation and diminishing the influence of the solid phase. Again in the analytical solution changes in Sr concentration and saturation with respect to the dissolving phase are not considered, in this case resulting in an $^{87}\text{Sr}/^{86}\text{Sr}$ closer to the solid-phase value.

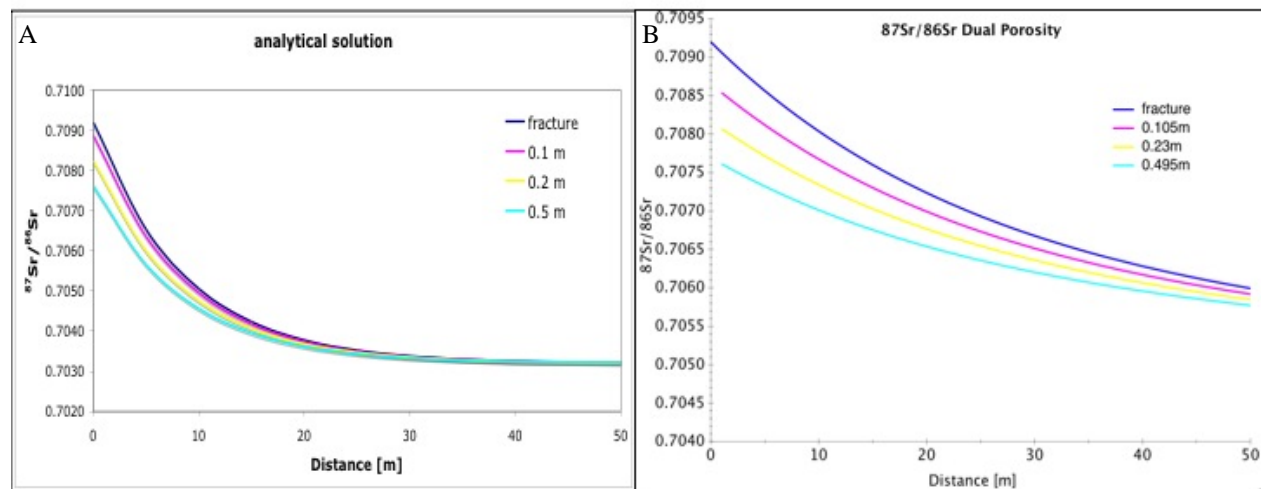


Figure 4. Dual porosity models with $L_d/b=2$ (A) DePaolo (2006) analytical solution showing the isotopic ratio at steady state in the fracture and in the pore fluid at a distance of 0.1, 0.2 and 0.5 m into the adjacent porous media block. (B) TOUGHREACT simulation showing the steady state (200 yr) fracture fluid isotopic ratios and pore fluid at distances of 0.105, 0.23 and 0.495 m into the adjacent porous media block.

CONCLUSIONS AND FUTURE RESEARCH

Using the TOUGHREACT program, we have simulated strontium isotopic exchange between a solid and a through-flowing fluid of unique $^{87}\text{Sr}/^{86}\text{Sr}$ ratios based on the analytical model of DePaolo (2006). The results indicate good agreement between the analytical and numerical solutions, particularly in light of the many differences in the scope and approach of these methods. These results suggest proper implementation of Sr isotopes as explicit species in the TOUGHREACT framework.

The principal differences between the DePaolo (2006) model and the TOUGHREACT simulations are based on the simplifying assumptions necessary to obtain the analytical solution. In the TOUGHREACT code, mineral dissolution and precipitation were allowed to occur as a function of saturation state with corresponding variations in aqueous chemical concentrations and abundance of dissolving phases. This treatment illustrates a more realistic scenario than the analytical solution, and shows that the difference in the apparent isotopic ratio of the fluid phase between single and dual porosity systems is even more pronounced than suggested by the analytical model. This result yields important implications for the use of isotopes as tools to identify hydrologic and geochemical properties such as reaction rates, recharge rates, and residence times. Furthermore, it provides a strong argument for analysis of isotopic data within a more complex numerical reactive transport program, one that can take into account the influence of time-evolving parameters and mixing of unique waters in a heterogeneous system.

The DePaolo (2006) model also presented results for oxygen isotope variation in single and dual porosity flow fields. Implementation of oxygen isotopes is somewhat more complex than those of strontium, because of mass-induced fractionation effects under transport and exchange regimes. Preliminary implementation of oxygen isotopes in the TOUGHREACT simulation indicates that good results can be obtained by establishing explicit ^{16}O and ^{18}O waters independent of the bulk H_2O solvent. Oxygen and strontium isotopes in the DePaolo (2006) model were demonstrated as an example of two isotopic systems with very different L_d values, leading to large differences in the distribution of each isotopic ratio within the fracture and pore fluids. The author suggested that using two such isotopic systems may provide enough data to back out information on fracture spacing. Application of this idea to appropriate sites, such as seawater flow in fractured basalt, should provide the opportunity to test this hypothesis using a more realistic numerical model.

ACKNOWLEDGMENT

This work was supported by the Director, Office of Science, and by the Biological and Environmental Research Program of the U.S. Department of Energy under Contract No. DE-AC02-05CH11231.

REFERENCES

- Bickle, M.J., Chapman, H.J., Wickham, S.M. and Peters, M.T., Strontium and oxygen-isotope profiles across marble silicate contacts, Lizzies Basin, East Humbolt Range, Nevada – constraints on metamorphic permeability contrasts and fluid-flow, *Contrib. Mineral. Petr.*, 121(4), 400–413, 1995.
- Blattner, P., and Lassey, K.R., Stable isotopic exchange fronts, Damkohler numbers and fluid-rock ratios, *Chem. Geol.*, 78(3-4), 381–392, 1989.
- Conrad, M.E., and DePaolo, D.J., Carbon isotopic evidence for biodegradation of organic contaminants in the shallow vadose zone of the Radioactive Waste Management complex, *Vadose Zone J.*, 3(1), 143–153, 2004.
- DePaolo, D.J., Isotopic effects in fracture-dominated reactive fluid-rock systems, *Geochim. Cosmochim. Acta*, 70(5), 1077–1096, 2006.
- Johnson, T.M., and DePaolo, D.J., Interpretation of isotopic data in groundwater-rock systems: Model developments and application of Sr isotope from Yucca Mountain, *Water Resour. Res.*, 30(5), 1571–1587, 1994.
- Johnson, T.M., and DePaolo, D.J., Reaction-transport model for radiocarbon in groundwater: The effects of longitudinal dispersion and the use of Sr isotope ratios to correct for water-rock interaction, *Water Resour. Res.*, 32(7), 2203–2212, 1996.
- Johnson, T.M., and DePaolo, D.J., Rapid exchange effects on isotope ratios in groundwater. 1. Development of a transport-dissolution-exchange model, *Water Resour. Res.*, 33(1), 187–195, 1997a.
- Johnson, T.M., and DePaolo, D.J., Rapid exchange effects on isotope ratios in groundwater. 1. Flow investigation using Sr isotope ratios, *Water Resour. Res.*, 33(1), 197–205, 1997b.
- Johnson, T.M., Roback, R.C., McLing, T.L., Bullen, T.D., DePaolo, D.J., Doughty, C., Hunt, R.J., Smith, R.W., Cecil, L.D., and Murrell, M.T., Groundwater “fast paths” in the Snake River Plain aquifer: Radiogenic isotope ratios as natural groundwater tracers, *Geology*, 28(10), 871–874, 2000.

- Lasaga, A.C., Chemical kinetics of water-rock interaction, *J. Geophys. Res.*, 89(NB6), 4009–4025, 1984.
- Maher, K., DePaolo, D.J., Christensen, J.N., U-Sr isotopic speedometer: Fluid flow and chemical weathering rates in aquifers, *Geochim. Cosmochim. Acta*, 70(17), 4417–4435, 2006.
- Manning, A.H., and Solomon, D.K., Constraining mountain-block recharge to the Eastern Salt Lake Valley, Utah with dissolved noble gas and tritium data, in *Groundwater Recharge in a Desert Environment: The Southwestern United States* (Hogan, J.F., Phillips, F.M., and Scanlon, B.R., eds.), *Water Science and Application* 9, AGU, 139–158, 2004.
- Massmann, G., Tichomirowa, M., Merz, C., and Pekdeger, A., Sulfide oxidation and sulfate reduction in a shallow groundwater system (Oderbruch Aquifer, Germany), *J. Hydrol.*, 278(1-4), 231–243, 2003.
- Singleton, M.J., Sonnenthal, E.L., Conrad, M.E., DePaolo, D.J., and Gee, G.W., Multiphase reactive transport modeling of seasonal infiltration events and stable isotope fractionation in unsaturated zone pore water and vapor at the Hanford site, *Vadose Zone J.*, 3(3), 775–785, 2004.
- Scanlon, B.R., Evaluation of methods of estimating recharge in semiarid and arid regions in the southwestern U.S., in *Groundwater Recharge in a Desert Environment: The Southwestern United States* (Hogan, J.F., Phillips, F.M., and Scanlon, B.R., eds.), *Water Science and Application* 9, AGU, 235–254, 2004.
- Singleton, M.J., Maher, K., DePaolo, D.J., Conrad, M.E., and Dresel, P.E., Dissolution rates and vadose zone drainage from strontium isotope measurements of groundwater in the Pasco Basin, WA unconfined aquifer, *J. Hydrol.*, 321(1-4), 39–58, 2006.
- Thomas, D.M., Paillet, F.L., and Conrad, M.E., Hydrology of the Hawaii Scientific Drilling Project borehole KP-1 2. Groundwater geochemistry and regional flow patterns, *J. Geophys. Res.*, 101(B5), 11683–11694, 1996.
- Xu, T.F., Sonnenthal, E.L., Spycher, N., Pruess, K., TOUGHREACT – A simulation program for non-isothermal multiphase reactive geochemical transport in variably saturated geologic media: Applications to geothermal injectivity and CO₂ geological sequestration, *Comput. Geosci.*, 32(2), 145–165, 2006.

GEOHERMAL

MODELING OF HYDROTHERMAL FLUID CIRCULATION AS A TOOL FOR VOLCANIC HAZARD ASSESSMENT

A. P. Rinaldi^(a), J. Vandemeulebrouck^(b), M. Todesco^(a)

(a) Istituto Nazionale di Geofisica e Vulcanologia
Sezione di Bologna

Bologna, 40133, Italy

e-mail: rinaldi@bo.ingv.it, todesco@bo.ingv.it

(b) Laboratoire de Geophysique Interne et Tectonophysique
Université de Savoie

Le Bourget du Lac Cedex, 73376, France

email: Jean.Vandemeulebrouck@univ-savoie.fr

ABSTRACT

Monitoring of geophysical and geochemical observables at the surface plays a main role in the understanding of—and the hazard evaluation of—active volcanoes. Measurable changes in these parameters should occur when a volcano approaches eruptive conditions. Hydrothermal activity is commonly studied as an efficient carrier of signals from the magmatic system. As the magmatic system evolves, the amount, temperature, and composition of magmatic fluids that feed the hydrothermal system change, in turn affecting the parameters that are monitored at the surface. Modeling of hydrothermal circulation, as shown in the past, may cause measurable gravity changes and ground deformation. In this work, we extend our previous studies and increase the number of observable parameters to include gas temperature, the rate of diffuse degassing, the extent of the degassing area, and electrical conductivity. The possibility of nonmagmatic disturbance needs to be carefully addressed to ensure a proper estimate of volcanic hazard.

INTRODUCTION

Volcanic hazard assessment is a major challenge in all countries where large communities reside near active volcanoes. The safety of the population requires that at any time, an appropriate alert level is achieved as eruptive conditions approach. This task is particularly complicated when long repose times elapse between subsequent eruptive events, and the unrest can last for decades before the actual eruption takes place. In this case, the state of volcanic activity needs to be carefully monitored in order to detect signals related to magma movement toward the surface. The fluids that feed fumaroles and hot springs in active volcanoes are a fundamental resource available for volcanic surveillance. In a volcanic region, a fraction of discharged fluids generally derives from magma degassing. If the magmatic source changes in time, because of a new material supply in the magma chamber or other differentiation processes, the volatiles could also change, affecting both the composition and flow rate

of fluids at the surface. Observed changes are generally caused by a complex interaction between the magmatic system and hydrothermal fluid circulation. Several changes in monitored parameters may be associated with the hydrothermal system rather than with the degassing magma, and may occur as the fluids ascend through porous rock.

High temperatures and pore pressures acting on porous rock can be responsible for ground deformation (Bonafede, 1991; Todesco et al., 2004; Hurwitz et al., 2007; Hutnak et al., 2009; Rinaldi et al., 2009a). Hydrothermal fluids can also influence self-potential and electrical resistivity, since these quantities depend on fluid flow pattern, temperature, and phase saturation. Through measurements carried out in various volcanic regions, many authors have inferred the main features of fluid circulation in the underground (Zlotnicki and Nishida, 2003; Finizola et al., 2004; Aizawa et al., 2009; Revil et al., 2008). The distribution of liquid-dominated, two-phase, and gas-dominated regions also determines the subsurface distribution of the fluid density. Changes in relative size or in the position of these regions can produce measurable gravity signals (Todesco and Berrino, 2005). Other studies have inferred the effects of fluid circulation as a fault lubricant and as a trigger for low-frequency seismic events (Bianco et al., 2004). Results also indicate that the amplitude of the observed changes mostly depend on the supply rate of magmatic fluids (Todesco, 2009). However, the state and properties of the degassing magma are not the only source that generates and influences the observable signals. Recent results highlight the role of rock properties in controlling the evolution of the parameters measured at the surface (Rinaldi et al., 2009b).

Since magmatic and hydrothermal processes may cause similar effects, the interpretation of signals collected at the surface is not always unequivocally constrained. A simultaneous analysis of different geophysical and geochemical observables is a sound approach for interpreting monitoring data and to infer a consistent conceptual model.

In this work, we extend our previous studies and increase the number of observable parameters to include gas temperature, the rate of diffuse degassing, and electrical conductivity. Following a well-established approach, we first simulate the evolution of the hydrothermal system and then compute the observables in a postprocessing calculation. The simulation of hydrothermal fluid circulation is based on a conceptual model previously developed for the Campi Flegrei (Chiodini et al., 2003; Todesco et al., 2004; Todesco and Berrino, 2005): the hydrothermal system is fed by fluids of magmatic origin and an unrest phase is simulated as a period of increased magmatic degassing. We quantify and compare the evolution of the considered observable parameters after a generic period of unrest. Note that we do not intend to reproduce the history of a particular system.

MODELING THE HYDROTHERMAL FLUID CIRCULATION

Hydrothermal fluid circulation is here simulated using the TOUGH2 code (Pruess et al., 1999), which is a multipurpose simulator describing the coupled flow of heat and multiphase and multicomponent fluids through a porous material.

In this paper, we consider water and carbon dioxide as fluid components. The 2-D computational domain is 10 km wide and 1.5 km deep (Figure 1), and discretized into 2,580 elements (radial dimensions from 25 to 3196 m and thickness from 5 to 25 m). Bottom and side boundaries are impervious and adiabatic. Atmospheric conditions are fixed along the upper boundary, which is open to heat and fluid flows. Figure 1 also show the properties of the porous medium used in the simulation, kept constant during the simulation. The shallow hydrothermal circulation is driven by the injection of a hot mixture of water and carbon dioxide. The inlet of hot fluids, placed at the bottom of the domain near the symmetry axis, is 150 m wide and discharges a mixture at a temperature of ~ 600 K.

As described in previous work (Chiodini et al., 2003; Todesco et al., 2004), this prolonged activity of the fluid source generates a wide two-phase plume, with a shallow single-phase gas region (Figure 2). The plume is characterized by high temperatures (contour in Figure 2) and is pressurized with respect to the hydrostatic gradient.

Initial conditions are obtained by simulating a long-lasting (thousands of years) injection of magmatic fluids. The prescribed flow rate at the inlet (1,000 tons/day of CO₂ and 2,400 tons/day of H₂O) reflects the data collected at the Campi Flegrei caldera and corresponds to a CO₂/H₂O molar ratio of 0.17 (Chiodini et al., 2003).

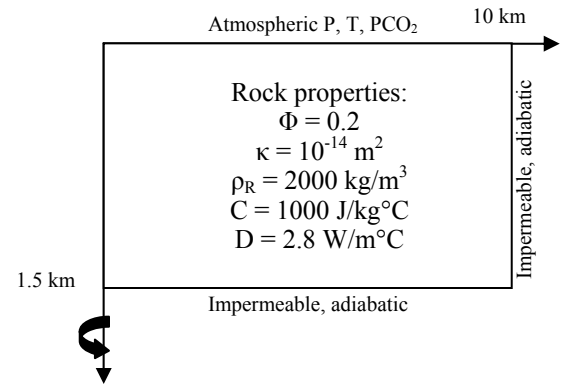


Figure 1. Computational domain and rock properties used in the hydrothermal fluid circulation. Fluid inlet is placed at the bottom near the symmetry axis. Symbols are: Φ porosity, κ permeability, ρ_R rock density, C rock specific heat, D rock thermal conductivity.

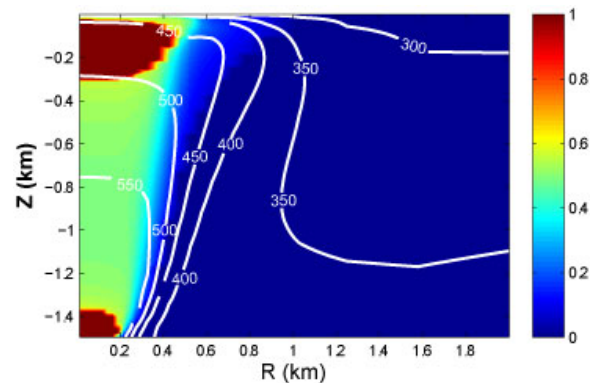


Figure 2. Gas volumetric fraction (color) and temperature distribution (contour) after the long-lasting injection of fluids. Two single phase gas zones are present in the domain (in red): near the inlet, and at shallow depth near the surface.

We are interested in the effects of a generic unrest to geophysical and geochemical observables. The unrest is simulated as a period (20 months) during which both the input of magmatic fluids and the CO₂ content increase (Table 1). The fluids are injected at the same, constant input enthalpy, corresponding to a temperature of 600 K. The unrest period is followed by a longer quiet period (100 months), during which the mass flow rate at the inlet returns to the initial lower values.

Table 1. Inlet conditions during the unrest and the following quiet period. The enthalpy does not change during the simulation and corresponds to a temperature of ca. 600 K.

	CO ₂ (ton/day)	H ₂ O (ton/day)	Molar ratio
Quiet	1000	2400	0.17
Unrest	6000	6100	0.40

The imposition of a larger discharge rate during the unrest is accompanied by pressure buildup and temperature changes. Also, the two-phase plume changes its shape and composition, owing to the different composition of injected fluids and the fact that pressure and temperature changes may enhance or reduce water evaporation. Detailed descriptions of the effect of the unrest on the two-phase plume can be found elsewhere (Rinaldi et al., 2009a, 2009b; Todesco, 2009; Todesco and Berrino, 2005; Todesco et al., 2003, 2004).

GEOPHYSICAL AND GEOCHEMICAL OBSERVABLES

As pointed out before, hydrothermal systems can generate a wide range of signals. Some observable parameters are directly related to fluid circulation and appear in the TOUGH2 output. Among these, we take into account in this work the amount and temperature of gas discharged at the surface. For other geophysical observables, a simple calculation is required. For example, it is possible to compute the compositional changes, considering the CO₂/H₂O molar ratio of the emitted gas. Such a calculation is made considering the average value of the molar ratio in the single-phase gas zone near the surface (Figure 2). Other observables can be derived from the TOUGH2 output, but require some postprocess calculation. Below, we present a background theory for electrical conductivity and gravity changes and ground displacement.

Background on Electrical Conductivity

Two main electrical conductivity mechanisms characterize the water-saturated porous medium. The first one is caused by the fluid flow inside the pore, through electromigration of anions and cations into the connected pore space. A second conduction mechanism occurs at the pore water-mineral interface, caused by a migration of the weakly adsorbed counterions (usually cations). We do not account for the effect of the electrical conductivity inside the grains, since measures performed on dry samples show very negligible values (Revil et al., 2002).

In this work, we follow the formulation of Revil et al. (1998) that takes into account the different behavior

of different charge carriers: cations and the anions. This formulation is based on the ‘‘Hittorf transport numbers,’’ which are the fraction of electrical current carried by the cations and anions in the free electrolyte. Similarly, it is possible to specify these numbers for surface conduction. Hittorf numbers are basically related to the ionic mobilities of the ions, and the electrical conductivity is given by combining the definitions of these numbers. Considering a solution with pH range 5–8, the counterions are mostly cations and the electrical conductivity is given by:

$$\sigma = \frac{\sigma_f}{F} \left[1 - t_{(+)} + F\xi + \frac{1}{2}(t_{(+)} - \xi) \left(1 - \frac{\xi}{t_{(+)}} + \sqrt{\left(1 - \frac{\xi}{t_{(+)}}\right)^2 + \frac{4F}{t_{(+)}}\xi} \right) \right] \quad (1)$$

where $F = \phi^{-m}$ is the electrical formation factor and represent the classical Archie’s law, confirmed by several works; ϕ is the medium porosity; and m is the cementation exponent. Since the commonly observed range of the cementation factor in rock is $3/2 < m < 5/2$, it is a good approximation to set $m = 2$. σ_f is the electrical conductivity of the pore fluid (in Sm^{-1}); depending upon the salinity of the fluid. $t_{(+)}$ is the Hittorf number for the cation in the electrolyte and represents the electrical current carried by the cations (Revil et al., 1998). ξ is the ratio between the surface electrical conductivity (σ_s) observed at the water-mineral interface and the pore fluid electrical conductivity (σ_f), observed in the pores.

The surface electrical conductivity can be written as a function of the distribution of the charge density per unit pore volume Q_V (in Cm^{-3}) and of the ionic mobility of the cations $\beta_{(+)}^f$ (in $\text{m}^2\text{s}^{-1}\text{V}^{-1}$):

$$\xi = \frac{\sigma_s}{\sigma_f} \approx \frac{\beta_{(+)}^f \bar{Q}_V}{\sigma_f} \quad (2)$$

In the case of fluid with NaCl, the ionic mobility is $\beta_{(+)} = 5.19 \cdot 10^{-8} \text{m}^2\text{s}^{-1}\text{V}^{-1}$ as shown by Revil et al. (1998). In the case of $\xi \ll 1$, as for high-salinity fluids, the electrical conductivity for a saturated porous medium can be approximated as follows:

$$\sigma = \frac{1}{F} (\sigma_f + \beta_{(+)} \bar{Q}_V) \quad (3)$$

Since there is no brine in our modeling of hydrothermal fluid circulation, we assume $\sigma_f = 0.1 \text{Sm}^{-1}$, to enhance the effect of the overall conductivity. This value is a good choice in the range of pure water conductivity (0.01Sm^{-1}) and water with high salinity (1Sm^{-1}).

The above formulation is valid for a saturated medium, but hydrothermal areas are often characterized by the presence of two immiscible or two-phase fluids occupying the pore space of the medium. The case we develop below is valid for two-phase fluids: the liquid phase is the electrolyte wetting the mineral grains and the gas-phase is considered an insulating fluid. Considering the formulation for the saturated medium, the influence of the gas-phase upon electrical conductivity can be taken into account introducing the transformation proposed by Waxman and Smits (1968):

$$\begin{aligned}\phi^m &\rightarrow \phi^m S_w^n \\ \bar{Q}_V &\rightarrow \bar{Q}_V / S_w\end{aligned}\quad (4)$$

where n is the saturation (or second) Archie exponent (generally $n = m$) and S_w is the pore volume space fraction occupied by liquid phase. A pore completely saturated in the liquid phase will have $S_w = 1$. Considering $m = n = 2$, the electrical conductivity as a function of the water saturation is given by:

$$\sigma = \phi^2 S_w^2 \left(\sigma_f + \beta_{(+)} \frac{\bar{Q}_V}{S_w} \right) \quad (5)$$

The presence inside a pore of a gas phase (like water vapor or CO_2), considered nonwetting and insulating, will increase the electrical conductivity at the pore surface.

For a variety of rock types, there is a strong relationship (Jardani and Revil, 2009) between the charge density per unit pore volume (\bar{Q}_V) and the permeability of the medium k , expressed in m^2 :

$$\log_{10} \bar{Q}_V = -9.2 - 0.82 \cdot \log_{10} k \quad (6)$$

A strong connection between these two parameters is valid since there exists a dependence of both on the specific surface area of the porous material.

Typically, as shown in several paper (Revil et al., 1998; Roberts, 2002; Vaughan et al., 1993), the electrolyte and surface conductivities are temperature dependent. From laboratory measurements (Revil et al., 1998), a linear temperature dependence is valid, both for the ionic mobility and for the brine conductivity:

$$\begin{aligned}\sigma_f &= \sigma_f(T_0) [1 + \alpha_f (T - T_0)] \\ \beta_{(+)} &= \beta_{(+)}(T_0) [1 + \alpha_{(+)} (T - T_0)]\end{aligned}\quad (7)$$

where T_0 is the reference temperature (300 K), and the coefficients $\alpha_f \approx 0.023 \text{ K}^{-1}$, and $\alpha_{(+)} \approx 0.037 \text{ K}^{-1}$ are temperature independent.

Gravity Changes and Ground Displacement

As pointed out by Todesco and Berrino (2005), changes in average fluid density generate a detectable gravity signal. The effect of a density changes on

gravity is evaluated as a sum of the contribution of each gridblock of the computational domain. Todesco and Berrino (2005) calculate the vertical component of gravitational attraction on the surface at the symmetry axis as:

$$\Delta g_z = GV \Delta \rho_f \frac{z}{L^3} \quad (8)$$

where G is the gravitational constant, V is the gridblock volume, $\Delta \rho_f$ its average fluid density, z its depth, $L^2 = r^2 + z^2$ its distance from the top of the symmetry axis, and r is the gridblock radius.

The vertical ground displacement is calculated using a mathematical model based on the linear theory of thermo-poro-elasticity and a system of distributed equivalent forces. (A full description of the displacement arising from hydrothermal circulation can be found elsewhere—Rinaldi et al., 2009a.) Each gridblock is considered as a potential source of deformation; then, the final displacement can be computed as a sum of the contribution of each element of the grid. Considering as observation point the symmetry axis at the surface, we have for each block:

$$u_z = \frac{1+\nu}{3\pi\mu} \Delta\theta V \frac{z}{R^3} \quad (9)$$

where $\Delta\theta = \Delta p/H + \alpha_s \Delta T$ represents the dilatation (compression) of the grid element. V and z are the volume and depth of the element. R is the distance of the observation point from the element. We use the following mechanical properties: $1/H = 1/K - 1/K'_s$ is the Biot's constant ($K = 5 \text{ GPa}$ is the isothermal, drained bulk modulus and $K'_s = 30 \text{ GPa}$ is the bulk modulus of the solid constituent), $\mu = 2 \text{ GPa}$ is the rigidity, $\nu = 0.25$ is the Poisson's ratio, and $\alpha_s = 10^{-5} \text{ K}^{-1}$ is the volumetric expansion coefficient.

Other approaches for ground deformation computing can be found elsewhere (Hurwitz et al., 2007; Hutnak et al., 2009; Todesco et al., 2004). In this work, we consider variation computed with respect to the initial steady-state condition.

RESULTING OBSERVABLES

In this section, temporal evolution and radial distribution of several observables deriving from the simulated hydrothermal fluid circulation will be analyzed.

Electrical Conductivity

We use Equation (5) to compute the electrical conductivity for each gridblock. The result is an electrical conductivity map over the entire domain, although a real measurement generally does not reach a depth of 1.5 km. Even if such a measurement were possible, the results are often biased, since a highly conductive layer (such as clay) may underestimate the conductivity in a deeper layer. However, we can

evaluate the electrical conductivity effect deriving from changes in water saturation and temperature at depth.

Since we are interested in studying the effect of a disturbance, we calculate the electrical conductivity with respect to the initial steady-state value, rather than the absolute values. Figure 3 shows the electrical conductivity changes at the end of the unrest period (20 months of simulation).

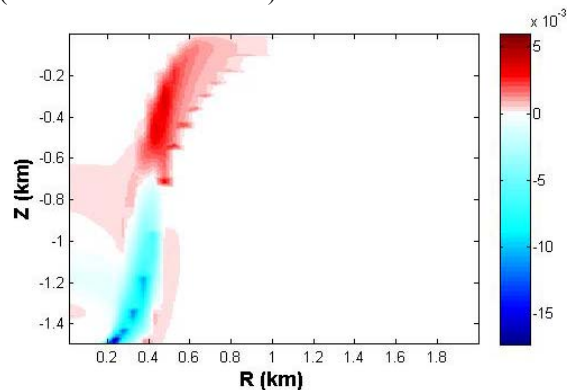


Figure 3. Changes in electrical conductivity (S/m) at the end of the unrest period (20 months).

The conductivity map presents some negative changes at depth (up to -0.015 S/m) near the inlet of magmatic fluids. Here, the gas phase, arising from the increased degassing, replaces the water-fluid phase. However, the temperature increases near the fluid source, beyond which there is also little increase in conductivity (0.001 – 0.002 S/m) at 400 m from the symmetry axis. The displaced fluids move toward the surface, after which we observe an increase in conductivity (up to 0.005 S/m) at shallower depth. Since most changes in temperature and water saturation happen at the border of the two-phase plume, electrical conductivity changes mainly at that location. Some minute changes occur inside the plume, which can be explained by considering the small front of condensation (for positive changes) or evaporation (negative changes).

The electrical conductivity changes at the end of simulation are shown in Figure 4. Also, in this case the changes are mostly confined to the border of the plume; however, at the end of the simulation, the two-phase plume is larger, and we observe mainly negative changes (-0.005 S/m). Some positive variations (0.002 S/m) are still present at shallower depth, caused by fluids movements, and at depth near the inlet, where heating persists at the end of simulation.

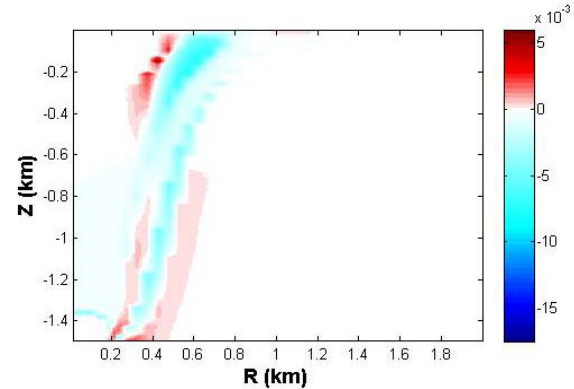


Figure 4. Changes in electrical conductivity (S/m) at the end of the simulation (120 months).

Temporal Changes

Analyzing the temporal trend of observable changes is essential for hazard evaluation. The temporal evolution of ground displacement, calculated at the surface on the symmetry axis, is shown in Figure 5 (line). Displacement presents an uplift at the beginning of the disturbance, as soon as the injection rate at the inlet is increased. Uplift reaches the maximum value (9 cm) at the end of the event. The quiet period is characterized by a slow subsidence that reflects the lower inflow of magmatic fluids at the inlet. The minimum ground elevation (-1 cm) is reached at the end of the simulation.

Figure 5 also shows the temporal evolution of the gravity changes caused by changes in average fluid density (dashed line). A positive trend characterizes the changes in gravity at the beginning of simulation, due to an increase in the average fluid density. The maximum value (40 μ Gal) is reached at the end of the unrest (20 months). As the simulation continues, the average fluid density declines, because the average gas fraction increases within the system. Then, gravity reaches a minimum value of -160 μ Gal at 80 months. Afterward, liquid water flows back toward the two-phase plume, after which the gravity changes begin again. When the simulation is over, a negative change of -100 μ Gal is still present.

The temporal evolution for the $\text{CO}_2/\text{H}_2\text{O}$ molar ratio and the emission temperature of the discharged gases at the surface are shown in Figure 6. The ratio is calculated as an average value of the shallow single-phase gas zone. When the disturbance begins, the molar ratio does not suddenly change, because the injected fluids spent some time before reaching shallower depth. The CO_2 -rich fluids injected during the disturbance period reach the surface (and modify the gas composition observed) only after a characteristic time, which depends on the flow rate at the source, the system geometry, and the rock permeability (Todesco, 2009).

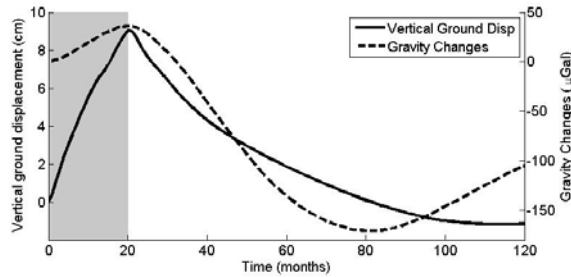


Figure 5. Temporal evolution of vertical ground displacement (line) and gravity changes (dashed line) at the symmetry axis. Shaded area represents the unrest period.

The $\text{CO}_2/\text{H}_2\text{O}$ molar ratio (Figure 6, line) reaches its maximum value (0.33) after 32 months of simulation. Afterward, the CO_2 content declines again, reflecting lower enrichment during the quiet period. At the end of simulation, the molar ratio reaches a value lower than steady-state.

Changes in emission temperature of discharged gas are also associated with the disturbance, despite their very low magnitude. The temporal evolution (Figure 6, dashed line) shows two local maximum. The first one corresponds with fluid arrival at the surface; it occurs at the same time (32 months) as the $\text{CO}_2/\text{H}_2\text{O}$ molar ratio maximum. A second maximum is attained at a later time (about 80 months), corresponding to an average heating of the system (see Rinaldi et al., 2009a).

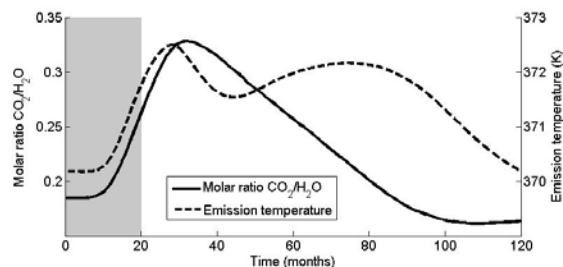


Figure 6. Temporal evolution of molar ratio $\text{CO}_2/\text{H}_2\text{O}$ (line) and temperature of discharged gas (dashed line). Shaded area represents the disturbance period.

Radial Changes

Radial pattern are also important in the observables analysis, since it would be useful to infer the extent of degassing zones. The degassing area can be easily related to the amount of discharged gases at the surface, but radial patterns in gravity changes may also play a role.

Figure 7 shows the radial distribution of the discharged gases and the gravity changes. The figure

is plotted at 32 months, which is when the $\text{CO}_2/\text{H}_2\text{O}$ molar ratio reaches its maximum value. From the amount of gas (Figure 7, line) we infer that the degassing area is about 500–600 m from the symmetry axis. We note that the maximum amount of discharged fluids (4 kg/s) is very low if compared with the amount of fluids injected at the inlet during the disturbance (140 kg/s).

Gravity changes are related to density changes, then, since these occur mostly at the border of the two-phase plume, a maximum (or minimum) in gravity changes will arise at a radial distance corresponding to the surface extension of the plume. Figure 7 (dashed line) shows a maximum of 150 μGal at a distance of about 600–700 m from the symmetry axis, almost the same value we can infer from the total gas flow.

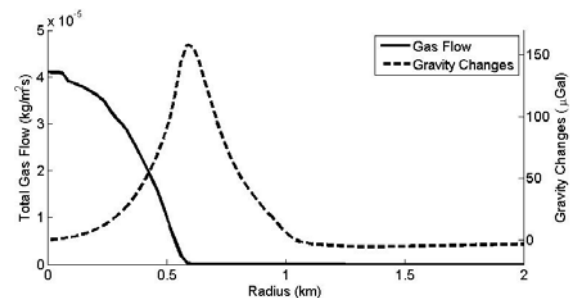


Figure 7. Radial distribution of gravity changes (dashed line) and amount of discharged gases at the surface (line) at $t = 32$ months, that is when the molar ratio $\text{CO}_2/\text{H}_2\text{O}$ reaches its maximum (Fig. 6).

The same analysis can be done at the end of the simulation. The results are much the same, as shown in Figure 8. The magnitude of total gas flow is one-half that of the disturbance period (2 kg/s), and we observe a very strong variation in gravity changes: the minimum value is about -500 μGal , due to a large quantity of gas near the surface.

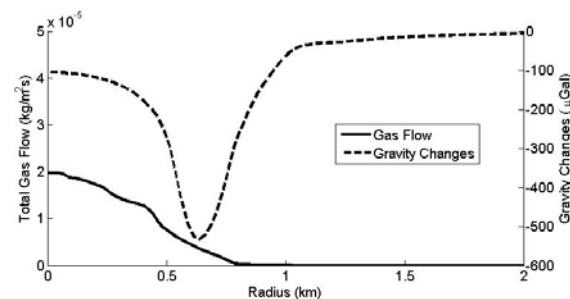


Figure 8. Radial distribution of gravity changes (dashed line) and amount of discharged gas at the surface (line) at the end of simulation (120 months).

Figure 9 shows the radial distribution of ground displacement calculated at different times. At the end of the disturbance (20 months, line in figure), the pattern of deformation looks like that of a Mogi-type, point source. The maximum uplift is right above the source and deformation vanishes within 4 km from the symmetry axis. A different pattern of deformation characterizes the subsidence. With time, changes in pressure and temperature become shallower along the border of the plume, then some spikes in displacement develop at 500-700 m from symmetry axis (Fig. 9, dashed line). At the end of simulation (Fig. 9, dot line), minor subsidence affects the axial region, and vertical displacement is mostly confined within 2 km from the symmetry axis.

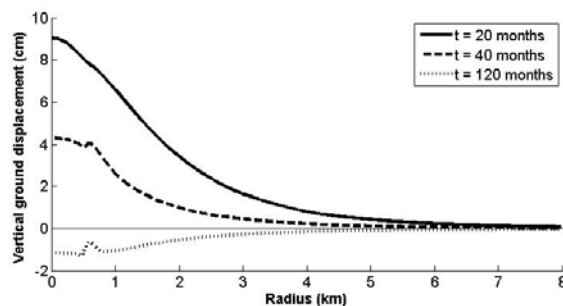


Figure 9. Radial distribution of vertical ground displacement at different time: 20 months (line), 40 months (dashed line) and 120 months (dot line).

CONCLUSION

Here we have presented an analysis of several geophysical and geochemical parameters. We have calculated the observables arising from changes in fluid circulation. The evolution of the hydrothermal system was simulated with the TOUGH2 numerical code (Pruess et al., 1999).

The evolution of the observables after a generic period of disturbance has been quantified and compared. Results show that increasing the fluid injection rate in our system (by a factor 3.5) results in measurable variations of surface signals.

The disturbance leads to a maximum uplift of the order of 10 cm, gravity changes up to 500 μGal and changes in electrical conductivity of the order of 10^{-2} Sm^{-1} . Changes in geochemical parameters were also observed, such as $\text{CO}_2/\text{H}_2\text{O}$ molar ratio, total gas flow at the surface and emission temperature of the discharged gas.

The studied parameters do not show always the same temporal evolution. Ground displacement and gravity changes react suddenly at the higher injection of magmatic fluids at the inlet, after which we can

easily discern when the disturbance is over. Other signals reach their maximum values after a characteristic time, depending on the flow rate at the source, the system geometry, and the rock permeability.

The evolution of the two-phase region over the entire simulation is associated with a complex pattern of variation along the surface, with peak values characterizing the edges of the plume. The extension of degassing area may subsequently be used as a benchmark for the measurements. Such an approach should emphasize the range of variations for several geophysical observables, such as electrical conductivity, gravity changes, and ground uplift.

An important result of this work is the analysis of the total gas flow through the ground surface. Although most of the observables present changes of the same order of magnitude as the observed variation, the values we found for the gas flow are underestimated compared to the measured changes in a real volcano, such as La Solfatara Volcano in the Campi Flegrei caldera (Italy). Such behavior may be explained by higher degassing at the bottom. However, the higher the fluid injection, the larger the observed signals at the surface. This difference in total gas flow may also mean that we are overestimating the gas dissolution in water, or that the gases may not redistribute in system in the same way we are simulating.

Although system properties and conditions strongly influence the calculated changes, our results support the importance of hydrothermal fluids in the surface changes of several geophysical and geochemical observables.

ACKNOWLEDGEMENT

The authors are grateful to A. Revil for helpful discussions. His comments greatly helped to improve this manuscript.

REFERENCES

- Aizawa, K., Y. Ogawa, and T. Ishido, Groundwater flow and hydrothermal systems within volcanic edifices: Delineation by electric self-potential and magnetotellurics, *J. Geophys. Res.*, 114(B01208), 2009.
- Bianco, F., E. Del Pezzo, G. Saccorotti, and G. Ventura, The role of hydrothermal fluids in triggering the July August 2000 seismic swarm at Campi Flegrei, Italy: Evidence from seismological and mesostructural data, *J. Volcanol. Geotherm. Res.*, 133, 229–246, 2004.
- Bonafede, M., Hot fluid migration: an efficient source of ground deformation: application to the 1982-1985 crisis at Campi Flegrei – Italy, *J. Volcanol. Geotherm. Res.*, 48, 187-198, 1991.

- Chiodini, G., M. Todesco, S. Caliro, C. Del Gaudio, G. Macedonio, and M. Russo, Magma degassing as a trigger of bradyseismic events: the case of Phlegrean Fields (Italy), *Geophys. Res. Lett.*, 30(8), 1434-1437, 2003.
- Finizola, A., A. Revil, E. Rizzo, S. Piscitelli, T. Ricci, J. Morin, B. Angeletti, L. Mocochain, and F. Sortino, Hydrogeological insights at Stromboli volcano (Italy) from geoelectrical, temperature and CO₂ soil degassing investigations, *Geophys. Res. Lett.*, 33(L17304), 2006.
- Hurwitz, S., L. B. Christiansen, and P. A. Hsieh, Hydrothermal fluid flow and deformation in large calderas: Inferences from numerical simulations, *J. Geophys. Res.*, 112(B02206), 2007.
- Hutnak, M., S. Hurwitz, S. E. Ingebritsen and P. A. Hsieh, Numerical models of caldera deformation: Effects of multiphase and multicomponent hydrothermal fluid flow, *J. Geophys. Res.*, 114(B04411), 2009.
- Jardani, A., and A. Revil, Stochastic joint inversion of temperature and self-potential data, *Geophys. J. Int.*, 2009.
- Pruess, K., C. Oldenburg, and G. Moridis, *TOUGH2 User's Guide, Version 2.0*, Report LBNL-43134, Lawrence Berkeley National Laboratory, Berkeley, Calif., 1999.
- Revil, A., L. M. Cathles III, S. Losh, and J. A. Nunn, Electrical conductivity in shaly sands with geophysical application, *J. Geophys. Res.*, 103(B10), 23925-23936, 1998.
- Revil, A., D. Hermitte, E. Spangenberg, and J. J. Cochemé, Electrical properties of zeolitized volcanoclastic materials, *J. Geophys. Res.*, 107(B8), 2002.
- Revil, A., et al., Inner structure of La Fossa di Vulcano (Vulcano Island, southern Tyrrhenian Sea, Italy) revealed by high-resolution electric resistivity tomography coupled with self-potential, temperature, and CO₂ diffuse degassing measurements, *J. Geophys. Res.*, 113(B07207), 2008.
- Rinaldi, A. P., M. Todesco, and M. Bonafede, Hydrothermal instability and ground displacement at the Campi Flegrei caldera, *Phys. Earth Planet. Int.*, 2009a.
- Rinaldi, A. P., et al., Heterogeneous hydrothermal system, *in preparation*, 2009b.
- Roberts, J. J., Electrical properties of microporous rock as a function of saturation and temperature, *J. App. Phys.*, 91(3), 2002.
- Todesco, M., Signals from the Campi Flegrei hydrothermal system: Role of a "magmatic" source of fluids, *J. Geophys. Res.*, 114(B05201), 2009.
- Todesco, M., and G. Berrino, Modeling hydrothermal fluid circulation and gravity signals at the Phlegrean Fields caldera, *Earth Planet. Sci. Lett.*, 240, 328-338, 2005.
- Todesco, M., G. Chiodini, and G. Macedonio, Monitoring and modelling fluid emission at La Solfatara (Phlegrean Fields, Italy). An interdisciplinary approach to the study of diffuse degassing, *J. Volcanol. Geotherm. Res.*, 125, 57-79, 2003.
- Todesco, M., J. Rutqvist, G. Chiodini, K. Pruess, and C. M. Oldenburg, Modeling of recent volcanic episodes at Phlegrean Fields (Italy): geochemical variations and ground deformations, *Geothermics*, 33, 531-547, 2004.
- Vaughan, P. J., K. S. Udell, and M. J. Wilt, The effects of steam injection on the electrical conductivity of an unconsolidated sand saturated with a salt solution, *J. Geophys. Res.*, 98(B1), 509-518, 1993.
- Waxman, M. H., and L. J. M. Smits, Electrical conductivities in oil-bearing shaly sands, *Soc. Pet. Eng. J.*, 8, 107-122, 1968.
- Zlotnicki, J., and Y. Nishida, Review on morphological insights of self-potential anomalies on volcanoes, *Surv. Geophys.*, 24, 291-338, 2003.

TOUGH2 MODELING OF COUPLED CO₂ FLUID FLOW AND HEAT TRANSFER IN GEOHERMAL RESERVOIRS WITH CO₂ AS WORKING FLUID

Jimmy B. Randolph, and Martin O. Saar

University of Minnesota
Department of Geology and Geophysics
e-mail: rando035@umn.edu

ABSTRACT

Ongoing research is examining the feasibility of using carbon dioxide (CO₂) as an alternative to water for the working fluid in geothermal energy capture. Utilizing CO₂ may permit more widespread implementation of geothermal power systems and has the benefit of negative greenhouse gas emissions through CO₂ sequestration. We present numerical simulations of coupled CO₂ fluid flow and heat transfer in geothermal reservoirs under conditions relevant for geothermal electricity generation. In particular, we examine reservoir cooling and pressure changes under a variety of CO₂ injection/production scenarios and reservoir characteristics.

MODELING OF HYDROLOGIC AND MAGMATIC INTERACTION AT MASAYA VOLCANO, NICARAGUA

S.C.P. Pearson ⁽¹⁾, C.B. Connor ⁽¹⁾, W.E. Sanford ⁽²⁾, K. Kiyosugi ⁽¹⁾ and H. Lehto ⁽¹⁾

⁽¹⁾University of South Florida, Dept. of Geology, 4202 East Fowler Avenue,
Tampa, Florida, 33620 USA

⁽²⁾U.S. Geological Survey, Mail Stop 431, Reston, Virginia 20192, USA
e-mail: spearson@mail.usf.edu

ABSTRACT

The interaction between magma and groundwater can play a pivotal role in volcanic eruptions. The location and style of this interaction is strongly affected by both the local and regional geological structures. By creating TOUGH2 models based on interpretations of magnetic data, and comparing model outputs with self-potential and CO₂ profiles, we were able to identify small-scale sealing faults dipping at 60° that redirect upward fluid flow. On a more regional scale, convection within the saturated zone along a 3–4 km fault on the flank of the Masaya Volcano can explain the diffuse degassing patterns seen at the surface. TOUGH2 models therefore allow us to improve understanding of the volcano-hydrologic system, its surface expressions, and its dominant controls, an understanding vital for improved eruption forecasting.

INTRODUCTION

Interaction between magma and groundwater is an important process in active volcanoes (Hurwitz et al., 2003). If magma heats groundwater directly, an initial phreatic eruption may occur before magma reaches the surface (e.g., Connor et al., 1996). In contrast, boiling of groundwater may create a hydrothermal system that can be in nonexplosive equilibrium with quiescently degassing magma for extremely long periods of time (Ingebritsen et al., 2006). Alternatively, direct interaction between groundwater and magma may result in violent phreatomagmatic eruptions (Morrissey et al., 2000). The Masaya Volcano in Nicaragua provides a natural laboratory for studies of long-term magma-groundwater interaction, because it is characterized by persistent, open degassing and a relatively shallow water table.

Synthesis of different datasets is necessary to provide a complete view of a shallow hydrothermal system, even on a local scale. Here, we create TOUGH2 models (Pruess, 1991) of the subsurface in an actively degassing area on the flank of Masaya Volcano, from interpretation of transient electromagnetic soundings (MacNeil et al., 2007) and magnetic profiles. We compare surficial model

outputs with CO₂ fluxes and self-potential (SP) measurements to deduce localized structures at Masaya Volcano. SP is a useful, if complex, indicator of fluid flux, because a negative SP anomaly is created by recharge of meteoric water (Sasai et al., 1997), and conversely, the interaction between moving pore fluid and the electric double layer at the pore surface generates an electric potential that causes a positive SP anomaly (Overbeek, 1952). CO₂ flux is a direct measure of flow of one component of fluid and may therefore be used as a proxy for the energy of the system (Chiodini et al., 2005). In low-temperature systems, this fluid generally results from boiling of the hydrothermal aquifer, although the porous medium through which the gases travel significantly affects the surface outflux (Chiodini et al., 1998; Evans et al., 2001; Lewicki et al., 2004).

We also created TOUGH2 models to attempt to understand the volcano-hydrologic system on a more regional scale. These models allow us to identify possible sources for diffuse degassing (fumarole) patterns observed within a 3–4 km fracture zone on the flank of Masaya Volcano. We can therefore determine configurations of the heat source at depth, valuable in understanding how the groundwater and magmatic systems are interacting and where. This, in turn, can greatly help in forecasting future volcanic eruptions, their magnitude, and their location.

MASAYA VOLCANO

Masaya Volcano is one of the most persistently active volcanoes in Central America (McBirney, 1956; Stoiber et al., 1986; Figure 1). It is located within 20 km of Managua, the capital city of Nicaragua, an area with over 2 million inhabitants. Large, explosive Plinian eruptions within the last 6,000 years (Williams, 1983; Wehrmann et al., 2006) have shown that it has the potential to impact Managua residents, their property, and their water resources (Johansson et al., 1998; MacNeil et al., 2007). The currently active (Santiago) crater has been the site of constant degassing since 1993 (Duffell et al., 2003; Stix, 2007) and has the largest reported noneruptive gas flux at any volcano (Stoiber et al., 1986; Horrocks et al., 1999; Burton et al., 2000;

Duffell et al., 2003). Gas flux and composition from the vent are very consistent (Horrocks et al., 1999) and imply a magma body of approximately 10 km^3 (Walker et al., 1993). The subsurface is highly fractured (Walker et al., 1993; Rymer et al., 1998; Williams-Jones et al., 2003).

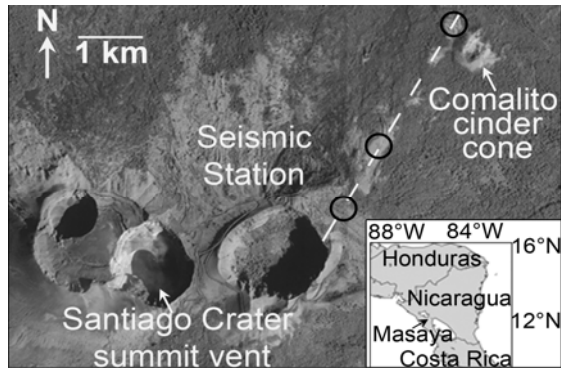


Figure 1. Aerial photograph showing the location of the study area on the flank of Masaya volcano. The dashed line represents the inferred fracture zone (Lewicki et al., 2003). Fumarole zones are highlighted by black circles. The inset is a map of the location within Nicaragua.

There is a subtle NE-trending fracture system extending 3–4 km from the summit crater to Comalito cinder cone, and beyond (Figure 1; Lewicki et al., 2003; Pearson et al., 2008). Elevated SP, CO_2 flux, and temperature suggest that this fracture zone is approximately 100 m wide. At least three distinct low-temperature ($\sim 65^\circ\text{C}$) fumarole zones occur along the fracture. The fumarole next to the Comalito cinder cone has some of the highest known carbon dioxide fluxes from low-temperature fumaroles, and the gases retain a magmatic component (Lewicki et al., 2003; St-Amand, 1998). This fumarole responds to changes in volcanic activity at the summit vents (Pearson et al., 2008).

These observations suggest that the hydrothermal system at Masaya Volcano is isolated within the Masaya caldera complex and is in equilibrium with the magmatic system. Vaporization of groundwater is on the order of 400 kg s^{-1} (Burton et al., 2000) and creates a hydrologic gradient about Santiago crater that causes flow of groundwater toward the volcano. The depth to the groundwater table is almost 250 m at Santiago crater and shallows to 50 m at Comalito cinder cone as a subdued reflection of topography (MacNeil et al., 2007). For the fumaroles along the fracture zone to respond to volcanic activity, this hydrologic system must be perturbed.

MODELING

The grid

We used the Petrasim interface to TOUGH2 to create models that simulate the interaction of a groundwater-air mixture with magmatic heat. We applied EOS3, using air as a simplified approximation of a magmatic gas heat source. The models comprised 900 cells over a regular 30×30 grid. As the data we were attempting to replicate were collected along profiles, we used only two dimensions, a reasonable assumption for the fault system. To represent fluid flow through a vertical fracture, we took advantage of the TOUGH2 code's ability to include the effect of gravity, and the negative z-direction corresponded to depth. The y direction was one unit cell width. Other parameters (Table 1) were inferred from previous studies by Chiodini et al. (2005), MacNeil et al. (2007), or are typical values for fractured basalt. The models were run for an infinite number of time steps over 3×10^9 s, or approximately 250 years, the last time that the fracture zone saw surface eruptive volcanic activity, and therefore a major change in its configuration.

Table 1. Parameters used in TOUGH2 models.

Parameter	Value	Units
Density	2000	kg/m^3
Porosity	0.3	
Wet heat conductivity	1.49	W/mC
Specific heat	840	J/kgC
Permeability of fumarole rock	1×10^{-13}	m^2
Permeability of fault	1×10^{-300}	m^2
Permeability of fractured rock	1×10^{-10}	m^2

LOCALIZED MODEL OF FUMAROLE ZONE

Magnetic profiles collected over a $150 \text{ m} \times 100 \text{ m}$ area at the middle fumarole zone on the flank of Masaya Volcano reveal a positive magnetic anomaly to the NW of the study area and a negative one to the SE (Figure 2a). Given that these are normally magnetized basalts of moderate magnetization, modeling shows that this could be explained by at least one dipping fault within the fumarole zone (Pearson et al., 2009 submitted; Figure 2a,b). SP and CO_2 profiles show an increase moving towards the SE, and then a rapid decrease (Figure 2b,c). One fault dipping at 60° would result in just one very high, single peak in both datasets, in contrast to the more gradual, and more numerous, peaks observed in the data. Therefore, TOUGH2 was used to create a more detailed model, where the effects of both groundwater and volcanism could be included to attempt to better replicate the data.

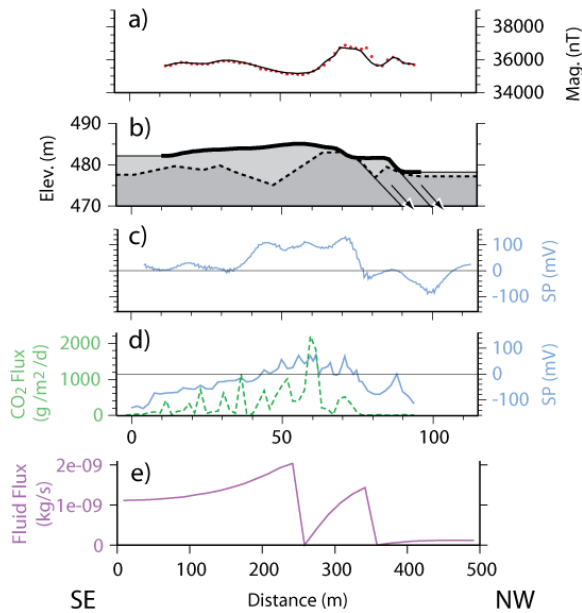


Figure 2. Geophysical data used to develop boundary conditions for Tough2 models. a) Observed magnetic anomaly (red dots) and calculated magnetic anomaly (solid line) used to infer geologic structure shown in (b). b) Light grey is a shallow, more permeable scoria layer. Arrows suggest the direction of fault slip in the layer below. c) SP profiles collected in 2004. d) SP (blue) and CO₂ (green) profiles measured nearby in 2006. e) Surface gas flux output from Tough2 model.

Method

To replicate the inferred faults within the fumarole zone, we included a second rock type that was relatively impermeable and created a barrier at approximately 60° to the surface. Although faults are generally seen as conduits, they can also serve as barriers to flow (Caine et al., 1996; Fairley et al., 2003; Marler and Ge, 2003). We propose that mineral precipitation, clay zones, and gouge along the faults have caused them to inhibit flow. Since all of the data collected were a reflection of the shallow system, only the vadose zone down to 250 m was considered. This was replicated by an equal mixture of air and water, with a single layer of air at the top to represent the surface. Different mixtures of air and water, and stratified variations in the proportions of each, were also modeled. Five hundred meters was encompassed in the models to cover the 100 m wide fault zone and the surrounding rock. The other boundary and initial conditions can be seen in Table 2.

Table 2. Conditions used in TOUGH2 models.

Parameter	Fumarole zone	Fracture zone
Length	500 m	3400 m
Depth	250 m	3400 m
Bottom BC	100°C 1.037 x 10 ⁵ Pa	100°C 3.29 x 10 ⁷ Pa
Top BC (fixed)	50% air 20°C 1.013 x 10 ⁵ Pa	100% water 20°C 1.013 x 10 ⁵ Pa
Vertical walls	No flow	No flow
Initial conditions	20°C Atmospheric pressure 50% air	20°C Hydrostatic pressure 100% water

The heat source below the fumarole zone is unconstrained. Other than the fact that magmatic gases are detected, nothing is known about the heat source and whether it is (a) magma directly below the fracture zone; (b) hot gases flowing from the crater; or (c) heat being transferred from the crater through the saturated zone. Therefore, we modeled three different bottom boundary conditions to represent these, all at 100°C: (a) heat injection; (b) air injection with an enthalpy of 1.509×10⁵ J/kg; (c) water injection with an enthalpy of 2.676×10⁶ J/kg. Rates of injection were determined experimentally by comparison with measured surface temperatures and gas fluxes.

Results

All of the models result in gases rising toward the surface and water sinking to the bottom (Figure 3). Since the temperatures are fixed at the top and the injection cells are at 100°C, the temperature profiles all look very similar. Fluid flux increases moving through the footwall toward the fault zone, becomes negligible in the fault zone, and increases again moving toward the next fault. Across the second fault, there is no fluid input at depth in the model, and a convection zone is developed in the hanging wall, which has much lower flux rates than those associated with rising hot fluids.

When heat is injected into the system at 1 J/s (Figure 3a) the maximum temperature is 90°C, and there is some circulation of water toward the faults. Air injection at 1×10⁻⁵ kg/s results in a maximum temperature of 42°C, but all of the water is driven out of the base of the model. Water injection at 5×10⁻⁷ kg/s results in a maximum, basal temperature of 100°C (Figure 3b). Both water and air rise towards the surface, but their flow is redirected along the faults. For both types of mass injection, higher rates result in unstable models.

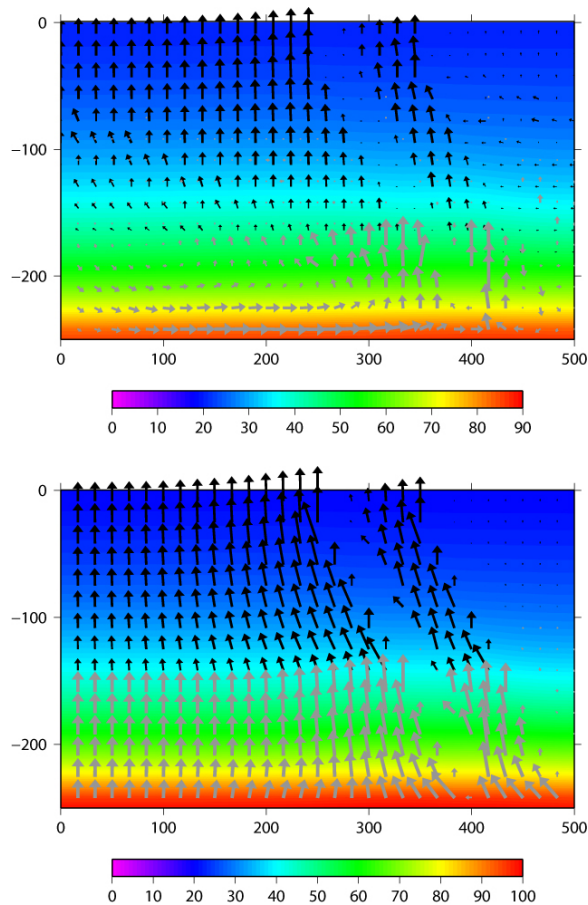


Figure 3. TOUGH2 model outputs showing injection of energy into an air-water mixture, with 2 relatively impermeable faults dipping SE at 60° . Black arrows represent gas flux, and gray arrows liquid flux. (a) heat injected at 1 J/s; (b) water injected at 5×10^{-7} kg/s. Gas flux is scaled by a factor of 200 and 500 respectively for comparison.

A thin, more permeable gravel layer, as suggested by magnetic modeling, inhibits and complicates flow very shallowly. With varying proportions of air and water, the circulation of water varies, but the gas flux at the surface remains essentially unchanged. When a stratified mixture of air and water is used to replicate the vadose zone, with all water at the bottom decreasing gradually to no water at the surface, flow at the surface is inhibited, and small pockets of air become trapped within convection cells of water at depth.

Discussion

The TOUGH2 models show an increase in gas flux moving towards the faults, with a decrease over them (Figure 3). This is in excellent agreement with the SP and CO_2 profiles (Figure 2). Therefore, low-

permeability fault models of the area appear to be supported, with more than one relatively impermeable fault dipping at 60° . These seal upward flow and redirect it along the underside of the fault.

The TOUGH2 models provide some constraints on the temperature source at depth. If air or another hot gas is injected, water is driven out of the base of the model, essentially drying out the system, which we do not observe. Injecting heat into the base of the model does result in feasible temperatures and the correct geometry of gas flux. This could correspond to very shallow magma, something that is unlikely in this system, or conduction of heat from the saturated zone. When hot water is injected into the shallow system, representing transfer of heat through the saturated zone, the surface gas flux again has the correct geometry, and the flux is twice that of injecting heat. This therefore seems more likely. To confirm the heat source and rates, drilling would be necessary, because the maximum temperature and water circulation at depth vary between the two models.

The magnetic model suggests a shallow scoria layer with a higher permeability. Our model shows that this does not produce the observed surface gas flux. Therefore, a distinct shallow layer, if present, must have a much more gradual permeability boundary with the host rock below. Varying the proportions of air and water within the system does not make a significant difference to surface gas flux; thus, we cannot use soil-moisture-content data to further refine the models. However, the TOUGH2 models show that air content is not systematically increasing approaching the surface, which is not likely anyway because of inhomogeneities within the subsurface.

REGIONAL MODEL OF FRACTURE ZONE

The distance between the Santiago Crater and the Comalito Cinder Cone along the fracture zone is approximately 3,400 m (Figure 1), and TEM soundings have detected the water table at between 51 and 59 m depth (MacNeil, 2007). The three fumarole areas are spaced irregularly along the fracture zone. There are two primary ways to focus these gases along the fracture: (1) localized heat sources at depth; or (2) convection along the fracture. Field observations provide some clues as to which is the more likely mechanism, but TOUGH2 models help to refine these theories.

Method

We created models using the parameters in Table 1 and conditions in Table 2, with variable injection along the bottom boundary. Since the depth to the heat source is unknown, a square grid of 3,400 m was

used for simplicity for models of the saturated zone. All models were homogeneous.

Two different models were tried to replicate localized heat sources at depth. The first included only the vadose zone, with depth down to 55 m and length of 3,400 m. This was similar to the fumarole models, with an equal mixture of air and water, but a layer of air at the surface. Water was injected at 100°C at three points along the bottom. The other model injected heat at 3 distinct points at the bottom of the saturated zone.

To see if convection occurs and could produce the configuration of heat and gas flux observed along the fracture, we created a uniform heat source along the bottom boundary. Heat was injected at different rates along the bottom of the saturated zone with a cell temperature of 100°C.

Results

When hot water is injected into the bottom of the vadose zone at 1 kg/s, hot plumes rise directly to the surface (Figure 4). However, this only occurs when the other cells of the bottom boundary condition are fixed at 20°C. When they are allowed to vary naturally, heat dissipates. When heat is injected at three distinct points into the base of the saturated zone at 20 000 J/s, three plumes develop with a maximum temperature of 74.5°C. Higher rates result in hotter plumes, and lower rates result in plumes that are too cool or do not even reach the surface.

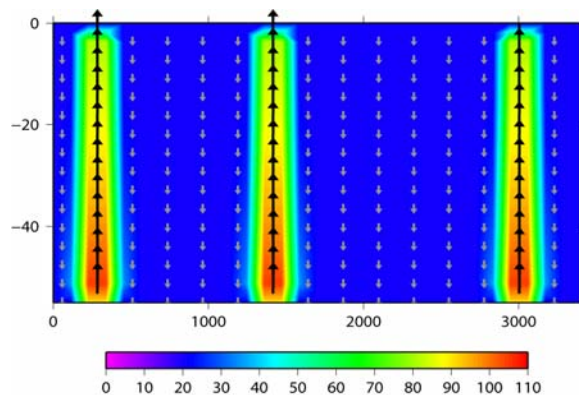


Figure 4. TOUGH2 model output showing hot water injected into a homogeneous air-water mixture to try to recreate the three fumarole zones observed from vadose zone circulation. Water (gray arrows) and gas (black arrows) rise along plumes and sink between them.

Injecting heat at 1667 J/s uniformly along the base of the model results in convection within the system. This creates three distinct zones of elevated

temperature and fluid flux (Figure 5). The maximum temperature is 65°C. Variations in injection rate result in differences in maximum temperature and in the number of plumes created.

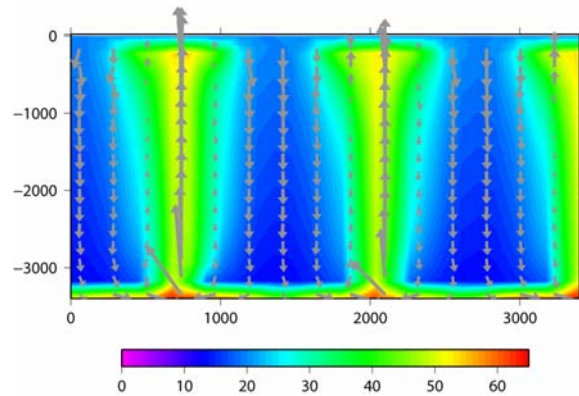


Figure 5. TOUGH2 model output showing heat injected uniformly along the base of the saturated zone. Three plumes still arise.

Discussion

Causes of fumarole zones

TOUGH2 models reveal that the most likely source for the three distinct fumarole zones is convection within the saturated zone. If the base of the vadose zone is kept cold in all but three zones, the elevated surface fluid flux and temperature could be a simple reflection of variations in fluid flux at depth. However, even given this unlikely scenario, CO₂ surveys at the fumarole zones on the flank of Masaya Volcano show that all three zones have fluxes of between 2,000 and 2,255 g m⁻² day⁻¹ that are remarkably consistent over extended periods of time. It is unlikely that all three zones would have entirely separate sources but the same surface gas fluxes. When the saturated zone is included, a comparison with the convective model shows that although three distinct sources create three plumes of heat and gas flux, the more simple uniform heat source also does. Therefore, it is more likely that there is one source, and that convection within the saturated zone is causing the fumarole zones observed at the surface.

With a constant heat source at depth, convection can develop in groundwater or in gases above the water table. The development of convection cells depends on the Rayleigh number, in porous media given by [Zhao et al., 2003]:

$$Ra = \frac{(\rho_0)^2 c_p g \beta \Delta T k_0 H}{\mu \lambda_0} \quad [1]$$

Substituting values appropriate for Masaya Volcano, found in Table 3 (Chiodini et al., 2005, MacNeil et al., 2007, and Zhao et al., 2003):

$$Ra = \frac{0.6^2 * 2000 * 9.81 * 7 \times 10^{-4} * 80 * 1 \times 10^{-10} * 55}{1.2 \times 10^{-5} * 1.43}$$

The Rayleigh number is 0.13 for gases within the vadose zone. The critical Rayleigh number is given by [Zhao et al., 2003]:

$$Ra_{critical}^{2D} = \frac{[1 + (H_3/H_2)^2]^2 \pi^2}{(H_3/H_2)^2}$$

$$Ra_{critical}^{3D} = \frac{[1 + (H_3/H_1)^2 + (H_3/H_2)^2]^2 \pi^2}{(H_3/H_1)^2 + (H_3/H_2)^2}$$

where H_1 is the length of the fracture, H_2 is its thickness, and H_3 its height. In this case the fracture is 100 m long, 3,400 m wide (as we are studying circulation dynamics along the fracture and not across it) and the depth to the water table (taken as the limit of the circulation regime) is 55 m. The critical Rayleigh number is 3.8×10^4 for the 2D case and 55 for the 3D case. Therefore, gases circulating within the vadose zone in the fracture will not advect. Even including a 50% mixture of water, the Rayleigh number is 8.8×10^3 , and so heat will be transferred by conduction rather than advection. If the saturated zone is included, the Rayleigh number is 1.6×10^5 . However, the critical Rayleigh number drops to 40 for the 2D case and 1.2×10^4 for the 3D case. Therefore, convection will readily occur within a saturated zone 3,400 m \times 3,400 m with a temperature difference of 80°C across it.

Table 3. Properties used in Equation (1). Where there are two values listed, the first is for water and the second for steam.

	Parameter	Value water / steam	Units
λ_0	Thermal conductivity	1.43	W/m°C
H	Depth to Water Table	55	m
k_0	Intrinsic Permeability	1×10^{-10}	m^2
c_p	Specific heat	4185 / 2000	J/kgK
ρ_0	Fluid density	1000 / 0.6	kg/m^3
β	Thermal expansion coefficient	$2 \times 10^{-4} / 7 \times 10^{-4}$	K^{-1}
μ	Dynamic viscosity	$1 \times 10^{-3} / 1.2 \times 10^{-5}$	Ns/m ²

The effect of permeability

Permeability is an extremely important factor in controlling fluid flow in faulted volcanic terrains (Todesco, 1995; Caine et al., 1996; Evans et al., 2001; Manzocchi et al., 2008). In our models, a homogeneous fracture is assumed, with a permeability of $1 \times 10^{-10} m^2$. If the lower permeability of the fumarole zone is used, it inhibits flow and prevents convection. However, it is likely that the bulk permeability is higher in this fracture than it is within the fumarole zone, where surrounding, unfractured rock is also included in the models. Caine et al. (1996) show that the response of fluid flux also depends on geometry of a fault or fracture zone. Where the damage width of a fault is negligible compared to its total width, strain is localized and flow is inhibited. In contrast, a damage width close to the total width of the fault causes strain to be evenly distributed and the fault to act as a conduit. It is therefore entirely possible that (in addition to permeability variations) the geometry of the fault and fracture zones is causing the difference in fluid flow.

There is some evidence, both conceptual and observational, for lateral heterogeneities along and within the fracture. Magnetic and GPR measurements suggest that there are faults within the 100 m wide fracture zone at various points along its length, which may seal or channel flow, and that the fracture dimensions vary along its length. Previous work by Méheust and Schmittbuhl (2001) and Neuville et al. (2006) have shown that fracture roughness can enhance or inhibit flow, but have not shown it to cause the strength of fluid flux variations that we observe at Masaya. As seen in the fumarole modeling, faults can focus flow into an area, but do not prevent flow on the scale seen at Masaya. Permeability can vary by several orders of magnitude within a fault (Manzocchi et al., 2008), and can form low-permeability zones with channels of high permeability (Marler and Ge, 2003; Fairley et al., 2003), but to create three distinct and comparatively strong zones of elevated flux at the surface, very specific heterogeneities would be required. The fault and fracture systems at Masaya Volcano are more extensive and less focused, suggesting that although heterogeneities are playing a role in channeling groundwater and gas flow, they are not the dominant factor.

CONCLUSION

TOUGH2 models are in excellent agreement with geophysical observations suggesting that within the central fumarole zone at Masaya Volcano, there are multiple shallow faults dipping at 60°. These faults channel flow through the hanging wall and inhibit flow across the faults to the footwall. TOUGH2

models show that flow of hot gases does not cause the temperature or fluid flux distribution observed, and therefore flow of hot water or heat from the saturated zone is the most likely cause of our surface observations. Magnetic models suggest a distinct, shallow, more permeable layer but TOUGH2 models show that this would inhibit gas flow and not result in the surface fluid flux distributions we observe. Therefore, a much more gradual change in permeability must occur across the different layers.

Within the fracture zone linking the active crater with the fumarole zones, TOUGH2 models show that convection within the saturated zone can create distinct fumarole zones, even with a constant, uniform heat source at depth. The three fumarole zones observed at Masaya Volcano may therefore be the result of injection of heat at 1667 J/s into the base of a 3400 m deep saturated zone, causing convection within the saturated zone.

TOUGH2 models are found to be a powerful tool to improve understanding of the hydrothermal system at both the regional and the local scales, particularly when combined with geophysical measurements. Knowledge of the geological controls on fluid flow help us to understand any changes in fumarole activity in relation to changes within the volcanic and hydrologic systems as a whole.

ACKNOWLEDGMENTS

We are grateful to staff at Instituto Nicaraguense de Estudios Territoriales. Field assistance from students from the University of South Florida Volcanology field class and from the Centro de Investigaciones Geocientíficas at the National Autonomous University of Nicaragua are also gratefully acknowledged.

REFERENCES

Burton, M. R., C. Oppenheimer, L. A. Horrocks, and P. W. Francis, Remote sensing of CO₂ and H₂O emission rates from Masaya Volcano, Nicaragua, *Geology*, 28(10), 915-918, 2000.

Caine, J. S., J. P. Evans, and C. B. Forster, Fault zone architecture and permeability structure, *Geology*, 24(11), 1025-1028, 1996.

Chiodini, G., R. Cioni, M. Guidi, B. Raco, and L. Marini, Soil CO₂ flux measurements in volcanic and geothermal areas, *Applied Geochem.*, 13(5), 543-552, 1998.

Chiodini, G., D. Granieri, R. Avino, S. Caliro, A. Costa, and C. Werner, Carbon dioxide diffuse degassing and estimation of heat release from volcanic and hydrothermal systems, *J. Geophys. Res.*, 110, B08204, 2005.

Connor, C. B., S. Lane-Magsino, J. A. Stamatakos, R. H. Martin, P. C. LaFemina, B. E., Hill, and S. Lieber, Magnetic surveys help to reassess volcanic hazards at Yucca Mountain, Nevada, *Eos Trans. AGU*, 78, 73-78, 1996.

Duffell, H. J., C. Oppenheimer, D. M. Pyle, B. Galle, A. J. S. McGonigle, and M. R. Burton, Changes in gas composition prior to a minor explosive eruption at Masaya Volcano, Nicaragua, *J. Volcanol. Geotherm. Res.*, 126(3-4), 327-339, 2003.

Evans, W. C., M. L. Sorey, B. M. Kennedy, D. A. Stonestrom, J. D. Rogie, and D. L. Shuster, High CO₂ emissions through porous media: transport mechanisms and implications for flux measurements and fractionation, *Chem. Geol.*, 177, 15-29, 2001.

Fairley, J., J. Heffner, and J. Hinds, Geostatistical evaluation of permeability in an active fault zone, *Geophys. Res. Lett.*, 30(18), 1962, 2003.

Horrocks, L., M. Burton, P. Francis, and C. Oppenheimer, Stable gas plume composition measured by OP-FTIR spectroscopy at Masaya Volcano, Nicaragua, 1998-1999, *Geophys. Res. Lett.*, 26(23), 3497-3500, 1999.

Hurwitz, S., K. L. Kipp, S. E. Ingebritsen, and M. E. Reid, Groundwater flow, heat transport, and water table position within volcanic edifices: implications for volcanic processes in the the Cascade Range, *J. Geophys. Res.*, 108, 2003.

Ingebritsen, S. E., W. E. Sanford, and C. E. Neuzil, Groundwater in Geologic Processes, *Cambridge University Press, Cambridge*, 2006.

Johansson, P.-O., C. Sharp, T. Alveteg, and A. Choza, The Framework for Ground Water Protection – the Managua Ground Water System as an Example, *Ground Water*, 37(2), 1998.

Lewicki, J. L., C. Connor, K. St-Amant, J. Stix, and W. Spinner, Self-potential, soil CO₂ flux, and temperature at Masaya Volcano, Nicaragua, *Geophys. Res. Lett.*, 30(15), 4, 2003.

Lewicki, J. L., G. E. Hilley, and C. Connor, *The scaling relationship between self-potential and fluid flow on Masaya volcano, Nicaragua*, in: Wanty, R. B., and R. R. Seal II (ed), *Water-Rock Interaction*, Taylor and Francis Group, London, 153-156, 2004.

- MacNeil, R. E., W. E. Sanford, C. B. Connor, S. K. Sandberg, and M. Diez, Investigation of the groundwater system at Masaya Caldera, Nicaragua, using transient electromagnetics and numerical simulation, *J. Volcanol. Geotherm. Res.*, 166(3), 217-232, 2007.
- Manzocchi, T., A. E. Heath, B. Palanathakumar, C. Childs, and J. J. Walsh, Faults in conventional flow simulation models; a consideration of representational assumptions and geological uncertainties, *Petroleum Geosci.*, 14, 91-110, 2008.
- Marler, J., and S. Ge, The permeability of the Elkhorn Fault Zone, South Park, Colorado, *Ground Water*, 41(3), 321-332, 2003.
- McBirney, A. R., The Nicaraguan volcano Masaya and its caldera, *Trans. Am. Geophys. Union*, 37(1), 83-96, 1956.
- Méheust, Y., and J. Schmittbuhl, Geometrical heterogeneities and permeability anisotropy of rough fractures, *J. Geophys. Res.*, 106(B2), 2089-2102, 2001.
- Morrissey, M., B. Zimanowski, K. Wohletz, and R. Buettner, *Phreatomagmatic fragmentation*, Encyclopedia of Volcanology, Academic Press, 431-445, 2000.
- Neuville, A., Toussaint, R., and J. Schmittbuhl, Hydro-thermal flow in a rough fracture. In *EHDRA Scientific Conference*, Soultz-sous-Forêts, France, 2006.
- Overbeek, J. T. G., *Electrochemistry of the double layer*, in: Kruyt, H. R. (ed), Colloid Science volume 1: irreversible systems, Elsevier, Amsterdam, 115-193, 1952.
- Pearson, S. C. P., C. B. Connor, and W. E. Sanford, Rapid response of a hydrologic system to volcanic activity: Masaya volcano, Nicaragua, *Geology*, 36(12), 951-954, 2008.
- Pearson, S. C. P., K. Kiyosugi, J. A. Saballos, C. B. Connor, W. E. Sanford, and H. Lehto, (submitted), Geological controls on fluid flow at Masaya volcano, Nicaragua, *Bull. Volc.*
- Pruess, K., *TOUGH2 - A General Purpose Numerical Simulator for Multiphase Fluid and Heat Flow*, Report LBL-29400, Lawrence Berkeley Laboratory, Berkeley, CA, 1991.
- Rymer, H., B. van Wyk de Vries, J. Stix, and G. Williams-Jones, Pit crater structure and processes governing persistent activity at Masaya volcano, Nicaragua, *Bull. Volcanol.*, 59, 345-355, 1998.
- Sasai, Y., J. Zlotnicki, Y. Nishida, P. Yvetot, P. Morat, H. Murakami, Y. Tanaka, Y. Ishikawa, S. Koyama, and W. Sekiguchi, Electromagnetic monitoring of Miyake-jima volcano, Izu Bonin Arc, Japan: A Preliminary Report, *J. Geomag. Geoelectr.*, 49, 1293-1316, 1997.
- St-Amand, K., The distribution and origin of radon, CO₂ and SO₂ gases and multifractal behavior of SO₂ at Masaya volcano, Nicaragua, Master's thesis, Univ. de Montreal, 1998.
- Stix, J., Stability and instability of quiescently active volcanoes; the case of Masaya, Nicaragua, *Geology*, 35(6), 535-538, 2007.
- Stoiber, R. E., S. N. Williams, B. J. Huebert, M. Sato, S. Matsuo, and C. King, Sulfur and halogen gases at Masaya Caldera complex, Nicaragua; total flux and variations with time, *J. Geophys. Res.*, 91(B12), 12215-12231, 1986.
- Todesco, M., Modeling of the geothermal activity at Vulcano (Aeolian Islands, Italy), *Proc. of the World Geothermal Congress '95., Int. Geotherm. Ass., Firenze*, 2, 1309-1314, 1995.
- Walker, J. A., S. N. Williams, R. I. Kalamarides, and M. D. Feigenson, Shallow open-system evolution of basaltic magma beneath a subduction zone volcano: the Masaya Caldera Complex, Nicaragua, *J. Volcanol. Geotherm. Res.*, 56(4), 379-400, 1993.
- Wehrmann, H., C. Bonadonna, A. Freundt, B. F. Houghton, and S. Kutterolf, Fontana Tephra: a basaltic Plinian eruption in Nicaragua, *Volcanic Hazards in Central America, Geol. Soc. Amer. Special Paper*, 412, 209-223, 2006.
- Williams, S. N., Plinian airfall deposits of basaltic composition, *Geology*, 11(4), 211-214, 1983.
- William-Jones, G., H. Rymer, and D. A. Rothery, Gravity changes and passive SO₂ degassing at the Masaya caldera complex, Nicaragua, *J. Volcanol. Geotherm. Res.*, (123), 137-160, 2003.
- Zhao, C., B. Hobbs, H. Mühlhaus, A. Ord, and G. Lin, Convective instability of 3-d fluid saturated geological fault zones heated from below, *Geophys. J. Int.* 155, 213-220, 2003.

FUTURE DIRECTIONS IN GEOTHERMAL MODELING

Michael J. O'Sullivan

Department of Engineering Science
University of Auckland, Auckland, New Zealand
e-mail: m.osullivan@auckland.ac.nz

ABSTRACT

The history of geothermal modeling is briefly reviewed, using a TOUGH2 model of Wairakei (New Zealand) as an example. The historical review provides the context for the development of a “wish list” for improvements in modeling technology. Matters discussed include: wellbore-reservoir interaction, surface features, groundwater levels, model calibration, very deep systems, fluid rock interaction, front-tracking, boiling zones, and chemistry.

GEOTHERMAL MODELING

The history of geothermal modeling goes back to the early 1970s (see O'Sullivan et al., 2001 and 2009, for more details). The starting point for the acceptance of numerical modeling by the geothermal industry was the 1980 Code Comparison Study (Stanford Geothermal Program, 1980). In that study, several geothermal simulators, including SHAFT79 (a predecessor of TOUGH2), were tested on a suite of six problems. The University of Auckland had an entrant in the Code Comparison Study that performed quite well, but we realized that the flexible grid structure and the ability to easily add new equations of state offered by MULKOM (the replacement for SHAFT79) made it superior to our code, and we have remained enthusiastic users of MULKOM and then TOUGH2 since the early 1980s.

Our modeling studies of Wairakei began in the early 1980s, at first with simple models (Blakeley and O'Sullivan, 1981, 1982), but by the late 1980s we had set up general 3-D models (see O'Sullivan et al., 2009). Most of the modifications we have made to TOUGH2 have resulted from our efforts to build bigger and better models of Wairakei. For example, we found that the original linear equation solver in MULKOM (MA28) could not handle a model with more than about 500 gridblocks. We therefore introduced conjugate gradient solvers (see Bullivant et al., 1991), which allow much larger models to be run. Conjugate gradient solvers were introduced into TOUGH2 at LBNL (Moridis and Pruess, 1998) and elsewhere at about the same time. We also carried out some work on the thermodynamics routines COWAT and SUPST to speed them up considerably.

Because of our interest in the Ohaaki geothermal system, which has high gas content, we developed an

equation of state (EOS) for mixtures of water and CO₂ (Zyvoloski and O'Sullivan, 1980; O'Sullivan et al., 1985). This became EOS2 in MULKOM, but was replaced in 1997 by an improved version developed by Battistelli et al. (1997).

From the mid 1980s until the present time, our model of Wairakei has grown from a small 3-D model of 301 gridblocks to large complex models of 10-30 K gridblocks (O'Sullivan and Yeh, 2007). This achievement was made possible by the effectiveness of TOUGH2, but the process has shown up areas where more research needs to be carried out and where further advances in modeling technology are desirable. These are discussed below.

WELLBORE – RESERVOIR INTERACTION

For modeling the future scenarios of geothermal systems, it is usual to operate each production well on deliverability, so that the production rate falls off as the pressure of the reservoir feed block declines. The simplest version of the deliverability formula available in TOUGH2 is

$$q_{\beta} = \frac{k_{r\beta}}{\nu_{\beta}} PI(p_{\beta} - p_{wb}) \quad (1)$$

Here, q_{β} is the mass production rate, $k_{r\beta}$ is the relative permeability, ν_{β} is the kinematics viscosity and P_{β} is the block pressure, all for phase β . PI is the productivity index, discussed in detail by Pruess et al. (1999), and P_{wb} is the flowing bottomhole pressure.

One of the difficulties with using (1) is the fact that for a fixed wellhead pressure, P_{wb} varies with the total mass flow q_m and the flowing enthalpy h_f . To accurately deal with this issue, it is necessary to couple a wellbore simulator with a reservoir simulator. This approach was taken by Hadgu et al. (1995) and Bhat et al. (2005), but has not been generally adopted, probably because the maximum time step permitted is likely to be controlled by wellbore processes and to be impractically small.

An alternative approach introduced by Murray and Gunn (1993) and also implemented in TOUGH2 (Pruess et al., 1999) is to generate a table of flowing bottomhole pressures defining the function below:

$$P_{wb} = f(q_m, h_f; P_{wb}, z, r_w) \quad (2)$$

In TOUGH2, this formula is implemented by an interpolation scheme based on tabular data pre-calculated with a wellbore simulator and read for a separate data file. We have used both (2) and a simplified version in the form

$$P_{wb} = f(h_f; P_{wb}, z, r_w) \quad (3)$$

This is implemented by reading in a table of values of P_{wb} vs h_f and using interpolation. The main use we have made of (3) is in ensuring that production wells in our Wairakei model are switched off when the feedzone enthalpy drops below 763.1kJ/kg (180°C).

A second difficulty with using (1) is that in many cases, geothermal wells have more than one feedzone. Again, the only way to model this situation accurately is to use a coupled wellbore-reservoir simulator. TOUGH2 offers an approximate method for modeling multifeed wells by means of the following formula for calculating the wellbore pressure in layer $l+1$ from that in layer l :

$$P_{wb,l} = P_{wb,l+1} + 0.5g(\rho_l^f \Delta z_l + \rho_{l+1}^f \Delta z_{l+1}) \quad (4)$$

Here, g is the acceleration of gravity and ρ_l^f is the flowing density in the well opposite layer l . The method used for calculating ρ_l^f is described by Pruess et al. (1999). The wellbore pressure at the deepest layer must be prescribed. At present the multifeed option cannot be combined with a rate and enthalpy-dependent P_{wb} defined by (2).

CONTROL OF PRODUCTION WELLS

We have introduced some minor modifications of the standard deliverability option in TOUGH2. The first option allows for the fact that a geothermal well may be operated in throttled state initially and then opened up over time. To represent this situation, the mass flow is calculated using

$$q_m = \min(q_{delv}, q_{max})$$

Here, q_{delv} is the mass flow calculated using (1), assuming that the well is fully open, and q_{max} is the target maximum flow. The flow restriction can be applied either to the total mass flow or to the total steam flow.

For most geothermal projects, as the total production from a group of wells falls away, make-up wells are introduced. We have included the automatic introduction of make-up wells as an option in TOUGH2. A group of wells is given "DMAK" as a well-type, the current wells are given a positive PI,

and the make-up wells are given a negative PI. The total mass flow (or steam flow) is compared with a target value, and when the total falls below 95% of the target, a make-up well is added. This process leads to a somewhat "saw-tooth" mass flow (or steam flow), oscillating above and below the nominated target. It would be useful to introduce a more sophisticated version of this make-up system that would produce a more constant total mass flow (or steam flow) and can handle the shutting down of make-up wells, if the reservoir pressure recovers as a result of the effects of injection or the condensation of steam zones.

Other options that would make TOUGH2 easier to use in simulating production for geothermal systems are: to be able to assign a particular well to a named separator, to be able to use a complex time schedule for wells on deliverability, and to be able to specify the separation process for each well (e.g., single flash, double flash, or binary plant). These options are not essential in terms of their effect on the reservoir behavior, but they would make it easier to carry out simulations of complex future scenarios without having to stop and restart the simulation several times.

LARGER, DEEPER MODELS

Almost all models of geothermal systems do not include the whole of the large-scale convective system. Thus, the base boundary condition must include some input of very hot water, corresponding to the upflow zone of the convective plume. It would be better to make the model large enough so that the whole convective system is contained in the model, and then the permeability structure would have to be compatible with the flow and temperature structure. We have recently moved somewhat in this direction with our model of Wairakei-Tauhara by adding extra layers, so that it is now 4 km deep. Probably more layers, extending the model down to 6–7 km, should be added and a larger area included.

The use of deeper models leads to the need for a thermodynamic EOS that can handle higher pressures and temperatures. We have implemented the IAPWS-97 thermodynamic formulation (Wagner et al., 2000), including the supercritical capability valid for pressures up to 100 MPa and temperatures up to 800°C (Croucher and O'Sullivan, 2008). This improvement allows for models of high temperatures and pressures to be used, provided that the fluid can be approximated as pure water. It would be very useful for models of other fields (such as Ohaaki and Ngawha) to have an EOS for mixtures of water, carbon dioxide, and sodium chloride that is accurate for temperatures and pressures ranging from atmospheric up to supercritical (pure water) conditions. This would require the extension of the

range of validity of the ECO2N fluid property module (Pruess, 2005).

Another EOS option that is required for modeling “gassy” geothermal fields such as Ohaaki and Ngawha, particularly in a carbon-conscious world, is one that can handle mixtures of water, air, and carbon dioxide. We have used a five-component EOS that can handle a mixture of water, methane, and air (broken down into its major components of N₂, O₂ and CO₂) for modeling coalbed methane extraction. Dropping the methane from this EOS would provide one possible approach, but the resulting module would include one more component than is really necessary.

MODEL CALIBRATION

The greatest challenge facing the geothermal modeling community is improvement in model calibration techniques. The calibration process involves two stages (O’Sullivan et al., 2001, Mannington et al., 2004).

- (i) Natural State Modeling
- (ii) History Matching

In natural state modeling, the permeability structure and location of the deep inflow are guessed, and then a simulation of the model to steady state is carried out. This steady state is assumed to be the natural or pre-exploitation state of the geothermal system that has developed over geological time (a concept that is open to some debate). Then the natural state temperature and the location of the surface outflows are compared to the measured data. If the match is not satisfactory, then adjustments are made to the permeability structure and deep inflows, and the process is repeated, possibly many times.

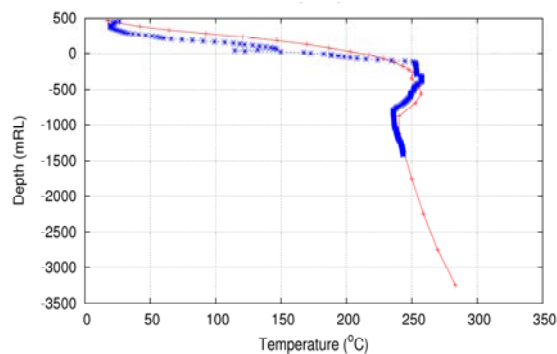


Figure 1. Natural state temperatures in one well for the Wairakei model (data - blue symbols, model - red line)

Once a reasonable natural-state model has been obtained (see Figure 1 for example), the results are used as the initial conditions for a simulation of the production and injection history, with the measured

mass flows being assigned to the appropriate model blocks. Then the pressure and enthalpy changes predicted by the model are compared to the data, and adjustments are made to the permeabilities and porosities to improve the model (Figures 2 and 3).

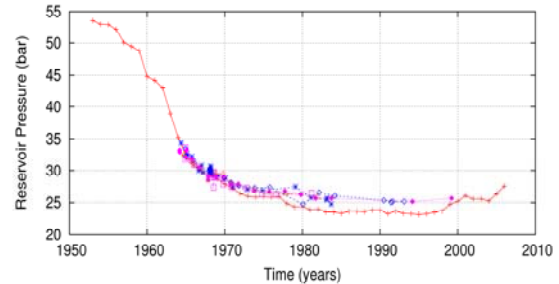


Figure 2. Pressure decline in the western borefield for the Wairakei model (data - blue symbols, model - red line)

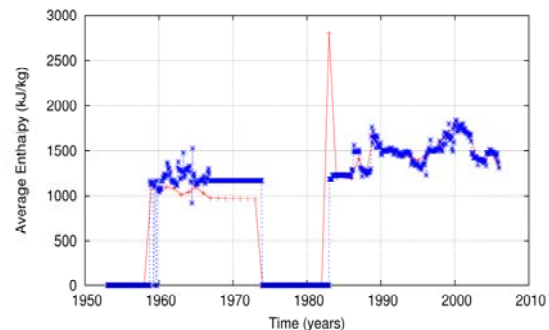


Figure 3. Enthalpy changes for one well in the Wairakei model (data—blue symbols, model—red line)

The process described above is appropriate for a convective geothermal system where the fluid is moving in the natural state. It is not so useful for warm water systems or hot dry rock systems, where conduction is the only heat-transfer mechanism and the reservoir fluid (hot water) does not move.

In hot water systems, the reservoir does not boil during production, and the production enthalpy does not change. However, in systems like Wairakei and Mokai (New Zealand), there is considerable boiling, and enthalpy changes are very useful for model calibration.

We have used three calibration techniques:

- (i) Manual calibration
- (ii) Inverse modeling with iTOUGH2 (Finsterle, 2007abc)
- (iii) Statistical sampling methods (Cui et al., 2007)

Suggestions for improving these methods will be discussed below.

Improved Manual Calibration

The basic idea of manual calibration is to determine where the model fit to the data is worst, and then to adjust the model structure to improve the fit. This is a slow process, because after each adjustment of the structure, the model must be re-run (possibly both the natural state and history match), and the results re-checked against the data. In some cases, it may not be obvious which reservoir parameters should be adjusted to improve the model, and then the skill and experience of the modeler can assist the process.

To speed up manual calibration and to make it less dependent on the modeler, an “expert system” approach may be useful—and this is one of our current research themes. The idea is to codify the various strategies followed by a modeler and to apply them in a systematic fashion. For example, in a natural state model, if block I is too hot, then the following steps should be followed:

- (i) Check flow directions for all connections between block I and other blocks.
- (ii) For flows into block I, if the neighboring block J is hotter, then decrease the permeability of block J. If block J is colder than block I, then increase the permeability of block J.
- (iii) Repeat for all blocks sending fluid into block I.

Several rules of this kind are currently used by modelers, but need to be formalized. There are many challenges to overcome in order to make such an expert system work, and there are several unanswered questions. For example: will it converge to a good solution in a reasonable time? It is worth noting that simple iterative methods for the numerical solution of Laplace’s equation, that have some similarities with the process described above, have a convergence rate that is dependent on the choice of a relaxation parameter.

Another problem with the process discussed above is the local nature of the adjustments proposed. In some cases it may be necessary to change the permeability over quite a large section of the model, in order to change the flow pattern sufficiently to achieve the required temperature change. In principle, it would be possible to track all streamlines entering the block in question and to adjust permeabilities along the streamlines.

With a scheme for local adjustment of permeabilities, based on fitting relatively sparse downhole temperatures, there is the problem of deciding whether to make a local or a global change. For example, if the rule suggests that rock-type IGNIM should have its horizontal permeability increased in block J, then should this change be implemented in all blocks with IGNIM as a rock-type? Or should a

new sub-rock-type IGNIX with a higher horizontal permeability be assigned to block J? Possibly both options should be tried, and the new rock-type IGNIX should only be accepted if it produces a substantially better result. That is, there should be some penalty discouraging fragmentation of the rock-types.

Improved Inverse Modeling

The basic idea of the inverse modeling approach, available through iTOUGH2 (Finsterle, 2007abc) for example, is to solve a nonlinear optimization problem. The unknowns are selected model parameters, and the objective function is the sum of squares of the difference between the model results and given data. What distinguishes inverse modeling of geothermal reservoirs from more traditional nonlinear optimization problems is the complexity of the calculation for the objection function, i.e., through the forward problem, which requires a TOUGH2 simulation.

The iTOUGH2 code is a very comprehensive package. It offers several optimization methods (Gauss-Newton, Levenberg-Marquardt, Downhill Simplex, Simulated Annealing, Grid Search) and very complete sensitivity analysis. Similar functionality has been achieved with the FEHM geothermal simulator (Zyvoloski, 1992) and the PEST inverse modeling code (Doherty, 2005). However, unanswered questions remain. Some are general and relate to the use of nonlinear least squares (see Fox, 2009). These will be discussed further in the next section.

Other problems are more specific to the application of iTOUGH2 to the calibration of geothermal models. In general, we have found iTOUGH2 to be a very useful tool for improving models that are already quite good. Conversely, if a model is not already fitting the data well, iTOUGH2 will probably not produce a model that is much better.

The difficulty with using iTOUGH2 (or any inverse modeling code) in calibrating a geothermal model is the choice of the variable parameters. At one extreme, each block in the model could be assigned different x, y, z permeabilities and porosities. This would result in a huge number of unknown parameters and is currently impractical. The simpler approach, and that which is usually used with iTOUGH2, is to assign a relatively small number of rock-types and then use the permeabilities and porosities of a subset of these rock-types as the parameters to be optimized. (See for example, Porras et al., 2007, Kiryukhin et al., 2008.) However, even if the optimal values for all parameters, for all rock-types, are determined by iTOUGH2, the resulting model is probably not going to be the best possible.

It might be possible to produce a better model by subdividing the zone assigned, say, to rock-type IGNIM into two new zones, labeled IGNIA and IGNIB, for example. Then iTOUGH2 could be re-run optimizing the parameters for IGNIA and IGNIB independently. We have had some success with this technique, but what is required is a more systematic approach with, say, an outer XiTOUGH2 code that controls the re-assignment of rock-types and calls iTOUGH2 to optimize parameter values for each new rock-type structure.

Statistical Sampling

As mentioned above, there are some fundamental problems with inverse modeling based on a least-squares-errors approach (see Fox, 2009). One difficulty is that a global optimum or even a local optimum found by a nonlinear optimization technique may not be a “good solution,” in the sense that the optimal parameter values may not be what a reservoir engineer expects or finds acceptable. What is really required is to identify a region of the multidimensional parameter space where good solutions are likely to be found. The statistical sampling tool for doing this is the multichain Monte Carlo (MCMC) technique (see Cui et al., 2006). The trouble with MCMC is that it requires a very large number of samples to be taken, or, in the context of geothermal modeling, a very large number of forward runs of TOUGH2 have to be carried out.

We have applied MCMC to calibrating a simple single-layer model using data from an extended test of a geothermal well. This is the same problem previously investigated with iTOUGH2 by Finsterle et al. (1997). We have also applied MCMC to a model of the Mokai geothermal system with some success. After two weeks of computation, the best natural state model produced by MCMC matches the downhole temperatures slightly better than the manually calibrated model.

Further advances with the MCMC technique are required to make it practically useful for calibrating geothermal models. Currently, we are investigating the use of a hierarchy of models ranging from a coarse grid to a fine grid, and we are investigating parallel rejection algorithms. As with inverse modeling techniques (e.g., iTOUGH2), MCMC is ideal for implementation on a cluster of computers in a distributed memory configuration. In the future, it may be possible to use a cluster of multicore processors, each running a parallelized version of TOUGH2 (see Moridis et al, 2008, Zhang et al, 2009).

None of the three methods discussed above can presently automatically deliver a well-calibrated model of a geothermal field.

FLUID-ROCK INTERACTION

At present, subsidence is a significant concern at the Wairakei-Tauhara geothermal field (Allis et al., 2009). To model subsidence, we have used temperature and pressure charges calculated with TOUGH2 as input for a rock-mechanics simulation using the ABAQUS package (ABAQUS, 2003). We had some success in matching the occurrence of the subsidence bowls (see Yeh and O’Sullivan, 2007). The results for the Wairakei bowl are shown in Figure 4.

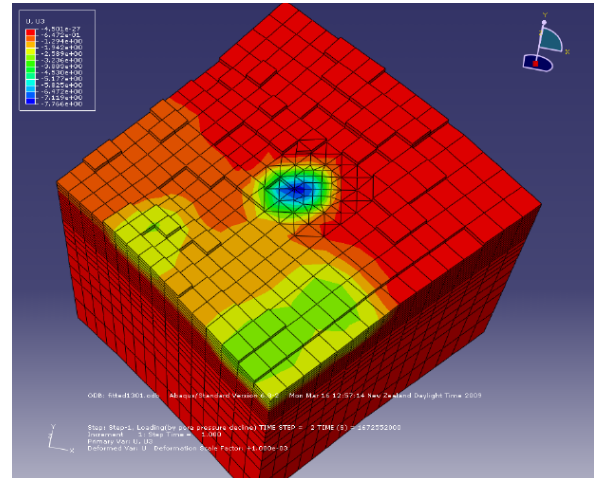


Figure 4. Model results for the Wairakei subsidence bowl.

The methods we have used for linking TOUGH2 and ABAQUS are very similar to those used by Rutqvist and Tsang (2003) and Pruess et al. (2004) for linking TOUGH2 and FLAC. The main problem to be dealt with is the interpolation of temperature and pressure data from the block-centered TOUGH2 grid onto the finite element grid used by ABAQUS. Although we have used a finer grid for the ABAQUS model than for the TOUGH2 model, at Wairakei the pressure and temperature changes are quite uniform over a large area, and therefore interpolation on to a finer grid is not difficult.

More challenging coupled fluid-rock interactions need to be modeled. For example, modeling the spreading of a fracture zone created by hydraulic fractures as part of a hot dry rock (or EGS) project is a problem that needs to be solved. Planners of EGS projects need to be able to calculate the size and permeability of the fractured zone created by hydraulic fracturing. The FEHM code includes some fluid-rock interaction capability that was used in a study of the Hijiori hot dry rock site (Tenma et al., 2008).

Some interesting studies of mass transfer through the ductile zone, below geothermal systems, have been

carried out by Fussels et al. (2009) and Regenauer-Lieb et al. (2009).

NUMERICS

As models get larger and more complex, the demand for improved computational speed and more accuracy follow. As pointed out by Pritchett (2007), processing power has increased dramatically, and its cost has decreased considerably. One feature of the present scene is the advent of cheap multicore computers, with quad-core computing becoming almost standard. Even 16-core machines are now relatively inexpensive. The new development of parallel versions of TOUGH+ (Zhang et al, 2009) will be able to take advantage of these new multicore machines. Distributed memory clusters may not be so effective for parallelizing TOUGH2, but are very useful for speeding up iTOUGH2.

The accuracy of the integrated finite difference or finite volume approach used in TOUGH2 is inevitably of low-order accuracy. We have achieved good results with an Euler-Lagrange approach for a 2-D single-phase flow (Croucher and O’Sullivan, 2004), but more work is required to implement it for two-phase flow and for general 3D flow. The implementation of an Euler-Lagrange approach in TOUGH2 would require some restriction on the choice of block structures. Probably finite element style grids would have to be used.

It would be very useful to be able to more accurately represent the expansion and contraction of boiling zones in geothermal systems. There are various “front-tracking” methods that might work, but again would probably require some restrictions on the design of the computational grid.

In various geothermal models that we have set up, we have used “bad” grids with two small blocks joining one large block and relatively poorly conditioned block structures. Pruess and Garcia (2000) showed how to improve computational accuracy when joining a coarse grid to a fine grid, but their work only considered simple grid structures. More research is required to generalize this approach for complex grids.

Mesh generation remains an issue for complex models. For 2-D models, triangulation can always be achieved, and in 3-D a general tetrahedral grid can be created. But better tools are still required for creating well-conditioned grids containing mostly quadrilaterals in 2-D or their equivalent in 3-D.

NEAR SURFACE BEHAVIOUR

In our model of Wairakei, we incorporate the unsaturated zone by using an air-water EOS and

extending our model up to the ground surface. Some other geothermal models take the water table as the top of the model. Our approach works satisfactorily, but does not track the movement of the water table very accurately, since the minimum layer thickness is 50 m. It would be useful to be able to handle the water table in a geothermal model similarly to the way unconfined aquifers are included in groundwater models.

A more sophisticated approach is required as the surface where $P = P_{\text{atmospheric}}$ may be partly boiling. Nevertheless, having the top surface of a model, either water or steam, able to move up or down through a gridblock would be a very useful advance in accurately representing near-surface behavior, such as the development of large areas of steaming ground.

Similarly, improved models of surface features such as hot springs and geysers would be useful. We have carried some modeling studies of these surface features (see Sapatdji et al., 1994), but we have not coupled these local models with our large-scale reservoir models. Currently, we use the DELV option to represent the hot springs as wells on deliverability, whose flow drops off as the pressure and/or enthalpy of the feed zone declines.

SUMMARY

We would like to be able to run bigger and better models of geothermal fields; we would like to be able to calibrate them better and more quickly; and we would like the models to be able to incorporate more complex reservoir behavior. Some of these aims can be met with current techniques, but others require more research.

1. Improved computation speed. The TOUGH+ code offers parallel computation as an option. All that is required is the development of a “TOUGH+Geothermal” in addition to the existing TOUGH+HYDRATE version (Moridis et al., 2008) and the TOUGH+CO2 version (Zhang et al. 2009). The development of a TOUGH+Geothermal module should not be not a difficult task.

2. Improved calibration methods. All three of the calibration methods discussed above (manual, inverse modeling, statistical sampling) require further research to make them work well.

3. Improved numerics. Our highest priority item in this category is the tracking of the movement of the water/steam table. This is probably achievable, and Euler-Lagrange methods could probably also be implemented in TOUGH2. We are less optimistic about implementing general front tracking into TOUGH2.

4. New EOSs. There are no fundamental impediments to the development of EOS modules that can handle mixtures of water and CO₂ (and perhaps NaCl) over a wide temperature and pressure range, although working out the details could be time consuming (e.g., Kissling et al., 2005).

5. Fluid-rock interaction. The problem of predicting the spread of a fracture zone in an HDR (EGS) project is challenging. More research is required.

We hope by the next TOUGH Symposium, we and others will have made progress on some of the topics discussed above.

REFERENCES

- ABAQUS Inc., Pawtucket, RI, *ABAQUS Analysis User's Manual Version 6.4*, 2003.
- Allis, R., C. Bromley and S. Currie, Update on subsidence in the Wairakei-Tauhara geothermal system, New Zealand, *Geothermics*, 38, 169-180, 2009.
- Battistelli, A., C. Calore and K. Pruess, The Simulator TOUGH2/EWASG for Modeling Geothermal Reservoirs with Brines and Non-Condensable Gas, *Geothermics*, 26(4), 437-464, 1997.
- Bhat, A., D. Swenson and S. Gosavi, Coupling the Hola wellbore simulator with TOUGH2, *Proc. 30th Workshop on Geothermal Reservoir Engineering*, Stanford University, Stanford, Calif., Jan. 31 – Feb. 2, 2005.
- Blakeley, M.R. and M.J. O'Sullivan, Simple models of the Wairakei reservoir, *Proc. 3rd New Zealand Geothermal Workshop*, Auckland, New Zealand, 131-136, 1981.
- Blakeley, M.R. and M.J. O'Sullivan, Modeling production and recharge at Wairakei, *Proc. 4th New Zealand Geothermal Workshop*, Auckland, New Zealand, 23-31, 1982.
- Bullivant, D.P., M.J. O'Sullivan and G.A. Zvoloski, Enhancements of the MULKOM geothermal simulator, *Proc. 13th New Zealand Geothermal Workshop*, Auckland, New Zealand, 175-182, 1991.
- Croucher, A.E., M.J. O'Sullivan, T. Kikuchi, and Y. Yasuda, Euler-Lagrangian tracer simulation with TOUGH2, *Geothermics*, 33(4), 503-520, 2004.
- Croucher, A.E. and M.J. O'Sullivan, Application of the computer code TOUGH2 to the simulation of supercritical conditions in geothermal systems, *Geothermics*, 37, 622-634, 2008.
- Cui, T., C.N. Fox, G. Nicholls and M.J. O'Sullivan, Bayesian Inference for Geothermal Model Calibration, *Proc. 28th NZ Geothermal Workshop*, Auckland, New Zealand, 9p., 2006.
- Doherty, J., *PEST: Model independent parameter estimation*, Watermark Numerical Computing, Corinda, Australia, 2005. www.sspa.com/pest
- Finsterle, S., K. Pruess, D.P. Bullivant and M.J. O'Sullivan, Application of inverse modeling to geothermal reservoir simulation, *Proc. 22nd Workshop on Geothermal Reservoir Engineering*, Stanford University, Stanford, California, 1997.
- Finsterle, S., *iTOUGH2 User's Guide*, Report LBNL-40040, Updated Reprint, Lawrence Berkeley National Laboratory, Berkeley, Calif., 2007a.
- Finsterle, S., *iTOUGH2 Command Reference*, Report LBNL-40041, Updated Reprint, Lawrence Berkeley National Laboratory, Berkeley, Calif., 2007b.
- Finsterle, S., *iTOUGH2 Sample Problems*, Report LBNL-40042, Updated Reprint, Lawrence Berkeley National Laboratory, Berkeley, Calif., 2007c.
- Fox, C.N., I'm sorry, but you have to do better than least-squares if you want to make quantitative estimates, Presentation at NZIMA Workshop on Energy, wind and water: algorithms for simulation, optimization and control, University of Auckland New Zealand, February, 2009.
- <http://www2.esc.auckland.ac.nz/EnergyWindWater/>
- Fussels, F., K. Regenauer-Lieb, J. Lui, R.M. Hough and F. De Carlo, Creep cavitation can establish a dynamic granular fluid pump in ductile shear zones, *Nature, Letters*, 459, 974-977, 2009.
- Hadgu, T., R.W. Zimmerman and G.S. Bodvarsson, Coupled reservoir-wellbore simulations of geothermal reservoir behavior, *Geothermics*, 24(2), 145-166, 1995.
- Kiryukhin, A.V., N.P. Asaulova and S. Finsterle, Inverse modeling and forecasting for the exploitation of the Puzhetsky geothermal field, Kamchatka, Russia, *Geothermics*, 37, 540-562, 2008.
- Kissling, W.M., Transport of three-phase hypersaline brines in porous media: theory and code implementation, *Transport in Porous Media*, 61, 25-44, 2005.
- Mannington, W.I., M.J. O'Sullivan and D.P. Bullivant, Computer modeling of the Wairakei-Tauhara geothermal system, New Zealand. *Geothermics*, 33(4), 401-419, 2004.

- Moridis, G.J. and K. Pruess, T2SOLV: An Enhanced Package of Solvers for the TOUGH2 Family of Reservoir Simulation Codes, *Geothermics*, 27(4), 415 - 444, 1998.
- Moridis, G.J., M.B. Kowalsky and K. Pruess, *TOUGH+Hydrate v1.0, User's Manual: A code for the simulation of system behavior in hydrate bearing geologic media*, Paper LBNL-149E, Lawrence Berkeley National Laboratory, Berkeley, Calif., 2008.
- Murray, L. and C. Gunn, Towards integrating geothermal reservoir and wellbore simulation: TETRAD and WELLSIM, *Proc. 15th NZ Geothermal Workshop*, Auckland, New Zealand, 1993.
- O'Sullivan, M.J., G.S. Bodvarsson, K. Pruess and M.R. Blakeley, Fluid and heat flow in gas-rich geothermal reservoirs, *Soc. Petrol. Eng. J.*, 25(2), 215-226, 1985.
- O'Sullivan, M.J., K. Pruess and M.J. Lippmann, State of the art of geothermal reservoir simulation, *Geothermics*, 30, 395-429, 2001.
- O'Sullivan, M.J. and A. Yeh, Wairakei-Tauhara Modeling Report, Uniservices and Department of Engineering Science, University of Auckland, 116 pp. (<http://www.mfe.govt.nz/rma/call-in-temihi/board-of-inquiry/evidence/11b-professor-osullivan.pdf>), 2007.
- O'Sullivan, M.J., A. Yeh and W.I. Mannington, A history of numerical modeling of the Wairakei geothermal field, *Geothermics*, 38, 155-168, 2009.
- Porras, E.A., T. Tanaka, H. Fujii and R. Itoi, Numerical modeling of the Momotombo geothermal system, Nicaragua, *Geothermics*, 36, 304-329, 2007.
- Pritchett, J.W., Geothermal reservoir engineering in the United States since the 1980s, *Geothermal Resources Council Transactions*, 31, 31-37, 2007.
- Pruess, K., C. Oldenburg, and G.J. Moridis, *TOUGH2 User's Guide, Version 2.0*, Report LBNL-43134, Lawrence Berkeley National Laboratory, Berkeley, Calif., 1999.
- Pruess, K. and J. Garcia, A systematic approach to local grid refinement in geothermal reservoir simulation, *Proc. World Geothermal Congress 2000*, Kyushu-Tohoku, Japan, 28 May-10 June, 2809-2814, 2000.
- Pruess, K., J. Garcia, T. Kavscek, C. Oldenburg, J. Rutqvist, C. Steefel and T. Xu, Code intercomparison builds confidence in numerical simulation models for geologic disposal of CO₂, *Energy*, 29, 1431-1444, 2004.
- Pruess, K., *ECO2N: A TOUGH2 Fluid property module for mixtures of water, NaCl and CO₂*, Report LBNL-57952, Lawrence Berkeley National Laboratory, Berkeley, Calif., 2005.
- Regenauer-Lieb, K., B. Hobbs, A. Ord, O. Gaede and R. Vernon, Deformation with coupled chemical diffusion, *Physics of the Earth and Planetary Interiors*, 172, 43-54, 2009.
- Rutqvist, J. and C-F Tsang, TOUGH-FLAC: A numerical simulator for analysis of coupled thermo-hydrologic-mechanical processes in fractured and porous geological media under multi-phase flow conditions, *Proc. TOUGH Symposium 2003*, Lawrence Berkeley National Laboratory, Berkeley, Calif., 2003.
- Saptadji, N.M., M.J. O'Sullivan and D.H. Freeston, Mathematical modeling of geysers at Rotorua geothermal field, New Zealand, *Geothermal Science and Technology*, 4(1), 37-75, 1994.
- Tenma, N., T. Yamaguchi and G.A. Zyvoloski, The Hijiori hot dry rock test site, Japan: evaluation and optimization of heat extraction from a two-layered reservoir, *Geothermics*, 37, 19-52, 2008.
- Wagner, W., J.R. Cooper, A. Dittman, J. Kijima, H.-J. Kretzschmar, A. Kruse, R. Mareš, K. Oguchi, H. Sato, I. Stöcker, O. Šifner, Y. Takaishi, I. Tanishita, J. Trübenbach, J. and Th. Willkommen, The IAPWS Industrial Formulation 1997 for the Thermodynamic Properties of Water and Steam, *ASME J. Eng. Gas Turbines and Power*, 122, 150-182, 2000.
- Yeh, A. and M.J. O'Sullivan, Computer modeling subsidence in geothermal fields, *Proc. 29th NZ Geothermal Workshop*, Auckland, New Zealand, 9p., 2007.
- Zhang, K., G.J. Moridis and K. Pruess, TOUGH+CO₂: A multiphase flow simulator for CO₂ Geologic Sequestration in Saline aquifers, Submitted to *Environmental Modelling and Software*, 2009.
- Zyvoloski, G.A. and M.J. O'Sullivan, Simulation of a gas-dominated two-phase geothermal reservoir, *Soc. Petrol. Eng. J.*, 20(1), 52-58, 1980.
- Zyvoloski, G.A., Z. Dash, and S. Kelkar, *FEHMN 1.0: Finite Element Heat and Mass Transfer Code, Rev. 1*, Los Alamos National Laboratory, Report LA-12062-MS, Los Alamos, NM, USA, 113pp., 1992.

SIMULATION OF POROUS MEDIUM GEOTHERMAL RESERVOIR CHARACTERISTICS WITH EXPLOITATION AND REINJECTION IN TIANJIN, CHINA

Haiyan Lei and Jialing Zhu

Geothermal Research & Training Centre, Tianjin University
92 Weijin Road, Nankai District
Tianjin, 300072, China
e-mail: leihy1216@yahoo.com

ABSTRACT

We have developed both conceptual and 3-D numerical models for the porous-medium Guantao (Ng) geothermal reservoir. These models used TOUGH2 software and were based on the natural state and production history of the study area, which covers an area of 532.86 km² in the Tanggu region, Tianjin, China. Mass flow and temperature histories of 20 production wells were simulated, primarily by adjusting well productivity indices and the permeabilities of the various rock types. Relatively good agreement was obtained between the measured and computed pressure profiles.

Pressure and temperature distributions of the porous Ng reservoir were projected for a single production pattern for the next 5 years, based on history matching simulations. The influence of different reinjection rates on reservoir pressure, temperature, and water level were studied. The results showed that the annual average water level drop for the entire study area is 3.4 m, and the annual average temperature drop is 0.1°C over 5 years under a single production pattern (no reinjection). The annual average water level drop is projected to be ~1.3 m under a 60% reinjection rate and 0.2 m under a 100% reinjection rate, after make-up wells are added, which constitute a doublet with the existing production well.

1. INTRODUCTION

The Neogene porous medium geothermal reservoir in Tianjin has been explored for many years (Wang and Zhu, 2003). Especially in the Tanggu area, large-scale reinjection has been carried out, owing to its longer exploitation history, advanced development, and the long-term dynamic monitoring at the Guantao (Ng) geothermal reservoir. Therefore, the study of a doublet system has been emphasized for the part of the Tanggu district that is our study area, which possesses typical pilot characteristics. This study area is located east of the Tanggu district in Tianjin. The overall size of this area is 532.86 km², with a centralized exploitation area of 160 km². Twenty production wells have been explored there since 2005, but as of yet no reinjection wells have been developed (Gao and Zeng, 2006).

2. CONCEPTUAL MODEL OF THE GEOTHERMAL SYSTEM

The study area crosses the depression of Beitang and Banqiao. The Beitang depression connects the Panzhuang uplift in the west with the boundary of the Cangdong fault, adjacent to the Ninghe River uplift in the north with the boundary of the Hangu fault. It connects the Banqiao depression in the south with the boundary of the Haihe River fault. Generally, the buried depth of the bedrock top surface is shallow in the west, whereas deep in the east, the thickness of Cenozoic ranges from 1300 to 5000 m (Zeng and Li, 2007). The Cangdong and Haihe faults have the greatest seismic impact on the Tanggu region. The study area is in the Huanghua Depression. A significant amount of data on subsurface pressures and temperatures, flow rates, and fluid enthalpy has been collected on the Tanggu geothermal field. Temperature and pressure measurements were made in wells under static conditions to estimate initial formation temperatures. These data provided the basic information needed to define initial, undisturbed, reservoir conditions. The conceptual model of the Ng geothermal reservoir in Tanggu is depicted in Figure 1.

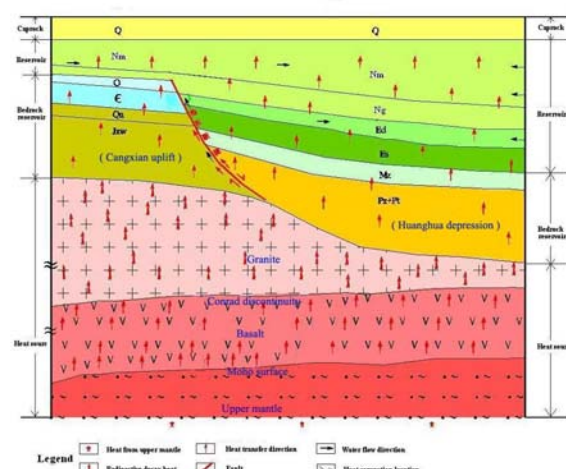


Figure 1. Conceptual model of Tanggu geothermal reservoir

3. NUMERICAL MODEL OF POROUS MEDIUM GEOTHERMAL RESERVOIR

3.1 Numerical model

A three-dimensional, porous-medium, numerical model was developed for the geothermal reservoir. The natural-state model was calibrated by matching the temperature profiles of 20 wells. The initial measured data were used in history matching and to analyze reservoir performance. The TOUGH2 (Pruess, 1987) simulator, which automatically estimates parameters of the reservoir, was used in the natural-state and history-matching simulations. Finally, the AUTOUGH2 (O’Sullivan, 2000) code was used to predict the performance of the reservoir under various assumed exploitation scenarios.

3.2 Parameters of the mathematic model

3.2.1 Initial conditions

Considering the relationship between the water-level drop of geothermal fluids and water-temperature changes in the wellbore, the geothermal reservoir pressure was used as the initial condition for the calculation, which seems reasonable, since water level varies with the density of geothermal fluids. Assuming that the fluid temperature changes linearly with the depth of geothermal wells, the geothermal reservoir pressure can be calculated by Equation (1):

$$P = \rho g (h - s) \tag{1}$$

where p , ρ , g , h , and s are reservoir pressure, density of geothermal fluids, gravitational constant, well depth, and water level, respectively.

The Ng geothermal reservoir pressure as measured in October 2005 was taken as the initial pressure field (Figure 2). Calculation of the temperature field mainly focuses on predictions of the further exploitation of the Ng geothermal reservoir. Thus, the temperature field under the current production state is taken as the initial temperature field (Figure 3).

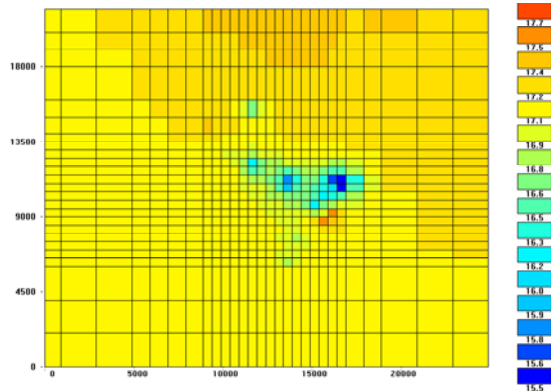


Figure 2. Initial pressure distribution of study area in Ng geothermal reservoir

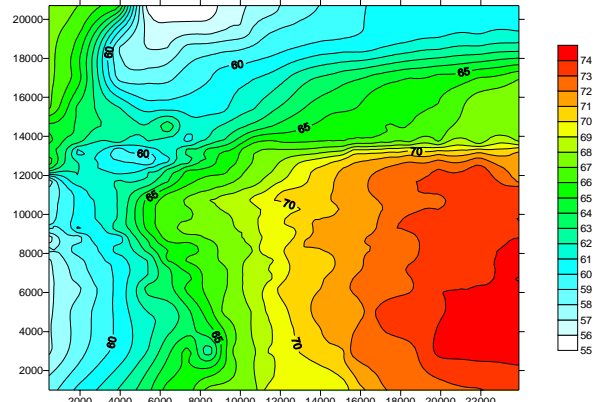


Figure 3. Initial temperature distribution of the study area in the Ng geothermal reservoir

3.2.2 Boundary conditions

According to the local geological data, the Ng geothermal reservoir is stable, and is hardly affected by the surrounding fractures. Based on the conceptual model of the Ng geothermal reservoir, the eastern and western parts of the study area are set as impervious boundaries, while the northern part is set as a recharging boundary and the southern part as a discharging boundary. It can be calculated that the mass flow of recharging and discharging are 89.64 t/h and 84.1 t/h, respectively.

3.2.3 Parameter of the Ng geothermal reservoir

Table 1. Numerical model parameters of the Ng geothermal reservoir

Cap rock	Temperature (°C)	55
	Thickness (m)	950-1300
	Permeability (10^{-12} m^2)	0.1-0.8
	Porosity	0.25
	Rock grain density (kg/m^3)	2109
	Rock grain specific heat ($\text{J/kg } ^\circ\text{C}$)	958
Ng geothermal reservoir	Formation heat conductivity ($\text{W/m } ^\circ\text{C}$)	1.5
	Permeability (10^{-12} m^2)	0.8-1.0
	Porosity	0.27-0.33
	Rock grain density (kg/m^3)	2103
	Rock grain specific heat ($\text{J/kg } ^\circ\text{C}$)	909
Formation heat conductivity ($\text{W/m } ^\circ\text{C}$)	1.6	

The simulation is mainly focused on fitting the dynamical monitoring data of 20 production wells that have been explored since 2005. Related reservoir

parameters could be adjusted reasonably by fitting the pressure of the geothermal wells—and permeability and porosity are important parameters in determining the reservoir pressure (Zhu and Zhang, 1996). The pressure drop is also constrained by the reservoir thickness and water mass flow. Judging from the parameters that undergo changes in the iterative simulation process, the reservoir pressure drops quickly under lower permeability, smaller layer thickness, and greater water mass flow. Table 1 provides the key numerical model parameters.

3.2.4 Meshmaker

For modeling purposes, the study area was assumed to be a rectangular prism 25 km long, 21.3 km wide, and 2.1 km deep. Figure 4 shows a plan view of the computational grid. The model has two horizontal layers ranging in thickness between 150 m and 1,100 m. Each layer has 700 gridblocks and 1112 nodes, their horizontal dimensions varying from 500 m×500 m to 2,000 m×2,000 m. The geothermal well is in the center of the model, covering an area of 500 m×500 m, with gridblocks of the smallest horizontal size within the model. Calculation time was divided into heating and nonheating periods, and the time step was set to 10 days during numerical simulation. The codes Mulgeom and Mulgraph (O’Sullivan and Bullivant, 1995) were used as pre- and postdata processors, and the mass flow of each production well is based on *in situ* utilization and measured data from Nov. 2005 to Dec. 2007.

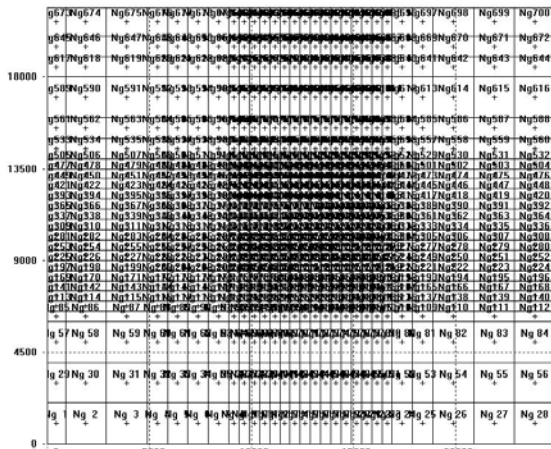


Figure 4. Plan view of the computational grid

4. SIMULATIONS OF GEOTHERMAL EXPLOITATION AND REINJECTION

4.1 History matching simulations

History-matching simulations began in Nov. 2005, and a total of 20 production wells were modeled. Figure 5 compares the measured and simulated pressure for four representative production wells

(TG07, TG17, TG28, TG23). The corresponding mesh number can be seen in Table 2. We can see that the simulations agree well with the monitoring data.

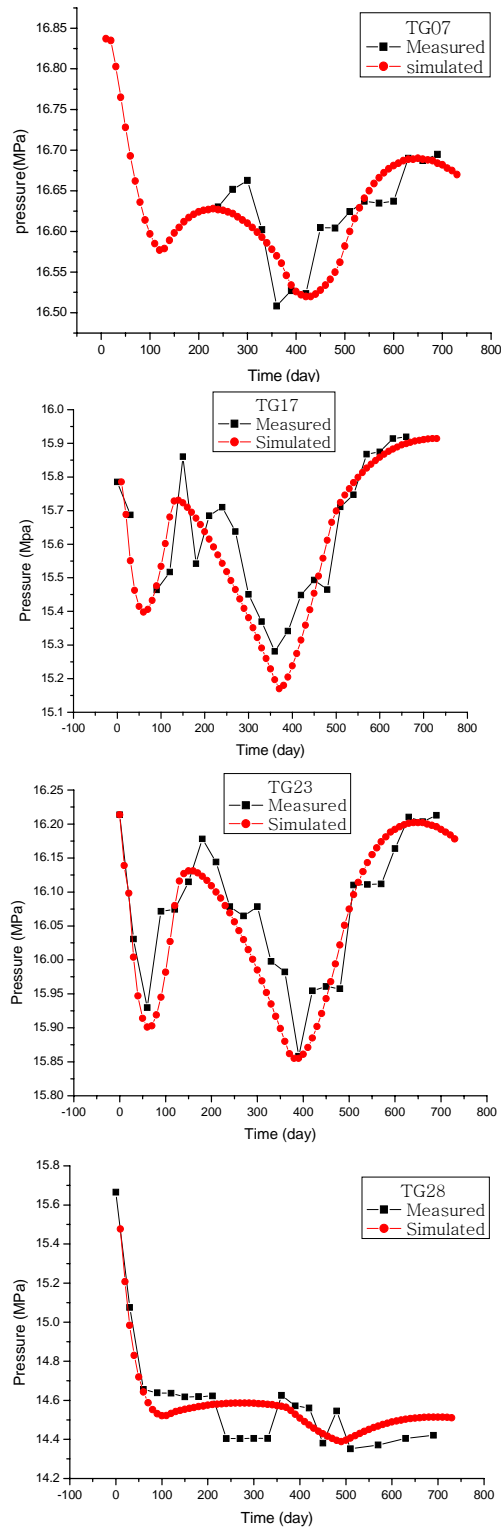


Figure 5. Comparison of measured and simulated pressure for four wells

Table 2. Corresponding mesh number of the four production wells

Production well	TG07	TG17	TG28	TG23
Corresponding mesh number	186	381	387	433

4.2 Prediction of pressure and temperature field under single production pattern

The pressure and temperature distribution of the Ng geothermal reservoir for the next 5 years are simulated based on the current exploitation state. Figures 6 and 7 give the pressure predictions of the four wells and the pressure distributions of the Ng geothermal reservoir without reinjection, respectively.

4.2.1 Pressure prediction

As shown in Figures 6 and 7, the pressure for the four wells will decrease over the next 5 years if there is no reinjection in the study area. The average annual water level drop is 3.4 m over the entire area, amounting to a maximum 4.1 m in the central area.

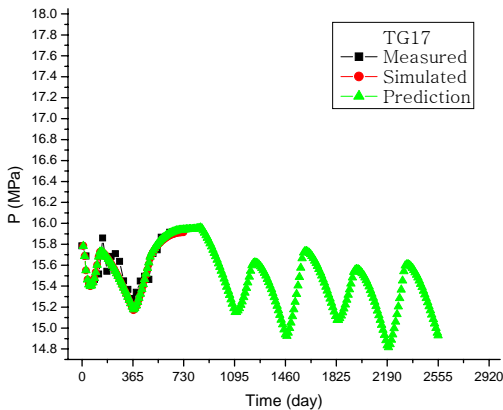
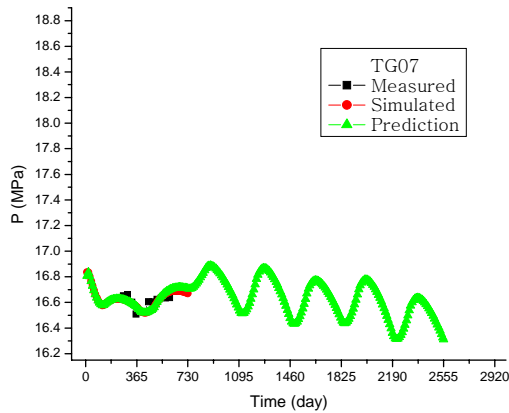
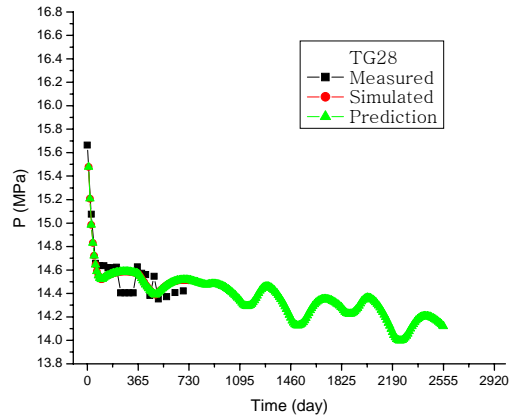
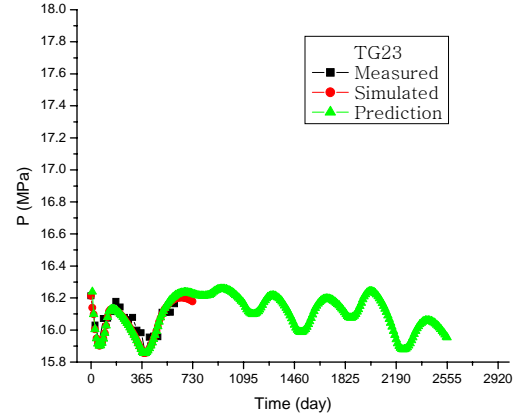


Figure 6. Pressure predictions for the four production wells over the next 5 years

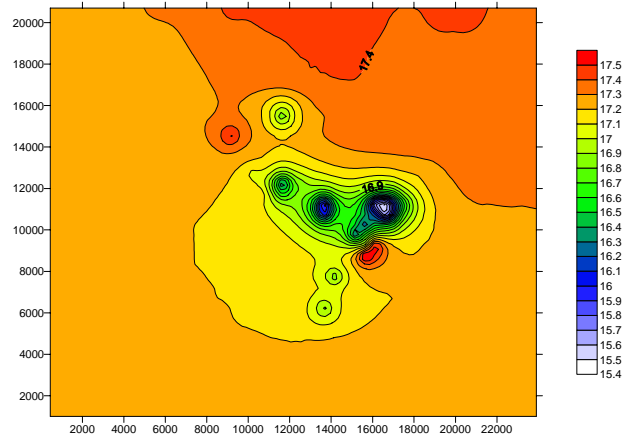


Figure 7. The pressure distribution of the Ng geothermal reservoir in 2012

4.2.2 Temperature prediction

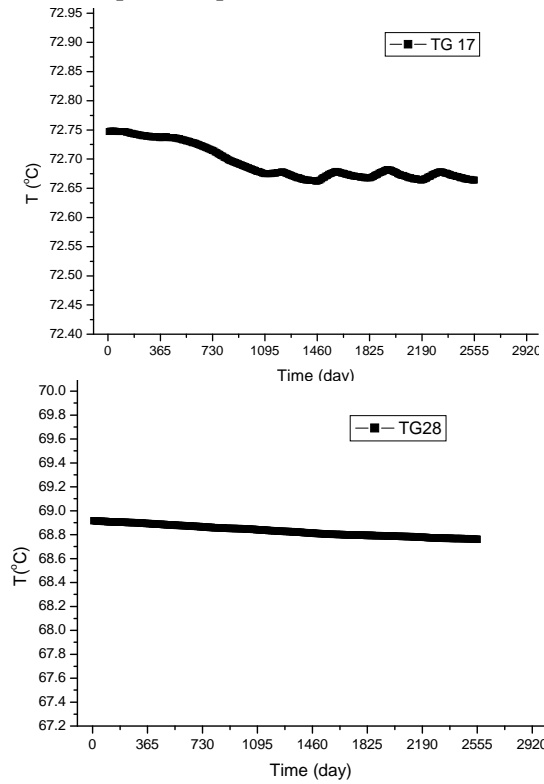


Figure 8. Temperature prediction for the two production wells in 5 years

Figure 8 shows the temperature drop for wells TG17 and TG28, which is around 0.1° over the next 5 years. Figure 9 gives the temperature distribution of the Ng geothermal reservoir in 2012; there is only a slight change compared to the initial temperature field, which can be neglected.

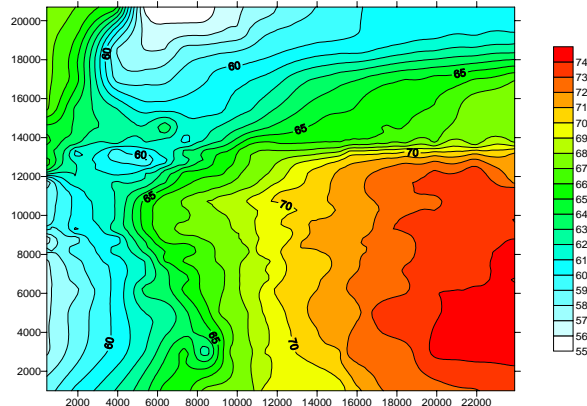


Figure 9. Temperature distribution of Ng geothermal reservoir in 2012

4.2 Future scenario simulations

4.2.1 Scenario 1 (60% reinjection with 35°C injected water)

In this scenario, the present-day production scheme is maintained. The objective is to investigate the pressure drawdown over the next 5 years. Corresponding reinjection wells, which are set in the periphery of the geothermal zone (Zhu, Wang and Lei, 2006), are added to the existing production wells at a distance of 800 m, based on the current exploitation state, which constitutes doublet wells with the ratio of mass flow of production to reinjection being 1:0.6. The separated water is reinjected at 35 °C.

4.2.2 Scenario 2 (100% reinjection with 35 °C injected water)

In this case, it is assumed that the reinjection rate is increased to the same as the production rate in order to further analyze the influence of reinjection on geothermal reservoir pressure.

4.2.3 Results of the predictive simulations

Results for the two scenarios are presented in Figures 10 and 11. Figure 10 shows that even though reinjection rate is not very large, the pressure drawdown of production wells slows down compared to the single production pattern after 5 years of operation. Well pressure for TG17 in the year 2012 will rise from 14.93 MPa without reinjection to 15.03 MPa with 60% reinjection, the equivalent of decreasing the annual water-level drop from 3.8 m to 1.8 m. Similarly, well pressure for TG28 will rise from 14.12 MPa without reinjection to 14.22 MPa with 60% reinjection, the equivalent of decreasing the annual water-level drop from 3.3 m to 1.3 m. In the entire study area, average water level increases 10.6 m in 5 years over the non-reinjection water level, i.e., the annual water level increases 2.12 m.

Figure 11 shows that the well pressure drops for TG17 and TG28 become slower than Scenario 1. Well pressure for TG17 further increases to 15.10 MPa with 100% reinjection in the year 2012, equivalent to decreasing the annual water-level drop from 3.8 m to 0.4 m. Similarly, well pressure for TG28 increases to 14.28 MPa with 100% reinjection, equivalent to an annual water-level drop of 0.1 m. Note that dynamic balance in the reservoir could be retained through Scenario 2. Considering the entire study area, the average water level increases 16.2 m in 5 years over the non-reinjection water level, i.e., the annual water level increases 3.24 m.

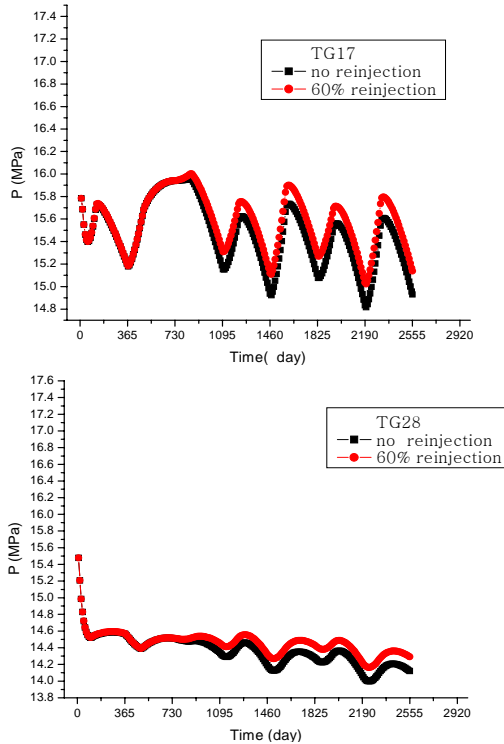


Figure 10. Pressure prediction of two wells with 60% reinjection

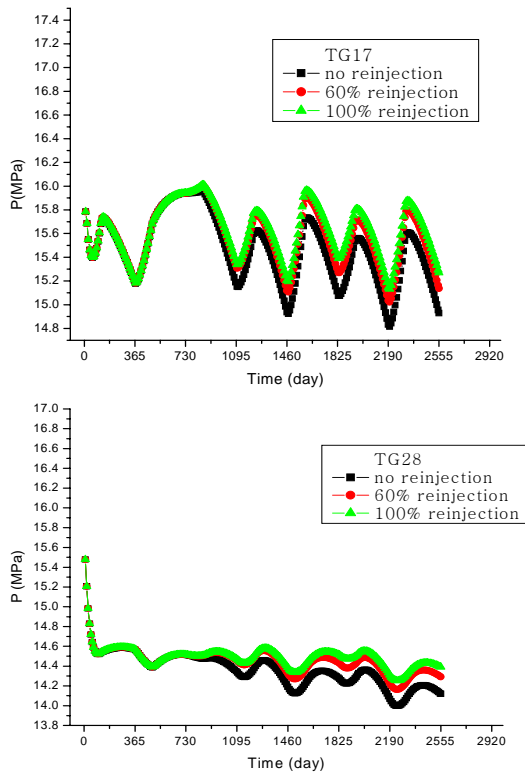


Figure 11. Pressure prediction of two wells with 100% reinjection

5. CONCLUSIONS

The results of numerical simulation can be summarized as follows:

- 1) A three-dimensional numerical model has been established for the Ng porous-medium geothermal reservoir in the Tanggu district, to simulate both its natural state and production history using the software TOUGH2.
- 2) Mass flow and discharge enthalpy histories of 20 production wells were automatically matched, primarily by adjusting well productivity indices and the permeabilities of the various rock types. Relatively good agreement was obtained between the measured and computed pressure profiles.
- 3) When there is no reinjection in the study area, the pressure of the Ng reservoir decreases over the next 5 years; the average annual water level drop is 3.4 m over the entire area, amounting to a maximum 4.1 m in the central area. The temperature of the Ng reservoir drops $\sim 0.1^{\circ}\text{C}$ in the next 5 years. This tiny variation can be neglected.
- 4) When the reinjection rate is 60%, the pressure drawdown of production wells slows down compared to the single production pattern. After 5 years of operation, the well pressure for TG17 rises from 14.93 MPa to 15.03 MPa, equivalent to decreasing annual water-level drop from 3.8 m to 1.8 m. Similarly, the well pressure for TG28 will rise from 14.12 MPa to 14.22 MPa, equivalent to decreasing annual water-level drop from 3.3 m to 1.3 m. The average water level for the whole study area increases 10.6 m in 5 years compared to the water level under a single production pattern, i.e., the annual water level increases 2.12 m.
- 5) When reinjection rate further increases to 100%, well pressure for TG17 rises to 15.10 MPa by the year 2012, which is the equivalent of an annual water level drop of 0.4 m. Similarly, well pressure for TG28 rises to 14.28 MPa, the equivalent of an annual water-level drop of 0.1 m, almost retaining the dynamic balance in the reservoir. Considering the entire study area, the average water level increases 16.2 m in 5 years over the water level under a single production pattern, i.e., the annual water level increases 3.24 m.

ACKNOWLEDGMENTS

The authors would like to express their thanks to the Tianjin Geothermal Exploration and Development-Designing Institute for supplying geological data and suggestions. The work was supported by The Ministry of Science and Technology of the People's

Republic of China, under contract No. 2006AA05Z425.

REFERENCES

- Kun, W., and Jialing, Z. Study on tracer test and reinjection of doublet system in Tianjin baserock reservoir (in Chinese), *ACTA Energiae Solaris Sinica*. 24(2), 162-166, 2003.
- Baozhu, Gao., and Meixiang, Z., Caused and prevention measures of clogging in the reinjection well of a geothermal double-well system (in Chinese), *Hydrogeology and Engineering Geology*. 34 (2), 75-80, 2007.
- Meixiang, Z., and Huijuan, L., The study on drilling technique of tertiary reservoir reinjection well, *Geology and Prospecting*. 43(2), 88-92, 2007.
- Jialing, Z., and Qi, Z. Numerical study on the geothermal resources assessment in Tuanbo landscape region, Tianjin (in Chinese), *ACTA Energiae Solaris Sinica*. 17(4), 336-343, 1996.
- Jialing, Z., and Kun, Wang, study of geothermal resources assessment and numerical simulation in the Tuanbo region (in Chinese), *GRC Transactions*, 167-170, 2002.
- O'Sullivan, M.J., *AUTOUGH2 Notes*. Geothermal Research Software. Department of Engineering Science, University of Auckland, 2000.
- O' Sullivan, M.J., and Bullivant, D.P., A graphical interface to the TOUGH family of flow simulators, in Proceedings of the Tough Workshop '95, Lawrence Berkeley Laboratory Report LBL-37200, Lawrence Berkeley National Laboratory, Berkeley, Calif., 1995.
- Pruess, K., *TOUGH2 User's Guide*, Earth Sciences Division Lawrence Berkeley Laboratory Report LBL-20700, Lawrence Berkeley National Laboratory, Berkeley, Calif., 1987.
- Jialing, Z., Kun, W., and Haiyan, L., The study on optimal exploitation scenario of reinjection around periphery of geothermal zone, *ACTA Energiae Solaris Sinica*. 27 (8). 794-799, 2006.

MODEL SIMULATION OF THE HENGILL AREA, SOUTHWESTERN ICELAND

Gunnar Gunnarsson*, Andri Arnaldsson+, and Anna Lilja Oddsdóttir*

*Reykjavik Energy, Bæjarháls 1, IS-110, Reykjavík, Iceland

+Vatnaskil Consulting Engineers, Suðurlandsbraut 50, IS-108 Reykjavík, Iceland
e-mail: gunnar.gunnarss@or.is

ABSTRACT

The Hengill Area is an important energy source for Reykjavík and the surrounding area, both for electricity and space heating. Two production fields are located in the area; Nesjavellir and Hellisheiði, and two other potential production fields are believed to be in the area.

We present numerical calculations of the entire Hengill Area, conducted using TOUGH2/iTOUGH2 software. The model contains nine layers consisting of 966 elements each. Geological survey data, down-hole measurements used to simulate the natural state of the system in the model, and production data from the fields have been used to calibrate the model parameters.

The model has been used to predict how production will affect the geothermal fields. Information gathered throughout the production history, such as drawdown and changes in enthalpy, have been used to reevaluate the size and production capacity of the production fields. Different production scenarios, such as production with and without reinjection, have been simulated. The model simulations have also been used to estimate the capacity of potential future production fields.

INTRODUCTION

The Hengill Area is located 20 km southeast of Reykjavík. It consists of the Hengill Central Volcano and fracture zones northeast and southwest of Mt. Hengill. A topographic map of the area is shown in Figure 1. The present production fields are Nesjavellir in the northwest part of the area, and Hellisheiði in the southwest part. The Nesjavellir Field has been in use since 1980; the Hellisheiði Field since 2006.

Two potential future fields exist in the Hengill Area; the Bitra field and the Hverahlíð field. Three exploration wells have been drilled in each of these fields, and three additional exploration wells are now (July 2009) being drilled in the Hverahlíð field.

A wealth of data is available to simulate the behavior of the present production fields. The geology has been studied extensively (Sæmundsson, 1967; Sæmundsson and Friðleifsson, 2003; Franzson et al.,

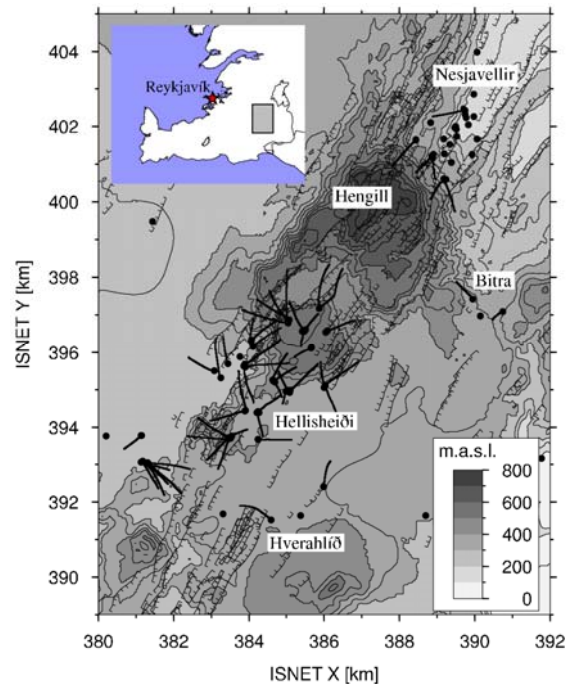


Figure 1. A topographic map of the Hengill Area showing the locations of present and potential production fields. Well heads are depicted as black dots, directional drilled wells as black lines, and fissures as comblike lines. The coordinates are in the local Icelandic system ISNET. The inset shows the location of the area in SW-Iceland.

2005) and geophysical surface measurements, mainly resistivity measurements, have been used for exploring the distribution of the geothermal activity (Arnason and Magnússon, 2001). Using geological survey and surface geophysics only, one has a relatively uncertain knowledge of the distribution of the temperature anomaly.

Numerous wells have been drilled in the current Nesjavellir and Hellisheiði production fields. Direct measurements of temperature and pressure have resulted in a comprehensive picture of the temperature anomaly of the fields. In the other parts of the Hengill area, such as Bitra and Hverahlíð fields, surface exploration with direct measurements in a few exploration wells will have to suffice in order to build a conceptual model of the system.

An existing large-scale TOUGH2/iTOUGH2 3D reservoir model has been developed to simulate the effects of production within the geothermal areas of the region (Björnsson et.al. 2006). That model, used to simulate production scenarios in the Nesjavellir and Hellisheiði fields, has been recalibrated using production data from Nesjavellir field (Björnsson, 2007), and is now considered to accurately predict the behavior of that field.

In recent years, several new wells have been drilled in the Hellisheiði field. Data acquired from down-hole measurements in the new wells has yielded accurate information on formation temperature and initial pressure of the Hellisheiði field.

THE CONCEPTUAL MODEL

The conceptual model of the area is based on its geology and estimated formation temperature. For Hellisheiði and Nesjavellir, the formation temperature is well known, due to numerous wells that have been drilled there. The formation temperatures of Bitra and Hverahlíð are not as well known, and therefore one has to rely on geological and geophysical surveys.

As mentioned above, a copious amount of new data is available from new wells in the Hellisheiði field. These data have changed our perception of the geothermal activity in the Hengill Area and challenged previous notions of a heat source under Mt. Hengill that feeds both the Hellisheiði and the Nesjavellir fields (Franzson et al, 2005).

The formation temperature profile at the depth of 1,000 m below sea level is depicted in Figure 2. The hottest formation temperature is found in the Nesjavellir Valley and in a relatively narrow belt in Hellisheiði. Local hot regions can also be seen in Hverahlíð and Bitra. There appears however, to be a local minimum in the formation temperature in the center of the area near Mt. Hengill.

The formation temperature in vertical cross sections in the Hellisheiði field are depicted in Figure 3 (The locations of the cross sections are shown in Figure 2.) As can be seen in the sections, the eastern and the northern boundaries of the Hellisheiði Field are characterized by an inverted temperature gradient.

Judging from the formation temperature distribution, we propose four separate heat sources in the area. The heat stems from intrusions in the crust and a deeper magma chamber. Here, it is assumed that hot fluid (low quantity with high enthalpy) is injected from below into the upper 2.5 km of the system.

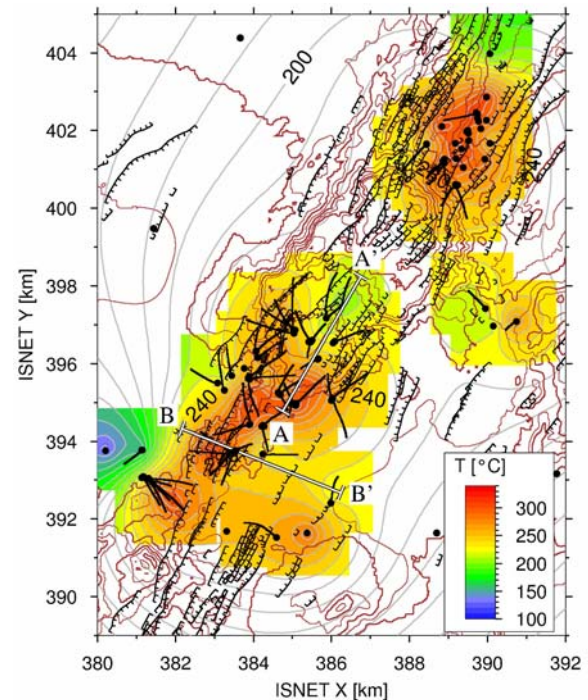


Figure 2: Formation temperature at 1000 m below sea level. The formation temperature is estimated from down-hole measurements.

The location of the heat sources are depicted in Figure 4. Shallower intrusions are also believed to provide heat to the system as well. The permeability of the formation is expected to be lower in the fractured zones, with these low permeability zones surrounded by higher permeability. The location of lower permeability is also shown in Figure 4.

NUMERICAL SIMULATIONS

Setting up the model

Numerical calculations based on the conceptual model were performed using the TOUGH2/iTOUGH2 software suite. The model consists of 9 layers having 966 elements, i.e., the total number of elements is 8694. The stratification of the model can be seen in Figure 5. The model is a square of size 100×100 km. Elements of the model at the core of the Hengill Area are shown in Figure 6. The inset in Figure 6 shows the model's location in SW-Iceland.

Boundary conditions of the model are assigned so that the top and bottom layers are maintained at constant pressure and temperature (referred to as “inactive”). The volume of the outermost elements is large compared to active part of the model, effectively making them “inactive.”

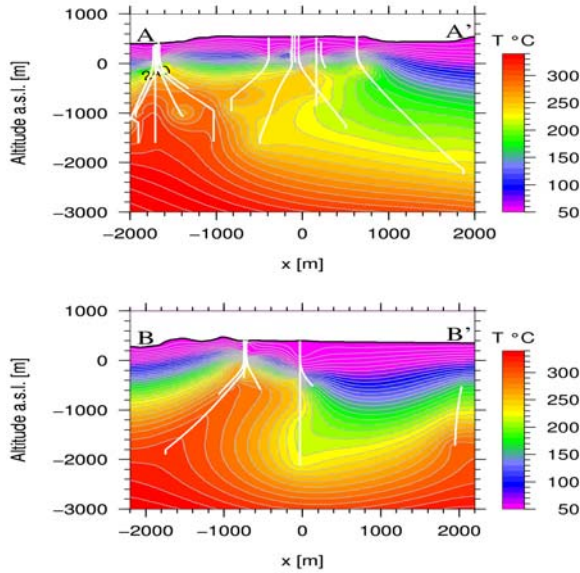


Figure 3: Vertical sections showing formation temperature calculated from downhole measurements. The white lines show the wells (the data points) used for calculating the temperature. Boundary condition is 5°C surface temperature and temperature of 500°C at 5 km depth. The locations of the sections are shown in Figure 2.

Temperature of the top layer is fixed at 15°C and the pressure at 10 bar. Temperature of the bottom layer in the vicinity of existing wells was estimated from the downhole measurements. Elsewhere it was set to 265°C , assuming a temperature gradient of $100^{\circ}\text{C}/\text{km}$ and temperature of 15°C in the top layer.

Net mass flow under natural conditions is only through the top and bottom. The bottom layer has low permeability. It is, however, high enough to allow limited amount of fluid to flow in and out, thus simulating flow of fluid from, and to, lower parts of the system.

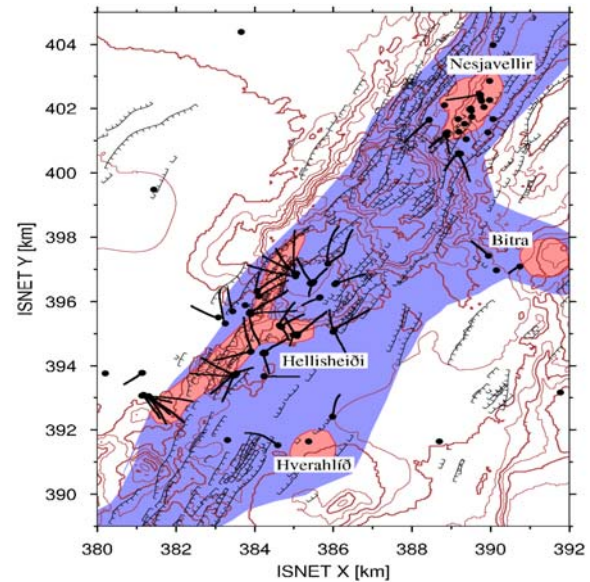


Figure 4: Conceptual model of the Hengill Area. Higher permeability is depicted with blue. That zone is expected to follow more or less the fracture zones. The heat sources are depicted as red.

Inactive upper layer simulates precipitation and the interaction of the geothermal system with the cold ground water system. Hot water can enter the groundwater, where it is washed away, and groundwater can flow into the geothermal system. The cap rock of the hot geothermal system has, however, a very low permeability, which limits flow between the groundwater and the geothermal system.

Knowledge of the lower parts of the system is scarce. The bottom of the deepest well is $\sim 3,000$ m under sea level. Most of the wells are significantly shallower, extending to $\sim 2,000$ m below sea level or higher. The range of depth is further limited by the difficulties in simulating the behavior of supercritical fluids.

Interaction of the model with deeper parts of the system is simulated through a fixed bottom temperature and heat sources in the H-layer (the second deepest layer). Both heat and hot fluid is injected into the H-layer in areas shown in Figure 6. The injected heat simulates heat flow from cooling intrusions. The injected hot fluid has high enthalpy and simulates the fluid that comes from lower parts of the system.

400 m	A	----- 300 m -----
	B	----- 50 m -----
	C	----- -200 m -----
	D	----- -400 m -----
	E	----- -650 m -----
	F	----- -950 m -----
	G	----- -1300 m -----
	H	----- -1850 m -----
-2500 m	I	----- -2300 m -----

Figure 5: The stratification of the model. The top of the model is 400 m above sea level and the bottom at 2500 m below sea level.

Another possibility for simulating the interaction of the model to the part below its range is to assign higher permeability to the subregions of the assumed heat and mass sources in the bottom layer. Pressure differences will drive the flow from and to the bottom layer, thus simulating the interaction of the upper geothermal system with its deeper roots.

This method of having permeable bottom areas has also been tested with the model. So far, it has not given as encouraging results as the method of injecting hot fluid and heat at fixed rate into the system.

Natural State

The natural state of the model is defined as the steady state without production. To reach a steady state, the entire model is given a temperature gradient of 100°C/km, and a fixed pressure and temperature in the top and bottom layers. The heat- and mass sources in the second deepest layer (the H-layer) then drive the system until it has reached equilibrium. The model is taken to be in a steady state when the time step of each iteration exceeds 10,000 years.

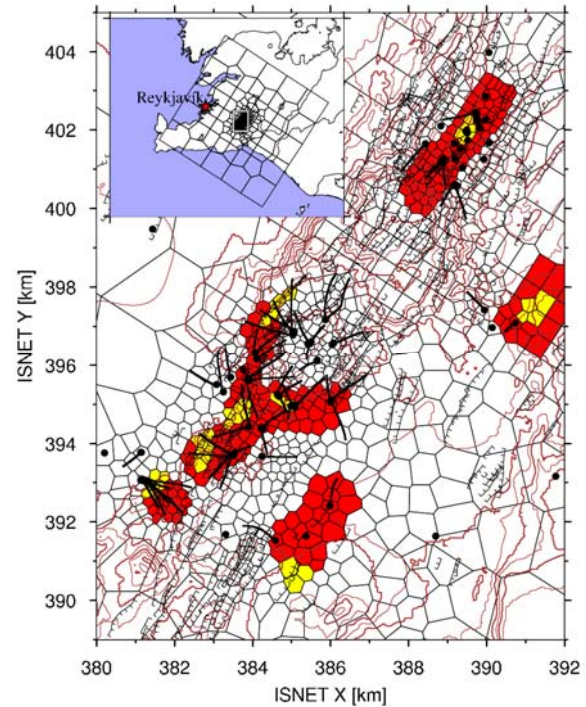


Figure 6. The elements in each layer in the center of the model. The colored areas show the elements where heat is introduced into the bottom of the model. The yellow elements are where hot fluid is introduced into the H-layer of the system. The inset shows how the whole model is located in SW-Iceland.

Calibrating the parameters

Permeability of the inner part of the system (i.e., the blue areas in Figure 4) is set high in layers E, F, G, and H. The upper layers of the system (B and C) are assigned low permeability, as are the top and bottom layers of the entire model. The areas surrounding the core of the system are given low permeability.

Injection of heat into the H-layer is set to a relatively low value. Mass of the injected fluid is set to ~1 kg/s per element, and the enthalpy is set to ~1500 kJ/kg. The steady state of this initial guess is then compared to measured values of formation temperature and initial pressure.

iTOUGH was used to fit the natural state of the model to the measured initial pressure and formation temperature. In Figure 7, calculated temperature (T_c) and pressure (P_c) are compared with formation temperature (measured temperature) T_m and initial (measured) pressure (P_m). The T_m and P_m are taken to be estimated values of formation temperature and initial pressure at the depth of the center of each layer in each well (excluded are Layers A and I). These values are compared with calculated values in the

elements that have their center closest to the well in the corresponding layer.

The dots in both graphs in Figure 7 are concentrated on the $y=x$ line. Temperature values are somewhat scattered, especially for the intermediate values. The pressure values are more concentrated on the $x=y$ line than the temperature values. In the calculations, pressure values for each layer do not vary much within a layer, as can be seen in Figure 7b.

Some work might still be done on the model in order to improve the agreement between measured and calculated values. The correlation is, however, relatively good. The correlation coefficient for temperature and pressure are 0.93 and 0.98, respectively.

The model was further calibrated using production data. A production history of Nesjavellir goes back to the 1980s. Due to this long production history, the model can be well calibrated there. The production history in Hellisheiði goes back to 2006. This is a short production history, making it difficult to improve the calibration significantly. The parameters of interest when calibrating the model using production data are mainly enthalpy of the fluid and drawdown. The drawdown depends on porosity and permeability, and can be used to calibrate these parameters.

Although it is more challenging to simulate the enthalpy of the fluid, it is included in the iTOUGH objectivity function, but its contribution is given lesser weight.

There are numerous methods for simulating the behavior of the wells in TOUGH2 (Pruess et al., 1999). We however, used the simple method of controlling the production rate. By monitoring the pressure in the feeding zone, the production rate was controlled in such a way that the pressure did not drop below a predefined value. It should be noted that we are working with a fractured medium, and the behavior of the well and its vicinity can be quite complicated.

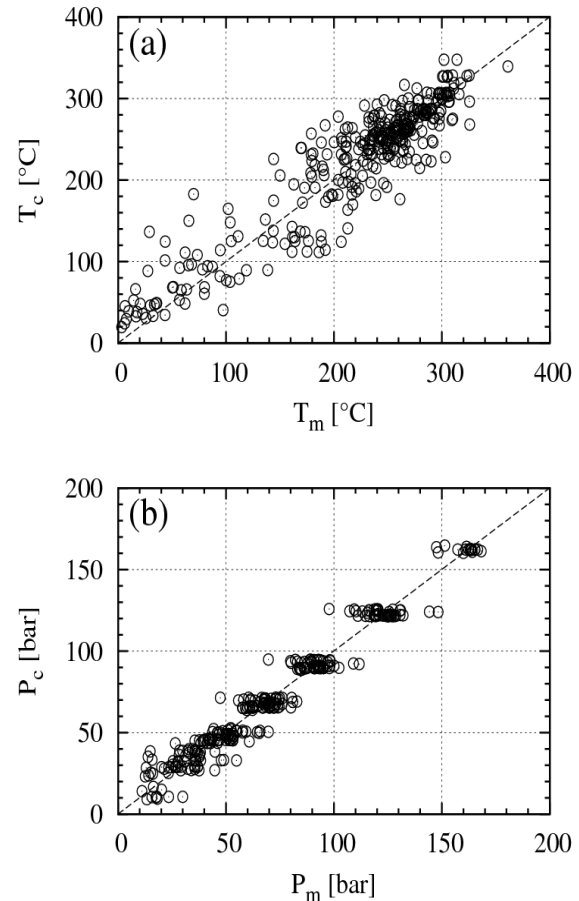


Figure 7: Comparison of measured and calculated variables. In (a) the calculated temperature (T_c) is plotted as function of measured temperature (T_m). In (b) calculated pressure (P_c) is compared with measured pressure (P_m).

The Calculated Natural State

The formation temperature measured in each well provides an incomplete picture of the distribution of the temperature anomaly, due to limited spatial resolution of measured data points. A simulation calibrated by using the downhole data gives a much broader picture of the temperature anomaly, in particular the shape of the convection cells and the flow therein. In Figure 8, the calculated formation temperature in the same cross sections as in Figure 2 and Figure 3 is shown. Calculated fluid flow is also depicted in Figure 8. Both the AA' cross section from the northern part of the Hellisheiði Field and the BB' section in the southern part of that field have a reversed temperature gradient at a depth below ~1,000 m b.s.l. This reversed temperature gradient is most likely caused by convection of the fluid in the formation. Using the simulation, it is also possible to predict (to some extent) what the temperature anomaly looks like in the vicinity of the drilling field.

Such predictions are helpful when deciding upon future exploration.

The shape of the temperature anomaly in the southern part of the Hellisheiði field is particular interesting (see Figure 8, section BB'). The most powerful wells are drilled near the western edge of the temperature anomaly—a very steep edge. These wells are drilled in mostly hyaloclastite bedrock, which has relatively high porosity and low matrix permeability (Frolova et al. 2005). However, the hyaloclastite formation has numerous fractures, which govern its permeability. The formation is extremely hot, and the wells drilled therein yield a high enthalpy fluid.

East of the high temperature in the hyaloclastite formation is a more permeable formation. The temperature there is lower, and the wells drilled there have lower enthalpy and an observed reversed temperature gradient.

From the simulation, it is evident that the reversed temperature gradient east of the hot heat source is due to convection. The simulation also predicts that a hot resource could be found at shallower depths east of the present drilling field. The policy in recent years has been to drill always deeper wells, and these wells have often gone through a hot formation into a cooler one. Drilling shallower wells into the hot shallow resource, without drilling through it, might result in higher enthalpy of the fluid. It will, in any case, result in less drilling cost.

Model Prediction

The main emphasis of the revision work for the Hengill Area model has been on Hellisheiði. The Nesjavellir Field is already well calibrated in the older version of the model, due to the long production history of the field. However, the conceptual model, on which it is based, is not entirely correct, as mentioned earlier. Limited information was available on the formation temperature of the Hellisheiði Field when the older version of the model was calibrated. The soundness of earlier assumptions has been called into question.

The present production at the Hellisheiði Field is 210 MW_e (4 x 45 MW_e high pressure units and a 30 MW_e low pressure unit). 330 kg/s of steam at 9 bar-a are needed to drive the high pressure units. By flashing water from the steam-water separators from 9 bar-a to 2 bar-a, steam is obtained for the low pressure unit.

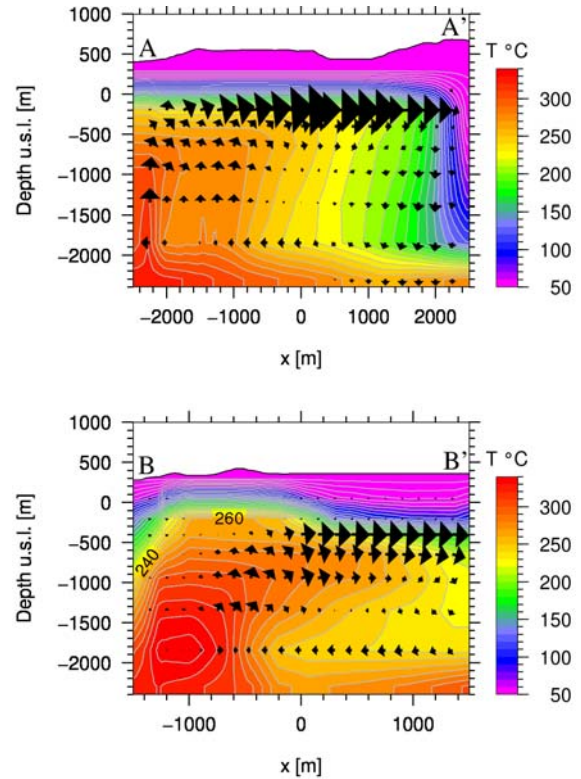


Figure 8: Formation temperature and flow in natural state as calculated by the model. The locations of the sections are shown in Figure 2.

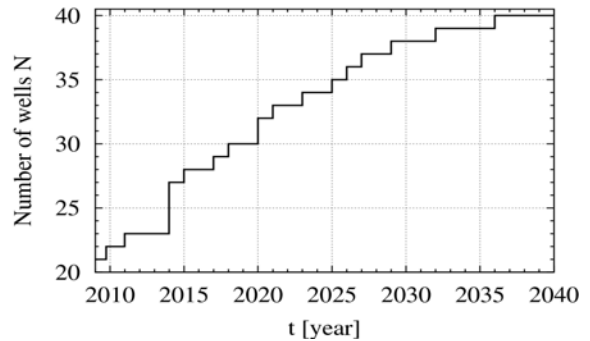


Figure 9: Number of well used during the production time

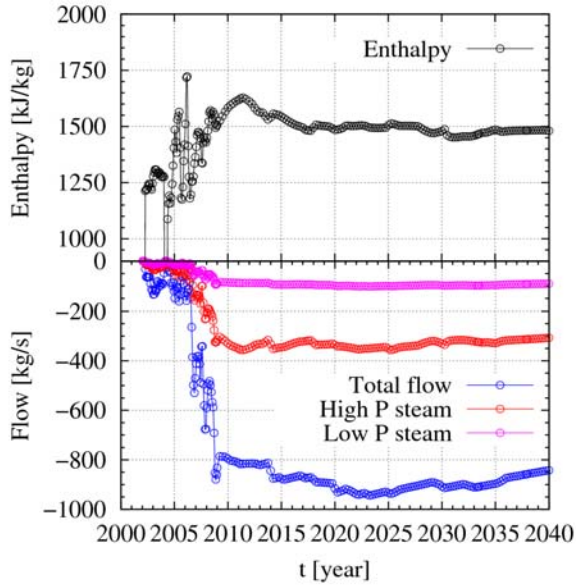


Figure 10: Enthalpy and production in the during the production time

In the simulations presented here, the aim was to extract mass from the system, which yielded 330 kg/s of high pressure steam. The water from the separators was enough to obtain the necessary amount of low pressure steam. For practical reasons, it is not always possible to obtain enough water for the low pressure steam production. The capacity of the current pipelines from the most productive parts of the field is still limited, which makes it preferable to use them to carry steam from wells that yield high enthalpy fluid, in order to maintain energy throughput. The power plant and the pipeline system are still under construction, and therefore it was assumed here that the transport of fluid is not an obstacle.

Reinjection of waste water was also simulated in the model. A total amount of 430 kg/s was injected into the southern and western edges of the field; the enthalpy of the injected water was set to be 504 kJ/kg.

To maintain constant enthalpy and minimize drawdown, new wells were introduced during the production time. The feed zones for most of the new wells were placed relatively shallow or in layers D and E. Because the temperature is close to the boiling point in the center of the production field, one can expect a higher proportion of steam in the upper layers when the pressure drops—thus, producing from the shallower layers yields higher enthalpy

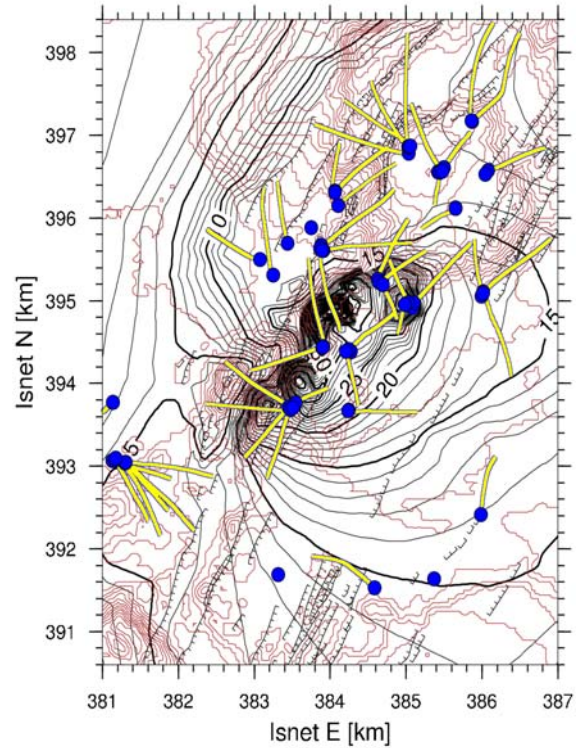


Figure 11: Drawdown in layer E in year 2040.

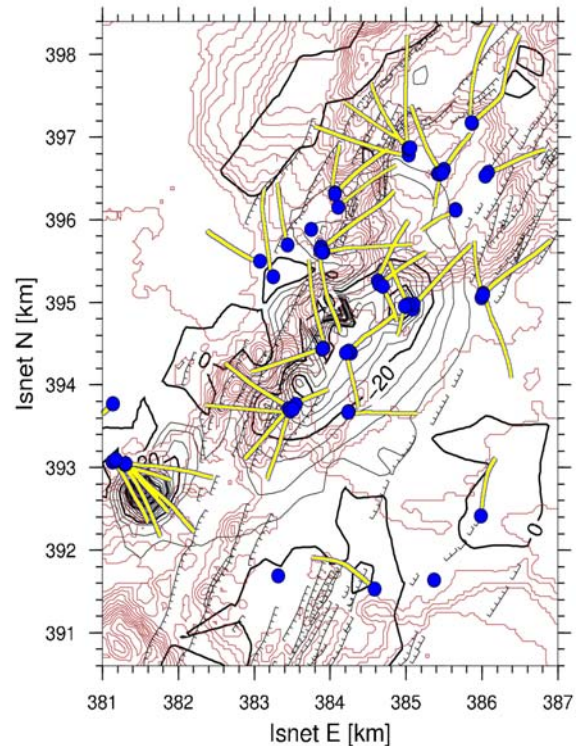


Figure 12: Temperature change of layer E in 2040

Figure 9 shows the number of wells used during the production time. During the simulations, 22 existing wells were used and 18 wells were introduced. On average, the new wells yielded 18 kg/s. The average

enthalpy of the extracted fluid is shown in Figure 10. Total flow from the system, along with the amount of high pressure steam (9 bar-a) and low pressure steam (2 bar-a), are plotted versus time in Figure 10. The enthalpy of the fluid increases at the beginning of production. It is assumed to reach a maximum in the year 2012, after which it begins to decrease. By introducing new wells with higher enthalpy, as discussed above, the average enthalpy can be kept around 1,500 kJ/kg.

There is a significant drawdown in the field due to production. In Figure 11 the drawdown in layer E (the layer where most wells have their feed zones) is shown. The pressure has dropped by more than 20 bar in the active area of the field by the year 2040.

In Figure 12, the temperature change in layer E in year 2040 is shown. The temperature has decreased by more than 20°C in the active area of the field. As mentioned earlier, the formation temperature in the central part of the production field is close to the boiling point. The pressure drop during production causes the fluid to boil and thus lowers the temperature of the formation. Flow from the edges of the system due to pressure drop and reinjection also cool the system. Ultimately, both the drawdown and the cooling of the system will have a significant effect on productivity by year 2040.

CONCLUSIONS

In recent years, numerous new wells have been drilled in the Hengill Area, southwestern Iceland. Most of the wells have been drilled in the Hellisheiði field. In light of recently acquired data from the new wells, a previously proposed conceptual model had to be revised.

Work has been undertaken to build a new conceptual model and consequently update the previously existing numerical model. In the new conceptual model, the geothermal fields in the Hengill Area are driven by separate heat sources located below the system, rather than a common heat source, as previously assumed. The revised model has been calibrated according to data from production histories and downhole measurements, with the aim of restructuring and simplifying the model. Presently, the model simulates fairly well the formation temperature and the initial pressure of the area.

Most emphasis has been on estimating the production capacity and sustainability of the present power production in Hellisheiði. According to the calculations presented, the Hellisheiði field can sustain a production of 330 kg/s of high pressure steam till 2040. By then, the drawdown and cooling of the field will have to be considered in the operation plan for the power plant.

These calculations are ongoing. The next steps will be to investigate more production scenarios, and recovery scenarios, in the Hellisheiði Field. The model also must be recalibrated according to the production data from Nesjavellir.

Two potential production fields, Hverahlíð and Bitra, are in the model. A provisional model prediction for the Hverahlíð field will soon have to be made, due to present interest in building a new power plant there.

REFERENCES

- Árnason K. and I. Magnússon, Geothermal activity in Hengill and in Hellisheiði, Results from resistivity measurements. Report OS-2001/091, Reykjavík. In Icelandic (English summary) 2001.
- Björnsson, G., E. Gunnlaugsson, and A. Hjartarson: Applying Hengill Geothermal Reservoir Model in Power Plant Decision Making and Environmental Impact Studies. Proceedings, Tough Symposium 2006. Lawrence Berkeley National Laboratory, Berkeley, California, 2006.
- Björnsson, G., 2007: Revised Conceptual Model of the Geothermal systems in Hengill and simple estimation of the Production Capacity of New Drilling Fields. OR internal report, in Icelandic, Nýjar virkjanir 3 – 2007
- Franzson, H., B.R. Kristjánsson, G. Gunnarsson, G. Björnsson, A. Hjartarson, B. Steingrímsson, E. Gunnlaugsson, and G. Gíslason: The Hengill-Hellisheiði Geothermal field – Development of a Conceptual Model. Proceedings, World Geothermal Congress 2005. Antalya, Turkey 24-29 April 2005.
- Frolova J., V. Ladygin, H. Franzson, O. Sigurðsson, V. Stefánsson, and V. Shustrov: Petrophysical Properties of Fresh to Mildly Altered Hyaloclastic Tuffs. Proceedings, World Geothermal Congress 2005. Antalya, Turkey 24-29 April 2005.
- Pruess, K., C. Oldenburg, and G. Moridis, *TOUGH2 User's Guide, Version 2.0*, Report LBNL-43134, Lawrence Berkeley National Laboratory, Berkeley, Calif., 1999.
- Sæmundsson K.: Vulkanismus und Tektonik des Hengill-Gebietes in Südwest-Island. Náttúrufræði-stofnun Íslands, Acta Naturalia Islandica. Vol. II, No. 7 105, 1967.
- Sæmundsson K. and Friðleifsson, G.Ó., 2003: Geological and Geothermal Map of the Hengill Area, Revision South of Mt. Hengill. Report ISOR-2003/020. In Icelandic including A1 size map.

A COMPUTATIONAL TECHNIQUE FOR ESTIMATING THE FRACTURE SURFACE AREA ADJACENT TO A NEWLY STIMULATED WELL WITHIN AN ENGINEERED GEOTHERMAL SYSTEM

Scott Fayer¹, Pete Rose¹, Susan Petty², Milind D. Deo³, and Tianfu Xu⁴

¹Energy and Geoscience Institute at the University of Utah
423 Wakara Way # 300
Salt Lake City, UT, 84108, USA
e-mail: sfayer@egi.utah.edu

ABSTRACT

In the creation of an Engineered Geothermal System (EGS), a reservoir is hydraulically stimulated by injecting water into wellbores under high pressure. This enhances permeability in marginally conductive fractures that are optimally oriented and critically stressed for shear failure. The objective of the hydraulic stimulation process is therefore to create a high-surface-area heat exchanger within the reservoir. Currently, no methods exist for characterizing the newly created fracture surface area, which is critical for estimating the success of the hydraulic stimulation and the performance of the incipient reservoir. In this paper, we present a computational technique for calculating the near-wellbore fracture surface area by inverting data from a single-well injection/backflow tracer test involving a thermally reactive tracer.

INTRODUCTION

The accurate measurement of fracture surface area within a geothermal system is a complex problem that needs further study, as currently no methods exist for characterizing the newly created fracture surfaces after a hydraulic stimulation. Providing onsite measurement, driven by computer-modeling technology, would benefit the geothermal industry by supplying the information needed to estimate the success of an ongoing stimulation through fracture characterization. Using such a method would give more control to field engineers and may end up decreasing cost and improving well longevity.

This problem will be addressed by modifying current tracing technologies commonly utilized during the development of a geothermal field. Stemming from existing tracer application, tracer pairing can be used for fracture characterization based on their physical properties. By selecting a pair of candidate tracers with different thermal decay kinetics, it will be possible to determine the newly created fracture surfaces after a hydraulic stimulation. This can be accomplished using both numerical techniques and the produced break through curve from a backflow injection.

The tracer pair is best formed using one conservative tracer and another that expresses thermal instability with first-order decay kinetics. Commonly used geothermal tracers that fit these requirements for simulation are Rhodamine WT and Fluorescein, which have both been well studied. Their thermodynamic constants are published and are often approved for tracer testing. These tracers make a good theoretical pair due to the conservative behavior of Fluorescein and the first-order decay of Rhodamine WT at geothermal temperatures.

The process begins with the continual injection of the tracer pair at fixed concentrations into the wellbore. After a shut-in period of arbitrary length, the well is produced and the concentration of each tracer measured at regular intervals to determine dilution degree. Since the two tracers have similar geometric and weight properties, they will experience similar adsorption and diffusion within the near-wellbore space. The thermally unstable tracer, Rhodamine WT, is produced with a lower concentration relative to the amount of thermal decay experienced. The amount of thermal decay can be considered proportional to the available surface area for heat transfer and to fracture surface area of contact.

The fracture surface area that would produce the tracer and thermal outputs measured in the injection/backflow experiment will work with standard inversion techniques (including, for example, iTOUGH2). If the input data are sufficiently constraining, only the calculated fracture-surface area could produce the measured tracer and fluid-temperature data, allowing this procedure to be utilized to determine the fracture-surface area that would produce the measured temperature increase. Although the overall objective is to provide a tool to determine the change in fracture surface area adjacent to single wells during a hydraulic stimulation, the proposed technique will also provide the starting point for measuring inner-reservoir fracture surface area in the future.

NUMERICAL METHOD

A 2D reactive transport model was developed using TOUGHREACT. This generic reservoir model simulates an eighth portion of the wellbore. Space is approximated by discretizing a specified area into equal dual porosity/dual permeability Cartesian zones with Dirichlet boundary conditions. The reservoir domain is balanced at 200°C, and system pressure was set above the vapor pressure to keep this model in the liquid phase. Fracture surface area was adjusted by changing the parameters using a dual porosity/dual permeability model. The main variable used to vary fracture surface area throughout each simulation was fracture spacing, which is proportional to the fracture density of a reservoir system. This model will demonstrate how an oppositional tracer pair changes in concentration throughout a range of fracture densities.

The method used was iterated over several fracture spacing values within the dual porosity/dual permeability module MINC. After a steady state was reached, the candidate tracer pairs were injected simultaneously at equal concentration. Thermal decay kinetics for both arbitrary tracers were chosen to match the model based on balancing computational cost and resolution, which best illustrates this method. The tracer pair, along with geothermal water, was injected for 4 days followed by a prompt 7-day shut-in. After 11 days, this model predicted that the arbitrary tracer pair had a sufficient concentration gradient to illustrate this method. At this time, a production well was established at the injection site, and flow was reversed using a rate comparable to the injection. This paper shows the relationship between changing fracture surface values and tracer product concentrations during the backflow injection reservoir system test (push-pull method).

RESULTS AND DISCUSSION

The curves were produced by modeling the concentration of an arbitrary tracer pair throughout the span of the backflow injection test. Tracer concentrations were measured at the injection, shut-in, and production points of the test. Using this schema, the curves below were created by varying fracture surface area settings within TOUGHREACT's dual porosity/dual permeability model. To study a wide range of fracture densities, the fracture spacing values chosen were 50, 100, 175, 250, and 400 m, while other parameters remained constant. The model depicted in Figure 1 illustrates the relationship of the concentration of two arbitrary candidate tracers over time at different fracture spacing.

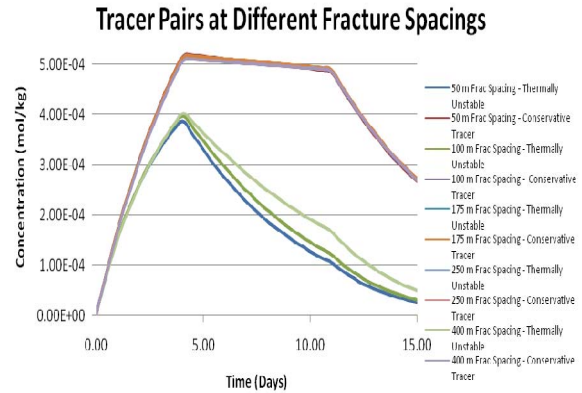


Figure 1. Arbitrary tracer pair concentration evolution over time. Measurements were taken in the fracture space near injection.

From this figure, it is clear that fracture density affects tracer concentration during a backflow injection test when thermal decay is a major contributor to the overall kinetics of a modeled tracer. The general trend can be seen in the “Less Stable Tracer” plots. The physical process is best described by the relationship of fracture spacing to temperature gradient. Primarily, as fracture spacing increases, fracture density decreases. This causes the temperature gradient to decrease, which is directly proportional to tracer decay over time.

It is important to notice the difference between the conservative and less stable tracers. While the less stable tracer changes more rapidly in concentration, the conservative tracer generally remains constant, and its concentration is practically independent of fracture density. This suggests the conservative tracer serves as a good control variable and provides a good background contrast for measuring fracture density when this model is later inverted.

This trend can also be characterized by measuring concentration difference between the tracer pair. Figure 2 shows this relationship. Here, the concentration of the conservative tracer is simply subtracted from the concentration of the less stable tracer.

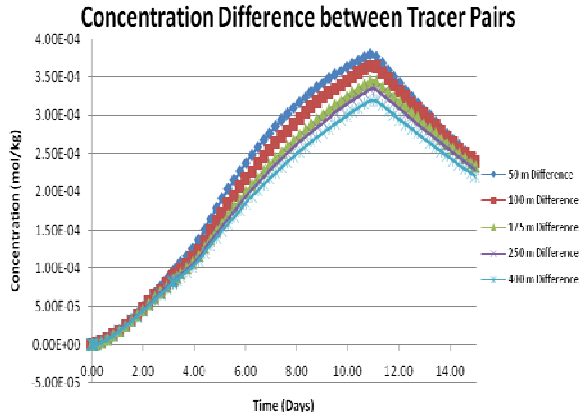


Figure 2. Conservative tracer minus less stable tracer over time. Measurements were taken in the fracture space near injection.

This graph illustrates that as systemic fracture spacing is decreased, the difference between the tracers becomes larger. This graph shows a convergence in concentration at the beginning and end of the simulation. This is a direct function of both the kinetic properties chosen and the characteristics of the injection and production sink and source in the model.

The temperature gradient change between the different degrees of fracture spacing is illustrated in Figure 3 below.

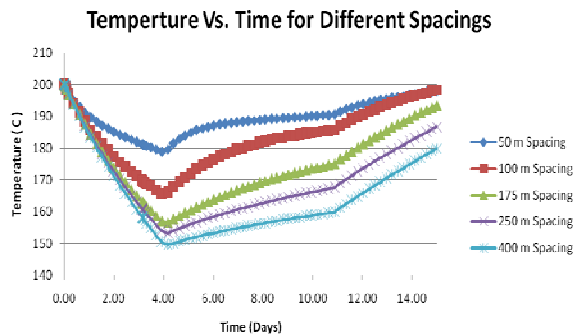


Figure 3. Temperature (°C) over time. Measurements were taken in the fracture space near injection.

This graph illustrates that as global fracture spacing is decreased, the transmissibility between the fractures and the matrix is increased. In this process, heat transfer becomes more involved at the fracture/matrix interface for lower spacing (i.e., heat loss reduced by an increased rate of heat transfer from the hotter matrix to the colder fracture). Therefore, during the 4-day injection period, temperature drop in the fracture happens at a much slower rate

for 50 m spacing compared to 400 m spacing. This is also seen at day 11 when the production begins.

In the next case, 3 simulations were run at 50 m fracture spacing. The thermal decay kinetics of the conservative tracer were held constant, while the decay kinetics of the less stable tracer were varied. The kinetic values for the less stable tracer were chosen as outlined in Table 1.

Table 1. Kinetic thermal decay values chosen to compare sensitivity

Model #	Kinetics of Conservative Tracer	Kinetics of Less Stable Tracer
1	Same as in Figures 1-3	Same as in Figures 1-3
2	Same as in Figures 1-3	Slightly Faster than Figures 1-3
3	Same as in Figures 1-3	Slightly Slower than Figures 1-3

Figure 4 shows the outcome of this simulation, and the results are shown in difference in concentration of the conservative tracer and the less stable tracer.

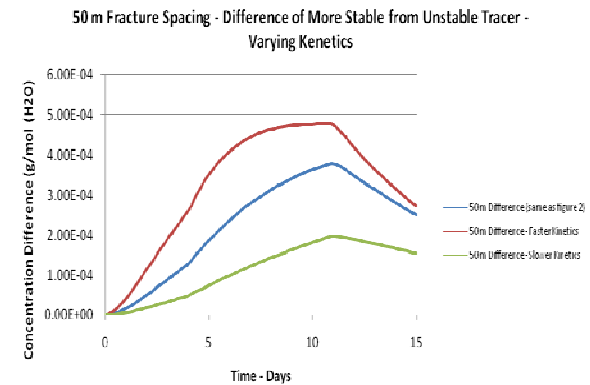


Figure 4. Conservative tracer minus less stable tracer over time. Only the Thermal Decay Kinetics of the Less Stable Tracer are varied. Measurements were taken in the fracture space near injection.

This figure illustrates that when the less stable tracer is chosen to have more sensitivity to temperature, the difference between the conservative and less stable tracer becomes larger. This suggests that in a field experiment, several variations of thermally unstable tracers can be used in a reservoir, depending on the physical properties. In addition, it may be possible to use more than two tracers to gather information about fracture density.

CONCLUSION

Using dual tracers and a novel computational method, it is possible to relate changes in tracer concentration to changes in fracture surface area. As previously stated, this method provides a convenient measurement for fracture characterization from a hydraulic stimulation. Using a conservative tracer as control due to its thermal stability, a less thermally stable tracer will provide contrast based on the available surface area for heat transfer. When only thermal decay is considered, changes in the amount of heat exchange between the matrix and fractures will be shown by the increased decay of a less stable tracer.

The figures above show the effect of tracer concentration by changing the effective fracture surface area. When the effective surface area is increased, transmissibility increases, and thermal energy is able to propagate faster from the matrix to the fractures. The result of this increase is a lower tracer concentration in response to a higher temperature gradient for a higher fracture surface area.

Currently, much work is being done to prepare this model for inversion. As discussed in both the abstract and the introduction, it would be very beneficial to use a backflow injection tracer profile to determine how the overall fracture surface area is changing during a stimulation event.

REFERENCES

- Adams, M., Davis, J. "Kinetics of Fluorescein Decay and its Application as a Geothermal Tracer." *Geothermics*, Vol 20, No 1 / 2, pg 53-66, 191
- Maloszewski, P., Zeber, A. "Mathematical Modeling of Tracer Behaviors in Short-Term Experiments in Fissured Rocks." *Water Resources Research*, Col 26, No 7, pg 1517-1528, July 1990
- Maloszewski, P., Zeber, A. "On the Theory of Tracer Experiments in Fissured Rocks with a Porous Matrix." *Journal of Hydrology*, No 79, pg 333-358, 1985
- Pruess, K., et al., "Tracer Testing for Estimative Heat Transfer Area in Fractured Reservoirs." *Proceedings World Geothermal Congress 2005*. Antalya, Turkey. pgs 24-29, April 2005
- Ptak, T., Schmid, G., "Dual-tracer Transport Experiments in a Physically and Chemically Heterogeneous Porous Aquifer: effective transport parameters and spatial variability." *Journal of Hydrology*. No 183, pgs 117-138, 1996
- Rose, P., et al., "The Application of Rodamine WT as a Geothermal Tracer." *Geothermal Resources Council. Transactions*, Vol 18, pgs 237-240, October 1994
- Xu, T., Pruess, K., "Modeling Multiphase Non-isothermal Fluid Flow and Reactive Geochemical Transport in Variably Saturated Fractured Rocks: 1. Methodology." *American Journal of Science*. Vol 301, pgs 16-33, January 2001.
- Xu, T., Zhang, G., and Pruess, K., "Use of TOUGHREACT to Simulate effects of Fluid Chemistry on Injectivity in Fractured Geothermal Reservoirs with High Ionic Strength Fluids." *PROCEEDINGS, 13th Workshop on Geothermal Reservoir Engineering*, Stanford University, Stanford, California, January 31-February 2, 2005, (pgs not listed).

ANALYSIS OF THE DOUBLET-WELL DISTANCE EFFECTS IN A POROUS MEDIUM GEOHERMAL RESERVOIR IN TIANJIN, CHINA

Jialing Zhu and Haiyan Lei

Geothermal Research & Training Centre, Tianjin University
92 Weijin Road, Nankai District
Tianjin 300072, China
e-mail: zhujl@tju.edu.cn

ABSTRACT

We established conceptual and mathematical models for a porous geothermal reservoir (study area of 532.86 km²) in Tianjin, China. As part of this project, history matching simulations were carried out for 2 years using TOUGH2. The results fit well with the measured data. Based on this observation, reservoir pressures and temperatures were further studied with doublet well distances ranging from 700 m to 250 m, under reinjections of (respectively) 60% and 100% of the separated water. The results indicated that the pressure of production wells increased slightly with decreasing doublet-well distances—because the funnel formed during production and reinjection processes interacted with each other as the well distances were reduced, and the injected cold water compensated for the pressure drop of the production well.

However, as expected, the reservoir temperature did not change when the well distance varied from 700 m to 350 m: injected cold water would have little influence on the production wells due to the larger flow resistance that exists in porous reservoirs. Also, most reinjection wells do not work during the nonheating period. The geothermal fluid could exchange heat sufficiently with the injected cold water, and accordingly, the cold front moves slowly and prolongs the thermal breakthrough. When the well distance further decreased to 250 m, the reservoir temperature visibly changed because of heat breakthrough. It could thus be concluded that the distance between the reinjection and production wells should be more than 250 m to avoid thermal breakthrough. Future work should involve further mesh subdivision, pressure and temperature modeling between production and reinjection wells, and funnel compensation effect analyses.

1 INTRODUCTION

Tianjin City is located in the north-central part of the North China Basin. This region is rich in porous medium geothermal resources from the Neogene rock system. The annual production rate is 1.5×10^7 m³ (Gao and Zeng, 2006), about half of the geothermal production rate of the entire city. Porous geothermal reservoirs are commonly found in China, and

remarkable achievements have been made in resource protection, large-scale reinjection tests, and research, based on its longer exploitation history and advanced development. Given this, the results from studies of reinjection into a porous medium geothermal reservoir in Tianjin could significantly promote sustainable geothermal development in other regions of China.

The study area—an area 532.86 km² in size, with a centralized exploitation area of 160 km²—is located east of the Tanggu district in Tianjin. Twenty production wells have been explored within the Ng geothermal reservoir since 2005, although no reinjection wells have yet been developed. All of the twenty wells were artesian at the beginning of exploitation, with static water levels close to the surface, and the initial runoff direction was from the northeast to the southwest, with gentle slopes. However, great changes have occurred in the original flow field due to different production rates in various regions. A drawdown funnel has formed in some high-production-rate areas and is still expanding, which has resulted in the runoff of geothermal fluids from the periphery to the center of Tianjin City.

2 GEOLOGICAL SETTING

2.1 Geological characteristics

The study area crosses the Beitang and Banqiao depression, The Cangdong and Haihe faults, the main faults in the area, have a strong local effect. The Cangdong fault lies in the western part of the study area, at the boundary of the Huanghua depression and the Cangxian uplift. The Cangdong fault strike is NNE-trending, inclined to SEE-trending. The angle of inclination ranges from 30° to 60°, which possesses the characteristics of a syngenetic fault and succession (Zeng and Li, 2007). The Haihe fault starts west of Zhuo in Heibei Province, runs along the path of Yongqing to Tianjin and the Tanggu District, and finally extends eastward to Bohai Sea along the Haihe River. The length of this fault on land is about 180 km. The Haihe River fault strike is NWW-trending, inclined to SSE-trending, with an inclination angle steep in the upper segment and gradual in the lower one. The Haihe Fault controls the sediment of the Paleocene Formation, which is the boundary of the Beitang and Panqiao depression.

2.2 Geothermal reservoirs.

There are two well-developed Neogene geothermal reservoirs in the Tanggu District, the Nm and Ng Group. Four wells in the Nm group reservoir were drilled in the Tanggu District by the end of 2007; their annual production rate is about $24.9 \times 10^4 \text{ m}^3$, with static water level of 62–72 m and annual water-level drawdown of 1.2 to 1.6 m (Lin and Wang, 2007). Taking Well TG13 as a representative well, its static water level was 71.37 m in December 2007, with average annual water-level drawdown of about 3.09 m from 2004 to 2007.

Up until the end of 2007, 35 wells (including one reinjection well) have been drilled in the Huanghua depression, where no Ng group reservoirs exist. The total annual production rate was $291.3 \times 10^4 \text{ m}^3$, the instantaneous production rate of a single well was 40 to $90 \text{ m}^3/\text{h}$, and the static water level was 70 to 90 m. Water level drawdown was 0.26 to 7.0 m, while the biggest dynamic water level was 107.83 m, which occurred in Well TG17. From Figure 1, we can see that geothermal wells are concentrated west and east of the Tanggu District, where two funnels have been formed, and the static water level decreases gradually.

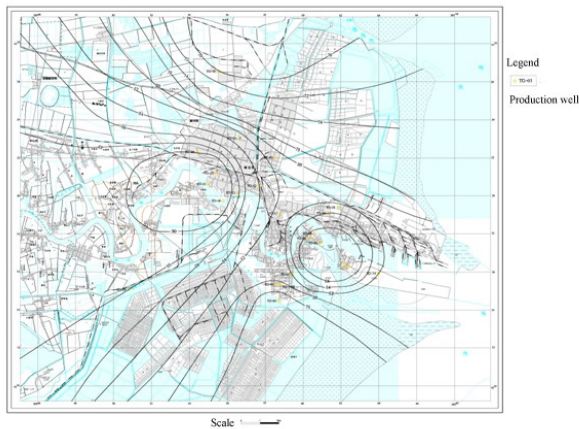


Figure 1. Isoline map of static water level in Ng reservoir in Tanggu district in 2007

2.3. Conceptual model of the geothermal system

According to our analysis of geothermal heat sources, reservoir, cap rock, fluid recharge, and run off conditions, we established a conceptual model of the geothermal system, based on the local geological conditions, which are mainly comprised of heat source, heat transfer, and the formation of geothermal resources, as shown in Figure 2.

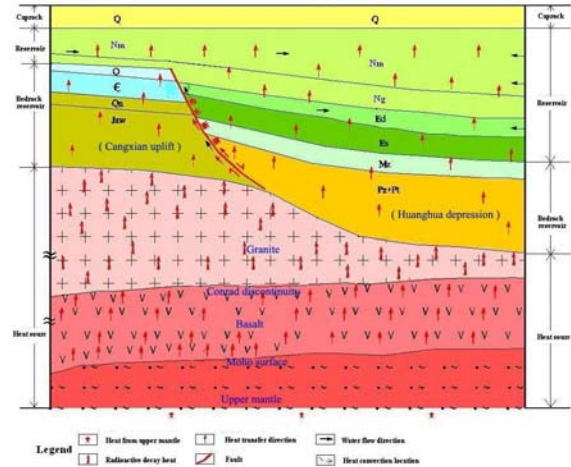


Figure 2. Conceptual model of the Tanggu geothermal reservoir

3 PARAMETER DETERMINATION

3.1 Basic mathematical model

Thermal breakthrough time needs to be estimated under different doublet well distances, i.e., the time from the initial injection until a significant cooling is observed in a production well. The mass conservation equation (Zhu and Wang, 2004) is:

$$\frac{\partial \phi \rho}{\partial t} = \frac{-\partial \phi S \rho_v}{\partial t} + \frac{\partial \phi (1-S) \rho_l}{\partial t} = -\nabla F + q_p \quad (1)$$

where subscript l , subscript v , F , q_p , ρ , Φ , and S are liquid phase, vapor phase, vector of mass matrix, external energy, density, porosity, and vapor saturation, respectively.

The energy conservation equation (conductivity and convection) is

$$\frac{\partial(Q/V)}{\partial t} = \frac{\partial(u\rho\phi + u_s\rho_s(1-\phi))}{\partial t} \quad (2)$$

$$= -\nabla G + \left(\frac{F_v}{\rho_v} + \frac{F_l}{\rho_l}\right)\nabla p + Q_u$$

where s , u , G , Q , V , and Q_u are solid phase, internal energy, energy matrix, energy, volume of reservoir, and external energy, respectively.

Equations (1) and (2) are related to one- or two-phase filtrations in a porous medium, where the rock matrix and fluid are considered to be in local thermal equilibrium. For a block of microvolume V_n of the field, the transfer equation (5) of mass and energy can be interpreted by Equations (3) and (4):

$$\frac{\partial \phi \rho}{\partial t} = \sum_{m=1}^N \frac{F_m A_m}{\tau} + q \quad (3)$$

$$\frac{\partial u_s}{\partial t} = \left(\frac{\partial u_s}{\partial t}\right)_\rho \frac{\partial u}{\partial t} + \left(\frac{\partial u_s}{\partial t}\right)_u \frac{\partial \rho}{\partial t} \quad (4)$$

$$\Delta U_n = \Delta t \frac{\frac{1}{V} \sum_{m=1}^N A_{nm} (G_{nm} - u_n F_{nm}) + (Q_n - Q'_n)}{\phi \rho + (1 - \phi) \rho_s \left[\left(\frac{\partial u_s}{\partial u}\right)_\rho + \left(\frac{\partial u_s}{\partial \rho}\right)_u \frac{\partial \rho}{\partial u \partial t} \right]} \quad (5)$$

3.2 Rock types

The Nm Group reservoir has rich thermal fluids. Light grayish green, yellow-powder sandstone and siltstone with medium sand are the primary water rocks, the average porosity being 33%. On the other hand, siltstone is the main lithology of Unit I of the Ng Group reservoir, including mudstone and sandy mudstone. Their average porosity is 27%–38%. In this area, Unit III of the Ng group is the dominant production reservoir; rock type is glutenite with a porosity of 20%–38% and permeability of (0.75-1.88) × 10⁻¹² m².

3.3 Boundary conditions

According to the local geothermal survey data, the Ng Group reservoir develops stably and is hardly ever affected by the ambient fractures. A water-level map of 2007 showed that the water level in this area gradually increased from the north to the south side. A funnel has formed in the central production area, but obvious runoff characteristics did not show up on either the east or west side. Therefore, the eastern and western parts of the study area were set as impervious boundaries, while the northern part was considered the recharging boundary and the southern part the discharging boundary.

3.4 Grid system

For simulation purposes, the study area was assumed to be a rectangular prism 25 km long, 21.3 km wide, and 2.1 km deep. Figure 3 shows the plan view of the computational grid. The model has two horizontal layers ranging in thickness between 150 m and 1,100 m. Each layer has 780 gridblocks, their horizontal dimensions varying from 250 m × 250 m to 2000 m × 2000 m. The geothermal well is in the center of the model, covering an area of 250 m × 250 m, which contains the gridblocks with the smallest horizontal size. Calculation time was divided into heating and nonheating periods, and the time step was set to 10 days during simulation. The codes Mulgeom and Mulgraph (O’Sullivan and Bullivant, 1995) were used as pre- and post-data processors. The mass flow of each production well was given based on *in situ* utilization. Measured data was from Nov. 2005 to Dec. 2007.

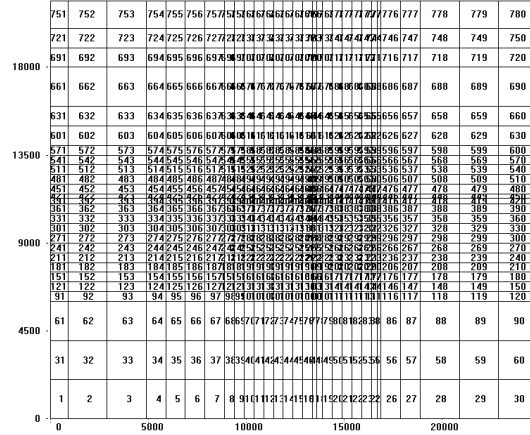


Figure 3. Plan view of the computational grid

3.5 Model calibration

The simulation is mainly focused on fitting the dynamic monitoring data of 20 production wells that have been explored since 2005. The related reservoir parameters could be adjusted reasonably by fitting the pressure of the geothermal well. The AUTOUGH2 code (O’Sullivan, 2000) was used to predict the performance of the reservoir. Permeability and porosity are key parameters in determining the reservoir pressure (Zhu and Zhang, 1996). The iteratively changing parameters show that the reservoir pressure drops quickly under the lower permeability, the smaller layer thickness, and the greater water mass flow (Wang and Zhu, 2003). Table 1 gives the numerical modeling parameters.

Table 1. Parameters of numerical model for the Ng geothermal reservoir

Cap rock	Temperature (°C)	55
	Thickness (m)	950-1300
	Permeability (10 ⁻¹² m ²)	0.1-0.8
	Porosity	0.25
	Rock grain density	2109
	Rock grain specific heat	958
	Formation heat	1.5
Ng geothermal reservoir	Permeability(10 ⁻¹² m ²)	0.8-1.0
	Porosity	0.27-0.33
	Rock grain density	2103
	Rock grain specific heat	909
	Formation heat	1.6
	conductivity (W/m. °C)	

3.6 History matching simulations

History matching simulations started from Nov. 2005. Two representative production wells (TG07 and TG17) were selected for modeling the water-level and temperature changes over 2 years. Figures 4 and 5 show the fitting of the simulated and measured curves of the two wells. We can see that the simulations agree well with the monitoring data.

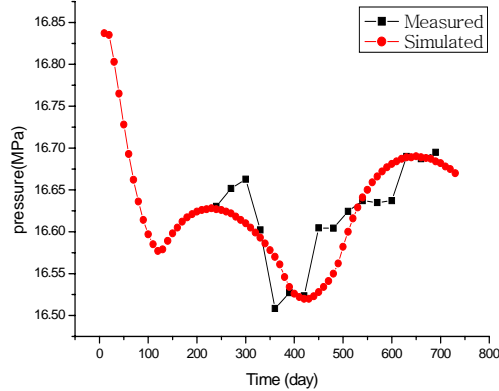


Figure 4. Comparison of measured and simulated pressure for Well TG07

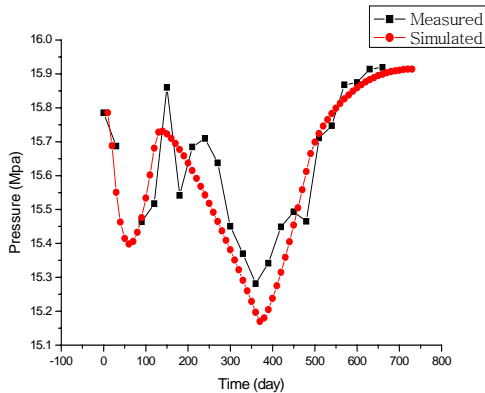


Figure 5. Comparison of measured and simulated pressure for Well TG17

4 SIMULATIONS OF PRESSURE AND TEMPERATURE OF N G RESERVOIR FOR DIFFERENT WELL DISTANCES

4.1 Simulation of temperature for different well distances

4.1.1 Comparison of temperature for different well distances

Assuming the reinjection rate is 60% of production, and the injected water temperature is 35 °C, we simulated the temperature change for TG07 and TG17 with a variety of doublet well distances (Figures 6 and 7).

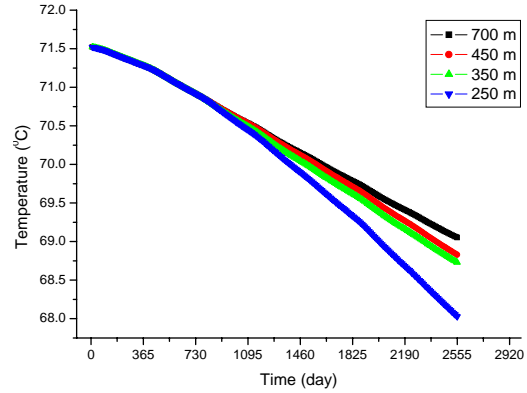


Figure 6. Temperature drop for Well TG07 under 60% reinjection rates

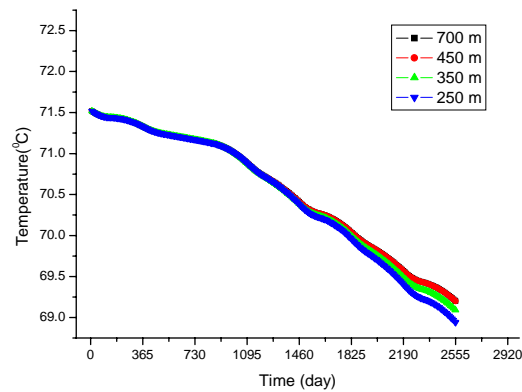


Figure 7. Temperature drop for well TG17 under 60% reinjection rates

When the reinjection rate is further increased to 100% of the production rate, and the injected water temperature remains at 35°C, similar temperature changes for TG07 and TG17 are obtained, as shown in Figures 8 and 9, respectively.

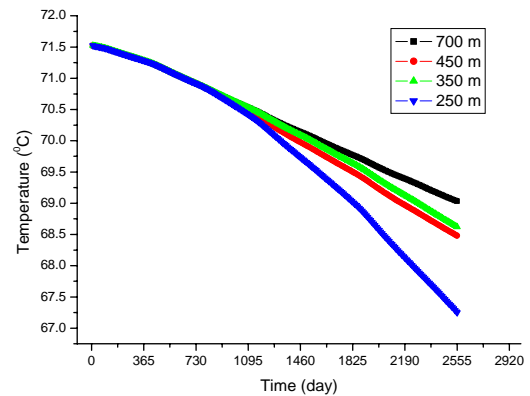


Figure 8. Temperature drop for well TG07 under 100% reinjection rates

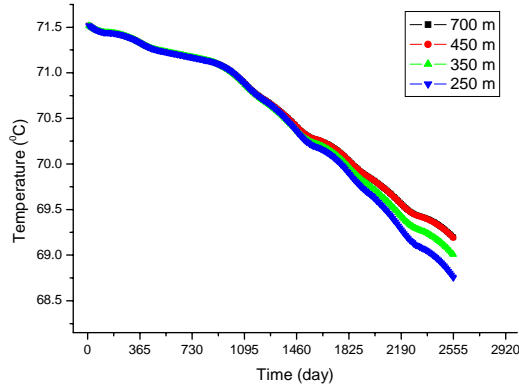


Figure 9. Temperature drop for well TG17 under 100% reinjection rates

It can be seen from Figures 6 and 7 that when the water temperature of TG07 and TG17 decreases 2.5°C, 5 years later when the doublet well distance is 700 m, the annual temperature drop is 0.5 °C, which is larger than that of the fracture reservoir. Considering the formation characteristics of porous medium reservoirs, its channel develops poorly, and radial flow recharge is dependent on hydraulic gradient. Much injected cold water will result in the reduction of temperature of water stored in the pore, which induces not only longer restoration time, but also the obvious temperature drop in geothermal fluid—that is the reason why the temperature drop in a porous reservoir is larger than that in a fractured reservoir.

Figures 8 and 9 show that when the reinjection rate is equal to production rate, and the injected water temperature is kept at 35°C, the declining trend of water temperature is similar to Figures 6 and 7, but it drops slightly more. This is because when the doublet well distances are reduced to some extent, the injected cold water would have a significant impact on the water temperature in a production well. Under those conditions, the bigger the mass flow of injected water, the lower the water temperature of the production well.

In Figures 6–9, we can also see no significant change of water temperature in TG07 and TG17 occurs when the doublet well distance gradually decreases from 700 m to 350 m. This is because the porous reservoir has a larger porosity, and the flow resistance of injected cold water is more substantial. Thus, water flows slowly, which has little influence on the production wells. In addition, most reinjection wells do not work during nonheating periods, which give injected cold water enough time to absorb the heat stored in the rock and exchange heat sufficiently with the geothermal fluid. Accordingly the movement of the cold front slows down and the thermal break through is prolonged significantly.

However, as the doublet well distance is further reduced to 250 m, an obvious drawdown of water temperature occurred in both TG07 and TG17 over 3–5 years. This is because the flow channel between injected cold water and geothermal fluids shortens at that time, even though the pore channels in the porous reservoir are not as good as those of the fractured reservoir. The mixed frontal area of cold and hot fluids would arrive at the production well after 3–5 years. Thermal breakthrough occurs and results in a sharp decline in geothermal fluid temperature.

4.1.2 Comparison of well temperature for the same well distance

A comparison of the water temperature for TG07 under 60% and 100% reinjection rates for the same well distance—with the temperature of the injected cold water 35°C—is shown in Figures 10 to 13.

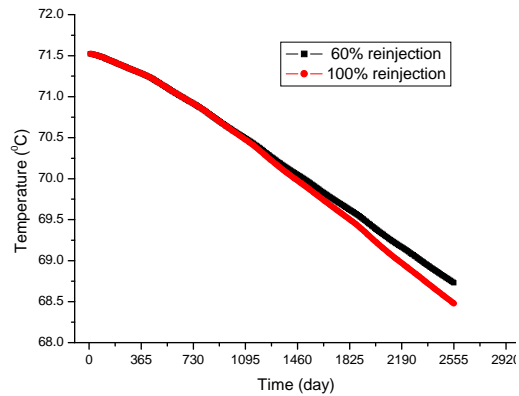


Figure 10. Water temperature prediction for the well distance of 700 m

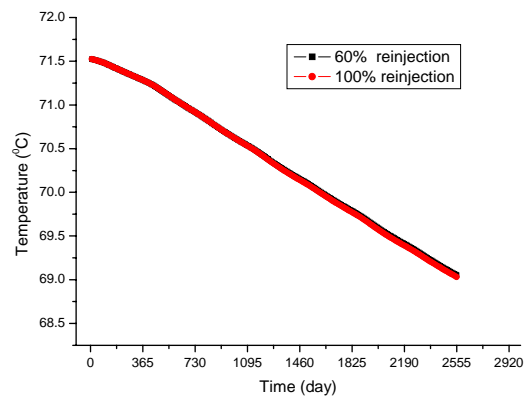


Figure 11. Water temperature prediction for the well distance of 500 m

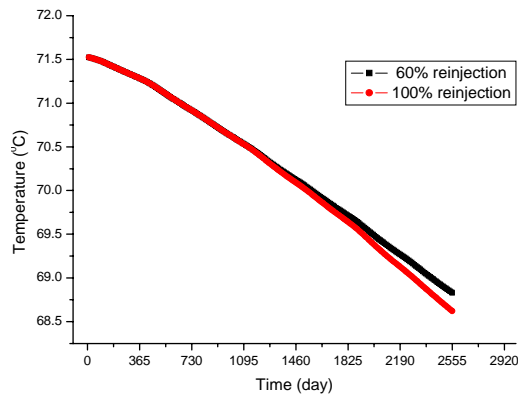


Figure 12. Water temperature prediction for the well distance of 350 m

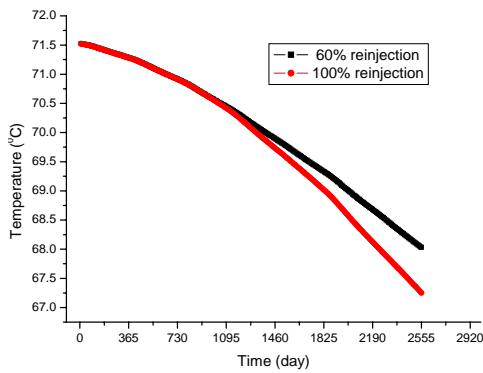


Figure 13. Water temperature prediction for the well distance of 350 m

Figures 10 to 13 give the comparison of water temperature of TG07 under 60% and 100% reinjection rate for the same well distances. It can be seen that when the well distance is 700 m, the injected water temperature has almost no impact on the temperature of geothermal fluids. However, decreasing the well distance and the injected water temperature results in lower geothermal fluids temperature. Compare to the condition of 60% reinjection rate and 35°C injected water. If the reinjection rate is raised to 100% whereas the injected water temperature is unchanged, the temperature differences are 0.01°C, 0.10°C, 0.18°C, 0.46°C in sequence, corresponding to the well distances of 700 m, 500 m, 350 m, and 250 m.

4.2 C omparison of pre ssure for di fferent w ell distances

Figures 14 and 15 show the simulated pressure predictions under 60% reinjection rate and 35°C injected cold water for TG07 and TG17, respectively.

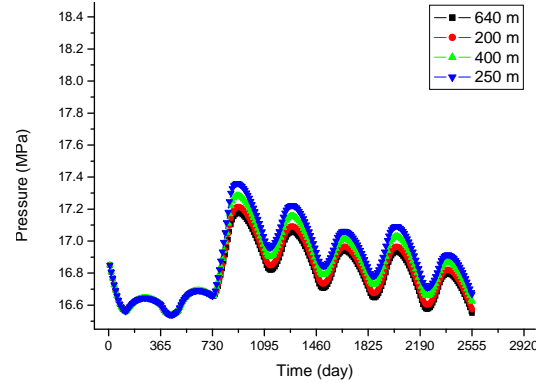


Figure 14. Pressure prediction for well TG07

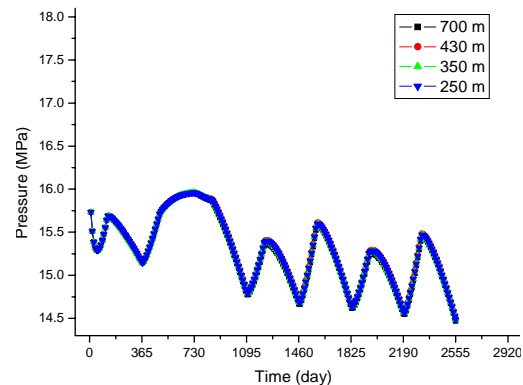


Figure 15. Pressure prediction for well TG17

We can see from these figures that the pressure for Wells TG07 and TG17 increases slightly as the doublet well distances decrease gradually, This is because both production and reinjection wells have their own funnel effect, which interact with each other as the well distance is reduced. Under these conditions, the injected cold water could compensate for the pressure drop in the production well, and the pressure of the reinjection well slightly declines accordingly. The smaller the well distance, the greater the funnel compensation effect. Therefore, the pressures in production and reinjection wells could compensate for each other and eliminate the mutual funnel effect at a certain well distance, if there is a good flow connection between them. Future work should be aimed to further subdivide the mesh, model the change in pressure and temperature fields between production and reinjection wells, and observe the funnel compensation effect.

5. CONCLUSIONS

The following conclusions can be drawn based on the above simulations:

- 1) A three-dimensional numerical model has been established for the Ng porous-medium geothermal reservoir in the eastern Tangu district, with TOUGH2 used for modeling the

- production history over 2 years. The results showed that simulated data agree well with the measured data.
- 2) When the reinjection rate and injected cold water temperature are 60% and 35°C, respectively, the annual water temperature drop for Well TG07 and TG17 is 0.5°C with the doublet well distance of 700 m. This is because the flow channel in the porous medium reservoir develops poorly, and large amounts of injected cold water would result in a decrease in the temperature of water stored in the pores—inducing not only longer restoration time, but also an obvious temperature drop in geothermal fluids.
 - 3) When the reinjection rate is increased to 100% of the production well, and injected water temperature is kept at 35°C, the water temperature drop for Wells TG07 and TG17 increases. This is because the injected cold water significantly affects water temperature in production wells under those conditions. The bigger the mass flow of injected water, the lower the water temperature of the production well.
 - 4) When the doublet well distance gradually decreases from 700 m to 350 m, no significant change in water temperature occurs in Wells TG07 and TG17. This is because the flow resistance of injected cold water in a porous reservoir is large, and the injected cold water has little influence on the production wells since the water flows slowly. In addition, most reinjection wells do not work during non-heating periods, which helps the injected cold water exchange heat sufficiently with the geothermal fluids, and accordingly, the cold front moves slowly and prolongs the thermal breakthrough.
 - 5) When the doublet well distance is further reduced to 250 m, water temperature obviously drops in Wells TG07 and TG17 after three and five years, respectively. This is because the flow channel between injected cold water and geothermal fluids shortens when the mixed cold and hot fluids arrive at production well, and thermal breakthrough occurs, resulting in a sharp decline in geothermal fluid temperature.
 - 6) The pressure in Wells TG07 and TG17 slightly increases as the doublet well distances gradually decrease. This is because the funnels formed during production and reinjection processes interact with each other as the well distance is reduced. The injected cold water compensates for the pressure drop in the production well. The smaller the well distance, the greater the funnel compensation effect.

- 7) Future work should include further mesh subdivision, pressure and temperature modeling between production and reinjection wells, and funnel compensation effect analysis.

ACKNOWLEDGMENT

The authors give special thanks to Tianjin Geothermal Exploration and Development-Designing Institute for geological data supply and suggestions. The work was supported by The Ministry of Science and Technology of the People's Republic of China, under contract No. 2006AA05Z425.

REFERENCES

- Baozhu, Gao., and Meixiang, Z., Caused and prevention measures of clogging in the reinjection well of a geothermal double-well system (in Chinese), *Hydrogeology and Engineering Geology*. 34 (2), 75-80, 2007.
- Jialing, Z., and Qi, Z. Numerical study on the geothermal resources assessment in Tuanbo landscape region, Tianjin (in Chinese), *ACTA Energetica Solaris Sinica*. 17(4), 336-343, 1996.
- Jialing, Z., and Kun, W., Reinjection tests in bedrock geothermal reservoir of Tianjin, *Transactions of Tianjin University*, 10(1), 67-70, 2004.
- Kun, W., and Jialing, Z. Study on tracer test and reinjection of doublet system in Tianjin baserock reservoir (in Chinese), *ACTA Energetica Solaris Sinica*. 24(2), 162-166, 2003.
- Li, L., and Liancheng, W., A discussion of the factors affecting geothermal reinjection in the geothermak reservoir of porous type in Tianjin, *Hydrogeology and Engineering Geology*. 35(6), 125-128.
- Meixiang, Z., and Huijuan, L., The study on drilling technique of tertiary reservoir reinjection well, *Geology and Prospecting*. 43(2), 88-92, 2007.
- O'Sullivan, M.J., *AUTOUGH2 Notes*. Geothermal Research Software. Department of Engineering Science, University of Auckland, 2000.
- O'Sullivan, M.J., and Bullicant, D.P., *TOUGH2 User's Guide*, Lawrence Berkeley Laboratory, Report LBL-37200, Lawrence Berkeley National Laboratory, Berkeley, Calif., 1995.
- O'Sullivan, M.J., *AUTOUGH2 Notes*. Geothermal Research Software. Department of Engineering Science, University of Auckland, 2000.

NUCLEAR WASTE

VERIFICATION OF NUMERICAL TOOLS THROUGH THERMO-HYDRO-GAS (THG) MODELING FOR A GEOLOGICAL REPOSITORY IN BOOM CLAY

Li Yu, Eef Weetjens, and Janez Perko

Institute for Environment, Health, and Safety, Belgian Nuclear Research Centre (SCK·CEN)
Boeretang 200, B-2400 Mol, Belgium
e-mail: lyu@sckcen.be

ABSTRACT

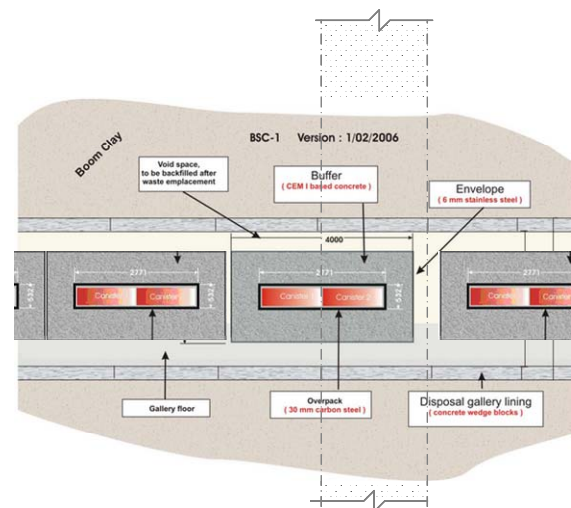
Verification of two numerical tools, TOUGH2-EOS5 module and CODE_BRIGHT, is carried out through three benchmark cases, including a 1D hydro-gas (HG) case, a 2D axi-symmetrical HG case with a constant hydrogen production rate, and a 2D axi-symmetrical thermo-hydro-gas (THG) case with time-varying heat and gas production rate. These benchmark cases for modeling the gas-driven migration of pore water under the combined effects of high gas pressure and high temperature are based on the Belgian multibarrier repository design for disposal of high-level waste (HLW). Comparisons between numerical results demonstrate that these two numerical tools give quite similar results in all three benchmark cases, thus providing evidence for the validity of these tools in solving HG and THG problems. The differences in the results obtained by two modeling tools are also analyzed.

INTRODUCTION

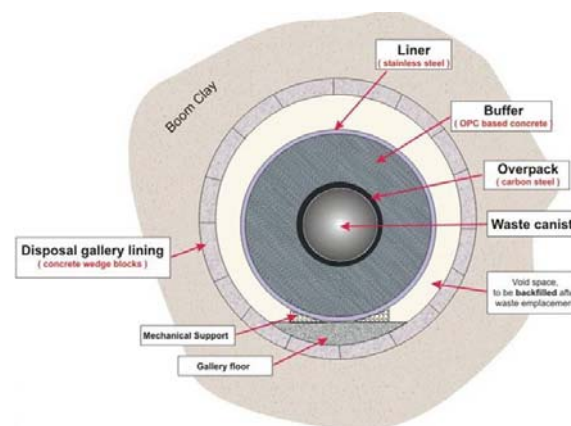
Within a geological disposal facility located in a formation with an extremely low permeability, accumulation of gas originating from the anaerobic corrosion of ferrous materials, microbiological degradation, and other gas generation processes may lead, for certain waste forms, to the buildup of gas pressure (Rodwell, 2000). Also, vitrified HLW and spend fuel (SF) release significant amounts of heat due to radioactive decay. Investigation of the gas-driven migration of aqueous-born contaminants under the combined effects of high gas pressure and high temperature in the multibarrier system is expected to become an increasingly important element of future safety cases for geological repositories in clay formations. Numerical models and tools will be critical in adequately understanding such complex systems. Through benchmark calculations and analyzing differences in the results obtained by using different modeling tools, proper application of the software and increased understanding of the kernel features can be assured. Confidence in simulation results will thereby increase.

Both TOUGH2 and CODE_BRIGHT are extensively used in evaluating nuclear waste disposal facilities. TOUGH2, developed primarily at Lawrence Berkeley National Laboratory (LBNL), can model multiphase and multicomponent flow by means of the

integral finite difference technique (Pruess, 2004). CODE_BRIGHT is a finite element code developed by the Technical University of Cataluña (UPC), Spain, for calculating displacements, liquid pressure, gas pressure, temperature, and salt content for boundary value problems in saturated or unsaturated soil (Olivella et al., 1996).



(a)



(b)

Figure 1. Schematic diagram of the Belgian disposal concept for vitrified HLW. (a) longitudinal section through a disposal gallery (b) Cross-section view of supercontainer (Wacquier et al., 2009)

The present Belgian disposal concept, referred to as "supercontainer" and under development since 2004, considers an engineered waste package entity in which the vitrified waste canister or spent fuel assemblies are placed. Figure 1 schematically illustrates a longitudinal and cross section of a vitrified HLW disposal gallery.

The supercontainer design for vitrified HLW considers disposal of two vitrified AREVA canisters in a watertight cylindrical carbon steel overpack fitted into a prefabricated concrete buffer. The cylindrical cavity between the overpack and the buffer will be filled with liquid mortar or similar cement-based filler, called 2nd phase concrete. After eight supercontainers are placed in a row along the disposal gallery, cementitious material will be backfilled between supercontainer and disposal gallery liner. Supercontainers will be placed such that sections of about 30 m length will be backfilled.

The underground disposal facility is assumed to be located at a reference depth of 220 m in a horizontal plane approximately in the middle of the Boom Clay. It will include spatially separated sections for ILW/HLW/SF. The inner diameter of the disposal galleries is about 3 m. The length of the disposal galleries depends on the waste type and its volumetric inventory, but is limited to 1,000 m for an individual gallery. The distance between the disposal galleries varies from 50 m to 120 m, depending on the heat emission of different types of waste.

Boom Clay is a marine sediment deposited about 30 My ago. At the Mol-Dessel nuclear site, the Boom Clay lies 186–289 m belowground. The Boom Clay layer is slightly dipping into the north-north-eastern direction with a slope of about 1–2% and increasing thickness with water-bearing sand layers situated above and below (Wemaere et al., 2008). Owing to its very low hydraulic conductivity (about 10^{-12} m/s) and the weak hydraulic gradient (about 0.02 m/m), the migration of liquids, dissolved gases, and other solutes in the undisturbed Boom Clay formation is dominated by diffusion (Marivoet et al., 1997).

THEORETICAL BACKGROUND

Mass and energy balance equations solved by TOUGH2 and CODE_BRIGHT can be written in the general form

$$\frac{d}{dt} \int_{V_n} M^k dV_n = \int_{V_n} \mathbf{F}^k \cdot \mathbf{n} d\Gamma_n + \int_{V_n} q^k dV_n \quad (1)$$

where M^k presents mass of component k (i.e., water, air components, solutes, etc.) or energy per volume; \mathbf{F}^k denotes mass flux of component k or heat flux; q^k is sinks/sources.

All the important constitutive laws used in solving the mass- and energy-balance equations implemented in the benchmark cases are listed below.

1) Water retention curve — the van Genuchten model (1980) is chosen for both codes, here expressed in terms of the effective saturation S_e .

$$S_e = \frac{S_l - S_{lr}}{S_{ls} - S_{lr}} = \left[1 + \left(\frac{P_g - P_l}{P_0} \right)^{\frac{1}{1-\lambda}} \right]^{-\lambda} \quad (2)$$

where S_l is liquid saturation; S_{lr} and S_{ls} are residual and saturated saturation of liquid, respectively; S_{gr} and S_{gs} are residual and saturated saturation of gas, respectively; P_g and P_l are gas and liquid pressure, respectively; P_0 and λ are fitting parameters and P_0 is normally taken as air entry pressure. Parameter λ corresponds to the shape parameter m in the original van Genuchten formulation.

2) Intrinsic permeability, k_{in} , is assumed to be isotropic and constant in both codes.

3) Relative permeability—Corey's theory is chosen for both codes.

$$k_{rl} = \hat{S}^4 ; \quad k_{rg} = (1 - \hat{S}^2)(1 - \hat{S})^2 \quad (3)$$

where $\hat{S} = (S_l - S_{lr}) / (1 - S_{lr} - S_{gr})$; k_{rl} and k_{rg} are relative permeability of liquid and gas phase, respectively. The relationship between relative permeability and liquid saturation is shown in Figure 2.

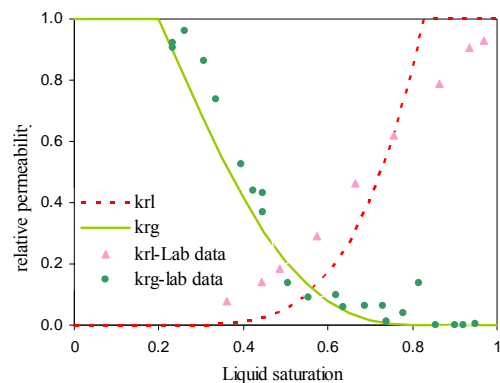


Figure 2. Relative permeability of Boom Clay

4) Dissolution of hydrogen in liquid phase—Henry's constant varies linearly with temperature in TOUGH2, while it is constant in CODE_BRIGHT.

5) Diffusion of dissolved gas in liquid phase—Diffusion coefficient for dissolved gas in liquid phase, D_l^g , in both codes are set to be constant in the benchmark cases. In CODE_BRIGHT, tortuosity τ is also set to be constant, while in TOUGH2, the relative permeability model is chosen for tortuosity:

$$\tau = \tau_0 \tau_\beta = \tau_0 k_{rl} \quad (4)$$

6) Vapor diffusion is considered exclusively in the nonisothermal case (Benchmark 3).

7) Gas/liquid viscosity—Viscosity of hydrogen is linearly interpolated as a function of temperature and gas pressure in TOUGH2. In CODE_BRIGHT, the viscosity is temperature dependent and expressed as:

$$\mu(\text{gas/liquid}) = A \exp\left(\frac{B}{273.15 + T}\right) \quad (5)$$

8) Liquid density—Density of water in CODE_BRIGHT is temperature and pressure dependent and expressed as:

$$\rho_l = \rho_{l0} \exp(\beta(P_l - P_{l0}) + \alpha(T - T_0)) \quad (5)$$

where ρ_{l0} is reference liquid density at reference pressure P_{l0} (0.1MPa) and reference temperature T_0 (0°C); β is compressibility coefficient; and α is volumetric thermal expansion coefficient for liquid.

9) Thermal conductivity—In CODE_BRIGHT, thermal conductivity in Fourier's law is water-saturation dependent and expressed as:

$$\lambda_T = \lambda_{sat} \sqrt{S_l} + \lambda_{dry} (1 - \sqrt{S_l}) \quad (7)$$

where λ_{sat} and λ_{dry} are thermal conductivities of the dry and water-saturated porous medium, respectively; S_l is as defined previously. To be consistent with TOUGH2, λ_{sat} and λ_{dry} are given the same values and treated as constants.

PARAMETERS

All the parameters used in the benchmarks are listed in Table 1 (Weetjens and Perko, 2008; manual of CODE_BRIGHT).

BENCHMARK 1: HG MODELING IN (1D)

Definition of benchmark 1

In Benchmark 1, a simple HG coupled modeling is carried out for a 1D problem to simulate the desaturation process due to gas pressure buildup (Figure 3). The whole domain is separated into two regions. Region I ($x=0-0.316$ m) represents the engineered barrier system (EBS) and Region II represents the host formation (Boom Clay). To simplify the problem, material properties of EBS are set to be the same as Boom Clay.

There is a fixed hydrogen injection rate at the left boundary of the system to simulate gas production as a result of anaerobic corrosion of the carbon steel overpack (corrosion rate is assumed to be $1\mu\text{m}/\text{year}$). Fixed gas and liquid pressures are prescribed at the right boundary to represent undisturbed far-field conditions. The entire domain is initially saturated

Table 1. Parameter set used in the benchmarks

porosity	η (m^3/m^3)	0.397 (Boom Clay)	0.104 (Lining/concrete buffer)	0.300 (2 nd phase concrete/ backfill)
Specific heat	C_p ($\text{Jkg}^{-1}\text{K}^{-1}$)	1100 (Boom Clay)	800 (others)	
Thermal conductivity	λ_T ($\text{Wm}^{-1}\text{K}^{-1}$)	1.0 (2 nd phase concrete/backfill)	1.7 (others)	
Water retention curve	S_{ls}	1		
	S_{lr}	0.012 (Boom Clay)	0.2 (others)	
	λ	0.355 (Boom Clay)	0.43 (others)	
	P_0 (MPa)	2.83 (Boom Clay)	0.5 (others)	
Intrinsic permeability	k_{in} (m^2)	4.6×10 ⁻¹⁹ (Boom Clay and concrete buffer) 4.6×10 ⁻¹⁷ (others)		
Relative permeability	S_{gr}	0.174 (Boom Clay)	0.2 (others)	
	S_{lr}	0.2 (Boom Clay)	0.25 (others)	
Diffusion of dissolved gas	D_T^g (m^2/s)	5×10 ⁻¹⁰ (realistic value)		
Gas viscosity (CODE_BRIGHT)	A (MPa·s)	8.8×10 ⁻¹²		
	B (K)	0		
Liquid viscosity (CODE_BRIGHT)	A (MPa·s)	0.21×10 ⁻¹¹		
	B (K)	1808.5		
Liquid density (CODE_BRIGHT)	P_{l0} (kg/m^3)	1002.6		
	β (MPa^{-1})	4.5×10 ⁻⁴		
	α ($^{\circ}\text{C}^{-1}$)	-3.4×10 ⁻⁴		
Henry's constant (CODE_BRIGHT)	K_H (MPa)	7215 (equivalent to 0.00077 moles (H ₂)/(kg (H ₂ O)×bar) at 25°C		

with a saturation degree of 1 and with a gas pressure of 0.1 MPa. Due to the excavation and backfilling of the tunnel, initial liquid pressure is set to 0.1 MPa in Region I to reflect near-field depressurization during construction, while hydrostatic pressure conditions of 2.3 MPa are assumed (220 m in depth) in Region II. Thermal effect is not considered in Benchmark 1, and the temperature is assumed to be 25°C over the entire domain. Five observation points are selected within the domain; their positions are listed in Figure 3.

In CODE_BRIGHT, gas and liquid pressures are outputted at each node, while liquid saturation is outputted for each element averaged from the element nodal values. In TOUGH2, all the results are outputted at the center of the volume element. In this benchmark, observation points are chosen to be node positions in CODE_BRIGHT, while center-of-volume elements were chosen in TOUGH2.

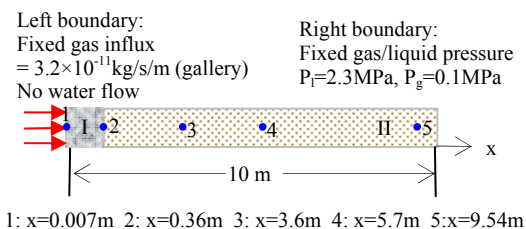


Figure 3. Schematic diagram of benchmark 1

Results of Benchmark 1

Time evolutions of gas/liquid pressure and gas saturation up to 100,000 years at five observation points are compared for the two codes in Figure 4. Because TOUGH2 does not output gas pressure

explicitly for saturated materials, comparisons between gas pressures are carried out only under unsaturated conditions. As illustrated in Figure 4, results from the two codes are quite similar before 3,000 years, when the gas pressure front reaches the right boundary (marked by B). The codes describe the process of resaturation and desaturation in a very similar manner.

When two-phase flow starts, gas pressure and gas saturation obtained by CODE_BRIGHT start to exhibit oscillations (after the transitional point A).

This may be due to the rapid decreasing relative liquid permeability defined in Corey's theory. When the gas pressure front reaches the right boundary, results from CODE_BRIGHT show an abrupt increase of gas pressure due to the sharp transition between an unsaturated element and the saturated boundary condition prescribed at the right boundary. The application of volume elements and the finite difference method makes results from TOUGH2 much more stable in such a situation.

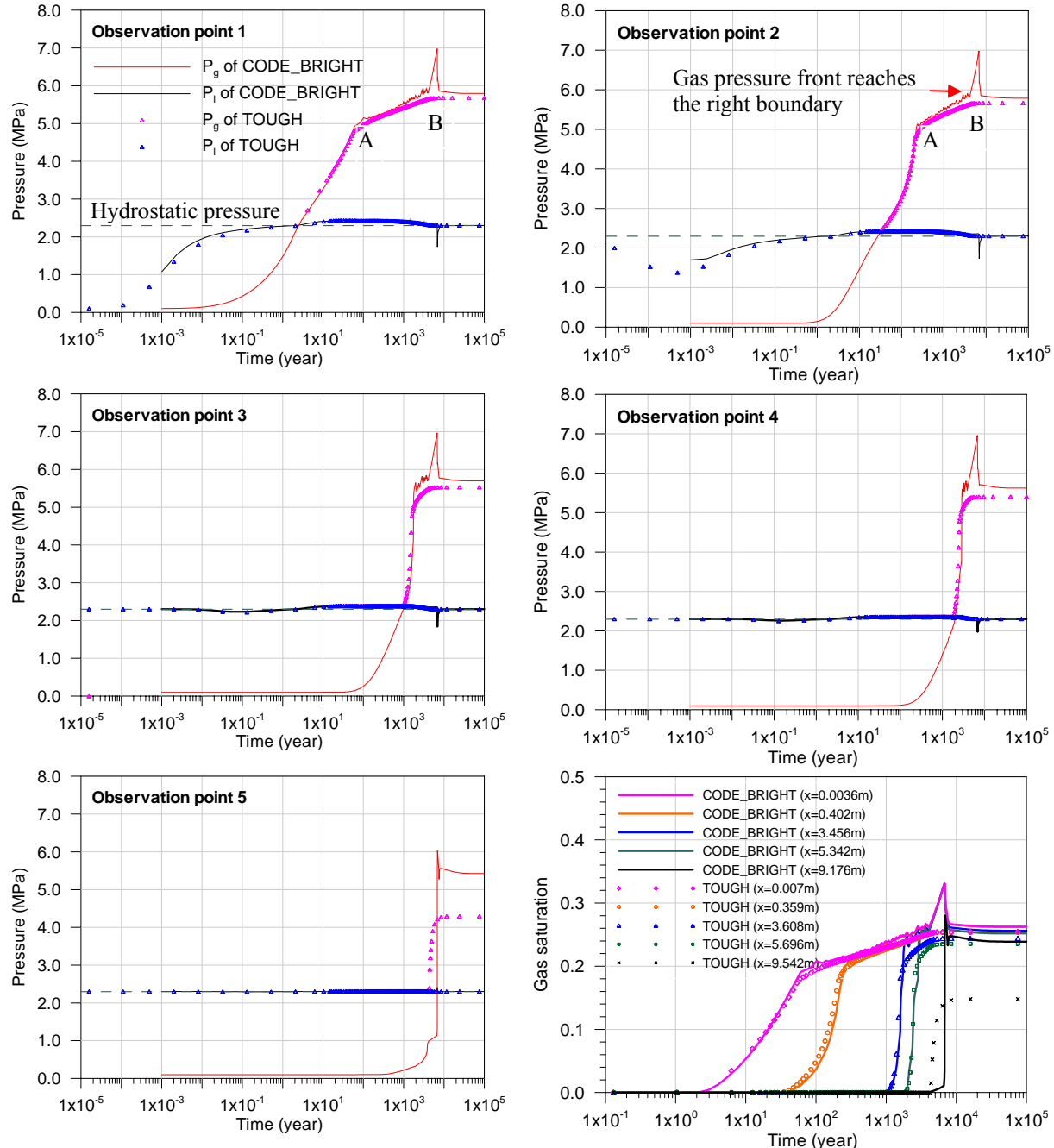


Figure 4. Comparison of time evolutions of gas, liquid pressure and gas saturation at five observation points between two numerical tools in Benchmark 1

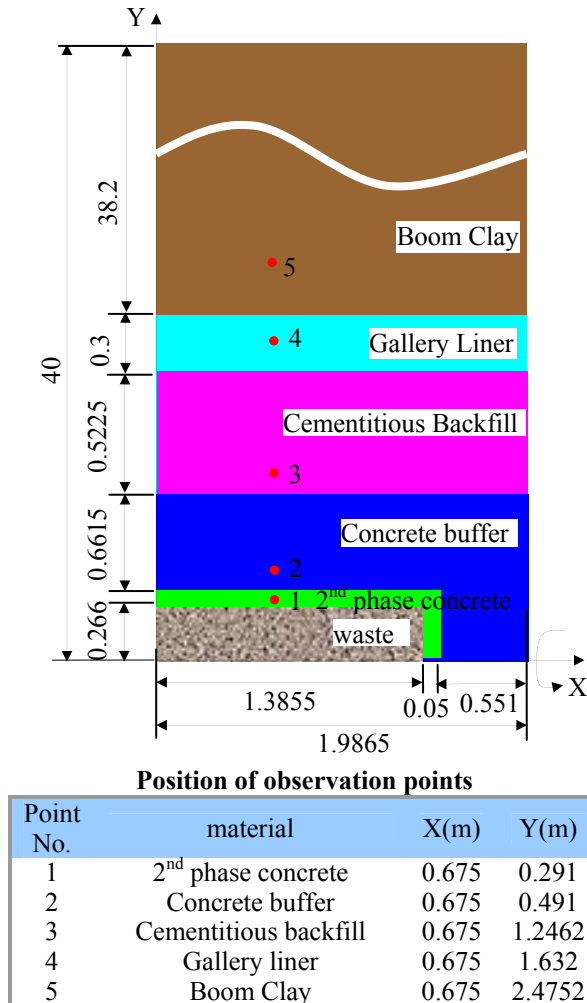


Figure 5. Conceptual model of Benchmark 2 (not to scale) unit: m

It is not surprising that gas saturation, and hence gas pressure at Point 5, is quite different for the two codes. In CODE_BRIGHT, the saturation is averaged from nodal values within the element of $8.81 \text{ m} < x < 9.542 \text{ m}$, while in TOUGH2, the output value is the central value of the element of $9.084 \text{ m} < x < 10 \text{ m}$. Obviously, the latter has a higher liquid degree than the former, which corresponds to a lower gas pressure/saturation.

BENCHMARK 2: HG MODELING (2D)

Definition of Benchmark 2

Benchmark 2 is defined based on the current Belgian disposal concept for vitrified HLW (Figure 1(a)) under isothermal conditions. This case involves 2D modeling of two-phase (liquid and gas) flow with constant hydrogen production.

The disposal gallery lies 220 m deep in Boom Clay and consists of five materials: 2nd phase concrete, concrete buffer, cementitious backfill, gallery liner

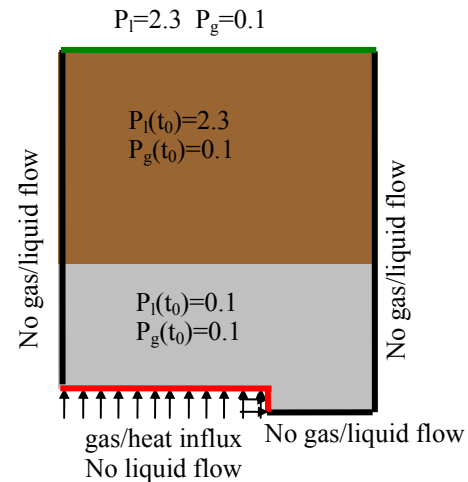


Figure 6. Initial and boundary conditions (unit: MPa)

and Boom Clay. Due to symmetrical conditions, only half a supercontainer (one canister) and corresponding Boom Clay volume is modeled as illustrated by the shaded area in Figure 1(a). Use of a cylindrical geometry of gallery and supercontainer further simplifies the problem into a 2D axis-symmetrical problem by neglecting the effect of gravity on gas/liquid flow (Figure 5). The parameter values for different materials used in the simulation are given in Table 1.

The model domain has a vertical extension of 40 m. Fixed gas/liquid pressures are assigned on the top as illustrated in Figure 6 to represent the unaffected boundary in the far field. Gas influx generated due to the corrosion of the overpack is applied uniformly on the interface of waste and 2nd phase concrete in CODE_BRIGHT, and distributed uniformly among all the volume elements of the 2nd phase concrete in TOUGH2. The total gas generation rate relative to one vitrified HLW canister is 0.475 mol/year , which is equivalent to $1.187 \times 10^{-11} \text{ kg/s/m}^2$ (overpack). The other boundaries are assumed to be impermeable to gas and liquid flow under symmetric conditions. Thermal effect is not considered in Benchmark 2, and the temperature is assumed to be 15.7°C in the whole domain.

Initially, in Boom Clay, hydrostatic conditions with a water pressure of 2.3 MPa at the repository level are assumed (brown color in Figure 6). Operation of disposal galleries under almost atmospheric conditions results in an initial liquid pressure of 0.1 MPa in the EBS, including gallery liner, cementitious backfill, concrete buffer, 2nd phase concrete (grey colour in Figure 6). In the repository period taken as the start of the calculation, the entire domain is set to be initially saturated with a degree of saturation of 1 and with initial gas pressure equal to 0.1 MPa.

The whole domain is meshed with a total of 2997 linear quadrilateral elements and 3116 nodes in CODE_BRIGHT, and discretized with 3160 volume elements in TOUGH2. Five observation points are selected in the entire domain; their positions are listed in the table of Figure 5.

Results of Benchmark 2

Time evolutions of gas/liquid pressure and gas saturation up to 20,000 years at five observation points are compared for the two codes. As illustrated

in Figure 7, both codes give quite similar time evolutions for gas and liquid pressures. Two-phase flow is limited in the region within concrete buffer by the end of 10,000 years. When two-phase flow starts, the same phenomenon as in Benchmark 1 appears, namely that gas pressure and gas saturation obtained by CODE_BRIGHT show oscillations at the transitional point, while they are quite smooth in the results obtained by TOUGH2. This is especially apparent in the gas saturation evolution plot.

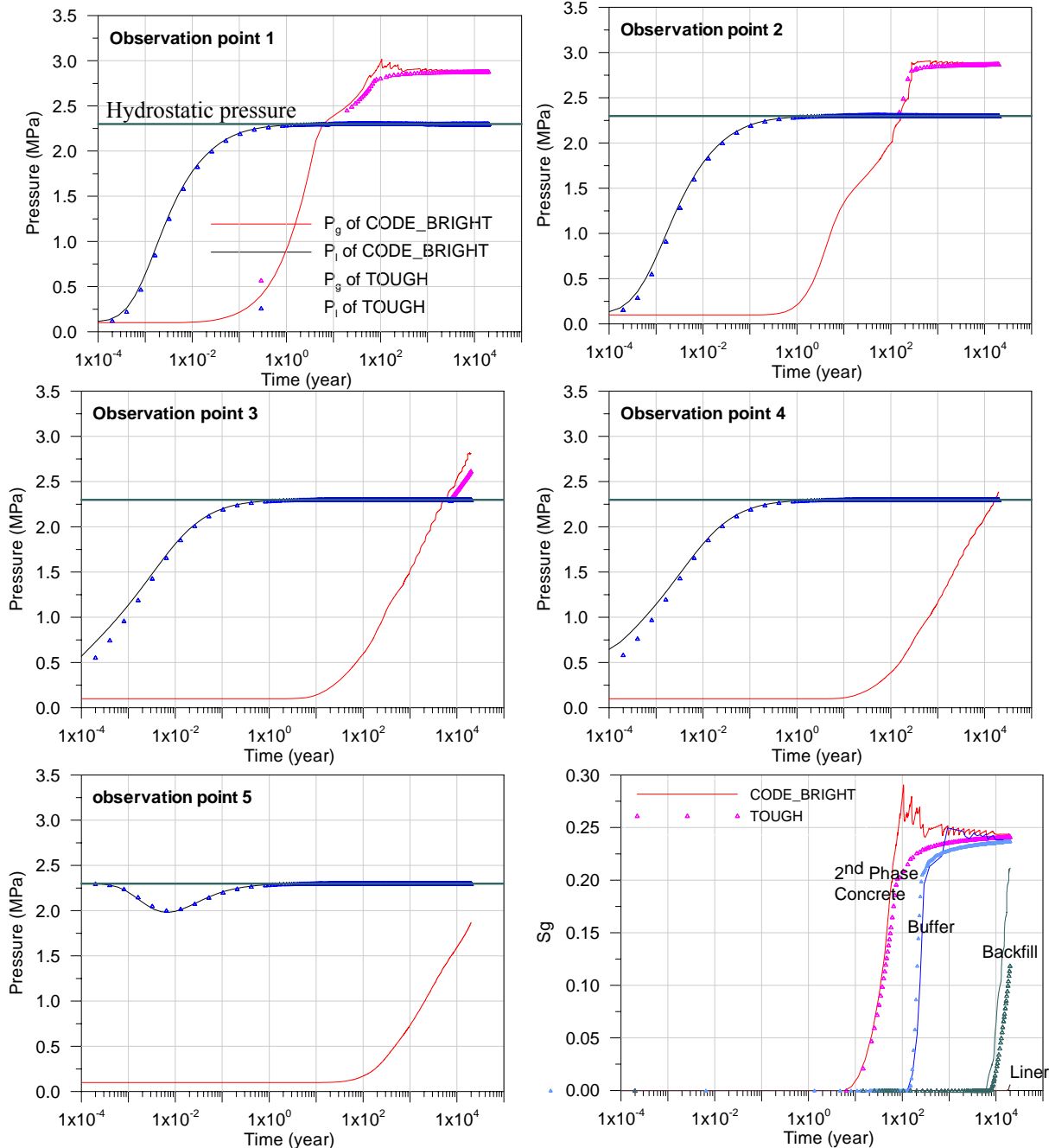


Figure 7. Comparison of time evolutions of gas, liquid pressure and gas saturation at five observation points between two numerical tools in Benchmark 2

BENCHMARK 3: THG MODELING (2D)

Definition of Benchmark 3

Benchmark 3 is defined using the same conceptual model as in Benchmark 2, but extended by coupling with heat transport. Heat is generated by radioactive decay of the vitrified HLW embedded in the super-container and decreases with time. Due to the

- P_g of CODE_BRIGHT
- P_l of CODE_BRIGHT
- ▲ P_g of TOUGH
- ▲ P_l of TOUGH

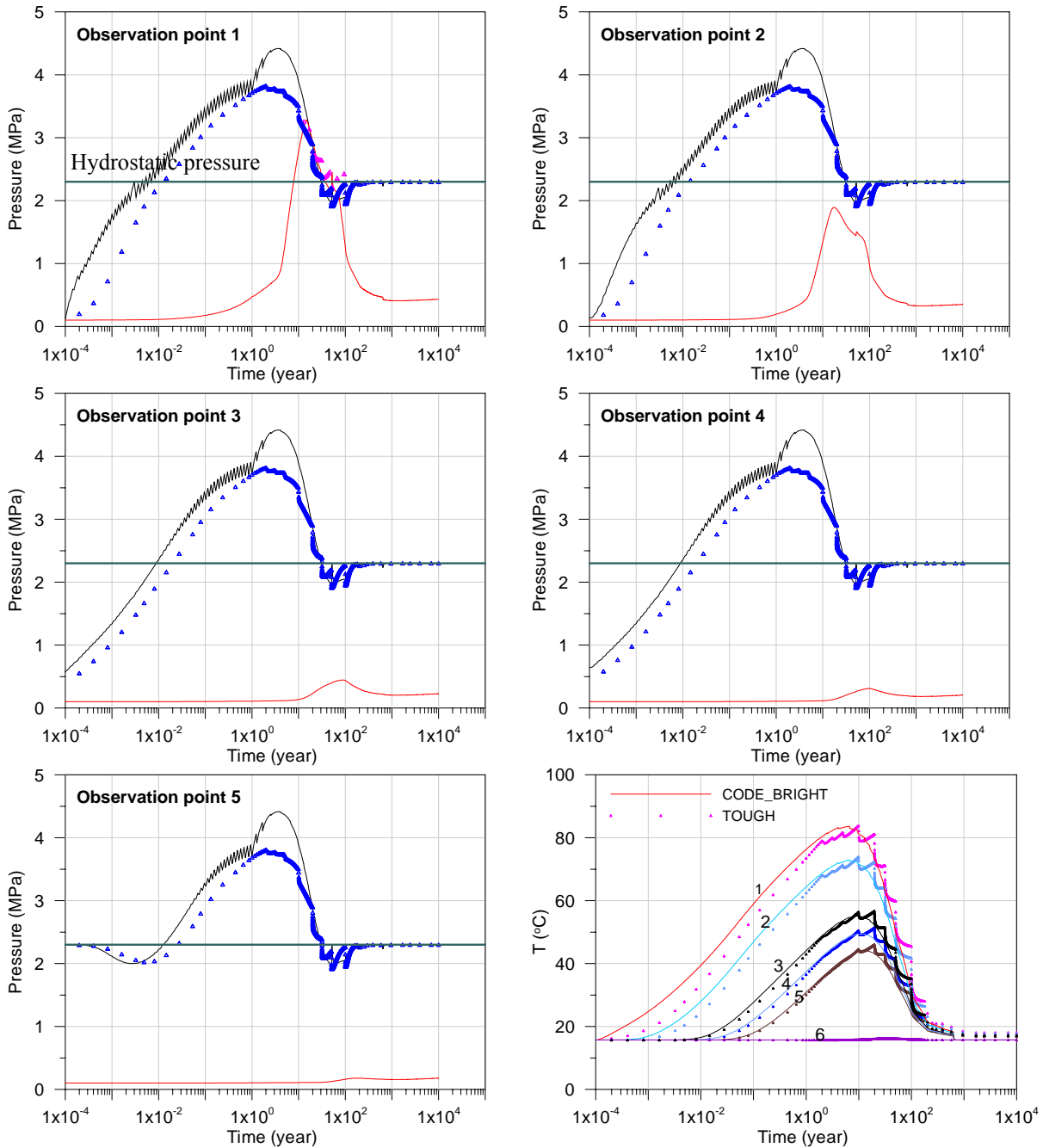


Figure 8. Comparison of time evolutions of gas, liquid pressure and gas saturation at five observation points between two numerical tools in Benchmark 3

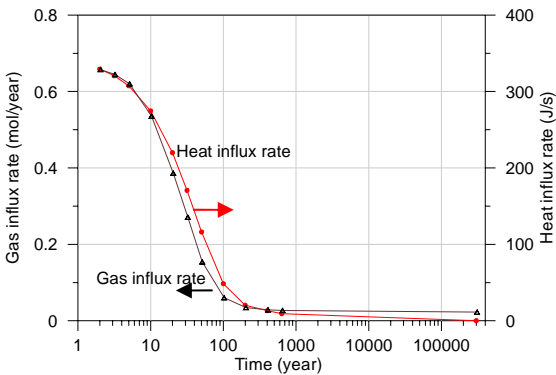


Figure 9. Hydrogen and heat influx in one canister in benchmark 3

dependency of corrosion rate on temperature, time-varying gas production rate is assumed in Benchmark 3 (Weetjens and Perko, 2008). In the numerical simulation, hydrogen and heat influx are simplified as piecewise linear functions (Figure 9) and applied uniformly along the interface of waste and the 2nd phase concrete in CODE_BRIGHT. In TOUGH2, the thermal source is distributed uniformly in the waste matrix, which is given a much higher thermal conductivity of $40 \text{ Wm}^{-1}\text{K}^{-1}$ to assume a fast homogeneous heat spreading.

Results of Benchmark 3

Time evolutions of gas/liquid pressure and temperature up to 10,000 years at five observations points are compared for the two codes. As shown in Figure 8, the codes produce comparable results. Increase of liquid pressure in the first five years is due to the thermal expansion of water. Its time scale is consistent with time evolution of temperature. The differences between liquid pressures mainly come from different definitions of the dependency of liquid density on temperature. From the liquid pressure curves of CODE_BRIGHT, it can be clearly seen that there are many oscillations before the appearance of the hump, which may be due to calculation instability. There is a good correspondence between temperature results, but CODE_BRIGHT gives a much smoother curve compared to TOUGH2.

CONCLUSIONS

Two numerical tools, TOUGH2 and CODE_BRIGHT, are mutually verified through three benchmark cases based on the most recent Belgian repository design: (1) HG coupled modeling for a 1D problem; (2) HG coupled modeling for a 2D axis-symmetrical problem; and (3) THG coupled modeling for a 2D axis-symmetrical problem. Comparisons between numerical results demonstrate that these two numerical tools produce similar results in all three benchmarks. The minor differences

between results obtained from the two numerical tools result in part from different discretizing methods and numerical techniques, and in part from several different constitutive laws.

CODE_BRIGHT is very sensitive to convergence parameters. During the calculation, convergence problems were sometimes encountered. The results reflect sharp oscillations at some critical points, while results from TOUGH2 are much more stable except for temperature.

Although both numerical tools can be used to simulate coupled multiphase flow problems, the results show that TOUGH2 is more stable and efficient in modeling two-phase flow problems. The advantage of CODE_BRIGHT is that it has provisions for solving mechanically coupled problems, and is easier to be implemented with self-defined constitutive laws.

ACKNOWLEDGMENTS

The authors wish to thank Dirk Mallants (SCK·CEN) for revisions on an earlier version of this paper.

REFERENCES

- Marivoet, J., Volckaert, G., Wemaerem I., Wibin, J., *Evaluation of elements responsible for the effective engaged does rates associated with the final storage of radioactive waste (EVEREST)*, VOL 2a, clay formation, site in Belgium, EC Report EUR 17449/2a EN, Luxembourg, 1997.
- Olivella, S., Gens, A., Carrera, J., Alonso, E.E., Numerical formulation for a simulator (CODE_BRIGHT) for the coupled analysis of saline media, *Engineering Computations* 13 (7), 87-112. 1996.
- Pruess K., The tough codes-a family of simulations tools for multiphase flow and transport processes in permeable media, *Vadoze Zone Journal* 3, 738-746, 2004.
- Rodwell, W.R. (eds), *Research into gas generation and migration in radioactive waste repository systems (PROGRESS)*, EC report, F14W-CT96-0024, Luxembourg, 2000.
- Wacquier, W., Van Humbeeck, H., *B&C Concept and Open Questions*, Note for ONDRAF/NIRAS, 2009-0146, 2009.
- Weetjens, E. and Perko J., *Report on first results of calculations on gas production and transport (PAMINA)*, SCK·CEN, Contract NO° FP6-036404, 2008.
- Wemaere, I., Marivoet, J., Labat, S., Hydraulic conductivity variability of the Boom Clay in north-east Belgium based on four core drilled boreholes, *Physics and Chemistry of the Earth* 33, 24-36, 2008.

BENTONITE ALTERATION DUE TO THC PROCESSES DURING THE EARLY THERMAL PERIOD IN A NUCLEAR WASTE REPOSITORY

Tianfu Xu¹, Rainer Senger², and Stefan Finsterle¹

¹Earth Sciences Division, Lawrence Berkeley National Laboratory, Berkeley, CA 94720, USA

²INTERA Inc., Schölslistrasse 12, CH-5408 Ennetbaden, Switzerland
e-mail: Tianfu_Xu@lbl.gov

ABSTRACT

After closure of an underground nuclear waste repository, the decay of radionuclides within the repository will elevate temperature, and the bentonite buffer will resaturate by water inflow from the host rock. The perturbations from these thermal and resaturation processes are expected to dissipate within a few hundred years. Here, we investigate coupled thermal-hydro-chemical processes and their effects on the short-term performance of a nuclear waste repository located in a clay formation considered by Nagra, Switzerland. Using a simplified geometric configuration and abstracted hydraulic parameters of the clayey formation, we examine chemical processes, coupled phenomena, and potential changes in porosity near the waste container during the early thermal period. The developed models are useful for evaluating the effect of water and mineral chemistry of the buffer and host rock on the repository performance for future site-specific studies.

INTRODUCTION

Simulating coupled thermal-hydrological-geochemical (THC) processes in the backfill material and near-field environment of a heat-generating nuclear waste repository requires site-specific and detailed information to assess the coupled processes and their impact at any particular site, and to develop engineering designs. Before moving into site-specific investigations, we explore general features and issues representing characteristics that are common and essential for many such systems. The present study is not related to any particular site. However, the geometric configuration and the hydraulic parameters and mineralogical composition of the clayey formation are abstracted from a nuclear waste repository concept considered in Switzerland (NAGRA, 2002). The reference design for canisters to be stored in a repository for spent fuel and high-level waste (SF/HLW) involves a cast steel body with about 20 cm wall thickness. The canisters are about 1 m in diameter and are surrounded by a 0.75-m thick bentonite buffer in emplacement tunnels which are 2.5 m in diameter (Figure 1). The repository tunnel is assumed to be in the water-saturated zone at a

depth of 650 m below the land surface; the host rock is referred to as Opalinus Clay.

It should be mentioned that the bentonite (clay) swelling process is not considered in this paper, because it is not included in the current TOUGHREACT simulator. The impact of clay swelling on porosity may be far higher than that of the geochemical interactions. Furthermore, the swelling is expected to affect the flow regime and retard resaturation. No redox reactions are considered in the simulations; the system evolves from an oxidizing to a reducing environment. However, here we concentrate our modeling analyses on the period of heat loading and water resaturation, and oxidizing conditions could prevail during this early stage.

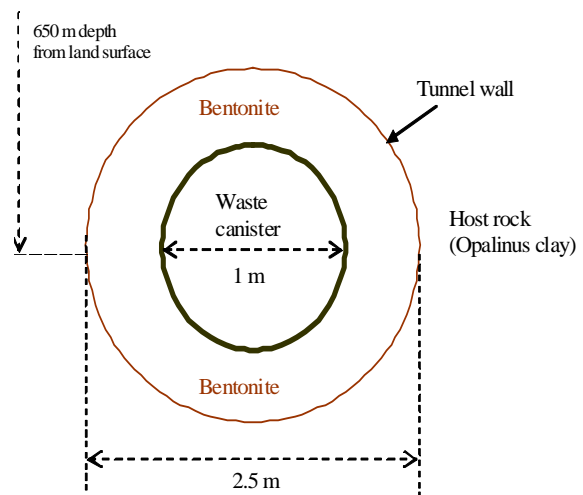


Figure 1. Schematic representation of a nuclear waste repository with a single waste canister, bentonite backfill, and Opalinus Clay host rock (NAGRA, 2002).

PROBLEM SETUP

Thermal and hydrological conditions

The present study employed a simplified model previously used by Senger et al. (2008) and Xu et al. (2008). The model is radially symmetric (Figure 1), i.e., it ignores the lateral no-flow boundary and gravity effects, which may represent general features

and issues related to a nuclear waste repository. The Opalinus Clay host rock is initially fully water-saturated with a background pressure of 65 bar. The outer boundary at a radial distance of 75 m was prescribed with a constant pressure of 65 bar.

The thermo-physical properties for the bentonite buffer and the Opalinus Clay host rock are summarized in Table 1. These parameters were taken from Xu et al. (2008) and Senger and Ewing (2008). Senger and Ewing (2008) reported simulation results for a 3D model of the thermo-hydrologic conditions in the vicinity of a backfilled emplacement tunnel for spent fuel. Their purpose was to quantify the coupled thermo-hydrologic evolution of temperature, saturation, and pressure through time, to determine potential non-uniform resaturation of the bentonite buffer, or potential localized accumulation of pore water in contact with the waste canister. The van Genuchten model (van Genuchten, 1980; Mualem, 1976) is used to describe the functional relationships between relative permeability and saturation, and capillary pressure and saturation for the different materials.

Table 1. Thermo-physical parameters used for bentonite and Opalinus Clay in the THC model

	Bentonite	Opalinus Clay
Porosity [-]	0.475	0.14
Permeability [m ²]	1×10^{-19}	1×10^{-20}
Pore compressibility (α/ϕ) [Pa ⁻¹]	3.58×10^{-9}	1.83×10^{-9}
Rock grain density (kg/m ³)	2700	2670
Rock specific heat (J/kg ^o C)	964	946.5
Thermal conductivity (W/m ^o C)	1.35	2.5
Two-Phase Parameter Model ¹	van Genuchten	
Residual liquid saturation [-]	0.3	0.5
Residual gas saturation [-]	0.02	0.02
van Genuchten parameter n [-]	1.82	1.67
Gas entry pressure [Pa]	1.8×10^7	1.8×10^7

¹van Genuchten (1980), Mualem (1976).

Time-dependent heat generation from the waste package was specified. A large density and an initial temperature of 150°C were specified for the gridblock representing the waste package, which produced the temperature evolution given in Figure 2, providing the inner boundary condition. This heat boundary specification was based on Figure 3.20a of the report of Senger and Ewing (2008), in which temperature reduced to about 55°C after 1,000 years. An initial temperature of 38°C was used for the remaining gridblocks of the model domain.

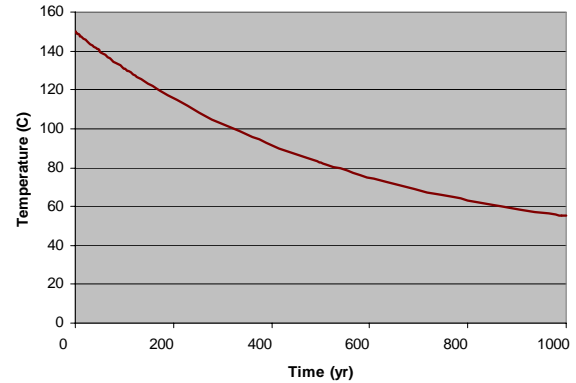


Figure 2. Temperature evolution at canister surface

Geochemical conditions

The initial mineral composition of bentonite and Opalinus Clay is given in Table 2. The MX-80 type of bentonite is used as the buffer material. It contains 75% montmorillonite. Montmorillonite-Na is the dominant clay mineral, which is assigned to have a volume fraction of 75%. The mineral content of Opalinus Clay was assigned based on Fernández et al. (2006). Smectite was substituted with montmorillonite in the present modeling for the portion of Opalinus Clay. Anhydrite precipitation was observed in some lab experiments for bentonite THC processes such as that of JNC (2000). Amorphous silica precipitation was reported in geothermal systems (Xu et al., 2004). Therefore, anhydrite and amorphous silica are considered here as secondary phases with initial volume fractions of zero, and they could be formed during the simulation time.

Two initial water chemical compositions were used: a dilute water for the bentonite, and the composition measured for BWS-A6 water (Fernández et al., 2006). Prior to simulating reactive transport, batch geochemical modeling of water-rock interaction for the two materials was conducted, equilibrating the initial water with the primary minerals listed in Table 2 at a temperature of 38°C. A reasonably short simulation time (10 years) is needed to obtain nearly steady-state aqueous solution compositions, which were then used as initial chemical conditions for reactive transport (THC) simulations.

Table 2. Initial mineral volume fractions and possible secondary mineral phases used in the THC simulations

Mineral	Volume percent in terms of solid	
	Bentonite	Opalinus Clay
Calcite	1.4	15.0
Quartz	15.1	18.0
Kaolinite	1.0	10.0
Illite		20.0
K-feldspar	6.5	3.0
Montmorillonite-Na	75	10.0
Montmorillonite-Ca		10.0
Chlorite		10.0
Dolomite		1.0
Siderite		3.0
Ankerite		1.0
Annite	1.0	
Anhydrite	0.0	0.0
Amorphous silica	0.0	0.0

Reaction kinetics

Reactive chemical-transport modeling requires not only a conceptual understanding of the mechanisms involved in the nucleation, precipitation, and dissolution of the suite of participating minerals, but also quantitative estimates of relevant kinetic parameters. In this work, a general rate expression was used, based on transition state theory (TST) (Lasaga et al., 1994; Steefel and Lasaga, 1994):

$$r = kA \left[1 - \left(\frac{Q}{K} \right)^\theta \right]^\eta \quad (1)$$

Here, r is the kinetic rate (positive values indicate dissolution, and negative values precipitation), k is a temperature-dependent rate constant (moles per unit mineral surface area and unit time), A is the specific reactive surface area per kg H₂O, K is the equilibrium constant for the mineral-water reaction written for the destruction of one mole of mineral, and Q is the reaction quotient. The parameters θ and η must be determined by experiment, but are commonly set equal to unity when experimental quantification is unavailable. The precipitation of secondary minerals is represented using the same kinetic expression as for dissolution.

For many minerals, the kinetic rate constant k can be summed from three mechanisms (Palandri and Kharaka, 2004):

$$k = k_{25}^{nu} \exp \left[\frac{-E_a^{nu}}{R} \left(\frac{1}{T} - \frac{1}{298.15} \right) \right] + k_{25}^H \exp \left[\frac{-E_a^H}{R} \left(\frac{1}{T} - \frac{1}{298.15} \right) \right] a_H^{n_H} + k_{25}^{OH} \exp \left[\frac{-E_a^{OH}}{R} \left(\frac{1}{T} - \frac{1}{298.15} \right) \right] a_{OH}^{n_{OH}} \quad (2)$$

where subscripts nu , H , and OH indicate neutral, acid, and base mechanisms, respectively, E is the activation energy, k_{25} is the rate constant at 25°C, R is the gas constant, T is absolute temperature, a is the activity of the species; and n is a power term (constant). Notice that parameters θ and η (see Equation 1) are assumed to be the same for each mechanism, and, for reasons noted above, are set to unity in the present work.

Mineral dissolution and precipitation rates are a product of the kinetic rate constant and reactive surface area, as represented by Equation (1). Calcite and anhydrite are assumed to react at equilibrium, because their reaction rates are rapid relative to the time frame being modeled. We include separate rate constants (k_{25}), activation energies (E), and reaction order (n) for processes catalyzed by H⁺ or OH⁻. At any pH, the total rate is the sum of the rates from all mechanisms. Catalysis by H⁺ or OH⁻ is considered only for mineral dissolution. Parameters for the rate law were taken from Palandri and Kharaka (2004), who compiled and fitted experimental data reported by many investigators. Parameters for montmorillonite were set to those of smectite.

If the aqueous phase supersaturates with respect to a potential secondary mineral, a small volume fraction such as 1×10^{-6} is used for calculating the seed surface area for the new phase to grow. The precipitation of secondary minerals is represented using the same kinetic expression as that for dissolution. However, because precipitation rate data for most minerals are unavailable, parameters for neutral pH rates only were employed to describe precipitation. Multiple kinetic precipitation mechanisms can be specified in an input file of the TOUGHREACT program (Xu et al., 2006), should such information become available.

Mineral reactive-surface areas are based on the work of Sonnenthal et al. (2005) and were calculated assuming a cubic array of truncated spheres constituting the rock framework. The larger surface areas for clay minerals result from smaller grain sizes

Cation exchange parameters

The Gaines-Thomas convention (Appelo, 1994) was used for cation exchange. In this convention, selectivities are calculated by using the equivalent fraction of the exchanged cations for the activity of the exchanged cations. It should be pointed out that selectivity is a relative concept. Na^+ was chosen as the reference. Therefore, Na^+ selectivity is equal to one. According to this definition, a lower selectivity corresponds to a higher exchange capacity. A divalent cation is in general more strongly exchanged than a monovalent cation. Parameters used for cation exchange reactions are listed in Table 3, which were taken from a report by JNC (2000). The cation exchange capacity (CEC) for bentonite was set to 105 meq/100g. The CEC for Opalinus Clay was assumed to be half of that of bentonite, or 52.5 meq/100g.

Table 3. List of cation exchange reactions considered for the THC modeling ($-X$ represents cation exchange sites)

Cation exchange	Selectivity (relative to Na^+)
$\text{Na}^+ + 0.5\text{Ca}-\text{X}_2 = 0.5\text{Ca}^{2+} + \text{Na}-\text{X}$	0.69
$\text{Na}^+ + 0.5\text{Mg}-\text{X}_2 = 0.5\text{Mg}^{2+} + \text{Na}-\text{X}$	0.67
$\text{Na}^+ + \text{K}-\text{X} = \text{K}^+ + \text{Na}-\text{X}$	0.42
$\text{Na}^+ + \text{H}-\text{X} = \text{H}^+ + \text{Na}-\text{X}$	1.88

Simulations

Four simulations were performed. The first, base-case simulation used parameters given in Tables 1 and 2. Mineral dissolution and precipitation rates are a product of the kinetic rate constant and reactive surface area, the magnitudes of which are highly uncertain and cover a wide range of values. Therefore, two sensitivity simulations (Simulations 2 and 3) were performed by decreasing and increasing the surface area by one order of magnitude from the base-case value. Simulation 4 includes cation exchange from the base case.

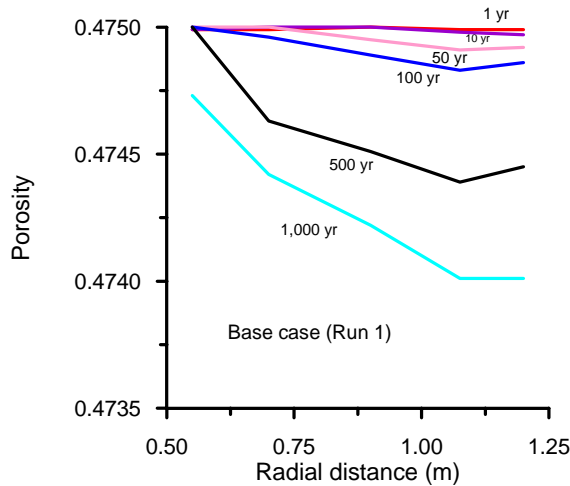
The nonisothermal reactive geochemical transport code TOUGHREACT (Xu and Pruess, 2001; Xu et al., 2006) was used. This code introduces reactive chemistry into the multiphase fluid and heat flow code TOUGH2 (Pruess et al., 1999). Interactions between mineral assemblages and fluids can occur under local equilibrium or kinetic rates. Precipitation and dissolution reactions can change formation porosity and permeability, and can also modify the unsaturated flow properties of the rock. A broad range of subsurface thermal-physical-chemical processes are considered under various thermohydrological and geochemical conditions of pressure, temperature, water saturation, ionic strength, and pH

and Eh. Temporal changes in porosity and permeability due to mineral dissolution and precipitation can be considered in the model. Mineral dissolution and precipitation are considered under kinetic conditions. Changes in porosity are calculated from changes in mineral volume fractions. Permeability changes can then be evaluated by consideration of several alternative models describing the porosity-permeability relationship, including a simple grain model of Kozeny-Carman, as used in the present study.

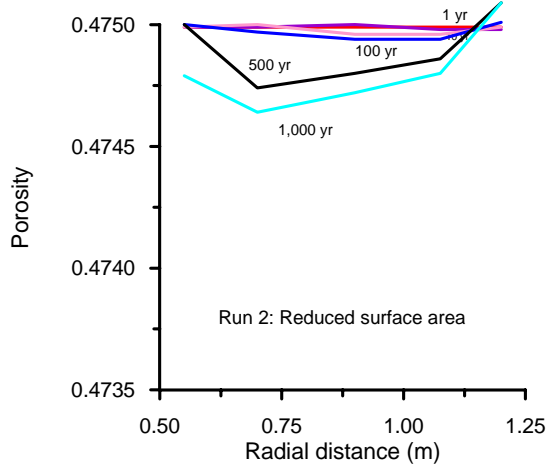
The program is run with different equation-of-state modules, depending on the phases and components of interest. Here, we use the EOS4 module to calculate the thermo-physical properties of the fluid mixture. In the EOS4 module, provision is made for vapor pressure lowering effects (see Pruess et al., 1999). Vapor pressure is expressed by Kelvin's equation, which is a function not only of temperature, but depends also on capillary pressure, which in turn is a function of saturation.

RESULTS

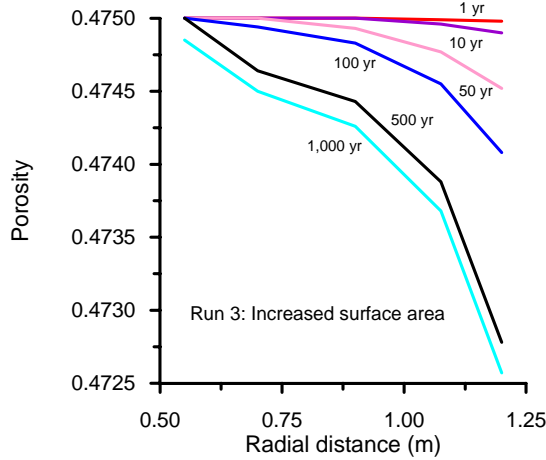
After closure of an underground nuclear waste repository, the decay of radionuclides elevates temperature, and the bentonite buffer resaturates through water flow from the surrounding host rock. The perturbations from these thermal and resaturation processes induce mineral dissolution and precipitation. Consequently, the porosity of the bentonite buffer is changed. The simulated porosity distribution at different times for different cases is presented in Figure 3. For the first three cases without cation exchange, porosity decreases from the initial value of 0.475, indicating that precipitation dominates. Changes in porosity are larger close to the interface between the bentonite buffer and Opalinus Clay host rock, because resaturation processes carry chemical constituents from the host rock. Decreases in porosity are smaller close to the canister surface. Decreases in reactive surface area (rate) result in reductions in mineral alteration and porosity change (compare Figure 3b to 3a). Conversely, increases in reactive surface area cause increases in mineral alteration and porosity change (compare Figure 3c to 3a). Considering cation exchange (Figure 3d), porosity mostly increases, but slightly decreases close to the interface with the host rock; it does not change close to the canister surface. Overall, no significant changes in porosity occur during the first 1,000 years of thermal and resaturation processes.



(a)

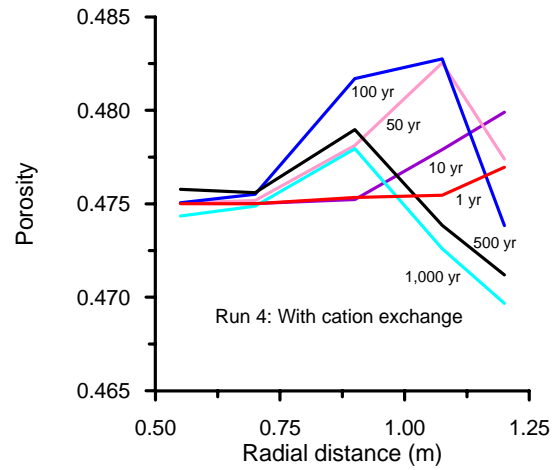


(b)



(c)

Figure 3. Distribution of porosity in bentonite buffer obtained with four simulation cases



(d)

Figure 3 (continued). Distribution of porosity in bentonite buffer obtained with four simulation cases

Montmorillonite-Na, the dominant mineral (with an initial volume fraction of 75%), dissolves in all four cases (Figure 4). Decreases in reactive surface area (rate) results in reductions in montmorillonite-Na dissolution. Conversely, increases in reactive surface area cause increases in its dissolution. Considering cation exchange results in a reduction in Montmorillonite-Na dissolution. The pattern of annite dissolution is similar to that of montmorillonite-Na (Figure 5). Calcite precipitates in most parts of the bentonite because its solubility decreases with temperature, but it dissolves close to the interface with the host rock supplying reactants for its precipitation close to the hot end of the canister surface (Figure 6). Calcite dissolution and precipitation is not sensitive to changes in surface area. K-feldspar precipitation occurs over the entire radial distance, with more precipitation close to the interface with the host rock (Figure 7). K-feldspar precipitation is proportional to changes in surface area. With cation exchange, less K-feldspar precipitates. Similar to K-feldspar, kaolinite precipitates over the entire thickness of the bentonite buffer, with more precipitation close to the interface with the host rock (Figure 8). The pattern of chlorite precipitation is the same as kaolinite (Figure 9).

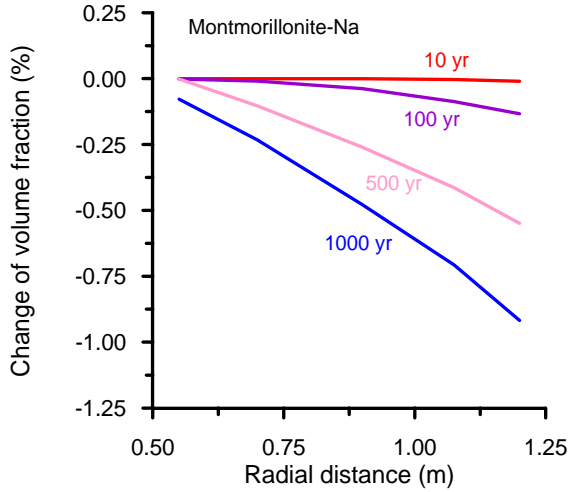


Figure 4. Change in volume fraction of montmorillonite-Na in bentonite buffer obtained for the base case

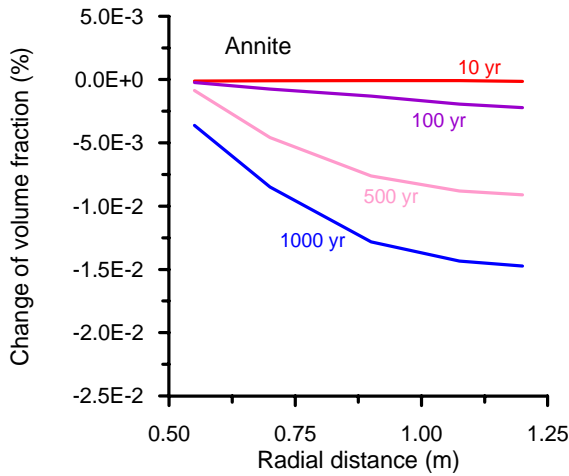


Figure 5. Change in volume fraction of annite in bentonite buffer obtained for the base case

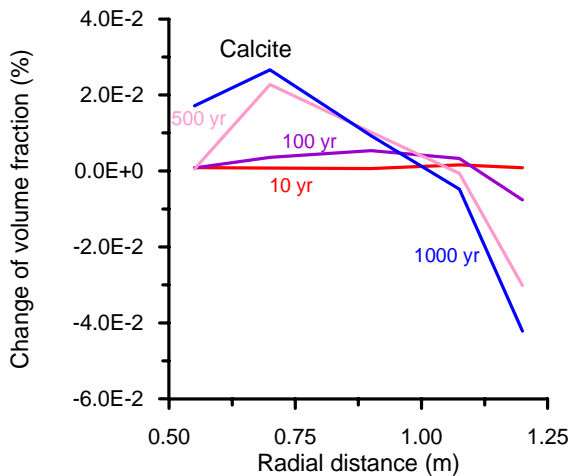


Figure 6. Change in volume fraction of calcite in bentonite buffer obtained for the base case

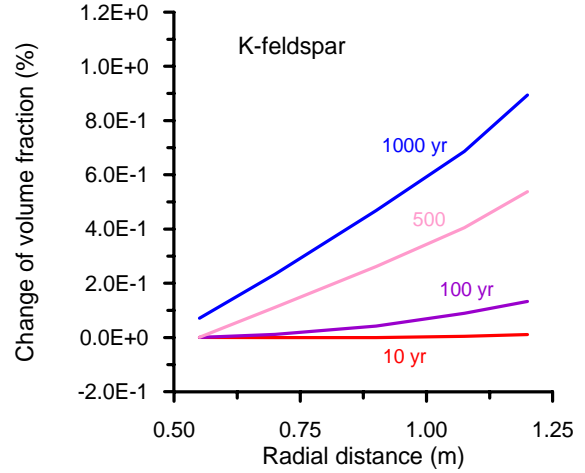


Figure 7. Change in volume fraction of K-feldspar in bentonite buffer obtained for the base case

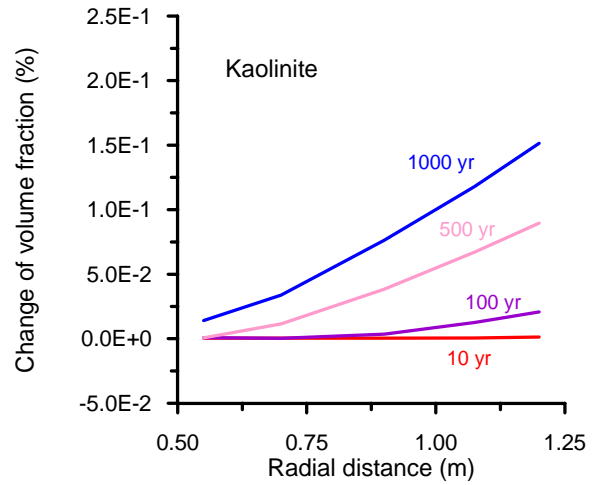


Figure 8. Change in volume fraction of kaolinite in bentonite buffer obtained for the base case

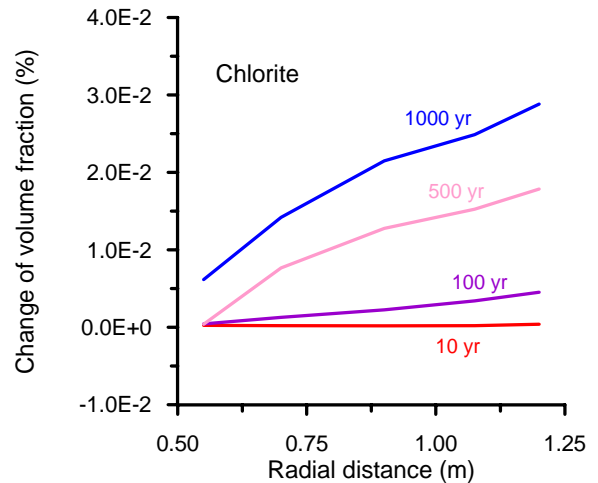


Figure 9. Change in volume fraction of chlorite in bentonite buffer obtained for the base case

SUMMARY AND CONCLUSIONS

A 1D radially symmetric model of a waste canister emplaced in a bentonite buffer in a deep repository in Opalinus Clay has been constructed, approximating general features and issues related to a nuclear waste repository. Using this model, mineral alteration and changes in porosity for the early thermal and resaturation processes in a nuclear waste repository were examined for different cases. The following conclusions can be drawn from the modeling analyses:

The perturbations from these thermal and resaturation processes result in a decrease in porosity, as precipitation dominates. Decreases in porosity are larger close to the interface between the bentonite buffer and the Opalinus Clay host rock, because resaturation processes carry chemical constituents from the host rock. Cation exchange indirectly affects mineral alteration, which in turn changes porosity. Overall, mineral alteration and changes in porosity during the 1,000 years period of thermal and resaturation processes are not significant, and do not significantly affect flow and transport properties

Montmorillonite-Na and annite dissolves throughout the model domain. Calcite precipitates in most parts, but it dissolves close to the interface between the backfill and the host rock, supplying reactants for its precipitation close to the hot end at the canister-backfill surface. Precipitation of K-feldspar, kaolinite, and chlorite occurs over the entire radial distance, with more precipitation close to the interface with the host rock.

The preliminary modeling presented here is for a simplified geometric configuration and the abstracted hydraulic parameters and mineralogy of the clayey formation. However, this modeling and the sensitivity analyses were useful in identifying the role of some physical and chemical parameters in the alteration of the bentonite buffer materials. The developed model may provide a useful tool for gaining a better understanding of the coupled chemical and physical processes, as well as the controlling conditions and relevant parameters, within a repository system.

ACKNOWLEDGMENT

This work was supported by the National Co-operative for the Disposal of Radioactive Waste (NAGRA) of Switzerland, and, in part, by the U.S. Dept. of Energy under Contract No. DE-AC02-05CH11231.

REFERENCES

- Appelo, C.A.J., Cation and Proton Exchange, pH Variations and Carbonate Reactions in a Freshening Aquifer, *Water Resour. Res.*, Vol. 30(10), 2793–2805, 1994.
- Fernández, R., Cuevas, J., Sánchez, L., de la Villa, R.V., Leguey, S., Reactivity of the cement-bentonite interface with alkaline solutions using transport cells, *Applied Geochemistry*, Vol. 21, 977–992, 2006.
- JNC, H12: Project to Establish the Scientific and Technical Basis for HLW Disposal in Japan, TN1410 2000-001, JNC, Tokai-mura, Japan, 2000.
- Lasaga, A.C., J.M. Soler, J. Ganor, T.E. Burch, K.L. Nagy, Chemical Weathering Rate Laws and Global Geochemical Cycles. *Geochimica et Cosmochimica Acta*, Vol. 58, 2361–2386, 1994.
- Mualem, Y., A new model for predicting the hydraulic conductivity of unsaturated porous media, *Water Resour. Res.*, Vol 12, 513–522, 1976.
- NAGRA, *Project Opalinus Clay: Safety Report. Demonstration of Disposal Feasibility (Entsorgungsnachweis) for Spent Fuel, Vitrified High-Level Waste and Long-Lived Intermediate-Level Waste*, NAGRA Technical Report NTB 02-05, NAGRA, Wettingen, Switzerland, 2002.
- Narasimhan, T.N., Witherspoon, P.A., An integrated finite difference method for analyzing fluid flow in porous media, *Water Resour. Res.*, Vol. 12, 57–64, 1976.
- Palandri, J., Y.K. Kharaka, A Compilation of Rate Parameters of Water-Mineral Interaction Kinetics for Application to Geochemical Modeling. US Geol. Surv. Open File Report 2004-1068, 64 pp., 2004.
- Pruess, K., C. Oldenburg, G. and Moridis, TOUGH2 User's Guide, Version 2.0, Report LBNL-43134, Lawrence Berkeley National Laboratory, Berkeley, Calif., 1999.
- Senger, R., T. Xu, P. Marschall, and S. Finsterle, Modeling approaches of two-phase flow phenomena associated with corrosion of SF/HLW canisters in a proposed repository in Opalinus clay, Switzerland, *Physics and Chemistry of the Earth*, 33, S317–S326, 2008.
- Senger, R., Ewing, J., Evolution of temperature and water content in the bentonite buffer: Detailed modelling of two-phase flow processes associated with the early closure period – complementary simulations. Report NAB 08-53 for NAGRA, INTERA Inc., Austin, Texas 78758, 2008.

- Sonnenthal, E., A. Ito, N. Spycher, M. Yui, J. Apps, Y. Sugita, M. Conrad, and S. Kawakami, *Approaches to modeling coupled thermal, hydrological, and chemical processes in the Drift Scale Heater Test at Yucca Mountain*. International Journal of Rock Mechanics and Mining Sciences, Vol. 42, 698–719, 2005.
- Steefel, C.I., Lasaga, A.C., A coupled model for transport of multiple chemical species and kinetic precipitation/dissolution reactions with applications to reactive flow in single phase hydrothermal system. *Am. J. Sci.*, Vol. 294, 529–592, 1994.
- van Genuchten, M. Th., A Closed-form equation for predicting the hydraulic conductivity of unsaturated soils, *Soil Sci. Soc. Am. J.*, Vol. 44, 892–898, 1980.
- Xu, T., Pruess, K., Modeling multiphase non-isothermal fluid flow and reactive geochemical transport in variably saturated fractured rocks: 1. Methodology, *American Journal of Science*, Vol. 301, 16–33, 2001.
- Xu, T., Sonnenthal, E.L., Spycher, N., Pruess, K., TOUGHREACT: A simulation program for non-isothermal multiphase reactive geochemical transport in variably saturated geologic media, *Computer & Geoscience*, Vol. 32, 145–165, 2006.
- Xu, T., R. Senger, and S. Finsterle, Corrosion-induced gas generation in a nuclear waste repository: Reactive geochemistry and multiphase flow effects, *Applied Geochemistry*, 23, 3423–3433, 2008.

NUMERICAL SIMULATION OF ATMOSPHERIC CARBONATION OF CONCRETE COMPONENTS IN A DEEP GEOLOGICAL RADWASTE DISPOSAL SITE DURING OPERATING PERIOD USING TOUGHREACT

L. Trotignon¹, P. Thouvenot¹, I. Munier², B. Cochepin², E. Piault¹, E. Treille², X. Bourbon² and S. Mimid¹

¹ CEA, Direction de l'Energie Nucléaire, DTN/SMTM/LMTE, CE Cadarache, France
² Andra, Scientific Division, Châtenay-Malabry, France
e-mail: laurent.trotignon@cea.fr, pascal.thouvenot@cea.fr, isabelle.munier@andra.fr

ABSTRACT

Simulations of atmospheric carbonation of concrete intermediate-low level waste (ILLW) disposal packages and concrete structural components are conducted to evaluate potential chemical degradations affecting these components during the operating period of a radioactive waste disposal repository, in a deep Callovo-Oxfordian (argillites) clay layer. Two-phase liquid water-air flow is combined with gas and diffusion processes, leading to a progressive drying of the concrete, gas displacement within the concrete, and an array of chemical reactions affecting the cement paste. The carbonation process is strongly dependent on the progression of the drying front inside the concrete, which in turn is sensitive to the initial water saturation and to nonlinear effects associated with permeability and tortuosity phenomenological laws.

Results obtained with a modified version of ToughReact-EOS4, in order to represent realistic tortuosity evolution of materials (CEM-I high performance concrete, argillites), are presented and commented upon.

AIM OF THE STUDY

Andra (2005) has elaborated on concepts to establish the feasibility of a high-level waste (HLW) and ILL waste disposal in a deep Callovo-Oxfordian argillite geological formation at the Meuse/Haute Marne site in the eastern part of the Paris Basin. During the operating period within an intermediate-level long-lived radioactive waste (ILLW) disposal zone (up to 100 y), a number of the concrete components (waste package containers, lining, and disposal cell backfill—Figure 1) will be subject to ventilation in order to guarantee operating safety and contribute to evacuation of residual heat from low- heat-emitting ILLW (temperatures below ~40°C are expected). Ventilating air will be drawn from the surface and exchange water and heat with the clay host rock that could lead to “dry” air conditions (relative humidity lower than 50%). This will generate a desaturation of concrete components, causing atmospheric carbonation to develop, potentially leading to a progressive lowering of pH inside the cement paste. This could trigger corrosion of the steel

reinforcement, which may have deleterious effects on the concrete.

Simplified approaches have been developed to model atmospheric carbonation processes (Bary et al., 2004, 2006; Thiery et al., 2007). However, a more complete and detailed modeling of this process is required, which can only be achieved with reactive transport tools. Preliminary simulations of carbonation processes performed within the framework of the CEA-Andra partnership were obtained in 1D geometry with a modified version of TOUGHREACT, taking into account extended tortuosity models of cement pastes. These simulations consider a complex mineralogical composition of cementitious and neofomed phases, as well as clogging processes due to precipitation/dissolution phenomena.

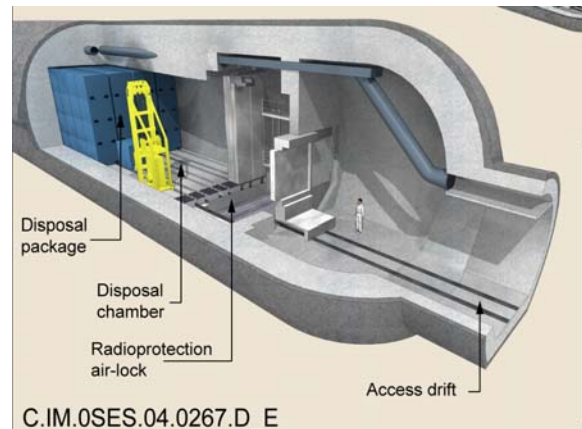


Figure 1. View of the ILLW disposal cell (~250 m long, ~10 m diameter). The concrete structure is in contact with the argillites host-rock. The ventilated vault is progressively filled with waste disposal packages during operating (after Andra(2005)).

CONCEPTUALIZATION OF ILLW DISPOSAL PACKAGES AND CONCRETE STRUCTURES

As shown by Figures 1 and 2, ILLW disposal components constitute a complex 3D system. That

being the case, the carbonation process is represented in this study in a simplified geometry:

- For waste disposal package simulations, a 1D half section of the package container (section = 0.11 m) is represented using a regular mesh of 11 cells of 5 mm. It is assumed that atmospheric carbonation occurs on both faces of the container. Boundary conditions are represented by a single-phase gas medium (air) of infinite volume, relative humidity of 40%, and temperature (25°C) and pressure (0.1 MPa). Initial liquid water saturation of the waste package concrete is assumed to be 0.6.

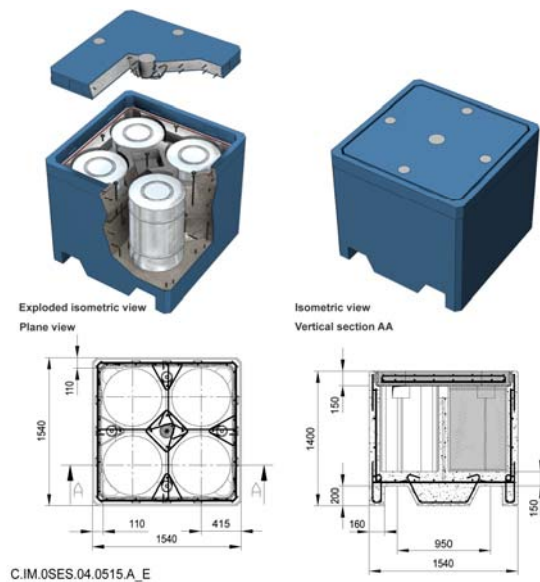


Figure 2. View of the ILLW waste package. The container has 0.11 m thick reinforced walls and contains four primary waste drums (after Andra(2005)).

- For concrete structures within a ILLW disposal cell, a 1D radial profile extending from $r=3.5$ m to $r=40$ m is simulated. Concrete liner and backfill (1.5 m thick) are in contact with an excavation-disturbed zone (EDZ), represented by a fractured zone (0.6 m thick) surrounded by a microfissured zone (4.5 m thick) and then an undisturbed argillite zone (~30 m thick). The mesh is progressive, from a 5 mm cell size at the air concrete boundary to a 1 m cell size at the other end of the system. The mesh includes 211 cells. At $r = 3.5$ m, boundary conditions are similar to that specified for waste-disposal-package simulations. At $r = 40$ m, constant pressure (4.5 MPa), temperature (25°C), and liquid saturation (0.98) are imposed. In the concrete, an initial pressure and liquid water saturation of respectively 0.1 MPa and 0.7 are

assumed. In the different argillites zones, the initial pressure and liquid saturation are assumed to be respectively 4.5 MPa and 0.98.

SIMULATED PROCESSES

Atmospheric carbonation of concrete in unsaturated conditions is a complex process that involves intricate couplings between transport of both liquid and vapor water and CO₂ in gas and liquid phases, capillary flow during drying of the concrete, and chemical reactions involving cement hydrates with CO₂ dissolved in the liquid water phase. Porosity modification is also associated with carbonation. Major processes considered in this work are:

- Darcy flow of liquid water and air, taking into account capillary forces and the Knudsen effect for gases
- Diffusion of gaseous and aqueous species
- Dissolution/precipitation of minerals, including the effect of temperature on reaction-rate constants
- Feedback of porosity variations on permeability and capillary properties, and thus effective diffusion coefficients

Drying of concrete components

Dripping is not considered in the present model and exportation of water out of the concrete is caused by water vapor diffusion from the external boundary of the component towards dry ventilation air. Thus, the nonlinear expression of tortuosity in the water vapor diffusion process (Thiery et al., 2007; Baroghel-Bouny et al., 2007) plays a key role in the initiation of atmospheric carbonation. For low-permeability concrete materials, expressions adopted for the diffusion coefficient are similar to the classical Millington and Quirk (1961) model developed for soils:

$$D_{i,j} = d_{0,i,j} \omega \omega^a S_i^b \quad (1)$$

where $D_{i,j}$ is the effective diffusion coefficient of component j in phase i , $d_{0,i,j}$ is the diffusion coefficient of component i in pure phase j , ω is the porosity, S_i is the relative saturation with respect to phase i . Exponent b (usually from 3 to 5) plays an important role in the dynamics of drying, because water vapor diffusion strongly increases only when some gas-saturation threshold is reached. Because of the corresponding nonlinear decrease with saturation of the liquid-water relative permeability, a dry-fringe formation starts at the component boundary as soon as capillary flow is unable to locally compensate for vapor diffusion.

Reactive transport

CO₂ diffuses from the single-phase gas boundary condition into the partially saturated pore space of concrete and dissolves in the pore water. Hydrates of the cement (mainly portlandite and CSH phases) are then subject to carbonation reactions, producing calcite and secondary minerals. A pH front progressively develops inside the concrete, from pH ~8.5 in regions where carbonation is complete, to pH ~13.3 in the unperturbed concrete. The evaporation of pore water also leads to the formation of Na-K-SO₄-OH brines, in which specific sulfate salts are likely to precipitate.

COMPONENTS PROPERTIES

Components involved in the simulations are a high-performance concrete (BHP CEM-I, based on pure Portland cement) and argillite rock (Andra, 2005).

Hydraulic and transport properties of components

Tables 1 and 2 summarize the main hydraulic and transport properties of the considered components. Wetting properties and relative permeability of the media are expressed using the van Genuchten-Mualem model described in Pruess et al. (1999).

Table 1. Concrete and argillites hydraulic properties

	BHP CEM-I	Bulk Argillites
Porosity	0.13	0.18
Intrinsic permeability (m ²)		
Water	9.5 10 ⁻²⁰	4.6 10 ⁻²⁰
Gas	8 10 ⁻¹⁷	4.6 10 ⁻¹⁸
Effective diffusion (m ² s ⁻¹) (Cl, liquid phase, 25°C)	9 10 ⁻¹²	2.8 10 ⁻¹¹
van Genuchten Pr (Pa)	2 10 ⁶	1.5 10 ⁷
van Genuchten n	1.54	1.49
Klinkenberg factor (Pa)	2 10 ⁵	2 10 ⁵

Table 2. Argillites EDZ hydraulic properties

	Fractured EDZ	Microfissured EDZ
Porosity	0.20	0.18
Intrinsic permeability (m ²)		
Water	9.2 10 ⁻¹⁷	9.2 10 ⁻¹⁹
Gas	9.2 10 ⁻¹⁵	9.2 10 ⁻¹⁷
Effective diffusion (m ² s ⁻¹) (Cl, liquid phase, 25°C)	3.6 10 ⁻¹¹	2.8 10 ⁻¹¹
van Genuchten Pr (Pa)	2 10 ⁶	8 10 ⁶
van Genuchten n	1.5	1.5

In these tables, materials are assigned an intrinsic permeability to gas larger than the intrinsic permeability to liquid. This feature is consistent with results reported in Baroghel-Bouny et al. (2007) and Thiery et al. (2007), who studied the drying of cement pastes. For argillites, a factor of 10² between gas and liquid intrinsic permeabilities was assumed. Microfissured argillites have hydraulic properties intermediate between those of argillites and fractured EDZ.

Composition of concrete

Concrete is composed of a mixture of aggregate (mainly calcite with some quartz) and cement paste. The model composition of the concrete (Table 3) was derived from data provided by Andra (2005) and Belarbi et al. (2006). Note that upon heating above 40°C, the equilibrium composition of the cement paste is predicted to evolve, because of the higher stability of Katoite_{Si} compared to Monocarboaluminat. The kinetics of this transition are considered to be fast.

Table 3. Mineralogical composition of concrete

Phase (volume fraction)	BHP CEM-I
Calcite	0.627
Portlandite	0.050
CSH 1.6	0.120
Monocarboaluminat	0.02
Ettringite	0.031
Hydrotalcite	0.003
Hydrogarnet-Fe (C3FH6)	0.018
Pyrite	-
Porosity	0.13

CSH 1.6 denotes a hydrated calcium silicate with a Ca/Si ratio of 1.6.

Composition of argillites

A reference composition model of argillites was derived from data published by Andra (2005) and Gaucher et al. (2006, 2007). This model is consistent with the pore-water chemistry of the argillite rock (Table 4).

The siderite considered here is an ideal mixture of 0.15 pure calcite and 0.85 pure siderite end-members.

Table 4. Mineralogical composition of argillites

Phase (volume fraction)	Bulk Argillites
Calcite	0.263
Quartz	0.185
Illite	0.221
Na-Smectite	0.02
Ca-Smectite	0.04
Microcline	0.056
Kaolinite	0.009
Dolomite	0.012
Siderite 0.85	0.006
Pyrite	0.007
Celestite	0.0006
Porosity	0.18

Secondary phases

Chemical reactions occurring at the air/concrete and argillite/concrete boundaries induce the precipitation of secondary minerals. The set of secondary phases considered in our simulations is summarized in Table 5. Secondary calcite was distinguished from aggregate calcite, with the latter considered an inert phase.

Table 5. Secondary phases

Phase type	Phases
Oxides	Magnetite, Amorphous silica
Hydroxides	Brucite, Gibbsite Fe(OH) ₃
Sheet silicates	Sepiolite
Zeolites	Phillipsite K, Phillipsite Ca Laumontite, Analcime Gehlenite, Heulandite
Other silicates	CSH 1.2, CSH 0.8 Straetlingite, Katoite_Si
Sulfates, chlorides and other salts	Gypsum, Anhydrite Burkeite, Syngenite Glaserite, Arcanite Glauberite, Polyhalite
Carbonates	Calcite, Nahcolite
Others	Hydrotalcite-CO ₃ Ettringite, Dawsonite

Kinetics of dissolution/precipitation reactions

Reactions occurring in the air/concrete/argillite system cover several orders of magnitude in kinetics, from very fast reactions, like gypsum dissolution, to very slow reactions, like quartz or illite dissolution. Because of the greater numerical stability of TOUGHREACT in the kinetic mode, it was decided to describe all solid/solution reactions in the pure

kinetic mode and avoid the mixed kinetic/equilibrium model. However, the reaction-rate constants for many phases, as well as the reactive surface areas, are not well known. A simplified approach was therefore adopted here, combining the best data from Palandri and Kharaka (2004) with information available at Andra on cementitious phases.

SIMULATION TOOLS

Thermodynamic database

The simulations were run using the Thermoddem lv12 (July 2008) database, developed by BRGM (Orléans, France).

Adaptation of TOUGHREACT-EOS4

The EOS4 module (Pruess et al., 1999) was used in this study for describing the drying of materials like concrete, in which pressure-lowering effects are noticeable. In addition, the choice of this EOS makes possible the correct treatment of two-phase flow together with reactive transport in such materials. However, several adaptations of the original EOS4 module available in TOUGHREACT Version 1.2 (YMP Q V3.1.1 July 2006) (Xu et al., 2004) were necessary:

- An extended model for porosity/saturation-dependent tortuosities was developed to allow material-generalized Millington-Quirk tortuosity laws as shown in Eq. (1),
- An additional factor was taken into account to fix a distinct intrinsic material permeability with respect to the gas phase (see Tables 1 and 2).

Time and space discretization

The two-phase reactive transport process simulated here combines two major features:

- Development of a drying front from the edge of the porous concrete component
- Transport in the gas phase of a strongly soluble reactive species, CO₂(g)

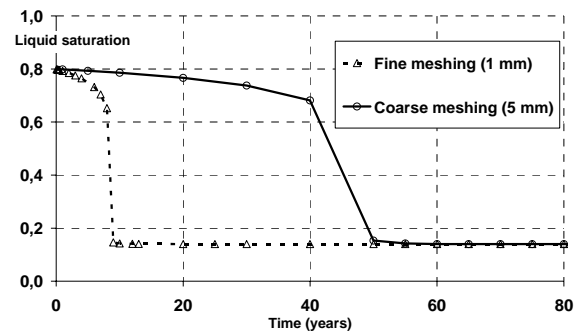


Figure 3. Effect of cell size on drying dynamics: evolution of liquid water saturation of waste package container in the mesh cell close to the dry air boundary.

It was found that the dynamics of drying are dependent on the size of the first discretization cell of concrete in contact with the dry air boundary condition (Figure 3). A large cell size delays drying, owing to control of the drying by water vapor diffusion. Among parameters influencing the kinetics of drying, note the nonlinear effects of the initial liquid water saturation of concrete (Figure 4) and of the b exponent in Equation (1) (Figure 5).

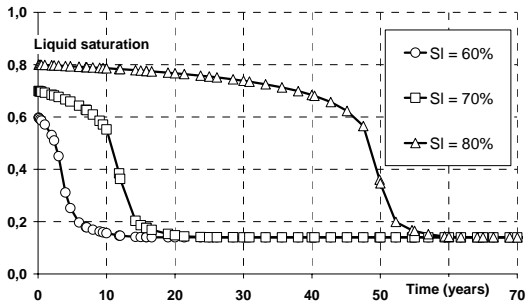


Figure 4. Effect of initial liquid water saturation on drying dynamics. Evolution of liquid water saturation in the mesh cell close to the dry air boundary) (meshing with $\Delta x = 5$ mm).

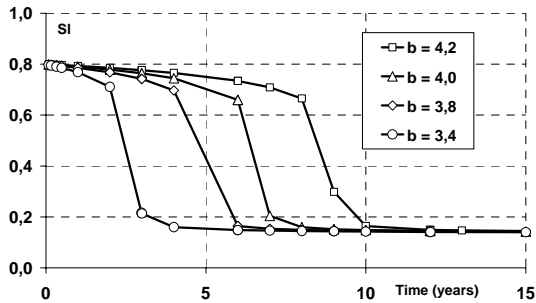


Figure 5. Effect b exponent of Eq. (1) on drying dynamics. Evolution of liquid water saturation in the mesh cell close to the dry air boundary) (mesh with $\Delta x = 1$ mm).

In the TOUGHREACT version used here, gas-phase transport is not iteratively coupled to reaction processes. It was therefore necessary to use a sequential noniterative approach (SNIA) for reactive transport, which requires small time steps, since gaseous CO_2 transport is a fast process (Fig. 6). It was therefore necessary to find a compromise in order to correctly describe the drying process, obtain sufficient detail about reaction fronts, and use the largest time-steps (keeping coupling errors small). The compromise found here was to take the smallest grid cells of 5 mm size; the time-step to be used then ranges from 10 to 50 s.

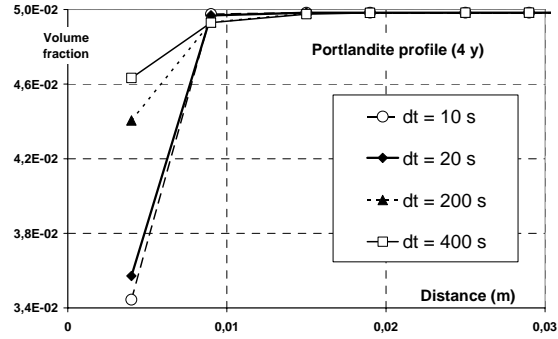


Figure 6. Effect of time-step magnitude dt on the spatial distribution of portlandite (BHP CEM-I, 25°C, 4 years).

Running cases

The runs were performed on a Linux workstation based on IntelXeon X5365 3 GHz processors. Duration of runs ranged from 30 to 180 days CPU to simulate 100 y of physical time.

CASES

Several conditions were explored to represent actual repository conditions in a schematic way, given that the heat source, the relative humidity of air, or vault ventilation may vary during realistic waste-disposal operations. Two cases are presented in this paper:

- Waste package (BHP CEM-I) at 25°C,
- BHP CEM-I components/argillite system, initially at 25°C and then submitted to hot (40°C) dry air at the concrete boundary.

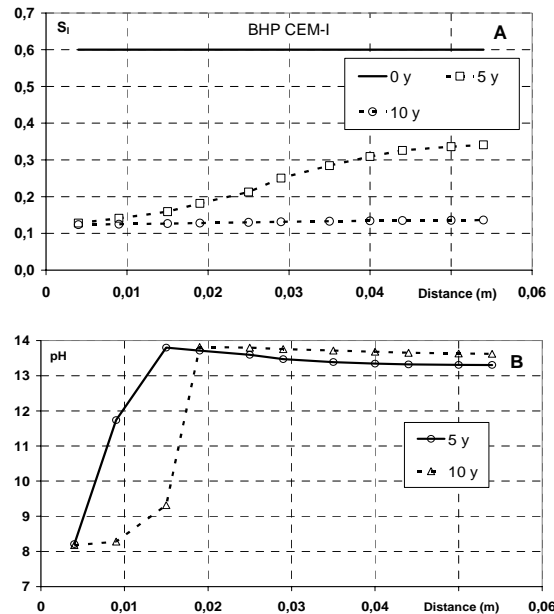


Figure 7. BHP CEM-I waste disposal package case (25°C): (A): Liquid water saturation (B) pH (along a half section of the container wall)

RESULTS

Waste disposal package test-case

With the assumption of an initial saturation of 0.6, complete drying of the waste package is fast (Figure 7a). After 10 y, the pH is depressed over a thickness of ~1.5 cm. The overshoot in pH, above the initial value of 13.25, results from a hydroxyl ion overconcentration caused by drying. Ionic strength reaches values of about 2.5 in the dried zones. In this range of ionic strength, the HKF model implemented in TOUGHREACT (Xu et al., 2004) gives fair estimations of activity coefficients for dissolved ions. Profiles for portlandite and secondary calcite (Figure 8a) show a retreat of portlandite on a total thickness of ~2 cm in 10 y.

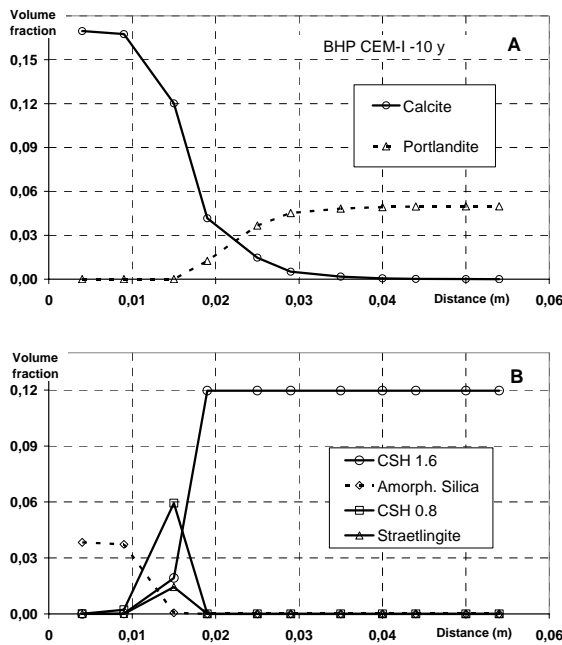


Figure 8. BHP CEM-I waste package case (25°C). (A): Calcite/Portlandite (B): CSH. (along a half section of the container wall)

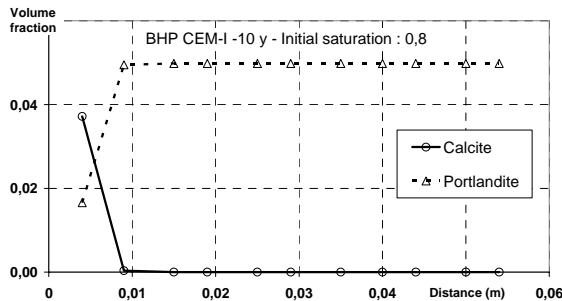


Figure 9. BHP CEM-I waste disposal package case (25°C) with initial saturation of 0.8. Calcite/Portlandite profile

Profiles for CSH phases (Figure 8b) show a degradation of CSH 1.6 towards secondary phases (CSH 0.8, Straetlingite) and ultimately amorphous silica. The degradation depth of CSH 1.6 corresponds to the depression zone in the pH profile (~1.5 cm in 10 y). Precipitation of small quantities of other secondary phases (gypsum, sepiolite, gibbsite, burkeite, syngenite) in the external alteration zone of the concrete is also predicted. If we assume an initial saturation of 0.8 in the concrete, the carbonation process is strongly delayed due to the long induction period prior to the development of the drying front. This results in carbonation depths of less than 1 cm in 10 y (Fig. 9).

Concrete structures/argillite test cases

BHP CEM-I engineered barrier/argillites system at 40°C at the air boundary

Results obtained after simulation of 8 years are shown here. At this time, the temperature gradient (Figure 10) extends through the entire concrete/argillite system. Temperatures from 40°C to 35°C are seen throughout the concrete zone.

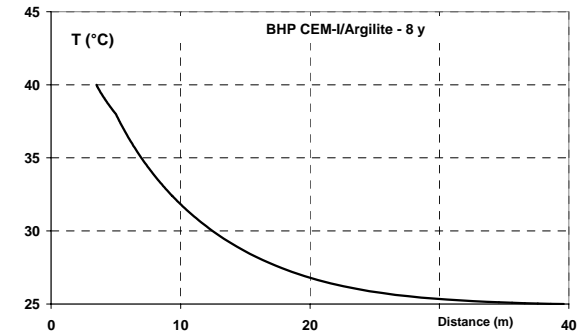


Figure 10. CEM-I/Argillite case (40°C). Temperature profile at 8 y.

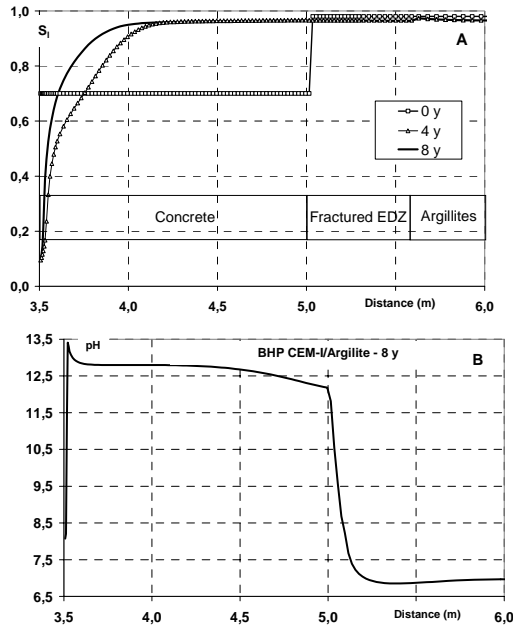


Figure 11. CEM-I/Argillites case (40°C). Liquid saturation and pH profiles at 8 y.

Liquid saturation in the concrete (Figure 11a) evolves with time due to both drying at the dry air boundary ($r=3.5$ m) and to water ingress from the host rock. This results, after 8 y, in a sharp desaturation front, extending over ~ 0.1 m, in which CO_2 gas will be able to diffuse rapidly and carbonate the concrete. The pH profile (Figure 11b) is depressed over about 2 cm at the air boundary, and then shows a maximum where the hydroxyl ions have been concentrated by evaporation.

A second pH front evolves around the other boundary of concrete, in contact with argillites, at $r = 5$ m. There, alkali and hydroxyl ions are free to diffuse towards the geological formation, as the medium is close to complete saturation. A broad pH weakening is therefore visible in the concrete, together with a pH front displaying a narrow foot (~ 0.1 m) inside the argillites. The calcite distribution near the dry air boundary (Figure 12a) displays a narrow peak, extending about 2 cm after 8 y, and a broader, low concentration extension over about 20 cm. The narrow peak corresponds to the zone of portlandite carbonation. The weak and broad extension seen in the calcite profile results from the conversion of monocarboaluminate into katoite Si that occurs around 38°C. This transformation involves simultaneous CSH uptake (in order to bring Si to the katoite) and portlandite/calcite production (in order to use the excess Ca and CO_3 left by the monocarboaluminate and CSH), as can be seen in Figure 12 a,b.

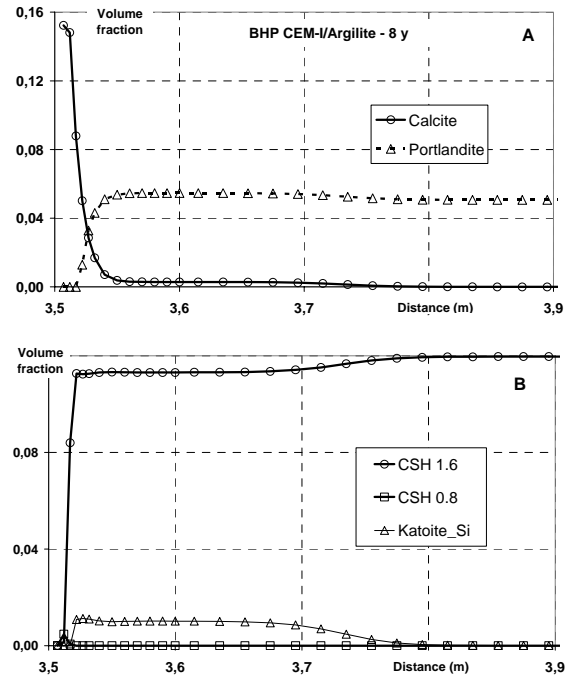


Figure 12. CEM-I/Argillites case (40°C). Minerals profiles at 8 y.

DISCUSSION

The two-phase reactive transport model presented in this work and applied, with 1D geometry, to subsystems found in ventilated ILL waste disposal cells—gives chemically consistent results:

- Transformation of portlandite and other cement hydrates to form calcite and various secondary products; the computed pH front matches well with these transformations;
- Formation of brines and deposition of salts in the parts of the concrete where drying occurs.

Note that the sulfate/carbonate salts predicted to precipitate (syngenite, burkeite) form in limited amounts (locally up to 0.01 vol. fraction) and were selected by database screening, not by experimental evidence. The progress and extent of these chemical transformations are, however, very sensitive to both the transport and hydraulic properties of the materials (concrete, EDZ, argillites). This is why a generalized form of the Millington-Quirk tortuosity model was implemented and tested—to better match the diffusion behavior of concrete. Results obtained among other cases on the waste package case (Figures 5 and 6) reveal that this is necessary but not sufficient to correctly tune the dynamics of drying, which are strongly coupled to carbonation. Gas transport in the partially saturated material is not a limiting process for carbonation, rather than solid/solution reactions and (perhaps also) gas/liquid

exchanges under low saturation conditions, in which the residual liquid phase occupies specific parts of the porous space (e.g., nanoporosity inside CSH phases). The time lag of 5 to 10 y necessary for drying of the 11 cm thick waste package (at 25°C) seems indeed underestimated when compared to recent experimental results obtained by Andra. Also, initial saturation conditions of the material will have some influence: if it is assumed that the initial saturation of concrete is 0.8 instead of 0.6, then the drying of the waste package would take ~50 y instead of about 10 y. Lower values of the liquid permeability of concrete may also produce a step-wise progression of the drying front, instead of behavior showing rapid percolation of gas through the sample at some moment. Also, it is known that carbonation reactions are very slow in a dry material. However, the dependence of chemical kinetics on water saturation is presently not included in TOUGHREACT, and this effect could not be explored.

Another salient feature of these simulations is related to numerical issues: the use of the SNIA approach could not be avoided, because gas transport is not coupled to carbonation reactions occurring between the solid and liquid phases. As a consequence, very small time steps had to be used to minimize operator splitting errors. Because the version of the TOUGHREACT code used here is not parallelized, computation duration is at the limit of what is reasonably achievable (1 month to 6 months CPU).

FUTURE DIRECTIONS OF WORK

This work will now follow three major directions:

- Improving the reactive transport model available in TOUGHREACT, to be able to describe water production/uptake by chemical reactions and the effects of liquid saturation on reaction kinetics;
- Improving material transport and hydraulic parameters to obtain more consistent predictions using the available experimental data, and then long- term predictions;
- Evaluating the possibility of improving code performance, for example by parallelizing parts of the numerical algorithm, to gain at least one order of magnitude in computation speed.

ACKNOWLEDGMENT

K. Pruess, T. Xu, and N. Spycher (Lawrence Berkeley National Laboratory) are gratefully acknowledged for their help in building and improving the TOUGH scripts and for their insightful remarks on multiphase physics. A. Burnol and F. Claret (BRGM) have helped us considerably with databases and script improvement. B. Bary and S.

Poyet (CEA/DEN LECBA) are acknowledged for their help on concrete physics.

REFERENCES

- Andra Dossier Argile, Agence Nationale pour la Gestion des Déchets Radioactifs, Châtenay-Malabry, France, 2005 (www.andra.fr).
- Bary B., Mügler C. Simplified modelling and numerical simulations of concrete carbonation in unsaturated conditions. *European Journal of Environmental and Civil Engineering*, 9/10, 1049-1072, 2006.
- Bary B., Sellier A., Coupled moisture: carbon dioxide-calcium transfer model for carbonation of concrete. *Cem. Concr. Res.*, 34, 1859-1872, 2004.
- Baroghel-Bouny, V., Thiery, M., Barberon, F., Coussy, O. et Villain G. Assessment of transport properties of cementitious materials. *European Journal of Environmental and Civil Engineering*, 11, 671-696, 2007.
- Belarbi R., Aït-Mokhtar A., Qin M. & Omicrine O. (2006) development of a simplified approach to model the moisture transfer in building materials. *Revue Européenne de Génie Civil*, 10/9, 1033-1048
- Gaucher E. et al. Modelling the porewater chemistry at the Callovo-Oxfordian formation at a regional scale. *C. R. Geoscience*, 338, 917-930, 2006.
- Gaucher E. et al. Caractérisation géochimique des forages PAC et nouvelles modélisations THERMOAR. Report BRGM/RP-54416-FR, BRGM, France, 2007.
- Millington R.J. and Quirk J.P. Permeability of porous solids. *Trans. Faraday Soc.*, 57, 1200-1207, 1961.
- Palandri J. L., Kharaka Y. K. A compilation of rate parameters of water-mineral interaction kinetics for application to geochemical modeling. US Geological Survey Open File Report 2004-1068. Menlo Park, California, USA., 2004.
- Pruess, K., C. Oldenburg, and G. Moridis, *TOUGH2 User's Guide, Version 2.0*, Report LBNL-43134, Lawrence Berkeley National Laboratory, Berkeley, Calif., 1999.
- Thiery M. Modélisation de la carbonatation atmosphérique des matériaux cimentaires. Prise en compte des effets cinétiques et des modifications microstructurales et hydriques. PhD Thesis, ENPC, Marne-la-Vallée, France, 2005.

Thiery M., Baroghel-Bouny V., Bourneton N., Villain G. et Stéfani C. Modélisation du séchage du béton. Analyse des différents modes de transfert hydrique. *European Journal of Environmental and Civil Engineering*, 11/5, 541-578, 2007.

Xu, T., Sonnenthal, E., Spycher, N. et Pruess K. TOUGHREACT user's guide: a simulation program for non-isothermal multiphase reactive geochemical transport in variably saturated geologic media. Report LBNL-55460, Lawrence Berkeley National Laboratory, Berkeley, Calif., 2004.

SIMULATION OF GAS MIGRATION AT THE SCALE OF A DISPOSAL CELL IN THE CONTEXT OF HIGH-LEVEL AND LONG-LIVED RADWASTE DISPOSAL IN A DEEP CLAY FORMATION DURING THE OPERATING PHASE

Eloi Treille, Jacques Wendling and Frédéric Plas

ANDRA, Scientific Division
Parc de la Croix Blanche, Châtenay-Malabry, France
e-mail: eloi.treille@andra.fr, jacques.wendling@andra.fr, frederic.plas@andra.fr

ABSTRACT

High-level and long-lived radioactive waste geological (HLW) disposal in the Callovo-Oxfordian deep clay layer, in the eastern part of the Paris Basin, is based primarily on the low water permeability of the clay host rock. This property also intrinsically returns to a low capacity of gas evacuation. Indeed, processes such as anoxic corrosion of metallic materials and radiolysis of organic waste will generate a significant amount of hydrogen over time. The effect of this gas on the safety performance of the components of the disposal system has to be evaluated for both the operating period and the postclosure period of the repository.

In that context, numerical simulations using TOUGH2/TOUGH2-MP were performed on a vitrified waste disposal cell and its access drift, for the early years of the operating-phase period. The objective was to investigate generation and migration of hydrogen within and outside a vitrified waste disposal cell, coupled with the desaturation of the near field of the drift and the coupled behavior of dry air and hydrogen within the disposal cell. Particular attention was focused on the form of hydrogen (expressed gas and dissolved), total gas pressure buildup, degree of gas saturation, gas pathways, concentrations of gases, and the exchanges of gases between the disposal cell and the drift within the disposal cell and its near field, up to the drift.

INTRODUCTION

The French National Radioactive Waste Management Agency (ANDRA) established the feasibility of a deep geological disposal of high-level and long-lived radioactivity waste in an argillaceous formation (ANDRA, 2005). The repository would be built in an indurated clay formation at around 500 m depth. One question relative to the performance of this repository concerns the impact of the (mainly) hydrogen gas generated by anoxic corrosion of metallic components. In this paper, these questions are addressed for HLW disposal zone with TOUGH2/TOUGH2-MP simulations. The numerical codes are tested in several geometrical configurations.

The general layout of the HLW disposal setup is shown in Figure 1. The disposal configuration comprises a disposal cell with waste disposal cell packages and some engineered components: tight radioprotection plug, swelling-clay sealing plug, concrete plug, tight protective cap, and an access drift with a concrete lining.

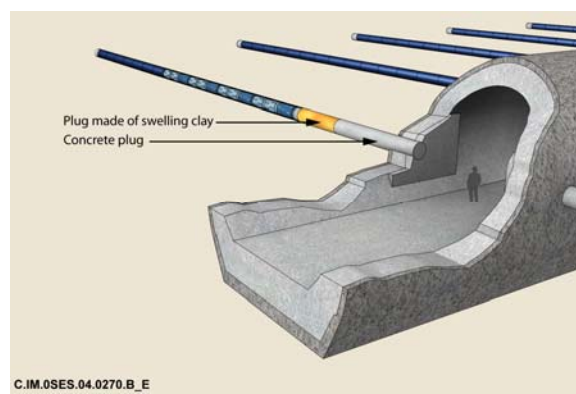


Figure 1. General layout of the HLW part of the repository: waste disposal cells: ~40 m length (Andra, 2005)

PHYSICAL PROCESSES

During the operating period of the repository, up to 100 years, the access drift will be ventilated and the surrounding rock will be progressively unloading and—to a certain extent—desaturating with air ventilation. Due to anoxic corrosion of steel components, hydrogen will be generated.

The processes taking place during this phase are:

- Aqueous phase: dissolution in the pore water (Henry's law) of gases (air and hydrogen) and transport by diffusion/advection.
- Gas phase: convection and diffusion of the different gas components (water vapor, air and hydrogen) in their expressed form.

The two-phase flow is described with a multiphase extension of Darcy's law. The flow and transport

processes are here considered to be under isothermal conditions (22°C).

The TOUGH2/TOUGH2-MP module EOS7R (multigas component context: water/air/RN1 component used for hydrogen) was selected for the different computations (Pruess et al., 1999; Zhang et al., 2008). The flow and transport processes are here considered to be under isothermal conditions (22°C).

GEOMETRY AND PARAMETERS

The geometry represents an axially symmetric simplification of an illustrative configuration of the disposal setup, as shown in Figure 2. The simulation domain has a horizontal extension of 51 m and a radial extension of 25 m.

Waste disposal packages are not part of the computational domain. Radioprotection plugs as well as protective caps are regarded as quite impermeable, so they are not included in the computational domain. The access drift, regarded as an infinite volume domain, is also not included in the computational domain. Distinction is not made between fractured and micro-fissured argillites.

The void between the metallic lining and the cell vault and wall (EDZ), and the lining itself, are assumed to be a homogenized domain represented by interface zones of small thickness (1 cm).

The main characteristic flow parameters are presented in Tables 1 and 2. We use the two-phase flow parametrization of the relative permeability and capillary-pressure-saturation constitutive relationship after van Genuchten–Mualem. Absolute permeability for the undisturbed argillites is considered to be isotropic, with a value of $2.32 \times 10^{-20} \text{ m}^2$ (geometric mean of values along the three principal axes). The absolute permeability for interface zones is three orders of magnitude larger in the longitudinal direction (10^{-13} m^2) than in the radial one (10^{-16} m^2).

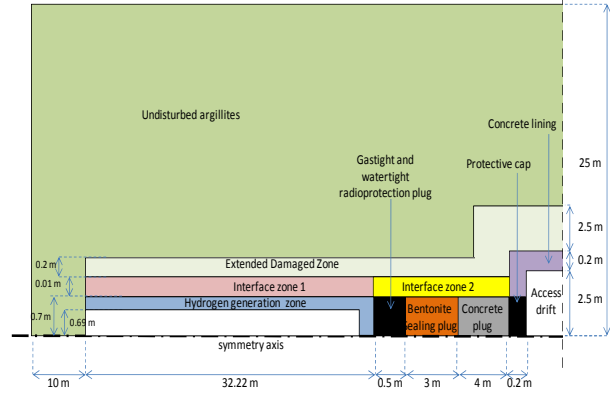


Figure 2. Geometry of the computational domain (diagram with distorted proportions)

Table 1. Hydraulic properties of the source zone, bentonite, and concrete

	Source zone	Bentonite plug	Concrete plug/lining	Unit
Porosity	1.00	0.35	0.15	-
Absolute permeability k	10^{-13}	10^{-19}	10^{-18}	m^2
van Genuchten Coefficient n	No	1.61	1.54	-
van Genuchten Pseudo gas entry pressure P_0	No	$1.8 \cdot 10^7$	$2.0 \cdot 10^6$	Pa

Table 2. Hydraulic properties of interface zones and undisturbed argillites

	Interface zones 1 et 2	Extended Damaged Zone	Undist. argillites	Unit
Porosity	0.10	0.20	0.18	-
Absolute permeability k	rad. 10^{-16} long. 10^{-13}	10^{-18}	$2.3 \cdot 10^{-20}$	m^2 m^2
van Genuchten Coefficient n	2.50	1.50	1.49	-
van Genuchten Pseudo gas entry pressure P_0	10^3	$8.0 \cdot 10^6$	$1.5 \cdot 10^7$	Pa

The rectangular mesh consists of 36,845 cells. The simulations are numerically demanding, since many different materials are taken into account at scales between 1 cm and several 10's of meters. High contrasts in permeability (up to 7 orders of magnitude) and capillarity properties of the different materials, as well as multicomponent diffusion processes in both aqueous and gaseous phases, lead to convergence problems in the numerical schemes. Most of these issues are solved by adapting spatial discretization. The different runs are performed on a 64-bit Linux cluster.

INITIAL AND BOUNDARY CONDITIONS

Initially, the rock mass is fully water saturated. The impact of the vertical gradient is neglected, and an initial pressure of 5 MPa is imposed along the upper horizontal boundary. Engineered components and interface zones are initially at the atmospheric gas-phase pressure and partially unsaturated with air. The initial liquid saturations are: 70% in the interface zones, 75% in the bentonite sealing plug, and 80% in the concrete plug and lining. The hydrogen generation zone is initially fully air saturated at the atmospheric pressure.

A constant atmospheric gas-phase pressure and 50% relative humidity (equivalent to 0.13 liquid phase saturation) are applied at the outer wall of the concrete lining. For symmetry reasons, other vertical boundaries are set to no-flow conditions.

The simulation period is 0 to 1,200 days (early years of the operating period). Hydrogen gas generation is uniform, with a cumulated constant rate of 133 mol/year for the entire source term zone.

MODELING RESULTS

Gas mass flows

As presented in Figure 3, prior to five months, the concrete lining and EDZ were depressurized and partially desaturated with air flow coming from the ventilated access drift. In the meanwhile, air moved from the hydrogen generation zone and interface zones, due to their resaturation, to EDZ and concrete lining. Air flow direction through the access drift was then inverted, due to gaseous hydrogen coming into the EDZ, in the near-field of the access drift.

From three years, there is almost no air flowing across the internal material boundaries.

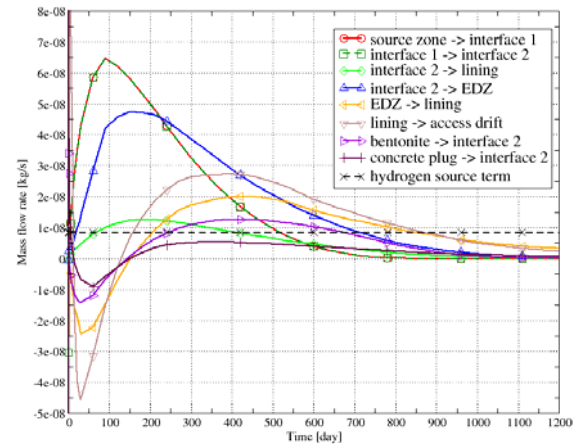


Figure 3. Mass flow rate of gaseous air through different internal material boundaries with time

Gaseous hydrogen flow coming out of interface zones regularly increases up to twenty months and decreases after thirty months (See Figure 4). About one quarter of this flow goes to the concrete lining, despite the very small area of the corresponding internal material boundary (0.04 m²). The remaining hydrogen coming from interface zones mainly flows towards EDZ (area of 33.5 m²). Also, some gas accumulates in the bentonite sealing plug, up to twenty months, before leaving again towards Interface Zone 2.

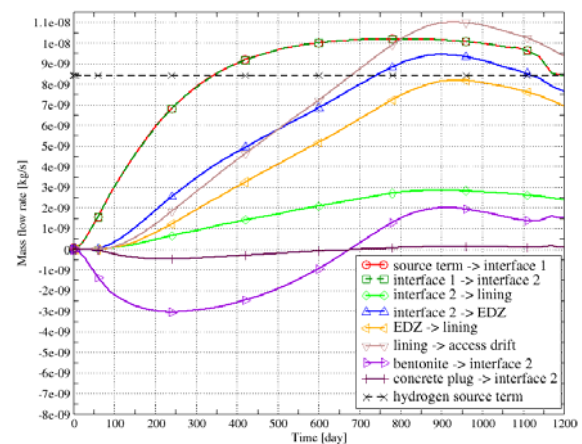


Figure 4. Mass flow rate of gaseous hydrogen through different internal material boundaries with time

Hydrogen flow in a dissolved form coming out of Interface Zone 1 (opposite to the hydrogen generation zone) greatly increases from 1,050 days. Most of this gas flows in dissolved form towards the bentonite sealing plug (See Figure 5).

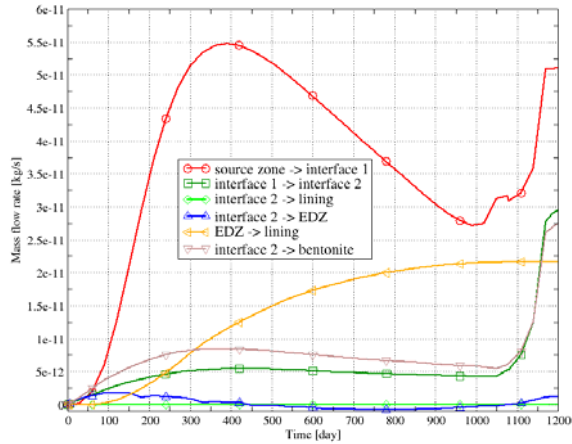


Figure 5. Mass flow rate of hydrogen in dissolved form through different internal material boundaries over time

Evolution of the saturation

Interface Zone 1 (opposite the hydrogen generation zone) is very quickly resaturated (within less than one day). After three years, the hydrogen generation zone is almost completely resaturated, as shown in Figure 6.

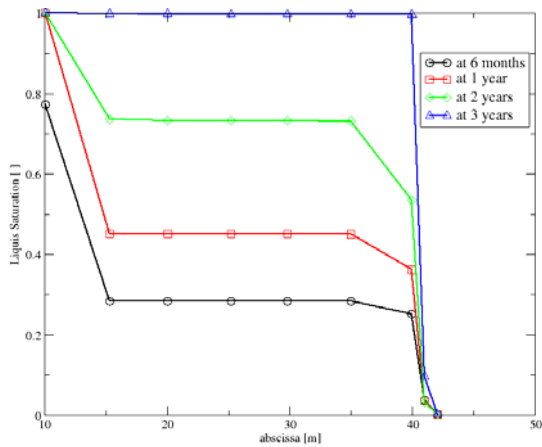


Figure 6. Space evolution of the liquid water saturation along the hydrogen generation zone, at different times

Undisturbed argillites come to partially saturated conditions in a very limited area, in the near field of the bentonite and concrete plugs (see Figure 8).

Evolution of the gas pressure

Despite the steady hydrogen generation, the gas pressure in the source zone reaches a maximum level of only 1.95 bars, after one year (see Figure 7). Due to the very high longitudinal permeability in the interface zones, hydrogen is quickly evacuated from the source zone, across Interface Zone 1.

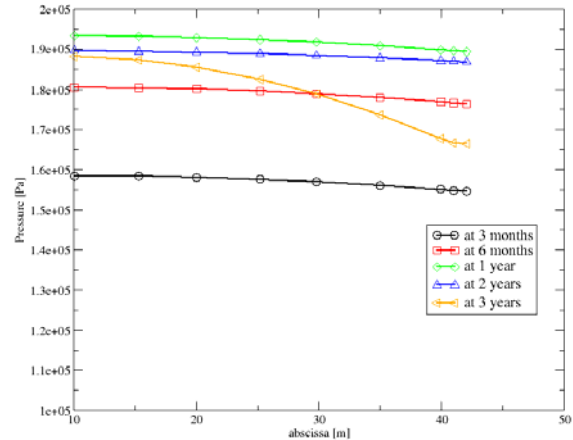


Figure 7. Space evolution of the gas pressure along the hydrogen generation zone, at different times

The gas pressure peaks at 3.1 bars in the bentonite sealing plug, close to the radial symmetry axis (see Figure 8). Gas pressure in the other engineered components and in the EDZ does not exceed 2.0 bars.

Evolution of the gas concentrations

A maximal level of hydrogen concentration is observed in the bentonite sealing plug, as the maximal gas phase pressure is reached. Gaseous hydrogen regularly flows into the EDZ, coming from interface zones (See Figure 9). Initially, maximal air concentrations are also present in unsaturated engineered components. Up to 20 months, due to air ventilation, air concentration raises in EDZ. Then, air present in EDZ is progressively replaced by gaseous hydrogen (See Figure 9).

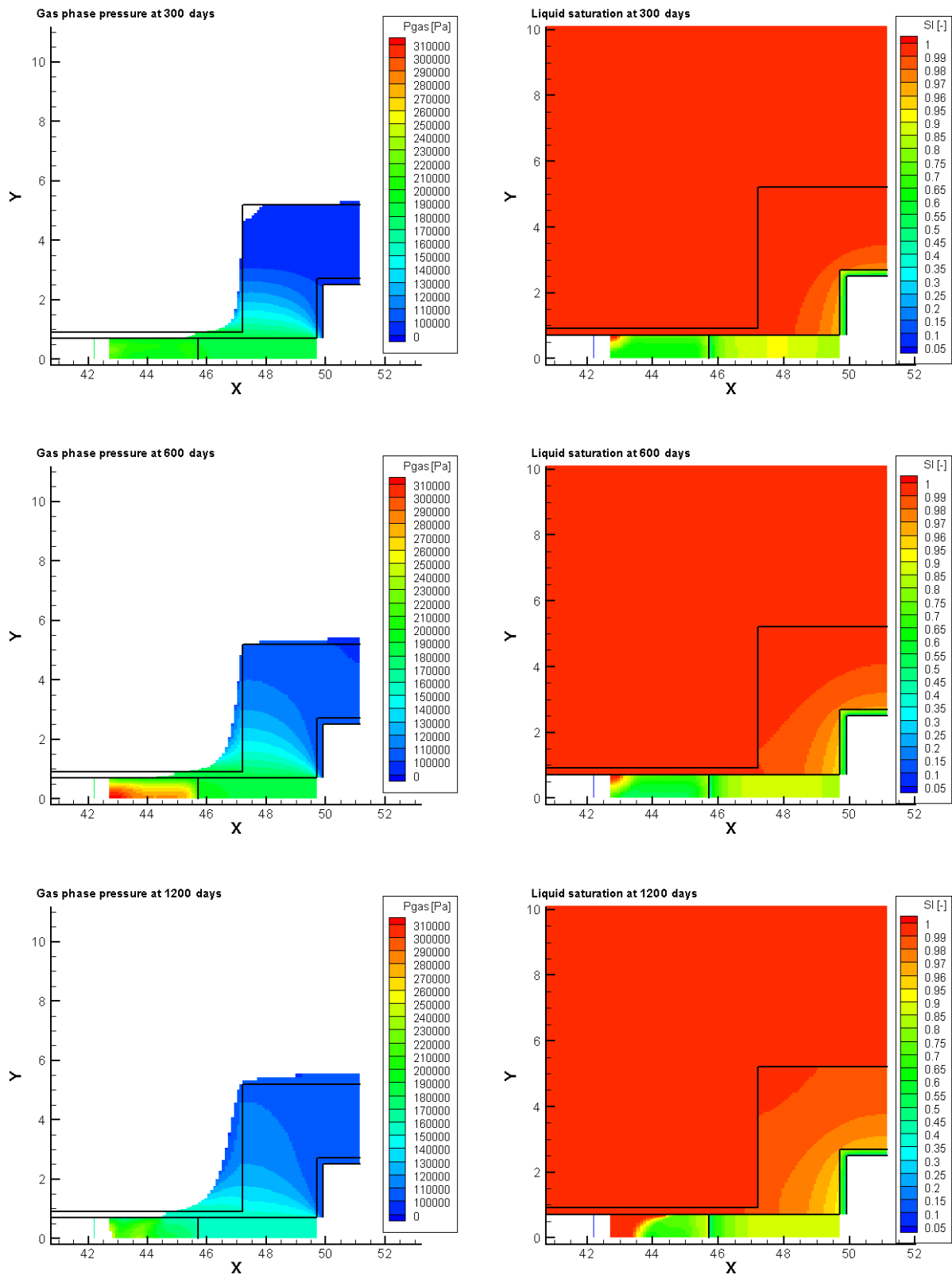


Figure 8. Spatial distribution of the gas pressure (left) and the liquid water saturation (right) (close-up around the engineered components and the access drift)

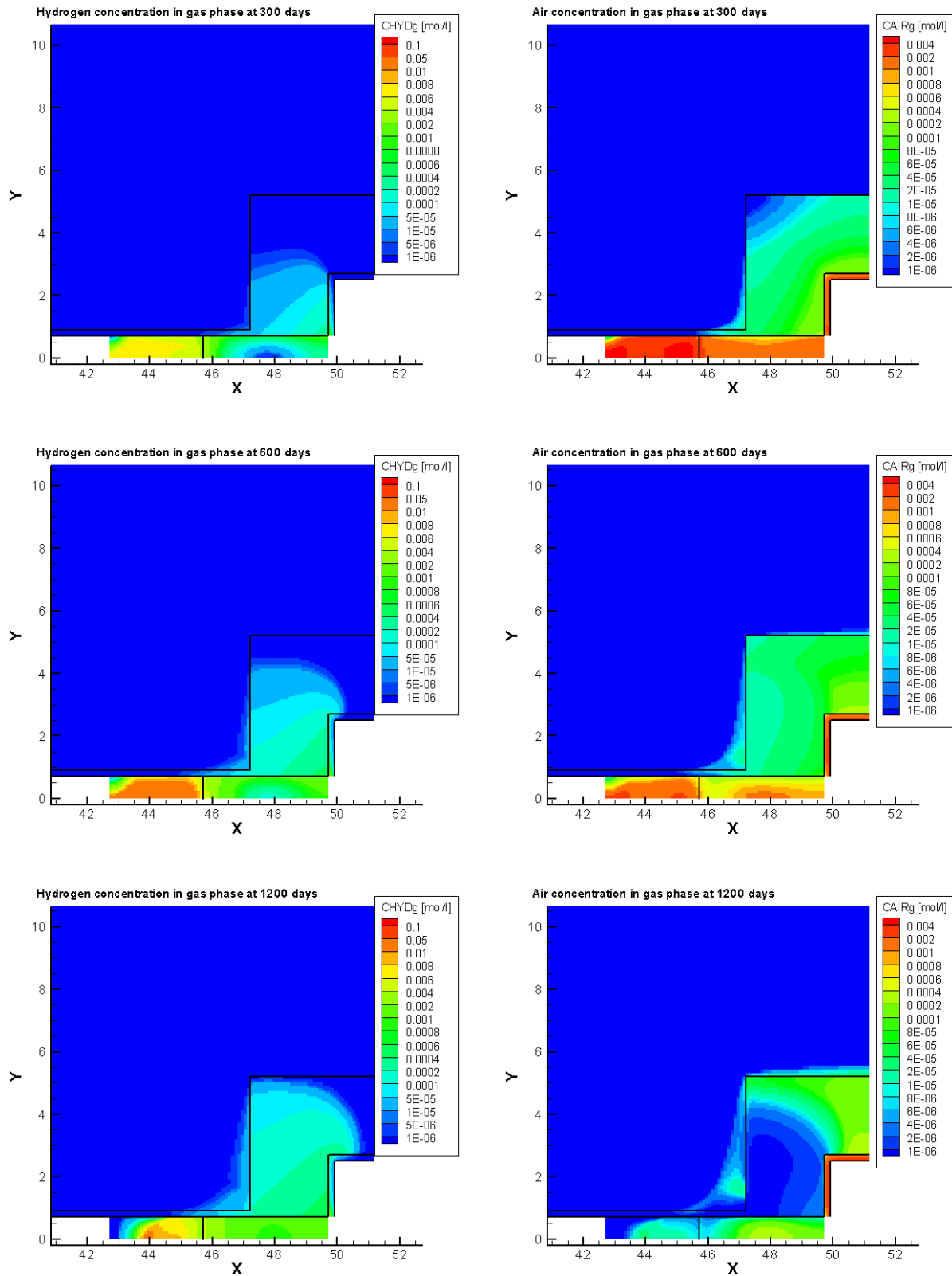


Figure 9. Spatial distribution of the hydrogen concentration (left) and the air concentration in gas phase (right) (close-up around the engineered components and the access drift)

FUTURE DIRECTIONS OF WORK

Additional sensitivity runs will be performed by changing some hydraulic properties of the interface zones and/or engineered components. The influence of the hydrogen generation rate and of the relative humidity of the ventilation air will also be examined. Numerical efforts must be done to improve the time-step management.

CONCLUSIONS

The objective of this study was to investigate the potential impact of hydrogen gas generated in the waste disposal packages at a high-level, long-lived radioactive waste geological (HLW) disposal site, in a deep clay formation, during the operating phase. We also took this opportunity to test the TOUGH2/TOUGH2-MP codes in a real multicomponent context.

Numerical simulations were performed in an axisymmetric configuration (horizontal symmetry axis), for early years of the operating-phase period. The problem was numerically challenging, because many different materials were taken into account at scales between 1 cm and several tens of meters, with high contrasts in permeability and capillarity properties.

The simulations focused on the gas transfer through the different internal material boundaries and the propagation of the gaseous components.

Simulation results show that a non-negligible hydrogen flow is likely to take place in the extended damaged zone (EDZ) and in the bentonite sealing plug. The internal material boundary between interface zones and concrete lining appears to be a preferential pathway. The total gas-pressure maximum is of three bars and is observed in the bentonite sealing plug. This maximal value corresponds to hydrogen accumulation in this engineered component. Undisturbed argillites are not affected by the gas propagation.

ACKNOWLEDGMENT

K. Pruess (Lawrence Berkeley National Laboratory) is gratefully acknowledged for his help and for his insightful remarks in using TOUGH2.

REFERENCES

- Andra (2005) Dossier Argile 2005. Agence Nationale pour la Gestion des Déchets Radioactifs, Châtenay-Malabry, France.
- Pruess, K., Oldenburg C., and Moridis G., *TOUGH2 User's Guide, Version 2.0*, Report LBNL-43134, Lawrence Berkeley National Laboratory, Berkeley, Calif., 1999.
- Zhang K., Wu Y., and Pruess, K., *User's Guide for TOUGH2-MP - A Massively Parallel Version of the TOUGH2 Code*, LBNL-315E, Lawrence Berkeley National Laboratory, Berkeley, Calif., 1999.

MODELING MULTIPHASE FLOWS FROM A REPOSITORY IN DIFFERENT GEOLOGICAL ENVIRONMENTS

Benjamin Swift, Andrew Hoch, Peter Jackson, Martin James, and Fiona Bate

Serco

B150, Harwell Science and Innovation Campus
Didcot, Oxfordshire, OX11 0QB, United Kingdom
e-mail: Ben.Swift@serco.com

ABSTRACT

The UK Nuclear Decommissioning Authority (NDA) is tasked with a range of functions, including developing a safety case to assess the safety and environmental implications of a geological disposal facility for radioactive waste.

Although current work is not specific to a particular geological environment, this does not preclude the NDA from investigating issues that will need to be taken into account once geological environments have been identified.

In particular: gases will be generated in the facility; non-aqueous phase liquids (NAPLs) may be present in the waste; and secondary NAPLs may be generated by radiation in the facility. The effects of these gases and NAPLs will need to be considered.

This paper summarizes recent work for the NDA to simulate the migration of gases and NAPLs from a geological disposal facility. The computer programs TOUGH2v2 and TMVOC respectively were used. In the course of this work, we made some developments to the way in which the computer programs are applied. These developments and some illustrative results are presented below.

INTRODUCTION

Geological disposal (i.e., the engineered emplacement of wastes in underground repositories at depths of several hundreds of meters) is widely accepted as the safe, secure and environmentally appropriate solution for radioactive wastes. In June 2008, the UK government published a White Paper (Defra etc., 2008) which set out a detailed framework for the long-term management of higher activity wastes. This makes it clear that geological disposal is the way forward, based on a voluntarism and partnership approach¹ with a local community. In particular, the government made the UK Nuclear Decommissioning Authority (NDA) the organization responsible for planning and delivering a geological disposal facility (GDF) in the UK.

Concepts for geological disposal

Concepts for geological disposal generally incorporate both engineered and natural barriers to radionuclide release, as part of a multibarrier approach to isolating radioactive waste from the surface environment. This is the underlying principle behind all international concepts for the disposal of intermediate level waste (ILW), high level waste (HLW) and spent fuel (SF). A schematic representation of a multibarrier approach is provided in Figure 1.

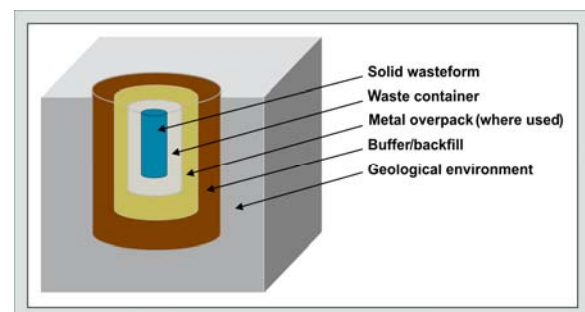


Figure 1. Schematic representation of a multibarrier approach for geological disposal

The UK safety case for a GDF is currently at an early stage of development, because neither a site nor a design has been chosen yet. The NDA calls it a “generic” safety case, and the strategy to demonstrate safety is also termed “generic” because it must cover a range of possible disposal environments and facility designs.

Geological environments

The range of geological settings in the UK that could be suitable for hosting a GDF¹ for higher-activity wastes is diverse. Concepts for geological disposal facilities in a variety of host rocks have been studied extensively by other countries, and it is possible to see how those concepts could be tailored to different UK waste inventories and UK geological environments. To demonstrate the feasibility of

¹ The UK government is using a voluntarism and partnership approach to site a GDF. This means an approach in which communities voluntarily express an interest in taking part in the site-selection process that ultimately will provide a site for a GDF.

building a safety case in a range of geological settings, the NDA is using the illustrative disposal concept examples listed in Figure 2.

Host rock	Illustrative Geological Disposal Concept Examples	
	ILW/LLW	HLW/SF
Higher strength rocks ^a	UK (Geological Disposal Concept for ILW/LLW, NDA)	Sweden (KBS-3V, SKB)
Lower strength sedimentary rock ^b	Switzerland (Opalinus Clay, Nagra)	Switzerland (Opalinus Clay, Nagra)
Evaporites ^c	United States (WIPP, US DoE)	Germany (Salt dome, DBE Technology)

- Higher strength rocks. The UK ILW/LLW and Swedish KBS-3V concepts were selected due to the availability of information.
- Lower strength sedimentary rock. The Swiss concepts for Opalinus Clay were selected because a recent OECD Nuclear Energy Agency review regarded the Nagra assessment as state-of-the-art. Information will be drawn, in addition, from: the French concept for Callovo-Oxfordian Clay, which has received strong endorsement from international peer review; and the Belgian super-container concept for disposal of HLW and SF in Boom Clay.
- Evaporites. The US concept for transuranic wastes at the Waste Isolation Pilot Plant (WIPP) was selected because of the wealth of information available from a licensed operating facility. The German concept for HLW/SF was selected due to the availability of information.

Figure 2. Illustrative disposal concept examples

Gases and NAPLs

The radioactive waste will continue to evolve, even after it are packaged. Some degradation processes will lead to generation of gas. There is a general consensus on the processes that will generate gas: corrosion; microbial action; and radiolysis (e.g. Rodwell et al., 2003). Corrosion of metals in wastes and containers will yield hydrogen; microbial degradation of various organic wastes will yield methane and carbon dioxide; radiolysis of water and certain organic materials in the packages will yield mainly hydrogen. Hydrogen will be the predominant gas formed; lesser amounts of methane and carbon dioxide will be formed. In addition, some active gases will be released in trace amounts, including tritium, carbon-14-labeled methane, and carbon dioxide, and radon. Finally, non-aqueous phase liquids (NAPLs) may be present in the wastes; and secondary NAPLs may be generated by radiation in a GDF.

The possible effects of these gases and NAPLs need to be considered, because they could:

- Affect the pathway by which radionuclides will migrate back to the surface environment; and
- Pressurize the GDF.

This paper summarizes recent work for the NDA to simulate the migration of gases and NAPLs from a GDF, and presents some illustrative results. In the absence of a specific geological environment, three example environments with contrasting properties are considered: higher strength rocks, lower strength sedimentary rock, and evaporites.

DEVELOPMENTS

The computer programs TOUGH2v2 and TMVOC² respectively were used to investigate the migration of gases and NAPLs from a GDF. In the course of this work, we made some developments to the way in which the computer programs are applied. These developments are summarized below.

Interfaces from CONNECTFLOW to TOUGH

CONNECTFLOW (<http://www.connectflow.com/>) is a software package for modeling groundwater flow and transport. It:

- Includes the NAMMU continuum porous medium (CPM) module;
- Includes the NAPSAC discrete fracture network (DFN) module; and
- Also can be used to nest NAMMU and NAPSAC submodels into a combined CPM/DFN model.

In many geological environments, both regional-scale groundwater flow models and local-scale multiphase flow models will be developed. To avoid duplication of effort, we have developed interfaces between CONNECTFLOW and the TOUGH suite of codes that will allow data from a groundwater flow model to be re-used in a multiphase flow model.

Generation of meshes

CONNECTFLOW has its own mesh generator, and also can read in mesh files generated by third-party mesh generators such as FEMGV³ and GiD⁴.

As a pragmatic way of developing a mesh generator for TOUGH2v2 or TMVOC, an output option was written that exports a mesh from CONNECTFLOW in a suitable format for import into the TOUGH suite of codes.

² TOUGH2v2 and TMVOC are programs for simulating coupled fluid and heat flows for multi-component, multiphase fluid mixtures in porous and fractured media (Pruess, 1987; Pruess, 1991; and Pruess *et al.*, 1999). They were developed by Lawrence Berkeley Laboratory.

³ <http://www.tnodiana.com/node/22/>

⁴ <http://gid.cimne.upc.es/>

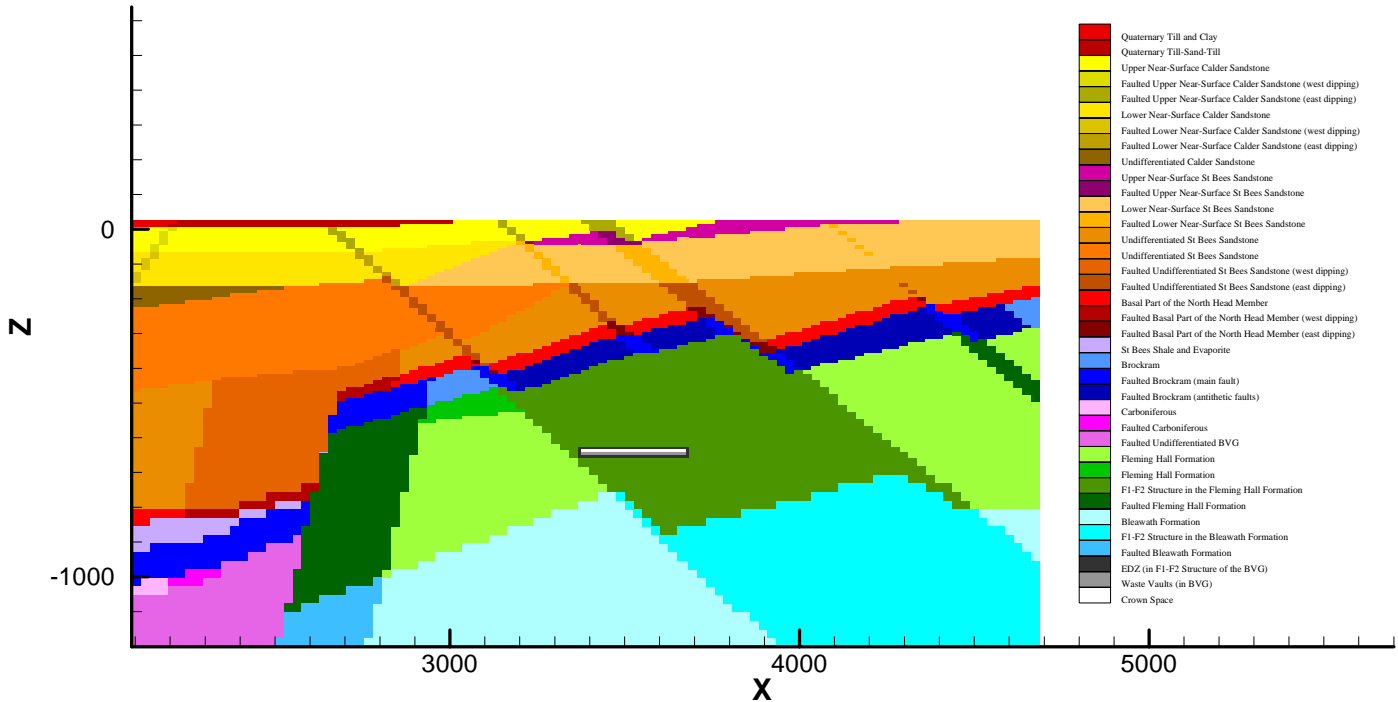


Figure 3. 2D model region showing a GDF and rock units (after Baker et al., 1997)

Setting of permeability and porosity

After creating a mesh, usually the next task is to assign the material properties (i.e., permeability and porosity). There are two interfaces between CONNECTFLOW and the TOUGH suite of codes that can be used to set material properties:

1. The first interface reads in both a TOUGH MESH file and an existing NAMMU (i.e., CPM) groundwater flow model. The elements in the TOUGH mesh are given a permeability and porosity based on the parameterization of the groundwater flow model. Figure 3 is an example of a TOUGH model obtained in this way.
2. The second interface is used if the underlying groundwater flow model is a DFN. In particular, NAPSAC has the capability to calculate equivalent continuum hydraulic properties (i.e., permeability and porosity). It can calculate the permeability tensor in individual mesh blocks for an arbitrary subdivision of the DFN. NAPSAC calculates the flows through a mesh block for an arbitrary head gradient, and then determines the six components of the permeability tensor that give the best fit (in a least-squares sense) to the flows. This capability originally was developed, tested, and applied by Jackson et al. (2000), and recently was extended to calculating equivalent continuum hydraulic properties for the TOUGH suite of codes.

In the case of the TOUGH suite of codes, a new data block called “PERM,” which lists the permeability tensor for each mesh block, is added to a TOUGH MESH file. Some minor modifications were also made to the TOUGH source code, to read in the “PERM” data block and to project the permeability tensor onto each of the connections with an element. (An example of the use of this interface is given in Leung et al., 2009.)

A refinement of the algorithm can be used to generate a TOUGH MINC⁵ file.

Setting of initial and boundary conditions

Finally, another interface between CONNECTFLOW and the TOUGH suite of codes can be used to set initial and boundary conditions. An output option can export the pressure calculated using a regional-scale CONNECTFLOW model to the TOUGH suite of codes (i.e., it writes a TOUGH INCON file).

⁵ The MINC (i.e. multiple interacting continua) model (Pruess, 1983; Pruess, 1992) is an extension of double continuum models. Double continuum models assume that the flow between the fractures and matrix blocks is “quasi-steady” (i.e., proportional to the local difference in average pressure between the fractures and matrix blocks). In contrast, the MINC method treats this flow in a fully transient way; it resolves the gradients that drive the flow by discretizing the matrix blocks into a nested sequence of volume elements.

Output options

The TOUGH suite of codes has rudimentary output facilities. To get around this limitation, we have customized the FORTRAN subroutine OUT so that it writes out the following data:

- Variables in a binary format for import directly into TecPlot360⁶;
- The masses of components (e.g. in selected rock types) in a CSV format for import into Excel;
- The flows of components (e.g. between selected rock types or across specified planes) in a CSV format for import into Excel; and
- The sources of components in a CSV format for import into Excel.

Job management

Often a calculation with the TOUGH suite of codes will involve a sequence of simulations. For example:

- First, equilibration of the system;
- Next, excavation of the facility and an operational phase, and
- Finally, a postclosure phase during which the repository resaturates.

We make extensive use of Linux scripts to manage a sequence of simulations. This helps to provide a robust audit trail. In particular, we use Perl scripts, with their advanced pattern-matching capabilities, to modify material properties, boundary conditions, source terms, etc.

Enhanced precision arithmetic

In some simulations with the TOUGH suite of codes, we have found it beneficial to use quadruple precision arithmetic to maintain accuracy.

A bug

The TOUGH input flag MOP(24) determines how to handle multiphase diffusive fluxes at interfaces. If MOP(24) is set to 1, then harmonic weighting of the separate liquid and gas-phase diffusivities is carried out. However, if MOP(24) is set to 0, then harmonic weighting of a “fully-coupled effective multiphase diffusivity” is carried out.

We have identified a problem with the scheme when MOP(24) is set to 0. Specifically, in a region where there are two phases and one of the mass fractions has a minimum, then the calculation of the “fully-coupled effective multiphase diffusivity” will give unphysical results (e.g., negative diffusivities). Therefore, we caution against setting MOP(24) to 0.

GAS IN HIGHER STRENGTH ROCKS

Gas migration models are sensitive to the details of the geological setting. In earlier studies of gas migration in “higher strength” rocks (e.g., Bate et al., 2006; Hoch et al., 2008; Hoch, 2008), many of the calculations were based on a model of the Sellafield region (Figure 3) that was developed for the *Nirex 97* analysis (Baker *et al.*, 1997). The NDA has used the setting of Sellafield to develop its understanding, because the site has been well-characterized.

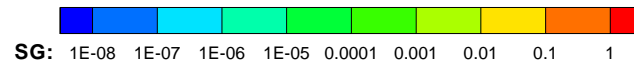
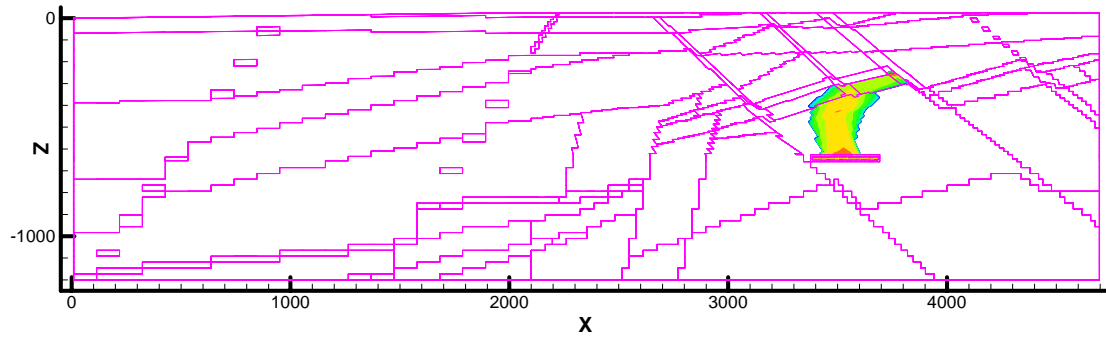
Some results

The results obtained using TOUGH2v2 to model gas migration in a “higher strength” rock are in accord with the expected evolution of the system.

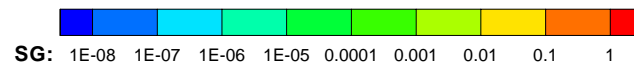
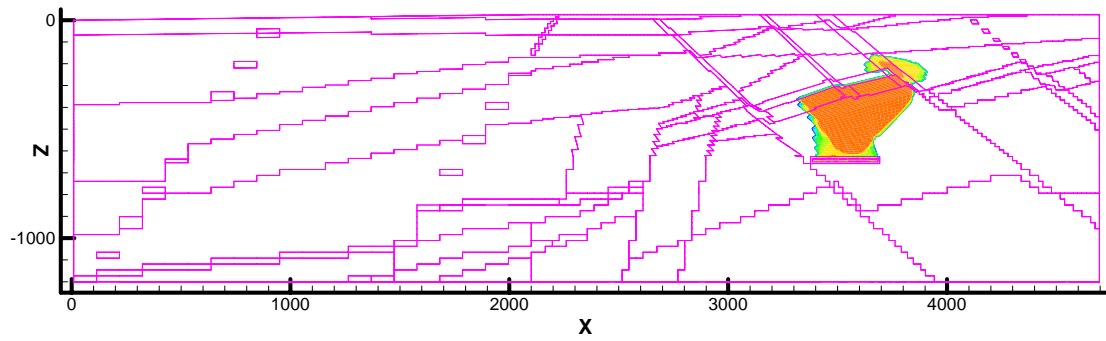
Once the gas pressure in the repository has risen sufficiently (in this particular case, to a fraction of hydrostatic pressure), free gas is able to migrate out of the repository. It then moves upward through the “higher strength” host rock and overlying rocks until it comes to a low-permeability formation with a high gas entry pressure, the Basal North Head Member (Figure 4a). The gas flows beneath the Basal North Head Member up to the location where a major fault breaks the continuity of the Basal North Head Member. A gas pocket forms. The pressure in the pocket increases and ultimately overcomes the gas entry pressure, and free gas moves from the pocket into the overlying St Bees Sandstone and then upward (Figure 4b). As the gas migrates, it dissolves in the groundwater, which is undersaturated with gas.

Later, the gas follows a second pathway. The pore water in the repository becomes saturated with gas. Dissolved gas from the repository is transported upward in the groundwater through the “higher strength” host rock and overlying rocks. As the groundwater rises, the pressure falls, and therefore some of the gas comes out of solution and collects in a second region of non-zero gas saturation below the Basal North Head Member (Figure 4c). Free gas flows along this pathway into, and ultimately through, the Basal North Head Member. As this free gas continues to migrate, it dissolves in the groundwater in the St Bees Sandstone (Figure 5).

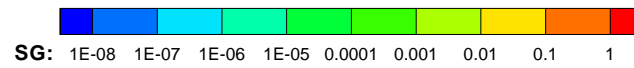
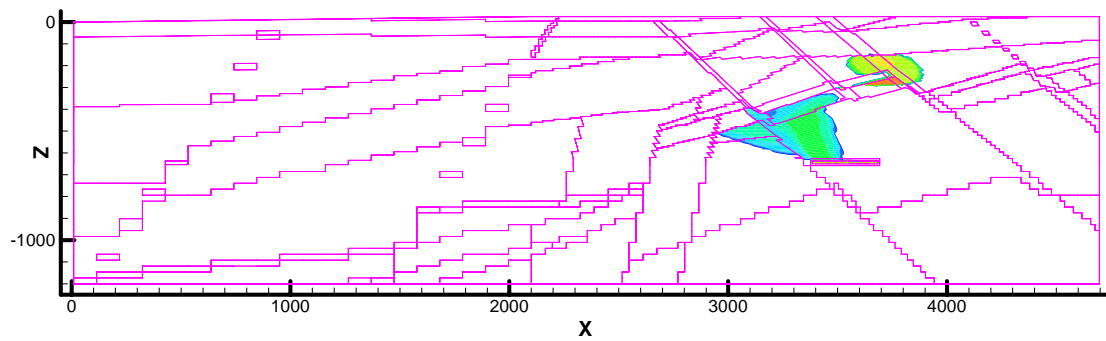
⁶ <http://www.tecplot.com/products/360/>



(a)



(b)



(c)

Figure 4. Gas saturation at: (a) 15 years post-closure; (b) 25 years post-closure; and (c) 240 years post-closure.

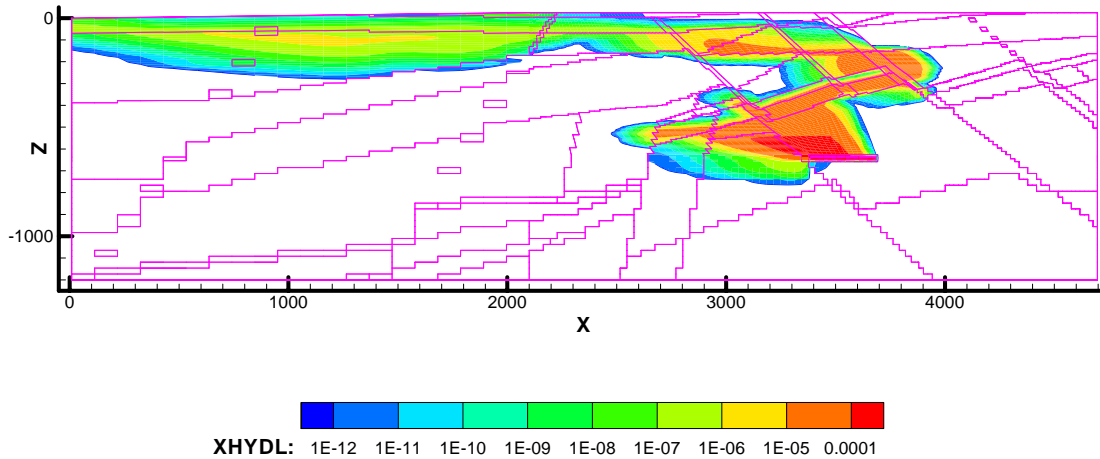


Figure 5. Mass fraction of gas dissolved in liquid at 240 years post-closure

Rock-matrix diffusion

The conceptual model of flow in a “higher strength” rock is that the flow takes place in a fracture system, but mass can be exchanged with a matrix system. (The matrix acts as a storage reservoir for fluid and solutes.) The MINC method (Pruess, 1983; Pruess, 1992) treats interporosity flow in a fully transient way; it does so by calculating a numerical approximation to the gradients (of pressure, concentration and temperature) which drive interporosity flow.

It is expected that some of the gas which dissolves in the groundwater (according to Henry’s Law) will diffuse from the fractures into the matrix. This process is called rock-matrix diffusion. A simple test case (for which a semi-analytical solution is available) investigated the capability of TOUGH2v2 with a MINC mesh to model rock-matrix diffusion (Hoch, 2008).

Figure 6 compares the semi-analytical solution and the TOUGH2v2 prediction for the concentration of solute in a fracture. These figures show that the TOUGH2v2 result agrees well with the semi-analytical solution for this problem, although, as expected, there is too much dispersion in the TOUGH2v2 prediction.

This test case identified that if rock-matrix diffusion is to be simulated correctly using TOUGH2v2, then a slightly nonstandard input of the model parameters is required. In particular, where usually the tortuosity of the fractured rock would have been specified, now

the correct input parameter is the product of the fracture porosity and the tortuosity.

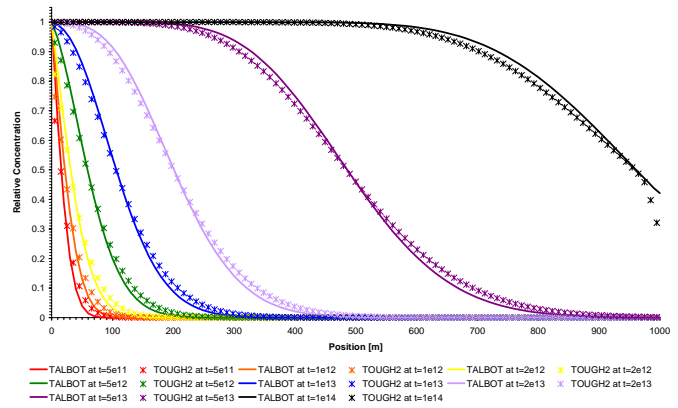


Figure 6. Comparison of TOUGH2v2 and semi-analytical (i.e. TALBOT) rock-matrix diffusion solution for profiles of concentration along the fracture at various times.

Heterogeneity

Results have been obtained also for a TOUGH2v2 calculation which included variability of the permeability field (Figure 7).

The gross features of the results are the same as those described in the previous subsections.

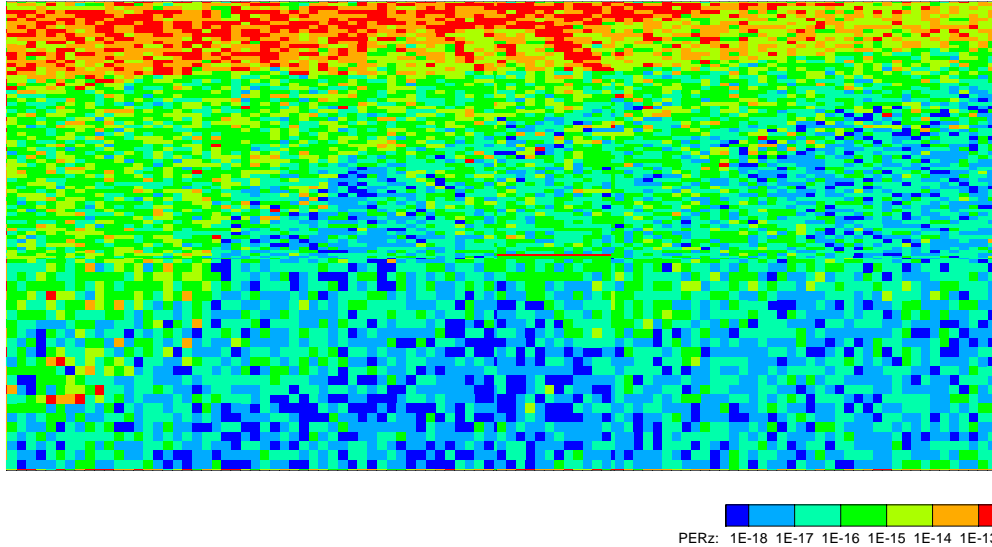


Figure 7. The z-component of the heterogeneous permeability field

GAS IN LOWER STRENGTH SEDIMENTARY ROCK AND EVAPORITES

Work has been carried out also on gas migration in “lower strength sedimentary” rock and “evaporites” (Hoch and Swift, 2008). This section shows some results for a “lower strength sedimentary” rock.

Some results

During the operational phase of the GDF, a region of drawdown develops around the vault. This region of drawdown continues to develop after closure. After closure of the GDF, the groundwater inflow to the vault decreases, and the pressure in the vault starts to increase. The pressure rises partly because the void volume available to the gas is reduced by water ingress, and partly because of the additional gas generated. When the pressure in the GDF has increased sufficiently, the pressure gradients are no longer high enough to prevent gas moving out of the vault into the host rock. Gas breaks through at the top boundary ~ 20,000 years after closure (Figure 8).

Limited availability of water

“Lower strength sedimentary” and “evaporite” host rocks raise some additional issues. Specifically, the inflow rate of water may restrict the generation rate of gases. A further modification to TOUGH2v2, which scales back the generation rate depending on the relative humidity in the facility, is used for these simulations.

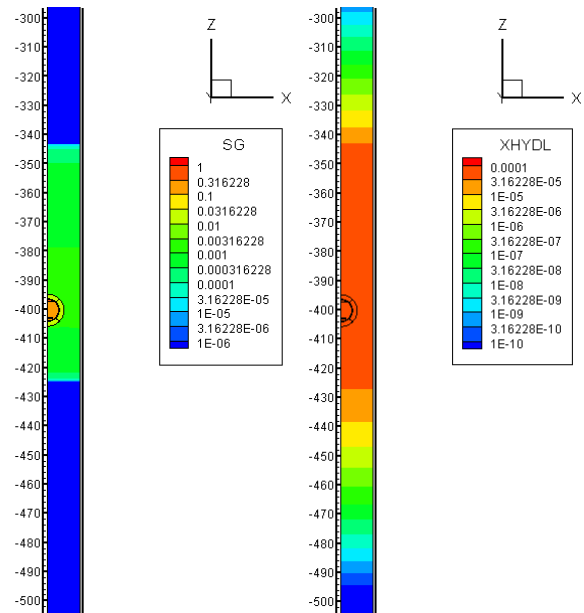


Figure 8 Gas saturation (left) and mass fraction of gas dissolved in liquid (right) at: 10,000 years post-closure

NAPL IN HIGHER STRENGTH ROCKS

Studies of NAPL migration (Swift, 2008) have been undertaken using essentially the same model as for the gas migration calculations in “higher strength” rocks discussed above. The calculations have been carried out for a typical light NAPL using TMVOC.

Some results

Migration of the NAPL shows qualitative similarities to the migration of gas, as expected, with the Basal North Head Member above the GDF providing a substantial barrier to migration. A NAPL phase evolves at this location within a thousand years, and then continues to build up. After several tens of thousands of years, small amounts have migrated past the barrier (Figure 9), but subsequently are dissolved in the groundwater, so that no NAPL phase occurs within 200 m of the ground surface. Some dissolved NAPL migrates into the top 100 m of the geosphere at concentrations around a hundredth of the solubility limit (which in any case is assumed to be very low at only 0.1 kg m^{-3}). Ultimately, dissolved NAPL migrates out of the model region across the left boundary.

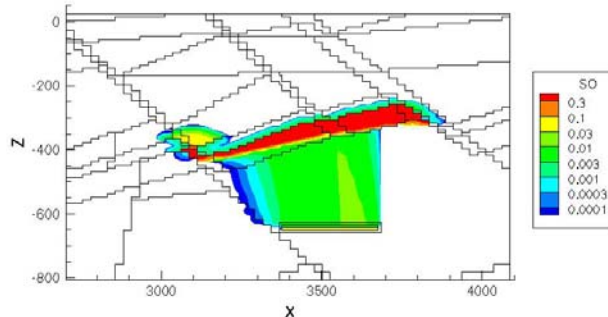


Figure 9 NAPL saturation after 10,000 years.

SUMMARY

This paper summarizes recent work for the NDA to simulate the migration of gases and NAPLs from a geological disposal facility. It describes some developments to the computer programs TOUGH2v2 and TMVOC, and presents some illustrative results.

ACKNOWLEDGEMENT

This work was funded by the United Kingdom's Nuclear Decommissioning Authority.

REFERENCES

Baker, A. J., D. A. Lever, J. H. Rees, M. C. Thorne, C. J. Tweed and R. S. Wikramaratna, *Nirex 97: An Assessment of the Post-Closure Performance of a Deep Waste Repository at Sellafield, Volume 4: The Gas Pathway*, Report S/97/012, Nirex, 1997.

Bate, F., C. P. Jackson and A. R. Hoch, *Gas Migration Calculations*, Report SA/ENV-0850, Serco, 2006.

Defra, BERR, Welsh Assembly Government, Department of the Environment Northern Ireland, *Managing Radioactive Waste Safely: A*

Framework for Implementing Geological Disposal, Cm7386, 2008.

Hoch, A. R., M. C. Thorne, B. T. Swift and F. Bate, *Update of the GPA (03) Assessment of the Consequences of Gas*, Report SA/ENV-0948 Issue 2, Serco, 2008.

Hoch, A. R., *Gas Migration and Rock Matrix Diffusion*, Report SERCO/TAS/000450/001, Serco, 2008.

Hoch, A. R., and B. T. Swift, *Post-closure Performance Assessment: Example Approaches for Gas Modelling in Generic Environments*, Report SERCO/TAS/000472/001 Issue 1, Serco, 2008.

Jackson, C. P., A. R. Hoch and S. Todman, Self-consistency of a Heterogeneous Continuum Porous Medium Representation of a Fractured Medium, *Water Resources Res.*, **36**, 189-202, 2000.

Leung, C. T. O., J. Rutqvist, R. W. Zimmerman and A. R. Hoch, *The Use of TOUGH-FLAC for Coupled Hydro-Mechanical Modelling of Fractured Rock Masses*, in *Proceedings, TOUGH Symposium 2009*.

Pruess, K., *GMINC – A Mesh Generator for Flow Simulations in Fractured Reservoirs*, Report LBL-15227, Lawrence Berkeley Laboratory, 1983.

Pruess, K., *TOUGH User's Guide*, Report LBL-20700, Lawrence Berkeley Laboratory, 1987.

Pruess, K., *TOUGH2 - A General Purpose Numerical Simulator for Multiphase Fluid and Heat Flow*, Report LBL-29400, Lawrence Berkeley Laboratory, 1991.

Pruess, K., *Brief Guide to the MINC Method for Modelling Flow and Transport in Fractured Media*, Report LBL-32195, Lawrence Berkeley Laboratory, 1992.

Pruess, K., C. Oldenburg and G. Moridis, *TOUGH2 User's Guide - Version 2.0*, Report LBNL-43134, Lawrence Berkeley National Laboratory, 1999.

Rodwell, W., S. Norris, W. Cool, M. Cuñado, L. Johnson, M. Mäntynen, W. Müller, P. Sellin, M. Snellman, J. Talandier, T. Vieno and S. Vines, *A Thematic Network on Gas Issues in Safety Assessment of Deep Repositories for Radioactive Waste (GASNET)*, Report EUR 20620 EN, European Commission, 2003.

Swift, B. T., *L-NAPL Migration Sensitivity Studies*, Report SERCO/TAS/002560/001 Issue 1, Serco, 2008.

BENCHMARK CALCULATIONS WITH TOUGH2-EOS9NT OF THE TRANSPORT OF RADIONUCLIDES THROUGH CLAY AND BENTONITE BARRIERS IN A GEOLOGICAL REPOSITORY

Manuel Lorenzo Sentís¹, Felix Altorfer¹, Georg Kosakowski²

¹Swiss Federal Nuclear Safety Inspectorate (ENSI)
CH-5232 Villigen-ENSI, Switzerland

²Paul Scherrer Institute (PSI)
CH-5232 Villigen-PSI, Switzerland
Email: manuel.sentis@ensi.ch

ABSTRACT

The Swiss Nuclear Safety Inspectorate is the supervisory authority for nuclear safety and radiation protection in nuclear facilities. It also supervises the preparations for the disposal of radioactive waste, which includes the review of safety assessments for geological repositories for all types of radioactive waste submitted by the Swiss implementer Nagra. In part, independent safety analyses were carried out using the code TOUGH2 (Pruess, 1999) and in particular the stand-alone module EOS9nT (Moridis, 1999) to check the calculations of the implementer.

To evaluate the capabilities of the code EOS9nT, a benchmark study was undertaken in collaboration with the Laboratory for Waste Management (LES) of the Paul Scherrer Institute (PSI). Results of four different codes were compared: Picnic, Frac3dvs, COMSOL, and EOS9nT. Picnic calculations were published by Nagra for a conceptual model of a geological repository within a feasibility study (project "Opalinus Clay") (Nagra, 2002). The results were reproduced by ENSI with Tough2-EOS9nT and COMSOL (COMSOL, 2006).

This report shows the conceptual model used for the calculations, the initial and boundary conditions, the simplifications and the parameters of the model. It explains the implementation of these elements in TOUGH2-EOS9nT and discusses the results of the calculations.

INTRODUCTION

In the feasibility study of Nagra, a site located in the geological formation called Opalinus Clay, in northern Switzerland, was selected. The geological repository would be located in the Opalinus Clay formation at a depth of 650 m. Canisters of about 1 m in diameter would be placed in the tunnels with an axial separation of 3 m. A bentonite backfill of 2.3 m diameter would be used as buffer and technical barrier around the canisters.

The purpose of this benchmark study was to estimate the release and transport of radionuclides from the

waste canister to the geosphere. The complex system of caverns and tunnels was simplified into a two-dimensional (Frac3dvs, COMSOL, EOS9nT) or as a one-dimensional (Picnic) conceptual model.

The conceptual model for the benchmark study is shown in Figure 1. The axial distances between canisters in an emplacement tunnel are conservatively neglected, thus reducing the calculation to a two-dimensional problem. Symmetry considerations allow us to simplify the model still further: It is only necessary to consider one emplacement tunnel, since the interactions between neighboring tunnels (separated by a distance of 40 m) are taken into account by setting no-flow conditions at the boundaries C and D in Figure 1. The distance between the emplacement tunnels and the nearest aquifers (boundaries A and B) were set to 40 m.

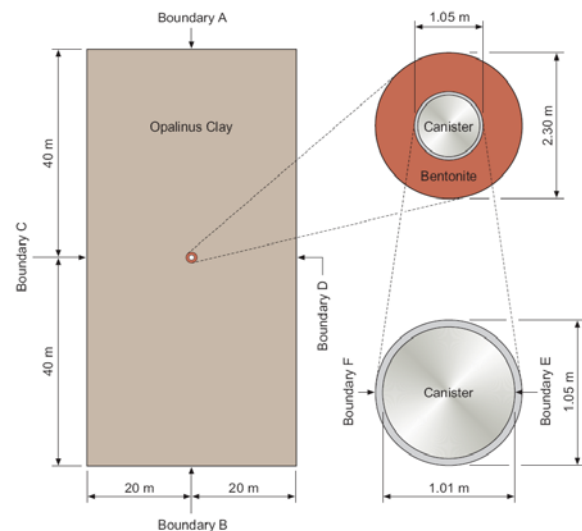


Figure 1. Conceptual model for the simulations (Kosakowski, 2004)

This benchmark concentrates on some critical radionuclides that show only a small retention in the different barriers of the geological repository: I-129, Ca-41, Cl-36, Se-79 and C-14. The release rates of these radionuclides (mass flow) from the steel waste canisters was provided in the form of a table and used as input for these calculations.

MODEL FOR THE CALCULATIONS

The different steps to prepare the model of Tough2-EOS9nT for the calculations are described schematically in Figure 2.

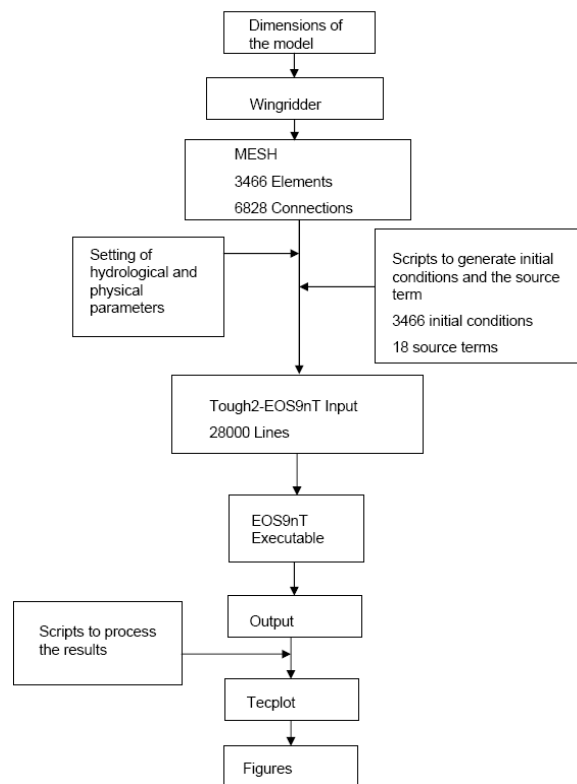


Figure 2. Sequential schema for the simulations

First, a mesh is created according to the conceptual model specified in Figure 1. A preprocessing program that produces a soft transition from the cylindrical elements of the system close to the canister to the rectangular geometry outside the canister was necessary. After testing several preprocessing programs it was decided to use the windows program WinGridder version 2.0 (Pan, 2001), developed by LBNL, which enabled creating the required cylindrical geometry—and was, besides, user-friendly.

A 2D rectangle in the xy-plane with the dimensions indicated in Figure 1 was created. To insert the nodes in the cylindrical part of the geometry, namely in the canister and in the bentonite filling, a script was made with Matlab to define the exact position of such nodes. To define the borders between different materials more accurately, some nodes were located regularly on both sides of each border between different materials and very close to it. These nodes were implemented by means of the internal objects in WinGridder called “boreholes.”

The rectangle mesh was generated with a nodal separation of 1 m. After node creation, the 2D-mesh was generated. An enlarged view of the region close to the canister is shown in Figure 3, with nodes indicated as red points, connections as red lines, and the Voronoi mesh as blue lines.

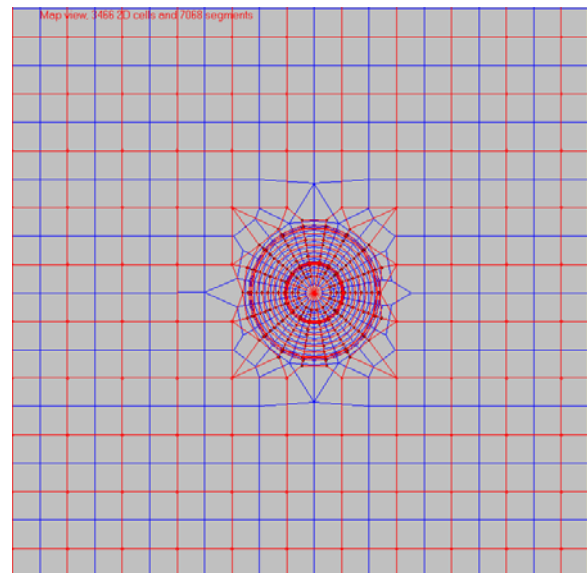


Figure 3. Mesh generated with WinGridder

The 3D mesh was generated by the standard procedure in WinGridder using the option “Designing a vertical structure.” One layer of 10 m was defined in the perpendicular direction. The 3D mesh was then revised to correct misalignments and wrong connections between the nodes. This structure in the xy-plane was then rotated to the xz-plane by interchanging the y and z coordinates and adapting the corresponding cosine of the direction of the connections between neighbor nodes in the CONNE card.

Once the mesh for TOUGH2 was finished, the next step, as shown in Figure 2, was to enter the parameters of the materials, the boundary, and the initial conditions into the TOUGH2-EOS9nT input.

INITIAL AND BOUNDARY CONDITIONS AND PARAMETERS OF THE MODEL

In the calculations, the bentonite backfill and the Opalinus Clay, assumed to be completely saturated, were modeled as homogeneous porous media without fractures. Due to the small values of the Darcy velocities, the dispersive transport of radionuclides was neglected in comparison with the diffusive transport.

We assigned hydraulic potentials of 0 m at the top boundary and 80 m at the bottom boundary. This setup corresponds to a hydraulic gradient of 1 m/m and was implemented with the standard procedure in TOUGH2, setting inactive elements in the top and bottom boundary, after having defined a linear variation in the hydraulic gradient between the top and bottom boundary as initial conditions (card INCON). In the inactive elements, these conditions remained constant.

The source term for these calculations is the release of radionuclides from the canister, provided in the form of tables for each of the radionuclides. They were obtained as result of previous near-field calculations with the STMAN suite of codes (Nagra, 2003). These tables are reported in Sentis et al., (2009). In Figures 6, 7, 8, 9 and 10, the release rates are plotted, together with the results of the simulations. The source term was implemented differently in the codes. For example in COMSOL the release of nuclides from the canister were implemented as a boundary condition in the outer boundary of the canister. In TOUGH2-EOS9nT a small volume surrounding the canister was added to the geometry of the model, as shown in Figure 1. The source term was implemented in this volume. The card GENER was used with 18 volume elements. This card is an extension of a card with the same name in TOUGH2 and allows additionally inputting the mass fractions of the tracers. Radionuclides are modeled in this volume as dissolved in a unit volume of water. The card GENER was prepared with the help of a script to read the data tables and to create automatically all necessary parameters of the GENER card. The material properties of bentonite and Opalinus Clay are shown in Table 1 and were taken from (Nagra, 2002) and (Kosakowski, 2004).

The parameters of the radionuclides used for these simulations are indicated in Table 2. Solubility limits for the radionuclides were not taken into account in these calculations. As seen in Table 2 from the radionuclides considered in these simulations, Ca-41 and I-129 have non-zero sorbing properties in bentonite and Opalinus clay, whereas the other three, namely C-14, Cl-36 and Se-79, are considered nonsorbing radionuclides. Sorption is described by a linear equilibrium model.

To calculate the correct effective diffusion coefficient in each material for a given porosity, the pore diffusion coefficient in bentonite and Opalinus Clay needs to be different in the different parts of the model domain. Since this is not possible within all codes, tortuosity was used to scale a constant pore diffusion coefficient to the designated effective diffusion coefficient.

Table 1. Material parameters for the Opalinus clay formation and for the bentonite filling of the tunnels (Nagra, 2002) and (Kosakowski, 2004)

Parameter	Unit	Value	
		Opalinus Clay	Bentonite
Hydraulic Conductivity in horizontal Direction K_x, K_y	m·s ⁻¹	1.0·10 ⁻¹³	1.0·10 ⁻¹³
Hydraulic Conductivity in vertical direction K_z	m·s ⁻¹	2.0·10 ⁻¹⁴	1.0·10 ⁻¹³
Bulk density ρ_t	kg·m ⁻³	2.43·10 ³	1.77·10 ³
Solid density ρ_k	kg·m ⁻³	2.72·10 ³	2.76·10 ³
Specific storage coefficient S_s	m ⁻¹	1·10 ⁻⁵	2·10 ⁻⁴

RESULTS

The next step was to create an executable of EOS9nT for the simulations, including some small changes in the EOS9nT code. Basically, these changes are related to the fact that the calculations extend in time for millions of years, and thus the time variables in seconds become large numbers. Similarly the maximum permitted number of time steps (originally 9,999 time steps) for the simulation in TOUGH2-EOS9nT had to be increased. The size of the time variables in the card TIMES was enlarged to allow the input of more significant figures for the time variables in seconds, thus increasing the precision of the results. The number of time variables within the card TIMES was also increased. Some changes were also made to make the format of the EOS9nT output more compatible with *ext.f* and with *Tecplot* (Tecplot, 2006).

For the solution of the transport equations in EOS9nT the conventional time-stepping method was used. The Laplace formulation option available in EOS9nT could not be used since the source term was time dependent, and this time dependence could not be described by a time function with a known Laplace transform.

The postprocessing of the results was made with the help of several scripts to sum the contributions for each radionuclide to the total mass flow from all the connections on the top and bottom boundaries. The time-dependent radionuclide mass flow over the upper and lower boundaries for a time span of 10 million years is similar in the four different codes.

The results of the simulations are shown in Figures 4–8 and were represented with the help of *Tecplot* (Tecplot, 2006). The red points represent the values of the source term used in the calculations.

methods implemented in the codes. Picnic uses a one-dimensional approximation for the transport in the geosphere, while the other codes use a two-dimensional approximation. Besides, TOUGH2-EOS9nT uses the integral finite difference method, whereas Picnic and Comsol use the finite element method, and Frac3dvs uses both the finite volume and finite difference methods.

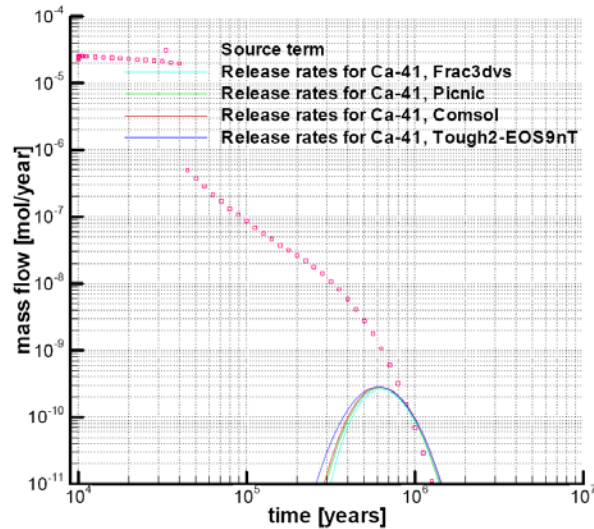


Figure 4. Geosphere release rates for Ca-41

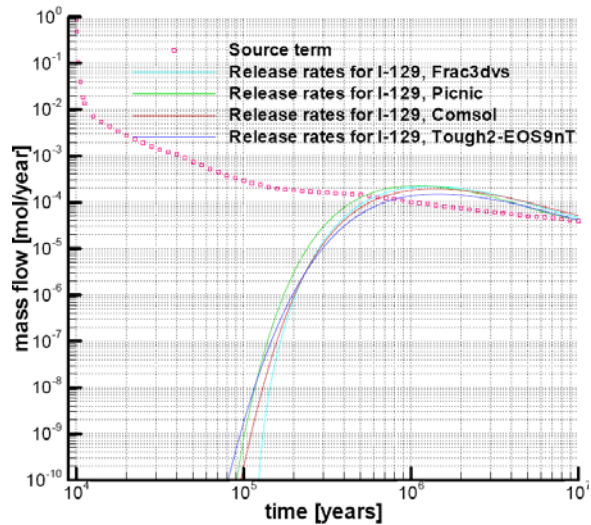


Figure 6. Geosphere release rates for Se-79

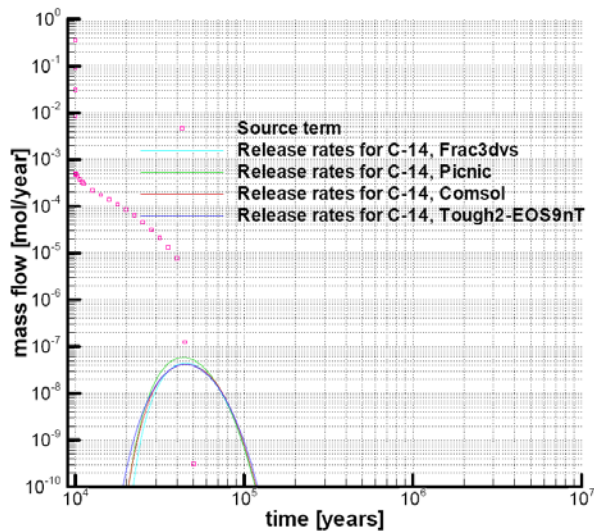


Figure 5. Geosphere release rates for C-14

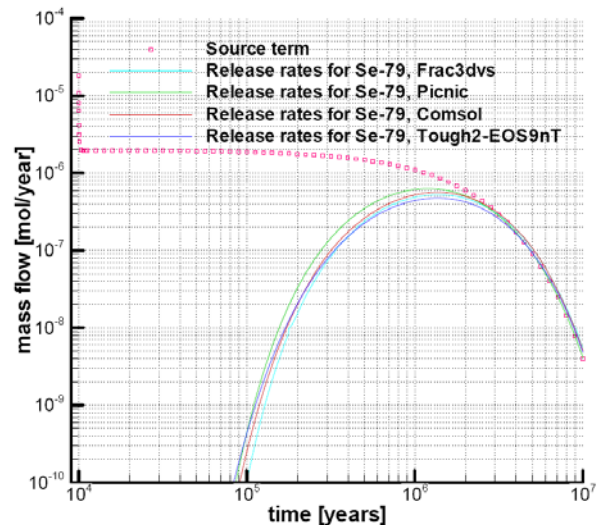


Figure 7. Geosphere release rates for I-129

Small variations in the results obtained with the codes can be explained by differences in the conceptualization and because of different numerical

The maxima of the mass flow values and the times of these maxima are summarized in Table 3 for the different codes and for the different radionuclides.

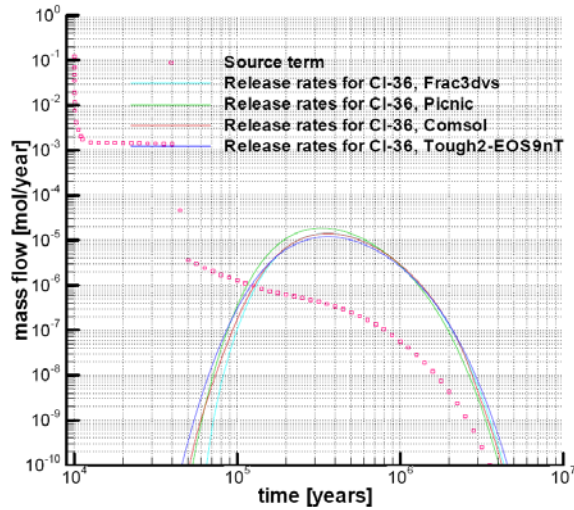


Figure 8. Geosphere release rates for Cl-36

CONCLUSION AND FUTURE TASKS

Based on these calculations, ENSI decided to continue using both COMSOL and TOUGH2-EOS9nT codes for assessing the calculations of the implementer Nagra within the sectoral plan in Switzerland that started in 2008.

Future calculations will include the assessment of homogeneous as well as fractured media. In the future, calculations decay chains with several radionuclides could also be considered. That represents an advantage of TOUGH2-EOS9nT over the former TOUGH2 module EOS7R, which was limited to simulations of decay chains with a maximum of two radionuclides.

Table 2. Material parameters for the different radionuclides used in this benchmark study, (Nagra, NTB 02-06) and (Kosakowski, 2004)

Parameter	Unit	Ca-41	C _{org} -14	Cl-36	I-129	Se-79
Molecular diffusion coefficient D_0	$\text{m}^2 \text{a}^{-1}$	$1.75 \cdot 10^{-2}$	$1.75 \cdot 10^{-2}$	$1.89 \cdot 10^{-3}$	$1.89 \cdot 10^{-3}$	$1.89 \cdot 10^{-3}$
Decay constant λ	a^{-1}	$6.73 \cdot 10^{-6}$	$1.21 \cdot 10^{-4}$	$2.31 \cdot 10^{-6}$	$4.41 \cdot 10^{-8}$	$6.3 \cdot 10^{-7}$
Half life $T_{1/2}$	a	$1.03 \cdot 10^5$	$5.73 \cdot 10^3$	$3 \cdot 10^5$	$1.57 \cdot 10^7$	$1.1 \cdot 10^6$
Bentonite	Unit	Ca-41	C _{org} -14	Cl-36	I-129	Se-79
Effective porosity ϕ_t	-	0.36	0.36	0.05	0.05	0.05
Effective diffusion coefficient D_e	m^2/s^{-1}	$2 \cdot 10^{-10}$	$2 \cdot 10^{-10}$	$3 \cdot 10^{-12}$	$3 \cdot 10^{-12}$	$3 \cdot 10^{-12}$
Distribution coefficient for sorption K_s	$\text{m}^3 \text{kg}^{-1}$	$3 \cdot 10^{-3}$	0	0	$5 \cdot 10^{-4}$	0
Tortuosity τ	-	1.0	1.0	1.0	1.0	1.0
Opalinus Clay	Unit	Ca-41	C _{org} -14	Cl-36	I-129	Se-79
Effective porosity ϕ_t	-	0.12	0.12	0.06	0.06	0.06
Effective diffusion coefficient D_e	m^2/s^{-1}	$1 \cdot 10^{-11}$	$1 \cdot 10^{-11}$	$1 \cdot 10^{-12}$	$1 \cdot 10^{-12}$	$1 \cdot 10^{-12}$
Distribution coefficient for sorption K_s	$\text{m}^3 \text{kg}^{-1}$	$1 \cdot 10^{-3}$	0	0	$3 \cdot 10^{-5}$	0
Tortuosity τ	-	0.15	0.15	0.278	0.278	0.278

Table 3. Comparison of the maximum values of the release rates for the different codes

Nuclide	Frac3dvs		Picnic		Comsol		Tough2-EOS9nT	
	Max. [mol/Jahr]	t _{max.} [Jahre]	Max. [mol/Jahr]	t _{max.} [Jahre]	Max. [mol/Jahr]	t _{max.} [Jahre]	Max. [mol/Jahr]	t _{max.} [Jahre]
Ca-41	2.6·10 ⁻¹⁰	6.3·10 ⁹	2.8·10 ⁻¹⁰	6.3·10 ⁵	2.8·10 ⁻¹⁰	6.2·10 ⁵	2.8·10 ⁻¹⁰	6.2·10 ⁵
C _{org} -14	4.5·10 ⁻⁸	4.5·10 ⁴	5.9·10 ⁻⁸	4.5·10 ⁴	4.2·10 ⁻⁸	4.6·10 ⁴	4.2·10 ⁻⁸	4.5·10 ⁴
Se-79	5.3·10 ⁻⁷	1.4·10 ⁶	6.3·10 ⁻⁷	1.3·10 ⁶	5.6·10 ⁻⁷	1.4·10 ⁶	4.8·10 ⁻⁷	1.4·10 ⁶
Cl-36	1.4·10 ⁻⁵	3.6·10 ⁵	1.9·10 ⁻⁵	3.2·10 ⁵	1.4·10 ⁻⁵	3.6·10 ⁵	1.2·10 ⁻⁵	3.6·10 ⁵
I-129	2.2·10 ⁻⁴	1.3·10 ⁶	2.3·10 ⁻⁴	1.3·10 ⁶	1.9·10 ⁻⁴	1.4·10 ⁶	1.5·10 ⁻⁴	1.4·10 ⁶

REFERENCES

- Pruess K., Oldenburg C., Moridis G., *Tough2 User's Guide, version 2.0*, 1999.
- Moridis G.J., Wu Y., Pruess K., *EOS9nT, A Tough2 module for the simulation of water flow and solute/colloid transport in the subsurfaces*, 1999.
- Nagra NTB 02-05, *Project Opalinus Clay – Safety Report Demonstration of Disposal feasibility for spent fuel; vitrified high-level waste and long-lived intermediate level waste (Entsorgungsnachweis)*. 2002, Nationale Genossenschaft für die Lagerung radioaktiver Abfälle, Wettingen.
- COMSOL, *Earth Science Module (Comsol Multiphysics 3.3)*, 2006, Comsol AB.
- COMSOL, *Comsol Multiphysics 3.3, User's Guide*. 2006.
- Kosakowski G., *Time-dependent Flow and Transport Calculations for Project Opalinus Clay (Entsorgungsnachweis)*, 2004, PSI-Report 04-10.
- Pan L., et al., *WinGridder An interactive grid generator for Tough2, User's Manual*, 2001.
- Nagra NTB 02-06, *Project Opalinus Clay: Models, Codes and Data for Safety Assessment - Demonstration of disposal feasibility for spent fuel, vitrified high-level waste and long-lived intermediate-level waste (Entsorgungsnachweis)*, 2002, Nagra, Nationale Genossenschaft für die Lagerung radioaktiver Abfälle.
- Sentis M.L., Altorfer F., Herfort M., *Benchmarkberechnungen für die Simulation der Ausbreitung ausgewählter Nuklide innerhalb von Bentonit- und Opalinustonsschichten mit den Rechenprogrammen Tough2-EOS9nT und COMSOL*, 2009, ENSI.
- Nagra NTB 02-03, *Projekt Opalinuston Synthese der geowissenschaftlichen Untersuchungsergebnisse - Entsorgungsnachweis für abgebrannte Brennelemente, verglaste hochaktive sowie langlebige mittelaktive Abfälle*. 2002, Nagra, Nationale Genossenschaft für die Lagerung radioaktiver Abfälle.
- Tecplot 360, *User's Guide*. Tecplot, Inc. 2006.

MODELING APPROACHES FOR INVESTIGATING GAS MIGRATION FROM A DEEP LOW/INTERMEDIATE LEVEL WASTE REPOSITORY (SWITZERLAND)

R. Senger¹, J. Ewing¹, K. Zhang², J. Avis³, P. Marschall⁴, I. Gaus⁴

¹Intera Inc. Swiss Branch, Schösslistr. 12, 5408 Ennetbaden, Switzerland, rsenger@interacom

²Earth Sciences Division, Lawrence Berkeley National Laboratory, Berkeley, CA 94720, USA, KZhang@lbl.gov

³Intera Eng. Ltd., 1 Raymond Street, Suite 200, Ottawa, Ontario, K1R 1A2, Canada, javis@interacom

⁴NAGRA, Hardstrasse 73, CH-5430 Wettingen, Switzerland, paul.marschall@nagra.ch

ABSTRACT

In low/intermediate-level waste (L/ILW) repositories, anaerobic corrosion of metals and degradation of organic materials produce mainly hydrogen, methane, and carbon dioxide. Gas migration in an L/ILW repository is thus an important component in the safety assessment of proposed deep repositories in low-permeability formations, because gas generation might produce excess pressures. The Swiss reference concept for the L/ILW repository consists of parallel caverns sealed off from a single access tunnel in a deep low-permeability claystone formation. The potential buildup of excess gas pressures in the backfilled emplacement caverns, after repository closure, was investigated in a series of two-phase flow models. In the first phase, a large-scale model was constructed, implementing the 3-D radial tunnel and cavern geometry with a simplified rectangular geometry. In the second phase, the potential impact of the detailed geometry of the engineered barrier system (EBS) and the associated heterogeneity inside the cavern was examined using detailed models of the repository caverns, tunnel seals, access tunnel, and surrounding host rock.

The transient hydrodynamic conditions associated with the excavation of the tunnels and caverns, subsequent waste emplacement, and backfilling of the underground openings were modeled with the 3-D models, representing partially saturated initial conditions at atmospheric pressures in the EBS for the start of the postclosure period. Gas generation was assumed to start under these partially saturated initial conditions.

The simulation results from the large-scale 3-D repository model show that, during the early postclosure period, simulated pressures can vary significantly between different parts of the repository; after 1,000 years the area of Test Facility still has not reached hydrostatic conditions, whereas the repository caverns developed overpressured conditions associated with gas generation in the caverns. The simulated pressure buildup in the emplacement caverns remained below the fracture pressure of the rock for realistic assumptions. Gas flow was largely limited to the EBS and the excavation disturbed zone (EDZ), thus gas flows

through and around the repository seal into the adjacent tunnel system.

INTRODUCTION

The National Cooperative for the Disposal of Radioactive Waste (NAGRA) has proposed the Opalinus Clay as possible host rock for a repository for low and intermediate-level waste (L/ILW). Opalinus Clay is characterized by a low permeability and is, therefore, an excellent barrier against radionuclide transport. Gas migration in an L/ILW repository is a critical component within the safety assessment of proposed deep repositories in low-permeability formations. In L/ILW repositories, anaerobic corrosion of metals and degradation of organic materials produce mainly hydrogen and methane. The generation, accumulation, and release of these gases from the disposal system may affect a number of processes that influence the long-term radiological safety of the repository.

After closure, the repository performance with respect to gas migration and pressure buildup will be affected not only by the two-phase properties of the EBS and surrounding host rock, but also by a variety of other geological, geotechnical, and waste-related factors. According to the generic repository concept (NAGRA 2008), the repository consists of as many as seven parallel caverns sealed off from a single access tunnel. Additional underground structures include a pilot facility, an underground rock laboratory (test area), a ventilation shaft, and a central operations area (Figure 1). To quantify gas migration from the L/ILW repository and to assess the risk of excess gas pressures developing in the backfilled caverns after repository closure, we developed a series of numerical models.

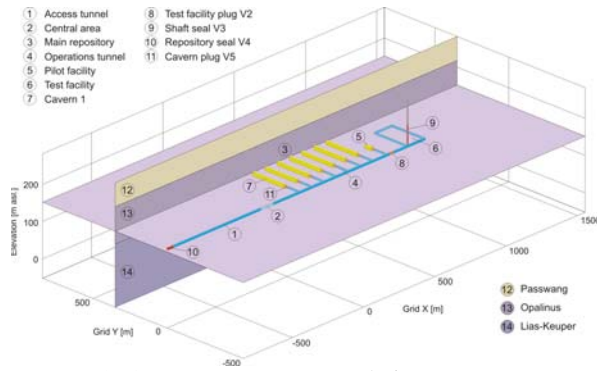


Figure 1. 3-D representation of the generic L/ILW repository with different EBS components

For the simulation of two-phase flow in the complex 3-D models, the parallel version of the two-phase flow simulator TOUGH2_MP (Zhang and Wu 2006) was used. The different gas components were represented by a single gas phase (air) using the TOUGH2 EOS3 module (Pruess et al. 1999). The development of the 3-D model geometries was automated using the visualization software mView (Calder and Avis, 2006).

Model Designs

The large-scale 3D model, representing the entire L/ILW repository, consists of 36 layers with 8329 elements per layer, for a total of 299,844 elements. The horizontal discretization used nested gridding, allowing refinement near the underground structures and a coarser mesh in the far field (Figure 2). The vertical extent of the model includes the Opalinus Clay, representing the host rock formation, with the adjacent Lias-Keuper below and Passwang formations above. The underground structures include the tunnel, seal, and cavern elements surrounded by an EDZ and the host rock (Figure 2).

The local-scale models include a detailed model of the repository seal (V4) and a 3-D model of the repository cavern, branch tunnel, and surrounding host rock.

The repository seal (V4) separating the access tunnel from the backfilled ramp at the contact of the Opalinus Clay and the overlying Passwang Formation represents a prescribed pressure boundary in the 3-D model (Figure 2). Functionally, this seal is intended to provide additional capacity for gas release from the repository while still maintaining low hydraulic permeability. The detailed seal configuration (Figure 3) was implemented in the 3-D repository seal model using a composite radial-rectangular mesh (Figure 4)

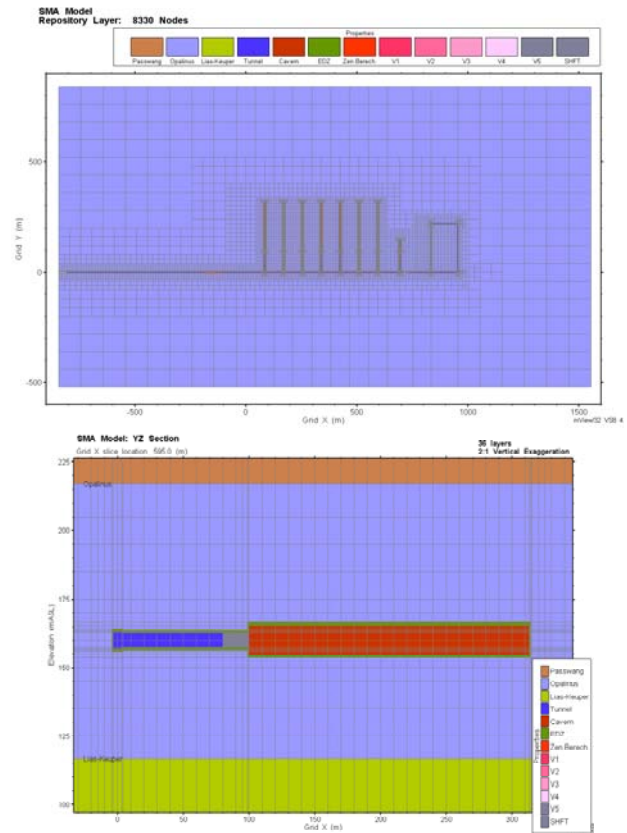


Figure 2. 3-D Model representation: plan view of the nested grid structure at the repository level (top), and vertical cross section parallel to the cavern axis (bottom).

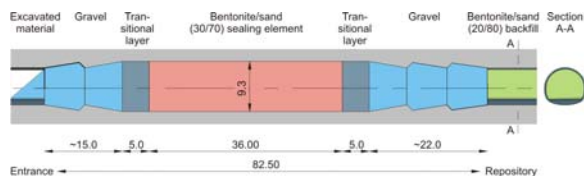


Figure 3. Components of the repository seal (V4).

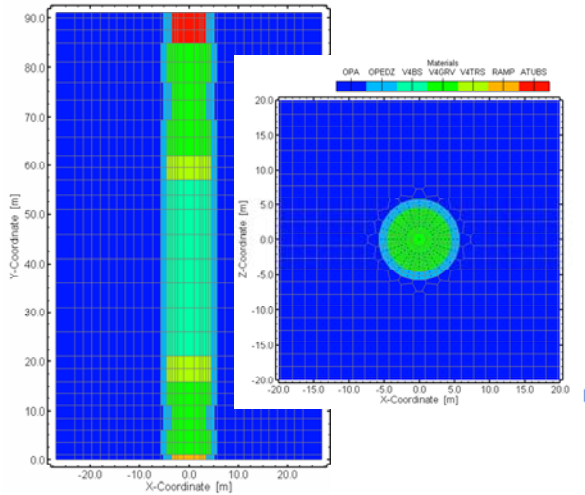


Figure 4. 2D XY and XZ Cross Sections of the 3D Repository Seal (V4) Model.

The repository cavern model represents the detailed configuration of a single cavern with the adjacent cavern seal and the branch tunnel (Figure 5).

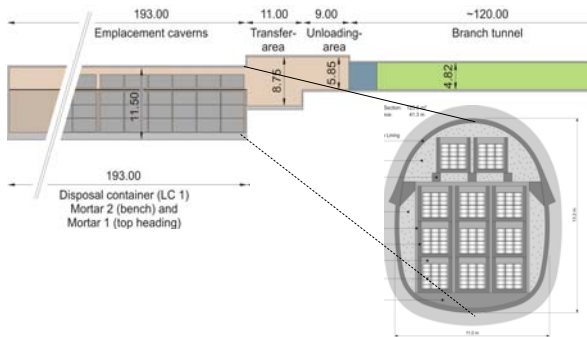


Figure 5. Geometry of the repository cavern, adjacent cavern seal (V5), and branch tunnel.

The detailed implementation of the different elements of the cavern and adjacent seal and tunnel sections in the detailed 3D cavern model are shown in Figure 6.

Because of the vertical symmetry plane along the axis of the cavern, only one half of the cavern geometry was implemented in the 3-D model. This accounts for the concrete containers with the different waste materials inside. The waste containers are separated by relatively small gaps which are backfilled with high-permeability mortar and are placed on a concrete fill of low permeability (Figure 6). Along the cavern axis, a detailed representation is employed for two columns of containers ~ 4 m long. The remainder of the cavern is represented by a single, composite container and surrounding backfill with proper volumetric representation of the different materials. Perpendicular to the cavern axis, the detailed discretization of the different materials (Figure 6, bottom) is maintained.

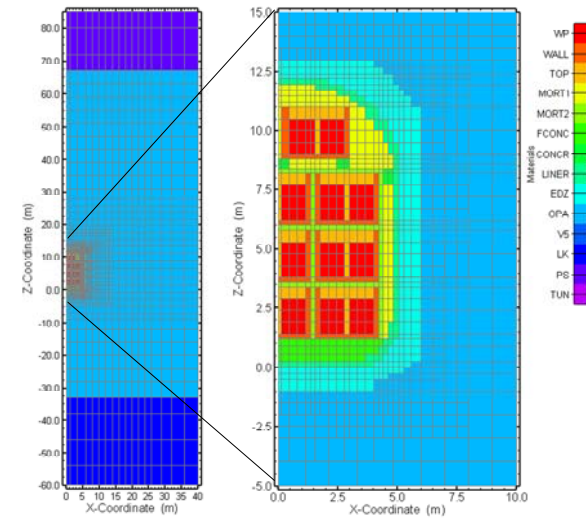
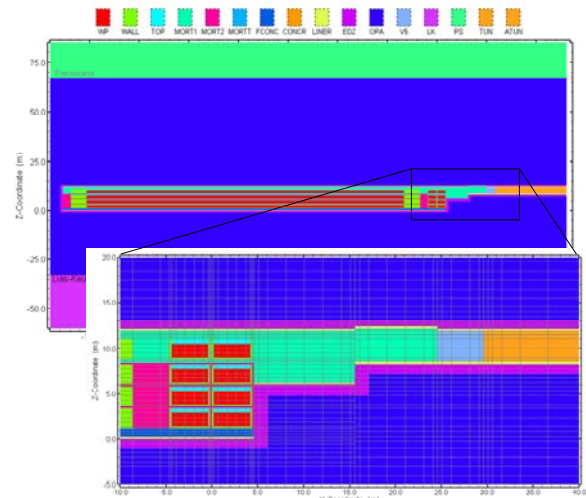


Figure 6. Repository Cavern Model: YZ section along the cavern axis (top) and XZ section perpendicular to the cavern axis (bottom).

Model Input

The input parameters of the host rock units and EBS represented in the different models are summarized in terms of hydraulic and two-phase flow properties in Tables 1 and 2, respectively. In the large-scale model, the cavern is represented by a single backfill material, whereas the local-scale cavern model accounts for numerous different materials characterized by as much as seven orders of magnitude variation in permeability (Table 1). Some variability in the capillary strength of the different materials is accounted for (Table 2).

Table 1. Summary of hydraulic properties

Host rock	k_h^2	Porosity ϕ	Compress. ¹ Cp [1/Pa]
	[m ²]		
Passwang	1.0E-17	0.10	2.6E-10
Opalinus Clay (k_x/k_z)	1.0E-20/ 2.0E-21	0.12	9.7E-10
Lias-Keuper	1.0E-20	0.10	2.6E-10
EBS Materials: Large-Scale Model			
Tunnel	1.0E-16	0.30	1.0E-9
Cavern	1.0E-15	0.25	1.0E-9
Cav.Seal (V5)	1.0E-17	0.30	1.0E-9
Rep.Seal (V4)	1.0E-18	0.30	1.0E-9
Shaft (V3)	1.0E-20	0.40	1.0E-9
Fac.Seal (V2)	1.0E-18	0.30	1.0E-9
Shaft (V3)	1.0E-20	0.40	1.0E-9
EBS Materials: Cavern Model			
Tunnel	1.0E-16	0.30	1.0E-9
Cav.Seal (V5)	1.0E-18	0.30	1.0E-9
Mortar-1	1.0E-12	0.30	3.3E-10
Mortar 2	1.0E-14	0.35	2.8E-10
Concrete (1)	1.0E-18	0.20	5.0E-10
Concrete (2)	1.0E-19	0.15	6.7E-10
Liner	1.0E-17	0.25	4.0E-10
WC-Wall	1.0E-19	0.15	6.7E-10
Waste	1.0E-19	0.20	5.0E-10
Seal (V4) Materials: Seal Model (see Fig. 3)			
Tunnel	1.0E-16	0.30	1.0E-9
V4(Bent/sand)	1.0E-18	0.30	1.0E-9
V4(Trans Lay.)	1.0E-17	0.20	1.0E-9
V4(Gravel)	1.0E-12	0.30	1.0E-9

Table 2. Summary of two-phase flow parameters

Host rock	Van Genuchten Model			
	P_0	n	Slr	Sgr
Passwang	1.0E+5	2	0.25	0.01
Opalinus Clay	1.8E+7	1.67	0.01	0.003
Lias-Keuper	1.0E+6	2	0.25	0.01
EDZ(OPA)	2.0E+6	1.67	0.2	0.001
EBS Materials: Large-Scale Model				
Tunnel	4.0E+3	2.5	0.3	0.0
Cavern	4.0E+3	2.5	0.3	0.0
Cav.Seal (V5)	4.0E+3	2.5	0.3	0.0
Rep.Seal (V4)	4.0E+3	2.5	0.3	0.0
Shaft (V3)	1.8E+7	1.82	0.01	0.001
Fac.Seal (V2)	4.0E+3	2.5	0.3	0.0
Shaft (V3)	1.8E+7	1.82	0.01	0.001
EBS Materials: Cavern Model				
Tunnel	4.0E+3	2.5	0.3	0.001
Cav.Seal (V5)	4.0E+3	2.5	0.3	0.001
Mortar-	5.0E+2	2.0	0.3	0.01
Concrete	2.0E+6	2.0	0.05	0.001
Liner	5.0E+4	2.0	0.2	0.001
Waste, Wall	2.0E+6	2.0	0.05	0.001
Seal (V4) Materials: Seal Model				
V4Bent/Sand	4.0E+3	2.5	0.3	0.001
V4(TransLay)	4.0E+3	2.5	0.3	0.001
V4(Gravel)	4.0E+3	2.5	0.3	0.001

Initial and Boundary Conditions

Initial conditions in the different host rock units are represented by hydrostatic pressures corresponding to the average elevation of the regional drainage systems. In the large-scale model, boundary conditions along the top and bottom model boundaries are prescribed hydrostatic pressures based on an average hydraulic head value of 415 m, corresponding to the initial hydrostatic conditions throughout the model. Lateral boundaries are represented by no-flow conditions, except for the interface of the access tunnel with the left boundary. This interface represents the subcrop of the repository seal (V4) with the top of the Opalinus Clay, where the tunnel seal connects to the backfilled access ramp (Figure 1). In this model, the inclination of the access tunnel is not accounted for.

In the underground structures, the initial pressure conditions during construction and emplacement were represented by atmospheric pressure conditions. Liquid pressure conditions correspond to the capillary suction pressure at the prescribed initial saturation. This capillary suction pressure was also used during the operational periods when the underground structures were ventilated.

Operational Periods : Construction and operational periods were represented by prescribed atmospheric pressures in the caverns, which include four sequences prior to the postclosure period:

- I. Exploration, construction and testing phase of the test laboratory: open caverns for 20 years—assume ventilation via prescribed suction pressure in the tunnel.
- II. Emplacement and operation: backfilled cavern for 15 years—prescribed atmospheric pressures and specified saturation of different backfill material (i.e., prescribed capillary pressures at the given saturation).
- III. Closure Phase 1: beginning of resaturation of emplacement caverns, and access tunnels with the test laboratory remaining open for 13 years.
- IV. Closure Phase 2: beginning of resaturation of tunnels and test laboratory with the ventilation shaft remaining open for 100 years.
- V. Post closure: beginning 148 years after the start of the operational period.

Gas Generation: The corrosion and degradation of the L/ILW waste produces mainly H₂ and CH₄, which result in gas generation rates in the emplacement caverns which decrease with time. According to the MIRAM 2005 waste inventory (NAGRA 2008), the “realistic” rate decreases from an initial rate of 6.65E+4 m³ STP/a at the onset of gas generation to 730 m³ STP/a after 1000 years, and to less than 60 m³ STP/a after 100,000 years. The different gas components associated with initial unsaturated

condition (air) and waste-generated gas (H_2 , CH_4) were represented by a single gas phase (air) using the TOUGH2 EOS3 module.

For the large-scale model, the time-varying gas generation rate is equally divided into the seven caverns and uniformly assigned along each cavern. For the local-scale cavern model, the corresponding rates for a single cavern are assigned in proportional amounts to each waste container (Figure 6). For the repository seal model, the gas flow rate through the access tunnel computed in the large-scale model (Figure 2) was used as a prescribed flow boundary at the upstream boundary of the seal, representing the access tunnel (Figure 5).

MODEL RESULTS

Modeling Strategy: The two-phase flow modeling of gas migration from an L/ILW repository involved three model configurations:

- (1) The large-scale model of the entire repository accounted for all the underground structures and the surrounding host rock and bounding formations (Figure 2). The focus of this model was to simulate the pressure buildup in the emplacement caverns and access tunnels, quantify the gas and liquid flow from the emplacement caverns through the EBS and into the surrounding host rock, and characterize the sensitivity of uncertain parameters on the pressure buildup.
- (2) The repository seal model, representing the different seal components, was designed to characterize the more detailed two-phase flow behavior through and around the seal.
- (3) The repository cavern model accounted for the detailed geometry of the different components inside the cavern. The focus of this model was to characterize the two-phase flow behavior associated with resaturation and migration of waste-generated gas from the waste container through the backfill and seals into the tunnels and surrounding host rock. In addition, the model should provide an effective property response for proper representation of the uniform backfill material assumed in the large-scale model

Large-Scale Model

The complete 3-D cavern near-field consists of the EBS model and the surrounding host rock. The various simulation cases involving the complete model are described in greater detail in NAGRA (2008). The results of a selected set of simulation cases are shown in terms of the repository pressure buildup in Figure 7 and summarized here. The reference case R_CM01 assumed a low permeability for the Opalinus Clay of $K_h = 1.E-20 \text{ m}^2$ and $k_z = 5.E-21 \text{ m}^2$ and the lowest permeability for the

repository seal (V4) of $1.E-19 \text{ m}^2$. The V4 seal has the objective of functioning as an engineered gas transport system (EGTS) in case of high pressure built-up. The simulated pressure buildup in the emplacement cavern reached a peak pressure of 8.9 MPa after 55,000 years (Figure 7). The second case (R_CM02) assumed an order of magnitude higher permeability of the repository seal ($1.E-18 \text{ m}^2$) compared to the reference case R_CM01. This resulted in a peak pressure of 6.05 MPa after 2,500 years. The effect of a greater host rock permeability ($k_h = 5.E-20 \text{ m}^2$, $k_z = 1.E-20 \text{ m}^2$) was examined in the case R_CM03, which resulted in a peak pressure of 5.5 MPa after about 8,000 years (Figure 7). In case R_CM04, the capillary strength was reduced from 18 MPa to 5 MPa and the residual water saturation (for relative permeability) was increased from 0 to 0.5. Case R_CM05 was modified from Case R_CM03, considering only the effect of the increased residual water saturation of the host rock and of the EDZ. An increase in residual water saturation for the Opalinus Clay from 0 to 0.5 (R_CM05) yielded a slightly higher peak pressure of 5.67 MPa after 7,750 years. The reduction in the capillary strength P_0 from 18 MPa to 5 MPa in the case R_CM04 resulted in a reduced pressure buildup to a maximum of 5.12 MPa after 2,250 years (Figure 7). All cases, except for Case R_CM01 (which assumed a very low seal permeability), yielded peak pressures below the frac pressure and below the inferred onset of pathway dilation.

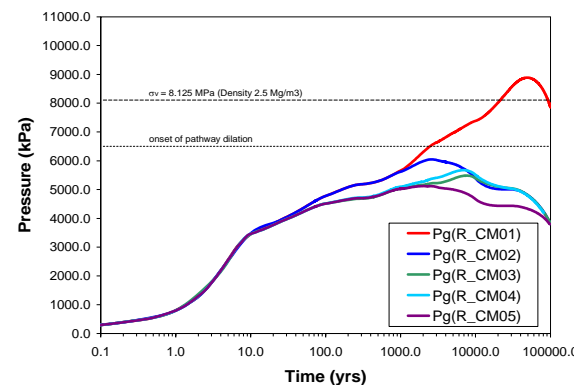


Figure 7. Large-Scale Model: pressure buildup in emplacement cavern for various parameter combinations; the different runs are described in the text.

The variations in pressure buildup at different locations in the underground structures are shown in Figure 8 for the simulation case R_CM02, which is characterized by higher permeability of the repository seal (V4 - EGTS) compared to the reference case R_CM01 (Table 1). The results show little difference in pressure buildup between the outside cavern (Cavern 1) and the central cavern (Cavern 4), both of which are characterized by early pressure increases from the initial atmospheric pressures to a peak

pressure of 6.1 MPa after about 2,500 years. The pressure upstream of the repository seal (V4) starts increasing after about 200 years and reaches a peak pressure of 5.2 MPa after about 2,500 years. After the peak, the pressure response follows the pressure in the repository cavern at an offset of a maximum of 1 MPa, decreasing to 0.5 MPa after 100,000 years (Figure 8). The pressure buildup at the tunnel seal increases above the pressure in the URL, which indicates resaturation of the access tunnel by water inflow from the ramp represented by a prescribed hydrostatic pressure at the model boundary.

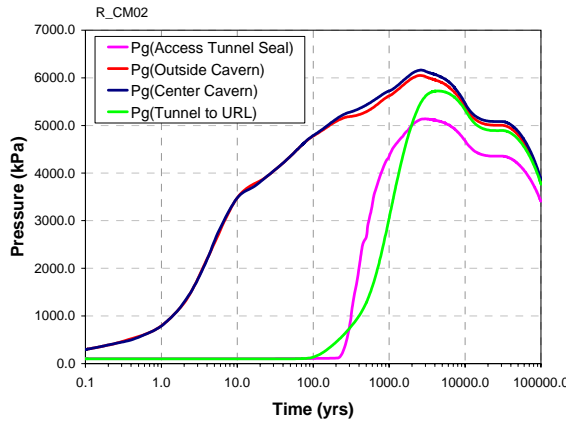


Figure 8 Large-Scale Model: L/ILW-Model Case R_CM02: pressure buildup in different locations of the emplacement cavern

The spatial distributions of gas pressure and gas saturation for the simulation run R_CM02 are shown in Figure 9. The pressure distribution after 1,000 years shows a non-uniform pressure distribution in the cavern and tunnels after 1,000 years as indicated by the differences in pressure buildup curves in

Figure 8. The pressures in between the caverns shows an early buildup above hydrostatic pressure, but subsequently a decrease, and the main pressure buildup is limited to the underground structures after 10,000 years (Figure 9, top right plot).

The simulated pressure and gas saturation along the vertical section through a single repository cavern after 1,000 years indicates water displacement from the cavern into the surrounding host rock and through the cavern seal into the branch tunnel (Figure 9, middle and bottom plots). The corresponding gas saturations indicate that the lower half of the cavern was resaturated and the waste-generated gas displaced the pore water from the repository. After 10,000 years, the water flow rates have decreased and much of the cavern indicates relatively high gas saturation. Most of the gas is migrating through the cavern seal into the branch and access tunnels, whereas the gas front into the surrounding host rock is limited to a few meters (Figure 9). That is, much of the waste-generated gas migrates through the repository seal (V4). Figure 10 shows the total flow of gas and water through the repository seal through time. The gas flow out of the model (at the contact between the seal and the ramp) starts after about 500 years. The liquid flow is negative at early time, indicating inflow of water through the seal into the access tunnel during the continued resaturation during the early postclosure period (Fig. 10). After about 500 years, the liquid flow is reversed as the gas front displaces some water through the repository seal. The computed gas flow rate in Figure 10 is used as input for the detailed repository seal model, described below.

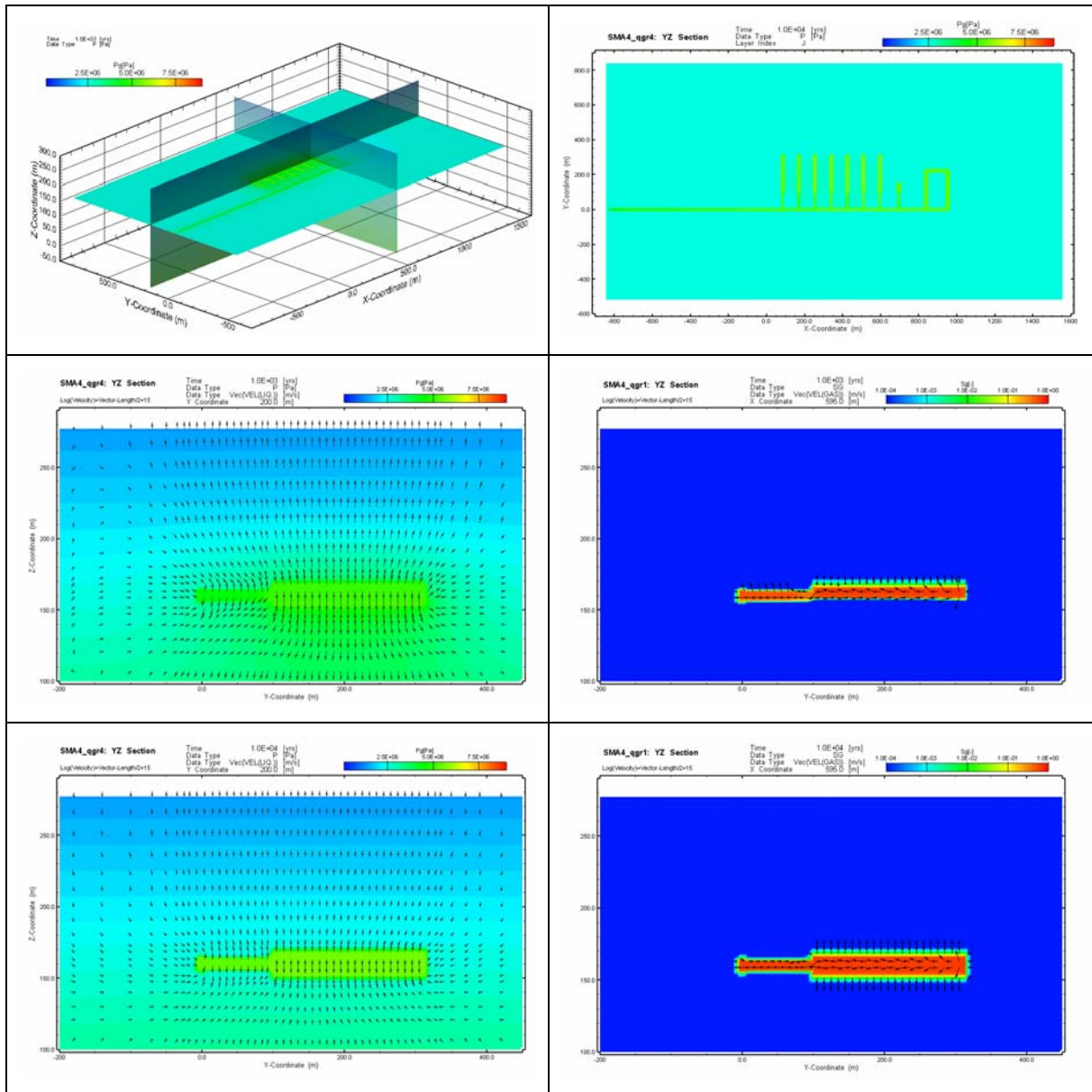


Figure 9. *L/ILW-Model Case R_CM02: 3D sections of pressure distribution after 1,000 years (top left) and in the repository plane after 10,000 years (top right); 2D vertical sections through a single emplacement cavern of pressure distributions and water fluxes (left), and gas saturations and gas fluxes (right), after 1,000, and 10,000 years.*

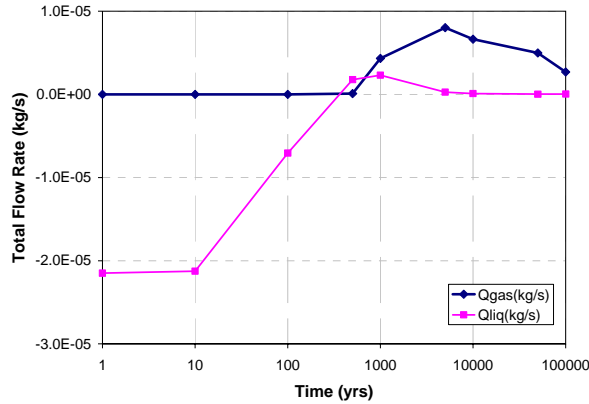


Figure 10 L/ILW-Model: Total flow (gas and liquid) through the repository seal (V4) (including EDZ) to the updip access ramp for Simulation Case R_CM02.

Repository Seal Model

The repository seal model (Figure 4) accounts for the detailed geometry and different components of the V4 seal. The operational periods, described above, are implemented as they relate to the seal and adjacent tunnel. The initial conditions for the postclosure phase are represented by partial saturation of the seal and depressurization in the surrounding host rock. For the simulation, all model boundaries are represented by a no-flow boundary, except for the tunnel segments, representing the contacts of the seal with the ramp and with the access tunnel. The contact of the seal with the ramp is represented by prescribed hydrostatic pressures. The tunnel segment representing the access tunnel accounts for the total volume of the access tunnel, which is assigned the prescribed gas flow rate computed from the large-scale model (Figure 10).

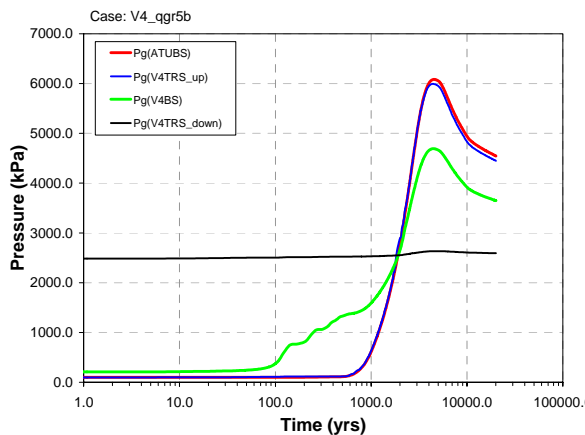


Figure 11. Repository Seal Model: Pressure buildup associated with the prescribed gas flow at the upstream boundary from the large-scale model (Fig. 10).

The results of the simulation in terms of the pressure buildup at different segments of the seal are shown in Figure 11. The simulated pressures in the access tunnel associated with the prescribed gas flow rate start to increase after about 500 years and reach a peak of 6.05 MPa after 4,000 years.

The corresponding saturation distribution is shown in Figure 12 for different times. The top plot depicts the maximum extent of the resaturation of the seal, indicating gas saturations remaining at the upstream side of the seal which consists of high-permeability gravel. The gas started to migrate from the access tunnel above the fully saturated bottom portion of the seal. The results after 4,700 years indicate that the gas front reached the ramp, corresponding to the pressure peak in Figure 11. The results indicate that the gas flow is limited to the seal and adjacent EDZ with only a minor penetration into the host rock.

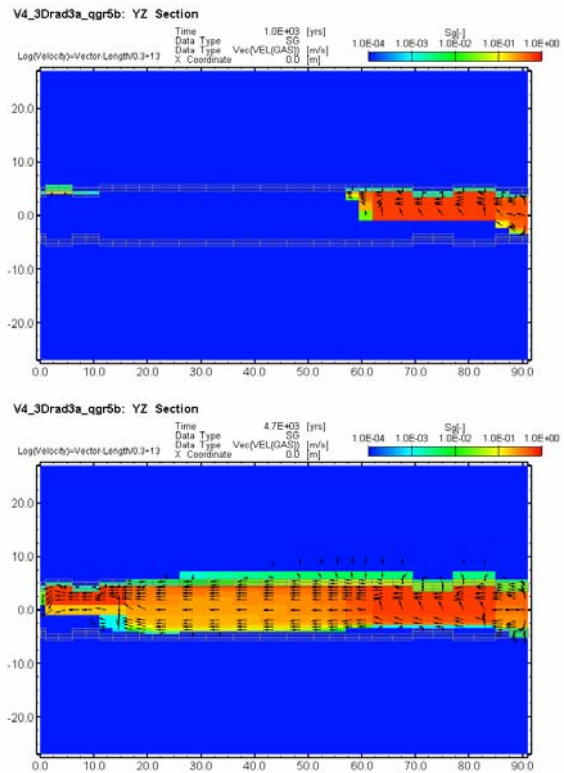


Figure 12. Repository Seal Model: Gas saturation and gas flow along the seal (YZ Section) after 1000 years (top) and 4,700 years (bottom); the outline mesh represents the EDZ zone in the model.

Repository Cavern Model

The repository cavern model (Figure 6) accounts for the detailed geometry and different components of the cavern including a liner at the contact with the surrounding EDZ. In comparison, the large-scale model assumed a single backfill material with

uniform properties. Similar to the large-scale model, the cavern model simulates the different operational phases, which are used as initial conditions for the postclosure phase.

The simulation results of the repository cavern model are shown in Figure 13. During early postclosure (after 1 year), the saturation distribution in the cavern indicates that, during the operational period, relatively little resaturation of the cavern occurs. In comparison, the large-scale model indicated that half the cavern became saturated halfway from the bottom. During gas generation, the gas pressures increased and displaced the pore water from the repository until most of the repository became fully gas saturated (Figure 9).

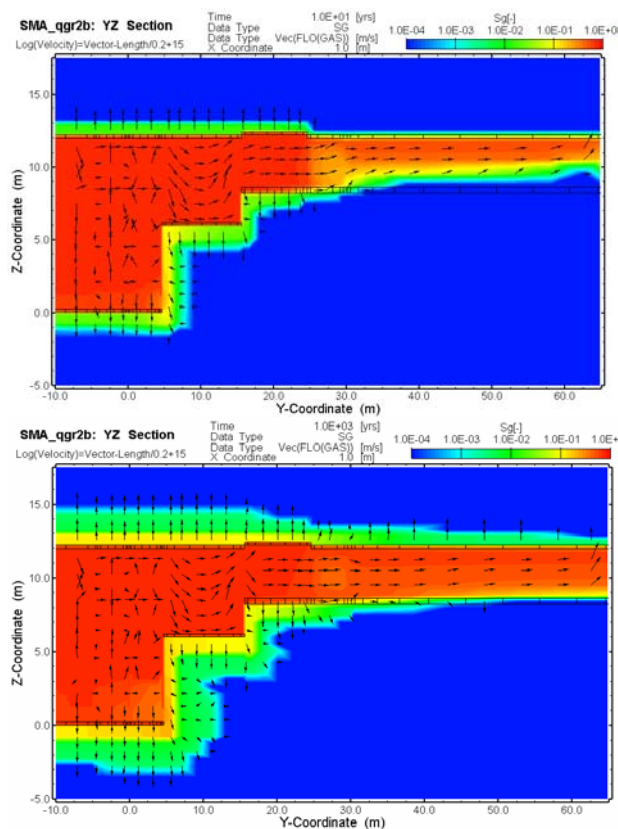


Figure 13 Repository Cavern Model: Gas saturation and gas flow along the YZ Section after 10 years (top) and 1,000 years (bottom); the outlined mesh represents the liner.

The detailed model of the repository cavern indicates that the lower part of the repository did not experience a significant decrease in gas saturation. Only the lower part of the branch tunnel exhibited some resaturation prior to the gas pressure buildup above hydrostatic pressures. The resulting early buildup in the cavern pressure was significantly lower compared to that in the large-scale model shown in Figure 8. The difference in the resaturation of the cavern between the large-scale model (Figure

9) and the detailed model (Figure 13) is the likely cause of this early pressure difference, resulting in a much greater initial storage volume for the accumulation of waste-generated gas. The differing resaturation behavior (being examined further) is likely caused by the finer discretization of the detailed model and/or the heterogeneity in the cavern materials, which included a liner with two orders of magnitude lower permeability than the uniform backfill material assigned to the entire cavern in the large-scale model.

SUMMARY

The numerical modeling study presented in this paper described a study for simulating two-phase flow behavior for a generic L/ILW repository in a low-permeability claystone formation. The repository consists of as many as seven parallel caverns which are sealed off from a single access tunnel. Additional underground structures include a pilot cavern, an underground test facility, a ventilation shaft, and a central area. To assess the possibility of buildup of excess gas pressures in the backfilled emplacement caverns after repository closure, a large site-scale two-phase flow model was constructed, complemented by detailed models of a single repository cavern and of the repository seal. Whereas the large-scale model focused on the pressure buildup in the emplacement caverns and access tunnels, and on the overall gas and liquid flow from the emplacement caverns through the EBS and into the surrounding host rock, the detailed models of the seal and of the single cavern provided a detailed characterization of the two-phase flow associated with the resaturation of the repository and the subsequent migration of waste-generated gas, from the repository caverns, through the EBS, and into the surrounding host rock.

ACKNOWLEDGMENTS

This study has been performed under contract from NAGRA, Switzerland.

REFERENCES

- Calder, N. & Avis, J.: mView User Manual, Version 4.0, 2006. Intra Engineering, Ottawa, Canada, 2006.
- Nagra: (Effects of post-disposal gas generation in a repository for low- and intermediate-level waste sited in the Opalinus Clay of Northern Switzerland. Nagra Tech. Rep. NTB 08-07. Nagra, Wettingen, Switzerland, 2008.
- Pruess, K., Oldenburg, C. & Moridis, G.: TOUGH2 user's guide, 2., LBNL Report, LBNL-43134, Berkeley, CA., 1999.
- Zhang, K., Wu, Y.S., Ding, C. & Pruess, K.: TOUGH2_MP: A parallel version of TOUGH2. Proceedings TOUGH2 Symposium 2003, Lawrence Berkeley National Laboratory, California, 2003.

ESTIMATION OF HUMIDITY DURING TUNNEL VENTILATION— SUPPORTED BY TOUGH2 CALCULATIONS OF LIQUID, VAPOR, AND HEAT TRANSPORT

Poppei Joachim, Mayer Gerhard, Hubschwerlen Nicolas, Guillaume Pépin*, Wendling Jacques*

AF-Colenco Ltd.
Taefernstrasse 26
5405 Baden, Switzerland
e-mail: joachim.poppei@afconsult.com
* ANDRA
1-7, rue Jean Monnet
92298 Châtenay-Malabry Cedex, France

ABSTRACT

The calculation of relative humidity in tunnels is a fundamental task when designing a repository ventilation system in a clay host rock. It requires complex numerical modeling of transient (forced) convective and conductive heat and fluid transport. The humidity of the tunnel air primarily depends (along with the meteorological conditions at the entrance) upon the thermal-hygric transitional conditions at the exposed rock surface of the tunnel walls. Some portions receive water influx while others receive heat influx from the waste already emplaced in other parts of the host rock.

The coupling between the transport processes in the host rock and the transfer processes along the tunnel wall is treated in a simplified manner. The processes described by coefficients for heat (Nusselt number) and vapor (Sherwood number) both depend on the ventilation velocity (Reynolds number). We discuss an approach involving supportive TOUGH2 computations for complex transport problems in the host rock. The results are processed and applied to the transient analysis of temperature and humidity changes in the ventilation air.

Analysis of the evaporation along a tunnel wall is supported by a one-dimensional radially symmetric EOS9 model. Results from the TOUGH2 computations with different Sherwood numbers are parameterized accordingly. The prevailing humidity along the tunnel wall is then determined with an iterative approach, whereby the humidity is controlled either by the ventilation (i.e., through the Sherwood number) or the leakage capacity of the host rock. Finally, the humidity changes in the ventilation air are derived from the computed diffusion of vapor along the boundary layer.

To calculate the heat transfer into the tunnel along its walls, we used the results from a complex geometric TOUGH2 model. The model considers different thermophysical parameters as well as the transient rates of heat production by the waste. At any given time, the heat transfer along the tunnel wall—with consideration of the then-prevailing heat production and ventilation velocity—causes a rise in air temperature and a corresponding decrease in relative humidity.

INTRODUCTION: CASE DESCRIPTION AND OBJECTIVES

The French radioactive waste management agency ANDRA is designing an underground tunnel system in a clay host rock, into which it intends to emplace radioactive waste. Figure 1 shows a schematic illustration of the repository. The horizontal emplacement tunnels, which will be sealed after waste emplacement, are accessible via access tunnels and vertical shafts that will remain open for an extended operational phase. Because the access tunnels and shafts need to be ventilated, the prognosis of the expected relative humidity is an essential issue. The humidity of the air in the access tunnels and shafts depends in part on the meteorological conditions at the entrance, but mostly on the thermal-hygric transitional conditions at the exposed rock surface in the tunnels and shaft.

In principle, the heat and mass exchange processes of the circulating air are relatively complex. If one considers all the physical effects along the boundary surfaces, the spatial and temporal changes of the turbulent flow and the complete coupling of the thermal-hygric transport processes, the underlying Navier-Stokes differential equations necessitate complex and time-consuming models of the turbulent flow dynamics, i.e., computational fluid dynamics (CFD).

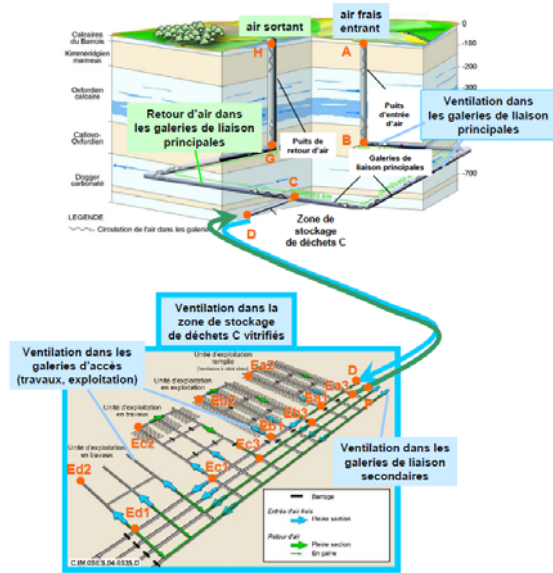


Figure 1. Schematic draft design of the underground repository

However, the situation analysis on the one hand, and the specifics of the task description on the other, justify conceptual considerations for the application of simplified solution approaches and robust (engineering technical) procedures. This approach must account for the important processes and should allow for comprehensive parameter variations.

The full scope of the project included consideration of all parts of the underground repositories and also processes such as transient heat transfer in shafts, pressure losses during ventilation, condensation, etc. For this paper, we concentrate on those parts and processes subjected to TOUGH2 calculations.

CONCEPTUAL MODEL

Simplified Geometrical Model

The complex system of tunnels and shafts may be described by a series of connected gallery sections, which are characterized individually in terms of horizontal or vertical orientation, position in the tunnel system, and specific thermal and/or hygric effects. Figure 2 shows the geometrical abstraction of the repository system for heat generating wastes, also called C-wastes. (Internationally, C-wastes are more commonly referred to as high-level radioactive wastes, or HLW.)

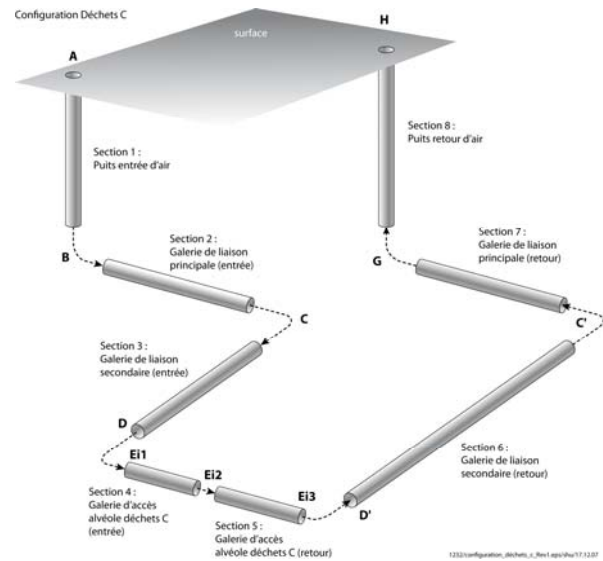


Figure 2. Geometrical abstraction for the C-waste configuration

The abstraction of the C-waste repository system consists of seven different gallery sections (see Figure 2):

- Section 1: “Puits entrée d’air” is the vertical access shaft to the repository. Fresh air comes down through this gallery (corresponds to $A \rightarrow B$).
- Section 2: “Galerie de liaison principale (entrée)” is a gallery section that conducts air to the waste zone. Air circulates in the main part of the gallery (corresponds to $B \rightarrow C$).
- Section 3: “Galerie de liaison secondaire (entrée)” is a gallery section situated in the waste zone that leads to C-waste access galleries. Air circulates in the main part of the gallery (corresponds to $C \rightarrow D$).
- Section 4: “Galerie d’accès alvéole déchets C (entrée)” is a gallery section along which the C-waste cells are situated and produce heat when in use (i.e., after heat emitting waste has been emplaced). Air circulates through the main part of the gallery (corresponds to $Ea1 \rightarrow Ea2$ or $Eb1 \rightarrow Eb2$ or $Ec1 \rightarrow Ec2$ or $Ed1 \rightarrow Ed2$, depending on the condition of use of the access gallery)
- Section 5: “Galerie d’accès alvéole déchets C (retour)” is a gallery section in which the air from the previous section is sent back to the secondary link gallery. During the construction phase, air circulates through a tube (smaller diameter). When the repository is in operation, i.e., after heat-emitting waste (C-waste) has been emplaced and produces heat, air circulates in a full-section waste gallery (corresponds to $Ea2 \rightarrow Ea3$ or $Eb2 \rightarrow Eb3$ or $Ec2 \rightarrow Ec3$ or $Ed2 \rightarrow Ed3$, depending on the conditions of use of the access gallery).

- Section 6: “Galerie de liaison secondaire (retour)” is a gallery section in which air returning from the previous section is sent back to a main link gallery. Air circulates in a tube which, in reality, is situated in the entry secondary link gallery, so the diameter is smaller than that of Section 3 (corresponds to $D \rightarrow C$).
- Section 7: “Galerie de liaison principale (retour)” is a gallery section conducting ventilation air from the secondary link gallery to the air output shaft. Air circulates into a tube that is physically located inside the main link gallery (Section 2) (corresponds to $C \rightarrow G$).
- Section 8: “Puits retour d’air” is the vertical air shaft in which air is sent back from the repository to the surface (corresponds to $G \rightarrow H$).

The following discussion focuses on two important processes, which are described in detail to exemplify the approach:

- Evaporation at the shaft or tunnel surface
- Heat transfer at an access tunnel wall (beyond which waste has already been emplaced, in Figure 2, Sections 4 and 5).

Basic Physical Assumptions

The task description asks for a prognosis of the changes in relative humidity of the circulating air at various locations, i.e., along different sections. The humidity of the air is conditioned by temperature, pressure, and vapor content. For this, the mixture of dry air and vapor is considered to be a mixture of ideal gases. Changes in the relative air humidity, along the path through the access and emplacement galleries and shafts, occur by way of (a) heat exchange of the circulating air with the surroundings (temperature change), (b) humidity exchange of the circulating air with the surroundings (change in water-vapor content), or (c) both processes. These heat- and mass-transfer processes need to be quantified to predict the effects on relative air humidity.

The dependency of vapor pressure at saturation (of pure water vapor) on temperature can be described with suitable equations such as the Magnus equation, Antoine equation or others.

The following basic assumptions are made with respect to convection:

- Convective flow is forced, turbulent, and hydraulically and thermally fully developed. One consequence of this basic assumption is that the transfer conditions for heat and mass (humidity) along the fluid-wall boundary are independent of the location along a section and may be described by a set of simplified, criteria-bound equations.

- Changes in the hygric property of the air may be characterized in a decoupled manner through heat exchange and/or humidity exchange.

An essential and basic assumption for our concept of humidity and heat exchange (mass and heat transfer) is that of quasi-steady-state conditions. The transport of air through the sections occurs many times faster than all other temporal changes.

It is also assumed that the source terms of heat and humidity at time t' may be characterized uniquely by the heat generation of the container at time t' and the humidity rate at time t' , respectively, and that they are mostly independent of the circulation system prior to t' .

The influence of the current ventilation rate on transfer processes is considered through the dependency of the dimensionless transfer coefficients (Nusselt and Sherwood numbers) on the Reynolds numbers. For the calculation of the Nusselt number, we consider the empirical relations to the Reynolds number for fully developed turbulent flow by forced convection in circular tubes, with Prandtl numbers on the order of 0.7 (correlations are given by Kakaç et al., 1987).

The humidity uptake of the ventilation air through evaporation may be described with the mass balance of the forced circulated air and the incoming water vapor. Transport of the water vapor in the boundary layer rock surface/air by diffusion may be considered in terms of a quasi steady-state application of the Sherwood number. For this purpose, the Lewis analogy for heat and mass transfer can be used.

The heat transport from waste containers into the adjacent rock was calculated with a complex TOUGH2 model. A radially symmetric TOUGH2 model was used to calculate the evaporation along tunnel and shaft walls. These models and their results are discussed below.

HEAT TRANSFER INTO THE GALLERY DUE TO HEAT GENERATED BY WASTES

Figure 3 illustrates the geometrical situation and the analytical task. A complex TOUGH2 model was used to consider the heat generated by the C-wastes and penetrating (retarded and reduced) the walls of the galleries.

This model is used to calculate the transient flow of heat generated by wastes into the gallery under certain transfer conditions at the wall surface (representing a scale of different Nusselt numbers).

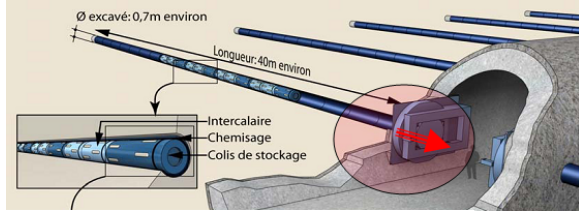


Figure 3. Illustration of the thermal issue: heat flow into the tunnel

Thermal Model Setup

The 3D mesh used for the simulation represents a section of the C-waste repository and is shown in Figure 4. The axis of the gallery is oriented in the x-direction ($y=0$, $z=0$). The emplacement tunnels are oriented in the z-direction, and y is the vertical direction.

For the purposes of modeling, the length of the mesh in the x-direction is half the distance between two neighboring emplacement tunnels (6.3 m). The length of the mesh in the z-direction is half the distance between two neighboring galleries (51.6 m). The height (y-direction) of the mesh is 4.5 m. Adjacent to the top elements, there is a semi-infinite domain with the same thermal properties as the clay host rock Callovo-Oxfordian (Material 1). The gallery has a concrete liner (Material 2) with an outer radius of 4 m. Due to symmetry, the model represents only one-fourth of the cross section.

In the mesh, the cross section of the emplacement tunnel is square. Next to the liner, there are nine concrete elements ($z=-8.5$ m) followed by six bentonite elements ($z=-11.5$ m) and one iron element ($z=-12$ m). Then follows a series of eight canister /

remblais pairs. Each canister element (Material 4) is 1.6 m long, whereas a remblais element (Material 5) is 2.4 m long.

To mimic the heat transfer resistance observed at interfaces between a solid (rock) and air, special “heat transfer elements” of thickness d were inserted in between the liner surface and the gallery boundary. The thermal conductivity of those elements λ_{HTE} is given by their thickness d , the Nusselt number Nu , the diameter of the gallery D , and the heat conductivity of air λ_a , as follows:

$$\lambda_{HTE} = Nu \cdot d \cdot \lambda_a / D \quad (1)$$

Thickness d was chosen to be 1 m.

Material parameters are summarized in Table 1.

The initial conditions were: full liquid saturation, a pressure of $1 \cdot 10^5$ Pa, and a temperature of 22°C for all elements in the mesh. The temperature in the gallery was kept constant by assigning very large volumes ($1 \cdot 10^{50}$ m³) to elements of Material 3.

No-flow boundary conditions were used for all mesh boundaries except for the bottom of the mesh. There, a heat exchange with a semi-infinite rock layer was assumed in effect by selecting the “Heat Exchange with Confining Beds” option in TOUGH2.

As each canister element in the mesh represents one-fourth of a real canister, the time-dependent heat generation rates of a canister were divided by 4 and applied to each canister element (Figure 4).

Table 1. Material parameters used for the TOUGH2 simulation

Material Nr.	Material name	Density [kg/m ³]	Porosity [-]	Rock grain specific heat [J/(kg K)]	Thermal conductivity (liquid water saturated) [W/(m K)]
1	Callovo-Oxfordian	2750	0.12	1000	2.0
2	Liner concrete	2750	0.12	1000	1.0
3	Gallery	2750	0.12	1000	1.0
4	Waste canister	6832	0.01	318	15.0
5	Remblais	2750	0.25	1500	1.4
6	Bentonite	2750	0.35	1350	1.4
7	Iron	7850	0.01	500	35.0
	Heat transfer elements	1000	0.99	10.0	see text

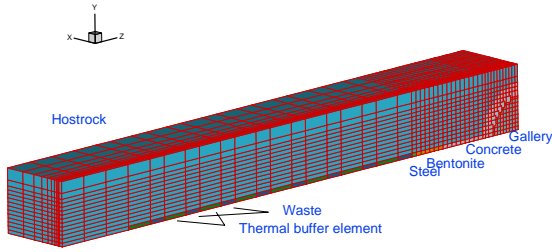


Figure 4. TOUGH mesh used to simulate heat transfer into the gallery. (The heat transfer elements between the liner concrete and the gallery, as well as the semi-infinite heat exchange layer above the mesh, are not shown)

Parameterization of TOUGH Results

The results of these calculations are transient heat flow densities at the wall surface, which depend on the time after the emplacement of wastes, t_w , and examples of transfer resistances which correspond to different Nusselt numbers.

The fundamental curve of heat flow density through the wall, neglecting a contact resistance (corresponding to an infinite transfer coefficient or infinite ventilation flow rates), \dot{q}_I , can be approximated by an algebraic step-function that depends only on the time after the emplacement of wastes t_w

$$\dot{q}_I = f(t_w) \quad (2)$$

To honor the actual flow rate (at any given time), the prevailing transfer coefficient and the increasing radius of a cooling mantle due to ventilation, the following parameterization was developed.

We considered a “surrogate” model consisting of a single-layer wall with a thermal conductivity λ_g . Its outward side is cooled with a heat-transfer coefficient α . In such a one-dimensional steady-state flow field, the relation between heat flow through a wall of thickness D with a contact coefficient α (\dot{q}_{III}), and the heat flow without such a contact resistance (\dot{q}_I), is given by

$$\frac{\dot{q}_{III}}{\dot{q}_I} = \frac{D}{\lambda_g + \frac{1}{\alpha}} = \frac{\frac{\alpha D}{\lambda_g} + 1}{\frac{\alpha r_0}{\lambda_a} + \frac{\lambda_g r_0}{\lambda_a D}} = \frac{Nu}{Nu + \frac{\lambda_g}{\lambda_a} \frac{2 \cdot r_0}{D}} \quad (3)$$

We replace the thickness D of the “surrogate wall” with the time-dependent thermal entrance depth D

$$D = r_0 + \sqrt{\pi a_g t_v} \quad (4)$$

$$a_g = \frac{\lambda_g}{(\rho \cdot c)_g} \dots \text{thermal diffusivity of rock}$$

t_v ... time after beginning of ventilation (corresponds approximately to t_w)

and fit the calculated curves of the complex 3D model with an “apparent” thermal conductivity for the rock λ_{ap} in (3) and (4). Examples of this parameterization with the fitted value are shown in Figure 5.

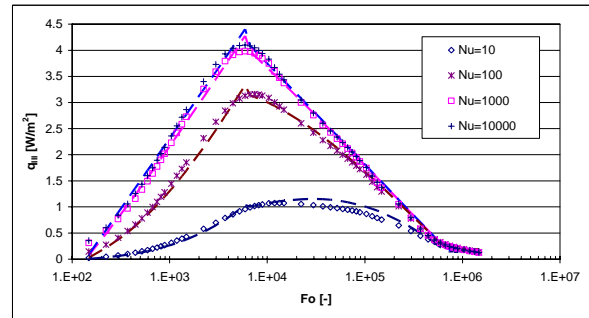


Figure 5. Comparison of calculated (with TOUGH2; dashed lines) and parameterized (dotted) curves of transient heat flow for different transfer conditions; plotted over dimensionless time, the Fourier

$$\text{number } Fo = \frac{a_g \cdot t_w}{r_0^2}$$

We then use this parameterization and the “apparent” thermal conductivity λ_{ap} to calculate for any actual flow field the attenuation of the heat transfer as a function of the flow velocity. Having the actual heat flow density at the wall surface, the temperature of the fluid in the gallery at a distance L from the entrance is given by

$$T_2(y=L) - T_e(y=0) = \frac{1}{\dot{m}_a \cdot c_p} \dot{q}_{III} [t_w, Nu[Re(\dot{V})]] \cdot 2\pi r_0 \cdot \int_0^L dy' = \frac{\dot{q}_{III} [t_w, Nu[Re(\dot{V})]] \cdot 2\pi r_0 \cdot L}{\dot{m}_a \cdot c_p} \quad (5)$$

Re ... Reynolds number

\dot{V} ... flow rate of ventilation

The vapor pressure saturation $p_s(T)$ can then be calculated with the Magnus or the Antoine equation. Without changes in the vapor partial pressure, the relative humidity φ for the (heated) air changes proportionally to it.

MASS TRANSFER BY EVAPORATION

We assume evaporation to be an isenthalpic process by simply adding water to (humid or dry) air. The

flow rates of water or vapor added by evaporation, \dot{m}_w , generally depend on the transmissivity and the leakage (or seepage) capacity of the surrounding rock, on the duration of ventilation, and on the prevailing ventilation conditions (especially flow rate and humidity). For practical reasons, we distinguish for this purpose between a potential flow or leakage rate of the host rock (f_{hr}) and a potential transfer rate at the surface, controlled by the mass-transfer coefficient or Sherwood number (f_{sh}), both per meter length of the ventilated shaft or tunnel.

The potential leakage (or seepage) rate controlled by the host rock, f_{hr} , was calculated for well-specified conditions with TOUGH2 EOS9. For these calculations, any film transfer was neglected (mass transfer coefficient $\beta = \infty$), i.e., the boundary condition at the wall surface was described as a Dirichlet type by pressure and humidity.

Evaporation Model Setup

A 1D radially symmetric mesh with a total of 61 elements was used. The parameters used to calculate the water flow to a shaft and to a gallery are summarized in Table 2.

Table 2. Modeling parameters used for water flow calculations with TOUGH2 (EOS9)

Parameter	Hostrock to gallery	Hostrock to shaft
Excavation radius [m]	3.5 (gallery)	6.0 (shaft)
Discretization (Radius, # elements), ...	(3.5 m, 1), (4.0 m, 30), (50.0 m, 30)	(6.0 m, 1), (7.0 m, 30), (50.0 m, 30)
Hostrock:		
k [m ²]	$5.1 \cdot 10^{-20}$	$8 \cdot 10^{-16}$
van Genuchten parameters:		
p_{ae} [MPa]	14.7	1.0
n	1.49	1.5
S_{lr}, S_{gr}	0.01, 0.0	0.0, 0.0
Initial liquid water pressure in hostrock and outer boundary	4.5 MPa	5 MPa
Temperature [°C]	22	
Relative humidity (liquid pressure) in gallery / shaft	0.1 (-314 MPa), 0.3 (-164 MPa), 0.5 (94.5 MPa), 0.9 (14.4 MPa)	

The calculated flow rates into the gallery and shaft are shown in Figure 6. For the shaft, the flow rate of about 1 m³/(m day) is found to be independent of the relative humidity in the shaft and the time. Therefore, it may be applied for any arbitrary conditions to calculate the change in air humidity.

Parameterization of TOUGH Results for the Calculation of Actual Evaporation

The flow rate into the gallery was more than four orders of magnitude smaller than the flow rate into the shaft. This was mainly due to the permeability of the host rock around the gallery, which was about 4 orders of magnitude lower than that around the shaft. A slight decrease in the flow rate with increasing relative humidity in the gallery was observed. The calculated potential leakage flow into the gallery (without film transfer at the surface), f_{hr} , and its dependency on the ventilation time t_v and the humidity of ventilated air could be approximated with a polynomial function.

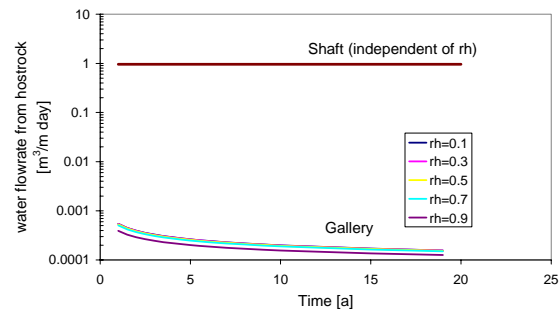


Figure 6. Simulated flow rate from hostrock into gallery and shaft

When considering a finite transfer coefficient at the surface, the transfer of vapor by diffusion in air, f_{sh} , can be described as depending on the Sherwood number:

$$f_{sh} = Sh \cdot \pi \cdot D_a \cdot \frac{\varphi_0 + \varphi_m}{2} [\rho_v(T_0) - \rho_v(T_m)] \quad (6)$$

and approximated (for numerical reasons) as follows

$$f_{Sh} \equiv Sh \cdot \pi \cdot D_a \cdot \frac{\varphi_0 + \varphi_m}{2} \cdot \frac{p_s(\bar{T}) \cdot M_v}{R \cdot \bar{T}} \cdot (\varphi_0 - \varphi_m)$$

with the mean temperature

$$\bar{T} = \frac{T_0 + T_m}{2}$$

The (mass transfer) Sherwood number is defined by

$$Sh = \frac{\beta \cdot 2r_0}{D_a} \quad (7)$$

with

β ... mass transfer coefficient [m/s]

D_a ... (molecular) diffusivity in air

and depends on the characterization of the fluid and on the Reynolds number.

To determine the Sherwood number, Sh , we can make use of the analogy of heat and mass transfer: Heat transfer and mass transfer are strongly analogous if the Lewis number (ratio of the Schmidt and Prandtl numbers) is one. For air, this criterion is about 0.6/0.7, i.e., it is almost satisfied. In this case, the same equations can be used to calculate the Nusselt and the Sherwood numbers as functions of the Reynolds number, by substituting the Schmidt number Sc for the Prandtl number:

$$Sc = \frac{\nu}{D_a} = \frac{\mu}{\rho \cdot D_a} \quad (8)$$

For the transfer of vapor to air, the Schmidt number Sc is about 0.6 (Kays and Crawford, 1993).

We now distinguish between two different situations: If for fully saturated conditions of air at the surface (i.e., $\varphi_0=1$), f_{Sh} acc. (6) is lower or equal to the calculated leakage rate, f_{hr} with $\varphi=\varphi_0=1$, the transfer of vapor is controlled by the transfer (Sherwood) condition. The transferred mass flow over a distance L is then

$$\dot{m}_w = f_{Sh}(\varphi_0=1) \cdot L = Sh \cdot \pi \cdot D_a \cdot \frac{1+\varphi_m}{2} \left[\frac{p_s(T_0) \cdot M_v}{RT_0} - \rho_v(T_m) \right] \cdot L \quad (9)$$

and the wall surface is fully saturated $\varphi_0=1$, because of the high leakage capacity of the host rock.

If, on the other hand, the calculated transfer rate, f_{Sh} , with $\varphi_0=1$, is higher than the potential leakage rate f_{hr} with $\varphi=\varphi_0=1$, the leakage of the host rock controls the transfer of vapor, and \dot{m}_w is calculated with f_{hr} . But in this case, the humidity at the surface, φ_0 , can be lower than one and has to be calculated iteratively:

$$\varphi_m \leq \varphi_0 \leq 1: \text{ where } f_{Sh}(\varphi_0) = f_{hr}(\varphi_0) \quad (10)$$

The leakage flow rates, f_{hr} , which depend on the duration of ventilation and on the prescribed relative humidity of the ventilated air at the surface, have been calculated for the shaft crossing the Oxfordian formation (permeability= $8 \cdot 10^{-16} \text{ m}^2$), and for the gallery in the Callovo-Oxfordian horizon (reference case $k_h=5 \cdot 10^{-20} \text{ m}^2$, $k_v=5 \cdot 10^{-21} \text{ m}^2$), and are given in Figure 6.

EXAMPLE APPLICATION

To finally calculate the evolution of the relative humidity throughout the tunnel system, we developed (1) an application taking into account the conceptual model with the multisection 1-dimensional geometry (the sections themselves are discretized), and made (2) an analytical computation taking into account the parameterized results of the TOUGH2 heat-transfer and mass-transfer calculations (as well as all the other necessary input parameters). A typical result for such a computation is illustrated in Figure 7 for a C-waste repository with the waste in place. The influence of the heat-generation and mass-transfer processes can clearly be observed along the shafts and gallery sections.

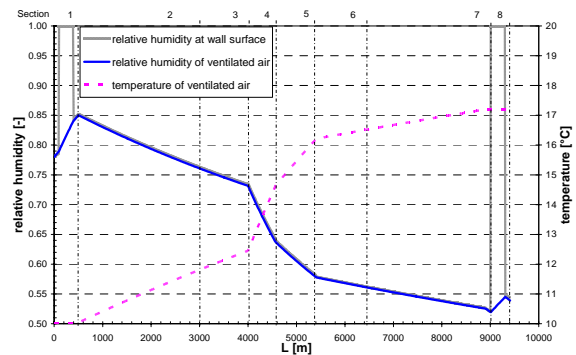


Figure 7. Examples of calculated relative humidity of air in the sections shown in Figure 2

CONCLUSIONS

The relative humidity of the air in tunnels depends strongly on the heat and humidity transfer conditions at the rock surface. In the case of forced turbulent convection, these may be defined relatively well through suitable indices (Nusselt and Sherwood numbers), which depend on the flow velocity (Reynolds number).

The situation is different for tunnel systems, where heat-generating wastes emplaced in sealed tunnels in the vicinity of open galleries give rise to additional heat transport. Another complicating factor occurs when fluid exchange is regulated not only by

convection, but also through the leakage capacity of the exposed rock wall. In these cases, TOUGH2 model calculations may provide the base for a parameterization that may be applicable even for frequently changing thermal-hygric properties of the ventilated air.

The approach presented here allows for fast approximating simulations of a variety of scenarios without time-consuming and complex models of the turbulent flow dynamics (CFD). This is advantageous, for example, when planning or optimizing the layout of facilities. Validating field investigations are currently being conducted in ANDRA's underground rock laboratory in Bure.

REFERENCES

- Kakaç, S., R. Shah, and W. Aung, *Handbook of single-phase heat transfer*, J. Wiley & Sons, 1987.
- Kays, W.M., and M.E. Crawford, *Convective heat and mass transfer*, McGraw-Hill Book Company, Second edition, 1993.

SYMBOLS

- a_g = thermal diffusivity of rock [m^2/s]
 c_p = specific heat capacity [$Ws/kg K$]
 d = model element thickness of "heat transfer elements" [m]
 D = thickness [m]
 D_a = diffusivity (of vapor) in air [m^2/s]
 f_{hr} = leakage flow rate from hostrock [$kg/(s \cdot m)$]
 f_{sh} = (Sherwood controlled) transfer rate of vapor [$kg/(s \cdot m)$]
 Fo = Fourier number [-]
 k_v, k_h = permeability (vertical, horizontal) [m^2]
 L = length [m]
 \dot{m}_a = mass flow rate (of air) [kg/s]

- \dot{m}_w = mass flow rate of water or vapor at the wall surface [kg/s]
 M_v = molar mass of vapor [g/mol]
 n = van Genuchten exponent [-]
 Nu = Nusselt number [-]
 p_{ac} = van Genuchten parameter air entry pressure [MPa]
 $p_s(T)$ = vapor saturation pressure [Pa]
 Pr = Prandtl number [-]
 \dot{q} = heat flow density [W/m^2]
 r_0 = (hydraulic) radius [m]
 R = ideal gas constant [$Ws/mol K$]
 Re = Reynold number [-]
 Sc = Schmidt number [-]
 Sh = Sherwood number [-]
 S_{gr} = residual gas saturation [-]
 S_{lr} = residual liquid saturation [-]
 t_v = time after ventilation began [s]
 t_w = time after emplacement of C-wastes [s]
 $T_{(m)}$ = (mean or bulk) temperature [K]
 T_e = entrance temperature [K]
 T_0 = wall temperature [K]
 \dot{V} = ventilation flow rate [m^3/s]
 y = coordinate or distance [m]

Greek letter symbols

- α = heat transfer coefficient [$W/m^2 K$]
 β = mass transfer coefficient [m/s]
 λ_a = thermal conductivity of air [$W/m K$]
 λ_{ap} = fit parameter (apparent thermal conductivity due to heat production) [$W/m K$]
 λ_g = thermal conductivity of rock [$W/m K$]
 λ_{HTE} = thermal conductivity of "heat transfer elements" [$W/m K$]
 μ = dynamic viscosity [$Pa s$]
 ν = kinematic viscosity [m^2/s]
 $\rho_{(a)}$ = density (of air) [kg/m^3]
 ρ_v = density of vapor [kg/m^3]
 $\Phi_{(m)}$ = (mean or bulk) relative humidity [-]
 ϕ_0 = relative humidity at wall surface [-]

REPOSITORY-SCALE MODELING OF THE LONG-TERM HYDRAULIC PERTURBATION INDUCED BY GAS AND HEAT GENERATION IN A GEOLOGICAL REPOSITORY FOR HIGH AND INTERMEDIATE LEVEL RADIOACTIVE WASTE— METHODOLOGY AND RESULTS

Andreas Poller², Carl Philipp Enssle¹, Gerhard Mayer¹, Jean Croisé¹, Jacques Wendling³

¹ AF-Colenco Ltd

Taefernstrasse 26, CH-5405 Baden, Switzerland

e-mail: carl-philipp.enssle@afconsult.com

² Formerly AF-Colenco Ltd

³ ANDRA, Parc de la Croix Blanche, Châtenay-Malabry, France

ABSTRACT

The current design of a repository for high- and intermediate-level radioactive waste in France consists of a complex system of different underground structures (ANDRA, 2005). For a comprehensive understanding of the long-term hydraulic evolution of the entire repository, numerical nonisothermal two-phase flow simulations are compulsory. A detailed numerical model of the entire repository system would require a tremendous computational effort and pose a laborious task with respect to the operability of the model. To handle these difficulties, we have developed an innovative method for the efficient hydraulic modeling of a complete repository system and its geologic environment. The method is based on the following: (i) Subdivision of the repository plane into a large number of “sectors” based on the position of seals and on other geometrical considerations, (ii) Exploitation of existing symmetries (inside or between sectors), (iii) Adoption of the “multiplication” concept, and (iv) Connection of the individual sectors at the drift interfaces to form the entire repository model. Each sector is modeled as a 3D block, and the entire model is computed with TOUGH2-MP. The method allows for a massive reduction in overall finite volume elements, and at the same time provides an adequate representation of the fine structures in the repository. The main characteristics of the method and its application to an entire repository system are presented.

INTRODUCTION

The French agency for the management of radioactive waste (ANDRA) is planning a deep geological repository for intermediate- to high-level radioactive waste in a claystone formation. One important question related to the long-term safety performance of the repository is the influence of heat and gas generated in the emplacement areas on the evolution of the fluid pressure and saturation fields in the repository and the host rock (ANDRA, 2005). Of particular interest is the potential for overpressure in the near field of the repository, because this could affect the

mechanical integrity of geotechnical and geologic barriers.

Achieving a good understanding of the hydraulic-system behavior of the repository requires numerical nonisothermal two-phase flow simulations. However, a detailed 3D modeling of the repository accounting for both the detailed structure at local scale and the global geometry of the gallery network would require a tremendous computational effort, even when using a high-performance code like TOUGH2-MP.

In this paper, we present an innovative method for the efficient hydraulic modeling of a complete repository system and its geologic environment, while still accounting for the detailed geometry at local scale. The method is illustrated by the example of an isothermal two-phase flow model for the entire repository system and some simulation results for the post-operational period.

SYSTEM DESCRIPTION

The general layout of the repository is presented in Figure 1. The repository design is envisaged as subdivided into three major zones: a large zone for high-level radioactive waste (zone HA), a zone for intermediate-level radioactive waste (zone MAVL) and a zone for infrastructure facilities and access shafts. Individual zones are connected through access and ventilation tunnels. The horizontal extent of the complete repository is several kilometers in width and length; the thickness of the host rock (Callovo-Oxfordien Clay) is around 130 m.

During the operational period (about 100 years), the complex network of drifts and disposal cells is ventilated under controlled conditions of relative humidity and atmospheric pressure, leading to a drawdown of hydraulic pressure in the near field of the repository, as well as to a desaturation of the host rock in the vicinity of the tunnels and caverns. At the end of the operational period, all repository structures are backfilled with specifically designed geomaterials. A set of hydraulic barriers (seals) is foreseen at the end of the emplacement drifts, at specific

locations within and between the major zones, as well as in the upper part of the access shafts, to hinder the transport of potentially contaminated fluids along the backfilled drifts and shafts.

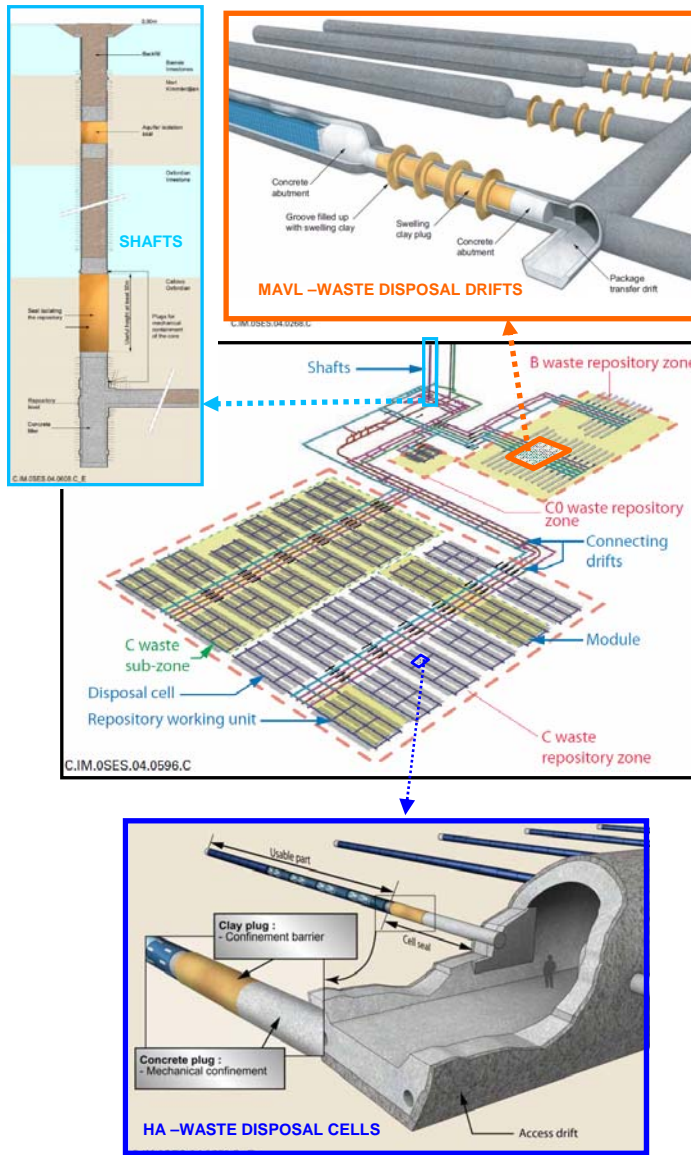


Figure 1. General repository layout (middle: “B-waste”=MAVL waste, “C-waste”=HA waste) with close-up on MAVL disposal area (top), HA disposal area (bottom) and schematic of shaft (top left) (ANDRA, 2005).

During the post-operational period, the waste containers (in particular those with high-level waste) emit heat, generated as a result of radioactive decay. Moreover, the chemical degradation of some waste components produces considerable amounts of gas (mostly hydrogen). Both processes have a strong impact on the resaturation of the repository system. The expected time scales of the transient thermal and

hydraulic processes until hydraulic equilibrium is reached were presented by ANDRA in 2005 (see Figure 2).

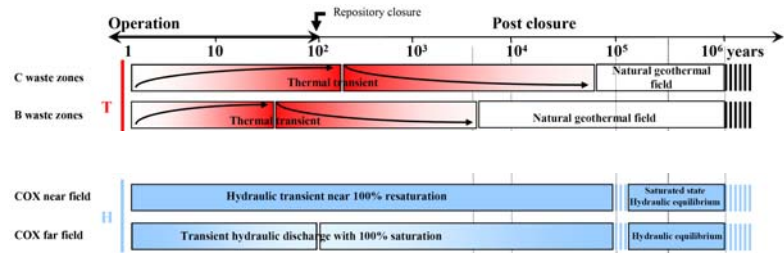


Figure 2. Chronogram of thermal and hydraulic phenomena affecting the repository (ANDRA, 2005)

METHODOLOGY

The complete lifetime of the repository is considered, i.e. the construction of the repository, the operational period and the post-closure period until the original natural hydraulic and thermal conditions are retrieved.

Modeled Processes

During the operational phase of the repository, the disposal and access drifts, as well as the access and ventilation shafts, are ventilated, and the host rock is progressively depressurized and desaturated. These processes can be modeled as simple unsaturated water flow. As soon as the drifts are backfilled and sealed, the post-operational period begins, and the principal processes to be considered are:

- Thermal dissipation into the formation (by convection and conduction) and an induced pore-water pressure increase resulting in comparably high water fluxes. (This process begins as soon as the waste packages are placed into the cells.)
- Resaturation of the backfill materials, due to the drainage towards the drifts and the suction of the backfill materials (at early times)
- Hydrogen gas generation and gas pressure buildup in the backfilled repository. (This process begins as soon as the waste packages are placed into the cells.)
- Flow of water into the host rock due to the gas pressure buildup (at later times). (This process begins as soon as the waste packages are placed into the cells.)
- Dissolution of hydrogen into the pore water and transport by diffusion/advection. (This process begins as soon as the waste packages are placed into the cells.)

- Advection and diffusion in the gas phase (in partially saturated materials). (This process begins as soon as the waste packages are placed into the cells.)

The gas-water flow is modeled as two-phase flow using the generalized Darcy's law and the relative permeability/capillary pressure concept. Advective/diffusive transport of hydrogen in the gas phase and the water phase is taken into account. Convective and conductive heat transport is also considered. Because of hydrogen being the dominant gas species, the TOUGH2-MP module EOS5 (water/hydrogen) is used for the computations (Pruess et al., 1999, Zhang et al., 2008).

Spatial discretisation

The simulation of the entire repository, including the geometrical details of the drifts, cells and shafts, would require a computational effort and operability far beyond the limits of today's possibilities, even if using a parallelized code like TOUGH2-MP on a medium size Linux-Cluster. Our experience shows that for the numerical problem at hand, the computation of up to several 100,000 gridblocks (finite volumes) is a practicable limit.

The principal idea of the new method presented here consists in the subdivision of the model domain, i.e., the repository and its host rock, including the underlying and overlying formations, into a number of individual 3D blocks, called "sectors." Each sector is then modeled using a conventional TOUGH2 mesh that represents the detailed geometry of the key materials within this sector. The size of the sectors is chosen such that the influence of the lateral boundaries on the hydraulic processes in the vicinity of the drifts is small. A sector allows the accurate local modeling of the gas-phase evolution in drifts and in the EDZs, the evolution of gas pressure, water pressure and water saturation in the drifts and cells, mass transfer from the drifts into the host rock (and vice versa), and mass transfer along the drifts, especially through the hydraulic barriers.

To model the hydraulic behavior of the entire repository during the post-operational period, all sectors are put together by means of hydraulic connections between the drifts present in each sector. This simple approach relies on the assumption that the vertical lateral boundaries of the sectors at some distance of the drifts can be considered no-flow boundaries or, in other words, that the capacity for lateral fluid transport along the drifts outweighs (by far) that for lateral fluid transport in the host rock. This is in fact justified for usual parameter values of backfill materials and the host rock. This does not hold, however, for the thermal evolution of the repository, because the dominant heat transport process in a repository in

a clay formation is heat conduction. Yet for sectors in which the lateral extent is large in comparison to the thickness of the host rock—which is the case for the current repository design—the thermal evolution in waste emplacement areas can be adequately modeled as well.

The key steps of the new method are (Figure 3):

- Subdivision of the repository plane into a large number of "sectors" based on the position of seals and on geometrical considerations (e.g., different drift types or dimensions). Each sector represents a 3D block of the geological pile (host rock and adjacent formations) and the repository components, like (for example) access drifts, sealed drifts, and emplacement cells.
- The existing symmetries (inside or between sectors) are used to reduce the number of gridblocks to be computed. In addition, the horizontal position of drifts is changed slightly to create additional symmetries.
- A "multiplying concept" is used in particular for the approximation of a series of emplacement cells along access drifts, as well as of a series of waste emplacement areas ("modules"; for example, see Figure 1). This concept has been justified by preliminary simulations, partly with detailed geometrical models, which showed that the pressure gradients along the handling and access drifts are very small.
- Several sectors are grouped to form a "zone" (e.g. a unit of high-level waste or a unit of intermediate level waste) by hydraulic connections at the drift interfaces. This enables the detailed geometrical representation of the individual sectors inside a zone (e.g., emplacement cell and portion of the access drift for the high level waste area).
- Interconnection of all zones at drift interfaces to form the model of the entire repository.

This approach is very flexible, since its modular structure allows the modeler to compute and test different configurations of the repository, as well as spatially different degrees of spatial discretization.

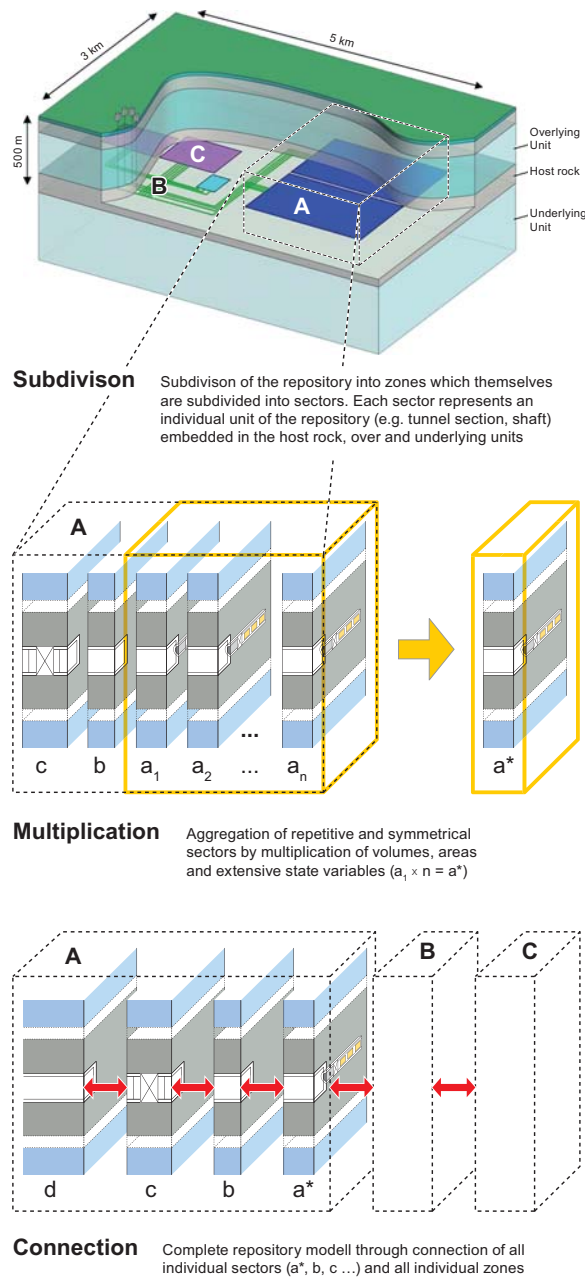


Figure 3. Schematic of the methodology for spatial discretisation: Subdivision into zones and sectors, multiplication and connection

Temporal evolution

The lifetime of the repository is modeled in 3 different phases:

- Phase 1: Instantaneous construction of all underground structures (drifts, cells, etc.) and ventilation at prescribed levels of relative humidity, pressure and temperature.
- Phase 2: Instantaneous emplacement of the waste and seals in emplacements structures. Ongoing ventilation in access drifts. Depending on the type

of waste (i.e. repository area), this phase has a different duration which is taken into account in the simulation.

- Phase 3: Postclosure phase. Instantaneous and simultaneous emplacement of backfill materials and seals in all drifts, caverns and shafts. Beginning of heat emission and gas production.

For Phases 1 and 2, the different sectors are modeled individually; for Phase 3, all sectors are connected.

MODELING AND RESULTS

This chapter describes the application of the method presented above to form a TOUGH2 model and shows some key results. The model is based on parameters, initial and boundary conditions within the possible value range for the envisaged repository as planned by ANDRA.

Not all chosen parameter values conform to the reference values; hence, the magnitude of fluxes and pressures presented below should not be considered as the reference for the HAVL-repository planned.

Layout, Geometry, Meshes, Physical Parameters, and Code

The model domain has a vertical extension of about 2000 m, which represents the thickness of the Callovo-Oxfordian Clay formation (130 m) and the over- and underlying formations. A schematic plan view of the model's general layout with zones and sectors is presented in Figure 4. The four zones considered are: the disposal zones for high-level waste (HA and CU3), the disposal zone for intermediate level waste (MAVL), the zone containing the infrastructure facilities and the shafts (PUDE), and the zone containing the primary access drift network (GLP). The individual zones are multiplied as follows to form the entire repository model: Zone HA by a factor of 4, zone GLP by a factor of 2, Zone MAVL by a factor of 2, the shafts [uw] by a factor of two.

Seals are located in the repository at different locations to hinder flow along the drift system. Seals between groups of sectors are modeled as individual sectors, discretized using hexahedral bricks. Shafts are discretized using axially symmetric blocks. Typical meshes used for the majority of sectors are presented in Figure 5.

The mesh generation and the connection of all sectors to form the complete model are performed using Python scripts, which allow a high degree of flexibility. In case of a rectangular representation of a radial feature, areas are scaled to the correct dimensions. The total number of elements in the model presented is about 40,000.

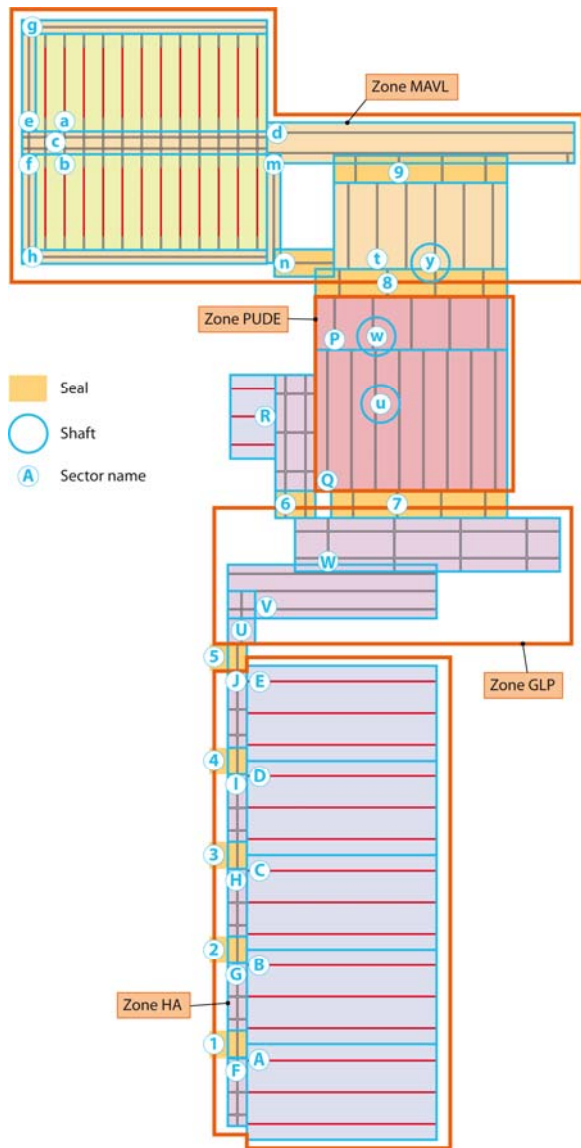


Figure 4. Schematic of a generic plan view of a part of the repository, with indication of zones (orange) and sectors (blue)

Characteristic flow parameters for a selection of materials are presented in Table 1. They show the large range of permeability and capillary-pressure values of the different materials, which indicates the high degree of complexity for numerical simulations. The two-phase flow parameterization of the relative permeability capillary pressure saturation constitutive relationship after van Genuchten–Mualem is used. Simulations were conducted with TOUGH2-MP (EOS5) for a simulation period of 1 million years. Computation time was about 16 h on 6 processors.

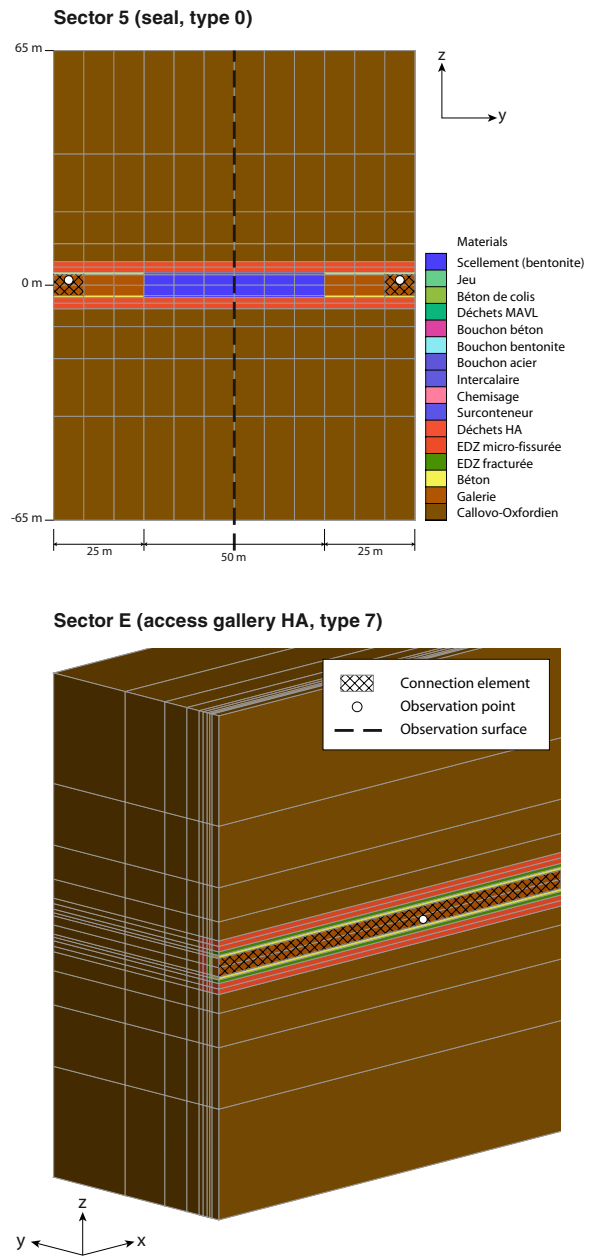


Figure 5. Typical meshes (3D blocks) used for the discretisation of each sector. Profile through bentonite plug (top), 3D view of HLW access gallery (bottom).

Table 1. Selection of characteristic material parameters for the simulations

	Waste Package (MAVL)	High performance cement (waste overpack)	Micro-fissured EDZ	Undisturbed Clay
Porosity ϕ [-]	0.3	0.15	0.18	0.18
Permeability k [m^2]	10^{-15}	$5 \cdot 10^{-19}$	$5 \cdot 10^{-18}$	$k_v=5 \cdot 10^{-21}$ $k_h=5 \cdot 10^{-20}$
van Genuchten coefficient n [-]	1.49	1.54	1.49	1.49
van Genuchten pseudo gas entry pressure P_0 [Pa]	$1 \cdot 10^4$	$2 \cdot 10^6$	$2 \cdot 10^6$	$1.5 \cdot 10^7$

Initial and Boundary Conditions

The rock mass is assumed to be fully water saturated at the start of the simulation. A hydraulic pressure gradient and a geothermal gradient are established. At the upper and lower boundaries of the host rock, two boundary conditions acting simultaneously are imposed. The first boundary condition is a constant pressure boundary condition, which corresponds to the hydraulic heads of the aquifers above and below the clay formation. The water saturation is set to 1, the hydrogen concentration is set to 0. The second boundary condition consists of 1D rock piles representing the adjacent formations of the host rock with constant temperature boundary conditions at the end of each pile. They correspond to surface atmospheric conditions and geothermal conditions at 3,000 m below ground level, respectively. The first boundary condition is practically impermeable to heat, the second one is impermeable to mass. All vertical boundaries are no-flow boundaries.

Results

Some selected results and the main characteristics are presented in the following figures.

Figure 6: Evolution of the gas pressure inside the backfilled drifts located in the zones HA, MAVL and GLP/PUDE. In Zone HA, the pressures culminate at 5.9 MPa in Sectors A–D and at 5.6 MPa in Sector E at around 5,000 years, and a second maximum at about the same level is reached after about 20,000 years. The gas phase disappears in the drift of the HA zone after around 80,000 years. In the MAVL zone, a first pressure peak is observed at around 500 years, the maximum is then reached after 10,000 years at around 6.5 MPa, and remains at this level for almost one century. The gas phase disappears in the drift of the MAVL zone after 200,000 years. In the GLP/PUDE zone, a similar evolution as in the MAVL zone is observed.

Figure 7: Evolution of the water saturation inside drifts located in the zones HA, MAVL and GLP/PUDE. The general evolution is a gradual resaturation that slows down after the gas pressure has reached its maximum values. For the MAVL and GLP/PUDE zones, even a slight desaturation occurs at times between 10,000 and 200,000 years.

Figure 8: Ribbon plot of the evolution of the mass of hydrogen in all the zones of the repository. For the purpose of a better visualisation, all mass sourcing from Zone HA are depicted as negative values, all mass sourcing from zone MAVL are positive. This plot shows in particular the amount of mass that transits through the different zones of the domain. The amount of hydrogen mass leaving the repository through the shafts is small in relation to the total mass produced.

Figure 9: Evolution of the cumulated hydrogen mass in sector E of Zone HA, of the cumulated outflow of hydrogen from sector E into the adjacent seal J (i.e. into the GLP zone), into the overlying aquifer (Oxfordien) and into the underlying aquifer (Dogger). In the long term, the hydrogen leaves the domain primarily by diffusion (as dissolved hydrogen) into the under- and overlying aquifers.

Figure 10: Evolution of the hydrogen fluxes from Zone HA to Zone GLP and from Zone MAVL to Zone PUDE. It shows that these fluxes vanish at different times: First, the flux coming from zone HA (5→U) at around 40,000 years, then much later the flux coming from Zone MAVL (8→P) at around 200,000 years.

CONCLUSIONS

A new methodology has been developed for repository-scale modeling of long-term hydraulic perturbation induced by gas and heat generation in a geological repository for high- and intermediate-level radioactive waste. It is based on the concept of subdivision into individual sectors, multiplication of sectors and (re-)connection of sectors by taking advantage of the symmetries in the repository layout. The script-based implementation enables a flexible and very efficient computation of the global hydraulic system behavior of the repository throughout its complete lifetime. A generic case was presented that demonstrates the power, flexibility, and computational efficiency of the developed method. The method can easily be applied to different repository layouts, and it can be run with geometrically more detailed submodels. It is currently being used in an ongoing project that investigates the hydraulic evolution of a realistic repository for different scenarios.

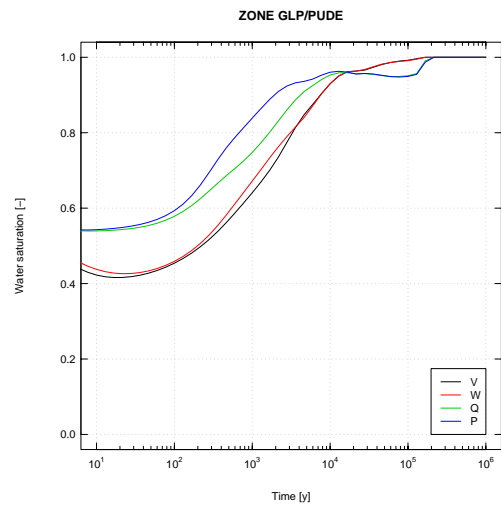
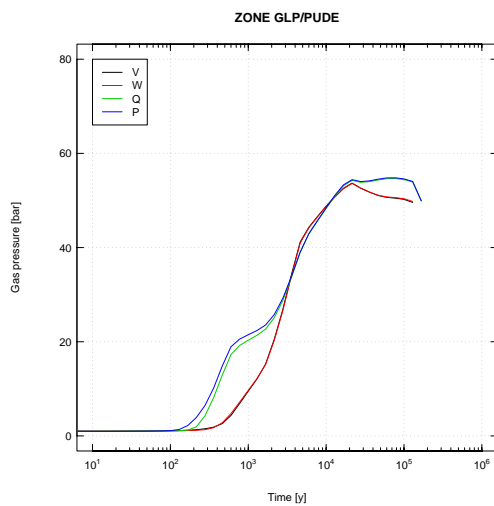
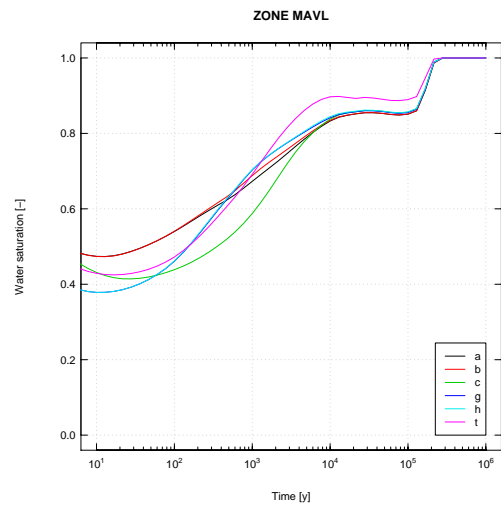
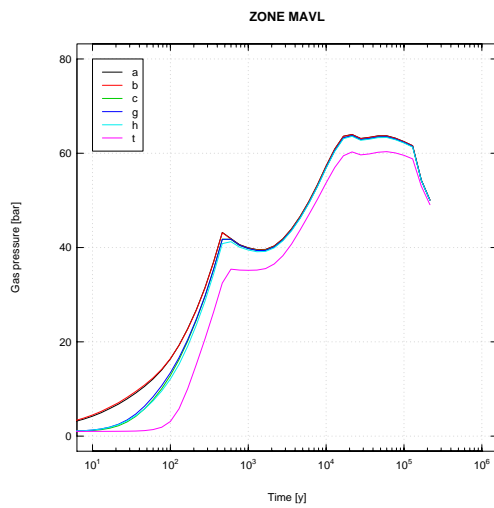
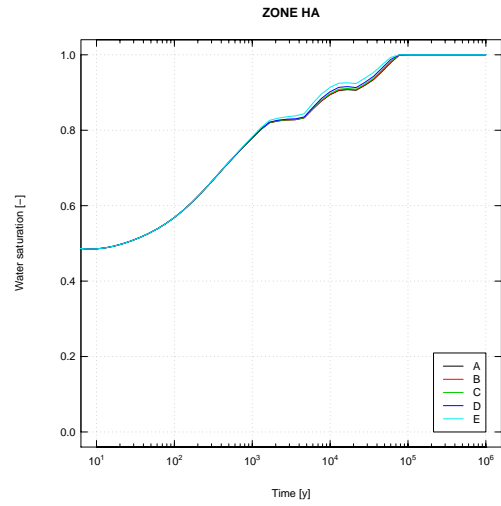
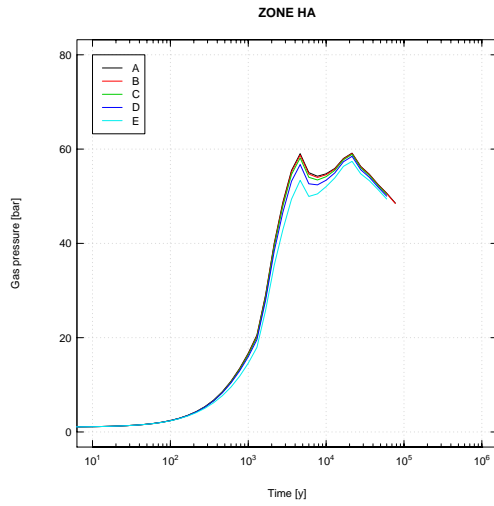


Figure 6. Evolution of the gas pressure at different locations in the repository

Figure 7. Evolution of the water saturation at different locations in the repository

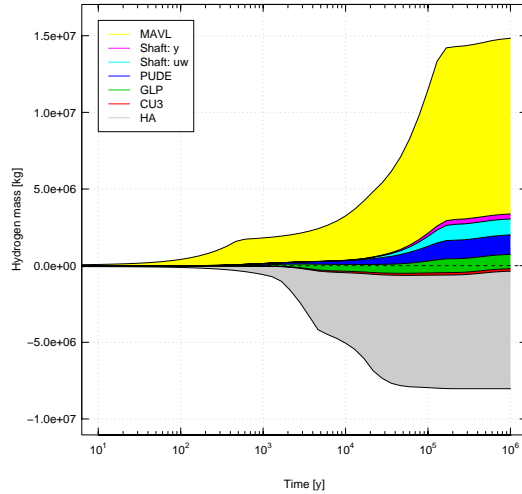


Figure 8. Temporal evolution of the cumulative H_2 mass for all zones of the repository (including the mass leaving the clay formation through the under- and overlying formations)

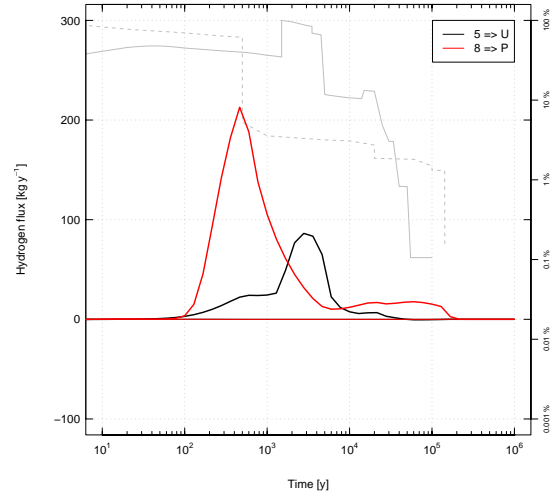


Figure 10. H_2 fluxes between different repository zones (red and black curves, left y-axis) and relative gas generation rate (grey: dashed line MAVL, continuous line HA, right y-axis)

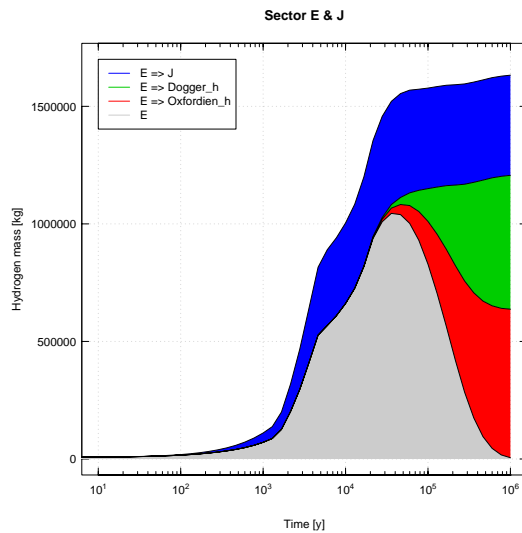


Figure 9. Temporal evolution of the cumulative H_2 mass generated in sector E (zone HA), with outflow towards sector J and the under- and overlying aquifers

REFERENCES

ANDRA: Dossier 2005 Argile, les recherches de l'Andra sur le stockage géologique des déchets radioactifs à haute activité et à vie longue, collection les Rapports, ANDRA, Châtenay-Malabry, France, 2005.

Pruess K., Oldenburg C. and Moridis G.: *TOUGH2 User's Guide, Version 2.0*, Report LBNL-43134, Lawrence Berkeley National Laboratory, Berkeley, Calif., 1999.

Zhang, K., J. Croisé, G. Mayer: *Modeling Studies of Gas Flow and Groundwater Pressure buildup for a Vitrified Nuclear Waste Disposal Site*, Proceedings of TOUGH Symposium 2009, Berkeley, California, 2009.

Zhang, K., Wu Yu-Shu, Pruess K.. User's guide for TOUGH2-MP – A Massively Parallel Version of the TOUGH2 Code, Report LBNL-315E, Lawrence Berkeley National Laboratory, Berkeley, Calif., 2008.

THERMO-HYDRAULIC ANALYSIS IN CASE OF GAS GENERATION IN A DISPOSAL FACILITY FOR VITRIFIED HIGH-LEVEL RADIOACTIVE WASTE IN BOOM CLAY

Janez Perko, Eef Weetjens, and Li Yu

SCK•CEN
Boeretang 200
2400 Mol, Belgium
e-mail: jperko@sckcen.be

ABSTRACT

The long-term safety of nuclear waste disposal is an important issue for all countries with a significant nuclear program. Repository disposal in deep geological formations is a promising option for managing high-level radioactive waste. The long-term safety of such a repository relies on a multibarrier system, including engineered and natural barriers, which should be evaluated for any anticipated factor that could have negative consequences on their performance. Specifically, assessment of gas generation and transport is a necessary part of a high-level radioactive waste (HLW) geological disposal facility safety assessment. Recent reports dealing with disposal of HLW and spent fuel have confirmed that anaerobic corrosion, which produces H₂ gas, will be the main contributor to gas production in the repository near field (Weetjens et al., 2006). In the case of disposal in low-permeability plastic clay formations, such as Boom Clay in Belgium, it is important to assess whether gas production rates can exceed the capacity of the near field to store and/or dissipate these gases.

The focus of this work is on coupling two-phase water and H₂ gas flow with a heat source originating from the heat-dissipating waste. The corrosion process and hence the intensity of the gas source is temperature dependent. The heat source is time dependent, owing to the decaying nature of the radioactive material. This property, in turn, makes the gas generation rate time dependent as well. The case presented in this work couples variable gas generation with a time-variable heat source. Due to large uncertainties related to the engineered materials to be used, two bounding-material permeabilities are chosen for comparison. Results demonstrate that the peak pressures for the isothermal and nonisothermal cases do not differ considerably in the case of high-permeability material. On the contrary, peak pressure differences are larger for low-permeability material, due to the thermal expansion of water as temperature increases. The analysis showed that the effect of pressure increase remains relatively local and should not affect the mechanical properties of the host Boom Clay formation. In the last part, we show the effect on hydrogen solubility at increased temperature. For this analysis, TOUGH2 (Pruess et al., 1999) had to be

modified, because the solubility of hydrogen is tabulated up to 25°C only, whereas the temperature in our case reaches 90°C. The function fitted to experimental hydrogen solubility data as a function of temperature is manually inserted into TOUGH2 source code. This increased its versatility considerably.

INTRODUCTION

Gas generation in the case of HLW geological disposal is in general not desirable, but due to several processes—including anaerobic corrosion of steel components, radioactive decay, radiolysis, and microbial activity—it cannot be avoided. Anaerobic corrosion of the steel engineered barrier system (EBS) is deemed to be the main contributor to gas production (Mallants et al., 2004). The gas originating from the anaerobic corrosion of steel components is hydrogen. When the gas production is sufficiently slow, gas can be completely dissolved in water and diffused away from the source. On the other hand, a high gas-production rate might result in a pressure buildup within the facility that can have two possibly detrimental effects: (1) it can cause engineered barriers to crack, thus providing a potential preferential water pathway, and (2) potentially contaminated water can be expelled from the disposal facility into the host formation. Apart from gas production, temperature also plays a role in the overall assessment. Temperature change affects most of the physical properties, such as viscosity, solubility, and thermal dilatation of water and surrounding host rock.

One of the most challenging issues in the calculation of such complex problems is dealing with uncertainties, including parameter uncertainty. The most sensitive parameters are the ones characterizing gas generation and transport and are related to EBS and host material hydraulic properties and to gas source rate (Weetjens et al., 2006). On the other hand, the thermal parameters of Boom Clay (Van Cauteren, 1994) and the thermal source evolution (Put et al., 1992) are much better characterized for the analysis of the heat transfer. For the uncertainty analysis of hydraulic properties and gas source, two bounding values are taken forward for comparison,

which should be descriptive enough for the purpose of this exercise.

The intention of this paper is to combine the effects of gas and heat transport on pressure within the facility, and to identify any critical combinations of material properties that would lead to EBS damage and possibly to loss of system performance.

Here, we first describe the model and its conceptualization, and then we provide numerical results for the selected calculation cases. In addition to the results of thermo-hydraulic couplings, the sensitivity of Henry's constant to temperature is also tested. This part represents an extension to the existing TOUGH2 code, in which hydrogen solubility is tabulated only up to 25°C. This refinement shows the sensitivity of pressure to hydrogen solubility.

CONCEPTUAL MODEL

In Belgium, the Belgian radioactive waste agency ONDRAF/NIRAS recently selected a supercontainer concept as the preferred option for disposal of vitrified HLW in Boom Clay. The decision is based on a multicriteria analysis (ONDRAF/NIRAS, 2004). In the reference design, every two waste canisters are enclosed within a carbon steel overpack. This overpack will be inserted into a prefabricated cylindrical buffer based on ordinary Portland cement, enclosed by a stainless steel envelope as shown in Figure 1. The cylindrical cavity between the overpack and the buffer will be filled with a concrete filler, called 2nd phase concrete (liquid mortar or similar). The top of the buffer is closed by pouring concrete, which forms the sealing plug. Eventually, the annular void between the supercontainer and the disposal gallery lining will be backfilled with cementitious material (Wickham et al., 2005). It is assumed that supercontainers will be placed end-to-end (without a gap), and that the spacing between neighboring disposal drifts is 50 m.

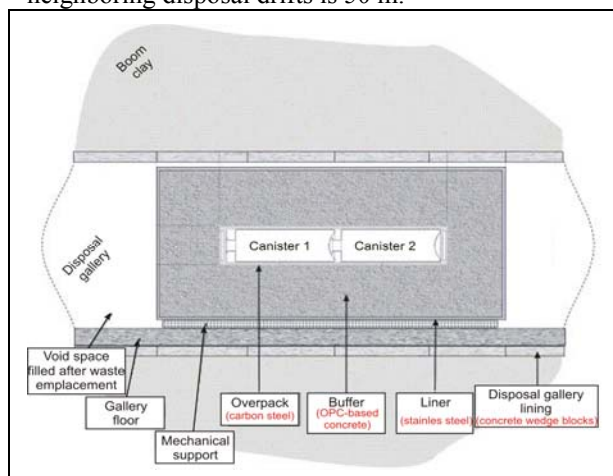


Figure 1. Longitudinal section of the supercontainer-OPC design

Numerical model

Based on the description above and neglecting the eccentricity and the mechanical support, one can simplify the geometry of the calculations to a 2D axis-symmetric grid, aligned with the axis of the gallery. Moreover, due to vertical symmetry, the model geometry can be reduced to one half of a supercontainer. The resulting model is shown in Figure 2. In reality, the disposal facility is assumed to be placed 220 m belowground. Our model, however, includes only 40 m of Boom Clay above it; the overlying aquifer is not included in the model. The interface between the top of Boom Clay and the overlying aquifer corresponds to infinite mixing in the large and permeable aquifer.

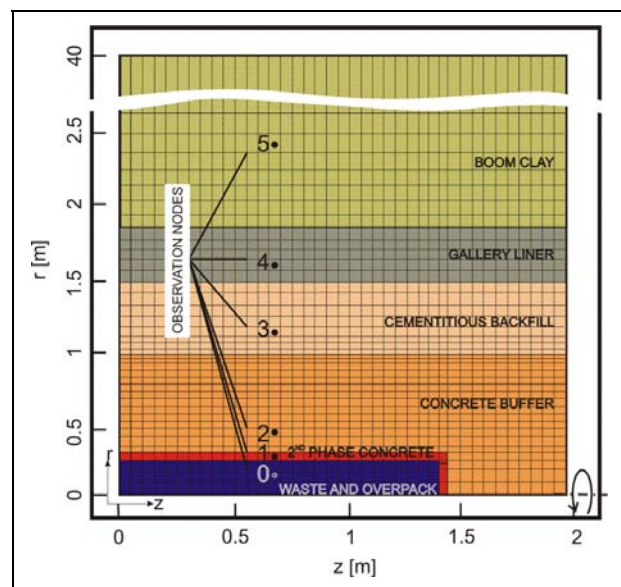


Figure 2. Axi-symmetrical model discretization with locations where the calculated primary values are recorded

Initial and boundary conditions

After supercontainer emplacement, the annular void spaces between the supercontainer and gallery lining will be backfilled with a cementitious material. Therefore, we assume that soon after disposal facility closure, all EBS will be initially at atmospheric pressure. A further assumption is that the pressure around the excavated Boom Clay remains at the hydrostatic pressure of 2.2 MPa. As such, the hydrostatic pressure is simplified in two ways: (i) water pressure will in reality follow the transition at the excavation boundaries, due to equilibration with an excavated tube, and (ii) hydrostatic pressure is constant throughout the domain, while a linear dependence with depth exists in reality. This simplification is used due to the axial symmetry of the model. Initially, the material is assumed to be fully saturated over the whole domain. This is

another simplification, because the Boom Clay will experience desaturation in the boundary layer due to excavation (Weetjens et al., 2008). Boundary conditions are as explained in Figure 3. The top boundary is set to a Dirichlet water pressure boundary condition with a value of 2.2 MPa. All other boundaries are Neumann pressure boundary conditions, also described as no-flow boundary conditions. Initial temperature is set at 15.7°C, which is the *in situ* temperature.

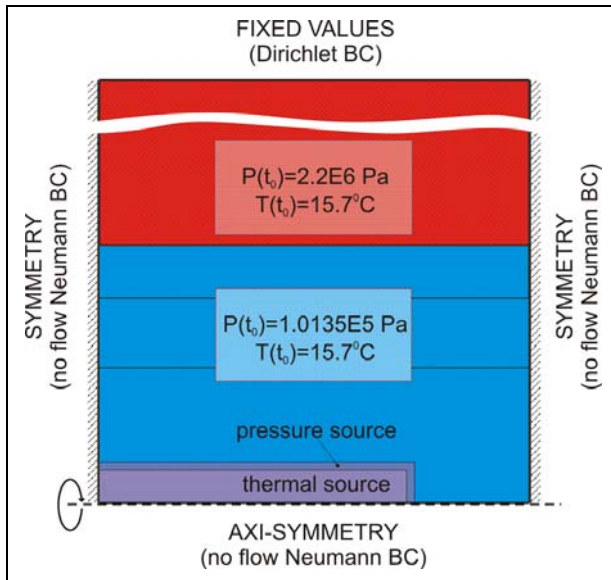


Figure 3. Initial and boundary conditions of the model

Source terms

The nature of the problem taken forward in this paper is a coupled thermo-hydraulic problem. As a consequence, pressure and heat sources need to be defined. Geometrically, however, the position of these sources is different. While the heat is generated in the waste region (denoted as thermal source in Figure 3), the pressure source is applied as a volumetric source within the second phase concrete. By nature, the pressure source should be defined as a boundary source originating from the overpack surface corrosion. Implementation of surface sources is not foreseen in TOUGH2. However, due to a relatively high permeability and small material thickness, the abovementioned adjustments to the source do not influence the results.

Thermal source

The heat produced by decay in the vitrified HLW is well approximated by a formula derived by Put (Put and Henrion, 1992). It can be written as

$$Q = \sum_i A_i e^{-\lambda_i t} \quad [\text{W/tHM}] \quad (1)$$

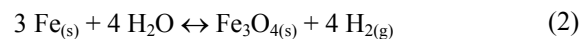
with the coefficients A_i and λ_i defined in Table 1 and t the time after waste production (i.e., vitrification). Put's formula is in good agreement with calculations made using the ORIGEN code and independent results from NAGRA (2002) and JNC, (2000). In the following calculations, a cooling time of 60 years was considered. For this reason ($t+60$) should be used in Equation (1). It is assumed that the amount of vitrified waste in canisters due to reprocessing of the spent fuel is 0.75% of the initial uranium mass. The source is implemented into TOUGH2 code by distribution of total heat over all thermal source elements in Figure 3.

Table 1. Coefficients for approximation of thermal source

A_1	A_2	A_3	A_4	A_5
5021	1205	27.04	0.7576	0.1
λ_1	λ_2	λ_3	λ_4	λ_5
$3.894 \cdot 10^{-1}$	$2.458 \cdot 10^{-2}$	$1.630 \cdot 10^{-3}$	$6.546 \cdot 10^{-5}$	0

Pressure source

There are many degradation reactions forming a variety of gas products. However, the dominant source of pressure is due to anaerobic corrosion of steel components and corresponding hydrogen production, as described above. Anaerobic corrosion is described here by the reaction that generates 4/3 mole of H_2 per mole of Fe, and involves production of magnetite, as written in Equation (2).



The evolution of hydrogen generation due to corrosion is highly concept dependent. First, the corrosion rate is dependent on local chemical conditions. Furthermore, the corrosion rate, and hence the rate of hydrogen production, is directly proportional to the exposed surface area of the steel EBS components. The steel-barrier thickness determines the duration of the gas generation process. Moreover, the surface area between the steel components and the surrounding porous media also determines how effectively the hydrogen can be dissipated by Fickian diffusion. Thus, the interplay of both phenomena determines whether gas will be accumulated in the near field or not. The pressure source term assumes a temperature-dependent corrosion rate enabled through an application of Arrhenius law. Temperature evolution in the second-phase concrete, to which the corrosion rate is linked, is calculated separately, because the link between thermal calculations and the gas source is not possible within TOUGH2 code. Two data points for the long-term uniform corrosion rate for anaerobic corrosion in a concrete environment (as a function of

temperature) were chosen from the literature: 0.1 $\mu\text{m}/\text{year}$ at 30°C and 1 $\mu\text{m}/\text{year}$ at 80°C (Kursten et al., 2004). Based on these data, a fit to Arrhenius law (3) is made.

$$k = A \cdot e^{\frac{-E_A}{RT}}, \quad (3)$$

with corrosion rate k [$\mu\text{m}/\text{year}$], fitting constant A [$\mu\text{m}/\text{year}$], activation energy E_A [J/mole], universal gas constant R [J/(mole \times K)] and temperature T [K]. The parameters E_A and the constant A were solved as variables to fit the given data points ($A=221475.4$ $\mu\text{m}/\text{year}$, $E_A=36153.41$ J/mole).

NUMERICAL EXAMPLES AND DISCUSSION

As described in the previous section, the analysis in this paper focuses on the coupled thermo-hydraulic problem for two bounding values of buffer permeability. The variation of buffer permeability is for two orders of magnitude, respectively from $4.6 \times 10^{-19} \text{ m}^2$ to $4.6 \times 10^{-21} \text{ m}^2$. The results will be given in terms of gas, capillary, and water pressure. Pressure analysis is important from the point of view of engineered-barrier mechanical stability and the host formation stability. Should the pressure approach or exceed the lithostatic pressure of the host formation, cracks could form, and further analysis and development of a more complex model would be required. The temperature is also an important factor that influences material properties and overall

behavior of the system, including dilatation. Another important material property is water saturation because of its relation to corrosion effects. For now, gas generation is based on the assumption that the corrosion rate is constant regardless of the saturation, although they might be linked because less water (required for the reaction in Equation (2)) is in contact with metal. These aspects, however, exceed the scope of the present paper. Desaturation is given indirectly in terms of capillary pressure denoted in graphs. Material properties used for the numerical analysis carried out are given in Table 2. Retention curve is defined by the van Genuchten (1980) formulation.

The first result shown in Figure 4 is related to the high-permeability case with a nonisothermal source. After 2.5 years, desaturation begins inside the second-phase concrete, where the source is located. Gas pressure reaches its peak at 20 years. Thereafter, gas pressure diminishes due to a decrease in the corrosion rate linked to temperature decrease. The end of the presence of a H_2 gas phase is at approximately 300 years. A capillary pressure (desaturation) is not observed at any observation element further from the source. This indicates the very localized effect of gas formation. The water pressure increase on the other hand is transmitted quickly outwards from the source. The maximal pressure is observed in the second-phase concrete, with a value of 2.85 MPa.

Table 2. Material parameters applied to the calculations

		Unit	Waste	Boom Clay	Lining	Backfill	Buffer	2 nd phase concrete
solid density	ρ_s	kg/m^3	7850	2650	2650	2650	2650	2650
porosity	η	-	0	0.391	0.104	0.3	0.104	0.3
permeability	k	m^2	0	$4.6 \cdot 10^{-19}$	$4.6 \cdot 10^{-17}$	$4.6 \cdot 10^{-17}$	$4.6 \cdot 10^{-19}$ ($4.6 \cdot 10^{-21}$)	$4.6 \cdot 10^{-17}$
Klinkenberg parameter	b	MPa	0	7.0	7.0	7.0	7.0	7.0
pore compressibility	β_p	MPa^{-1}	0	$7.50 \cdot 10^{-3}$	$3.83 \cdot 10^{-5}$	$3.83 \cdot 10^{-5}$	$3.83 \cdot 10^{-5}$	$3.83 \cdot 10^{-5}$
relative permeability curve								
shape parameter	λ	-		0.355	0.430	0.430	0.430	0.430
residual water saturation	S_{lr}	-		0.20	0.25	0.25	0.25	0.25
maximum water saturation	S_{ls}	-		1.00	1.00	1.00	1.00	1.00
residual gas saturation	S_{gr}	-		0.174	0.20	0.20	0.20	0.20
capillary pressure function								
shape parameter	λ	-		0.355	0.430	0.430	0.430	0.430
residual water saturation	S_{lr}	-		0.012	0.20	0.20	0.20	0.20
maximum water saturation	S_{ls}	-		1	1	1	1	1
shape parameter	α	m^{-1}		$3.47 \cdot 10^{-3}$	$1.96 \cdot 10^{-2}$	$1.96 \cdot 10^{-2}$	$1.96 \cdot 10^{-2}$	$1.96 \cdot 10^{-2}$
air entry pressure	P_0	MPa		2.83	0.50	0.50	0.50	0.50
heat transport								
thermal conductivity	λ_T	$\text{Wm}^{-1}\text{K}^{-1}$		1.7	1.7	1.0	1.7	1.0
specific heat	C_p	$\text{Jkg}^{-1}\text{K}^{-1}$		1100	800	800	800	800

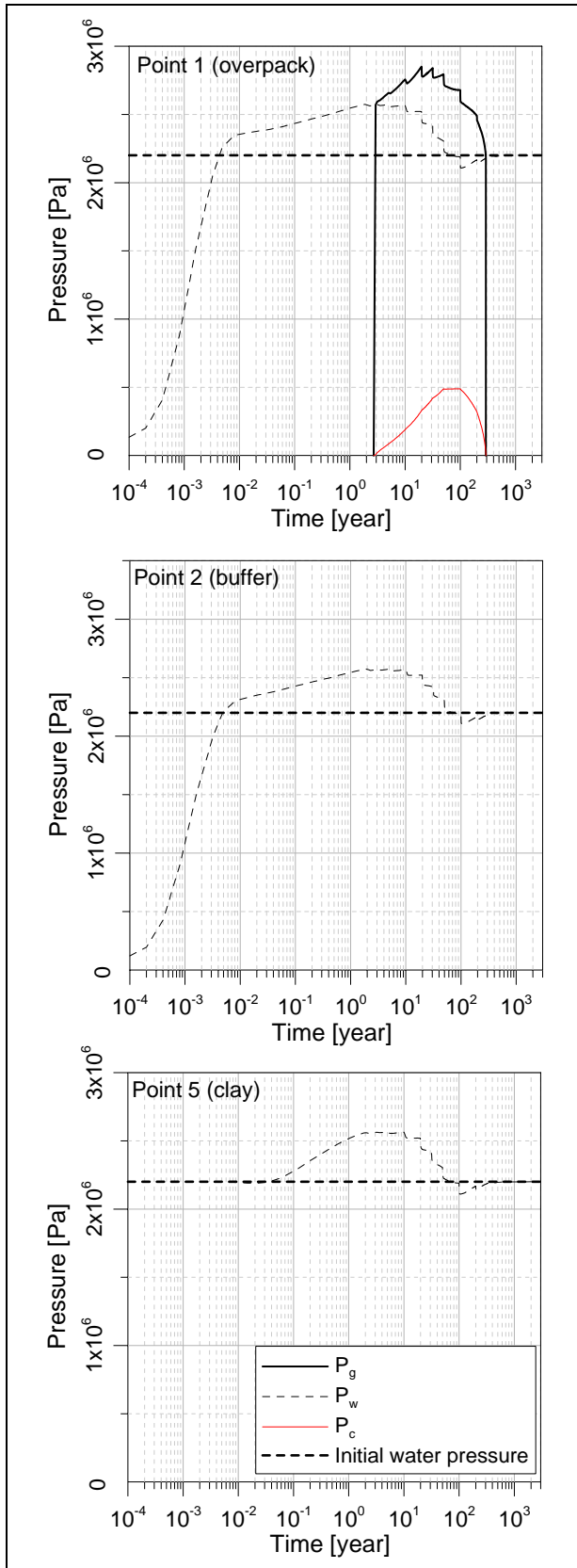


Figure 4. Pressure evolution in high-permeability buffer case

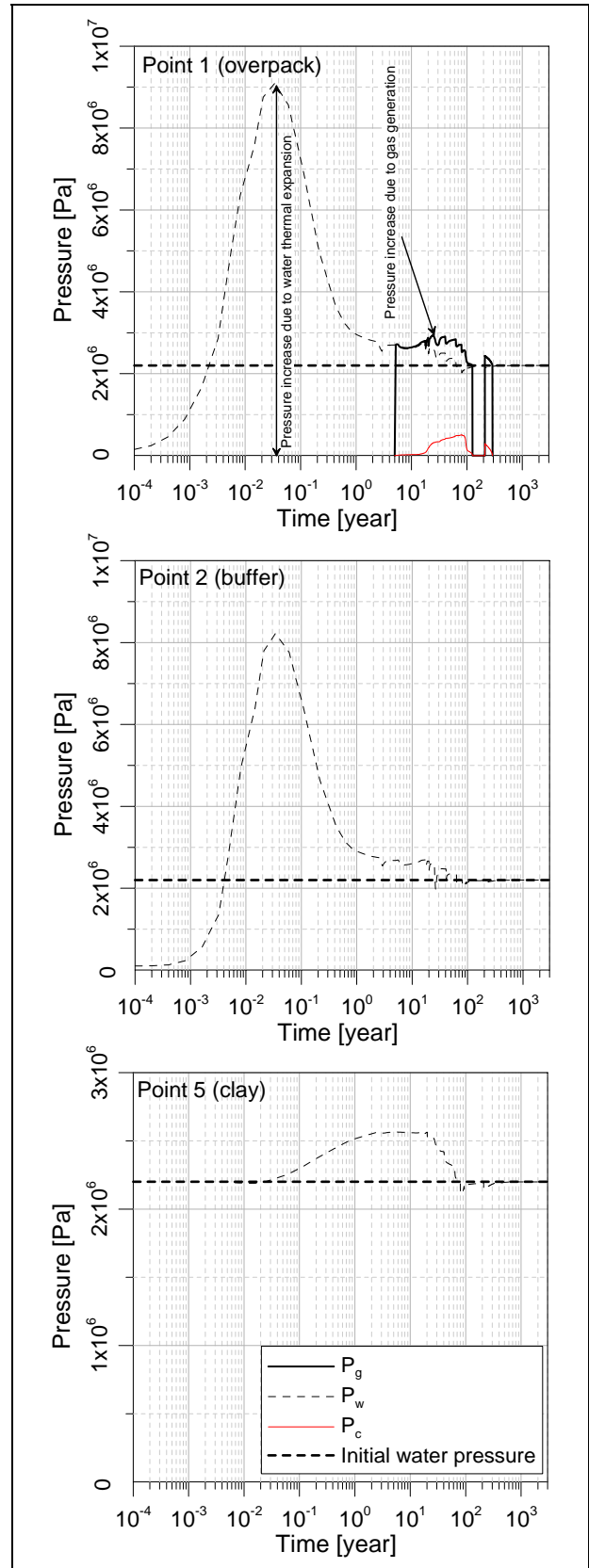


Figure 5. Pressure evolution in low-permeability buffer case

The second results are related to a low-permeability buffer concrete (i.e., 100x lower than that of Boom Clay) in combination with a heat source. In this case, it is expected that expanding water cannot be evacuated fast enough. Therefore, water expansion results in a high water pressure, corresponding to the temperature increase as indicated in Figure 5. It can be seen that very high water pressures exceeding 9 MPa are calculated in the vicinity of the thermal source very soon after. This pressure would damage engineered barriers, after which our present model is no longer valid (i.e., cracks formed in the concrete). The pressure in the Boom Clay (observation point 3) is similar to the high permeability case in Figure 4.

The last case is an extreme case, in which the heat source is applied in a saturated near-field environment. However, in the case of a low-permeability buffer, the EBS is unsaturated for the time period of 20–80 years (Weetjens and Perko, 2008). Upon saturation, the heat source term will already be considerably lower, and the water pressure increase due to water expansion would be less significant.

Effect of hydrogen solubility

Most of the parameters (e.g., diffusion and solubility) are temperature dependent. In the TOUGH2 code, the majority of the parameters are defined within the temperature range applicable to HLW disposal facility (up to 90°C), while the solubility of hydrogen in the pore water is defined only until 25°C, and a constant value is assigned for higher temperatures. The solubility is defined by Henry's law, which states that at a certain temperature, the amount of a given gas dissolved in a given type and volume of liquid is directly proportional to the partial pressure of that gas in equilibrium with that liquid. In the case of hydrogen production, the solubility defines the amount of hydrogen stored in water before the gas phase starts to form. The aim is to assess the influence of a more realistic temperature-dependent solubility, with literature values valid within the considered temperature range. Experimental values are obtained from Perry's chemical engineers' handbook (Perry and Green, 1984). From the experimental data, we derived the best fit in the form of function that was hard coded in the code. The best fit function derived is shown in Equation (4):

$$H(T)=a+b \cdot T+c \cdot T^2+d \cdot \exp(-e \cdot T), \quad (4)$$

where constants a, b, c, d and e are defined as $a=-6.88401 \times 10^{-10}$, $b=7.35462 \times 10^{-12}$, $c=-2.08518 \times 10^{-14}$, $d=8.59034 \times 10^{-10}$ and $e=1.07349 \times 10^{-2}$.

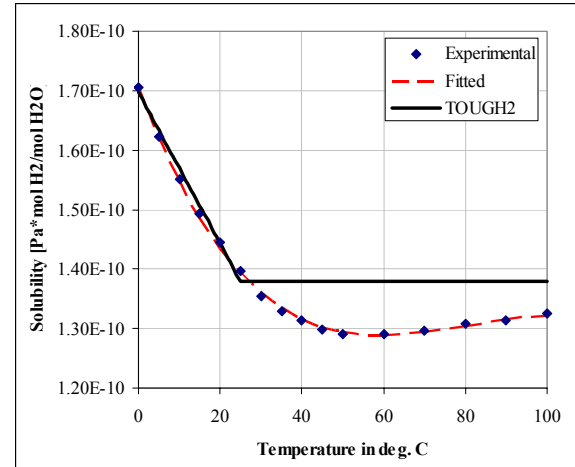


Figure 6. Comparison between solubility values used for comparison

Comparison between TOUGH2 formulation, experimental data, and fit is presented in Figure 6. The original formulation in TOUGH2 is obviously well approximated until 25°C, while major differences are observed at higher temperatures.

Numerical results are presented for two examples with a variable heat source, observed at observation point 1 (second phase concrete). The first example is with a high buffer permeability (Figure 7, top), and the second example is with a low buffer permeability (Figure 7, bottom). The results from the simplified linear relation with cutoff (TOUGH2) are plotted with a dashed line, while the new results from the fitted function in Equation (4) are represented with solid lines.

In the example with a high-permeability buffer material, differences in pressure evolution are negligible. Small differences are observed in the second-phase concrete, while no difference is noticeable farther from the source (not shown here). Larger differences are observed if a lower-permeability buffer is simulated (Figure 7, bottom). The peak pressure, which in this case is due to thermal expansion of the pore water, is slightly higher and occurs slightly later. The formation of a gas phase (after about 3 years) occurs earlier compared to the original TOUGH2 implementation. This can be explained by the lower solubility of gases with higher temperatures in the fitted equation (4). The difference between the original (simplified) and the improved solubility formulation diminishes with the distance from the source (results not shown).

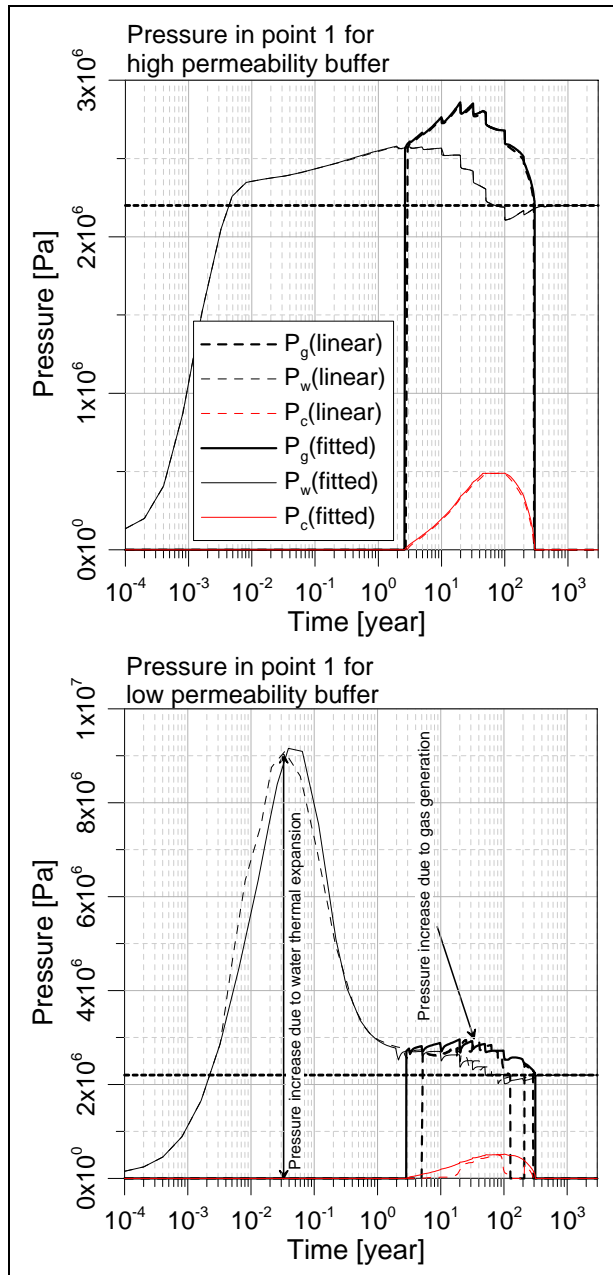


Figure 7. Pressure analysis for different solubility formulations.

In the low-permeability case, the peak water pressure (due to thermal expansion of water) close to the overpack reaches 9.09 MPa for the simplified formulation and 9.16 MPa in the improved solubility formulation, while the peak gas pressures reached 2.95 MPa in the simplified and 2.96 MPa in the improved solubility formulation.

For the high-permeability case, the difference is negligible and limited to 0.01 MPa: the gas peak pressures reach 2.85 MPa for the simplified and 2.86 MPa for the improved solubility formulation.

CONCLUSIONS

The results presented in this paper should not be regarded as absolute values, but rather as a sensitivity exercise with the intention to identify possible detrimental pressure conditions for the EBS and Boom Clay. In general, most previous analyses regarding an HLW disposal facility in the Boom Clay were carried out separately for each physical process, e.g., pressure analysis due to gas generation, temperature field due to heat generation, etc.

Taking into account coupled thermo-hydraulic relationships when analyzing the gas issue reveals that, assuming given conditions, the effect of the heat source on the resulting pressure might be much larger than the hydrogen production itself. The magnitude of pressure increase depends tightly on the respective permeability of the concrete buffer. Again, it is important to view the results in the correct perspective. The conceptual model in this analysis is still subject to serious limitations, and should be subject to further refinement. In addition to gaining better knowledge on permeability, the following properties should be thoroughly investigated: the corrosion reaction and resulting hydrogen production is considered to be independent from water saturation. Further, desaturation does not occur only due to partial gas pressure increase, but also because of water consumption (Equation (2)). This leads to further desaturation and, in turn, to a decrease in hydrogen production. One other property observed to have high impact on the sensitivity is the nature of the retention curve. Not only do the respective parameters of the van Genuchten equation play a major role in pressure evolution—so does the type of retention curve definition (van Genuchten, Brooks and Corey, ...).

In general, one can conclude that, based on the assumed corrosion rates, a free gas will be formed inside the container buffer, but the effect stays relatively localized and the integrity of the Boom Clay is not threatened. Also, high pressures resulting from a temperature increase in the waste stay localized, with only a minor water-pressure increase observed in the Boom Clay.

Implementation of an improved solubility dependence, valid for higher temperatures, showed that although the original equation expressing the temperature dependency of the hydrogen solubility in water implemented in TOUGH2 is very simplified, this simplification does not substantially influence the results. Differences, albeit small, are more pronounced for the low-permeability buffer case.

ACKNOWLEDGMENT

This work is partly undertaken in the framework of the EC-funded project PAMINA and partly as

support for the national Belgian program under the supervision, and with the financial support, of NIRAS/ONDRAF, the Belgian Agency for Radioactive Waste and Enriched Fissile Materials.

DISCLAIMER

The findings and conclusions in this paper are those of the authors and do not necessarily represent the official position of the Belgian Agency for Nuclear Waste and Fissile Materials ONDRAF/NIRAS.

REFERENCES

JNC, H12: *Project to establish the Scientific and Technical Basis for HLW Disposal in Japan*. Project overview report TN1410, JNC, Japan, 2000.

Kursten B., E. Smailos, I. Azkarate, L. Werme, N. Smart, G. Santarini. *COBECOMA: State-of-the-art document on the CORrosion BEhaviour of COntainer MAterials*. EC, Luxembourg, 2004.

Mallants, D. and D. Jacques, *Performance Assessment for Deep Disposal of Low and Intermediate Level Short-Lived Radioactive Waste in Boom Clay*. SCK•CEN, report R-3793, 2004.

NAGRA, *Calculations of the Temperature Evolution of a Repository for Spent Fuel, vitrified high-Level Waste and Intermediate Level Waste in Opalinus Clay*. NAGRA, Technischer Bericht NTB 01-04, 2002.

ONDRAF/NIRAS. *Multi-criteria Analysis on the Selection of a Reference EBS Design for Vitrified High Level Waste*. ONDRAF/NIRAS, Brussels, 2004.

Perry R.H. and D. Green. *Perry's chemical engineers' handbook. Sixth edition*. McGraw-Hill Co, 1984.

Pruess K., C. Oldenburg and G. Moridis. *TOUGH2 User's Guide, version 2.0*. Lawrence Berkeley National Laboratory, Berkeley, 1999.

Put, M. and P. Henrion. *Modelling of radionuclide migration and heat transport from an HLW-repository in Boom Clay*, EC, Nuclear Science and Technology, Luxembourg, EUR 14156, 1992.

van Cauteren, L. *Evaluatie van de warmtegeleidbaarheid en de warmtecapaciteit van de Boomse klei*. Nota ref. 250 94-0605. ONDRAF/NIRAS, Brussel, 1994.

van Genuchten, M.Th. A closed-form equation for predicting the hydraulic conductivity of unsaturated soils. *Soil Sci. Soc. Am. J.*, 44:892-898, 1980.

Weetjens, E. and J. Perko. *Performance assessment methodologies in application to guide the development of the safety case: Report on the first results of calculations on gas production and transport*. PAMINA M 3.2.2 Report, Revision 1, 2008.

Weetjens, E. and X. Sillen. *Mass and Energy Balance Calculations for the Supercontainer Concept*. Report, SCK•CEN, Mol, 2006.

Wickham S.M., M.B. Crawford and D.G. Bennett. *Belgian Supercontainer Design for HLW and Spent Fuel Disposal*. Evaluation of the Reference Design. Galson Sciences LTD, Oakham, 2005.

GLACIAL EROSION OF THE BENTONITE BUFFER

Matti Liukkonen and Markus Olin

VTT – Technical Research Centre of Finland
P.O. Box 1000, VTT Espoo, FI-02044 VTT, Finland

e-mail: Matti.Liukkonen@vtt.fi

ABSTRACT

According to the KBS-3 concept, the bentonite buffer is an essential part of a safe nuclear waste repository in the granitic bedrock. Glacial erosion of the bentonite buffer may occur due to potential intrusion of low-saline groundwater during the highly variable flow conditions following a glaciation period. The stability of the bentonite buffer is influenced by divalent cations, particularly pore-water calcium, present both in the bentonite pore water and in soluble minerals. As long as calcium containing minerals are present in the bentonite, calcium loss into fresh groundwater coming into contact with the bentonite can be replenished by the dissolution of these minerals. When a mineral is depleted near to the water flow interface, the gel may form a sol, which can be carried away by the groundwater flow. This exposes new gel to the water flow, and a steady state mass loss rate of the bentonite may be attained.

The main focus of this modeling study is on the changes in composition of the cation exchangers before and, especially, after a glacial period. The bentonite composition will change, to at least some degree, prior to the glacial period. The system will therefore reach a state of equilibrium during the different groundwater periods prior to the glacial period. From the point of view of preserving the beneficial characteristics (density and Na- content) of the bentonite buffer, it is essential to estimate whether the Na -bentonite will ultimately transform into mixed Ca/Na -bentonite.

The simulation results show that the colloid formation capacity remains low, even during the intrusion of glacial melt waters, since the cation exchanger changes from sodium to calcium one.

In this PetraSim simulation, a 1-D model of the composition of the cation exchangers was applied using the Gaines-Thomas model. The RESTART module was applied to simulating the long-term effects of groundwater and glacial melt water on repository conditions.

INTRODUCTION

The assessment relates to the KBS-3 disposal concept in which copper canisters with a cast-iron insert containing spent nuclear fuel are surrounded by

bentonite clay and deposited at saturation in granitic rock. Hedin (2006) A reference evolution of KBS-3 repositories over the entire one-million-year assessment period is studied to gain an understanding of the overall evolution of the system as a basis for scenario selection and analysis. After closure of the final repository, the groundwater composition is assumed to change from saline to brackish during the period prior to infiltration by glacial melt waters. As a base variant for the simulation, the external conditions during the first 125,000-year glacial cycle are assumed to be similar to those experienced during the last Weichesealian glacial cycle (Hedin, 2006)

In the Nordic region, deep underground final repositories for spent nuclear fuel will be affected by one or more glacial periods before their radioactivity falls to a level comparable to that naturally present in bedrock. The safety of these repositories relies to a large extent on the beneficial properties of the bentonite buffer surrounding the waste capsules. Glacial erosion of the bentonite buffer may occur due to the potential intrusion of very-low-saline groundwater following deglaciation (Hedin, 2006).

The infiltration of low-saline water may affect the colloid formation potential of the bentonite buffer. Thus, the density and swelling pressures of the bentonite buffer may change. The stability of the bentonite buffer against colloid formation is maintained by divalent cations, particularly calcium, as well as groundwater, pore water, exchangeable cations, and certain soluble minerals. As long as calcium-containing minerals are present in the bentonite, calcium loss into fresh groundwater coming into contact with the bentonite can be replenished by the dissolution of these minerals. When a mineral is consumed nearest to the flowing water, the gel may form a sol, which can be carried away by the groundwater flow. This exposes new gel to the water flow, and a steady-state mass loss rate of the bentonite may be attained (Liu, 2006).

BENTONITE BUFFER

The chemical stability of bentonite is largely dependent on the divalent cation concentrations in the pore water contained in the bentonite. When the bentonite initially contains divalent cationic minerals of relatively high solubility, such as gypsum or

anhydrite, the calcium cation concentration in the pore water will be buffered by the dissolution of these minerals and exceed the critical coagulation concentration for montmorillonite. When these calcium-containing minerals are depleted by diffusion into the passing water, the calcium concentration in the pore water of the bentonite may drop below the critical coagulation concentration for montmorillonite, and the gels may disperse into the water as colloidal particles and be carried away by the flowing groundwater (Liu, 2006).

As clay loss becomes extensive, the bulk density of the bentonite buffer will be noticeably reduced, and the buffer may lose some of its swelling capacity. The assumption of constant depth of clay intrusion into the fracture becomes no longer valid (Liu, 2006).

Under normal conditions, the uptake of water and resulting swelling of the bentonite buffer is counteracted by the walls of the deposition hole and, as a result, swelling pressure develops within the bentonite. Possible fractures intersecting the deposition hole may, however, commence swelling without the development of swelling pressure. Thus, part of the buffer could transfer to the aqueous phase and be transported with the groundwater (Hedin, 2006).

MODELING

A range of phenomena must be taken into account in the safety assessment of a spent fuel repository. Computational modeling is a useful tool for broadening understanding in this area. The main modeling interests in terms of different process classes of the bentonite buffer are: (i) minimization of hydraulic conductivity near the waste canister; (ii) maintaining the planned chemical conditions; (iii) delaying and limitation of the release of radionuclides; and (iv) limitations on the stresses acting on the canister (Olin et al., 2008).

The chemical conditions in the bentonite buffer within the repository are affected by temperature, the composition of the fluids, diffusion and advection phenomena, the surface area of minerals, and the texture of porous media. In addition, thermal gradients from the radioactive spent fuel have an effect, as well as alteration of the characteristics of the bentonite buffer and copper canister. Because of the great complexity of phenomena and processes, the coupled models for the evolution of the bentonite buffer have had to be simplified. An essential part of the assessment concerns the quantification of both repository evolution and dose risk consequences through mathematical modeling. Other key requirements of the assessment include appropriately defined models that represent proper

conceptualizations of the processes to be modeled, and quality assured input data (Olin et al., 2008).

The modeling concept is the infiltration of low-salinity glacial melt water into the bentonite buffer in a final deposition hole during a glacial period. The infiltrating low-salinity water alters the colloid formation potential of the bentonite buffer.

In the simulation, the grids of the EOS-1 module model were defined using the regular division method. The model used 21 calculation cells representing screw-like hole samples to describe the behavior of the water-bentonite interface and bentonite buffer. The length of each rectangular calculation cell was 17.5 mm and the height and width 35 mm. In the parameterization, the first cell on the right-hand side was selected to simulate a rock fracture with infiltrating water. The volume of the first cell was also set to infinite size to represent a large quantity of infiltrating water. The other cells were selected to simulate the bentonite buffer material, with its cation exchange properties and bentonite pore water. The bentonite is assumed to be fully saturated, and mass transfer is diffusive in isothermal 25°C temperature. All aqueous species present were selected for the simulation. However, surface complexes are not taken into account in the current PetraSim revision 4.2.1118. Therefore, it is assumed that the pH buffering capacity of the montmorillonite is not taken into account.

The transformation of the cation exchangers of the bentonite buffer in long-term nuclear waste deposition was simulated. Groundwater compositions in the cycles were selected according to the Weichselian R-scenario.

Saline groundwater was at first assumed to prevail for the next 10,000 years following closure of the system. The groundwater was assumed to correspond to Olkiluoto's current saline OLSO groundwater. The groundwater composition was assumed to become brackish over time due to land uplift, and the brackish groundwater period was assumed to last for up to 100,000 years. Its composition was assumed to correspond to Olkiluoto's current KR20 brackish/saline groundwater. Finally, following the glacial period, a 1,000-year period of dilute glacial melt water infiltration was assumed.

The exact composition and dwell times of the different groundwater types are relatively unknown. In the adjustment of the length of the time step, the diffusion rate is a limiting factor, since the time-step length should be in relation to the diffusion rate. Even a relatively short step causes an overflow error of the time and iteration step counters in the input files. However, since these have no effect on the output results, they were manually adjustable.

The Restart module of the PetraSim software was used for the simulations. This option allows the use of TOUGHREACT results from the end of a previous run, with the geological conditions used as initial conditions in a subsequent run. The Restart module was used in this simulation for the two later groundwaters: KR20 and glacial melt waters, after the initial OLSO water. (Pruess et al., 1999)

The maximum time step is proportional to the size of a grid cell, which strongly increases the time calculation with increased spatial resolution. To ensure that the time and space discretizations produce a physically correct solution, the time-step size must at least respect a “Neumann” criterion:

$$N_{Neuman} = \frac{2D_p \Delta t}{\Delta x^2} \leq 1 \quad (1)$$

where D_p is the pore diffusion coefficient ($D_p = \tau D_0$), in which (D_0) has a maximum value of $1E-9 \text{ m}^2/\text{s}$ in the bentonite system, and Δx (m) and Δt (s) refer to the space and time steps.

The dimensionless value N_{Neuman} is restricted by the condition $N_{Neuman} \leq 1$. In the current simulation, taking into account this criterion, a maximum time step of $1E6$ s was allowed for spatial discretizations of 17.5 mm in the model.

MODEL DATA

The bentonite used in the simulation is Wyoming type MX-80 sodium bentonite. Its properties correspond to Posiva’s plans for the final repository project (Pastina, 2006). However, there is significant variation in the content of minor accessory minerals, due partly to a lack of quality demands regarding specific accessory minerals in many commercial products (Karlund et al., 2006).

As Table 1 shows, the initial cation exchange equilibrium composition corresponds to MX-80 bentonite in accordance with the Gaines-Thomas model (Hedin, 2006; Pastime, 2006).

As Table 2 shows, the material properties of the saturated bentonite buffer correspond to the Posiva plans. The porosity was determined from the proposed dry density. The tortuosity was determined from the empirical relation of Ochs (2004). For diffusivity, free water-phase diffusivity was used. In this simulation, albite, calcite, cristobalite, gypsum, muscovite, and quartz are the primary minerals, and chalcedony and k-feldspar are the secondary minerals. The majority of the mineral kinetic data was derived from Palandri (2004). The chalcedony data was derived from Savage (2006).

Montmorillonite acts as an inert cation exchanger in the simulation.

Table 3 shows the accessory minerals of montmorillonite according to the Posiva data (Pastina, 2006; Hedin, 2006). The mineral volume fractions are derived from the mineral grain densities given in the THERMODDEM database (Blanc et al. 2007). Table 4 shows the cation exchange selectivity parameters for the thermodynamic model (Bradbury, 2003). Table 5 shows the assumed compositions of the different waters during the repository period. OLSO groundwater is used as the initial saline water (Laaksoharju, 2005), KR20 groundwater as the brackish/saline water (Wersin et al., 2007), and, finally, dilute glacial melt water (Andersson et al., 2007). The pH values of the waters were defined using the H_2O concentration and H^+ activity value in accordance with the PetraSim procedure. Figure 1 shows the glacial time scale of the modeled system.

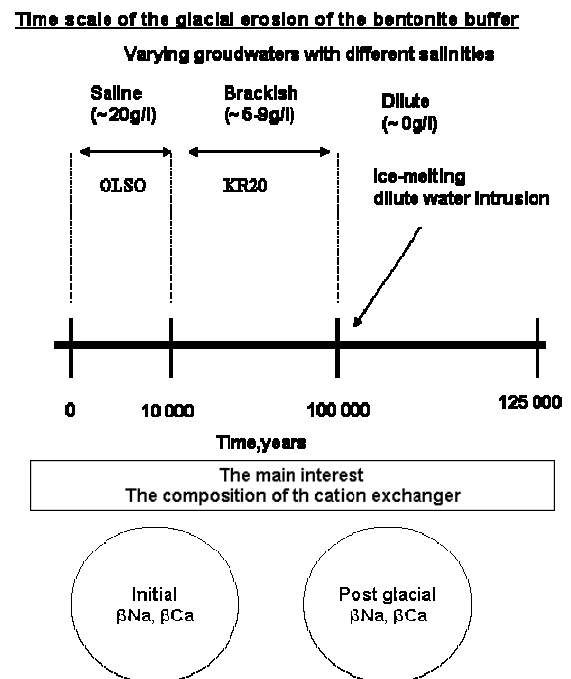


Figure 1. Glacial time scale

In the adjustment of the initial pore water composition of bentonite according to the composition of the cation exchangers, the Cl^- content of the solution is set low enough to hinder the formation of electrical imbalance. With this adjustment, the cation exchanger composition is derived for the desired cation formula, thus allowing the activity coefficients to be ignored. The initial composition of the pore water is consequently low, and the entire chemical system is balanced with low-ionic-strength pore water. Finally, the equilibrated bentonite pore water is placed in contact with the groundwater.

Table 1. Composition of the cation exchanger of Posiva MX-80 bentonite in equivalent fractions (CEC = 75 meq/100 g). Pastina (2006)

Na	Ca	Mg	K
0.72	0.18	0.08	0.02

Table 2. Material properties of the bentonite buffer Pastina (2006) Hedin (2006)

Quantity	Value
Density	2,737 kg/m ³
Permeability	2.75E-21 m ²
Diffusivity	1E-9 m ² /s
Porosity	0.424
Tortuosity	0.12

Table 3. Composition of MX-80 bentonite. Pastina (2006), Hedin (2006)

Mineral	Volume fraction	Grain size	Surface area cm ² /g
Albite	0.0314	0.001	9.8
Calcite	0.00303	0.001	9.8
Chalcedony	0	0.001	9.8
Cristobalite	0.0234	0.001	9.8
Gypsum	0.00831	0.001	9.8
K-Feldspar	0	0.001	9.8
Muscovite	0.0386	0.001	151.6
Quartz	0.031	0.001	9.8

Table 4. Cation exchange selectivity parameters for the thermodynamic model. Bradbury (2003)

Reaction	K	K PetraSim
$K + NaX = KX + Na^+$	0.60	0.251
$Ca^{2+} + 2NaX = CaX_2 + 2Na^+$	0.41	0.624
$Mg^{2+} + 2NaX = MgX_2 + 2Na^+$	0.34	0.676

Table 5. Composition, pH and ionic strength (I) of groundwaters and glacial melt water (mol/l).

	OLSO	KR20	Glacial
Na	0.21	0.11	6.5e-6
K	5.4e-4	2.8e-4	3.8e-6
Ca	0.1	0.03	3.3E-6
Mg	2.3E-3	2.6E-3	4.1E-6
Cl	0.41	0.18	2.3E-5
HCO ₃	1.6E-4	5.5E-4	4.9E-7
SO ₄ ²⁻	4.4E-5	2.1E-4	5.2E-7
SiO ₂ (aq)	4.1E-5	3.6E-4	1.7E-7
AlO ₂	3.7E-8	3.7E-8	3.7E-8
pH	7.2	7.4	5.8
I	0.515	0.218	3.34E-5

RESULTS

The composition of the cation exchangers in the initial conditions and in the subsequent restart simulations with different waters and cations are shown as a function of the length of bentonite buffer. In addition, the composition of the cation exchangers with different waters is shown as a function of time.

Saline groundwater (OLSO)

The OLSO groundwater is Na-dominated, with a Na/Ca molar concentration ratio of 2.1. As Figure 2 shows, after 10,000 years the initial Na- bentonite is transformed into a mix of virtually equal Na/Ca-fraction bentonite.

In the outer areas of the bentonite buffer, the transformation is much more pronounced, and the Ca-fraction clearly exceeds the Na- fraction. In this area, Ca accumulates and the Na -fraction remains relatively constant. Due to diffusion mass-transfer inertia, the composition distribution is unequally divided in the innermost areas of the bentonite. Here, the Ca- and Na- fractions are relatively equal. At the same time, the K - and Mg- fractions decrease to relatively insignificant fractions. In the outer area of the bentonite buffer, the decrease of K and Mg fractions is relatively strong.

Thus, according to the simulation results, the conditions are not favorable for the formation of colloids when the bentonite buffer is in contact with OLSO groundwater. However, bentonite of virtually equal Na/Ca -fraction may be prone to colloid formation if the repository conditions are not fully static.

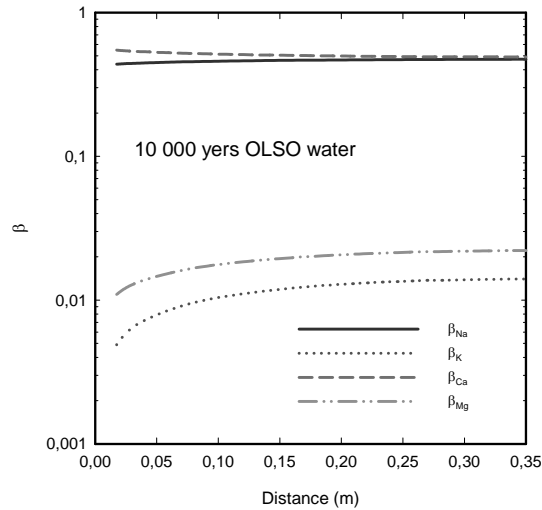


Figure 2. Equivalent fractions of cation exchangers with saline OLSO groundwater after 10,000 years

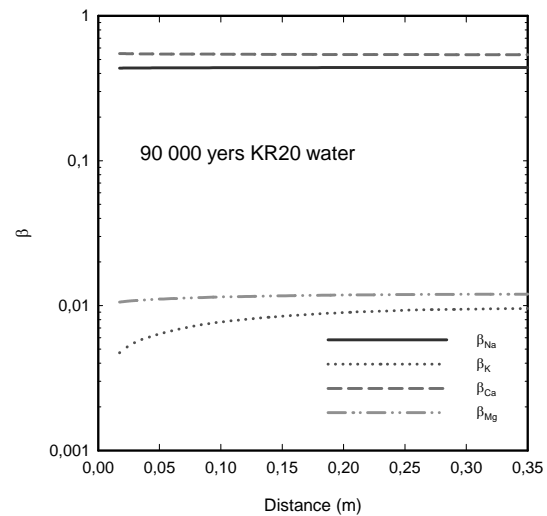


Figure 3. Equivalent fractions of cation exchangers with saline KR20 groundwater after 90,000 years

Brackish/saline groundwater (KR20)

Figure 3 shows the equilibrium fractions of the cation exchangers with saline/brackish KR20 groundwater. During long-term deposition, the groundwater composition is assumed to change from saline to saline/brackish. This is a relatively long time period, assumed to last until the end of the next deglaciation period. The brackish water was assumed to most likely correspond to KR20 groundwater. The brackish groundwater, with a Na/Ca molar concentration ratio of 3.7, is much more highly dominated by Na than the saline OLSO water.

By the time the infiltration of saline/brackish KR20 groundwater commences, the preceding OLSO groundwater will already have been equilibrated with the bentonite. The KR20 results show the Ca-fraction to exceed the Na-fraction throughout the buffer. Their flattened curves indicate the stagnant conditions relative to their change in composition. The equivalent fractions of the K- and Mg-cation exchangers are still insignificant. The curve of Mg shows stagnation, whereas the curve of K is relatively steep with assumed unfinished mass transfer.

According to the simulation results, the composition of cation exchangers is markedly Ca-dominated with brackish/saline groundwater. Thus, the probability of colloid formation is reduced. However, the simulation results with KR20 water show that the Ca-fraction of the exchangers has as divalent cation dominant role, since the high Na/Ca-molar concentration ratio could not change the virtually equal Na/Ca-bentonite to Na-bentonite.

Dilute glacial melt water

After the glaciation period, the groundwater composition finally converts to dilute glacial melt water with a Na/Ca molar concentration ratio of 2. The ratio is same as in the case of OLSO. Thus, the Ca-fraction can be assumed to dominate the composition of exchangers. The deglacial melt-water period is relatively brief. The cation exchangers of the bentonite will have been equilibrated by the preceding waters.

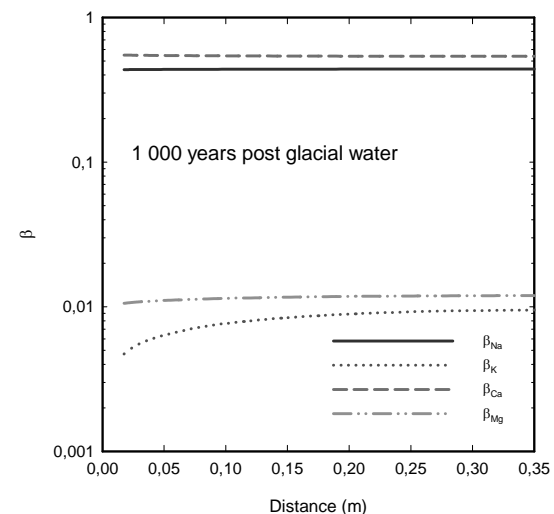


Figure 4. Equivalent fractions of cation exchangers after 1,000 years of post glacial water

Figure 4 shows the equilibrium fractions of the cation exchangers with postglacial water. The simulation

results are relatively similar to KR20 groundwater. The composition of the exchangers is Ca dominated. The composition curves of the cations are stagnant, with the exception of K. The curve of K is relatively steep; mass transfer can thus be assumed to be unbalanced. However, the compositions of K and Mg are, in this case relatively insignificant as well. Their composition also remains relatively unscathed

compared with the previous brackish groundwater simulation.

According to the simulation results, the tendency for transformation of Na-bentonite into mixed Na/Ca bentonite remains with postglacial waters. Thus, the colloid formation probability remains low in the case of intrusion of dilute glacial melt waters.

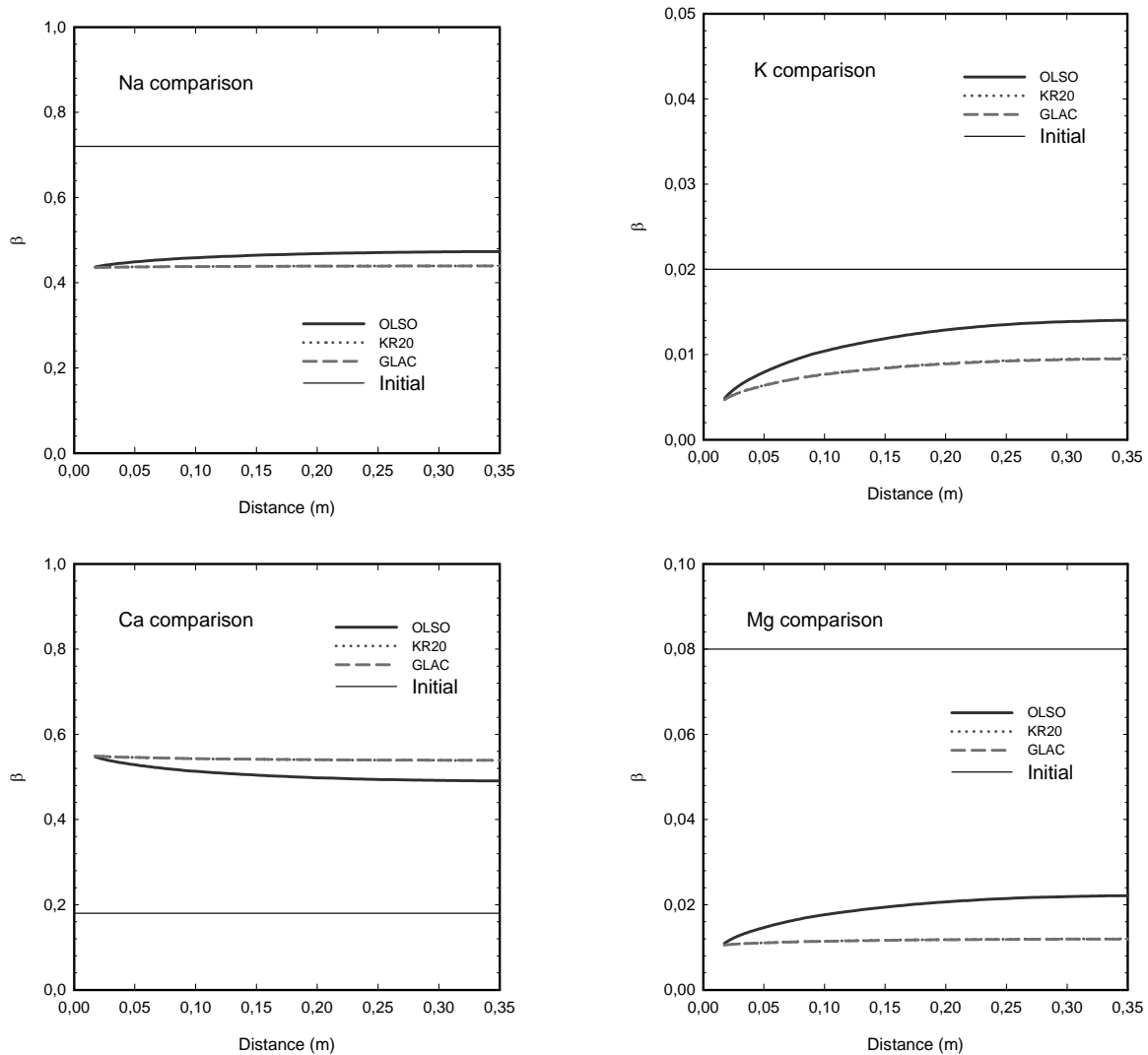


Figure 5. Equivalent fractions of cation exchangers for Na, K, Ca and Mg with different waters

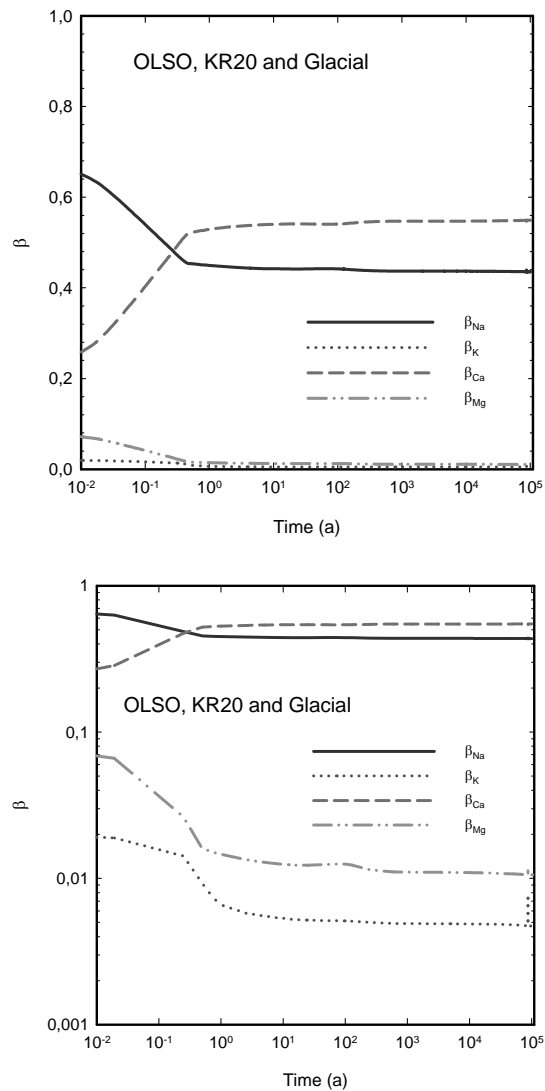


Figure 6. Ion-exchanger fraction near to the groundwater as a function of time. Top: linear fraction scale. Bottom: log scale. Note the log time scale for both figures.

Cation exchanger comparison

Figure 5 shows the equivalent fractions of the cation exchangers with different waters. The equivalent fraction of Na decreases strongly with OLSO water. Its values do not initially fall equally, and only at the end of glacial melt water period does the distribution appear to reach completion. The relative decrease in Na -fraction is high.

The equivalent fraction of K also decreases strongly with OLSO water, but the relative drop is not as large. The material change curve is relatively steep. Mass transfer appears to remain ongoing at the end of the glacial period.

Whereas the equivalent fraction of Ca also increases strongly during the OLSO water period, the changes stabilize by the end of the glacial period. The curve Ca -fraction flattens considerably, indicating stagnancy conditions.

The equivalent fraction of Mg decreases most dramatically of all during the OLSO water period. However, the decrease stagnates by the glacial water period.

The effect of time

The composition of the cation exchangers in the second simulation in the outer part of the buffer against the groundwater are shown in Figure 6 as a function of time. Initially, the Na- and Ca-fractions respectively decrease and increase relatively strongly. After slightly over half a year, the Ca-fraction exceeds Na. From here on, with all waters, the Ca-fraction dominates at the expense of Na.

The K-fraction decreases smoothly in two stages, reaching stagnancy within 100 years. The Mg-fraction undergoes a similar decrease, with changes in Mg-fraction reaching full stagnancy considerably later within 500 years.

CONCLUSIONS

The study simulated the changes in cation exchanger composition properties of Posiva's MX-80 Na bentonite during long-term repository conditions. The groundwater compositions varied from initial saline OLSO, to brackish/saline KR20, and finally to dilute glacial melt water.

According to the simulation, from the OLSO groundwater phase onward, Ca begins to relatively rapidly dominate the composition of the cation exchangers at the expense of Na, with the cation exchanger composition ultimately changing to correspond to mixed Ca/Na -bentonite.

The subsequent brackish/saline KR20 groundwater and dilute glacial melt water periods have only a slight effect on the cation exchangers compared with the end of the saline OLSO groundwater period. On the whole, the composition of the cation exchangers remains dominated by Ca from the beginning of the OLSO groundwater period to the end of the dilute glacial melt water period. The Ca dominated even with a higher Na/Ca-molar concentration ratio KR 20 water, due to its divalent cation charge.

Correspondingly, according to the simulation results, the other cations in the exchangers, K and Mg, have an insignificant impact on the composition of the exchangers, with even the initial value of the equivalent fraction of Mg being relatively high.

The transformation of the cation exchangers is relatively rapid in the outer part of the buffer, where it takes less than one year for the Ca-fraction to reach the Na-fraction. After this, the conditions stagnate despite changing water conditions.

The equivalent fractions of K and Mg become significantly low relatively rapidly. The fraction of K decreases relatively gradually, reaching stagnation within 100 years, whereas the fraction of Mg undergoes an initial strong decrease, reaching full stagnancy much later, not until 500 years.

The simulation results show that the colloid formation capacity remains low, even during the intrusion of glacial melt waters, since the cation exchanger changes from sodium to calcium. However, the transformation of Na-bentonite to mixed Na/Ca-bentonite is most acute in the outer parts of the buffer. Composition differences exist in the bentonite buffer due to slow diffusion mass transfer. During the OLSO water period, at least, the bentonite has relatively equal Na- and Ca-fractions. A possible consequence of this could be susceptibility to colloid formation if repository conditions are not static.

ACKNOWLEDGMENTS

The study was jointly funded by the Finnish Research Programme on Nuclear Waste Management (KYT2010). We extend warm thanks to Aku Itälä and Merja Tanhua-Tyrkkö for their kind assistance with the PetraSim simulation procedure.

REFERENCES

- Andersson, J., H. Ahokas, J. A. Hudson, L. Koskinen, A. Luukkonen, J. Löfman, V. Keto, P. Pitkänen, J. Mattila, A.T.K. Ikonen, M. Ylä-Mella, Olkiluoto site description 2006, Report POSIVA 2007-03, Posiva Oy, Olkiluoto, Finland, 2007.
- Blanc, P., A. Lassin, P. Piantone, THERMODDEM – A database devoted to waste minerals, BRGM, Orleans, France, 2007.
- Bradbury, M.H., B. Baeyens, Pore water chemistry in compacted re-saturated MX-80 bentonite, J. Contam. Hydrol. (1-4)61, 329-338, 2003.
- Hedin, A., Long-term safety for KBS-3 repositories at Forsmark and Laxemar – a first evaluation, Main Report of the SR-Can project, Technical Report SKB TR-06-09, Svensk Kärnbränslehantering AB, Stockholm, Sweden, 2006.
- Karland, O., S. Olsson, U. Nilsson, Mineralogy and sealing properties of various bentonites and smectite-rich clay materials, Technical Report SKB-TR-06-30, Kärnbränslehantering AB, Stockholm, Sweden, 2006.
- Laaksoharju, M., S. Wold, The colloid investigations conducted at the Äspö Hard Rock Laboratory during 2000–2004, Technical Report SKB-TR-05-20, Svensk Kärnbränslehantering AB, Stockholm, Sweden, 2005.
- Liu, J., I. Neretnieks, Physical and chemical stability of the bentonite buffer, Report SKB R-06-103, Svensk Kärnbränslehantering AB, Stockholm, Sweden, 2006.
- Ochs, M., C. Talerico, SR-Can, data and uncertainty assessment, Migration parameters for the bentonite buffer in the KBS-3 concept. Technical Report SKB-TR-04-18, Kärnbränslehantering AB, Stockholm, Sweden, 2004.
- Olin, M., M. Tanhua-Tyrkkö, V-M. Pulkkanen, A. Itälä, K. Rasilainen, A. Seppälä, M. Liukkonen, Thermo-Hydro-Mechanical-Chemical (THMC) Modelling of the bentonite barriers in final disposal of high level nuclear waste, COMSOL Conference, Hannover, Germany, 4 - 6 Nov., 2008.
- Palandri J.L., Y.K. Kharaka, A compilation of rate parameters of water-mineral interaction kinetics for application to geochemical modelling, Open File Report 2004-1068, U.S. Geological Survey, 2004.
- Pastina, B., P. Hellä, Expected evolution of a spent nuclear fuel repository at Olkiluoto, Report POSIVA 2006-05, Posiva Oy, Olkiluoto, Finland, 2006.
- Pruess, K., C. Oldenberg, G. Moridis, TOUGH2 User's Guide, Version 2.0, Report LBNL-43134, Lawrence Berkeley National Laboratory, Berkeley, Calif., 1999.
- Savage, D., D. Noy, M. Mihara, Modelling the interaction of bentonite with hyperalkaline fluids, Appl. Geochem, 17(3), 207-223, 2002.
- Wersin, P., M. Birgersson, S. Olsson, O. Karland, M. Snellman, Impact of corrosion-derived iron on the bentonite buffer within the KBS-3H disposal concept - the Olkiluoto site as case study, Report Posiva 2007-11, Posiva Oy, Olkiluoto, Finland, 2007.

THE USE OF TOUGH-FLAC FOR COUPLED HYDROMECHANICAL MODELING OF FRACTURED ROCK MASSES

Colin T. O. Leung¹, Jonny Rutqvist², Robert W. Zimmerman¹, and Andrew R. Hoch³

¹Department of Earth Science and Engineering, Imperial College, London SW7 2AZ, UK
c.leung08@imperial.ac.uk; r.w.zimmerman@imperial.ac.uk

²Earth Sciences Division, Lawrence Berkeley National Laboratory, Berkeley, CA 94720
jrutqvist@lbl.gov

³Serco TAS, Harwell Science and Innovation Campus, Didcot OX11 0QB, UK
andrew.hoch@serco.com

ABSTRACT

This paper presents the progress in development and application of TOUGH-FLAC for coupled hydro-mechanical modeling of fractured rock masses. The study is part of the international collaborative research project called DECOVALEX (DEvelopment of COupled models and their VALidation against EXperiments in nuclear waste isolation). The current DECOVALEX project includes a task aimed in part at simulating coupled fluid flow, transport and mechanical deformation in a two-dimensional (2D) 20 m × 20 m fracture network that is based on real data. We study this problem using three different model approaches based on TOUGH-FLAC and a discrete fracture network flow and transport simulator called NAPSAC. First, we use NAPSAC to provide a baseline flow simulation with exact representation of the discrete fractures. Using NAPSAC, we also perform a simplified coupled stress-flow analysis correlating fracture permeability to the stress field without a performing a full stress-strain analysis. Second, we use TOUGH-FLAC and a fine-scale regular mesh to conduct a full coupled hydromechanical analysis, but with a simplified continuum representation of discrete fractures. Finally, we intend to solve the problem using a dual-continuum representation of the fractured media in which NAPSAC is utilized to derive equivalent continuum properties. This paper describes the approaches and presents a few completed simulation results.

INTRODUCTION

An assessment of the performance of a geological disposal facility (GDF) for radioactive wastes needs to account for coupled thermal (T), hydrological (H), mechanical (M) and chemical (C) processes. Recognizing the importance of the topic, an international collaborative research project called DECOVALEX (DEvelopment of COupled models and their VALidation against EXperiments in nuclear waste isolation) was started in the early 1990s to develop and test models of coupled THMC processes in fractured rock. In DECOVALEX, different models for coupled THMC processes in fractured rock have

been tested against data from laboratory and field experiments, and applied to a number of benchmark test cases designed to be relevant for assessment of the performance of an underground disposal facility for radioactive waste.

The current phase of DECOVALEX, which is scheduled to run from 2008–2011, includes a task (Task C) aimed in part at simulating fluid flow and transport in a two-dimensional 20 m × 20 m fracture network based on real data (Figure 1). The rock mass will be subjected to various hydraulic gradients, as well as to various states of hydrostatic and deviatoric stress (Figure 2).

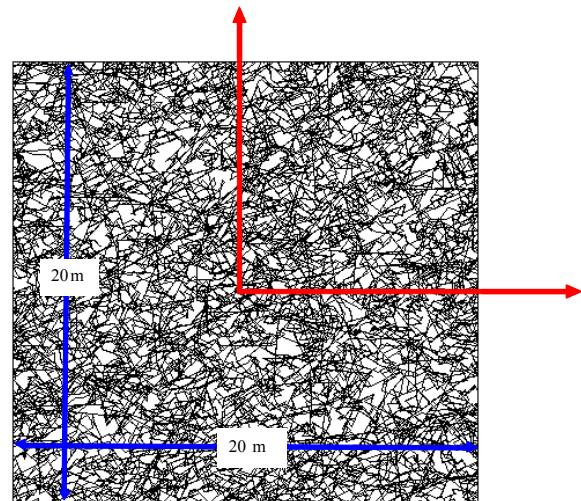


Figure 1. 2D BMT fracture network

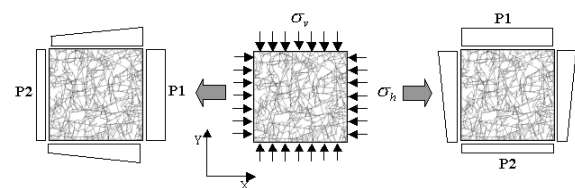


Figure 2. 2D BMT hydraulic and mechanical boundary conditions

In this paper, we present the test case, our modeling approaches, and some initial modelling results. We first present our use of NAPSAC, a discrete fracture network (DFN) flow and transport simulator, to predict the variation of hydraulic transmissivity with stress. NAPSAC assumes one-way coupling, in the sense that the imposed stress field changes the apertures of the individual fractures, but the displacement of the fractures does not alter the stress field. This is done by imposing a macroscopic stress at the outer boundary of the region, after which the fracture apertures, and hence their transmissivities, are modified in response to the normal and shear stresses that are projected from the macroscopic stresses onto the individual fracture planes. Various forms of coupling will be investigated.

We will compare the NAPSAC results with those obtained using a fine-scale TOUGH-FLAC model. This approach employs full coupling between the hydraulic behaviour, simulated within TOUGH, and the mechanical behaviour, which is handled by FLAC (Rutqvist et al., 2002, Rutqvist and Tsang, 2003). In these simulations, the model domain is discretized in a very fine regular continuum mesh, and the hydromechanical properties of each individual gridblock are adjusted depending on whether the gridblock is intersected by a fracture. Thus, we represent discrete features by adjusting the properties of the continuum element, and we may therefore denote such an approach as a discrete continuum (DC) model. Currently, we use NAPSAC to derive the permeability of each individual gridblock, and a simple reduction in stiffness and strength of elements along fracture traces.

Finally, we also intend to use a third approach, in which NAPSAC is first used to compute “effective” properties, which are then exported to a coarse-scale TOUGH-FLAC model for a dual-continuum representation of the fractured media. Ultimately, the predictions of these three approaches will be compared and critically contrasted.

THE BENCHMARK TEST

The test case, denoted Task C in the current DECOVALEX 2011 project, consists of a 2D Benchmark Test (BMT) of fluid flow and transport in a two-dimensional fracture network based on real data. The model parameters, including fracture and matrix data as well as mechanical and hydraulic boundary conditions, were prescribed by the project coordinators (Hudson et al., 2008).

Fracture System

The fracture system, consisting of 7767 fractures, is provided for each modeling team (Fig. 1). Each fracture is defined by two end points and an aperture.

The fracture lengths range between 0.5 m to more than 30 m. The apertures are correlated with the fracture lengths, following the equations described by Baghbanan and Jing (2007). Apertures in this fracture set vary between 1 and 200 microns.

Mechanical and Hydraulic Boundary Conditions

Fluid flow through the fracture system is driven by a constant pressure gradient of magnitude $\Delta P = 200$ kPa, imposed across the 20 m fracture network. The hydrostatic pressure at the centre of the model is 200 kPa. Gravity effects are not considered.

Shear stresses are induced by changing the ratio of the stress field applied along the vertical and horizontal boundaries of the fracture system. A uniform vertical stress of 5 MPa is specified at the top and bottom surfaces. A horizontal stress, with vertical/horizontal stress ratios of 1, 2, 3, and 5, is applied at the right- and left-hand side boundaries to induce shear within the fracture system.

DFN MODELING USING NAPSAC

The first set of calculations was carried out using the computer program NAPSAC (Serco TAS, 2008). NAPSAC is software to simulate flow and transport through fractured rock. The models are based on a direct representation of the discrete fractures making up the flow-conducting network.

NAPSAC fracture flow algorithm

NAPSAC can be used to simulate steady-state constant-density groundwater flow in a fracture network. The basic algorithm is very simple. Assuming the fracture transmissivity is related to the fracture aperture by the “cubic law” (Zimmerman and Bodvarsson, 1996), the flow in each fracture is determined numerically using a Galerkin finite-element approach. Then the flow in the overall network is obtained by combining the flows in the different fractures, using the constraints that:

- i. The groundwater pressure is continuous between two intersecting fractures.
- ii. Groundwater is conserved at an intersection, so that groundwater which flows out of one fracture flows into the other.

Full details of this algorithm are given in the NAPSAC Technical Summary (Serco TAS, 2008).

Normal Stress and Aperture Coupling

NAPSAC has built-in capabilities to calculate stress/aperture coupling. For example, it is noted from the program documentation (Serco TAS, 2008) that NAPSAC can model normal stress/aperture coupling using the following linear law:

$$e = \max \left\{ e_o - \frac{(\sigma - \sigma_o)}{k_n}, e_{\min} \right\} \quad (1)$$

where e is the aperture, e_o is the initial aperture, e_{\min} is the residual aperture, σ is the applied normal stress, σ_o is the initial normal stress, and k_n is the fracture normal stiffness.

For the 2D BMT, it is suggested that the stress/aperture coupling should be modeled according to the methods described by Baghbanan and Jing (2008). The normal stress and aperture coupling relationship in NAPSAC has been modified to comply with the specification of the 2D BMT.

The stress/aperture coupling suggested by Baghbanan and Jing is based on a hyperbolic relation defined in Bandis et al. (1983):

$$\sigma_n = \frac{k_{no} \delta}{1 - (\delta / \delta_m)} \quad (2)$$

where σ_n is the normal stress, k_{no} is an empirical parameter representing the initial normal stiffness, δ is the fracture closure, and δ_m is the maximum possible fracture closure.

The equation can be rearranged into

$$\frac{\delta}{\delta_m} = \frac{(\sigma_n / \sigma_{no})}{(\sigma_n / \sigma_{no}) + 1} \quad (3)$$

where $\sigma_{no} = k_{no} \delta_m$, and σ_n / σ_{no} is the normalised normal stress.

Baghbanan and Jing (2008) assumed that the minimum value of δ / δ_m is 0.9, when the corresponding value of σ_n / σ_{no} is greater than 9. It was furthermore assumed that the critical value of the normalized normal stress σ_n / σ_{no} is 10.

Substituting this into $\sigma_{no} = k_{no} \delta_m$ gives $k_{no} = \sigma_{nc} / 10 \delta_m$. Substituting this back into equation (2) gives

$$\sigma_n = \frac{\sigma_{nc} \delta}{10(\delta_m - \delta)} \quad (4)$$

In the present study, it is assumed that δ_m is related to the initial aperture of the fracture h_i by $\delta_m = 0.9 h_i$. Substituting this into Equation (4) and rearranging gives the normal stress/aperture relationship that will be used in the model:

$$\delta = \frac{9 \sigma_n h_i}{\sigma_{nc} + 10 \sigma_n} \quad (5)$$

Finally, we take $\sigma_{nc}(\text{MPa}) = 0.487 h_i(\mu\text{m}) + 2.51$, as used by Baghbanan and Jing (2007).

Figure 3 compares the difference in coupled behavior between the linear relationship given by Equation (1)

and the nonlinear one given by Equation (5), for a 50 μm fracture, which is fairly typical for the 2D BMT system. The range of normal stress applied to the fracture network is from zero to up to 25 MPa. The graphs show that within the range of normal stress, there are significant differences in aperture using the two relationships.

For the 2D BMT simulations, Equation (5) is used, instead of the linear law (1), to model normal stress/aperture coupling.

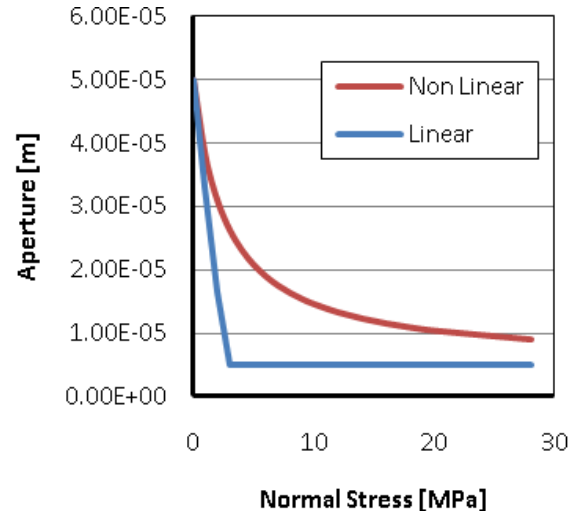


Figure 3. Comparing the linear and nonlinear models for stress-aperture coupling

Shear dilation

Initially, the following strategy was suggested to model shear dilation. Shear displacement varies linearly with shear stress until slipping occurs. After slipping occurs, the normal displacement due to shear dilation of the fracture is proportional to any additional shear displacement after slip (see Fig. 4).

After slip has occurred, shear displacement is no longer dependent uniquely on the shear stress. After shear slip occurs, according to this model, shear stress would not increase any further, and so shear displacement and shear stress no longer follow a linear relationship. Loading history of the fracture network is not defined in this project, and there is no way to determine the dilation without assuming additional parameters.

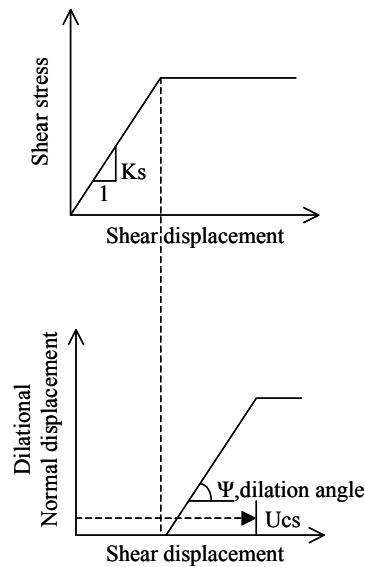


Figure 4. Strategy initially suggested for modeling shear dilation

For the current 2D BMT modeling, it is assumed that slip does not occur between the fractures, to simplify the simulations. It is assumed that shear displacement is directly proportional to shear stress, and the component of dilation due to shear is directly proportional to the shear displacement.

DFN model results

First, the permeability of the 2D BMT fracture system for the case with no applied stress was calculated as $k_{xx} = 6.66 \times 10^{-13} \text{ m}^2$ and $k_{zz} = 1.06 \times 10^{-12} \text{ m}^2$. These are the horizontal and vertical permeability components of the full permeability tensor calculated by NAPSAC. The 2D BMT fracture network was modeled as a 3D system with uniform thickness, so there will be permeability calculated in the transverse y -direction. The cross terms k_{xz} and k_{zx} are an order of magnitude smaller than k_{xx} or k_{zz} , and so the principal directions of the permeability tensor are very close to the (x, z) axes of the in-plane coordinate system.

Next, the permeabilities were calculated for four vertical/horizontal stress ratios of 1, 2, 3, and 5. The results are presented in Figure 5 in the form of permeability normalized against the value in the stress-free case. At a stress ratio of 1, i.e., an isotropic stress of 5 MPa, the permeabilities in both the x and y directions have been reduced to less than one-third of their original stress-free values. When the stress ratio increases, the permeabilities continue to decrease as a result of further closure of fractures. Our current stress-vs-permeability coupling approach for the NAPSAC does not result in any substantial effect of shear dilation on permeability.

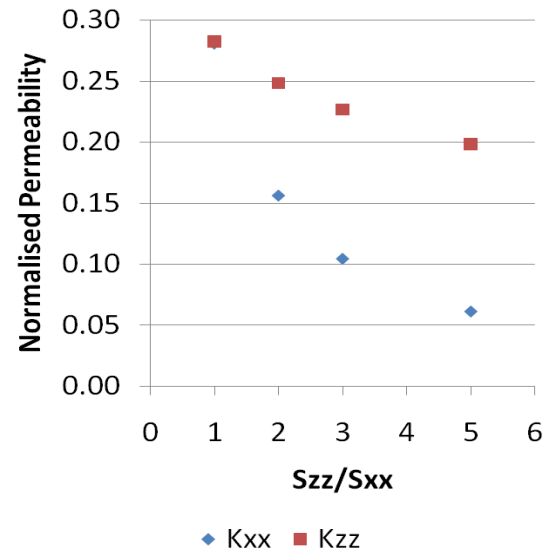


Figure 5. Normalized permeability versus stress ratio. The permeability values are normalized to the values at zero stress.

DC MODELING USING TOUGH-FLAC

The second set of calculations is carried out using the using the fine-scale TOUGH-FLAC modeling approach. In this case, we discretize the $20 \times 20 \text{ m}$ domain in 400×400 gridblocks, leading to a total of 160,000 gridblocks, each with a side length of 0.05 m. We first explore the possibilities of modeling fluid flow with TOUGH2 and geomechanical processes with FLAC3D, before attempting to consider the hydromechanical coupling in TOUGH-FLAC.

DC modeling of fluid flow in TOUGH2

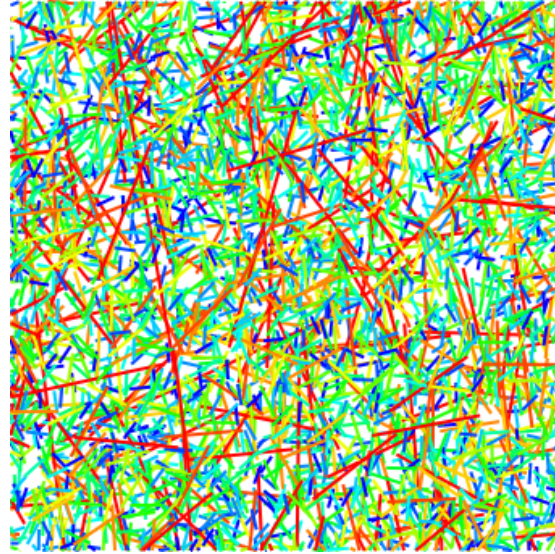
Modeling of fluid flow in TOUGH2 using a similar so-called quasi-explicit approach has been explored by Doughty et al. (2002) as well as Ito and Seol (2003). Doughty et al. (2002) simply assigned new material indicators for a gridblock intersected by a fracture. Special material properties, essentially increased permeability, was assigned for elements along fractures. Ito and Seol (2003) developed a mesh generator that adds fracture elements along a fracture trace with appropriate fracture-matrix connections and calculated gridblock interface area based on fracture aperture. It uses the TOUGH2 permeability modifier factor, enabling consideration of a large number of fractures with different permeabilities. Both approaches, in particular the one developed by Ito and Seol (2003), would be applicable in the present case. However, in this study, we first explore the use of an existing capability of the NAPSAC code to calculate equivalent hydraulic

properties for gridblocks of continuum fluid flow codes.

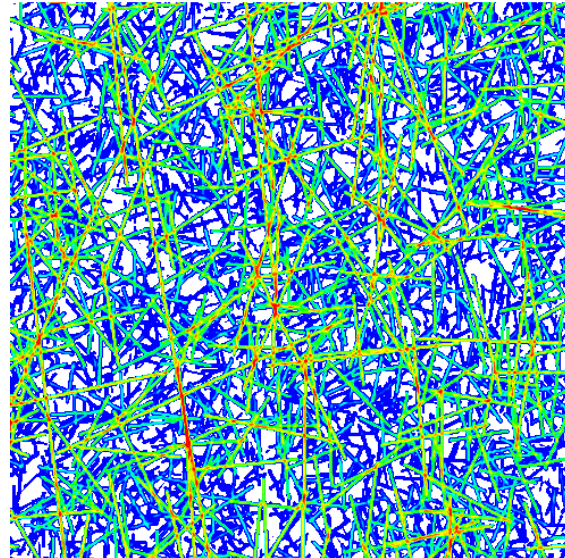
The NAPSAC capability for calculating continuum equivalent hydraulic properties (porosity and permeability) was originally developed, tested, and applied by Jackson et al. (1999) using the finite element flow and transport code NAMMU. This capability has recently been extended to calculating equivalent properties for TOUGH2. Using this approach, the NAPSAC can calculate the permeability tensor on individual blocks for an arbitrary subdivision of the original fracture network model. In the case of the very fine mesh applied in this study, there may be just one or two fractures (or, indeed, none) intersecting a gridblock. NAPSAC calculates the flows through the gridblock for an arbitrary head gradient, and then determines the six components of the permeability tensor that give the best fit (in a least-squares sense) to the flows.

In the case of TOUGH2, a new data block called "PERM" is added to the mesh file listing the permeability tensor for each gridblock. Some modifications were made to the TOUGH2 source code, first to read in the "PERM" data block, and second to project the permeability tensor onto each of the connections with an element. Figure 6 presents the resulting permeability distribution for the initial aperture at stress free conditions.

Figure 7 present the vertical fluid flow distribution along the lower boundary in the case of a vertical hydraulic gradient. The locations of the highest outflow correlate with the locations high permeability fractures in Figure 6.



(a)



(b)

Figure 6. Comparison of (a) the distribution of NAPSAC fracture transmissivities, and (b) the NAPSAC-derived permeability distribution in TOUGH2 fine mesh model

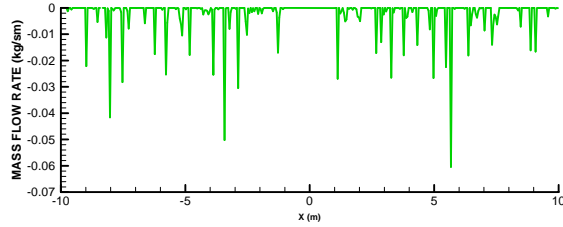


Figure 7. Vertical flow distribution along the lower boundary for the case of a vertical flow gradient under uniform initial stress of 5 MPa.

DC modeling of geomechanics in FLAC3D

For modeling the geomechanical behavior of the fractured rock mass, we represent fractures by softening and weakening grid elements intersected by a fracture trace. In this first, exploratory analysis testing of this model approach, the softening effect of an intersecting fracture trace was represented by a simple 1D formula considering fracture stiffness (Young’s modulus of intact rock) and grid size. Moreover, the weak elements were assigned Mohr-Coulomb properties with a very low cohesion (1 MPa) and a friction angle of 27 degrees. Although isotropic elastic and elasto-plastic models were applied, anisotropic fracture deformation behavior can still be achieved, because most substantial shear and normal deformation will automatically tend to occur, respectively, along and normal to the trace of weak fracture elements.

Figure 8 presents the calculated volumetric strain for stress ratios of 3 and 5. At a stress ratio of 3, the volumetric strain is compressive as a result of the increasing compressive stress. At a stress ratio of 5, substantial volumetric expansion can be observed as areas of white contour color. These are located preferentially along preferentially along traces of shear zones observed in Figure 9. These shear zones do not necessarily align with pre-existing fracture traces, but are rather formed through the shearing of the intensively fractured rock mass.

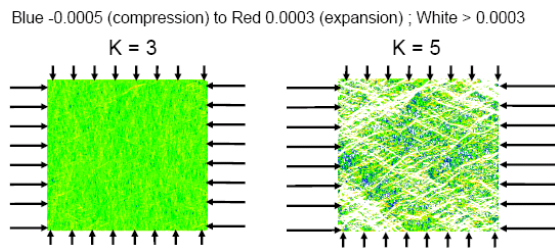


Figure 8. Calculated volumetric strain when increasing the horizontal stress from 5 MPa to 15 MPa (K = 3) and 25 MPa (K = 5)

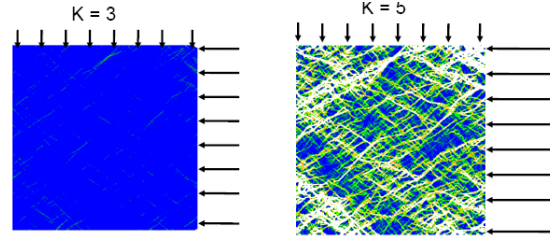


Figure 9. Calculated shear strain when increasing the horizontal stress from 5 MPa to 15 MPa (K = 3) and 25 MPa (K = 5)

Coupled fluid flow and geomechanics using TOUGH-FLAC

The evolution of permeability along fractures can be calculated using a relationship between stress (or strain) and permeability for the fracture elements. In a first test of our approach to model fractures, we employ the following simple relationship between permeability and volumetric strain:

$$k = k_o(1 + \beta \Delta \epsilon_v) \tag{6}$$

where k_o is initial (reference) permeability, and β is a factor to relate permeability to volumetric strain. By using volumetric strain, we can consider both elastic fracture normal closure with associated compressive volumetric strain and decreased permeability, as well as shear dilation with associated expansive volumetric strain and permeability increases.

In this calculation, we assumed $\beta = 500$, which resulted in permeability increases by as much as a factor of about 10,000 in zones of the highest volumetric strain. Using the simple correction of permeability, the permeability of subvertical fractures decreased somewhat with increasing horizontal stress, whereas the permeability increased for fractures oriented optimally for shear. For a vertical hydraulic gradient, the outflow distribution changes with a general decrease in total flow, although the flow increases at certain locations as a result of local fracture shear.

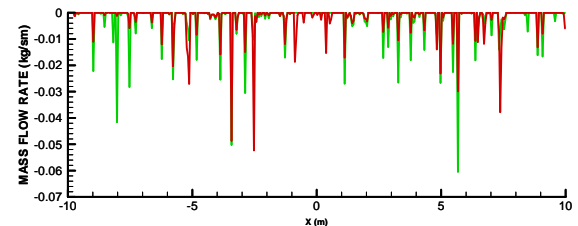


Figure 10. Vertical flow distribution along the lower boundary for the case of a vertical flow gradient and a stress ratio K = 1 (green) and K = 5 (red)

CONCLUDING REMARKS

In this paper, we presented the progress in development and application of TOUGH-FLAC for coupled hydromechanical modeling of fractured rock masses. For this study, we also utilize the discrete fracture network code NAPSAC for code comparison and for deriving equivalent hydraulic properties of the TOUGH-FLAC model.

First, we applied NAPSAC to provide a baseline flow simulation with exact representation of the discrete fractures. Using NAPSAC, we also performed a simplified coupled stress-flow analysis correlating fracture permeability to the stress field without a performing a full stress-strain analysis. Currently, the simplified NAPSAC model cannot properly handle fracture shear reactivation. However, we are at present implementing an improved algorithm that can consider shear dilation of individual fractures embedded in an elastic medium.

Second, we applied TOUGH-FLAC and a fine mesh discretization to model the coupled hydromechanical behavior of the intensively fractured rock mass. The permeability of the fine mesh elements were derived using NAPSAC code. The geomechanical behavior of the fractured rock mass was simulated in a FLAC3D analysis, using an equivalent fine mesh in which fracture elements along the trace of a fracture plane were assigned weaker and softer geomechanical properties. We tested the approach for the coupled analysis in which permeabilities of individual elements were corrected as a function of volumetric strain. The results of this analysis demonstrated how the geomechanical changes of the fractured rock mass affect the fluid flow distribution across the system in a complex way.

A more detailed comparison of the two approaches is under way. In addition, a third approach of using a coarser TOUGH-FLAC mesh with equivalent properties derived from NAPSAC will be tested and compared to the above approaches. The third approach can be expanded and applied in 3D, and might eventually be the best choice for analyzing the coupled hydromechanical performance of large-scale fractured rock masses.

ACKNOWLEDGMENT

This work was co-funded by the UK Nuclear Decommissioning Authority (NDA), and the Engineering and Physical Sciences Research Council of the UK (EPSRC).

REFERENCES

- Baghbanan, A., and L. Jing, Hydraulic properties of fractured rock masses with correlated fracture length and aperture, *International Journal of Rock Mechanics*, 44, 704-719, 2007.
- Baghbanan, A., and L. Jing, Stress effects on permeability in a fractured rock mass with correlated fracture length and aperture, *International Journal of Rock Mechanics*, 45, 1320-1334, 2008.
- Bandis, S. C., A. C. Lumsden, and N. Barton, *Fundamental of rock joint deformation*, *International Journal of Rock Mechanics*, 20, 249-268, 1983.
- Doughty C., R. Salve, and J. S. Y. Wang, Liquid release tests in unsaturated fractured welded tuff: II Numerical modeling. *Journal of Hydrology*, 256, 80-105, 2002.
- Hudson, J., I. Neretnieks, and L. Jing, DECOVALEX-2011 Technical Definition of the 2D BMT Problem for Task C, 2008.
- Ito, K., and Y. Seol, A 3-dimensional discrete fracture network generation to examine fracture-matrix interaction using TOUGH2. *Proceedings of the TOUGH symposium 2003*, Lawrence Berkeley National Laboratory, Berkeley, May 12-14, 2003a.
- Jackson, C. P., A. R. Hoch, and S. Todman, Self-consistency of a heterogeneous continuum porous medium representation of a fractured medium. *Water Resources Research* 36, 189-202, 2000.
- Rutqvist, J., Y.-S. Wu, C.-F. Tsang, and G. S. Bodvarsson, A modeling approach for analysis of coupled multiphase fluid flow, heat transfer, and deformation in fractured porous rock, *International Journal of Rock Mechanics*, 39, 429-442, 2002.
- Rutqvist, J., and C.-F. Tsang, TOUGH-FLAC: A numerical simulator for analysis of coupled thermal-hydrologic-mechanical processes in fractured and porous geological media under multi-phase flow conditions. *Proceedings of the TOUGH Symposium 2003*, Lawrence Berkeley National Laboratory, Berkeley, May 12-14, 2003.
- Sercu TAS, NAPSAC Technical Summary: Release 9.6, Sercu Report SA/ENV/CONNECTFLOW/12, 2008.
- Zimmerman, R. W., and G. S. Bodvarsson, Hydraulic conductivity of rock fractures, *Transport in Porous Media*, 23, 1-29, 1996.

A STRUCTURED APPROACH TO THE DERIVATION OF EFFECTIVE PROPERTIES FOR COMBINED WATER AND GAS FLOW IN THE EDZ

G. W. Lanyon, Fracture Systems Ltd., Tregurrian, Ayr, St. Ives, TR26 1EQ, UK; bill@fracture-systems.co.uk
R. Senger, INTERA Incorporated, Swiss Branch, Schloesslistr. 12, CH-5408 Ennetbaden, Switzerland;
P. Marschall, NAGRA, Hardstrasse 73, CH-5430 Wettingen, Switzerland.

ABSTRACT

Gas generation from corrosion of waste canisters is a key issue in assessing the long-term safety of a proposed repository for spent fuel and high-level waste (SF/HLW) sited in the Opalinus Clay formation of Northern Switzerland.

This paper describes the development of a structured approach to abstracting the complex geoscientific models of two-phase flow through the Excavation Damage Zone to simplified models suitable for use within a Probabilistic Safety Assessment.

INTRODUCTION

Gas generation from corrosion of waste canisters and accumulation in the backfilled emplacement tunnels is a key issue in assessing the long-term radiological safety of the proposed repository for spent fuel and high-level waste (SF/HLW) sited in the Opalinus Clay formation of Northern Switzerland. As part of NAGRA's Probabilistic Safety Assessment (PSA) initiative, two-phase flow of gas and water, along the Excavation Damage Zone (EDZ) of a Spent Fuel/High-Level Waste (SF/HLW) emplacement tunnel, was investigated within the "EDZ Converter" study. Previous studies of single-phase fluid flow and solute transport have represented flow in the EDZ using effective homogeneous hydraulic/transport properties. In contrast, gas flow along the EDZ is expected to be controlled by small-scale variability, leading to distinct gas flow channeling.

This paper describes modeling studies performed in support of the development of an "EDZ converter" for NAGRA's PSA studies. The aim is to develop a defensible, transparent abstraction process from complex, "realistic" geoscientific models to simplified models suitable for PSA. The concept of the "EDZ converter" is illustrated in Figure 1, showing the adjustable model inputs (parameter uncertainty and variability in the geoscientific model), a fixed abstraction process, and end-user outputs for PSA.

The modeling concept for the "EDZ converter" consists of successive model abstractions, starting from detailed geoscientific models and ending with a homogeneous pipe-like representation of the EDZ, which is suitable for PSA purposes. The model abstraction process includes three different models:

- Model 1: a discrete fracture network (DFN) model, which describes the EDZ to the best geoscientific knowledge. The DFN model is used for the simulation of single-phase flow and solute transport.
- Model 2: a stochastic continuum model, which describes the EDZ by concentric shells around the backfilled tunnel with a heterogeneous continuum porous medium (CPM) representation. The abstracted stochastic continuum model is implemented with the TOUGH2 code (Pruess et al., 1999) to simulate two-phase flow in the heterogeneous medium.
- Model 3: a simplified continuum model, which describes the EDZ using a highly simplified geometry e.g. concentric shell around the backfilled tunnel or "process zone" with homogeneous flow/transport parameters. This final abstraction uses the characteristic pressure and two-phase flow responses from the stochastic continuum model to calibrate the homogeneous hydraulic and two-phase flow parameters.

DFN MODEL OF THE EDZ

The overall structural model of the EDZ is shown in Figure 2. The model is based on results from laboratory tests and numerical modeling (NAGRA, 2002a,b) together supported by results from investigations at the Mont Terri Rock Laboratory (e.g., Bossart et al., 2004; Martin and Lanyon, 2003). The pronounced bedding fabric of the Opalinus Clay is assumed to be subhorizontal at repository depth (~500 m) and results in a distinctive structure with two large buckling zones formed by bedding-plane failure in the roof and floor of the excavation and smaller damage zones in the tunnel sidewalls containing unloading fractures. The buckling zones include subvertical shear structures that bound the failure zone and a kink zone shear structure in the central part. In addition, more highly disturbed bedding planes are associated with the top and base of each buckling zone.

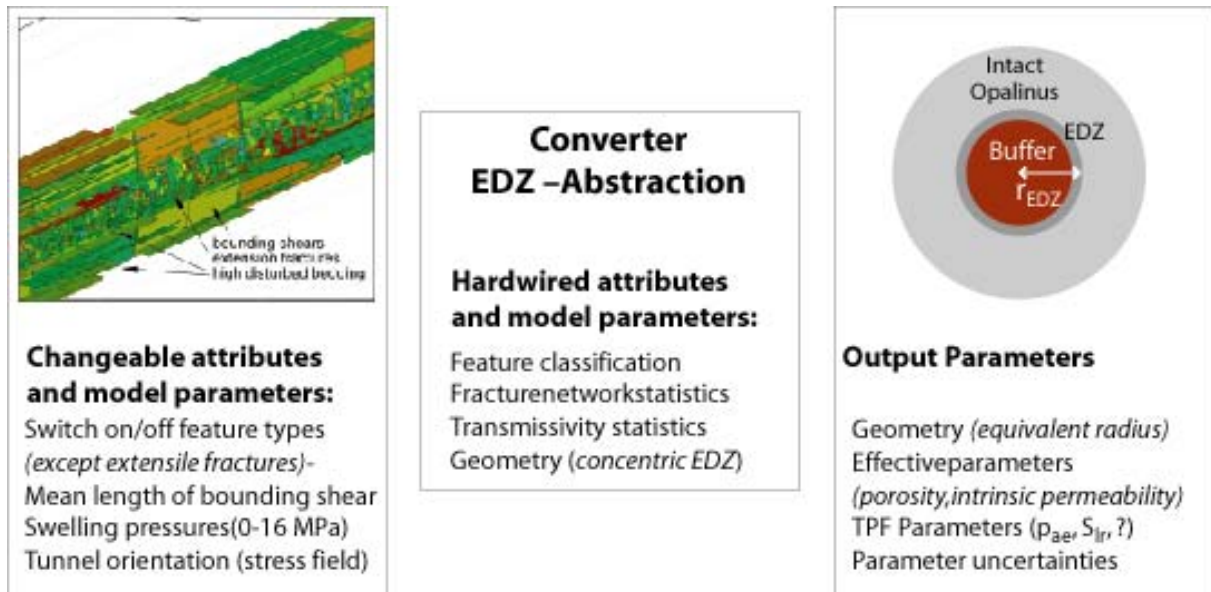


Figure 1. Components of the EDZ converter: input side (definition of changeable attributes / experts), hardwired EDZ abstraction procedure and output for the end users (PSA model)

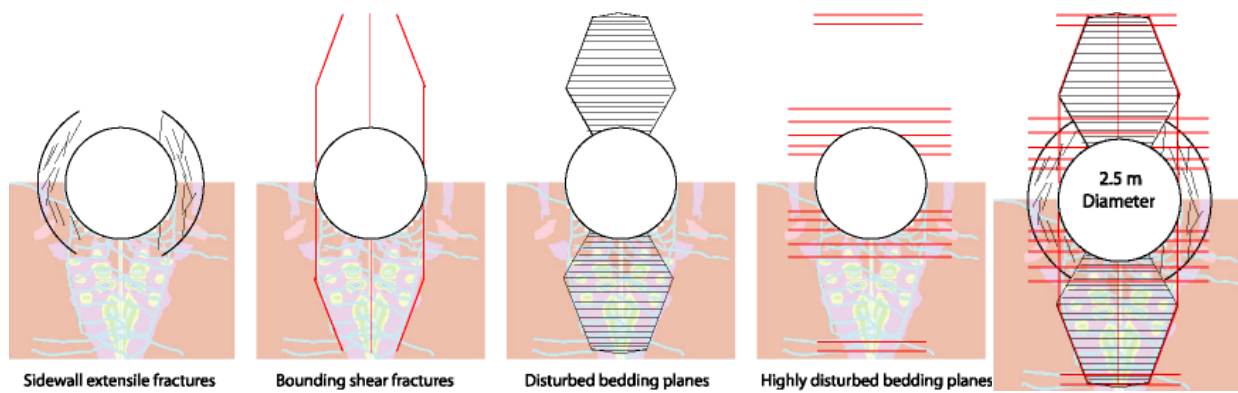


Figure 2. Structural model of EDZ in Opalinus Clay: fracture families and complete network

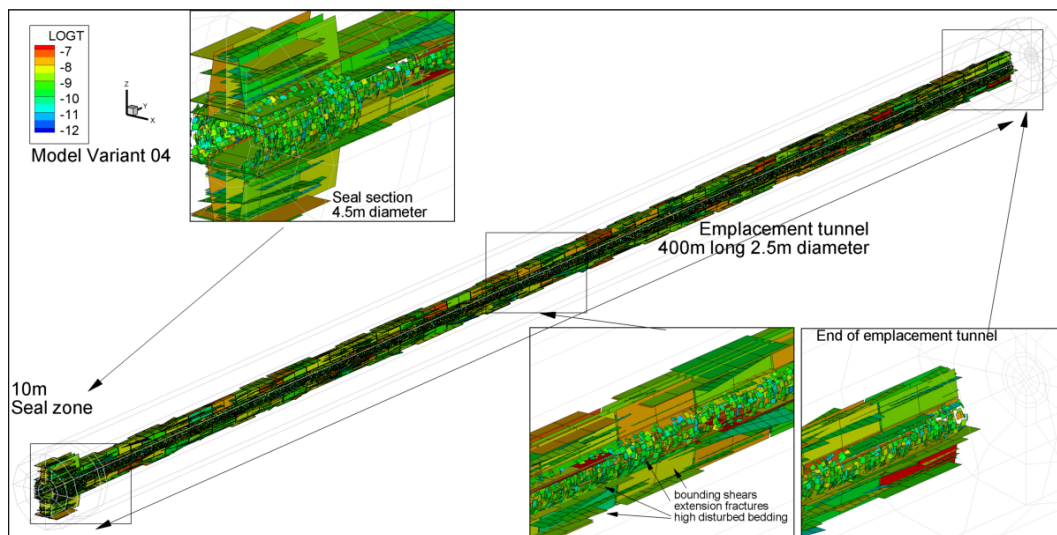


Figure 3. Realization of one variant of EDZ DFN model. Fractures colored by \log_{10} transmissivity (m^2/s)

The structural model has been implemented as a DFN model using the hybrid CPM/DFN code CONNECTFLOW (Hartley & Holton 2004). Several variants of the structural model were identified (parameter variations), and multiple realizations were created for each variant. Figure 3 shows one realization from one variant that was used for the TOUGH2 modeling described in later sections.

STOCHASTIC CONTINUUM MODEL

The realization shown in Figure 2 was transformed into a continuum representation. Effective properties of each continuum element were calculated from the DFN model using the upscaling method of Jackson et al. (2000) implemented in CONNECTFLOW. This method calculates the equivalent permeability tensor for subregions of the DFN by fitting to the flow (calculated in the DFN model) across the subregion for differing hydraulic gradients. The consistency of the approach is illustrated in Figure 4, where the total conductance along the tunnel as calculated by the DFN and CPM models is compared for 10 realizations and several different continuum meshes.

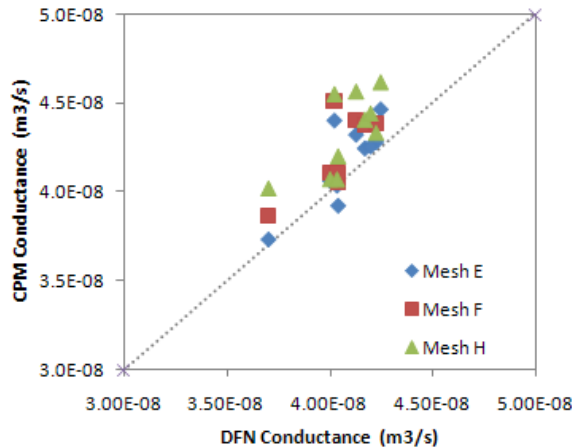


Figure 4. Comparison of CPM and DFN EDZ conductance for 10 DGN realizations and three different CPM meshes

The CONNECTFLOW CPM representation was then converted into a TOUGH2 model. The permeability of each TOUGH2 element was described by a permeability modifier calculated as the ratio of the maximum principal permeability of the tensor for that element divided by the permeability of the undisturbed rock. This modifier varied from 1 to over 10⁶ (highly permeable regions), as shown in Figure 5. In addition to permeability variations, the porosity can be varied based on the apertures or effective hydraulic aperture representation of the individual element blocks derived from the DFNs.

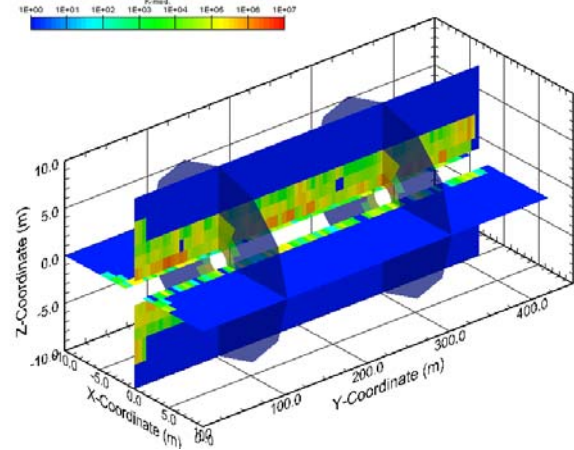


Figure 5. 3D variation in permeability modifier

The capillary pressure–saturation relationship for each element can be scaled by the capillary strength parameter (i.e., van Genuchten parameter $1/\alpha=P_0$) as a function of permeability. A typical scaling relationship between capillary strength and permeability is given by Leverett (1941) as:

$$P_0' = P_0 \sqrt{\frac{k_0}{k}}$$

or by a cubic law function:

$$P_0' = P_0 \sqrt[3]{\frac{k_0}{k}}$$

where P_0 and k_0 are the reference values of capillary strength and permeability, respectively, and are defined as material properties for the entire EDZ region. The reference permeability of the EDZ of $k_0 = 10^{-20} \text{ m}^2$ corresponds to the undisturbed host rock. The corresponding reference capillary strength was assumed to be $P_0 = 2 \times 10^6 \text{ Pa}$; the reference porosity is $\phi = 0.12$. Model parameters are listed in Table 1.

The CPM model incorporates the DFN as heterogeneous distributions of representative permeabilities and porosities at the scale of the discretized CPM blocks. In theory, the variations in permeability and porosity could be represented by variations of the different parameters of the van Genuchten model. In a first approximation, only the capillary strength parameter (P_0) was assumed to be a function of permeability using the Leverett function. All other van Genuchten parameters were assumed to be constant.

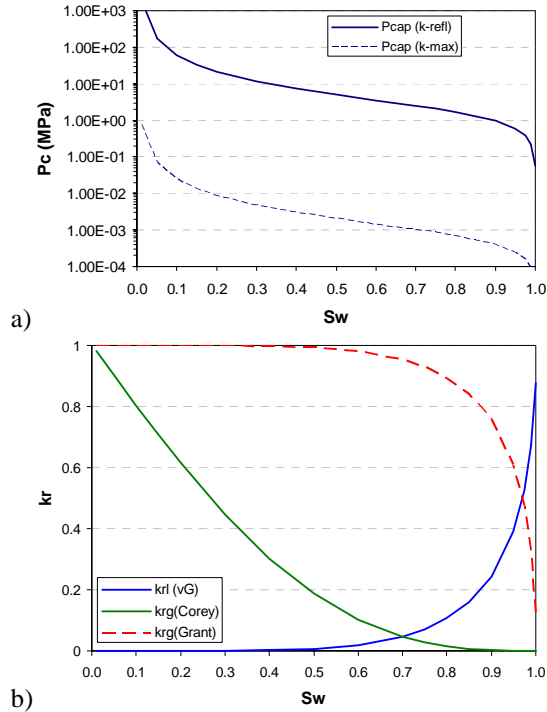


Figure 6. Functional relationship for capillary pressure (top) and relative permeability (bottom) for the van Genuchten/Mualem model.

The range in the capillary pressure curves based on the range in permeability of the EDZ is shown in Figure 6, indicating a range of more than three orders of magnitude between the higher capillary pressure (corresponding to the reference permeability k_0) and the lowest capillary pressure (corresponding to the highest permeability in the CPM model—Figure 6). A residual gas saturation of $S_{gr} > 0$ is assumed, indicating a Corey model for the gas relative permeability curve.

The model domain considered in TOUGH2 is shown in Figure 7, together with the two different gas injection scenarios.

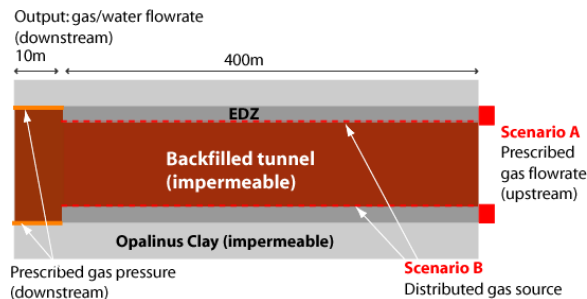


Figure 7. Schematic depiction of model domain with two different gas injection variants

At the left model boundary, a 10 m thick seal of uniform low permeability is assumed. In the actual model, gas injection is along the left vertical boundary (for Scenario A) or along the radial interface between the tunnel and the EDZ (for Scenario B). Constant gas injection rates were prescribed corresponding to the conservative and pessimistic H_2 generation rates of 0.112 and 0.04 m^3-H_2/a per tunnel meter, respectively (NAGRA, 2002a, b).

TOUGH2 simulations were performed using the EOS3 module for air and water. For this, the H_2 gas generation rates were converted to the mole-equivalent air-mass injection rates. Solubility of air in water according to Henry’s law was considered, but no diffusion in either liquid or gas phases was assumed.

Gas migration through the EDZ, as represented in the CPM model, was simulated to obtain characteristic responses in terms of pressure buildup and gas/water flow through the heterogeneous CPM model. The two-phase flow simulation of gas migration through the EDZ represented by the CPM model for the two gas injection variants. Focus is on injection Scenario A, because of numerical difficulties encountered in the simulation of Scenario B. In addition, a second realization (corresponding to a different DFN model variant) was used for comparison of the simulated pressure and gas/water flow responses.

Figure 8 shows the evolution of gas pressure and saturation within the model over the first 1000 years. The gas front extends farther in the vertical direction according to the greater extent of the higher permeability EDZ. The gas saturation distributions indicate that the gas front reaches the downstream boundary after about 500 years.

SIMPLIFIED CONTINUUM MODEL

The simplified model used a radially symmetric mesh with the symmetry axis parallel to the cavern axis. The overall dimensions were the same as those of the CPM model. The 10 m radial extent was subdivided into 5 radial columns corresponding to the radial discretization of the CPM model. The horizontal dimension of the model domain (420 m) is composed of variable length vertical slices (5 to 20 m length) for a total grid size of 5×27 .

The simulated pressure buildup and gas breakthrough responses from the CPM model for Scenario A were used as calibration data to estimate effective properties for a simplified homogeneous model of the EDZ.

Gas pressure (Pa)

Gas saturation (-)

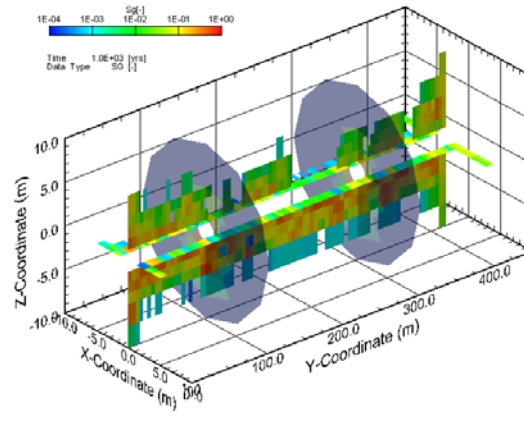
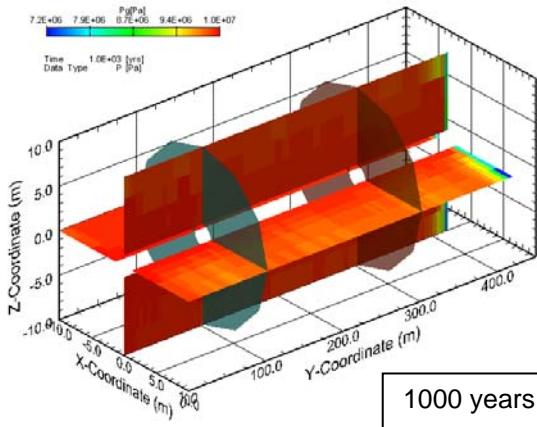
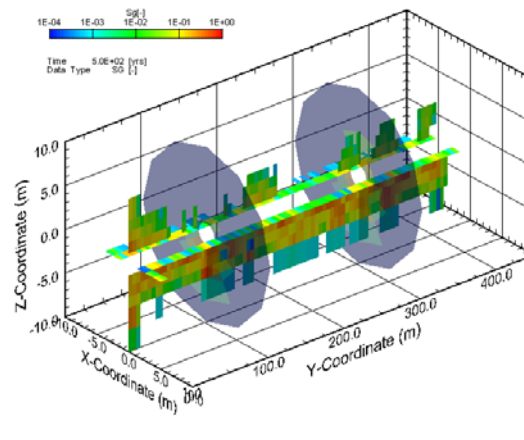
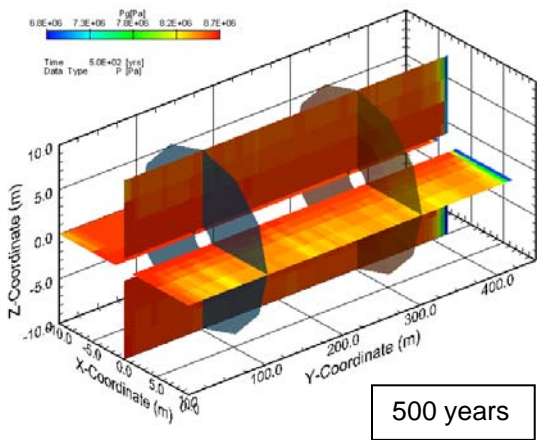
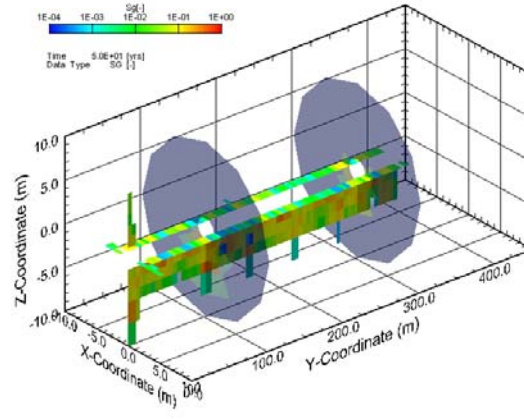
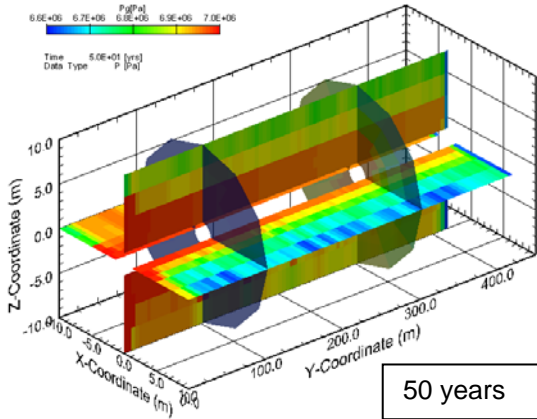


Figure 8. Gas pressure and gas saturation distribution along 3D section through the CPM model after 50, 500, and 1,000 years from beginning of gas injection. The scale of the pressure range changes for the different time steps to show the internal variation at early times.

In the first runs, only three parameters were selected for optimization using the inverse code ITOUGH2 (Finsterle, 1999):

- Radial permeability (k_r)
- Horizontal permeability (k_h)
- Capillary strength (vG : $\alpha = 1/P_0$)

These parameters correspond to the variations in permeability and capillary strength in the CPM model. In subsequent runs, the following additional parameters were included for the optimization:

- Porosity (ϕ)
- Shape factor ($vG - m$)
- Residual water saturation (S_{ir})

In the CPM model, the ϕ , vG - m , and S_{ir} were kept constant, whereby the two-phase parameters define a van Genuchten model for the water relative permeability curve (k_{rl}) and a Corey model for the gas relative permeability curve based on a residual gas saturation of $S_{gr} > 0$. The Corey curve indicates significant phase interference where $k_{rl} + k_{rg} < 1$. In comparison, the Grant gas relative permeability ($k_{rg} = 1 - k_{rl}$) indicates no phase interference, resulting in much higher gas mobility. The Grant model is defined by assuming $S_{gr} = 0$, which is typically used to represent preferential gas flow paths in continuum approximations of fractured-porous rocks. Sensitivity simulations with the homogeneous model indicated that a Grant k_{rg} curve is required to reproduce the relatively fast gas migration in the CPM model.

For the inverse simulations, 50 calibration points were interpolated on a log-time scale from the simulated pressure buildup and gas flow curves (see Figure 9). The focus for the calibration was on the peak pressure response and gas breakthrough and less on the early-time data. In a subsequent run, water flow was included in the calibration (Figure 10). Initial model runs fitting only permeability and capillary strength produced a relatively poor fit to the pressure data, and parameter estimates did not represent a statistically valid representation of the CPM model. The inverse simulation was repeated with the additional optimization parameters. Results indicate a better fit of the pressure response, reproducing well the pressure peak (Figure 9).

The estimated parameters for the homogeneous model are summarized in Table 2, together with relevant statistical information from the inverse simulation (Table 3). The homogeneous model indicates a significant anisotropy with higher EDZ permeability along the tunnel axis and lower permeability perpendicular to the tunnel axis. The estimate of the vG - α parameter representing the capillary strength ($\alpha = 1.83E-7$ 1/Pa or $P_0 = 5.47$ MPa) is greater than the reference value of $P_0 = 2.0$ MPa

corresponding to the reference permeability k_0 of the undisturbed rock ($k_0 = 10^{-20} \text{m}^2$). The estimate of the vG - m parameter decreased compared to the reference value, causing a steeper rise in the capillary pressure curve and a slight reduction in the relative permeability for liquid and a corresponding increase in the relative permeability for gas. The covariance/ correlation matrix in Table 3 indicates a relatively high correlation between the van Genuchten's α and m parameters. A positive correlation indicates an increase in m , and a corresponding increase in α would yield similar results.

The estimated residual water saturation indicates a significant percentage of mobile water (i.e., affected by the gas displacement). The porosity did not indicate a significant change (Table 2), corresponding to the relatively large pore volume affected by the gas flow. This is to be expected during injection in Scenario A, which induces a piston-type flow regime with the total gas injected at the upstream boundary and discharged at the downstream boundary, represented by a 10 m thick section with the low reference permeability of $k_0 = 10^{-20} \text{m}^2$, corresponding to the intact EDZ in the CPM model.

The results of the inverse simulations indicated a reasonable fit of the gas breakthrough curve, but the computed water flow at the downstream boundary at late time was noticeably higher than the rate from the CPM model.

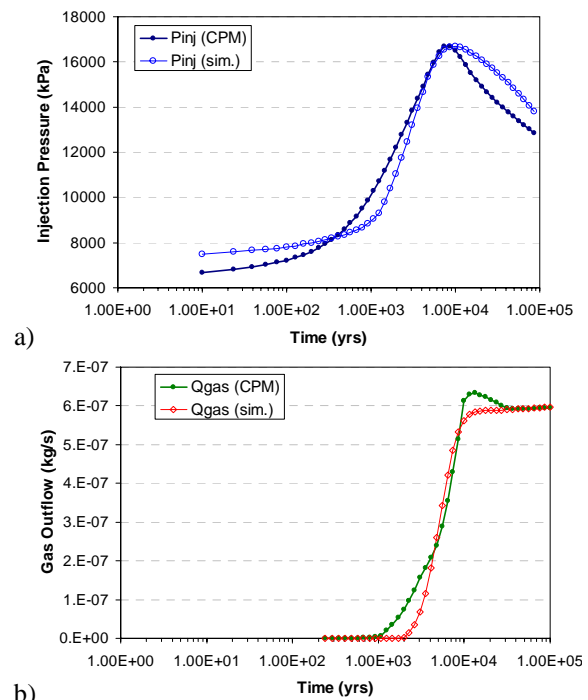


Figure 9. CPM and fitted homogeneous model calculated injection pressure and gas flow. Fit to gas pressure and flow.

In the following case, the inverse simulation takes into account the simulated water flow in the CPM model as calibration points. Results indicate a poorer fit of the pressure response (Figure 10) compared to that in Figure 9. The overall pattern of the water flow response is reasonably well reproduced, particularly the general decrease after gas breakthrough, but the fit of the gas breakthrough curve is decreased. The statistical analysis indicates a relatively high sensitivity of the water flow, compared to the pressure and gas flow, and a decrease in some of the parameter correlations compared to those in Table 1. Simulations were also performed with higher gas injection rates, but are not discussed here.

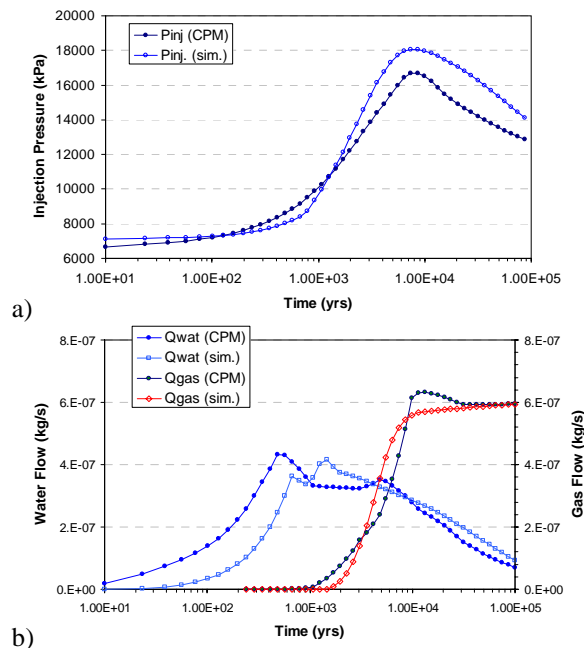


Figure 10. CPM and fitted homogeneous model calculated injection pressure and gas flow. Fit to pressure, gas and water flow.

Even though the inverse simulation gave a fair fit of the CPM model results, the statistical analysis of the inverse modeling indicated that the homogeneous model is not a statistically valid representation of the heterogeneous CPM model (relatively large residuals and non-uniform residual distribution). However, the inverse modelling indicates sufficient sensitivity of the different parameters and of the different calibration data (i.e., pressure, gas flow, and water flow) to obtain effective parameters for a homogeneous model that can produce a qualitatively optimal fit of the responses of the CPM model.

CONCLUSIONS

The TOUGH2 simulation results demonstrate that the simulated responses (pressure and gas/water flow) from the CPM model can be used for the calibration of effective parameters for a homogeneous model.

Overall, the calibrated parameters reproduced reasonably well the CPM model responses.

It should, however, be remembered that the modeling represents the first step in development of a structured methodology for treatment of solute and water flow through the EDZ, and several issues were identified that need further examination.

- The homogeneous model may be revised to be consistent with the effective property calculation used for the DFN/CPM for single-phase liquid flow.
- The inverse modelling requires refinement with regard to the relative contribution of the different data sets (i.e., pressure, gas flow).
- Further consistency checks regarding the observed two-phase flow behavior are needed between the CPM model and the homogeneous model.

REFERENCES

- Bossart, P., Meier, P.M., Moeri, I., Trick, T., Mayor J.C., Structural and hydrogeological characterization of the excavation-disturbed zone in the Opalinus Clay *Applied Clay Science* Vol 26, Issues 1-4, pp 429-448, August 2004.
- Finsterle, S.: ITOUGH2 User's Guide, Lawrence Berkeley National Laboratory, LBNL-40040, 1999.
- Hartley L.J., Holton, D., *CONNECTFLOW (Release 8.0) Technical Summary Document*, Serco Assurance Report, 2004.
- Jackson C.P., A.R. Hoch and S. Todman, Self-consistency of a heterogeneous continuum porous medium representation of a fractured medium *Water Resour. Res.*, 36(1), 189, 2000.
- Martin, C.D., Lanyon, G.W., *EDZ in Clay Shale: Mont Terri*, Mont Terri Technical Report. 2001-01, 2003.
- NAGRA, *Project Opalinus Clay: Safety report. Demonstration of disposal feasibility for spent fuel, vitrified high-level waste and long-lived intermediate-level waste (Entsorgungsnachweis)*. NAGRA Technical Report NTB 02-05. Nagra, Wettingen, Switzerland, 2002a.
- NAGRA, *Projekt Opalinuston – Synthese der geowissenschaftlichen Untersuchungsergebnisse. Entsorgungsnachweis für abgebrannte Brennelemente, verglaste hochaktive sowie langlebige mittelaktive Abfälle*. NAGRA Technical Report NTB 02-03. NAGRA, Wettingen, Switzerland, 2002b.
- Pruess, K., Oldenburg, C., Moridis, G., 1999, TOUGH2 User's Guide, Version 2.0, Lawrence Berkeley National Laboratory, LBNL-43134.

Table 1. Summary of reference hydraulic and two-phase parameters

Material	K^2 [m/s]	k_h^2 [m ²]	Porosity C	p [1/Pa]	Specific Storage ¹
EDZ	1.00E-13	1.02E-20	0.12	1.7E-9	2.60E-06

Material	Capillary Pressure ¹ Relativ			e Permeability ²		
	$P_o n$		Slr	m	Slr	Sgr
EDZ	2.00E+06	1.67	0.00	0.40	0.00	0.003
¹ – van Genuchten				² – van Genuchten / Mualem		
$P_c = P_o \cdot (S_{ec}^{n/(1-n)} - 1)^{1/n}$ $S_{ec} = \frac{S_l - S_{lr}}{1 - S_{lr}}$ $m = 1 - 1/n$				$k_{r,l} = S_e^{0.5} \cdot [1 - (1 - S_e^{1/m})^m]^2$ $k_{r,g} = 1 - k_{r,l} \rightarrow S_{gr} = 0 (Grant)$ $k_{r,g} = (1 - S_e)^2 (1 - S_e^2) \rightarrow S_{gr} > 0 (Corey)$ $S_e = \frac{S_l - S_{lr}}{1 - S_{gr} - S_{lr}}$		

Table 2. Best-fit parameters, standard deviations, and sensitivities for the fit to gas pressure and flow (Figure 9)

ESTIMATED PARAMETER	V/L/F	INITIAL GUESS	BEST ESTIMATE	STANDARD DEVIATIONS			SENSITIVITY	
				COND.	MA	RG. C/M	OUTPUT	OBJ. FUNC.
Kr	LOG10	-20.000	-20.100	0.154	0.229	0.670	706.500	37.181
Kh	LOG10	-18.000	-17.900	0.148	0.268	0.554	1158.000	36.673
Por	VALUE	0.120	0.110	0.001	0.013	0.054	1259.300	3853.969
Slr	VALUE	0.500	0.380	0.020	0.159	0.127	200.200	350.762
vG m	VALUE	0.401	0.808	0.005	0.063	0.073	646.700	6486.816
α	LOG10	-6.301	-6.420	0.007	0.117	0.060	6581.100	2291.873
Inj. Pressure							128.720	
Gas Flow							10423.00	

Table 3. Covariance/correlation of estimated parameters for the fit to gas pressure and flow (Figure 9)

Covariance(L+D)/Direct Correlation(U) Matrix of Estimated Parameters						
Kh		Kr	Por	Slr	vG m	α
Kh	5.25E-02	-0.51	0.199	-0.235	-0.094	0.088
Kr	-2.53E-02	7.17E-02	-0.207	0.329	0.18	-0.222
Por	7.69E-04	1.88E-03	1.81E-04	0.932	0.966	-0.975
Slr	2.88E-03	2.58E-02	2.04E-03	2.54E-02	-0.82	0.845
vG m	1.24E-03	-2.26E-03	2.01E-04	3.21E-03	4.02E-03	0.996
α	-4.05E-03	-1.45E-02	-8.15E-04	-7.10E-03	5.19E-03	1.37E-02

CHEMICAL EVOLUTION OF BENTONITE BUFFER IN A FINAL REPOSITORY OF SPENT NUCLEAR FUEL DURING THE THERMAL PHASE

Aku Itälä & Markus Olin

VTT Technical Research Centre of Finland
P.O.Box 1000
Espoo, FI-02044 VTT, Finland
e-mail: aku.itala@vtt.fi

ABSTRACT

Finnish spent nuclear fuel final disposal is planned to be based on the KBS-3 concept (Figure 1). Within this concept, the role of the bentonite buffer is considered central. The aim of the study was to model the evolution of the final repository during the thermal phase (heat-generating period of spent fuel) when the bentonite is initially only partially saturated. There is an essential need to determine how temperature influences saturation and how both of these factors affect the chemistry of bentonite.

INTRODUCTION

In Finland, bentonite will be used as a buffer material in high-level radioactive waste disposal. Upon saturation with groundwater, bentonite swells and thus seals repository tunnels. However, the thermal, hydrological, mechanical and chemical phenomena and processes taking place in the bentonite buffer may change the mechanical and chemical properties

of the bentonite. Determination of the long-term stability of bentonite under final repository conditions must be based on modeling, since empirical testing would require millennia to implement.

In this work, we concentrate on modeling the temperature effects on bentonite during the thermal phase. However, the complexity of the *in situ* conditions and computing power limitations preclude models that include all processes. We are therefore forced to consider only simplified repository site models.

To make the modeling more concrete, an example experimental case was adapted: the Long Term Test of Buffer Materials (LOT) A-2 parcel test at the Äspö Hard Rock Laboratory (HRL) in Sweden (Karlund et al., 2008). This experiment was modeled, and the experimental results have been compared with the model.

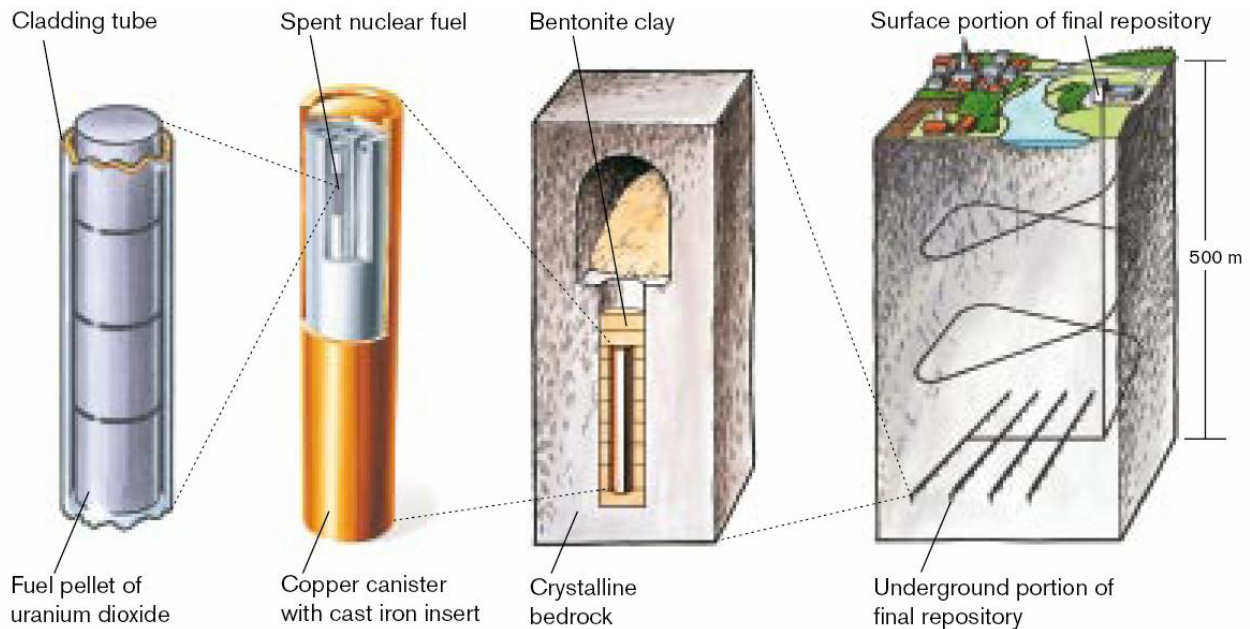


Figure 1. The KBS-3V spent nuclear fuel final disposal concept (SKB - Swedish Nuclear and Waste Management Co, 2006)

Differences in the thermodynamic properties of minerals cause a redistribution of minerals within the bentonite. For example, laboratory tests indicate gypsum dissolution and anhydrite precipitation near the heater-bentonite interface. Incoming groundwater will also affect the bentonite pore water. Since these changes may affect the properties of bentonite, it must be determined whether these phenomena are to be taken into account in safety management.

GOAL

The first aim was to investigate the thermal (T), hydraulic (H), and chemical (C) phenomena affecting the bentonite. Comprehensive knowledge of the composition of bentonite after the thermal phase is crucial for estimating the long-term safety of nuclear waste final disposal repositories.

The second aim was to improve the modeling capabilities at VTT (Technical Research Centre of Finland) to understand the bentonite evolution problem and to create a model that could in turn be used to model the final repository site, planned to be constructed in Olkiluoto.

EXPERIMENT

The LOT test experiment A2 parcel test and its results were used in this model as reference data (118 Karnland, Ola 2008). In the LOT tests, relatively small test parcels (see Table 1) are exposed to field conditions at Äspö HRL. The LOT test series includes three test parcels with similar conditions to those in a Kärnbränslesäkerhet 3 (KBS-3V) repository, and four test parcels with adverse conditions.

Table 1. Dimensions in LOT A2 parcel test

Hole depth	4 m
Cylinder diameter	0.28 m
Cylinder height	0.1 m
Copper inner diameter	0.1 m
Copper wall thickness	0.004 m
Borehole diameter	0.3+0.01 m
Depth	450 m
Copper tube length	4.7 m
Hole height	8 m
Water Pressure	1.2 Mpa

The A2 parcel is an adverse conditions parcel—*adverse* in this case referring to conditions that accelerate alteration processes (higher temperature and higher temperature gradient). The A2 parcel was placed in a vertical borehole in granitic rock. After approximately 5–6 years exposure, the test parcel was lifted and partitioned for examination. The results of these examinations were used as a reference. Test parcel dimensions were smaller compared to the KBS-3V deposition hole, in order to shorten the water saturation period, to achieve a higher

temperature gradient over the buffer material and to ease the uplift of the test parcel (Karnland et al., 2008).

The standard maximum temperature limit for final disposal repositories is 90°C. In the A2 test, the maximum temperature was set to 120–150°C. A 5–year period in these conditions covers a significant proportion of the thermal load in a KBS-3V repository with respect to kinetically controlled slow processes.

Test Site Description

The test site depth was ~450 m from the surface. The rock consists mainly of Äspö diorite. The A2 hole was 8 m deep and situated 33 m from the tunnel entrance. The water pressure was kept higher than the vapor pressure at the test temperature, and the water inflow rate was kept low enough to prevent piping erosion. Because this rate of water inflow was too low, it was decided to introduce external water via a supply hole, with water pressure into the hole ~1.2 MPa, through titanium tubes. The test site dimensions are presented in Table 1, and the test parcel is illustrated in Figure 2 (Karnland et al., 2008) below.

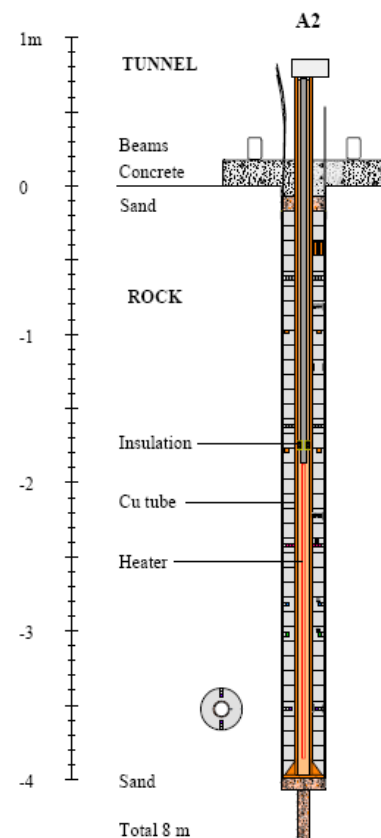


Figure 2. Scaled schematic drawing of the A2 test parcel (Karnland et al., 2008)

MATERIAL

Research has shown that sodium bentonite is currently the most viable material for isolating radioactive materials, due to its multiple beneficial characteristics (Wersin, 2003):

1. In case of canister failure, the migration of the majority of contaminants (radionuclides) is retarded almost completely, via sorption to the reactive clay surfaces.
2. Bentonite's ability to swell makes it an efficient barrier against contaminant migration.
3. Bentonite constitutes a mechanical and chemical zone of protection around the canister.
4. Bentonite has high thermal conductivity, thus serving to efficiently dissipate heat emitted by the waste.

Bentonites (montmorillonite clays) differ by mineralogical composition. The type chosen for final repository use, MX-80, is extracted, for example, from Wyoming (USA) and is a commercial material supplied in powder form. The MX-80 material consists mainly of sodium montmorillonite clay with small amounts of quartz, tridymite, cristobalite, feldspars, sulfides and other trace minerals (Karnland et al., 2008).

MODEL

Modeling Concept

The chemical phenomena occurring in the bentonite barrier in a disposal site depend on numerous factors, such as the rate of iron corrosion, the reaction temperature, the composition of the interaction fluid, the diffusion coefficients of the solutes, and the reactive surface area of minerals. Owing to the complexity of their estimation and mutual couplings, consideration of all of these parameters within a single model remains highly challenging. Certain simplifications must, therefore, be made. The model presented in this article is a simplified model, and its limitations as such must be recognized.

It is assumed that three phases (solid, liquid, and gas) are present in the modeled porous medium. The basic component of the solid montmorillonite is assumed to be insoluble, but able to absorb ions and exchange them with solution. Precipitated minerals are assumed to be part of the solid phase. The gas phase consists of water vapor and air, while the liquid phase consists of water, dissolved air, and other dissolved species. Local equilibrium is assumed for all chemical reactions, excluding mineral reactions with kinetics. Equilibrium is a limiting case for kinetics when transport is slow compared to reaction rates.

The model was created using the PetraSim user interface of the TOUGH2 and TOUGHREACT programs. The applied model is a thermo-hydro-chemical coupled model, meaning no mechanical alterations and effects are considered. The purpose of the model was to match the results as closely to the experimental results as possible, and thus the time frame was limited to ten years (the LOT A2 parcel test duration was approximately 6 years).

Modeling Program

TOUGHREACT EOS3 was used to model the reactive unsaturated transport processes in 1-D, and the grid was pitched at uniform intervals. The model constructed was a simplified model. The idea was to simplify the real 3-D model in which the copper canister producing heat is surrounded by bentonite and a rock matrix that contains a traversing water conducting fracture. The model can be simplified to 1-D because the changes in the bentonite are highest at the fracture location and diminish with increasing distance from the fracture. Thus, the worst possible scenario is in the fracture position. Figure 3 shows the model grid.

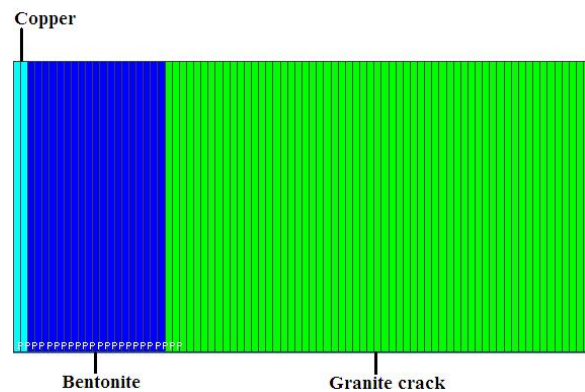


Figure 3. 1-D grid with 80 pitched cells at uniform intervals

Whereas the grid is simple, the phenomena at play within an actual system of this type are complex. The light blue cell on the left represents the heat source, i.e., the heat coming from the decay of spent fuel and the inert copper canister (1 cm). The green zone is granitic rock (29.5 cm) containing relatively free moving water. The dark blue zone is the bentonite (9.5 cm), which is initially partially saturated or virtually dry. The rightmost cell is a magnified water source. As such, the chemistry and water concentration in that cell remains constant. The bentonite has an initial water-mineral content and cation exchange capacity, and it interacts with the granitic Äspö groundwater outside the bentonite block. The copper canister is inert, exclusive of its heat production.

PetraSim version 4.1.0219 was used. A newer version of the PetraSim (4.2.1118) user interface, which uses newer versions of TOUGH2 and TOUGHREACT, is also available, but we were unable to produce consistent results with this version. The newer version produced a number of anomalous results, and the cation exchanger compositions were also calculated apparently incorrectly. The reasons for this are unclear.

Model parameters

The model parameters for these models were taken from different sources (Karnland et al., 2008), (Karnland et al., 2008), (Jacinto et al., 2009), (Arthur and Zhou, 2005) (Wersin, 2003), (Karnland et al., 2006). Some of the parameters were approximated according to the data. Table 2 shows the material parameters, and Table 3 shows the water-retention parameters used. The water-retention parameters for the fracture were set for constant saturation of the rock.

Table 2. Material parameters

Parameter	Granite		
	Bentonite	fracture	Copper
Pressure [Pa]	NTP	1.20E+06	NTP
Cation exchange capacity [meq/100g]	75		
Rock grain density [kg/m ³]	2 750	2 650	8 960
Diffusion coefficient [m ² /s]	2.00E-09		
Wet Heat Conductivity [W/(mC)]	1.3	2	2
Dry Heat Conductivity [W/(mC)]	0.3		
Porosity	0.43	0.14	0.01
Intrinsic Permeability [m ²]	3.00E-21	5.00E-11	0
Tortuosity	0.124	0.2	
Specific Heat [J/(kgC)]	2 500	784	385

Table 3. Water retention parameters: van Genuchten for the bentonite and Fatt&Klikoff for the granite fracture.

	Bentonite	Granite fracture
λ	0.338	
S_{ir}	0.4	0.999
S_{is}	1	
S_{gr}	0	
P_0	14.12 MPa	
P_{max}	140 MPa	

Besides material parameters, chemical data were needed for the model. Table 4 shows the bentonite mineral volume fractions in the model. Bolded minerals are inert.

Table 4. Mineral mass and volume fractions

Minerals	Mass fraction	Volume fraction
Gypsum CaSO ₄ ·2(H ₂ O)	0.17	0.0012
Anhydrite CaSO ₄	0.17	0.0009
Quartz SiO ₂	15.00	0.0897
Montmorillonite		
Na_{0.2}Ca_{0.1}Al₂Si₄O₁₀(OH)₂(H₂O)₁₀	76.00	0.4236
K-Feldspar KAISi ₃ O ₈	7.00	0.0427
Calcite CaCO ₃	0.70	0.0040
Chalcedony SiO ₂ (crystalline)	0.96	0.0057
Sum	100	0.568

The mineral kinetics were taken from Palandri and Kharaka (2004) with the exception of chalcedony, which was assumed to be at equilibrium. Also, groundwater, bentonite pore water, and ion exchanger composition were needed for the initial state and are shown in Table 5. The bentonite pore water was chosen so that the ion exchanger was initially filled correctly (Tournassat et al., 2007).

Table 5. Groundwater, bentonite pore water, and cation exchanger composition

Variable	Bentonite pore water composition		Cation exchanger composition (equivalent fractions/[meq/100g])
	[mmol/l]	[mmol/l]	
pH	6.9	8.62	
Na ⁺	100	9.972·10 ⁻⁴	0.808/60.6
K ⁺	0.28	2.79·10 ⁻⁷	0.009/0.675
Ca ²⁺	47.3	7.603·10 ⁻¹¹	0.128/9.6
Mg ²⁺	2.40	3.838·10 ⁻¹¹	0.055/4.125
Cl ⁻	178	1·10 ⁻³	
SO ₄ ²⁻	4.60	traces	
HCO ₃ ⁻	0.44 ¹	traces	
Al ³⁺	traces	traces	
H ₄ SiO ₄ (aq)	traces	traces	
O ₂ (aq)	traces	traces	

RESULTS

The results were fairly realistic. The obtained results were so numerous that they can be addressed here in part only. A full discussion of the results will be presented in a master thesis due for publication in August 2009 (Itälä, 2009).

Properties

A number of key properties were given special observation. Figure 4 shows the temperature and temperature gradient in the bentonite and part of the rock matrix. As one can see, the temperature gradient is approximately 4.7°C/cm, and the temperature 130–85°C in the bentonite. The bentonite was shown to saturate within approximately one year (Figure 5), which correlates closely with the LOT test report (Karnland et al., 2008).

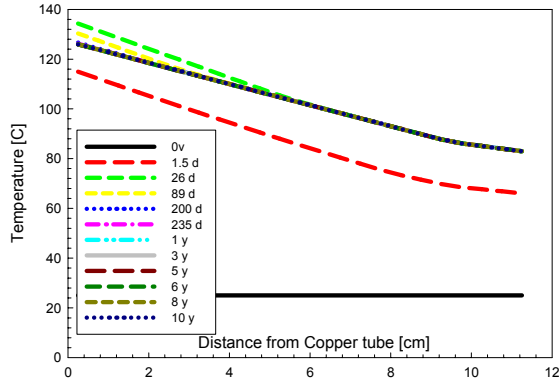


Figure 4. Temperature evolution as a function of distance from the copper tube, over time.

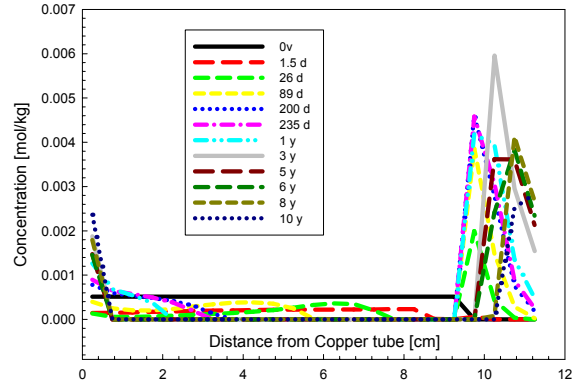


Figure 6. Anhydrite volume fractions as a function of distance from the copper tube, over time.

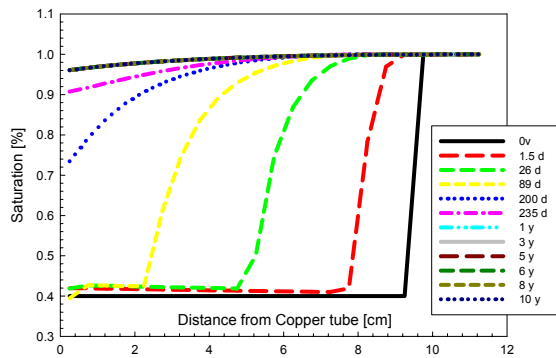


Figure 5. Saturation as a function of distance from the copper tube, over time

Other significant properties were pH and porosity. The change in porosity from 0.43 to 0.431 is so small that it does not affect the water flow or diffusion velocity. The reduction in pH is due to lack of surface complexation and also to higher temperature, which increases production of OH⁻ and H⁺ ions.

Minerals

Chalcedony is in equilibrium, and some equilibrium processes occur. Some calcite appears to dissolve near the copper (heat source) surface and gypsum dissolves within a couple of days. Quartz and K-Feldspar are almost stable. The most interesting of the minerals was, however, anhydrite. Figure 6 shows the anhydrite profile. It appears that when sulfate is diffusing out and calcium is coming in, anhydrite precipitates near the rock surface. Anhydrite also starts to precipitate near the copper surface due to high temperature.

Primary Species

The main primary species affecting the system were: Na⁺, Mg²⁺, Ca²⁺, K⁺, Cl⁻, and SO₄²⁻. Other species present are not discussed here. The calcium profile (Figure 7) shows calcium diffusing from the groundwater to the bentonite.

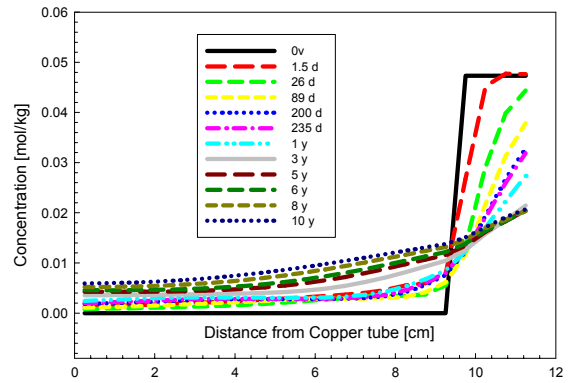


Figure 7. Total aqueous calcium component concentrations as a function of distance from the copper tube, over time

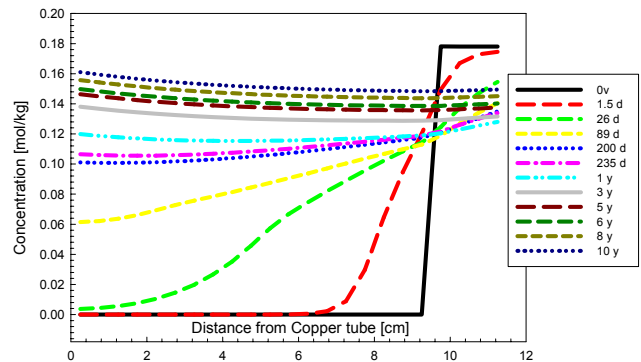


Figure 8. Total aqueous chloride component concentrations as a function of distance from the copper tube, over time

The chloride concentration increases with saturation and diffusion continues, although the diffusion profile is slightly anomalous compared to the boundary conditions (Figure 8.). Both sodium and sulfate ions diffuse out from the bentonite, due to increasing sodium concentrations in the bentonite resulting from cation exchange reactions (Figures 9 and 12) and an initial increase in sulfate concentrations caused by dissolution of gypsum (Figure 10).

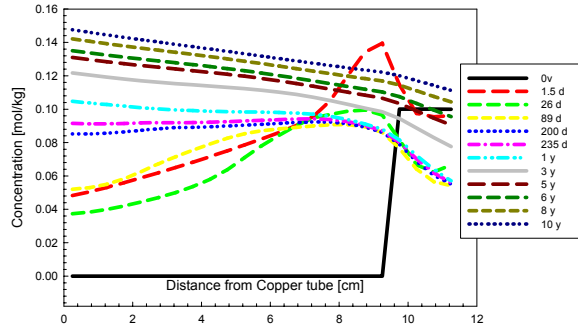


Figure 9. Total aqueous sodium component concentrations as a function of distance from the copper tube, over time

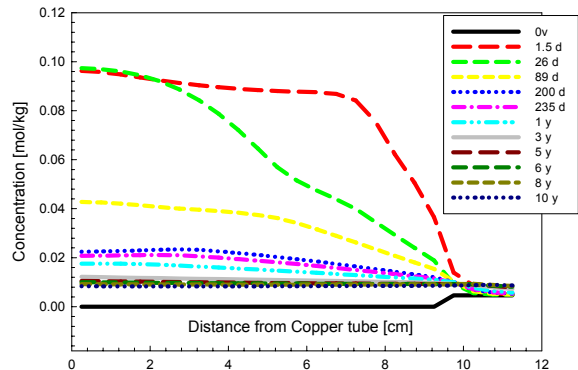


Figure 10. Total aqueous sulfate component concentrations as a function of distance from the copper tube, over time

Magnesium concentrations in the bentonite increase due to diffusion from groundwater and cation exchange. Potassium concentrations increase initially due to diffusion, but later, the direction of diffusion moves outwards to the rock matrix as the concentration in the bentonite exceeds that of the groundwater due to cation exchange.

Cation Exchanger

The cation exchanger composition changes are shown in the figures below as meq/100 g. It appears that calcium enters the cation exchanger and sodium exits (Figures 11 and 12). Calcium levels are, however, higher near the bentonite rock interface due to incoming calcium and, thus, the concentrations are

not balanced equally and equilibrium is not yet reached. The sodium content decreases, with the changes greatest near the rock surface (Figure 12). Potassium and magnesium also exit the exchanger and are replaced by calcium (Figures 13 and 14).

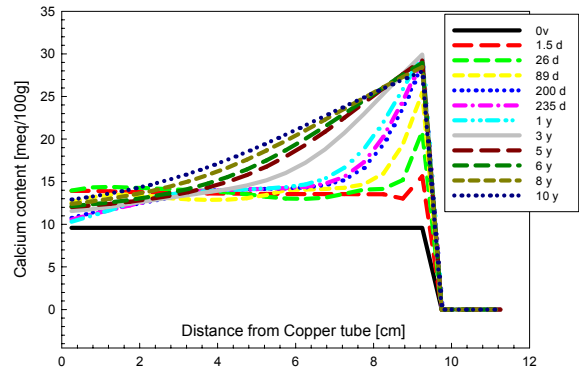


Figure 11. Calcium content [meq/100g] in the cation exchanger as a function of distance from the copper tube, over time

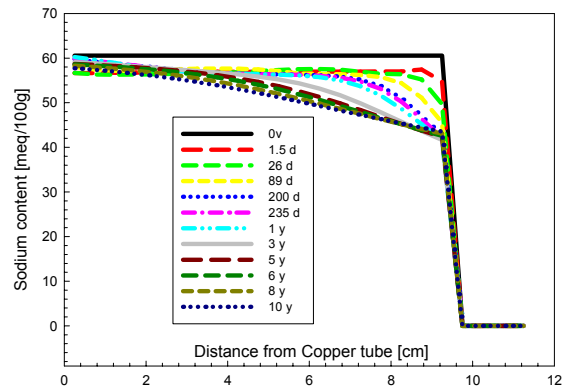


Figure 12. Sodium content [meq/100g] in the cation exchanger as a function of distance from the copper tube, over time

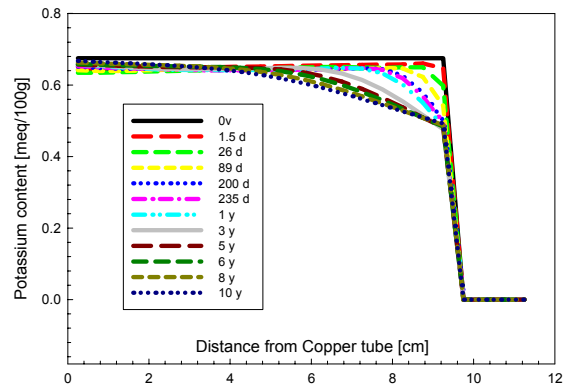


Figure 13. Potassium content [meq/100g] in the cation exchanger as a function of distance from the copper tube, over time

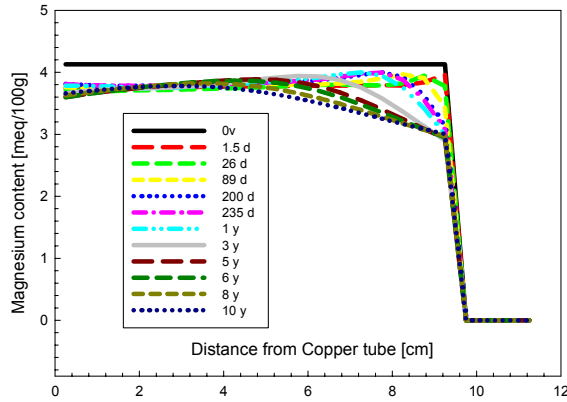


Figure 14 Magnesium content [meq/100g] in the cation exchanger as a function of distance from the copper tube, over time

DISCUSSION (VALIDITY)

Whereas the majority of the results appear to be qualitatively correct, their validity is open to a number of questions. The following limitations were applied to the creation of the model:

1. The calculation time of the model was limited to ten years, since the principal aim was to obtain calculated results that were as close as possible to the measured values, and because the LOT A2- parcel test duration was approximately six years.
2. Montmorillonite was chosen as the insoluble solid phase with constant ion exchange capacity.
3. The calculations were carried out in one dimension to simplify the system. The grid was thus created with one cell only in the y and z directions, and multiple cells in the x direction.

The model itself also contained the following limitations:

1. A major source of uncertainty is the fact that the model does not take into account the three different water types present in bentonite: the interlayer water, double layer water, and free water. The model assumes that all water content is accessible to solutes for transport and geochemical reactions.
2. THC predicted concentrations systematically overestimate measured values near the heater and show probably sharper gradients than those of measured data. This is because the model does not take into account bentonite swelling/shrinkage (or water

evaporation near the copper-bentonite interface).

3. TOUGHREACT does not include surface complexation: protonation/deprotonation of surface edge sites.
4. Even though THC processes are expected to alter the capillary strength parameter ($1/\alpha$), this effect has not been included in these models.
5. Diffusion coefficient is assumed constant for all ions and neutral molecules.
6. Swelling and rock mechanics are not included.
7. All material parameters are constant, and functions such as temperature cannot be added.
8. The model was 1-D, whereas a realistic model should be 3-D.

Furthermore, data limitations of THC modeling include:

1. General lack of kinetic data for environmental and geochemical processes is a major drawback. Laboratory-based values are not necessarily applicable to the field situation.
2. It is not well understood how to take handle a lack of equilibrium among redox couples.
3. Reactive surface areas and grain radii of minerals are highly uncertain, due to lack of data.
4. Uncertainties in thermodynamic data, especially at higher temperatures, may exist.
5. Van Genuchten function parameters for partial saturation in rock and bentonite are not well known, and no data is given for different temperatures.

CONCLUSIONS

The results show similarity with experimental data. However, the results are open to question, and further study is needed to confirm the validity of the results. The parameters used should be applied to other modeling programs, and the results compared.

Furthermore, more experimental data is needed (see discussion section for details). Constructing surface complexation in TOUGHREACT would be of key importance with respect to modeling the final repository of nuclear waste.

THC models could be improved by incorporating mechanical and geochemical coupling to account for porosity changes caused by swelling phenomena. This would lead to fully coupled THMC models (where M = mechanical).

ACKNOWLEDGMENTS

The study is jointly funded by the Finnish Research Programme on Nuclear Waste Management (KYT2010). The reference material is provided courtesy of Clay Technology AB. Many thanks to our colleague Merja Tanhua-Tyrkkö for our many fruitful discussions.

REFERENCES

- Arthur, R. and W. Zhou, *Reactive-Transport Model of Buffer Cementation*, 2005:59, SKI, Stockholm Sweden, 2005.
- Itälä, A., Chemical Evolution of Bentonite Buffer in a Final Repository of Spent Nuclear Fuel During Thermal Phase, Master of Science Thesis, Tampere University of Technology, Tampere, 2009 [on print].
- Jacinto, A. C., M. V. Villar, R. Gómez-Espina and A. Ledesma, Adaptation of the van Genuchten expression to the effects of temperature and density for compacted bentonites, *Applied Clay Science*, 42(3-4), 575-582, 2009.
- Karnland, O., S. Olsson, A. Dueck, M. Birgersson, U. Nilsson and T. Hernan-Håkansson, *LOT project - Long Term Test of Buffer Material. Parcel A2 field and laboratory draft report*. Clay Technology AB, Lund, Sweden, 2008.
- Karnland, O., S. Olsson and U. Nilsson, *Mineralogy and sealing properties of various bentonites and smectite-rich clay materials*, TR-06-30, SKB Swedish Nuclear Fuel and Waste Management Co, Stockholm Sweden, 2006.
- Palandri, J. L. and Y. K. Kharaka, A Compilation of Rate Parameters of Water-Mineral Interaction Kinetics for Application to Geochemical Modeling, 64, 2004.
- SKB-Swedish Nuclear Fuel and Waste Management Co. *Long-term safety for KBS-3 repositories at Forsmark and Laxemar - a first evaluation. Main report of the SR-Can project*, SKB-TR-06-09, Stockholm, Sweden, 2006.
- Tournassat, C., H. Gailhanou, C. Crouzet, Two cation exchange models for direct and inverse modelling of solution major cation composition in equilibrium with illite surfaces, *Geochimica et Cosmochimica Acta*, 71(5), 1098-1114, 2007.
- Wersin, P., Geochemical modelling of bentonite porewater in high-level waste repositories, *Journal of Contaminant Hydrology*, 61(1-4), 405-422, 2003.

MODELING PH EVOLUTION IN THE NEAR FIELD OF A CEMENTITIOUS REPOSITORY

Andrew Hoch¹, Fred Glasser², Graham Baston¹ and Victoria Smith¹

¹ Serco TAS, Harwell Science and Innovation Campus, Didcot OX11 0QB, United Kingdom
e-mail: Andrew.Hoch@serco.com

² Chemistry, University of Aberdeen, King's College, Aberdeen AB24 3FX, United Kingdom
e-mail: F.P.Glasser@abdn.ac.uk

ABSTRACT

The program TOUGHREACT has been applied to predict spatial and temporal changes in the chemical conditions within an underground disposal facility for radioactive waste. The model represents a single waste package, which is filled with an encapsulation grout, placed in an underground vault, and surrounded by a cementitious backfill. Groundwater from the host rock flows into the vault and through the backfill. The package is assumed to be situated close to the upstream edge of the vault.

This model has been used to examine the interactions between different groundwater compositions, the backfill, and various grout formulations. In most cases, the model predicts a reduction in the backfill porosity due to precipitation and dissolution reactions, particularly at the upstream edge of the vault. The degree to which this occurs depends on the groundwater composition. The groundwater flow is reduced significantly, which results in a high pH environment being maintained for longer periods than would have been predicted if the effects of changing porosity on groundwater flow had not been allowed for.

The model also predicts that precipitation and dissolution reactions will occur in the grouts close to the interface with the backfill, reducing the porosity there significantly. This isolates the grouts from the backfill, so that the pH within the grouts is unchanged over an extended period.

INTRODUCTION

In the United Kingdom, one possible concept for disposing of intermediate- and certain low-level radioactive wastes involves the placing of grouted waste packages in the vaults of a geological disposal facility (GDF), which are then surrounded by a cementitious backfill. The backfill, as part of a "multibarrier concept" to limit the migration of radionuclides from the wastes, will be required to maintain a high pH environment (in which the solubility of many radionuclides will be low) for a long period.

Formulations for a possible backfill, NRVB, and for a number of waste encapsulation grouts have been developed.

The physical and chemical properties of the GDF's near field will evolve as groundwater percolates through the facility and chemical reactions occur. It is important to understand these processes, so as to be able to predict the long-term effectiveness of the near field in limiting radionuclide release and migration.

Expected evolution of pH in the backfill

The hydrated backfill will contain a number of solid phases, with the exact mineral assemblage depending on both the formulation and the curing temperature. For "fresh" NRVB hydrated under typical repository conditions, the main components are expected to be alkali (i.e., Na, K) hydroxides, calcium hydroxide (Ca(OH)₂), calcium-silica-hydrate (CSH) gels, calcium carbonate, and hydrated calcium aluminates. A significant proportion of the alkali hydroxides will dissolve in the initial pore water, and will condition the pore water to a high pH (i.e. >13). As groundwater replaces the initial pore water, the chemistry will be dominated by the dissolution of Ca(OH)₂ and leaching of CSH. The dissolution of Ca(OH)₂ will maintain the high pH of the pore water (i.e., ~12.5) until it is exhausted, and then the pH will be buffered by CSH phases with a relatively high calcium-silicon molar ratio (Ca/Si). During this period, the pH is likely to drop, as the incongruent dissolution of CSH phases will remove calcium and hydroxide ions preferentially, thereby lowering the Ca/Si ratio and reducing the capacity of the system to buffer the pH. The formation of secondary minerals (e.g., brucite, ettringite, hydrogarnet, hydrotalcite and monocarboaluminate) may occur due to reactions between the inflowing groundwater, the backfill, and the wastes (especially those containing magnesium, sulphur, or aluminium). The secondary minerals could continue to buffer the pH.

Context

Previously, models have been developed that predict the long-term capacity of the near field to buffer the pH (e.g., Gould et al., 2001; Heath and Hunter, 2009). These models represented the effects of both waste and groundwater interactions with the cementitious materials. However, the models were concerned with reactions on the scale of a vault, and not on the scale of a single waste package. More recently, reactive transport computer programs have

been applied to predict pH evolution on the scale of a waste package (Small and Thompson, 2008), and, even more locally, within cracks through the backfill (Swift et al., 2008).

This paper identifies the mineral phases likely to be present in both the backfill and the encapsulation grouts at times soon after disposal, and then proposes a model for the evolution of the cement mineralogy, including the incongruent dissolution of CSH gels. The model was implemented using the program TOUGHREACT (Xu et al., 2004), and then the evolution of pH in the GDF was simulated over a timescale of 50,000 years. The model includes: aqueous speciation; equilibrium chemical reactions; and rate-dependent precipitation and dissolution reactions. In addition, the model calculates changes in transport properties (i.e., porosity and permeability) due to precipitation and dissolution reactions; and couples the changes in transport properties to the groundwater flow. Thus, effects such as “clogging” of pores due to carbonation (i.e., formation of calcite) are treated in a more realistic manner.

NUMERICAL METHOD

System under consideration

The model is of a 3 m^3 box, which contains both waste and grout, assumed to be situated towards the upstream boundary of a disposal vault (Figure 1).

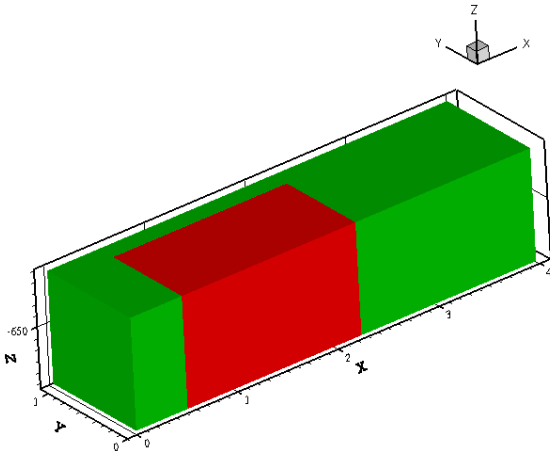


Figure 1. Geometrical model, showing the waste and encapsulation grout inside a 3 m^3 box (colored red) and the surrounding backfill (colored green). Because of symmetry, only half of the 3 m^3 box is represented. Groundwater flows into the backfill across the surface $X = 0$.

Groundwater from the host rock flows into the vault, through about half a meter of backfill, and then

through the 3 m^3 box. Because the grout has a lower permeability than the backfill, groundwater is channeled around the waste package. For simplicity, the steel container is not modeled.

Geometrical model

The 3 m^3 box and its surrounding backfill were simulated in two dimensions using TOUGHREACT (Xu et al., 2004). Assuming horizontal groundwater flow and vertical symmetry planes (both symmetry planes are aligned with the groundwater flow; one cuts through the mid-point of the waste package, and the other cuts through the backfill halfway between adjacent waste packages), only one half of the 3 m^3 box was modeled (Figure 2). The downstream edge of the model was chosen sufficiently far away that it would not affect behavior near the 3 m^3 box.

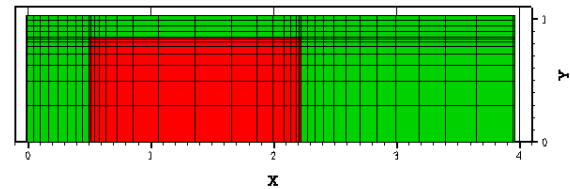


Figure 2 TOUGHREACT grid, showing refinement of the grid all around the 3 m^3 box and also at the upstream edge of the backfill. Groundwater flows into the backfill across the surface $X = 0$.

The geometry of the model was represented using a grid with 456 elements. The grid was refined at the interface between the grout and the backfill, and also at the upstream edge of the backfill. When refining the grid, consideration was given to the implications of the Courant and von Neumann stability conditions for time-step size, and the practicalities of running the model over a period of 50,000 years.

Chemical model

The hydration phases present in an encapsulation grout will depend on factors such as temperature and age. Reactions will continue for some time after encapsulation of the waste, and that could affect the subsequent evolution of pH in the GDF. Therefore, a review of current understanding was carried out and used to derive starting compositions for both the backfill and the grouts.

Backfill composition

The formulation of NRVB¹, which involves a mix of ordinary Portland cement (OPC), hydrated lime (i.e., calcium hydroxide) aggregate, limestone flour and water, is designed to give a cementitious material with high porosity. Holland and Tearle (2003) have considered the probable hydration phases for various conditions. Using information from that study, and assuming aluminum is partitioned equally between hydrogarnet and monocarboaluminate², led to the backfill composition in Table 1.

Table 1. Initial backfill composition (volume fraction)

Mineral	Formula	NRVB
Al-ettringite	$\text{Ca}_6\text{Al}_2(\text{SO}_4)_3(\text{OH})_{12}\cdot 26\text{H}_2\text{O}$	0.0375
Calcite	CaCO_3	0.1784
Monocarboaluminate	$\text{Ca}_4\text{Al}_2(\text{CO}_3)(\text{OH})_{12}\cdot 5\text{H}_2\text{O}$	0.0338
Si hydrogarnet	$\text{Ca}_3\text{Al}_2(\text{SiO}_4)_{0.8}(\text{OH})_{8.8}$	0.0194
CSH (Ca/Si = 4)	$\text{Ca}_{0.80}\text{Si}_{0.20}\text{O}_{1.20}\cdot 0.80\text{H}_2\text{O}$	0.2343
CSH (Ca/Si = 5.67)	$\text{Ca}_{0.85}\text{Si}_{0.15}\text{O}_{1.15}\cdot 0.85\text{H}_2\text{O}$	0.0095
Porosity*	—	0.2000
Un-reactive volume	—	0.2871

* A total porosity of about 0.5 has been measured (Francis *et al.*, 1997) using a combination of mercury intrusion porosimetry (for large pores) and nitrogen desorption (for small pores). However, experiments on the transport of tritiated water through NRVB (Harris and Nickerson, 1995) give a smaller value of about 0.2. This paper prefers the latter value.

Grout composition

Three grouts were considered:

- 3 parts blast furnace slag, 1 part ordinary Portland cement (3:1 BFS/OPC);
- 9 parts blast furnace slag, 1 part ordinary Portland cement (9:1 BFS/OPC); and
- 3 parts fly ash, 1 part ordinary Portland cement (3:1 PFA/OPC).

Typical “simplified” compositions for BFS, PFA and OPC were identified from the literature.

It is presumed the waste will be kept in storage for a period of about 100 years following encapsulation, and sufficient water will be present to ensure hydration of the grout over that period. In particular, all of the slag, but only 90% of the fly ash (taking account of unreactive crystalline phases) will react.

Hence, the hydration phases present in the grouts could be calculated. For example, in the case of the two BFS/OPC grouts it was assumed that:

- Ettringite is formed, consuming available SO_3 .
- “MgO” is present as hydrotalcite. (Hydrotalcite is considered more plausible than brucite, which is not observed in slag-rich cement pastes.)
- The remaining “ Al_2O_3 ” is present as stratlingite. (Stratlingite is considered the most realistic way to account for aluminum without forming large amounts of gibbsite, $\text{Al}(\text{OH})_3$.)
- The remaining “Ca” and “Si” form CSH gels.

In the case of 3:1 PFA/OPC grout, the only difference was to assume that:

- The remaining “Al” is present in the form of aluminum silicates with a low Al/Si ratio. Halloysite, $\text{Al}_2\text{Si}_2\text{O}_5(\text{OH})_4$, was chosen as the best mineral to represent the hydration phases.

These assumptions led to the grout compositions in Table 2.

Table 2. Initial Grout Composition (volume fraction)

Mineral	3:1 BFS/OPC	9:1 BFS/OPC	3:1 PFA/OPC
Al-ettringite	0.029	0.011	0.077
Calcite	0.007	0.003	0.011
CSH (Ca/Si = 1.1)	0.458	—	—
CSH (Ca/Si = 0.86)	—	0.423	—
CSH (Ca/Si = 0.70)	—	—	0.523
Hydrotalcite	0.123	0.139	0.043
Stratlingite	0.383	0.424	—
Halloysite	—	—	0.345

Solid solution model for CSH

CSH gels are amorphous, metastable, and exhibit incongruent dissolution with the preferential release of Ca. A number of approaches to thermodynamic modeling of these solid solution systems have been proposed (e.g., Bruno *et al.*, 2007; Berner, 1988; Kulic and Kersten, 2001; Walker *et al.*, 2007).

Recently, Lichtner and Carey (2006) have presented an approach to incorporating the thermodynamics and kinetics of solid-solution formation into reactive transport models. Their approach represents the continuously variable solid-solution composition by a discrete set of stoichiometric solids that cover the composition range, and is combined with a kinetic formulation of the rates of reaction. An advantage of this algorithm is that modeling solid-solutions is similar to modeling pure mineral phases, with the exception of a “weighting factor” applied to the

¹ NRVB is only a possible backfill material. The use of NRVB in this study is due to the availability of chemical information for it.

² Hydrogarnet is known to be the dominant phase at higher temperatures, such as those likely to occur during curing, but becomes unstable as the temperature falls to 25°C. Monocarboaluminate is expected to form at lower temperatures.

reaction rates of stoichiometric solids. The algorithm was implemented in TOUGHREACT.

Carey and Lichtner (2007) applied the algorithm to modeling CSH degradation, with portlandite and amorphous silica as end members. Unfortunately, the equilibrium constants Carey and Lichtner used for the end members (i.e., portlandite and silica) are inconsistent with values in the Nagra/PSI Chemical Thermodynamic database we use in this paper. To get around this problem, the fit of Carey and Lichtner was adjusted “by eye” to give a modified fit (Figure 3) consistent with the Nagra-PSI database.

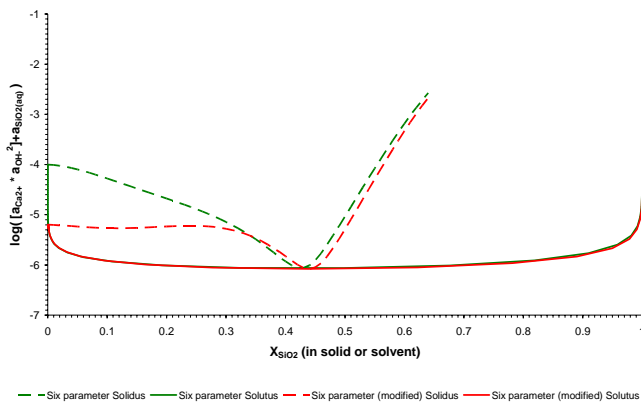


Figure 3 Carey and Lichtner’s (2007) fit (green lines) of their CSH model to Chen et al. (2004) data and our modified fit (red lines)

Groundwater composition

Four groundwater compositions³ (see Table 3) were considered:

Table 3. Groundwater Composition (at 25°C)

	Saline (mol kg ⁻¹)	High Carbonate (mol kg ⁻¹)	Low Carbonate (mol kg ⁻¹)	Clay (mol kg ⁻¹)
Na	3.7×10^{-1}	8.4×10^{-3}	8.2×10^{-2}	3.2×10^{-2}
K	4.4×10^{-3}	3.8×10^{-5}	2.5×10^{-4}	7.1×10^{-3}
Mg	5.7×10^{-3}	3.3×10^{-5}	6.8×10^{-4}	1.4×10^{-2}
Ca	2.9×10^{-2}	8.8×10^{-5}	4.8×10^{-2}	1.5×10^{-2}
Sr	2.0×10^{-3}	2.0×10^{-5}	9.9×10^{-4}	1.1×10^{-3}
Al	1.7×10^{-6}	4.6×10^{-7}	5.4×10^{-8}	6.9×10^{-9}
C	1.0×10^{-3}	2.8×10^{-3}	1.6×10^{-4}	3.0×10^{-3}
Si	2.5×10^{-4}	1.1×10^{-4}	7.6×10^{-5}	9.4×10^{-5}
Cl	4.2×10^{-1}	5.3×10^{-3}	1.7×10^{-1}	3.0×10^{-2}
SO ₄ ²⁻	1.2×10^{-2}	2.8×10^{-4}	6.4×10^{-3}	3.4×10^{-2}
pH	7.22	8.75	7.73	7.00

³ The use of these groundwater compositions is due entirely to the existence of appropriate data sets, and in no way prejudices any future site-selection programme.

- The first, “Saline,” is sample DET5 from Sellafield borehole RCF3 (Bond and Tweed, 1995) and is a typical saline groundwater.
- The second, “High Carbonate,” is sample DET6 from Dounreay, and has a high concentration of carbonate.
- The third, “Low Carbonate,” is sample DET8 from Dounreay and contains the lowest concentration of carbonate. Consequently, calcite precipitates at a slower rate, and the pores in the backfill do not clog.
- The fourth, “Clay,” is from the Callovo-Oxfordian (COX) argillite, and has high concentrations of magnesium and sulfate.

Thermodynamic database

The thermodynamic database used in the modeling was derived as follows. The Nagra/PSI Chemical Thermodynamic database (Hummel et al., 2002), which has been widely applied to model cement chemistry, was converted to a suitable format for use with TOUGHREACT. Next, this database was augmented to include hydrolysis reactions for cement phases based on the thermodynamic data given by Lothenbach et al. (2006; 2008) and Matschei et al. (2007), the so-called CEMDATA07 dataset.

Kinetic parameters

In general, the precipitation and dissolution reactions were controlled by kinetic-rate expressions based on Transition State Theory (Xu et al., 2004).

The kinetic parameters are shown in

Table 4 below.

Transport model

The region modeled was taken to be at steady state initially (i.e., at time $t = 0$), and the temperature was taken to be 25°C.

On the faces of the model perpendicular to the y-axis, the boundary conditions were taken to be no-flow of water or of aqueous species, because these faces correspond to planes of symmetry. On the other faces of the model, Dirichlet boundary conditions were specified for all of the variables, i.e., their values were prescribed.

For all the groundwater compositions except “Clay”, the specified value of the pressure was equal to the sum of the hydrostatic pressure and a linear pressure gradient in the x-direction chosen to give an initial specific discharge of $9.0 \times 10^{-11} \text{ ms}^{-1}$. (This flow is appropriate for a fractured, crystalline host rock.) In the case of “Clay”, the host rock permeability is lower, and the initial specific discharge was chosen to be $3.2 \times 10^{-13} \text{ ms}^{-1}$.

Table 4. Mineral molar volumes and reaction rates

Mineral	Formula	Molar Volume (cm ³ mol ⁻¹)	Reaction Rate (mol m ⁻² s ⁻¹)	Reactive Area (m ² g ⁻¹)	Note
Al-ettringite	Ca ₆ Al ₂ (SO ₄) ₃ (OH) ₁₂ •26H ₂ O	707	1.12 × 10 ⁻¹²	9.8	(1)
Calcite	CaCO ₃	37	1.44 × 10 ⁻⁷	1	(2)
Monocarboaluminate	Ca ₄ Al ₂ (CO ₃)(OH) ₁₂ •5H ₂ O	262	6.31 × 10 ⁻¹²	5.7	(1)
Si hydrogarnet	Ca ₃ Al ₂ (SiO ₄) _{0.8} (OH) _{8.8}	143	1.12 × 10 ⁻¹²	10	(3)
Portlandite	Ca(OH) ₂	33.226	2.24 × 10 ⁻⁸	16.5	(2)
CSH	—	—	2.75 × 10 ⁻¹²	41	(1)
SiO ₂ (am)	SiO ₂	29	—	1	(4)
Hydrotalcite	Mg ₄ Al ₂ (OH) ₁₂ CO ₃ •3H ₂ O	220	1.12 × 10 ⁻¹²	10	(3)
Stratlingite	Ca ₂ Al ₂ SiO ₂ (OH) ₁₀ •3H ₂ O	216	1.00 × 10 ⁻¹²	10	(5)
Halloysite	Al ₂ Si ₂ O ₅ (OH) ₄	100	1.00 × 10 ⁻¹²	10	(5)
Brucite	Mg(OH) ₂	30	1.00 × 10 ⁻⁷	1	(6)
Gypsum	CaSO ₄	73	1.00 × 10 ⁻⁷	1	(6)
Monosulfoaluminate	Ca ₄ Al ₂ (SO ₄)(OH) ₁₂ •6H ₂ O	309	6.31 × 10 ⁻¹²	5.7	(1)

- (1) These data (*i.e.* rates and surface areas) are from the doctoral dissertation of Isabel B. Keller (2004), submitted to the Swiss Federal Institute of Technology Zurich. Also, see Baur *et al.* (2004).
(2) See Marty *et al.* (2009) and references therein.
(3) Set similar to ettringite. Also, see Marty *et al.* (2009).
(4) TOUGHREACT includes a kinetic model specifically for SiO₂(am), which was used in this study.
(5) No data found. Assumed to be similar to ettringite.
(6) Brucite and gypsum were assumed to have reaction rates and surface areas similar to those of calcite.

The transport parameters are shown in Table 5.

Table 5. Transport Parameters

	Backfill	Grout
Permeability	10 ⁻¹⁶ m ²	10 ⁻¹⁸ m ²
Initial porosity	0.2*	0.2
Tortuosity	0.15**	0.005***

* A total porosity of about 0.5 has been measured (Francis *et al.*, 1997) using a combination of mercury intrusion porosimetry (for large pores) and nitrogen desorption (for small pores). However, experiments on the transport of tritiated water through NRVB (Harris and Nickerson, 1995) give a smaller value of about 0.2. This paper prefers the latter value.

** This was calculated from the intrinsic diffusion coefficient of tritiated water, which has been measured to be 6.0 10⁻¹¹ m²s⁻¹ (Harris and Nickerson, 1995), and the capacity factor, which has been measured to be 0.2. The aqueous molecular diffusion constants are assumed to be 2 10⁻⁹ m²s⁻¹.

*** A typical intrinsic diffusion coefficient for both sulfate resistant Portland cement and BFS/OPC is about 2.0 10⁻¹² m²s⁻¹ (Harris and Nickerson, 1995).

The porosity of the different materials will change due to mineral precipitation and dissolution reactions. The changes in porosity will cause changes in permeability, which were estimated using the Kozeny-Carman relationship (Xu *et al.*, 2004).

RESULTS AND DISCUSSION

Detailed results are presented only for a 3 m³ box of 3:1 BFS/OPC grout surrounded by backfill, through which groundwater “Saline” percolates.

The predicted evolution of pH over a 50,000-year time scale is illustrated in Figure 4.

In the region where groundwater flows into the model, initially the pH drops, but after 2,500 years, no significant change is observed. The reason for this behavior is a decrease in the porosity of the region due to precipitation of minerals, mainly of calcite (Figure 5, Figure 6). As the porosity decreases, the flow also decreases (Figure 5). Eventually the backfill becomes sealed off by a layer of calcite, produced by the reaction of carbonate in the groundwater with calcium from the backfill. The carbonation of cement surfaces is an effect that is well-documented (Cowie and Glasser, 1992; Harris *et al.*, 2003), and so, in this respect, the model predictions agree with experimental observations. In addition to calcite precipitation, some hydrotalcite formation is predicted (Figure 6). Finally, brucite and gypsum form at early times, but their volume fractions decrease after about 2,500 years, coinciding with a drop in the pH due to dissolution of CSH.

The other region where there are significant mineral changes, with a corresponding decrease in porosity, is close to the interface between the grout and the backfill. In the grout, monocarboaluminate and CSH form as species from the calcium-rich backfill porewater diffuse into the grout. In the backfill, Al-ettringite forms as aluminium diffuses from the grout into the backfill

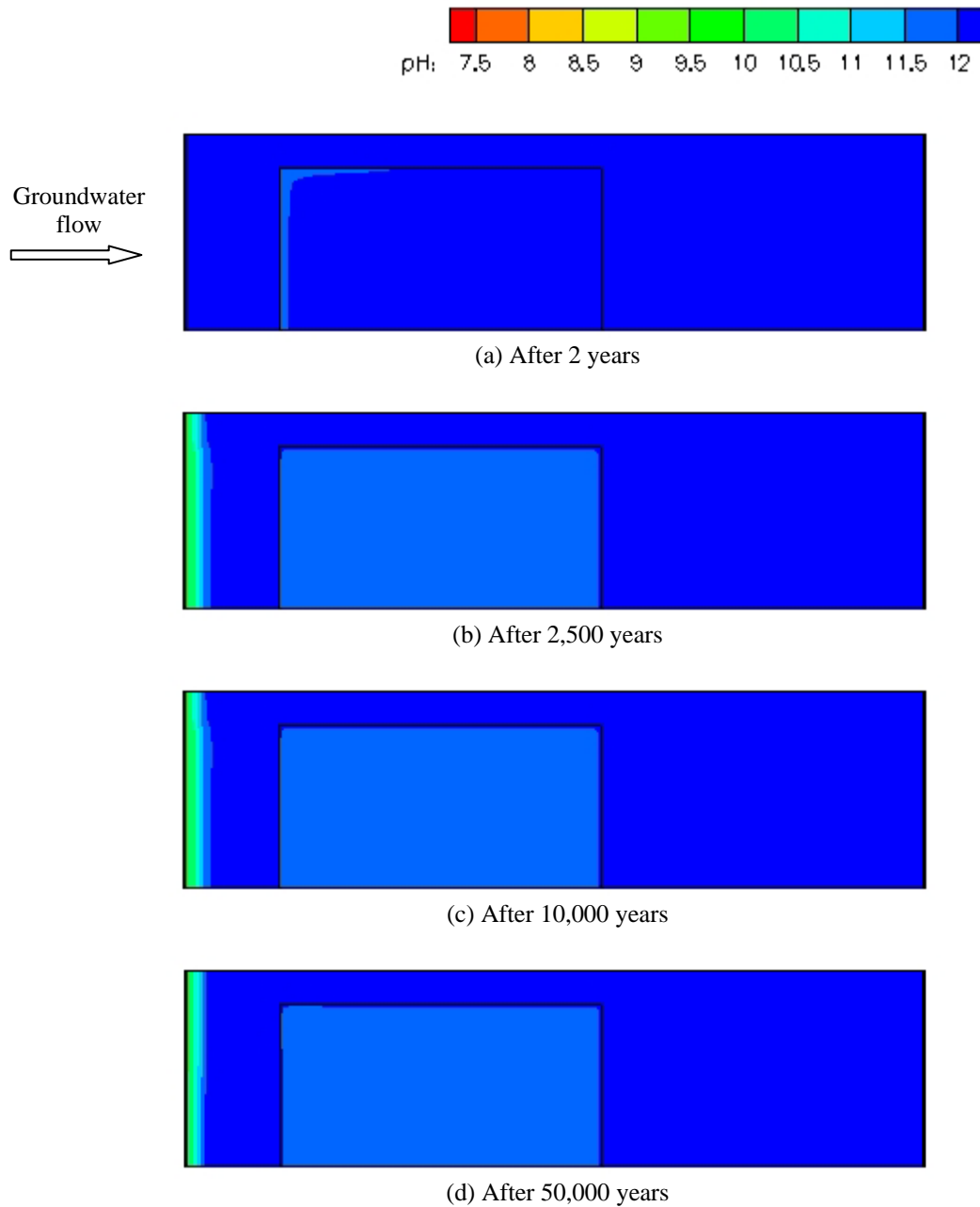


Figure 4. Predicted evolution of pH over a period of 50,000 years (for groundwater with a “Saline” composition flowing through backfill surrounding a 3:1 BFS / OPC grout).

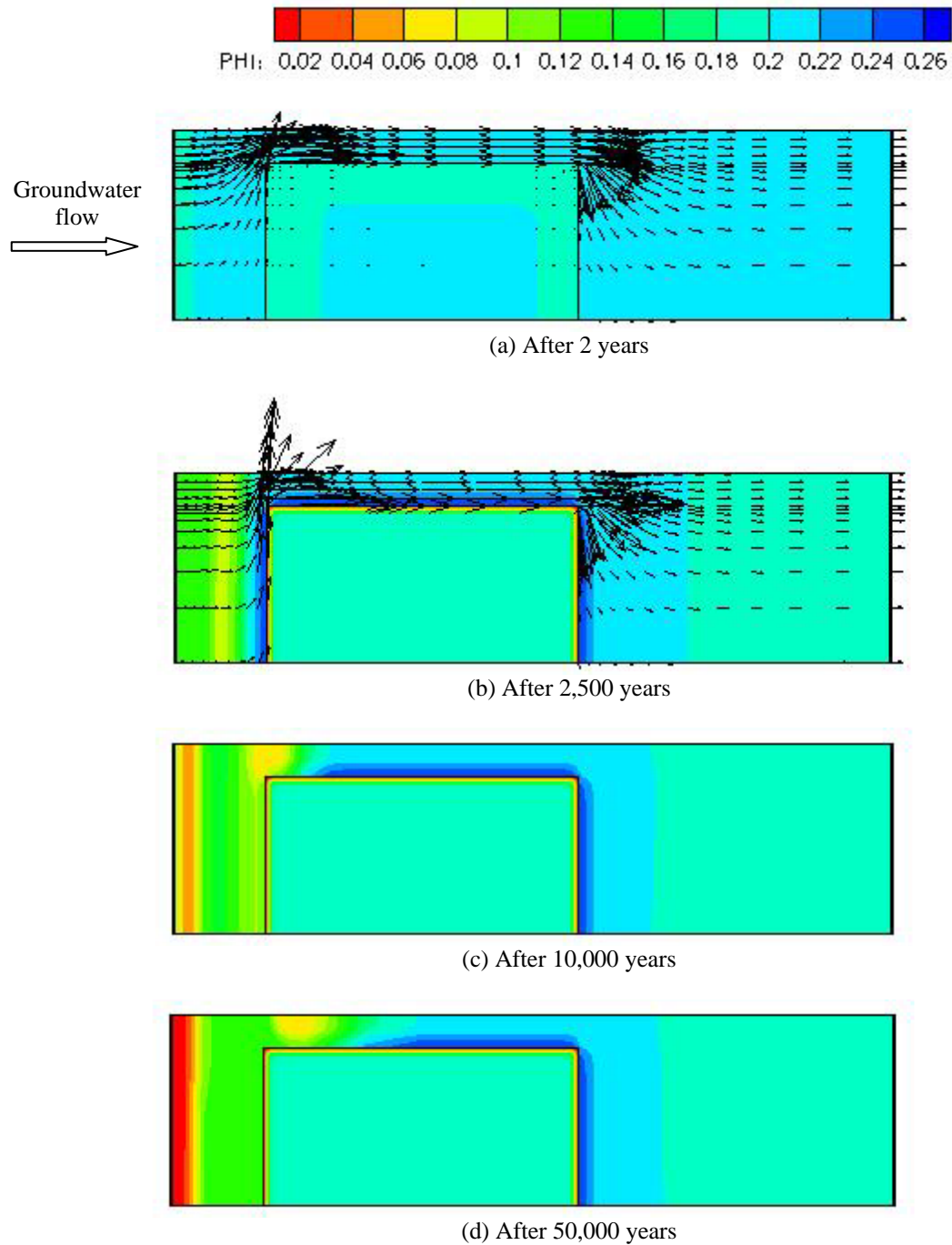


Figure 5 Predicted changes in porosity and groundwater flow over a period of 50,000 years (for groundwater, with a “Saline” composition flowing through backfill surrounding a 3:1 BFS / OPC grout). The flow vectors at 10,000 and at 50,000 years cannot be seen because the flow is very low.

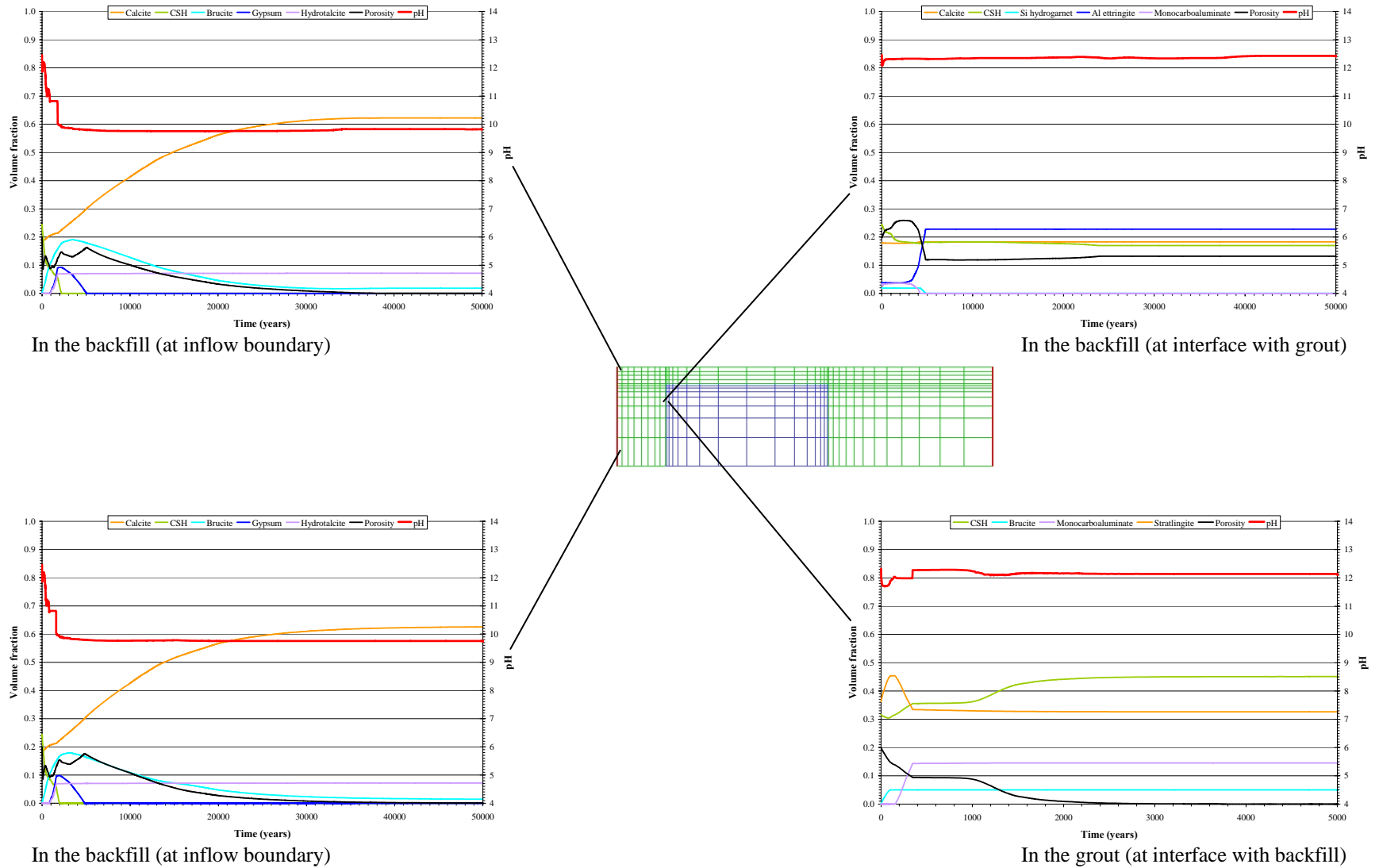


Figure 6 Predicted changes in the volume fractions of some key minerals over a period of 50,000 years (for groundwater with a “Saline” composition flowing through backfill surrounding a 3:1 BFS / OPC grout).

Variant simulations considered different groundwater compositions and different grout formulations.

Depending on the carbonate concentration of the groundwater, sufficient calcite may or may not form in the region where groundwater flows into the model to clog the pores of the backfill. For example, although calcite forms for the “Low Carbonate” groundwater, it is not enough to fill the porosity over a period of 50,000 years. In the case of the “Clay” groundwater, brucite and gypsum form as well as calcite.

The other region where there are significant mineral changes is close to the interface between the grout and the backfill. Results have been presented above for BFS/OPC grouts in contact with the backfill. For the PFA/OPC grout, Al-ettringite again forms in the backfill. In the grout, a significant fraction of the halloysite reacts with Ca^{2+} from the backfill to form stratlingite. This reaction occurs only close to the edge of the grout, and the bulk of the grout remains unaltered.

UNCERTAINTIES

There are some simplifications and uncertainties in the model, which mean that caution is needed when interpreting the results for the evolution of pH in the GDF.

The formation of calcite in cementitious materials which have been exposed to carbonate has been observed in experimental studies, and so is likely to occur in the GDF. However, the TOUGHREACT model assumes a simple Kozeny-Carman expression to relate changes in permeability to changes in porosity. The predicted timescale for calcite to clog the pores in the backfill depends on this assumption, and therefore is uncertain. The situation is further complicated by the possibility that most of the groundwater actually may flow through cracks in the backfill.

The reactions at the interface between the backfill and the grouts also are uncertain. Although predicted by thermodynamic modeling, some of the reactions may not occur. However, if the grouts do react with the backfill to form a low-permeability “skin,” then the mobility of radionuclides from out of the waste packages would be reduced significantly. This could be an important conclusion.

Despite these reservations, the TOUGHREACT model represents a significant step forward in representing the effects of mineral reactions on groundwater flow to predict evolution of chemistry in the near field.

SUMMARY

A TOUGHREACT model has been used to examine the interactions between the cementitious backfill in a disposal facility for radioactive waste, different grout formulations, and various groundwater compositions.

In most cases, the model predicts a reduction in the backfill porosity due to precipitation and dissolution reactions, particularly at the upstream edge of the vault. The degree to which this occurs depends on the groundwater composition. In some cases, the reactions seal the backfill, preventing further ingress of groundwater, which results in a high pH (i.e., $\text{pH} > 12$) environment being maintained thereafter. In other cases, the rates of groundwater flow are reduced significantly, which results in a high pH environment being maintained for longer periods than would have been predicted if the effects of changing porosity on groundwater flow had not been allowed for.

The model also predicts that precipitation and dissolution reactions will occur in the grouts close to the interface with the backfill, reducing the porosity significantly there. This isolates the grouts from the backfill, so that the pH within the grouts is unchanged over an extended period. However, there is some uncertainty about whether the reactions that are assumed to occur at the interface between the grouts and the backfill are correct; further investigation is needed to validate this aspect of the model.

ACKNOWLEDGEMENT

We are grateful to Fiona Hunter for her help with preparing this paper.

This work was funded by the United Kingdom’s Nuclear Decommissioning Authority.

REFERENCES

- Baur, I., P. Keler, D. Mavrocordatos, B. Wehrli and C. A. Johnson, Dissolution-precipitation Behaviour of Ettringite, Monosulfate, and Calcium Silicate Hydrate, *Cement and Concrete Res.*, **34**(2), 341-348, 2004.
- Berner, U. R., Modelling the Incongruent Dissolution of Hydrated Cement Minerals, *Radiochim. Acta*, **44/55**, 387-393, 1988.
- Bond, K. A., and C. J. Tweed, *Groundwater Compositions for the Borrowdale Volcanics Group, Boreholes 2, 4 and RCF3, Sellafield, Evaluated Using Thermodynamic Modelling*, Report NSS/R397, Nirex, 1995.

- Bruno, J., D. Bosbach, D. Kulik and A. Navrotsky, *Chemical Thermodynamics of Solid Solutions of Interest in Nuclear Waste Management, a State-of-the-art Report*, Volume 10 of the "Chemical Thermodynamics" Series, OECD Nuclear Energy Agency, 2007.
- Carey, J. W., and P. C. Lichtner, Calcium Silicate Hydrate (C-S-H) Solid Solution Model Applied to Cement Degradation Using the Continuum Reactive Transport Model FLOTRAN, in: eds. B. Mobasher and J. Skalny, *Transport Properties and Concrete Quality: Materials Science of Concrete*, special volume, 73-106, American Ceramic Society, 2007.
- Chen, J. J., J. J. Thomas, H. F. W. Taylor and H. M. Jennings, Solubility and Structure of Calcium Silicate Hydrate, *Cement and Concrete Res.*, **34**(9), 1499-1519, 2004.
- Cowie, J., and F. P. Glasser, The Reaction Between Cement and Natural Waters Containing Dissolved Carbon Dioxide, *Adv. in Cem. Res.*, **4**(15), 119-134, 1992.
- Gould, L. J., A. W. Harris and A. Haworth, *Calculation of the Volume of Backfill Required in the Near Field of a Repository*, Report AEAT/ERRA-2270, AEA Technology, 2001.
- Francis, A. J., R. Cather and I. G. Crossland, *Nirex Safety Assessment Research Programme: Development of the Nirex Reference Vault Backfill*, Report S/97/014, Nirex, 1997.
- Harris, A. W., M. C. Manning and W. M. Tearle, *Carbonation of Nirex Reference Backfill*, Report SERCO/ERRA-0454, Serco, 2003.
- Harris, A. W., and A. K. Nickerson, *The Mass-transport Properties of Cementitious Materials for Radioactive Waste Repository Construction*, Report NSS/R309, Nirex, 1995.
- Heath, T. G., and F. M. I. Hunter, *Calculation of Near-field pH Buffering: Effect of Polymer Encapsulant*, Report SA/ENV-0909, Serco, 2009.
- Heath, T. G., F. M. I. Hunter, S. Magalhaes and V. Smith, *Spreadsheet Model for the Impact of Waste Packages on Local pH Conditioning*, Report SERCO/TAS/000356/01 Issue 1, Serco, 2009.
- Holland, T. R., and W. M. Tearle, *A Review of NRVB Mineralogy*, Report SERCO/ERRA-0455, Serco, 2003.
- Hummel, W., U. Berner, E. Curti, F. J. Pearson and T. Thoenen, *Nagra/PSI Chemical Thermodynamic Data Base 01/01*, Report NTB 02-16, Nagra, 2002.
- Kulic, D. A., and M. Kersten, Aqueous Solubility diagrams for Cementitious Waste Stabilisation Systems: II, End-member-stoichiometries of Ideal Calcium Silicate Hydrate Solid Solutions, *J. Am. Ceram. Soc.*, **84**, 3017-26, 2001.
- Lichtner, P. C., and J. W. Carey, Incorporating Solid Solutions in Reactive Transport Equations using the Discrete-composition Approach, *Geochim. et Cosmochim. Acta*, **70**, 1356-1378, 2006.
- Lothenbach, B., T. Matschei, G. Möschner and F. P. Glasser, Thermodynamic Modelling of the Effect of Temperature on the Hydration and Porosity of Portland Cement, *Cement and Concrete Res.*, **38**(1), 1-18, 2008.
- Lothenbach, B., and F. Winnefeld, Thermodynamic Modelling of the Hydration of Portland Cement, *Cement and Concrete Res.*, **36**(2), 209-226, 2006.
- Marty, N. C. M., C. Tournassat, A. Burnol, E. Giffaut and E. C. Gaucher, Influence of Reaction Kinetics and Mesh Refinement on the Numerical Modelling of Concrete/Clay Interactions, *J. Hydrol.*, **364**, 58-72, 2009.
- Matschei, T., B. Lothenbach and F. P. Glasser, Thermodynamic Properties of Portland Cement Hydrates in the System CaO-Al₂O₃-SiO₂-CaSO₄-CaCO₃-H₂O, *Cement and Concrete Res.*, **37**(10), 1379-1410, 2007.
- Small, J.S., and O. R. Thompson, *Development of a Model of the Spatial and Temporal Evolution of pH in Cementitious Backfill of a Geological Repository*, Report Nexia Solutions (07) 8869, Nexia Solutions, 2008.
- Swift, B. T., P. B. Bamforth, A. R. Hoch, C. P. Jackson, D. A. Roberts and G. M. N. Baston, *Cracking, Flow and Chemistry in NRVB*, Report SERCO/TAS/000505/01 Issue 1, Serco, 2008.
- Walker, C.S., D. Savage, M. Tyrer and K. Vala Ragnarsdottir, Non-ideal Solid Solution Aqueous Solution Modeling of Synthetic Calcium Silicon Hydrate, *Cement and Concrete Res.*, **37**(4), 502-511, 2007.
- Xu, T., E. Sonnenthal, N. Spycher, and K. Pruess, *TOUGHREACT User's Guide: a Simulation Program for Non-isothermal Multiphase Reactive Geochemical Transport in Variably Saturated Geologic Media*, Report LBNL-55460, Lawrence Berkeley National Laboratory, 2004.

NATURAL CONVECTION IN TUNNELS AT YUCCA MOUNTAIN AND IMPACT ON DRIFT SEEPAGE

Halecky, N.¹⁺², J.T. Birkholzer¹, P.F. Peterson²

¹Lawrence Berkeley National Laboratory, Berkeley, CA

²University of California at Berkeley, Berkeley, CA

e-mail: nehalecky@lbl.gov

ABSTRACT

The decay heat from radioactive waste that is to be disposed in the proposed geologic repository at Yucca Mountain (YM) will significantly influence the moisture conditions in the fractured rock near emplacement tunnels (drifts). Additionally, large-scale convective cells will form in the open-air drifts and will serve as an important mechanism for the transport of vaporized pore water from the fractured rock in the drift center to the drift end. Such convective processes would also impact drift seepage, as evaporation could reduce the build up of liquid water at the tunnel wall. To study such processes, we previously developed and applied an enhanced version of TOUGH2 (Pruess et al., 1999) that solves for natural convection in the drift. Results from this study were then used as a time-dependant boundary condition in a high-resolution seepage model, allowing for a computationally efficient means for simulating these processes.

INTRODUCTION

The unsaturated tuffs at Yucca Mountain, Nevada, are being considered as a geological repository for the disposal of high-level nuclear waste in the United States. Decay heat, from the emplaced spent nuclear fuel and defense wastes, would significantly alter the thermal hydrological (TH) conditions in the host rock and the waste emplacement tunnels. Pore water vaporization, transport and the subsequent condensation results in changes in saturation and fluxes throughout the surrounding rock. Characterizing and understanding these liquid water and vapor transport processes is critical for evaluating the performance of the repository, in terms of water-induced canister corrosion and subsequent radionuclide containment.

Previous computational fluid dynamic studies have shown the formation of large-scale natural convection cells along the length of the drifts, a result of temperature differences between the heated and cool sections of the drift (Webb et al. 2003). These convective cells could provide an effective mechanism for moisture transport of pore water, evaporated from the rock formation, from the heated drift centers to the cool drift ends (where no waste is emplaced). To understand these processes, a new module was developed for TOUGH2 (Pruess et al., 1999), allowing the solving of natural convection

processes in open cavities. The new module simultaneously handles (a) the flow and energy transport processes in the unsaturated fractured rock, (b) the flow and energy transport processes in the cavity, and (c) the heat and mass exchange at the rock-cavity interface.

Recent studies employed TOUGH2 with the new module to simulate the impact of natural convection on the future TH conditions of a full 3D drift domain, including the in-drift environment and the surrounding fractured rock (Birkholzer et al., 2006, 2008). Results from these studies showed a large increase in the moisture transport away from the heated drift center, and a subsequent reduction in the relative humidity (RH) of the in-drift environment, suggesting a substantial increase in the evaporative potential at the drift wall when compared to a case with no natural convection.

In this paper, we present a new procedure for investigating the complex coupled behavior between natural convection and its impact on drift seepage. Previous studies investigating thermally driven flow processes and their impact on seepage neglected the presence of open drifts as conduits for gas and vapor transport along the drift axis (e.g., Birkholzer et al., 2004), thus neglecting an important mechanism for seepage reduction. To better understand what role the natural convective processes might have on minimizing seepage of percolation water into the tunnels, a high-resolution seepage model was developed based on existing seepage models; however, now additionally employing the new natural convection module. Because an increased grid resolution was needed to allow for heterogeneity in element permeability near the drift wall, computational limitations prevented simulation of an entire drift in the new model. Instead, the time dependent in-drift response from the previous full-drift and rock model (temperature, pressure, and relative humidity) was used as a Dirichlet boundary source for the high-resolution seepage model. Three different infiltration input sources were used as sensitivity cases to account for the variations in subsurface flow expected at Yucca Mountain.

BASIC TH PROCESSES

At Yucca Mountain, the heat emanating from the waste packages (horizontally emplaced cylindrical

canisters about 5 m long, with a small gap in between them) will be effectively transferred to the drift walls, mostly via thermal radiation. At early stages after emplacement, temperatures in the partially saturated formation near the drifts will heat up to above-boiling conditions. As a result, the initially mostly stagnant pore water in the rock matrix will become mobile through boiling (see Figure 1a). Vaporization causes a pressure increase, which will drive the vapor away from the boiling region, both into more distant rock regions (where the vapor will condense and enhance liquid fluxes) as well as back into the drifts (where relative humidity will increase). At later times, when temperatures will decrease below boiling, the rock mass near the drifts will gradually rewet (Figure 1b).

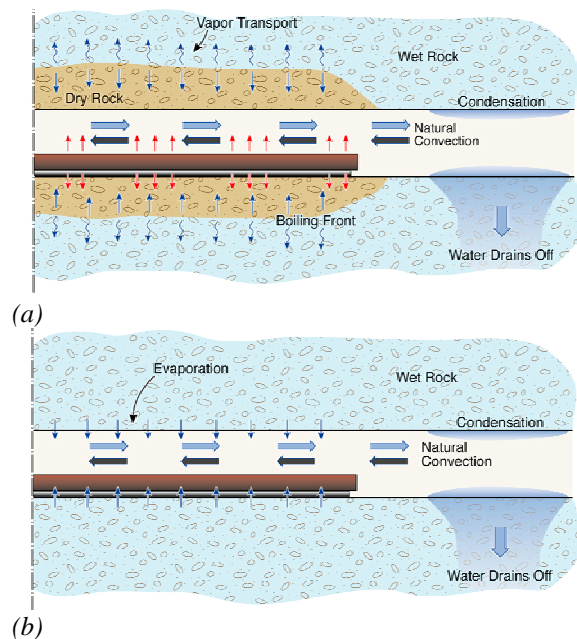


Figure 1. Schematic of expected TH processes along emplacement drift for (a) boiling conditions and (b) sub-boiling conditions. (modified from Webb and Reed, 2004).

Natural Convection Processes

Vapor entering the emplacement drifts from the fractured porous rock is subject to effective radial and axial mixing transport as a result of natural convection processes. Axial mixing can reduce the overall moisture content in heated drift sections because of the presence of the unheated drift ends (turnouts). Principles of thermodynamics suggest that the maximum amount of vapor that can be present in air decreases with declining temperature. Thus, the warm vapor-rich gases moving from heated drift sections toward the drift turnouts—caused by natural convection processes—will be depleted of most of their vapor content through condensation on cooler rock surfaces. (As shown in Figure 1, the condensate will drain away from the repository into underlying rock units.) At the same time, vapor-poor gas will

circulate towards the emplacement sections of the drifts, thereby reducing the moisture content in these areas (Birkholzer et al., 2006, 2008).

Seepage Processes

Seepage refers to the flow of liquid water into emplacement drifts. Water tends to divert around underground openings because of capillarity, behavior well known as the capillary barrier. This condition arises, for example, when coarse-grained soils are overlain by fine-grained soils. Across this boundary, the stronger negative capillary pressure developed in the fine-grained material prevents water from entering the larger pores of the underlying coarse-grained material (Birkholzer et al., 1999). In the case of zero capillarity (as in the case of the open drift), seepage into the drift can only occur if the capillary pressure in the rock close to the drift walls becomes zero; i.e., the fractured rock becomes locally saturated. Local saturation in the rock can occur due to a disturbance to the flow field (caused by the presence of the drift opening) and more importantly by spatial heterogeneity that promotes channelized flow and local ponding (Birkholzer et al., 1999). Parameters that have the largest impact on seepage at ambient temperatures are the

- amount of percolation flux above the drifts (amount of water arriving at the drift wall),
- local heterogeneity of the fracture flow field (the orientation of fractures to the drift opening), and
- capillary strength of the fractures close to the wall (the amount of water the rock can hold) (Birkholzer et al., 1999).

We refer to thermal seepage when considering the possibility of seepage during the time period that the flow around drifts is perturbed from heating. When the surrounding rock is above boiling temperatures, a superheated dryout region forms around the drifts, serving as a barrier to seepage since percolating liquid water is vaporized prior to reaching the drift wall (Birkholzer et al., 2004). Later, when rock temperatures return to below-boiling conditions, seepage is impacted by the thermodynamic conditions in the drifts. Natural convection would reduce seepage by reducing the RH of the local in-drift environment and thus increasing evaporation of water at the drift wall.

MODELING APPROACH

During times with thermal perturbations due to decay heat, the in-drift environment is impacted by axial vapor transport via natural convection. These processes occur over the length of the entire drift and, therefore, require the modeling of a full-scale drift tunnel (including drift turnout, where no waste is emplaced) along with the surrounding host rock.

Developing a model that captures and solves both seepage and natural convection processes

simultaneously would require an extremely complex discretization and significant computational resources. We instead propose a unique method to use the time varying, thermodynamic response of the in-drift domain from our previously developed full-drift & rock natural convection model (referred from here on as the *nat-co model*) as a time-dependent boundary condition for the in-drift domain for a high-resolution seepage model (referred from here on as the *seepage model*). This allows us to not need to model the entire length of the drift in the seepage model, helping to reduce the grid complexity by an order of magnitude. Because such time-dependant, in-drift boundary conditions, generated from the *nat-co model*, will have a large impact on seepage, we will describe again the details of this model and follow with details for the seepage model.

Nat-Co Model: The previous Full-Drift & Rock Natural Convection Model

Our previous studies developed a full-drift and rock natural convection model to understand the effect that natural convection has on vapor transport in a drift at YM.

Modeling Framework for Fractured Rock Mass

The modeling framework for simulating the TH conditions in the near-field fractured rock was adopted from existing TH models for Yucca Mountain (e.g., Birkholzer et al., 2004). The TOUGH2-EOS4 simulator (Pruess et al., 1999) accounts for convective and diffusive movement of gaseous and liquid phases of components water and air (under pressure, viscous, capillary, and gravity forces); transport of latent and sensible heat; phase transition between liquid and vapor; and vapor pressure lowering. The fractured rock was described using a dual permeability concept, assuming two separate but interacting continua that superpose with each other in space. One continuum describes flow and transport in the fractures; the other describes flow and transport in the rock matrix. We assume the emplacement drift is located in the Topopah Spring Tuff lower lithophysal unit (Ttpltl), and use rock properties of this geologic strata for the entire fractured rock mass.

Modeling Framework for Emplacement Drifts

In principle, the mass and heat transport processes occurring in an open drift could be modeled with a CFD simulator that would solve the mass, momentum, and energy conservation equations, including their turbulent contributions (e.g., Webb and Reed, 2004). However, solving the turbulent velocity fields expected in heated drift sections would require fine spatial and temporal resolution. Not only would this result in highly time-consuming simulation runs, but would also necessitate complex coupling approaches, because of the large

discretization disparities between the drift and the fractured rock.

To approximate the effects of natural convection, we followed the methodology described in Webb and Reed (2004), and assumed that the axial transport of vapor and air can be simplified as a binary diffusion process of the air-vapor mixture, using effective mass dispersion coefficients calculated from complementary CFD flow field simulations. By approximating natural convection as a binary diffusion process, the in-drift heat and fluid flow processes can, in principle, be simulated with the standard methodologies applied for Darcy-type flow and transport (such as those implemented in TOUGH2), with the drift represented as a specific solution subdomain that requires certain code modifications and parameter specifications. A new drift simulation version of TOUGH2 was developed that can solve simultaneously for heat and fluid flow within the drift and in the surrounding rock mass (Birkholzer et al., 2006, 2008).

Model Setup

Three-dimensional simulations runs were performed for a simplified geometrical representation of an emplacement drift located in one of the southern panels of the repository (Figure 2). The model domain comprises the entire unsaturated zone, having the ground surface as the upper model boundary and the groundwater table as the lower model boundary. In the axial drift direction (y-direction), symmetry allows for reducing the model to half of the drift length. Thus, the simulated drift comprises half of the typical emplacement section length (300 m), followed by a 80-m unheated section away from the symmetry axis (Figure 2). The total length of the model domain in y-direction is 520 m. Symmetry assumptions can also be used to reduce the model domain in the x-direction, perpendicular to the drift axis. The current repository design of parallel drifts can be represented as a series of symmetrical, identical half-drift domains with vertical no-flow boundaries between them. Thus, the numerical mesh can be limited to a lateral width of 40.5 m, extending from the drift center to the midpoint between drifts.

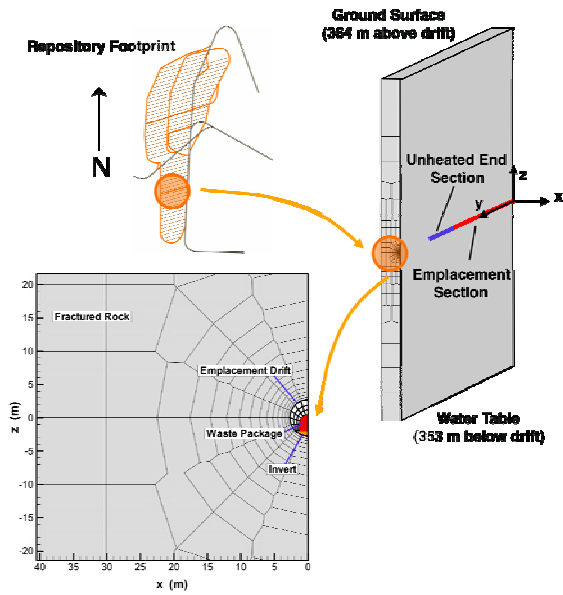


Figure 2. Schematic showing geometry of 3D domain of full-drift & rock natural convection model (not to scale).

Different climate stages occurring in the future are realized by three percolation flux inputs that change with time and are imposed at the upper model boundary (Table 1). Decay heat is modeled by setting a time-varying, average thermal linear load (TLL) boundary condition on the waste package element with initial value of 1.45 kW/m.

Table 1. Climate Scenario Input

Climate Stage	Time (years)	Infiltration rate (mm/yr)
Modern	0 to 600	6
Monsoon	600 to 2000	16
Glacial	> 2000	25

As pointed out before, natural convection was treated as a binary diffusion process in this study, with effective diffusion coefficients derived from CFD studies. There is, however, considerable uncertainty as to the magnitude of these coefficients. Two vastly differing sets of dispersion values were derived in Webb and Reed (2004), representing first-order estimates for the possible range of natural convection conditions in Yucca Mountain drifts (see Table 2). To account for this uncertainty, we run three main simulation cases, one with strong convective mixing (Case 1), the second with moderate convective mixing (Case 2), and the third with no convective mixing, assuming only binary diffusion of air and vapor (Case 3). All other material properties and the model boundary conditions are described elsewhere (e.g., Birkholzer et al., 2006), and shall not be repeated here.

Table 2. Convective Mixing Cases

Case	Dispersion Coefficient (m ² /s)
Case 1: Strong convective mixing	0.1
Case 2: Moderate convective mixing	0.004
Case 3: No convective mixing	2.14E-05

This nat-co model was then run with the three convective mixing cases. In short it was shown that Case 1 (strong convective mixing) causes considerable transport of vapor from heated drift sections to the unheated end, and gives rise to reduced relative humidity along the length of the drift when compared to the case with moderate and no convective transport (Figure 3). It is this time-varying response (temperature, pressure, and RH) that will serve as a boundary condition input for the seepage model. We expect that the strong convective mixing case will significantly reduce seepage at the drift wall due to the increased evaporative potential.

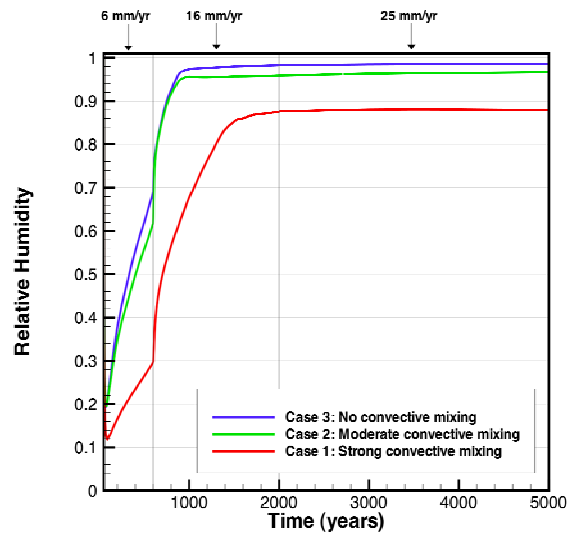


Figure 3. Evolution of relative humidity of in-drift element at the drift center in the full-drift & rock natural convection model for all three convective mixing cases.

Seepage Model: High-Resolution Seepage Model

To investigate the impact of the natural convection, in-drift thermodynamic response on seepage, we developed a high-resolution seepage model, based on existing TH seepage models (e.g., Birkholzer et al., 2004). The seepage model employs all the same framework as the nat-co model explained above, but with additional modeling details given below.

The fractured rock mass is modeled in the same manner described previously in the nat-co model, however it has a more finely gridded mesh in the x-z plane, allowing for prescribing a heterogeneous fracture permeability field to the region of rock next to the drift wall (fracture permeability was constant in the nat-co model). The specific realization chosen for the permeability field contains a highly permeable region next to a low-permeability region near the rock-drift interface, a scenario beneficial for seepage as it allows for local ponding at the wall (Figure 4). It is this region that we will be observing in greater detail.

Another key element of seepage modeling is the implementation of a small capillary-strength parameter for the fracture continuum in drift vicinity. This parameter relates the fracture saturation to the capillary pressure and is derived from inverse modeling and calibration to niche liquid-release tests conducted at Yucca Mountain (Birkholzer et al., 2004). This calibrated parameter incorporates potential effects from permeability changes due to excavation effects, small-scale wall roughness, high-frequency episodicity from small-scale flow processes, film flow, drop formation, discrete fractures that may terminate at the wall, artifacts of finite discretization, and, effects from lithophysal cavities.

Before dripping, liquid water that encounters the drift wall is likely to form a film over the local surface of the wall. Following the methodologies of Ghezzehei et al. (2004), we will assume film evaporation occurs at the drift wall, and that the area available for such film evaporation is proportional to the fracture saturation and the drift wall surface of the seeping gridblock.

Model Setup

Seepage is a local event, and occurs over regions of rock on the order of less than a meter. While the in-drift thermodynamic conditions are dependent on the amount of percolation water evaporated into the drift (during sub-boiling conditions), the additional amount of water arriving due to a seepage event is trivial when compared to the total amount of water arriving over the length of the drift. When also considering natural convection, we can assume that the in-drift is well-mixed, or that there is no significant change in the local thermodynamic conditions of the in-drift domain nearby a seepage event. We consider this by developing a quasi-3D model, with boundary conditions prescribed in the same manner as the nat-co model. The model again extends from the mountain surface to the water table, yet now incorporates only a 25 meter long section of the drift, divided into 9 layers (Figure 4). The grid contains about 17,000 grid blocks and 70,000 connections.

Seepage is most likely to occur in drift regions where the local percolation flux is much higher than the average percolation, a possible result of intermediate-scale heterogeneity leading to flow focusing. To account for the possibility of locally higher flux arriving at a drift region, we consider three flow focusing cases by increasing the average input percolation flux prescribed at the model upper boundary by factors of 10 and 20 (Table 3). We restrict the flux increase to a thin (0.25 m) flow focusing layer in the model, preventing any transport of liquid between this layer and the adjacent layer (Figure 4) while still allowing heat transfer in the axial direction. It is this layer of locally focused flux that we will pay attention to.

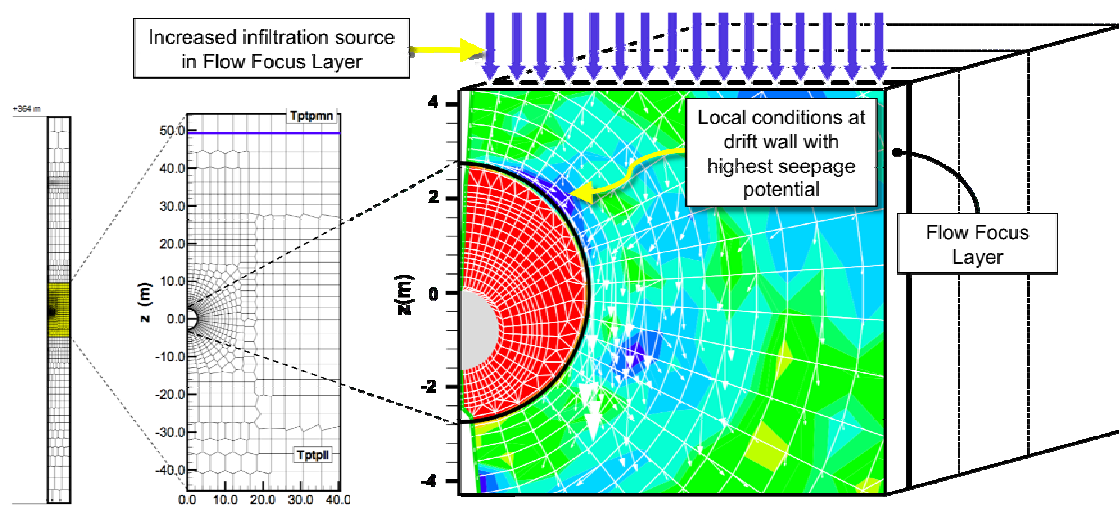


Figure 4. Schematic showing geometry of 3D domain of high-resolution seepage model (not to scale). Contour plot shows sample fracture saturation of near-field rock.

Table 3. Infiltration Rate Input Flow Focusing Sensitivity Cases

Flow Focusing Case	Infiltration rate (mm/yr)	Climate Scenario
No Flow Focusing (mean infiltration scenario)	6 16 25	Modern Monsoon Glacial
Flow Focusing Factor 10	60 160 250	Modern Monsoon Glacial
Flow Focusing Factor 20	120 320 500	Modern Monsoon Glacial

A time-dependent boundary condition (temperature, pressure, and relative humidity), generated from the nat-co model, is implemented as a Dirichlet boundary condition in the in-drift domain of the seepage model. Specifically, the waste package element is assigned a prescribed temperature defining the heat output of the waste packages. Another Dirichlet boundary is defined at the end of the in-drift region, opposite the flow focusing layer, with prescribed temperature, pressure and RH assigned to the in-drift elements. These prescribed in-drift conditions account for the effect of natural convection.

MODEL RESULTS

The goal of this study is to evaluate the potential impact that natural convection has on drift seepage, which is largely affected by the local in-drift thermodynamic conditions.

First, we will look at temperature response at the drift wall from 50 to 5000 years (the time scale for all future plots). Climate stages are distinguished by vertical grey lines on the plot, and the corresponding percolation rates are given at the top of the plot. Figure 5 depicts the temperature response in the focus-20 case, for the most seepage-prone element (that having the largest permeability) at the drift wall, represented by the solid lines and also the temperature of the time-dependant in-drift Dirichlet boundary condition, represented by the dashed lines. Temperatures begin around 150 °C early after emplacement of waste at year 50, then cool to the boiling temperature (96 °C) around year 800, and eventually drop to below 60 °C by year 5000. Although not plotted, similar behaviors are observed in the other flow focusing cases (focus-10, and mean), with slightly higher temperatures due to the decrease in the percolation flux. Also, we observe the temperature of the seepage element for the strong convective mixing case (red lines) is lower than that for the other two convective mixing cases, which is

due to the more effective heat removal from the drift center due to enhanced axial vapor transport.

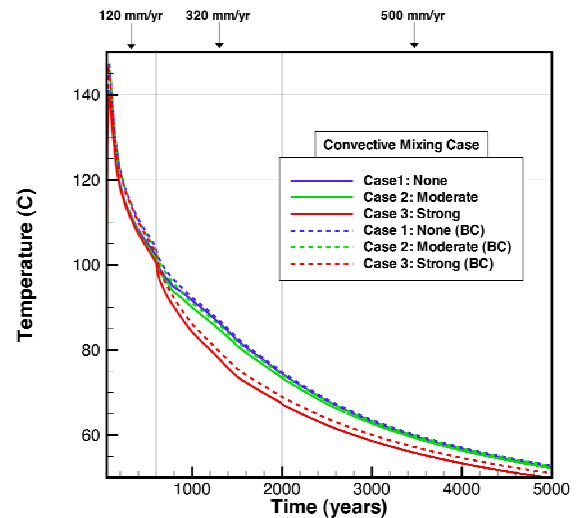


Figure 5. Temperature evolution in seepage-prone element at drift wall (solid line) and boundary source (dashed line) for Flow Focusing 20 case.

More important to predicting thermal seepage is the fracture saturation in the seepage element. Seepage can occur when the capillary pressure in the gridblocks next to the wall is higher (less negative) than the threshold pressure (defined in Birkholzer et al., 2004). For the properties used in this simulation, such conditions exist when the fracture saturation at the wall exceeds about 0.5. Also, the threshold pressure for seepage increases slightly (becomes less negative) with elevated temperatures because of liquid density changes. Therefore, at higher temperatures, the threshold saturation for seepage may be slightly higher than 0.5.

Figure 6 shows fracture saturations for each flow focusing case in three different plots. Figure 6.a gives the saturations for each convective mixing case for the mean infiltration rate. The fractures are completely dry in all cases for the first 800 years as the rock temperature during this time remains above boiling. Rewetting occurs soon thereafter in the no convection case (blue line) and moderate (green line) convective mixing cases, as the temperature drops below boiling, allowing the presence of liquid water. The increase in the infiltration rate at year 2000, due to the transition to glacial climate, promotes a jump in the fracture saturations, which slowly increases with time after (a result of declining temperature). For the strong convective mixing case (red line), no water is observed near the drift wall until well after 3000 years, showing the evaporative potential of natural convection processes. A similar behavior is observed for the focus-10 case, depicted in Figure 6.b, however now with much larger fracture saturations and earlier rewetting of the fractured rock.

The focus-20 case (Figure 6.c) shows an even larger response in fracture saturations for all convective mixing cases due to the increase of the infiltration rate input. In this case we now observe the saturations reaching the threshold, around 0.5 for all cases. For both the no and moderate convective mixing cases, this occurs around year 2000. The strong convective mixing case reaches critical saturation much later, around year 3300. It is at these critical values where we can expect seepage might occur.

Finally, the seepage percentage, for both ambient and thermal seepage, is plotted in Figure 7 for the focus-20 case. The seepage percentage is defined as the ratio of the liquid flux that seeps into the drift to the total liquid flux percolating with constant infiltration rate through a cross-sectional area corresponding to the footprint of the drift. To note, for the time periods plotted, no seepage was observed in the other flow focusing cases (focus-10 and mean cases), as was expected from the fracture saturation plots.

In Figure 7, no ambient seepage is observed for the modern climate scenario (120 mm/yr). However, during the monsoon and glacial climate scenarios, the capillary barrier is overcome and seepage percentages of 6% (320 mm/yr) and 16% (500 mm/yr) are achieved (a seepage percentage of 16% means that 16% of the percolation water arriving at the drift wall is seeping into the drift). Although we observe ambient seepage in the monsoon climate, thermal seepage is not present until the glacial climate infiltration rate is reached. As expected, the start of seepage corresponds to the fracture saturations reaching their threshold values. At the year 2000, we see the result for the no convective mixing case jumps immediately to a 2% seepage percentage, and increases from this time on, eventually reaching about 8% of the percolation rate.

Similarly, the moderate convective mixing case sees seepage start around year 2100, but always remains slightly below seepage in the no convective mixing case. This is because even moderate convective mixing allows for some removal of moisture from the drift walls and thereby reduces seepage. The strong convective mixing case sees a substantial decrease in the seepage rate and a later start around 3200 years. At year 5000, with a seepage percentage of only 3.5%, the strong convective mixing case has significantly lower values than in the 7% and 8% observed in the moderate and no convective mixing cases. As suggested earlier, these results show that strong convective mixing due to natural convection can reduce seepage significantly.

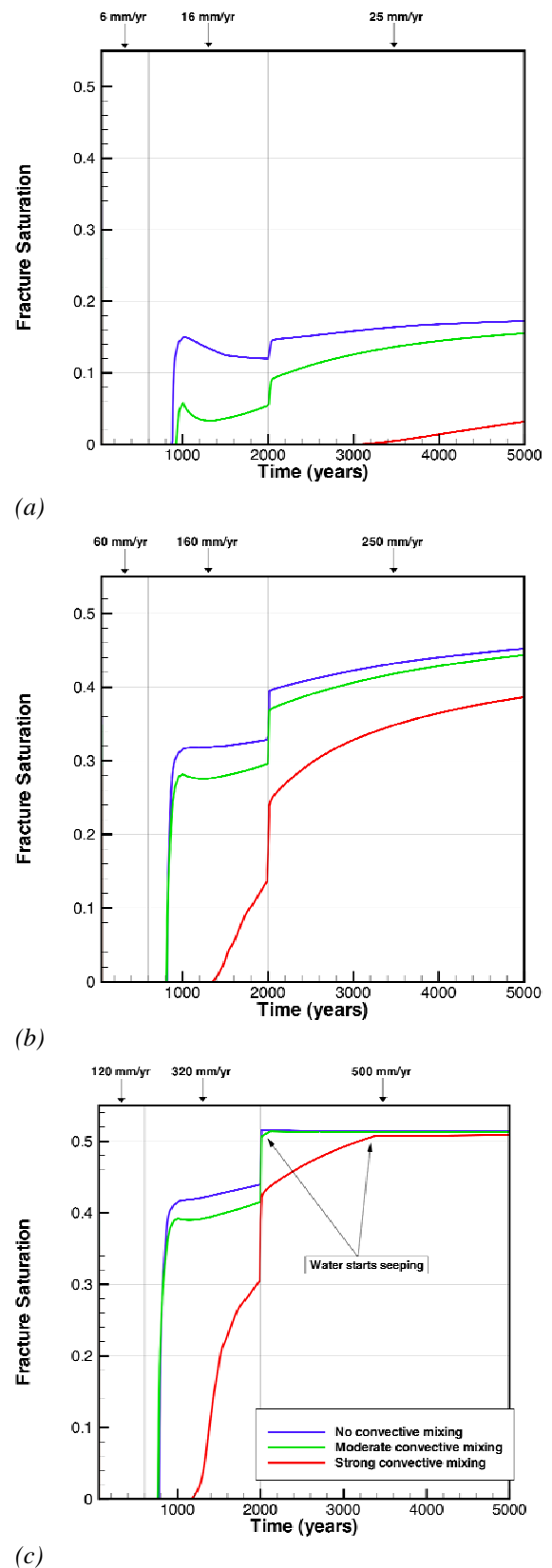


Figure 6. Fracture saturation at the drift wall for flow focusing cases: (a) Case 1 - none (mean infiltration) (b) Case 2 - factor-10 and (c) Case 3 - factor-20.

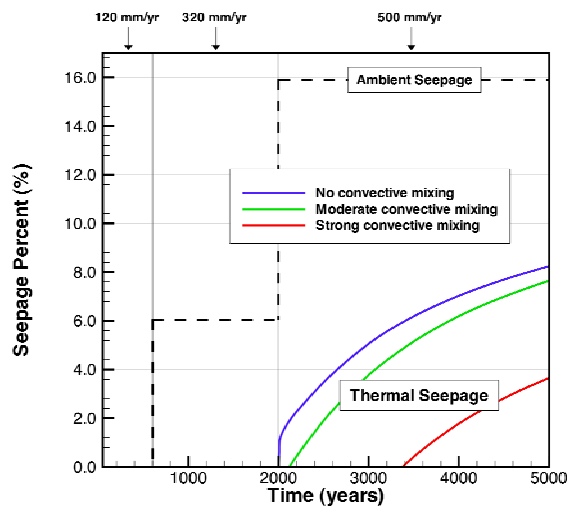


Figure 7. Seepage percentage for the flow focus-20 case for both ambient (dashed lines) and thermal (solid lines) seepage. (No seepage is observed in either the focus-10, or no-focus cases).

SUMMARY AND CONCLUSIONS

A numerical study was conducted to explore the impact that natural convection processes have on the reduction of drift seepage at the Yucca Mountain repository. A new TOUGH2 seepage model was developed based on existing seepage models and employed results from a previous natural convection model. This natural convection model coupled existing modeling approaches for predicting heat and mass transport in the rock mass with modules that approximate in-drift convection as a binary diffusion process.

Quasi three-dimensional simulations runs were performed for a detailed geometrical representation of an emplacement drift cross-section plus surrounding fractured rock located in one of the southern panels of the repository. Three simulation cases were analyzed, representing different degrees of convective mixing in drifts as determined from CFD studies reported in the literature along with three different flow focusing cases, to capture the effect of a flow-focused event. Our simulation results demonstrate the importance of in-drift natural convection on seepage reduction. Strong convective mixing convection:

- causes considerable delay in the rewetting of the fracture rock, and also the seepage, in all flow focusing cases.
- reduces the maximum fracture saturations achieved at the drift wall
- significantly reduces the amount of seepage into the drift when compared to the other convective mixing cases.

These natural convection effects are expected to improve the performance of the repository, since smaller relative humidity values, with reduced local seepage, form a more desirable waste package environment. While the results of our study have demonstrated the importance of natural convection in assessing the future TH conditions in Yucca Mountain drifts, it is important to consider that we have employed several limiting model assumptions that are valid for a comparative evaluation of natural-convection sensitivity cases, but may not allow for a realistic quantitative representation.

ACKNOWLEDGMENT

This work was supported by the Director, Office of Civilian Radioactive Waste Management, Office of Science and Technology and International, of the U.S. Department of Energy. Much thanks to input and assistance with the parallelized version of TOUGH2 goes to Dr. Keni Zhang, LBNL.

REFERENCES

- Birkholzer, J.T., G. Li, C.F. Tsang, and Y.W. Tsang, "Modeling Studies and Analysis of Seepage into Drifts at Yucca Mountain," *Journal of Contaminant Hydrology*, 38 (1-3), pp. 349-384, 1999.
- Birkholzer, J.T., S. Mukhopadhyay, and Y.W. Tsang, "Modeling Seepage into Heated Waste Emplacement Tunnels in Unsaturated Fractured Rock," *Vadose Zone Journal*, 3, 819-836, 2004.
- Birkholzer, J.T., S.W. Webb, N. Halecky, P. Peterson, and G.S. Bodvarsson, "Evaluating the Moisture Conditions in the Fractured Rock at Yucca Mountain – The Impact of Natural Convection in Heated Emplacement Drifts," *Vadose Zone Journal*, 5(4), pp. 1172-1193, 2006.
- Birkholzer, J.T., N. Halecky, S.W. Webb, P. Peterson, and G.S. Bodvarsson, "A Modeling Study Evaluating the Thermal-Hydrological Conditions in and Near Waste Emplacement Tunnels at Yucca Mountain," *Journal of Nuclear Technology*, 163(1), pp. 147-164, 2008.
- Ghezzehei, T. A., R. C. Trautz, S. Finsterle, P. J. Cook, and C. F. Ahlers "Modeling Coupled Evaporation and Seepage in Ventilated Cavities," *Vadose Zone Journal*, 3:806-818, 2004.
- Pruess, K., C. Oldenburg, and G. Moridis, "TOUGH2 User's Guide, Version 2.0," LBNL-43134, Berkeley, California, 1999.
- Webb, S.W., and A. Reed, "In-Drift Natural Convection and Condensation," MDL-EBS-MD-000001 REV 00, Yucca Mountain Project Report, Bechtel SAIC Company, Las Vegas, Nevada, 2004.

MODELING THE HYDROGEN GENERATION AND MIGRATION FROM AN EMPLACEMENT DRIFT WITH INTERMEDIATE-LEVEL RADIOACTIVE WASTE: IMPACT OF WATER CONSUMPTION AND WATER DEPENDENT CORROSION RATE

Jean Croisé¹, Gerhard Mayer¹, Jean Talandier², Jacques Wendling²

¹ AF-Colenco Ltd

Taefernstrasse 26, CH-5405 Baden, Switzerland

e-mail: jean.croise@afconsult.com

² ANDRA

Parc de la Croix Blanche, Châtenay-Malabry, France

ABSTRACT

The corrosion of metals contained in intermediate-level waste under reduced chemical conditions will lead to the production of hydrogen gas during the postclosure phase of a radioactive waste repository. According to previous investigations by ANDRA (see, e.g., Talandier et al., 2006), the period of concern covers several 1,000 years after closure of a repository in an argillaceous formation. The limited transport efficiency of host rock with low permeability and high capillary resistance might cause, among other things, significant desaturation and pressure buildup within the emplacement drifts. On the other hand, water availability could be limited as a result of (1) low host-rock permeability and (2) desaturation due to the ventilation of the drifts during the operational phase of the repository. In previous numerical simulations, it was assumed that under the reducing chemical conditions prevailing in the repository, the corrosion rate would be a function of the available metal surface and temperature only. In this paper, simulation results based on new phenomenological functions implemented in TOUGH2 are presented. These functions allow taking into account (i) the saturation dependency of the hydrogen-gas generation rate, (ii) the water consumption caused by the corrosion process and (iii) the total metal mass available for corrosion.

The simulations (1D and 2D) provide insight into the system behavior from the construction of the drift to postclosure conditions: including evolution of the gas pressure and saturation within the drift, and of the argillaceous formation around it.

INTRODUCTION

The French Agency for the Management of Radioactive Waste (ANDRA) is currently investigating the feasibility of deep geological disposal of radioactive waste in an argillaceous formation (ANDRA, 2005). The repository is planned to be built in a claystone formation around 500 m bgl.

Waste and materials used to confine the waste will lead to gas production during their degradation processes. The study presented in the paper concerns the intermediate-level radioactive waste (ILW—the general layout of the ILW disposal is presented in Figure 1) and a particular type of package containing magnesium alloys. This kind of alloy is known to have a very high corrosion rate when in contact with alkaline water. The potential outcome is a rapid increase in gas pressure, and the potential impact of such increased pressure on a repository must be studied. Consequently, 1D radial and 2D vertical simulations of the water and gas flow were performed.

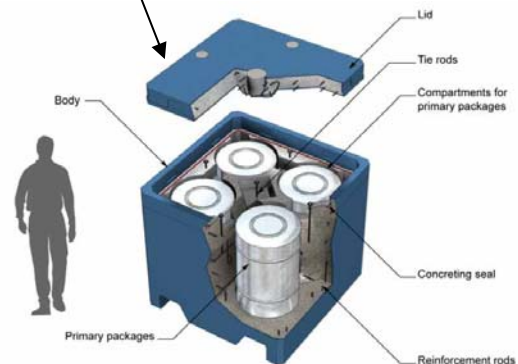
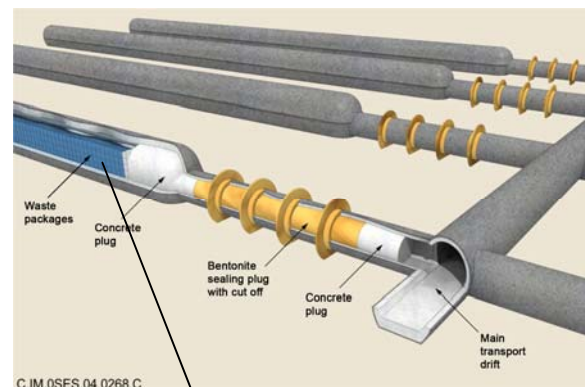


Figure 1. Layout of the ILW part of the repository and details of the waste package (ANDRA, 2005)

PROCESSES

General processes

During the operational phase of the repository, the disposal and access drifts, as well as the access and ventilation shafts, will be ventilated, and the host rock will be progressively depressurized and desaturated. As soon as the drifts are backfilled and sealed with bentonite plugs, resaturation of the host rock (clay) and the backfill material starts. Because of the corrosion of magnesium alloys in the waste packages, hydrogen might be produced for up to 10'000 years.

The processes taking place during and after the hydrogen generation are:

- Dissolution into the pore water and transport by diffusion/advection
- Advection of and diffusion in the gas phase

The gas flow is described as two-phase flow, using Darcy's law and the relative permeability concept. Flow and transport processes are considered to be isothermal. The TOUGH2 module EOS5 (water/hydrogen) was used for the computations (Pruess et al., 1999).

Corrosion model

In this paper, the corrosion process of magnesium alloys are addressed in terms of gas generation and water consumption. No other chemical or physical effect is considered. This simplified model is, however, based on experimental observations. Corrosion of magnesium happens when water (liquid) is available and when it is alkaline (e.g., after migrating through concrete). Furthermore, a threshold water saturation of the pore space is needed to initiate corrosion. Summarizing, the corrosion model is based on the following components:

- A maximum hydrogen generation rate is prescribed, based on the metal surface available for corrosion and a corrosion rate assuming complete water saturation of the void space in the waste.
- A linear dependency is assumed between the hydrogen gas generation and the water (liquid) saturation (e.g., with a threshold value and a linear increase with saturation).
- The water consumption rate is specified based on the stoichiometry of the corrosion reaction (when 1 mole of hydrogen is formed, two moles of water are consumed).
- Gas generation stops when the total magnesium alloy mass is corroded.
- The maximum production rate happens at 100% water saturation.

This model has been implemented into TOUGH2 and tested for different parameters. Examples of gas generation rates as a function of liquid saturation are presented in Figure 2 below.

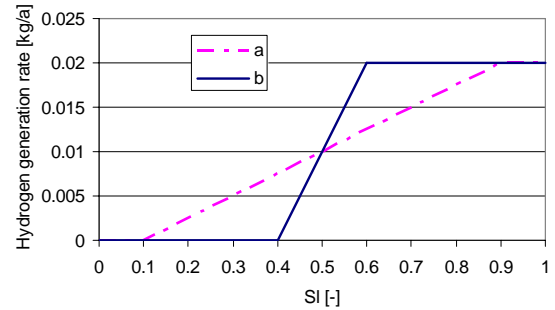


Figure 2. Example of gas generation rates depending of the liquid (water) saturation

The model was parameterized as follows (see Colenco, 2008):

$$r_g = \begin{cases} 0 & S < S_0 \quad \text{OR} \quad \int r_g(t)dt > M_g \\ r_{g,max} \frac{S - S_0}{S_1 - S_0} & S_0 \leq S \leq S_1 \\ r_{max} & S \geq S_1 \end{cases}$$

$$r_w = r_g \cdot w_r$$

with:

r_g	Gas generation rate [kg/s]
M_g	Gas reservoir mass, i.e. the upper limit of cumulative generated gas mass [kg]
t	Time [s]
$r_{g,max}$	Gas generation rate at saturations equal to or above S_1 [kg/s]
S	Liquid saturation [-]
S_0	Minimum liquid saturation required to initiate gas generation [-]
S_1	Threshold liquid saturation required for maximum gas generation rate [-]
r_w	Water consumption rate (negative) [kg/s]
w_r	Ratio of water consumption rate to gas generation rate [kg/s/kg/s]

MODELING AND RESULTS

Geometry, Mesh, and Physical Parameters

The simulation domain has a vertical extension of about 130 m, which represents the thickness of the Callovo-Oxfordian formation. The 2D configuration considered is a half plane through the disposal drift. In the cross section of the drift, 12 waste packages (each of them containing four primary waste containers—see Figure 1) are placed in a 3×4 arrangement). The width of the domain is 36 m, corresponding to half the distance between neighboring disposal drifts. Details of the material are taken into account in the simulation: a waste package with a high performance cement overpack, emplacement voids, concrete back-

fill, fractured excavation disturbed zone, micro-fissured disturbed zone and undisturbed clay (see Figure 3). The 1D configuration is a radial case with all the materials taken into account as in the 2D configuration (with the exception of the anisotropic permeability of the undisturbed clay, for which a geometric mean of the vertical and horizontal values was taken) and equivalent volumes and interfaces to the 2D configurations. This 1D radial configuration was developed to allow a quick preliminary investigation of general system behavior.

Characteristic flow parameters for a selection of materials are presented in Table 1. The two-phase flow parametrization of the relative permeability capillary pressure saturation constitutive relationship after van Genuchten–Mualem is used (see, e.g., Croisé et al., 2006).

Initial and Boundary Conditions

The rock mass is assumed to be fully water saturated at the start of the simulation. At the upper and lower boundaries of the simulation domain, a constant pressure is imposed that corresponds to the hydraulic heads of the aquifers above and below the clay. Due to the symmetry of the disposal configuration with a horizontally placed array of disposal drifts, the vertical boundaries are set to no-flow conditions. The lifetime periods of the repository are modeled as follows:

- Instantaneous construction of the repository
- Repository kept opened at atmospheric pressure and ventilated with controlled air relative humidity of 50%
- Instantaneous closure with materials at prescribed initial water saturation levels, and simulation of resaturation with hydrogen generation and water consumption for a 10,000-year period
- Corrosion is assumed to start as soon as the water saturation inside the waste exceeds a level of 0.1 of the pore space.

The materials inside the disposal drift present different degrees of initial water saturation: dry conditions in the waste package, 100% for the concrete backfill and the high performance cement overpack. The emplacement voids between waste packages are considered to be initially unsaturated.

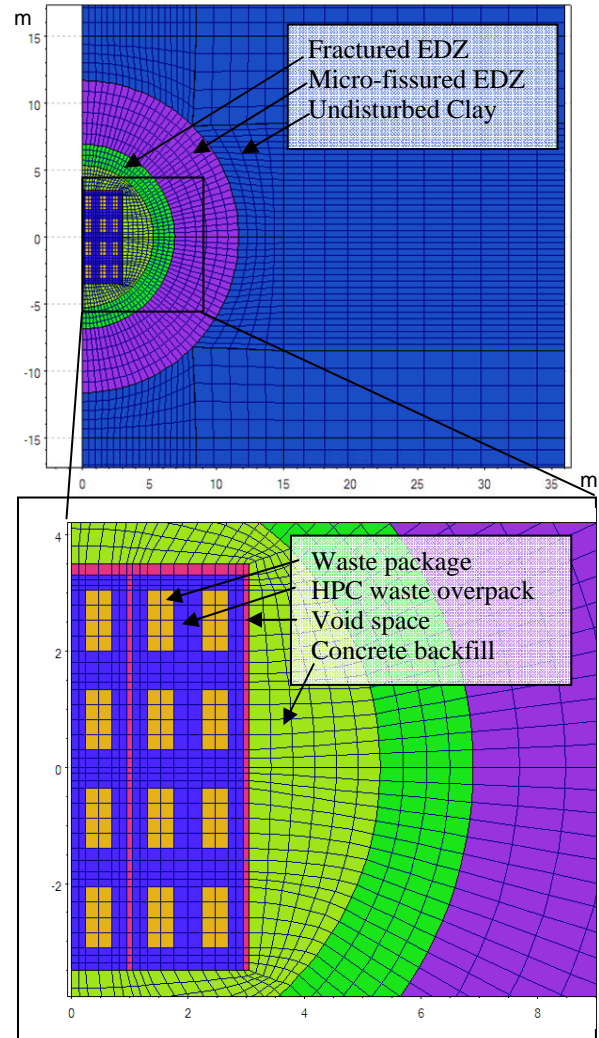


Figure 3. Schematic view of the geometry and mesh of the 2D configuration; 2 zooms on the interior of the disposal drift and its near field.

Table 1. Selection of characteristic material parameters for the simulations.

	Waste Package	High performance cement (waste overpack)	Micro-fissured EDZ	Undisturbed Clay	Unit
Porosity ϕ	0.3	0.15	0.18	0.18	-
Permeability k	10^{-15}	$5 \cdot 10^{-19}$	$5 \cdot 10^{-18}$	$k_v=5 \cdot 10^{-21}$ $k_h=5 \cdot 10^{-20}$	m^2
Van Genuchten coefficient n	1.49	1.54	1.49	1.49	-
Van Genuchten pseudo gas entry pressure P_0	$1 \cdot 10^4$	$2 \cdot 10^6$	$2 \cdot 10^6$	$1.5 \cdot 10^7$	Pa

Results

The simulations, performed with a modified version of TOUGH2-EOS5, cover 0–10,000 years. Diffusion processes in the gas and water phases have been neglected in the 2D simulation results presented below, since they were shown to have only a small impact on the results in preliminary simulations.

Two “flooding” scenarios of the waste packages have been investigated. In the first (Scenario A), the waste packages are considered to be flooded without delay when water flows into the emplacement drift. In this case, due to the gradual resaturation, the hydrogen source term is strongly limited by the availability of the water. In the second (Scenario B), the waste package is considered to become accessible to water inflow at the end of the resaturation and pressure re-equilibration phase of the emplacement drift. In this case, the water flow rate into the packages is much higher right from the start, and hence the hydrogen gas generation rate is much higher than in the Scenario A.

Results of 1D simulations

The 1D radial simulations performed showed that:

- For both scenarios (A and B), it is essential to take into account the corrosion model as described above, in order to obtain a realistic assessment of the gas pressure buildup in the emplacement drift. Computations based on corrosion rates taken independent of the saturation level lead to unrealistic high-pressure buildup.
- Due to the low inflow rates into the emplacement drifts (about 0.2 l/day/m) during the resaturation period, the impact of water consumption (corrosion) on gas pressure buildup is not negligible and must therefore be taken into account.

The results of five 1-D simulations are presented in Figure 4. These simulations are based on Scenario A and the following corrosion rates at full water saturation: Case 1, 0 mm/year (=“natural resaturation”); Case 2, 1 mm/year; Case 3, 0.1 mm/year; Case 4, 6.8 $\mu\text{m}/\text{year}$; Case 5, 0.68 $\mu\text{m}/\text{year}$. From top to bottom, the figure shows gas pressure inside the waste package, water saturation in the waste package, water inflow rate into (+) the emplacement drift, hydrogen gas production rate, and mass of magnesium remaining in the emplacement drift.

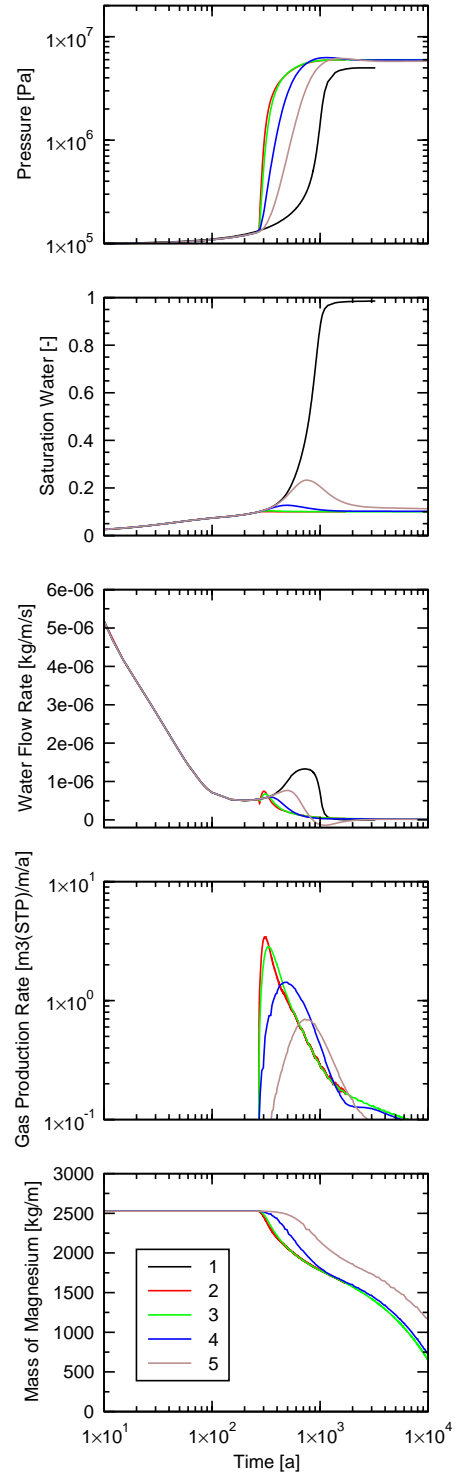


Figure 4. 1D simulation results for natural resaturation conditions (Case 1) and 4 different corrosion rates (Cases 2-5)

As soon as the water saturation reaches 0.1 inside the waste package (at around 300 years), hydrogen gas is generated, and a pressure rise is observed. In comparison, Case 1 (natural resaturation) shows how the pressure continues to smoothly increase up to the hydrostatic level. However the pressure buildup remains at a level less or only slightly above the natural undisturbed value, due to the available storage volume of the emplacement drift. The water saturation rises to a maximum value and then decreases again, due to the increasing gas pressure; it then reaches a level very close to the threshold saturation necessary for switching on the corrosion. Water fluxes out of the emplacement drift are generated when the gas pressure is higher than the water pressure outside the drift plus the capillary pressure. At ~2000 years, the hydrogen generation rate also strongly diminishes due to the low water saturation level in the emplacement drift. Some magnesium mass is still remaining in the drift at 10,000 years.

Results of 2D simulations

Scenario A

The simulation results obtained for Scenario A are provided in Figures 5–8. Two corrosion rates at saturation are investigated: Case 2: 1 mm/year and Case 3: 0.1 mm/year.

In Figure 6, the same diagrams as in Figure 4 are presented for the Cases 2 and 3. Pressure and saturation are presented for a point in the lowest right waste package ($x=2.58\text{m}$, $z=-2.97\text{m}$). Figures 5, 7, and 8 show the spatial distribution of the following variables at times 150 years, 1000 years and 7000 years, respectively:

- Pressure (of the gas phase in the partly saturated areas of the model domain; of the water in the fully water saturated areas): upper left figure
- Gas-phase saturation: upper right figure
- Percentage of corroded magnesium in the waste packages: lower left figure
- Relative hydrogen generation rate: lower right figure

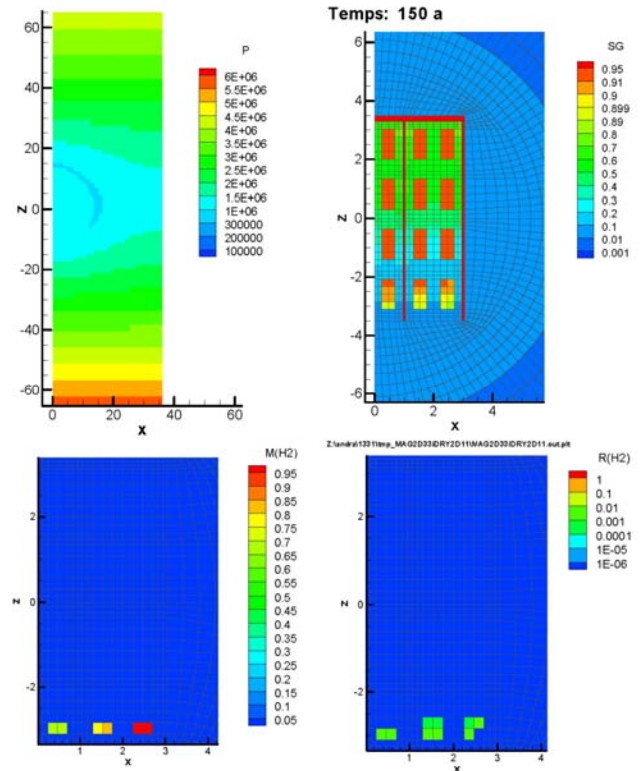


Figure 5. 2D simulation results Scenario A, corrosion rate 1 mm/year, $t=150$ years

The waste resaturates vertically from the bottom to the top of the drift. The emplacement drift is progressively filled with water, and the magnesium originally in place mostly corrodes gradually from the bottom to the top of the drift. The hydrogen generation zone is moving vertically. In Case 2 (max. corrosion rate of 1 mm/year) the hydrogen generation rate is slightly higher than in Case 3 (max. corrosion rate of 0.1 mm/year). The maximum gas pressure in the drift never exceeds the hydrostatic level. Overall, the time evolutions are very similar, indicating that the gas generation is highly controlled by the resaturation process of the drift.

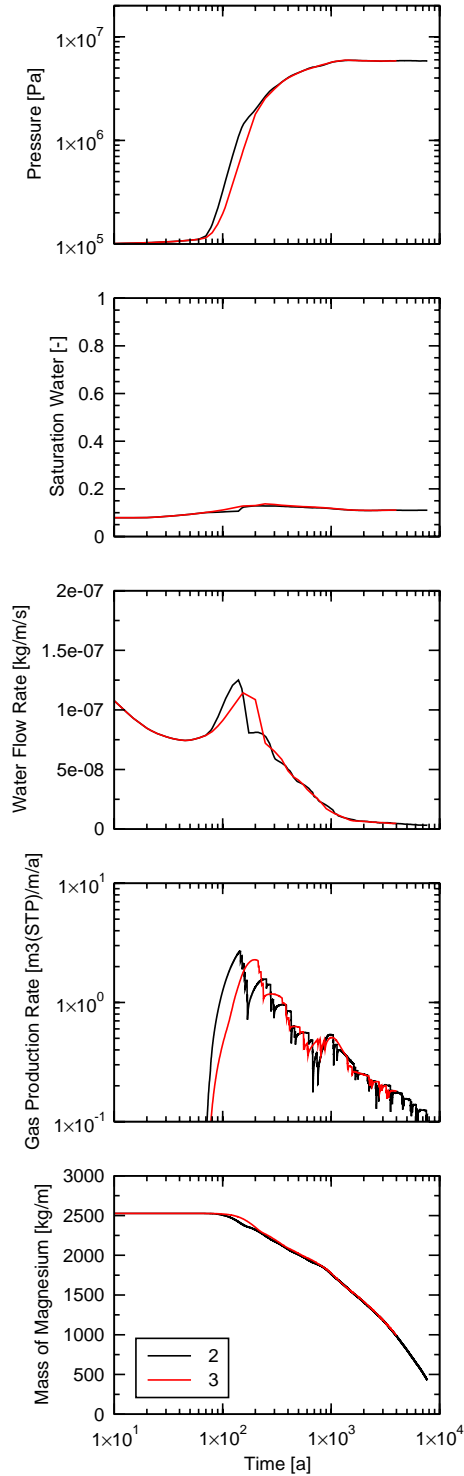


Figure 6. 2D simulation result: Scenario A, corrosion rate 1 mm/year (black line) and 0.1 mm/year (red line); pressure and saturation at the lowest right waste package ($x=2.58m, z=-2.97m$)

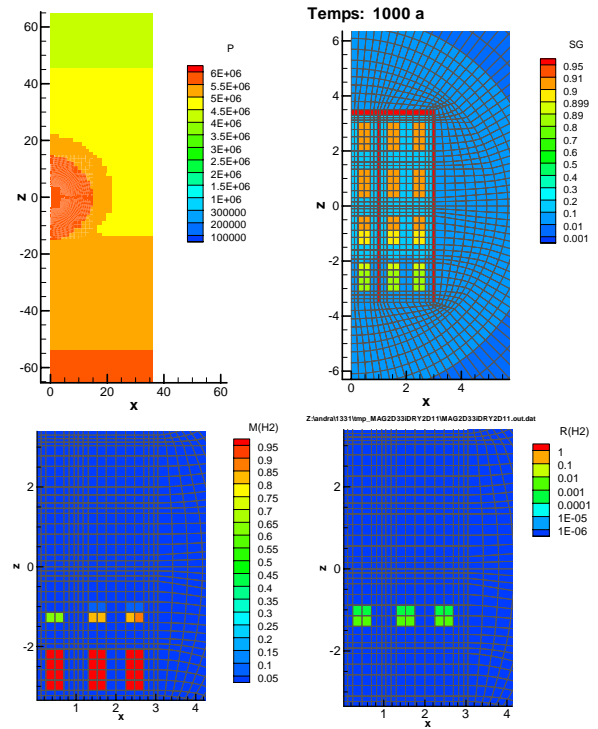


Figure 7. 2D simulation results Scenario A, corrosion rate 1 mm/year, $t=1000$ years

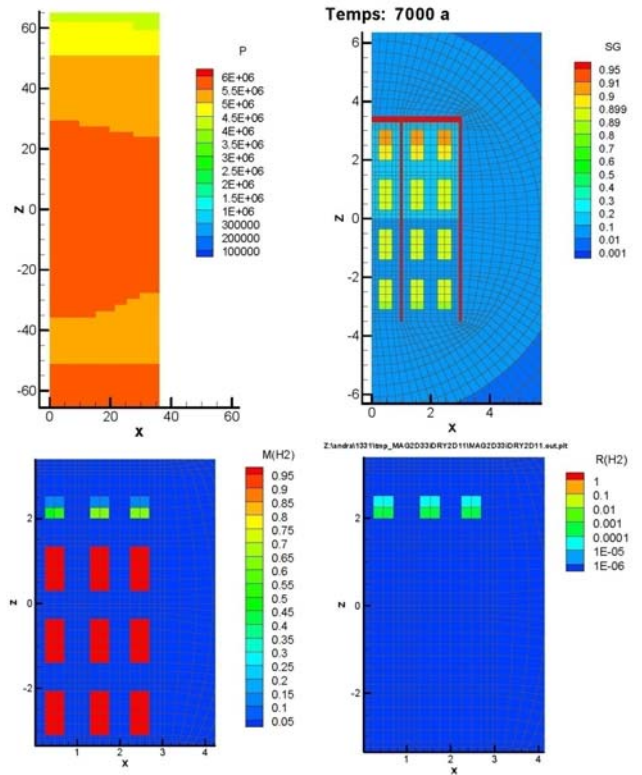


Figure 8. 2D simulation results Scenario A, corrosion rate 1 mm/year, $t=7000$ years

Scenario B

This scenario can be understood as a bounding case in terms of pressure buildup. Both hypotheses—(1) maximum pressure difference between formation and waste packages, and (2) instantaneous failure of all waste packages—are highly conservative. The simulation results obtained for Scenario B are provided in Figures 9–12. As in Scenario A, two corrosion rates at saturation are investigated: Case 2 (1 mm/year) and Case 3 (0.1 mm/year).

Due to the high water pressure in the formation near the drift (around 5 MPa) at the start of resaturation, the inflow rates are large, and all the waste packages could start to corrode at the same time. The pressure buildup is therefore larger and happens at earlier times than in the scenario A. The larger availability of water causes higher total hydrogen generation rates, and at 10,000 years the entire magnesium mass is corroded. The maximum pressure is around 12 MPa at 10 years.

The time evolution of the buildup process presents the same general shape in the two simulation cases, but the magnitudes of the variables pressure, saturation and production rates differ significantly. The last waste packages to be entirely corroded are situated in the middle of the drift.

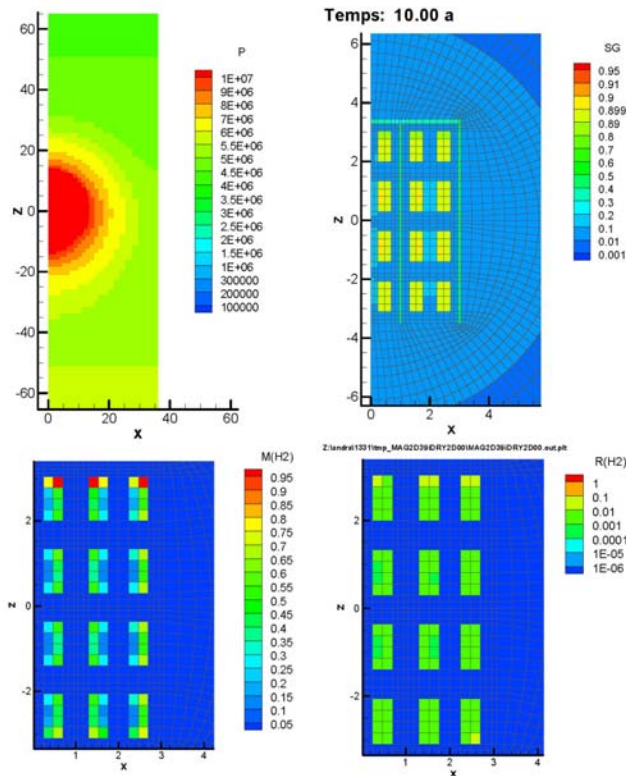


Figure 9. 2D simulation results Scenario B, corrosion rate 1 mm/year, $t = 10$ years

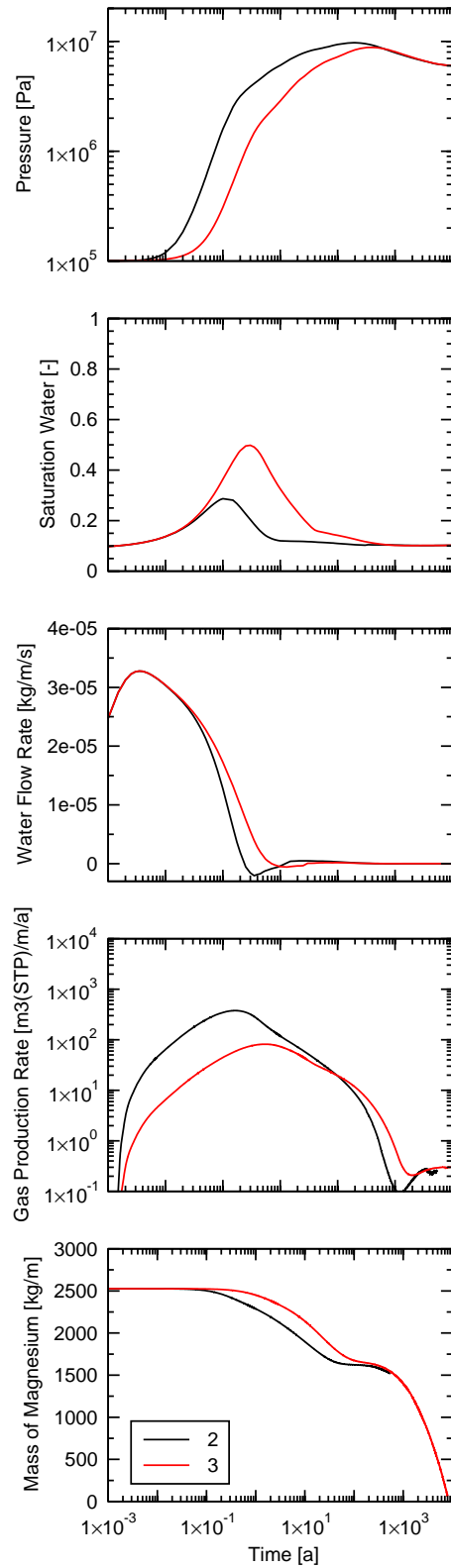


Figure 10. 2D simulation results Scenario B, corrosion rate 1 mm/year (black line) and 0.1 mm/year (red line); pressure and saturation at the lowest right waste package ($x = 2.58\text{m}$, $z = -2.97\text{m}$)

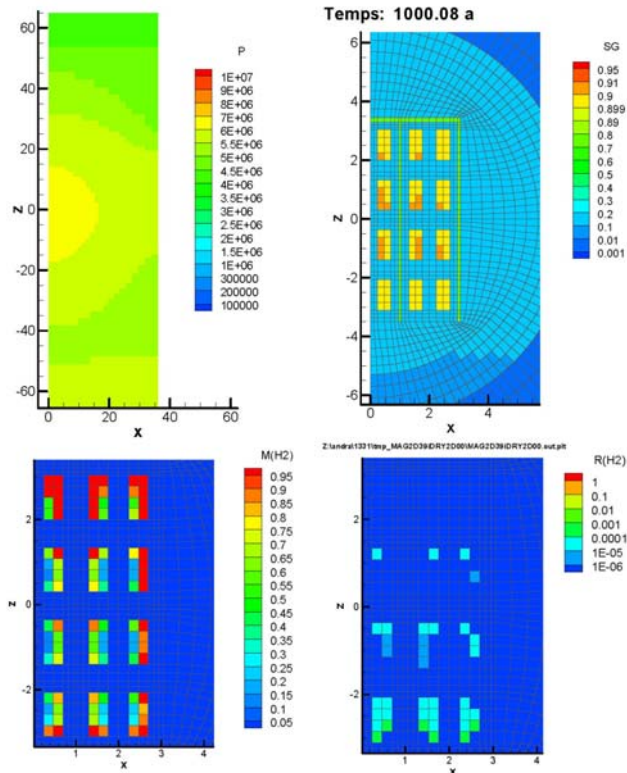


Figure 11. 2D simulation results Scenario B, corrosion rate 1 mm/year, $t = 1000$ years

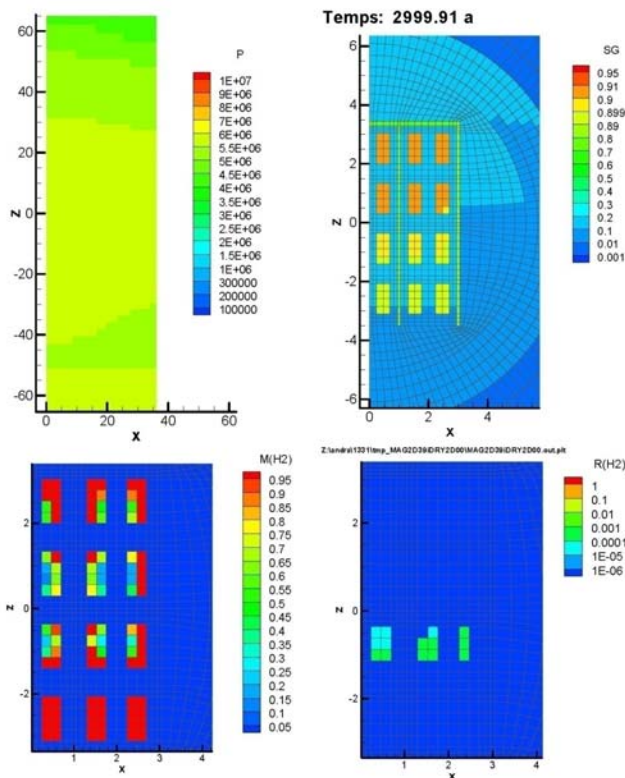


Figure 12. 2D simulation results Scenario B, corrosion rate 1 mm/year, $t = 3000$ years

CONCLUSIONS

In this paper, we presented a simplified corrosion model that we implemented in TOUGH2. It was developed for the simulation of hydrogen generated by corrosion of metals in the context of deep radioactive waste disposal. This model allows taking into account the dependency of the hydrogen gas generation rate on water saturation, the water consumption due to the reaction under anaerobic corrosion, and the ceasing of corrosion when all the metal mass available has been corroded. We presented the results of 1D and 2D simulations, performed for a typical emplacement drift for magnesium-bearing waste packages in a clay host rock, showing the potential of this simplified corrosion model. Results demonstrated the importance of water availability for the assessment of gas pressure buildup in the emplacement drift. In particular, the time for which the waste package might stay impervious to water is an important parameter for assessing hydrogen generation over time, and therefore pressure buildup in the drift. The model can be readily extended to take into account experimental findings on hydrogen generation of metals under reductive conditions as well as more waste-specific conditions. This makes it a good tool for further design investigations.

REFERENCES

- ANDRA: Dossier 2005 Argile, les recherches de l'ANDRA sur le stockage géologique des déchets radioactifs à haute activité et à vie longue, collection les Rapports, ANDRA, Châtenay-Malabry, France, 2005.
- Colenco : Modélisation du transfert des gaz dans une alvéole de déchets B contenant des déchets magnésiens en phase de post-fermeture, Rapport ANDRA, DRP0CPE008015, 105 p., 2008.
- Croisé J., Mayer G., Marschall P., Matray J.M., Tanaka T. and Vogel P.: Gas Threshold Pressure Test Performed at the Mont Terri Rock Laboratory (Switzerland): Experimental Data and Data Analysis. Oil & Gas Science and Technology – Rev. IFP, Vol. 61(5), pp.631-645, 2006.
- Pruess K., Oldenburg C. and Moridis G.: TOUGH2 User's Guide, Version 2.0, Report LBNL-43134, Lawrence Berkeley National Laboratory, Berkeley, Calif., 1999.
- Talandier, J., G. Mayer, J. Croisé, Simulations of the hydrogen migration out of intermediate-level Radioactive Waste Disposal Drifts Using TOUGH2, Proceedings of TOUGH Symposium 2006, Berkeley, California, 2006.

INJECTION OF NUCLEAR ROCKET EXHAUST AND WATER INTO A DEEP UNSATURATED ZONE

Clay A. Cooper and David L. Decker

Desert Research Institute, Division of Hydrologic Sciences
2215 Raggio Pkwy
Reno, NV 89512
e-mail: clay.cooper@dri.edu

ABSTRACT

Nuclear rocket engine technology is being considered as a means of interplanetary vehicle propulsion for a manned mission to Mars. Significant additional technological research and development is required before nuclear-based rocket propulsion can be integrated into an interplanetary vehicle—including firing full-scale nuclear rocket engines in a test and evaluation facility designed to safely handle and evaluate engine performance. Testing of nuclear engines in the 1950s and 1960s was accomplished by directing engine exhaust gases into the atmosphere, a practice that is no longer acceptable. Injection into deep unsaturated zones of radioactive exhaust gases and water vapor associated with the testing of nuclear rocket engines is being considered as a way of sequestering radionuclides from the environment. Numerical simulations were conducted to determine the ability of an unsaturated zone with the hydraulic properties of Yucca Flat alluvium at the Nevada Test Site to contain gas-phase radionuclides. In these simulations, gas and water vapor were injected for two hours at a temperature of 600°C and with rates of 14.5 kg s⁻¹ and 15 kg s⁻¹, respectively, in varying thicknesses of alluvium with an intrinsic permeability of 10⁻¹¹ m² and porosity of 0.35. The simulation results show that during a test of an engine, gaseous radionuclides should not migrate to the land surface for injection intervals deeper than 200 m. A significant component of the nuclear engine test facility design is the injection of water at the engine exhaust nozzle to cool the engine exhaust. This water is rapidly converted to superheated steam that is then co-injected into the unsaturated zone simultaneously with the radioactive exhaust gas. This gaseous/vapor injectate will cool and condense within several meters of the injection point and drain downward. The nearly horizontal hydraulic groundwater gradient present in Yucca Flat, however, should limit lateral migration of any condensate that may drain downward and reach the water table.

INTRODUCTION

Background

Recurring interest by NASA to send a crewed mission to Mars has rekindled interest in nuclear

engine technology. Nuclear rocket engine technology was developed and successfully demonstrated under the Nuclear Engine for Rocket Vehicle Applications (NERVA) program between 1955 and 1972. A total of 23 engines were tested at a facility located in Jackass Flats on the Nevada Test Site, at power levels up to 4,000 MW (megawatts) with engine run times up to an hour. The long-run time capability of nuclear rocket engines provides a significantly higher specific impulse than traditional chemical engines. The use of nuclear engines will in turn reduce the overall interplanetary flight time, with a consequent reduction in flight risk. At the Nevada Test Site, nuclear rocket engines were mounted onto a testing platform, and exhaust gases were released to the atmosphere. The NERVA program also successfully demonstrated an exhaust gas scrubber system that removed all radiogenic material from the gas stream from a 45 MW engine test.

To achieve the level of performance necessary for an engine design intended for a Mars mission, an extensive ground-based test and evaluation program is necessary. In addition, power requirements for a Mars-capable engine are large enough that design of a scaled-up NERVA scrubber system may be cost prohibitive. Rather than scrubbing radiogenic exhaust gases, Howe et al. (2001) proposed the sequestration of gases in a deep unsaturated zone. They identified the pressure, liquid saturation, and temperature fields associated with injection of exhaust associated with a full-scale test. In concept, a nuclear rocket engine is mounted to a containment structure over a large diameter well head. The well is cased from the surface to a depth sufficient to prevent near surface rupture or wall failure from heat and gas ablation. Below the upper stem casing, the borehole is either uncased or is lined with perforated casing. The perforated casing allows rocket exhaust gases to be injected into the vadose zone, which acts as a reservoir for these constituents, thereby reducing the possibility of atmospheric release of radiogenic gas. The full-scale nuclear rocket test will produce hydrogen gas at a temperature of several thousand degrees centigrade. This exhaust gas stream will be cooled to <600°C with a spray of liquid water (which is immediately vaporized) at the rocket exhaust nozzle (Figure 1).

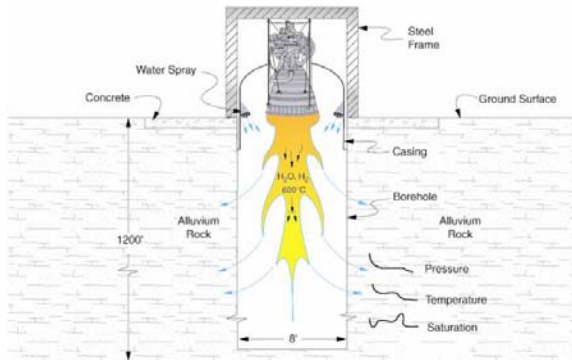


Figure 1. Schematic of a full-scale nuclear rocket engine test stand with vadose zone exhaust sequestration (after Howe et al., 2001).

The injectate will also contain radionuclides produced by the degradation of the nuclear furnace reactor. Principal radiogenic constituents of concern are radioisotopes of the noncondensable gases krypton and xenon. The gas pressure within the borehole is not expected to exceed 0.24 MPa without impacting the successful operation of the engine.

To extend the work reported by Howe et al. (2001), we developed a numerical model to simulate the scenario depicted in Figure 1, occurring in the unsaturated zone at the Nevada Test Site. In addition to investigating the pressure, temperature, and liquid (gas) saturation fields associated with injection, gaseous radionuclide transport was included in the model. Results are compared to those of Howe et al. (2001) where possible.

An important requirement for the sequestration of radioactive gases is a deep unsaturated zone. The deepest unsaturated zone at the NTS is located within Yucca Flat, the location of atmospheric and subsurface nuclear tests. In the center of the Yucca Flat basin, there is over 500 m of Quaternary alluvium which is underlain by Tertiary volcanic rocks.

APPROACH AND METHODS

Development of Numerical Model

The model was implemented into the TOUGH2 simulator (Pruess et al., 1999) with the EOS7r equation of state module. Two active phases were simulated (gas and liquid) with five components: air, water, radiogenic tracer (^{85}Kr), tracer decay product (stable ^{85}Ru), and heat.

The flow equations for the gas and aqueous phases are modeled with Darcy's law, solute transport in both phases is handled by Fick's law, and conductive heat transport is modeled with Fourier's law. A complete description of the governing equations and their implementation is described in Pruess et al. (1999).

The computational domain was arranged as radially symmetric flow, with an injection borehole in the center. The domain size extends from the face of the borehole (2 m radius) to 10,000 m, which is large considering the 100 yr time scale of the model. Vertically, the domain exists from the land surface to the 490 m deep water table. The hydraulic boundary conditions are prescribed flux along the interval within the borehole undergoing injection and zero flux along the rest of the borehole, prescribed pressure along the upper and lower horizontal boundaries, and prescribed pressure along the vertical boundary 10,000 m from the borehole. The input data and initial conditions are presented in Table 1 for a "reference" simulation.

The carrier gas in the model is air, while that in the actual engine test will be hydrogen. Figure 2 shows the relationship between the densities of hydrogen and air over the temperature range of the test. Air density was obtained from tabulated data (CRC Press, 89th Ed.) while hydrogen density was calculated from Boyle's Law. The molecular weight of diatomic hydrogen is 2 g mol⁻¹ while that for air at ~100 percent relative humidity in the unsaturated zone is between 16 g mol⁻¹ (pure water vapor) and 28 g mol⁻¹ (dry air). For all temperatures, the air density is ~10 times that of hydrogen, making hydrogen buoyant in relation to the subsurface air, a process not accounted for in the model. Figure 2 also shows the viscosity relationship between the two gases; the viscosity ratio between the two favors buoyancy of hydrogen over air by a factor between 2 and 3. Viscosity for both air and hydrogen were calculated from Sutherland's formula (Crane, 1988). The radioactive isotope ^{85}Kr , was mixed with the carrier gas (air and water vapor). This gas phase mixture was injected uniformly and at the same temperature across the borehole face; i.e., there were no allowances for a pressure drop within the borehole. The ratio of gas densities suggests that buoyant hydrogen gas as a separate gas phase would rise when immersed in air, but is not accounted for in the model.

Table 1. Input data and initial conditions for reference simulation.

Input Data Parameters	Value
Intrinsic permeability, m ²	10 ⁻¹¹
Porosity	0.35
Diffus. coeff. gas phase tracer, m ² s ⁻¹	2.62 x 10 ⁻⁵
Residual liquid saturation	0.0206
Capillary pressure curve	van Genuch.
Relative permeability curve	van Genuch.
van Genuchten m (=1-1/n)	0.291
van Genuchten α, Pa ⁻¹	0.0017
Injection interval, m	variable
Injection time, hours	2
Injection rate, water, kg s ⁻¹	15.0
Injection rate, "air," kg s ⁻¹	14.5
Enthalpy of injected water, J kg ⁻¹	1.463 x 10 ⁶ ^a
Enthalpy of injected air, J kg ⁻¹	6.57 x 10 ⁵ ^a
Tracer half-life, yr	10.76
<i>Initial conditions</i>	
Parameter	Value
Liquid saturation	0.3
Formation pressure (gas static), MPa	0.12 at water table
Formation temperature, °C	25

^a approx. 600°C

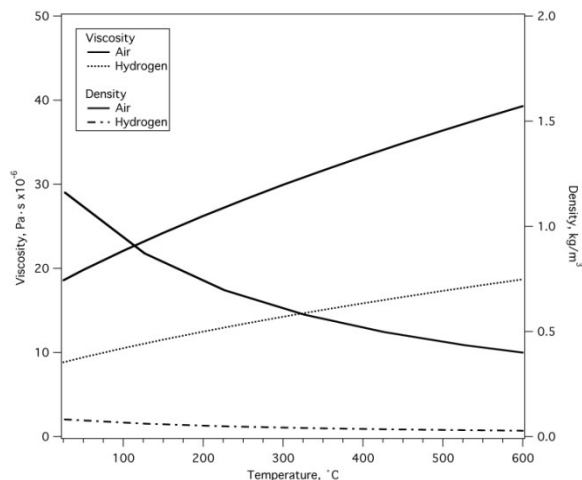


Figure 2. Mass density and dynamic viscosity as a function of temperature for air and hydrogen at 1 bar pressure.

SIMULATION RESULTS

A simulation in which the 600°C radioactive gas was injected into a 20 m injection interval for two hours is used as a "reference" case. Figure 3 shows the pressure, saturation, and temperature fields over a four-hour period. The pressure field extends out to approximately 20 m, while the formation temperature and liquid saturation are affected by the injectate to a distance of less than four meters from the edge of the borehole (note that hot colors show greater liquid saturation on the liquid saturation scale). The injectate immediately condenses upon entering the formation, which increases the liquid saturation within the vicinity of the borehole. The low grid resolution does not capture centimeter-scale behavior such as the downward drainage of water (gridblock heights are 10 m).

The mass fraction field of a gas tracer (as tracer density to gas density, X_g^{Kr} with the properties of ⁸⁵Kr) for the same simulation is shown in Figure 4. The initial inventory for a two hour test is estimated as 283 mg radioactive Kr and Xe. For a two-hour test, the rate of injection is 3.93×10^{-8} kg s⁻¹. Radionuclides do not reach the land surface during the 100-year simulation. Within the first year of transport, the horizontal extent of radionuclide transport is less than 160 m from the borehole. At approximately 10 years, radionuclides extend between 250 and 300 m from the borehole.

When the reference simulation was modified by increasing the injection interval from 20 m to 160 m (Figure 5), low levels of radionuclides come to within 50 m of the land surface in 10 years. The horizontal extent of radionuclides is only slightly smaller than for the 20 m injection interval simulation.

A simulation was run to compare our results with those of the WAFE computer model presented in Howe et al. (2001). The WAFE calculations did not include a tracer gas, so only the flow simulation can be compared. In this simulation, the injectate gas flow rate was lowered to 4.9 kg s⁻¹ and the water flow rate was raised to the slightly higher value of 15.6 kg s⁻¹, to match the values used in Howe et al. (2001). A comparison between the liquid saturation fields of Howe et al. (2001) and this work is shown in Figure 6. The location of maximum liquid saturation (2.2 m from the center of the borehole) is the same for both simulations, even though the injection interval of Howe et al. was over 300 m long. The difference between the injection intervals probably accounts for the higher liquid saturation in our model, as injection was confined to a narrower zone.

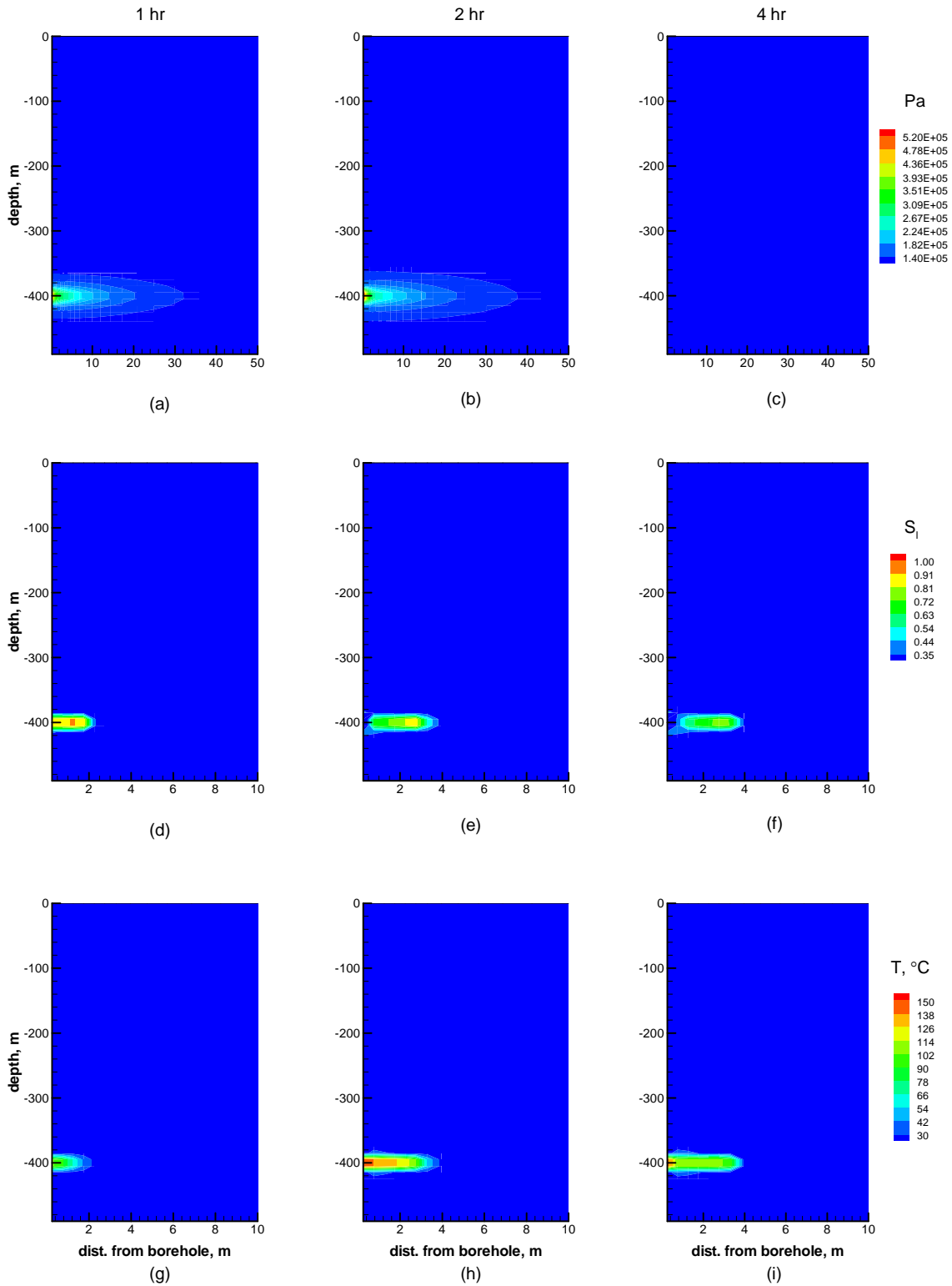


Figure 3. Pressure, liquid saturation, and temperature fields over a period of four hours after the start of injection. Injection stopped after two hours.

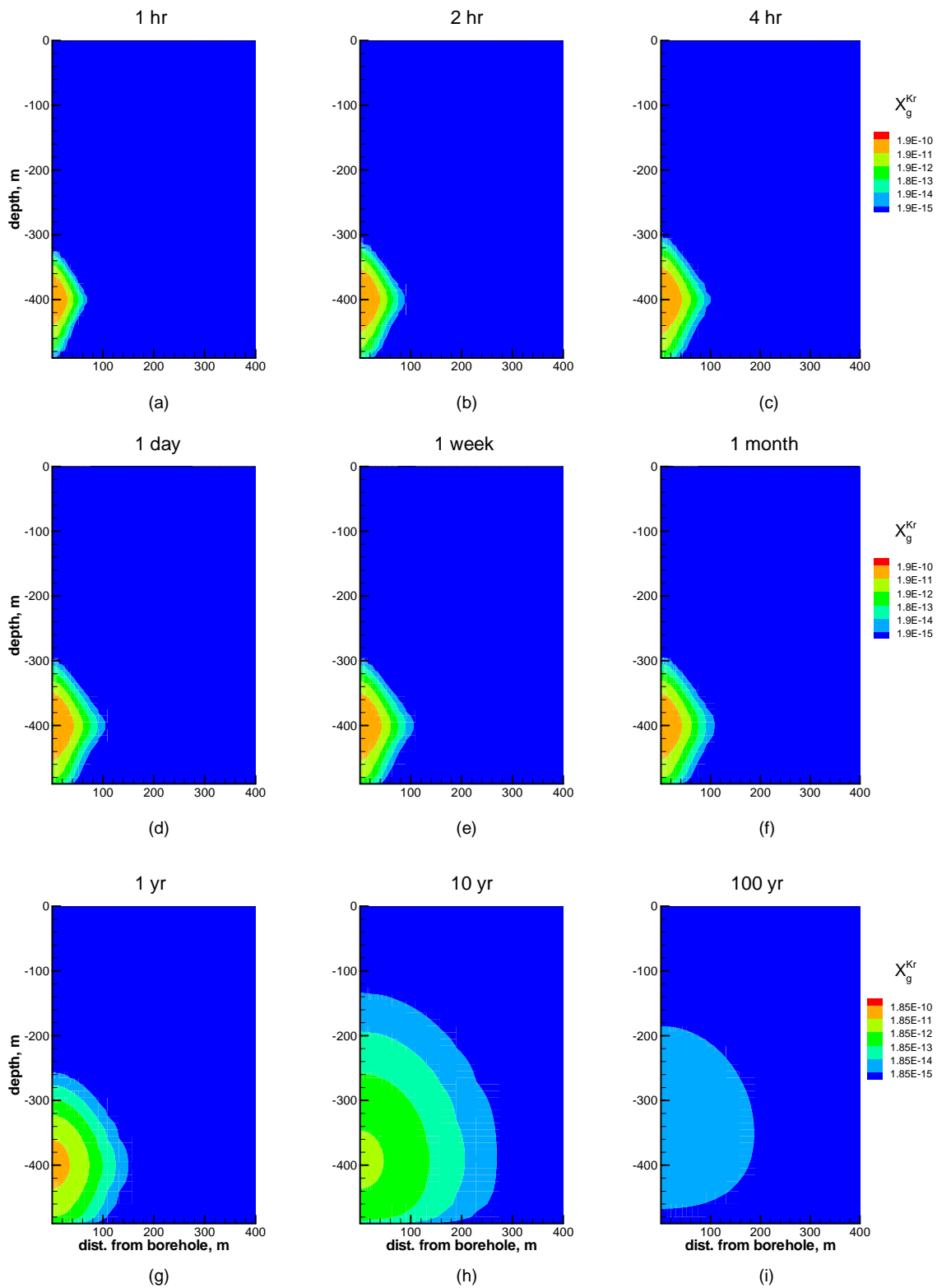


Figure 4. Mass fraction of ^{85}Kr between 1 hr and 100 yr through a 20 m interval. The period of injection was between zero and 2 hr.

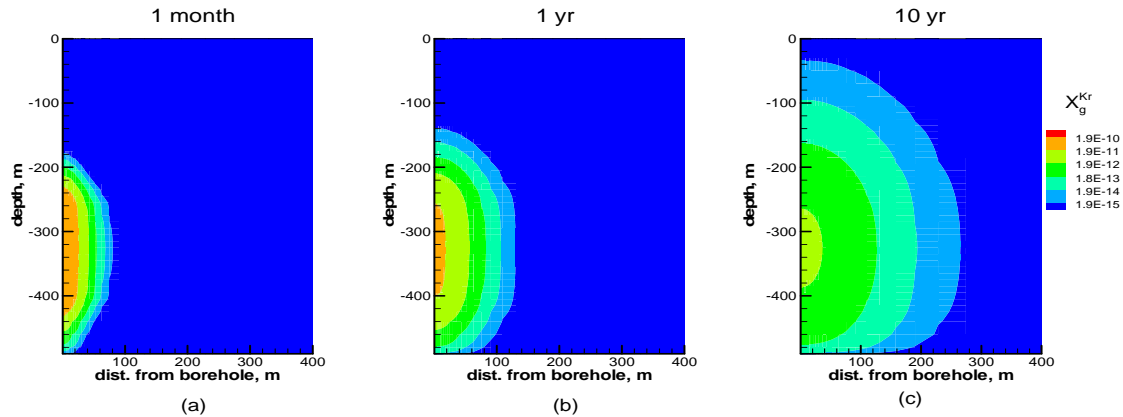


Figure 5. Mass fraction of ^{85}Kr for 3 times after gas injection through a 160 m interval

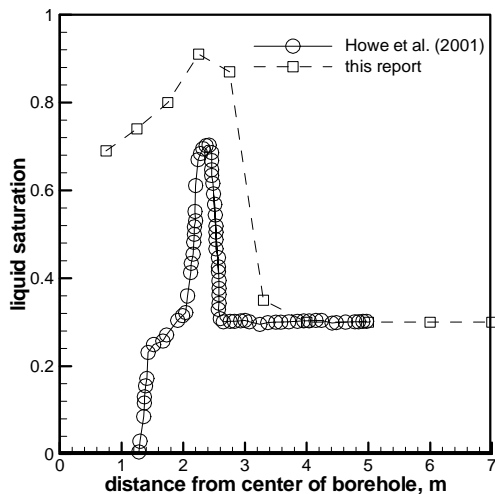


Figure 6. Comparison of liquid saturation in the alluvium to the simulation of Howe et al., 2001.

SUMMARY AND CONCLUSIONS

The simulations performed were conducted to evaluate the efficacy of using the Nevada Test Site unsaturated zone as a repository for the mass of water, water vapor, and gases produced from a nuclear rocket engine test. The simulations were constructed with homogeneous and isotropic permeability fields. For a narrow (20 m) and deep (300 m) injection zone, the results suggest that injected radionuclides will not reach the land surface. Similarly, the amount of water injected is not enough to result in the downward drainage. These simplified models suggest that the unsaturated zone is capable of sequestering radionuclides at the prescribed mass flow rates without exceeding the specified design pressure within the borehole. The results give merit that a conceptual design for a rocket test facility has merit, but will require more detailed information on the spatial

distribution of subsurface permeability, porosity, and moisture content.

ACKNOWLEDGMENTS

This work was supported by the Idaho National Lab – Battelle Energy Alliance (award no. 00060606). We thank Jenny Chapman, Roger Jacobson, Chuck Russell, and David Shafer for careful reviews of an earlier version of this manuscript.

REFERENCES

- Bechtel Nevada, A hydrostratigraphic framework model and alternatives for the groundwater flow and contaminant transport model of corrective action unit 98: Frenchman Flat, Clark, Lincoln and Nye Counties, Nevada, DOE/NV/11718-1064 Bechtel Nevada for US DOE, 2005.
- Crane Company, *Flow of fluids through valves, fittings, and pipe*, Technical Paper No. 410 (TP-410), 1988.
- CRC Press, *Handbook of Chemistry and Physics*, 89th Edition.
- Gonzales, J.L., S.L. Drellack, and M.J. Townsend, *Descriptive narrative for the hydrogeologic model at the Yucca Flat corrective action unit, an interim report*, Las Vegas, NV Bechtel Nevada, 1998.
- Gonzales, J.L., and S.L. Drellack, *Addendum to the descriptive narrative for the hydrogeologic model at the Yucca Flat corrective action unit: Northern extension*, Las Vegas, NV Bechtel Nevada, 1999.
- Howe, S.D., B. Travis, and D.K. Zerkle, Safe testing of nuclear rockets. *Journal of Propulsion and Power*, 17(3) 534-539, 2001.

- Laczniak, R.J., J.C. Cole, D.A. Sawyer, and D.A. Trudeau, *Summary of hydrogeologic controls on ground-water flow at the Nevada Test Site, Nye County, Nevada*, U.S. Geological Survey Water-Resources Investigations Report 96-4109, 1996.
- Pruess, K., C. Oldenburg, and G. Moridis, *TOUGH2 User's Guide, Version 2.0*, Report LBNL-43134, Lawrence Berkeley, Berkeley, Calif., 1999.
- Simmons, A.M., *Yucca Mountain Site Description*, TDR-CRW-GS-000001 Rev. 02 ICN 01, 2004.
- U.S. Department of Energy (DOE), United States Nuclear Tests, July 1945 through September 1992, DOE/NV-209 (Rev. 15), 2000.
- U.S. Geological Survey, National Water Information System: Web Interface. Ground-water Reports, Nevada, Water years 2005, <http://nwis.waterdata.usgs.gov/nv/nwis/gwlevels>.
- Young, M., C. Cooper, S. Sharpe, J. Miller, and D. Shafer, *Upward advection: dynamic simulation of vadose zone moisture flux*, Desert Research Institute, Division of Hydrologic Sciences Publication No. 45192, 2002.

MODELING STUDIES OF GAS FLOW AND GROUNDWATER PRESSURE BUILDUP FOR A VITRIFIED NUCLEAR WASTE DISPOSAL SITE

Keni Zhang¹, Jean Croisé², and Gerhard Mayer²

¹Earth Sciences Division, Lawrence Berkeley National Laboratory, Berkeley, CA 94720, USA

²AF-Colenco Ltd, Täferstrasse 26, CH-5405 Baden, Switzerland

e-mail: KZhang@lbl.gov

ABSTRACT

Significant quantities of hydrogen can be produced by the corrosion of metal components. It is necessary to forecast gas migration and groundwater pressure buildup in the context of deep geological radioactive waste disposal. One of the major problems in representing gas migration in a radioactive waste repository is that of simultaneously modeling all gas sources and transfer pathways constituted by the network of underground drifts and the surrounding low-permeability rock. In 2006, the French National Agency for Radioactive Waste Management (ANDRA) launched an international multiphase flow simulation benchmark exercise for modeling such a two-phase flow system. The exercise was designed to compare the performance of the numerical methods being used to resolve the designed problems. This paper presents the results of Test Case 2 of the exercise completed by the authors, which has been awarded the first prize as the only best-performing team. The three-dimensional model represents a fraction of a repository with vitrified waste. The model simulates ambient pressure and flow conditions (considering evacuation effect) after placement of wastes, with full consideration of two-phase initial and boundary conditions. Isothermal conditions are assumed. Time-dependent gas sources are applied to the model. Since the natural environment is unable to evacuate the entire amount of hydrogen in a dissolved state, a free gas phase is formed within the disposal structures. The model is used to study the dissipation of those gases to determine their influence on the transient phases throughout the lifetime of the repository, and to investigate possible pressure buildup, which may introduce a risk of damage to the host rock. We use the model to investigate how the presence of gas in the repository influences the nature of water flow around the disposal structures and the resaturation transient processes. The TOUGH2-MP code, a parallel multiphase flow simulator, has been adopted for this study.

INTRODUCTION

Gas migration in a radioactive waste repository is a critical component in the safety assessment of deep geological storage. Several European countries are currently investigating the feasibility of deep

geological disposal of radioactive waste in low-permeability formations. The French Agency for the Management of Radioactive Waste (Andra) proposes to build a repository in an argillaceous formation (Andra, 2005), an indurated clay formation approximately 500 m below ground surface. Such a proposed repository raises a question related to the long-term performance of the repository, namely the impact of the hydrogen gas generated in the waste on the pressure and saturation fields within the repository and the host rock. In the repositories, anaerobic corrosion of metals produces hydrogen. The generation, accumulation, and release of the gas from the disposal system may affect a number of processes that influence long-term radiological safety of the repository. These processes may include (1) excess gas/water pressures affecting the mechanical integrity of the barrier system and the surrounding rock, (2) expulsion of contaminated water from the waste package due to gas buildup, and (3) transport of volatile radionuclides through the surrounding geological barriers.

Numerical simulations provide an effective approach for investigating the processes of pressure buildup due to gas generation and its influence on the repository system. A numerical model for such purposes must be able to simulate different stages of a repository: ambient conditions, operational phase of the repository, and closure after placement of wastes. After closure, the repository performance with respect to gas migration and pressure buildup will be affected not only by the two-phase properties of the surrounding barriers, but also by a variety of other geological, geotechnical, and waste-related factors. The model needs to account for the relevant processes associated with the migration of waste-generated gas, and also to incorporate the complex geometry of a deep repository, such as regional hydrogeologic framework, caverns, tunnels, and seals. These processes have been investigated by Talandier et al. (2006) using simplified 2D and 3D models. Senger et al. (2008) developed 3D models for the Swiss radioactive waste repository site by treating hydrogen as air in the simulations. Full consideration of such a three-dimensional site-scale complex system represents a large computational challenge.

In 2007, ANDRA launched an international multiphase flow simulation benchmark exercise, named Couplex-Gaz, for modeling waste-generated gas flow systems. Couplex-Gaz was designed to compare the accuracy and efficiency of the numerical methods being used to resolve the nonlinear equation system associated with gas transfers and groundwater in porous media, and to provide relevant representations of those transfers at large spatial scales. The exercise consists of two simulation cases. The first case is a relatively simple 2D model (similar to a 2D case presented in Talandier et al., 2006), and the second case is a 3D site-scale model, which is more computationally challenging. The team formed by the authors of this paper has been awarded the first prize. In this paper, we will discuss the approaches used in the model development and simulation results.

The three-dimensional model represents a fraction of a repository with vitrified waste. We used an integrated finite difference (IFD) method for the model simulation. The model considers a system with two-phase initial and boundary conditions and time-dependent gas sources from metal corrosion. In the repository, hydrogen is partially dissolved in the water and also partially exists as a free gas. The dissipation processes of those gases are examined to determine their influence on the transient phases throughout the lifetime of the repository, and to investigate possible pressure buildup, which may introduce the risk of damage to the waste-containing materials. Gas present in the repository may influence the nature of water flow around the disposal structures. Simulations were run by the parallel two-phase flow simulator TOUGH2-MP (Zhang et al., 2001, 2008; Wu et al. 2002). The simulator has been successfully applied to large-scale simulations for nuclear waste disposal site characterization, such as in the work of Zhang et al. (2003) and Senger et al. (2008).

MODEL SETUP

Problem Description and Conceptual Model

During construction of the repository facilities and the operational phase of the repository, drifts and shafts are ventilated, and the host rock is depressurized and desaturated. At the end of operation, the access drifts are backfilled and sealed with bentonite plugs. As described in Andra (2006), the part of the repository containing high-level vitrified waste is taken into account. After closure, resaturation of the host rock and backfill material starts. At the same time, corrosion of steel in the waste packages causes hydrogen to be generated in a repository (containing high-level radioactive waste) for 50,000 years after closure of the facility (Andra, 2006). The generated gas will first dissolve in the

pore water and then transport through advection and diffusion into the host rock and backfill materials within the drifts. Excessive amounts of hydrogen cannot be fully dissolved, and a free gas phase will be formed. Continuing generation of the gas will lead to pressure buildup in the repository and surrounding rock. After 50,000 years, metals are completely consumed, and no more hydrogen will be produced. The free gas in the repository will slowly dissipate, and the pressure in the system will recover to initial conditions. We have developed a model to simulate the entire process—from the transient phases throughout the lifetime of the repository—and to investigate possible pressure buildup, which may introduce of the risk of damage to waste-containing materials.

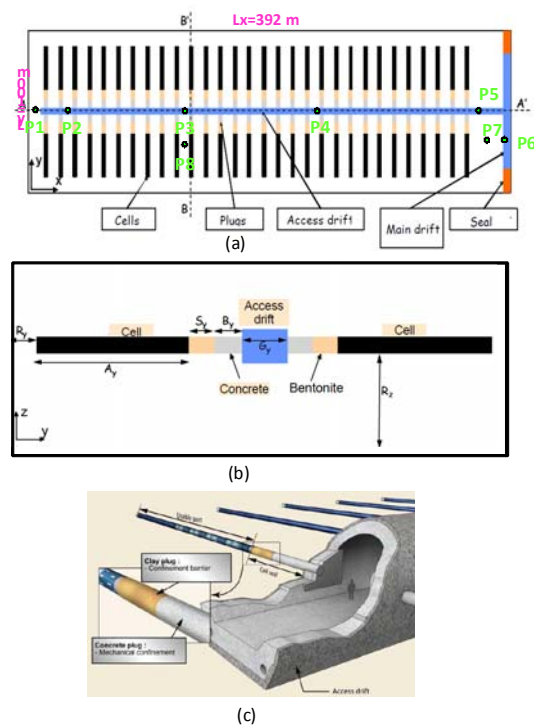


Figure 1. (a) Horizontal plane view of the model domain; (b) Vertical view of the model domain; (c) General concept of the high level cell in the repository (Modified from Andra 2005 and Andra, 2006)

The model represents a fraction of the repository for an area of vitrified waste consisting of two rows of 30 cells (Figure 1). Only half of the plane (Figure 1a) needs to be considered in the three-dimensional model, owing to its symmetry along the access drift. The domain has a vertical extension of about 130 m, which represents the thickness of the Callovo-Oxfordian clay at the potential disposal site. The width of the domain is 50 m and corresponds to half the distance between neighboring disposal drifts, while the length of the domain, which covers all the 30 cells, is 392 m. The length of each waste cell is 30

m, sealed by a 3 m bentonite plug and then supported by a 4 m concrete plug (Figure 1b, c). The repository is placed ~500 m below ground level.

Fluid flow in the repository involves multiphase transient flow processes. These flow and transport processes are considered to be isothermal with a constant temperature of 30°C. For gas flow, a mixture of gases is evolved, with hydrogen being the chief constituent. In this study, all gases are treated as hydrogen. Hydrogen dissolution in the pore water follows Henry's law; gas and water flow are governed by a multiphase extension of Darcy's law:

$$V_{\beta} = -\frac{kk_r^{\beta}(S_{\beta})}{\mu_{\beta}}(\nabla P_{\beta} + \rho_{\beta}g\nabla z) \quad (1)$$

where β denotes the phase of the fluid (aqueous or gaseous), k is the intrinsic permeability, k_r^{β} is relative permeability for phase β , μ_{β} is the viscosity, ρ_{β} is the density, g is the gravity of acceleration, z is the altitude, and V_{β} is Darcy's velocity for phase β .

Diffusion processes in the gas and water phases are described by Fick's Law. The diffusive flux for the binary mixture of hydrogen and water vapor can be written as:

$$f^g = \rho_g D_{H2/vap}^g \nabla X_{H2}^g \quad (2)$$

where g represents gas phase, $D_{H2/vap}^g$ is the diffusion coefficient of hydrogen in the water vapor, and ∇X_{H2}^g is the gradient of mass fraction of hydrogen gas.

The diffusive flux for the dissolved hydrogen is written as:

$$f^w = \rho_w D_{H2}^w \nabla X_{H2}^w \quad (3)$$

where w represents the liquid water phase, D_{H2}^w is the diffusion coefficient of hydrogen in the water, and ∇X_{H2}^w is the gradient of mass fraction of the dissolve hydrogen.

In this study, the following expressions for the diffusion coefficients were chosen (Pruess, et al. 1999).

$$D_{H2}^w = \frac{\omega}{\tau^2} \cdot k_r^w \cdot D_{H2}^{w,0} \quad (4)$$

and

$$D_{H2}^g = \frac{\omega}{\tau^2} \cdot k_r^g \cdot D_{H2}^{g,0} \quad (5)$$

with ω the porosity, τ a tortuosity coefficient, $D_{H2}^{w,0}$ and $D_{H2}^{g,0}$, the free diffusion coefficients in the water and in the gas phase.

The model solves mass-balance equations by the integrated finite difference method. The equations are set up by combining mass balance, advection flux, and diffusion flux, and solved by supplementing with a number of constitutive equations. These constitutive correlations express the interrelationships and constraints of physical processes, variables, and parameters. The van Genuchten model (1980) has been selected to express capillary pressure in relation to the effective saturation of the medium. Relative permeability is expressed by integrating the forecasting model proposed by Mualem (1976) into van Genuchten's capillary model.

Simulation Code

The simulations conducted in this study are computationally challenging, because of the site-scale three-dimensional grid and the complex nonlinear processes involved. The TOUGH2-MP (Zhang et al., 2008) is adopted for these simulations. The EOS5 fluid property module (Pruess et al., 1999) is selected for describing the thermodynamics of hydrogen gas. The module was developed for studying the behavior of groundwater systems in which hydrogen releases are taking place. TOUGH2-MP is an efficient parallel simulator for large-scale general purpose multiphase flow simulations developed at Lawrence Berkeley National Laboratory. The parallel simulator is a three-dimensional, fully implicit model that solves large, sparse linear systems arising from discretization of the partial differential equations for mass and energy balance in porous and fractured media. The simulator was developed based on the TOUGH2 code (Pruess et al., 1999) and inherits all the process capabilities of the TOUGH2 code, including a comprehensive description of the thermodynamics and thermophysical properties of fluids with multiple components, modeling single and/or multiple-phase isothermal or non-isothermal flow processes. TOUGH2-MP uses MPI for parallel implementation, the METIS software package (Karypis and Kumar, 1998) for simulation domain partitioning, and the iterative parallel linear solver package Aztec (Tuminaro et al., 1999) for solving linear equations by multiple processors. The parallel simulator is equipped with a very efficient interprocessor communication scheme and demonstrates excellent efficiency and scalability.

Initial and Boundary Conditions

At the top and bottom boundaries of the simulation domain, a constant pressure is imposed corresponding to the hydraulic heads of the aquifers above and below the clay rock. The pressures for the top and bottom boundaries are specified as 4.2 MPa and 5.5 MPa respectively. Top and bottom of the domain are fully water saturated, and no hydrogen dissolves in the water. Due to the symmetry of the disposal configuration with horizontally placed array of disposal drifts, the lateral sides of the model domain are set to no-flow conditions for both water and gas. A constant pressure of 4.85 MPa at the entrance of the main drift is imposed, where the seal for the main drift is located and is fully saturated.

The model initial conditions represent flow conditions immediately after closure of the repository system. The entire host formation is fully water saturated; other facilities (such as the backfilled drift, concrete supports, bentonite plugs, and drift seals) are 70% water saturated and 30% gas saturated. The partially saturated materials have a gas pressure equal to 1 atmosphere, and their corresponding water pressure is deduced from the gas pressure and the capillary pressure, by applying van Genuchten models for each materials.

The initial conditions are obtained by first specifying constant pressure at the model top and bottom boundary and running the model to steady state. The steady state represents ambient conditions of pressure under steady-state equilibrium between aquifers on the top and bottom of the domain. These steady-state conditions are then used as the starting point for a second run segment, which simulates the operational phase of the repository by specifying a constant pressure at the entrance of the main drift, giving 0.7 of water saturation for engineering materials as requested and running the model for a short period. The impact of ventilation in the operational period is neglected. Initial conditions, representing the conditions at the end of repository operation, are then created by modifying the output of the second segment run with changing gas pressure and gas saturation for the gridblocks of the man-made facilities to the given conditions. Full saturation of the host rock in the vicinity of the waste packages is a rather unrealistic but conservative assumption with respect to pressure buildup, and may also cause numerical difficulty. To improve the model convergence performance, small gas saturation (1%) is assigned to the surrounding gridblocks of the waste packages.

Gas generation is simulated by providing a gas-production term for each disposal cell. It is imposed on the external surface of the cylinder that schematically represents the cell. Generation rates are

given as: from 0 to 4,500 years, $Q=100$ mol/year/cell; from 4,500 to 20,000 years, $Q=15$ mol/year/cell; from 20,000 to 50,000 years, $Q=1$ mol/year/cell. After 50,000 years, no hydrogen gas will be generated.

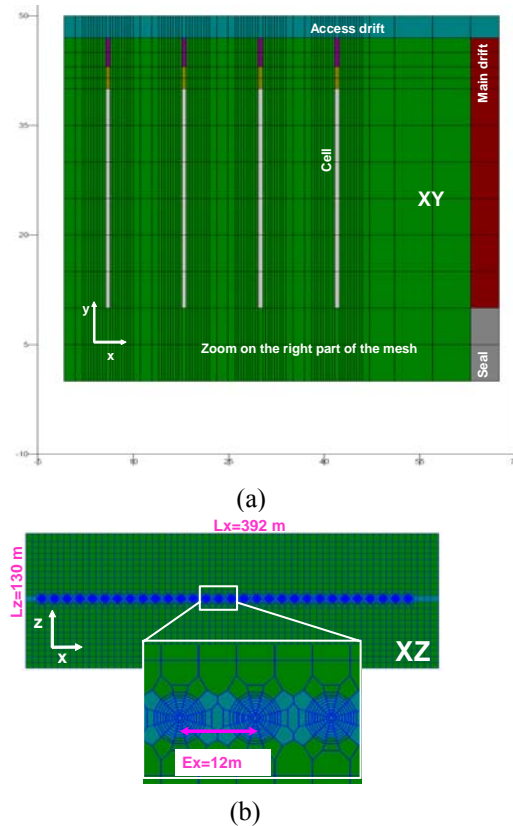


Figure 2. Cross-sectional view of the 3D mesh: (a) in xy plan (zoom on the right part of the mesh with the main drift and the 4 first cells), (b) in xz plan.

Model Mesh and Input Parameters

A three-dimensional unstructured mesh was created based on the model domain definition by Andra (2006) using WinGridder (Pan et al., 2001). In the mesh, waste packages (cells), bentonite plugs, and concrete supports share the same circular section. All sections of the access and main drifts are square. Disposal cells are positioned at half height in the access drift and in the calculation domain. There are 30 cells along the one side of the access drift. Cylindrical gridding is adopted around waste cells (Figure 2a), whereas rectangular grids are used for the geological domains that are some distance away from the waste packages, because the host rock is anisotropic in permeability. We use refined grids around waste cells to capture the radial transport near the emplacement drift of the waste package. Figure 2 shows a portion of the cross-sectional view of the 3D mesh in xy and xz plans. The mesh consists of 62,401 gridblocks and 184,260 connections.

The materials to be taken into account in the simulation include the backfill of the drift, the bentonite and concrete of the drift seals, and the Callovo-Oxfordian clay. The cell is constituted of a material impermeable to both water and gas. Table 1 provides the parameters used in the modeling study. Free diffusion coefficients in gas and aqueous phases are $2.13\text{E-}05$ and $1.0\text{E-}09$ for water, and $9.5\text{E-}05$ and $5.961\text{E-}09$ for hydrogen, respectively. Comparing to the advection flow, the diffusion flux is relatively small at early stage. To facilitate the simulation run, the diffusion effect is neglected for the first 5,000-year simulation.

Table 1. Physical parameters for the rocks (from ANDRA 2006)

Parameter (at 30°C)	Materials						
	Cell	Concrete	Bentonite	Backfill	Seal	COX	
K_r [m ²]	0	$1.0 \cdot 10^{-13}$	$1.0 \cdot 10^{-22}$	$6.0 \cdot 10^{-13}$	$1.0 \cdot 10^{-13}$	$5.0 \cdot 10^{-21}$	
K_a [m ²]		Kv=Kh					$5.0 \cdot 10^{-20}$
Porosity [%]	25	30	35	35	30	15	
Specific storage coefficient [m ³]	$4.0 \cdot 10^{-06}$	$2.3 \cdot 10^{-06}$	$4.4 \cdot 10^{-06}$	$4.0 \cdot 10^{-06}$	$3.0 \cdot 10^{-06}$	$2.3 \cdot 10^{-06}$	
Two-phase flow parameters							
S_{gr} [%]	0	0	0	0	0	0	
S_{or} [%]	1	1	1	1	1	40	
Van Genuchten parameters							
n [-]	1.5	1.54	1.61	1.42	1.5	1.49	
P_r [Pa]	$3 \cdot 10^4$	$2 \cdot 10^6$	$16 \cdot 10^6$	$6 \cdot 10^5$	$5 \cdot 10^6$	$15 \cdot 10^6$	
τ (Tortuosity)	1	2	4.5	2	2	2	

RESULTS AND DISCUSSION

The simulation was run up to the time when the gas phase in the model domain has disappeared, which is expected to be several ten-thousands of years. The results of the simulation were depicted as gas pressure and saturation history curves at 9 observation locations and 2D spatial distribution contours of simulated pressure and gas saturation. In addition, hydrogen fluxes at different locations are also presented. The observation points are mainly located at the repository horizon. Figure 1 shows the eight observation locations at the repository level. Observation points P1, P2, P3, P4, and P5 distribute along the access drift, and the P6 is in the main drift. P7 and P8 are located in the host rock between drifts (see Figure 1a). P9 is located right above the access drift and between P3 and P4. The maximum pressure buildup is expected to appear at the repository horizon.

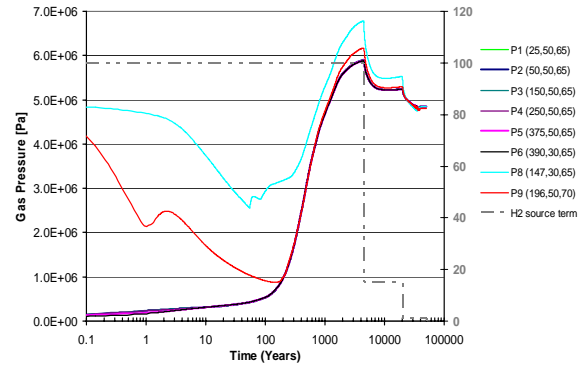


Figure 3. Gas pressure changes with time at the observation locations

Figure 3 shows the evolution of gas pressure at the eight observation locations (no P7). The figure also shows the corresponding hydrogen generation rate (mol/year/cell; see left y axis). The maximum pressure buildup appears at 4,500 years at all observation locations. The time of peak pressure corresponds to the time when hydrogen generation rate starts to drop. Gas pressures in the whole drift are similar at all times. Higher pressures are observed in the host rock at P7, P8, and P9. Figure 4 shows gas pressure at the time 2,000, 3,000, 4,500, and 5,000 years at the repository horizon ($z=65\text{m}$). The contour plots show that the maximum pressure buildup appears in the host rock surrounding the cell. Pressure buildup reaches a maximum pressure of about 7000 kPa after 4500 years, followed by a significant decline. The gas pressure in a vertical plane of the access drift is presented in Figure 5.

Figure 6 shows gas saturation change over time at observation locations. The drifts and tunnels have an initial gas saturation of 0.3. After closure of the repository system, gas saturation in the drift drops significantly in the first several hundred years, even though a significant amount of hydrogen is generated by the nuclear waste during this period. This is due to the gas storage capacity of the drift and the slow resaturation process resulting from the low-permeability rock. The waste-generated hydrogen then migrates vertically into the host rock and horizontally along the drift towards the seal of the main drift, both as a free gas phase and dissolved in pore water. The transport through advection and diffusion into the host rock causes gas saturation reduction (see Figure 6). After 4,500 years, the gas dissipation rate is higher than the generation rate. With the increase in gas generation rate and decrease in dissipation rate, an excessive amount of hydrogen cannot be fully dissolved, and a free gas phase will be formed. This free gas accumulation causes gas saturation to increase. Figure 6 indicates that gas saturation at the observation locations in the host rock is very small, and not much free gas can transport into the surrounding host rock.

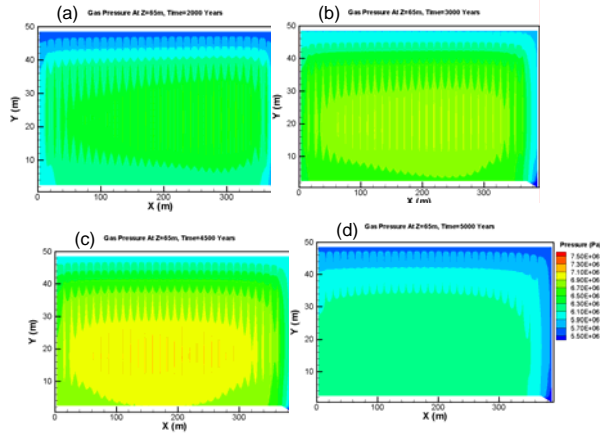


Figure 4. Gas pressure distributions at the repository horizon at time: (a) 2000 years; (b) 3000 years; (c) 4500 years; and (d) 5000 years.

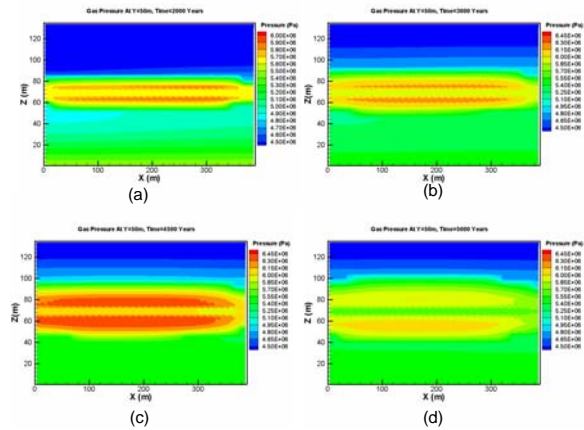


Figure 5. Gas pressure distributions in the vertical plane XZ of the access drift at time: (a) 2000 years; (b) 3000 years; (c) 4500 years; and (d) 5000 years.

Cumulative hydrogen escapes from the modeling domain mainly through top and bottom boundaries, and the sealed main drift entrance. The rates of the hydrogen fluxes through the top and bottom boundaries at different times are presented in Figure 7. The gas flux first arrives at the top and bottom boundaries in around 4,900 years. The flux rate reaches the peak value of 97.5 mol/year at the bottom boundary at 18,000 years, and 137.4 mol/year reaches the top boundary at time 22,500 years. Most hydrogen at the top and bottom boundaries is dissolved in water and leaves the domain through diffusion. Figure 8 shows the rate of gas flux in the drift at different locations and times. At early times (0.01 to 10 years), some initial high gas fluxes into the drift are observed, due to the initial small desaturation of the cells near field. These early fluxes vanish at around 100 years. The amount of hydrogen having being transported through the drift is small.

Starting with the pressurization phase (100–4500 years), caused by the combined effect of the continuous gas production and the low permeability of the host rock, the rate increases from left to right and to the entrance of the drift. This result indicates that the hydrogen gas accumulates in the drift, transports to the seal of the main drift, and escapes from there. After 30,000 years, the hydrogen fluxes through the main drift seal vanish, and the hydrogen continues to escape the domain through diffusion at the top and bottom boundaries.

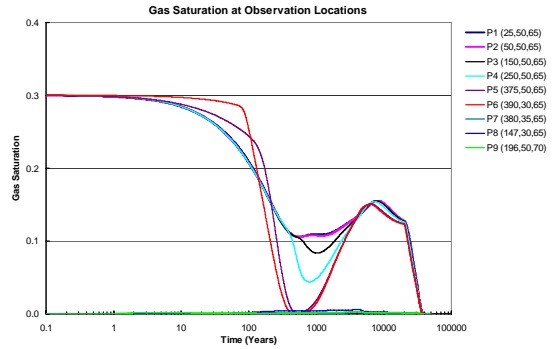


Figure 6. Gas saturation changes at the observation locations

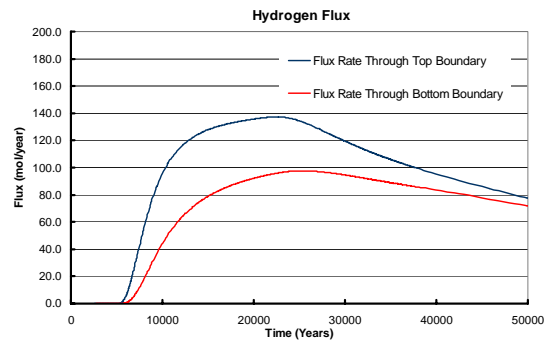


Figure 7. Evolution of hydrogen total (advective and diffusive) fluxes at the top and bottom boundary

The first 100-year simulation was run using an increased number of processors (2 to 32) to investigate computational efficiency. Figure 9 shows the speedups obtained by using different numbers of processors and for different parts of the simulation. By increasing the number of processors, the total execution time was reduced from 1,486 seconds using two processors to 110 seconds using 32 processors. The parallel code thus demonstrates very good performance. Total execution time is reduced to less than half when doubling the processor numbers in some cases (e.g., from 4 to 8, and from 8 to 16 processors). Figure 9 indicates that a superlinear effect is introduced by the part for solving the linear equations.

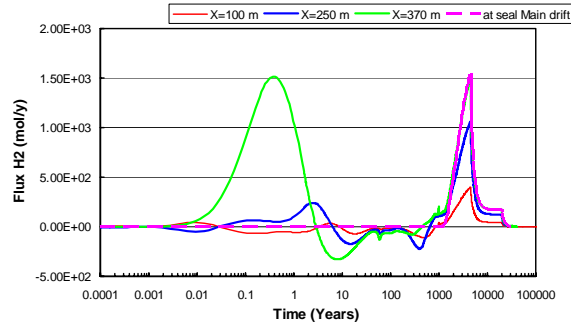


Figure 8. Evolution of hydrogen flux at different locations in the drift

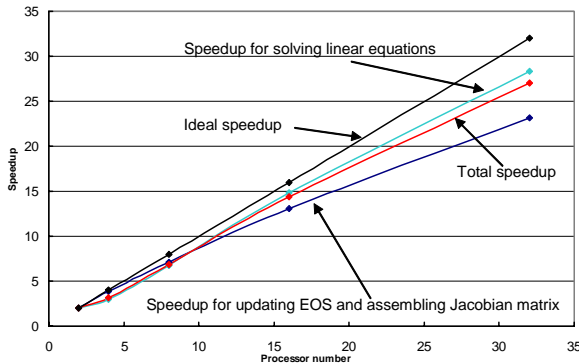


Figure 9. Speedups for the different parts of the parallel simulations

CONCLUSIONS

This paper presents the results obtained with TOUGH2-MP on the benchmark exercise Couplex-gaz 2, proposed by Andra in 2006. A 3D model is developed to study the dissipation of waste generated hydrogen from a line of 60 high-level waste cells horizontally emplaced along an access drift in a 500 m deep repository within a clay formation. This model simulates the transient hydraulic (single and two-phase) flow throughout the lifetime of the repository and investigates possible pressure buildup which may introduce of the risk of damage to the clay host rock and engineered barriers. The model fully represents hydrogen gas migration in a radioactive waste repository, simulates simultaneously all gas sources and the transfer pathways constituted by the network of underground drifts, and takes into account the time-dependent gas generation source term.

Simulation results indicate that the maximum pressure level obtained in the repository is controlled by the gas generation rate, the gas-filled volume initially available in the backfilled drifts, and the main-drift-seal permeability. The main long-term hydrogen dissipation process is the diffusion of the dissolved hydrogen towards the top and bottom boundaries of the Callovo-Oxfordian Clay.

ACKNOWLEDGEMENTS

The authors would like to thank Lehua Pan for his help in creating the model mesh.

REFERENCES

- Andra, Dossier 2005 Argile, les recherches del'Andra sur le stockage géologique des déchets radioactifs à haute activité et à vie longue, collection les Rapports, Andra, Châtenay-Malabry, France, 2005.
- Andra, couplex-gaz test case 2: 3d modelling of a disposal area for vitrified waste. Andra report, 2006.
- Karypsis, G. and V. Kumar, V, *METIS: A Software Package for Partitioning Unstructured Graphs, Partitioning Meshes, and Computing Fill-Reducing Orderings of Sparse Matrices*, V4.0, Technical Report, Department of Computer Science, University of Minnesota, 1998.
- Mualem, Y., A New Model for Predicting the Hydraulic Conductivity of Unsaturated Porous Media, *Water Resour. Res.*, Vol. 12(3), pp. 513 - 522, NNA.19881228.0005, 1976.
- Pan, L., J. Hinds, C. B. Haukwa, Y. S. Wu, and G. S. Bodvarsson, WinGridder - An interactive grid generator for TOUGH, Version 1.0 User's Manual, LBNL-42957, Lawrence Berkeley Laboratory, Berkeley, California, 2001.
- Pruess, K, C. Oldenburg, and G. Moridis, *TOUGH2 User's Guide*, V2., Lawrence Berkeley National Laboratory Report LBNL-43134, Berkeley, CA, 1999.
- Senger, R., K. Zhang, J. Avis, and P. Marschall, *Three-dimensional Modeling of gas Migration in a Deep Low/Intermediate Level Waste Repository (Switzerland)*, Proceedings of XVII international conference on computational methods in water resources, San Francisco, California (Abs.), 2008.
- Talandier, J., G. Mayer, J. Croisé, *Simulations of the hydrogen migration out of intermediate-level Radioactive Waste Disposal Drifts Using TOUGH2*, Proceedings of TOUGH Symposium 2006, Berkeley, California, 2006.
- Tuminaro, R.S., M. Heroux, S. A. Hutchinson, and J. N. Shadid, *Official Aztec User's Guide*, Ver 2.1, Massively Parallel Computing Research Laboratory, Sandia National Laboratories, Albuquerque, NM, 1999.
- Van Genuchten, M.Th. A Closed-Form Equation for Predicting the Hydraulic Conductivity of Unsaturated Soils, *Soil Sci. Soc.*, Vol. 44, pp. 892 - 898, NNA.19911009.0008, 1980.

- Wu, Y. S., K. Zhang, C. Ding, K. Pruess, and G. S. Bodvarsson, An Efficient Parallel-Computing Method for Modeling Nonisothermal Multiphase Flow and Multicomponent Transport in Porous and Fractured Media, LBNL-47937, *Advances in Water Resources*, Vol. 25, pp.243-261, 2002
- Zhang, K., Y.S. Wu, C. Ding, K. Pruess, and E. Elmroth, *Parallel computing techniques for large-scale reservoir simulation of multi-component and multiphase fluid flow*, Paper SPE 66343, Proceedings of the 2001 SPE Reservoir Simulation Symposium, Houston, Texas, 2001.
- Zhang, K., Y. S. Wu, and G. S. Bodvarsson, Massively Parallel Computing Simulation of Fluid Flow in the Unsaturated Zone of Yucca Mountain, Nevada, LBNL-48883, *Journal of Contaminant Hydrology*, pp.381-399, 2003
- Zhang, K., Y.S. Wu, and K. Pruess, *User's guide for TOUGH2-MP—A massively parallel version of the TOUGH2 code*. Report LBNL-315E, Lawrence Berkeley National Laboratory, Berkeley, CA, USA, 2008.

NUMERICAL METHODS

TOUGHREACT VERSION 2.0

Tianfu Xu, Eric Sonnenthal, Nicolas Spycher, Guoxiang Zhang¹, Liange Zheng, and Karsten Pruess

Earth Sciences Division
Lawrence Berkeley National Laboratory
One Cyclotron Road
Berkeley, CA 94720, USA
e-mail: Tianfu_Xu@lbl.gov

ABSTRACT

TOUGHREACT is a numerical simulation program for chemically reactive nonisothermal flows of multiphase fluids in porous and fractured media, and was developed by introducing reactive chemistry into the multiphase fluid and heat flow simulator TOUGH2 V2. The first version of TOUGHREACT was released to the public through the U.S. Department of Energy's Energy Science and Technology Software Center (ESTSC) in August 2004. It is among the most frequently requested of ESTSC's codes. The code has been widely used for studies in nuclear waste isolation, CO₂ geological sequestration, and geothermal energy development, environmental remediation, and increasingly for petroleum applications. Over the last several years, many new capabilities have been developed. To effectively serve our in-house projects and to share the advances with the user community, we incorporated these new capabilities into Version 2 of TOUGHREACT. Major additions and improvements in Version 2 are discussed here. Two application examples are presented to illustrate the applicability, (1) Denitrification and sulfate reduction, and (2) long-term fate of injected CO₂ for geological sequestration.

INTRODUCTION

TOUGHREACT is a numerical simulation program for chemically reactive nonisothermal flows of multiphase fluids in porous and fractured media (Xu and Pruess, 2001; Spycher et al., 2003; Sonnenthal et al., 2005; Xu et al., 2006; Xu, 2008; Zhang et al., 2008; Zheng et al., 2009). The program was written in Fortran 77 and developed by introducing reactive chemistry into the multiphase fluid and heat flow simulator TOUGH2 (Pruess et al., 1999). The program can be applied to one-, two- or three-dimensional porous and fractured media with physical and chemical heterogeneity. The code can accommodate any number of chemical species present in liquid, gas, and solid phases. A variety of subsurface thermal, physical, chemical, and

biological processes are considered under a wide range of conditions of pressure, temperature, water saturation, ionic strength, and pH and Eh.

Processes for fluid flow and heat transport are the same as the original TOUGH2. Transport of aqueous and gaseous species by advection and molecular diffusion is considered in both liquid (aqueous) and gas phases. Depending on computer memory and CPU performance, any number of chemical species in the liquid, gas, and solid phases can be accommodated. In the 2004 version, aqueous complexation, acid-base, redox, gas dissolution/exsolution, and single-site cation exchange are considered under the local equilibrium assumption. Mineral dissolution and precipitation can proceed either subject to local equilibrium or kinetic conditions.

Over the last several years, many new capabilities have been developed within different research projects at Lawrence Berkeley National Laboratory. To effectively serve our in-house projects and to share the advances with the user community, we incorporated these new capabilities into Version 2 of TOUGHREACT. Major additions and improvements in Version 2 include

- Intra-aqueous reaction kinetics and biodegradation,
- Surface complexation models including double layer,
- Multi-site exchange,
- Improvements on reactive surface area algorithm for mineral-water reactions, and fugacity coefficient corrections for gas-water reactions,
- Improvement on coupling and mass balance between chemistry and physics parts including changes in rock and fluid properties due to reactions, and accounting

¹ Current address: Shell International E&P Inc. Houston, TX 77079, USA

for CO₂ fixed as carbonates in flow simulation (for using ECON module).

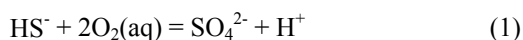
- Improvement on functionalities such as printout mineral reaction rate, and both aqueous component and species concentrations in different unit options,
- Improvement on computational efficiency.

Here, we present the general formulations for solving the chemical system of equations. Then we present kinetic rate expressions for intra-aqueous reactions and biodegradation, rate laws for mineral dissolution and precipitation implemented in our reactive transport simulator. Finally, we give two application examples to illustrate new features in TOUGHREACT Version 2.

MATHEMATICAL FORMULATION

Modeling flow and transport in geologic media are based on space discretization by means of integral finite differences (IFD). The IFD method gives a flexible discretization for geologic media that allows the use of irregular grids, which are well suited for simulation of flow, transport, and fluid-rock interaction in multiregion heterogeneous and fractured rock systems. TOUGHREACT uses a sequential iteration approach. An implicit time-weighting scheme is used for individual components of flow, transport, and kinetic geochemical reaction. The chemical transport is solved on a component-by-component basis. The solution methods for solving flow and transport have been presented in our previous papers. Here we only present the method for solving the system of mixed equilibrium-kinetic reaction equations, which is solved on a gridblock-by-gridblock basis by Newton-Raphson iteration.

The primary equations for the chemical system are based on mass balance in terms of primary (basis) species. In contrast to aqueous equilibrium, species involved in kinetic reactions, such as redox couples, are independent and must be considered as primary species (Steeffel and MacQuarrie, 1996). For example, for the reaction



under kinetic conditions, both HS⁻ and SO₄²⁻ must be placed in the primary species list. Thus, all redox reactions making use of these species must be decoupled in the input of the thermodynamic database.

Details on the formulation for solving the mixed equilibrium-kinetics system of equations are given in Xu (2008). Here we present the final Jacobian equations only. By denoting residuals of mass-

balance of each component *j* as F_j^c (which are zero in the limit of convergence), we have

$$\begin{aligned} F_j^c &= (c_j - c_j^0) && \text{primary species} \\ &+ \sum_{k=1}^{N_x} \nu_{kj} (c_k - c_k^0) && \text{equilibrium aqueous complexes} \\ &+ \sum_{m=1}^{N_p} \nu_{mj} (c_m - c_m^0) && \text{equilibrium minerals} \\ &- \sum_{n=1}^{N_q} \nu_{nj} r_n \Delta t && \text{kinetic minerals} \\ &- \sum_{l=1}^{N_a} \nu_{lj} r_l \Delta t && \text{kinetics among primary species} \\ &= 0 && j = 1 \dots N_c \end{aligned} \quad (1)$$

where superscript 0 represents time zero; Δt is the a time step; *c* are concentrations; subscripts *j*, *k*, *m*, and *n* are the indices of primary species, aqueous complexes, minerals at equilibrium, and minerals under kinetic constraints, respectively; *N_c*, *N_x*, *N_p*, and *N_q* are the number of corresponding species and minerals; ν_{kj} , ν_{mj} , and ν_{nj} are stoichiometric coefficients of the primary species in the aqueous complexes, equilibrium, and kinetic minerals, respectively; r_n is the kinetic rate of mineral dissolution and precipitation (positive for dissolution and negative for precipitation—units used here are moles of mineral per kilogram of water per time), for which a general multi-mechanism rate law was used (see below, Equation 3); *l* is the aqueous kinetic reaction (including biodegradation) index, *N_a* is total number of kinetic reactions among primary species, and r_l is the kinetic rate which is in terms of one mole of product species per unit time. For product species, the stoichiometric coefficients ν_{lj} are positive, for reactant species, they are negative.

According to mass-action equations, concentrations of aqueous complexes c_k can be expressed as functions of concentrations of the primary species c_j . Kinetic rates r_n and r_l are functions of c_j . (The expression for r_l and r_n will be presented in the next section.) No explicit expressions relate equilibrium mineral concentrations c_m to c_j . Therefore, *N_p* additional mass-action equations (one per mineral) are needed. Notice that gas dissolution/exsolution, cation exchange, and surface complexation are included in TOUGHREACT, but for simplicity the formulation is not shown here.

RATE EXPRESSIONS

Intra-aqueous kinetics and biodegradation

A general rate expression for intra-aqueous kinetic reaction and biodegradation has been incorporated into TOUGHREACT. Following the expression of Curtis (2003) and adding multiple mechanisms (or pathways), a general rate law used is:

$$r_i = \sum_{s=1}^M \left[\begin{array}{l} k_{i,s} \quad \text{rate constant} \\ \times \prod_{j=1}^{N_l} \left(\gamma_j^{v_{i,j}} C_j^{v_{i,j}} \right) \quad \text{product terms} \\ \times \prod_{k=1}^{N_m} \frac{C_{i,k}}{K_{M_{i,k}} + C_{i,k}} \quad \text{Monod terms} \\ \times \prod_{p=1}^{N_p} \frac{I_{i,p} + C_{i,p}}{I_{i,p}} \quad \text{inhibition terms} \end{array} \right] \quad (2)$$

where r_i is the reaction rate of the i -th reaction, M is the number of mechanisms or pathways, s is the mechanism counter, k is a rate constant, (often denoted v_{\max} , maximum specific growth constant for biodegradation), γ_j is the activity coefficient of species j , C_j is the concentration of species j (with biodegradation, the product term is usually biomass concentration), $v_{i,j}$ is a stoichiometric coefficient, N_l is the number of reacting species in the forward rate term (called product terms), N_m is the number of Monod factors (Monod terms), $C_{i,k}$ is the concentration of the k -th Monod species, $C_{i,p}$ is the concentration of the p -th inhibiting species, $K_{M_{i,k}}$ is the k -th Monod half-saturation constant of the i -th species, N_p is the number of inhibition factors (inhibition terms), and $I_{i,p}$ is the p -th inhibition constant. Equation (6) accounts for multiple mechanisms and multiple products, Monod, and inhibition terms, which can cover many rate expressions

Mineral dissolution and precipitation

The general rate expression used in TOUGHREACT is taken from Lasaga et al. (1994):

$$r_n = \pm k_n A_n \left| 1 - \left(\frac{Q_n}{K_n} \right)^{\theta} \right|^{\eta} \quad (3)$$

where n denotes kinetic mineral index, positive values of r_n indicate dissolution, and negative values precipitation, k_n is the rate constant (moles per unit mineral surface area and unit time) which is temperature dependent, A_n is the specific reactive surface area per kg H_2O , K_n is the equilibrium constant for the mineral-water reaction written for the

destruction of one mole of mineral n , and Q_n is the reaction quotient. The parameters θ and η must be determined from experiments; usually, but not always, they are taken equal to one.

For many minerals, the kinetic rate constant k can be summed from three mechanisms (Palandri and Kharaka, 2004), or

$$k = k_{25}^{nu} \exp \left[\frac{-E_a^{nu}}{R} \left(\frac{1}{T} - \frac{1}{298.15} \right) \right] + k_{25}^H \exp \left[\frac{-E_a^H}{R} \left(\frac{1}{T} - \frac{1}{298.15} \right) \right] a_H^{n_H} + k_{25}^{OH} \exp \left[\frac{-E_a^{OH}}{R} \left(\frac{1}{T} - \frac{1}{298.15} \right) \right] a_{OH}^{n_{OH}} \quad (3)$$

where superscripts or subscripts nu, H, and OH indicate neutral, acid, and base mechanisms, respectively, E_a is the activation energy, k_{25} is the rate constant at 25°C, R is gas constant, T is absolute temperature, a is the activity of the species; and n is an exponent (constant). The rate constant k can be also dependent on other species such as Al^{3+} and Fe^{3+} . Two or more species may be involved in one mechanism. A general form of species dependent rate constants (extension of Equation 3) is implemented in TOUGHREACT as

$$k = k_{25}^{nu} \exp \left[\frac{-E_a^{nu}}{R} \left(\frac{1}{T} - \frac{1}{298.15} \right) \right] + \sum_i k_{25}^i \exp \left[\frac{-E_a^i}{R} \left(\frac{1}{T} - \frac{1}{298.15} \right) \right] \prod_j a_{ij}^{n_{ij}} \quad (4)$$

where superscripts or subscripts i is the additional mechanism index, and j is species index involved in one mechanism that can be primary or secondary species. TOUGHREACT currently considers up to five additional mechanisms and up to five species involved in each mechanism.

ROCK AND FLUID PROPERTY CHANGES

Changes in porosity and permeability

Temporal changes in porosity and permeability due to mineral dissolution and precipitation can modify fluid flow path characteristics. This feedback between flow and chemistry is considered. Changes in porosity are calculated from changes in mineral volume fractions. Four different porosity-permeability relationships were implemented in TOUGHREACT. One is a commonly used cubic Kozeny-Carman grain model. Laboratory experiments have shown that modest decreases in porosity due to mineral precipitation can cause large

reductions in permeability. This is explained by the convergent-divergent nature of natural pore channels, where pore throats can become clogged by precipitates while disconnected void spaces remain in the pore bodies. A relationship proposed by Verma and Pruess (1988), with a more sensitive coupling of permeability to porosity than the Kozeny-Carman relationship was found to better capture injectivity losses in a geothermal example (Xu et al., 2004):

$$\frac{k}{k_0} = \left(\frac{\phi - \phi_c}{\phi_0 - \phi_c} \right)^n \quad (5)$$

where ϕ_c is the value of “critical” porosity at which permeability goes to zero, and n is a power law exponent. Equation (5) is derived from a pore-body-and-throat model in which permeability can be reduced to zero with a finite (“critical”) porosity remaining.

Permeability and porosity changes will likely result in modifications to the unsaturated flow properties of the rock, which is treated by modification of the capillary pressure function using the Leverett scaling relation.

Changes in aqueous phase density

Mineral dissolution and precipitation changes concentrations of aqueous species. The resulting changes aqueous density and viscosity are considered in TOUGHREACT Version 2 when the ECO2N fluid flow module is used. The total mass fraction (X_s) of all dissolved species (including Na^+ , Cl^- , HCO_3^- , $\text{CO}_2(\text{aq})$, Ca^{2+} , Mg^{2+} , Fe^{2+} , NaHCO_3 , CaHCO_3^+ , MgHCO_3^+ , and FeHCO_3^+) was calculated in the chemistry module as

$$X_s = \frac{\sum_{i=1}^{N_T} w_i c_i}{1000 + \sum_{i=1}^{N_s} w_i c_i} \quad (6)$$

where subscript i is aqueous species index, N_T is the total number of aqueous species, w is molecular weight of an aqueous species (g/mol), c is the species concentration (mol/kg H_2O). Then, the values of X_s are passed to the ECO2N fluid flow module, and density and viscosity of the aqueous phase are calculated using NaCl as proxy, in addition to the consideration of pressure and temperature.

The current implementation of density calculations is an approximation. Future improvement should account for all dissolved species in the solution, considering temperature-dependent parameters and partial molal volumes of aqueous species, which

could be connected to a Pitzer ion-interaction model such as that implemented by Zhang et al. (2008).

APPLICATION EXAMPLES

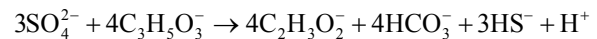
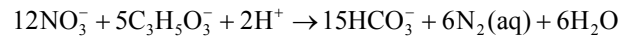
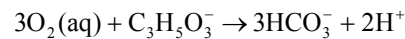
TOUGHREACT V2.0 has been applied to a wide variety of geological and environmental problems. Here, we only give two examples: (1) Denitrification and sulfate reduction, and (2) long-term fate of injected CO_2 for geological sequestration.

Denitrification and sulfate reduction

To test the applicability of TOUGHREACT to reactive transport of denitrification and sulfate reduction, the column experiments of von Gunten and Zobrist (1993) were modeled. Their experiments were designed to simulate infiltration of an organically polluted river into an aquifer. Thus, synthetic river water, including an organic substrate (lactate) and electron acceptors of oxygen, nitrate and sulfate, were injected into columns filled with river sediments.

Biodegradation kinetics

Three major microbially mediated reactions are involved in the experiments. Three electron acceptors are reduced, while dissolved organic matter (DOC) using lactate ($\text{C}_3\text{H}_5\text{O}_3^-$) in the experiment, are oxidized as follows:



The bacterial reaction rates due to three different electron acceptors are given in the following Equations. Denitrification is inhibited by oxygen, and sulfate reduction is inhibited by both oxygen and nitrate.

$$r_b^{\text{O}_2} = k_b^{\text{O}_2} X_b \left(\frac{C_{\text{DOC}}}{K_{\text{DOC}}^{\text{O}_2} + C_{\text{DOC}}} \right) \left(\frac{C_{\text{O}_2}}{K_{\text{O}_2} + C_{\text{O}_2}} \right) \quad (7)$$

$$r_b^{\text{NO}_3} = k_b^{\text{NO}_3} X_b \left(\frac{C_{\text{DOC}}}{K_{\text{DOC}}^{\text{NO}_3} + C_{\text{DOC}}} \right) \left(\frac{C_{\text{NO}_3}}{K_{\text{NO}_3} + C_{\text{NO}_3}} \right) \left(\frac{I_{\text{O}_2 \rightarrow \text{NO}_3}}{I_{\text{O}_2 \rightarrow \text{NO}_3} + C_{\text{O}_2}} \right) \quad (8)$$

$$r_b^{SO_4} = k_b^{SO_4} X_b \left(\frac{C_{DOC}}{K_{DOC}^{SO_4} + C_{DOC}} \right) \left(\frac{C_{SO_4}}{K_{SO_4} + C_{SO_4}} \right) \left(\frac{I_{O_2 \rightarrow SO_4}}{I_{O_2 \rightarrow SO_4} + C_{O_2}} \right) \left(\frac{I_{NO_3 \rightarrow SO_4}}{I_{NO_3 \rightarrow SO_4} + C_{NO_3}} \right) \quad (9)$$

The overall biotic reaction rate is expressed as

$$r_b = r_b^{O_2} + r_b^{NO_3} + r_b^{SO_4} - bX_b \quad (10)$$

where X_b is biomass concentration (mg/l), b is decay constant. In this example, biomass is assumed not subject to transport and growth. Most of the bacteria are fixed on the solid phase within geologic media. The rate parameters for Equations (7) through (9) are given in Table 6 of Xu (2008).

A general multiregion model for hydrological transport interacting with microbiological and geochemical processes was used (Figure 1). The applicability of this enhanced multiregion model for reactive transport of denitrification and sulfate reduction was evaluated by comparison with column experiments (Figures 2 and 3). The matches with measured nitrate and sulfate concentrations were achieved by adjusting the interfacial area between mobile and immobile regions. The values of 38 m^2 per m^3 bulk medium for the initial period and 75 m^2 for the late period were calibrated. The match and parameter calibration suggest that TOUGHREACT is not only a useful interpretative tool for biogeochemical experiments, but also can produce insight into the processes and parameters of microscopic diffusion and their interplay with biogeochemical reactions. Details on the problem setup and results can be found in Xu (2008).

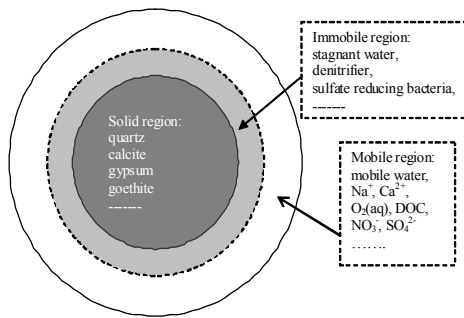


Figure 1. Schematic representation of a multiregion model for resolving local diffusive transport

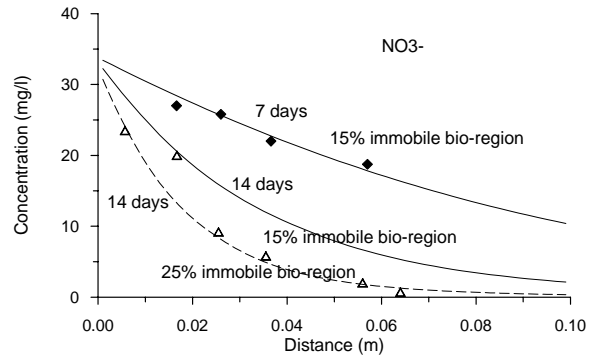


Figure 2. Nitrate concentrations obtained with the multiregion model after 7 and 14 days, together with measured data

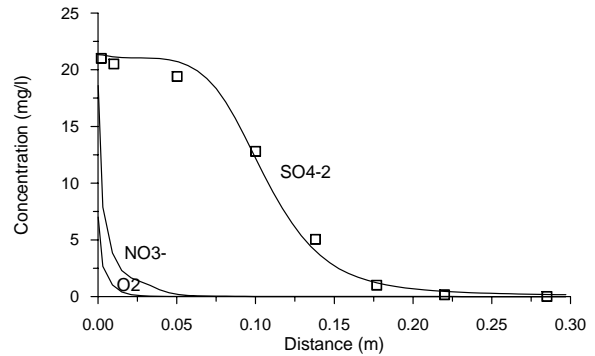


Figure 3. The simulated concentration profiles (lines) of sulfate, nitrate, and oxygen at steady-state (35 days), together with measured data of sulfate along the column

Long-term fate of injected CO₂

CO₂ injected into a deep saline sandstone formation (storage reservoir) will tend to migrate upwards towards the cap rock, because the density of the supercritical CO₂ phase is lower than that of water (aqueous phase). In the upper portions of the reservoir, CO₂ dissolution into brine decreases pH and induces mineral dissolution and complexing with dissolved ions such as Na⁺, Ca²⁺, Mg²⁺, and Fe²⁺ to form NaHCO₃, CaHCO₃⁺, MgHCO₃⁺, and FeHCO₃⁺. Over time, these dissolution and complexing processes will increase CO₂ solubility, enhance solubility trapping, and will increase the density of the aqueous phase. Aqueous phase will then move downward due to gravity, giving rise to “convective mixing.” These processes, together with changes in rock properties induced by CO₂ injection into a U.S. Gulf Coast sandstone formation, have been studied using a generic 2D radial well flow model. Hydrological and geochemical conditions and parameters are taken from Xu et al. (2007).

Numerical simulation results indicate that considering mineral alteration (reaction) is significant for increasing aqueous density, enhancing solubility trapping (Figures 4 and 5) and obtaining mineral trapping (Figure 6), which are important for long-term CO₂ geological sequestration. The mineral trapping starts at late stage (about 100 years) and then increases linearly with time. The reaction-driven convection mixing by aqueous density increase occurs slowly, on the order of several hundred years. Amounts of CO₂ trapped in different phases and variations of different storage modes with time are estimated. After 1,000 years, 9% of the injected CO₂ could be trapped in the solid (mineral) phase, 28% in the aqueous phase, and 63% in the gas phase.

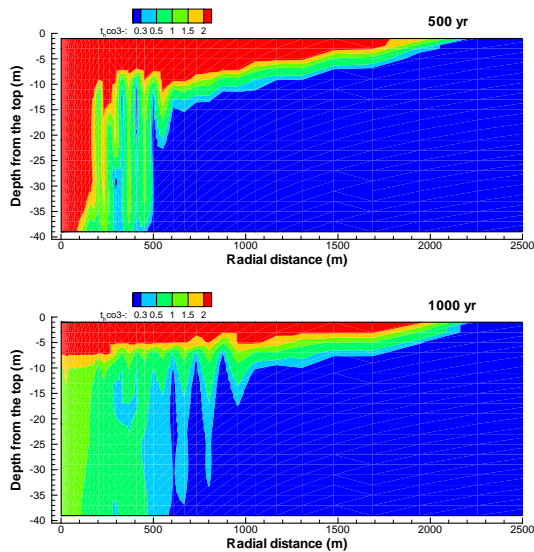


Figure 4. Distribution of total dissolved CO₂ (mol/kg H₂O) at different times for the 2-D radial model.

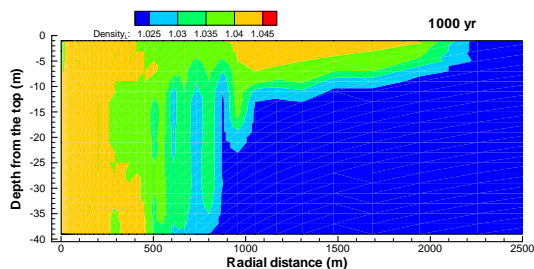


Figure 5. Distribution of aqueous phase (water) density (kg/L) after 1,000 years

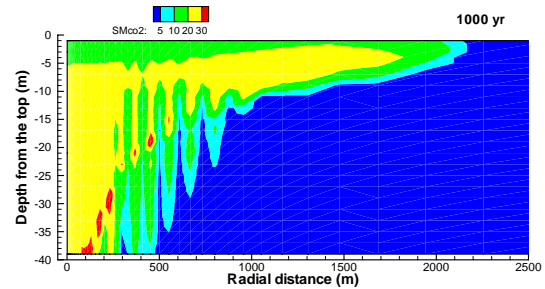


Figure 6. Cumulative sequestration of CO₂ by precipitation of carbonate minerals after 1,000 years (units of kg/m³ medium)

Mineral alteration and CO₂ trapping capability depends on the primary mineral composition. Precipitation of siderite and ankerite requires Fe²⁺, which can be supplied by the dissolution of iron-bearing minerals, such as chlorite, or by reduction of Fe³⁺ in small amounts of hematite. Variation in Ca content in Plagioclase significantly affects carbonate mineral precipitation, and thus CO₂ mineral trapping. The time required for mineral alteration and CO₂ sequestration depends on the rates of mineral dissolution and precipitation, which are products of the kinetic rate constant and reactive surface area. The current simulated mineral alteration pattern is generally consistent with available mineralogy observed at natural high-pressure CO₂ gas reservoirs. Details are discussed in Xu et al. (2007).

The present reactive transport modeling studies did not consider medium heterogeneities and geometric complexities. The “numerical experiments” presented here give a detailed view of the dynamical interplay between coupled hydrologic and chemical processes, albeit in an approximate fashion. A critical evaluation of modeling results can provide useful insight into changes in water chemistry and the long-term CO₂ storage and performance.

ACKNOWLEDGMENT

The development of TOUGHREACT was supported by various DOE program offices, and documentation of Version 2 was supported by the Zero Emission Research and Technology project (ZERT), of the U.S. Department of Energy under Contract No. DE-AC02-05CH11231 with Lawrence Berkeley National Laboratory.

REFERENCES

Curtis, G.P., Comparison of approaches for simulating reactive solute transport involving organic degradation reactions by multiple terminal electron acceptors, *Computer & Geoscience*, 29, 319-329, 2003.

- Lasaga, A.C., Soler, J.M., Ganor, J., Burch, T.E., Nagy, K.L., Chemical weathering rate laws and global geochemical cycles, *Geochimica et Cosmochimica Acta*, 58, 2361-2386, 1994.
- Palandri, J., Kharaka, Y.K., A compilation of rate parameters of water-mineral interaction kinetics for application to geochemical modeling, US Geol. Surv. Open File Report 2004-1068, 64 pp, 2004.
- Pruess, K., Oldenburg, C., Moridis, G., TOUGH2 user's guide, Version 2.0. Lawrence Berkeley Laboratory Report LBL-43134, Berkeley, California, 192 pp, 1999.
- Sonnenthal E., Ito, A., Spycher, N., Yui, M., Apps, J., Sugita, Y., Conrad, M., Kawakami, S., Approaches to modeling coupled thermal, hydrological, and chemical processes in the Drift Scale Heater Test at Yucca Mountain. *International Journal of Rock Mechanics and Mining Sciences*, 42, 6987-719, 2005.
- Spycher, N.F., Sonnenthal, E.L., Apps, J.A., Fluid flow and reactive transport around potential nuclear waste emplacement tunnels at Yucca Mountain, Nevada, *Journal of Contaminant Hydrology*, 62-63, 653-673, 2003.
- Steefel, C. I., and K. T. B. MacQuarrie, Approaches to modeling of reactive transport in porous media, In Lichtner, P. C., Steefel, C. I., and Oelkers, E. H. (eds.), *Reactive transport in porous media: Reviews in Mineralogy*, Mineral Society of America, 34, 83-129, 1996.
- Verma, A., Pruess, K., Thermohydrological conditions and silica redistribution near high-level nuclear wastes emplaced in saturated geological formations. *Journal of Geophysical Research*, 93, 1159-1173, 1988.
- von Gunten, U. and Zobrist, J., Biogeochemical changes in groundwater infiltration systems: column studies. *Geochim. Cosmochim. Acta*, 57: 3895-3906, 1993.
- Xu, T., Pruess, K., Modeling multiphase non-isothermal fluid flow and reactive geochemical transport in variably saturated fractured rocks: 1. Methodology. *American Journal of Science*, 301, 16-33, 2001.
- Xu, T., Ontoy, Y., Molling, P., Spycher, N., Parini, M., Pruess, K., Reactive transport modeling of injection well scaling and acidizing at Tiwi Field, Philippines. *Geothermics*, 33(4), 477-491, 2004.
- Xu, T., J. A. Apps, K. Pruess, and H. Yamamoto, Numerical modeling of injection and mineral trapping of CO₂ with H₂S and SO₂ in a sandstone formation, *Chemical Geology*, 242/3-4, 319-346, 2007.
- Xu, T., Incorporation of aqueous reaction kinetics and biodegradation into TOUGHREACT: Application of a multi-region model to hydrobiogeochemical transport of denitrification and sulfate reduction. *Vadose Zone Journal*, 2008-7, 305-315, 2008.
- Zhang, G., N. Spycher, E. Sonnenthal, C. Steefel, and T. Xu, Modeling reactive multiphase flow and transport of concentrated aqueous solutions, *Nuclear Technology*, 164, 180-195, 2008.
- Zheng, L., Apps, J.A., Zhang, Y., Xu, T., Birkholzer, J., On mobilization of lead and arsenic in groundwater in response to CO₂ leakage from deep geological storage. Submitted to *Chemical Geology*, 2009.

SIMULATION OF NON-DARCY POROUS MEDIA FLOW ACCORDING TO THE BARREE AND CONWAY MODEL

Yu-Shu Wu, Bitao Lai, and Jennifer L. Miskimins

Colorado School of Mines
Golden CO 80401 USA
e-mail: ywu@mines.edu

ABSTRACT

Non-Darcy porous media flow has been traditionally handled using the *Forchheimer* equation. However, recent experimental studies have shown that the *Forchheimer* model is unable to fit laboratory results at high flow rates. On the other hand, the non-Darcy flow model proposed by Barree and Conway (2004, 2007) is capable of describing the entire range of relationships between flow rate and potential gradient from low- to high-flow rates through proppant packs. In this paper, we present a numerical model by incorporating the Barree and Conway model into a general-purpose reservoir simulator for modeling single-phase and multiphase non-Darcy flow in porous and fractured media. The numerical formulation is based on the TOUGH2 methodology, i.e., spatial integral-finite-difference discretization, leading to an unstructured grid, followed by time discretization carried out with a backward, first-order, finite-difference method. The final discrete nonlinear equations are handled fully implicitly by Newton iteration. In the numerical approach, flow through fractured rock is handled using a general multicontinuum approach, applicable to both continuum and discrete fracture conceptual models. To validate the model, we use analytical solutions to verify our numerical model results for both single-phase and multiphase non-Darcy flow.

INTRODUCTION

Darcy's law, describing a linear relationship between volumetric flow rate (or Darcy velocity) and pressure (or potential) gradient, has been the fundamental principle in analyzing flow processes in reservoirs. Darcy's law has been used exclusively in reservoir studies; however, there is considerable evidence that high-velocity non-Darcy flow occurs in oil and gas reservoirs, such as for flow in the formation near oil or gas production, groundwater pumping, and liquid-waste-injection wells. Effects of non-Darcy or high-velocity flow regimes in reservoirs have been observed and investigated for decades (e.g., Tek et al., 1962; Scheidegger, 1972; Katz and Lee, 1990; Wu, 2002). Studies performed on non-Darcy flow in porous media at early times have focused mostly on single-phase flow conditions in petroleum reservoir engineering (Tek et al., 1962; Swift and Kiel, 1962; Lee et al., 1987). Some investigations have been

conducted for non-Darcy flow in fractured reservoirs (Skjetne et al., 1999) and for non-Darcy flow into highly permeable fractured wells (e.g., Guppy et al., 1981, 1982). Other studies have concentrated on finding and validating correlations of non-Darcy flow coefficients (e.g., Liu et al., 1995), and modeling efforts (e.g., Wu, 2002).

The Forchheimer equation (1901) has been exclusively used for analysis of non-Darcy flow through porous media, and it has been extended to multiphase flow conditions (Evans et al., 1987; Evans and Evans, 1988; Liu et al., 1995; Wu, 2001 and 2002). In recent developments, laboratory studies and analyses have shown that the Barree and Conway model is able to describe the entire range of relationships between flow rate and potential gradient from low- to high-flow rates through porous media, including those in transitional zones (Barree and Conway, 2004 and 2007; Lopez, 2007).

This paper summarizes our continuing study of single-phase and multiphase non-Darcy flow in reservoirs according to the Barree and Conway model (Lai et al., 2009; Wu et al., 2009). The objective of this study is to present a mathematical method for quantitative analysis of single-phase multiphase non-Darcy flow through heterogeneous porous and fractured rock, based on the Barree and Conway's model. In this paper, we construct a mathematical and numerical model by incorporating the Barree and Conway model into a general-purpose reservoir simulator for modeling single-phase and multiphase non-Darcy flow in porous and fractured media. The numerical formulation is based on the TOUGH2 methodology, i.e., spatial integral-finite-difference discretization, leading to an unstructured grid, followed by time discretization carried out with a backward, first-order, finite-difference method. The final discrete nonlinear equations are handled fully implicitly by Newton iteration. In the numerical approach, flow through fractured rock is handled using a general multicontinuum approach, applicable to both continuum and discrete fracture conceptual models. As a demonstration of model validation and application efforts, we use analytical solutions to verify our numerical model results for both single-phase and multiphase non-Darcy flow.

BARREE-CONWAY MODEL AND LABORATORY RESULTS

Barree and Conway (2004) proposed a new model for nonlinear flow in porous media, one that does not rely on the assumptions of constant permeability or a constant β (non-Darcy flow coefficient in the Forchheimer model). In their model, Darcy's law is still assumed to apply, but the apparent permeability, as a general nonlinear function of flow rate, is introduced to replace the constant, intrinsic permeability of Darcy's law for one-dimensional linear flow as:

$$v = -\frac{k_{app}}{\mu} \frac{\partial P}{\partial L} \quad (1)$$

where v is superficial or Darcy velocity. The apparent permeability, k_{app} , is defined as:

$$k_{app} = k_{min} + \frac{(k_d - k_{min})}{(1 + R_e^F)^E} \quad (2)$$

and the Reynolds number is defined as,

$$R_e = \frac{\rho v}{\mu \tau} \quad (3)$$

The Barree and Conway model, (1) and (2), is a physically based correlation. It provides a single equation to describe the entire range of flow velocities versus pressure or potential gradient, from low-flow-rate Darcy to high-flow-rate non-Darcy flow regimes. At low flow rates, the Barree and Conway model collapses into Darcy's law with a constant permeability, k_d ; it converges to the Forchheimer analysis for the intermediate flow rate. The Barree and Conway model provides a plateau area at high rates, which indicates a constant permeability (or minimum permeability), consistent with laboratory and finite element modeling results. In particular, considerable experimental validation efforts have been completed using proppant packs and nitrogen gas non-Darcy flow apparatuses (Lopez, 2007; Lai et al., 2009). Their experimental data are analyzed using a regression method for both Forchheimer and Barree and Conway models; some example results are shown in Figure 1 (Lai et al., 2009). As shown in Figure 1, the experimental data agree extremely well with the Barree and Conway model across the entire flow velocity range, from low to high gas flow rates. The Forchheimer quadratic correlation overestimates the associated pressure drop, while the Forchheimer cubic correlation underestimates the pressure drop at high gas flow rates. All sample data taken to date show similar agreement with the Barree and Conway equation across the observed wide flow spectrum (Lai et al., 2009).

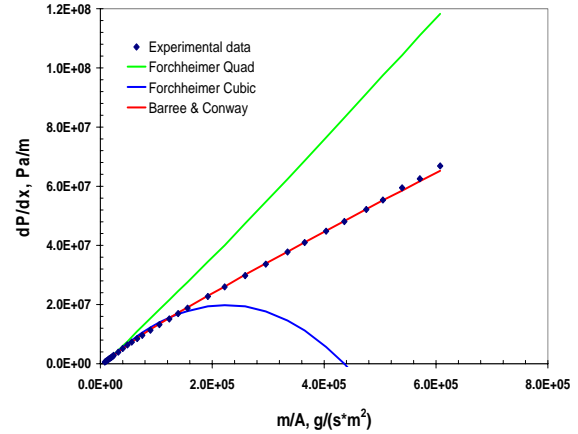


Figure 1. Results of pressure gradient versus mass flow rate for a ceramic 20/40 proppant under a confining stress of 27.5 MPa (The experimental data (blue diamonds) agree with the Barree and Conway model (red) from low to high flow rates. The Forchheimer quadratic correlation (green) overestimates the pressure drop, while the Forchheimer cubic correlation (blue) underestimates the pressure drop at high gas flow rates).

Using the Reynolds number, Equation (3), and the following dimensionless variable,

$$\eta = \frac{k_{app}}{k_d} = \frac{k_{min}}{k_d} + \frac{1 - \frac{k_{min}}{k_d}}{(1 + N_{Re})^E} \quad (4)$$

Figure 2 summarized all the test data taken to date using the dimensionless form of the Barree and Conway model (Lopez, 2007; Lai et al., 2009). Figure 2 demonstrates that all of the experimental data collapse into one single curve, which can be fitted using the Barree and Conway model in a dimensionless form. One plateau of the log-dose equation format is clearly observed at low Reynolds numbers, representing Darcy's flow range. When converted to field units, the test data shown in Figure 2 cover field gas production rates from less than 707.2 m³/D to more than 283,168 m³/D, demonstrating that the Barree and Conway model is accurate across the intervals of interest for the industry.

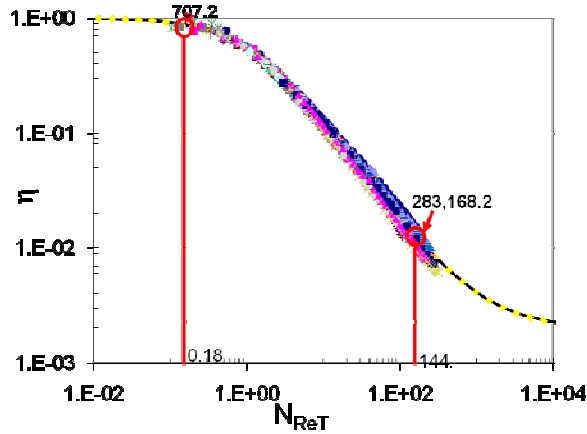


Figure 2. Dimensionless plot of all tested proppants using the Barree and Conway model.

Barree and Conway (Barree and Conway, 2007) have recently extended their model to multiphase non-Darcy flow. With this extension, single-phase and multiphase volumetric flow rate (namely Darcy velocity with Darcy flow) for non-Darcy flow of phase β may be described in a vector form for multidimensional flow (Wu et al., 2009),

$$-\nabla\Phi_{\beta} = \frac{\mu_{\beta}\mathbf{v}_{\beta}}{k_d k_{r\beta} \left(k_{mr} + \frac{(1-k_{mr})\mu_{\beta}\tau}{\mu_{\beta}\tau + \rho_{\beta}|\mathbf{v}_{\beta}|} \right)} \quad (5)$$

where $\nabla\Phi_{\beta}$ is the flow potential gradient,

$$\nabla\Phi_{\beta} = (\nabla P_{\beta} - \rho_{\beta}g\nabla D) \quad (6)$$

and ρ_{β} is the density of fluid β ; \mathbf{v}_{β} is the volumetric velocity vector of fluid β , P_{β} is the pressure of the fluid, g is gravitational acceleration, and D is the depth from a datum. In Equation (5), k_{mr} is the minimum permeability ratio (k_{min}/k_d) at high rate, relative to Darcy's permeability (fraction); $k_{r\beta}$ is the relative permeability to fluid β ; and μ_{β} is the viscosity of fluid β . Equation (5) is used as the Barree and Conway model in this work to replace Darcy's law in modeling single-phase and multiphase flow in reservoirs.

MATHEMATICAL MODEL

A multiphase system in a porous or fractured reservoir is assumed to be similar to the black oil model, composed of three phases: oil, gas, and water. For simplicity, three fluid components (water, oil, and gas) are assumed to be present only in their associated phases; and single-phase flow is treated as a special case of multiphase flow in this work. Each phase flows in response to pressure, gravitational, and capillary forces according to the multiphase extension of the Barree and Conway model of (5) for non-Darcy flow. In an isothermal system containing

three mass components, three mass-balance equations are needed to fully describe the system, as described in an arbitrary flow region of a porous or fractured domain for flow of phase β ($\beta = w$ for water, $\beta = o$ for oil, and $\beta = g$ for gas),

$$\frac{\partial}{\partial t}(\phi S_{\beta}\rho_{\beta}) = -\nabla \cdot (\rho_{\beta}\mathbf{v}_{\beta}) + q_{\beta} \quad (7)$$

where S_{β} is the saturation of fluid β ; ϕ is the effective porosity of formation; t is time; and q_{β} is the sink/source term of phase (component) β per unit volume of formation, representing mass exchange through injection/production wells or due to fracture and matrix interactions.

Equation (7), the governing of mass balance for three phases, needs to be supplemented with constitutive equations that express all the secondary variables and parameters as functions of a set of primary thermodynamic variables of interest. The following relationships will be used to complete the description of multiphase flow through porous media:

$$S_w + S_o + S_g = 1 \quad (8)$$

The capillary pressures relate pressures between the phases. The aqueous- and gas-phase pressures are related by

$$P_w = P_g - P_{cgw}(S_w) \quad (9)$$

where P_{cgw} is the gas-water capillary pressure in a three-phase system and assumed to be a function of water saturation only. The oil pressure is related to the gas phase pressure by

$$P_o = P_g - P_{cgo}(S_w, S_o) \quad (10)$$

where P_{cgo} is the gas-oil capillary pressure in a three-phase system, which is a function of both water and oil saturations. For formations, the wettability order is (1) aqueous phase, (2) oil phase, and (3) gas phase. The gas-water capillary pressure is usually stronger than the gas-oil capillary pressure. In a three-phase system, the oil-water capillary pressure, P_{cow} , may be defined as

$$P_{cow} = P_{cgw} - P_{cgo} = P_o - P_w \quad (11)$$

The relative permeabilities are assumed to be functions of fluid saturations only (i.e., not affected by non-Darcy flow behavior). The relative permeability of the water phase is described by

$$k_{rw} = k_{rw}(S_w) \quad (12)$$

of the oil phase by

$$k_{ro} = k_{ro}(S_w, S_g) \quad (13)$$

and the gas phase by

$$k_{rg} = k_{rg}(S_g) \quad (14)$$

The densities of water, oil, and gas, as well as their viscosities, can in general be treated as functions of pressure.

NUMERICAL MODEL

Equations (7) and (5), as described by the Barree and Conway's model, for single-phase and multiphase non-Darcy flow of gas, oil and water in porous media, are highly nonlinear and in general need to be solved numerically. In this work, the methodology for using a numerical approach of TOUGH2 (Pruess et al., 1999) to simulate the non-Darcy flow consists of the following three steps: (1) spatial discretization of the mass conservation equation; (2) time discretization; and (3) iterative approaches to solve the resulting nonlinear, discrete algebraic equations. A mass-conserving discretization scheme, based on finite or integral finite-difference or finite-element methods (Pruess et al., 1999) is used and discussed here. Specifically, non-Darcy flow equations, as discussed in the Mathematical Model section above, have been implemented into a general-purpose, three-phase reservoir simulator, the MSFLOW code (Wu, 1998). As implemented in the code, Equation (7) can be discretized in space using an integral finite-difference or controlled-volume finite-element scheme for a porous and/or fractured medium. The time discretization is carried out with a backward, first-order, finite-difference scheme. The discrete nonlinear equations for water, oil, and gas flow at node i are written as follows:

$$\left\{ (\phi S_\beta \rho_\beta)_i^{n+1} - (\phi S_\beta \rho_\beta)_i^n \right\} \frac{V_i}{\Delta t} = \sum_{j \in \eta_i} (flow_\beta)_{ij}^{n+1} + Q_{\beta i}^{n+1} \quad (15)$$

where n denotes the previous time level; $n+1$ is the current time level; V_i is the volume of element i ($i=1, 2, 3, \dots, N$, N being the total number of elements of the grid); Δt is the time step size; η_i contains the set of neighboring elements (j), porous or fractured block, to which element i is directly connected; and “ $flow_\beta$ ” is a mass flow term between elements i and j for fluid β , defined by Equation (16) implicitly. For flow between two gridblocks, the mass flow term “ $flow_\beta$ ” can be evaluated directly (Lai et al., 2009; Wu et al., 2009) as,

$$flow_{\beta,ij} = A_{ij} \rho_\beta v_\beta = \frac{A_{ij}}{2\mu_\beta} \left\{ \frac{-[\mu_\beta^2 S_\beta \tau - \Delta\Phi_{\beta,ij} k_d k_{r\beta} k_{rm} \rho_\beta] + \sqrt{[\mu_\beta^2 S_\beta \tau - \Delta\Phi_{\beta,ij} k_d k_{r\beta} k_{rm} \rho_\beta]^2 + 4\mu_\beta \rho_\beta \Delta\Phi_{\beta,ij} k_d k_{r\beta} \mu_\beta S_\beta \tau}}{2} \right\} \quad (16)$$

where A_{ij} is the common interface area between connected elements i and j . All the parameters, such as permeability, relative permeability, density, and viscosity, need a proper averaging or weighting of properties at the interface between the two elements i

and j ; A_{ij} is the common interface area between the connected blocks or nodes i and j ; and the discrete flow potential gradient is defined in an integral finite difference as,

$$\Delta\Phi_{\beta,ij} = \frac{(P_{\beta,i} - \rho_{\beta,ij+1/2} g D_i) - (P_{\beta,j} - \rho_{\beta,ij+1/2} g D_j)}{D_i + D_j} \quad (17)$$

In (16), the mass sink/source term at element i , $Q_{\beta i}$ for phase β , is defined as

$$Q_{\beta i} = q_{\beta i} V_i \quad (18)$$

In the model formulation, Darcy permeability, relative permeability, and other non-Darcy flow parameters, such as minimum permeability ratio, k_{mr} , and characteristic length, τ , are all considered as flow properties of the porous media and need to be averaged between connected elements in calculating the mass flow terms. In general, the weighting approaches used are (1) that absolute permeability is harmonically weighted along the connection between elements i and j , (2) relative permeability is upstream weighted, and (3) non-Darcy flow coefficients are arithmetically averaged.

Newton/Raphson iterations are used to solve Equation (15). For a three-phase flow system, $3 \times N$ coupled nonlinear equations must be solved, including three equations at each element for the three mass-balance equations of water, oil, and gas, respectively. The three primary variables (x_1, x_2, x_3) selected for each element are oil pressure, oil saturation, and gas saturation, respectively. In terms of the three primary variables, the Newton/Raphson scheme gives rise to

$$\sum_m \frac{\partial R_i^{\beta, n+1}(x_{m,p})}{\partial x_m} (\delta x_{m,p+1}) = -R_i^{\beta, n+1}(x_{m,p}) \quad (19)$$

for $m = 1, 2, \text{ and } 3$

where index $m = 1, 2, \text{ and } 3$ indicates the primary variable 1, 2, or 3, respectively; p is the iteration level; and $i = 1, 2, 3, \dots, N$, the nodal index. The primary variables are updated after each iteration,

$$x_{m,p+1} = x_{m,p} + \delta x_{m,p+1} \quad (20)$$

A numerical method is used to construct the Jacobian matrix for Equation (19), as outlined by Forsyth et al. (1995).

Boundary Condition: Similarly to Darcy flow handling, first-type or Dirichlet boundary conditions denote constant or time-dependent phase pressure, and saturation conditions. These types of boundary conditions can be treated using the large-volume or inactive-node method (Pruess et al., 1999), in which a constant pressure/saturation node may be specified with a huge volume while keeping all the other

geometric properties of the mesh unchanged. However, caution should be taken in (1) identifying phase conditions when specifying the “initial condition” for the large-volume boundary node and (2) distinguishing upstream/injection from downstream/production nodes. Once specified, primary variables will be fixed at the big-volume boundary nodes, and the code handles these boundary nodes exactly like any other computational nodes.

Flux-type or Neuman boundary conditions are treated as sink/source terms, depending on the pumping (production) or injection condition, which can be directly added to Equation (15). This treatment of flux-type boundary conditions is especially useful for a situation where flux distribution along the boundary is known, such as dealing with a single-node well. More general treatment of multilayered well-boundary conditions is discussed in Wu et al. (1996) and Wu (2000).

HANDLING NON-DARCY FLOW IN FRACTURED MEDIA

The technique used in the current model for handling non-Darcy flow through fractured rock follows the dual-continuum methodology (Warren and Root, 1963; Kazemi, 1969; Pruess and Narasimhan, 1985; Wu, 2002). The method treats fracture and matrix flow and interactions using a multicontinuum numerical approach, including the double- or multiporosity method (Wu and Pruess, 1988), the dual-permeability method, and the more general “multiple interacting continua” (MINC) method (Pruess and Narasimhan, 1985). As shown in Wu and Qin (2009), the generalized dual-continuum, MINC method, can handle any flow processes of fractured media, with matrix size varying from as large as the model domain of interest to as small as a representative elementary volume (REV) of zero volume. In general, the fracture network can be continuous in a pattern, randomly distributed, or discrete.

The non-Darcy flow formulation, Equations (5) and (7), and (15) and (16), as discussed above, is applicable to both single-continuum and multicontinuum media within fracture or matrix. Using the dual-continuum concept, Equations (7) and (15) can be used to describe multiphase flow, respectively, both in fractures and inside matrix blocks when dealing with fractured reservoirs. Special attention needs to be paid to treating fracture/matrix flow terms with Equations (15) and (16) for estimation of mass exchange at fracture/matrix interfaces using a double-porosity approach. In particular, special attention should be paid to selecting characteristic lengths of non-Darcy flow distance between fractures and matrix crossing the interface, for the double-porosity or the nested discretizations may be approximated using the results for Darcy flow

(Warren and Root, 1965; Pruess, 1983; Wu, 2002). However, the flow between fractures and matrix can still be evaluated using Equation (16) and the characteristic distance for flow crossing fracture/matrix interfaces for 1-D, 2-D, and 3-D dimensions of rectangular matrix blocks, with characteristic distances, based on a quasi-steady flow assumption (Wu, 2002).

When using the Barree and Conway model for handling non-Darcy flow through a fractured rock with the numerical formulation using the generalized TOUGH2 multicontinuum approach, the problem essentially becomes how to generate a mesh that represents both the fracture and matrix systems. Several fracture-matrix subgridding schemes exist for designing different meshes for different fracture-matrix conceptual models (Pruess, 1983). Once a proper mesh of a fracture-matrix system is generated, fracture and matrix blocks are specified to represent fracture or matrix domains, separately. Formally, they are treated in exactly the same way in the solution of the discretized model. However, physically consistent fracture and matrix properties and modeling conditions must be appropriately specified for fracture and matrix systems, respectively.

MODEL VERIFICATION AND APPLICATION

In this section, we use analytical solutions to verify the numerical scheme implemented for modeling single-phase and multiphase non-Darcy flow in reservoirs, and demonstrate application of the numerical model.

Comparison with An Analytical Solution for 1-D, Single-Phase Steady-State Flow: Lai et al. (2009) presented an analytical solution for steady-state incompressible fluid flow:

$$P(x) = P_i - \frac{\dot{m}}{A} \left(\frac{\dot{m}}{A} + \mu\tau \right) (L-x) \quad (21)$$

$$\left(\mu k_d \tau + \frac{\dot{m}}{A} k_d k_{mr} \right) \rho$$

where \dot{m} is fluid mass-flow rate at inlet; and P_i is pressure at outlet. The analytical solution (21) is used to check the numerical results of modeling 1-D, single-phase flow. In numerical discretization, a 1-D linear reservoir formation 10 m long, with a unit cross-sectional area, is represented by a 1-D uniform linear grid of 1,000 elements with $\Delta x = 0.01$ m. The parameters used for this comparison are listed in Table 1. We compare two cases with different minimum permeability and characteristic length values, where Case 1 is $k_{min} = 0.1$ Darcy and $\tau = 100,000$ (1/m); and Case 2 is $k_{min} = 1.0$ Darcy and $\tau = 10,000$ (1/m). In the two scenarios, the pressure at the outlet boundary is maintained at 10^7 Pa, and a constant mass production rate is proposed at $x = 0$ for

both the analytical and numerical solutions. The numerical calculation is carried out until steady state is reached. Figure 3 shows the comparison results from the two solutions and indicates that excellent results are obtained from the numerical simulation, as compared to the analytical solution. Figure 3 also shows that the pressure distributions for the two scenarios are nearly linear along the linear flow direction, because under incompressible, constant mass or volumetric flow conditions, the effective permeability is essentially constant along the flow system.

Table 1. Parameters Used for Model Verification of Checking of Numerical Simulation Results against the Analytical Solution, as Shown in Figure 3.

Parameter	Value	Unit
Cross section area	$A = 1$	m^2
Darcy permeability	$k_d = 10$	Darcy
Minimum permeability	$k_{min} = 0.1, 1.0$	Darcy
Viscosity	$\mu = 0.001$	$Pa \cdot s$
Characteristic length	$\tau = 100,000, 10,000$	$1/m$
Density	$\rho = 1,000$	kg/m^3
Mass production rate	$\dot{m} = 5$	kg/s
Pressure at outer boundary	$P_i = 10^7$	Pa

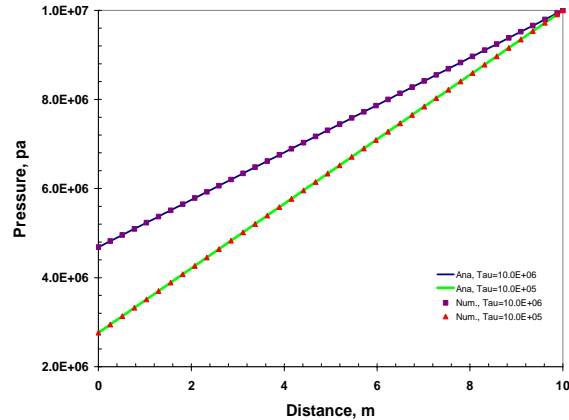


Figure 3. Comparison between the analytical and numerical solutions for 1-D steady-state flow in a linear system (The analytical solution for Case 1 is shown as a solid blue line, while the numerical solution for Case 1 is shown as purple squares. The analytical solution for Case 2 is shown as a solid green line, while the numerical solution for Case 2 is shown as red triangles).

Comparison with the Buckley-Leverett Type Analytical Solution: Wu et al. (2009) presents a Buckley-Leverett type analytical solution for non-Darcy displacement according to the Barree and Conway model, and we use the analytical solution to examine the numerical model formulation as well as the correctness of its numerical implementation. The

physical flow model is a one-dimensional linear porous medium, which is at first saturated uniformly with a nonwetting fluid ($S_o = 0.8$) and a wetting fluid ($S_w = S_{wr} = 0.2$). A constant volumetric injection rate for the wetting fluid is imposed at the inlet ($x = 0$), starting from $t = 0$. The relative permeability curves used for all the calculations in this paper are shown in Figure 4. Properties of the rock and fluids used are listed in Table 2.

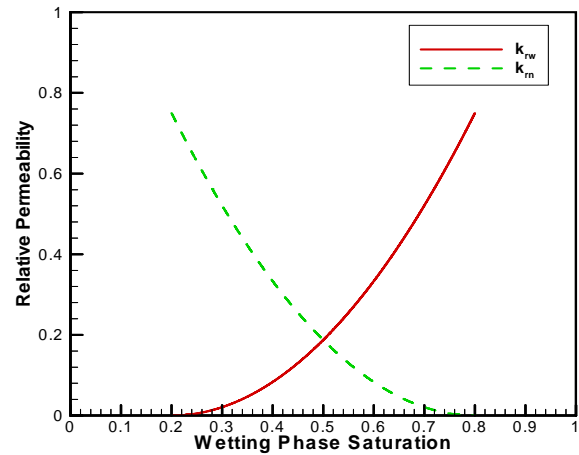


Figure 4. Relative-permeability curves used in analytical and numerical solutions for Barree and Conway non-Darcy displacement.

Table 2 Parameters for the non-Darcy Displacement Example.

Parameter	Value	Unit
Effective Porosity	$\phi = 0.30$	
Darcy permeability	$k_d = 10$	Darcy
Minimum permeability	$k_{min} = 0.1, 1.0$	Darcy
Characteristic length	$\tau = 10,000$	$1/m$
Wetting Phase Density	$\rho_w = 1,000$	kg/m^3
Wetting Phase Viscosity	$\mu_w = 1.0 \times 10^{-3}$	$Pa \cdot s$
Nonwetting Phase Density	$\rho_n = 800$	kg/m^3
Nonwetting Phase Viscosity	$\mu_n = 5.0 \times 10^{-3}$	$Pa \cdot s$
non-Darcy Flow Constant	$C_\beta = 3.2 \times 10^{-6}$	$m^{3/2}$
Injection Rate	$q = 1.0 \times 10^{-5}$	m^3/s

The resulting fractional flow and its derivative curves are shown in Figure 5. Note that fractional flow curves change also with the non-Darcy model parameters due to changes in pressure gradient and flow rate for different non-Darcy flow parameters under the same saturation.

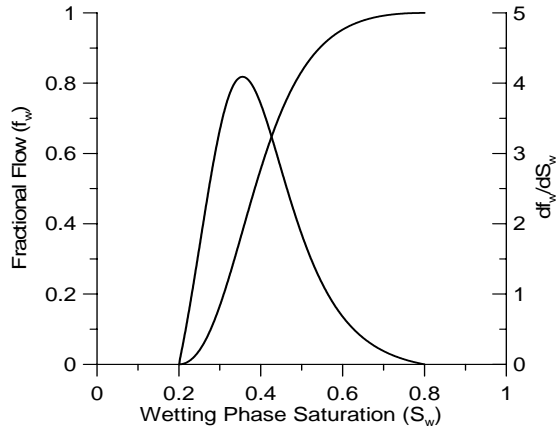


Figure 5. Fractional flow and its derivative curves with respect to wetting phase saturation in the non-Darcy displacement system.

For the comparison, to reduce the effects of discretization on numerical simulation results, very fine, uniform mesh spacing ($\Delta x = 0.01$ m) is chosen. A one-dimensional 5 m linear domain is discretized into 500 one-dimensional uniform gridblocks. The comparison between the analytical and numerical solutions is shown in Figure 6. The figure indicates that the numerical results are in excellent agreement with the analytical prediction of the non-Darcy displacement for the entire wetting-phase sweeping zone. Except at the shock, advancing saturation front, the numerical solution deviates only slightly from the analytical solution, resulting from the typical “smearing front” phenomenon of numerical dispersion effects when matching the Buckley-Leverett solution using numerical results (Aziz and Settari, 1979).

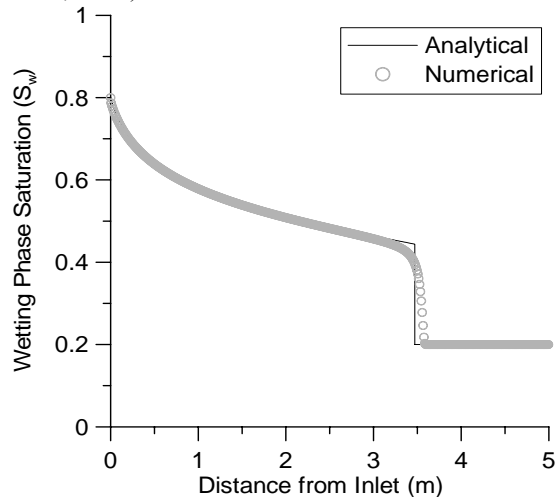


Figure 6. Comparison between displacement saturation profiles calculated from analytical and numerical solutions after 10 hours of injection.

Model Application: The application example presents a radial flow problem of single-phase non-Darcy using the numerical model to calculate

transient pressure at an injection well. The reservoir formation is a 10 m thick, uniform, radially infinite system (approximated by $r_e = 10,000,000$ m in the numerical model) represented by a 1-D radial grid of 1,202 radial increments with a Δr size that increases logarithmically away from the well radius ($r_w = 0.1$ m). The formation is initially at a constant pressure of 10^7 Pa and is subjected to a constant volumetric injection rate of $1,000$ m³/d at the well, starting at $t = 0$. Parameters used for the simulation study are listed in Table 3. Figure 7 presents the results of the simulated transient pressure responses at the well and a comparison for the two subject cases with different minimum permeability and characteristic length values—for Case 1: $k_{min} = 0.1$ Darcy and $\tau = 100,000$ (1/m) and Case 2: $k_{min} = 1.0$ Darcy and $\tau = 10,000$ (1/m). In Figure 7, the lower, dashed curve shows the results for Case 1 and the upper, solid curve shows the results for Case 2. The larger pressure increases in Case 2 indicate the greater flow resistance for the Case 2 system, as the value of the characteristic length, τ , becomes smaller. Note also that in both cases, the later time pressure responses have a linear relationship with time on the semi-log plot, which is similar to Darcy flow behavior.

Table 3. Parameters used for simulation transient checking numerical, as shown in Figure 6.

Parameter	Value	Unit
Darcy permeability	$k_d = 10$	Darcy
Minimum permeability	$k_{min} = 0.1, 1.0$	Darcy
Viscosity	$\mu = 0.001$	Pa · s
Reference density	$\rho = 1,000$	kg/m ³
Volumetric Injection rate	$q = 1,000$	m ³ /d
Total compressibility of fluid and rock	$C_T = 6.0 \times 10^{-10}$	1/Pa
Well radius	$r_w = 0.1$	m
Formation thickness	$h = 10$	m
Initial formation gas pressure	$P_i = 10^7$	Pa

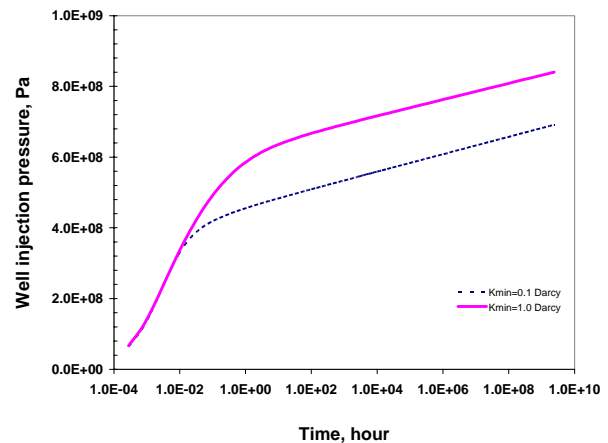


Figure 7. Transient pressure responses simulated at an injection well for 1-D radial flow. The dashed blue line shows the results for Case 1, while the solid magenta line shows the results for Case 2. Higher resistance is demonstrated in the Case 2 system.

SUMMARY AND CONCLUSIONS

This paper presents a general mathematical model and numerical approach for incorporating the Barree and Conway (2004, 2007) model into single-phase and multiphase non-Darcy flow simulations. The model formulation is implemented into a general reservoir simulator for multidimensional non-Darcy flow in porous and fractured media. In numerical solutions, the multiphase non-Darcy flow formulation is solved using an unstructured grid with regular or irregular meshes for multidimensional simulation, while flow in fractured rock is handled using a general TOUGH2 multi-continuum approach. To check the numerical scheme implemented, we use analytical solutions to verify our numerical model results for both single-phase and multiphase non-Darcy flow, and demonstrate the model application in single-phase transient radial flow.

Acknowledgements

The authors wish to thank the members of the Fracturing, Acidizing, Stimulation Technology (FAST) Consortium located at the Colorado School of Mines and the Stimlab Proppant Consortium for their support. The authors would also like to acknowledge support from Sinopec Inc. of China, through the National Basic Research Program of China (973 Program), "Study the Fundamentals of the Carbonate Karst Reservoir Development 2006CB202400."

REFERENCES

- Aziz, K. and A. Settari, *Petroleum Reservoir Simulation*, Applied Science, London, 1979.
- Barree, R.D. and, M.W. Conway, Multiphase Non-Darcy Flow in Proppant Packs. Paper SPE 109561, presented at the 2007 Annual Technical Conference and Exhibition, Anaheim, CA, 11-14 November, 2007.
- Barree, R. D. and, M. W. Conway, Beyond Beta Factors: A Complete Model for Darcy, Forchheimer and Trans-Forchheimer Flow in Porous Media. Paper SPE 89325 presented at the 2004 Annual Technical Conference and Exhibition, Houston, Texas 26-29 September, 2004.
- Evans, E. V. and R. D. Evans, Influence of an immobile or mobile saturation on non-Darcy compressible flow of real gases in propped fractures, *J. Petroleum Technology*, Vol. 40, No. 10, pp.1343-1351, 1988.
- Evans, R. D., C. S. Hudson and J. E. Greenlee, The effect of an immobile liquid saturation on the non-Darcy flow coefficient in porous media, J.

- SPE Production Engineering, *Trans. AIME*, Vol. 283, pp.331-338, 1987.
- Forchheimer, P., *Wasserbewegung durch Bode*, ZVDI (1901) 45, 1901.
- Forsyth, P. A., Y. S. Wu and K. Pruess, Robust Numerical Methods for Saturated-unsaturated Flow with Dry Initial Conditions in Heterogeneous Media. *Advance in Water Resources* 18, p. 25-38, 1995.
- Guppy, K. H., H. Cinco-Ley, H. J. Ramey, Jr. and F. Samaniego, Non-Darcy flow in wells with finite-conductivity vertical fractures, *Soc. Pet. Eng. J.*, pp.681-698, 1982.
- Guppy, K. H., H. Cinco-Ley, and H. J. Ramey, Jr., Effects of non-Darcy flow on the constant-pressure production of fractured wells, *Soc. Pet. Eng. J.*, pp.390-400, 1981.
- Katz, D. L. and R. L. Lee, *Natural Gas Engineering, Production and Storage*, Chemical Engineering Series, McGraw-Hill Book Co. Inc., New York, 1990.
- Kazemi, H., Pressure Transient Analysis of Naturally Fractured Reservoirs with Uniform Fracture Distribution. *SPEJ*, 451-62. *Trans., AIME*, 246, 1969.
- Lai, B, J. L. Miskimins, and Y. S. Wu, Non-Darcy Porous Media Flow According to the Barree and Conway Model: Laboratory and Numerical Modeling Studies, SPE-122611, Presented at the 2009 Rocky Mountain Petroleum Technology Conference, 14-16 April, 2009, Denver, CO, 2009.
- Lee, R. L., R. W. Logan and M. R. Tek: Effects of turbulence on transient flow of real gas through porous media, *SPE Formation Evaluation*, pp.108-120, 1987.
- Liu, X., F. Civan and R. D. Evans, Correlations of the non-Darcy flow coefficient, *J. Canadian Petroleum Technology*, Vol. 34, No. 10, pp.50-54, 1995.
- Lopez. H. D., Experimental Analysis and Macroscopic and Pore-level Flow Simulations to Compare Non-Darcy Flow Models in Porous Media. PhD dissertation, Colorado School of Mines, Golden, Colorado, 2007.
- Pruess, K., C. Oldenburg, and G. Moridis, *TOUGH2 User's Guide, Version 2.0*, Report LBNL-43134, Berkeley, California: Lawrence Berkeley National Laboratory, 1999.

- Pruess, K. and Narasimhan, T. N., A practical method for modeling fluid and heat flow in fractured porous media, *Soc. Pet. Eng. J.*, 25, pp.14-26, 1985.
- Pruess, K., GMINC - A mesh generator for flow simulations in fractured reservoirs, Report LBL-15227, Berkeley, California: Lawrence Berkeley National Laboratory, 1983.
- Scheidegger, A. E. *The Physics of Flow through Porous Media*, University of Toronto Press, 1972.
- Skjetne, E., T. K. Statoil and J. S. Gudmundsson, Experiments and modeling of high-velocity pressure loss in sandstone fractures, SPE 56414, Presented at the 1999 SPE Annual Technical Conference and Exhibition, Houston, Texas, 3-6, October, 1999.
- Swift, G. W. and O. G. Kiel, The prediction of gas-well performance including the effects of non-Darcy flow, *J. Petroleum Technology, Trans. AIME*, Vol. 222, 791-798, 1962.
- Tek, M. R., K. H. Coats and D. L. Katz, The effects of turbulence on flow of natural gas through porous reservoirs, *J. Petroleum Technology, Trans. AIME*, Vol. 222, pp.799-806, 1962.
- Warren, J.E., and P. J. Root, The behavior of naturally fractured reservoirs, *Soc. Pet. Eng. J., Trans., AIME*, pp.245-255, 228, 1963.
- Wu, Y. S., B. Lai, and J. L. Miskimins, Simulation of Multiphase Non-Darcy Flow in Porous and Fractured Media, SPE-122612, to be presented at the 2009 SPE Annual Technical Conference and Exhibition held in New Orleans, Louisiana, USA 4-7 October 2009.
- Wu, Y. S. and G. Qin, A General Numerical Approach for Modeling Multiphase Flow and Transport in Fractured Porous Media, *Communications in Computational Physics*, (accepted), 2009.
- Wu, Y. S., Numerical Simulation of Single-Phase and Multiphase Non-Darcy Flow in Porous and Fractured Reservoirs. *Transport in Porous Media* 49 (2): 209-240, 2002.
- Wu, Y. S., Non-Darcy Displacement of Immiscible Fluids in Porous Media, *Water Resources Research*, Vol. 37, No. 12, pp.2943-2950, 2001
- Wu, Y. S. A virtual node method for handling wellbore boundary conditions in modeling multiphase flow in porous and fractured media, LBNL-42882, *Water Resources Research*, Vol. 36, NO. 3, pp.807-814, 2000.
- Wu, Y. S., MSFLOW: *Multiphase Subsurface Flow Model of Oil, Gas and Water in Porous and Fractured Media with Water Shut-off Capability, DOCUMENTATION and User's Guide*, Walnut Creek, California, 1998.
- Wu, Y. S., P. A. Forsyth and H. Jiang, A consistent approach for applying numerical boundary conditions for subsurface flow, *Journal of Contaminant Hydrology* 23: 157-185. 1996.
- Wu, Y. S. and K. Pruess, and P. A. Witherspoon, Flow and displacement of Bingham non-Newtonian fluids in porous media, *SPE Reservoir Engineering*, 369-376, 1992.
- Wu, Y. S. and K. Pruess, A multiple-porosity method for simulation of naturally fractured petroleum reservoirs, *SPE Reservoir Engineering*, 3, pp. 327-336, 1988.

A Multiple-Continuum Model for Simulating Single-Phase and Multiphase Flow in Naturally Fractured Vuggy Reservoirs

Yu-Shu Wu¹, Zhijiang Kang², Yuan Di³, Thanh Nguyen¹, and Perapon Fakcharoenphol¹

¹Colorado School of Mines, Golden CO USA

²SINOPEC, Beijing, China

³Peking University, Beijing, China

ABSTRACT

The existence of vugs or cavities in naturally fractured reservoirs has long been observed. Even though these vugs are known for their large contribution to reserves of oil, natural gas, or groundwater, few quantitative investigations of fractured vuggy reservoirs have been conducted. In this paper, a multiple-continuum conceptual model is presented, based on geological data and observations of core samples from carbonate formations in China, to investigate single-phase multiphase flow behavior in such vuggy fractured reservoirs. The conceptual model has been implemented into a three-dimensional, three-phase reservoir simulator with a generalized multiple-continuum modeling approach. The conceptual model considers fractured vuggy rock as a triple- or multiple-continuum medium, consisting of (1) highly permeable and well-connected fractures, (2) low-permeability rock matrix, and (3) various-sized vugs. The matrix system may contain a large number of small or isolated cavities, whereas vugs are larger cavities, indirectly connected to fractures through small fractures or microfractures. Similar to the conventional double-porosity model, the fracture continuum is primarily responsible for the occurrence of global flow, while vuggy and matrix continua, providing storage space, are locally connected to each other and interacting with globally connecting fractures. In addition, flow in fractured vuggy reservoirs may be further complicated by occurrence of non-Darcy and other nonlinear flow behavior, because of large pore space and high-permeability flow channels. To account for such complicated flow regime, our model formulation includes non-Darcy flow, using the multiphase extension of the *Forchheimer* equation, as well as flow according to parallel-wall fracture and tube models, based on solutions of flow through a parallel-wall, uniform fracture and Hagen-Poiseuille tube flow.

INTRODUCTION

Naturally fractured reservoirs existing throughout the world represent a significant amount of the world oil and gas reserves, water, and other natural resources. In the past half century, significant progress has been made towards understanding and modeling of flow processes in fractured rock (Barenblatt et al. 1960;

Warren and Root, 1963; Kazemi, 1969; Pruess and Narasimhan, 1985). However, most studies have focused primarily on naturally fractured reservoirs without taking large cavities into consideration. Recently, characterizing vuggy fractured rock has received attention, because a number of fractured vuggy reservoirs have been found worldwide that can significantly contribute to reserves and the production of oil and gas (Kossack and Curpine, 2001; Rivas-Gomez et al., 2001; Lui et al., 2003; Hidajat et al., 2004; Camacho-Velazquez et al., 2005; Kang et al., 2006; Wu et al., 2006).

Among the commonly used conceptual models for analyzing flow through fractured rock, dual-continuum models (i.e., double- and multiporosity, and dual-permeability models) are perhaps the most popular approaches for fractured reservoir modeling studies. In addition to the traditional double-porosity concept, a number of triple-porosity or triple-continuum models have been proposed (Closemann, 1975; Wu and Ge, 1983; Abdassah, and Ershaghis, 1986; Bai et al. 1993; Wu et al. 2004; Kang et al. 2006; Wu et al. 2006) to describe flow through fractured rock. In particular, Liu et al. (2003), Camacho-Velazquez et al. (2005); and Wu et al. (2007) present several new triple-continuum models for single-phase flow in a fracture-matrix system that includes cavities within the rock matrix (as an additional porous portion of the matrix). In general, these models have focused on handling different level/scaled heterogeneity of rock matrix or fractures (e.g., subdividing the rock matrix or fractures into two or more subdomains with different properties for single-phase and multiphase flow) in such fractured reservoirs.

Based on these conceptual models, mathematical modeling approaches to flow through fractured reservoirs in general rely on continuum approaches and involve developing conceptual models, incorporating the geometrical information of a given fracture-matrix system, setting up mass and energy conservation equations for fracture-matrix domains, and then solving discrete nonlinear algebraic equations. The commonly used mathematical methods for modeling flow through fractured rock include: (1) an explicit discrete-fracture and matrix model (e.g., Snow, 1969), (2) the dual-continuum method, including double- and multiporosity, dual-permeability, or the

more general "multiple interacting continua" (MINC), or the TOUGH2 method (e.g., Warren and Root, 1963; Kazemi, 1969; Pruess and Narasimhan, 1985; Pruess et al. 1999), and (3) the effective-continuum method (ECM) (e.g., Wu, 2000a). Among these three commonly used approaches, the dual-continuum method has been perhaps the most used in application. This is because it is computationally less demanding than the discrete-fracture approach, and it can handle fracture-matrix interactions under multiphase flow, heat transfer, and chemical transport conditions in fractured reservoirs.

This paper summarizes our recent study of modeling flow in fractured vuggy reservoirs, based on an oilfield example of fractured vuggy reservoirs. In particular, we discuss the issues and the physical rationale for how to conceptualize fracture-vuggy-matrix systems, and how to represent them using a numerical modeling approach. The objective of this paper is to: (1) present a general triple-continuum conceptual model to include effects of different-sized vugs and cavities on single-phase and multiphase flow processes in naturally fractured vuggy reservoirs; (2) describe a methodology for numerically implementing the proposed triple-continuum conceptual model; and (3) present examples for verifying and applying the proposed model.

OBSERVATION AND CONCEPTUAL MODEL

As observed, for example, in the carbonate formations of the Tahe Oilfield in western China, a typical fractured vuggy reservoir consists of a large and well-connected, fractured, low-permeability rock matrix, as well as a large number of varying-sized cavities or vugs. As shown in outcrops of the reservoir layers in Figures 1-(a), 2-(a), and 3-(a), these vugs and cavities are irregular in shape and vary in size from millimeters to meters in diameter. Many of the small-sized cavities appear to be isolated from fractures. In this paper, we use "cavities" for small caves (with sizes of centimeters or millimeters in diameter), while "vugs" represent larger cavities (with sizes from centimeters to meters in diameter). Several conceptual models for vugs are shown in Figures 1, 2, and 3: (1) vugs are indirectly connected to fractures through small fractures or microfractures (Figure 1); (2) vugs are isolated from fractures or separated from fractures by rock matrix (Figure 2); and (3) some vugs are directly connected to fractures and some are isolated (Figure 3). In reservoirs, there are many more vug varieties and spatial distributions than those shown in Figures 1-(a), 2-(a), and 3-(a), some of which may be approximated by the conceptual models of Figures 1-(b), 2-(b), and 3-(b), or their combinations. Under no circumstances, however, is

there a requirement for uniform size distribution patterns for vugs and cavities in this study.

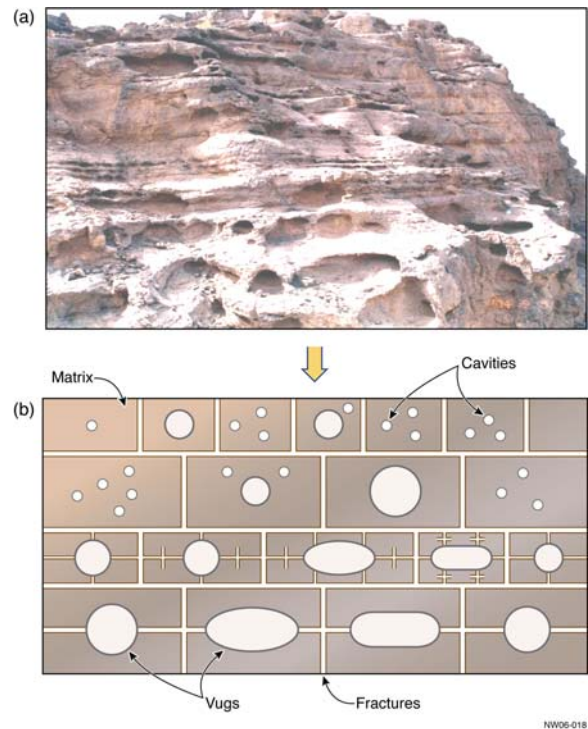


Figure 1. Schematic of conceptualized fractured vuggy formation as a multiple-continuum system with different-scale fractures, various vugs and cavities; (a) outcrop pictures and (b) conceptual model

Similar to the conventional double-porosity concept (Warren and Root, 1963), large fractures or the fracture continuum are conceptualized to serve as main pathways for global flow, while vuggy and matrix continua, mainly providing storage space as sinks or sources, are locally connected to each other, as well as directly or indirectly interacting with globally connecting fractures. Note that vugs and cavities directly connected with fractures (e.g., Figure 3) are considered part of the fracture continuum. More specifically, as shown in Figures 4, 5, and 6, we conceptualize the fractured-vug-matrix system as consisting of (1) "large" fractures (or fractures), *globally connected* on the model scale to wells; (2) various-sized vugs or cavities, which are *locally connected* to fractures either through "small" fractures or through the rock matrix; and (3) rock matrix, which may contain a number of cavities, *locally connected* to large fractures and/or to vugs.

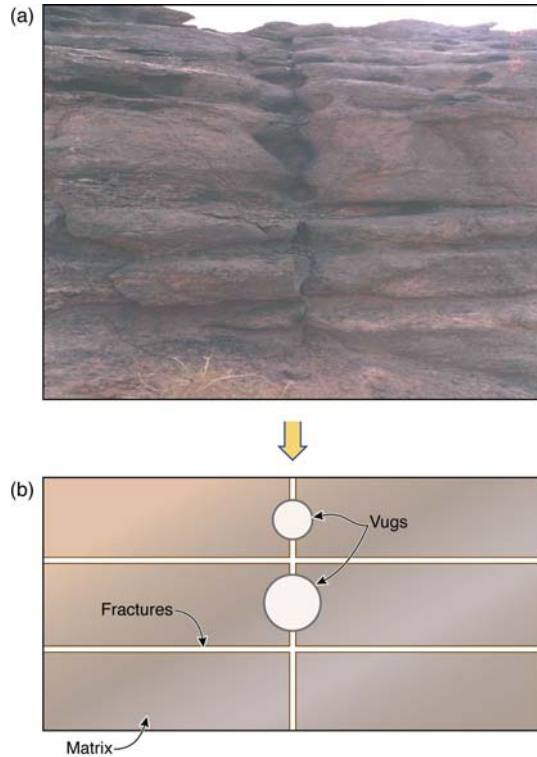


Figure 2. Schematic of conceptualized fractured vuggy formation as a discrete fracture system with well connected, (a) outcrop pictures and (b) conceptual model

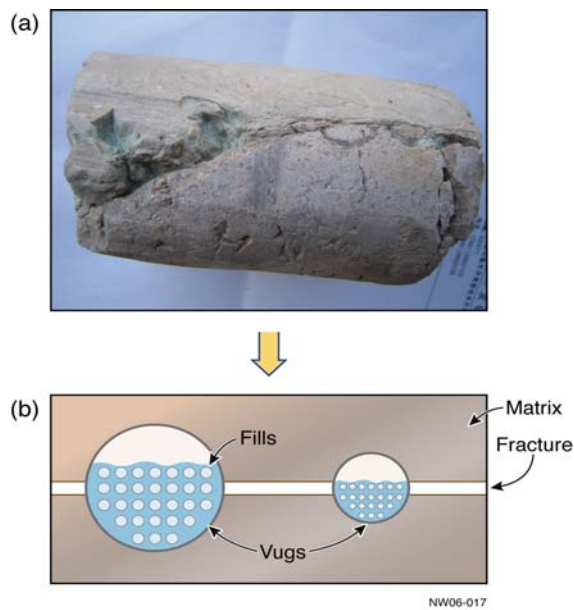


Figure 3. Schematic of conceptualized fractured vuggy formation as a fracture-vug-matrix system with well partially filled vugs: (a) core sample and (b) conceptual model

In principle, the discussed triple-continuum model can be considered to be a natural extension of the generalized multicontinuum (MINC) approach (e.g., Pruess and Narasimhan, 1985; Wu and Pruess, 1988; Wu et al., 2004). In this approach, an “effective” porous medium is used to approximate the fracture, vugs, or rock matrix continua, by considering the three continua to be spatially overlapping and interacting to each other. The triple-continuum conceptual model assumes that an approximate thermodynamic equilibrium exists locally within each of the three continua at all times. Based on this local equilibrium assumption, we can define thermodynamic variables, such as fluid pressures and saturation, for each continuum. Note that the triple-continuum model is not limited to the orthogonal idealization of the fracture system or a uniform size or distribution of vugs and cavities, as those illustrated in Figures 1, 2, and 3. Irregular and stochastic distributions of fractures and cavities can be handled numerically, as long as the actual distribution patterns are known (Pruess, 1983).

MATHEMATICAL MODEL

A multiphase isothermal system in fractured vuggy reservoirs is assumed to involve three phases: oil, gas, and water. Each phase flows in response to pressure, gravitational, and capillary forces according to Darcy's law. Note that in this work, single-phase flow is considered as a special case of multiphase flow. Therefore, three mass-balance equations fully describe the system in an arbitrary flow region of the porous, fractured, vuggy domain:

For gas flow,

$$\frac{\partial}{\partial t} \left\{ \phi (S_o \bar{\rho}_{dg} + S_g \rho_g) \right\} = -\nabla \cdot (\bar{\rho}_{dg} \mathbf{v}_o + \rho_g \mathbf{v}_g) + q_g \quad (1)$$

For water flow,

$$\frac{\partial}{\partial t} (\phi S_w \rho_w) = -\nabla \cdot (\rho_w \mathbf{v}_w) + q_w \quad (2)$$

For oil flow,

$$\frac{\partial}{\partial t} (\phi S_o \bar{\rho}_o) = -\nabla \cdot (\bar{\rho}_o \mathbf{v}_o) + q_o \quad (3)$$

where the Darcy's velocity of phase β ($\beta = g$ for gas, $= w$ for water, and $= o$ for oil) is defined as,

$$\mathbf{v}_\beta = -\frac{k k_{r\beta}}{\mu_\beta} (\nabla P_\beta - \rho_\beta \mathbf{g} \nabla D) \quad (4)$$

In Equations (1)–(4), ϕ is the effective porosity of the medium; ρ_β is the density of phase β at reservoir conditions; $\bar{\rho}_o$ is the density of oil, excluding

dissolved gas, at reservoir conditions; $\bar{\rho}_{dg}$ is the density of dissolved gas (dg) in oil phase at reservoir conditions; μ_β is the viscosity of phase β ; S_β is the saturation of phase β ; P_β is the pressure of phase β ; q_β is the sink/source term of component β per unit volume of the medium, representing mass exchange through injection/production wells or due to fracture-matrix-vug interactions. To continue, g is the gravitational acceleration; k is the absolute/intrinsic permeability (tensor) of the medium; $k_{r\beta}$ is the relative permeability to phase β ; and D is depth.

Equations (1), (2) and (3), governing mass balance for three-phase fluid flow, need to be supplemented with constitutive equations that express all the secondary variables and parameters as functions of a set of key primary thermodynamic variables. The following relationships will be used to complete the description of multiphase flow through fractured porous media:

$$S_w + S_o + S_g = 1 \quad (5)$$

In addition, capillary pressure and relative permeability relations are also needed for each continuum, which are normally expressed in terms of functions of fluid saturations. The densities of water, oil, and gas, as well as the viscosities of fluids, can in general be treated as functions of fluid pressures.

NUMERICAL FORMULATION

The governing equations, as discussed above, for multiphase flow in fractured vuggy reservoirs have been implemented into a general-purpose, three-phase reservoir simulator, the MSFLOW code (Wu, 2000b). As implemented numerically, Equations (1), (2) and (3) are discretized in space using an integral finite-difference or control-volume finite-element scheme for a porous-fractured-vuggy medium. Time discretization is carried out with a backward, first-order, finite-difference scheme. The discrete nonlinear equation for water, oil, and gas flow at Node i is written as follows:

$$\left\{ (\phi S_\beta \rho_\beta)_i^{n+1} - (\phi S_\beta \rho_\beta)_i^n \right\} \frac{V_i}{\Delta t} = \sum_{j \in \eta_i} F_{\beta,ij}^{n+1} + Q_{\beta i}^{n+1} \quad (6)$$

where superscript n denotes the previous time level; $n+1$ is the current time level; V_i is the volume of element i (porous or fractured block); Δt is time step size; η_i contains the set of neighboring elements (j) (porous, vuggy, or fractured) to which element i is directly connected; $F_{\beta,ij}$ is the mass flow term for phase β between elements i and j ; and $Q_{\beta i}$ is the mass sink/source term at element i of phase β .

The “flow” term ($F_{\beta,ij}$) in discrete Equation (6) for multiphase flow between and among the triple-continuum media, along the connection (i, j), is given by

$$F_{\beta,ij} = \lambda_{\beta,ij+1/2} \gamma_{ij} [\psi_{\beta j} - \psi_{\beta i}] \quad (7)$$

where $\lambda_{\beta,ij+1/2}$ is the mobility term to phase β , defined as

$$\lambda_{\beta,ij+1/2} = \left(\frac{\rho_\beta k_{r\beta}}{\mu_\beta} \right)_{ij+1/2} \quad (8)$$

Here, subscript $ij+1/2$ denotes a proper averaging or weighting of properties at the interface between two elements i and j ; and $k_{r\beta}$ is the relative permeability to phase β . In Equation (7), γ_{ij} is transmissivity and is defined, within the integral finite-difference scheme (Pruess et al. 1999), as

$$\gamma_{ij} = \frac{A_{ij} k_{ij+1/2}}{D_i + D_j} \quad (9)$$

where A_{ij} is the common interface area between connected blocks or nodes i and j ; D_i is the distance from the center of block i to the interface between blocks i and j ; and $k_{ij+1/2}$ is an averaged (such as harmonically weighted) absolute permeability along the connection between elements i and j . The flow potential term in Equation (4) is defined as

$$\psi_{\beta i} = P_{\beta i} - \rho_{\beta,ij+1/2} g D_i \quad (10)$$

where D_i is the depth to the center of block i from a reference datum. The mass sink/source term at element i , $Q_{\beta i}$ for phase β , is defined as

$$Q_{\beta i} = q_{\beta i} V_i \quad (11)$$

Note that Equation (6) has the same form regardless of the dimensionality of the model domain, i.e., it applies to one-, two-, or three-dimensional analyses of multiphase flow through fractured vuggy porous media. In our numerical model, Equation (6) is written in a residual form and is solved using Newton/Raphson iteration fully implicitly.

HANDLING FRACTURES AND VUGS

The technique used in this work for handling multiphase flow through fractured vuggy rock follows the dual- or multi-continuum methodology, or TOUGH2 technology (Warren and Root, 1963; Pruess and Narasimhan, 1985; Wu and Pruess, 1988). With this dual-continuum concept, Equations (1), (2), (3), and (4) can be used to describe multiphase flow

along fractures and inside matrix blocks, as well as fracture-matrix-vug interaction. However, special attention needs to be paid to treating interporosity flow in the fracture-matrix-vug triple continua. Flow terms between fracture-matrix, fracture-vug, and vug-matrix connections are all evaluated using Equation (6). However, the transmissivity of (9) will be evaluated differently for different types of inter-porosity flow. The fracture-matrix flow, γ_{ij} , is given by

$$\gamma_{FM} = \frac{A_{FM} k_M}{l_{FM}} \quad (12)$$

where A_{FM} is the total interfacial area between fractures (F) and the matrix (M) elements; k_M is the matrix absolute permeability; and l_{FM} is the characteristic distance for flow crossing fracture-matrix interfaces. For fracture-vug flow, γ_{ij} is defined as

$$\gamma_{FV} = \frac{A_{FV} k_V}{l_{FV}} \quad (13)$$

where A_{FV} is the total interfacial area between the fracture (F) and vugs (V) elements; l_{VM} is a characteristic distance for flow crossing vug-matrix interfaces; and k_V is the absolute vuggy permeability, which is the actual permeability of small fractures that control flow between vugs and fractures (Figure 1). Note that for the case in which vugs are isolated from fractures, as shown in Figures 5 and 6, no fracture-vug flow terms need to be calculated, because they are indirectly connected through the matrix. For vug-matrix flow, γ_{ij} is evaluated as

$$\gamma_{VM} = \frac{A_{VM} k_M}{l_{VM}} \quad (14)$$

where A_{VM} is the total interfacial area between the vug (V) and matrix (M) elements, and l_{VM} is a characteristic distance for flow crossing vug-matrix interfaces.

Table 1 summarizes several simple models for estimating characteristic distances in calculating interporosity flow within fractures, vugs, and the matrix, where we have regular one-, two-, or three-dimensional large fracture networks, each with uniformly distributed small fractures connecting vugs or isolating vugs from fractures (Figures 4, 5, and 6). The models in Table 1 rely on the quasi-steady-state flow assumption of Warren and Root (1963) to derive

characteristic distances for flow between fracture-matrix and (through small fractures) fracture-vug connections. Another condition for using the formulation in Table 1 is that fractures, vug, and matrix are all represented by only one gridblock. In addition, the flow distance between large fractures (F) and vugs (V), when connected through small fractures, is taken to be half the characteristic length of the small fractures within a matrix block (Figure 4). Furthermore, the interface areas between vugs and the matrix should include the contribution of small fractures for the case of Figure 4. Interface areas between fractures and the matrix, and between fractures and vugs through connecting small fractures, should be treated using the geometry of the large fractures alone. This treatment implicitly defines the permeabilities of the fractures in a continuum sense, such that bulk connection areas are needed to calculate Darcy flow between the two fracture continua.

Table 1. Characteristic distances* for evaluating flow terms between fractures, vugs, and matrix systems

Fracture Sets	1-D	2-D	3-D
Dimensions of Matrix Blocks (m)	A	A, B	A, B, C
Characteristic F-M Distances (m)	$l_{FM} = A/6$	$l_{FM} = AB / 4(A+B)$	$l_{FM} = 3ABC/10 / (AB+BC+CA)$
Characteristic F-V Distances (m)	$l_{FV} = l_x$	$l_{FV} = \frac{l_x + l_y}{2}$	$l_H = \frac{l_x + l_y + l_z}{3}$
Characteristic V-M Distances ¹ (m)	$l_{VM} = a/6$	$l_{VM} = ab / 4(a+b)$	$l_{VM} = 3abc/10 / (ab+bc+ca)$
Characteristic V-M Distances ² (m)	$l_{VM} = (A-d_c) / 2$	$l_{VM} = \frac{A+B-2d_c}{4}$	$l_H = \frac{A+B+C-3d_c}{6}$

* Note in Table 1, A, B, and C are dimensions of matrix blocks along x, y, and z directions, respectively.

¹ Characteristic V-M distances are estimated for the case (Figure 4), i.e., vuggy-matrix connections are dominated by small fractures, where dimensions a, b, and c are fracture-spacings of small fractures along x, y, and z directions, respectively.

² Characteristic V-M distances are used for the case (Figures 5 and 6), i.e., vugs are isolated from fractures.

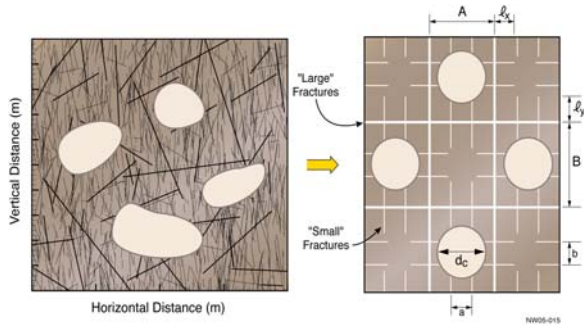


Figure 4. Conceptualization#1 of fractured vuggy rock as a triple-continuum system with vugs indirectly connected to fractures through small fractures

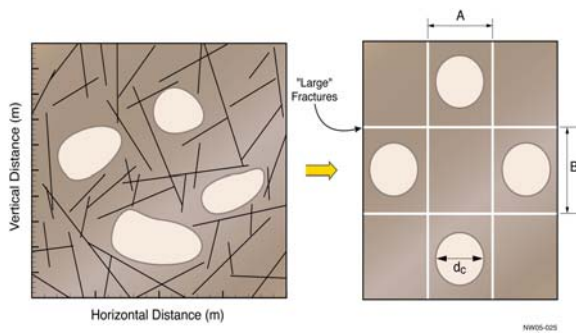


Figure 5. Conceptualization#2 of fractured vuggy rock as a triple-continuum system with vugs isolated from or indirectly connected to fractures through rock matrix

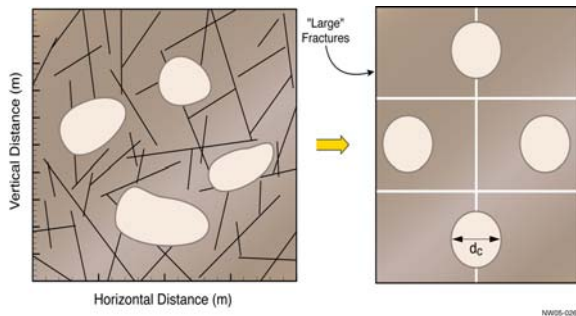


Figure 6. Conceptualization#3 of fractured vuggy rock as a triple-continuum system with partial vugs isolated from

The MINC concept (Pruess, 1983; Pruess and Narasimhan, 1985) is extended to generate a triple-continuum grid, which is a key step in modeling flow through fractured-vuggy rock. We start with a primary or single-porous medium mesh that uses bulk volume of formation and layering data. Then, we use geometric information for the corresponding fractures and vugs within each formation subdomain or each finite-difference gridblock of the primary mesh. Fractures are lumped together into the fracture

continuum, while vugs with or without small fractures are lumped together into the vuggy continuum. The rest is treated as the matrix continuum. Connection distances and interface areas are then calculated accordingly, e.g., using the relations listed in Table 1 and the geometric data of fractures. Once a proper mesh for a triple-continuum system is generated, fracture, vuggy, and matrix blocks are specified, separately, to represent fracture or matrix continua.

HANDLING NON-DARCY'S AND OTHER COMPLICATED FLOW

Flow regime may be more complicated within fracture-vuggy reservoirs or through faults or fault zones, because of (1) the high permeability of fractures and (2) large pores, such as vugs and larger-aperture fractures, in vug or fault zones. Several common scenarios are discussed below:

No-Darcy Flow: In addition to Darcy flow, as described in Equations (4) or (7), non-Darcy flow may also occur between and among the multiple continua within fault zones. A general numerical approach for modeling non-Darcy flow (Wu, 2002) can be directly extended to the multiple-continuum model of this work for flow in fractured or fault zones. Volumetric flow rate (namely Darcy velocity for Darcy flow) for non-Darcy flow of each fluid may be described using the multiphase extension of the Forchheimer equation:

$$-(\nabla P_w - \rho_w \mathbf{g}) = \frac{\mu}{k} \mathbf{v}_w + \theta \rho_w \mathbf{v}_w |\mathbf{v}_w| \quad (15)$$

θ is the non-Darcy flow coefficient, an intrinsic rock property with units of m^{-1} under non-Darcy flow conditions.

Note that no matter what type the flow (i.e., Darcy flow, non-Darcy flow, or the following pipe-type flow), the discrete mass-balance equation of (6) is always valid. For the case of non-Darcy flow, the flow term ($F_{\beta,ij}$) in Equation (7) along the connection (i, j), between elements i and j, is numerically replaced by (Wu, 2002):

$$F_{\beta,ij} = \frac{A_{ij}}{2(k\theta)_{ij+1/2}} \left\{ -\frac{1}{\lambda_\beta} + \left[\left(\frac{1}{\lambda_\beta} \right)^2 - \bar{\gamma}_{ij} (\psi_{\beta j} - \psi_{\beta i}) \right]^{1/2} \right\} \quad (16)$$

$$\bar{\gamma}_{ij} = \frac{4(k^2 \rho_w \theta)_{ij+1/2}}{D_i + D_j} \quad (17)$$

Flow in Parallel-Wall Fracture or Tube: In general, flow along connecting paths of large-aperture fractures or vugs through narrow pores or fractures may be too fast or openings too large to describe using Darcy's law. In particular, when these large-aperture fractures vuggy connections could be approximated as a single (or parallel) fracture or tube within fault zones, solutions of flow through a parallel-wall, uniform fracture or Hagen-Poiseuille tube-flow solution (Bird et al. 1960) may be extended to describe such flow in Equation (9):

$$\gamma_{ij} = \frac{wb^3}{12(D_i + D_j)} \quad (18)$$

for fracture-type connection and,

$$\gamma_{ij} = \frac{\pi r^4}{8(D_i + D_j)} \quad (19)$$

for tube-type connection. In (18) and (19), b is fracture aperture, w is fracture width, and r is tube radius. Similarly, flow solutions for both laminar and turbulent flow through the simple geometry of vug-vug connections can be used for flow between these vuggy connections.

COMPARISON WITH ANALYTICAL SOLUTION

We compared the numerical model to analytical solutions (Lui et al., 2003; Wu et al., 2004; Wu et al., 2007). The verification problem concerns typical single-phase transient flow towards a well that fully penetrates a radially infinite, horizontal, and uniformly vuggy fractured reservoir. Numerically, a radial reservoir ($r_e = 10,000$ m) of 20 m thick is represented by a 1-D (primary) grid of 2,100 intervals. A triple-continuum mesh is then generated using a 1-D vuggy-fracture-matrix conceptual model, consisting of a horizontal large-fracture plate network with a uniform disk-shaped matrix block. Uniform spherical vugs are contained inside the matrix and connected to fractures through small fractures. Fracture, vugs and matrix parameters are given in Table 2.

Figure 7 compares numerical-modeling results with the analytical solution for a single-phase transient flow case (in terms of dimensionless variables). Excellent agreement exists between the two solutions, which provides verification of the numerical formation and its implementation. Note that there are very small differences at very early times ($t_D < 10$ or 0.2 seconds) in the two solutions in Figure 7, which may occur because the analytical solution, long-time asymptotic and similar to the Warren-Root solution, may not be valid for $t_D < 100$.

Table 2. Parameters used in the single-phase flow problem in the triple-continuum, fractured vuggy reservoir

Parameter An	al/Num. Comparison	Basecase of Sensitivity	Unit
Matrix porosity	$\phi_M = 0.263$	$\phi_M = 0.200$	
Fracture porosity	$\phi_F = 0.001$	$\phi_F = 0.001$	
Vuggy porosity	$\phi_V = 0.01$	$\phi_V = 0.010$	
Fracture spacing	$A = 5$	$A = 1.0$	m
Small-fracture spacing	$a = 1.6$	$a = 0.2$	m
F characteristic length	$l_x = 3.472$	$l_x = 0.4$	m
F-M/F-V areas per unit volume rock	$A_{FM} = A_{FV} = 0.61$	$A_{FM} = 6.0,$ $A_{FV} = 0.356$	m^2/m^3
Reference water density	$\rho_i = 1,000$	$\rho_i = 1,000$	kg/m^3
Water phase viscosity	$\mu = 1 \times 10^{-3}$	$\mu = 1 \times 10^{-3}$	Pa•s
Matrix permeability	$k_M = 1.572 \times 10^{-16}$	$k_M = 1.0 \times 10^{-16}$	m^2
Fracture permeability	$k_F = 1.383 \times 10^{-13}$	$k_F = 1.0 \times 10^{-12}$	m^2
Small-fracture or vug permeability	$k_V = 1.383 \times 10^{-14}$	$k_V = 1.0 \times 10^{-13}$	m^2
Water Production Rate	$q = 100$	$q = 864$	m^3/d
Total compressibility of three media	$C_F = C_M = C_V = 1.0 \times 10^{-9}$	$C_F = C_M = C_V = 1.0 \times 10^{-10}$	1/Pa
Well radius	$r_w = 0.1$	$r_w = 0.1$	m
Formation thickness	$h = 20$	$h = 10$	m

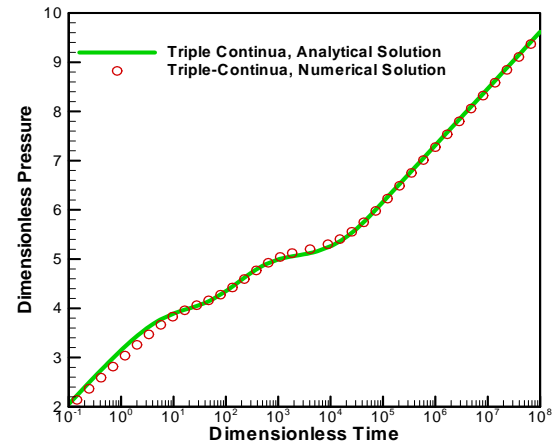


Figure 7. Comparison between analytical and numerical solutions for single-phase transient flow through fractured vuggy formation

SENSITIVITY RUN

To investigate flow behavior and the contribution of vug parameters in triple continuum vuggy fractured reservoirs, Conceptualizations #1 and #2 (Figure 4 and 5) together with varied fracture, vug, and matrix parameters were numerically modeled. An infinite radial reservoir 10 m thick is represented by a 1-D (primary) radial grid of 1,101 grids. Single-phase reservoir simulation was used to generate sets of pressure transient data. Base-case fracture, vug and matrix parameters are also given in Table 2.

Comparison of simulation results between Conceptualizations #1 and #2 are shown in Figure 8. It is clear that fracture and vug connections (F-V) play a major role in behavior. Conceptualization#1, which has an F-V connection, generates triple porosity behavior, whereas simulation results from Conceptualization#2, which does not have an F-V connection, yields double porosity. To explain this observation, one must consider well-to-reservoir connections. In these simulation cases, an injector well connects exclusively to the fracture continuum. Consequently, fluid flow starts from fractures and propagates into another connected continuum. Conceptualization#1, the start of fluid flow in a vug continuum, takes place before the matrix continuum because the vug has larger permeability. In contrast, the beginning of fluid flow in the vug of Conceptualization#2 cannot be clearly identified, because it is dominated by flow in the matrix, since the vug does not directly connect to the fracture. As a result, the vug is acting like additional storage or source to the matrix.

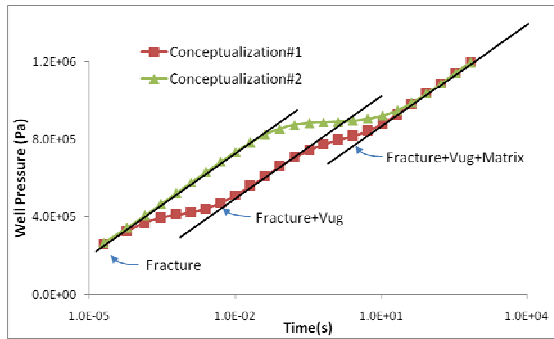


Figure 8. Comparison between Conceptualization#1 and Conceptualization#2 for basecase fracture, vug, and matrix parameters

Figures 9 and 10 show results from sensitivity to vug porosity. It is observed that vug porosity controls the appearance of interporosity flow in Conceptualization#1's simulation results. In contrast, it does not affect flow behavior in Conceptualization#2. This observed behavior is caused by F-V connectivity. In Conceptualization#1 which has F-V connections, changes in vug rock properties directly influence flow behavior in the vug continuum. In contrast, Conceptualization#2, which does not have F-V connections, flow in the vug is controlled by matrix properties; as such, changing vug porosity does not affect the flow behavior.

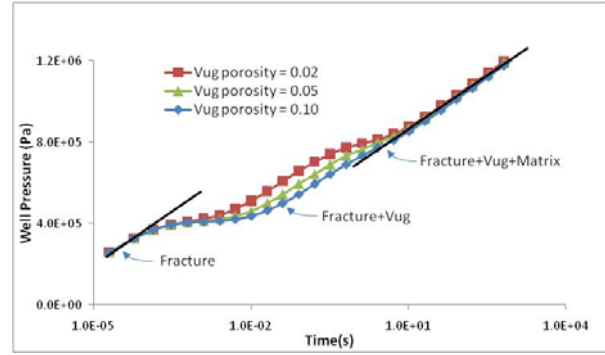


Figure 9. Sensitivity runs on vug porosity for Conceptualization#1

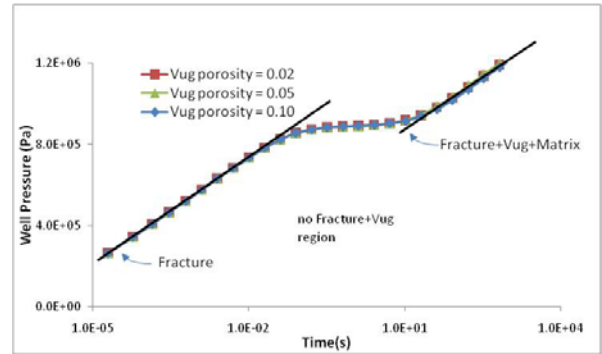


Figure 10. Sensitivity runs on vug porosity for Conceptualization#2

Figure 11 and Figure 12 illustrate sensitivity results of vug permeability in Conceptualization#1 and Conceptualization#2, respectively. Vug permeability in Conceptualization#1 controls time when flow in the vug starts. The larger the permeability, the sooner the flow in the vug takes place. However, changes in vug rock properties influence flow behavior in Conceptualization#1, but not in Conceptualization#2. The same reason for the previous sensitivity is also applicable in this case.

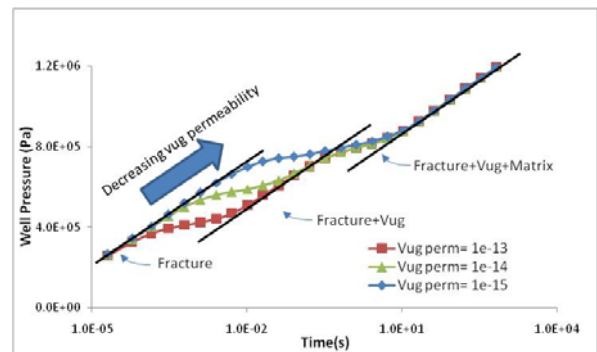


Figure 11. Sensitivity runs on vug permeability for Conceptualization#1

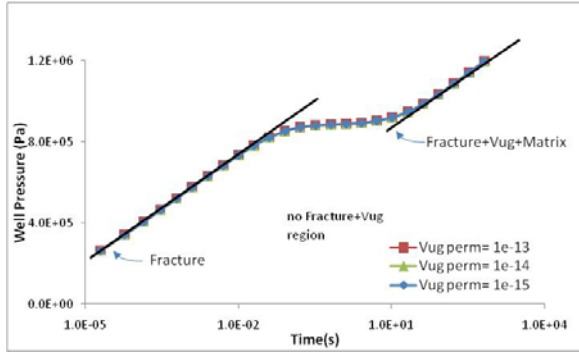


Figure 12. Sensitivity runs on vug permeability for Conceptualization#2

Figure 13 and Figure 14 show results of sensitivity on matrix permeability of Conceptualization#1 and Conceptualization#2, respectively. Both figures indicate the effect of changing matrix permeability. It is observed that matrix permeability controls the beginning of fluid flow in the matrix. The larger the permeability, the sooner the flow in the matrix starts.

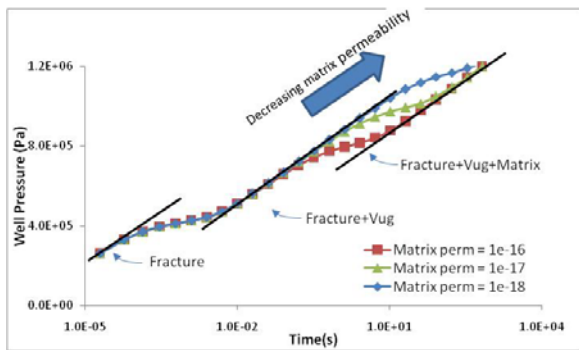


Figure 13. Sensitivity runs on matrix permeability for Conceptualization#1

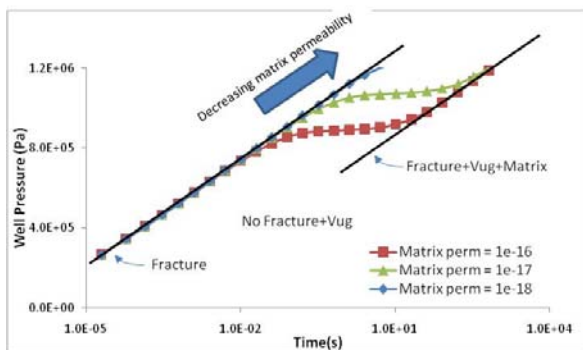


Figure 14. Sensitivity runs on matrix permeability for Conceptualization#2

CONCLUDING REMARKS

Based on observations in several oilfields of fractured vuggy reservoirs, we present a physically based conceptual and numerical model for simulating single-phase and multiphase flow in fractured vuggy rock, using a triple-continuum medium approach. The proposed multicontinuum concept is a natural extension of the classic double-porosity model, with the fracture continuum responsible for conducting global flow, while vuggy and matrix continua, providing storage space, are locally connected as well as interacting with flow through globally connecting fractures. Specifically, the proposed conceptual model considers fractured vuggy rock as a triple- or multiple-continuum medium, consisting of (1) highly permeable fractures, (2) low-permeability rock matrix, and (3) various-sized vugs. In addition, our model formulation includes non-Darcy flow, using the multiphase extension of the *Forchheimer* equation, and flow according to parallel-wall fracture and tube models.

The proposed conceptual model has been implemented into a general numerical reservoir simulator using a control-volume, finite-difference approach, which can be used to simulate single-phase as well as multiple-phase flow in 1-D, 2-D and 3-D reservoirs. We provide a verification example for the numerical scheme by comparing numerical results against an analytical solution for single-phase flow. As application examples, we apply the proposed mathematical model to sensitivity studies of transient triple-porosity flow behavior and parameter effects.

ACKNOWLEDGMENTS

This work was supported in part by the National Basic Research Program of China (973 Program), “Studying the Fundamentals of the Carbonate Karst Reservoir Development 2006CB202400” of the Research Inst. of Petroleum Exploration and Development of Sinopec Corp, and by the MECERS of Colorado School of Mines.

REFERENCES

- Abdassah, D. and Ershaghis I., Triple-porosity system for representing naturally fractured reservoirs, *SPE Form. Eval.*, 1, 113–127, 1986.
- Bai, M., Elsworth, D., and Roegiers, J.C., Multiporosity/multipermeability approach to the simulation of naturally fractured reservoirs, *Water Resour. Res.* 29, 1621–1633, 1993.
- Barenblatt, G.I., Zheltov, I.P., and Kochina, I.N., Basic concepts in the theory of seepage of

- homogeneous liquids in fissured rocks, *PMM, Sov. Appl. Math. Mech.*, 24(5), 852–864, 1960.
- Bird, R.B., W.E. Steward, E.N. Lightfoot. *Transport Phenomena*, John Willey & Sons, Inc., New York, London, Sydney, 1960.
- Camacho-Velazquez, R., M. Vasquez-Cruz, R. Castrejon-Aivar, and V. Arana-Ortiz, Pressure transient and decline-curve behavior in naturally fractured vuggy carbonate reservoirs, *SPE Reservoir Evaluation & Engineering*, 95-111, April, 2005.
- Closemann, P.J., The aquifer model for fissured fractured reservoir, *Soc. Pet. Eng. J.*, 385–398, 1975.
- Hidajat, I., K. Mohanty, M. Flaum, and G. Hirasaki, Study of vuggy carbonates using NMR and X-Ray CT scanning, *SPE Reservoir Evaluation & Engineering*, 365-377, October, 2004.
- Kang, Z., Y.S. Wu, J. Li, Y. Wu, J. Zhang, and G. Wang, Modeling multiphase flow in naturally fractured vuggy petroleum reservoirs, PSE-1-2356, Presented at the 2006 SPE Annual Technical Conference and Exhibition, San Antonio, Texas, 24-27 Sempember, 2006.
- Kazemi, H., Pressure Transient Analysis of Naturally Fractured Reservoirs with Uniform Fracture Distribution. *SPEJ*, 451–462. *Trans.*, AIME, 246, 1969.
- Kossack and Curpine, A methodology for simulation of vuggy and fractured reservoirs, SPE-66366, Presented at the SPE Reservoir Simulation Symposium, Houston, Texas, 11-14, February, 2001.
- Liu, J.C. G.S. Bodvarsson, and Y.S. Wu, Analysis of pressure behavior in fractured lithophysal reservoirs, *Journal of Contaminant Hydrology*, 62-62, 189-211, 2003
- Pruess K., Oldenburg, C., and Moridis, G., TOUGH2 User's Guide, Version 2.0, Report LBNL-43134, Berkeley, California: Lawrence Berkeley National Laboratory, 1999.
- Pruess, K. and Narasimhan, T.N., A practical method for modeling fluid and heat flow in fractured porous media, *Soc. Pet. Eng. J.*, 25, 14-26, 1985.
- Pruess, K., GMINC-A mesh generator for flow simulations in fractured reservoirs, Report LBL-15227, Berkeley, California: Lawrence Berkeley National Laboratory, 1983.
- Rivas-Gomez et al., Numerical simulation of oil displacement by water in a vuggy fractured porous medium, SPE-66386, Presented at the SPE Reservoir Simulation Symposium, Houston, Texas, 11-14, February, 2001.
- Snow, D.T., A parallel plate model of fractured permeable media, Ph.D. Dissertation, University of California, Berkeley, Californian, 1965.
- Warren, J.E. and Root, P.J., The behavior of naturally fractured reservoirs, *Soc. Pet. Eng. J.*, 245–255, *Trans.*, AIME, 228, 1963.
- Wu, Y.S., C. Ehlig-Economides, G. Qin, Z. Kang, W. Zhang, B. Ajayi, and Q. Tao, A Triple Continuum Pressure Transient Model for A Naturally Fractured Vuggy Reservoir, SPE-110044, presented at the 2007 SPE Annual Technical Conference and Exhibition held in Anaheim, California, 11–14 November 2007
- Wu, Y.S., G. Qin, R.E. Ewing, Y. Efendiev, Z. Kang and Y., A Multiple-Continuum Approach for Modeling Multiphase Flow in Naturally Fractured Vuggy Petroleum Reservoirs, SPE-104173, Presented at the 2006 SPE International Oil & Gas Conference and Exhibition, Beijing, China, 5–7 December, 2006.
- Wu, Y. S., H. H. Liu, And G. S. Bodvarsson, A triple-continuum approach for modeling flow and transport processes in fractured rock, *Journal Of Contaminant Hydrology*, 73, 145-179, 2004.
- Wu, Y.S., Numerical simulation of single-phase and multiphase non-Darcy flow in porous and fractured reservoirs, *Transport In Porous Media*, Vol. 49, No. 2, pp.209-240, 2002.
- Wu, Y.S., On the effective continuum method for modeling multiphase flow, multicomponent transport and heat transfer in fractured rock, Book chapter of “*Dynamics of Fluids in Fractured Rocks, Concepts and Recent Advances*”, AGU Geophysical Monograph 122, American Geophysical Union, Washington, DC, 299–312, 2000a.
- Wu, Y.S., A virtual node method for handling wellbore boundary conditions in modeling multiphase flow in porous and fractured media, *Water Resources Research*, 36 (3), 807-814, 2000b
- Wu, Y.S. and Pruess K., A multiple-porosity method for simulation of naturally fractured petroleum reservoirs, *SPE Reservoir Engineering*, 3, 327-336, 1988.
- Wu, Y.S. and J.L. Ge, The transient flow in naturally fractured reservoirs with three-porosity systems, *Acta, Mechanica Sinica, Theoretical and Applied Mechanics*, Beijing, China, 15(1), 81–85, 1983.

VALIDATION OF MARTHE-REACT COUPLED SURFACE AND GROUNDWATER REACTIVE TRANSPORT CODE FOR MODELING HYDRO SYSTEMS

D. Thiéry, N. Jacquemet, G. Picot-Colbeaux, C. Kervévan, L. André, M. Azaroual

BRGM, Groundwater Division, M2H unit
BP 36009
45060 Orléans, France
e-mail: d.thiery@brgm.fr

ABSTRACT

This paper presents the validation of the computer code MARTHE-REACT enabling the simulation of reactive transport in hydrosystems. MARTHE-REACT results from coupling the MARTHE code (flow and transport in porous media) with the chemical simulator TOUGHREACT. The resulting coupled model takes advantage of the functionalities already available in each of the two codes. In particular, it is now possible to simulate flow, reactive mass, and energy transfer in both saturated and unsaturated media (vadose zone), taking into account the soil-atmosphere exchange (rainfall, evapo-transpiration), and runoff into rivers and infiltration. Four examples of verification are presented in comparison with calculations using the reference coupled codes TOUGHREACT, PHAST, PHREEQC, and MARTHE-SCS.

- 1) Continuous injection of acidified CO₂-rich aqueous phase into a fictitious limestone core sample. Simulations performed with several transport schemes are compared with results from PHREEQC and MARTHE-SCS.
- 2) Injection of CO₂-saturated water into a Dogger carbonate reservoir (Paris Basin, France). The reservoir is modeled with a 2D radial geometry. Chemical simulations are compared with those obtained using the TOUGHREACT code.
- 3) Diffusion of acidified water within a cap rock overlying the Dogger aquifer, in which (hypothetical) large amounts of CO₂ are stored.
- 4) Carbonated brine percolation through a weathered cement sample for 7 days, accounting for coupled advection-diffusion-reactions having various kinetics. These simulations are compared with those obtained with the TOUGHREACT code.

The coupling in MARTHE-REACT is based on a sequential noniterative algorithm, so that parallelization of the chemical calculations has been easily implemented. Preliminary results on a 64-processor computer show a dramatic decrease of needed CPU time, even with a moderately complex geometry.

INTRODUCTION

To accurately model complex, real-world aquifer systems and their chemical interactions, it is necessary to combine a detailed groundwater flow model with a geochemical model. For instance, the PHREEQC (Parkhurst and Appelo, 1999) public domain code couples a very detailed chemical simulator with a simple 1D transport scheme. In addition, PHREEQC has been coupled to several transport codes. For instance, in PHAST (Parkhurst et al.), it is coupled with a 3D transport scheme. In PHT3D (Prommer et al., 2003), it is coupled with a MODFLOW model. In HP1 (Simunek et al. 2006), it is coupled with the 1D vadose zone transport code HYDRUS_1D. TOUGHREACT (Xu et al. 2004) is a widely used multiphase mass and energy transport code integrating a chemical simulator. To model complex hydrosystems, TOUGHREACT has been integrated into the MARTHE (Thiéry, 1990, 1993, 1995a,b, 2007) flow and transport code. This paper presents a validation of this new tool.

NUMERICAL TOOL

The computer code MARTHE-REACT, resulting from the coupling of the flow and transport code MARTHE with the chemical simulator of TOUGHREACT, is briefly described below.

The TOUGHREACT Code

TOUGHREACT is a nonisothermal multicomponent reactive fluid flow and geochemical transport simulator that can be applied under various thermo-hydrological and geochemical conditions of pressure, water saturation, and ionic strength. It is a reference code extensively used for extreme conditions (high temperatures, high pressure, high salinity, etc.).

The MARTHE Flow and Transport Code

MARTHE (Modelling Aquifers with Rectangular cells, Transport and Hydrodynamics) is a 3D code for flow and hydro-dispersive transport in porous media. Mass and energy transfer are modeled in both saturated and unsaturated media using the Richards equation, taking into account soil-atmosphere interactions (rainfall, evapo-transpiration), and runoff into rivers and infiltration. The flow calculations follow a finite volume approach using irregular

parallelepipedic cells, with the possibility of nested grids or radial grids. Based on a kinematic wave approach, flow in river networks is coupled to groundwater flow. Mass and energy transport occur simultaneously in the groundwater system and in the surface network. Several transport schemes are available, which may be selected according to the kind of problem at hand: finite difference transport, method of characteristics (MOC), total variation diminishing (TVD) (Thiéry, 1995a). Temperature and fluid density variations are also taken into account (Thiéry, 2007).

THE COUPLING APPROACH

MARTHE has already been coupled to specific chemical simulators (SCS) (Kervévan et al., 1998, Thiéry 1995b), and the approach used to couple it with the TOUGHREACT chemical simulator is essentially the same. Flow calculations and mass and energy transport are performed by the MARTHE code with no modifications. Chemical simulations are performed by the chemical part of the TOUGHREACT code. The coupling sequence is the following at each time step: (1) coupled flow calculation in aquifers and river networks integrating evaporation, infiltration, runoff, overflow etc.; (2) transport in aquifer and river networks of each primary dissolved chemical species; (3) chemical reactions in each aquifer cell and river reach using the concentrations at the end of the time step. There is no iteration; hence, it is a SNIA (sequential non iterative algorithm) scheme. The important point is that with this sequential scheme, after transport, the chemical reaction calculations are independent in each cell.

This coupling method has several advantages: because the chemical calculations are independent, the chemical reactor extracted from TOUGHREACT is totally independent of any grid or time sequence. As a matter of fact, on each call, the reactor knows only one mesh and one time step duration. This guarantees the independence of both codes and also enables a very simple parallelization. Another advantage is that several chemical simulators may be implemented independently in MARTHE. The user of the code may then select the chemical simulator that is most appropriate to the problem, or the chemical simulator that he/she knows the best.

VALIDATION TEST 1: CONTINUOUS INJECTION OF ACIDIFIED CO₂-RICH AQUEOUS PHASE INTO A FICTITIOUS LIMESTONE CORE SAMPLE

Problem Description

This validation case simulates the percolation of an aqueous solution enriched with CO₂ into a pure calcite cylindrical core initially saturated with a

solution of water, in equilibrium with calcite in atmospheric pCO₂. The simulations were used for the pre-dimensioning and interpretation of experiences with percolation of water acidified by CO₂ dissolved in a Lavoux limestone core (Kervévan et al., 2007). The core properties are given in Table 1.

Table 1. Calcite core geometry and parameters

Core length	10 cm
Core diameter	4 cm
Kinematic porosity	30 %
Longitudinal dispersivity	1 cm
Temperature	25°C
Injection rate	20 cm ³ .h ⁻¹

The composition of the water initially saturating the core was calculated by equilibrating pure water with calcite under atmospheric conditions (CO₂ pressure of 3.16×10^{-4} bar). The composition of the injected water has been calculated by equilibrating pure water containing 5×10^{-7} mol.kg_{H₂O}⁻¹ of CaCl₂ with a 1 bar CO₂ pressure.

Simulations

The concentrations after one hour of injection were calculated with PHREEQC and MARTHE-REACT. The calculations performed with PHREEQC correspond to a discretization of the core into 80 cells 1.25 mm long, with a time step of 84.9 seconds. The time step in PHREEQC is constrained by the need for a Courant number equal to 1; therefore, since the filtration velocity is 0.0147 mm/s, the time step must be set at 84.9 seconds.

Calculations with MARTHE-REACT were performed with 100 cells, different transport schemes and different time steps (10 s or 60 s). Figure 1 and Figure 2 show that the pH profile and dissolved calcium profile calculated with PHREEQC and MARTHE-REACT are very similar, except very near the core ends.

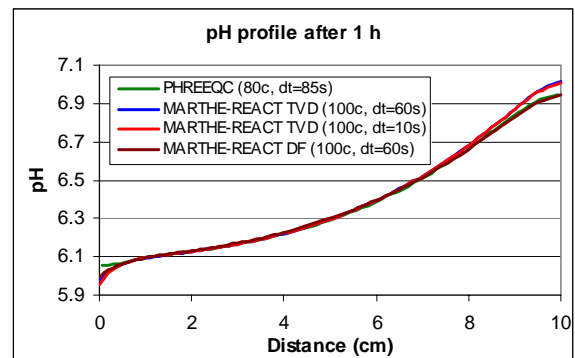


Figure 1. Comparison of pH profile, calculation with PHREEQC and MARTHE-REACT.

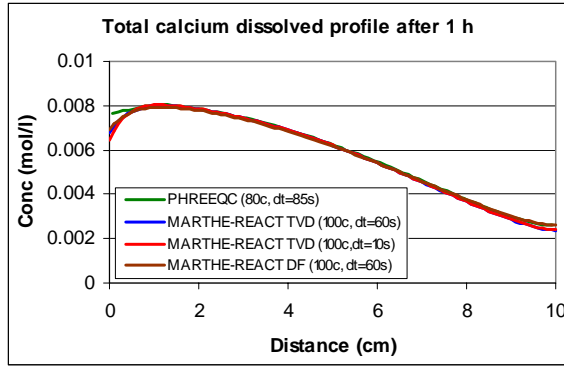


Figure 2. Comparison of total dissolved calcium concentration profile. Calculation with PHREEQC and MARTHE-REACT.

Calculations with MARTHE coupled with specific chemical simulators (MARTHE+SCS) yielded comparable results (Kervévan et al., 2007). Also note that the calculations are much faster with MARTHE-REACT: 1 second of CPU time for 100 cells and 100 time steps, as compared to 600 seconds of CPU time for PHREEQC for 80 cells and 43 time steps.

VALIDATION TEST 2: INJECTION OF CO₂ SATURATED WATER INTO A DOGGER CARBONATE RESERVOIR

Problem Description

This validation case, following the work of André et al. (2007), uses a simple 2-D radial model to simulate the CO₂ behavior near the injection well of the Dogger Reservoir (Paris Basin, France). The well field is modeled (Figure 3) as a circular region of 100,000 m radius and 20 m thickness. At the center, a well injects dissolved CO₂ into the formation water.

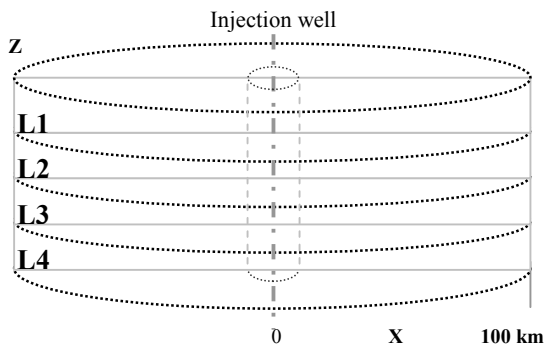


Figure 3. Two-dimensional radial geometry of the Dogger reservoir model with four layers (L1, L2, L3 and L4).

Porosity and permeability are homogeneous. The formation parameters are given in Table 2. The reservoir temperature is assumed to be uniform (75°C), and a hydrostatic pressure is considered

initially as fixed in the outermost column of the grid during the simulation. No exchanges of fluids are considered above or below the system.

Table 2. Injection of CO₂ into the Dogger reservoir: geometry and parameters.

Aquifer thickness	20 m
Permeability	1.10^{-13} m^2
Compressibility	Water compressibility only
Kinematic porosity	15 %
Diffusion	0
Dispersivities	0
Temperature	75°C
Transport method	Finite Differences
Total injected flow	$20.10^{-3} \text{ m}^3/\text{s}$

The injected solution corresponds to the formation water in equilibrium at 75°C with a CO₂ pressure of 180 bars (the initial reservoir pressure). Consequently, to be in equilibrium with this gas phase at such pressure, the water contains 1.25 moles of carbonates / kg H₂O.

The reservoir composition is defined in the André et al. simulation (2007) and initially contains a solution at equilibrium with the reservoir rocks at a constant temperature of 75°C. The chemical composition of the formation water and injected CO₂-saturated water are presented in Table 3. The 12 minerals of reservoir rock are similar to the André et al. study, including 70% calcite, 10% dolomite, 5% siderite, 5% illite, 5% albite and 5% K-feldspar (in volume fraction). Kaolinite, chalcedony, magnesite, dawsonite, anhydrite, and halite are not initially present in the reservoir, but are allowed to precipitate. Dissolution and precipitation of minerals follow kinetic laws.

Table 3. Chemical composition of formation water and injected water (in mol/kgH₂O)

Formation water		CO ₂ -saturated water	
Temperature	75 °C	Temperature	75 °C
pH	6.7	pH	3.0
Alkalinity	427.0	Total Carbon	1.080
Na	$7.734 \cdot 10^{-2}$	Na	$7.734 \cdot 10^{-5}$
K	$9.051 \cdot 10^{-4}$	K	$9.051 \cdot 10^{-7}$
Ca	$2.860 \cdot 10^{-3}$	Ca	$2.860 \cdot 10^{-6}$
Mg	$2.777 \cdot 10^{-3}$	Mg	$2.777 \cdot 10^{-6}$
Al	$1.976 \cdot 10^{-7}$	Al	$1.976 \cdot 10^{-10}$
Fe	$2.856 \cdot 10^{-5}$	Fe	$2.856 \cdot 10^{-8}$
Cl	$7.049 \cdot 10^{-2}$	Cl	$7.049 \cdot 10^{-5}$
SO ₄	$6.985 \cdot 10^{-3}$	SO ₄	$6.985 \cdot 10^{-6}$
SiO ₂	$8.476 \cdot 10^{-4}$	SiO ₂	$8.476 \cdot 10^{-7}$

Simulations

The geologic formation is assumed to be infinite-acting and homogeneous, with a total thickness of 20 m. A 2D radial grid (X, Z) has been chosen. The aquifer thickness (Z axis) is divided into four layers

(L1, L2, L3 and L4), and the radial direction (X axis) is divided into 100 columns, with radius following a logarithmic progression starting from 0.2 m for the injection well to 10.115 m at the outermost limit, 100,000 m away. The total grid then has 400 cells.

Simulations are realized for 1 year of CO₂-saturated water injection with MARTHE-REACT and TOUGHREACT. Effects of temperature on flow are taken into account in both simulations. Due to the water compressibility, the hydraulic calculation is performed in a transient state. Because of the small size of the injection cell, a time step of 24 seconds was selected for the entire simulation (after some smaller time steps at the very beginning).

Simulation results (Figure 4) are compared in terms of pH (A), porosity (B) and variation of minerals— (C) carbonates and (D): alumino-silicates. The results are identical in the four layers; only the first layer profiles along the radial distance from the injected well are presented. One can observe an acidification of the reservoir in the first few meters around the well (pH = 3) involving total dissolution of carbonates (calcite and dolomite) and minor dissolution of alumino-silicates (Albite, K-feldspar and illite). This high dissolution has an impact on porosity, which increases (15% initially and 87% after 1 year).

Further within the reservoir, pH is controlled by calco-carbonic equilibrium (pH = 4.8) where carbonates are still present. In the nonaffected zone, minor chemical reactions occur where formation water is at near-equilibrium with mineralogical assemblage. Within these simulations all the observations related to chemical reactivity are similar to André et al results (2007). MARTHE-REACT and TOUGHREACT results are identical.

Similarly, simulations have been done for a reactivity study of the Keuper sandstone aquifer, using the MARTHE-REACT simulator. The work is described by Picot-Colbeaux et al. (2009, in the same Tough Symposium) where the aquifer is represented by a 2D radial geometry with three layers, each layer having their own permeability and porosity. In this case, flow, chemical reactivities, and transport vary between layers, from the injected well to the outermost column.

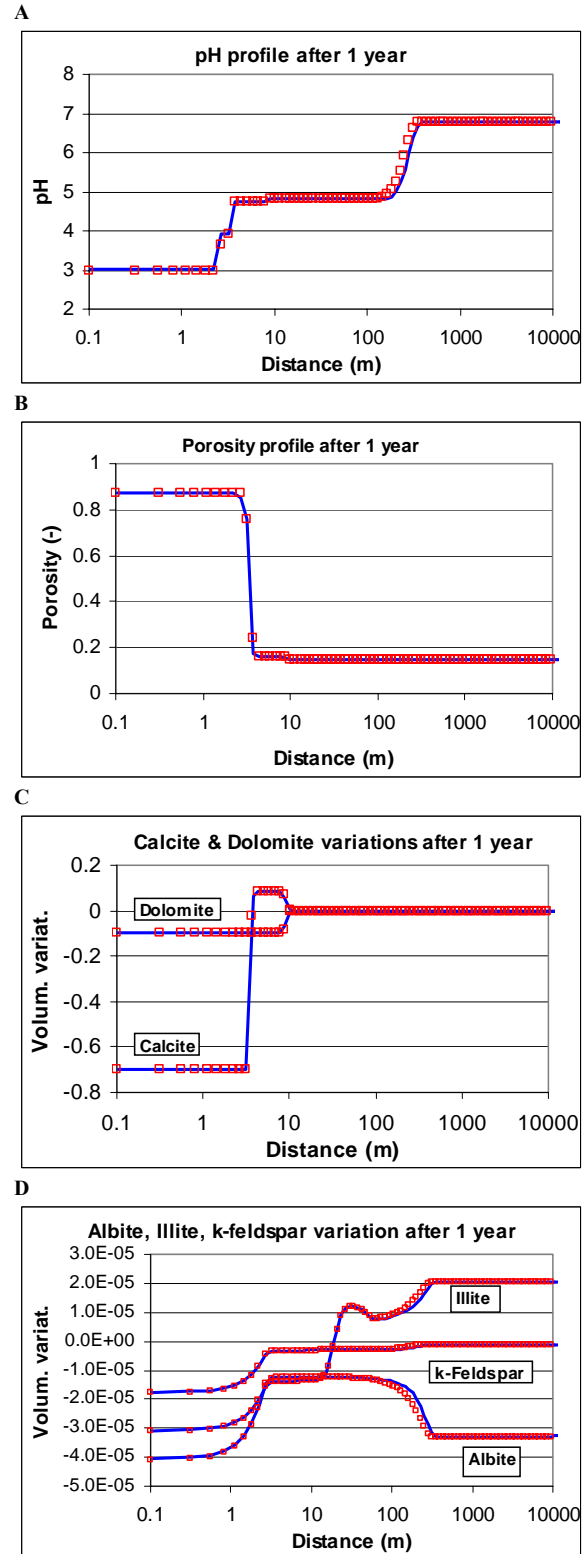


Figure 4. Variation of pH, porosity and mineral volume fractions (V_{min}/V_s) in the first layer of Dogger aquifer from the injection cell to the outermost after 1 year of CO₂-saturated water injection. MARTHE-REACT (solid line) and TOUGHREACT (open squares).

VALIDATION TEST 3: DIFFUSION OF ACIDIFIED WATER WITHIN A CAP ROCK OVERLYING THE DOGGER AQUIFER

Problem Description

This validation case hypothetically simulates the vertical diffusion of acidified water from the Dogger aquifer into its overlying clay cap rock (Kervévan et al., 2009). The cap-rock formation is mainly composed of calcite, montmorillonite-Na, and quartz. There are eight primary minerals, initially present in the formation, and four secondary minerals. Because the permeability is very low, the advection flow is considered as negligible, and only molecular diffusion is taken into account. The system is modeled as a vertical 1D domain, with vertical dimension large enough to be considered as semi-infinite during the simulation duration of 10,000 years (Table 4).

Table 4. Clay caprock geometry and parameters.

Domain length	10 m
Kinematic porosity	15 %
Diffusion	$10^{-11} \text{ m}^2 \cdot \text{s}^{-1}$
Temperature	80°C
Transport method	Finite Differences

The acidified water in the Dogger aquifer, at the lower end of the domain, is a brine at 80 °C, with a CO₂ pressure of 150 bars and pH of approximately 4.8. The initial brine in the cap rock, mainly composed of NaCl (0.26 mol/kgw), has a pH of approximately 6.5. The detailed mineralogy and brine compositions assumed, as well as the kinetic laws used for describing dissolution and precipitation processes, lead to a relatively complex coupled problem that includes 12 mineral phases.

Simulations

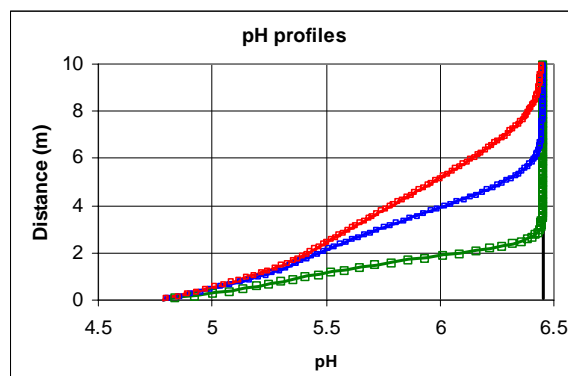
Coupled transport and reactions have been simulated with MARTHE-REACT, TOUGHREACT, PHREEQC, and PHAST. The domain was discretized into 100 cells of 10 cm length. For MARTHE-REACT simulations, the 10,000-year simulation period was divided into 6 small time steps, followed by 1,999 time steps of 5 years duration. TOUGHREACT also used time steps of 5 years after 30 time steps increasing progressively. Figure 5 and Figure 6 compare, for some dissolved elements and some minerals, the concentration profiles calculated with MARTHE-REACT (solid line) and with TOUGHREACT (open squares). These figures show that the simulation results are identical. Simulations were also performed with PHREEQC and PHAST codes, with chemical formulations and water compositions approximately the same. The results with PHAST, described in Kervévan et al. (2009), are comparable with MARTHE-REACT (or TOUGHREACT) for the pH and dissolved carbon

profiles—reasonably close for some minerals and quite different for others. The discrepancies are most probably due to the differences in the TOUGHREACT and PHREEQC chemical reactors.

Parallelization

A simple parallelization of the chemical calculations has been implemented in MARTHE-REACT code. This same simulation on a cluster of 16 processors resulted in a reduction of the CPU time by a factor of 11, compared to a nonparallel simulation on the same computer.

A



B

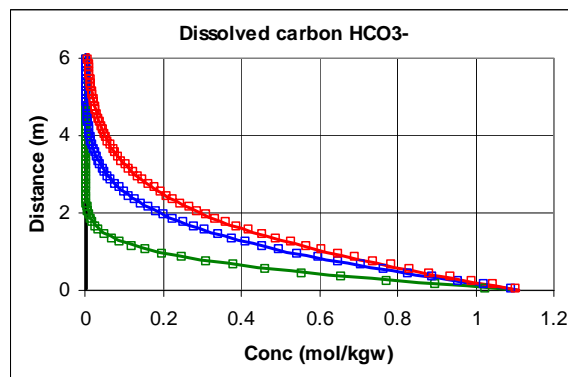


Figure 5. Diffusion in clay caprock: Profiles after 1000 years (green), 5000 years (blue) and 10000 years (red). A: pH, B: Dissolved carbon. MARTHE-REACT (solid line) and TOUGHREACT (open squares)

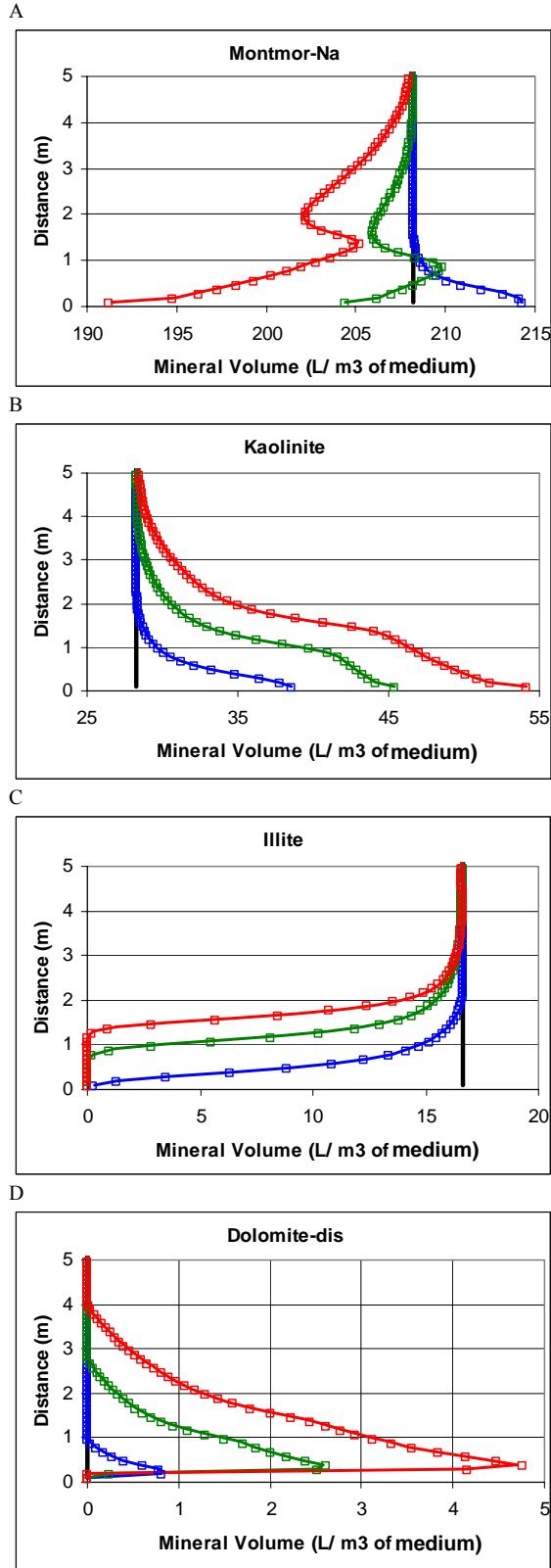


Figure 6. Diffusion in clay caprock: Profiles after 1000 years (blue), 5000 years (green) and 10000 years (red). A to D: minerals. MARTHE-REACT (solid line) and TOUGHREACT (open squares)

VALIDATION TEST 4: CARBONATED BRINE PERCOLATION THROUGH A POROUS CEMENT

Leakage via the cement sheath of the wells is an issue for the long-term safety of CO₂ geological storage. The reactivity of cement with the fluids (gas, brine) occurring in the host reservoir at high pressure and high temperature can result in their alteration. Well cement-CO₂ interactions in the context of CO₂ geological storage have been investigated via reactive transport modeling (Jacquemet, 2006; Carey and Lichtner, 2007) with the aim of reproducing *in situ* or experimental observations. As a test, we modeled, with MARTHE-REACT, the percolation of a carbonated brine through a cementitious porous channel. This feature represents a defect in a well cement sheath. The model is based on an experiment by IFP (French Institute of Petroleum). This percolation experiment has already been modeled with TOUGHREACT by Jacquemet (2009) in the framework of the CO2GEONET project (Rochelle et al., 2009).

Problem Description

An acid brine percolates over 7 days through a 40 mm long cementitious porous channel, whose properties are given in Table 5. The cement is initially composed of four primary minerals, and later, of 5 potential secondary minerals (Table 6). The initial interstitial cement water results from the equilibrium of pure water with the primary cement minerals, and hence is very basic: its pH is 10.8. The injected water is composed of a NaCl solution (0.4 mol/kgw) equilibrated with a CO₂ pressure of 5 bar at a temperature of 80°C: its pH is 3.5.

Table 5. Cement porous channel geometry and parameters.

Length	40 mm
Permeability	3.5 10 ⁻¹⁵ m ²
Kinematic porosity	60 %
Diffusion	0
Longitudinal dispersivity	0
Temperature	80°C
Transport method	Finite Diff.

Table 6. Initial cement mineral assemblage.

Mineral	% Volume
Calcium Silicate Hydrates (CSH 1.6, C/S=1.6)	60
Portlandite (CH)	20
Katoite	10
Calcium monosulfoaluminate (AFm)	10
CSH 1.2 (C/S=1.2)	0
CSH 0.8 (C/S=0.8)	0
Amorphous silica, calcite and aragonite	0

Simulations

The coupled transport and reaction was simulated with MARTHE-REACT and TOUGHREACT. The core was discretized into 100 cells of 0.4 mm length. The 7-day simulation period was divided into time steps of 2 seconds duration. This time-step duration was chosen because it corresponds to a reasonable Courant number of 1.02.

Figure 7 and Figure 8 compare profiles calculated with MARTHE-REACT and with TOUGHREACT. The profiles show that the simulation results are very close. A small discrepancy appears: the reactions with TOUGHREACT are slightly faster (around 1 or 2%), which might result from a small difference in the hydraulic parameter definition. The models predict very similar evolutions. Because of the slow reaction kinetics compared to the quick advection, the pH decreases dramatically, which results in a strong dissolution of the cement. Porosity increases from 60% to ~100% after 3 days of injection.

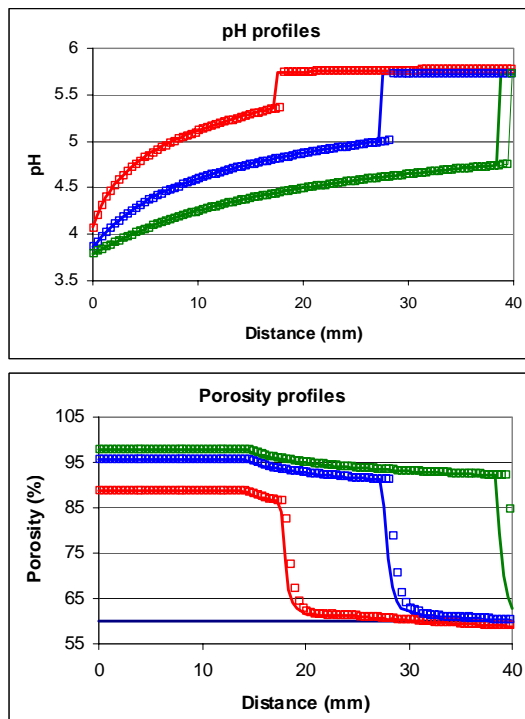


Figure 7. Carbonated brine percolation through a cement. Profiles after 1 day (red), 2 days (blue) and 3 days (green). Top: pH, bottom: porosity. MARTHE-REACT (solid line) and TOUGHREACT (open squares).

Note that a transient calcite precipitation (up to 3 days) allows the initial porosity to be conserved in the second half of the channel. Amorphous silica deposits quickly at a distance of 14 mm and reaches a 6% volume fraction, without the possibility of dissolving. This is the only mineral significantly

present at the end of the simulation, and the resultant porosity is 94 %.

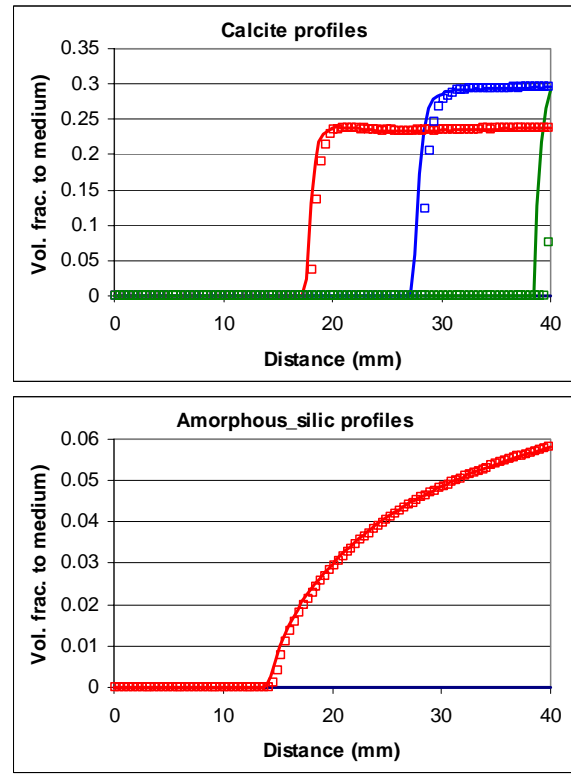


Figure 8. Carbonated brine percolation through a cement. Profiles after 1 day (red), 2 days (blue) and 3 days (green). Top: calcite, bottom: amorphous silica. MARTHE-REACT (solid line) and TOUGHREACT (open squares).

CONCLUSIONS

A set of coupled reactive transport simulations performed with the MARTHE-REACT code was compared with TOUGHREACT and other codes. It appears that the results are the same, which is a verification of the coupling of TOUGHREACT chemical simulator with the MARTHE code. The value of MARTHE-REACT is that it integrates efficient transport schemes and is adapted to the simulation of unconfined aquifers and complex hydrosystems. Validation of reactive transport simulations through the vadose zone are scheduled.

ACKNOWLEDGMENT

The research described in this paper was carried out in the framework of the "PROCHE PUITs" project, financially supported by the ANR (French National Research Agency) and the Research Division of BRGM.

REFERENCES

- André, L., P. Audigane, M. Azaroual, A. Menjot, Numerical modeling of fluid-rock chemical interactions at the supercritical CO₂-liquid interface during CO₂ injection into a carbonate reservoir, the Dogger aquifer (Paris Basin, France), *Energy Conversion & Management*, 48, 1782-1797, 2007.
- Carey, J.W., Lichtner, P.C., *Calcium silicate hydrate (C-S-H) solid solution model applied to cement degradation using the continuum reactive transport model FLOTRAN*. In : Mobasher, B. and Skalny, J., editors, *Transport Properties and Concrete Quality: Materials Science of Concrete*, Special Volume, pp. 73-106. American Ceramic Society; John Wiley & Sons, Inc. 2007
- Jacquemet, N., Durabilité des matériaux de puits pétroliers dans le cadre d'une séquestration géologique de dioxyde de carbone et d'hydrogène sulfuré. Thèse, Université Henri Poincaré, Nancy. 2006. Available on: <http://tel.archives-ouvertes.fr/tel-00084391/>.
- Jacquemet, N., Reactive transport modelling of a carbonated brine percolation experiment through a well cement. BRGM report No. BRGM/RP-57183-FR, part of the Deliverable 3, JRAP-14, CO₂GEONET project, 30 p, 2009, restricted.
- Kervévan, C., Lanini S., Audigane P., *Étude comparative des algorithmes de couplage des codes chimie-transport utilisés au BRGM*, Report BRGM/RP-54904-FR, 66 p., 11 Fig., 2007.
- Kervévan, C., Audigane, P., Jacquemet, N., *Géocarbonate « Intégrité », volet 5 : Modélisation de l'impact géochimique d'un stockage de CO₂ sur la couverture sus-jacente*. Report BRGM/RP-57220-FR, 106 p., 51 fig., 2009.
- Kervévan, C., Thiéry D., Baranger P., SCS: Specific Chemical Simulators dedicated to chemistry-transport coupled modelling Part III - Coupling of SCS with the hydro-transport modelling software MARTHE. Goldschmidt Conference 1998, Toulouse, Mineralogical magazine, Vol. 62 A, p. 773-774, 1998.
- Parkhurst, D.L., Appelo, C.A.J., *User's guide to PHREEQC (version 2): a computer program for speciation, batch-reaction, one-dimensional transport, and inverse geochemical calculations*. U.S.G.S. Water Investigations Report 99-4259, 312pp, 1999.
- Parkhurst, D.L. Kipp, K.L., Engesgaard, P. and S.C. Charlton, PHAST — *A program for simulating ground-water flow, solute transport and multicomponent geochemical reactions*, U.S.G.S. Techniques and Methods vol. 6-A8 154 pp., 2004.
- Picot-Colbeaux, G., Pettenati M., Thiéry D., Kervévan C., André L., Azaroual M., Numerical modeling of fluid-rock chemical interactions during CO₂ saturated water injection into a sandstone reservoir using MARTHE-REACT code, TOUGH Symposium 2009, 14-16 September, submitted.
- Prommer, H., Barry, D., and Zheng, C., PHT3D - A MODFLOW/MT3DMS based reactive multi-component transport model. *Ground Water*, 42 (no. 2): 247-257, 2003.
- Rochelle, C., Milodowski, A.E., Bateman, K., Lécolier, E., Jacquemet, N., Durucan, S., Shi, Ji.-Q., *Report on laboratory experiments and modelling*. Deliverable JRAP-14/3, CO₂GEONET project, 2009, restricted.
- Simůnek, J., Jacques, D., Van Genuchten, M.T. and D. Mallants, Multicomponent geochemical transport modeling using Hydrus-1D and Phreeqc. *JAWRA*, 42(6), 1537-1547, 2006.
- Thiéry, D., *Software MARTHE. Modelling of Aquifers with a Rectangular Grid in Transient state for Hydrodynamic calculations of hEads and flows. Release 4.3*. Report BRGM 4S/EAU n° R32548, 1990.
- Thiéry, D., Modélisation des aquifères complexes - Prise en compte de la zone non saturée et de la salinité. Calcul des intervalles de confiance. *Revue Hydrogéologie*, 1993, n° 4, p. 325-336.
- Thiéry, D., *Modélisation 3D du transport de masse avec le logiciel MARTHE version 5.4*. Report BRGM R 38149 DR/HYT 95, 171 p. 1995a.
- Thiéry, D., *Modélisation des écoulements avec interactions chimiques avec le logiciel MARTHE. Version 5.5*, Report BRGM n° R 38463 HYT/DR 95. 1995b.
- Thiéry, D., *Modélisation 3D des écoulements à densité variable avec le logiciel MARTHE version 6.9*. Report BRGM n° RP-55871-FR, 88 p., 23 fig., 2007.
- Xu, T., Sonnenthal E., Spycher N., Pruess K., *TOUGHREACT User's Guide: A Simulation Program for Non-isothermal Multiphase Reactive Geochemical Transport in Variably Saturated Geologic Media*, Lawrence Berkeley National Laboratory Report LBNL-55460, 2004.

AN UPDATE ON PETRASIM—CURRENT STATUS AND FUTURE DEVELOPMENTS

Daniel Swenson¹, Alison Alcott², Brian Hardeman¹

¹Thunderhead Engineering, 403 Poyntz Ave., Suite B, Manhattan, KS, 66502
1.785.770.8511, swenson@thunderheadeng.com

²RockWare Inc., 2221 East St. #1, Golden, CO 80401
1.303.278.3534 x108, alison@rockware.com

ABSTRACT

PetraSim, a graphical user interface for TOUGH2 model creation, analysis, and results display, has undergone continual development since its first release in August, 2002. PetraSim supports TOUGH2, T2VOC, TMVOC, TOUGHREACT, TOUGH-Fx/HYDRATE. It allows the analysts to focus on the model, while automatically handling the complex details of simulator input and results. The TOUGH2 versions of PetraSim include the corresponding TOUGH2 simulation software executables. PetraSim is currently at version 4.2 and includes support for ECO2N, the equation of state used to model carbon sequestration.

New features to be included in version 5.0 include: grid-independent description of the conceptual model; import of existing TOUGH2 models created using Meshmaker; improved import of geometry from Surfer and other modeling software; support for larger models using TOUGH2-MP, the parallel version of TOUGH2; and several other interface enhancements.

Use of PetraSim and the TOUGH2 programs will be demonstrated in this poster session.

PETRASIM FEATURES

PetraSim provides four key features that help speed and simplify the use of the TOUGH2 and TOUGH-Fx family of codes: (1) use of a high-level model description based on geometric features of the reservoir, (2) presentation of the required input options grouped in a logical format with appropriate default options activated, (3) automatic writing and execution of the input file, and (4) rapid access to visualization of results. PetraSim is interactive, with immediate visual confirmation of any user actions.

Problem Description/Conceptual Model

PetraSim allows the user to define regions and wells as high-level geometric entities, independent of the grid. For example, *Figure 1* shows a model in which internal material boundaries, once defined, can then be used to assign properties to the regions created by the boundaries. This description is independent of the

mesh. When the grid is created, the cell properties will inherit the proper material values and initial conditions from the region in which they are located.

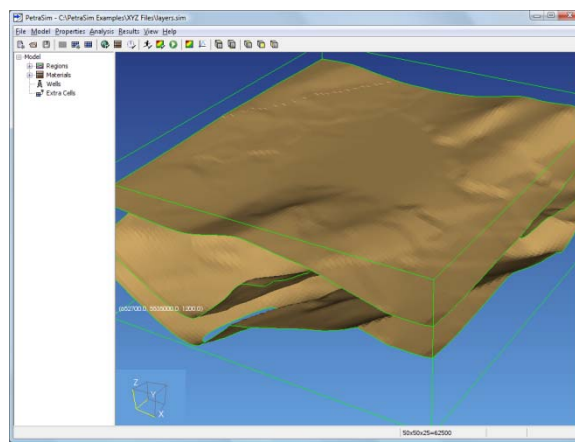


Figure 1. Model with internal material boundaries

Figure 1 also illustrates several options for high-level interaction with the model. On the left of the window is a tree that displays features in the model. Using the tree, the user can select a specific feature. Alternately, the model can be manipulated in the 3D display and features selected with the mouse. In either case, once a feature is selected, all associated properties can be modified.

Grid Definition

An appropriate grid for an analysis must satisfy several constraints: (1) it must be able to capture the essential features of the reservoir, such as stratigraphic layers with different material properties; (2) it must be sufficiently refined to accurately represent regions of high gradient in the solution; and (3) it must satisfy the requirements of the simulator for proper convergence of the solution. A prismatic 3D grid is guaranteed to satisfy the convergence requirements of TOUGH2 and is used in PetraSim.

PetraSim gives the option of creating grids by simply specifying the number of cells to be used on each edge (along with an optional size factor for geometrically increasing cell sizes) or the option of using an input similar to the Meshmaker input for TOUGH2. To specify the Meshmaker input, the user

fills a table that defines the direction, number of repeated cells, and the cell sizes. There is no limitation on grid size.

In addition, the user can specify contours that define the top and bottom of the grid. This can be used to represent topography, such as mountains and valleys. Above and below this contour, the cells will be disabled and not included in the analysis. A grid created using internal boundaries and a contour to define the surface topography is illustrated in **Figure 2**. As can be seen, the disabling of cells enables the representation of topography, while still maintaining the proper convergence properties for TOUGH2.

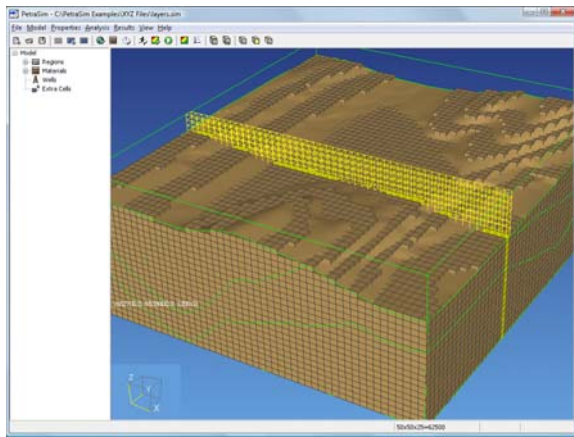


Figure 2. Prismatic grid defined on model

In the future, more general grids can be added, since TOUGH2 uses the integral finite difference method. However, for convergence to the correct solution, the integral finite difference method requires that the mesh satisfy the Voronoi condition (that is, boundaries of the elements must be formed by planes which perpendicularly bisect the lines between volume centers). Generation of such grids is relatively simple in 2D, but algorithms are much more complex for a general 3D Voronoi grid.

Gridlines can be edited, deleted, or inserted interactively. This editing is performed in the Grid Editor window. It is important to remember that the model has a grid, but the grid is not the model. The model is a higher level, grid-independent, description of the reservoir.

Input of Model Properties

A properly designed user interface can guide the user through the model definition process, organizing into logical groupings input that may appear in many locations in a simulator input file. The interface can ease learning for a beginning user and act as a reminder for an experienced user.

The definition of material properties in TOUGH2 is shown in **Figure 3**. The left pane allows the user to select any existing material or create a new one. In the right pane, the user can edit properties of the selected material. This includes MINC data (only activated if the MINC option has been enabled) and, under Relative Perm, the capability to select and preview relative permeability and capillary functions, as shown in **Figure 4**.

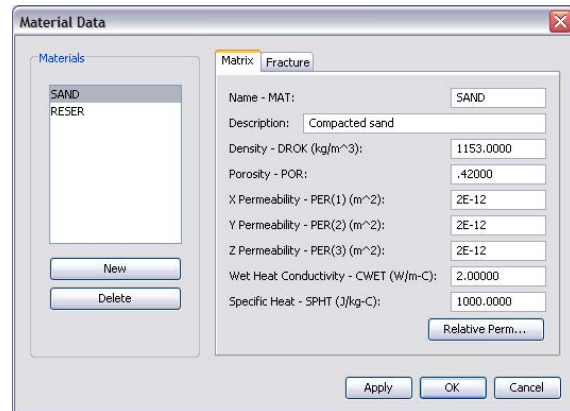


Figure 3. TOUGH2 material definition

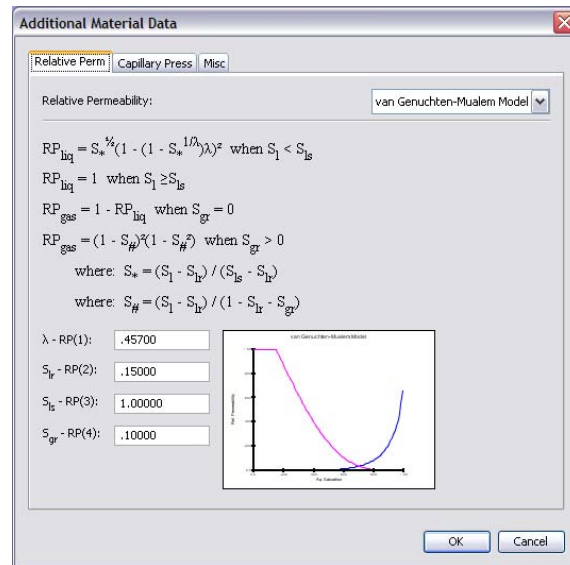


Figure 4. Selection and preview of relative permeability functions

Figure 5 illustrates the organization of the solution parameters of TOUGH2. Again, common parameters have been grouped in an arrangement that helps the user understand and specify all parameters from one location. Similar organization is used for the solver and other solution parameters.

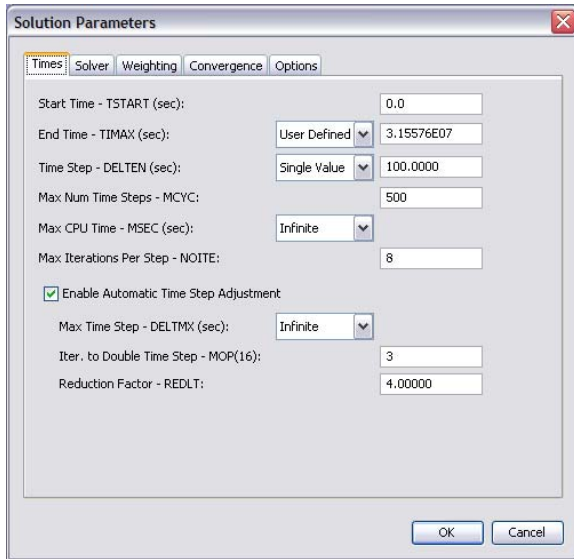


Figure 5. Solution controls dialog

Editing of Cell Properties

After the grid is defined, cell properties may be edited directly. This is accomplished in the Grid Editor window, which allows the user to select a grid layer and edit any cell in that layer (Figure 6). The user can view the grid on any plane (XY, YZ, XZ) and on any layer in that plane.

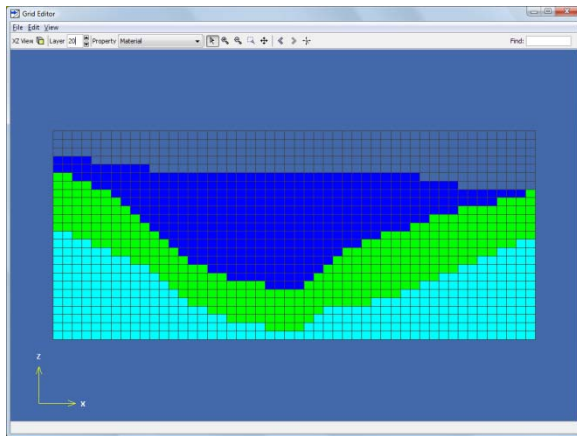


Figure 6. Grid editor

To help orient the user to which cells are being edited, PetraSim can highlight the current layer being edited. In the Grid Editor, the user can also select cells to define sources and sinks (Figure 7).

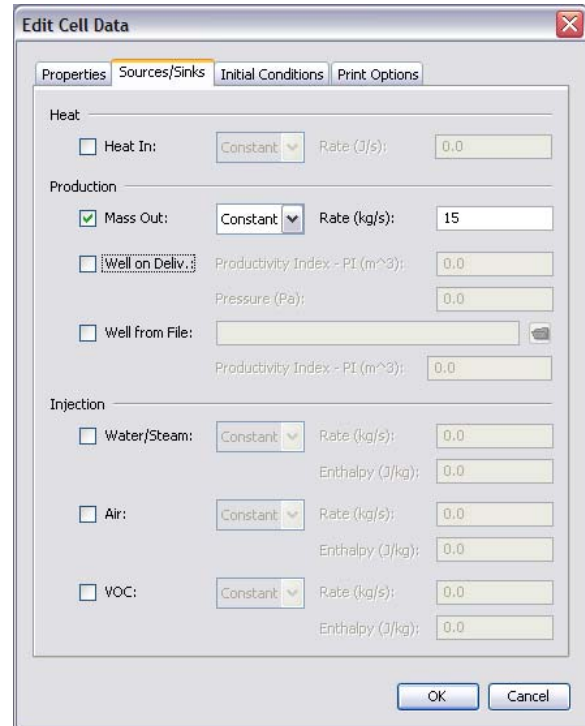


Figure 7. Defining a source or sink in the Grid Editor

Writing a Simulator Input File

The purpose of a pre-processor is to automatically write the simulator input file in a correct format and without intervention by the user. In PetraSim, this task is performed by a function that accesses the model, the grid, and all other data necessary to write the file.

A portion of an example file is shown in Figure 8. Since the TOUGH2 program has not been modified, the input file written by PetraSim is in standard TOUGH2 format. Because PetraSim is writing the file, there is no need to keep the file small. Each element, connection, and initial condition is written explicitly. It can also be seen that the elements are given sequential numerical names. It is intended that the user never need know or examine these names. Any type of data, such as the definition of a source or sink, knows the associated cell and correctly writes the cell name when the simulator input file is written.

The resulting input file is correctly formatted and ready for input to TOUGH2.

```

3dfivespot.dat - Notepad
TOUGH2 Analysis
ROCKS-----1-----2-----3-----4-----5-----6-----7-----8
POMED 3 2650.0 0.010000 6.00e-015 6.00e-015 2.1000 1000.0
      0.0 0.0 2.1000 0.0 0.0
      3 0.300000 0.050000
      1 0.0 1.0 0.0 0.0
MULTI-----1-----2-----3-----4-----5-----6-----7-----8
      1 2 6
PARAM-----1-MOPF 1.23456789012345678901234-----5-----6-----7-----8
8 1 200 1.00000000 0000 03 000 0 1.9000
      0.0 1.50e+009 100.0 0.0 0.0 9.8100 4.0 1.0
      1.00e-005 1.0 1.0 1.0
SOLVR-----1-----2-----3-----4-----5-----6-----7-----8
5 Z1 00
ELEM-----1-----2-----3-----4-----5-----6-----7-----8
1 POMED 110028.86 0.0 -476.1905 22.7273 -279.5833
2 POMED 110028.86 0.0 -428.5714 22.7273 -279.5833
3 POMED 110028.86 0.0 -390.9524 22.7273 -279.5833
4 POMED 110028.86 0.0 -333.3333 22.7273 -279.5833
5 POMED 110028.86 0.0 -285.7143 22.7273 -279.5833
6 POMED 110028.86 0.0 -238.0952 22.7273 -279.5833
7 POMED 110028.86 0.0 -190.4762 22.7273 -279.5833
8 POMED 110028.86 0.0 -142.8571 22.7273 -279.5833
9 POMED 110028.86 0.0 -95.2381 22.7273 -279.5833
10 POMED 110028.86 0.0 -47.6190 22.7273 -279.5833
11 POMED 110028.86 0.0 -1.28e-013 22.7273 -279.5833
12 POMED 110028.86 0.0 47.6190 22.7273 -279.5833
13 POMED 110028.86 0.0 95.2381 22.7273 -279.5833
14 POMED 110028.86 0.0 142.8571 22.7273 -279.5833
15 POMED 110028.86 0.0 190.4762 22.7273 -279.5833
16 POMED 110028.86 0.0 238.0952 22.7273 -279.5833
17 POMED 110028.86 0.0 285.7143 22.7273 -279.5833
18 POMED 110028.86 0.0 333.3333 22.7273 -279.5833
19 POMED 110028.86 0.0 380.9524 22.7273 -279.5833
20 POMED 110028.86 0.0 428.5714 22.7273 -279.5833
21 POMED 110028.86 0.0 476.1905 22.7273 -279.5833
22 POMED 110028.86 0.0 476.1905 68.1818 -279.5833
23 POMED 110028.86 0.0 -428.5714 68.1818 -279.5833
    
```

Figure 8. Portion of TOUGH2 input file created by PetraSim

Integrated Solution

Thunderhead Engineering has received a license from the U.S. Department of Energy that allows the integrated distribution of TOUGH2 executables. Therefore, to run the analysis, all the user needs to do is select Analysis->Run TOUGH2, and the analysis will proceed, using the integrated executable. During the solution, progress is displayed (Figure 9).

If the user owns their own license for the TOUGH2 source code (which can be obtained separately from the U.S. DOE), PetraSim can be used to write the input file. Then the user can edit the input file to accommodate any specific input changes needed to run their version of TOUGH2.

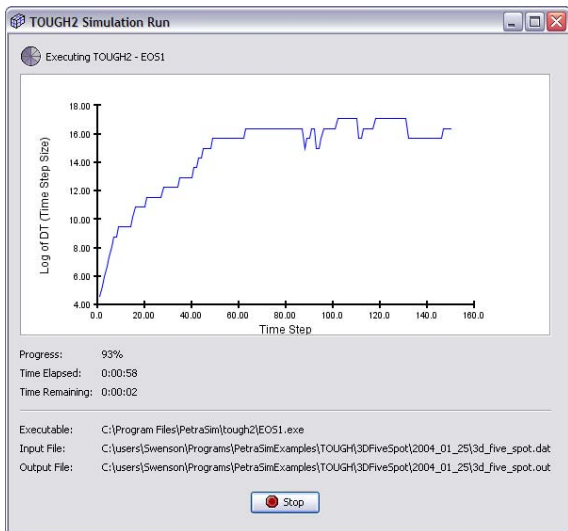


Figure 9. Graphical display of solution progress and time step size

Visualization

After the solution is completed, either 3D or time history plots of the results may be made. Figure 10 shows an example of an iso-surface plot of temperature. PetraSim uses a common results display component for all simulators. Extensions to TOUGH2 output comma separated value (CSV) files in addition to the normal simulator-specific output. The CSV files provide a consistent format that can be used by both PetraSim and external tools such as MS Excel.

As shown in Figure 10, once the data is read, the user can select any available variable and time for plotting. The user can rotate, pan, and zoom the image interactively. Image details, such as the number of iso-surfaces and the data range, can be controlled. Also, cutting planes can be defined on which the results are contoured. Vectors can be used to display items such as fluid flow. Finally, the user can export the data in a simple X, Y, Z, value format for import into other presentation quality graphics programs, such as TECPLOT. In PetraSim, results are readily accessible to rapidly evaluate the analysis.

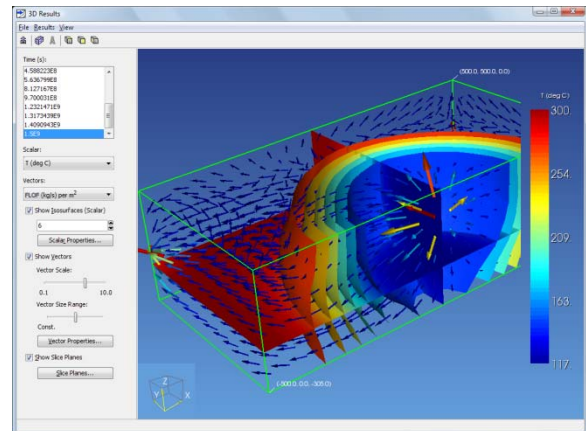


Figure 10. Iso-surface plot of temperatures

In a similar manner, time history plots of results may be made (Figure 11). A common time history display component is used, with different translators to read the different simulator results files. For TOUGH2, the FOFT file is read.

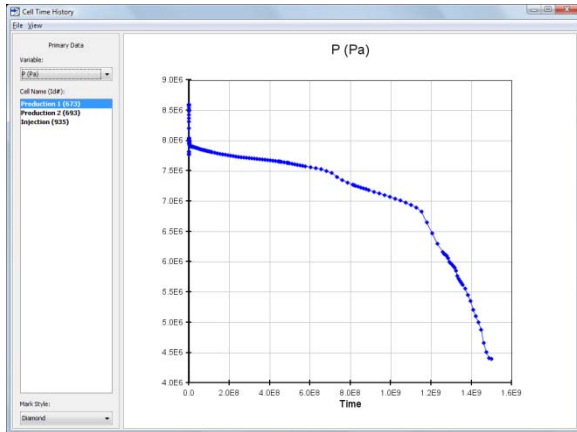


Figure 11. Time history plot (from TOUGH2 FOFT file)

As illustrated in **Figure 11**, the user can select any saved data and make a time history plot. If a cell was given a user-defined name, this name will be available for selecting the plot data. Once any plot is made, the data can be exported in a format that can be read in a spreadsheet or other presentation quality graphics program.

OTHER FEATURES IN PETRASIM

Some of the other features in PetraSim include:

- Support for nongeometric “extra cells” in the model. Many modelers use nongeometric cells to represent special boundary conditions. The user can input a table of cells, defining the connections to existing cells in the model.
- The ability to add an image, such as a map, in the 3D view (**Figure 12**).
- A find cell feature in the 2D grid editor that allows the user to search for a cell by cell ID.
- Line plots to visualize results along a line in 3D.
- PetraSim User and Examples Manuals.

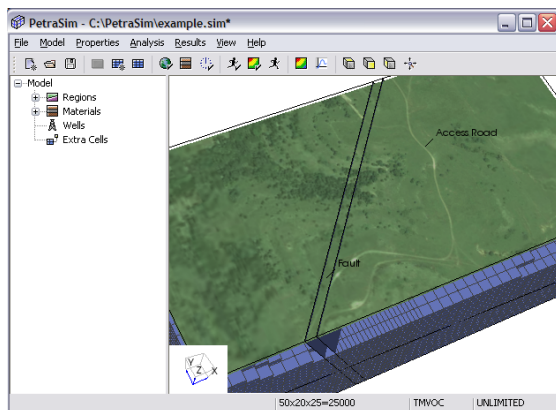


Figure 12: Graphic image superimposed on model

FEATURES TO BE INCLUDED IN VERSION 5

Development has begun on version 5 of PetraSim. Some of the features to be included are:

- Extension of the grid-independent conceptual model to include assignment of boundary conditions by feature, rather than assignment by cell. The goal is for the model to become completely independent of the mesh.
- Import of existing TOUGH2 models that use Meshmaker grids.
- Improved import of geometry from Surfer and other modeling software.
- Support for larger models using TOUGH2-MP, the parallel version of TOUGH2.
- User interface enhancements such as speeding the opening and display of large models.

OBTAINING PETRASIM

A 30-day trial version of PetraSim can be downloaded at www.petrasim.com. Sales are through RockWare (www.rockware.com). Licenses are available for education (free), research, and commercial use.

ACKNOWLEDGEMENTS

Original development of PetraSim was a joint venture between Thunderhead Engineering and GeothermEx, with primary funding from a Department of Energy Phase II Small Business Innovative Research grant.

REFERENCES

Pruess, K., C. Oldenburg, and G. Moridis, TOUGH2 User's Guide, Version 2. 0, Earth Sciences Division, Lawrence Berkeley National Laboratory, LBNL-43134, November 1999.

STATUS OF TOUGH-FLAC AND RECENT APPLICATIONS

Jonny Rutqvist

Lawrence Berkeley National Laboratory, Berkeley, USA
e-mail: jrutqvist@lbl.gov

ABSTRACT

This paper presents the current status of the TOUGH-FLAC simulator for multiphase fluid flow and geomechanics, including recent code developments and applications. The most significant new development is a revised architecture compared to the earlier attempts, enabling a more rigorous and tight coupling procedure with improved computational efficiency. The applications presented in this paper are related to modeling of crustal deformations caused by deep underground fluid movements and pressure changes as a result of both industrial activities (the In Salah CO₂ Storage Project and the Geysers Geothermal Field) and natural events (the 1960s Matsushiro Earthquake Swarm). Finally, the paper provides some perspectives on the future of TOUGH-FLAC in the light of its applicability to practical problems and the need for high-performance computing capabilities for field-scale problems, such as industrial scale CO₂ storage and enhanced geothermal systems. It is concluded that despite some limitations to fully adapting a commercial code such as FLAC3D for some specialized research and computational needs, TOUGH-FLAC is likely to remain a pragmatic simulation approach with increasing number of users in both academia and industry.

INTRODUCTION

In the 2003 TOUGH symposium, TOUGH-FLAC was presented as a pragmatic approach for modeling coupled multiphase flow, heat transport and geomechanics, by linking the two established codes TOUGH2 and FLAC3D (Rutqvist et al., 2002; Rutqvist and Tsang, 2003a). In this approach, TOUGH2 (Pruess et al., 1999) is used for solving multiphase flow and heat transport equations, whereas FLAC3D (Itasca, 2006) is used for solving geomechanical stress-strain equations. The two codes are sequentially coupled, but a TOUGH-FLAC simulation runs seamlessly on a PC. A great advantage with the adopted approach is that both codes are continuously developed and widely used in both academia and industry.

The earliest developments of TOUGH-FLAC at the Lawrence Berkeley National Laboratory (LBNL) were presented in Rutqvist et al. (2002) and Rutqvist and Tsang (2003a). The simulator has since been applied to study coupled geomechanical aspects

under multiphase flow conditions for a wide range of applications, including nuclear waste disposal (Rutqvist and Tsang, 2003b; Rutqvist et al., 2005; Rutqvist et al., 2008a, Rutqvist et al., 2009c), CO₂ sequestration (Rutqvist and Tsang, 2002; Rutqvist and Tsang, 2005; Rutqvist et al., 2006a; Rutqvist et al., 2007; Rutqvist et al., 2008b; Rutqvist et al., 2009b), geothermal energy extraction (Rutqvist et al., 2006b; Rutqvist and Oldenburg, 2008), naturally occurring CO₂ upwelling with surface deformations (Todesco et al., 2004; Cappa et al., 2009), and gas production from hydrate-bearing sediments (Rutqvist and Moridis, 2008; 2009; Rutqvist et al., 2009a).

These applications have been accompanied with exploratory code developments. The most significant new development is a revised architecture compared to the earlier attempts, enabling a more rigorous and tight coupling procedure with improved computational efficiency. This development occurred when coupling the newly released TOUGH+ code to FLAC3D for the analysis of the geomechanical performance of hydrate-bearing sediments (Rutqvist and Moridis, 2008; 2009). In addition, new modules have been developed for material behaviors and modeling of hydrate bearing sediments and thermo-elastoplastic behavior of unsaturated soils. The development of thermo-elastoplastic model of unsaturated soils involves implementation of a version of the Barcelona Basic Model using the user-defined model option in FLAC3D and is described in detail in Rutqvist et al. (2009d).

This paper presents the current TOUGH-FLAC approach and some recent applications of TOUGH-FLAC since the last TOUGH symposium in 2006. The applications presented are related to modeling of crustal deformations caused by deep underground fluid movements and pressure changes as a result of both industrial activities and natural events. These application examples include analysis of ground-surface deformations measured by satellite (InSAR) at the In Salah industrial scale CO₂ injection site in Algeria and at the Geysers Geothermal field in California. The third example involves ground surface deformation during upwelling of CO₂ rich fluid associated with the 1960s Matsushiro earthquake swarm in central Japan. The paper concludes with some perspectives on the future of TOUGH-FLAC in the light of its applicability to practical problems and the need for high-performance computing capabilities for very large-scale problems,

such as for the analysis of industrial scale CO₂ sequestration sites and enhanced geothermal systems.

TOUGH-FLAC STRUCTURE

This description of the TOUGH-FLAC structure follows the most recent developments applied to studies of geomechanical performance of gas hydrates by coupling FLAC3D to the newly released TOUGH+ code (Rutqvist and Moridis, 2008; 2009). However, some of these ideas are concurrently being implemented for the coupling of FLAC3D to TOUGH2 as well. In this approach, the two constituent codes—TOUGH+ (or TOUGH2) and FLAC3D—are linked through a coupled thermal-hydrological-mechanical (THM) model (Figure 1). Depending on the problem and specific porous media (e.g., fractured rock, unsaturated clay, or hydrate-bearing sediments), a number of coupling functions have been developed.

In Figure 1, the data exchanges between TOUGH+ and FLAC3D are illustrated with arrows going through the central THM model. The arrow on the right-hand side of Figure 1 shows the transmission of the effective stress σ' and strain ε (that are computed in FLAC3D) to TOUGH for calculation of the updated porosity ϕ and the corresponding porosity change $\Delta\phi$. This mechanically induced $\Delta\phi$ has an immediate effect on fluid flow behavior. For example, if a change in σ' and ε causes ϕ to decrease, the pore pressure is expected to rise, especially if the permeability is low.

For a porous deformable media, two models for mechanically induced porosity changes are implemented in the most recent version of linking FLAC3D to TOUGH+

- (i) A poroelastic model (based on the approach proposed by Settari and Mourits, 1998) that considers macroscopic stress/strain changes and grain deformability
- (ii) An empirical model (proposed by Rutqvist and Tsang, 2002) that describes a nonlinear change in porosity as a function of the effective mean stress

The $\Delta\phi$ computed from either of these models is used to estimate changes in k by means of empirical equations. The updated ϕ and k values are in turn used to estimate changes in the hydraulic and wettability properties of the porous medium (i.e., aqueous- and gas-phase relative permeabilities k_{rA} and k_{rG} , and capillary pressure P_c) by employing appropriate scaling equations.

For fractured media, a similar exponential empirical model has been applied to correct permeability for changes in the stress field (e.g., Rutqvist et al., 2002; 2008a).

The arrow on the left side of Figure 1 depicts the flow of data obtained from TOUGH+ (or TOUGH2) (namely the pressure P , temperature T , and phase saturations S_β) to FLAC3D for processing and estimation of their impact on the effective stress $\alpha\Delta P_\beta$ (α being Biot's effective stress parameter), as well as on thermal and swelling strains (ε_T and ε_{sw} , respectively). Capabilities for modeling of moisture swelling and geomechanical behavior of unsaturated soil has recently been implemented into TOUGH-FLAC (see Rutqvist et al., 2009d). In this model, the swelling can either be introduced as a function of phase saturation or as a function of suction (or capillary pressure, P_c) using the Barcelona Basic Model for elastoplastic behavior of unsaturated soils (Rutqvist et al., 2009d).

Additionally, changes in P , T , and S_β may also result in changes in other mechanical properties listed in Figure 1. These include the bulk modulus K , the shear modulus G , the cohesion C , and the coefficient of internal friction μ . For example, in the case of hydrate-bearing sediment, geomechanical properties change as a function of solid-phase saturations, i.e., hydrate and ice saturations (S_H and S_I , respectively). In the case of unsaturated soil, the bulk modulus and friction angle is a function of suction.

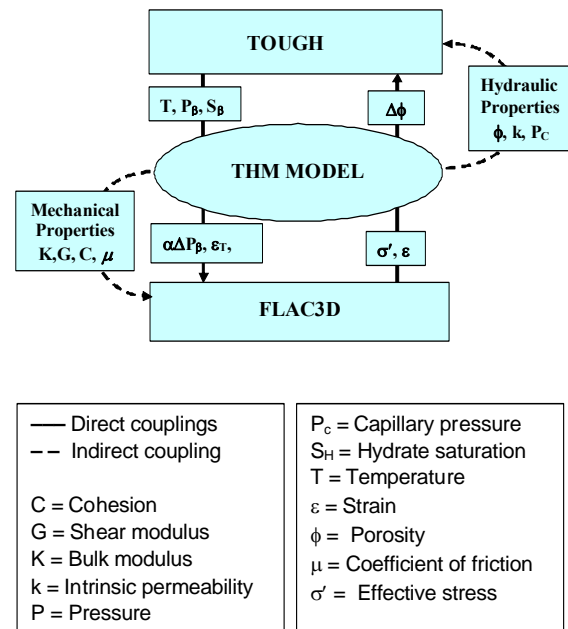


Figure 1. Schematic of linking TOUGH family code such as TOUGH+ and TOUGH2 with FLAC3D for a coupled THM simulation.

In the current TOUGH-FLAC modeling approach, FLAC3D is invoked from TOUGH+ (or TOUGH2) using a system call. This is different from the earliest version, in which TOUGH2 multiphase flow

simulation was invoked from FLAC3D. Invoking the quasistatic mechanical calculation from the multiphase flow simulation enables tighter and more rigorous coupling and improved efficiency. For example, it is now possible to invoke FLAC3D in each Newton iteration and when calculating the Jacobian in TOUGH+. The coupling to the FLAC3D code is still made possible through the use of the FLAC3D FISH programming capability, which enables access to internal FLAC3D arrays and parameters. However, the Itasca Consulting Group (who develops and maintains FLAC3D) has provided new FISH variables for a more efficient transfer of TOUGH parameter directly to the FLAC3D grid-elements, avoiding the previously tedious interpolation between TOUGH mid-element nodes and FLAC3D corner nodes.

In the new TOUGH+ version, three coupling schemes are available:

- (i) *Jacobian*: This is the highest level of iterative coupling, in which all the geomechanical and flow parameters are continuously updated (in every Newtonian iteration of every time step), and their changes are accounted for in the computation of the Jacobian matrix.
- (ii) *Iterative*: In this scheme, the geomechanical and flow parameters are corrected at the end of each Newtonian iteration of each time step, and the contribution of their changes between Newtonian iterations are not accounted for in the computation of the Jacobian matrix.
- (iii) *Time-step*: This represents the weakest coupling option and involves correction of the geomechanical and flow parameters once in (i.e., at the end of) each time step. As in the iterative scheme, the parameter changes do not contribute to the computation of the Jacobian matrix.

The full Jacobian option is a sequentially implicit scheme, whereas the iterative and the time-step coupling options are sequentially explicit schemes. The full Jacobian scheme is necessary for problems in which pore-volume (direct) couplings dominate, i.e., when a mechanically induced $\Delta\phi$ gives rise to a relatively strong and rapid change in pore pressure, and where it is necessary to rigorously preserve the fluid mass and heat balances. In problems where the so-called property changes (indirect) couplings dominate, iterative or time-step coupling schemes are sufficient.

RUNNING A TOUGH-FLAC SIMULATION

A TOUGH-FLAC simulation is typically developed according to the steps in Figure 2. The user first develops numerical grids for the two codes that should have the same geometry and element numbering. The user then typically runs a TOUGH

simulation test to make sure that the TOUGH code can execute the specific problem setup without consideration of the mechanical coupling. This may include an initially steady-state TOUGH simulation to establish initial conditions, including vertical gradients of pressure and temperature. Similarly, a FLAC3D simulation may be conducted to assure correct input of (for example) mechanical boundary conditions and to establish initial equilibrium stress gradients.

Thereafter, the TOUGH-FLAC simulation is set up. This involves preparing a binary file called FLAC3D.sav that should contain the geomechanical model, as well as essential FLAC3D FISH routines that handle the link from FLAC3D to TOUGH+ (or TOUGH2). The simulation is initiated by starting a TOUGH+ simulation with geomechanical option activated. The first time FLAC3D is invoked, it restores information and the initial mechanical state from a binary file called FLAC3D.SAV. It runs to a mechanical equilibrium and then saves the new mechanical state to the FLAC3D.SAV. This procedure of restoring, running to a new mechanical equilibrium, and saving to the binary file is repeated every time the FLAC3D mechanical calculation is invoked. The simulation runs seamlessly without need for user interference and produces required outputs for simulation times defined in the TOUGH+ input file.

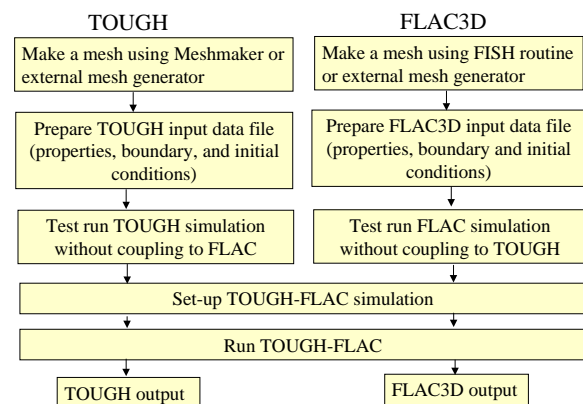


Figure 2. Steps for developing a coupled TOUGH-FLAC simulation of a particular problem.

MODELING COUPLED FLUID FLOW AND CRUSTAL DEFORMATIONS

This section summarizes recent TOUGH-FLAC simulations of crustal deformations caused by deep underground fluid movements and pressure changes as a result of both industrial activities (the In Salah CO₂ storage project and the Geysers Geothermal Field) and natural events (The 1960s Matsushiro Earthquake Swarm).

In Salah Industrial CO₂ Storage Project

The In Salah Gas Project in Algeria has been injecting 0.5–1 million tonnes CO₂ per year over the past four years into water-filled strata at a depth of about 1,800 to 1,900 m. Unlike most CO₂ storage sites, the permeability of the storage formation is relatively low and comparatively thin, with a thickness of about 20 m. To ensure adequate CO₂ flow-rates across the low-permeability sand-face, the In Salah Gas Project decided to use long-reach (about 1 to 1.5 km) horizontal injection wells. In a related ongoing research project, LBNL uses field data and TOUGH-FLAC modeling to assess the effectiveness of this approach and to investigate monitoring techniques to evaluate the performance of a CO₂-injection operation in relatively low-permeability formations.

In the fall of 2006, a preliminary reservoir-geomechanical analysis using TOUGH-FLAC indicated that surface deformations on the orders of centimeters would be feasible during CO₂ injection at In Salah. This preliminary simulation was conducted in a 3D model (10×10×4 km) shown in Figure 3. As a result, LBNL decided to explore the possibility of using the satellite-based interferometry (InSAR) for detecting ground-surface deformations related to the CO₂ injection. InSAR data were acquired and analyzed by Tele-Rilevamento (TRE) in Italy, using a state-of-the-art permanent scatterer method (PS), enabling determination of millimeter-scale surface deformations. The results processed in 2007 and later published in Vasco et al. (2008a, b) were remarkable, because the observed uplift could be clearly correlated with each injection well with uplift bulges of several kilometers in diameter centered on each injection well (Figure 4). Measured uplift occurred within a month after start of the injection, with the rate of uplift ~5 mm per year, amounting to about 1.5 cm in the first 3 years of injection.

In subsequent TOUGH-FLAC analysis including measured geomechanical properties as well as actual injection flow and pressure history, Rutqvist et al. (2009) showed that the observed uplift magnitude can be explained by pressure-induced, poro-elastic expansion of the 20 m thick injection zone. For example, Figure 5 shows a calculated uplift magnitude of 1.2 cm after 3 years of injection, which is similar to the measured uplift at injection well KB501. Figure 6 shows a comparison of the evolution of calculated and measured uplift. Again, the results shows that the observed uplift magnitude can be explained by pressure-induced, poro-elastic expansion of the 20 m thick injection zone. However, there could also be a significant contribution from pressure-induced deformations within a 100 m thick zone of shaly sands immediately above the injection zone. Thus, the modeling indicates that the CO₂ and native brine is not displaced out of the injection zone,

but is contained at depth below that 900 m thick overburden sealing formation.

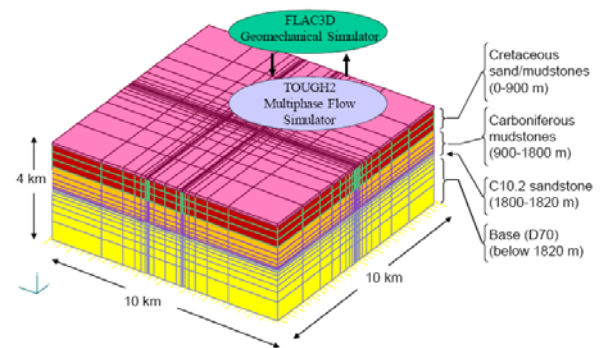


Figure 3. Model geometry for the TOUGH-FLAC coupled reservoir-geomechanical analysis of CO₂ injection and ground surface deformations at Krechba. The model is centered on one CO₂ injection well (Rutqvist et al., 2009).

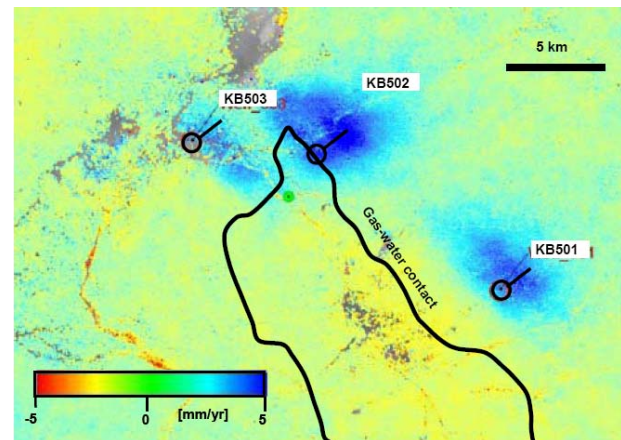


Figure 4. InSAR data of rate of vertical displacements for the first 3 years of CO₂ injection (Rutqvist et al., 2009).

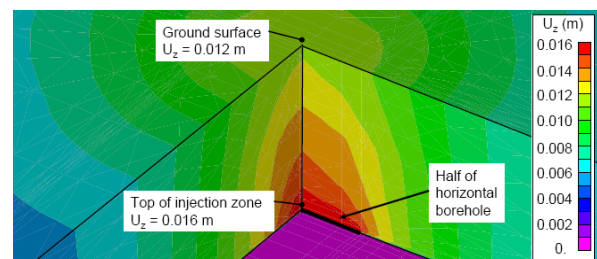


Figure 5. Simulated vertical displacement after 3 years of injection with a caprock permeability of $k=1 \times 10^{-21} \text{ m}^2$ (Rutqvist et al., 2009).

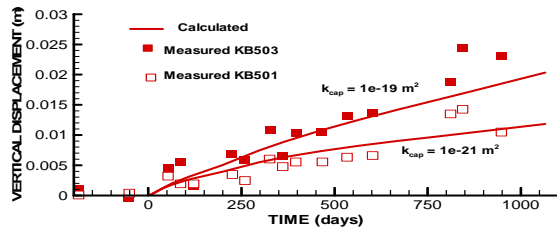


Figure 6. Comparison of simulated vertical ground uplift for two different values of caprock permeability (solid lines) to that of measured ground uplift above injection wells KB501 and KB503 (symbols). (Rutqvist et al., 2009).

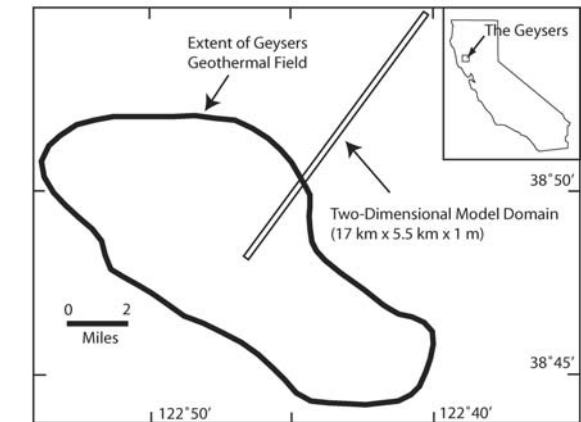
The Geysers Geothermal Field

The Geysers is the site of the largest geothermal electricity generating operation in the world and also one of the most seismically active regions in northern California (Majer and Peterson, 2007). It is a vapor-dominated geothermal reservoir system, which is hydraulically confined by low-permeability rock units. As a result of the high rate of steam withdrawal, the reservoir pressure declined until the mid-1990s, when increasing water injection rates resulted in a stabilization of the steam reservoir pressure. However, the water injection has also resulted in an increased level of seismicity at The Geysers, which has raised concerns regarding the social, environmental, and economic impacts on the local communities (Majer and Peterson, 2007).

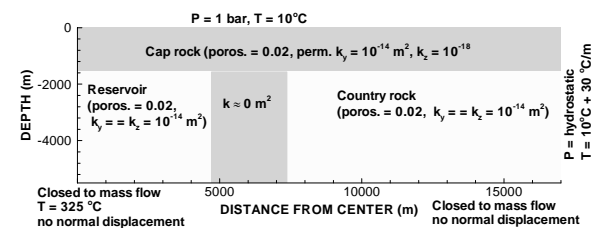
The TOUGH-FLAC simulator was used for coupled reservoir-geomechanical analysis of the Geysers geothermal operation, and in particular to study the cause and mechanisms of seismicity. As part of this study, TOUGH-FLAC was employed for studying reservoir-wide coupled geomechanical responses using a generic reservoir-geomechanical simulation of a NE-SW cross-section of the NW-SE trending Geysers geothermal field (Figure 7). Details of the model setup and results of this analysis have been presented several papers (Rutqvist et al., 2006, Rutqvist and Oldenburg 2008). This includes derivation of appropriate rates of steam production and water injection derived from field-wide data at The Geysers from 1960 through 2005. In this paper, we focus on the modeling of large-scale crustal deformations and ground-surface deformations observed by the InSAR.

InSAR data were acquired for the area around the Geysers to investigate whether such data could be useful for constraining the geomechanical model, and for providing mechanical-strain boundary conditions. In an initial calculation, it was found that the estimated compressive regional strain rate in the area

would not significantly impact the stress evolution within the Geysers over the 44-year production period. Observed vertical displacement, on the other hand, could be very useful for constraining and validating the choice of large scale poro-elastic and thermo-elastic model parameters. Earlier published leveling and GPS surveys show that from 1977 to 1996, ground settlement occurred on the order of 0.4 to 0.8 m at a rate of up to 4 cm per year (Mossop and Segall, 1997).



(a)



(b)

Figure 7. Domain and boundary conditions for a coupled geomechanical reservoir Geysers model aligned NE-SW across The Geysers geothermal field. (A) Location of two-dimensional model domain, and (B) half-symmetric model with hydraulic properties and boundary conditions (Rutqvist and Oldenburg, 2008).

Archival InSAR images were acquired of approximately monthly satellite passes over the region for a seven-year period, from 1992 to 1999. (After 1999, this particular satellite was out of service.) The data was analyzed by TRE on behalf of LBNL. Figure 8 shows vertical displacement along a profile across the Geysers roughly parallel to the two-dimensional model shown in Figure 7a. The results in Figure 8 indicate a continuous settlement over the seven-year period, with a maximum settlement of 0.2 m at the center of the field.

Figure 9 presents comparison of measured and calculated vertical displacements. The agreement between the measured and calculated surface deformations is surprisingly good considering the simplified generic TOUGH-FLAC model representation of The Geysers. The agreement provided a validation of the deformation model, including the choice of elastic properties, which also was supported by comparison to the previously published leveling and GPS data. The model was then used to calculate the injection-induced stress changes and their relative contribution to the cause and mechanisms of induced seismicity (Rutqvist and Oldenburg, 2008).

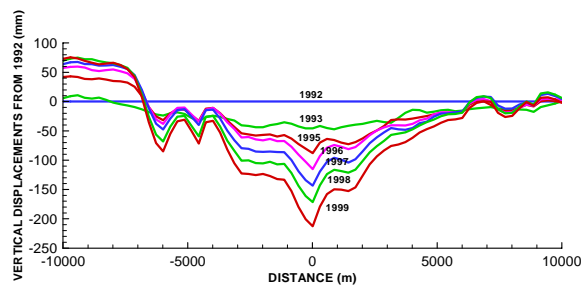


Figure 8. InSAR evaluated evolution of vertical surface displacement from 1992 to 1999 in a profile across the field.

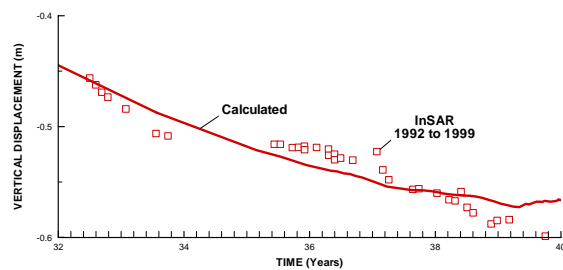


Figure 9. Comparison of calculated and InSAR evaluated vertical displacements focused comparison from year 32 to 40 (1992 to 1999) since the start of the steam production at The Geysers.

The 1960s Matsushiro Earthquake Swarm

This application example of TOUGH-FLAC was part of a collaborative research project between LBNL and Japanese organizations to study the 1960s Matsushiro Earthquake Swarm in Central Japan as a natural analogue for CO₂ leakage. During the five-year term of the swarm, between 1965 to 1970, approximately 60,000 earthquakes were felt, and ten million tons of CO₂-bearing water appeared at the ground surface, flowing up through newly created surface ruptures (Figure 10a). Ground deformations were observed with a maximum uplift of about 0.7 m as well as a strike slip motion along two intersecting faults (Figure 10b). One part of the research project was to use coupled multiphase flow and geomechanical modeling with TOUGH-FLAC to understand the role

of a deep CO₂ source on the initiation and propagation of the fault ruptures that resulted in the Matsushiro Earthquake Swarm (Cappa et al., 2009).

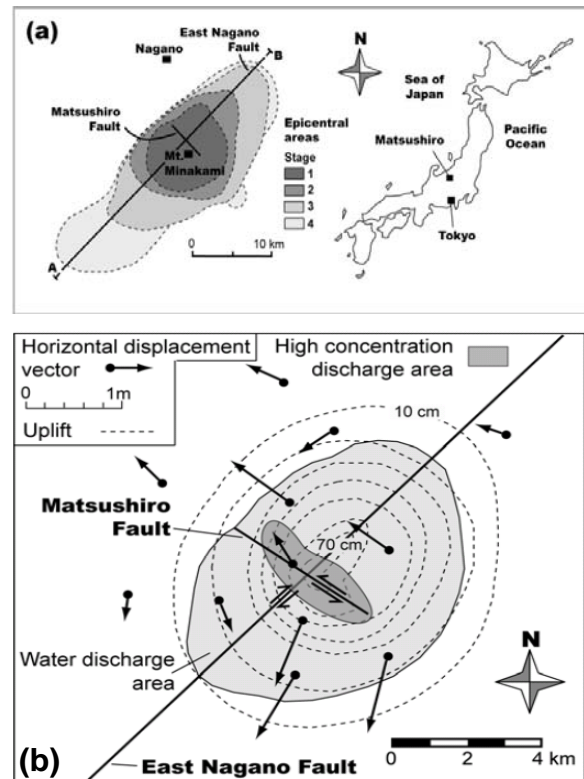


Figure 10 (a) Tectonic features and time series of epicentral areas, and (b) areas of maximum uplift, horizontal displacements and water discharge induced in September 1966 during the Matsushiro earthquake swarm (Cappa et al., 2009).

The coupled CO₂ fluid flow and geomechanical processes, including fault motion and associated permeability changes, were modeled. A model for fault permeability changes with fault reactivation was implemented into the TOUGH-FLAC simulator. A series of two and three-dimensional simulations were conducted to identify key parameters and to investigate possible causes and mechanisms behind the Matsushiro Earthquake Swarm.

Figure 11 shows the three-dimensional model domain with the two intersecting faults and the deep source of CO₂ rich fluid at the bottom of the model. Figure 12 presents simulation results of the ground-surface uplift and evolution of surface geochemical changes. The geomechanical analysis explains the cause of the Matsushiro Earthquake Swarm as overpressure resulting from the upwelling CO₂-rich fluid.

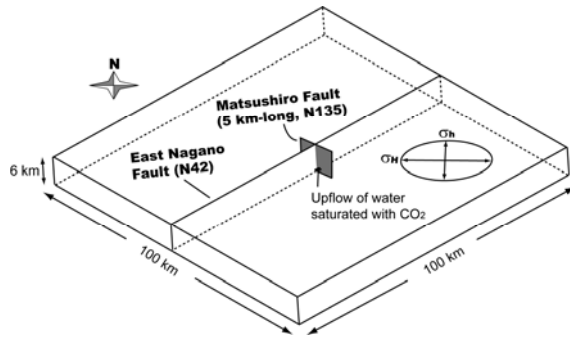


Figure 11 Model geometry including the Matsushiro and East Nagano earthquake faults. Stress orientation (Cappa et al., 2009).

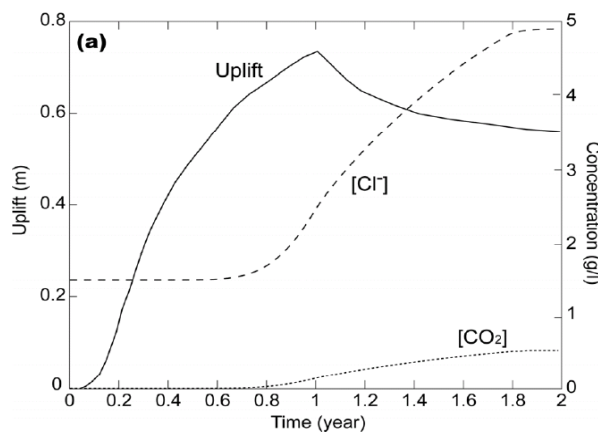


Figure 12 Calculated uplift and $[Cl^-]$ and $[CO_2]$ concentration at the ground surface (at the intersection between the Matsushiro and East Nagano faults (Cappa et al., 2009).

The mechanisms of earthquakes are attributed to shear failure initiated by reduced effective stress on pre-existing fracture planes within and near the two main faults. It is concluded that the *in situ* 3-D stress regime, as well as fault strength and permeability, are likely the most important parameters that control the nucleation, propagation, arrest, and occurrence of the earthquake swarm during its 2-year migration through the seismogenic crust. Moreover, surface deformation and increased seismicity were precursors to the CO_2 surface release, since these mechanical responses were detected up to a year before any chemical changes were measured at the ground surface.

DISCUSSION AND CONCLUDING REMARKS

Over the past 8 years, TOUGH-FLAC has been successfully applied to a wide range of problems related to coupled multiphase fluid flow and geomechanical processes in geological media. One of the advantages with this approach is that both the

TOUGH family codes and FLAC3D are already established and are continuously developed in their respective fields, and therefore model developments can be focused on the coupling of the two codes. The approach is not a completely closed black-box commercial package, but rather provides considerable flexibility for a wide range of applications. Another great advantage with this approach is that it promotes multidisciplinary collaboration among hydrologists (who may be familiar with TOUGH) and geomechanists (who may be familiar with FLAC3D) to solve complex coupled problems that might be difficult to grasp for one person. One good example is the development and application of TOUGH-FLAC for the geomechanical performance of gas hydrates.

In parallel with the development and application of TOUGH-FLAC, several research groups have been working with similar or alternative approaches for considering geomechanical coupling in the TOUGH family codes. This includes, but is likely not limited to, Gosavi and Swenson (2005), Javeri (2007), Hurwitz et al. (2007) and Taron et al. (2009). Gosavi and Swenson (2005) linked TOUGH2 to the finite element code GeoCrack3D for a more tightly coupled code, and later applied it to geothermal energy applications. Javeri (2007) employed linked TOUGH2 and FLAC3D in a similar manner to Rutqvist et al. (2002) and applied it to study geomechanical effects of gas generation and pressure buildup in a nuclear waste repository. Hurwitz et al., (2007) linked TOUGH2 to the coupled hydromechanical finite element code Biot2 and applied it to study hydrothermal fluid flow and deformation in large calderas, inspired by earlier TOUGH-FLAC modeling of similar phenomena reported in Todesco et al. (2004). Finally, Taron et al. (2009) applied coupled TOUGHREACT and FLAC3D to study coupled THMC phenomena for hot dry rock geothermal extraction applications.

The linking of TOUGH family codes and FLAC3D requires the coupling of a reservoir simulator to a mechanical code, a problem that has been studied in depth by Settari and others (e.g., Settari and Mourits, 1998). It is a delicate operation to correctly change the porosity of the reservoir simulator upon a change in stress or strain in the mechanical code. The ideas of Settari and others have been implemented in the new FLAC3D to TOUGH+ coupling as one alternative poro-elastic model. The correct poro-elastic consideration is important when comparing simulation results to that of fully coupled poro-elastic finite element models of the Biot type. However, as described by Settari and Mourits (1998), in practice it is more important to consider the nonlinear stress-dependent effects on porosity and permeability over the range of stress expected in a problem. Such properties may be derived directly from laboratory data and fitted to theoretical or empirical functions (e.g.,

Liu et al., 2009) or by calibration to field experiments (e.g., Rutqvist et al., 2008).

Despite the success in applying TOUGH-FLAC to a wide range of geoscience and engineering problems, one drawback with the current TOUGH-FLAC simulator is that it runs exclusively on a Windows platform (because FLAC3D only runs on Windows), which prevents us from applying the approach on existing Unix clusters for massive parallel processing. Therefore, other options for capturing geomechanics in the TOUGH family codes, including the use of geomechanical research codes with full access to the source code, will be explored in the near future. This will also include coupling to TOUGHREACT and may be conducted within the framework of future developments of TOUGH+. However, because FLAC3D is a commercial code that is continuously improved and maintained for practical applications, TOUGH-FLAC is likely to remain as a pragmatic approach with increased number of users, especially for applications requiring advanced multiphase flow analysis linked with geomechanics of complex, highly nonlinear and/or time-dependent constitutive behavior.

ACKNOWLEDGMENTS

This paper was completed with funding from the Assistant Secretary for Fossil Energy, Office of Natural Gas and Petroleum Technology, through the National Energy Technology Laboratory, and Assistant Secretary for Energy Efficiency and Renewable Energy, Geothermal Technologies Program, of the U.S. Department under the U.S. Department of Energy Contract No. DE-AC02-05CH11231. Reviews by Hui-Hai Liu and Dan Hawkes at LBNL are greatly appreciated. I would like to thank my collaborators (most of them co-authors in cited papers) for their contributions to the development and application of TOUGH-FLAC, especially George Moridis and Yu-Shu Wu at LBNL, as well as Edward Dzik and Christine Detournay at ITASCA, Minneapolis. I would also like to thank Chin-Fu Tsang at LBNL for his initial encouragement and promotion of TOUGH-FLAC, an approach that has been much more useful than I initially thought.

REFERENCES

Cappa, F., J. Rutqvist, and K. Yamamoto, Modeling crustal deformation and rupture processes related to upwelling of deep CO₂ rich fluids during the 1965–1967 Matsushiro Earthquake Swarm in Japan, *Journal of Geophysical Research*, accepted June, 2009.

Gosavi, S., and D. Swenson, Architecture for a coupled code for multiphase fluid flow, heat transfer and deformation in porous rock. PROCEEDINGS, Thirtieth Workshop on

Geothermal Reservoir Engineering Stanford University, Stanford, California, January 31–February 2, 2005.

- Hurwitz, S., L.B. Christiansen and P.A. Hsieh, Hydrothermal fluid flow and deformation in large calderas: Inferences from numerical simulations, *Journal of Geophysical Research*, 112, BO2206, 2007.
- Itasca Consulting Group, FLAC3D, Fast Lagrangian Analysis of Continua in 3 Dimensions, Version 2.0. Five volumes, Minneapolis, Minnesota, Itasca Consulting Group, 2006.
- Javeri, V., Three dimensional analysis of combined gas, heat and nuclide transport in a repository in clay rock including coupled thermo-hydro-geomechanical processes, *Physics and Chemistry of the Earth*, 33, S252–S259, 2007.
- Liu, H.H., J. Rutqvist, and J.C. Berryman, On the relationship between stress and elastic strain for porous and fractured rock, *Int J Rock Mech & Min Sci* 46, 289–296, 2009.
- Majer, E.L., and J.E. Peterson, The impact of injection on seismicity at The Geysers, California Geothermal Field, *Geothermics*. 44, 1079–1090, 2007.
- Mossop, A.P., and P. Segall, Subsidence at The Geysers geothermal field, N. California from a comparison of GPS and leveling surveys, *Geophys. Res. Letter*, 24, 1839–1842, 1997,
- Pruess, K., C. Oldenburg, and G. Moridis, *TOUGH2 User's Guide, Version 2.0*, Report LBNL-43134, Lawrence Berkeley National Laboratory, Berkeley, Calif., 1999.
- Pruess, K., J. García, J.T. Kowsek, C. Oldenburg, J. Rutqvist, C. Steefel, and T. Xu, Code intercomparison builds confidence in numerical simulation models for geologic disposal of CO₂, *Energy* 29, 1431–1444, 2004.
- Rutqvist, J., and G.J. Moridis, Numerical Studies on the Geomechanical Stability of Hydrate-Bearing Sediments, *Society of Petroleum Engineers SPE Journal*, 14, 267–282, SPE-126129, 2009.
- Rutqvist, J., G.J. Moridis, T. Grover, and T. Collett, Geomechanical response of permafrost-associated hydrate deposits to depressurization-induced gas production, *Journal of Petroleum Science and Engineering*, 67, 1–12, 2009a.
- Rutqvist, J., D. Vasco, and L. Myer, Coupled reservoir-geomechanical analysis of CO₂ injection at In Salah, Algeria. 9th International Conference on Greenhouse Gas Control Technologies (GHGT-9), Washington D.C., Nov 16–20, 2008. *Energy Procedia*, 1, 1847–1854, 2009b.
- Rutqvist, J., D. Barr, J.T. Birkholzer, K. Fujisaki, O. Kolditz, Q.-S. Liu, T. Fujita, W Wang, and C.-Y. Zhang, A comparative simulation study of

- coupled THM processes and their effect on fractured rock permeability around nuclear waste repositories. *Environ Geol*, 57, 1347–1360, 2009c.
- Rutqvist, J., Y. Ijiri, and H. Yamamoto, Implementing the Barcelona Basic Model into TOUGH-FLAC for analysis of geomechanical behavior of unsaturated soils. Proceedings of the TOUGH symposium 2009, Lawrence Berkeley National Laboratory, Berkeley, Sept 14–16, 2009d.
- Rutqvist, J., and G. Moridis, Development of a Numerical Simulator for Analyzing the Geomechanical Performance of Hydrate-Bearing Sediments. Proceedings of the 42th U.S. Rock Mechanics Symposium, San Francisco, California, USA, June 29-July 2, 2008: American Rock Mechanics Association ARMA, Paper No. 139, 2008.
- Rutqvist, J., and Oldenburg C.M., Analysis of injection-induced micro-earthquakes in a geothermal steam reservoir, Geysers Geothermal Field, California. Proceedings of the 42th U.S. Rock Mechanics Symposium, San Francisco, California, USA, June 29-July 2, 2008: American Rock Mechanics Association ARMA, Paper No. 151, 2008.
- Rutqvist, J., B. Freifeld, K.-B. Min, D. Elsworth, and Y. Tsang, Analysis of thermally induced changes in fractured rock permeability during eight years of heating and cooling at the Yucca Mountain Drift Scale Test. *Int J Rock Mech & Min Sci*, 45, 1373–1389, 2008a.
- Rutqvist, J., J.T. Birkholzer, and C.-F. Tsang, Coupled reservoir-geomechanical analysis of the potential for tensile and shear failure associated with CO₂ injection in multilayered reservoir-caprock systems. *Int. J. Rock Mech. & Min. Sci.*, 45, 132–143, 2008b.
- Rutqvist, J., J. Birkholzer, F. Cappa, and C.-F. Tsang, Estimating maximum sustainable injection pressure during geological sequestration of CO₂ using coupled fluid flow and geomechanical fault-slip analysis. *Energy Conversion and Management*, 48, 1798–1807, 2007.
- Rutqvist, J., J.T. Birkholzer, and C.-F. Tsang, Modeling hydrological and geomechanical processes related to CO₂ injection in a faulted multilayer system. 8th International Conference on Greenhouse Gas Control Technologies, Trondheim, Norway, June 19-22, 2006a.
- Rutqvist, J., J.T. Birkholzer, F. Cappa, C. Oldenburg, and C.-F. Tsang, Shear-slip analysis in multiphase fluid-flow reservoir engineering applications using TOUGH-FLAC. Proceedings of the TOUGH symposium 2006, Lawrence Berkeley National Laboratory, Berkeley, California, May 15–17, 2006b.
- Rutqvist, J., and C.-F. Tsang, Coupled hydromechanical effects of CO₂ injection. In: Tsang C.F., Apps J.A., editors. *Underground Injection Science and Technology*. Elsevier, 649–679, 2005.
- Rutqvist, J., D. Barr, R. Datta, A. Gens, M. Millard, S. Olivella, C.-F. Tsang, and Y. Tsang Y, Coupled thermal-hydrological-mechanical analysis of the Yucca Mountain Drift Scale Test – comparison of field results to predictions of four different models. *Int. J. Rock mech. & Min. Sci.*, 42, 680–697, 2005.
- Rutqvist, J., and C.-F. Tsang, TOUGH-FLAC: A numerical simulator for analysis of coupled thermal-hydrologic-mechanical processes in fractured and porous geological media under multi-phase flow conditions. Proceedings of the TOUGH symposium 2003, Lawrence Berkeley National Laboratory, Berkeley, May 12–14, 2003a.
- Rutqvist, J., and C.-F. Tsang, Analysis of thermal-hydrologic-mechanical behavior near an emplacement drift at Yucca Mountain, *Journal of Contaminant Hydrology*, 62–63, 637–652, 2003b.
- Rutqvist, J., and C.-F. Tsang, A study of caprock hydromechanical changes associated with CO₂ injection into a brine aquifer. *Environmental Geology*, 42, 296–305, 2002.
- Rutqvist, J., Y.-S. Wu, C.-F. Tsang, and G. Bodvarsson, A modeling approach for analysis of coupled multiphase fluid flow, heat transfer, and deformation in fractured porous rock, *Int. J. Rock mech. & Min. Sci.* 39, 429-442, 2002.
- Settari, A., and F.M. Mourits, A Coupled reservoir and Geomechanical Simulation System, *SPE Journal*, 27(9), 219-226, SPE paper 50939, 1998.
- Taron, J., D. Elsworth, and K.-B. Min, Numerical simulation of thermal-hydrologic-mechanical-chemical processes in deformable, fractured porous media. *International Journal of Rock Mechanics & Mining Sciences*, 46, 842–854, 2009.
- Todesco, M., J. Rutqvist, G. Chiodini, K. Pruess, and C.M. Oldenburg, Modeling of recent volcanic episodes at Phlegrean Fields (Italy): geochemical variations and ground deformation. *Geothermics*, 33, 531–547, 2004.

A PARALLEL SECOND-ORDER ADAPTIVE MESH ALGORITHM FOR REACTIVE FLOW IN GEOCHEMICAL SYSTEMS

George S. H. Pau, Ann S. Almgren, John B. Bell, Michael J. Lijewski,
Eric Sonnenthal, Nic Spycher, Tianfu Xu, Guoxiang Zhang

Lawrence Berkeley National Laboratory
1 Cyclotron Road MS50A-1148
Berkeley, CA 94720, USA
e-mail: gpau@lbl.gov

ABSTRACT

We present a second-order accurate adaptive algorithm for solving reactive transport flow in geochemical systems. A Strang-splitting approach is used to numerically decouple the transport component and the reaction component of the problem. The transport component is solved using a second-order accurate IMPES-like algorithm that exhibits excellent control of numerical dispersion. The numerical scheme for the reaction component uses reaction network details from the chemistry module of TOUGHREACT, COREREACT, and VODE, a high-order ODE integrator, to maintain second-order accuracy of the algorithm. The algorithm is implemented within an adaptive refinement framework that uses a nested hierarchy of logically rectangular grids with simultaneous refinement of the grids in both space and time. The integration algorithm on the grid hierarchy is a recursive procedure in which coarse grids are advanced in time, fine grids are advanced multiple steps to reach the same time as the coarse grids, and the data at different levels are then synchronized. Numerical examples are presented to demonstrate the algorithm's accuracy and convergence properties. We conclude with a simulation of a reactive salt dome problem.

INTRODUCTION

Accurate modeling of a reacting flow has many important ramifications in geologically important problems such as carbon sequestration and environmental remediation. The increasing role of simulation in the analysis and decision-making process places significant demands on the fidelity of the simulation codes. However, coupling between transport and reaction can be complex due to scale differences in both space and time, placing severe demands on computational methodology.

One of the challenges in simulation of reactive flow lies in the large number of chemical species in a geochemical system. In addition, the reaction rates can be disproportionately high compared to the flow rate, posing significant difficulties in devising an

efficient numerical algorithm. In Steefel and MacQuarrie (1996), the number of species that needs to be tracked during transport is significantly reduced by assuming local equilibrium between aqueous species. Precipitation and dissolution are the only reactions with finite rates, which are usually slower than reaction rates between aqueous species. Even with this simplification however, small time steps may still be needed to integrate the reaction equations accurately, especially if the reaction rates are strongly nonlinear function of species' concentrations. Grid resolution requirements can also be steep since reactions occur at the pore scale. A fully implicit approach to simulating geochemical system can thus be computationally very demanding.

In this work, we develop a second-order accurate adaptive scheme for the accurate simulation of reactive flow. We describe the details of our method and how we make use of a reaction module of TOUGHREACT, COREREACT, in the next section. We then solve several geochemical systems based on our method to demonstrate its convergence properties and accuracy. We also compare our results to TOUGHREACT.

NUMERICAL SCHEME

The formulation of the chemical system we use follows Steefel and MacQuarrie (1996). Aqueous species are assumed to be in local equilibrium and only precipitation and dissolution reactions are finite-rate reactions. The species in a chemical system can be divided into primary and secondary species. This formulation allows the mass conservation equations to be written down in terms of the concentration of aggregated species c_i^t , defined as

$$c_i^t = c_i^p + \sum_{j=1}^{N_s} \nu_{ji} c_j^s, \quad i = 1, \dots, N_p \quad (1.1)$$

where c_i^p and c_j^s are the concentration of the primary and secondary species, N_p and N_s are the number of primary and secondary species, and ν_{ij} are the stoichiometric coefficients. We utilize databases in COREREACT in our code development efforts.

The operator-split formalism (Day and Bell, 2000) is used to computationally decouple the problem into two independent operators that represent the transport and reaction components. The transport operator is based on the total velocity formulation that decomposes the mass conservation equations and Darcy's law into an elliptic pressure equation and a system of parabolic equations. This allows us to employ the second-order IMPES-like discretization approach described in Pau et al. (2009). The reaction component is described by a coupled system of pointwise nonlinear ordinary differential equations (ODEs). These ODEs can be very efficiently and accurately solved by the VODE solver, a high-order adaptive ODE integrator developed by Brown et al. (1989). Reaction rates are computed based on COREACT. The flow and reactions operators are then coupled using the Strang-splitting approach, which consists of the following sequential steps within a time step Δt :

1. We advance the reaction operator for $\Delta t/2$ to obtain solution at $t + \Delta t/2$ using VODE;
2. We integrate the flow operator for an interval of Δt based on the discretization described earlier; and finally
3. We advance the reaction operator for another $\Delta t/2$ to obtain solution at $t + \Delta t$ using VODE.

The operator-splitting approach we have adopted here is somewhat similar to the sequential noniterative algorithm option of TOUGHREACT. However, there are significant differences between our method and TOUGHREACT in how the individual operators are handled, as well as in the coupling scheme itself. The TOUGHREACT flow module uses a fully implicit temporal discretization coupled with a first-order upstream weighting to compute spatial derivatives. This approach provides a robust discretization, but requires the solution of a large nonlinear system of algebraic equations. In our sequential approach, we first solve the pressure equation to determine a total velocity and then solve the component conservation equations in total velocity form. Discretization of each component is tailored to reflect its underlying mathematical character. The pressure equation is solved implicitly using a finite difference method. The mass conservation equations are solved semi-explicitly using an explicit second-order Godunov method for advection and an implicit Crank-Nicolson discretization of diffusion, resulting in excellent control of numerical dispersion.

The reaction module of TOUGHREACT uses fixed time steps and Newton's method to solve the

resulting systems of nonlinear ODEs. In contrast, the VODE solver applied here utilizes an automatic adaptive time subcycling procedure to numerically integrate the ODEs to the desired level of accuracy. Also, the Strang-splitting approach is formally second-order accurate, while the sequential noniterative approach is only first-order accurate. These enhancements allow our method to work in many cases where TOUGHREACT fails with the sequential noniterative algorithm option.

The extension of the aforementioned single-grid algorithm to an adaptive hierarchy of nested rectangular grids follows the algorithmic details outlined in Pau et al. (2009). The structured-grid adaptive mesh refinement approach, introduced for gas dynamics by Berger and Colella (1989), was first applied to porous media flow by Hornung and Trangenstein (1997) and by Propp (1998). We note that the use of adaptive mesh refinement strategies in reactive flow is particularly advantageous, because it allows the simulation to efficiently capture localized phenomena, such as localized reactions, steep concentration gradients, and saturation fronts. As we will show later, grid resolution strongly influences the solutions of reactive flow. Dynamic gridding capability then allows efficient amortization of computing resources. Figure 1 shows a snapshot of the grid for a problem where the specie AB is formed along the center of the domain where aqueous solutions of A and B mix. Two successive levels of fine grids are placed where gradients of the species' concentrations are steep.

The adaptive mesh refinement (AMR) framework used here can be efficiently parallelized (Rendleman et al., 2000). The reaction component of the procedure is a pointwise operation and thus trivially parallelizable. The parallelization of the flow operator, which involves solving an elliptic equation, is less efficient, but the code is scalable up to several thousands CPUs. In most cases, since the computational cost of the reaction operator dominates the total computational cost, good scaling behavior is usually achieved.

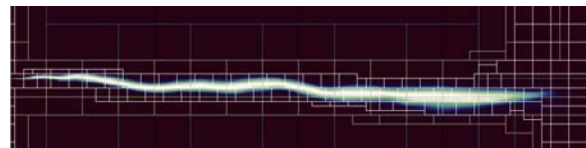


Figure 1. AMR grid with two levels of refinement. Refinement criterion is based on sum of concentration gradients of all components. Shown is the component $AB_{(aq)}$ of a simple reaction $A_{(aq)} + B_{(aq)} \rightleftharpoons AB_{(aq)}$.

RESULTS

We first look at the convergence properties of the method based on a simple kinetic reaction with a finite rate. This is followed by a more realistic geochemical system that utilizes the TOUGHREACT framework. We conclude the section with a simulation of a reactive salt dome problem. Comparisons are made to results using TOUGHREACT and its sequential iterative algorithm option.

Convergence Properties

As a first test, we consider a simple reaction where $A_{(aq)} + B_{(aq)} \leftrightarrow AB_{(aq)}$, with a finite reaction rate. The problem setup for this test is shown in Figure 2. The 2D rectangular domain is of width $W = 4$ m and height $H = 1$ m. The top and bottom boundaries are impermeable. Fluid flows into the domain from the left boundary and flows out of the domain at the right boundary. The domain is initially filled with aqueous solution of A. Aqueous solution of B is then injected into the domain from the left boundary with a smoothly increasing injection rate to prevent the initial discontinuity in the rate from affecting the determination of the theoretical convergence rate. For the same reason, the permeability function varies vertically from 200 mD at the center of the domain to 100 mD at the top and bottom boundaries. The time step is determined based on a fixed Courant-Friedrichs-Levy (CFL) number of 0.5.

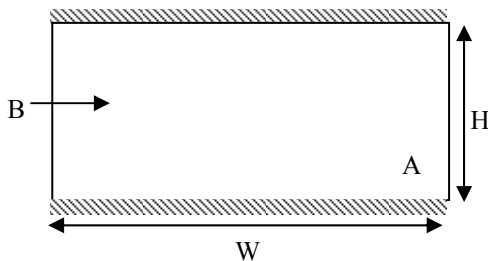


Figure 2. Configuration for the test problem. The domain is initially filled with Solution A. Solution B is then injected into the domain from the left boundary.

Table 1 shows the discrete L_1 and L_2 norms of the difference between the concentration of A obtained on each grid and that obtained on the next finer grid, and the resulting convergence rates. The rate between the two columns of error norms is defined as $\log_2(\epsilon_l/\epsilon_r)$ where ϵ_l and ϵ_r are the errors shown in the columns to the left and right of the rate columns. It clearly demonstrates the second-order convergence property of the algorithm.

Table 1. Convergence rate of algorithm

Δx	$1/2^4$	rate	$1/2^5$	rate	$1/2^6$
L_1	1.68e-2	2.00	4.21e-3	2.00	1.05e-3
L_2	2.82e-2	1.99	7.12e-3	1.99	1.79e-3

In addition to maintaining the second-order accuracy of our method, the use of VODE has the added advantage of having an adaptive time-stepping procedure that automatically subcycles the reactions in time to achieve the desired level of accuracy. As a second test, we compare our approach to TOUGHREACT based on a simple chemical system that examines the precipitation of calcite, using the same physical setup shown in Figure 2. The system involves seven primary species (H_2O , H^+ , Ca^{2+} , Na^+ , HCO_3^- , Cl^- and $CaCO_{3(s)}$) and 11 secondary species. The domain's size is given by $H = 0.01$ m and $W = 0.1$ m. It is initially saturated with $CaCl_{2(aq)}$ (0.4 mol/kg water). $NaHCO_{3(aq)}$ in concentration of 0.8 mol/kg water is then injected from the left boundary at a speed of 1.12354×10^{-6} m/s. Under these conditions, calcite will precipitate, with the precipitation front moving from one end to the other. We will compare the concentration of calcite we obtained along the length of the simulation domain with results from TOUGHREACT.

As shown in Figure 3, results based on our method for $\Delta t = 10$ s and 1 s are identical. On the other hand, solutions obtained from TOUGHREACT for $\Delta t = 5$ s and 0.1 s deviate significantly, suggesting that even at $\Delta t = 0.1$ s, the solution from TOUGHREACT has not converged to an accurate solution. Furthermore, the peak decreases as Δt is decreased, suggesting that solutions from our method are closer to the converged value. The discrepancy can be attributed to the fact that the precipitation rate is a discontinuous function of the species' concentrations for this particular problem (i.e., the rate equation is not a continuously differentiable function through the equilibrium point). A very small time step is needed to resolve this discontinuity. VODE's adaptive time integration scheme is able to automatically resolve this discontinuity to the desired accuracy efficiently without using a fixed small time step. We finally note that if the sequential noniterative algorithm option is used in TOUGHREACT, an incorrect solution is obtained. The above observations thus suggest that when reactions are not too stiff, our method is able to treat nonlinearity in the reaction rate accurately.

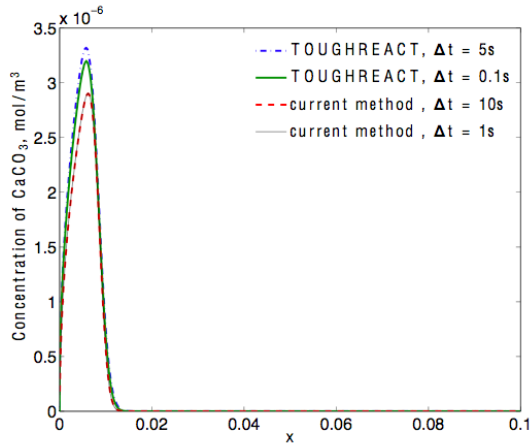


Figure 3. Comparison of the concentration of $\text{CaCO}_{3(s)}$ determined by TOUGHREACT and current method for different time steps.

Resolution effect in reactive flow

We now consider the simulation of an experimental setting reported in Redden et al. (2007) and shown in Figure 4. We again consider a chemical system involving the precipitation of CaCO_3 . The simulation domain of size $0.075 \text{ m} \times 0.6 \text{ m}$ is initially filled with aqueous species in low concentration, and these species are in equilibrium. High concentrations of aqueous CaCl_2 (0.4 mol/kg water) and aqueous NaHCO_3 (0.8 mol/kg water) are respectively injected from the left and right half of the lower boundary of the domain with a Darcy velocity of $1.67 \times 10^{-4} \text{ m/s}$.

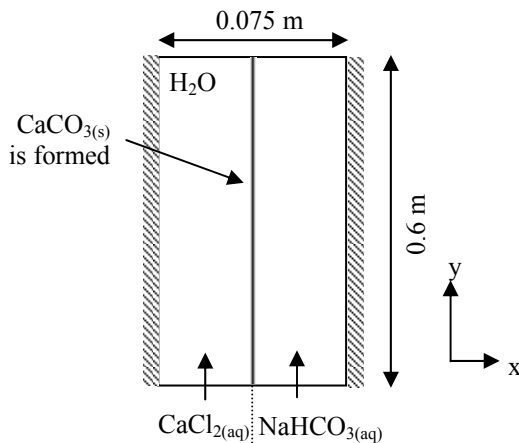


Figure 4. Configuration for problem in Redden et al. (2007). The domain is initially filled with H_2O . $\text{CaCl}_{2(aq)}$ and $\text{NaHCO}_{3(aq)}$ are respectively injected from the left and right half of the lower boundary of the domain.

Upon mixing, CaCO_3 will form along y , the vertical axis, and at center of the domain where the two aqueous solutions mix with each other through diffusion. Experimental results in Redden et al. (2007) show that precipitate will form along the entire y -axis.

Figure 5 shows how the precipitate varies along y at different resolutions; the grid resolutions are increased by placing levels of successively finer grids using our AMR scheme. The higher-resolution result captures the mixing, and thus reactions that occur close to the inlet. It thus qualitatively matches the experimental result shown in Redden et al. (2007). At coarser resolutions, precipitate only begins to form at some distance away from the inlet. It is clear from Figure 5 that resolution plays an important role in the simulation of reactive flow.

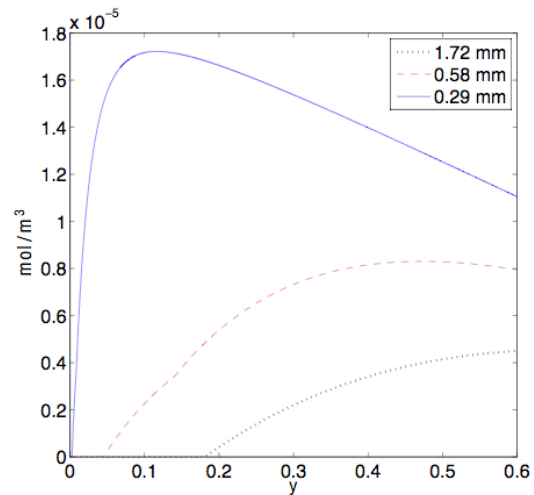


Figure 5. Concentration of the precipitate determined from grids at different resolutions

Interaction between complex flow dynamics and reaction

Here, we consider a salt dome problem coupled with the geochemical system described in the previous section. We consider a small rectangular domain of size $3 \text{ m} \times 9 \text{ m}$ as shown in Figure 6, and two solutions A and B (Table 2). An aqueous solution of CaCl_2 is allowed to diffuse into the domain at $3 \text{ m} < x < 6 \text{ m}$ along the bottom boundary. The bottom, left and right boundaries are otherwise impermeable. The top boundary is an inflow/outflow boundary where a pressure gradient 0.01 atm/m is applied. We will examine four different cases to demonstrate the interaction between flow and reaction by varying the species and densities of solutions A and B. These four cases are described in Table 2. The density of the CaCl_2 solution is 1007 kg/m^3 . Concentrations of the species are as given in the previous section.

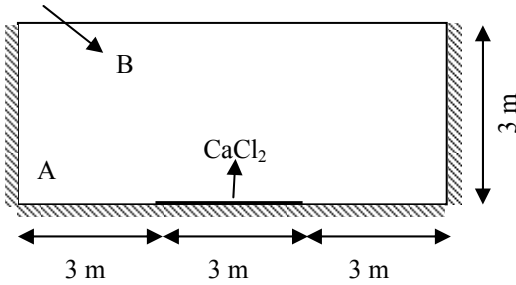


Figure 6. Configuration for the salt dome problem with reaction. CaCl_2 diffuses into the domain, which is initially filled with solution A, from the center of the bottom boundary. Solution B flows into the domain from the top boundary due to the pressure gradient applied at the top boundary.

Table 2. Cases considered. The density is the density of aqueous solutions A or B.

Case	Solution A		Solution B	
	Species	Density, kg/m^3	Species	Density, kg/m^3
1	NaHCO_3	997.16	NaHCO_3	997.16
2	NaHCO_3	1018	H_2O	997.16
3	H_2O	997.16	NaHCO_3	997.16
4	H_2O	997.16	NaHCO_3	1018

As previously, the reaction of $\text{NaHCO}_{3(\text{aq})}$ with $\text{CaCl}_{2(\text{aq})}$ causes the precipitation of $\text{CaCO}_{3(\text{s})}$. The concentrations of the $\text{CaCO}_{3(\text{s})}$ after 3×10^7 s for all the case 1-4 are shown in Figure 7. In Case 1, we see that the continual replenishment of NaHCO_3 leads to large amounts of $\text{CaCO}_{3(\text{s})}$ precipitation. In Case 2, as H_2O squeezes out $\text{NaHCO}_{3(\text{aq})}$, the buildup of $\text{CaCO}_{3(\text{s})}$ is less. In Cases 3 and 4, there is no reaction until $\text{NaHCO}_{3(\text{aq})}$ has advanced to a point where it mixes with $\text{CaCl}_{2(\text{aq})}$. This results in lower concentrations of $\text{CaCO}_{3(\text{s})}$ compared to Cases 1 and 2. The concentration of $\text{CaCO}_{3(\text{s})}$ in Case 4 is also lower than that in Case 3 because the heavier $\text{NaHCO}_{3(\text{aq})}$ in Case 4 leads to less mixing. We note that there is no precipitate in the right lower corner, indicating that the flow dynamics is such that there is a region where $\text{NaHCO}_{3(\text{aq})}$ does not mix with $\text{CaCl}_{2(\text{aq})}$.

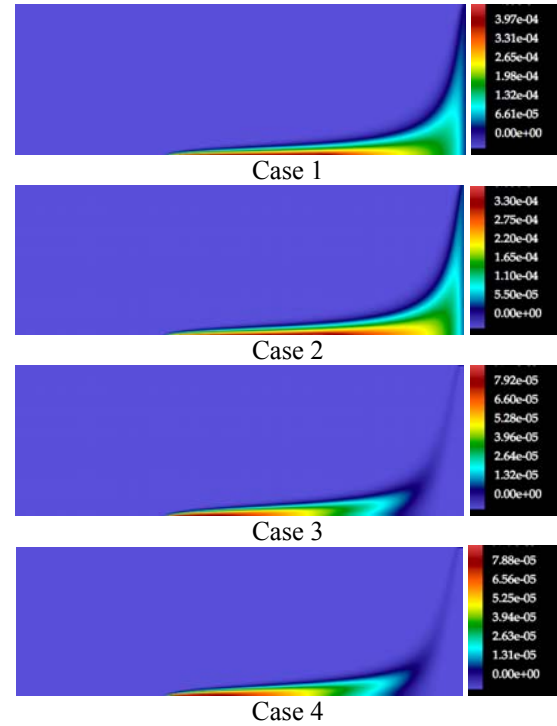


Figure 7. Calcite distribution in mol/dm^3 for cases described in Table 2 at time 3×10^7 s

CONCLUSION

This paper describes a second-order accurate algorithm for reactive flow that utilizes the reaction module of TOUGHREACT. Distinctions are made between the current code and TOUGHREACT. We demonstrated the second-order accurate convergence property of our method. We also showed that the use of AMR allows efficient resolution of localized reactions and flow features, resulting in accurate determination of the solution. Finally, we looked at a reactive salt dome problem, in which we captured the complex interaction between transport and reaction.

ACKNOWLEDGMENT

Support for this work was provided by the LDRD program at Lawrence Berkeley National Laboratory under Contract DE-AC02-05CH11231. This research used resources of the National Energy Research Scientific Computing Center, which is supported by the Office of Science of the U.S. Department of Energy under Contract No. DE-AC02-05CH11231.

REFERENCES

- Bell, J., M. Berger, J. Saltzman, and M. Welcome, A Three-dimensional Adaptive Mesh Refinement for Hyperbolic Conservation Laws, *SIAM J. Sci. Statist. Comput.*, 15(1), 127-138, 1994.
- Berger, M. J. and P. Colella, Local Adaptive Mesh Refinement for Shock Hydrodynamics, *J. Comp. Phys.*, 82 (1), 64-84, 1989.
- Brown P. N., G. D. Byrne, and A. C. Hindmarsh, VODE: A Variable Coefficient ODE solver, *SIAM J. Sci. Stat. Comput.*, 10, 1038-1051, 1989.
- Day, M. S. and J. B. Bell, Numerical Simulation of Laminar Reacting Flow with Complex Chemistry, *Combust. Theory Modeling*, 4(4), 535-556, 2000.
- Hornung, R. D. and J. A. Trangenstein, Adaptive Mesh Refinement and Multilevel Iterations for Flow in a Porous Media, *J. Comp. Phys.*, 136, 522-545, 1997.
- Pau, G. S. H., A. S., Almgren, J. B. Bell, and M. J. Lijewski, A Parallel Second-Order Adaptive Mesh Algorithm for Incompressible Flow in Porous Media, *Phil. Trans. R. Soc. A*, 2009.
- Propp, R. M., *Numerical Modeling of a Trickle Bed Reactor*, Ph.D. Thesis, Dept. of Mechanical Engineering, Univ. of California, Berkeley, 1998.
- Redden G. D., D. Fox, Y. Fujita, Y. Fang, T. Scheibe, and A. Tartakovsky, Fluid Flow, Solute Mixing and Precipitation in Porous Media, in *Proceedings of the 2nd International Conference on Porous Media and its Applications in Science and Engineering*, Kauai, Hawaii, June 17-21, 2007.
- Rendleman, C. A., V. E. Beckner, M. J. Lijewski, W. Y. Crutchfield, and J. B. Bell, Parallelization of Structured, Hierarchical Adaptive Mesh Refinement Algorithms, *Computing and Visualization in Science*, 3 (3), 147-157, 2000.
- Steeffel, C. I. and K. T. B. MacQuarrie, Approaches to Modeling of Reactive Transport in Porous Media, *Reviews in Mineralogy and Geochemistry*, 34(1), 85-129, 1996.
- Xu, T., E. Sonnenthal, N. Spycher, and K. Pruess. *TOUGHREACT User's Guide: A Simulation Program for Non-isothermal Multiphase Reactive Geochemical Transport in Variable Saturated Geologic Media*, Report LBNL-55460, Lawrence Berkeley National Laboratory, Berkeley, Calif., 2004.

A DUAL-CONTINUUM APPROACH FOR MODELING COUPLED HYDROMECHANICAL PROCESSES

Hui-Hai Liu and Jonny Rutqvist

Earth Sciences Division
Lawrence Berkeley National Laboratory
Berkeley, CA 94720
e-mail: hhliu@lbl.gov

ABSTRACT

Mechanical deformation processes in fractured rock and their coupling to hydrological processes are important for many practical applications. The objective of this study is to develop a dual-continuum approach for modeling coupled hydromechanical processes associated with fluid flow and mass transport in fractured rock that has often been conceptualized as a dual-continuum system. Considering that fluid flow occurs in pore volumes (including fracture apertures), we first develop a so-called pore-space conservation equation for deformed fractured rock, and then combine this equation with fluid mass balance to derive governing equations for multiphase flow. Constitutive relationships are also presented for describing stress dependence of hydraulic properties and effective mechanical parameters for bulk rock mass (as a function of the corresponding parameters for fracture and matrix continua). The developed approach has been incorporated to TOUGH2 under a condition of constant total stress and applied to simulating CO₂ injection processes at In Salah site, Algeria.

INTRODUCTION

Coupled hydraulic and mechanical-deformation processes in fractured rock are important for many energy-development and environment-management applications, such as geothermal energy development, oil and gas extraction, nuclear waste disposal, geological sequestration of carbon dioxide, and deep well injection of liquid and solid wastes. Recently, considerable attention has been given to development of numerical models for simulating these coupled processes and assessing their impacts on different aspects of these applications (Rutqvist et al., 2001; Jing and Hudson, 2002).

Several approaches are available in the literature for modeling hydraulic (flow and transport) and mechanical processes in fractured rocks, such as the continuum approach and the discrete-fracture-network approach. In the continuum approach, fractures are considered to be sufficiently ubiquitous and distributed in such a way that they can be meaningfully described statistically (Barenblatt and Zheltov, 1960; Warren and Root, 1963). In other words, connected fractures and rock matrix are

viewed as two overlapping interacting continua. Considerable effort has also been made with respect to modeling mechanical deformation processes and their coupling with flow processes in this dual continuum system (e.g., Wilson and Aifantis, 1982; Bai et al., 1993; Berryman and Wang, 1995). These studies generally highlight the importance of carefully considering dual continuum behavior in flow and mechanical deformation processes, as well as their coupling, resulting from dramatic differences between fracture and matrix (hydraulic and mechanical) properties.

The primary objective of this work is to present formulations (governing equations and constitutive relationships) for coupled hydraulic and mechanical processes associated with multiphase flow in a dual-continuum system. This is motivated by two observations of previous studies documented in the literature. First, most of the earlier studies of coupled hydromechanical processes in dual continuum systems were focused on single-phase flow (e.g., Wilson and Aifantis, 1982; Bai et al., 1993; Berryman and Wang, 1995), rather than multiphase flow. Second, in commonly used coupled hydromechanical models (codes), the coupling between hydraulic and mechanical-deformation processes is implemented mainly through the mass conservations of the fluid component and solid phase. Since fluid flow occurs in pore spaces (or within fractures), rather than in the solid mass, it is more straightforward to study the coupling between fluid-flow and rock deformation through a governing equation that focuses on the “conservation” of pore space during the deformation. This paper will provide a derivation of such a governing equation.

GOVERNING EQUATIONS

We will first derive an equation for “conservation” of pore space during deformation, and then present the fluid-component mass balance equations for the dual continuum system. As previously indicated, such a derivation procedure may be more preferable simply because fluid flow occurs in pore spaces (or fracture apertures).

Pore space conservation

Consider a control volume (v_c [m³]) with fixed boundaries in the deformed rock mass (i.e., homogeneous and isotropic). For this control volume, the concept of pore-space conservation can be defined as the increase in pore space (storage term) for the rock mass within the control volume during a unit time, and is equal to the sum of net pore-space flux into the control volume due to solid flow (advection term) and local expansion of pore space (expansion term) for the given volume during that unit time.

It is easy to show that the storage and advection terms are $\frac{\partial(v_c \phi_j)}{\partial t}$ and $-v_c \nabla \cdot (\phi_j V_{s,j})$, respectively, where ϕ_j [-] is porosity for continuum j and defined as the ratio of pore volume for that continuum to the total volume of rock mass (including all the continua), t [s] is time, and V_s [m/s] is the solid velocity vector.

The expansion term can be derived from bulk volume change and solid-phase volume change for a unit rock volume. Using the definition of strain, bulk-volume change can be expressed as

$$dv_j = v_{0,j} d\varepsilon_{v,j} \quad (1)$$

where v [m³] is the bulk rock volume, ε_v [-] is the volumetric strain that is considered positive for expansion in this study, and v_0 is the rock volume under zero stress conditions. The subscripts can be $j = f$ and $j = m$, referring to the fracture and matrix continuum, respectively. Similarly, solid volume change can be given as

$$dv_{s,j} = v_{s,j} d\varepsilon_{s,j} \quad (2)$$

where the subscript s refers to the solid phase. Using the definitions of the solid and bulk rock volumes, one can obtain

$$v_{s,j} = (1 - \phi_j) v_{0,j} \quad (3)$$

Hooke's law further provides the following relationships

$$d\varepsilon_{s,j} = \frac{d\sigma_{s,j}}{K_{s,j}} \quad (4)$$

$$d\varepsilon_{v,j} = \frac{d\sigma_j}{K_j} \quad (5)$$

where $\sigma_{s,j}$ [Pa] and $K_{s,j}$ [Pa] are the (average) normal stresses acting on the solid phase and the solid-phase modulus of the continuum j , respectively. The

variables σ_j [Pa] and K_j [Pa] are the respective (average) effective stress and the bulk modulus for the continuum j . Considering that the effective stress is defined with respect to the bulk rock mass (including both the solid phase and the pore space), we can relate it to $\sigma_{s,j}$ by (Fjær et al., 2008)

$$d\sigma_j = (1 - \phi_j) d\sigma_{s,j} + (\phi_j - \alpha_j) dP_j \quad (6)$$

Combining Eqs. (1) through (6) yields the following expansion term

$$\frac{\partial(v_j - v_{s,j})}{\partial t} = \Phi_j v_c \left(\alpha_j \frac{\partial \varepsilon_{v,j}}{\partial t} - \frac{(1 - \alpha_j)(\phi_j - \alpha_j)}{K_j} \frac{\partial P_j}{\partial t} \right) \quad (7)$$

where $\alpha_j = 1 - \frac{K_j}{K_{s,j}}$ is the Biot's coefficient for the continuum j , $\Phi_j = \frac{v_{0,j}}{v_c}$ is the volume fraction of j th continuum (in the control volume) under unstressed conditions, and the volume difference $v_j - v_{s,j}$ is equal to the pore volume for that continuum within the control volume.

So far, we have obtained mathematical expressions for all three terms (storage, advection, and expansion) of the pore-space conservation equation. Thus, the conservation equation can be given as

$$\frac{\partial \phi_j}{\partial t} + \nabla \cdot (\phi_j V_{s,j}) = \Phi_j \left(\alpha_j \frac{\partial \varepsilon_{v,j}}{\partial t} - \frac{(1 - \alpha_j)(\phi_j - \alpha_j)}{K_j} \frac{\partial P_j}{\partial t} \right) \quad (8)$$

Eq. (8) is our new equation to establish the fundamental relationship among porosity, solid-phase flow and local strain during rock deformation processes. For simplicity, our derivation has focused on a relatively simple case (i.e., homogeneous and isotropic rock mass), although it can be extended to more complex situations.

Fluid mass conservation

Fluid mass conservation equations are fundamental equations that need to be solved for determining multiphase flow processes in fractured rock. A fluid mass conservation (balance) equation can be written as (Olivella, 1994; Pruess, 1991; Rutqvist et al., 2001)

$$\frac{\partial M_{j,\psi}^k}{\partial t} + \nabla \cdot \mathbf{q}_{j,\psi}^k - \mathbf{Q}_{j,\psi}^k = 0 \quad (9)$$

where $M_{j,\psi}^k$ [kg] is the liquid mass with j th continuum per unit control volume of fractured rock, k is the mass component (such as water, air, or CO₂), and ψ is the phase (gas, liquid, or solid). The symbol

$q_{j,w}^k$ [kg/s] represents liquid flux (within the j th continuum) with respect to the spatial reference system, and $Q_{j,w}^k$ [kg/s] is the source/sink rate of component k per unit volume. By combining Eqs. (8) and (9), the following equation can be derived (Liu and Rutqvist, 2009)

$$\frac{\partial(M_{j,w}^k)}{\partial t} + \nabla \cdot q_{j,w}^k + \frac{M_{j,w}^k}{\phi_j} \left(\Phi_j \alpha_j \frac{\partial \varepsilon_{v,j}}{\partial t} - \Phi_j \frac{(1-\alpha_j)(\phi_j - \alpha_j)}{K_j} \frac{\partial P_j}{\partial t} - \frac{\partial \phi_j}{\partial t} \right) - Q_{j,w}^k = 0 \quad (10)$$

The third term in our new Eq. (10) is an additional term owing to mechanical deformation, as compared with the fluid mass-balance equations commonly used in reservoir simulators (e.g., Pruess, 1991).

Momentum conservation

The momentum-conservation equation is a fundamental relation used for simulating rock deformation processes. While details regarding derivation of this equation are available in the literature (e.g., Jaeger et al., 2007; Fjær et al., 2008), we present it here just for the sake of completeness. In the absence of an inertia term (commonly assumed for modeling coupled hydro-mechanical processes), the momentum conservation can be expressed as (Rutqvist et al., 2001)

$$\nabla \cdot \sigma_T + \rho_m \mathbf{g} = 0 \quad (11)$$

where σ_T [Pa] is the total stress tensor, \mathbf{g} [m/s²] is the acceleration vector for gravity, and ρ_m [kg/m³] is the bulk density, including contributions from both the fluid and solid phases.

CONSTITUTIVE RELATIONSHIPS

In addition to governing equations, constitutive relationships (among hydraulic and mechanical parameters and related variables) are needed for solving the coupled hydro-mechanical processes. Constitutive relationships for uncoupled hydraulic and mechanical processes have been very well documented in the literature (Pruess, 2001; Jaeger et al., 2007). In this paper, we focus on those relationships related to coupling between hydraulic and mechanical deformation processes for the dual continua.

Stress-dependent hydraulic properties

The coupling between hydraulic and mechanical processes is largely determined by the stress dependence of hydraulic properties, which is closely

related to the stress-strain relationships in fractured rock. Recently, Liu et al. (2009) present a general relationship between stress and elastic strain for porous and fractured rock. They divide a rock body conceptually into two distinct (soft and hard) parts and define the soft part to a fraction of the pore volume subject to a relatively large degree of relative deformation. They show that the theoretical predictions of this method are generally consistent with both empirical expressions (from field data) and laboratory rock experimental data.

Based on their theory, the bulk modulus K_j [Pa] for the j th continuum is given by (Liu et al., 2009)

$$K_j = \frac{1}{\frac{\gamma_{e,j}}{K_{e,j}} + \frac{\gamma_{t,j}}{K_{t,j}} \exp\left(-\frac{\sigma_j}{K_{t,j}}\right)} \quad (12)$$

where subscripts 0 , e , and t denote the unstressed state, the hard part and the soft part, respectively, of a rock body, and K_e and K_t are the bulk moduli of the two parts. The constants $\gamma_{e,j}$ and $\gamma_{t,j}$ represent volumetric fractions of hard and soft parts at unstressed conditions $\gamma_{e,j} + \gamma_{t,j} = 1$.

The matrix porosity is related to stress by (Liu et al., 2009):

$$\phi_m = \phi_{e,m} (1 - C_e \sigma_m) + \gamma_{t,m} \exp\left(-\frac{\sigma_m}{K_{t,m}}\right) \quad (13)$$

where C_e is a constant and

$$\phi_{e,m} = \phi_{0,m} - \gamma_{t,m} \quad (14)$$

Subscripts m and 0 refer to the matrix continuum and unstressed state, respectively. When the term $C_e \sigma_m$ [-] is much smaller than unity, the above equation can be approximately reduced to

$$\phi_m = \phi_{e,m} + \gamma_{t,m} \exp\left(-\frac{\sigma_m}{K_{t,m}}\right) \quad (15)$$

Once the matrix porosity-stress relationship is available (Eqs. (13) and (14)), the relationship between permeability and stress can be easily obtained using empirical relations between permeability and porosity (a function of stress). Note that Eqs. (12)-(15) are developed for isotropic and homogeneous media under hydrostatic press conditions. For a more general condition involving different principle-stress values at a location, an

average of these stresses needs to be used in these equations. We acknowledge that this is an approximation and reserve the subject of a more accurate treatment to future research.

Liu et al. (2009) also derived a relationship for the stress-dependence of fracture aperture (for a single fracture) that relates the fracture aperture b [m] and porosity to the effective normal stress by

$$\frac{b}{b_0} = \frac{\phi_f}{\phi_{0,f}} = \gamma_{e,f} + \gamma_{t,f} \exp\left(-\frac{\sigma_f}{K_{t,f}}\right) \quad (16)$$

Then, the stress-dependence of fracture permeability can be easily determined from the cubic law that states that fracture permeability is proportional to the cube of the fracture aperture (a function of stress [Eq. 16]). However, Eq. (16) is developed by considering normal stress only and should be used when fracture planes are perpendicular to principal stresses. Additionally, these equations are valid for a single fracture. For a fracture network consisting of single fractures perpendicular to principal-stress directions, the stress-dependence of fracture-continuum permeability and porosity can be derived from the single-fracture relationship (Eq. [16]). Such a derivation was provided by Rutqvist et al. (2002).

Effective parameters for dual continua

A geomechanical simulator generally models bulk deformation (including both fractures and rock matrix). It is necessary to develop expressions of effective parameters for such a dual-continuum system that allow appropriate information transfer between geomechanical and reservoir simulators.

One important parameter for modeling coupled hydromechanical processes is the effective stress that depends on both the total normal stress, σ_T [Pa], and the fluid pressure. The effective (normal) stress for a single continuum can be expressed as (Jaeger et al., 2007)

$$\sigma = \sigma_T + \alpha P \quad (17)$$

where P [Pa] is the fluid pressure. For a dual continuum system under hydrostatic stress conditions (with the total stress assumed to be the same in both continua at a given point), we have (based on Hooke's law)

$$d\varepsilon_{v,m} = \frac{dv_m}{v_{0,m}} = \frac{d(\sigma_T + \alpha_m P_m)}{K_m} \quad (18)$$

$$d\varepsilon_{v,f} = \frac{dv_f}{v_{0,f}} = \frac{d(\sigma_T + \alpha_f P_f)}{K_f} \quad (19)$$

$$d\varepsilon_v = \frac{dv}{v_0} = \frac{dv_m + dv_f}{v_0} = \Phi_f d\varepsilon_{v,f} + \Phi_m d\varepsilon_{v,m} = \frac{d\sigma_{eff}}{K_{eff}} \quad (20)$$

Combining Eqs. (18) to (20), we obtain the effective modulus K_{eff} [Pa] and stress σ_{eff} [Pa] for a dual continuum system given by

$$K_{eff} = \frac{1}{\frac{\Phi_f}{K_f} + \frac{\Phi_m}{K_m}} \quad (21)$$

$$\sigma_{eff} = \sigma_T + \frac{\Phi_f K_{eff}}{K_f} P_f + \frac{\Phi_m \alpha_m K_{eff}}{K_m} P_m \quad (22)$$

Eqs. (21) and (22) are developed under hydrostatic stress conditions. The same conditions have also been used in previous studies of dual-continuum mechanical behavior (e.g., Berryman and Wang, 1995), while their derivation procedure is much more complicated.

A SENSITIVITY STUDY

As previously discussed, our governing equation (10) for fluid flow is different from those commonly used in reservoir simulators in that it includes an additional storage term that describes the effects of rock deformation on fluid flow. In this section, the importance of this additional storage term is evaluated through a sensitivity study. This evaluation is important because it can determine whether the considerable effort needed to modify the conventional reservoir simulators is warranted for modeling coupled hydromechanical processes.

The sensitivity study was conducted using a numerical model of CO₂ geological sequestration developed for the In Salah Gas Project in central Algeria. This is the world's first on-shore industrial scale project of CO₂ storage. The source of the CO₂ is the natural gas produced from this area (which is high in CO₂). Nearly one million tonnes of CO₂ per year are being injected since August 2004 into a relatively low-permeability, 20 m thick, water-filled carboniferous sandstone at a depth of about 1,800 to 1,900 m, around the Krechba gas field (Fig. 1). To ensure adequate CO₂ flow-rates across the low-permeability sand-face, the In Salah Gas Project decided to use long-reach (about 1 to 1.5 km) horizontal injection wells. The storage formation is an excellent analogue for much of North-West

Europe and of the U.S. midwestern region, where large storage capacity will be required if CO₂ capture and geological storage (CCS) is to make a significant contribution to reducing CO₂ emissions. (The formation into which CO₂ is injected is known to contain well-connected fractures (Iding and Ringrose, 2008).) Note that here we focus on the evaluation of the relative importance of the additional storage term in Eq. (10) (corresponding to a Biot's coefficient value of one), rather than on the detailed hydromechanical processes involved in the CO₂ geological sequestration of the In Salah Gas project. The latter will be reported on elsewhere.

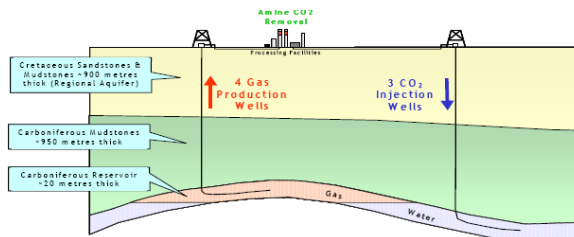


Figure 1. A schematic cross section of In Salah site (Wright, 2008).

Because the formation where CO₂ injection occurs is relatively thin (20 m thick), we used a two-dimensional fine-grid model to represent this formation. We assumed that the total stress was invariant during the CO₂ injection. In this case, changes in the effective stress are totally determined by changes in fluid pressure. To model this problem of CO₂ geological sequestration in deep aquifers, we used the TOUGH2 reservoir simulator (Pruess, 1991) with the ECO2N module (describing the equation-of-state of the H₂O+NaCl+CO₂ system)(Pruess, 2005). For this study, TOUGH2 was modified to include the additional storage term in the governing equation for fluid flow, and the stress dependence of the hydraulic properties.

The numerical model was calibrated against wellhead pressure (WHP) data observed from the In Salah Project site (Fig. 2). The pressure difference in Fig. 2 is defined as the difference between the WHP and its value without injection. In this part of the study, we considered this difference to be the same as difference between bottom hole pressure (BHP) and its ambient value. (This is admittedly a rough approximation, and refinement of our simulation results with more accurately estimated BHP difference will be performed in the future.) During model calibration, the measured flow rates at the injection well are directly taken as model inputs. The calibrated parameters are the fracture permeability under ambient conditions and the mechanical properties of Eq. (16). In general, injection pressure data for $t < 200$ days were used to determine the

ambient fracture permeability because stress-dependent behavior becomes more pronounced at the high-pressure differences that are expected at later time. The calibrated fracture permeabilities were 35 md and 7 md, respectively, in the two horizontal directions (along and perpendicular to the horizontal well). During calibration, the fracture porosity under ambient conditions was assumed to be 1%. The calibrated fracture mechanical properties (Eq. [16]) were $\frac{\gamma_{e,f}}{\gamma_{t,f}} = 8$ and $K_{t,f} = 3$ MPa, consistent with the fracture property values reported in Liu et al. (2009).

The calibrated model was then used to predict the injection pressure (at the injection well) as a function of time. The injection rate was assumed to be constant for the next 20 years, and equal to the average injection rate during the last 100 days of the period used for model calibration. After 20 years, injection stops. The simulated injection pressures are shown in Fig. 3.

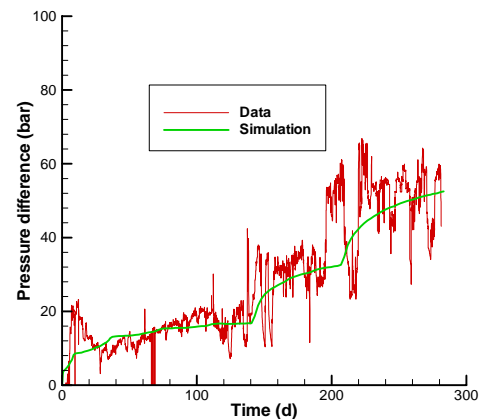


Figure 2. Comparison between simulated and observed pressure differences.

Note that the simulated results with and without the storage term (in Eq. [10]) are almost identical, suggesting that this new term has little effect on simulated pressure evolution at the injection borehole. We examined this issue in a number of simulation cases and obtained similar results. In one particular case, the results practically coincided even when the matrix porosity decreased by 70% and the injection rate increased by 100% (as compared with those used to obtain the simulation results of Fig. 3). These significant parameter changes were deemed sufficiently large to increase the contribution of the storage term of equation (10), but the results did not conform to the expectations. This finding indicates that the additional storage term may not be needed for practical applications as long as the stress-dependence of hydraulic parameters (e.g., porosity

and permeability) is considered. This can considerably simplify the “partial” coupling approach because modifications of governing equations for fluid flow (used in the corresponding reservoir simulator) are then unnecessary.

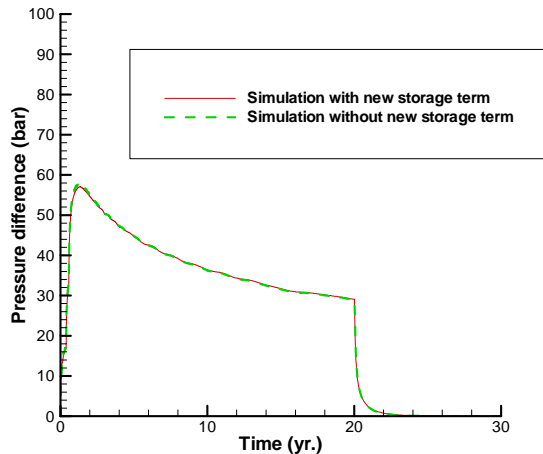


Figure 3. Simulated injection pressures with and without considering the new storage term in the governing equation for fluid flow (Eq. [10]).

CONCLUDING REMARKS

This paper presents a systematic approach to modeling coupled hydraulic and mechanical deformation processes in a dual continuum system. A pore-space conservation equation is developed to describe pore-space evolution resulting from the coupled process. This equation is particularly useful for investigating fluid flow in deformed fractured rock simply because fluid flow occurs in rock voids. Combining this new equation with fluid mass balances allows us to derive governing equations for fluid flow in fractured rock. Compared with the corresponding equations employed in traditional reservoir simulators, our governing equations include an additional storage term resulting from mechanical deformation. We conducted a sensitivity study using data from a CO₂ geological sequestration project (In Salah Gas Project). Our results demonstrate that consideration of this additional storage term has little effect on simulated fluid flow processes, as long as the stress-dependence of hydraulic properties is considered in the reservoir simulators.

ACKNOWLEDGMENT

We appreciate that Dr. George J. Moridis from LBNL provided thorough and constructive comments on the preliminary version of the paper. This work was supported by the Assistant Secretary for Fossil Energy, Office of Sequestration, Hydrogen, and Clean Coal Fuels of the U.S. Department of Energy under Contract No. DE-AC02-05CH11231. Especially, we like to acknowledge In Salah JIP and their partners BP, StatoilHydro, and Sonatrach for providing field data and valuable discussions.

REFERENCES

- Bai, M., D. Elsworth, and J. C. Roegiers, Multiporosity/multipermeability approach to the simulation of naturally fractured reservoirs. *Water Resour. Res.* 29, 1621-1633, 1993.
- Berryman, J.G., and H. F. Wang, The elastic coefficients of double-porosity models for fluid transport in jointed rock. *J. Geophys. Res.* 100(B12), 24611-24627, 1995.
- Fjær, E., R. M. Holt, P. Horsrud, A. M. Raen, and R. Risnes, *Petroleum related rock mechanics* (2nd Edn). Elsevier, Boston, 491 pp, 2008.
- Iding, M., and P. Ringrose, Evaluating the impact of fractures on the long-term performance of the In Salah CO₂ storage site. *9th International Conference on Greenhouse Gas Control Technology, GHGT-9*, Washington D.C., 16-20 Nov, 2008.
- Jaeger, J.C., N. G. W. Cook, and R. W. Zimmerman, *Fundamentals of rock mechanics* (4th Edn). Blackwell Publishing, Malden, 2007.
- Jing, L., and J. A. Hudson, Numerical methods in rock mechanics. *Int J Rock Mech Mining Sci* 39, 409-427, 2002.
- Liu, H.H, J. Rutqvist, and J. G. Berryman, On the relationship between stress and elastic strain for porous and fractured rock. *Int J Rock Mech Mining Sci.* 46, 289-296, 2009.
- Liu, H.H and J. Rutqvist, Coupled hydromechanical processes associated with multiphase flow in fractured rock. *Journal of Petroleum Science and Engineering* 2009 (in review).

- Olivella, S., J. Carrera, A. Gens, and E. E. Alonso, Nonisothermal multiphase flow of brine and gas through saline media. *Transp Porous Media* 15, 271-293, 1994.
- Pruess, K., *TOUGH2- A general purpose numerical simulator for multiphase fluid and heat flow*. Lawrence Berkeley National Laboratory Report LBL-29400, 1991.
- Pruess, K., *ECO2N- A TOUGH2 fluid density module for mixtures of water, NaCl, and CO₂*. Lawrence Berkeley National Laboratory Report LBL-57952, 2005.
- Rutqvist, J., L. Borgesson, M. Chijimatsu, A. Kobayashi, L. Jing, T. S. Nguyen, J. Noorishad, C. F. Tsang, Thermohydromechanics of partially saturated geological media: governing equations and formulation of four finite element models. *Int J Rock Mech Mining Sci.* 38, 105-127, 2001.
- Rutqvist, J., Y. S. Wu, C. F. Tsang, and G. S. Bodvarsson, A modeling approach for analysis of coupled multiphase fluid flow, heat transfer, and deformation in fractured porous rock. *Int J Rock Mech Mining Sci* 39, 429-442, 2002.
- Wilson, R.K., and E. C. Aifantis, On the theory of consolidation with double porosity. *Int. J. Eng. Sci.* 20, 1009-1035, 1982.
- Wright, I., Satellite monitoring at In Salah. *Seventh annual conference on carbon capture & sequestration*, Pittsburg, Pennsylvania, 5-8 May, 2008.

A USER-FRIENDLY GRAPHICAL INTERFACE FOR TOUGHREACT

You Li, Marcin Niewiadomski, Edward Trujillo, Surya Prakash Sunkavalli
University of Utah, Department of Chemical Engineering
50 S. Central Campus Drive - 3290 MEB
Salt Lake City, UT 84112 U.S.A.
edward.trujillo@utah.edu

ABSTRACT

TOUGHREACT is a powerful simulator for multi-phase fluid, heat, and chemical transport. However, it has a steep learning curve, and the creation of the input files is time intensive, particularly for heterogeneous and complex geometries such as those experienced in simulating mining rock piles and formations. TOUGHER is an application developed—by the Acid Rock Drainage research group of the Department of Chemical Engineering at the University of Utah—to develop models rapidly and be able to visualize the simulation results in an intuitive way. It also reduces the chance of mistakes while creating complex models and makes debugging easier. The application is written in C++ and can be run on any computer with a Windows or Linux operating system. This poster paper will describe the overall structure of the application and give some examples of how it interfaces with the TOUGHREACT program. In particular, it will be shown how the application can generate a grid system for a rock pile containing several distinct geological layers, how the properties of each layer are set, and how the input sections (ELEM and CONNE) for TOUGHREACT are generated automatically. In addition, visualizing the flow and chemical output files generated by TOUGHREACT for a particular rock pile will be demonstrated, including the handling of transient vector as well as transient scalar data.

INTRODUCTION

One of the difficulties in working with any simulation software is to create an error-free input file that the software can use to run the simulation. This is the case for TOUGH2 [Pruess, 1999] and TOUGHREACT [Xu, 2004], in which the user must define the system, create a geometry that resembles the system, and assign properties to the various components in that geometry. This is especially difficult if one is simulating reactive flow in heterogeneous porous media, such as that in underground geologic formations and human-made mining rock piles. Our research group is particularly interested in modeling acid rock drainage (ARD), an environmental problem affecting the mining industry. We

have created a software application to make TOUGHREACT more user-friendly and faster for setting up the input files for this particular problem; the application also visualizes the results from TOUGHREACT, so users can view the results in a more intuitive way. While our software does not create all the files necessary to run TOUGHREACT, it does help develop the most labor-intensive aspects. It is geared towards creating physical models of porous media more easily, rock piles in particular.

DESIGN AND IMPLEMENTATION

TOUGHER was designed using the following libraries (see Figure 1):

- OpenGL: for rendering the model.
- Qt(toolkit): for graphical user interface and networking support.
- Qwt: for plotting.

There are three major components of TOUGHER:

- A rendering engine that displays the model and visualization.
- A model generator that generates TOUGHREACT models.
- A post processor that processes the output files so they can be visualized.

Each of these will be described separately below.

TOUGHER COMPONENTS

Rendering Engine

The rendering engine is the foundation of TOUGHER. All major interactions between the program and user are achieved through the visualization generated by the rendering engine. The core of the rendering engine contains two parts:

1. A package of data structures to store TOUGHREACT data and model information: ROCK, MULTI, PARAM, SOLVR, RPCAP, ELEM, CONNE, GENER.
2. A displaying engine implemented with OpenGL to display the data structures.

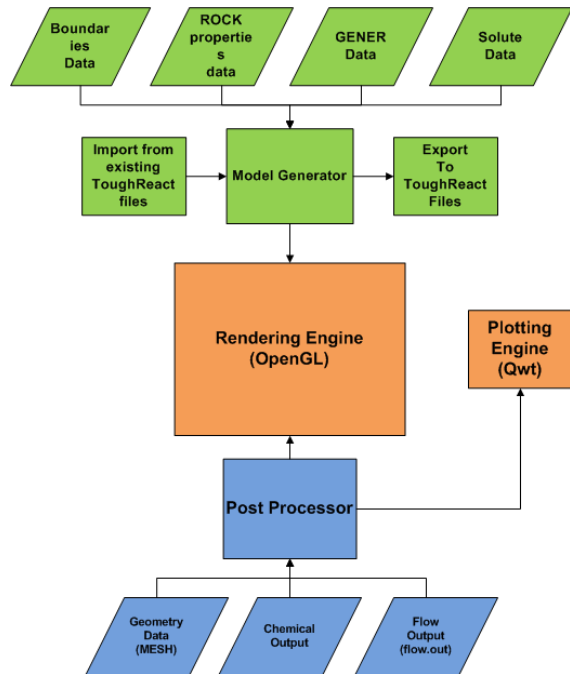


Figure 1. Design Chart for TOUGHER

The engine is used in both model generation and output visualization. Since both tasks share many common data structures, the rendering engine is versatile enough to function without much modification.

Model Generator

The model generator is one of the most important and definitive components of TOUGHER. Our project was based on the idea of creating a program that would make model generation of a rock pile in TOUGHREACT easier and faster.

The basic concept of the model generator is like building physical models with LEGO® blocks. A model of a rock pile can be divided into multiple layers based on different rock properties, and between two layers there is a boundary. A model is made up of many user-defined boundaries. Basically the steps involved are:

1. A list of boundaries and rock properties are defined by the user either in 2D or 3D format (see Figure 2). Thus, a coordinate system must be defined and for a 2D Cartesian coordinate system, the boundaries must be defined in terms of X and Y coordinates.
2. X cell size and Y cell size are chosen by the user.
3. The layers are sorted from lowest in elevation to highest.
4. Starting from the bottom-left, add blocks with size X*Y and corresponding rock properties until

the next boundary is reached. Continue until the top boundary is reached.

5. Add X cell size to the current X value if the result is smaller than the maximum X value for the boundaries; otherwise, stop building (see Figure 3). The concept is simple and easy to implement, but it has a few limitations:
 - The grid can only be rectangular, and all cells have the same size.
 - All boundaries must have the same number of points with the same set of X values
 - This method only works for 2D mesh.

Post Processor

The post processor is used for output visualization. The tasks of the post processor are twofold:

1. Parse chemical output files and store the results.
2. Parse flow output files and translate the data into vector data.

Since the chemical output files already have a format that is easy to read, the post processor simply reads in all the information contained in the files and displays them with the rendering engine (Figure 4).

This procedure becomes more complicated for flow data, because the flow output files only contain vector information along a connection. In our 2D Cartesian coordinate case, all the connections are either vertical or horizontal. Therefore, all the vectors in one cell need to be combined to create a new vector that shows the correct direction and relationship.

Figure 5 shows a section of a model with new vectors generated by the post processor. The arrows indicate the direction of the vectors, and the length of the arrows indicate the magnitude of the vectors.

To illustrate how our program works, we will go through a simple example of a layered rock pile. At the start of our program, the user sees a blank screen divided into an upper section and a lower section (see Figure 6). The upper section has two tabs, one for viewing the model and the other for transient plotting. The lower section has two types of tabs – New input file and visualization. These are used to create a new input file to TOUGHREACT and to visualize the results after running TOUGHREACT. To begin constructing a new model, the user clicks on the new input file tab, which contains four subtabs called Model Generation, Rocks, Gener and Solute.inp. Each of these will be described below.

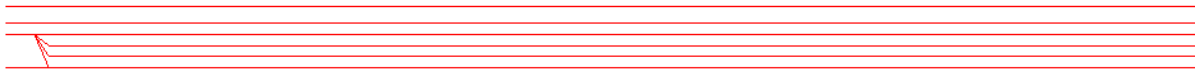


Figure 2. Boundaries

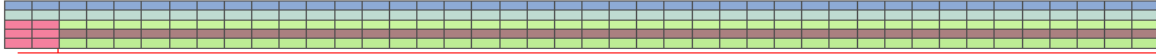


Figure 3. Cells generated

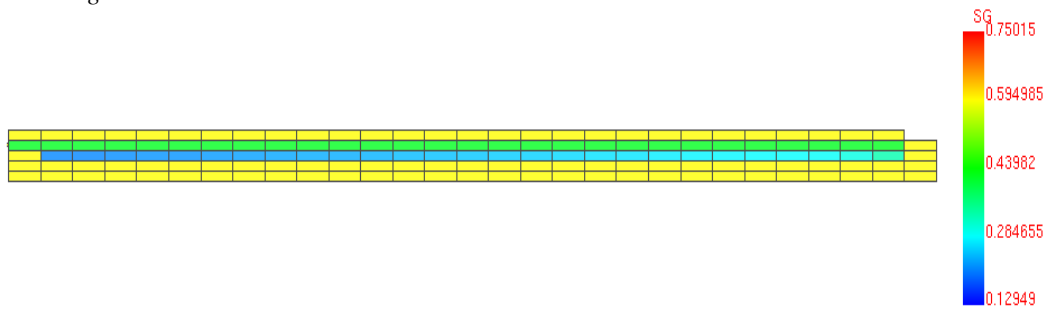


Figure 4. Chemical output showing saturation of gas

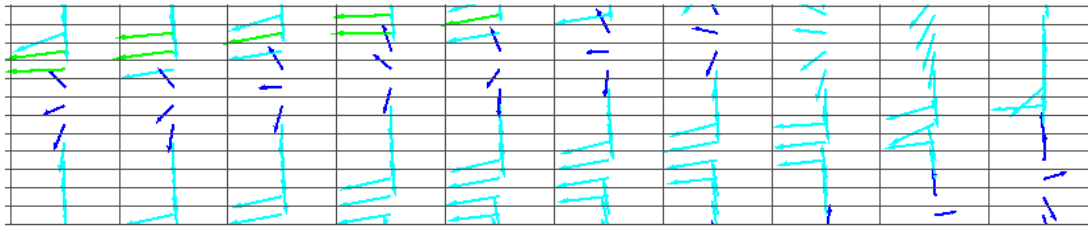


Figure 5. Vectors showing velocity of liquid in several different geological layers

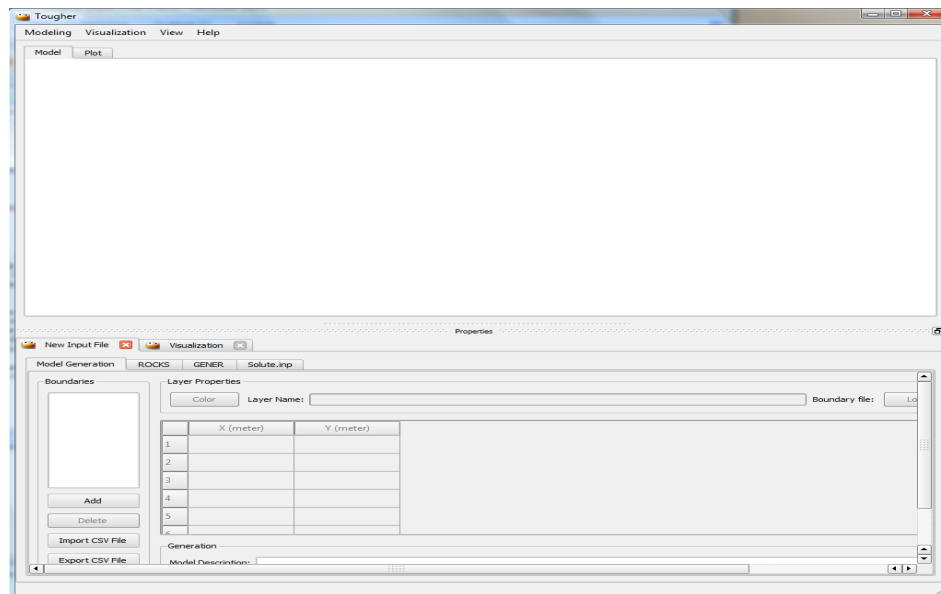


Figure 6. Overview of TOUGHER'S interface at the start of the program

EXAMPLE**Mesh**

As stated above, we first need to define the boundaries of the rock pile layers in a 2D Cartesian coordinate system. To make it easier, TOUGHER accepts CSV files with the format as shown in the Figure 7.

The highlighted portion shows a single boundary in the CSV file. The first row is the boundary name followed by the X and Y values of points that define the boundary. The boundaries (BASE, LEFT, B1, B2, etc.) are divided by an empty column.

Once this is done, the user can import this into the TOUGHER program through the Model Generation section (tab).

Figure 8 is a window used in our program under the Model Generation tab:

- The left panel shows a list of boundaries (described by the CSV file), with buttons that gives the user the option to add/remove boundaries. The buttons to import and export CSV files are also shown here.
- The color button (in Layer Properties) changes the color of the selected layer. Normally, a boundary's color is assigned randomly.
- The layer name is for identification purpose only.
- After the layer name are the boundary file button and the material button. These buttons are used to load a single boundary coordinate file and to define the properties (material) of each layer, as assigned in the ROCKS section described below.
- At the center are the X and Y values of points in the selected boundary.

	A	B	C	D	E	F	G	H	I	J
1	BASE			LEFT			B1			B2
2	30	0		30	22.8		30	22.8		30
3	40	0		40	22.8		40	22.8		40
4	50	0		50	22.8		50	22.8		50
5	60	0		60	0		60	7.6		60
6	70	0		70	0		70	7.6		70
7	80	0		80	0		80	7.6		80
8	90	0		90	0		90	7.6		90
9	100	0		100	0		100	7.6		100
10	110	0		110	0		110	7.6		110
11	120	0		120	0		120	7.6		120

Figure 7. A CSV file with boundaries information

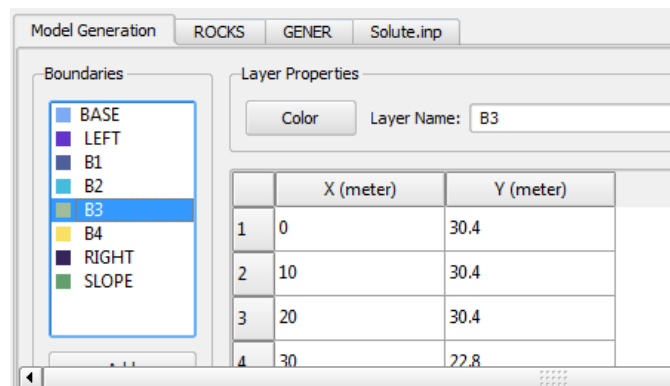


Figure 8. User interface for defining boundaries and Layers

Rock Properties

Rock or layer properties can be defined by clicking the ROCKS tab (see Figure 8). Figure 9 shows a window for setting rock properties.

The rock properties section corresponds to the material drop-down list in the previous section. The fields are exactly matched to the ROCKS section in the TOUGHREACT input file.

Generation Terms

This section (the GENER tab, Figure 10) creates the data corresponding to the GENER section of TOUGHREACT input files, which allows a layer:

- To have infinite volume
- To have mass injection/production
- To have heat injection/production



Figure 9. User interface for rock properties

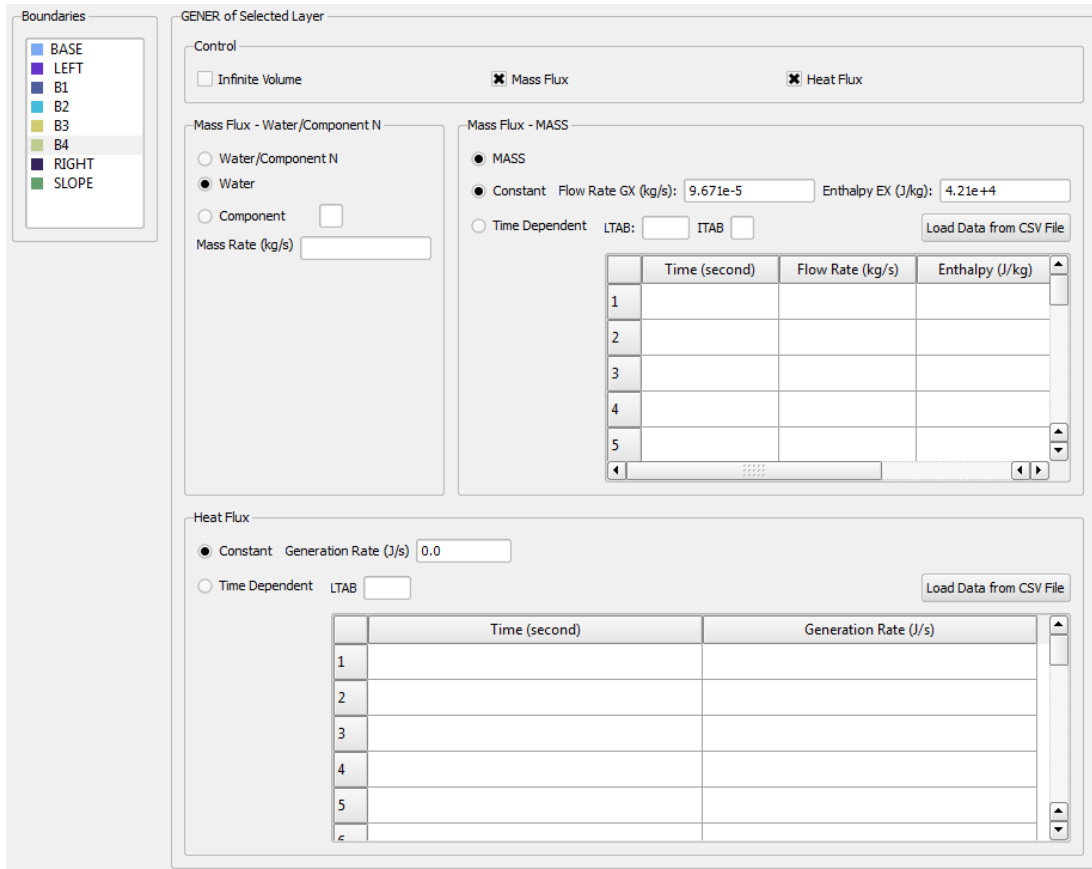


Figure 10. User interface for generation terms

Solute.Inp Data

If the user decides to include solute.inp data, the information is placed in the solute.inp section (tab). Figure 11 shows this part of the program. Notice that this section only partially creates the solute.inp file. More information needs to be filled in manually.

Generate Toughreact Files

After setting up all the sections mentioned above, the user can now generate a model. To do this, the user needs to go back to the model generation section. The lower portion contains the generation section. In this section, the user specifies:

- A name for the model. This text will be displayed at the first line of the TOUGHREACT input file called flow.inp (This text is optional)

- Grid X size
- Grid Y size
- Grid Z size
- Rotation angle. This angle is the counter-clockwise positive angle from horizon in degrees. This is useful if the model has been rotated to optimize the gravity vector. In other words, even though the layers show as horizontal layers on the screen, they are oriented by this angle with respect to gravity (see Figure 12).
- After hitting the Generate button, a model will be generated.

Figure 13 shows an example of a complex rock pile generated using our program.



Figure 11 User interface for solute.inp data

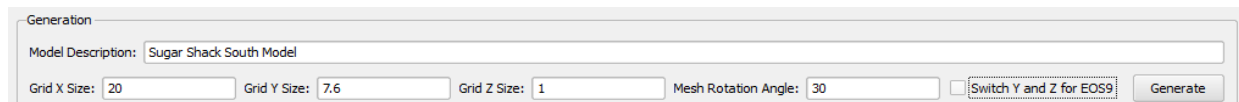


Figure 12 Model generation settings

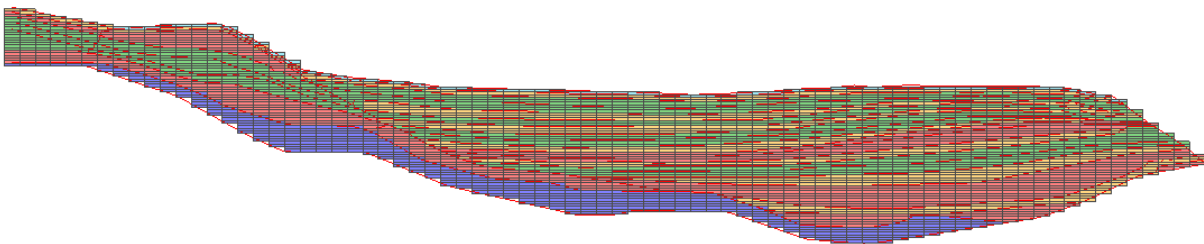


Figure 13. Sample model generated by TOUGHER. This is a model of a hypothetical rock pile that is approximately 1,500 feet long and 100 feet thick. This model has 26 geological layers and is built with 3,008 elements with 5,844 connections among them.

OUTPUT VISUALIZATION

Not only can TOUGHER generate models, it can also visualize the results from TOUGHREACT runs. Before loading the output files, though, the mesh data needs to be loaded into the software from the flow.inp or MESH file.

Visualize Chemical Data

Multiple files can be loaded at once, and the user can visualize the data from all of them (see Figure 14). After loading the files, the user simply:

1. Selects a file
2. Selects a time step
3. Selects a species

Visualize Flow Data

Visualization of chemical data and flow data is done in a similar way. But since there will be only one file containing flow information, flow.out, the user merely needs to select a time step and a type of flow to visualize (see Figure 15).

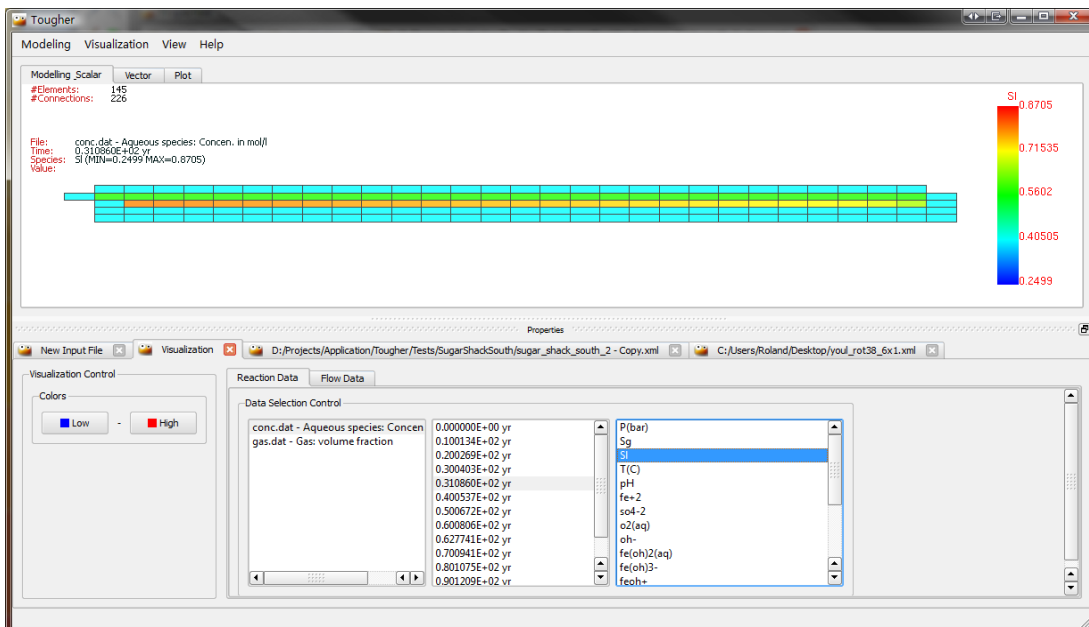


Figure 14. Sample visualization of water saturation values for a simple rock pile.

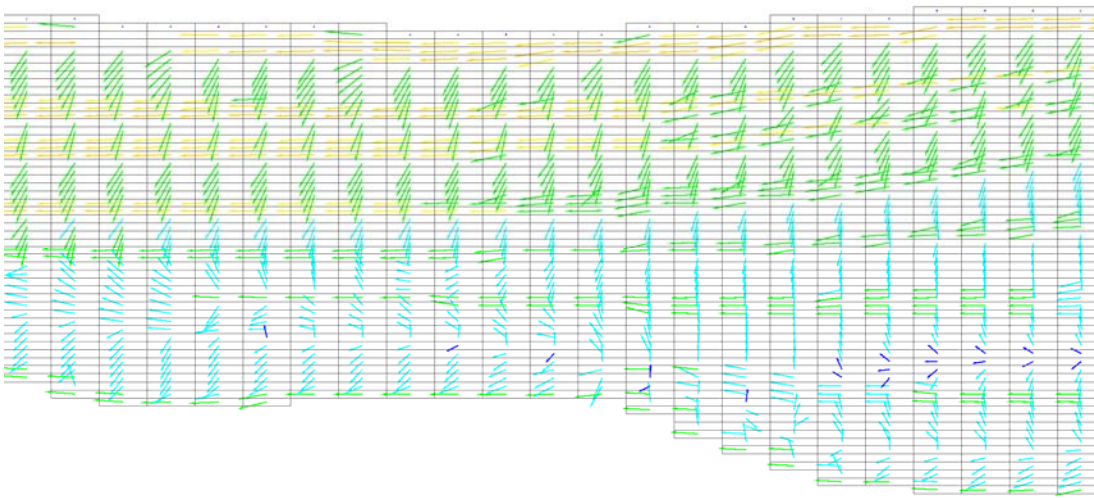


Figure 15. An example of visualizing only a portion of the flow data (velocity vectors) for a complex rock pile such as that shown in Figure 13.

CONCLUSIONS

A user-friendly interface program to TOUGHREACT has been developed that helps generate the mesh for a layered geological formation and define the properties of those layers. The program can also be used to visualize the output from a TOUGHREACT run, including transient flow vector data.

ACKNOWLEDGMENTS

This project was funded by Chevron Mining Inc. (formerly Molycorp, Inc.) for which we are grateful. We would also like to thank everyone in the large multidisciplinary team associated with this project for their helpful suggestions and comments during the development of these models.

REFERENCES

- Pruess, K., C. Oldenburg, and G. Moridis, *TOUGH2 User's Guide, Version 2.0*, Report LBNL-43134, Lawrence Berkeley National Laboratory, Berkeley, Calif., 1999.
- Xu, Tianfu, E. Sonnenthal, N. Spycher and K. Pruess, *TOUGHREACT User's Guide: A Simulation Program for Non-isothermal Multiphase Reactive Geochemical Transport in Variably Saturated Geologic Media*, Report LBNL-55460, Lawrence Berkeley National Laboratory, Berkeley, Calif., September 2004.

WHAT'S NEW IN iTOUGH2?

Stefan Finsterle

Lawrence Berkeley National Laboratory
Earth Sciences Division, One Cyclotron Rd., MS 90-1116
Berkeley, CA 94720
e-mail: SAFinsterle@lbl.gov

ABSTRACT

iTOUGH2 provides inverse modeling capabilities for the TOUGH suite of nonisothermal multiphase flow simulators. By running TOUGH simulations multiple times for different input parameter sets, iTOUGH2 can be used for parameter estimation through automatic model calibration, for formalized sensitivity analyses to identify which parameters can be estimated accurately given available data (or to determine what data are needed to accurately estimate parameters of interest), or for assessing the uncertainty of model predictions. Furthermore, iTOUGH2 provides a useful framework for running TOUGH simulations with added capabilities, such as automatic modification of state variables at user-specified locations and times, automatic calculation of steady-state distributions in TOUGH simulations, generation of realistic heterogeneous fields (i.e., spatially correlated permeability or porosity fields that are conditioned to point measurements), and for simplifying otherwise tedious tasks, such as generating time-series output of state variables. iTOUGH2 is continuously updated in response to scientific challenges and user needs. For example, the code was expanded to allow for the joint inversion of hydrogeological and geophysical data. To accomplish this, interfaces to external geophysical forward simulators were established, and appropriate petrophysical relationships were introduced that link the classical TOUGH state variables to properties that affect the geophysical signals to be matched during the joint inversion. A similar approach is used for the analysis of geochemical data. To efficiently and robustly solve these joint inverse problems with their increased parameter and observation spaces, the optimization algorithms have been adapted to better handle strong correlations and large differences in parameter sensitivities. These new capabilities, as well as other iTOUGH2 enhancements and additions, are described in this paper.

INTRODUCTION

The first version of the iTOUGH2 simulation-optimization code (<http://esd.lbl.gov/iTOUGH2>) was released in 1994, providing automatic model calibration capabilities for the 1991 version of the TOUGH2 nonisothermal multiphase flow and transport simulator (Pruess, 1991). Ever since, iTOUGH2 has been

continuously updated to enhance both its forward and inverse modeling capabilities. Specifically, many newly developed equation-of-state modules have been incorporated into the iTOUGH2 framework. New user features have been added, mainly driven by the need to avoid user intervention during a simulation run, which are not acceptable when automatically performing multiple forward simulations as part of an inversion. This requirement led to the development of features that are useful also in standard forward simulations. For example, iTOUGH2 provides means to make minor adjustments to element and connection data after mesh generation; to connect steady-state and transient simulations without user interference; to change state variables and select rock properties at discrete simulation times; to extract time series of state variables or simple functions of these state variables; to specify time-varying Dirichlet boundary conditions; and to send signals to the code during execution to trigger certain actions, notably the graceful termination of the simulation. Most importantly, iTOUGH2 provides simple parameterizations of certain aspects of the conceptual model, so these aspects can be subjected to parameter estimation or uncertainty analyses. The most prominent example is the parameterized generation and mapping of spatially correlated property fields using the GSLIB geostatistical library (Deutsch and Journel, 1992).

In addition to enhancing forward modeling capabilities, iTOUGH2's optimization algorithms, as well as the related sensitivity and uncertainty propagation analyses, have been refined, and new user features have been added to make iTOUGH2 more useful, more robust, and more efficient. Many of these developments were driven by the recent inclusion of geophysical data into a joint inversion framework, which called for more convenient data input, the addition of regularization by a smoothness criterion, parameterization at pilot points, and a more robust inversion by suitably truncating the parameter space. In addition, new global minimization algorithms were added, and the sensitivity analysis option expanded.

Table 1 provides an overview of recent iTOUGH2 enhancements; some will be discussed in more detail in the remainder of this paper.

Table 1. Summary of Recent iTOUGH2 Developments

Capability Description	Command	Reference
<i>Forward Model</i>		
Geostatistical simulation	GSLIB	Deutsch and Journel (1992); Finsterle and Kowalsky (2007, 2008)
Hysteresis	HYSTE	Doughty (2007, 2009)
Time stepping	MOP(16)=0 MOP(16)=1	TOUGH2 output file
TMVOC	-	Pruess and Battistelli (2002)
EOS7C	-	Oldenburg et al. (2004)
ECO2N	-	Pruess (2005)
Geophysics	GEOPH	Kowalsky et al. (2007)
<i>Inverse Model</i>		
Pilot points	>> PILOT POINT	Finsterle and Kowalsky (2007)
Geostatistical parameters	>> NUGGET >> SILL >> RANGE >> ANISOTROPY >> ROTATION	Finsterle and Kowalsky (2007)
Global search	>> EVOLUTION >> HARMONY	Finsterle and Zhang (in preparation)
Jacobian	>>> BROYDEN >>> SKIP	Finsterle (2009)
Regularization	>> SMOOTH	Finsterle (2009)
Tikhonov matrix	-	Finsterle (2009)
Truncation	>>>> TRUNCATED	Finsterle (2009)
Spatial data	>>> MAP >>> PROFILE >>> SECTION	Finsterle (2009)
Temporal data	>>>> INDIVIDUAL WINDOWS	Finsterle (2009)
Zero-value and no data	>>>> NO DATA >>>> ZERO DATA	Finsterle (2009)
<i>General</i>		
Module structure	-	File it2stubs.f
Distribution	-	esd.lbl.gov/TOUGH+

FORWARD SIMULATION CAPABILITIES

In essence, iTOUGH2 simply solves the forward model multiple times for different parameter combinations, extracts select output from these individual runs, and uses this information to perform a formal sensitivity analysis, parameter estimation by automatic model calibration, and uncertainty propagation analysis. The forward simulator, which implements the conceptual model of the system to be studied, is thus the engine of iTOUGH2, i.e., any improvement of forward simulation capabilities most critically affect the value and usefulness of iTOUGH2. It should also be noted that iTOUGH2 can be used for conventional forward simulations, which thus can benefit from the enhancements in the forward model discussed in this section.

Geostatistical Simulation

Heterogeneity is a defining feature of the subsurface, which significantly affects the natural behavior and response to external forcing. Identifying, describing, and simulating heterogeneity in itself is challenging, since it results from a combination of deterministic and stochastic processes on multiple scales.

Geostatistical methods are one way to characterize subsurface heterogeneity using a relatively small number of parameters, which capture average spatial features in a hydrogeologic data set. These parameters can then be used to predict (in a statistical sense) probable distributions of that property by weighted interpolation (e.g., kriging) or geostatistical simulation.

Three methods (kriging, sequential Gaussian simulation, and sequential indicator simulation) of the geostatistical software library GSLIB (Deutsch and Journel, 1992) have been implemented into iTOUGH2 for the convenient generation of spatially correlated permeability or porosity fields. These fields are first generated on regular two- or three-dimensional grids, which are then mapped onto the TOUGH mesh. Since field generation and mapping are fully integrated into iTOUGH2 (Finsterle and Kowalsky, 2007), the impact of random heterogeneity on simulation results can be examined using Monte Carlo simulations, where a new property field is generated for each Monte Carlo realization. Moreover, iTOUGH2 can be used for soil structure identification, as described below.

Hysteresis

Multiphase flow behavior is critically affected by the capillary pressure and relative permeability curves, which govern the driving force and flow resistance for a given saturation. Inverse modeling has been used extensively to determine the parameters of these curves. (For a review of related iTOUGH2 applica-

tions, see Finsterle, 2004.) Moreover, a careful residual analysis may indicate that the functional form of the standard characteristic curves is inappropriate to represent retention properties and phase interference. This may be caused by a multimodal pore-size distributions, or dynamic effects that lead to hysteresis. Hysteresis is a well-documented phenomenon that particularly affects the trapping of the nonwetting phase—a crucial issue for the long-term geological sequestration of CO₂ (Doughty, 2007). A sophisticated hysteresis model has been implemented into iTOUGH2 (Doughty, 2009). Not only does it consider hysteresis in the capillary pressure function, but also in the relative permeability curves, whereby the amount of residual nonwetting phase saturation is in itself a history-dependent parameter (Figure 1). The parameters of the hysteresis model can be estimated by inverse modeling or subjected to uncertainty analyses.

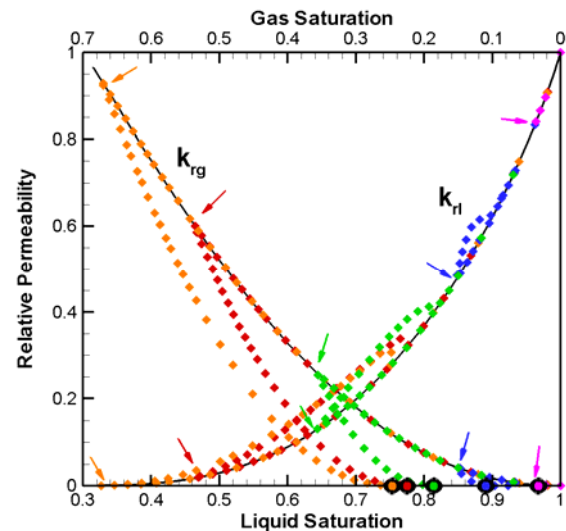


Figure 1. Hysteretic relative permeability paths taken during CO₂ plume migration (from Doughty, 2007), showing history-dependent residual gas saturation values as black-outlined dots.

Time Stepping

Two new time-stepping schemes have been implemented. The first calculates an increase or decrease in time-step size as a simple function of the number of Newton-Raphson iterations needed to reach convergence. The second approach uses the maximum change in saturation to guide time stepping. These alternative schemes generally increase the efficiency of a forward simulation.

Equation-of-State (EOS) Modules

The suite of TOUGH simulators is continuously expanded in response to new scientific insights or application needs. The TOUGH developer team enhances process descriptions and adds new fluid property modules to be able to handle specific com-

binations of components, phases, and processes. (For a discussion of recent developments, see Finsterle et al., 2008.) Many of these fluid property modules have been incorporated into the inverse modeling framework of iTOUGH2. Among the most prominent of these modules are (a) TMVOC (Pruess and Battistelli, 2002) for nonisothermal three-phase flow of water, multiple noncondensable gases, and multiple volatile organic compounds, (b) EOS7C (Oldenburg et al., 2004) for nonisothermal two-phase flow of water, brine, CO₂ or N₂, and air, and (c) ECO2N (Pruess, 2005) for nonisothermal two-phase flow of water, brine, and CO₂. Additional EOS modules have been and will be linked to iTOUGH2 as needed.

Geophysical Postprocessing

Geophysical methods are employed to infer the geologic structure of the subsurface. In addition, geophysical data may be sensitive to changes in fluid saturations, salinity, or temperature, and can thus be used to image the system state and its temporal evolution.

iTOUGH2 attempts to improve subsurface imaging and parameter estimation by jointly inverting hydrological, thermal, geochemical, and geophysical data. The fundamental concept is described in Kowalsky et al. (2005). Within this frame, geophysical attributes need to be calculated for each gridblock as a function of porous-medium and fluid properties as well as the system state. Petrophysical models are used to establish a link between hydrogeological properties and state variables used in TOUGH2 and the corresponding geophysical attributes (e.g., electrical resistivity or seismic velocity); the latter are then used in a geophysical forward model to calculate geophysical signals, such as voltage or arrival time. These geophysical data can then be used—along with hydrological, thermal, or geochemical data—in the joint inversion framework discussed below.

Postprocessing TOUGH2 output at select simulation times to generate attributes used as input to geophysical simulators is a first step for the joint hydrogeophysical inversion approach. This link has been established for different geophysical methods, including ground penetrating radar (GPR), electrical resistance tomography (ERT), resistivity data, and seismic data. Other geophysical methods (microgravity, self-potential, and controlled source electromagnetics) are currently being investigated.

INVERSE MODELING CAPABILITIES

Any advance in the forward modeling capabilities of the TOUGH suite of simulators calls for enhancements in the inversion framework. Not only do the number and type of parameters and observable variables change as new processes or fluid compositions are considered—The nature of the inverse problems

and associated challenges in solving them also change. In particular, making iTOUGH2 a platform for joint inversions of different data types for the estimation of spatially distributed parameters, using high-resolution geophysical data, mainly required the implementation of new algorithms and user features. Some of them are described in the following subsections.

Pilot Points

The geostatistically generated property fields discussed above can be conditioned on given values at certain locations. While conditioning is usually invoked to honor measured values, it also can be used to adapt so-called pilot points (RamaRao et al., 1995). In this approach, property values at the pilot points are the parameters of calibration. This approach couples geostatistics and optimization. Changing the permeability at one of the pilot points influences the permeability field in the vicinity of the point within approximately one correlation length. Distributing pilot points over the model domain allows iTOUGH2 to modify the heterogeneous field during an inversion, improving the match to the measured data of the system response, and at the same time acknowledging the geostatistical properties of the field (as well as measured permeabilities). An application of the pilot point method using iTOUGH2 is presented in Kowalsky et al. (2005) and Finsterle and Kowalsky (2008).

Estimation of Geostatistical Parameters

In the context of inverse modeling, the soil structure is usually considered a part of the (fixed) conceptual model, i.e., parameters representing soil properties are estimated under the assumption that the geometry of subsurface features (e.g., stratigraphic layers, inclusions, intrusions, man-made structures) are known and correctly captured in the model. However, estimates of feature-related property values may be severely biased if the underlying description of the soil structure is wrong. Given the (partly) stochastic nature of subsurface heterogeneity, it is unlikely that the geometry of these features is correctly captured throughout the model domain.

Geostatistical simulation is one way to describe and generate soil structures that resemble subsurface heterogeneity. If combined with the pilot point method, these structures can be conditioned on site-specific property data, or—as proposed here—site-specific observations of any types of data that are sensitivity to the details of the heterogeneity. Classical geostatistics directly analyzes data of the attribute of interest (or of attributes that are statistically correlated to the property to be described by geostatistical parameters). In our approach, we infer these geostatistical parameters through inverse modeling of flow and transport data that are affected by the heteroge-

neous soil structure. For example, the amount of water infiltrating into a heterogeneous soil, or point observations of water content along a borehole, depend on the variability, continuity, size, and orientation of sand and gravel deposits and the clay lenses embedded in them (Figure 2). These geometric characteristics are geostatistically described by the nugget effect, sill value, correlation length, anisotropy ratio, and orientation of the semivariogram. Given the sensitivity of the observed data to changes in the soil structure, these geostatistical parameters can thus be estimated by model calibration. The pilot point method accounts for the fact that we are interested in a single realization with site-specific locations of clay lenses, rather than an abstract universe of random realizations. The estimation of geostatistical parameters using a joint hydrological-geophysical inversion approach is demonstrated in Finsterle and Kowalsky (2007).

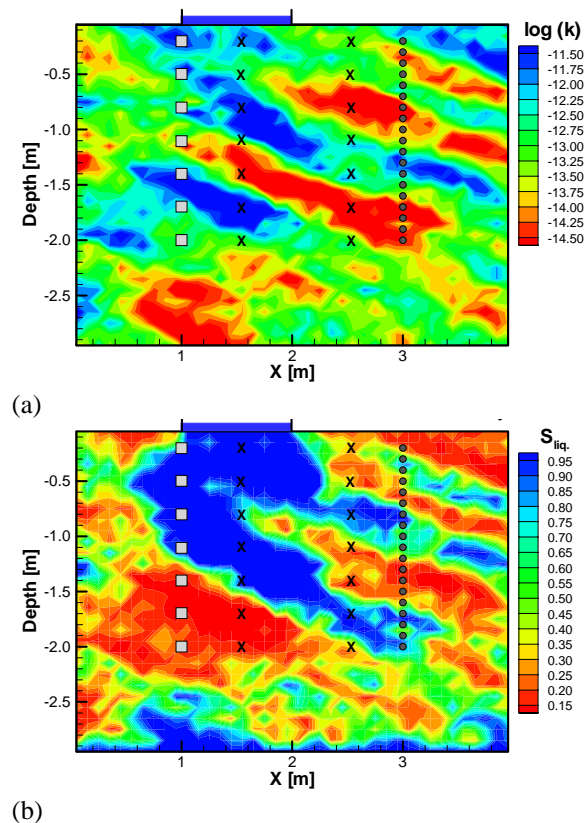


Figure 2. (a) Spatially structured random permeability field; locations of neutron probes in boreholes (squares); location of GPR antennas (squares: transmitting; circles: receiving); and position of pilot points (crosses); (b) liquid saturation distribution after one day of ponded infiltration.

Global Minimization Algorithms

Most minimization algorithms take advantage of some assumed properties of the objective function, such as linearity, smoothness, differentiability, con-

convexity, quadratic behavior near the minimum, etc. If these assumptions are appropriate, derivative-based minimization algorithms are very efficient in identifying the minimum of the objective function. However, these algorithms are generally only able to identify a local minimum in the vicinity of the starting point of the optimization. If the topology of the objective function contains multiple local minima, as is likely the case for strongly nonlinear models or management optimization problems that include complex, potentially discontinuous cost functions, these local algorithms have to be started from multiple points in the parameter space to examine whether the solution is indeed a global minimum.

iTOUGH2 currently contains three minimization algorithms that attempt to identify the global minimum of an objective function exhibiting multiple local minima: Simulated Annealing, Differential Evolution Algorithm, and Harmony Search. These heuristic algorithms have two common features: They (1) attempt to examine the entire parameter space using trial parameter sets that are usually generated using a stochastic process; the search narrows as the algorithm proceeds towards a minimum; and (2) they occasionally accept uphill steps to escape local minima. As a result of these two properties, global minimization algorithms are generally much less efficient than derivative-based algorithms. Insights into the properties of the objective function should therefore be used to choose the most appropriate minimization algorithm for a given problem. The global search algorithms will be documented in Finsterle and Zhang (in prep.).

Re-evaluation of the Jacobian Matrix

Gradient-based minimization algorithms require the repeated evaluation of the Jacobian matrix, which contains the partial derivatives of the observable variables at the calibration points with respect to the parameters to be estimated. In iTOUGH2, these sensitivity coefficients are calculated numerically by means of finite differences. This step amounts to the largest computational burden of the inversion, as $(n+1)$ forward runs are needed, where n is the number of parameters.

Evaluation of the Jacobian matrix by the perturbation method can be embarrassingly parallelized (Finsterle, 1998), which somewhat alleviates the problem. As an alternative method, the Broyden rank-one update has been implemented in iTOUGH2. In this method, the Jacobian matrix is updated using the value of the objective function obtained at an additional point in the parameter space. Such additional evaluations are readily available, for example, when a trial parameter set is tested as part of the minimization algorithm. A full finite-difference re-evaluation is automatically performed if the Broyden approximation leads to a

significant change of the convexity of the Hessian, as measured by its trace.

Regularization

Underdetermined or otherwise ill-posed inverse problems are often solved by adding a regularization term, i.e., by including additional information such as prior knowledge about the parameters to be estimated, or a smoothness constraint. The former is simply a weighted difference between the prior parameter value and its estimate; the latter is a weighted difference between pairs of parameter estimates. Minimizing these regularization terms ensures that the estimate is not too far away from its prior value, or that differences between estimates remain small, which—if applied to spatially distributed parameter values—is identical to smoothing the image. Note that these regularization terms need to be appropriately weighted against the information provided by the calibration data.

Regularization has been implemented into iTOUGH2 mainly to enable tomographic-type imaging using the joint inversion of geophysical and hydrological data. For this application, differences between properties estimated at neighboring gridblocks or zones are reduced to obtain a smoother image. However, the smoothness constraint can be imposed on any parameter pair, even if they do not pertain to spatial proximity. For example, this regularization feature can be used to keep estimates of residual saturation in the capillary pressure and relative permeability curves similar. In the extreme, the weight of this constraint could be increased such that the two residual saturation values are virtually synchronized (which would be more conveniently achieved by hardwiring a deterministic correlation in the forward model).

Truncated Levenberg-Marquardt Algorithm

The Levenberg-Marquardt algorithm is a local, second-order minimization method for nonlinear optimization problems that has been proved robust and efficient for most iTOUGH2 applications. It can be viewed as a flexible combination of the robustness of a steepest-descent method and the efficiency of a second-order Gauss-Newton method. For strongly nonlinear models, if the parameter vector \mathbf{p} of length n is far away from the optimum parameter set, the Hessian is not necessarily a positive-definite matrix, and the local approximation ($\mathbf{J}^T \mathbf{C}_{zz}^{-1} \mathbf{J}$) used by the Gauss-Newton method may not lead to an efficient or successful parameter step $\Delta \mathbf{p}$. In the Levenberg-Marquardt method, the approximation to the Hessian is made positive definite by adding an $n \times n$ diagonal matrix $\lambda \mathbf{D}$ to the Fisher Information Matrix (FIM):

$$\Delta \mathbf{p} = (\mathbf{J}^T \mathbf{C}_{zz}^{-1} \mathbf{J} + \lambda \mathbf{D})^{-1} \mathbf{J}^T \mathbf{C}_{zz}^{-1} \mathbf{r}$$

Here, \mathbf{J} is the Jacobian matrix, \mathbf{C}_{zz} is the covariance matrix of the expected modeling and measurement errors used for scaling, and vector \mathbf{r} holds the residuals, i.e., the differences between the measured and model-calculated observable variables.

The scalar λ is the so-called Levenberg (1944) parameter, which is updated according to a scheme proposed by Marquardt (1963) depending on the success or failure to reduce the objective function. For large values of λ (usually during the early stage of the optimization far away from the minimum), a robust but small step along the steepest descent direction is taken; for $\lambda \rightarrow 0$ (near the minimum), $\Delta \mathbf{p}$ approaches a Gauss-Newton step with its quadratic convergence rate.

\mathbf{D} is a diagonal matrix also known as the Tikhonov matrix. In the simplest case, \mathbf{D} is the identity matrix. Earlier versions of iTOUGH2 used the diagonal of the scaled FIM, which gave \mathbf{D} an appropriate weighting.

The new approach proposed here is to perform a singular value decomposition (SVD) of the scaled FIM, and then use the diagonal element of the FIM divided by the singular values as the diagonal elements of the Tikhonov matrix. The parameter associated with the largest singular value (i.e., that with the overall highest sensitivity that is least correlated with all the other parameters) will perform a near-Gauss-Newton step, whereas the step size of relatively insensitive, strongly correlated parameter combinations (which lead to instability because they amplify noise) will be reduced, making the inversion more efficient and more stable, as parameters with a singular value approaching zero are essentially fixed.

The order of the singular values can also be used to automatically truncate the parameter space (i.e., using a subspace inversion method that separates out the calibration null space; Tonkin and Doherty, 2009). Starting with a relatively large number of parameters, only those above the so-called truncation level will be updated during the inversion. If the ratio of the eigenvalue and the largest eigenvalue is above a critical level, the parameter is included; otherwise, the parameter is (temporarily) de-activated, i.e., not updated and excluded from the next evaluation of the Jacobian matrix. Since the set of active parameters may change as the inversion proceeds, a full Jacobian matrix for all originally selected parameters needs to be evaluated after a user-specified number of iterations.

The efficiency and robustness of the truncated Levenberg-Marquardt algorithm make it the method of choice for most iTOUGH2 inversions.

Input of Measured Data

iTOUGH2 solves a nonlinear optimization problem by automatically calibrating a transient flow and transport model against time-series data measured at select points in space, usually inlets and outlets of experimental laboratory columns, or wells and boreholes in the field. Conversely, geophysical data are spatially extensive, but are taken only once or (at the most) a few times. To accommodate spatially extensive data sets, new input formats have been implemented in iTOUGH2, where the user provides coordinates of measurement locations (either along a borehole, a two-dimensional profile, or in three-dimensional space) along with the corresponding observation (or multiple observations, if multiple geophysical surveys are taken at different times). These spatial data taken at only a few select times can still be combined with extensive time series data taken at only a few select spatial locations. An automatic time window feature supports the combination of such data sets.

CONCLUDING REMARKS

iTOUGH2 enhances the usefulness and power of the TOUGH suite of nonisothermal multiphase flow simulators by providing capabilities for formalized sensitivity analyses, inverse modeling, and uncertainty propagation analyses. It helps the TOUGH user understand and evaluate the impact of certain parameters and conceptual features on model predictions, and to quantitatively relate the model to laboratory or field data. Moreover, certain (forward) modeling tasks are more conveniently performed if executed through iTOUGH2.

iTOUGH2 is continuously updated, in part in response to new developments of the TOUGH forward model, and in part to include new inversion algorithms and analytical tools. As soon as new features are sufficiently tested and fully documented, they are released to the community through LBNL's Technology Transfer Department, see <http://esd.lbl.gov/TOUGH+/software-itough2.html>

Scientific needs and user requests will determine future iTOUGH2 developments. In general, the inverse modeling framework is considered robust enough to make iTOUGH2 available for the solution of universal inverse problems that involve diverse forward models; an appropriate interface is currently being developed.

ACKNOWLEDGMENT

I would like to thank all developers and users of TOUGH2 and iTOUGH2 for their direct and indirect contributions to these codes over the years. This work was supported by the U.S. Dept. of Energy under Contract No. DE-AC02-05CH11231.

REFERENCES

- Deutsch, C. V., and A. G. Journel, *GSLIB—Geostatistical Software Library and User's Guide*, Oxford University Press, New York, 1992.
- Doughty, C. Modeling geologic storage of carbon dioxide: comparison of non-hysteretic and hysteretic characteristic curves, *Energy Conversion and Management*, 48, 1768–1781, 2007.
- Doughty, C., *User's Guide for Hysteretic Capillary Pressure and Relative Permeability Functions in iTOUGH2*, Report LBNL-2483E, Lawrence Berkeley National Laboratory, Berkeley, Calif., August 2009.
- Finsterle, S., *Parallelization of iTOUGH2 Using PVM*, Report LBNL-42261, Lawrence Berkeley National Laboratory, Berkeley, Calif., October 1998.
- Finsterle, S., Multiphase inverse modeling: Review and iTOUGH2 applications, *Vadose Zone J.*, 3: 747–762, 2004.
- Finsterle, S., *iTOUGH2 Command Reference*, Report LBNL-40041 (Rev.), Lawrence Berkeley National Laboratory Report, 2009. (also: esd.lbl.gov/iTOUGH2/Command/command.html)
- Finsterle, S., and M.B. Kowalsky, *iTOUGH2-GSLIB User's Guide*, Report LBNL/PUB-3191, Lawrence Berkeley National Laboratory, Berkeley, Calif., June 2007.
- Finsterle, S., and M. B. Kowalsky, Joint hydrological-geophysical inversion for soil structure identification, *Vadose Zone J.*, 7:287–293, 2008.
- Finsterle, S., C. Doughty, M.B. Kowalsky, G.J. Moridis, L. Pan, T. Xu, Y. Zhang, and K. Pruess, Advanced vadose zone simulations using TOUGH, *Vadose Zone J.*, 7:601–609, 2008.
- Finsterle, S., C. Doughty, M.B. Kowalsky, G.J. Moridis, L. Pan, T. Xu, Y. Zhang, and K. Pruess, Advanced vadose zone simulations using TOUGH, *Vadose Zone J.*, 7:601–609, 2008.
- Finsterle, S., and Y. Zhang, *Global Optimization Algorithms in iTOUGH2*, Lawrence Berkeley National Laboratory, Berkeley, Calif., (in prep.)

- Kowalsky, M., S. Finsterle, J. Peterson, S. Hubbard, Y. Rubin, E. Majer, A. Ward, and G. Gee, Estimation of field-scale soil hydraulic parameters and dielectric parameters through joint inversion of GPR and hydrological data, *Water Resour. Res.*, 41, W11425, 2005.
- Levenberg, K., A method for the solution of certain nonlinear problems in least squares, *Quart. Appl. Math.*, 2, 164–168, 1944.
- Marquardt, D.W., An algorithm for least squares estimation of nonlinear parameters, *SIAM J. Appl. Math.*, 11, 431–441, 1963.
- Oldenburg, C.M., G.J. Moridis, N. Spycher, and K. Pruess, *EOS7C Version 1.0: TOUGH2 Module for Carbon Dioxide or Nitrogen in Natural Gas (Methane) Reservoirs*, Report LBNL-56589, Lawrence Berkeley National Laboratory, Berkeley, Calif., 2004.
- Pruess, K., *TOUGH2—A General-Purpose Numerical Simulator for Multiphase Fluid and Heat Flow*, Report LBL-29400, Lawrence Berkeley Laboratory, Berkeley, Calif., 1991.
- Pruess, K., C. Oldenburg, and G. Moridis, *TOUGH2 User's Guide, Version 2.0*, Report LBNL-43134, Lawrence Berkeley National Laboratory, Berkeley, Calif., 1999.
- Pruess, K. and A. Battistelli, *TMVOC, A Numerical Simulator for Three-Phase Non-isothermal Flows of Multicomponent Hydrocarbon Mixtures in Saturated-Unsaturated Heterogeneous Media*, Report LBNL-49375, Lawrence Berkeley National Laboratory, Berkeley, Calif., April 2002.
- Pruess, K., *ECO2N: A TOUGH2 Fluid Property Module for Mixtures of Water, NaCl, and CO₂*, Report LBNL-57952, Lawrence Berkeley National Laboratory, Berkeley, Calif., 2005.
- RamaRao, B. S., A. M. LaVenue, G. de Marsily, and M. G. Marietta, Pilot point methodology for automated calibration of an ensemble of conditionally simulated transmissivity fields, 1. Theory and computational experiments, *Water Resour. Res.*, 31, 475–493, 1995.
- Tonkin, M., and J. Doherty, Calibration-constrained Monte Carlo analysis of highly parameterized models using subspace techniques, *Water Resour. Res.*, 45, W00B10, doi:10.1029/2007WR006678, 2009.

DEVELOPMENT AND APPLICATIONS OF A TURBULENT TRANSPORT NETWORK MODEL COUPLED WITH TOUGH2

G. Danko and D. Bahrami
Mackay School of Earth Sciences and Engineering,
University of Nevada, Reno
Reno, NV 89557
danko@unr.edu, dbahrami@unr.edu

J.T. Birkholzer
LBNL, Earth Sciences Division, MS 90-1116
One Cyclotron Rd.
Berkeley, CA 94720
JTBirkholzer@lbl.gov

ABSTRACT

A new numerical method is described for the conjugate solution of two discrete submodels, involving (1) a transport network and (2) a porous media. The transport network submodel describes the thermal-hydrologic transport processes in the flow channel system with laminar or turbulent flow and convective heat and mass transport, using MULTIFLUX. The porous media submodel, TOUGH2, is used to solve for the heat and mass transport in the rock mass. The new model solution method extends the application fields of TOUGH2 by integrating it with turbulent flow and transport in a discrete flow network system. Man-made tunnels or fractures in geologic formations often need thermal and hydrological calculations. The common feature of the tasks is that transport processes in a network of flow channels are coupled to those in the surrounding rock mass. We present demonstrational results for the proposed nuclear waste repository at Yucca Mountain for the transport processes within a waste emplacement drift and the surrounding rock mass. The natural, convective air flow field, as well as heat and mass transport in a representative emplacement drift during post-closure, are explicitly simulated in the new model. The simulation results suggest that large-eddy turbulent flow, as opposed to small-eddy flow, dominate the drift air space for at least 5,000 years following waste emplacement. The direction and magnitude of the air circulation patterns are both strongly affected by the heat and moisture transport processes in the surrounding rock, justifying the need for the new model.

INTRODUCTION

A research project was conducted with the purpose of increasing the understanding of the coupling between thermo-hydrological-airflow processes (THA) (including air and vapor movement)

in the in-drift, near-field, and mountain-scale systems at Yucca Mountain (YM). Specific aims are (1) to configure, test, and verify a novel, efficient, numerical-computational, coupled THA model; and (2) to evaluate, at different stages after waste emplacement, the coupled, in-drift heat, moisture, and air flow transport with evaporation, condensation, and seepage of water into drifts from the near-field rock mass embedded in a mountain-scale geologic unit. These objectives are met by developing a multiscale modeling approach that (1) integrates in-drift and in-rock process models, with new laminar or turbulent air flow components; and (2) allows for studying the storage environment in various emplacement drifts, without applying excessive conservatism in the modeling assumptions.

The key elements of the new modeling approach are: (1) the separation of the rock-mass model element of the host geological formation from the in-drift model element of the engineered nuclear waste emplacement system; (2) the detailed, general model solution of the rock mass with a porous-media, thermal-hydrologic model, in this case, TOUGH2 (Pruess et al., 1999); (3) the detailed model solution of the internal components of the emplacement drift and the air space with a lumped-parameter CFD (Computational Fluid Dynamics) model; and (4) the dynamic recoupling of the separate tasks (2) and (3) iteratively at each time instant and boundary element at the drift wall. All key model elements are simultaneously applied during simulation within the MULTIFLUX (MF) framework (Danko, 2008), a software developed at the University of Nevada, Reno (UNR), for solving coupled heat, mass, and air flow modeling tasks. The solutions to the separate tasks are accomplished in a new way, allowing for efficient and dynamic recoupling, by using the NTCF (Numerical Transport Code Functionalization) technique (Danko, 2006).

In previous work, the solution for the coupled system comprising the rock mass and waste emplacement drift domains has been approximated within one monolithic domain as a classic solution to the heat and mass transport problem using a porous-media model, either TOUGH2 (Pruess et al., 1999) or NUFT (Nitao, 2000). Sandia National Laboratory (SNL, 2008) developed such an approximate model for a three-dimensional (3D) panel by representing a full emplacement drift and the surrounding rock mass. The heat and moisture transport processes in both the rock mass and the air space in the emplacement drifts were modeled with NUFT. The in-drift transport processes were approximated with an equivalent dispersion model. Birkholzer et al. (2006, 2008) further improved the monolithic modeling concept using TOUGH2. Monolithic models, however, can only approximate the air flow field and its effects on heat and moisture transport within the air space of the emplacement drift. Air flow during the first few thousands of years becomes dominantly turbulent, and the flow regime exceeds the modeling capabilities of the porous-media codes, all involving only the law of Darcy flows. In addition, the contrast in permeabilities between the in-rock and in-drift model domains are simply too large (on the order of 10^{11}) to be solvable within one numerical solution framework. For example, the average permeability in the fractured rock mass at Yucca Mountain is on the order of 10^{-12} m² (BSC, 2008), while permeability, k , of the open air space in the emplacement drift is as high as 10^{-1} m², assuming Darcy flow and using the $k=r^2/8$ formula where r is the radius of the drift.

Solutions for just the in-drift environment, separated from the other model elements of the porous rock, have also been published. Bechtel SAIC Company (BSC, 2004) solved for the temperature and humidity distribution in the in-drift emplacement system using a two-step approach. First, in a 70 m long section of the in-drift domain, the 3D heat transport and air flow were modeled using a commercial CFD model, FLUENT (BSC, 2004). The CFD model was coupled to a hollow rock cylinder surrounding the emplacement drift, in which heat transport per conduction was assumed, driven by a prescribed temperature boundary condition at some distance in the rock wall. The solution excluded moisture transport and was used to evaluate an equivalent, effective dispersion coefficient in the drift air space under the single driving force of temperature-induced buoyancy effects. In a second step, the moisture transport was modeled in an entire emplacement drift, using a separate, lumped-parameter network model that used the dispersive transport coefficients derived from the FLUENT-based CFD model. In this separate moisture transport model, the availability of moisture was assumed prescribing 100% relative humidity at the drift wall along the emplacement drift. While this combined solution included some simulated thermal interactions between the rock mass and

in-drift domains, it did not consider the diffusive and convective interactions regarding moisture transport. Passive vapor transport from an impermeable surface at saturated vapor pressure may be either higher or lower relative to the real moisture flux, which is generally comprised of two components: (1) convective flux, which may include superheated steam, driven by the total pressure gradient; and (2) diffusive flux, driven by the humidity concentration gradient. Even the moisture flow direction at a drift surface element cannot be known without a coupled model. Hao et al. (2006) developed a double-diffusion CFD solver for a two-dimensional slice normal to the drift axis of an emplacement drift, also with prescribed boundary conditions, but without being coupled to the rock mass and without iterating between the two different, but conjugate model domains.

In previous work, we have conducted numerical tests with the fully coupled MF framework, including comparison with published results obtained using an alternative, albeit simplified model (Birkholzer et al., 2006; 2008) involving a large model domain. Comparisons showed good agreement between the results from the monolithic model (Birkholzer et al., 2006, 2008) and those from the coupled MF model, configured with equivalent dispersion transport processes along the axial direction of the emplacement drift (Danko et al., 2008). The current paper goes beyond the previous MF model configurations of equivalent dispersion. The new software and model version of MF allows for explicit calculation of the velocity field in the emplacement drift, determining the natural air movement driven by temperature and humidity variations within the air space, and the resultant heat and moisture transport processes due to natural convection after closure. The paper describes the new results involving large-eddy, laminar or turbulent heat, moisture, and air flows.

MULTI-SCALE, COUPLED NUMERICAL-COMPUTATIONAL MODEL

Model Concept

The numerical simulator MF Version 5.0 is used in the evaluation of the coupled in-drift airflow field, caused by natural convection, is explicitly and iteratively solved within MF, using its lumped-parameter solver for the Navier-Stokes equation.

Thermal-hydrologic Model of the Rockmass

The multiscale rock mass model is identical to that of a previous study (Danko et al., 2008). The rock mass surrounds a representative drift in the middle of an emplacement panel. The length of the drift is 760 m, with two 80 m long end sections where no waste is emplaced. The length of the unheated sections are kept at 80 m, the same length used by Birkholzer et al (2006; 2008) in order to evaluate agreements and/or differences caused by

transport model components instead of arrangement geometry. It has been pointed out before by Danko et al. (2008) that the axial moisture transport and the humidity in the emplacement drift are quite sensitive to the length of the unheated sections. The unheated drift sections are connected to the undisturbed and also unheated edges, which provide a dominantly conductive heat sink to the heated portion of the rock mass around the center of the emplacement drift. This arrangement, described in Danko et al. (2008), manifests a strongly 3D temperature field in and around the drift with cooler temperatures around the drift ends. Likewise, the representative NTCF model, a surrogate model using response functions based on the TOUGH2 thermal-hydrologic porous-media code, is also used unchanged.

It is sufficient to refer to a previous study (Danko et al., 2008) for the NTCF model representing the rock-mass response. Along the length of the drift, 44 individual mountain-scale divisions are applied. The relationship between the set of input T , P , and output qh , qm temporal variations for each drift section define the corresponding dynamic, mountain-scale rock-mass NTCF model for heat and moisture. The following matrix equation terms are selected for the NTCF model (Danko et al., 2008):

$$qh = qh^c + hh \cdot (T - T^c) + \langle T \rangle \cdot hm \cdot (P - P^c) \quad (1)$$

$$qm = qm^c + mh \cdot (T - T^c) + \langle T \rangle \cdot mm \cdot (P - P^c) \quad (2)$$

The hh , hm , mh , and mm dynamic admittance matrices are identified based on Eqs (1) and (2) by fitting qh and qm to TOUGH2 data. The NTCF model identification method follows the technique described in Danko (2006). The model for each drift-section perfectly reproduces qh^c and qm^c , the central output fluxes from TOUGH2, for $T=T^c$ and $P=P^c$, the central input boundary conditions, that are included in the preselected set of boundary conditions.

Other T and P input variations can produce outputs from the NTCF model for qh and qm without actually re-running TOUGH2. For the coupled in-rock and in-drift model, 454 drift-scale NTCF models are generated from the mountain-scale NTCF models by scaling, following the technique used in Danko et al. (2008).

CFD Models for Heat, Moisture, and Air Flow Transport in the Emplacement Drift

The lumped-parameter, in-drift CFD model domain is also identical to that in a previous study (Danko et al., 2008). However, the heat, mass, and air flow transport connections within the emplacement drift are re-configured according to the three different model approaches in Cases A through C.

In all cases, the energy balance equation in the CFD model of MF is used in a simplified form, as follows, for an x -directional flow with v_i velocity in a flow channel of cross section dy by dz (and with no convective heat

transport in y and z directions while considering the x -directional flow):

$$\rho c \frac{\partial T}{\partial t} + \rho c v_i \frac{\partial T}{\partial x} = \rho c a \frac{\partial^2 T}{\partial x^2} + \rho c a \frac{\partial^2 T}{\partial y^2} + \rho c a \frac{\partial^2 T}{\partial z^2} + \dot{q}_h \quad (3)$$

In Equation (3), ρ and c are density and specific heat of moist air, respectively; a is the molecular or eddy thermal diffusivity for laminar or turbulent flow; and \dot{q}_h is the latent heat source or sink for condensation or evaporation. In this equation, a equals the molecular diffusivity in all directions, as moisture transport by convective air flow is explicitly modeled. The second and the third terms on the right-hand-side of Equation (3) represent heat conduction (or effective heat conduction) in the y and z directions, normal to the x axis of the flow channel; these terms are substituted with expressions for transport connections using heat transport coefficients for flow channels bounded by solid walls (Danko, 2008). Equation (3) is discretized and solved numerically and simultaneously along all flow channels for the temperature field T in MF.

The simplified moisture transport convection-diffusion equation in the CFD model of MF is similar to Equation (3) as follows:

$$\frac{\partial \rho_v}{\partial t} + v_i \frac{\partial \rho_v}{\partial x} = D \frac{\partial^2 \rho_v}{\partial x^2} + D \frac{\partial^2 \rho_v}{\partial y^2} + D \frac{\partial^2 \rho_v}{\partial z^2} + \dot{q}_{cm} + \dot{q}_{sm} \quad (4)$$

In Equation (4), ρ_v is the partial density of water vapor; D is the molecular or eddy diffusivity for vapor, calculated from the thermal diffusivity, a , which is substituted specifically according to Cases A, B, or C, as explained for Equation (3); \dot{q}_{cm} is the moisture source or sink due to condensation or evaporation; and \dot{q}_{sm} is the vapor flux in superheated steam form.

The Navier-Stokes momentum-balance equation for 3D flow of the bulk air-moisture mixture is used as follows, following Welt et al. (1984):

$$\rho \left(\frac{\partial v_x}{\partial t} + \mathbf{v} \cdot \nabla v_x \right) = \rho g_x - \frac{\partial P b}{\partial x} + F_x \quad (5a)$$

$$\rho \left(\frac{\partial v_y}{\partial t} + \mathbf{v} \cdot \nabla v_y \right) = \rho g_y - \frac{\partial P b}{\partial y} + F_y \quad (5b)$$

$$\rho \left(\frac{\partial v_z}{\partial t} + \mathbf{v} \cdot \nabla v_z \right) = \rho g_z - \frac{\partial P b}{\partial z} + F_z \quad (5c)$$

The viscous terms in Equations (5a–c) can be expressed with the viscous normal-stress (σ), and shear-stress (τ) components as:

$$F_x = \frac{\partial(\sigma_{xx})_v}{\partial x} + \frac{\partial \tau_{yx}}{\partial y} + \frac{\partial \tau_{zx}}{\partial z} \quad (6a)$$

$$F_y = \frac{\partial \tau_{xy}}{\partial x} + \frac{\partial(\sigma_{yy})_v}{\partial y} + \frac{\partial \tau_{zy}}{\partial z} \quad (6b)$$

$$F_x = \frac{\partial \tau_{xz}}{\partial x} + \frac{\partial \tau_{yz}}{\partial y} + \frac{\partial (\sigma_{zz})_v}{\partial z} \quad (6c)$$

The viscous force terms in Equations (5a–6c) are integrated along the grid lines of the flow channels and expressed as a function of the convective air flow components in the emplacement drift.

The lumped-parameter CFD model approach allows for reducing the number of discretization elements in the computational domain. MF allows for defining connections between lumped volumes, applying direct heat and moisture transport relations between them. The current, lumped-parameter CFD model in the drift applies $18 \times 454 = 8172$ nodes for the heat, and the same number of nodes for the moisture transport as well as for air flow transport. Each WP is represented by two nodes (Danko et al., 2008), with one additional node for the gap between neighboring containers. CFD nodes are in the airway along four longitudinal lines in a half-cross-section of the drift on either side of the symmetry line: (1) close to the floor; (2) close to the drip shield; (3) close to the drift wall at mid-height; and (4) above the drip shields, with 454 nodes on each line (Danko et al., 2008). The drift wall is assumed to be separated from the rock with a 10^{-5} m thick still air layer representing the rock-air interface, and acting as a coupling layer of insignificant resistance to transport of heat and moisture. Both the drift wall and the thin coupling layer are represented by 454 nodes each along three longitudinal lines spanning the drift length—at the invert, sidewall, and roof. The airspace under the drip shields is also modeled by four lines, each having 454 nodes. Half of the drip shield on either side of the symmetry line is lumped into four nodes defining four lines, two on the top and two on the side. Each air space, one above and one under the drip shield, also includes one steam transport line. Heat and moisture transport are modeled using heat and moisture transport coefficients at the WP, drift wall, and at each side of the drip shield. Three-dimensional thermal radiation between solid surfaces is also included in the CFD model. The radial, tangential, and axial velocity components are all explicitly modeled and calculated in MF.

Coupled In-rock NTCF and In-drift CFD Models

The NTCF (approximating the rock-mass response) and CFD models are coupled on the rock-air interface by MF until the heat and moisture fluxes are balanced at the common surface temperature and partial vapor pressure at each surface node and time instant. Two iteration loops are used to balance the in-rock and in-drift transport processes on the rock-air interface:

1. Heat-flow-balance iteration between the NTCF and airway CFD models for each time division
2. Moisture-flow-balance iteration between the NTCF and airway CFD models for each time division

An outer iteration loop is used to determine the natural air flow field in the closed air space of the emplacement drift. For each set of balanced results from iterations 1 and 2, the air flow velocity field is solved based on the new, updated temperature and vapor-pressure distribution in an outside balance loop, until no significant change is observed between consecutive iterations.

The simulation results obtained from the CFD model elements are temperature, relative humidity, and water condensate variations within the emplacement drift, including their distributions on the drift wall boundary. In the current study, we focus on these in-drift conditions. In other studies, the main focus may be directed to the processes in the rock mass and not in the drift, such as in Birkholzer et al. (2006; 2008). Temperature, humidity, and moisture flow distributions in the rock mass, already coupled to the in-drift processes, are given by the TOUGH2 porous-media model. Read-out of saturation and/or moisture flow results in the rock mass from TOUGH2 at any time instant can be made during the MF runs at the end of a successful iteration for heat and moisture flow balances.

COUPLED SIMULATION RESULTS

The simulation results for the drift wall temperature are shown in Figure 1 along the emplacement drift length and at selected time periods. Likewise, Figures 2 and 3 show the relative humidity and the condensate rate distributions, respectively.

The MF model predicts no condensation in the emplacement area for several thousand years; in contrast the condensation model described in BSC (2004) predicts small rates until approximately 3,000 years. Beyond 3,000 years, small rates in condensation appear in the MF model results, due to a decrease in efficiency of the axial, in-drift vapor transport, which in turn leads to an increase in relative humidity. The in-drift environment at higher relative humidity and under a convective vapor influx from the rock mass into the still relatively hot mid-drift section shows small rates of condensation at some surface areas in the MF results. This may be explained by the complex, coupled boundary interactions, which include convective vapor fluxes between the in-drift and in-rock domains in the MF model.

Further results from the new model solution are given for the natural, axial, and cross-sectional air flows in the drift. The open air cross section of the emplacement drift is divided into eight segments, four over and four under the drip shields, forming eight longitudinal air distribution lines. The lumped-parameter CFD model for air flow applies 16 velocity components, eight along horizontal lines parallel with the drift axis and eight transversal, normal to the drift axis at each drift cross section in the present model configuration. The velocity components

and their positive directions are defined in Figures 4 and 5 for the air space above and under, respectively, the drip shields. Along a full drift, $454 \times 18 = 8172$ velocity components are determined from the lumped-parameter model calculation.

The MF model calculation results for the velocity components along the drift length at Year 300 are given in Figure 6. Results for other time periods show similar, albeit complex behavior, but are omitted from this paper for brevity. As shown, neither the horizontal nor the cross-sectional velocity components are constant along the drift length. The variation in the horizontal velocity components, $v_1^H \dots v_8^H$, indicates that the recirculation loops are "leaky"—that is, the flows are short-circuited with small bypass flows in the drift air space. Nevertheless, the formation of a continuous, horizontal, large-scale eddy, half-drift length in size, is unmistakable.

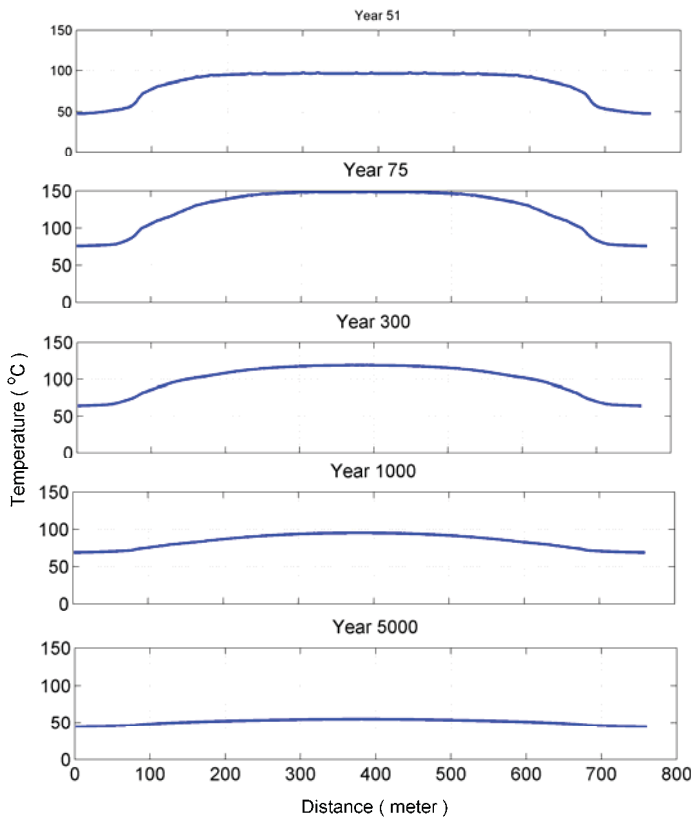


Figure 1. Drift invert temperature variation with drift length at selected postclosure time periods

Figure 7 is a schematic diagram of the dominant, averaged, natural axial air-recirculation loops in the air space inside and outside the drip shield. A simplified axial air flow pattern diagram is shown in Figure 8. Visualizing the air recirculation loops as dominant flow patterns, one loop under and one over the drip shields,

helps in understanding the simulation results and the nature of the flow field.

No such axial air flow loops have been reported in previous studies for Yucca Mountain. The Natural Convection and Condensation studies conducted in BSC (2004) show dominantly cross-sectional, but no axial large-eddy flows, probably due to a much shorter drift length and the very different boundary conditions used in the FLUENT CFD model. The open flow cross section in the drift is divided into unequal surface areas in the present model; therefore, the horizontal velocities do not sum to zero. However, the flow rates in each cross section strictly satisfy continuity, meaning that the inbound and outbound mass flow rates sum to zero.

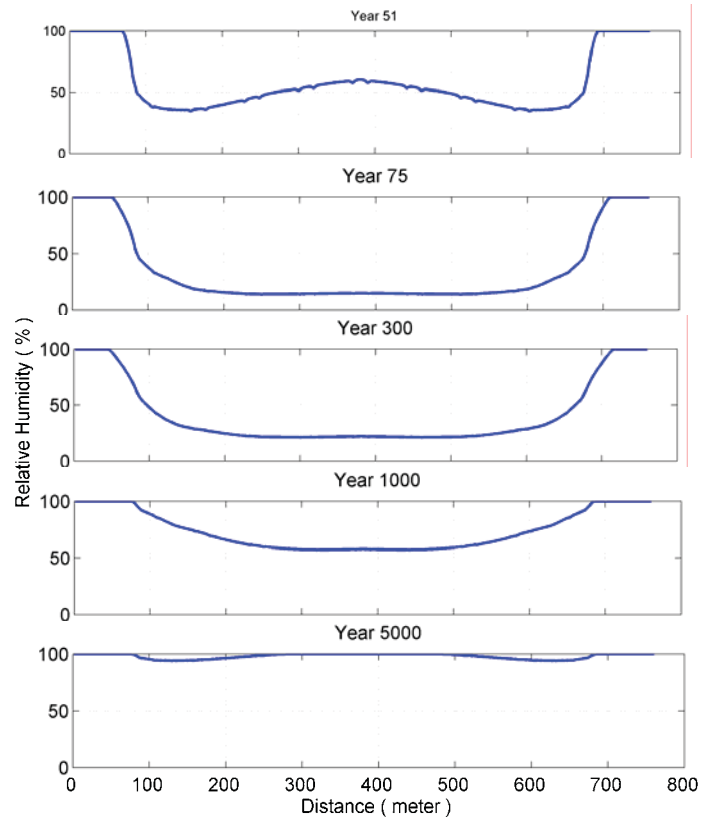


Figure 2. Drift invert relative humidity variation with drift length at selected postclosure time periods

The variation in the velocity components, v_1^V and v_8^V , of the cross-sectional circulation loops is especially strong along the drift length. In fact, the direction of the circulation reverses along the drift length perhaps multiple times, as indicated by the positive and negative signs of the velocity components, shown in Figure 6b. The ruggedness of the curves is caused by the disturbed cross section and velocities in the gaps between the individual WPs.

The boundary conditions on the full drift surface in the MF model includes a rich variation of temperature and humidity, fully coupled and balanced with the in-rock TOUGH2 model. The natural driving force for the horizontal and transversal air circulations come from air density variations due to temperature and humidity changes. The change in the rotational direction of the transversal velocities along the drift length indicates that the air density change due to humidity variation becomes dominant over the change in air density due to temperature variation at the cold and humid drift sections. This fact agrees with what common sense would dictate.

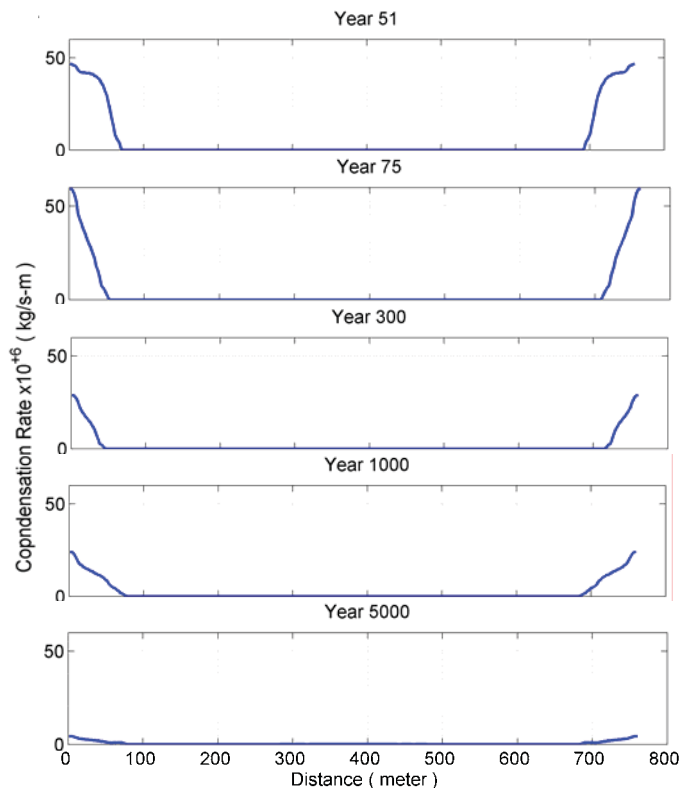


Figure 3. Drift condensation flux variation with drift length at selected post-closure time periods

In a hot drift section, the transversal air circulation is expected to be dominantly temperature driven, causing upward air flow in the drift center. In a cold drift section with high relative humidity, the effect of vapor content on the air density may overwhelm that of temperature. More humid and lighter air may rise over the drift wall and descend in the drift center, reversing the transversal circulation loop direction.

The simulation results suggest that large-eddy turbulent flow, as opposed to small-eddy flow, dominates the drift air space for at least 5000 years following waste emplacement. The size of the longitudinal eddy equals half of the drift length. The large-eddy flow structure

apparent from the MF results appears to predict a strong axial heat and moisture transport. In other words, conditions would be drier in most of the drift sections where waste is emplaced, and would be wetter in the end sections where no waste is emplaced.

This mechanism should be further explored and analyzed for the optimization of the design and the benefit of waste storage and isolation.

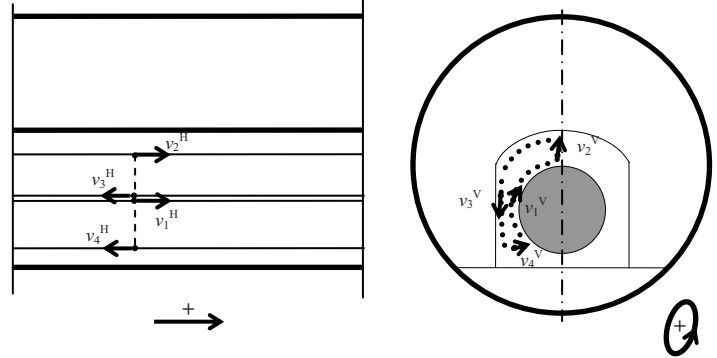


Figure 4. Definition of velocity components at a given cross section under the drip shield

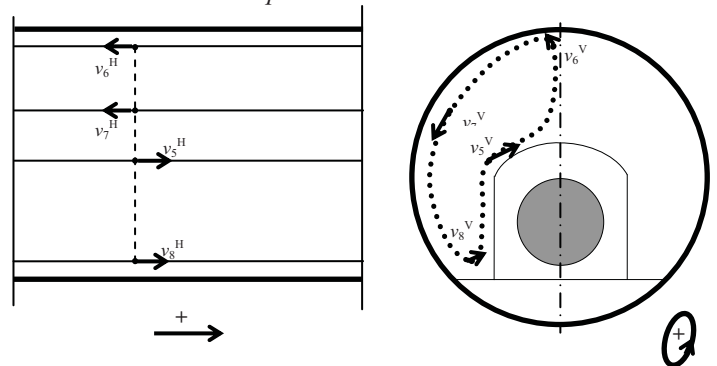


Figure 5. Definition of velocity components at a given cross section outside the drip shields.

CONCLUSIONS

1. A fully-coupled, in-drift and near-field, in-rock model is configured and applied for the solution of a complex thermo-hydrologic-airflow problem at Yucca Mountain for a full emplacement drift, embedded in a mountain-scale rock mass with edge cooling.
2. The new model includes an explicit, natural air flow field solver within the drift air space during post-closure. From the new model, natural, buoyancy-driven air flow loops are predicted in both axial and transversal directions in a full emplacement drift.
3. Simulated results are given for temperature, humidity, and condensation rates on the drift wall along the full length of an emplacement drift, using the new version of the MF model. Future modeling studies could benefit greatly from such an analysis.

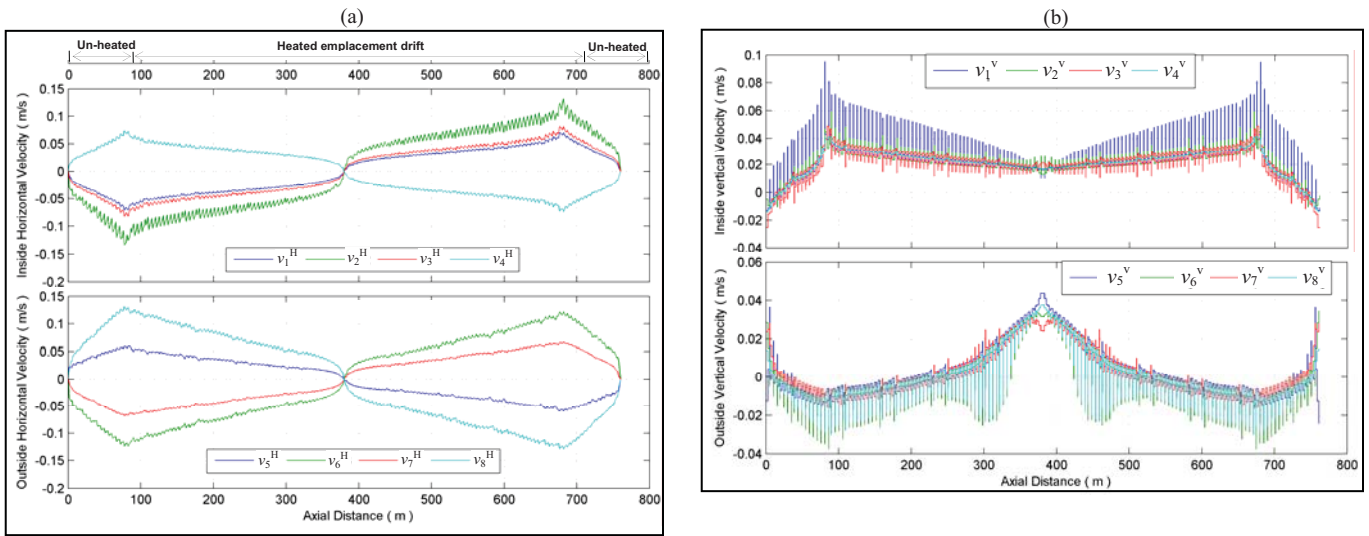


Figure 6. Spatial distribution of the axial (horizontal) (a) and cross-sectional (transversal) (b) velocity components along eight air streams outside and inside the drip shield air spaces at Year 300 after waste

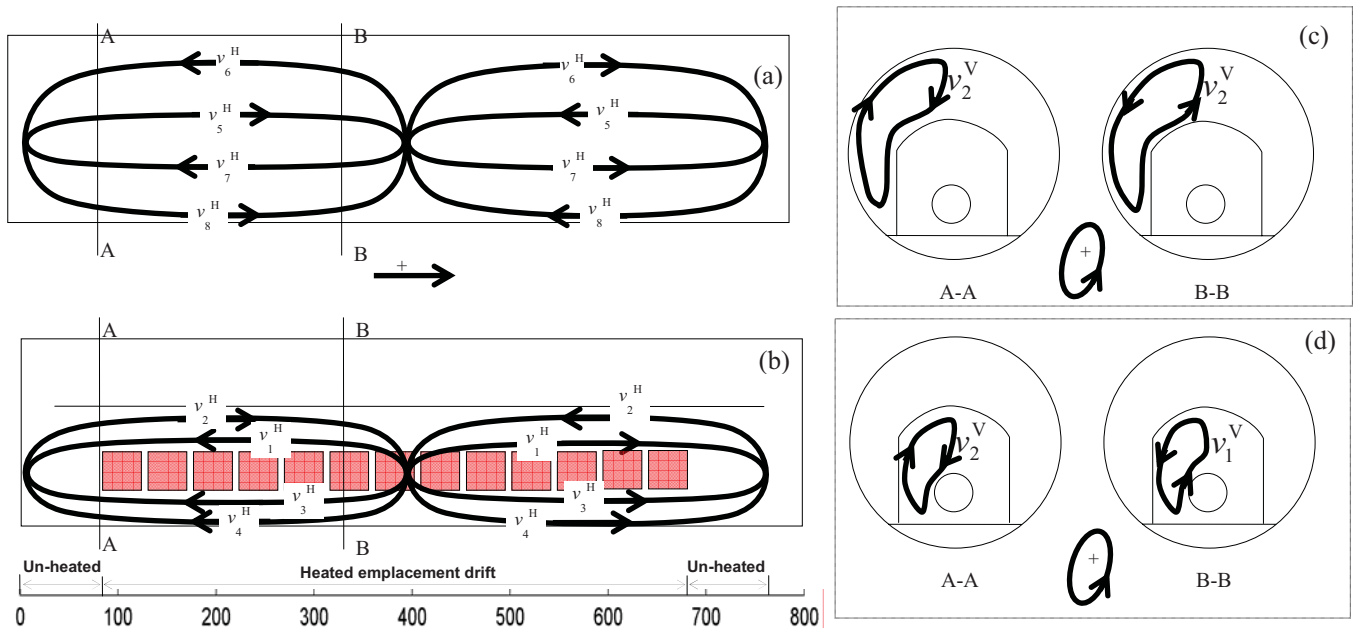


Figure 7. Schematic diagram of the natural, axial air-recirculation loops over (a); and under (b) drip shields. Cross-sectional air flow loops over (c); and under (d) drip shields at two locations along the drift are also shown.

4. The MF model predicts no condensation on the drift wall in the emplacement area for several thousand years, then the onset of small rates at around 5,000 yrs. By contrast, the condensation model used in the license application for YM (BSC, 2008) predicts small rates until approximately 3,000 yrs, and no significant condensation on the drift wall after that time. These differences likely stem from several factors, including

transport process model elements, and boundary coupling between the in-drift and in-rock domains. Further studies are recommended with comparison between MF model results and appropriate field data.

5. Large-eddy turbulent flow, as opposed to small-eddy flow, seems to dominate the drift air space for at least 5000 years, as evidenced by the 3D velocity field distribution.

6. The size of the longitudinal eddy equals half of the drift length for periods of time during postclosure. The implications of the strong axial transport mechanism should be further explored and analyzed.

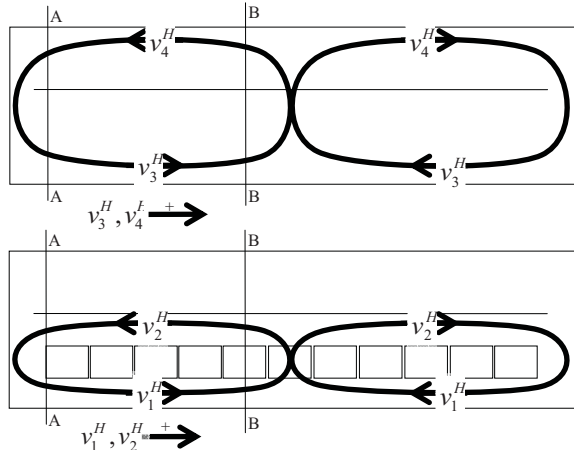


Figure 8. Dominant, averaged, drift-scale natural air flow patterns in one emplacement drift

ACKNOWLEDGEMENTS

This manuscript has been authored by Lawrence Berkeley National Laboratory and University of Nevada, Reno, under Contract No. DE-AC02-05CH11231 with the U.S. Department of Energy. Financial support from Nye County, Nuclear Waste Project Office is also acknowledged. The United States Government retains and the publisher, by accepting the article for publication, acknowledges that the United States Government retains a non-exclusive, paid-up, irrevocable, worldwide license to publish or reproduce the published form of this manuscript, or allow others to do so, for United States Government purposes. The views expressed in this article are those of the authors and do not necessarily reflect the views or policies of the United States Department of Energy, Lawrence Berkeley National Laboratory, or the University of Nevada, Reno.

REFERENCES

- Birkholzer, J., N. Halecky, S.W. Webb, P.F. Peterson, G.S. Bodvarsson, The Impact of Natural Convection on Near-Field TH Processes at Yucca Mountain. Proceedings, 11th International High-Level Nuclear Waste Conference, April, Las Vegas, NV, 2006.
- Birkholzer, J.T., Halecky, N., Webb, S.W., Peterson, P.F., Bodvarsson, G.S., A Modeling Study Evaluating the Thermal-Hydrological Conditions in and Near Waste Emplacement Tunnels at Yucca Mountain. *Journal of Nuclear Technology*, July, 163, 2008.
- Bechtel SAIC Company (BSC), *In-drift natural convection and condensation*. Yucca Mountain Project Report, MDL-EBS-MD-000001 REV 00, Bechtel SAIC Company, Las Vegas, NV, 2004.
- Danko, G., *MULTIFLUX V5.0 Software Qualification Documents*. Software Tracking Number: 1002-5.0-00, Prepared for the Berkeley National Laboratory at University of Nevada, Reno, 2008.
- Danko, G., 2006. Functional or Operator Representation of Numerical Heat and Mass Transport Models, *Journal of Heat Transfer*, 128, 162-175, 2006.
- Danko, G., Birkholzer, J., and Bahrami, D.. *Coupled In-Rock and In-Drift Hydrothermal Model Study for Yucca Mountain*. *Journal of Nuclear Technology*, July, 163, 2008.
- Hao, Y. Nitao, J.J., Buscheck, T.A. and Sun, Y., *Double Diffusive Natural Convection in a Nuclear Waste Repository*. Proceedings, 11th International High-Level Radioactive Waste Management Conference, Las Vegas, NV, 615-622, 2006.
- Nitao, J. *NUFT, Flow and Transport code V3.0s*. Software Configuration Management, Yucca Mountain Project – STN: 10088-3.0S-00, 2000. Prepared at the Lawrence Livermore National Laboratory.
- Pruess, K., C. Oldenburg, and G. Moridis, *TOUGH2 User's Guide, Version 2.0*. Report LBNL-43134, Lawrence Berkeley National Laboratory, Earth Sciences Division, Berkeley, California, 1999.
- Sandia National Laboratory (SNL), *Multiscale Thermohydrologic Model*. ANL-EBS-MD-000049, Rev. 03, Bechtel SAIC Company, 2008.
- Welty, J. R., Wicks, C.E., and Wilson, R.E.. *Fundamentals of Momentum, Heat, and Mass Transfer*. 3rd edition, Wiley and Sons, 612-614, 1984.